

Bengt Friman
Claudia Höhne
Jörn Knoll
Stefan Leupold
Jørgen Randrup
Ralf Rapp
Peter Senger
Editors

LECTURE NOTES IN PHYSICS 814

The CBM Physics Book

Compressed Baryonic Matter in
Laboratory Experiments

Lecture Notes in Physics

Founding Editors

W. Beiglböck
J. Ehlers
K. Hepp
H. Weidenmüller

Editorial Board

B.-G. Englert, Singapore
U. Frisch, Nice, France
F. Guinea, Madrid, Spain
P. Hänggi, Augsburg, Germany
W. Hillebrandt, Garching, Germany
M. Hjorth-Jensen, Oslo, Norway
R. A. L. Jones, Sheffield, UK
H. v. Löhneysen, Karlsruhe, Germany
M. S. Longair, Cambridge, UK
M. Mangano, Geneva, Switzerland
J.-F. Pinton, Lyon, France
J.-M. Raimond, Paris, France
A. Rubio, Donostia, San Sebastian, Spain
M. Salmhofer, Heidelberg, Germany
D. Sornette, Zurich, Switzerland
S. Theisen, Potsdam, Germany
D. Vollhardt, Augsburg, Germany
W. Weise, Garching, Germany

The Lecture Notes in Physics

The series Lecture Notes in Physics (LNP), founded in 1969, reports new developments in physics research and teaching – quickly and informally, but with a high quality and the explicit aim to summarize and communicate current knowledge in an accessible way. Books published in this series are conceived as bridging material between advanced graduate textbooks and the forefront of research and to serve three purposes:

- to be a compact and modern up-to-date source of reference on a well-defined topic
- to serve as an accessible introduction to the field to postgraduate students and nonspecialist researchers from related areas
- to be a source of advanced teaching material for specialized seminars, courses and schools

Both monographs and multi-author volumes will be considered for publication. Edited volumes should, however, consist of a very limited number of contributions only. Proceedings will not be considered for LNP.

Volumes published in LNP are disseminated both in print and in electronic formats, the electronic archive being available at springerlink.com. The series content is indexed, abstracted and referenced by many abstracting and information services, bibliographic networks, subscription agencies, library networks, and consortia.

Proposals should be sent to a member of the Editorial Board, or directly to the managing editor at Springer:

Christian Caron
Springer Heidelberg
Physics Editorial Department I
Tiergartenstrasse 17
69121 Heidelberg / Germany
christian.caron@springer.com

B. Friman · C. Höhne · J. Knoll · S. Leupold ·
J. Randrup · R. Rapp · P. Senger (Editors)

The CBM Physics Book

Compressed Baryonic Matter in Laboratory
Experiments

 Springer

Editors

Bengt Friman
GSI Helmholtzzentrum für
Schwerionenforschung
Planckstr. 1
64291 Darmstadt
Germany

Claudia Höhne
II Physikalisches Institut
Justus-Liebig-Universität Gießen
Heinrich-Buff Ring 16
35392 Gießen
Germany

Jörn Knoll
GSI Helmholtzzentrum für
Schwerionenforschung
Planckstr. 1
64291 Darmstadt
Germany

Stefan Leupold
Uppsala University
Division of Nuclear and Particle Physics
Box 516
75120 Uppsala
Sweden

Jørgen Randrup
Nuclear Science Division
Lawrence Berkeley National Laboratory
1 Cyclotron Road
Berkeley, CA 94720
USA

Ralf Rapp
Department of Physics & Astronomy
and Cyclotron Institute
Texas A & M University
College Station, TX 77843-3366
USA

Peter Senger
GSI Helmholtzzentrum für
Schwerionenforschung
Planckstr. 1
64291 Darmstadt
Germany

B. Friman et al. (Eds.): *The CBM Physics Book*, Lect. Notes Phys. 814, (Springer-Verlag Berlin Heidelberg 2011), DOI 10.1007/978-3-642-13293-3

Lecture Notes in Physics ISSN 0075-8450 e-ISSN 1616-6361
ISBN 978-3-642-13292-6 e-ISBN 978-3-642-13293-3
DOI 10.1007/978-3-642-13293-3
Springer Heidelberg Dordrecht London New York

Library of Congress Control Number: 2010935525

© Springer-Verlag Berlin Heidelberg 2011

This work is subject to copyright. All rights are reserved, whether the whole or part of the material is concerned, specifically the rights of translation, reprinting, reuse of illustrations, recitation, broadcasting, reproduction on microfilm or in any other way, and storage in data banks. Duplication of this publication or parts thereof is permitted only under the provisions of the German Copyright Law of September 9, 1965, in its current version, and permission for use must always be obtained from Springer. Violations are liable to prosecution under the German Copyright Law.

The use of general descriptive names, registered names, trademarks, etc. in this publication does not imply, even in the absence of a specific statement, that such names are exempt from the relevant protective laws and regulations and therefore free for general use.

Cover design: Integra Software Services Pvt. Ltd., Pondicherry

Printed on acid-free paper

Springer is part of Springer Science+Business Media (www.springer.com)

Preface

The understanding of aggregates of matter in terms of its elementary constituents and their interactions is a problem of fundamental interest with far reaching ramifications in science and technology. Much like the electromagnetic force between atomic nuclei and electrons gives rise to a rich variety of macroscopic materials, the strong (nuclear) force is expected to generate intricate matter structures and phases at the subatomic level, at densities of about a trillion times larger than ordinary matter and beyond.

The theoretical foundation of the Strong Force, Quantum Chromodynamics (QCD), is well established, as part of the Standard Model of Elementary Particles, with quarks and gluons as the fundamental degrees of freedom. However, key phenomena in strong interactions have evaded a profound understanding to date, most notably the confinement of quarks and gluons into hadrons and the generation of mass. These phenomena are believed to be intimately related to phase changes in strongly interacting matter, which is one of the main motivations for the research addressed in the present book. In nature, hot deconfined matter (the so-called Quark-Gluon Plasma) filled the early universe, just a few microseconds after the Big Bang, while present-day compact stars may contain cold and baryon-rich quark matter in their interior. The prospect of creating and studying this fundamental form of matter in modern-day laboratory experiments is truly fascinating. It enables a close interplay of experimental data and theoretical interpretation which is pivotal for scientific progress in this field. Nearly forty years of nuclear collision experiments, at laboratories across the world, have led to spectacular new insights, including the discovery of new forms and novel properties of matter.

Some of these developments have identified the regime of high baryon densities as a particularly interesting one. This is the main motivation for the proposed Compressed Baryonic Matter (CBM) experiment at the Facility for Antiproton and Ion Research (FAIR) at GSI in Darmstadt. Closely related science will be pursued in a complementary fashion in an “energy scan” at the existing Relativistic Heavy-Ion Collider (RHIC) at Brookhaven National Laboratory. The ambitious goals of these projects have increased the need

for a detailed, yet comprehensive, assessment of the current theoretical understanding of matter at high baryon densities, in order to help develop and focus the capabilities of future detectors and accelerators. Such an assessment constitutes the first main objective of the present “CBM Physics Book”, and as such is intended to render the latter a useful resource for experienced researchers in the field. As the project evolved, the scope of the CBM Physics Book expanded from the originally envisaged more specific discussion of the physics of high baryon density. The positive feedback and broad participation of contributors suggested a more general presentation of the physics of strongly interacting matter. The Editorial Board seized this opportunity to implement various pedagogical components, including more elementary introductory sections and intermediate summaries of the main Parts of the book. A rather general overall introduction on “Facets of Matter” is intended to be accessible to an interested non-expert. The pedagogic measures are aimed at realizing a second main objective: to make the physics of hot and dense matter in heavy-ion collisions accessible to entry-level graduate students starting their research in this field.

The CBM Physics Book is structured into five topical units (“Parts”). [Part I](#) surveys the bulk properties of strongly interacting matter, including its equation of state and phase structure. [Part II](#) discusses elementary (hadronic) excitations of QCD matter, which, in particular, provide the conceptual basis for “probing” its properties. [Part III](#) addresses the concepts and models regarding the space-time dynamics of nuclear collision experiments – tools essential to connect bulk-matter properties and its excitations to experimental data. A compilation of relevant observables from current and past high-energy heavy-ion facilities is presented in [Part IV](#), augmented by theoretical predictions specific to CBM. [Part V](#) finally gives a brief description of the experimental concepts and components underlying the CBM detector.

The official start of the CBM-Book project may be associated with a “kick-off” meeting of approximately 30 world-leading scientists in June of 2005 at GSI (Darmstadt). At this meeting four topical working groups were initiated, one for each of the four original parts of the book, in a process open to anyone interested and willing to join. The fifth part was added later to reflect progress in design studies of the detector. Each working group consisted of up to a dozen scientists headed by two to three elected conveners. The conveners were entrusted with organizing the collection of the scientific material and combining it into a topical unit for each part of the book. The scientific efforts were further supported by several 1 week workshops held at the International Center for Theoretical Nuclear Physics and Related Areas (ECT*) in Trento in 2006 and at GSI in the following years.

The CBM Physics Book is based on an impressive number of high-quality contributions authored by leading scientists in the field, as listed at the beginning of each part. These contributions represent forefront research on diverse aspects of strongly interacting matter. While covering the topic from a broad

perspective as indicated above, CBM-specific connections have been stipulated throughout.

The approximately 4-year process of putting together the final volume of $\sim 1,000$ pages required substantial organizational efforts. About 2 years into the project the necessity for another level of editorial work became evident, which led to the formation of the Editorial Board (EB). Its members naturally emerged as the leading conveners of each part, S. Leupold (Part I), R. Rapp (II), J. Knoll (III+technical editing), J. Randrup (Part III), P. Senger (IV+V), C. Höhne (Part V), as well as B. Friman (executive summary). Their task was to establish overall coherence of the material by suitable adjustments in the structure of the various parts, e.g. by incorporating umbrella paragraphs to improve the connections of sections and chapters. Summaries of each part highlight the main points with topical foci that may serve as a quick reference.

The EB hopes that the large efforts devoted by the many contributing scientists toward completion of this book will stimulate further progress in the field of strongly interacting matter in particular, and in the applications and developments of concepts for describing strongly coupled systems, in general. It ultimately remains with the reader to judge in how far the objectives of this book have been realized. The EB expects that significant parts of this book will have to be rethought, rewritten and augmented when confronted with the reality of experimental data. It will be exciting to witness these developments in the years to come.

The combination of the primary research review character of this book with components of a more pedagogical design may fit quite suitably the format of “Lecture Notes in Physics”. The EB is very grateful to the editors of Springer Verlag for the opportunity to publish the present volume in this series.

The primary thanks go to all our scientific colleagues, listed below, who have contributed in various ways to the completion of this book, be it as contributing authors or as conveners collecting and distilling the material, towards a well tuned presentation of the different parts. Many thanks are also in order to the numerous colleagues who contributed ideas, discussion or other pertinent material, thereby opening valuable perspectives on various aspects of this book. Further thanks are also in order to the students performing simulations for the design study of the future detector. Without all their help the book would not have developed into its present form. Despite the broad authorship, the vast scope of the physics of strongly interacting matter inevitably implies that possibly some important results have not got covered in a complete fashion, or might have simply got overlooked. While thanking all the authors for their valuable contributions, the EB apologizes to researchers whose work was not appropriately covered or cited.

The EB gratefully acknowledges Frank Wilczek’s prelude to this book sharing his thoughts on strongly interacting matter. Finally, the EB thanks GSI, the CBM collaboration and the ECT* for supporting the progress in compiling this book with pertinent scientific workshops and meetings.

Conveners:

E. Bratkovskaya²⁰ (Part IV), C. Fuchs^{25,39} (Part III), C. Höhne^{21,12} (Part V), B. Kämpfer^{16,17} (Part II), J. Knoll^{12,23} (Part III), S. Leupold⁴⁰ (Part I), J. Randrup⁴ (Part III), R. Rapp¹¹ (Part II), K. Redlich^{13,43} (Part I), P. Senger¹² (Part IV, V), and M. Stephanov¹⁰ (Part I).

Contributing authors:

J. Aichelin³², A. Andronic¹², F. Antinori³⁵, R. Averbeck¹², R. Bellwied¹⁵, D. Blaschke^{43,18}, M. Bleicher²⁰, M. Bluhm¹⁶, E. Bratkovskaya²⁰, W. Cassing²¹, P. Danielewicz²⁸, A. Dumitru^{33,7}, Z. Fodor⁴⁴, V. Friese¹², B. Friman¹², C. Fuchs^{25,39}, M. Harada³¹, J. Heuser¹², T. Hilger¹⁷, C. Höhne^{21,12}, R. Holzmann¹², Y. Ivanov^{29,12}, B. Kämpfer^{16,17}, F. Karsch^{5,6}, S.D. Katz^{44,8}, M. Kitazawa²⁴, T. Klähn¹, J. Knoll^{12,23}, C.-M. Ko¹¹, T. Kunihiro²⁶, A. Larionov^{29,19}, Y. Leifels¹², S. Leupold⁴⁰, D. Miśkowiec¹², T. Peitzmann⁴¹, H. Petersen²⁰, P. Petreczky⁶, J. Randrup⁴, R. Rapp¹¹, C. Ratti³⁷, A. Rebhan⁴², K. Redlich^{43,13}, F. Riek¹¹, D. Rischke^{19,20}, D. Röhrich³, K. Rummukainen^{24,34}, C. Sasaki³⁰, B.-J. Schaefer²², E. Scapparini³⁸, P. Senger¹², E. Shuryak³⁷, J. Steinheimer²⁰, M. Stephanov¹⁰, M. Thaler³⁰, R. Thomas^{16,17}, L. Tolos²⁰, V. Toneev^{18,12}, S. Typel^{12,30}, F. Uhlig¹², H. van Hees¹¹, R. Vogt^{27,14}, J. Wambach^{13,12}, F. Weber³⁶, W. Weise³⁰, F. Wilczek⁹, P. Zhuang², and S. Zschocke^{16,17}

Affiliations:

¹Argonne National Laboratory, Argonne, IL, USA

²Tsinghua University Beijing, Beijing, China

³University of Bergen, Bergen, Norway

⁴Lawrence Berkeley National Laboratory, Berkeley, CA, USA

⁵University of Bielefeld, Bielefeld, Germany

⁶Brookhaven National Laboratory, Upton, NY, USA

⁷RIKEN BNL Research Center, Upton, NY, USA

⁸Eötvös University, Budapest, Hungary

⁹Massachusetts Institute of Technology (MIT), Cambridge, MA, USA

¹⁰University of Illinois, Chicago, IL, USA

¹¹Texas A&M University, College Station, TX, USA

¹²GSI Helmholtzzentrum für Schwerionenforschung, Darmstadt, Germany

¹³Technical University of Darmstadt, Darmstadt, Germany

¹⁴University of California at Davis, Davis, CA, USA

¹⁵Wayne State University, Detroit, MI, USA

¹⁶Forschungszentrum Dresden-Rossendorf, Dresden, Germany

¹⁷Technical University of Dresden, Dresden, Germany

¹⁸Joint Institute of Nuclear Research (JINR), Dubna, Russia

¹⁹Frankfurt Institute for Advanced Studies (FIAS), Frankfurt, Germany

²⁰University of Frankfurt, Frankfurt, Germany

- ²¹University of Gießen, Gießen, Germany
- ²²University of Graz, Graz, Austria
- ²³University of Heidelberg, Heidelberg, Germany
- ²⁴University of Helsinki, Helsinki, Finland
- ²⁵Martin-Gerbert-Gymnasium, Horb am Neckar, Germany
- ²⁶Kyoto University, Kyoto, Japan
- ²⁷Lawrence Livermore National Laboratory, Livermore, CA, USA
- ²⁸Michigan State University, East Lansing, MI, USA
- ²⁹Kurchatov Institute Moscow, Moscow, Russia
- ³⁰Technical University of Munich, Munich, Germany
- ³¹Nagoya University, Nagoya, Japan
- ³²SUBATEC Nantes, Nantes, France
- ³³Baruch College, New York, NY, USA
- ³⁴University of Oulu, Oulu, Finland
- ³⁵Istituto Nazionale di Fisica Nucleare, Padova, Italy
- ³⁶San Diego State University, San Diego, CA, USA
- ³⁷State University of New York, Stony Brook, NY, USA
- ³⁸Universita di Torino and INFN, Torino, Italy
- ³⁹University of Tübingen, Tübingen, Germany
- ⁴⁰Uppsala University, Uppsala, Sweden
- ⁴¹Utrecht University, Utrecht, The Netherlands
- ⁴²Technical University of Vienna, Vienna, Austria
- ⁴³University of Wrocław, Wrocław, Poland
- ⁴⁴University of Wuppertal, Wuppertal, Germany

Acknowledgement

We gratefully acknowledge the careful reading of the manuscript by H. Gies, T. Schäfer and J. Schaffner-Bielich ([Part I](#)), U. Mosel ([Part II](#)), W. Cassing ([Part III + IV](#)), P. Danielewicz ([Part III](#)), R. Bellwied, R. Averbeck and N. Xu ([Part IV](#)).

For enabling and performing simulations and feasibility studies of the CBM experiment we want to thank M. Al-Turany, D. Bertini, S. Das, M. Deveaux, T. Galatyuk, D. Gonzalez-Diaz, S. Gorbunov, M. Kalinsky, R. Karabowicz, Y. Kharlov, I. Kisel, S. Kiselev, A. Kiseleva, M. Klein-Bösing, I. Korolko, D. Kresan, E. Kryshen, A. Lebedev, S. Lebedev, A. Maevskaya, M. Prokudin, M. Rhyshinsky, and I. Vassiliev.

Contents

Prelude by Frank Wilczek	1
References	10
General introduction	11
Facets of matter	11
Executive summary	26
 Part I Bulk Properties of Strongly Interacting Matter	
1 Introduction	41
2 QCD and its thermodynamics	47
2.1 QCD and its symmetries	47
2.1.1 QCD basics	47
2.1.2 Systematic approaches and models	53
2.1.3 Symmetries of QCD	56
2.2 Phases of QCD	65
2.2.1 General thermodynamics	65
2.2.2 Types of phase transitions	74
2.2.3 QCD phase diagram at low temperatures	81
2.2.4 QCD transitions and chiral symmetry	85
2.2.5 Universality and QCD transitions	89
2.2.6 Order parameters and changes in the symmetry pattern	92
3 Equation of state and phase boundaries of strongly interacting matter	101
3.1 The coupling constant expansion of the QCD pressure	101
3.1.1 Perturbative expansion at high temperatures	102
3.1.2 Quark mass effects and pressure in real QCD	104
3.1.3 Beyond perturbation theory	107
3.1.4 Resummation methods	108

3.1.5	Perturbative expansion at finite chemical potential . . .	111
3.1.6	Summary of the present status	114
3.2	Thermodynamic properties from lattice QCD	116
3.2.1	Lattice formulation	117
3.2.2	Lattice methods at finite chemical potential	119
3.2.3	The equation of state from lattice QCD	124
3.2.4	The transition temperature at vanishing chemical potential	132
3.2.5	Results for the location of the transition line and of the critical point	133
3.2.6	Generalized susceptibilities and fluctuations	138
3.2.7	Further discussion	142
3.3	The nuclear equation of state from many-body theory	146
3.3.1	Models for the nuclear equation of state	146
3.3.2	Equation of state in symmetric and asymmetric nuclear matter	151
3.3.3	Connection to QCD	155
3.3.4	Summary of the present status	156
3.4	Compact star constraints on the high-density equation of state	158
3.4.1	Constraints from bulk properties	162
3.4.2	Constraints from compact star cooling	173
3.4.3	Relation to nuclear collisions	178
3.4.4	Summary	181
3.5	Color superconducting phases of QCD matter	182
3.5.1	Color superconductivity at asymptotically large densities	183
3.5.2	Color superconductivity at intermediate densities	188
3.5.3	Color superconductivity at low densities: Bose-Einstein condensation of diquark molecules	194
4	Model descriptions of strongly interacting matter near deconfinement	197
4.1	Statistical model and particle production in heavy-ion collisions	197
4.1.1	Statistical approach – grand canonical formalism	198
4.1.2	Canonical formulation of strangeness conservation	200
4.1.3	Model description of experimental data	202
4.2	Hadronic resonances – important degrees of freedom below deconfinement	209
4.2.1	Charge density fluctuations in a hadronic medium	210
4.2.2	Charge density fluctuations in lattice gauge theory	212
4.2.3	Lattice gauge theory results and hadron resonance gas predictions	212
4.3	The QCD equation of state near the transition line within a quasi-particle model	215

4.3.1	Basic relations	216
4.3.2	Concept of quasi-particles	216
4.3.3	The Rossendorf quasi-particle model at vanishing chemical potential	217
4.3.4	Baryon density effects and susceptibilities	220
4.3.5	A family of equations of state	223
4.3.6	The critical end point	224
4.4	Wilson line degrees of freedom and deconfinement	228
4.4.1	Pure Yang-Mills $SU(N)$ gauge theory	229
4.4.2	QCD: finite pion masses	233
4.5	Phase diagram and thermodynamics of the PNJL and PQM models	237
4.5.1	The NJL model	237
4.5.2	Introducing the PNJL model	239
4.5.3	Parameter fixing	241
4.5.4	Thermodynamics at finite chemical potential	243
4.5.5	Phase diagram	247
4.5.6	The Polyakov-quark-meson model	249
4.5.7	Quark-meson parameters	251
4.5.8	Polyakov-loop potential parameters	252
4.5.9	Phase structure and thermodynamic variables	254
4.5.10	Summary of the present status	258
4.6	Probing the QCD phase boundary with fluctuations	260
4.6.1	Charge density fluctuations near the critical end point	260
4.6.2	Charge density fluctuations in the presence of spinodal phase separation	262
4.7	The renormalization group method and the critical structure of QCD medium	266
4.7.1	Renormalization group methods	267
4.7.2	QCD in an RG framework	275
4.7.3	The phase diagram of the quark-meson model	281
4.7.4	Summary of the present status	285
4.8	Strongly coupled quark gluon plasma	286
4.8.1	Why is it strongly coupled?	286
4.8.2	Radial, elliptic and conical flows	288
4.8.3	Classical strongly coupled non-Abelian plasmas	290
4.8.4	Quantum mechanics of the quasiparticles	292
4.8.5	The magnetic side of sQGP and confinement	293
4.8.6	AdS/CFT correspondence and conformal sQGP	298
4.8.7	AdS/CFT correspondence predictions for sQGP	301
5	Summary	307
	References	313

Part II In-Medium Excitations

1	Introduction	337
2	Electromagnetic probes and light vector mesons	343
2.1	Brief overview of experimental status and interpretation	344
2.2	Emissivity of strongly interacting matter	345
2.2.1	Electromagnetic correlation function and thermal emission rates	345
2.2.2	Electromagnetic spectral function in vacuum	346
2.2.3	Low-density expansions and chiral mixing	349
2.3	Sum rules	350
2.3.1	QCD sum rules	351
2.3.2	Chiral sum rules and axialvector spectral function	360
2.4	Vector mesons in medium: hadronic models	364
2.4.1	ρ meson	366
2.4.2	ω meson	382
2.4.3	ϕ meson	384
2.5	Thermal dilepton rates	386
2.5.1	Lattice QCD	386
2.5.2	Hadronic approaches	388
2.5.3	RG approach: vector manifestation	390
2.6	Thermal photon rates	392
2.6.1	Direct single photons	392
2.6.2	Diphotons and in-medium “ σ ”	395
3	Hadronic resonance spectroscopy	401
3.1	Meson resonances	402
3.2	Baryon resonances	404
3.2.1	Chiral symmetry of baryons	405
3.2.2	Baryon masses and QCD condensates	405
3.2.3	Baryon resonance decays in heavy-ion collisions	407
4	Strangeness	411
4.1	Kaons in dense matter	412
4.1.1	Mean field dynamics	412
4.1.2	Effects non-linear in density	413
4.1.3	Coupled channel dynamics	416
4.1.4	Kaons in pion matter	423
4.1.5	Chiral symmetry restoration	425
4.2	Strange baryons	426
4.2.1	QCD sum rules	426
4.2.2	Hadronic models	427
4.2.3	Exotica	428

5	Open charm probes	429
5.1	Perturbative calculation of charm-quark production near threshold	431
5.1.1	Resummation	432
5.1.2	Charm-quark production in pp collisions	434
5.2	Charm-quark interactions in the QGP	438
5.2.1	Energy loss of charm quarks at high momentum	438
5.2.2	Charm diffusion and nonperturbative correlations in the QGP	441
5.2.3	Charm dilepton decays	448
5.3	Charm chemistry and thermal models	449
5.4	QCD sum rules	451
5.4.1	Open charm mesons	451
5.4.2	Remarks on J/ψ	454
5.5	Charm hadrons in medium	455
5.5.1	Cold nuclear matter	455
5.5.2	Hot pion gas	458
5.5.3	Hot and dense nuclear matter	458
5.5.4	Charm baryons	462
6	Charmonium	465
6.1	Charmonium in equilibrium	466
6.1.1	Color screening and quarkonium	466
6.1.2	Free energy of static quarks in lattice QCD	466
6.1.3	Spectral functions and Euclidean correlators	469
6.1.4	Charmonium spectral functions and potential models	470
6.2	Charm(onium) production within the statistical hadronization model	471
6.2.1	Introduction	471
6.2.2	Assumptions and ingredients of the statistical hadronization model	473
6.2.3	Energy dependence of charmed hadrons yield	477
6.2.4	Effects of in-medium modification of charmed hadrons masses	478
6.2.5	Conclusions	480
6.3	Charmonium transport in hot and dense medium	481
6.3.1	Introduction	481
6.3.2	Normal and anomalous J/ψ suppression	483
6.3.3	Regeneration	489
6.3.4	Transverse-momentum distributions	492
6.3.5	Charmonia in heavy-ion collisions at low energies	495

7	Excitations of color-superconducting matter	499
7.1	Color superconductivity in the QCD phase diagram	499
7.2	Strong decays of mesonic resonances	500
7.3	Pre-critical phenomena of color superconductivity	503
8	Summary and relations to observables	509
	References	513

Part III Collision Dynamics

1	Introduction	533
1.1	General features	535
1.2	Collision geometry and dynamical scales	536
1.3	Degrees of freedom	539
1.4	Relation to the equation of state	541
2	Cascade models	543
2.1	Intra-nuclear cascade models	543
2.2	The linear cascade model (rows-on-rows)	544
2.3	Parton cascades	546
2.4	String models	547
3	Kinetic transport models	549
3.1	Potentials and mean fields	550
3.2	Two-body collisions (Boltzmann equation)	552
3.2.1	Boltzmann-Langevin dynamics	553
3.3	Transport theory with dynamical spectral functions	555
3.3.1	From the golden rule to the Kadanoff-Baym equations	557
3.3.2	Generalised transport equations with dynamical spectral functions	562
3.3.3	Generalised collision term C_{loc}	563
3.3.4	Gradient terms	564
3.3.5	The virial limit	566
3.3.6	Non-additivity of perturbative rates	569
3.3.7	Physical processes in dense matter	573
3.3.8	Detailed balance and two-particle irreducible (2PI) method	574
3.4	Beyond binary collisions	576
3.4.1	Phenomenological quasi-free ansatz for multi-particle processes	576
3.4.2	Intermediate resonances	577
3.4.3	Transport with dynamical spectral functions	577
3.4.4	Inclusion of many-body collisions in transport simulations	578
3.4.5	Higher-order processes within the quasi-particle picture	579

3.4.6	Recent progress and challenges	580
3.5	Specific implementations	583
3.5.1	Initialization	583
3.5.2	Solution methods	583
3.5.3	Boltzmann-equation model BEM (MSU)	585
3.5.4	GiBUU (Giessen)	586
3.5.5	BRoBUU (Budapest/Rosendorf)	587
3.5.6	Relativistic BUU (Texas A&M/Stony Brook)	588
3.5.7	Relativistic BUU (Catania/Munich/Tübingen)	589
3.5.8	A Relativistic Transport ART (Texas A&M)	590
3.5.9	A Multi-Phase Transport AMPT (Texas A&M)	591
3.5.10	Hadron String Dynamics HSD	592
3.5.11	Quark-Gluon String Model QGSM	593
4	Many-body models	595
4.1	Molecular dynamics with phase-space smearing	596
4.1.1	IQMD: Isospin Quantum Molecular Dynamics	597
4.1.2	Relativistic Quantum Molecular Dynamics	598
4.1.3	UrQMD: Ultra-relativistic Quantum Molecular Dynamics	599
4.2	Quantum many-body approaches	600
4.2.1	Fermionic molecular dynamics	601
4.2.2	Antisymmetrized molecular dynamics	603
4.2.3	Quantal Langevin dynamics	604
5	Fluid dynamics	607
5.1	General framework	607
5.2	One-fluid hydrodynamics	608
5.3	Multi-fluid hydrodynamics	609
5.3.1	Three-fluid model	610
5.3.2	Phase conversion within non-equilibrium chemistry ...	611
5.4	Collective modes	614
5.5	Viscous fluid dynamics	615
5.6	Hybrid models	617
5.7	Fluid dynamics inspired models	619
5.8	Decoupling and freeze-out	620
5.9	Collision source imaging (HBT) and final-state correlations ..	628
6	Characteristic results	635
6.1	Gross characteristics of nucleus–nucleus collisions	635
6.2	Benchmarks	641
6.3	Mean-field dynamics	642
6.4	Collective flow	644
6.5	Rare probes	653

7	Status, perspectives and challenges	657
7.1	Summary of dynamical concepts	658
7.1.1	Micro-dynamical concepts	658
7.1.2	Macroscopic transport dynamics	660
7.2	Model overview	661
7.3	High-density challenge	663
7.4	Phase transitions	664

References	667
-------------------	-----

Part IV Observables and Predictions

1	Introduction	683
2	Exploring the QCD phase diagram	687
3	Review of experimental observations	693
3.1	Probing dense nuclear matter: results from GSI	693
3.1.1	Kaons in dense nuclear matter	694
3.1.2	Probing the nuclear equation-of-state with subthreshold kaon production	700
3.1.3	Conclusions	703
3.2	Probing hot and dense hadronic matter: results from AGS	704
3.2.1	Identified particle spectra	705
3.2.2	Strange particle measurements	706
3.2.3	Antibaryon production	708
3.2.4	HBT studies	709
3.2.5	Elliptic and directed flow studies	711
3.2.6	Conclusions and perspectives for FAIR	712
3.3	Searching for the phase transition: results from SPS	714
3.3.1	Initial energy density	716
3.3.2	Hadronic expansion	717
3.3.3	Strangeness enhancement and chemical equilibrium	718
3.3.4	J/ψ suppression	720
3.3.5	In-medium modification of the ρ meson	721
3.3.6	Energy dependence of relative strangeness production	721
3.3.7	Conclusions and perspectives for FAIR	723
3.4	Probing partonic matter: results from RHIC	724
3.4.1	Jet quenching	724
3.4.2	Hydrodynamical elliptic flow	726
3.4.3	Constituent Quark (NCQ) Scaling of elliptic flow	727
3.4.4	Hadronic resonance measurements	728

4	Hadron production	731
4.1	Excitation functions of hadron yields	731
4.2	Excitation functions of hadron ratios	736
4.3	Conclusions and perspectives for FAIR	741
5	Transverse mass spectra	743
5.1	Beam energy dependence of transverse mass distributions	743
5.2	Particle mass dependence of transverse mass distributions	745
5.3	Conclusions and perspectives for FAIR	746
6	Collective flow	747
6.1	General considerations	747
6.2	Nucleon flow and the nuclear equation-of-state	748
6.3	Elliptic flow and partonic collectivity	750
6.4	Collective flow and phase transitions	752
6.5	Conclusions and predictions for FAIR energies	755
7	Dileptons	759
7.1	General overview	759
7.2	Lessons from the CERN-SPS	761
7.2.1	Invariant mass spectra	761
7.2.2	Transverse mass spectra	767
7.3	Dielectrons at RHIC	768
7.4	Dielectrons at BEVALAC and SIS	769
7.5	Conclusions and predictions for FAIR energies	772
8	Open and hidden charm	775
8.1	General overview	775
8.2	Charm in transport models	778
8.3	Charmonia from kinetic rate equations	781
8.4	The statistical hadronization model	785
8.5	Open charm in dense matter	787
8.6	Conclusions and predictions for FAIR energies	790
9	Fluctuations and correlations	795
9.1	Fluctuations and correlations in a thermal system	797
9.2	Fluctuations and correlations of conserved quantities	798
9.3	Electric charge fluctuations	800
9.4	Particle multiplicity ratio fluctuations	803
9.5	Correlation between baryon number and strangeness	805
9.6	Higher-order moments of the fluctuations	807
9.7	Fluctuations of the mean transverse momentum	809
9.8	Observable consequences of a first-order transition	811
9.8.1	Kinematic observables	812
9.8.2	Chemical observables	814
9.9	Observable consequences of a critical end point	816

9.10	Summary and concluding remarks	818
10	Dibaryons, hypernuclei and strange nuclear systems at FAIR	821
11	Summary	827
	References	831
 Part V CBM Experiment		
1	Introduction	851
1.1	Exploring dense baryonic matter in the laboratory	851
1.2	The facility of antiproton and ion research	855
1.3	Nuclear matter research at FAIR	856
1.3.1	Experiments at SIS100	856
1.3.2	Experiments at SIS300	863
2	The CBM detector concept	865
2.1	The Silicon Tracking System (STS)	867
2.2	The Micro-Vertex Detector (MVD)	868
2.3	The Ring Imaging CHerenkov detector (RICH)	869
2.4	The Transition Radiation Detector (TRD)	870
2.5	The Muon Chamber system (MuCh)	870
2.6	The timing Resistive Plate Chambers (RPC)	871
2.7	The Electromagnetic CALorimeter (ECAL)	871
2.8	The Projectile Spectator Detector (PSD)	872
2.9	Online event selection and data acquisition	872
3	Feasibility studies	875
3.1	Track and vertex reconstruction	875
3.2	Hadron identification	877
3.3	Hyperon reconstruction	881
3.4	Event-by-event fluctuations	882
3.5	Open charm	886
3.6	Identification of vector mesons via lepton pairs	890
3.6.1	Electron simulations	891
3.6.2	Muon simulations	896
3.7	Direct photons	904
3.8	Expected particle yields	906
4	Experiments complementary to CBM	909
4.1	The NICA/MPD project at JINR	909
4.2	The NA61 experiment at the CERN-SPS	910
4.3	The RHIC energy scan program	911

References	913
Overview of heavy-ion experiments	915
A.1 Introduction	915
A.2 FOPI – a 4π detector for heavy ion collisions at SIS	916
A.2.1 Introduction	916
A.2.2 The detector	916
A.2.3 Experimental program and results	917
A.3 The HADES detector at SIS/GSI	921
A.4 The KaoS experiment at SIS/GSI	924
A.5 Summary of AGS experiments	927
A.5.1 E802 – E859 – E866 – E917	927
A.5.2 E814 – E877	928
A.5.3 E810 – E891	929
A.5.4 E895	930
A.5.5 E910	931
A.6 The CERES (NA45) experiment at the SPS/CERN	933
A.7 The NA49 experiment at the SPS/CERN	935
A.8 The NA57 (WA97) experiment at the SPS/CERN	938
A.8.1 Experimental setup and observables	938
A.8.2 Results	939
A.9 The NA60 experiment at the SPS/CERN	941
A.9.1 Experimental setup	941
A.9.2 Observables, event characterization	942
A.9.3 Performance	942
A.9.4 Running conditions	942
A.9.5 Results and outcomes	943
A.9.6 Advantages and limitations	943
A.10 The WA98 experiment at the SPS/CERN	945
A.10.1 Experimental setup	945
A.10.2 Trigger and observables	946
A.10.3 Performance	946
A.10.4 Results	947
A.10.5 Advantages and limitations	948
A.11 The BRAHMS experiment at RHIC/BNL	950
A.11.1 Experimental setup	950
A.11.2 Observables	951
A.11.3 Performance	951
A.11.4 Running conditions	952
A.11.5 Results	952
A.11.6 Advantages and limitations of the experimental approach	953
A.12 The PHENIX experiment at RHIC/BNL	955

A.12.1 Experimental setup	955
A.12.2 Main results and publications	957
A.13 The PHOBOS experiment at RHIC/BNL	960
A.13.1 Experimental setup	960
A.13.2 Main results and publications	962
A.14 The STAR experiment at RHIC/BNL	963
A.14.1 Experimental setup	963
A.14.2 Main results and publications	965
A.15 The ALICE experiment at the LHC/CERN	969
Index	973

Prelude to compressed baryonic matter

Frank Wilczek

Center for Theoretical Physics, Department of Physics,
Massachusetts Institute of Technology,
Cambridge, MA 02139, USA

Why study compressed baryonic matter, or more generally strongly interacting matter at high densities and temperatures? Most obviously, because it's an important piece of Nature. The whole universe, in the early moments of the big bang, was filled with the stuff. Today, highly compressed baryonic matter occurs in neutron stars and during crucial moments in the development of supernovae. Also, working to understand compressed baryonic matter gives us new perspectives on ordinary baryonic matter, i.e. the matter in atomic nuclei. But perhaps the best answer is a variation on the one George Mallory gave, when asked why he sought to scale Mount Everest: Because, as a prominent feature in the landscape of physics, it's there. Compressed baryonic matter is a material we can produce in novel, challenging experiments that probe new extremes of temperature and density. On the theoretical side, it is a mathematically well-defined domain with a wealth of novel, challenging problems, as well as wide-ranging connections. Its challenges have already inspired a lot of very clever work, and revealed some wonderful surprises, as documented in this volume.

Despite – or rather because of – all this recent progress, I think the best is yet to come. Central questions have not been answered. What is the phase diagram? What is in the interior of a neutron star? And more broadly: How can we make better use of QCD in nuclear physics? Its equations should, in principle, contain all the answers; but in practice we struggle. With more powerful accelerators and detectors, bigger and faster computers, and improved insight, we are advancing on these issues. The latest investigations also raise new questions: Why does quark-gluon plasma, near its crossover temperature, behave remarkably like a perfect liquid, perhaps well described by a simple strong-coupling theory? Does cold baryonic matter at ultra high density really form the color-flavor locked state, where weak coupling methods borrowed from the theory of superconductivity describe the physics of confinement and chiral symmetry breaking? Can we build out from the profound simplicity apparently discovered in those idealizations, to make them more realistic and comprehensive?

Part of the appeal of the study of compressed baryonic matter is that it presents four distinct aspects: analytic theory, laboratory experiments, astrophysical observations, and last but certainly not least numerical “experiments”. I'd like to make a few comments about each of these aspects, in turn.

Analytic theory

The foundation of QCD is uniquely secure. Once the numerical values of quark masses and an overall coupling are given, the equations of QCD are defined with mathematical precision.¹ Quantum theory, special relativity, and the profound embodiment of those principles in gauge field theory, impose such powerful consistency constraints that the theory does not allow any significant modification nor additional parameters.

Indeed, the situation is even a little better than the preceding counting of parameters indicates, due to the phenomenon of dimensional transmutation. Let me take a moment to elaborate on that profound feature of QCD. Since we are discussing a theory wherein quantum mechanical fluctuations and relativistic motion are all-pervasive, it is appropriate to adopt Planck's constant \hbar and the speed of light c as our units for action, so that $\hbar = c = 1$. In this system, the unit of any physical quantity is some power of mass, its mass dimension. With that understanding, we can appreciate the power of the dimensional transmutation principle, which is this:

Dimensional Transmutation Principle: If, in the formulation of QCD, one re-scales all the quark masses by a common constant, and at the same time makes an appropriate (nonlinear) change in the coupling constant, one obtains a new theory in which all *dimensionless* – that is, numerical – quantities retain the same values as in the original theory.

In other words, the new theory differs from the old only in an overall change of the unit of mass, or equivalently length^{-1} . The dimensional transmutation principle is an immediate consequence of the fact that the coupling “constant” is not simply a numerical quantity; its definition brings in a length scale. We could, for instance, define the coupling constant as the “charge” appearing in the “Coulomb’s law” for forces between quarks at short distances; but since in QCD the analogue of Coulomb’s law is not accurately valid, we obtain a distance-dependent, running coupling constant. We can freely specify some conventional value for g_0 the coupling. The physically defined coupling $g(l)$, which depends on the distance l , takes this value at some length l_0 , where $g(l_0) = g_0$. Thus we can trade the conventional, numerical quantity g_0 for the physical quantity $l_0(g_0)$ it points to. But l_0 has dimensions of length, or inverse mass. So what might have appeared to be a freely specifiable numerical quantity is actually another freely specifiable mass parameter, on the same footing as the quark masses. If we rescale all the masses by a common factor, we have merely changed the standard by which we measure mass (or length). What might have appeared to be a one-parameter family of essentially different theories, with different values of the coupling constant, is actually just one theory, viewed through lenses of differing magnification. If

¹ If neither of the discrete symmetries parity P or time reversal T are imposed, one must also specify the notorious θ term. Empirically, this term is known to be very nearly zero.

we discount that trivial difference, one additional parameter can be disposed of.

QCD Lite is the version of QCD wherein the masses of the u, d , and s quarks are taken to zero and the masses of the c, b and t quarks are taken to infinity (so that in effect the heavy quarks are neglected). We expect on theoretical grounds that QCD Lite provides an excellent qualitative and a reasonable semi-quantitative approximation to real-world QCD in many applications. In particular, QCD Lite supports confinement and chiral symmetry breaking and it yields, for baryon number $|B| \leq 1$, an excellent approximation to the spectrum of real-world QCD². Those expectations are borne out by numerical studies of the two theories.

There are a handful of cases where we can make analytic prediction in QCD. The most basic and most useful, by far, is in the regime of short-distance or high-energy processes, where we can apply renormalization group methods. We can exploit asymptotic freedom, and calculate short-distance or high-energy behavior using ordinary perturbation theory around free quark and gluon fields [2]. It is not always obvious (to say the least) what aspects of a complex process involving hadrons really reflect short-distance behavior. Over the years the scope of perturbative QCD has expanded enormously, from its original base in deep inelastic scattering and other current-induced processes (the Age of Operators) to include many aspects of jet physics, heavy quark physics, and more. In the modern Age of Quarks and Gluons, the operating principle is the Jesuit Credo, that it is more blessed to ask forgiveness than permission. One starts by assuming tentatively that the quantity of interest, such as (say) the probability of producing a jet within a given energy range and solid angle, can be calculated by pretending that quarks and gluons are the physical degrees of freedom of QCD, and then checks whether higher orders in perturbation theory render that starting assumption untenable. This principle has been extremely fruitful and successful, giving us valuable and – so far – reliable guidance regarding the applicability of perturbation theory. These ideas dominate the interpretation of accelerator experiments at the high energy frontier; for example, experimenters routinely speak of measuring cross-sections for producing quarks or gluons, meaning of course the jets calculated using those concepts.

It's long been known that perturbation theory can also be applied to describe QCD at asymptotically high temperatures, to calculate such things as the energy density and pressure. Intuitively, keeping in mind the Jesuit Credo, this seems utterly reasonable: At high temperatures, taking noninteracting quarks and gluons as the starting point, the corrections to bulk properties due to interactions seem likely to be small, since most of those quarks and gluons will be highly energetic, and thus weakly interacting. Indeed, until fairly recently it was widely anticipated that the temperatures required to

² However the quark-hadron continuity principle [1], which is closely connected to color-flavor locking, suggests that “Nuclear Physics Lite”, for $|B| > 1$, is quite different from real nuclear physics.

produce a nearly ideal gas of quarks and gluons might not be terribly large. After all, in deep inelastic scattering approximate free-field behavior sets in at remarkably low energies – this is the phenomenon of precocious scaling. The truth is more interesting, as we’ll discuss further below.

A different regime of highly compressed baryonic matter supports a most remarkable analytic theory [3]. This is the regime of large chemical potential, or in other words high baryon number density, and low temperature. Here methods borrowed from the BCS theory of superconductivity come into play. Starting from free quarks, one derives large fermi surfaces. Therefore the relevant low-energy excitations, involving transitions between occupied and unoccupied states near the fermi surface, involve quarks with large momenta. Such quarks can be expected to be weakly interacting, so we seem – at first glance – to have a simple “quark soup”. There are two problems with that picture, however. First, it fails to consider the gluons. And the gluons are indeed problematic. While their electric interactions are screened by the quarks, their magnetic interactions are not screened, and the unscreened magnetic interactions among gluons lead to infrared divergences, invalidating our hypothesis of weak coupling. Second, it fails to take into account that there are many low-energy quark-quark excitations with the same quantum numbers. This means that we’re doing *degenerate* perturbation theory among those states. (This too is signaled by infrared divergences.) In degenerate perturbation theory, even small perturbations can make qualitative changes. Specifically, quark-quark pairs with equal and opposite 3-momenta $\pm\mathbf{p}$ are subject to the same Cooper pairing instability that leads, in ordinary condensed matter systems, to superconductivity in metals or to superfluidity in liquid He³. Remarkably, these two problems can be resolved analytically. The quarks have an attractive interaction, which triggers a version of superconductivity for the color gauge interaction, analogous to ordinary superconductivity for electromagnetism. In more detail: Quarks form a pairing condensate. For three quarks with negligible masses a particularly simple and beautiful symmetry breaking pattern, the so-called color-flavor locking, appears to be energetically favored. In this state the quarks pair as

$$\begin{aligned}\langle q_L^{a\alpha\mu} q_L^{b\beta\nu} \rangle &= -\langle q_R^{a\alpha\mu} q_R^{b\beta\nu} \rangle \\ &= \epsilon^{\mu\nu} (\kappa_{\bar{3}} (\delta^{a\alpha} \delta^{b\beta} - \delta^{a\beta} \delta^{b\alpha}) + \kappa_6 (\delta^{a\alpha} \delta^{b\beta} + \delta^{a\beta} \delta^{b\alpha}))\end{aligned}\tag{1.1}$$

Here μ, ν are Dirac spinor indices, α, β are color indices, and a, b flavor indices, $\kappa_{\bar{3}} \gg \kappa_6$ are coefficients of pairing in antitriplet and sextet color channels, and momentum dependence has been suppressed. This pairing has many interesting features. It breaks the color gauge and chiral flavor symmetries down to a diagonal global flavor group, according to

$$SU(3)_c \times SU(3)_L \times SU(3)_R \rightarrow SU(3)_\Delta\tag{1.2}$$

where the residual symmetry transformations are of the form (g, g^*, g^*) . The “spontaneous breaking” of color symmetry produces gaps in both the gluon and the quark sector. The correlation between left-handed (L) and right-handed (R) quark fields breaks chiral symmetry. The modified form of the symmetry generators has as a consequence that the elementary excitations around the new ground state have integer electric charge; and indeed the whole spectrum of low-lying states resembles what one expects for the confined phase of this theory. So we have here a weak-coupling implementation of the main qualitative features that distinguish perturbative from non-perturbative QCD! The deep point is that the color-flavor locked ground state is constructed non-perturbatively, following the ideas of the Bardeen-Cooper-Schrieffer (BCS) theory of superconductivity – here weak interactions, in the context of degenerate perturbation theory, do indeed trigger drastic reorganization of the ground state.

Very recently another front of analytic work on compressed QCD has opened up [4]. This is inspired, on the theoretical side, by the AdS/CFT correspondences of string theory. In the right circumstances, those correspondences allow one to map strong coupling problems in four-dimensional gauge field theory onto problems in five-dimensional classical general relativity. On the experimental side, we have indications that the initial fireball of material produced in heavy ion collisions, which probably broadly resembles QCD near equilibrium at $T \sim 150\text{--}200$ MeV, is characterized by strong effective coupling. The observed fireball behaves as a near-perfect ideal liquid, rather than an ideal gas! Unfortunately QCD is not a case where AdS/CFT applies directly, nor is it manifestly close to one, so considerable guesswork is involved in application of AdS/CFT ideas to reality. It’s still early days in this field, however, and the possibility of connecting five-dimensional general relativity to observations is so startling and deep that it must be pursued vigorously.

Finally, there is another class of analytic theory that can be applied to the QCD of condensed matter [5]. This is the theory of second-order critical points. Both the strength and the weakness of this theory is that it is so general (“universal”); it is largely independent of the microscopic dynamics. Second-order critical points are associated with change in symmetry, and the low-energy, long-wavelength behavior near such critical points is dominated by critical fluctuations. Those modes and their interactions are described by effective theories, which depend only on the symmetries (here: chiral symmetry). The effective theories relevant to second-order transitions in QCD are much simpler than QCD itself, but they can be exploited to make detailed quantitative predictions that should also hold in QCD itself.

Cosmology and astrophysics

As I mentioned earlier, compressed baryonic matter filled the early universe, and is the stuff of neutron stars and supernovae.

QCD and asymptotic freedom, by enabling us to extrapolate and draw consequences from the laws of physics to the ultra-extreme conditions of the early big bang with confidence and precision, provide the intellectual foundation for modern early universe cosmology. At present, however, the link between cosmological or astrophysical observations and fundamental theory is quite tenuous. In cosmology, I'm afraid this situation appears unlikely to change.³ The problem is that the evolution of the universe, even in its dynamic early stages, is very slow on strong-interaction time scales, so that accurate equilibrium is likely to be maintained. If at any stage the equilibrium were inhomogeneous, due to phase separation at a first-order transition or even fluctuations at a second-order transition, then one might hope that some historical memory would be imprinted on nuclear abundances, or in gravity waves. But the emerging consensus is that real-world QCD at very small chemical potential, which is what we encounter in conventional cosmology, does not support either sharp phase transitions or large equilibrium fluctuations. So, barring a very major deviation from orthodox expectations (e.g., Affleck-Dine baryogenesis [6]) no observable relic of the early strong dynamics seems likely to survive.

Astrophysics is, I think, much more promising. It's not entirely ridiculous to think that in the foreseeable future we'll have mass-radius relations for a good sample of neutron stars, rich measurements of neutrino emission in a few supernova explosion, and measurements of gravity wave emission accompanying the final infall of binary systems that include neutron stars. These signals, and perhaps others, will in coming years provide a rich flow of information from the world of compressed baryonic matter. We should get ready for it!

There's also an ongoing revolution in the experimental study of high-energy cosmic rays. Perhaps there are opportunities for extreme QCD here, either in the description of the interactions of heavy nucleus primaries or in modelling the sources; but these are complex subjects, where QCD contributes to only a small share of the uncertainties.

Laboratory experiments

I shall be very brief here, since the material on this topic in the body of the book speaks ably for itself.

³ I'd love to be wrong about that!

Although by now we almost take it for granted, it's important to remember that the most fundamental prediction of QCD at high temperatures is both simple and spectacular:

At low temperatures strongly interacting matter should be well described using separate hadrons. In fact below $T \lesssim 125$ MeV or so, it should be basically a gas of pions, with 3 bosonic degrees of freedom. But at high temperatures, strongly interacting matter should be described as a plasma of quarks and gluons, with 36 fermionic and 16 bosonic degrees of freedom! (Three flavors and three colors of quarks and antiquarks, each with two spin states; eight gluons each with two polarization states.) In fact we find, both upon numerical solution of the theory and in experiments, that within a remarkably narrow range of temperatures things do change dramatically. By $T \gtrsim 170$ MeV or so the energy density is pretty nearly that of a gas of free quarks and gluons, with 36 fermionic and 16 bosonic degrees of freedom! This enormous quantitative change, of course, serves to dramatize the qualitative change that underlies it. Quarks and gluons, once famous for being confined and elusive, have dropped their masks and come to center stage.

While this zeroth-order success is gratifying, closer examination reveals that the situation is far from straightforward. It's long been known, from the numerical work, that while the energy density quickly approaches its predicted asymptotic value, the pressure lags. So the weak-coupling theory is suspect near the transition temperature. (Though tour-de-force calculations in perturbation theory, involving high orders and some resummations, work significantly better.) And here experiment produced perhaps its greatest surprise: while the *thermodynamic* properties of the plasma near $T \sim 150$ MeV are not so different from those of an ideal gas of quarks and gluons, the *transport* properties point to very strong interactions. Indeed, the plasma appears to have very small shear viscosity, so that it more resembles an ideal liquid. Were we to think in terms of standard kinetic theory – which is no doubt too naive – this phenomenon would point to a tiny mean free path.

Clearly, it will be interesting to observe whether, or to what extent, these surprising properties survive at the higher temperatures that will be explored in heavy ion collisions at the LHC. Speaking more broadly, it will be highly interesting to explore how the asymptotically free ultra-short distance and ultra-high energy behavior of hadronic matter connects to the distinctly different intermediate-scale and overall transport behavior. At LHC there will be enough phase space and luminosity to exploit c and even b quarks, and very high energy photons, dimuons, and jets, with rich statistics, and really engage these issues.

Another important goal of future experiments is to map out the phase structure of hadronic matter, as a function of temperature *and* baryon number density. In this regard an interesting target is a possible true second-order phase transition (a tricritical point). Such a transition should be accompanied by critical fluctuations, which might leave signatures visible even within

the daunting environment around heavy ion fireballs. These possibilities will be explored both at the Relativistic Heavy Ion Collider (RHIC) and the new Facility for Antiproton and Ion Research (FAIR).

Finally, it is appropriate to mention that the classic experimental probe of hadronic structure, deep inelastic scattering, remains interesting and relevant. The “gluonization” of hadrons, as they are analyzed by virtual photons of large Q^2 , is a fundamental phenomenon, that connects in important but poorly understood ways to dominant interaction mechanisms between high-energy hadrons (diffractive scattering and diffractive dissociation). These issues can also be studied for nuclei, of course, and should give insight into some fundamental questions. Is there a dynamically defined variety of quark, in a piece of the nuclear wave function, that is shared among different nucleons, or are all of them, uniformly, strictly confined? I sense that this is a domain where accurate experimental work might connect with new analytical ideas.

Numerical experiments

Numerical solution of the equations of QCD, usually called lattice gauge theory, is a subject that has achieved major triumphs [7]. Confinement and spontaneous chiral symmetry breaking have been demonstrated convincingly. Going far beyond those qualitative results, it has been demonstrated by direct calculation that the rigid microscopic equations of QCD, based on quarks and gluons, reproduces the rich spectrum of low-energy hadrons that is observed in Nature. Numerical work also revealed the striking temperature dependence of the energy density and pressure, mentioned earlier, well in advance of its experimental confirmation [8]. No other technique on the horizon comes close to competing with the use of sophisticated discretisation techniques, clever algorithms and powerful computers for addressing these and many other issues (e.g., evaluating matrix elements of weak and electromagnetic currents, heavy quark spectroscopy) quantitatively. Where lattice gauge theory can be applied, it is generally unrivalled.

Unfortunately, however, lattice gauge theory is not well adapted to deal with some other central questions and opportunities in QCD. All known algorithms degrade badly for problems that cannot somehow be phrased as the evaluation of positive-definite integrals – in gigantic spaces, to be sure. But the partition function of QCD at finite chemical potential is, when cast into an integral, not positive definite; one has the notorious fermion sign (actually phase) problem. The final answer is much smaller than the various, largely cancelling, contributions to it. Existing numerical techniques thereby lose most of their power, and today we have no meaningful ability to investigate QCD at high baryon number density by direct solution of equations, even though we know exactly what the equations are.

Different but equally severe problems appear when we try to investigate high-mass, high-spin resonances. That is a pity, because QCD exhibits remarkably simple regularities in the high-spin regime, so it's tempting to conjecture that a good analytic or semi-analytic theory awaits discovery.

I'd like to take this opportunity to mention a pet idea of mine, that I think merits attention. As just mentioned, known numerical techniques in quantum field theory are extremely powerful when applied to positive-definite integrals, though they founder for oscillatory ones. This difficulty creates a barrier to direct simulation of nuclear matter or investigation of its phase diagram. There is, however, the possibility of dodging it, by pursuing what I call "lattice lattice gauge theory". That is, one can insert sources belonging to *real* representation of the gauge group. These do not lead to sign or phase problems. Thus lattices of fixed sources in real representations provide user-friendly model systems. The spacing of the source lattice can and should be varied independently of the spacing in the numerical grid; this is what I mean by lattice gauge theory. We can vary the dimensionality, the type of lattice, the gauge group(s), and the representation(s) present; we can also include temperature or even (at a high price) dynamical fermions.

As a concrete example, we could consider putting octet sources on a cubic lattice in pure glue QCD. At large separation these sources will induce a lattice of individuated glueballs. At small separation, the glueballs will start to overlap, and presumably there will be a transition to a screening "metallic" state. This is an analogue of the Mott transition, which is a central research area in today's condensed matter physics. There might also be an intermediate state with flux directed between pairs of neighboring sources, in the spirit of Anderson's resonating valence bond (RVB) hypothesis. The point is we don't have to guess, we can calculate.

In QCD models of this kind could shed light on the nature of glueballs or (with dynamical fermions) $Gq\bar{q}$. They could also supply a *very* crude, but tractable, caricature of nuclear matter, and it would be interesting to compare their Mott transition density to the density of nuclear matter. For exploring quasi-chemical questions, which might be the most fascinating, it would probably be advisable to make do with finite groups, and to invest more heavily in some of the other bells and whistles I mentioned before.

Even were this program to prove wildly successful, it would of course only be a stopgap. To get quantitative results for highly condensed baryonic matter, worthy of the challenges posed by Nature and the opportunities afforded by QCD, we will need fundamentally different numerical methods. In conventional lattice gauge theory the starting point is the no-particle, Fock vacuum. Probably, as suggested by color-flavor locking, the key is to start with a better approximation to the true ground state, generated numerically through an appropriate variational principle.

As evidenced by this volume, the study of compressed baryonic matter is paying off handsomely. Old questions are being answered; but the answers lead us to better, more ambitious questions, and leave us hungry for more.

References

1. T. Schäfer, F. Wilczek, *Quark description of hadronic phases*. Phys. Rev. D **60**, 074014 (1999). [3](#)
2. R. Ellis, W. Stirling, B. Webber, *QCD and Collider Physics* (Cambridge University Press, Cambridge, 1996). [3](#)
3. M. Alford, K. Rajagopal, T. Schäfer, and A. Schmitt, *Color superconductivity in dense quark matter*. Rev. Mod. Phys. **80**, 1455 (2008). [4](#)
4. S. Gubser and A. Karch, *From gauge-string duality to strong interactions: a Pedestrian's guide*, Annu. Rev. Nucl. Part. Sci. **59**, 145 (2009). [5](#)
5. K. Rajagopal and F. Wilczek, The condensed matter physics of QCD. In *Handbook of QCD* (M. Shifman (ed.), pp. 2016–2151 (World Scientific, Singapore, 2001). [5](#)
6. I. Affleck and M. Dine, *A new mechanism for baryogenesis*. Nucl. Phys. B **249**, 361 (1985). [6](#)
7. I. Montvay and G. Münster, *Quantum Fields on a Lattice* (Cambridge University Press, Cambridge, 1997). [8](#)
8. C. DeTar and U. Heller, *QCD Thermodynamics from the Lattice*, Eur. Phys. J. A **41**, 405 (2009). [8](#)

General introduction

In this introductory part we first present a primer, “facets of matter”, which is intended for non-experts and young students, who would like to enter this research field. After a brief historical overview, the main physics concepts and research objectives addressed in this book are elucidated, using illustrative examples known from standard physics text books. For the more experienced researcher, the subsequent executive summary reviews the main accomplishments and physics goals presented in the five topical parts of the book.

Facets of matter

In the course of the past century, unprecedented progress has been achieved in our understanding of the fundamental laws of nature and their implications for the complex structure of the world at all scales, ranging from the sub-structure of elementary hadrons to the universe as a whole. The revolutionary concepts of special and general relativity and quantum mechanics have resolved many of the puzzling experimental findings that had accumulated by the beginning of the twentieth century, such as the particle-wave duality. A new wave of enthusiasm inspired the physicists those days. New theoretical frameworks for the basic laws of physics appeared. A wealth of novel so far unknown phenomena were predicted, many of them later on experimentally verified. A famous example is the conjecture suggested from the relativistic formulation of quantum mechanics that each elementary particle has an antiparticle partner, a particle with the same mass and spin but opposite attributes such as electric charge.

Together with the progress in technology, sophisticated devices were developed capable to accelerate elementary particles. Electrons, protons and even heavy atomic nuclei could be boosted to higher and higher energies. It permitted the exploration of the sub nanometer world of atoms and even the femtometer scales (10^{-15} m) of atomic nuclei and their constituents. Probing

the laws of nature at incessantly finer scales has revealed the existence of a surprisingly large number of elementary particles and provided the means to study their interactions and thus to understand their relationships.

As a result two further interactions were identified in addition to the familiar gravitational and electromagnetic forces. These are the *strong interaction* that causes nucleons to bind into atomic nuclei and the *weak interaction* responsible for certain radioactive transformation processes, such as the β decay that turns a neutron into a proton. While essentially dormant in our familiar terrestrial world, the strong interaction plays an active role in stellar environments. It provides the energy that powers stars such as our sun by causing individual nucleons to fuse into light nuclei. Ultimately the evolution of the universe from the Big Bang to its current state with more than one hundred billion of galaxies each containing billions upon billions of stars, with associated (and possibly inhabited) planetary systems, is the result of the subtle interplay of all four fundamental forces.

The combination of quantum mechanics with special relativity led to the presently most powerful formulation of fundamental physics: *Quantum Field Theory*. This conceptual framework forms the basis for the *Standard Model of Particle Physics*, according to which nature at its fundamental level consists of elementary “matter” particles (which all have half-integer intrinsic spin and are categorised as *fermions*) that interact by the exchange of *boson* field quanta (having integer spin).

A prominent part of the Standard Model is *Quantum Electrodynamics* (QED) which governs the properties of the familiar matter surrounding us in our daily life. The electromagnetic force is mediated by the *photon*, the quantum of light. The photon itself is uncharged but carries one elementary unit of intrinsic spin and has a vanishing mass, which gives rise to the long range of the electric force. The most familiar elementary particles that interact electromagnetically are the electron, which by convention carries one negative unit of elementary charge, $-e$, and the proton carrying the positive elementary charge $+e$. Like the others, the neutron, though electrically neutral, can be deflected by a magnetic field due to its spin. Neutron and proton are the building blocks of atomic nuclei. QED is by far the best established physical theory, experimentally verified to a precision of about 12 numerical digits. Because of this unrivalled success, this type of quantum field theory, which contains so-called *gauge* fields, was generalised to describe all fundamental interactions. This framework then led to the successful formulation of a unified theory of the *strong* force, the *electromagnetic* force and the *weak* force, while it has not yet been possible to encompass the fourth (and weakest) force, *gravity*, into such a unifying scheme.

One of the most important advances in physics during the twentieth century arose from recognising the essential role played by *symmetries* (or invariances). They govern the character of the fundamental interactions. In particular, invariances under temporal translation, spatial translation or spatial rotation, which are all continuous transformations, imply the funda-

mental conservation laws for energy, momentum and angular momentum, respectively. Furthermore, the discrete symmetries associated with particle-antiparticle conjugation and spatial reflection (parity) allow us to organise the elementary particles into certain groups and to characterise the features of their mutual interactions. In particular, the existence of *quarks* as the fundamental entities in strong-interaction physics was postulated on the basis of symmetry considerations. Their invention and subsequent discovery brought a transparent systematics into the increasing zoo of *hadrons* produced in high-energy collision experiments. There are two known categories of hadrons: *Baryons* (from the Greek word βαρυς meaning *heavy*), such as protons and neutrons, which can be thought of as composed of three quarks, and *mesons* (from the Greek word μεσος meaning *medium*), which contain a quark and an antiquark. The strong interaction has the particular feature, called *confinement*, that the elementary constituents, namely the quarks, do not appear in isolation.

Like the electron, the quarks carry half a unit of intrinsic spin. As an unusual feature, however, they have fractional electric charges of $\frac{2}{3}e$ or $-\frac{1}{3}e$. Initially just three different types of quarks were needed to explain the hadrons known those days: the very light *u* (for “up”) and *d* (for “down”) quarks with masses of about 2 and 6 MeV,¹ forming e.g. protons and neutrons as (*uud*) and (*udd*) bound states, and a somewhat heavier (≈ 95 MeV) *s* quark, explaining the so called strange hadrons. The property that distinguishes the different quark types is called *flavour*. The lightness of these quarks gives rise to a special symmetry, called *chiral symmetry*. It coins the spectrum of the very light hadrons by a very special mechanism, denoted as *spontaneous symmetry breaking*, cf. p. 19.

It is fascinating to reconcile that the clue for the quark story was not derived from studies of strong interacting physics. Rather *weak* interaction processes delivered compelling arguments that further quark flavours must exist. Two *lepton* families were known those days: the electron *e* together with its associated neutrino, (*e*, ν_e), and the muon and its neutrino (μ , ν_μ), respectively. These families should have corresponding partner families in the quark sector, each consisting of two quark flavours. The missing link was indeed soon provided by the observation of a very heavy meson with unexpected long lifetime: the famous “*J/ψ* meson”. It established the existence of the *c* (“charm”) quark with a mass of about 1.2 GeV as the partner of the *s* quark. The existence of an as yet unknown third quark-lepton family was even postulated. The argumentation based on intricate symmetry considerations in connection with certain symmetry violating weak-decay processes, known as CP violation.² Indeed both, a very heavy lepton, called “*τ* lepton”,

¹ It became customary to quote the masses in terms of the energy needed to create that mass, i.e. in MeV= 10^6 eV (mega electron volt) or GeV= 10^9 eV (giga electron volt). For example comparison the masses of electron, proton and neutron are 0.511, 938.3 and 939.6 MeV, respectively.

² The CP-symmetry refers to the symmetry with respect to the simultaneous particle-antiparticle conjugation, normally referred to as “charge conjugation” (C), and the reflec-

as well as two further very heavy quark flavours, with symbols b (for “bottom” or “beauty”) and t (for “top” or “truth”), were then experimentally verified in the following years. These theoretical and experimental successes, awarded by several Nobel prices, founded the nowadays accepted *Standard Model of Particle Physics* with its three quark-lepton families.

What is not directly manifest in the spectrum of hadrons, though, is the way the quarks interact strongly with each other. Here again symmetry arguments gave the hint: the *strong* charge has to come in three different varieties, referred to as *colours* (a term that has nothing to do with our visual perception). Although initially not intended, this nomenclature provides a convenient association: the combination of two or more strong charges resembles the mixing of ordinary colours. In particular, the confinement property requires the total strong charge of any hadron to vanish (i.e. to be “colour neutral” or “white”). Thus, the three colour charges of the constituent quarks in a baryon have to cancel each other, while for mesons the colour charges of the quark and its antiquark partner have to be opposite (“complementary”).

The resulting fundamental theory describing the strong interaction is therefore named *Quantum Chromodynamics* (QCD) – from the Greek word $\chi\rho\omega\mu\alpha$ meaning colour. In analogy with QED, the elementary particles, here quarks and antiquarks, interact via bosonic gauge fields. These quanta are called *gluons*, since they serve to “glue” the quarks together. While there is only one type of photon in QED, which is electrically neutral, in QCD there is an octet of gluons, corresponding to the various elementary ways of transforming one colour into another.³ The gluons themselves also carry colour charge, which permits them to also interact among themselves, a property which is believed to ultimately be responsible for confinement.

While the strong and the electromagnetic interactions conserve the total net flavours (flavour minus antiflavour), the weak interaction can change the flavour on time scales that are typically sub-nano seconds. Due to the dramatic drop in temperature during the very early evolution of the universe, all initially created heavy-flavour hadrons quickly decayed into up and down flavours and the electrons as present in the stable matter around us today. The further expansion and cooling led to a plasma of very light nuclei (predominantly protons) and electrons, which subsequently combined into electrically neutral atoms (mostly hydrogen) only about 300,000 years later. First galaxies were finally formed after a further few hundred million years.

Parallel to the advances at the elementary level, significant progress was achieved in the understanding of many-body systems such as macroscopic matter. As known from our daily life, a given substance, such as water, can appear in various forms (called *phases*). Depending on the ambient pres-

tion in space denoted as “parity” (P). This symmetry was observed to be violated in certain weak decay processes.

³ One might naively have expected there to be nine types of gluon, three colours times three anticolours. However the colour neutral combination must be excluded, leaving eight independent transformations.

sure and temperature water exists in the form of vapour, liquid and solid. The preference for one phase over another results from the interplay of the binding forces between the constituents (e.g. the water molecules), which tend to organise the system into regular structures, and the thermal motion, which drives the system towards disorder. Any given thermodynamic condition usually favours one particular phase over the others. Therefore, by changing the thermodynamic parameters (i.e. the temperature (T), pressure (p), etc.), one can control which phase is preferred and cause the substance to undergo corresponding phase transformations. These properties are conveniently summarised in a *phase diagram*, which delineates the various phases of the substance as a function of the thermodynamic variables, much like a map shows the areas of various countries.

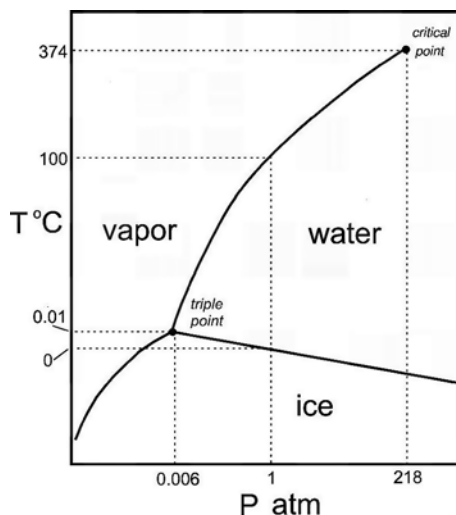


Fig. 1 Phase diagram for water delineating the thermodynamic domains of the familiar gas, liquid and solid phases in the temperature (T) versus pressure (p) presentation (the scales are *not* linear). The three phase boundaries come together at the *triple point*, situated just above 0°C , while the liquid-gas phase boundary terminates at the *critical point*; above the critical temperature there is a smooth transition from the liquid to the vapour phase. [The figure was adapted from http://serc.carleton.edu/research_education/equilibria/phaserule.html.]

The phase diagram of water with its three phases of vapour, liquid and (one of several forms of) ice is illustrated in Fig. 1 in the (p, T) plane. Each point on the phase diagram represents a large uniform and thermally equilibrated system of the particular substance at the specified values of pressure p and temperature T . Neighbouring points located on opposite sides of a phase border line represent different phase configurations with the same pressure and temperature which can *coexist*, i.e. they can be simultaneously present under the same thermodynamic conditions. However, they differ in their microscopic

organisation and, as a result, they generally have different particle or energy densities. In the latter case one talks about a *first order phase transition*. The crossing of such a phase boundary, i.e. transforming the substance from one phase to the other (such as the change of water into vapour), requires the supply or removal of a certain amount of energy (called the *latent heat*) as well as some degree of compression or expansion. Furthermore, for thermodynamic conditions along a phase boundary the substance will generally appear as a *phase mixture*, e.g. with droplets of the high-density phase immersed in the low-density phase or vice versa. For water, ordinary fog represents such a phase mixture, situated somewhere along the upper-right phase-boundary line in Fig. 1, where liquid droplets coexist with the vapour. However, the particular geometrical organisation of such phase mixtures (e.g. the droplet sizes) depends on specific properties beyond those of uniform matter, such as the surface tension, and cannot be depicted on a standard thermodynamic phase diagram.

A phase separation line may end in a so called *critical end point*, where the differences between coexisting phases cease. The study of the physical properties of a substance under thermodynamic conditions close to the critical point has been a central research interest for decades in condensed matter physics. Systems show some universal behaviour that permits different substances to be classified into certain *universality classes*. Beyond the critical point there is a smooth *crossover* between the phases. This occurs for water, which has a liquid-vapour critical point situated near the upper-right corner of Fig. 1. Furthermore, the simultaneous coexistence of three phases occurs when three phase boundary lines come together in a *triple point*, as it happens for water (see Fig. 1).

Besides the familiar three phases discussed above (gaseous, liquid, and solid) nature exhibits several more phases of matter. Of particular importance in the context of this book is the *plasma* phase, which can be formed at high densities or pressures. Under such conditions the normally electrically neutral atoms (or molecules) of a gas become ionised as some of their outer electrons become unbound and mobile. The electromagnetic forces between these charged constituents are then of primary importance. These conditions are encountered during an electric discharge, in the interior of stars such as our sun, or in large gaseous planets like Jupiter and Saturn.

In addition to the phases discussed above, which principally concern the spatial organisation of the constituents of a system, there are also phase transformations associated with internal degrees of freedom, such as the spin of the constituents. Perhaps the most familiar example of such a phenomenon is *ferromagnetism*, known since ancient times and manifested by the spontaneous magnetisation of certain materials (such as iron) when cooled below the so-called Curie temperature. Another more modern example is superconductivity, the sudden drastic drop of the electric resistance in a conducting material, when its temperature is brought below a critical value.

Both of those examples are particularly relevant to the present discussion. They represent common place illustrations of the concept of *spontaneous symmetry breaking*, a phenomenon that plays a fundamental role in the standard model of particle physics. For the case of a ferromagnet, the thermal preference for disorder prevails at high temperature and the individual spins of the constituents have random orientations. At low temperature, however, the attraction between parallel spins overwhelms the thermal noise and causes the spins to become mutually aligned. It should be noted that even though the basic interactions favour no particular direction, the system automatically settles into one particular (not a priori determined) orientation, thus spontaneously breaking the rotational symmetry. Furthermore, because differently oriented aligned states have the same energy, it takes essentially no energy to introduce a gentle spin wave into an aligned system (see Fig. 2). There is thus no lower bound in the excitation spectrum (it is *gapless*), a characteristic feature of phases exhibiting spontaneous breaking of a continuous symmetry.

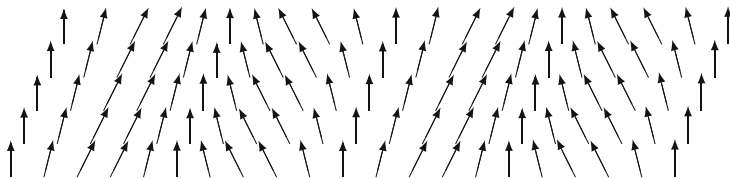


Fig. 2 Illustration of a spin wave in the spontaneously broken phase where all the individual spins are (approximately) aligned along a common (here vertical) direction.

Common to all phase transitions is that symmetry considerations play an import role in characterising the properties of the phase transition. Different substances with identical symmetry properties generally exhibit similar phase-transition behaviours particularly in the vicinity of the critical point.

An important facet of matter concerns its response to external perturbations such as the application of electric and magnetic fields. Often a given material responds quite differently from what would be naively expected from the properties of its constituents. For example, although the elementary carriers of the electric current in matter are negatively charged electrons, there are materials whose electric properties are most conveniently described as if the mobile particles carry a positive charge. This phenomenon has led to the notion of *quasi-particles*, dynamical entities that behave like particles with modified properties: a particle moving through matter interacts with the surrounding particles and polarises the medium. The resulting *collective* excitation can be effectively expressed as if the perturbing particle had acquired a modified mass and/or charge. A widely known example of such a phenomenon is the change of the index of refraction in a dielectric medium, such as glass or water. In the medium, a photon of given frequency propagates with a different velocity than in vacuum, with the consequence that

a light ray will be deflected in the medium relative to its direction outside. Moreover, in bulk matter, excitation modes exist that behave similar to particles or waves, such as e.g. spin waves or acoustic waves (called *phonons*), although they have no counter part in the spectrum of the stable particles.

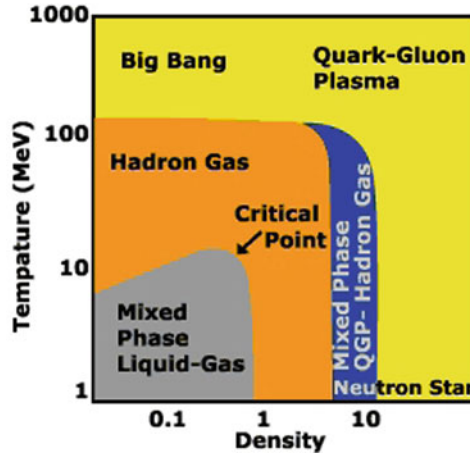


Fig. 3 The hypothetical phase diagram for strongly interacting matter in the plane of net baryon density (in units of the nuclear bulk density) and temperature (in MeV), both scales being logarithmic. At low temperatures, nuclear matter has a liquid-gas type phase transition and the corresponding region of phase coexistence is highlighted (*grey*). When the temperature and/or (net) density is raised sufficiently, the hadrons dissolve into a quark-gluon plasma. At low temperature, the deconfinement transition is presumably of first order with an associated region of phase coexistence (*blue*), whereas a smooth crossover happens at low density. Also the matter conditions prevailing during the Big Bang or existing in the interior of neutron stars are indicated. [The figure is from <http://www.lbl.gov/abc/wallchart/chapters/09/0.html>.]

In the present book we are interested in matter governed by the *strong force*, rather than the matter encountered in our ordinary terrestrial world, which is bound by the electromagnetic force. One form of such matter, though at zero temperature, exists inside large atomic nuclei and is referred to as *nuclear matter*. The associated scales of force and density exceed the familiar scales of ordinary terrestrial matter by more than twelve orders of magnitude (i.e. by factors beyond 10^{12}). In order to obtain such densities one would have to compress our planet into a sphere of less than a few hundred meters in diameter. The typical binding forces in nuclear matter are in the range of $\sim 10 \text{ MeV/fm} = 10^{22} \text{ eV/m}$, which vastly exceeds the typical strength of chemical bonds between atoms, $\sim 10^9 \text{ eV/m}$. Nuclear matter of even higher densities exists in the interior of compact (neutron) stars. Furthermore, strongly interacting matter in the form of a hot *quark-gluon plasma* (QGP) prevailed during the first microseconds of the early universe.]

Many of the various facets of normal matter discussed above are also expected to appear in the strong-interaction regime, i.e. in QCD matter. In particular, different phases are expected to occur as the temperature and density are changed as illustrated in Fig. 3. Together with the change of the matter conditions, the properties of particles moving through the matter are also expected to be strongly modified.

It is a characteristic feature of QCD that the mutual coupling between quarks and gluons decreases as the collision energy is raised, a property referred to as *asymptotic freedom*. Because of this inherent feature, one expects that the quarks and gluons will essentially become free in matter at very high temperatures T . Far before this asymptotic scenario, already at temperatures of $T \approx 150\text{--}200\text{ MeV}$, conditions are reached where the hadrons dissolve into individual quarks forming a *quark-gluon plasma*. Similar to an ordinary plasma, the colour charged particles (quarks, antiquarks and gluons) can then move throughout the entire volume of the system. Our current understanding of QCD suggests that this transformation occurs in a smooth manner as the temperature is raised, provided that the net baryon density ρ or the associated chemical potential μ is small. However, at large values of ρ (or μ) one expects a true phase transition from a confined (hadronic) to a deconfined (plasma) phase. It is a major goal of the compressed baryonic matter (CBM) experiment to investigate these phenomena. The associated critical point forms a natural focus for these efforts.

At very low temperatures and densities the confined phase primarily consists of individual nucleons and a few very light composite nuclei. As the density is raised, nuclear liquid becomes the favoured state. The associated liquid-gas phase transition is of first order. It has been the subject of extensive experimental investigations in the 1980s and 1990s. At densities significantly larger than those in ordinary nuclei (possibly present in the interior of neutron stars), one may encounter a variety of ordered phases with novel properties, most notably colour charge superconductors. Unfortunately, it appears to be unlikely that these dense but relatively cold phases could be produced in collision experiments, in which large compressions tend to be accompanied by large temperatures.

A particularly important symmetry in particle physics is *chirality* (from the Greek word $\chi\epsilon\iota\rho$ meaning *hand*), which characterises the orientation of a particle's internal spin relative to its direction of motion. As illustrated in Fig. 4, a quark's spin can be oriented either along its velocity (giving it a



Fig. 4 Illustration of left- and right-handed quarks: the direction of motion is given by the *black arrows*, while the direction of the spin rotation is given by the *curved arrows*; for left- or right-handed particles the spin direction is anti-parallel or parallel to the direction of motion, respectively.

right-handed chirality) or in the opposite direction (giving it a left-handed chirality). In the sector of *up* and *down* flavours the basic QCD interaction has approximate *chiral symmetry*, because the masses of the *u* and *d* quarks nearly vanish. One might therefore expect that the resulting hadrons (bound solutions to the QCD field equations) would reflect this property by appearing in (approximately) degenerate chiral pairs.

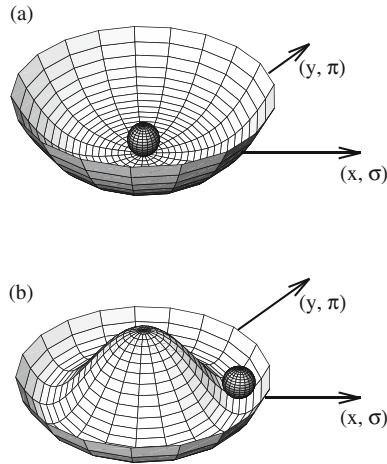


Fig. 5 Pictorial representation of spontaneous symmetry breaking in terms of a ball moving in a rotationally symmetric potential, assuming that this “effective” potential can change with temperature. At high temperature (*top*) the ball achieves its stable position in the potential minimum which is located at the centre: so the equilibrium configuration preserves the symmetry. Towards low temperatures (*bottom*) the effective potential changes its form taking the shape of a *sombrero*, or a “Mexican hat”, thus energetically disfavoring the central region. While the potential is still rotationally symmetric, the ball has to spontaneously settle in an asymmetric configuration at the bottom of the potential. [The figure is from V. Koch, Int. J. Mod. Phys. **E6** 203-250 (1997).]

However, this is not what is found in nature, where the chiral partners exhibit large mass differences. This apparent paradox was resolved by a mechanism analogous to the spontaneous magnetisation of a ferromagnet below the Curie temperature (illustrated in Fig. 5), namely the concept of spontaneous breaking of chiral symmetry. Then the earlier discussed gap-less feature of the ideal excitation spectrum suggests the existence of certain modes related to chiral symmetry that are nearly massless. Such modes indeed exist in the form of the π mesons (*pions*), whose masses ($m_\pi \approx 140 \text{ MeV}$) are abnormally small. The fact that the pion masses are non zero is due to the small but finite masses of the *u* and *d* quarks which explicitly break the symmetry. This leads to a slight preference for one particular chiral direction, much like the tendency of ferromagnetic material to align its magnetisation with the orientation of an externally applied magnetic field. In the bottom picture

of Fig. 5 this explicit symmetry breaking is achieved by slightly tilting the Mexican hat, which defines a minimum at a preferred position due to a “soft” restoring force along the bottom of the potential. The concept of chiral symmetry, even extended to include the relatively light strange quark, turns out to be a powerful tool for understanding the mass spectrum of light hadrons.

With respect to the properties of hadronic matter, the chirally broken phase occurs at low temperatures and/or low densities of the phase diagram. Much like the spontaneous magnetisation in a ferromagnet, though, it is expected that the chiral symmetry breaking will gradually weaken as the temperature or the density is increased. This eventually leads to novel phases of strongly interacting matter in which chiral symmetry is (approximately) restored. Such a change in the hadronic environment causes dramatic modifications in the hadronic excitation spectrum. In particular, in the chirally restored phase the mass distributions of chiral partners would become (nearly) identical. Furthermore there are conjectures that the chiral transition may occur in close proximity to, or even simultaneously with, the deconfinement–confinement transition.

In addition to the fundamental aspects raised above, experimental investigations of compressed baryonic matter would also elucidate a number of astrophysical issues: What does matter look like under the very large gravitational pressure in the interior of neutron stars? Do nucleons still exist there or does matter melt into matter of quarks? What limits the total mass of a neutron star? How does a *super nova* collapse and the subsequent explosion of the burnt out star evolve? Do such processes create the composition of elements that we find in our planetary system?

The opportunity to analyse such forms of matter in all its facets in the laboratory is truly fascinating. However, it is not as straight forward as the investigation of ordinary matter. Neither are there appropriate vessels to contain this kind of matter and to exert pressure on it, nor is there any standard flame that could heat it. The only possibility is to collide two heavy nuclei, so that they inter-penetrate and compress but also heat each other due to the microscopic collisions (see Fig. 6). Still, the analysis of such collision events is intricate due to the transient nature of the reaction, where the object of interest, the compressed and heated zone is of finite small size and fades away in the very short time of less than 10^{-22} s. Furthermore, there is no light by which one can illuminate the collision scene in order to watch and record the event, like with a movie camera, as we are used in daily life observations. Rather the only observation comes through the reaction products themselves, i.e. the particles emitted from the reaction zone into the detectors. Thereby the different nature of the various particle species can provide information on different aspects of the collision event. The most abundant particles produced are hadrons. Due to their strong interactions with their environment, they tend to quickly adjust to the evolving conditions and therefore mostly reflect the conditions that prevailed during the later stages of the collision event. However, there are also electromagnetic “flashes” of photons and pairs of elec-

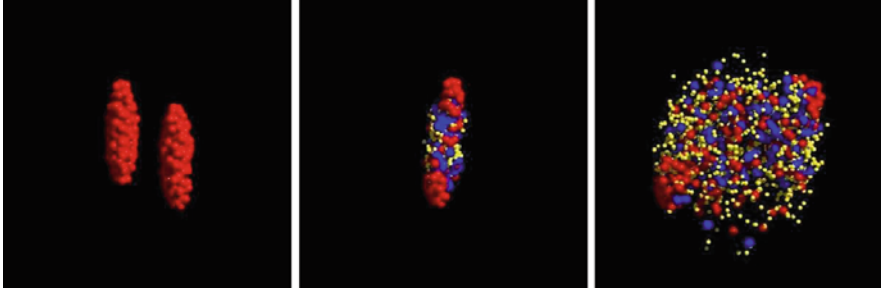


Fig. 6 Three snapshots illustrating a nuclear collision of two uranium nuclei in a future CBM experiment with a projectile energy per nucleon of 23 GeV on a fixed target. The snapshots are taken in the reference frame in which both nuclei have the same but opposite velocities. *Left frame:* The two incident nuclei (with the incident nucleons in *red*) are Lorentz contracted as the incident velocities are already close to the speed of light. The *middle frame* shows the moment of highest compression, i.e. the configuration of interest, while the *right frame* displays the expansion stage, when most of the particles already no longer interact strongly. The final situation is called *freeze-out*. The newly created baryon resonances are in *dark blue*, while the created mesons are given in *yellow color*. The pictures resulting from a simulation code calculation are extracted from a movie on <http://th.physik.uni-frankfurt.de/~weber/CERNmovies/>.

trons and positrons emitted that are hardly affected at all during their propagation through the collision zone. Since these so-called *penetrating probes* tend to be produced primarily when and where the system is hottest, they are particularly suited as “messengers” of this stage.

In order to perform such experiments, accelerators are needed that are capable of accelerating atomic nuclei to the desired energies. The most efficient workhorses in this respect are *synchrotrons*. These are circular accelerators that work a bit like hammer throwers, operating at more than a million turns per second. In each turn the ionised atoms gain further energy through alternating electric fields, while magnets with synchronised field strengths hold them on their circular orbits inside the ring. Once the desired beam energy is reached, a short pulse of ions is directed onto a suitable target, usually a foil sufficiently thin to ensure that the collisions occur at time intervals long enough to permit the detection system to complete the event recording. The construction of a modern heavy-ion accelerator facility is a complex project that challenges the frontiers of science, technology and engineering. The variety of physical conditions opened to experimental exploration has steadily grown as the accelerators have become ever more powerful and the associated detectors have acquired ever more sophisticated capabilities.

The field of high-energy nuclear collisions, often called relativistic heavy-ion physics, originally evolved around the BEVALAC facility at the Lawrence Berkeley Laboratory in the 1970s. Subsequently, beams of higher quality and intensity became available in the same energy range of 1–2 GeV at GSI in Darmstadt (SIS 18). At these energies it was possible to study hot and com-

pressed matter within the confined phase region only. The deconfined region could not be probed until it became possible to generate ultra-relativistic beams, where the kinetic energies of the particles far exceeded their rest masses, as first achieved at the Brookhaven AGS and at the CERN SPS. In all of these early experiments the accelerated nuclei were bombarded on a stationary target as explained above. Much higher effective collision energies can be achieved with a so-called collider, in which two beams collide head-on. Over the past several years, the main experimental activity in the field has occurred at the Brookhaven Relativistic Heavy Ion Collider (RHIC). Even much higher collision energies will soon be available at the CERN Large Hadron Collider (LHC).

In collisions at the very high energies characteristic of the collider facilities, a large number of newly created particles will fill the collision zone which by far surpasses the number of incident particles. As the newly created particles are balanced with respect to their matter–antimatter content, the net baryon density is relatively small in such matter. Therefore one explores the baryon-poor (but very hot) region of the phase diagram (Fig. 3), where a cross-over transition from the quark-gluon plasma to the hadron gas is expected.

Complementary to the research activities at the colliders, there is a strong scientific interest to explore the first-order phase transition region and the critical end point. For this purpose one needs to generate collision events that lead to much higher net baryon densities at relatively moderate temperatures. It follows from the above discussion that such matter is best investigated at lower collision energies, where the degree of stopping is then larger, and the amount of newly produced particles is less. There are currently several efforts underway worldwide towards this goal. In particular, a planned energy scan at RHIC will carry out a series of measurements at the lowest possible collision energies for the primary purpose of finding evidence of the expected critical end point. Furthermore, the Facility for Antiproton and Ion Research (FAIR) soon being constructed at GSI (see Fig. 7) will offer nuclear beams of unprecedented quality and intensity. At one of the experimental sites a dedicated detection system, the CBM detector (see Fig. 8), will be built for the purpose of studying compressed baryonic matter, in particular to search for the expected first-order phase transition. Finally, vigorous planning is in progress at JINR in Dubna, Russia, for the construction of a Nuclotron-based Ion Collider fAcility (NICA) for the purpose of studying strongly interacting matter in the mixed phase.

The nuclear beams for the CBM experiment, like the beams for other users at FAIR, will originate from an ion source at GSI. The ions are first sent through and pre-accelerated by the existing UNILAC/SIS-18 facility, displayed on the left side of Fig. 7, before being injected into the new double synchrotron SIS 100/300 (upper right portion of the diagram in Fig. 7), which will have a circumference of 1,100 m.

A single high-energy nucleus–nucleus collision at RHIC or LHC typically produces thousands of reaction products. Even at the lower energies rele-

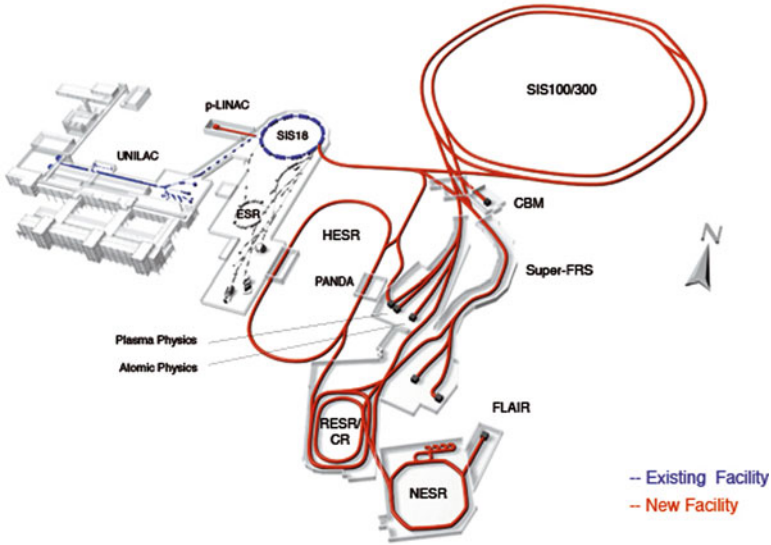


Fig. 7 FAIR, the new Facility for Antiproton and Ion Research under construction at GSI. The double synchrotron SIS 100/300 directly provides the nuclear beams for the CBM experiment. In parallel operation it can also feed complementary experiments with beams, where mostly secondary beams of antiprotons or rare nuclear isotopes are produced by means of a production target, filtered by the new fragment separator (super FRS) and subsequently stored and further manipulated in special purpose storage rings, such as the HESR for antiproton research at the PANDA detector or for Nuclear structure and atomic and plasma physics investigations at the other rings.

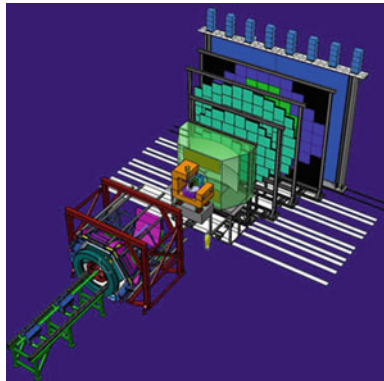


Fig. 8 The detector complex planned for the CBM (Compressed Baryonic Matter) experiment at FAIR. Some explanations are given in the text. The complete detector description can be found in [Part V, Chap. 2](#).

vant for exploring the high-density region there will typically be hundreds of particles per collision event – mostly neutrons, protons and pions. The experimental task of detecting these reaction products, i.e. identifying their species and measuring their mass, energy and emission angle, requires a detection system that is optimised for the specific physics objective. The proposed CBM detector is shown schematically in Fig. 8. It is a multi-particle detector, which is able to resolve and to detect most of the particles simultaneously emitted in a collision event. It consists of several detector layers, each serving a different purpose for the complex detection strategy. It enables to trace rare probes such as particles carrying multiple strangeness or charm quarks. It is further capable of singling out the extremely rare electron–positron or muon pairs, that carry the message from the hottest part of the collision zone.

It is obviously a difficult task to anticipate the outcome of such collisions, to identify the novel physics phenomena that may occur, and to determine how they are best observed. In an attempt to provide a useful resource for this challenging endeavour, the present book reviews the status of the field, discusses important recent developments, and outlines future prospects and perspectives, as well as important theoretical challenges. The highlights of the various parts of this book are summarised in the subsequent “Executive Summary”. [Part I](#) concentrates on topics related to the bulk properties of strongly interacting matter, its phase structure and the equation of state. [Part II](#) considers medium modifications of hadrons travelling through such a medium. [Part III](#) discusses the various dynamical treatments developed for the description of the collision dynamics. Relevant experimental observations and their physical interpretations, together with specific predictions for the CBM experiment are reviewed in [Part IV](#). Finally [Part V](#) describes the technical aspects of the CBM detector complex.

Executive summary

The purpose of this book is to describe our present understanding of the physics of hot and dense strongly interacting matter, with emphasis on aspects relevant for the planned nuclear-collision experiments in the intermediate beam energy range of 10–50 AGeV, as seen in the target rest frame. Such experiments are foreseen at RHIC (BNL, USA), FAIR (GSI, Germany) as well as NICA (JINR, Russia). It is expected that nuclear collisions at these energies will produce matter at moderate temperatures and high baryon densities. These research programs present unprecedented opportunities for exploring the phase diagram of Quantum Chromodynamics (QCD) at densities and temperatures complementary to those probed in nuclear collisions at the highest energies at RHIC and LHC. In particular, in the indicated energy range, it is expected that the properties of hot hadronic matter and of the deconfinement/chiral phase transition can be probed at the highest baryon densities available in laboratory experiments.

The topics addressed in this book are organized into five main parts, preceded by an elementary introduction to the properties of strongly interacting matter at high densities and temperatures and to the relevant experiments (*Facets of Matter*). First the properties of strongly interacting matter in thermal equilibrium are addressed in [Part I](#), while the in-medium properties of particles and excitation modes in such systems are discussed in [Part II](#). The theoretical tools required for describing the transient dynamical situations of the nuclear collision experiments are presented in [Part III](#). They provide the bridge between the bulk matter properties on the one hand, and the experimentally observed data on the other. The data aspects are discussed in [Part IV](#), where besides the results from dynamical models for already completed experiments also predictions for the planned future experiments are discussed. Finally, in [Part V](#) the conceptual designs for the projected second-generation type experiments in this beam-energy range are presented. This part also includes an appendix summarising the various first-generation experiments at AGS, SPS and RHIC.

I BULK PROPERTIES OF STRONGLY INTERACTING MATTER

A unified theoretical description of the thermodynamics of strongly interacting matter at all densities and temperatures does not yet exist. Our present understanding of this subject is based on results obtained with a variety of approaches ranging from systematic solutions of QCD on a computational lattice to effective models that exhibit some of the relevant symmetries of QCD.

Symmetries play a crucial role in the classification of the various phases and phase transitions. An instructive example is provided by the approximate chiral symmetry of QCD, which arises from the smallness of the masses of

the u and d quarks. Chiral symmetry is spontaneously broken at low temperatures and densities and thereby plays a crucial role in the generation of hadron masses, leading to a significant mass splitting of the so-called chiral partners (such as the ρ and a_1 mesons), which would otherwise be degenerate. The spontaneous breaking of chiral symmetry is reflected in a non-vanishing expectation value of the quark condensate. In strongly interacting matter at sufficiently high values of the temperature and/or density chiral symmetry is restored and, accordingly, the quark condensate is very small. Thus, the quark condensate is an order parameter that characterizes the spontaneous breaking of chiral symmetry. Because the u and d masses are in fact not strictly zero, chiral symmetry is not exact and, consequently, the chiral phase transformation is generically not of second order. At finite temperature and vanishing baryon density it is most likely of the crossover type, similar to the gradual ionization of a gas (leading to an electromagnetic plasma) as the temperature is raised. Model calculations suggest that at low temperatures and finite baryon densities the transition is of first order. Consequently, there should be a critical end point somewhere in the plane of temperature and baryo-chemical potential.

The deconfinement phase transformation is also related to an approximate global symmetry, namely the center symmetry of the color gauge group (the center of the $SU(3)$ group is $Z(3)$). This symmetry is exact for infinitely heavy quarks but only approximate for physical quark masses. A suitable order parameter for the deconfinement transformation is the so-called Polyakov loop, which is related to the free energy of a single quark. The $Z(3)$ symmetry is broken in the deconfined phase and the order parameter is non-vanishing, while it is restored in the confined phase where the order parameter vanishes.

So far lattice QCD simulations are well established at vanishing baryon chemical potential μ_B . First results for finite but still small μ_B have recently been obtained using various methods for extrapolating from $\mu_B = 0$. At low temperatures and densities systematic calculations involving a low-temperature and low-density expansion are available in the framework of chiral perturbation theory. Conversely, at very high temperatures and/or baryon chemical potentials QCD is, due to asymptotic freedom, weakly interacting and perturbative calculations of thermodynamic functions become applicable. Unfortunately, at the densities and temperatures of interest here, neither of these methods can be applied with confidence. Consequently, much of our present understanding of hot and dense matter is based on results obtained in various effective models. Although some of these models are constrained by the model-independent results obtained in lattice QCD, chiral perturbation theory and perturbative QCD, the predictions at temperatures near the expected deconfinement/chiral transition, in particular at non-zero densities, remain model dependent. Consequently, progress in this field requires intensive exchanges between theory and experiment as well as the development of novel theoretical methods for describing the truly non-perturbative phenomena of strongly interacting matter near the phase transition.

Chapter 2 introduces QCD and the thermodynamics of strongly interacting matter. The relevant symmetries of the QCD Lagrangian are identified and the systematic approaches as well as the models used to describe the thermodynamics of QCD are presented. The general features of thermodynamics of phase transitions are also discussed and universality arguments that can be used to classify phase transitions based on their symmetry breaking pattern are applied to the QCD phase transformations. Then, in Chap. 3, systematic approaches to the thermodynamics of strongly interacting matter are introduced and subsequently Chap. 4 discusses a variety of models used for the description of strongly interacting matter near deconfinement.

II IN-MEDIUM EXCITATIONS

The symmetries of QCD are essential not only for characterizing its phase diagram but also for determining its spectrum of excitations. In Part II the properties of in-medium excitations are discussed and utilized to link observables with symmetry and transport properties of QCD at finite temperature and density. One basic idea is that the spontaneous breaking of chiral symmetry (SBCS) is reflected in the properties of hadrons. Thus, by studying hadron properties in matter one can explore the (partial) restoration of the chiral symmetry including, e.g., the connections to hadronic mass generation. Another central idea is to use (hadrons containing) the heavier strange and charm quarks to access (chemical and kinetic) transport properties of the QCD medium.

The in-medium modifications of hadrons are best explored with so-called *penetrating* (electromagnetic) probes, since they escape essentially unaffected from the strongly interacting medium. The relations of dileptons and photons to the in-medium properties of hadrons are discussed in Chap. 2. The light vector mesons ρ , ω and ϕ play a special role due to their direct decay into dileptons (e^+e^- or $\mu^+\mu^-$ pairs). The dilepton production rate probes the in-medium current-current correlation function, which is sensitive to the in-medium spectral functions of the vector mesons. Thus, the dilepton invariant-mass spectrum, measured in heavy-ion collisions, is expected to unveil the in-medium properties of the light vector mesons.

The ρ meson has been at the center of attention because it is short lived and hence likely to decay inside the medium, and because of its strong connection with chiral symmetry. However, since experimental access to the chiral partner of the ρ meson, the a_1 meson, in the medium is extremely difficult, one has to resort to other means to clarify the characteristics of chiral symmetry restoration. A basic problem here is that the fate of e.g. the ρ meson mass spectrum in matter is not uniquely determined by chiral symmetry. Hence, various effective hadronic models, satisfying constraints of chiral symmetry, can imply different dynamics and therefore predict different properties of the

ρ mass spectrum at finite temperature and density. A program is outlined which utilizes chiral sum rules to connect chiral order parameters (as evaluated, e.g., in lattice QCD) with in-medium ρ and a_1 properties computed within effective models which, in turn, can be tested in dilepton experiments. Eventually, hadronic spectral functions may be computed directly from lattice QCD.

Much progress has been achieved in recent years. It is discussed how a large variety of constraints, derived e.g. from QCD sum rules and from elementary reactions on ground-state nuclei, are implemented into effective hadronic models presently employed to compute dilepton production rates. These approaches yield a broadening (and ultimately “melting”) of the ρ meson spectral function without an appreciable shift of its mass. This is in contrast to the vector manifestation approach, where both the ρ mass and its coupling to dileptons approach zero as chiral symmetry restores. The close connection to production rates for single photons (and, to a lesser extent, to photon pairs) is pointed out. The enhancement of dileptons found in nucleus–nucleus collisions is largely consistent with the broadening scenario, and, in particular, identifies baryons as the prevalent source of medium effects. This implies that the energy range of FAIR, where baryon-rich matter is produced, appears ideal for the next generation of dilepton experiments.

Chapter 3 discusses the spectroscopy of hadronic resonances in the light quark (u, d) sector. The in-medium mass distribution of the $\Delta(1232)$, $\rho(770)$ and possibly “ $\sigma(500)$ ”, close to the freeze-out transition, may be observed via the invariant-mass spectra of the decay products. Such data could provide information complementary to that obtained from the penetrating probes, in particular from the dilepton spectrum of the ρ meson. For the Δ resonance $\pi^\pm p$ invariant-mass spectra have been measured at BEVALAC/SIS and RHIC energies, without conclusive evidence for the relevance of medium effects. Such an analysis is rather challenging due to large backgrounds and resonance widths, combined with phase space and rescattering effects. This also applies to $\pi^+\pi^-$ spectra which are particularly interesting due to the close connection of ρ and σ mesons to chiral symmetry.

The role of strangeness is addressed in Chap. 4. The strange (s) quark is considerably more massive than u and d quarks. However, on the scale of SBSCS, the s quark may be considered light and therefore treated on the same footing as u and d quarks. In nuclear collisions, however, s quarks differ in an important aspect from u and d in that there are essentially no s and \bar{s} in the initial state. Strangeness-carrying hadrons in the final state have to be produced in the collision, rendering them an important messenger of flavor chemistry in nuclear reactions. For example, the production of strangeness is expected to be enhanced in a deconfined, chirally restored QGP, due to a much reduced mass threshold for (bare) $s\bar{s}$ pairs compared to, e.g., kaon-antikaon pairs. In nuclear collisions at AGS energies and above, the multiplicity of strange particles is consistent with the saturation of phase space, which is not the case in elementary hadron-hadron collisions. However, the

connection to QGP formation is still somewhat tentative since at this point other effects cannot be excluded from playing an important role in the chemical relaxation of the strangeness degrees of freedom. Chapter 4 focuses on in-medium modification of anti-/kaons and their coupling to baryonic excitations, which is particularly relevant close to the threshold for strangeness production, i.e., at SIS/BEVALAC energies. Analogous considerations may apply to charm production near threshold, to be explored at FAIR. (One should realize, however, that the timescales for strangeness and charm production are presumably rather different and thus the analogy may be of limited use.) A lowering of the \bar{K} energy in matter, as predicted by model calculations, implies an enhanced production in nucleus-nucleus collisions close to the production threshold. The observed enhancement of the \bar{K} multiplicity compared to elementary reactions at SIS energies is, at least on a qualitative level, consistent with this picture.

Chapters 5 and 6 address the physics of charm in nuclear collisions which plays a prominent role in the analysis of the produced medium. The c quark is heavy compared to the typical temperatures in the hot collision region. Consequently, the population of charm quarks ought to be determined in early hard collisions and remains unaffected by lower-energy secondary reactions in the QGP and in the hadronic phase. The number of charm quarks should therefore follow from an extrapolation of binary nucleon-nucleon collisions. At present, neither experimental proton-proton data nor perturbative QCD calculations can deliver the desired accuracy for the elementary production processes at the relevant collision energies near threshold.

As discussed in Chap. 5, if a reliable baseline for the initial spectra can be established, open charm is an ideal probe to study the transport properties of the medium and to possibly gain insight into hadronization mechanisms. Roughly speaking, the c quark is sufficiently light to undergo significant rescattering in the medium, yet heavy enough not to (fully) equilibrate, thus carrying information especially on the early phases of the medium produced in nuclear collisions. A theoretically appealing aspect is the possibility of a Brownian motion treatment of charm diffusion.

In Chap. 6 the study of hidden-charm bound states (charmonia) in nuclear collisions is presented. Charmonium production in nucleus-nucleus collisions is believed to probe the properties of the potential between two heavy quarks, as well as pertinent dissociation mechanisms. Originally, a suppressed production of J/ψ mesons was suggested as a signal of deconfinement, as a consequence of color-Debye screening melting the hidden-charm bound states. However, at present, the problem appears to be much more involved than anticipated. While significant suppressions have been observed at SPS and RHIC, their levels are very similar, despite an increase of the collision energy by more than an order of magnitude. It has been suggested that this is due to a competition between enhanced charmonium suppression, on the one hand, and charm coalescence becoming increasingly important at higher energies, on the other hand. Much activity is presently devoted to the problem of in-

medium charmonium properties in both lattice QCD and potential models, as described in Chap. 6. This work has advanced the understanding of color screening and melting of charmonia in a hot environment. Phenomenological applications are discussed in the framework of transport approaches including both dissociation and regeneration mechanisms. A more stringent connection between theory and phenomenology, and additional measurements at LHC and FAIR, will contribute to clarifying the fate of charmonia in the QGP and the relation to observables.

Finally, Chap. 7 discusses selected aspects of color-superconductivity, the state of matter expected at very high baryon densities and low temperatures. In particular, the excitation spectrum in a two-flavor color superconductor (2SC phase), as well as precritical phenomena in normal quark matter near the transition to the superconducting phase, are discussed. Other aspects of color superconductivity were explored in Sect. 3.5 of Part I.

III COLLISION DYNAMICS

Many of the theoretical concepts discussed in Parts I and II are formulated for idealised systems that are uniform in density and temperature and in global thermodynamic equilibrium. However, the experimental situation in relativistic nuclear collisions is very different. There one expects strong non-equilibrium effects, requiring non-equilibrium many-body approaches to describe the reaction dynamics and ultimately provide the bridge between the observables properties of the reaction products and those of the idealized uniform and static systems of strongly interacting matter. Since a full dynamical treatment of such collisions is intractable, one must resort to reduced schemes that are computationally practical. These range from kinetic transport models of the Boltzmann equation type on the microscopic level to macroscopic (multi) fluid approaches. In this part of the book, we review the various dynamical frameworks and models employed for the description of nuclear collisions, as well as the further conceptual developments needed for extending their applicability to the FAIR energy range.

The introductory chapter, Chap. 1, covers the general features, like collision geometry, typical time scales, the relevant degrees of freedom at various beam energies, as well as the achieved densities and the relation to the equation of state. Chapter 2 describes the simplest, and historically earliest, microscopic transport treatments, the so-called cascade models. There the participating particles move on straight trajectories, while accumulating the effects of sequential random binary collisions that are treated according to elementary cross sections. Later on, refinements based on perturbative QCD were introduced to compute the early highly non-equilibrium state of nuclear collisions at very high energies.

In the beginning of Chap. 3 the most commonly used transport approaches are presented. They rest on the Boltzmann-Uehling-Uhlenbeck equation, which includes an effective one-body field that governs the motion of the individual particles in between their binary collisions. The latter may be either Pauli suppressed (for fermions) or (less commonly) Bose enhanced (for bosons). Kinetic models of this type are well justified for dilute systems, where single-particle excitations are well approximated by quasiparticles of infinite lifetime. At collision energies above 1 A GeV hadron resonances with broad spectral widths will be produced. Also stable particles will acquire non-trivial spectral functions due to the high collision rates in the dense medium. Therefore a large portion of this chapter is devoted to the transport treatment of particles with broad spectral widths. This includes the derivation of generalized phase-space transport equation from the underlying quantum Kadanoff-Baym equations by means of a systematic gradient expansion, questions of detailed balance and unitarity, as well as issues of conservation laws. A further important facet of transport in dense systems is the relevance of multi-particle collisions. General aspects of this problem are discussed and various implementations are presented. Chapter 3 closes with descriptions of the various specific transport models which are presently used. After some general remarks on the technical issues, each model is briefly presented.

In Chap. 4 the attention is turned to many-body models, which are capable of retaining many-body correlations. The most extensively used versions for simulating nuclear collisions from low up to relativistic energies are the so called quantum molecular dynamics (QMD) models. In these treatments, the mean-field dynamics described above is replaced by classical many-body dynamics subjected to smooth two-body forces that can be density and momentum dependent. In order to obtain smooth phase-space densities, each particle is represented by a Gaussian in phase space, while the strong short-range part of the interactions is still represented by a collision term as in the Boltzmann treatments. True quantum mechanical schemes were developed on the basis of Slater determinants built from single-particle Gaussian wave packets. While these fermionic (FMD) or anti-symmetrised (AMD) molecular dynamics approaches are capable of delivering even quantitative results for nuclear structure and can be applied to low-energy collisions, applications to high-energy nuclear collisions are not foreseen.

Dynamical instabilities, such as those caused by phase transitions, may occur during the evolution. Such scenarios were addressed in the context of multi-fragmentation at lower beam energies, where the liquid-vapour phase transition causes the expanding system to condense into nuclear clusters of various sizes. In order to meet this challenge, a variety of dynamical schemes were developed that account for fluctuations beyond the average dynamics. Of particular importance are Boltzmann-Langevin and the Quantum-Langevin approaches. While their applications have so far been relatively limited, due to the significant computational requirements, such techniques may become important also for the dynamics related to the transition between the quark-gluon plasma and the hadronic resonance gas.

Macroscopic transport approaches in terms of fluid dynamical concepts are described in Chap. 5. They offer an alternative to the kinetic descriptions above discussed and provide a direct link between the equation of state (EoS) discussed in Part I and the collision dynamics. In ideal hydrodynamics, which assumes instantaneous local equilibration, the EoS is the only dynamical input needed. The corresponding evolution is then generally isentropic. However, there are circumstances where ideal hydrodynamics fails. One such situation occurs during the initial stage of the collision, where the bulk of the matter has the character of two counter-streaming hadronic or partonic currents. At high energies, the equilibration of such a system is within ideal hydrodynamics attained instantaneously in an idealized shock front, while a more realistic description involves a gradual approach to equilibrium. Another case concerns the dynamics of phase separation occurring when bulk matter evolves into a mechanically unstable state. In ideal fluid dynamics, the lack of a finite spatial scale precludes a proper treatment of such instabilities. A more realistic treatment is obtained by allowing for the finite relaxation time scales encoded in the coefficients of shear and bulk viscosity, as well as heat transport.

Various strategies have been developed to circumvent such problems. Particularly powerful are hybrid approaches that link kinetics with fluid dynamics and multi-fluid concepts that model the mutual thermalisation between the fluid components by a phenomenological dissipative coupling. Recently also viscous fluid dynamics treatments have been developed and applied. Fits to elliptic flow data from RHIC suggest a very small shear viscosity which has led to the expectation that the matter near the QCD phase boundary is strongly coupled. Non-equilibrium multi-fluid models can also accommodate a first-order phase transition from the quark-gluon plasma to the hadronic phase. Due to the reduction of the entropy density across the transition, the phase conversion takes time during which the volume significantly grows, new hadrons are created and the normal temperature drop due to the expansion is compensated by the release of latent heat. The resulting approximate chemical equilibration among the hadrons at the end of the transition has provided support for the use of thermal freeze-out models for the observed yields, cf. Part IV.

Once the system is dilute, the particles also decouple kinetically and become free. In most hydrodynamic calculations the decoupling is treated arbitrarily as a sudden freeze-out on a hyper-surface, a crude concept that is not void of deficiencies. Indeed recent progress indicates that a sudden freeze-out is not possible; the typical time scale that emerges for the freeze-out process is of the same order as the expansion time scale. A discussion of these developments is followed by a brief review on the use of final-state correlations for imaging of the source (HBT) in the context of the finite decoupling duration.

In Chap. 6 the characteristic dynamical behavior such as the various flow phenomena are discussed in some detail. In the last chapter the status of the field is briefly reviewed and perspectives for future developments as well as the challenges lying ahead are outlined.

IV OBSERVABLES AND PREDICTIONS

Progress in the exploration of hot and dense strongly interacting matter requires, on the one hand, a comprehensive set of high quality data, and on the other hand dynamical models that make contact between theoretical concepts and experimental observables. [Part IV](#) reviews the relevant experimental data, the corresponding results of simulations as well as predictions for observables that are not yet measured in the intermediate energy range. This part starts with an outline of the physics program of the Compressed Baryonic Matter (CBM) experiment at FAIR.

Chapter 2 gives an overview of our present knowledge of the QCD phase diagram. The challenging goal of the future experiments at RHIC and FAIR is to discover the most prominent landmarks of the QCD phase diagram - the theoretically anticipated first-order phase transition and the corresponding critical endpoint. Furthermore, the dependence on beam energy of the region in the phase diagram probed in nuclear collisions is discussed on a qualitative level.

The highlights of the experiments conducted so far at SIS, AGS, SPS and RHIC are presented in Chap. 3. In particular, data relevant for the extraction of the nuclear equation of state, data on strangeness production, studies of the fireball geometry using HBT correlations, data on collective flow, jet quenching as well as measurement of hadronic resonances are discussed.

The measured excitation function of hadron abundances is discussed and compared to results of various model calculations in Chap. 4. The general trend of particle yields can be understood in terms of a transition from baryon-dominated matter below to meson-dominated matter above the low SPS energy range. However, the observation of a sharply peaked structure in the ratio of strangeness-to-entropy as a function of energy cannot be reproduced by purely hadronic models.

In the same beam energy range, the excitation function of the inverse slope parameters of the transverse mass spectra of strange mesons measured in heavy-ion collisions exhibits a step-like structure which also is in disagreement with the expectations of hadronic models. Moreover, the inverse slope parameter rises with increasing mass of the particle species up to about the proton or Λ mass, and then drops for particles with higher masses such as Ω and charmonium. This observation indicates that the heavy particles containing strange and charm quarks are produced in the early (partonic) phase of the collision. These features of the transverse mass spectra are reviewed in Chap. 5.

The collective flow of particles is discussed in Chap. 6. At FAIR energies and above, the elliptic flow is driven by the pressure generated in the reaction volume and it is therefore a sensitive probe of the equation of state of strongly interacting matter. At RHIC energies the elliptic flow exhibits partonic collectivity, i.e. its strength scales with the number of constituent

quarks. Hydrodynamical calculations suggest that the elliptic flow disappears at the phase transition.

The data on lepton-pair production in nuclear collisions measured at the BEVALAC, at SIS, SPS and RHIC are presented in Chap. 7 together with various theoretical interpretations. The yields and invariant mass distributions of dileptons produced in proton–nucleus collisions are in agreement with the expected contributions from known lepton-pair sources such as vector mesons and other hadronic sources (the so called cocktail) – in the case of electron–positron pairs these include e.g. Dalitz decays of pions and Delta resonances. The dilepton invariant mass spectra obtained in nucleus–nucleus collisions, however, exhibit an enhancement above the cocktail in the mass range between 0.3 and 1 GeV/ c^2 , which is attributed to a broadening of the ρ meson mass distribution in the dense and hot nuclear medium. The slope of the transverse momentum distribution of the lepton pairs rises with increasing invariant mass up to about 1 GeV/ c^2 and then falls again, indicating a partonic source for lepton pairs with invariant masses above 1 GeV/ c^2 .

The production of charm in nuclear collisions is reviewed in Chap. 8. A significant suppression of J/ψ production relative to that obtained by scaling of proton–proton scattering is observed in central collisions of heavy nuclei at SPS and RHIC. Indeed, the suppression is larger than expected from extrapolation of the influence of cold nuclear matter. However, the theoretical interpretation of these results is subject of debate. On the one hand, within transport models, the suppression of both J/ψ and ψ' is attributed solely to collisions of the charmonium with comovers. On the other hand, the solution of kinetic rate equations within an expanding thermal fireball, suggest that interactions in the QGP are responsible for an important contribution to the dissociation of J/ψ . Furthermore, in models of the latter type, the suppression of ψ' mesons is mainly due to the decay into a pair of $D\bar{D}$ mesons in the hadronic phase, a process which requires a reduction of the D meson mass in the medium. The resulting ratio of J/ψ to D meson yields computed within a hadronic transport model (HSD) is larger than that obtained in the statistical hadronization model, where the yields of hadrons containing charmed quarks are determined by assuming canonical chemical equilibrium (the total number of charm quarks is fixed in the initial hard collisions) near the phase boundary. In order to narrow down the range of theoretical interpretations, data on open charm and on transverse spectra of charmed hadrons will be very valuable. For instance, the flow of D mesons encode information on the transport properties of open charm in strongly interacting matter, and, hence, on the dynamics of charm-carrying degrees of freedom in the fireball.

In Chap. 9, critical fluctuations and correlations of various observables are discussed as signatures for phase transitions in general and for the QCD critical endpoint in particular. Thermodynamic and mechanical instabilities are expected in the vicinity of the critical end point, and in the presence of a first-order phase transition when the bulk of the fireball enters the corresponding spinodal region. If, as a consequence of these instabilities, the

plasma is decomposed into “blobs”, which hadronize independently at different locations in space with distinct flow velocities, fluctuations in event-by-event correlations of the proton rapidity difference and in the strange particle abundance are expected. Indeed, event-by-event fluctuations of the K -to- π ratio have been observed in central Pb+Pb collisions at the SPS. However, the interpretation of these data is still under debate. Finally, the idea that relative charge fluctuations are suppressed in a QGP environment relative to a hadron gas, and hence may serve as a signal for deconfinement is discussed.

In Chap. 9 it is also noted that fluctuation signals from the QGP may be severely reduced by subsequent hadronic interactions. The point is made, that a careful scrutiny of relevant processes, such as resonance scattering and decay, is clearly needed. Furthermore, it is noted that fluctuations of conserved quantities, such as charge and baryon number, depend strongly on the actual kinematic domain experimentally covered. To properly account for detector acceptance and for the event classes employed in the analysis, detailed transport simulations are required.

The prospects for producing composite objects with multiple units of strangeness in heavy-ion collisions is discussed in Chap. 10. According to model calculations, the yield of meta-stable exotic multi-hypernuclear clusters (consisting of nucleons and hyperons) increases with increasing baryon density and reaches a maximum at FAIR energies. Such objects can be identified e.g. via their weak decay into a pair of Λ hyperons plus nucleons.

The most promising experimental observables and diagnostic probes of dense and hot baryonic matter produced in high-energy heavy-ion collisions are summarized in Chap. 11. It is pointed out that progress in this field is dependent on a comprehensive set of new high-quality experimental data and that novel theoretical tools are needed to trace the observables back to the early phases of the collision where matter presumably was in the form of partons.

V THE CBM EXPERIMENT

The goal of the CBM (Compressed Baryonic Matter) experiment at FAIR is to explore the phase diagram of strongly interacting matter in the region of high baryon densities. The CBM research program, as outlined in Chap. 1 of Part V, addresses the equation of state of baryonic matter, the deconfinement phase transition and its critical endpoint, chiral symmetry restoration at high baryon densities, and the in-medium properties of hadrons. The corresponding key observables comprise low-mass vector mesons decaying into lepton pairs which serve as penetrating probes, hidden and open charm produced at threshold beam energies, (multi-) strange particles, and global features like collective flow and event-by event fluctuations. Lepton pairs and particles containing charm quarks have not yet been measured in heavy-ion collisions

at AGS and low SPS energies, and only very little data on multi-strange hyperons have so far been recorded. The CBM experiment at FAIR is designed to perform these measurements with unprecedented precision.

The CBM detector concept is outlined in Chap. 2. The experimental challenge is to identify both hadrons and leptons, and to select events containing charm or lepton pairs in a heavy-ion environment with up to about 1,000 charged particles per central collision at reaction rates of up to 10 MHz. Such measurements require fast and radiation-hard detectors, self-triggered read-out electronics, a high-speed data acquisition system, and online event selection based on full track reconstruction.

In Chap. 3 the results of feasibility studies are presented, demonstrating that both frequently produced as well as rare particles can be measured with excellent statistics within beam times of several weeks. Finally, a brief review of complementary experimental approaches such as the NA61 experiment at CERN SPS, the RHIC beam energy scan program and the NICA project at JINR in Dubna, currently under consideration, is given in Chap. 4. The subsequent appendix covers technical features and main accomplishments of past and present detector arrangements employed in high-energy heavy-ion reaction experiments.

Part I

Bulk Properties of Strongly Interacting Matter

Conveners: S. Leupold^{1,a}, K. Redlich^{2,3}, and M. Stephanov⁴

Authors, who contributed to the various chapters or sections given in brackets:

A. Andronic⁵ [4.1], D. Blaschke^{2,6,a,b} [3.4], M. Bluhm^{7,a,c,d} [4.3], A. Dumitru^{8,9} [4.4], Z. Fodor¹⁰ [3.2], B. Friman⁵ [3.3, 4.6], C. Fuchs^{11,a} [3.3], B. Kämpfer^{7,12,a,c,d} [4.3], F. Karsch^{13,14} [3.2], S.D. Katz^{10,15} [3.2], T. Klähn^{16,a} [3.4], S. Leupold^{1,a} [1, 2.1, 2.2, 5] J. Randrup¹⁷ [2.2], C. Ratti^{18,a,e} [4.5], A. Rebhan¹⁹ [3.1], K. Redlich^{2,3} [4.1, 4.2, 4.6], D. Rischke^{20,21} [3.5], K. Rummukainen^{22,23,f} [3.1], C. Sasaki²⁴ [4.6], B.-J. Schaefer²⁵ [4.5, 4.7], E. Shuryak¹⁸ [4.8], M. Stephanov⁴ [2.1, 2.2], M. Thaler^{24,a,e} [4.5], J. Wambach^{3,5} [4.5, 4.7], F. Weber^{26,g} [3.4], W. Weise^{24,a,e} [4.5], S. Typel^{5,24,h} [3.4]

Affiliations:

¹Uppsala University, Uppsala, Sweden; ²University of Wrocław, Wrocław, Poland; ³Technical University of Darmstadt, Darmstadt, Germany; ⁴University of Illinois, Chicago, IL, USA; ⁵GSi Helmholtzzentrum für Schwerionenforschung, Darmstadt, Germany; ⁶Joint Institute of Nuclear Research (JINR), Dubna, Russia; ⁷Forschungszentrum Dresden-Rossendorf, Dresden, Germany; ⁸Baruch College, New York, NY, USA; ⁹RIKEN BNL Research Center, Upton, NY, USA; ¹⁰University of Wuppertal, Wuppertal, Germany; ¹¹Martin-Gerbert-Gymnasium, Horb am Neckar, Germany; ¹²Technical University of Dresden, Dresden, Germany; ¹³Brookhaven National Laboratory, Upton, NY, USA; ¹⁴University of Bielefeld, Bielefeld, Germany; ¹⁵Eötvös University, Budapest, Hungary; ¹⁶Argonne National Laboratory, Argonne, IL, USA; ¹⁷Lawrence Berkeley National Laboratory, Berkeley, CA, USA; ¹⁸State University of New York, Stony Brook, NY, USA; ¹⁹Technical University of Vienna, Vienna, Austria; ²⁰University of Frankfurt, Frankfurt, Germany; ²¹Frankfurt Institute for Advanced Studies (FIAS), Frankfurt, Germany; ²²University of Helsinki, Helsinki, Finland; ²³University of Oulu, Oulu, Finland; ²⁴Technical University of Munich, Munich, Germany; ²⁵University of Graz, Graz, Austria; ²⁶San Diego State University, San Diego, CA, USA

Support:

^aGSi Darmstadt

^bHelmholtz-Gesellschaft, Grant VH-VI-041

^cBMBF 06DR136

^dEU FP6 I3HP

^eBMBF

^fAcademy of Finland, Grants 104382 and 114371

^gNational Science Foundation, Grant PHY-0457329, and Research Corporation

^hDFG cluster of excellence “Origin and Structure of the Universe”

Leupold, S. et al.: *Part I Bulk Properties of Strongly Interacting Matter*.

Lect. Notes Phys. **814**, 39–334 (2011)

DOI 10.1007/978-3-642-13293-3_3

© Springer-Verlag Berlin Heidelberg 2011

Chapter 1

Introduction

Quantum Chromodynamics (QCD) shows a rich phase structure mainly related to changes of its symmetry properties. Accordingly, the equation of state is dominated by rather different degrees of freedom depending on the values for the temperature and the chemical potentials. At low temperatures and low chemical potentials hadrons are the relevant degrees of freedom. Chiral symmetry is spontaneously broken whereas the center symmetry of color $SU(3)$ (the symmetry aspect underlying confinement) is not. Systems at high temperatures are governed by quarks and gluons. This, however, does not imply that such a quark-gluon plasma is a weakly interacting gas for the temperatures reachable by heavy-ion collisions. In the quark-gluon plasma chiral symmetry is restored while the center symmetry is broken. Also at low temperatures, but high chemical potentials quarks determine the bulk properties. The dynamics, however, is related to the excitations near the Fermi surface where diquark correlations play an important role leading to color superconductivity. Concerning the transition from one phase of matter to another one, it is expected that when increasing the temperature at low chemical potentials a crossover from hadronic matter to the quark-gluon plasma takes place. For larger chemical potentials this changes to a first order transition. (Note that this issue is not completely settled yet, see e.g. [1, 2] for differing opinions.) The critical point which appears at the end of the first-order transition line is an important aspect of the phase diagram both from the theoretical and the experimental point of view. A sketch of our present-day understanding of the phase diagram of QCD is depicted in Fig. 1.1.

The pressure as a function of the temperature and the chemical potential(s), i.e. the equation of state, is one of the most important characteristics of QCD matter. The precise knowledge of the pressure of QCD has obvious phenomenological significance for the analysis of heavy-ion collision experiments, e.g. for the determination of collective flow and as an essential ingredient for a hydrodynamic treatment. In the early Universe the total pressure was dominated by the QCD degrees of freedom for temperatures larger than

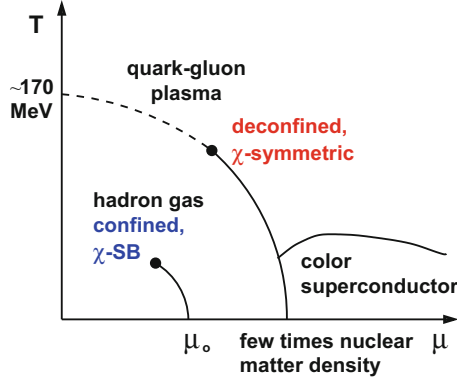


Fig. 1.1 Sketch of our present-day understanding of the QCD phase diagram at finite temperature T and non-zero quark chemical potential μ . It shows a crossover region at low μ (*dashed*) which turns to a true phase transition at a non-zero critical value of the quark chemical potential. The phase transition line starts with a 2nd order phase transition point as an end-point of a line of 1st order transitions. The latter extend to higher chemical potentials and lower temperatures until the region of color superconductivity is reached. (The line at smaller T and smaller μ which also ends in a critical point is the liquid-gas phase transition of nuclear matter).

the transition temperature. Because the pressure contributes strongly to the rate of the expansion of the Universe, it may affect the evolution of various cosmological relics: so far, the spectrum of the primordial gravitational waves [3, 4] and the relic densities of various dark matter candidates [5–9] have been studied in this context. The knowledge of the pressure to better than $\sim 1\%$ level is necessary for precise quantitative analysis. Neutron stars are macroscopic objects where the stability is guaranteed by the Pauli principle of nucleons (together with a repulsive short-range interaction). Therefore the structure of a neutron star is dictated by the strong interaction (and, of course, gravity). The key ingredient that enters the stability condition is precisely the equation of state.

It is important to understand which regions of the phase diagram depicted in Fig. 1.1 are accessed by nature or accessible by experiment: The early Universe traversed the phase diagram essentially downward along the temperature axis, i.e. for vanishing chemical potential. Neutron stars, on the other hand, probe the strong interaction at very small temperatures, but high chemical potential. The question whether the interior of a neutron star is already in a (superconducting) quark phase constitutes an active field of research. Ultrarelativistic heavy-ion reactions reach the transition region between hadronic and quark-gluon matter. It should be noted, however, that one has to evaluate for each reaction to what extent the hot system created in the center of a heavy-ion collision reaches local equilibrium. In that sense it might be somewhat oversimplified to attribute a position in the phase dia-

gram of Fig. 1.1 to the product of a heavy-ion reaction. With these words of caution one can say that typically the higher the reaction energy the closer the created system is located near the temperature axis. Hence, it is the crossover region close to the temperature axis which is explored by the experiments at the Relativistic Heavy-Ion Collider in Brookhaven (RHIC) or at the Large Hadron Collider at CERN (LHC) which reach the largest energies. To find a true phase transition and eventually the critical end point one presumably has to go to lower bombarding energies. Whether a color superconducting phase can be reached by a heavy-ion collision depends on the critical temperature of these low-temperature phases. At present one has to rely on models which in part yield sizable temperatures on the order of about 50 MeV. This is below the temperatures reached in the matter created in heavy-ion collisions, but it is sufficiently close to stimulate the hope that some precursor effects of a color superconducting phase might already be visible. Clearly dedicated observables are necessary to study the properties of strongly interacting matter in the region of the true phase transitions. The CBM experiment at FAIR is designed to explore this region.

In principle, one would like to describe all areas of the phase diagram depicted in Fig. 1.1 and the corresponding equation of state by first principle QCD calculations. The corresponding two tools, lattice QCD and perturbative QCD, however, have their intrinsic limitations: Perturbative QCD can only be applied at large enough temperatures and/or large enough chemical potentials where the non-perturbative aspects (e.g. confinement) have faded away. Also there, resummation techniques are necessary, since naive loop expansions are not equivalent to coupling constant expansions and since the QCD coupling constant is still sizable for the temperature and density regimes of interest (heavy-ion collisions, neutron stars). In contrast to perturbative QCD, lattice QCD can also be applied to the non-perturbative regime. Limitations occur, however, for finite chemical potentials and for quantities which are sensitive to the smallness of the up and down quark masses. Only very recently it became possible to perform lattice calculations in the range of realistic quark masses. It should also be mentioned that aside from the phase diagram there are also many other quantities which are of interest for the characterization of a strongly interacting system, e.g. transport properties or spectral informations (cf. Part II). Also such quantities are difficult to assess within lattice QCD.

At very low temperatures and low chemical potentials there is still another systematic approach to describe strongly interacting systems: chiral perturbation theory. It accounts for the smallness of the up and down quarks and for broken chiral symmetry in a systematic way. However, it does not work any more in the region where hadron resonances start to influence the properties of a strongly interacting system. In view of the present day limitations of first principle calculations and systematic approaches, also effective models are a valuable tool to determine the equation of state and the phase structure of strongly interacting matter. Such models use either hadronic degrees

of freedom with properties based on phenomenology or degrees of freedom closer related to the basic ingredients of QCD, like dressed quarks, quark bound states or Wilson lines. The respective region of applicability of the various approaches is illustrated in Fig. 1.2. In this figure the main empha-

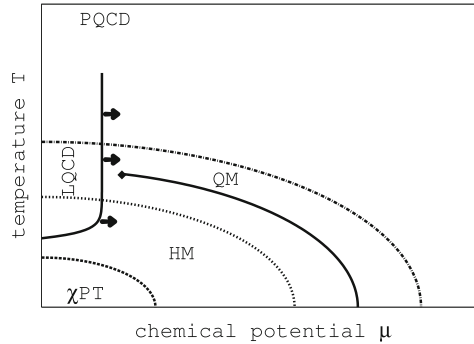


Fig. 1.2 Regions of applicability of various approaches to the phase diagram of QCD. For simplicity only the phase line between hadronic matter and the quark-gluon plasma is displayed (the full line which terminates in a critical end point), while the color superconducting phase and the liquid-gas transition are not shown. The label “ χ PT” denotes chiral perturbation theory, “LQCD” lattice QCD, “PQCD” perturbative QCD, “HM” hadronic models and “QM” quark models. Recent developments in lattice QCD aim at the extension of this first principle method to larger chemical potentials. This is indicated by the *arrows*. See main text for details.

sis lies on the transition from hadronic matter to the quark-gluon plasma. (The corresponding transition line is the full line which ends in the critical point discussed above.) Therefore, the other transition lines depicted in Fig. 1.1 are left out here for simplicity. As already discussed, perturbative QCD (labeled by “PQCD” in Fig. 1.2) is only applicable where the temperature T and/or the chemical potential is large. The applicability region of Lattice QCD (LQCD) is depicted by the full line. Lattice QCD can deal in principle with arbitrary temperatures, but only with small chemical potentials. Recent progress in lattice QCD pushes the reachable chemical potentials to larger values. This is indicated in Fig. 1.2 by the arrows. At very low temperatures the bulk properties are determined by the lightest hadrons, the pions. Since their mass is determined by the very light up and down quark masses, the pions are typically too heavy in present-day lattice QCD calculations. Therefore, the applicability region of lattice QCD roughly ends at the domain of chiral perturbation theory (χ PT) – the dashed line. Obviously, there are regions in the phase diagram depicted in Fig. 1.2 where none of the systematic approaches (PQCD, LQCD, χ PT) works. There one has to rely on models to get qualitative or semi-quantitative insights. Of course, hadronic models (HM) work only in the hadronic phase, i.e. their border (dotted line) is be-

low the phase transition line. In principle, quark models (QM) could work below and above the transition between hadronic matter and the quark-gluon plasma. Typically, however, they do not reliably describe the hadronic matter with its large number of degrees of freedom. Around the phase transition and especially for large chemical potentials, on the other hand, quark models are the only tool which one can apply so far (various kinds of quark models will be discussed below). Therefore, a realistic border for the applicability region of quark models is given by the dotted and the dashed line. An interesting aspect is the fact that the regions of both hadronic and quark models have an overlap with the region of lattice QCD. Therefore, lattice QCD can provide valuable cross-checks or constraints for these models.

The present part of the book is essentially structured in three chapters: Chap. 2 contains a general introduction to QCD and its thermodynamics. Chapter 3 is a scan through the phase diagram of strongly interacting matter. Chapter 4 collects various approaches towards the description of the properties of matter near the phase transitions or crossovers.

An introduction to QCD and its symmetry properties is provided in Sect. 2.1. Systematic approaches to the strong interaction are briefly introduced and the fundamental difference to effective models is pointed out. A discussion of general aspects of thermodynamics and an overview of the phases of QCD is given in Sect. 2.2.

In Chap. 3 the phase diagram (see Figs. 1.1 and 1.2) is scanned through – roughly from top left to bottom right: Calculations of the equation of state using perturbative QCD are reviewed in Sect. 3.1. This method is applicable for high temperatures. Results from lattice QCD for the equation of state and other thermodynamic quantities of interest as well as for the location of the critical point are presented in Sect. 3.2. We recall that this critical point separates the crossover region (between hadronic and quark-gluon matter) present at low baryo-chemical potential from the true phase transition region at higher baryo-chemical potential. Approaching higher chemical potentials and lower temperatures one leaves the region where first principle approaches can be reliably applied. The determination of the nuclear equation of state from hadronic models (“hadronic many-body theory”) is reviewed in Sect. 3.3. At least for the late stage of a heavy-ion collision the system crosses the regime where at present hadronic many-body theory is the best tool at hand. Properties of cold and dense strongly interacting matter as can be found in neutron stars are discussed in Sect. 3.4. Interestingly, the observed properties of neutron stars constrain the equation of state obtained from hadronic and/or quark models. In that way one obtains crosslinks relevant for the equation of state which enters the description of heavy-ion collisions. Chapter 3 ends with a review of the color superconducting phases present at high chemical potentials and low temperatures in Sect. 3.5. It is noticeable that at least for extremely high chemical potentials perturbative QCD can be used again.

Chapter 4 concerns the physics in the vicinity of the transition from hadronic to quark-gluon matter. In Sect. 4.1 the statistical thermal model for particle production yields is presented. In Sect. 4.2 it is demonstrated that below, but close to the transition region the thermodynamic properties of hadronic matter can be described in terms of a hadron resonance gas. Above, but close to the transition region, the quark-gluon plasma has properties which are rather different from a free gas of gluons and quarks. One well established approach which introduces quark and gluon quasi-particles is presented in Sect. 4.3. The role of the dynamics of the Polyakov loop for the deconfinement phase transition is discussed in Sect. 4.4. In Sect. 4.5 quark models are discussed which account for the confinement as well as for the chiral symmetry aspect of the transition from hadronic to quark-gluon matter. Polyakov loop and constituent quark degrees of freedom are combined on a mean field level. In Sect. 4.6 the role of fluctuations is highlighted focusing on first order phase transitions out of equilibrium. Here one of the quark models introduced in the previous section is used for illustration. Model calculations which go beyond mean field approaches by using renormalization group methods are presented in Sect. 4.7. A possible connection between QCD on one hand and conformal field theory and gravity theory on the other is discussed in Sect. 4.8.

Finally an executive summary is presented in Chap. 5 which highlights the connection of the presented approaches to the CBM experiment and points to future developments.

Chapter 2

QCD and its thermodynamics

2.1 QCD and its symmetries

The present section provides an introduction to QCD and its symmetry properties. Also systematic approaches to the strong interaction are briefly introduced and the fundamental difference to models is pointed out.

2.1.1 QCD basics

It is commonly accepted at present that Quantum Chromodynamics (QCD) is the theory of the strong interaction. The theory posits that the observed strongly interacting particles, namely the hadrons, arise as particle excitations in a quantum field theory of quarks and gluons as fundamental degrees of freedom. Six different types of quarks, called quark flavors, exist: up (u), down (d), strange (s), charm (c), bottom (b) and top (t). Some of their properties are collected in Table 2.1. The quarks carry fractional (electric and

Table 2.1 Some basic properties of quarks and gluons. The electric charge is given in multiples of $|e|$ where e is the charge of an electron. The spin is given in multiples of \hbar . Note that the quark masses depend on the renormalization scheme and scale (see [10] for details).

Particle	Mass [MeV/ c^2]	Electric charge	Baryon number	Spin
u	1.5–3.0	2/3	1/3	1/2
d	3–7	−1/3	1/3	1/2
s	95 ± 25	−1/3	1/3	1/2
c	$(1.25 \pm 0.09) \cdot 10^3$	2/3	1/3	1/2
b	$(4.20 \pm 0.07) \cdot 10^3$	−1/3	1/3	1/2
t	$(174.2 \pm 3.3) \cdot 10^3$	2/3	1/3	1/2
g	0	0	0	1

baryonic) charge. In addition, the up, down and strange quarks are very light objects. All experimental searches for such light states or for states with fractional charge have failed. This fact – which is far away from being completely understood – is called *confinement*.

As will be discussed below in Sect. 2.1.3 confinement is associated to a symmetry: the center symmetry. This symmetry changes its pattern in a hot and/or dense strongly interacting system. Quarks and gluons will become deconfined and form a quark-gluon plasma. For later use concerning thermodynamics it is illustrative to count the light degrees of freedom on the elementary level of QCD, i.e. the light quarks and gluons (where “light” means every state which is significantly lighter than, e.g., 1 GeV):

$$\begin{array}{lcl} \text{quarks: (part.+antip.)} \times \text{spin} \times \text{flavor} \times \text{color} & = & 2 \times 2 \times 3 \times 3 = 36 \\ \text{gluons:} & \text{polar.} \times \text{color} & = 2 \times 8 = 16 \end{array}$$

Thus one finds in total 52 light degrees of freedom.

Instead of the pattern of states which one would naively expect (more or less free quarks and gluons) one finds a rather complex hadronic world which consists of states with integer electric and baryonic charges. These states are rather heavy as compared to the (lightest) quark masses (cf. Table 2.2). The spectrum starts after a gap of roughly 1 GeV. There is, however, an

Table 2.2 Low-lying hadronic states (selection) and some of their properties [10]. Top part mesons, bottom part baryon octet.

Particle	Mass [MeV/c ²]	Electric charge	Baryon number	Spin
π^0	134.9766	0	0	0
π^\pm	139.57018	± 1	0	0
K^\pm	493.677	± 1	0	0
K^0, \bar{K}^0	497.648	0	0	0
η	547.51	0	0	0
ρ^0, ρ^\pm	775.5	0, ± 1	0	1
ω	782.65	0	0	1
K^*	891.66	0, ± 1	0	1
η'	957.78	0	0	0
ϕ	1,019.460	0	0	1
p	938.27203	1	1	1/2
n	939.56536	0	1	1/2
Λ	1,115.683	0	1	1/2
Σ^+	1,189.37	1	1	1/2
Σ^0	1,192.642	0	1	1/2
Σ^-	1,197.449	-1	1	1/2
Ξ^0	1,314.83	0	1	1/2
Ξ^-	1,321.31	-1	1	1/2
...

exception: one finds comparatively light pseudoscalar states (as compared to other hadrons), the pions – including the strangeness sector one additionally has the kaons and the eta meson.

Again one can count the light degrees of freedom:

$$3 (\text{pions}) + 4 (\text{kaons}) + 1 (\text{eta}) = 8$$

Hence in the hadronic world one only has the 8 types of light pseudoscalars as compared to the 52 light degrees of freedom counting quarks and gluons. As already pointed out, one expects that quarks and gluons are liberated in a strongly interacting medium at sufficiently large densities/temperatures. If such a transition¹ happens, the relevant degrees of freedom significantly change from about 8 to about 52. (For the sake of this simple qualitative argument interactions are neglected.) Therefore one can expect sizable changes e.g. in the energy density or pressure as a function of the temperature. A detailed discussion of the phases of QCD is given in Sect. 2.2.

Confinement or not, global symmetries of the fundamental theory are manifest in the hadron spectrum. The isospin symmetry, under which proton and neutron transform as an SU(2) doublet² is the manifestation of the corresponding SU(2) symmetry of QCD between the up and down quarks. The approximate SU(3) symmetry under which proton, neutron and six hadron resonances (strange hyperons Σ , Ξ and Λ) transform as an octet is the manifestation of the approximate flavor symmetry between the up, down and strange quarks, which transform in the fundamental representation of flavor SU(3) (cf. Fig. 2.1). In SU(3), to obtain an octet representation one should

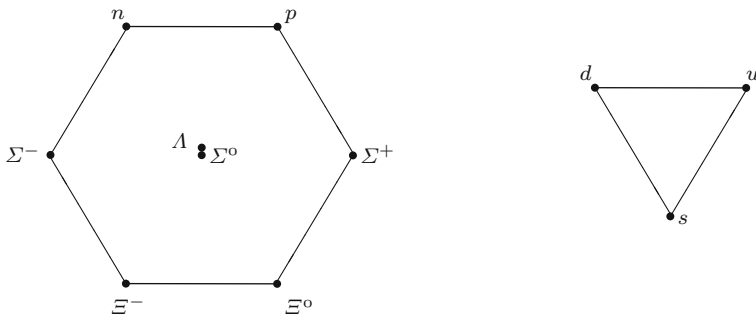


Fig. 2.1 The lowest-lying baryon multiplet (*left*) and the fundamental triplet (*right*) of flavor SU(3).

¹ “Transition” is used here in a loose sense. It might be a true phase transition or a rapid crossover. Details are discussed below in Sect. 2.2.

² SU(N) denotes the group of special unitary transformations in N dimensions ($N \geq 2$), whose determinant is 1. The group is non-commutative and hence non-Abelian.

take a product of three fundamental representations – i.e., there are three quarks in a baryon.

A further symmetry of QCD which is not manifest in the spectrum of hadrons is called *color* – which gives the name to the theory. Unlike flavor, the color symmetry is a *local* symmetry or, more appropriately, invariance of QCD. Like the U(1) local gauge invariance of QED, the local color invariance also requires vector boson fields; these are the gluons. As there are three fundamental colors required (e.g. “red”, “green” and “blue”), QCD gauge invariance obeys a color SU(3) symmetry, defining QCD as a non-commutative, i.e. non-Abelian gauge theory.

SU(3)_{flavor} and SU(3)_{color} are two completely different sets of transformations in QCD, completely independent from each other, though they form similar group structures. Quarks transform under (i.e., carry) both flavor (u , d , s for up, down and strange quarks³) and the three color. Gluons, like photons, are emitted by currents. Unlike photons, gluons do not only carry momentum and spin, but also color. The color of the gluon is determined by the colors of quarks before and after the emitting transition. There are eight gluons corresponding to nine pairs of initial times final quark colors minus one which correspond to a singlet under SU(3)_{color}.

In quantum field theory the gluons are described by eight 4-vector potentials A_μ^a , $a = 1, \dots, 8$, or matrix valued 4-vector $A_\mu \equiv A_\mu^a \lambda^a / 2$, where λ^a are eight linearly independent 3×3 Gell-Mann matrices. Each flavor of quark is described by three (color) Dirac 4-spinor fields q^c , $c = 1, 2, 3$, where $q = u, d$ or s and we suppress Dirac spinor indices.

The most general, relativistically invariant, renormalizable Lagrangian density for a theory of 3 flavors of quarks with SU(3) color gauge invariance is given by [11]:

$$\mathcal{L}_{\text{QCD}} = -\frac{1}{2} \text{Tr} F_{\mu\nu} F^{\mu\nu} + \sum_{q=u,d,s} \bar{q} (i\gamma^\mu D_\mu - m_q) q, \quad (2.1)$$

with the gauge covariant derivative $D_\mu = \partial_\mu - igA_\mu$ and the gluon field strength $F_{\mu\nu} = \frac{i}{g} [D_\mu, D_\nu]$. For a single color component the field strength reads

$$F_{\mu\nu}^a = \partial_\mu A_\nu^a - \partial_\nu A_\mu^a + gf^{abb'} A_\mu^b A_\nu^{b'} \quad (2.2)$$

which demonstrates that gluons also interact with themselves and not only with quarks.

The Lagrangian density (2.1) and the corresponding action

³ For the present discussion the heavy quarks c , b and t are ignored. For the symmetry considerations which will follow below and also for the thermodynamics the heavy quarks are not of much concern. Note, however, that the heavy quarks are interesting probes to explore strongly interacting matter, cf. the Parts II “In-Medium Excitations” and IV “Observables and predictions”

$$S_{\text{QCD}} = \int dt \int d^3x \mathcal{L}_{\text{QCD}} \quad (2.3)$$

define QCD on the classical level. One convenient way to obtain the corresponding *quantum* field theory is the path integral formalism. In addition, this formalism yields a close connection to the thermodynamic partition function. In vacuum, the central quantity to obtain observables is the transition amplitude which transports a given field configuration Φ_1 at time t_1 to another configuration Φ_2 at time t_2 [11]:

$$\begin{aligned} \langle \Phi_1 | e^{-iH(t_2-t_1)} | \Phi_2 \rangle &\sim \int \mathcal{D}[q, \bar{q}, A_\nu^a] \exp \left(i \int_{t_1}^{t_2} dt \int d^3x \mathcal{L}_{\text{QCD}}[q, \bar{q}, A_\nu^a] \right) \\ &= \int \mathcal{D}[q, \bar{q}, A_\nu^a] e^{iS_{\text{QCD}}} \end{aligned} \quad (2.4)$$

with the Hamiltonian H . On the other hand, in a (sufficiently large) many-body system which is in thermal equilibrium all thermodynamical quantities can be obtained from the grand canonical partition function [12]

$$Z := \text{tr} e^{-(H-\mu N)/T} = \sum_n \langle n | e^{-(H-\mu N)/T} | n \rangle. \quad (2.5)$$

Here T denotes the temperature and μ is the chemical potential associated with the conservation of baryon number (see Sects. 2.1.3 and 2.2 below). N denotes the baryon number operator.

In addition, the expectation value for an observable \mathcal{O} is given by

$$\langle \mathcal{O} \rangle := \frac{\text{tr} [\mathcal{O} e^{-(H-\mu N)/T}]}{Z}. \quad (2.6)$$

It is important to note here that the states $|n\rangle$ in (2.5) form an arbitrary complete set of states, i.e. they are not necessarily eigen states of H .

The formal similarity between $e^{-iH(t_2-t_1)}$ in (2.4) and $e^{-(H-\mu N)/T}$ in (2.5) can be exploited to represent also the partition function by a path integral

$$\begin{aligned} Z &\sim \int \mathcal{D}[q, \bar{q}, A_\nu^a] \exp \left[- \int_0^{1/T} dt \int d^3x \left(\mathcal{L}_{\text{QCD}}^E[q, \bar{q}, A_\nu^a] - \frac{1}{3} i \mu q^\dagger q \right) \right] \\ &= \int \mathcal{D}[q, \bar{q}, A_\nu^a] e^{-S_{\text{QCD}}^E} \exp \left[\int_0^{1/T} dt \int d^3x \frac{1}{3} i \mu q^\dagger q \right] \end{aligned} \quad (2.7)$$

where $\mathcal{L}_{\text{QCD}}^E/S_{\text{QCD}}^E$ is the Euclidean Lagrangian/action. Changing from Minkowski to Euclidean space accounts for the fact that the “time” integration

is now along an imaginary time running from 0 to $-i/T$. The expectation value (2.6) can be represented in a corresponding way. We note that the chemical potential enters (2.7) in a simple way: Starting from the action S_{QCD}^E each field that transforms nontrivially under the action of the baryon charge operator (such as the quark fields in QCD) should have its time derivative extended, $\partial_0 q \rightarrow \partial_0 q + \frac{i}{3}\mu q$, where $\frac{1}{3}$ is the baryon charge of the quark. This is analogous to the coupling of an external electrostatic potential to a charged particle.

On a grid the sum over all possible field configurations can be performed by the Monte-Carlo method provided that the statistical weight of a given configuration is a positive definite function, i.e. allows for a probabilistic interpretation. This condition is indeed satisfied by $e^{-S_{\text{QCD}}^E}$ which appears in (2.7), but not by $e^{iS_{\text{QCD}}}$ appearing in (2.4). Therefore time-dependent quantities cannot be evaluated with such a Monte-Carlo approach. Also the appearance of a finite chemical potential in (2.7) makes the exponent complex-valued and the exponential function non-positive definite. Ways to circumvent that problem are discussed in much more detail below in Sect. 3.2.

The Monte-Carlo evaluation of path integrals like the one in (2.7) constitutes the lattice QCD approach towards strongly interacting systems. More details and applications of this technique to thermodynamical quantities can be found in Sect. 3.2 below. For the limiting case $T \rightarrow 0$ (and $\mu = 0$) one can even describe vacuum properties by appropriate choices for the observable \mathcal{O} in (2.6). Note, however, that for the vacuum case only static quantities (like masses) can be calculated in lattice QCD, no dynamical ones like reaction rates. After this brief introduction of path integrals and a first look at thermodynamic quantities we return to some elementary properties of QCD.

One can see that the QCD Lagrangian (2.1) has only one parameter – the dimensionless coupling constant, g , besides the quark masses. Gauge invariance together with renormalizability are powerful constraints. Such a theory must have an enormous predictive power (in a loose sense of predictions per free parameter).

The most remarkable property of QCD is asymptotic freedom – the physical coupling defined, e.g., through a process of scattering, tends to zero as the characteristic momentum transfer of the defining process Q tends to infinity: $g^2(Q) \sim 1/\log Q$. In a simpler language, translating the momentum transfer to a space resolution, the coupling vanishes at short distances.

Moreover, because of the renormalization group running of the physical coupling, the theory is more appropriately described by a scale, rather than a dimensionless coupling (this is known as dimensional transmutation). This scale is usually defined as a scale Q at which the running coupling would become of order unity. This is the characteristic hadronic scale, typically taken as $\Lambda_{\text{QCD}} = 200$ MeV. For example, the size of a proton is of order $\hbar c/\Lambda_{\text{QCD}} = 1$ fm.

The running coupling constant $\alpha_s = \frac{g^2}{4\pi}$ is depicted in Fig. 2.2 taken from [10]. Due to the smallness of the coupling constant QCD perturbation the-

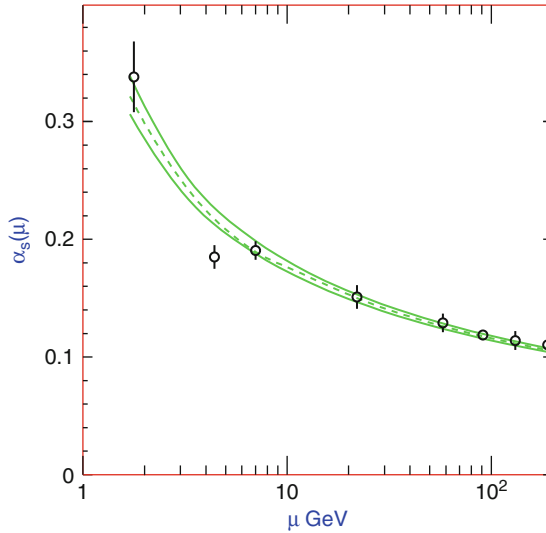


Fig. 2.2 The running coupling constant α_s of QCD [10].

ory becomes applicable in the high energy regime for quantities which are insensitive to low energies [11]. At lower energies, however, the results of perturbative QCD become unreliable. At least one sees that the strong coupling constant strongly rises. This suggests that it is possible that the strong interactions rearrange things in such a way that one can no longer simply read off the relevant degrees of freedom from the Lagrangian density. Therefore the rise of the strong coupling constant with decreasing energy/momentum is compatible with (but no proof of) confinement.

2.1.2 Systematic approaches and models

At present, we are not able to fully solve QCD.⁴ Nonetheless for certain kinematical regimes and for specific problems we can develop systematic approaches towards QCD. In addition, we have a whole plethora of hadronic and quark models at hand. The principal difference between systematic approaches and models is that in the former case one knows – at least in principle – how to systematically improve the calculations. A non-exhaustive list of systematic approaches which is relevant for the forthcoming discussions is given here:

- Perturbative QCD [11]: One deals with free quarks and gluons as the basic objects. Every quantity is calculated as an expansion in terms of the cou-

⁴ Actually this is true for any quantum field theory besides some toy models.

pling constant α_s , i.e. one approximates full QCD by a Taylor expansion in α_s . This approach is only applicable for high energies where the running coupling is small enough (cf. Fig. 2.2) and where the quarks and gluons are the relevant degrees of freedom. Concerning thermodynamics one can apply perturbative QCD to the regimes of high temperatures and/or high chemical potential, since in these regimes the high-momentum modes play the dominant role. Obviously, for the behavior and interactions of these high-momentum modes perturbation theory can be applied since the running coupling becomes small. Note that some non-perturbative features are intertwined with standard perturbation theory for the calculation of thermodynamic properties (see Sects. 3.1 and 3.5 for details).

- Chiral perturbation theory [13–16]: Full QCD is approximated by an effective theory for the light pseudoscalar mesons (and nucleons), i.e. one takes into account the stable⁵ hadrons which are the relevant degrees of freedom at low momenta. This effective theory contains free parameters which ideally one would like to determine from QCD. So far one has to fit them to experimental data. One obtains a Taylor expansion in terms of energies and (Goldstone boson) masses. For a given order in this Taylor expansion the pattern of chiral symmetry breaking (see Sect. 2.1.3) reduces the number of otherwise infinitely many free parameters to a finite number (which rises with the desired order in the expansion). Obviously this approach is applicable for low energies where mesonic and baryonic resonances are not excited. Concerning thermodynamics one can apply chiral perturbation theory to the regime of low temperatures and low chemical potentials, since there the lowest excitations play the dominant role. This approach will be of use in Sect. 2.2.6 to calculate the onset of in-medium changes for various order parameters.
- Lattice QCD [17]: One approximates full continuum QCD by (full!) QCD on a grid, i.e. with a finite grid point distance $a \neq 0$ and a finite volume $V \neq \infty$. In principle one can improve the calculation by working with a higher number of grid points. In addition, one can check how the calculated quantities scale with the number of grid points to judge how close one already is to the continuum and infinite volume limit [18]. Clearly, lattice QCD is a powerful tool to learn about QCD especially since it is not restricted to very low or high energies/temperatures like chiral perturbation theory or QCD perturbation theory, respectively. Nonetheless, also lattice QCD has some inherent restrictions which have already been partly discussed after Eq. (2.7). In contrast to the previously discussed approaches one cannot calculate dynamical quantities within lattice QCD. Therefore, the dynamics of a nucleus–nucleus collision is out of reach. On the other hand, concerning thermodynamical quantities this is of no concern and one can use lattice QCD at least in principle for arbitrary high or low temperatures. More severe in that context is the restriction to small

⁵ “Stable” with respect to the strong interaction.

chemical potentials. How this problem is tackled is discussed in more detail in Sect. 3.2. A second problem concerns the light quark masses. In lattice QCD the action of fermions is transformed to a functional determinant which is a nonlocal object. The computational effort grows with the number of lattice sites which are correlated by this determinant. On the other hand, how many lattice sites are effectively correlated, is determined by the dimensionful quantity which sets the largest scale (in coordinate space), i.e. in practice by the smallest quark mass. At present, it is not possible to deal with quark masses as low as the physical up and down quark masses. There is yet another problem with fermions on the lattice: Due to the lattice boundary conditions the fermion determinant actually contains more degrees of freedom than one has in the continuum (fermion doublers). One ad hoc method to deal with that problem is to take roots of the determinant (staggered fermions). Another one is to give a large mass to the doublers which grows to infinity when the continuum limit is approached (Wilson fermions). The latter method, however, violates chiral symmetry (see below). In principle, one expects chiral symmetry to become restored in the continuum limit, but for all practical calculations – which always have a finite grid distance, no matter how small it is – one sacrifices an important symmetry. A third method, which is theoretically most satisfying, but numerically most costly, is to use an action which exactly obeys a lattice chiral symmetry (chiral fermions). In the continuum limit the latter turns into the ordinary chiral symmetry. These issues are taken up again in Sect. 3.2.

As should have become clear from the previous discussion there are still areas and problems where none of the systematic approaches can be applied: Concerning elementary processes (e.g. hadron scattering) there is the regime of intermediate energies which is dominated by the appearance of hadronic resonances. Neither chiral perturbation theory nor perturbative QCD (using quarks and gluons) can be applied here. Of course, the same is true for more complicated reactions, e.g. nucleus–nucleus collisions, in the corresponding energy regime. Therefore, hadronic models are applied to such problems. For the description of strongly interacting many-body systems one has to switch from hadronic to quark models, if one proceeds from below to temperatures close to the transition and above. Concerning thermodynamic quantities this is especially necessary for large chemical potentials and low temperatures where lattice QCD cannot be applied.

It is important to understand the following interrelation between models and systematic approaches: Models are mandatory for the areas where the systematic approaches do not work. However, these models typically have a region where they overlap with the applicability region of one of the systematic approaches. This opens the possibility to constrain parameters of the models. Especially fits of models to lattice QCD calculations are an important tool to improve hadron or quark models or to fix their parameters. Various such hadronic and quark models are discussed in later sections of this

book. Of course, another constraint for these models comes from the symmetries obeyed by the strong interaction. These symmetries are discussed in the following.

2.1.3 Symmetries of QCD

To figure out the symmetries of a physical system is an important aspect to understand the observed pattern, e.g. of the mass spectrum. Selection rules and the appearance of multiplets (degenerate states) are classical examples for the importance of symmetries. Even more, if one has a problem at hand where the underlying theory cannot be fully solved, symmetries can still lead to a qualitative understanding. Especially the phase structure of QCD is dictated by its symmetries. Most important in that respect are chiral, center and color symmetry. Their changes with temperature and/or chemical potential lead to the hadronic phase, the quark-gluon plasma and the color superconducting state. These aspects will be outlined in the present section.

Symmetries can be realized in different ways in a given physical system: First, the symmetry might be either exact or only approximately realized. Second, one has to distinguish between the interaction which governs the system and the physical state. Third, a symmetry might exist on the classical level, but be destroyed on the quantum level. The most simplest case appears, if both the interaction and the physical state are invariant with respect to a symmetry transformation. This situation is called Wigner-Weyl phase. In this case one finds the celebrated selection rules etc. If the symmetry is only approximate one observes some (small) violations of the consequences which follow from the symmetry. But also these violations show a pattern which can be understood from the approximate symmetry.

If only the interaction obeys the symmetry, but not the physical state, the system is in the Nambu-Goldstone phase. Such a symmetry is called “hidden” or “spontaneously broken.” A classical example is a ferro magnet: The spin-spin interaction is invariant with respect to rotations. However, the energetically favored physical state is the one where all spins are aligned. This causes a macroscopic magnetization which points in some direction. Clearly, rotational invariance is broken. If a continuous symmetry is spontaneously broken one finds a massless state (gapless excitation) in the excitation spectrum, the Goldstone mode. Another feature of a spontaneously broken symmetry is the change of the symmetry pattern as a function of temperature. For the ferro magnet there is a critical temperature, the Curie temperature, where the system changes from the low-temperature Nambu-Goldstone phase to the high-temperature Wigner-Weyl phase. The magnetization serves as an order parameter of this symmetry transition. An order parameter is non-vanishing when the symmetry is spontaneously broken and vanishes when the symmetry is restored. If the symmetry is only approximately realized in a system,

the Goldstone modes are not exactly massless (gapless), but light. Also the order parameter might not completely vanish in the Wigner-Weyl phase.

Finally, a symmetry might exist only for the classical version of the interaction. If it does not exist for the corresponding quantum theory one calls it an “anomaly”. In the path integral representation (cf. e.g. (2.4)) this implies that the action is invariant while the integration measure is not. Still, the classical symmetry leaves its marks in the quantum system.

In the following we will discuss the symmetries of QCD. We will see that the symmetry structure of QCD is so rich that all cases (Wigner-Weyl and Nambu-Goldstone phases, anomalies) appear here. The results are summarized in Table 2.3.

Table 2.3 Exact and approximate symmetries of QCD; note that the consequences given in the last column are only a selection. The symmetries which hold only approximately are explicitly broken. See main text for details.

Symmetry	Vacuum	High T	Low T , high μ	Order parameter	Consequences
(Local) color $SU(3)$	Unbroken	Unbroken	Broken	Diquark condensate	Color superconductivity
$Z(3)$ center symmetry	Unbroken	Broken	Broken	Polyakov loop	Confinement/deconfinement
Scale invariance	Anomaly			Gluon condensate	Scale (Λ_{QCD}), running coupling
Chiral symmetry $U_L(N_f) \times U_R(N_f) = U_V(1) \times SU_V(N_f) \times SU_A(N_f) \times U_A(1)$					
$U_V(1)$	Unbroken	Unbroken	Unbroken	—	Baryon number conservation
Flavor $SU_V(N_f)$	Unbroken	Unbroken	Unbroken	—	Multiplets
Chiral $SU_A(N_f)$	Broken	Unbroken	Broken	Quark condensate	Goldstone bosons, no degenerate states with opposite parity
$U_A(1)$	Anomaly			Topological susceptibility	Violation of intrinsic parity

As already mentioned in Sect. 2.1.1 the QCD Lagrangian (2.1) is invariant with respect to local color transformations

$$\begin{aligned}
 q(x) &\rightarrow {}^g q(x) := g(x) q(x) \\
 A_\mu(x) &\rightarrow {}^g A_\mu(x) := g(x) \left(A_\mu(x) + \frac{i}{g} \partial_\mu^x \right) g^\dagger(x)
 \end{aligned}
 \tag{2.8}$$

where we have introduced the local transformation

$$g(x) = e^{ig\Theta^a(x)\lambda^a/2} \tag{2.9}$$

utilizing the Gell-Mann matrices λ^a acting on the color indices of the quarks. Θ^a are arbitrary real numbers, $a = 1, \dots, 8$. It is the local gauge invariance with respect to color $SU(3)$ which leads to the fact that both the quark-

gluon and the gluon-gluon interaction strength are determined by the same coupling constant g . As a gauge theory QCD has a lot of similarities to QED. In particular, there are QED governed systems which show a transition to a superconductor at sufficiently low temperatures. From the point of view of symmetries, QED gauge invariance is spontaneously broken in the superconducting phase. Electron pairs condense and the photons obtain a (Meissner) mass, i.e. magnetic fields cannot penetrate the superconducting region. The corresponding effect is observed for QCD: At low temperatures, but very high chemical potentials one enters the regime of color superconductivity. Quark pairs condense and this diquark condensate serves as an order parameter of spontaneously broken color $SU(3)$. For more details see Sect. 3.5.

A symmetry which is closely interrelated with the local color symmetry is the center symmetry (for a recent introductory report see [19]). Some formal considerations are necessary to identify this symmetry: First we note that in the definition of the partition function in (2.5) the very same state appears as a bra and as a ket vector (since it has to represent the trace). In the path integral representation (2.7) this translates to boundary conditions for the fields: Gluon/quark fields must be periodic/antiperiodic in Euclidean time, i.e.

$$A_\mu(t + 1/T, \mathbf{x}) = A_\mu(t, \mathbf{x}), \quad q(t + 1/T, \mathbf{x}) = -q(t, \mathbf{x}). \quad (2.10)$$

Clearly, the boundary condition (2.10) places constraints on the allowed gauge transformations which appear in (2.8). As it will turn out in the following, the center symmetry is a good symmetry of a purely gluonic theory (Yang-Mills theory), i.e. it becomes a symmetry of QCD, when the quarks are neglected. Therefore, we first concentrate on the gluons and neglect the quark fields in (2.7). In order to fulfill the boundary condition (2.10) for the gluon vector potential, we consider first gauge transformations which are strictly periodic in (Euclidean) time $g(\mathbf{x}, x_4 + \beta) = g(\mathbf{x}, x_4)$. Every physical quantity must be invariant under these gauge transformations. In addition we can find topologically non-trivial transformations that are periodic up to a constant twist matrix $h \in SU(3)$

$$g(t + 1/T, \mathbf{x}) = h g(t, \mathbf{x}). \quad (2.11)$$

Such a transformation turns a strictly periodic vector potential A_μ into

$${}^g A_\mu(t + 1/T, \mathbf{x}) = h {}^g A_\mu(t, \mathbf{x}) h^\dagger. \quad (2.12)$$

Still the gauge transformed vector potential ${}^g A_\mu$ must obey the boundary condition (2.10). Therefore, the twist matrices h are limited to the center $Z(3)$ of the gauge group $SU(3)$. By definition, the elements of the center commute with all group elements. They are multiples of the unit matrix,

$$h = z \mathbb{1}, \quad z = \exp(2\pi i n/3), \quad n = 1, 2, 3. \quad (2.13)$$

The symmetry with respect to the transformations (2.11) which obey (2.13) is called center symmetry. Note that for a given gauge transformation $g(x)$ the center symmetry with respect to h is a global transformation and should not be considered as a subgroup of the local gauge group.

Now we turn to the quarks. Here the $Z(3)$ symmetry gets explicitly broken in the presence of dynamical quark fields: The crucial point is that the quarks are antiperiodic in Euclidean time, cf. (2.10). Indeed, under a twisted transformation a quark field transforms into

$${}^g q(t + 1/T, \mathbf{x}) = g(t + 1/T, \mathbf{x}) q(t + 1/T, \mathbf{x}) = -z g(t, \mathbf{x}) q(t, \mathbf{x}) = -z {}^g q(t, \mathbf{x}). \quad (2.14)$$

To maintain the boundary condition (2.10) one is restricted to $z = 1$ so that the center symmetry disappears. Nonetheless, the center symmetry is useful as an approximate symmetry of QCD which becomes exact, if the dynamical quarks are neglected.

Note, that we always stress the word “dynamical” in the context of quarks. Indeed, the center symmetry is an important aspect of the theory in particular in the presence of *static* quarks. Here, the connection between the center symmetry and confinement appears, as will be discussed next: We recall that – neglecting dynamical quarks – the QCD action is $Z(3)$ invariant. However, other physical quantities need not necessarily be invariant under the center symmetry transformations. In particular, the global $Z(3)$ symmetry can break spontaneously. We now use static quark fields to probe the physics of the gauge fields. Such infinitely heavy test quarks are described by the Polyakov loop (a Wilson loop closed around the periodic Euclidean time direction)

$$L(\mathbf{x}) = \text{Tr } \mathcal{P} \exp \left[ig \int_0^{1/T} dt A_0(t, \mathbf{x}) \right] \quad (2.15)$$

where \mathcal{P} denotes path ordering of the exponential. The Polyakov loop is a complex scalar field that depends on the spatial position \mathbf{x} of the static color source. It transforms non-trivially under $Z(3)$ transformations,

$${}^g L(\mathbf{x}) = z L(\mathbf{x}). \quad (2.16)$$

On the other hand, it is invariant under strictly periodic gauge transformations (with $z = 1$) as it should be for a gauge invariant physical quantity.

The partition function for a system of gluons in the presence of a static infinitely heavy test quark is given by

$$Z_Q = \int \mathcal{D}[A_\nu^a] L(\mathbf{x}) \exp(-S_{\text{YM}}^E) \quad (2.17)$$

where the (Euclidean) Yang-Mills action S_{YM}^E is obtained from the QCD action by dropping the quark fields. Obviously, the thermal expectation value

of the Polyakov loop

$$\langle L \rangle = \frac{1}{Z} \int \mathcal{D}[A_\nu^a] L(\mathbf{x}) \exp(-S_{\text{YM}}^E) = \frac{Z_Q}{Z} = \exp(-\beta F) \quad (2.18)$$

is just the ratio of the partition functions of the gluon systems with and without the external color source. Therefore, this expectation value measures the free energy F of the static test quark. This aspect connects the center symmetry to confinement: At low temperatures color is confined and the free energy of a single quark is therefore infinitely large ($F = \infty$). Hence, in the confined phase $\langle L \rangle = 0$. On the other hand, at high temperatures asymptotic freedom suggests that quarks and gluons become deconfined. There F is finite and $\langle L \rangle = L_0 \neq 0$ in the deconfined phase. From (2.18) we know that L transforms non-trivially under center symmetry transformations. Therefore, a non-zero expectation value L_0 implies that the $Z(3)$ symmetry is spontaneously broken at high temperatures in the deconfined phase. Thus, $\langle L \rangle$ qualifies as an order parameter of deconfinement. It is unusual that a symmetry is realized at low temperatures, but gets spontaneously broken at high temperatures. However, we note that the center symmetry is not a symmetry of the Hamiltonian, but of the action. In fact, it is easy to understand why the center symmetry must break spontaneously at high temperatures: In the limit $1/T \rightarrow 0$ the integral in (2.15) extends over shorter and shorter Euclidean time intervals and hence $L_0 \rightarrow \text{Tr} \mathbb{1} = 3$, the number of colors. As we will see below in Sect. 2.2.6 the expectation value of the Polyakov loop is still useful as an order parameter even in the presence of dynamical quarks which break the center symmetry explicitly (cf. also Sect. 4.4). In this case, the center symmetry can only be regarded as an approximate symmetry of QCD. This is a first example for an approximate symmetry which still leaves its trace in the phenomenology of QCD. Next we turn to another simplification of QCD which reveals other approximate symmetries.

As outlined in Sect. 2.1.1 the masses of the three light quarks are (much) smaller than typical hadronic scales ($\approx 1 \text{ GeV}$). Therefore mass terms of the light quarks can be treated as a perturbation of a Lagrangian where these masses are dropped,

$$\mathcal{L}_0 = -\frac{1}{2} \text{Tr} F_{\mu\nu} F^{\mu\nu} + \bar{\psi} i \gamma_\mu D^\mu \psi \quad (2.19)$$

where now ψ collects the three light quark fields

$$\psi = \begin{pmatrix} u \\ d \\ s \end{pmatrix}. \quad (2.20)$$

The Lagrangian (2.19) does not contain any dimensionful parameter. The corresponding classical theory possesses dilation invariance, i.e. the corresponding action is invariant with respect to the following transformations of

fields and space-time variables:

$$\begin{aligned} x &\rightarrow x' = e^{-\sigma} x, \\ \psi(x) &\rightarrow \psi'(x') = e^{3\sigma/2} \psi(x), \\ A_\mu(x) &\rightarrow A'_\mu(x') = e^\sigma A_\mu(x). \end{aligned} \tag{2.21}$$

Here σ is an arbitrary real number, $\sigma \in \mathbb{R}$. If this symmetry was realized, QCD would look the same at all distances, since no scale is provided by the theory. Consequently all hadrons (and even all nuclei) would be massless. Even more important, there would be no running, i.e. scale dependence of the coupling constant. Of course, this dilation symmetry is explicitly broken by the quark masses. But even then, one would expect no running of the coupling at high energies where all quark (and hadron masses can safely be neglected. However, the dilation symmetry is an anomaly, i.e. the (approximate) symmetry exists only on the classical level, but is spoiled by quantum effects. In that way, Λ_{QCD} , the scale of QCD, emerges from quantization. One calls this effect “trace anomaly” for the following reason: Still one can define an order parameter associated with this anomaly, namely the expectation value of the trace of the energy-momentum tensor $\Theta_{\mu\nu}$, given by

$$\langle \Theta_\mu{}^\mu \rangle = \underbrace{\frac{\beta_{\text{QCD}}}{g^3} \langle \text{Tr} F_{\mu\nu} F^{\mu\nu} \rangle}_{\text{dominant}} + \sum_{q=u,d,s} (1 + \gamma_{\text{QCD}}) m_q \langle \bar{q}q \rangle. \tag{2.22}$$

The last term on the right hand side of (2.22) comes from the explicit breaking of the dilation symmetry due to the finite quark masses. On the other hand, the first term, the “gluon condensate,” is actually the numerically dominant one. It solely comes from quantum effects encoded in β_{QCD} , the beta function of QCD which governs the running of the coupling constant. We note in passing that quantum effects influence also the last term on the right hand side of (2.22) via the scale dependence of the quark masses controlled by γ_{QCD} . Below in Sect. 2.2.6 we will compare the temperature dependence of the gluon condensate and therefore of the trace anomaly with the temperature dependence of other order parameters.

If the masses of the quarks are neglected their chirality (handedness) becomes a good quantum number: A free massless Dirac particle does not change its chirality. Even more important, also the QCD interaction does not change it and the gluons couple to the left- and right-handed states with the same strength. Formally this can be seen by splitting the quark fields into left- and right-handed contributions, $\psi = \psi_L + \psi_R$. The Lagrangian (2.19) becomes⁶

⁶ Note that \bar{q}_L means $(q_L)^\dagger \gamma_0$.

$$\begin{aligned} \mathcal{L}_0 = & -\frac{1}{2} \text{Tr} F_{\mu\nu} F^{\mu\nu} + \bar{u}_L i\gamma_\mu D^\mu u_L + \bar{u}_R i\gamma_\mu D^\mu u_R + \bar{d}_L i\gamma_\mu D^\mu d_L \\ & + \bar{d}_R i\gamma_\mu D^\mu d_R + \bar{s}_L i\gamma_\mu D^\mu s_L + \bar{s}_R i\gamma_\mu D^\mu s_R \end{aligned} \quad (2.23)$$

where we have explicitly displayed all flavor components to stress that one has just six copies of basically the same object, a massless quark with fixed handedness. Neglecting the quark masses is called “chiral limit”. Since the interaction does not distinguish between the different flavors one can mix them without changing the physics. One can perform this mixing independently for the left- and for the right-handed sector. This suggests a symmetry with respect to a large group, namely the chiral group $U_L(3) \times U_R(3)$. For the following discussion it is more appropriate to structure this group in a somewhat different way,

$$U_L(N_f) \times U_R(N_f) = U_V(1) \times SU_V(N_f) \times SU_A(N_f) \times U_A(1), \quad (2.24)$$

and to discuss separately the implications of the various subgroups. The indices V and A indicate “vector” and “axial(-vector)” and refer to the Lorentz transformation properties of the conserved currents which are attributed to the respective symmetry. We have also taken the freedom to use the number of flavors N_f instead of 3. In that way we are more flexible to discuss isospin symmetry ($N_f = 2$) separately.

Global transformations with respect to $U_V(1)$ just change the phase of all quark species in the same way. The corresponding conserved charge is the baryon number. This symmetry is present in the QCD Lagrangian (2.1) not only in the massless limit (2.19). Therefore, the baryon number is an exactly conserved quantum number of the strong interaction and serves to specify different types of hadrons (baryons, antibaryons, mesons, cf. Tables 2.1 and 2.2). An isolated many-body system is also characterized by a fixed baryon number which can be incorporated grand canonically by a baryo-chemical potential μ (see also Sect. 2.2).

Next we study the following chiral transformations $U \in SU_V(3) \times SU_A(3)$ which leave the Lagrangian (2.19) invariant:

$$\psi \rightarrow U\psi, \quad A^\mu \rightarrow A^\mu \quad (2.25)$$

with

$$U = e^{i\alpha_a \tau_a} e^{i\beta_a \tau_a \gamma_5} \quad (2.26)$$

with flavor matrices τ_a and arbitrary real numbers α_a, β_a with $a = 1, 2, 3$. We note in passing that $\alpha_a = \pm\beta_a$ results in purely right/left-handed transformations which leave the respective other component untouched.

The symmetry with respect to $SU_V(3)$ is extremely well realized for the subgroup $SU_V(2)$ of u and d (isospin symmetry). This is due to the smallness of the difference between m_u and m_d (cf. Table 2.1). Mass splitting within

the isospin multiplets are on the order of a few MeV. Also the symmetry breaking pattern with respect to the rest of $SU_V(3)$ which involves the heavier strange quark mass is well understood – at least for the masses. Turning to $SU_A(N_f)$ we note that a generator (there are three/eight independent ones for $SU_A(2)/SU_A(3)$) of such an axial transformation changes sign under parity transformation $L \rightarrow R$. Thus, acting on a state of definite parity, e.g., a proton at rest, such a generator should create another state with opposite parity. If the chiral symmetry was realized trivially, we would have observed such opposite parity partners for hadrons, including the proton, with small mass splitting (vanishing in the chiral limit). There are no such single-particle states. On the other hand, spontaneous breaking of a continuous symmetry, such as the chiral symmetry, by the vacuum of QCD would mean that the vacuum is degenerate. There is a continuum of such vacua and the action of $SU_A(2)$ on the vacuum would transform different vacua into each other (as a rotation would in a ferro magnet). Furthermore, the action of each generator of chiral $SU_A(N_f)$ on the vacuum creates a pseudoscalar particle, whose rest energy is zero, by the symmetry; this is a reflection of the Goldstone theorem. These particles – three π mesons for $SU_A(2)$ – are observed, albeit with small masses ($m_\pi \ll m_\rho, m_p$, cf. Table 2.2) which are due to nonzero m_u and m_d . For $SU_A(3)$ one finds the flavor octet of light pseudoscalars, i.e. besides the pions one has the kaons and the eta (cf. Table 2.2).

One of the clearest indications that the chiral symmetry is hidden (spontaneously broken) can be seen in the τ -decay data of $\tau \rightarrow \nu_\tau + n\pi$: The weak interaction couples to the left-handed quark currents, i.e. to $V - A$ with

$$V_\mu^b = \frac{1}{2} \bar{\psi} \gamma_\mu \tau^b \psi, \quad A_\mu^b = \frac{1}{2} \bar{\psi} \gamma_\mu \gamma_5 \tau^b \psi. \quad (2.27)$$

(Note that this axial-vector flavor current A_μ^b should not be mixed up with the gluon potential A_μ .) Decays with even (odd) number of pions contribute to V (A). Therefore one can obtain from the τ -decay both spectral informations, the one contained in V and the one contained in A . On the other hand, V and A are connected by a chiral transformation. Thus, if chiral symmetry was realized for the vacuum and its excitation spectrum, the spectral informations contained in V and A would be the same – up to small differences of a few MeV. These spectral informations are obtained from the (Fourier transforms (FT) of the) correlators, schematically $v_1 \sim \text{FT}\langle VV \rangle$. These spectra and their difference are shown in Fig. 2.3. One observes the ρ -peak in the vector (v_1) channel, the bump of the a_1 in the axial-vector (a_1) channel and broad structure at higher energies.⁷ Thus the difference between the two spectra does not vanish, not even approximately. Obviously, in vacuum chiral symmetry is hidden.

⁷ In principle, there is also the one-pion contribution in the axial-vector channel which is not displayed since it would be a delta function at the invariant mass of the pion.

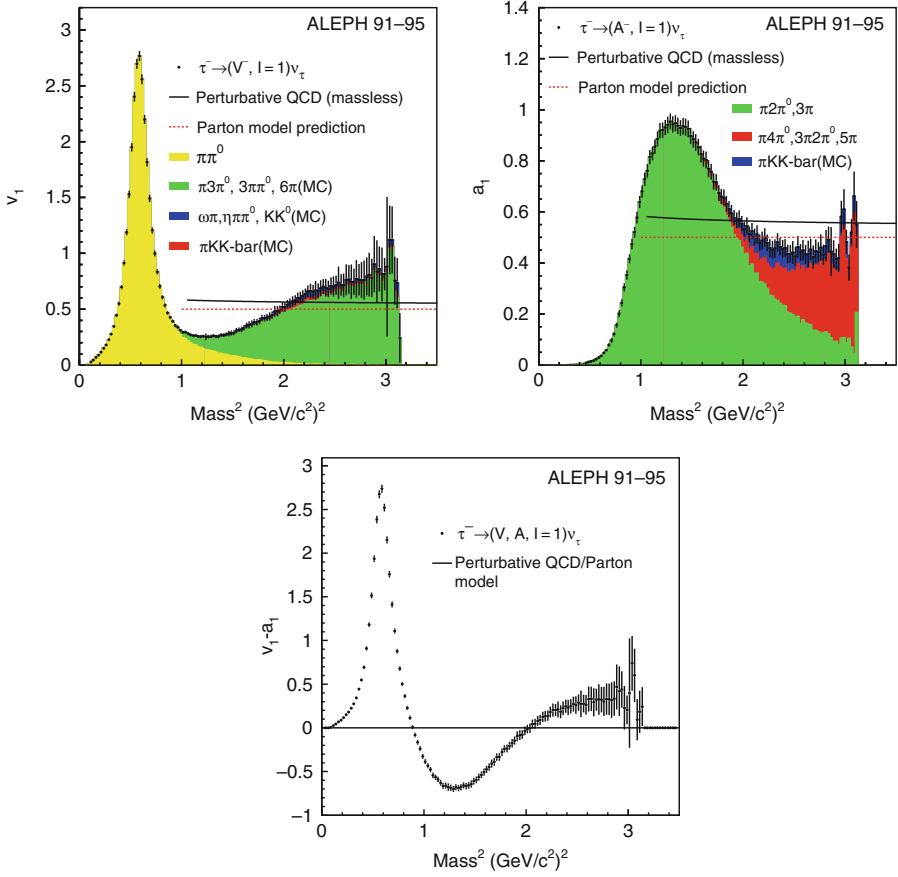


Fig. 2.3 Isovector-vector and isovector-axialvector spectra and their difference as obtained by the ALEPH collaboration [20].

The situation is very similar to the already mentioned ferro magnet: In spite of a rotational invariance of the spin–spin interaction, in the ground state (“vacuum”) all spins are aligned which causes a macroscopic magnetization pointing in some direction chosen to be the z axis. Therefore, full rotational invariance is broken down to the symmetry with respect to rotations around the z axis. The excitation spectrum in the z direction is distinct from the excitation spectrum in the x or y direction, just like in QCD the v -spectrum is distinct from the a -spectrum. If the ferro magnet is heated, the magnetization vanishes and rotational invariance gets restored. The magnetization is an order parameter for the breakdown of full rotational invariance. In Sect. 2.2.6.1, order parameters of chiral symmetry breaking are introduced and their dependence on energy and particle density (or temperature and chemical potential) is discussed.

Finally we turn to the last subgroup on the right hand side of (2.24), the $U_A(1)$ symmetry. If this symmetry was realized and unbroken, we would not find interactions which violate the intrinsic parity.⁸ The decay of the omega meson (intrinsic parity $+1$) into three pions (intrinsic parity -1) is a counter example. On the other hand, if the symmetry was hidden, there should be a ninth Goldstone boson connected to it. The appropriate candidate would be the η' meson which, however, is too heavy (cf. Table 2.2). In fact, the $U_A(1)$ symmetry is destroyed by quantization, i.e. it is an anomaly.

The symmetry pattern of QCD is summarized in Table 2.3. One column concerns the order parameters connected to the possible restoration or breaking of the respective symmetry as a function of temperature T or baryochemical potential μ . These order parameters are further discussed in Sect. 2.2. In the present Sect. 2.1 we have only scratched the surface of thermodynamics and phase transitions. Section 2.2 is devoted to a much more detailed discussion of these issues.

2.2 Phases of QCD

We discuss here the most relevant thermodynamics framework as well as symmetry and universality arguments with a bearing on the phase structure of strongly interacting matter.

2.2.1 General thermodynamics

Due to the vast number of excited degrees of freedom in a many-body system, e.g. a system created in a heavy-ion collision, it is both impractical and uninteresting to consider individual microscopic states. Rather, it is desirable to consider entire ensembles of individual states characterized by suitable macroscopic parameters. This approach forms the foundation for statistical mechanics which takes a particular simple form in the thermodynamic limit dealing with idealized systems that are spatially uniform and sufficiently large to render finite-size effects insignificant. We start this section with a brief reminder of general thermodynamic features of particular relevance to our subsequent discussion.

⁸ The intrinsic parity is defined as $P(-1)^s$ where P denotes the parity of the state and s its spin [21].

2.2.1.1 Microcanonical treatment

Most basic is the microcanonical ensemble which encompasses, with equal probability, all microstates within a narrow energy band around specified values of the energy E as well as possible other quantite is of interest, such as conserved “charges”. The key quantity is the entropy which is the logarithm of the number of states in the ensemble, $S(E, V) = \ln \Omega(E, V)$. In the thermodynamic limit of uniform bulk matter, the volume V acts as a trivial scaling parameter and it is therefore convenient to work with the corresponding intensive variables. The control parameter is then the *energy density* $\varepsilon = E/V$ and the key thermodynamic function is the *entropy density* $\sigma(\varepsilon) = S/V$, which then depends only on the ratio $E/V = \varepsilon$. This simplest case is illustrated in Fig. 2.4 for an idealized system having a first-order phase transition.

For scenarios relevant to compressed baryonic matter, it is required to specify also some (or all) of the conserved charges, such as the net baryon

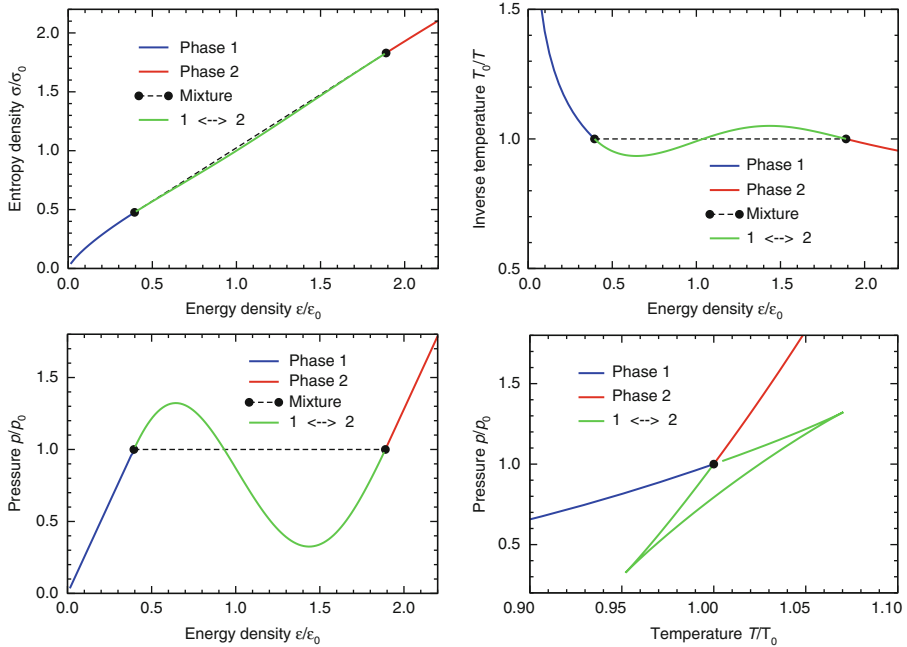


Fig. 2.4 First-order phase transition for a system without conserved charges. The entropy density $\sigma(\varepsilon)$ (*upper left*) exhibits a convex anomaly and, consequently, there are two separate points (*dots*) that have a common tangent (lying above $\sigma(\varepsilon)$). These points represent the coexisting low-density (*blue*) and high-density (*red*) phases. Between these the uniform phase (*green*) is thermodynamically unstable, so a Gibbs phase mixture (*dashed black line*) is preferred. The entropy density $\sigma(\varepsilon)$ determines the inverse temperature $\beta(\varepsilon) = \partial_\varepsilon \sigma = 1/T$ (*upper right*), and these two functions combine to give the pressure $p(\varepsilon) = T\sigma - \varepsilon$ (*lower left*). While $\sigma(\varepsilon)$, $T(\varepsilon)$ and $p(\varepsilon)$ are all single-valued functions, the convexity in $\sigma(\varepsilon)$ causes $\beta(\varepsilon)$ and $p(\varepsilon)$ to be non-monotonic. As a consequence, the equation of state $p(T)$ (*lower right*) is triple-valued in the coexistence region.

number B , the net electric charge Q , and the net strangeness S . To illustrate this case, we discuss the microscopic ensemble characterized by a given energy E and a given “particle number” N which represents, for example, the net baryon number. (The treatment can readily be extended to an arbitrary number of such additional charges, although it becomes increasingly tedious.) The starting point is then the entropy $S(E, N, V)$. This key function responds to changes in the specified parameters as follows,

$$\delta S = \beta \delta E + \alpha \delta N + \pi \delta V , \quad (2.28)$$

where the coefficients are simply related to the temperature T , the chemical potential μ , and the pressure p ,

$$\beta = \frac{1}{T} = \left(\frac{\partial S}{\partial E} \right)_{NV} , \quad \alpha = -\frac{\mu}{T} = \left(\frac{\partial S}{\partial N} \right)_{EV} , \quad \pi = \frac{p}{T} = \left(\frac{\partial S}{\partial V} \right)_{EN} . \quad (2.29)$$

In the thermodynamic limit, S , E , and N are proportional to V and we need only consider the corresponding densities, $\sigma \equiv S/V$, $\varepsilon \equiv E/V$, and $\rho \equiv N/V$, in terms of which we have

$$\text{Temperature} \quad : \quad 1/T = \beta(\varepsilon, \rho) = \partial_\varepsilon \sigma(\varepsilon, \rho) , \quad (2.30)$$

$$\text{Chemical potential} : -\mu/T = \alpha(\varepsilon, \rho) = \partial_\rho \sigma(\varepsilon, \rho) , \quad (2.31)$$

$$\text{Pressure} \quad : \quad p/T = \pi(\varepsilon, \rho) = \sigma(\varepsilon, \rho) - \beta(\varepsilon, \rho)\varepsilon - \alpha(\varepsilon, \rho)\rho . \quad (2.32)$$

A familiar example of a first-order phase transition occurs for nuclear matter⁹ in the temperature range of the nuclear binding energy per nucleon ($0 < T < 20$ MeV) around and below the nuclear saturation density $\rho_0 = 0.16 \text{ fm}^{-3}$. Due to the interplay between the long-range attraction and the short-range repulsion of the force between nucleons, the system behaves like a Van der Waals gas. As a result, nuclear matter behaves as a liquid at densities near the saturation value, where as it is a gas of individual nucleons at low densities. Various thermodynamic representations of this nuclear liquid-gas phase transition (cf. Sect. 2.2.3.4) are schematically illustrated in various representations in Fig. 2.5.

Phase equilibrium:

By considering two such thermodynamic systems in contact and demanding that the resulting total entropy $S = S_1 + S_2$ be stationary, $\delta S = 0$, one finds that the systems are in mutual thermodynamic equilibrium if their intensive quantities match, $\beta_1 = \beta_2 = \beta_0$, $\alpha_1 = \alpha_2 = \alpha_0$, and $\pi_1 = \pi_2 = p_0$, i.e. if they have the same temperature, chemical potential, and pressure. It readily follows that the tangents of the entropy density function $\sigma(\varepsilon, \rho)$ at the two coexistence phase points (ε_1, ρ_1) and (ε_2, ρ_2) are identical,

⁹ Details on many-body descriptions of nuclear matter can be found in Sect. 3.3.

$$\sigma(\varepsilon_1, \rho_1) + \beta_0(\varepsilon_2 - \varepsilon_1) + \alpha_0(\rho_2 - \rho_1) = \sigma(\varepsilon_2, \rho_2) . \quad (2.33)$$

Thermodynamic stability:

To second order, the response of the entropy $S(E, N, V)$ to variations in the ensemble parameters E , N , and V can be written as $S \approx S_0 + \delta S + \delta^2 S$, where S_0 is the entropy of the reference ensemble. The thermodynamic stability properties are therefore determined by the eigenvalues of the curvature matrix of the entropy function. We first note that if E and N are changed in proportion to the change in V , then the entropy also changes in proportion to V since the densities ε and ρ remain unchanged. For this trivial scaling, the

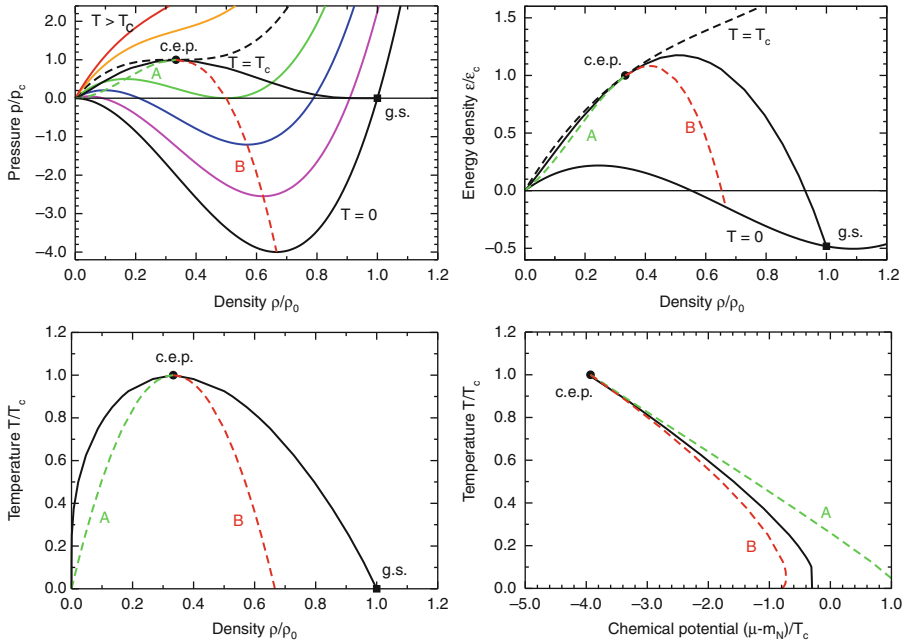


Fig. 2.5 The phase diagram for nuclear matter in different representations, calculated in a schematic model (a classical gas in a density-dependent mean field with properties similar to a Van der Waals gas). In all four representations, the *solid line* delineates the phase coexistence boundary which starts in the zero-temperature vacuum, goes through the critical endpoint (c.e.p.), and terminates at nuclear matter in its ground state (g.s.); in any of the diagrams, two thermodynamically coexisting pieces of bulk matter are represented by a pair of phase points that lie on the phase coexistence boundary and have the same value of the ordinate. The spinodal boundaries are shown by the *dashed curves*, the lower one in green (A) and upper one in red (B). *Top left:* The equation of state $p(\rho, T)$ for a number of temperatures (this representation is closely related to the familiar Van der Waals diagram that shows the pressure p versus the volume per particle, $v = 1/\rho$). *Top right:* The same boundaries in the ρ - ε phase plane. In both *upper panels* the lines at constant temperature $T=0$ and $T=T_c$ are also indicated. *Bottom left:* The boundaries in the ρ - T phase plane. *Bottom right:* The boundaries in the μ - T phase plane, in which the lower and upper branches of the phase coexistence boundary coincide.

second variation vanishes, $\delta^2 S = 0$. So the associated curvature eigenvalue is zero and the scaling mode can be left out of further consideration.

The response to a change of non-scaling type is determined by the curvature properties of the entropy *density*, as encoded into the curvature matrix,

$$\begin{pmatrix} \sigma_{\varepsilon\varepsilon} & \sigma_{\varepsilon\rho} \\ \sigma_{\rho\varepsilon} & \sigma_{\rho\rho} \end{pmatrix} \equiv \begin{pmatrix} \partial_\varepsilon^2 \sigma(\varepsilon, \rho) & \partial_\rho \partial_\varepsilon \sigma(\varepsilon, \rho) \\ \partial_\varepsilon \partial_\rho \sigma(\varepsilon, \rho) & \partial_\rho^2 \sigma(\varepsilon, \rho) \end{pmatrix}. \quad (2.34)$$

When $\sigma(\varepsilon, \rho)$ is concave, as is normally the case, both (generally all) eigenvalues are negative, and a(ny) small change in ε and ρ produces a decrease of the entropy density. Such a uniform system is therefore mechanically stable. (However, the system may be only metastable thermodynamically, as explained below.) But as soon as one of the eigenvalues is positive, the corresponding density changes will increase the entropy density and the uniform system is then mechanically unstable. This instability reflects the thermodynamic preference of the system for splitting into two different systems in mutual equilibrium and is thus characteristic of a first-order phase transition.

It is important to recognize that the phase points representing these co-existing systems generally lie well outside the region of convexity (as seen in Figs. 2.4 and 2.5). Therefore, generally, the intermediate phase region within which a uniform system is thermodynamically unstable consists of an outer region where the entropy density is still concave and an inner region where it is convex. In the convex region (often referred to as the spinodal region) small undulations of uniform matter are amplified which leads towards a phase separation, whereas uniform matter in the concave coexistence region is mechanically metastable, i.e. it is stable against small modulations whereas sufficiently large redistributions may increase the entropy and lead to phase separations. Thus, in Fig. 2.5, within the lower metastable region (situated between the low-density phase coexistence boundary and spinodal A) the system is an undercooled gas of nucleons, while within the upper metastable region (between the high-density phase coexistence boundary and spinodal B) contains superheated nuclear liquid.

These general features are easily understood from the simpler (chargeless) case illustrated in Fig. 2.4. This figure also brings out the fact that when σ is convex its first derivatives are non-monotonic. Therefore, the relationship between the underlying mechanical densities ε and ρ and the corresponding thermodynamic quantities T and μ is not one-to-one in the phase-coexistence region. (For example, the “equation of state” $p(T, \mu)$ is triple-valued throughout that region.) As a result, those latter variables are sometimes less convenient in the presence of a phase transition. This is especially true for dynamically evolving systems, where the mechanical densities (ε and ρ) change continuously and are partly subjected to conservation laws, while the thermodynamic variables (T, μ, p, σ, \dots) are not (see e.g. Sect. 5.3.2, Fig. 5.2 in Part III “Collision Dynamics”).

The microcanonical framework presented above is most relevant for situations where the system is characterized by definite values of the mechanical parameters (E , N , and V), as tends to be the case for isolated systems or in microscopic dynamical treatments.

2.2.1.2 Canonical treatment

When the system can exchange energy with its environment only the average value of the energy can be specified. This is done in terms of the temperature T , or its inverse β . The density of states $\Omega(E, N, V)$ is then replaced by the corresponding Legendre transform, the canonical partition function,

$$Z_T(N, V) = \int dE \Omega(E, N, V) e^{-E/T} = V \int d\varepsilon e^{V[\sigma(\varepsilon, \rho) - \beta(\varepsilon, \rho)\varepsilon]} . \quad (2.35)$$

While we here consider only the thermodynamic limit of uniform matter, the above relationship between the canonical partition function and the density of states holds generally. Here and below we denote thermodynamic quantities in the canonical or grand canonical treatment by subscripts T or $T\mu$, respectively.

An expansion of the entropy density to second order around the value $\bar{\varepsilon}_T(\rho)$ determined by the vanishing of the linear term in the exponent, $\partial_\varepsilon \sigma(\varepsilon, \rho) \doteq \beta$, makes it possible to carry out the integral in the saddle point approximation (if the curvature of the entropy is negative at that point, $\partial_\varepsilon^2 \sigma(\varepsilon, \rho) < 0$). Up to an additive constant, this procedure yields

$$\zeta_T(\rho) \equiv \frac{1}{V} \ln Z_T(N) = \sigma(\bar{\varepsilon}_T(\rho), \rho) - \beta \bar{\varepsilon}_T(\rho) , \quad (2.36)$$

in terms of which we may recover the energy density as well as express the chemical potential and the pressure,

$$\begin{aligned} \bar{\varepsilon}_T(\rho) &= \partial_\beta \zeta_T(\rho) , \\ \alpha_T(\rho) &= -\frac{\mu_T(\rho)}{T} = \partial_\rho \zeta_T(\rho) , \\ \pi_T(\rho) &= \frac{p_T(\rho)}{T} = -\rho^2 \partial_\rho \frac{\zeta_T(\rho)}{\rho} . \end{aligned} \quad (2.37)$$

We note that the transformation from the microcanonical to the canonical description requires that the function $\beta(\varepsilon, \rho)$ can be inverted to give $\bar{\varepsilon}_T(\rho)$. While this is always possible locally, it cannot be done globally inside a phase coexistence region where β is a non-monotonic function of ε (see Fig. 2.4).

2.2.1.3 Grand canonical treatment

The grand canonical treatment is appropriate for systems that can also exchange conserved charge(s) (“particles”) with the environment. The basic quantity is then the normalization constant for the Gibbs ensemble, $\mathcal{Z}_{T\mu}(V) = \sum_k \exp(-E_k/T + \mu N_k/T)$, where the sum is over all individual states k (cf. Eq. (2.5)). Thus it can be expressed as a Legendre transform of the microcanonical phase-space volume $\Omega(E, N, V) = \sum_k = \exp(S(E, N, V))$,

$$\begin{aligned} \mathcal{Z}_{T\mu}(V) &= \int dN \int dE \Omega(E, N, V) e^{-E/T - \mu N/T} \\ &= V \int d\rho \int d\varepsilon e^{V[\sigma(\varepsilon, \rho) - \beta(\varepsilon, \rho)\varepsilon - \alpha(\varepsilon, \rho)\rho]}, \end{aligned} \quad (2.38)$$

where $\beta = 1/T$ and $\alpha = -\mu/T$. While we here consider only the thermodynamic limit of uniform matter, the above relationship between the grand partition function and the density of states holds generally. (The analogous relation for the canonical partition function $Z_T(N, V)$ was given in Eq. (2.35).) The integral may be carried out in the saddle point approximation, in which the entropy density $\sigma(\varepsilon, \rho)$ is expanded to second order around any phase point $(\bar{\varepsilon}, \bar{\rho})$ at which the linear term in the exponent vanishes, requiring $\partial_\varepsilon \sigma(\varepsilon, \rho) \doteq \beta$ and $\partial_\rho \sigma(\varepsilon, \rho) \doteq \alpha$. For each such stationary phase point, the resulting Gaussian integral can then be carried out provided that the eigenvalues of the local curvature matrix of $\sigma(\varepsilon, \rho)$ are negative.

More generally, the grand canonical treatment requires that the functions $\beta(\varepsilon, \rho)$ and $\alpha(\varepsilon, \rho)$ can be inverted to give $\bar{\varepsilon}_{T\mu}$ and $\bar{\rho}_{T\mu}$. When this is possible, we obtain the grand potential $\mathcal{Z}_{T\mu}(V)$, where

$$\xi_{T\mu} \equiv \frac{1}{V} \ln \mathcal{Z}_{T\mu}(V) = \sigma(\bar{\varepsilon}_{T\mu}, \bar{\rho}_{T\mu}) - \beta \bar{\varepsilon}_{T\mu} - \alpha \bar{\rho}_{T\mu} = \pi_{T\mu}, \quad (2.39)$$

From this key function we can then recover the mechanical densities, $\bar{\varepsilon}_{T\mu} = \partial_\beta \xi_{T\mu}$ and $\bar{\rho}_{T\mu} = \partial_\alpha \xi_{T\mu}$. We note that $p_{T\mu} = T\xi_{T\mu}$ which is recognized as the first law of thermodynamics, $E = TS + \mu N - pV$. Furthermore, we readily find the familiar relations $\sigma = \partial_T p$ and $\rho = \partial_\mu p$.

An important advantage of the Gibbs ensemble is that the associated grand partition function can be expressed as an integral over paths or as field configurations evolving in imaginary time. This connection has already been introduced in Sect. 2.1, Eq. (2.7).

2.2.1.4 Phase structure

We close this general reminder of thermodynamics by a brief discussion of phase structure. As an illustration, we show in Fig. 2.5 the phase diagram for nuclear matter in various representations.

In the presentation of the microcanonical treatment, we saw already how the phase structure of a given system can readily be determined by considering the curvature properties of the entropy density in the ρ - ε phase plane: The occurrence of one or more positive eigenvalues in the entropy curvature matrix signals the presence of a first-order phase transition. The associated region of thermodynamic instability is delineated by pairs of phase points (ρ_1, ε_1) and (ρ_2, ε_2) that represent systems that have matching values of temperature, chemical potential, and pressure and therefore can coexist in mutual thermodynamic equilibrium. In the thermodynamically stable region, the relationship between the mechanical variables (ε and ρ) and the thermodynamic variables (T and μ) is one-to-one and the transformation between the different treatments discussed above is simple.

By contrast, inside the phase region of thermodynamic instability the inverse relations are triple-valued and one must carefully keep track of the overlaid phase sheets. Generally, the instability region consists of an outer region adjacent to the border within which the entropy remains concave and these systems are mechanically metastable (it would require a finite disturbance to induce a thermodynamic phase separation). But in the central region, where the entropy function turns convex (in one or more dimensions), uniform matter is mechanically unstable and even small deviations from uniformity will become amplified and such matter will seek to phase separate spontaneously.

The canonical representation describes the system in terms of the temperature T and the density ρ . For a given temperature T , a first-order phase transition is present if two different densities, ρ_1 and ρ_2 have the same chemical potential μ . As the temperature is increased, the corresponding coexistence densities grow progressively similar until they coincide at $T = T_c$, the critical temperature. These coexistence points, from $(\rho_1, T = 0)$ through (ρ_c, T_c) to $(\rho_2, T = 0)$ delineate the unstable region which again can be divided into a metastable region adjacent to the boundary and a central region characterized by spinodal instability. We note that this representation yields a continuous behavior of the various quantities, such as the entropy density $\sigma_T(\rho)$, the pressure $p_T(\rho)$, and the chemical potential $\mu_T(\rho)$.

In the grand canonical representation the density ρ is replaced by the chemical potential μ and, as a result, the entire unstable phase region collapses into a single phase-transition line across which the various quantities (such as $\bar{\rho}_{T\mu}$, $\bar{\varepsilon}_{T\mu}$, and $p_{T\mu}$) are discontinuous. This line, which thus represents a cut rather than a boundary, terminates at the critical point (μ_c, T_c) where there is a second-order phase transition.

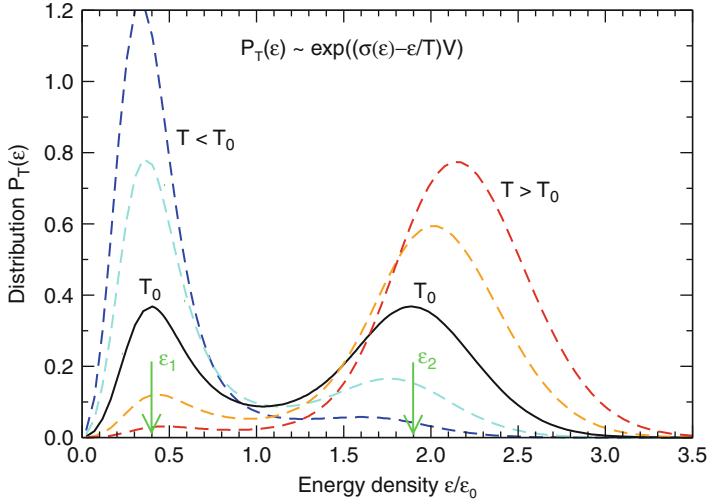


Fig. 2.6 The (normalized) integrand $P_T(\varepsilon) \sim \exp((\sigma(\varepsilon) - \varepsilon/T)V)$ in the expression for the canonical partition function $Z_T(V)$ for the idealized chargeless case displayed in Fig. 2.4, shown for a narrow range of temperatures near the coexistence value T_0 for which the energy densities ε_1 and ε_2 are in thermodynamic equilibrium. (Here and in Fig. 2.4 the softest point, where the speed of sound squared has its minimum, has been used as a scale for ε , σ , and p .)

Crossing the phase boundary:

The Legendre transforms from the microcanonical to the canonical (2.35) or grand canonical (2.38) descriptions provide a useful mean for elucidating how a phase boundary may be crossed while maintaining global thermodynamic equilibrium. To illustrate this, we consider the schematic example exhibited in Fig. 2.4 where there are no conserved charges. The integrand in the Legendre transform is then $\exp((\sigma(\varepsilon) - \beta\varepsilon)V)$ and, for any specified value of T , this function expresses the relative weight $P_T(\varepsilon)$ of the different values of ε in the canonical ensemble. Figure 2.6 shows $P_T(\varepsilon)$ for a range of temperatures near the coexistence temperature T_0 . In the stable regions well below or above T_0 , $P_T(\varepsilon)$ displays a single peak around the value $\bar{\varepsilon}_T$. But near T_0 the distribution turns bimodal, exhibiting peaks centered near the coexistence values ε_1 and ε_2 . (We note that $P_T(\varepsilon)$ is convex in the spinodal region for any T .) Since the peaks have their maxima where the exponent in the Legendre integrand is stationary, the corresponding two values of $\partial_\varepsilon \sigma(\varepsilon)$ are identical and therefore the peaks are shifted in the same direction, e.g. they both move down when T is decreased from T_0 while they move up when T is increased from T_0 .

As T is increased from below to above T_0 , the strength steadily shifts from the lower peak to the higher one. Right at the phase coexistence tempera-

ture $T = T_0$ the two peak values are identical, $P_T(\varepsilon_1) = P_T(\varepsilon_2)$ (though the relative strengths of the two bumps clearly differ). It is important to note that the average energy at a given temperature, $\langle \varepsilon \rangle_T = \int \varepsilon P_T(\varepsilon) d\varepsilon$ increases continuously with T but exhibits a rapid rise at T moves past T_0 . As the volume is increased the peaks become narrower and in the thermodynamic limit, $V \rightarrow \infty$, only the one with the highest value remains significant. Thus, in this limit the energy density $\bar{\varepsilon}_T$ jumps from ε_1 to ε_2 at T_0 and the intermediate region of energy density cannot be addressed within the framework of global thermodynamic equilibrium.

After the above illustration, we now turn to the more realistic case where we have one conserved charge and let us first consider the canonical treatment. The exponent in the Legendre transform (2.35) is then $[\sigma(\varepsilon, \rho) - \varepsilon/T]V$ and, for specified values of T and ρ , a given ε value contributes to the integral (2.38) in proportion to $P_{T\rho} \sim \exp([\sigma(\varepsilon, \rho) - \varepsilon/T]V)$. Above the critical temperature, $T > T_c$, $P_{T\rho}(\varepsilon)$ has only one peak (centered at $\bar{\varepsilon}_T(\rho)$). But as T is decreased below T_c , the distribution $P_{T\rho}(\varepsilon)$ bifurcates and displays two peaks centered at the corresponding coexistence energies, $\varepsilon_1(T)$ and $\varepsilon_2(T)$, signaling the presence of a first-order transition.

Finally, let us consider the grand canonical description of systems with one conserved charge, as considered above. The exponent in the Legendre transform (2.38) is then $p(\varepsilon, \rho)V$ and, for specified values of T and μ , a given phase point (ρ, ε) contributes to the Legendre transform (2.38) in proportion to $P_{T\mu}(\rho, \varepsilon) \sim \exp(p(\varepsilon, \rho)V)$. Away from the coexistence region $P_{T\mu}(\rho, \varepsilon)$ displays only one peak (centered at $(\bar{\rho}_{T\mu}, \bar{\varepsilon}_{T\mu})$). But for (μ, T) phase points near the transition line the distribution $P_{T\mu}(\rho, \varepsilon)$ displays two peaks that are centered near the corresponding coexistence values, (ρ_1, ε_1) and (ρ_2, ε_2) . Their relative prominence changes as the phase point is moved across the transition line, the peak values being equal just at the crossing.

2.2.2 Types of phase transitions

We discuss here a number of phase transitions that are particularly relevant to the topic of this book.

2.2.2.1 Spontaneously broken symmetries: QCD chiral symmetry

Global symmetries often play essential role in determining the phase structure of a system. We recall that there are two ways a global symmetry can be realized on (thermodynamic) states. Trivial: transformation of the symmetry acting on every quantum state in the ensemble maps the ensemble on itself. Spontaneously broken: transformation creates another ensemble which, by symmetry, must have exactly the same values of ε and (if the generators of

the symmetry and the baryon charge commute) of n . The typical example of the spontaneous breaking of a symmetry is a uniaxial ferromagnet below the Curie temperature. The symmetry, Z_2 in this case, flips all spins. Below the Curie temperature such transformation creates a state with flipped magnetization – a distinct macroscopic state.

It is clear that in the situation where the vacuum, or thermal state is degenerate, the variables such as energy and baryon density, which are identical for different degenerate states, are not sufficient to describe the system fully. One can specify the state further by using another variable which is not invariant under the symmetry transformation. Such a variable is called *order parameter*. For example, magnetization is an order parameter in the case of the ferromagnet. In the case of QCD the choice convenient theoretically is the chiral condensate – the expectation value of the quark bilinear operator $\langle \bar{q}q \rangle$. This issue is further discussed below in Sect. 2.2.6.

A point worth keeping in mind is that unlike energy or baryon number, the operator $\bar{q}q$ does not commute with the Hamiltonian of QCD, i.e, the stationary states are not eigenstates of the chiral condensate. This is not a problem, because each individual state can be characterized by the expectation value of $\bar{q}q$ in this state. What we do have to take into account, however, is that the operator $\bar{q}q$ being a product of two quantum fields at the same point has short distance singularities. To define $\bar{q}q$ properly one needs to regularize it, e.g., by splitting the points. Unlike energy or baryon number, which by virtue of being conserved quantities, are insensitive to renormalization, the operator $\bar{q}q$ and its expectation value depends on the renormalization procedure and the associated scale. Therefore, the definition of the chiral condensate should be accompanied by the specification of the renormalization procedure and scale, which is what we shall always imply. It is helpful that the dependence on the scale is weak (logarithmic) and thus, in practice, we will not need to worry about this issue. We shall imply the renormalization scale on the order of 1 GeV in what follows. Experimental data indicate that the value of the chiral condensate in vacuum is approximately

$$\langle \bar{u}u \rangle \approx \langle \bar{d}d \rangle \approx (-250 \text{ MeV})^3. \quad (2.40)$$

One important advantage of the order parameter such as $\bar{q}q$ is that this operator enters linearly into the Hamiltonian. The coefficient m_q is the parameter which explicitly breaks the chiral symmetry. It is the analog of the magnetic field H in the case of the ferromagnet. For non-zero m_q the probability distribution is skewed – favoring the value of $\langle \bar{q}q \rangle$ which minimizes the energy for given m_q . Since, by conventional choice of sign, the contribution to the energy is $+m_q \bar{q}q$, positive mass favors negative chiral condensate. It is worth pointing out that the quark mass, similar to the operator $\bar{q}q$, is renormalization dependent (there is no mass shell for a quark), but the product $m_q \bar{q}q$ is not – and it is a matter of fact that only this combination emerges

in all physically observable relations, e.g., the pion mass is proportional to $m_q \langle \bar{q}q \rangle$.

The value of pressure also depends on m_q . Viewing the pressure $p(T, \mu)$ as the Legendre transform of the energy $\varepsilon(s, n)$, according to Eqs. (2.39) and (2.36), it is easy to show that

$$\left. \frac{\partial p}{\partial m_q} \right|_{T, \mu} = - \left. \frac{\partial \varepsilon}{\partial m_q} \right|_{s, n} = - \langle \bar{q}q \rangle, \quad (2.41)$$

where derivatives are taken with corresponding arguments fixed, as indicated.

2.2.2.2 Second-order transitions

Similarly to the rotational symmetry in the ferromagnet, the spontaneously broken chiral symmetry in QCD is restored at some critical temperature.

Using the order parameter as an additional thermodynamic variable, one can see how the phase transition is accomplished by looking at the probability distributions of that order parameter in an ensemble at given T (and μ). In the broken phase there will be two (or more, depending on the type of symmetry and the order parameter, or even a manifold of) distinct peaks related by the symmetry, which merge into a single peak at the critical temperature. Such a transition is called *second-order* phase transition.

The symmetry is not necessary for the second order phase transition. One can achieve such a transition generically by tuning parameters to maintain two coexisting peaks of the probability distribution at equal height, as they converge. On the phase diagram this corresponds to staying on the first-order transition line and moving towards the critical point, where the transition ends. Ordinary critical points are therefore often referred to as second order transitions.

However, if the two coexisting peaks are related by a (spontaneously broken) symmetry, their heights are automatically the same. This eliminates one additional tuning parameter needed to achieve criticality. As a result second-order transitions are more ubiquitous among symmetry restoration transitions, than among generic phase transitions. In QCD, *in the chiral limit*, this allows a whole line of critical points on a $T\mu$ phase diagram to exist – as is the case with chiral restoration transition in QCD for low μ (see below). Only a single critical point survives from this line when the chiral symmetry is *explicitly* broken by the quark masses.

Of course, a broken symmetry can also be restored by a generic first order transition – if the peak corresponding to symmetric phase emerges and outgrows the broken symmetry peaks before the latter converge.

Similar to the critical point, the symmetry restoration transition is also a branching point for the partition function Z as a function of the symmetry breaking parameter (H in ferromagnet, or m_q in QCD). It is a point

where pressure and all other thermodynamic functions are singular. On the $T\mu$ plane, the phases with different realizations of the symmetry (trivial vs spontaneously broken) must be separated by a continuous line of such critical points (or by a first order transition line).

Very generically, the order parameter can be used to predict that a phase transition must be associated with a singularity (non-analyticity) of some sort in thermodynamic functions. Indeed, if the order parameter is *exactly* zero in some phase (usually, because it is protected by an exact symmetry), the analyticity must be lost at the phase boundary so that the order parameter can change its value (to non-zero value in the broken phase).

2.2.2.3 Critical behavior at a second-order phase transition

The most important property of the second-order phase transition is the divergence of the correlation length. If we consider local values of variable such as energy, density or order parameters, these values fluctuate. The correlation length of these fluctuations in a *generic* thermodynamic system is of the order of the characteristic microscopic length ($1/\Lambda_{\text{QCD}}$ in QCD, or interatomic spacing in a ferromagnet). This is not the case at a critical point (second-order transition) – the correlation length becomes infinite.

This phenomenon can be described using the effective potential for the order parameter. We denote the order parameter generically as σ . To describe spatial correlations we consider probability distribution for a spatially varying parameter $\sigma(\mathbf{x})$, $\mathcal{P}[\sigma(\mathbf{x})]$. To determine the correlation length ξ we calculate the thermal expectation value of $\sigma(\mathbf{x})\sigma(\mathbf{y})$,

$$\langle \sigma(\mathbf{x})\sigma(\mathbf{y}) \rangle = \int \mathcal{D}\sigma(\mathbf{x}) \mathcal{P}[\sigma(\mathbf{x})] \sigma(\mathbf{x})\sigma(\mathbf{y}) \sim \exp(-r/\xi), \quad (2.42)$$

for $r \equiv |\mathbf{x} - \mathbf{y}| \rightarrow \infty$.

The logarithm of the probability density \mathcal{P} defines the corresponding *Ginzburg-Landau effective potential* $\Omega[\sigma(\mathbf{x})]$ as a functional of $\sigma(\mathbf{x})$ which we expand in spatial derivatives of $\sigma(\mathbf{x})$:

$$-\log \mathcal{P}[\sigma(\mathbf{x})] \equiv \Omega[\sigma(\mathbf{x})]/T = \int d^3\mathbf{x} [V(\sigma) + (1/2)(\nabla\sigma)^2 + \dots] \quad (2.43)$$

(we chose normalization of σ to reduce the gradient term to the above canonical form).

Mean-field critical behavior:

The saddle point, or mean-field, or Gaussian approximation to the path integral in Eq. (2.42) amounts to expanding $\Omega[\sigma(\mathbf{x})]$ around its minimum – a constant (mean – hence the name) field σ_0 and dropping all terms beyond

quadratic. The Gaussian path integral is then easy to take:

$$\langle \sigma(\mathbf{x})\sigma(\mathbf{y}) \rangle_{\text{mean field}} = \sigma_0^2 + \frac{\exp(-r/\xi)}{r}, \quad \text{with} \quad r = |\mathbf{x} - \mathbf{y}|, \quad (2.44)$$

where the correlation length ξ is related to the curvature of the potential $V(\sigma)$ at its minimum:

$$\xi = (V''(\sigma))^{-1/2} \Big|_{\sigma=\sigma_0}, \quad (2.45)$$

At the critical point (or second order phase transition), two coexisting minima of V continuously merge into one, and the curvature vanishes. Thus ξ diverges. If the curvature vanishes linearly with a parameter which is being varied, e.g., temperature, as it is generically the case, the correlation length diverges as

$$\xi \sim |T - T_c|^{-1/2}, \quad (2.46)$$

where T_c denotes the critical temperature. This is the well-known result of the Ginzburg-Landau theory of the phase transitions, which is not correct generically, as we discuss now.

The mean-field/saddle-point approximation, or neglecting terms beyond quadratic in $\Omega[\sigma]$ is not justified in most cases, in particular, very close to the transition, where the correlation length becomes very large compared to typical microscopic scale. This approximation is valid only if the non-Gaussian terms (higher order than σ^2) can be neglected in $\Omega[\sigma(\mathbf{x})]$. For example, the leading higher order term, $\lambda\sigma^4$, would be negligible compared to the quadratic term $\xi^{-2}\sigma^2$ if $\lambda\sigma^2 \ll \xi^{-2}$ (for simplicity we consider $\sigma_0 = 0$). The typical value of σ^2 relevant in this case could be estimated as the Gaussian (mean-field) average of $\sigma(\mathbf{x})\sigma(\mathbf{y})$ at $|\mathbf{x} - \mathbf{y}| \sim \xi$.¹⁰ Using the correlator Eq. (2.44), or by a simple dimensional counting, we find $\sigma^2 \sim \xi^{2-d}$, where $d = 3$ is the dimension of space. Thus, higher order terms, i.e., non-Gaussian fluctuations, are negligible if

$$\lambda\xi^{d-4} \ll 1 \quad \text{--- Ginzburg criterion.} \quad (2.47)$$

For $d < 4$ (that includes the relevant case $d = 3$) the mean-field approximation is invalid for large ξ . The value $d = 4$ is the *upper critical dimension* for this critical field theory.

Non-mean-field critical behavior, scaling and universality:

¹⁰ The naive average $\langle \sigma^2 \rangle$ is the correlator $\langle \sigma(\mathbf{x})\sigma(\mathbf{y}) \rangle$ at $\mathbf{x} \rightarrow \mathbf{y}$, and it is divergent. This short-distance divergence can be regularized by subtracting the same average at $\xi = \infty$, since the short-distance behavior is independent of ξ . This counterterm arises naturally from additive renormalization (shift) of T_c . The subtracted value of $\langle \sigma^2 \rangle$ is of order ξ^{2-d} as stated in text.

To anticipate and/or understand the correct result beyond the mean-field approximation, one observes that at the critical point, i.e., in the limit $\xi \rightarrow \infty$ the system becomes *scale invariant*. Therefore, one should expect the correlator to follow a power law:

$$\langle \sigma(\mathbf{x})\sigma(\mathbf{y}) \rangle \sim \frac{1}{r^{1+\eta}}, \quad \text{for} \quad r = |\mathbf{x} - \mathbf{y}| \ll \xi, \quad (2.48)$$

where η is the critical exponent. Calculation of the exponent η (which equals twice the anomalous dimension of the order parameter field σ) requires application of *renormalization group* methods to the 3-dimensional field theory defined by the action $\Omega[\sigma(\mathbf{x})]$ at the critical point $\xi \rightarrow \infty$. (A review of the renormalization group method is given in Sect. 4.7.)

One of the remarkable consequences of the renormalization group is the *universality* of critical phenomena. Indeed, the critical indices are determined by critical points of the effective theory for the order parameter σ and do not depend on the detailed microscopic nature of the order parameter or the underlying microscopic theory itself. The critical behavior of different microscopic theories fall into broad *universality classes*, each described by a critical point of a 3-dimensional theory. In general, microscopic theories which have the same global symmetries, and their pattern of breaking/restoration at their respective critical points, fall in the same universality class.

Another important critical exponent is defined by the power at which the correlation length diverges at the critical point:

$$\xi \sim |T - T_c|^{-\nu} \quad (2.49)$$

This exponent is related to the anomalous dimension of the mass operator, i.e., the term σ^2 , of the critical field theory. In the mean field theory of Ginzburg-Landau $\eta = 0$ and $\nu = 1/2$. In the most common universality class of the Ising model (described by a single-component scalar field theory), $\eta \approx 0.04$ and $\nu \approx 0.63$.

The divergence of the correlation length Eq. (2.49) is the source of the non-analyticity of all thermodynamic functions at the critical point. For example, the divergence of the susceptibility of the order parameter

$$\chi = \int d^3\mathbf{x} \langle \sigma(\mathbf{x})\sigma(\mathbf{y}) \rangle \quad (2.50)$$

can be calculated by substituting Eq. (2.48) into Eq. (2.50) for $r \ll \xi$ and truncating the diverging integral at $r \sim \xi$:

$$\chi \sim \xi^{2+\eta} \sim |T - T_c|^{-\nu(2+\eta)}. \quad (2.51)$$

We see that the exponent γ defined as $\chi \sim |T - T_c|^{-\gamma}$ is not independent, but is related to η and ν . The same is true about other commonly used exponents α , β , δ , etc.

The scaling invariance means that for large but finite ξ , the value of ξ remains the only relevant scale in the system. If we change ξ by an arbitrary factor s (e.g., by changing $T - T_c$), and then rescale all the quantities by appropriate powers of s then all relations must remain correct.¹¹ In other words, the system is self-similar under scaling transformation.

The scaling invariance at the critical point allows to apply simple dimensional counting, in which all non-trivial properties are in the anomalous scaling dimensions of the variables. For example, assigning, by convention, scaling dimension $[r] = -1$ to distance, we see that according to Eq. (2.48) the order parameter has the scaling dimension $[\sigma] = (1 + \eta)/2$, and according to Eq. (2.49) the thermal variable $t = T - T_c$ has scaling dimension ν .

Using this counting, for example, one can derive the dependence of the correlation length on the value of the external symmetry breaking parameter h , which in the Ising model is the magnetic field, which introduces a term $h\sigma$ into $\Omega(\sigma)$. It is easy to see that at $t = 0$ correlation length will be finite for $h \neq 0$ and will diverge when $h \rightarrow 0$. The scaling dimension of h can be found from $[h\sigma d^3x] = 0$: $[h] = 3 - (1 + \eta)/2 = (5 - \eta)/2$. Therefore, by scaling, at $t = 0$ the relationship between ξ and h must be

$$\xi \sim h^{-2/(5-\eta)}. \quad (2.52)$$

This is a non-rigorous, but a very handy way of generating many useful scaling relations.

As another example, given the above scaling dimensions $[t] = \nu$ and $[h] = (5 - \eta)/2$, the correlation length must depend on t and h as

$$\xi = h^{-2/(5-\eta)} F(x), \quad \text{where } x = h t^{-(5-\eta)\nu/2}, \quad (2.53)$$

and $F(x)$ is a dimensionless function of the “dimensionless” scaling variable x .¹² This function is universal and it obeys $F(0) = \text{const}$ to match Eq. (2.52), and $F(x \rightarrow \infty) \sim x^{(5-\eta)/2}$ to match Eq. (2.49). A particularly relevant example for us will be the approach to the critical point along a ray $t/h = \text{const} < \infty$. Because $(5 - \eta)\nu/2 > 1$, we find $x \rightarrow 0$ along this ray and Eq. (2.53) shows that ξ grows with h as in Eq. (2.52). I.e., ξ grows with the same power for all $t/h = \text{const}$ rays, except along the temperature axis $h = 0$, where it grows fastest (2.49).

¹¹ Up to inverse powers of the correlation length – the corrections to scaling, which vanish as $\xi \rightarrow \infty$.

¹² It is customary to write $x = h t^{-\beta\delta}$, which is equivalent to Eq. (2.53), if one expresses β and δ in terms of the two independent exponents η and ν .

2.2.3 QCD phase diagram at low temperatures

After this general introduction we shall now tour the QCD phase diagram in the T - μ plane. One can expect the phase diagram of QCD to have many subtleties. We can anticipate some of these by noticing that there are several small parameters, whose interplay may produce subtle, competing effects that will lead to new states of matter: the up and down quark masses are small on the natural mass scale of QCD. In addition, the strange quark mass is comparable to the QCD scale, and it might produce additional exotic states in the phase diagram, especially in the low- T region. In realistic environments, one must also take electromagnetism into account. We shall not even try to attack the full problem. Instead, we shall strip as much from it as we possibly can while still keeping the most basic QCD features in. We shall find that even such a “stripped” version of QCD (F. Wilczek coined the name “QCDLite” for it) is an interesting and challenging problem.

Thus we consider pure $SU(3)_{\text{color}}$ QCD with (i) electroweak interactions turned off and with (ii) two massless quarks. There is then an exact $SU(2)_L \times SU(2)_R \times U(1)_B$ global symmetry of the action, which is spontaneously broken down to $SU(2)_V \times U(1)_B$ at zero and sufficiently low temperatures by the formation of a condensate, $\langle \bar{q}q \rangle$. Many features of QCD indicate that this is a reasonable approximation, e.g., the lightness of pions, the success of current algebra relations, etc. (We will comment below on the inclusion of electromagnetic interactions and strange quarks.) This theory is described by the grand canonical partition function given in Eq. (2.7).

Both the temperature T and the baryo-chemical potential μ (as well as the pressure p) are intensive parameters. For a system in thermodynamic equilibrium, these quantities are the same for any of its smaller subsystems. In contrast, the densities, such as the entropy density s and the baryon density n , of extensive quantities can differ for two subsystems even when they are in equilibrium with each other. This happens in the phase coexistence region, e.g., a glass containing water and ice. It is more convenient to describe the phase diagram in the space of intensive parameters, T and μ (the pressure is not an independent parameter, but a function of T and μ). In particular, the first-order phase transition which we shall encounter is characterized by one value of μ but two values of n – the densities of the two coexisting phases (cf. the corresponding discussion in Sect. 2.2.1, illustrated in Fig. 2.5). Another reason for working with these coordinates is that first-principle lattice calculations (cf. Sect. 3.2) are performed using T and μ as independent variables that can be controlled while the densities are measured. The results of relativistic heavy-ion collision experiments are also often analyzed using this set of parameters.

2.2.3.1 Zero temperature

We begin by considering the phase diagram as μ is varied along the line $T = 0$. Strictly speaking, we are not dealing with *thermodynamics* here since the system is in its ground state. This fact leads to a simple property of the function $n(\mu)$, where from now on n denotes the number density of fermions: Below some value μ_0 one finds (see e.g. [22] for more details)

$$n(\mu) = 0 \quad \text{for} \quad \mu < \mu_0 . \quad (2.54)$$

What is the value of μ_0 ? As a trivial example, consider a free theory of massive fermions with mass m carrying one unit of baryon charge. One finds $\mu_0 = m$ for such a theory. When $\mu > m$, the ground state is the Fermi sphere with radius $p_F = \sqrt{\mu^2 - m^2}$. Therefore, $n(\mu) = (\mu^2 - m^2)^{3/2}/(3\pi^2)$. Thus, we see that, even in a trivial theory, the function $n(\mu)$ has a singularity at $\mu = \mu_0$. The existence of some singularity at the point $\mu = \mu_0$, $T = 0$ is a robust and model independent prediction. This follows from the fact that a singularity must separate two phases distinguished by the value of the density n , which plays the role of the order parameter: the function $n(\mu) \equiv 0$ cannot be continued to $n(\mu) \neq 0$ without a singularity.

2.2.3.2 Nuclear matter

The exact value of μ_0 and the form of the singularity are somewhat different in QCD and in the real world (QCD+) which includes other interactions, most notably electromagnetic interactions. Since we are not primarily interested in this $T = 0$ low-density region we just state that the difference between μ_0 and the nucleon mass is small on typical hadronic scales and refer to [22] for further details.

For larger values of the chemical potential, i.e. for $\mu - \mu_0 = \mathcal{O}(10\text{--}200 \text{ MeV})$, we traverse the domain of nuclear physics with the possibility for various phase transitions. In particular, a transition to neutron matter ($Z \ll A$) is probably similar to the transition in QCD at $\mu = \mu_0$. In this domain, one may encounter such phenomena as nuclear matter crystallization [23, 24], superconducting phases of neutron matter and quark matter [25–28], and, due to the strange quark in QCD+, kaon condensation [23, 29] and a transition to strange quark matter [30, 31]. Moving along the μ axis to the right is equivalent to increasing the pressure: $p = \int n d\mu$. Thus, this picture is roughly what one might encounter in moving towards the center of a neutron star from the iron crust at the surface.

Our knowledge of $n(\mu)$ is scanty for densities of order one to ten times n_0 and $\mu - \mu_0 = \mathcal{O}(10\text{--}200 \text{ MeV})$ both in QCD and in QCD+. We can only be sure that $n(\mu)$ is a monotonically increasing function, which follows from the requirement of thermodynamic stability.

2.2.3.3 Quark matter

The behavior of $n(\mu)$ again becomes calculable in the region of very large $\mu \gg \Lambda_{\text{QCD}}$. In that case, the Pauli exclusion principle forces the quarks to occupy ever higher momentum states, and, due to asymptotic freedom, the interaction of quarks near the Fermi surface is (logarithmically) weak. The baryon charge density is proportional to the volume of a Fermi sphere of radius $\mu/3$, $n(\mu) \approx N_f(\mu/3)^3/(3\pi^2)$. At low temperatures, only quarks near the Fermi surface contribute to the Debye screening of the gauge fields. The square of the screening mass, m_D^2 , is proportional to the area of the Fermi surface: $m_D^2 \sim g^2\mu^2$. This means that color interactions are screened on lengths $\mathcal{O}(1/g\mu) = \mathcal{O}(\sqrt{\ln(\mu/\Lambda_{\text{QCD}})}/\mu)$. This motivates the conclusion that nonperturbative phenomena such as chiral symmetry breaking should be absent at sufficiently large μ . Therefore, in QCD with two massless quarks one should expect at least one other phase transition, at a value of μ which we define as μ_1 – a transition characterized by the restoration of chiral symmetry.

The situation in QCD+, with a strange quark, is somewhat more subtle. As has been observed by Alford, Rajagopal and Wilczek [32] at sufficiently large μ one must reach a phase in which chiral symmetry is broken by a completely different mechanism than it is in the QCD vacuum, the mechanism which the authors named Color-Flavor-Locking (CFL). The CFL phase of QCD+ is a subject of many recent studies (see, e.g., [33–36] for reviews). The mass of the strange quark again crucially affects the phase diagram. The question of whether this transition to CFL occurs from the chirally symmetric phase $\mu_{\text{CL}} > \mu_1$, or before the chirally symmetric phase even sets in at zero T is open.¹³ Sending m_s to infinity will relieve us from this question.

What is the value of μ_1 in QCD, and is it finite? Very little reliable information about the phase transition at μ_1 is available. However, several different approaches agree on the conclusion that the value of μ_1 is finite and that $\mu_1 - \mu_0$ is on the order of the typical QCD scale $\Lambda_{\text{QCD}} \approx 200 \text{ MeV} \approx 1 \text{ fm}^{-1}$. For example, equating the quark pressure minus the MIT bag constant to the pressure of nuclear matter yields such an estimate (see, e.g., [38]). A simpler thermodynamic model, which is similar to the MIT bag, but neglects the pressure on the nuclear matter side gives $\mu_1 = 3\sqrt{\pi}B^{1/4} \approx 1.1 \text{ GeV}$. Here, we should also point out another interesting distinction between QCD and QCD+: the effect of the strange quark in QCD+ is to decrease the value of μ_1 compared to that of QCD. It has even been conjectured that this effect might be sufficient to drive μ_1 below μ_0 , which would make normal nuclear matter metastable [30, 31]. Another model which predicts the phase transition at finite μ_1 is the Nambu-Jona-Lasinio model, which focuses on the degrees of freedom associated with the spontaneous chiral symmetry breaking and leads to a similar estimate for μ_1 [39].

¹³ Perhaps, there is no transition at all, as conjectured by Schäfer and Wilczek [37].

What is the order of this phase transition? The MIT bag model predicts that it is a first-order transition since the density, n , of the baryon charge is discontinuous. Unfortunately, analysis of the Nambu-Jona-Lasinio model shows that the order of the transition depends on the values of parameters, most notably, on the value of the cutoff. A larger cutoff leads to a second-order transition, a smaller to a first-order transition [39]. A random matrix model at $T = 0$ predicts a first-order phase transition [40]. Here we shall use more general methods to analyze features of the phase diagram of QCD at finite density *and* temperature. We base our subsequent analysis of the phase diagram of QCD with two massless quarks on the following expectations: (i) $\mu_1 \sim \mu_0 + \mathcal{O}(200 \text{ MeV})$ and (ii) the transition is of first order.

2.2.3.4 Nuclear liquid-gas transition at finite T and μ

We have used the density n as an order parameter, to show that there is a singularity at $\mu = \mu_0$ and $T = 0$. It was important for that argument that n is exactly zero for all $\mu < \mu_0$. At nonzero T , however, n is not strictly 0 for any $\mu > 0$. Hence, at finite T the density n cannot be used to predict phase transitions as it can at zero T .

Nevertheless, we can use a continuity argument to deduce that the first-order phase transition at $T = 0$, $\mu = \mu_0$ has to remain a first-order phase transition for sufficiently small T . Therefore, there must be a line emerging from the point $T = 0$, $\mu = \mu_0$ in the $T - \mu$ diagram Fig. 2.9. One can think of this transition as boiling the nuclear fluid. Indeed, the basic character of the nuclear force, being attractive at large distances but strongly repulsive at short distances, invariably leads to a behavior similar to that of a Van der Waal gas. The corresponding properties of this liquid-gas phase transition were illustrated and discussed in more detail in connection with Fig. 2.5, in which the features of the nuclear two-phase system were displayed in different thermodynamic representations.

As there is no symmetry-breaking order parameter which distinguishes the two phases, there is no reason why these two phases cannot be connected analytically. As in a typical liquid-gas transition, it is natural to expect that the first-order phase transition line terminates at a critical point with the critical exponents of the three-dimensional Ising model. The temperature of this critical point can be estimated from the binding energy per nucleon in cold nuclear matter, $T_0 = \mathcal{O}(10 \text{ MeV})$, cf. Figs. 2.5 and 2.9. Signatures of this point are seen in heavy-ion collisions at moderate energies (i.e., $\approx 1 \text{ GeV}$ per nucleon), and the critical properties of this point have been studied through measurements of the yields of nuclear fragments [38, 41]. In particular, the reported critical exponents are in agreement with those of the three-dimensional Ising model [41].

Additional phase transitions which might occur at $T = 0$ would give rise to additional phase transition lines. One could expect two generic situations. If

there is a breaking of a global symmetry (e.g., translational symmetry in the case of nuclear matter crystallization), the phase transition line must separate such a phase from the symmetric phase at higher temperature without any gaps in the line. Otherwise, the transition can terminate at a critical point.

2.2.4 QCD transitions and chiral symmetry

Now we turn to the more general case where the temperature is not small or vanishing. Symmetry considerations will help to characterize the different phases of QCD.

2.2.4.1 Chiral symmetry argument

In the chiral limit – the idealized limit when 2 lightest quarks, u and d , are taken to be massless, the Lagrangian of QCD acquires chiral symmetry $SU(2)_L \times SU(2)_R$, corresponding to $SU(2)$ flavor rotations of (u_L, d_L) and (u_R, d_R) doublets independently. The ground state of QCD breaks the chiral symmetry spontaneously locking $SU(2)_L$ and $SU(2)_R$ rotations into a single vector-like $SU(2)_V$ (isospin) symmetry and generating 3 massless Goldstone pseudoscalar bosons – the pions. The breaking of the chiral symmetry is a non-perturbative phenomenon.

At sufficiently high temperature $T \gg \Lambda_{\text{QCD}}$, due to the asymptotic freedom of QCD, perturbation theory around the approximation of the gas of free quarks and gluons (quark-gluon plasma – QGP) should become applicable. In this regime chiral symmetry is not broken. Thus we must expect a transition from a broken chiral symmetry vacuum state to a chirally symmetric equilibrium state at some temperature $T_c \sim \Lambda_{\text{QCD}}$. The transition is akin to the Curie point in a ferromagnet – where the rotational $O(3)$ symmetry is restored by thermal fluctuations (chiral $O(4) = SU(2) \times SU(2)$ symmetry in QCD). Thermodynamic functions of QCD must be singular at the transition point – as always when the transition separates thermodynamic states with different realization of global symmetry.

Thus, the region of broken chiral symmetry on the $T\mu_B$ phase diagram must be separated from the region of the restored symmetry by a closed boundary as shown in Fig. 2.7.

2.2.4.2 Pisarski-Wilczek argument

The chiral symmetry argument alone is not sufficient to determine the *order* of the temperature driven chiral symmetry restoration transition. A more elaborate argument, based on universality, advanced by Pisarski and Wilczek

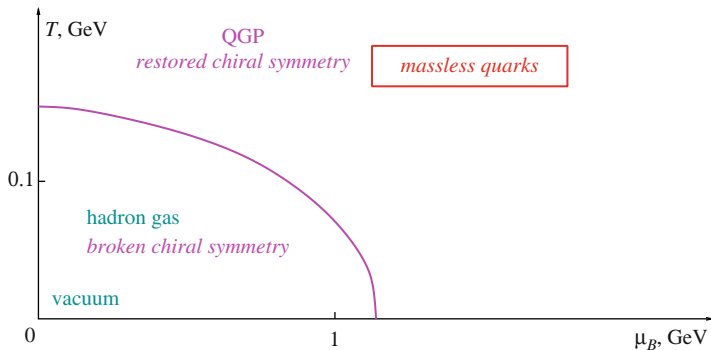


Fig. 2.7 Phase diagram of QCD with massless quarks dictated by the chiral symmetry argument. The order of the transition (*solid magenta line*) is not determined by this simplest argument.

[42] asserts that the transition *cannot* be of second order for *three massless* quarks.

In a simplified form, the logic of [42] is as follows. Let us assume that the transition is of the second order. Then the critical behavior of the system (long-distance behavior of correlation functions, singular contributions to thermodynamic functions, etc.) is determined by the long-wavelength modes which, in the case of the second order transition in a theory with N_f light quarks, are the $N_f^2 - 1$ pions of the spontaneously broken $SU(N_f)_A$ axial flavor symmetry plus the critical mode – the magnitude of the chiral condensate $\sigma \sim \bar{q}q$.

Universality implies that the critical behavior is the same as in any local theory in 3 dimensions with the same global symmetry breaking pattern and the same set of critical modes. In our case, a representative example of the universality class is an $SU(N_f) \times SU(N_f)$ sigma model of an $N_f \times N_f$ matrix-valued field Σ . It turns out, that for $N_f = 3$, the model cannot be critical: there is a relevant term *cubic* in the order parameter field, $\det \Sigma$, which always destabilizes the symmetric minimum of the effective potential for Σ via a first order transition, before the curvature of the minimum vanishes (i.e., before criticality is reached). Hence, QCD with $N_f = 3$ massless quark flavors must undergo a *first* order chiral restoration transition.

2.2.4.3 $N_f = 2$ chiral limit and tricritical point

For *two massless* quarks the transition can be either second or first order. As lattice and model calculations show, both possibilities are realized depending on the value of the strange quark mass m_s and/or the baryo-chemical potential μ_B .

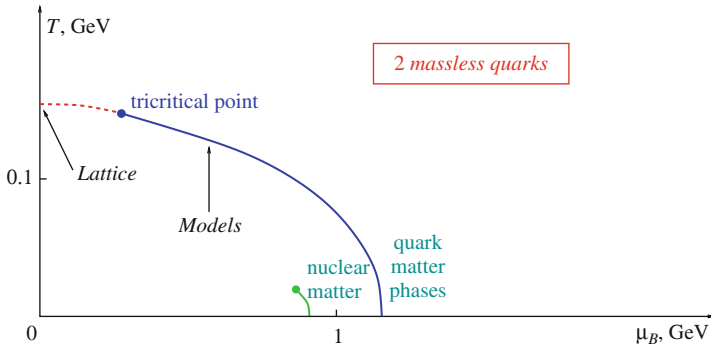


Fig. 2.8 The order of the chiral symmetry restoration transition for 2 massless and one massive quarks. The *dashed line (red)* is the second order transition, the *solid line (blue)* is the first order transition. In the low T region: chiral symmetry is broken in nuclear matter. Details of the phase structure at high μ_B are omitted.

The point on the chiral phase transition line where the transition changes order is called tricritical point, see Fig. 2.8. The location of this point is one of the unknowns of the QCD phase diagram with 2 massless quarks. In fact, even the order of the transition at $\mu_B = 0$, which many older and recent studies suggest is of the second order (as shown in Fig. 2.8) is still being questioned (see, e.g., recent review [43]).

Neither can it be claimed reliably (model or assumption independently) that the transition, if it begins as a 2nd order at $\mu_B = 0$, changes to first order. However, numerous model calculations show this to be the case. Lattice calculations also support such a picture. Recent advances in the understanding of QCD at low T and large μ_B , reviewed, e.g., in [33–36], also point at a first order transition (at low- T , high- μ_B) from nuclear matter to color superconducting quark matter phase. Figure 2.8 reflects this consensus.

At low temperature, nuclear matter (which is expected to be still bound in the chiral limit) should be placed on the broken symmetry side of the chiral transition line as shown in Fig. 2.8.

2.2.4.4 Physical quark masses and crossover

When the up and down quark masses are set to their observed finite values, the diagram assumes the shape sketched in Fig. 2.9. The second order transition line (where there was one) is replaced by a crossover – the criticality needed for the second order transition in Fig. 2.8 requires tuning chiral symmetry breaking parameters (quark masses) to zero. In the absence of the exact chiral symmetry (broken by quark masses) the transition from low- to high-temperature phases of QCD need not proceed through a singularity. Lat-

tice simulations do indeed show that the transition is a crossover for $\mu_B = 0$ (most recently and decisively [44], see also [43] for a review).¹⁴

This transitional crossover region is notoriously difficult to describe or model analytically – description in terms of the hadronic degrees of freedom (resonance gas) breaks down as one approaches crossover temperature (often called T_c), and the dual description in terms of weakly interacting quarks and gluons does not become valid until much higher temperatures. Recent terminology for the QCD state near the crossover ($T \sim (1 - 2)T_c$) is strongly coupled quark-gluon plasma (sQGP).

Transport properties of sQGP have attracted considerable attention. For example, generally, the shear viscosity η is a decreasing function of the coupling strength. The dimensionless ratio of η/\hbar to the entropy density s tends to infinity asymptotically far on either side of the crossover – in dilute hadron gas ($T \rightarrow 0$) and in asymptotically free QGP ($T \rightarrow \infty$). Near the crossover η/s should thus be expected to reach a minimum [45]. The viscosity can be indirectly determined in heavy-ion collisions by comparing hydrodynamic calculations to experimental data. Such comparison [46] indeed indicates that the viscosity (per entropy density) of this “crossover liquid” is relatively small, and plausibly is saturating the lower bound conjectured in [47].

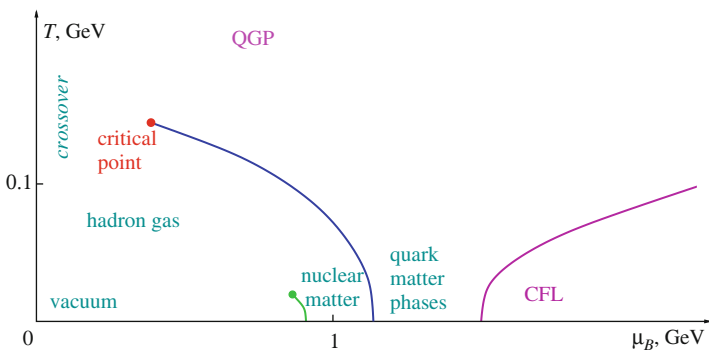


Fig. 2.9 The contemporary view of the QCD phase diagram with physical quark masses – a semiquantitative sketch.

2.2.4.5 Physical quark masses and the critical point

The first order transition line is now ending at a point known as the QCD critical point or end point.¹⁵ The end point of a first order line is a critical point

¹⁴ This fact is technically easier to establish than the order of the transition in the chiral limit – taking the chiral limit is an added difficulty.

¹⁵ The QCD critical point is sometimes also referred to as *chiral* critical point which sets it apart from another known (nuclear) critical point, the end-point of the transition separating nuclear liquid and gas phases (see Fig. 2.9). This point occurs at much lower temperatures $\mathcal{O}(10 \text{ MeV})$ set by the scale of the nuclear binding energies (see Sect. 2.2.3).

of the second order. This is by far the most common critical phenomenon in condensed matter physics. Most liquids possess such a singularity, including water. The line which we know as the water boiling transition ends at pressure $p = 218$ atm and $T = 374^\circ\text{C}$. Along this line the two coexisting phases (water and vapor) become less and less distinct as one approaches the end point, resulting in a single phase at this point and beyond.

In QCD the two coexisting phases are hadron gas (lower T), and quark-gluon plasma (higher T). What distinguishes the two phases? As in the case of water and vapor, the distinction is only quantitative – one is denser than the other – and more obviously so as we approach the critical point, where even the quantitative distinction vanishes. In QCD the situation is similar – since the chiral symmetry is explicitly broken by quark masses, the two phases cannot be distinguished by realizations (broken vs restored) of any global symmetry.¹⁶

It is worth pointing out that beside the critical point, the phase diagram of QCD in Fig. 2.9 has other similarities with the phase diagram of water. A number of ordered quark matter phases must exist in the low- T high- μ_B region, which are akin to many (more than 10) confirmed phases of ice. This issue is discussed in much more detail in Sect. 3.5. For asymptotically large μ_B , QCD with 3 quark flavors must be in a color-flavor locked (CFL) state [32, 33, 35, 36]. Concerning the location of the QCD critical point we refer to the QCD lattice calculations in Sect. 3.2.

2.2.5 Universality and QCD transitions

2.2.5.1 Universality at the $N_f = 2$ chiral restoration transition

At those values of μ for which the chiral symmetry restoration transition is of second order, the singularities of the thermodynamic observables can be described using universality and scaling principles. In the symmetry broken phase the full chiral symmetry $\text{SU}(2)_L \times \text{SU}(2)_R$ is broken down to an $\text{SU}(2)$ subgroup, the isospin. The critical theory can be written in terms of σ and π fields as a linear $\text{O}(4)$ sigma model (in accordance with $\text{SU}(2) \times \text{SU}(2) \sim \text{O}(4)$), in which the symmetry is spontaneously broken down to $\text{O}(3)$ by a non-vanishing expectation value of the σ field.

¹⁶ The last statement may appear to contradict the observation that an asymptotically free gas of quarks and gluons is different from the hadron gas: the quarks and gluons are confined in the latter, while they are free in the former. However, deconfinement – a powerful concept to discuss the transition from hadron to quark-gluon plasma, strictly speaking, does not provide a distinction between the phases. In QCD (not pure Yang-Mills theory), because of the light quarks, even in vacuum ($T = 0$) the confining potential cannot rise infinitely – a quark-antiquark pair inserted into the color flux tube breaks it. The energy required to separate two test color charges from each other is finite (see also the discussion of center symmetry and the Polyakov loop in Sects. 2.1.3, 4.4 and 4.5).

The exponents for the $O(4)$ sigma-model universality class are $\nu \approx 0.75$ and $\eta \approx 0.04$. The correlation length ξ diverges at the chiral transition according to Eq. (2.49). The chiral order parameter $\sigma \sim \langle \bar{q}q \rangle$ vanishes as

$$\sigma \sim |T - T_c|^\beta \quad (2.55)$$

where $\beta = \nu(1 + \eta)/2 \approx 0.39$.

2.2.5.2 Universal properties of the tricritical point

By analogy with an ordinary critical point, where *two* distinct coexisting phases become identical, one can define the tricritical point as a point where *three* coexisting phases become identical simultaneously. A tricritical point marks an end-point of three-phase coexistence. In order to see this in QCD, it is necessary to consider another dimension in the space of parameters – the quark mass m_q – see Fig. 2.10. This parameter breaks chiral symmetry explicitly. In such a three-dimensional space of parameters, one can see that there are two surfaces (symmetric with respect to $m_q \rightarrow -m_q$ reflection) of first-order phase transitions emanating from the first-order line at $m_q = 0$. On these surfaces or wings with $m_q \neq 0$, two phases coexist: a low density phase and a high density phase. There is no symmetry distinguishing these two phases since chiral symmetry is explicitly broken when $m_q \neq 0$. Therefore, each surface can have an edge which is a line of critical points. These lines, or wing lines, emanate from the tricritical point. The first-order phase transition line can now be recognized as a line where three phases coexist: the high T

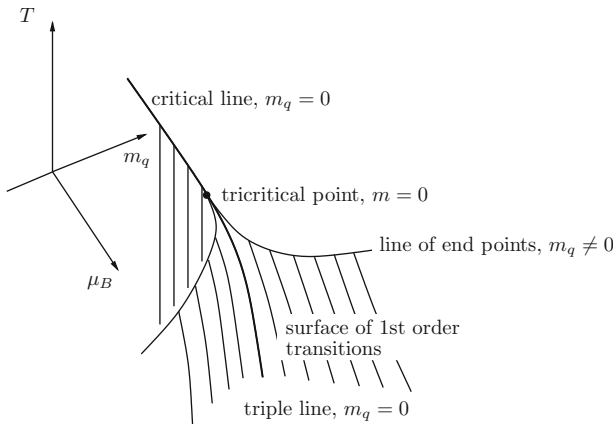


Fig. 2.10 A three-dimensional view (T, μ_B, m_q) of the QCD phase diagram near the tricritical point.

and density phase and two low density and T phases with opposite signs of m_q and, hence, also of $\langle \bar{q}q \rangle$. This line is called, therefore, a triple line.

Critical behavior near the tricritical point can now be inferred from universality. The upper critical dimension for this point is 3. Therefore the scaling behavior near this point is described by mean field exponents with only logarithmic corrections. The effective Landau-Ginzburg theory for the long-wavelength modes, $\sigma \sim \langle \bar{q}q \rangle$, near this point requires a σ^6 potential. In particular, the following exponents in the symmetry plane $m_q = 0$ are readily found using mean field σ^6 theory (as noted above, the actual singularities include additional, logarithmic corrections [48]). The discontinuity in the order parameter $\langle \sigma \rangle = \langle \bar{q}q \rangle$ along the triple line as a function of the distance from the critical point μ_3 , T_3 (measured either as $T_3 - T$ or $\mu - \mu_3$) behaves like

$$\Delta \langle \bar{q}q \rangle \sim (\mu - \mu_3)^{1/2}. \quad (2.56)$$

The discontinuity in the density, $n = dV/d\mu$, across the triple line behaves like

$$\Delta n \sim (\mu - \mu_3)^1. \quad (2.57)$$

The critical behavior along the second-order line is everywhere the same as at the point $\mu = 0$, $T = T_c$: the $\sigma \sim \langle \bar{q}q \rangle$ vanishes on the second-order line with three-dimensional $O(4)$ exponents Eq. (2.55). At the tricritical point, however, the exponent with which $\langle \bar{q}q \rangle$ vanishes is given by Landau-Ginzburg theory as

$$\langle \bar{q}q \rangle \sim (T_3 - T)^{1/4}. \quad (2.58)$$

There are many other universal properties in the vicinity of a tricritical point which can be derived from the σ^6 Landau-Ginzburg theory. One can, for example, show that the $m = 0$ second-order line, the wing lines, and the triple lines approach the triple point with the same tangential direction: The second-order line approaches from one side while the wing lines and the triple line approach from the opposite side. For a more detailed description of the properties of tricritical points, see [48].

2.2.5.3 Scaling and universality at the QCD critical point

For fixed $m_q \neq 0$ one finds a line of first order transitions which ends in a critical point (cf. Fig. 2.10). What is the universality class of the QCD critical point? The critical point is an end-point of a first order transition (coexistence curve) between two phases, which are not distinguished by any symmetry. This type of critical points is the most common and corresponds to Ising model, or liquid-gas phase transition universality class. The critical points of this class are described by a field theory for a single-component

scalar field $\phi = \sigma - \sigma_0$.¹⁷ In the Ising model, the role of ϕ is played by the magnetization. In QCD, as in the liquid-gas case, the field to play the role of the order parameter, can be chosen to be any thermodynamic variable which jumps across the first order transition, e.g., $\langle \bar{q}q \rangle$, n or even ε , or any linear combination thereof. The most common, convenient, and natural choice is $\langle \bar{q}q \rangle$ since this is the same order parameter which is relevant also near the tricritical point, and simplifies a unified description of real QCD as well as its chiral limit.

The signatures of the critical point depend crucially on the magnitude of the correlation length, which is a function of the distance $|T - T_E|$ and $|\mu - \mu_E|$ from the critical point. Applying universality and scaling, one can describe this dependence near the critical point in terms of the universal critical exponents, which for the Ising model universality class are given by $\nu \approx 0.63$ and $\eta \approx 0.04$. Near the critical point the correlation length behaves as

$$\xi \sim |a(T - T_E) + b(\mu - \mu_E)|^{-2/(5-\eta)} \quad (2.59)$$

where a and b are some non-universal coefficients. Along the direction where the linear combination in Eq. (2.59) vanishes the universal scaling predicts that $\xi \sim |a'(T - T_E) + b'(\mu - \mu_E)|^{-\nu}$ with different coefficients a' , b' .

One consequence of this is that, because $\nu > 2/(5 - \eta)$ for the Ising model universality class, the region around the critical point where the correlation length ξ exceeds a given value ξ_0 (a contour line) is stretched along the direction where the particular combination given in Eq. (2.59) vanishes. For qualitative illustrations we refer to [49] and to Sect. 4.7.

The divergence of the correlation length ξ translates into the divergence of susceptibilities. For example, the baryon number susceptibility ξ_B diverges as $\xi^{2+\eta}$ as the susceptibility of the order parameter should Eq. (2.51). Since susceptibilities are proportional to the magnitude of fluctuations, a critical point could be discovered in heavy-ion collisions by observing a non-monotonous behavior (rise and fall) of fluctuation signatures [50–52] as the phase diagram of QCD is scanned, e.g., by varying the collision energy.

2.2.6 Order parameters and changes in the symmetry pattern

2.2.6.1 Order parameters of chiral symmetry breaking

One of the most direct order parameters of chiral symmetry breaking is the pion decay constant f_π defined by

¹⁷ Pion excitations $\boldsymbol{\pi}$ are massive throughout the $T\mu$ plane at $m_q \neq 0$ and decouple from the critical theory.

$$\langle 0 | A_\mu^b | \pi^c(p) \rangle = i \delta^{bc} f_\pi p_\mu. \quad (2.60)$$

Here A_μ^b is the axial-vector current introduced in (2.27). In a medium (denoted by Ω) the appropriate generalization is $\langle \Omega | A_\mu^b | \pi^c(p) \rangle = i \delta^{bc} f_\pi p_0$ (see e.g. [53]). Unfortunately, model-independent calculations of in-medium changes of f_π are only available for very special in-medium situations (see below).

As already discussed, frequently used order parameters are the two-quark condensates $\langle \bar{u}u \rangle$, $\langle \bar{d}d \rangle$ and $\langle \bar{s}s \rangle$ or the corresponding two- or three-flavor averages. As compared to the pion decay constant there are much more calculations available for the in-medium changes of the two-quark condensates (see below). The problem with these condensates, however, is that there is so far no relation derived from first principles which directly connects two-quark condensates with observable quantities.¹⁸ In addition, the two-quark condensates might vanish even if chiral symmetry is still broken (see e.g. [55]).

As a complementary order parameter one might use a particular four-quark condensate [56, 57]

$$\langle \mathcal{O}_{\chi\text{SB}} \rangle = \langle (\bar{u}\gamma_\mu\gamma_5\lambda^a u - \bar{d}\gamma_\mu\gamma_5\lambda^a d)^2 - (\bar{u}\gamma_\mu\lambda^a u - \bar{d}\gamma_\mu\lambda^a d)^2 \rangle \quad (2.61)$$

which is related to the second moment of the difference of spectra $v_1 - a_1$ shown in Fig. 2.3. Therefore, this four-quark condensate is closely connected to an observable quantity. If $v_1 - a_1$ vanishes, also the four-quark condensate (2.61) has to vanish. More general, if chiral symmetry is restored, both the two- and this particular four-quark condensate must vanish. Note, however, that strictly speaking the opposite is not true. In any case, it is instructive to compare the in-medium behavior of two- and four-quark condensate to obtain estimates for intrinsic uncertainties.

2.2.6.2 In-medium changes of order parameters

In this section the in-medium dependence of the order parameters introduced above is discussed. At least in principle the temperature dependence of these order parameters can be studied within lattice QCD. However, also lattice QCD has some inherent restrictions and problems which improve only rather slowly and only gradually with increasing computer power: One problem concerns the treatment of light quarks. It turns out that with the present computational power it is difficult to deal with quarks which are as light as they are in reality (cf. Table 2.1). On the other hand, the size of the light quark masses determines the pion mass. Starting with too heavy quarks lattice QCD calculations unavoidably result in too heavy pion masses. Therefore the properties of pions and all observables which are rather sensitive to the

¹⁸ In the famous Gell-Mann–Oakes–Renner relation [54] the two-quark condensate appears together with the quark mass which is also not an observable.

light quark masses cannot be directly determined from the lattice so far. (Unfortunately it is not always clear a priori for a given observable how sensitive to the quark masses it actually is.) We have already discussed a second problem: The inclusion of a finite baryo-chemical potential μ causes the appearance of a weighting function in (2.7) which is no longer positive definite.

For these reasons also other approaches to the in-medium change of order parameters have their merits and are used in the following. Among the systematic approaches discussed in Sect. 2.1.2 chiral perturbation theory is an important tool to determine in-medium changes as long as the system under consideration is sufficiently dilute (see below). Concerning finite temperature systems the calculations from lattice QCD and from chiral perturbation theory are to some extent complementary: The latter can only be used reliably at low temperatures. There, the most abundant particles are the pions which are too heavy in present day lattice calculations. Therefore, at least the onset of the change of an order parameter might come out too weak in lattice calculations, but can be reliably determined from chiral perturbation theory.

The temperature change (for $\mu = 0$) of the two-quark condensate and of the Polyakov loop has been calculated within lattice QCD [58]. A remarkable aspect found there is the fact that both transitions seem to appear at exactly the same temperature. This aspect is far from being completely understood. In addition, it is not clear whether this fact remains true for finite chemical potentials. Indeed, one cannot generally expect that all order parameters drastically change at the very same temperature. As a counter example we already refer to Fig. 2.14 below: There the in-medium change of the two-quark and the gluon condensate as obtained from a resonance gas model are compared. One observes that the gluon condensate drops much later than the two-quark condensate. Details about the resonance gas model are discussed below. Concerning further results from lattice QCD we refer to Sect. 3.2.

To understand not only the transition region, but also the onset of in-medium changes we concentrate for the rest of this section on the hadronic phase and on analytical calculations. We focus on order parameters of chiral symmetry breaking and on the trace anomaly. Note that the Polyakov loop is not accessible by purely hadronic models.

Concerning analytical calculations, model independent statements can be made for (i) a system at low temperature and vanishing baryo-chemical potential and (ii) a system at finite baryo-chemical potential and vanishing temperature. System (i) is described by a gas of pions as the lightest degrees of freedom. If the temperature is low enough, all heavier states are suppressed by their thermal Boltzmann factors and can safely be neglected. System (ii) is described by a Fermi sphere of nucleons. If the baryon density is low enough one can neglect the nucleon–nucleon interactions. For higher temperatures and/or densities model assumptions must be added to determine the change of the order parameters.

We now present in a compact list the changes of the introduced order parameters in leading order of the pion and nucleon density, respectively. Afterwards we will comment on the different results and discuss further improvements:

$$\begin{aligned}
\frac{f_\pi(T)}{f_\pi} &= 1 - \frac{2\varrho_{\pi,s}}{3f_\pi^2}, \\
\frac{f_\pi(\varrho_N)}{f_\pi} &= 1 - (0.26 \pm 0.04) \frac{\varrho_N}{\varrho_0}, \\
\frac{\langle \bar{q}q \rangle_{\text{pionic med.}}}{\langle \bar{q}q \rangle_{\text{vac}}} &= 1 - \frac{\varrho_{\pi,s}}{f_\pi^2}, \\
\frac{\langle \bar{q}q \rangle_{\text{nucl. med.}}}{\langle \bar{q}q \rangle_{\text{vac}}} &= 1 - \frac{\sigma_N \varrho_N}{f_\pi^2 M_\pi^2} \approx 1 - 0.3 \frac{\varrho_N}{\varrho_0}, \\
\frac{\langle \mathcal{O}_{\chi\text{SB}} \rangle_{\text{pionic med.}}}{\langle \mathcal{O}_{\chi\text{SB}} \rangle_{\text{vac}}} &= 1 - \frac{8\varrho_{\pi,s}}{3f_\pi^2}, \\
\frac{\langle \mathcal{O}_{\chi\text{SB}} \rangle_{\text{nuclear med.}}}{\langle \mathcal{O}_{\chi\text{SB}} \rangle_{\text{vac}}} &= 1 - \frac{2\sigma_N \varrho_N}{f_\pi^2 M_\pi^2} \approx 1 - 0.7 \frac{\varrho_N}{\varrho_0}
\end{aligned} \tag{2.62}$$

with the quark field q denoting u or d , the scalar pion density¹⁹

$$\varrho_{\pi,s} = 3 \int \frac{d^3k}{(2\pi)^3} \frac{1}{2E_k} \frac{1}{e^{E_k/T} - 1} \xrightarrow{M_\pi \rightarrow 0} \frac{1}{8} T^2 \tag{2.63}$$

the nuclear density $\varrho_N = 4 \int \frac{d^3k}{(2\pi)^3} \Theta(k_F - |\mathbf{k}|)$, the nuclear saturation density ϱ_0 and the nucleon sigma term $\sigma_N \approx 45 \text{ MeV}$.

Comparing the respective formulae of (2.62) which are in the same column shows that a bold extrapolation of these formulae to the point where the respective order parameter vanishes would lead to different critical densities. This indicates a breakdown of the linear-density approximation. In other words, one should not trust any of the formulae of (2.62) to the point where the respective order parameter vanishes. For such large pion/nucleon densities higher order terms in the respective density become important. Such effects are in general hard to account for in a model independent way. In addition, increasing the density of cold nuclear matter this system might not end up in a chirally restored phase, but in a color superconductor with some remaining chiral symmetry breaking. (This depends on the type of color superconductor, see Sect. 3.5 for more details.)

The leading order change of the pion decay constant with temperature (i.e. for system (i)) has been worked out e.g. in [59, 60]. The corresponding case of cold nuclear matter (system (ii)) has been studied e.g. in [53]. Model independent results for the change of f_π beyond the leading order in the respective density are not available so far.

¹⁹ Note that a scalar density is only a well-defined concept for a non-interacting system.

The quark condensate is obtained from the logarithmic derivative of the partition function with respect to the quark mass [61]. Also here, for cold nuclear matter there are no model independent results beyond the leading order. For a pion gas described by chiral perturbation theory the situation is better. The partition function and its quark mass derivative have been evaluated in [61] up to three loops.²⁰ The result in lowest order in the pion density (i.e. neglecting interactions) is included in (2.62). The result of the full three-loop calculation is depicted in Fig. 2.11. Recently this result has

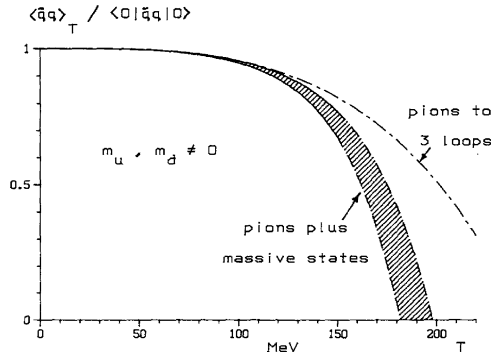


Fig. 2.11 Drop of the quark condensate in an interacting pion gas plus non-interacting other hadron states [61]. The shaded area signals the uncertainty for the resonance sigma terms.

been generalized to flavor $SU(3)$ by considering a gas of pions, kaons and etas [62]. The result is shown in Fig. 2.12. Since the kaons and etas are (much) heavier than the pions the former are less populated in a thermal medium. This explicit flavor breaking causes a different thermal behavior of the strange quark condensate as compared to the sum of up and down quark condensate.

For the finite-temperature calculations presented above the medium contained only Goldstone bosons. One can improve on that (with minor model assumptions) by taking into account all known hadron species – albeit neglecting their interactions (resonance gas approximation). One can look at this approximation from two different points of view: First, it is a generalization of the linear-density approximation used in (2.62) by considering also other degrees of freedom. Second, one might start from the stable states, i.e. pions and nucleons and their flavor partners. Going beyond the linear-density approximation means to account for correlations between the stable states. Clearly the strongest correlations appear just in the channels where hadronic resonances are formed. The latter line of reasoning already indicates

²⁰ “One-loop” corresponds to non-interacting pions.

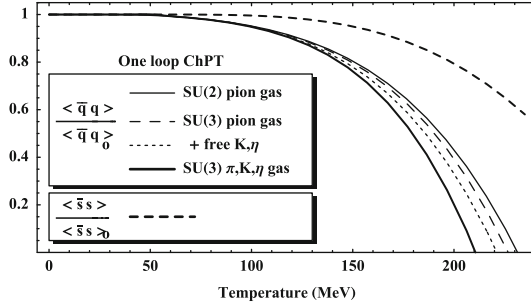


Fig. 2.12 Drop of the quark condensates in a gas of pions, kaons and etas [62]. (Note that the label “One loop ChPT” concerns the scattering phase shifts and corresponds to a three-loop evaluation of the pressure).

that the resonance gas approximation can be meaningful at finite temperatures, but not for cold nuclear matter. In the latter system one would need nucleon–nucleon correlations to go beyond the linear-density approximation. Clearly they are not encoded in hadronic resonances. Nonetheless, one can use the resonance gas also for finite baryo-chemical potential – as long as the temperature is not too low. For vanishing chemical potential the resonance gas approximation – together with the three-loop evaluation of the pressure within chiral perturbation theory (see above) – has been used in [61] to determine the drop of the quark condensate. Actually one would need the sigma terms for all resonances. Strictly speaking this information is not available. Simple estimates can be made and an error attributed to the results. This leads to Fig. 2.11. An extension of the resonance gas approximation to finite baryo-chemical potential is shown in Fig. 2.13 where the contour line is displayed for which the (up and down) quark condensate vanishes. In the right panel of Fig. 2.13 the end point on the right hand side of the respective contour line corresponds to the case of vanishing temperature. As already discussed one should not trust the resonance gas approximation in this area.

The drop of the four-quark condensate (2.61) in a pion gas in leading order in the density has been calculated in [64]. The dependence on the nuclear density cannot be calculated model independently. Using the large- N_c approximation [65] (where N_c denotes the number of colors) one gets the result given in (2.62). With the same approximation (large- N_c) the drop of the four-quark condensate can be calculated for a resonance gas along the same lines as for the two-quark condensate [63]. The results are also shown in Fig. 2.13. Interestingly, the line where the four-quark condensate vanishes remains constant in energy density for a large range of baryon densities. The differences between the lines shown in Fig. 2.13 might be seen as an uncertainty for the determination of the line of chiral symmetry restoration. For a discussion of further uncertainties (concerning the resonance sigma terms) see [63].

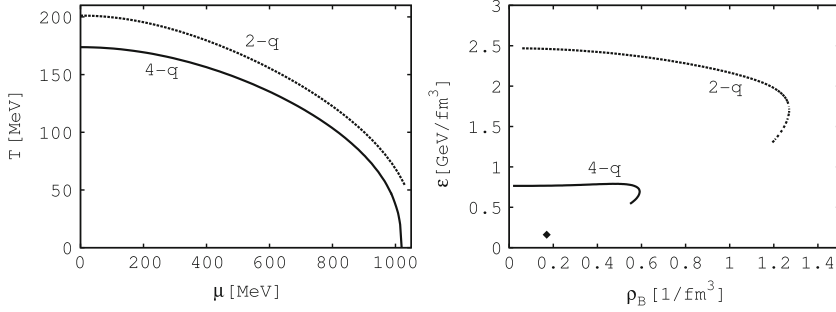


Fig. 2.13 Vanishing of two-quark (2-q) and four-quark (4-q) condensate, respectively, in a resonance gas as functions of temperature T and baryo-chemical potential μ (*left panel*) and as functions of energy density ϵ and baryon density ρ_B (*right panel*). See [63] for details. For orientation, the point of cold nuclear matter has been included in the *right panel* (diamond).

The resonance gas approximation can also be used to determine the in-medium change of the gluon condensate. This is depicted in Fig. 2.14 in comparison to the change of the two-quark condensate [66].²¹ One observes that the gluon condensate is still nearly constant in the region where the two-quark condensate already vanishes. Only at higher temperatures also the gluon condensate drops. As already discussed this is in qualitative contrast to the comparison between two-quark condensate and Polyakov loop which according to lattice calculations change at the very same temperature – at least for vanishing chemical potential. Hence not all condensates have their drastic changes at the very same point.

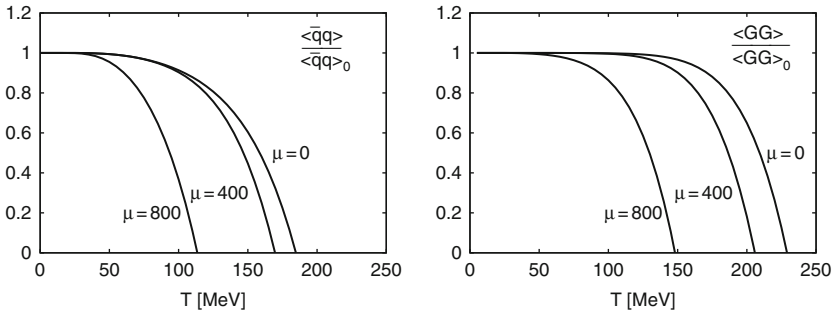


Fig. 2.14 Comparison of temperature and μ dependence of two-quark (*left*) and gluon condensate (*right*) [66]. Both condensates are normalized to their respective vacuum values. The chemical potential $\mu = \mu_B$ is given in MeV.

²¹ Note that the assumption in [61, 63] about the resonance sigma terms deviates to some extent from the corresponding assumption made in [66] which is based on [67], cf. the corresponding discussion in [63].

From the hadronic calculations one gets a chiral transition with a temperature of roughly 200 MeV for vanishing chemical potential. This temperature drops with increasing chemical potential. The energy density at the transition is roughly $1 \text{ GeV}/\text{fm}^3$ with large uncertainties. Actually these numbers are in good agreement with lattice calculations. Further applications of the resonance gas approximation are discussed in Sect. 4.2. The presented analytical calculations describe the drop of order parameters in purely hadronic scenarios. It should be clear that such calculations do not tell whether in the end there is a phase transition or only a crossover. Such deeper questions involve the relevant degrees of freedom of both sides of the transition. Therefore one needs lattice QCD to shed light on these questions (see Sect. 3.2).

Chapter 3

Equation of state and phase boundaries of strongly interacting matter

In the present chapter our knowledge about the different areas of the QCD phase diagram is reviewed, starting at high temperatures and vanishing baryo-chemical potentials and ending up at low temperatures and high net baryon densities.

3.1 The coupling constant expansion of the QCD pressure

As is well known by now, at temperatures substantially below the critical temperature T_c hadronic matter behavior is accurately described by a hadron resonance gas [10]. However, near the critical temperature things become quite complicated: the system is fully non-perturbative and numerical lattice Monte Carlo simulations remain the only first principles method for obtaining reliable results. The status of these simulations is described in Sect. 3.2. (Concerning the hadron resonance gas see also Sect. 4.2.) At temperatures sufficiently far above the critical temperature, well into the quark-gluon plasma phase, the QCD coupling constant becomes small and perturbative methods are applicable. However, this is not the whole story: due to the *infrared singularities* in the gluonic sector, the perturbative loop expansion breaks down at some finite order, as shown by Linde [68] and Gross et al. [69] already more than 25 years ago. For the pressure this happens at order g^6 .

The perturbative expression for the pressure has recently been calculated to order $g^6 \ln 1/g$, the highest perturbatively computable order, first at vanishing baryon chemical potential μ by Laine et al. [70], but soon generalized to non-zero μ by Vuorinen [71, 72]. These calculations are valid for $T \gtrsim 2T_c$, $\mu \lesssim \pi T$. At large μ and arbitrary T the result is known to order g^4 [73].

A striking feature of the coupling constant expansion is the slow convergence. Only at temperatures higher or around $\sim 100T_c$ the convergence

becomes uniform. This is due to the large value of the QCD coupling constant even significantly above the transition temperature. This causes significant deviations from the ideal Stefan-Boltzmann law; at $T \sim 10T_c$ these are still of order 12%, and at $100T_c$ 7%.

The perturbative calculations mentioned above are done using massless quarks. While non-vanishing quark masses pose no fundamental problems for perturbation theory, the computations become technically very cumbersome, and the result is known only to order g^2 [74, 75]. However, in [75] an interpolation method was used to estimate the effect of physical quark masses to the full perturbative pressure. This was then connected to the resonance gas behavior at low temperatures, resulting in a phenomenological result for the physical QCD pressure for all temperatures.

For precision results it would be important to know the pressure also at order g^6 and higher. Because this is the lowest order where genuinely non-perturbative physics starts to contribute, the magnitude of these contributions can be significant. This problem can be addressed using a combination of perturbative analysis and lattice Monte Carlo simulations of effective 3-dimensional theories [76–78].

The slow convergence of the perturbative expansion has spurred the development of various approaches to reorganize the perturbative expansion so that the convergence improves, especially at temperatures close to the transition temperature. These resummation techniques [79–91] have the feature that these include some relevant physical ingredients – Debye screening mass, for example – in the definition of the method. Thus, as opposed to the standard perturbation theory which is an expansion around vacuum, these include thermal quasiparticles from the outset. The cost to pay is that the methods are somewhat non-systematic, and it becomes technically very difficult to calculate the results to high orders.

3.1.1 Perturbative expansion at high temperatures

The expansion of the QCD pressure is now known up to order $g^6 \ln 1/g$, after 25 years of effort. In parametric order the expansion in terms of QCD coupling constant g is as follows:

$$\begin{aligned}
p/p_{\text{SB}} = & 1 && \text{Stefan-Boltzmann ideal gas} \\
& + g^2 && \text{2-loop (Shuryak 78 [92], Chin 78 [93])} \\
& + g^3 && \text{resummed 2-loop (Kapusta 79 [74])} \\
& + g^4 \ln 1/g && \text{resummed 2-loop (Toimela 83 [94])} \\
& + g^4 && \text{resummed 3-loop (Arnold, Zhai 94 [95, 96])} \\
& + g^5 && \text{resummed 3-loop (Zhai, Kastening 95 [97])} \\
& + g^6 \ln 1/g && \text{resummed 4-loop (Laine et al. 03 [70])} \\
& + g^6 && \text{not perturbatively computable (Linde 80 [68])}^1 \\
& + g^7 && \\
& + \dots &&
\end{aligned} \tag{3.1}$$

Here the ideal gas Stefan-Boltzmann pressure for SU(3) gluons and N_f massless quarks is

$$p_{\text{SB}} = \frac{\pi^2 T^4}{45} \left(8 + \frac{21 N_f}{4} \right). \tag{3.2}$$

Explicit expressions for the coefficients can be found in [70]. Recently the calculation was extended to the order $O(g^6 \ln 1/g)$ pressure in the full electroweak standard model [99, 100]. It should be noted that the expansion contains odd powers and logarithms of g , not present in standard perturbative expansions at $T = 0$. Moreover, the g^6 term is not computable in loop expansion [68, 69]. These facts are due to infrared divergences which are inevitable at finite temperature perturbation theory; these divergences are of physical origin and give rise to a hierarchy of energy scales which will be discussed below. It is possible to proceed further in the large N_f -limit, where all-orders result in the full (T, μ) -plane has been obtained [101–104].

The coefficients of the expansion depend on temperature T , chemical potentials μ , and the number of quark flavors N_f . We shall first assume that the quarks are massless and that the quark chemical potentials are zero; mass effects and finite baryo-chemical potential will be discussed further below.

How well does the expansion work? In Fig. 3.1 the pressure is shown term by term for $N_f = 0$ case, and compared with the available lattice data [105, 106]. We can see that the convergence of the perturbative expansion is very slow and non-uniform; only when $T \gtrsim 40 \dots 100 A_{\overline{\text{MS}}}$ there is apparent term-by-term convergence. On the left panel of Fig. 3.1 the unknown g^6 -coefficient has been tuned so that the result fits the lattice simulation data [105, 106] at $T = 3\text{--}4 A_{\overline{\text{MS}}}$. While this gives a surprisingly good fit (the behavior even approximates the lattice results all the way down to T_c), this is probably spurious: there is no reason to assume that the remaining higher order terms would give a negligible contribution. Indeed, the dependence on the unknown g^6 coefficient is large: adjusting it within a reasonable range we obtain the family of curves on the right panel in Fig. 3.1.

That said, it can be expected that the true pressure of QCD will be close to the fitted curve on the left panel of Fig. 3.1; i.e. the fitted g^6 -term is a fair

¹ partial non-perturbative result (Renzo et al. 06) [98]

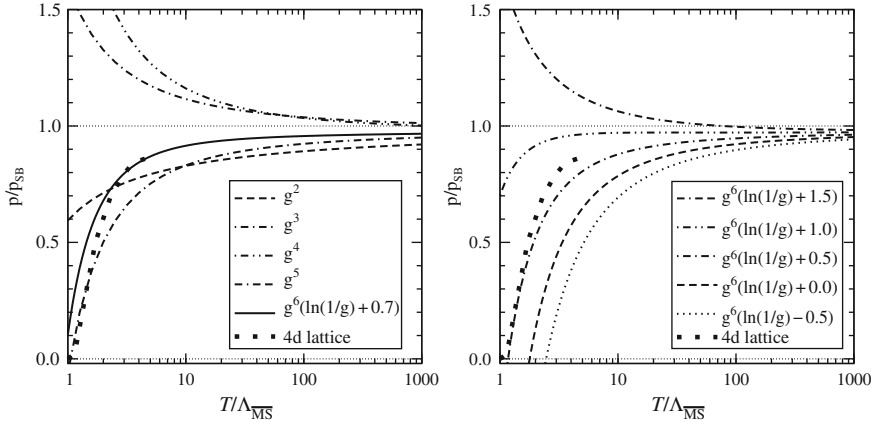


Fig. 3.1 *Left:* Perturbative QCD pressure order-by-order at $N_f = 0$, normalized to the ideal gas pressure, as a function of $T/\Lambda_{\overline{MS}}$ (to convert to units of T_c , use $T_c/\Lambda_{\overline{MS}} \approx 1.2$). The last term is plotted using an optimized $O(g^6)$ constant for the fit to the lattice data [105, 106]. The latter are the *dots* labeled by “4d lattice”. *Right:* Dependence of the $O(g^6)$ result on the so far undetermined constant [70].

approximation of all the remaining higher order contributions. Thus, from a practical point of view, one can take the lattice+fitting perturbative curve to be currently the best available result for the pressure. This approach has been analyzed in detail by Laine and Schröder in [75]. The resulting pressure for pure glue ($N_f = 0$) QCD is shown on Fig. 3.2. The obtained interpolating curve is an accurate determination of the pressure of the theory.

The slow convergence of the perturbative expansion indicates that the QCD plasma remains effectively strongly coupled up to temperatures somewhat larger than $10T_c$. At $T \sim 10\Lambda_{\overline{MS}} \sim 8T_c$, the interpolating curve still deviates $\sim 12\%$ from the Stefan-Boltzmann gas value.

3.1.2 Quark mass effects and pressure in real QCD

In the calculations leading to the results shown in Fig. 3.1 quark masses were set to zero. (In the actual figures $N_f = 0$, thus the masses do not matter.) However, the real masses of the strange and charm quarks cannot be neglected if we want to obtain precise results for the pressure. While non-zero quark masses do not cause any conceptual problems for perturbation theory, in practice the computations become technically cumbersome. In this case the pressure has been calculated only up to order $O(g^2)$, originally by Kapusta almost 30 years ago [74], and recently in a more complete form by Laine and Schröder [75].

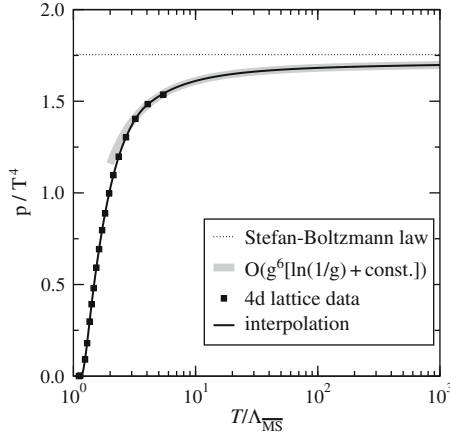


Fig. 3.2 The pressure in quenched QCD ($N_f = 0$), obtained by matching the unknown $O(g^6)$ constant of the perturbative result to lattice data ([75], lattice data [105, 106]). The continuous curve is an interpolation of the perturbative and lattice results.

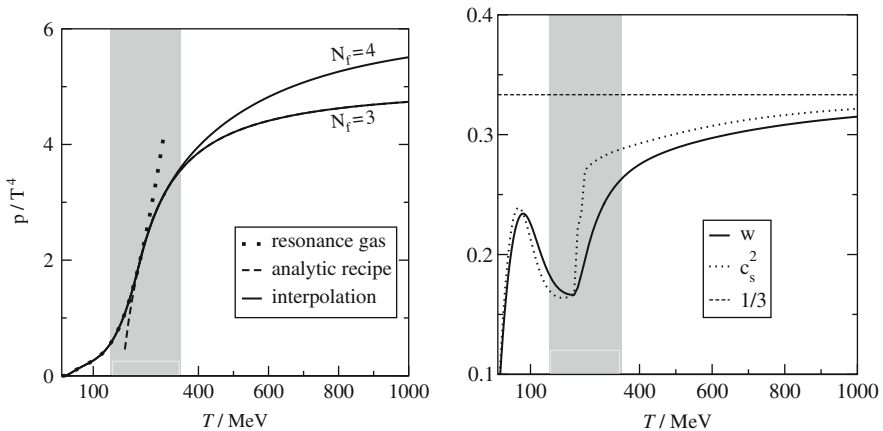


Fig. 3.3 *Left:* The pressure of physical QCD, obtained by interpolating the low-temperature hadron resonance gas model and the high-temperature perturbative result including 3 (u,d,s) and 4 (u,d,s,c) quarks with physical masses. The *shaded region* is the transition region. *Right:* The “equation of state” $w = p/e$ and the square of the speed of sound c_s^2 , using the phenomenological result for $N_f = 4$ pressure. $1/3$ is the free field value for both quantities [75].

While the full $O(g^6 \ln 1/g)$ result has not been calculated, it is nevertheless possible to approximate the contribution of the massive quarks to the full perturbative pressure. It is obvious that when we change the mass of one flavor from zero to infinity while keeping the other quark masses at zero, we are smoothly interpolating between N_f and $N_f - 1$ massless flavors (and at the same time the pressure decreases). Thus, what is needed is a prescription for interpolating the known boundary values to the physical quark masses.

The choice of the interpolation method is not unique. One way to proceed is to define an effective number of massless quark flavors, N_f^{eff} , by matching the pressure at order g^2 :

$$p_{g^0+g^2}(m_q = 0, N_f^{\text{eff}}) = p_{g^0+g^2}(m_q^{\text{phys.}}). \quad (3.3)$$

The full pressure can be estimated by inserting N_f^{eff} to the known $O(g^6 \ln 1/g)$ -formula for massless quarks. Alternatively, as was done in [75], we can calculate a *correction factor*

$$\frac{p_{g^0+g^2}(m_q^{\text{phys.}}, N_f = 4)}{p_{g^0+g^2}(N_f = 0)} \quad (3.4)$$

and multiply the full $N_f = 0$ pressure with this correction. Naturally, here one could also use the known perturbative result for $N_f = 4$, $m_q = 0$ as the baseline which is corrected, but $N_f = 0$ has the advantage that the quenched pressure is well determined near the transition by lattice simulations.

In [75] the pressure in the low temperature phase is modeled using the hadron resonance gas model [10]; this has been recently observed to match the lattice simulations with dynamical fermions quite well near the critical temperature, if the resonance masses are adjusted to correspond to the (unphysical) quark masses used in simulations [107] (cf. Sect. 4.2). The resonance gas gives the pressure directly in physical units, and the phenomenological high-temperature curve is matched to that by tuning $\Lambda_{\overline{\text{MS}}}$ so that the slopes of the curves match in the transition/crossover region. The resulting pressure is shown on the left panel in Fig. 3.3. The curves have been computed using physical quark masses for u,d,s-quarks and u,d,s,c-quarks ($N_f = 3$ and 4). It can be readily observed that the charm quark gives a significant contribution to the pressure already almost immediately above the transition region.

In addition to the pressure itself, its first and second derivatives have important thermodynamic applications. The equation of state and the speed of sound can be expressed as dimensionless ratios

$$w(T) = \frac{p(T)}{e(T)} = \frac{p(T)}{Tp'(T) - p(T)} \quad (3.5)$$

$$c_s^2(T) = \frac{p'(T)}{e'(T)}, \quad (3.6)$$

where $e(T)$ is the energy density. These are shown for the physical $N_f = 4$ pressure on the right panel of Fig. 3.3 [75].

Clearly, there is a significant amount of structure around the critical region. Here the transition is, by construction, continuous (at most second order): the derivative of the pressure is tuned to be continuous through the transition region. The discontinuity is seen in higher order derivatives, especially in c_s^2 , which jumps almost discontinuously when we go over to the perturbative

curve. A jump in c_s^2 would indicate a second order transition, whereas in a smooth crossover all derivatives are continuous. Obviously the results remain quite sensitive to the interpolation between the low- and high-temperature domains, and precise numerical lattice simulations in the transition region are required. Furthermore, the phenomenological approach used here cannot describe the chiral phenomenology of full QCD near the transition temperature.

Recent lattice simulations with dynamical quarks indicate that the transition is most likely a continuous crossover [108–111]; see also Sect. 3.2. They also show w and c_s^2 to go significantly below the minimum shown in Fig. 3.3 in the transition region. Also, these quantities either decrease or remain at most constant when the temperature is decreased; hence, the peak seen in Fig. 3.3 around $T \sim 100$ MeV is missing. This is due to the unphysically heavy quarks used in simulations, making lattice pions significantly heavier than the physical ones. Thus, available lattice data cannot be directly compared with the phenomenological physical pressure, and simulations with much lighter quarks are needed.

3.1.3 Beyond perturbation theory

It would be very interesting to know the non-perturbative $O(g^6)$ coefficient for the pressure, because it receives contributions from very different physics than the lower orders. In order to calculate it (and higher order terms) we have to rely on numerical lattice Monte Carlo simulations. Perhaps the most efficient way to access these terms is to use simulations of 3-dimensional *effective theories*.²

The derivation of these theories relies on the fact that at high enough temperatures the QCD coupling constant g is small, and we have a hierarchy of dynamical scales $\pi T \gg gT \gg g^2T$. The “hard” πT scales include all non-static bosonic modes and all fermionic modes. The “soft” electric and “supersoft” magnetic scales, gT and g^2T , describe only static bosonic 3-dim. modes. A crucial point here is that the infrared divergences rendering the physics non-perturbative affect only scales g^2T . Thus, we can integrate over $k \sim \pi T$ – modes and, in turn, over $k \sim gT$ – modes perturbatively, obtaining effective theories describing scales $k \lesssim gT$ (Electrostatic QCD, EQCD) and $k \lesssim g^2T$ (Magnetostatic QCD, MQCD), respectively [112–115]. These theories are purely bosonic and 3-dimensional, thus very suitable for numerical analysis, while still fully retaining the non-perturbative infrared physics of QCD. In particular, the theory describing g^2T -scales (MQCD) is just 3-dimensional SU(3) gauge theory.

² Effective theories are also used to organise the perturbative calculations described in Sect. 3.1.1.

We emphasize here that while the effective theories can be used to calculate non-perturbative contributions to the coupling constant expansion, they cannot describe phenomena where the expansion fails, e.g. physics at very close proximity to the transition temperature. In this case one has to rely on standard full 4-dimensional lattice simulations.

Let us look at the ongoing progress in the determination of the $O(g^6)$ contribution to the pressure. This term is a sum of two parts: a genuinely non-perturbative part involving scale g^2T (and calculable from MQCD), and the perturbatively computable “matching” part including contributions from scales πT , gT . Here the non-perturbative part turns out to be simpler to evaluate: it can be elegantly and robustly computed using lattice simulations of MQCD [77, 78]. On the other hand, the perturbatively computable part remains undetermined. In order to determine it full 4-loop calculations in finite- T QCD are required, which is technically an extremely challenging problem.³ Thus, the full resolution of the order g^6 term for the QCD pressure awaits for the completion of this 4-loop calculation.

To go beyond $O(g^6)$ again becomes more difficult. However, the static part of $O(g^7)$ coefficient (involving scales gT and g^2T but not πT) can be calculated with lattice simulations of EQCD. This has been attempted in [76]. While the method was seen to work well in describing the overall behaviour of the pressure, the precision of the results was not sufficient to determine the $O(g^7)$ coefficient. Substantially increased accuracy is needed in order to resolve the issue.

3.1.4 Resummation methods

So far, we have only discussed systematic order-by-order expansions in the QCD coupling constant. While this is a well-defined and robust approach, it is obvious that the convergence of the expansion is bad, as seen from Fig. 3.1. Various “resummation” methods have been developed to address this issue. These reorganize the expansion in a way which tries to improve the convergence, especially at temperatures closer to the transition temperature. There are several non-equivalent ways to do the resummation: these go under names “screened perturbation theory” (SPT) [79, 80, 88, 89], “hard thermal loop effective theory” (HTLPT) [82, 90, 91], and “ Φ -derivable” approximations [81, 85–87, 117]. These approaches have been recently reviewed in [118, 119].

An essential feature in these approaches is that typically some relevant thermal phenomenology is included in the formalism from the outset: quasi-particles, Debye screening, damping, etc. Thus, as opposed to standard per-

³ Recently, 4-loop $O(g^6)$ pressure has been computed by Gynther et al. for massless $O(N)$ scalar theory, where it is perturbatively computable [116]. One of the aims of this computation was to explore methods for handling the more challenging QCD 4-loop computation.

turbation theory which is an expansion around empty vacuum, the starting point here is a “thermal” vacuum around which to make the expansion. The price to pay is that the expansions typically cannot be carried out to as high order as in perturbation theory. Thus, these approaches typically reproduce the standard perturbative expansion (3.1) only to some low order, depending on truncations, but include certain contributions from all higher orders. However, none of these approaches includes the physics of the super-soft magnetostatic g^2T -sector (neither does the standard perturbation theory, of course).

In addition to the “physical” approaches listed above, purely mathematical extrapolation schemes have been introduced. These are constructed, based on the first few terms of the perturbative series, using Padé approximants [120–122] or Borel summation techniques [123, 124]. However, we shall not discuss these methods here further.

Let us look closer at screened perturbation theory [79], which is the simplest of the above approaches. Consider a scalar field ϕ Lagrangian, to which we add and subtract an extra mass term. One is interpreted as a change of the original mass, the other one as a perturbation:

$$\mathcal{L} = \mathcal{L}_0 + m^2\phi^2 + \delta\frac{g^2}{4!}\phi^4 - \delta m^2\phi^2 = \mathcal{L}'_0 + \delta\mathcal{L}'_{\text{int}}. \quad (3.7)$$

If $\delta = 1$ we obtain the original theory, and the loop expansion of the modified theory becomes an expansion in δ . The mass parameter m^2 is a priori completely arbitrary, and it becomes an optimization parameter. At finite temperature the optimal values are close to the thermal screening mass of the scalar theory, which is of order gT . In scalar theory this approach leads to dramatic improvement in convergence over the standard perturbation theory [88]. However, inclusion of thermal mass to the “free” Lagrangian leads to temperature-dependent counterterms which can cause difficulties in calculations.

The screened perturbation theory cannot be directly applied to non-Abelian gauge theories. The generalization to QCD is the hard thermal loop perturbation theory (HTLPT), which is also based on adding and subtracting a correction term:

$$\mathcal{L} = [\mathcal{L}_{\text{QCD}} + (1 - \delta)\mathcal{L}_{\text{HTL}}]_{g^2 \rightarrow \delta g^2} \quad (3.8)$$

Again, $\delta = 1$ is the standard QCD, and the expansion is done around $\delta = 0$. Here \mathcal{L}_{HTL} is constructed so that already the free propagator ($\delta = g^2 = 0$) gives thermal quasiparticles, screening (Debye mass), and Landau damping. All of these phenomena depend on electric modes gT . Thus, the starting point of the expansion is more physical, and the hope is that the expansion is better behaved. However, the calculations become technically very difficult already at 2-loop level. For quenched QCD the pressure has been calculated by Andersen et al. to 2-loop order [90], with the result shown in Fig. 3.4.

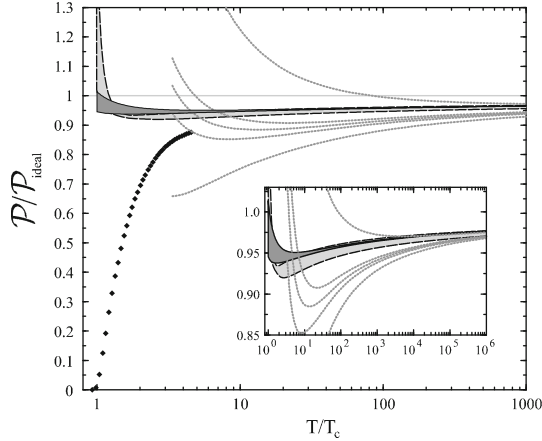


Fig. 3.4 The pressure calculated using hard thermal loop perturbation theory to 1-loop (*light gray band*) and 2-loop (*dark gray*) order. The calculation is compared to 4-dim. lattice data (*dots*) and to effective theory results obtained in [76] and discussed in Sect. 3.1.3 [90].

Comparing HTLPT with the standard perturbation theory we can see that the stability of the expansion is, indeed, greatly improved. However, near the transition temperature it overshoots the 4-dimensional lattice results significantly where data is available. The 2-loop result includes the standard perturbative result up to order $g^4 \ln 1/g$ after which they differ; especially the physics of the magnetic sector is not included in HTLPT.

It has been suggested that the too large value for the HTLPT pressure can be due to the fact that it does not describe the hard modes correctly to high enough accuracy in coupling constant expansion. Thus, in [125] a hybrid approach was advocated: apply screened perturbation theory to EQCD. In this approach the hard $\sim T$ modes are treated using normal perturbation theory as EQCD is derived. The results obtained appear to match the available lattice results better than with the direct HTLPT calculation [118, 125].

In the third resummation method mentioned above, “ Φ -derivable” approach, the variational parameter is not the mass term as in SPT but the full exact propagator. The method was derived already in the 1960s by Luttinger and Ward [126] and Baym [117]. It is based on the fact that the thermodynamic potential can be expressed in terms of an expansion of 2-particle irreducible (2PI) skeleton graphs. While the Φ -derivable approach has several desirable features it is also very difficult to solve, and in practice one has to rely on approximations. Like the HTLPT, when applied to a scalar field theory it offers considerably improved convergence of the expansion of the pressure. The method has been applied to QCD pressure by Blaizot et al. [85–87] and Peshier [81]; for all details, we refer therein. While the results, especially for entropy, numerically are close to the results obtained with

HTLPT or lattice simulations, it is very difficult to push these calculations beyond leading order.

3.1.5 Perturbative expansion at finite chemical potential

At high temperature and quark chemical potential $\mu \ll T/g$ the perturbative expansion remains as sketched in Eq. (3.1). The calculation of its coefficients has been carried out for massless quarks to order $g^6 \ln g$ by Vuorinen [72].

The problems with the convergence of the perturbative series are somewhat milder in the contributions to the pressure involving the chemical potential. The results obtained in strict perturbation theory [72], at least when using an optimized choice of the renormalization scale, agree reasonably both with results from resummations based on Φ -derivable approximations [127, 128] and with available lattice data [129, 130] as long as the temperature is not too close to the deconfinement transition. Figure 3.5 shows a comparison [104] of the perturbative three-loop result for $\Delta P = P(T, \mu) - P(T, 0)$ with lattice data from [130], where the difference between the optimized perturbative result and the lattice data is about 10% at the upper end of the temperature range considered. This difference is in fact of the order of the estimated discretization errors [131].

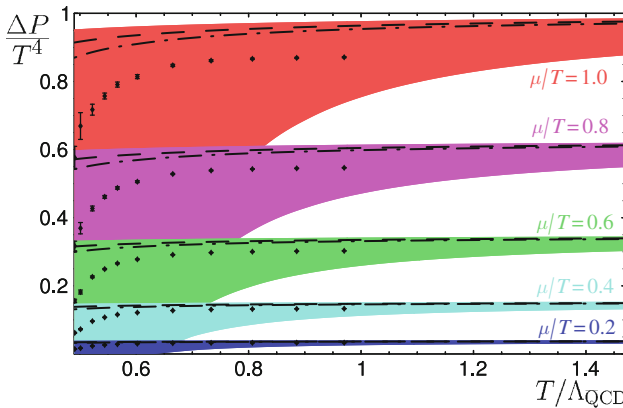


Fig. 3.5 The difference $\Delta P = P(T, \mu) - P(T, 0)$ divided by T^4 given by the three-loop result of [72] for $\mu/T = 0.2, \dots, 1.0$ (bottom to top) versus lattice data from [130] (not yet continuum-extrapolated!) assuming $T_c^{\mu=0} = 0.49 \Lambda_{\text{QCD}}$ [132]. Dashed and dash-dotted lines correspond to the perturbative result with two different choices of optimized renormalization scales and the shaded areas display the spread when the renormalization scale is varied by a factor of 2 about the central value.

The perturbative expansion of diagonal quark number susceptibilities follows the same pattern as shown in Eq. (3.1), except that now the coefficient of order g^6 is perturbatively computable (albeit not computed so far).

Off-diagonal susceptibilities $\chi_{ij} = \partial^2 P / \partial \mu_i \partial \mu_j$ with different flavor indices $i \neq j$ differ in that the perturbative expansion at the point $\mu_i = \mu_j = 0$ starts only at order $g^6 T^2 \ln 1/g$. In QCD one finds for massless quarks [127]

$$\chi_{i \neq j}|_{\mu=0} \sim -\frac{10}{9}(\alpha_s/\pi)^3 T^2 \ln 1/\alpha_s. \quad (3.9)$$

This term is due to C -odd contributions to the dimensionally reduced effective theory of EQCD [133–135]. Initially lattice results at high temperature [136] appeared to be in contradiction with (3.9), which was interpreted as a further indication of the nonperturbative nature of the quark-gluon plasma. However, newer lattice results now do agree in sign and order of magnitude [137, 138]. A detailed quantitative comparison of the perturbative results for both diagonal and off-diagonal susceptibilities with (3-dimensional) lattice simulations of EQCD has recently been carried out in [139].

At zero temperature and high chemical potential the perturbative expansion of the pressure does not involve odd powers of the coupling g , but does involve $\ln 1/g$ terms starting at order g^4 . In contrast to the results obtained at high temperature and chemical potential $\mu \ll T/g$, the nonanalytic terms in the coupling constant require a resummation of nonstatic self energy contributions, namely the so-called hard-dense-loop (HDL) part [140–143]. On the other hand, perturbation theory at zero temperature is free of Linde’s magnetic mass problem [68] which at finite temperature renders the contribution proportional to $g^6 T^4$ nonperturbative. A complete result of the $T = 0$ high- μ pressure to order g^4 has been obtained already in 1977 by Freedman and McLerran [144–146] and subsequently by Baluni [147], but the coefficient to order g^4 involved sizeable numerical uncertainties. An accurate calculation to order g^4 has been provided more recently by Vuorinen [72].

At small nonzero temperatures $T \ll g\mu$, the perturbative series is more complicated and involves logarithms and fractional powers of g and of T/μ . Physically, this is caused by the weakly screened low-frequency magnetic fields rather than electrostatic Debye screening. The leading temperature contribution to the pressure is of order $g^2 T^2 \mu^2 \ln T^{-1}$, which gives rise to a $T \ln T^{-1}$ term in the low-temperature entropy characteristic of non-Fermi-liquid (NFL) behavior (also referred to as “anomalous specific heat”). The (positive) coefficient of this logarithmic term was calculated first by Holstein et al. in 1973 [148] (corrected 1995 in [149]) for a nonrelativistic electron gas, where its effect is probably too small for experimental detection. In QCD, which has 8 times more gauge bosons and a much larger coupling, the effect is correspondingly bigger. Moreover, it has been shown in [150] that the $T \ln T^{-1}$ term is not modified by (perturbative) higher order corrections even when the logarithm gets nonperturbatively large. A complete calculation of the leading term beyond logarithmic accuracy was performed by Ipp et al.

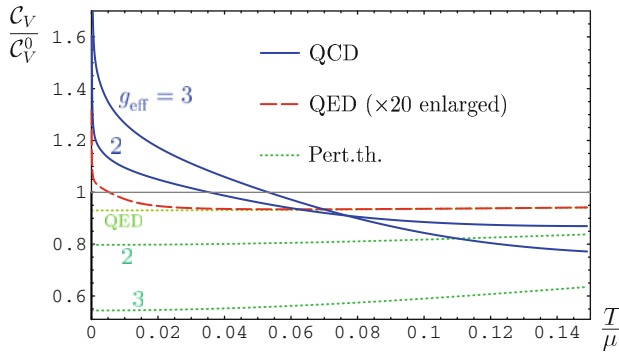


Fig. 3.6 Non-Fermi-liquid specific heat for low-temperature (but non-superconducting) massless QCD and QED normalized to the Stefan-Boltzmann result. With $g_{\text{eff}}^2 \equiv g^2 N_f/2$, $g_{\text{eff}} = 2$ and 3 correspond to $\alpha_s \approx 0.32$ and 0.72 , respectively, in $N_f = 2$ QCD. The *dotted lines* represent the naive perturbative result to order g^2 . The QED result is enlarged by a factor 20 to make its tiny NFL effects visible in this plot.

[151, 152] (the corresponding NFL term in the quark propagator was later calculated completely in [153]). If one defines the NFL regime by the criterion that the T -dependent contribution to the interaction pressure is positive rather than (as usually the case) negative, the upper temperature of the NFL regime is obtained as [73]

$$\frac{T_{\text{NFL}}}{\mu} \approx 0.064(N_f/2)^{1/2}g. \quad (3.10)$$

This temperature is at the same time a rather sharp lower limit for the applicability of dimensional reduction and the effective theory EQCD. Because of the smallness of the prefactor in (3.10) the latter actually permits remarkably low values of T/μ . For temperatures below T_{NFL} one finds strong deviations from naive, unresummed first-order perturbation theory, leading eventually to a specific heat in excess of the Stefan-Boltzmann value as shown in Fig. 3.6.

As discussed in detail later in Sect. 3.5, at sufficiently small temperatures ($T \propto \exp(-3\pi^2/\sqrt{2}g)$ and therefore not visible in a series expansion in g) one expects a transition to a color superconducting phase which limits the above NFL regime for normal-conducting quark matter from below. Extrapolating the weak-coupling results for T_{NFL} and for the critical temperature of color superconductivity to larger coupling, the perturbative result suggests a small but finite range of NFL behavior as displayed in Fig. 3.7.

The effects of the anomalous specific heat of normal quark matter and the specific heat expected for the various phases of color superconductivity on neutron star cooling have been studied in [154]. This crucially involves also

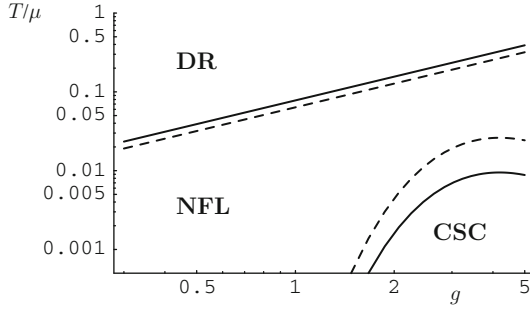


Fig. 3.7 The dividing line between the regime of dimensional reduction (DR) which is governed by the effective theory of EQCD and that of non-Fermi-liquid behavior (NFL) as given by Eq. (3.10) for $N_f = 3$ (full lines) and $N_f = 2$ (dashed lines), in comparison with the weak-coupling result ((3.59) for a spin-zero condensate) for the critical temperature of color superconductivity (CSC) when extrapolated to large coupling.

NFL effects on the neutrino emissivity through the NFL quark dispersion relations [153].

3.1.6 Summary of the present status

The pressure of the quark-gluon plasma phase is of fundamental importance in heavy-ion collision experiments and precision cosmology. At very high temperatures the QCD coupling constant becomes small and perturbation theory is applicable. The perturbative expansion for the pressure of high-temperature QCD is now known up to order $g^6 \ln 1/g$ [70], 29 years after the first non-trivial $O(g^2)$ contribution was obtained. This is the highest order fully computable in perturbation theory. The results are physically applicable when $T \gtrsim 2 - 3T_c$ and $\mu \lesssim \pi T$.

The most striking features of the perturbative expansion are the slow convergence and large order-by-order fluctuations in the expansion. These signal the well-known fact that QCD remains strongly coupled also within the quark-gluon plasma. Despite the large fluctuations, it is possible to fit the perturbative result to the pressure determined with quenched lattice simulations [70, 75]. Thus, combining these two results, we obtain interpolated quenched QCD pressure for all temperatures. From the resulting curve we can observe that deviations from the ideal gas Stefan-Boltzmann law are significant: at $T \sim 2T_c$, the deviation is $\sim 30\%$, at $T \sim 10T_c$ 12% , and even at $T \sim 100T_c$ around 7% . Thus, deviations from the ideal gas are significant at all temperatures relevant for heavy-ion experiments.

In order to go beyond $g^6 \ln 1/g$ non-perturbative lattice simulations are required. The non-perturbative part of the $O(g^6)$ contribution has already

been measured from lattice simulations; however, in order to relate this to QCD pressure, a perturbative 4-loop matching computation is required. This has not been accomplished yet.

At low temperatures and high quark chemical potential, where lattice QCD is unfortunately unavailable, the perturbative expansion obtained by means of dimensionally reduced effective theories breaks down for $T \lesssim 0.1g\mu$. For such temperatures the perturbative expansion, which has been worked out to order g^4 , involves the nonstatic hard-dense-loop effective theory. It is no longer restricted to orders below g^6 , since Linde's magnetic mass problem [68] disappears in the limit of zero temperature. However, as discussed below in Sect. 3.5, at parametrically exponentially small (but potentially sizeable) temperatures important additional contributions are provided by phases of color superconductivity. Above the critical temperature of color superconductivity, the perturbative result suggests a small but finite range of non-Fermi-liquid behavior of QCD, involving a characteristic anomalous specific heat contribution.

For full QCD the pressure has been calculated only for massless quarks. However, because the pressure behaves smoothly when the quark masses are varied, it is possible to use an interpolation in order to obtain a phenomenological result for QCD with a physical quark mass spectrum. Combining the high-temperature perturbative pressure with a hadron resonance gas behavior at low temperature, we obtain a "best effort" result for the full QCD pressure at all temperatures [75]. One of the striking features is that the charm quark mass has a significant effect almost immediately above the transition temperature. It is important to understand the interrelations between such a "best effort" result and the results from lattice QCD: On the one hand, the calculation of the pressure within lattice QCD typically uses too heavy up and down quark masses (see, however, the most recent results discussed in Sect. 3.2). Therefore, the results from a combined resonance gas plus perturbative QCD calculation might be regarded as more physical. On the other hand, without calculations from lattice QCD we would not know whether the resonance gas results are reasonable (see also Sect. 4.2). In addition, the description of the pressure in terms of resonance gas + perturbative expansion will certainly be incorrect in some details; for example, the way these two expansions are glued together at T_c determines the nature of the transition. Hence, full lattice QCD is still the most powerful guideline in the transition region from hadronic to quark-gluon matter. The next section is devoted to the results for thermodynamic properties obtained with this first-principle method.

3.2 Thermodynamic properties from lattice QCD

During recent years our knowledge of the thermodynamics of strongly interacting elementary particles greatly advanced [58]. Lattice calculations now allow to study also the thermodynamics at non-zero quark chemical potential (μ_q). Most of the approaches developed for this purpose [155–159] are still limited to the regime of high temperature and small values of the chemical potential, $T \gtrsim 0.9 T_0$, $\mu_q/T \lesssim 1$ (where T_0 denotes the transition temperature at vanishing chemical potential). An exception is the density of state method which can be used at larger chemical potentials (see below) [160]. In spite of the fact that most approaches are limited to small chemical potentials, they already allow to analyze the density dependence of the QCD equation of state in a regime relevant for a wide range of energies explored by heavy-ion experiments and may even be sufficient to establish or rule out the existence of a second order phase transition point in the QCD phase diagram. The existence of such a critical point as endpoint of a line of first order phase transitions that separates at low temperature the low and high density regions in the QCD phase diagram, is suggested by many phenomenological models. For small values of μ_q/T lattice calculations suggest that the transition from low to high temperature is not a phase transition; the transition during which bulk thermodynamic quantities, e.g. the energy density, change rapidly and the chiral condensate drops suddenly, is a continuous, rapid crossover. It thus has been speculated [50] that a 2nd order phase transition point exists somewhere in the interior of the QCD phase diagram. The generic form of the QCD phase diagram which is not without dispute in the lattice community [1, 2] is shown in Fig. 1.1.

In the past five years considerable progress was made to explore this phase diagram and determine some of its features even quantitatively (especially for $\mu_q = 0$). At non-zero μ_q the infamous sign problem prohibits direct lattice calculations. Therefore there was little progress for a long time. Recently, several methods have been introduced to circumvent this problem and make predictions for small μ_q values. At large chemical potentials where the sign problem becomes the most severe, usually QCD-like models are applied on the lattice. These will not be discussed here.

In the following we will first discuss some important aspects of the techniques developed in lattice QCD. Especially we will focus on the problem how to extract information at non-vanishing chemical potential. Afterwards we will present recent lattice results for the equation of state, the transition temperature, the location of the critical point and various susceptibilities.

3.2.1 Lattice formulation

We recall from Sect. 2.2 that thermodynamical quantities can be obtained from the partition function which can be given by a Euclidean path-integral (cf. Sect. 2.1, Eq. (2.7)):

$$Z = \int \mathcal{D}U \mathcal{D}\bar{\Psi} \mathcal{D}\Psi e^{-S_E(U, \bar{\Psi}, \Psi)}, \quad (3.11)$$

where U and $\bar{\Psi}, \Psi$ are the gauge and fermionic fields and S_E is the Euclidean action. Note that here the gauge links U instead of the gauge potentials A_ν are used to characterize the gauge fields. This representation is more appropriate for the discretized version of QCD. The formal integral $\mathcal{D}U \mathcal{D}\bar{\Psi} \mathcal{D}\Psi$ is carried over all possible gauge and fermionic field configurations. Note, that the above expression is formally the same as the partition function in statistical mechanics. One has to take all gauge and fermionic field configurations, calculate the corresponding Euclidean actions and use them as Boltzmann-weights for the summation. The lattice regularization of the QCD action is not unique. There are several possibilities to use improved actions which have the same continuum limit as the straightforward unimproved ones. On the one hand the advantage of improved actions is that the discretization errors are reduced and therefore a reliable continuum extrapolation is possible already from larger lattice spacings. On the other hand, calculations with improved actions are usually more expensive than with the unimproved one.

Usually S_E can be split up as $S_E = S_g + S_f$ where S_g is the gauge action containing only the self interactions of the gauge fields and S_f is the fermionic part. The gauge action has one parameter, the gauge coupling g . In lattice QCD one uses instead $\beta = 6/g^2$. This quantity should not be confused with the inverse temperature.⁴ The parameters of S_f are the quark masses m_f and the chemical potentials μ_f , where f denotes the quark flavor. For the fermionic action the two most widely used discretization types are the Wilson and staggered fermions. As most recent works at finite T and μ_f apply staggered fermions in the following we focus on this case.

The fermionic part of the action is always bilinear, so the Grassmann-integration can be carried out according to

$$\int \mathcal{D}\bar{\Psi} \mathcal{D}\Psi e^{-\bar{\Psi} M(U) \Psi} = \det M(U), \quad (3.12)$$

where M is the fermion matrix depending on the gauge fields. Staggered fermions describe four flavors (usually referred to as “taste”) of quarks, therefore the fourth root trick is usually applied to get the partition function of

⁴ Increasing $\beta = 6/g^2$ corresponds to decreasing the gauge coupling. In turn, this is connected to a decrease of the lattice spacing a due to asymptotic freedom. The temperature is connected to the inverse of the lattice spacing, cf. Eq. (3.14) below. Thus increasing $\beta = 6/g^2$ effectively *increases* the temperature.

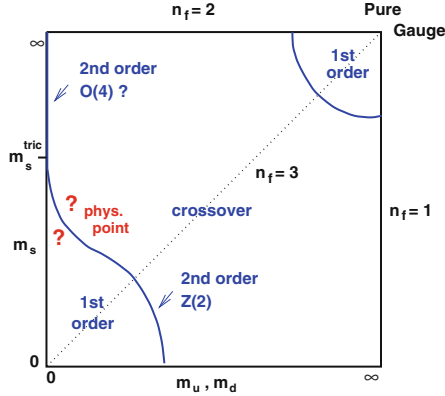


Fig. 3.8 The order of the phase transition (at vanishing chemical potential) as a function of the quark masses [58].

N_f flavors⁵:

$$Z = \int \mathcal{D}U [\det M(U)]^{N_f/4} e^{-S_g(U)}. \quad (3.13)$$

The appearance of the fractional power of the determinant leads to some difficulties which will be discussed later. Note, however, that this is only specific to the staggered formulation. Possible future studies with Wilson fermions will not suffer from these difficulties.

To understand the results presented in the following for different number of flavors it is useful to introduce the following notation used in the lattice community: N_f flavor lattice calculations mean N_f flavors with same mass, whereas lattice calculations with $2 + 1$ flavors mean 2 light flavors and one heavier one. (Of course, this is closest to the physical situation of the two light flavors up and down and the heavier strange one.) As already discussed in Sect. 2.2 the order of the transition from hadronic matter to the quark-gluon plasma depends on the number of active flavors and their masses. For three quarks and for vanishing chemical potential this is depicted in Fig. 3.8.

For the actual calculations finite lattice sizes of $N_s^3 N_\tau$ are used. The physical volume and the temperature are related to the lattice extensions as:

$$V = (N_s a)^3, \quad T = \frac{1}{N_\tau a}. \quad (3.14)$$

Therefore lattices with $N_\tau \geq N_s$ are usually referred to as zero temperature lattices while the ones with $N_\tau \ll N_s$ are finite temperature lattices.

⁵ The locality of a theory with fourth root is recently intensively studied; see e.g. [161–163].

3.2.2 Lattice methods at finite chemical potential

In lattice QCD the computation of Z (or more often its derivatives) is done via Monte-Carlo techniques involving importance sampling. An ensemble of configurations is generated with the distribution $p \propto (\det M)^{N_f/4} e^{-S_g(U)}$. This requires, however, that the fermionic determinant is positive and real. It is easy to understand the importance and the consequences of this condition by using the simplest importance sampling method, the Metropolis algorithm. The usual Metropolis update of any system consists of two steps. In the first step one changes the field configuration (in QCD it means one changes the gauge configuration U). We denote this change by $U \rightarrow U'$. This change of the gauge field would result in a change of the Euclidean action. Thus, this new gauge configuration would give another Boltzmann-weight in the partition function (see Eq. (3.11)). In the second step the suggested U' can be accepted or rejected by the following probability

$$P(U \rightarrow U') = \min [1, \exp(-\Delta S_g) \det(M[U']) / \det(M[U])] . \quad (3.15)$$

Since the probability is a real number between 0 and 1, the above expression can be interpreted as a probability only for real positive determinants. The positivity of the fermionic determinant is guaranteed for $\mu = 0$ and for purely imaginary μ -s by the γ_5 hermiticity of the fermion matrix (Dirac operator):

$$\gamma_5 M \gamma_5 = M^\dagger \Rightarrow \det(\gamma_5) \det(M) \det(\gamma_5) = \det(M)^* \Rightarrow \det(M) = \det(M)^* . \quad (3.16)$$

It also follows from this equation that the eigenvalues of M and M^\dagger are the same. Therefore the eigenvalues of M are either real or come in complex conjugate pairs. In the continuum, or in the staggered regularization the real eigenvalues can only be positive, equal to the quark mass, so the determinant is positive. (For Wilson fermions the positivity is only guaranteed close to the continuum limit or using an even number of degenerate quark flavors.)

Unfortunately, at non-zero chemical potentials the determinant can have arbitrary complex values. Even if we take the real part of the integrand (since we know that Z is real) the sign is not always positive thus spoiling the above Metropolis accept/reject step and any other importance sampling method. This is the infamous sign problem: direct simulations applying importance sampling at $\mu > 0$ are not possible.

Recently several methods have been developed to extract information for finite μ from simulations at zero or purely imaginary μ values. These techniques are, however still restricted to finite T and relatively small μ . The validity region in *baryonic* chemical potential is approximately $\mu \lesssim 3T$. The three up to now most successful methods will be discussed in the following.

3.2.2.1 Multi-parameter reweighting

One of the possibilities to extract information at $\mu \neq 0$ is the Glasgow method [164]. It is based on a reweighting in μ . An ensemble is generated at $\mu = 0$ and the ratio of the fermion determinants at finite μ and $\mu = 0$ is taken into account as an observable. This method was used to attempt to locate the phase transition at low T and finite μ , however it failed even on lattices as small as 4^4 . The reason is the so-called overlap problem. The generated configurations (only hadronic ones) do not have enough overlap with the configurations of interest (e.g. in the case of a phase transition a mixture of hadronic and quark-gluon dominated ones).

A simple, but powerful generalization of the Glasgow method is the overlap improving multi-parameter reweighting [165]. The partition function at finite μ can be rewritten as:

$$\begin{aligned} Z &= \int \mathcal{D}U e^{-S_g(\beta, U)} [\det M(m, \mu, U)]^{N_f/4} \\ &= \int \mathcal{D}U e^{-S_g(\beta_0, U)} [\det M(m_0, \mu = 0, U)]^{N_f/4} \\ &\quad \times \left\{ e^{-S_g(\beta, U) + S_g(\beta_0, U)} \left[\frac{\det M(m, \mu, U)}{\det M(m_0, \mu = 0, U)} \right]^{N_f/4} \right\}, \quad (3.17) \end{aligned}$$

where the second line contains a positive definite action which can be used to generate the configurations and the terms in the curly bracket in the last line are taken into account as an observable. The expectation value of any observable can then be written in the form:

$$\langle O \rangle_{\beta, m, \mu} = \frac{\sum O(\beta, m, \mu) w(\beta, m, \mu)}{\sum w(\beta, m, \mu)} \quad (3.18)$$

with $w(\beta, m, \mu)$ being the weights of the configurations defined by the curly bracket of Eq. (3.17).

The main difference from the Glasgow method is that reweighting is done not only in μ but also in the other parameters of the action (at least in β , but possibly also in m). This way the overlap can be improved. If the starting point (β_0 , m_0 and $\mu_0 = 0$) is selected to be at the $\mu = 0$ transition point then a much better overlap can be obtained with transition points at higher μ . A schematic figure shows the main differences between the two techniques (see Fig. 3.9). One can in general define the best weight lines along which – starting from a given point (β_0, m_0, μ_0) – the overlap is maximal. This can be done e.g. by minimizing the spread of the w weights.

There is still one potential problem with reweighting methods: The overlap between the different configurations might shrink with increasing volume [159, 166, 167]. Hence the observable (3.18) one is interested in might dissolve

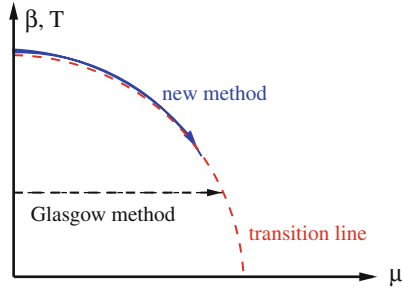


Fig. 3.9 Comparison of the Glasgow method and the new (multi-parameter reweighting) method. The Glasgow method collects an ensemble deep in the hadronic phase, attaches weights to the individual configurations and attempts to get information about the phase diagram, thus information about configurations on the other side of the transition line. There is no overlap between the original typical configurations (hadronic phase) and the configurations of the new phase. This is the reason why the method fails. The new technique (overlap improving multi-parameter reweighting) determines the transition line in a different way. First one tunes the system to the transition point at $\mu=0$. At this point the configuration ensemble contains configurations from both phases. A simultaneous reweighting is done in β (or in other words in the temperature – cf. footnote 4) and also in μ . Since we are looking for the transition line, thus for an equal “mixture” of the two phases, a careful change of the two parameters keeps the system in this mixed phase. The overlap between $\mu=0$ and $\mu \neq 0$ is much better, the transition line can be determined.

into numerical noise when approaching the infinite volume limit. We will come back to that point below when comparing the three different techniques.

3.2.2.2 Taylor expansion with and without multi-parameter reweighting

The use of Eq. (3.17) requires the exact calculation of determinants on each gauge configuration which is computationally expensive, in particular for large lattices. Instead of using the exact formula, one can perform a Taylor expansion for the determinant ratio in the weights [156] (for simplicity assuming no reweighting in the mass):

$$\ln \left[\frac{\det M(\mu)}{\det M(0)} \right]^{N_f/4} = \sum_{n=1}^{\infty} \frac{\mu^n}{n!} \frac{\partial^n \ln [\det M(0)]^{N_f/4}}{\partial \mu^n} \equiv \sum_{n=1}^{\infty} R_n \mu^n. \quad (3.19)$$

Taking only the first few terms of the expansion one gets an approximate reweighting formula. The advantage of this approximation is that the coefficients are derivatives of the fermion determinant at $\mu = 0$, which can be well approximated stochastically. Indeed, the problem mentioned above – that the overlap between different configurations might shrink with increasing vol-

ume – is of no concern here since everything is well-behaved at vanishing chemical potential. On the other hand, due to the termination of the series and the errors introduced by the stochastic evaluation of the coefficients it might appear that this Taylor expansion method does not work for as large μ values as the full technique. Indeed, it has been shown in [168] that even for very small lattices (i.e. 4^4) the phase of the determinant is not reproduced by the Taylor expansion for $a\mu \geq 0.2$.

From Eqs. (3.17) and (3.19) one sees that a Taylor expansion is performed for the exponent, i.e. the action, of the integrand of the path integral. The reweighting technique as the basis of (3.19) is important for the determination of the transition line (cf. Fig. 3.9). However, for the calculation of thermodynamic quantities, e.g. the pressure, in a given phase one can directly start with the partition function displayed in the first line of Eq. (3.17). One performs a Taylor expansion just for the (logarithm of the) partition function, i.e. for the whole path integral and not for the exponent of the integrand. We already refer to Eq. (3.28) below which forms the basis for the results presented later for the pressure at non-vanishing chemical potential and for the susceptibilities.

3.2.2.3 Simulations at imaginary μ

The fermion determinant is positive definite, if we use a purely imaginary chemical potential. Hence, reweighting techniques are not required in this case. If the transition line $T_c(\mu)$ is an analytic function, we can determine it for imaginary μ values and analytically continue back to real values of μ [158, 159, 169]. The analytic continuation is in general impossible from just a finite number of points. However, taking a Taylor expansion in μ or μ/T one gets:

$$\frac{T_c(\mu) - T_c(0)}{T} = a_2 \left(\frac{\mu}{T}\right)^2 + a_4 \left(\frac{\mu}{T}\right)^4 + \dots \quad (3.20)$$

The coefficients a_i can be determined from imaginary μ simulations. One simply measures $T_c(\mu)$ for imaginary μ -s and fits it with a finite order polynomial in μ/T . Recently, a generalization of this method was proposed by using a more general form of the action which still preserves the positivity of the fermion determinant [170].

Recently, instead of using the grand-canonical partition function a canonical approach was also applied to study QCD at non-zero density [171, 172]. This technique involves a Fourier integral for which the fermion determinant at imaginary μ values is needed. The sign problem emerges as fluctuations during the evaluation of this Fourier integral.

3.2.2.4 Differences and similarities of the three techniques

Although the three described methods seem different they are intimately connected. The connection between exact reweighting and Taylor expansion is obvious: The latter is an approximation of the former. Using all non-vanishing orders in the Taylor expansion should give exactly the same results as exact reweighting, provided that the latter still works well in the infinite volume limit.

The connection between reweighting and analytic continuation is not so straightforward. Since the phase diagram for imaginary μ is fitted by a polynomial it yields the μ derivatives at $\mu = 0$ (the closest point to the real μ domain, since μ^2 is the natural variable). In this sense it should give the same results as the Taylor expansion method in the same order. Thus, under the condition specified above and for moderate μ values the imaginary μ method should also agree with exact reweighting.

Indeed, the agreement of all three methods is demonstrated in Fig. 3.10 for a model case. In order to avoid difficulties when comparing different discretizations, different quark masses, different choices to transform lattice data into physical units and exact/non-exact Monte-Carlo generators the three methods have been applied using identical circumstances. The same phase diagram as in [159] is taken and the corresponding determination for the curvature of the transition line is used. The result of [159] is perfectly reproduced (up to four digits) by multi-parameter reweighting with full determinants and

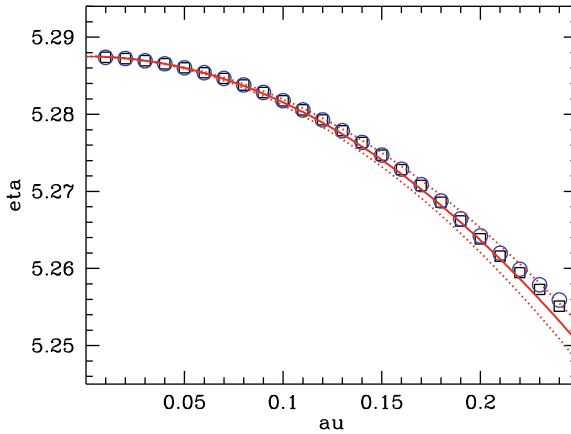


Fig. 3.10 The $N_f = 2$ phase diagram of [159] obtained via analytic continuation from imaginary μ (solid line; dotted lines show the uncertainty) and the same system calculated by exact multi-parameter reweighting (boxes) and Taylor expansion up to μ^4 order (circles) [173]. There is a perfect agreement. To enhance the differences the results were matched at $\mu = 0$ within the uncertainties. The errors are smaller than the symbol sizes. The labels “au” and “eta” denote chemical potential and temperature, respectively, in lattice units.

also by the Taylor expansion technique [173]. As the chemical potential gets larger the results start to deviate. This might be attributed to the higher order μ terms, which are missing both from the imaginary chemical potential method and from the Taylor expansion technique.

As we mentioned previously in the case of staggered fermions a fractional power of the fermion determinant is taken in order to have less than four flavors. For $\mu > 0$ this leads to an additional difficulty. The fourth root of a complex number cannot be taken unambiguously. There are several ways to circumvent this problem. It has been shown in [174] that near the continuum limit these ambiguities disappear and a unique fourth root can be defined. It has also been argued, however, that current lattices are not yet close enough to the continuum in this sense. The procedure the authors of [174] propose does not work on today's lattices. An alternative method to choose among the Riemann leaves is given in [155] which assumes analyticity of the fourth root along the real μ axis. Close to the continuum where the previous procedure can be applied the two methods choose the same roots. Since both Taylor expansion and analytic continuation from imaginary chemical potentials implicitly assumes analyticity they correspond to the same choice.

After this introduction into the calculational techniques of lattice QCD at finite chemical potentials we turn to the presentation of results.

3.2.3 The equation of state from lattice QCD

To determine the equation of state (EoS) we introduce the grand canonical potential, $\Omega(T, V, z_f)$, normalized such that it vanishes at vanishing temperature,

$$\Omega(T, V, z_f) = T \ln Z(T, V, z_f) - p_0 \quad . \quad (3.21)$$

The quantity $p_0 = \lim_{T \rightarrow 0} T \ln Z(T, V, 1)$ denotes the vacuum contribution to the pressure.

Here T denotes the temperature, V the volume, and $z_f = e^{\mu_f/T}$ is a set of fugacities related to the chemical potentials μ_f for different quark flavors, e.g. $f = u, d, s$ for up, down and strange quarks.

From (3.21) we obtain pressure (p) and energy density (ϵ)

$$p = \frac{1}{V} \Omega(T, V, z_f) \quad , \quad \epsilon = \frac{T^2}{V} \frac{\partial \Omega(T, V, z_f)/T}{\partial T} \quad , \quad (3.22)$$

which both vanish at vanishing temperature. Using these relations one can express the difference between ϵ and $3p$, i.e. the thermal contribution to the trace of the energy-momentum tensor $\Theta_\mu^\mu(T)$, in terms of a derivative of the pressure with respect to temperature, i.e.

$$\frac{\epsilon - 3p}{T^4} = T \frac{\partial}{\partial T} (p/T^4) \quad , \quad (3.23)$$

In a lattice calculation of bulk thermodynamic quantities Eq. (3.23) is, in fact, the basic observable that is determined. The pressure is then obtained through integration and it then is straightforward to extract the energy density.

Net particle numbers in different flavor channels are obtained as derivatives with respect to the corresponding quark chemical potentials or fugacities,

$$\frac{n_f}{T^3} = \frac{1}{VT^3} \frac{\partial p/T^4}{\partial \mu_f/T} = \frac{z_f}{VT^3} \frac{\partial p/T^4}{\partial z_f} \quad . \quad (3.24)$$

With this one also obtains the entropy density for non-zero values of the chemical potentials,

$$\frac{s}{T^3} = \frac{\epsilon + p}{T^4} - \sum_f \frac{n_f \mu_f}{T^4} \quad . \quad (3.25)$$

We stress that the normalization process introduced here for the grand canonical potential, Eq. (3.21), puts the pressure and energy density to zero in the vacuum; in practice this means they are set to zero at a suitably chosen small temperature value. As a consequence any non-perturbative structure of the QCD vacuum, e.g. quark and gluon condensates, which may lead to a non-vanishing vacuum pressure and/or energy density will show up as non-perturbative contributions to the high temperature part of these thermodynamic observables. This is similar to the normalization used e.g. in the bag model as well as the hadronic resonance gas, but differs from the normalization used e.g. in perturbative calculations at high temperature and phenomenological (quasi-particle) models used to describe the physics of the high temperature phase of QCD. This should be kept in mind when comparing results for the EoS with analytic and model calculations. Note also that these ambiguities in normalizing pressure and energy density at zero temperature drop out in the entropy density.

At present there are several groups which perform lattice calculations for finite temperature (and density). Concerning the presentation of results we will not collect all results of all groups, but rather concentrate in the present Sect. 3.2.3 mainly on results from the RIKEN-BNL-Columbia-Bielefeld collaboration.

3.2.3.1 Vanishing baryon number density

Most information on the structure of the high temperature phase of QCD and the nature of the transition itself has been obtained through lattice calculations performed in the limit of vanishing baryon number density or vanishing quark chemical potential ($\mu_f = 0$). We recall that this limit is most relevant

for our understanding of the evolution of the early universe and also is the regime which can be studied experimentally in heavy-ion collisions at RHIC (BNL) and soon also at the LHC (CERN). The experimental accessibility of this regime of dense matter also drives the desire to go beyond a qualitative analysis of the QCD phase transition and to aim at a numerically accurate determination of basic parameters that characterize the thermodynamics of dense matter at high temperature.

The transition to the high temperature phase of QCD is related to the restoration of chiral symmetry as well as deconfinement; the sudden decrease of the chiral condensate at the transition temperature T_0 and the sudden liberation of quark and gluon degrees of freedom, which leads to a rapid increase in the energy density, are clearly visible in many numerical calculations.

The deconfining features of the QCD transition are often discussed in terms of the Polyakov loop expectation value, which gives the change in free energy of a thermal medium due to the presence of an external static quark source (cf. Sect. 2.1, Eq. (2.18)),

$$e^{-F_q(T)} = \langle L \rangle \equiv \lim_{|\mathbf{x}| \rightarrow \infty} (\langle L(\mathbf{0}) L^\dagger(\mathbf{x}) \rangle)^{1/2}, \quad (3.26)$$

where $L(\mathbf{x})$ denotes the Polyakov loop defined at a lattice site \mathbf{x} . In Fig. 3.11 we show some results for the chiral condensate [175] and the Polyakov loop expectation value [176].

While the early studies of the QCD equation of state with dynamical quark degrees of freedom have been performed with only moderately light quarks and quark masses that have been held fixed in units of the temperature [131, 177, 178], computing resources now improved to use a more realistic setup. Recent studies of the equation of state therefore concentrated on calculations with a realistic or almost realistic quark mass spectrum performed

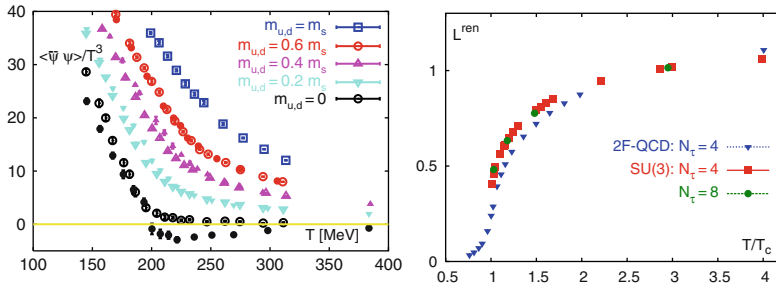


Fig. 3.11 *Left:* The light quark chiral condensate in QCD with 2 light up, down and a heavier strange quark mass (*open symbols*) and in 3-flavor QCD with degenerate quark masses (*full symbols*) [175]. *Right:* The Polyakov loop expectation value in the SU(3) gauge theory and in 2-flavor QCD [176].

along lines of constant physics, i.e. with light and strange quark masses fixed in units of hadron masses rather than the temperature [109, 110, 179, 180]. To reduce cut-off effects induced by the finite lattice spacing in the high temperature limit and in order to improve on the chiral properties of the discretized fermionic part of the QCD Lagrangian, recent calculations have been performed with improved staggered fermions, that remove $\mathcal{O}(a^2)$ discretization errors in bulk thermodynamic observables [109, 179, 180]. These calculations have been performed on lattices with temporal extent $N_\tau = 4$ and 6. We show in Fig. 3.12 the results for $(\epsilon - 3p)/T^4$ obtained in calculations with two different improved actions, asqtad [109, 179] and p4fat3 [180, 181]. The calculations performed with these two different actions still differ somewhat on coarse lattices with temporal extent $N_\tau = 4$. They are, however, in remarkably good agreement for $N_\tau = 6$.

The results shown in Fig. 3.12 have been obtained with the physical value of the strange quark mass and almost physical light quark mass values that correspond to a pion mass of about 210 MeV. The scale that is used to define the temperature scale has been determined from properties of the zero temperature, heavy quark potential, i.e. the distance r_0 at which the slope of the potential takes on a particular value,

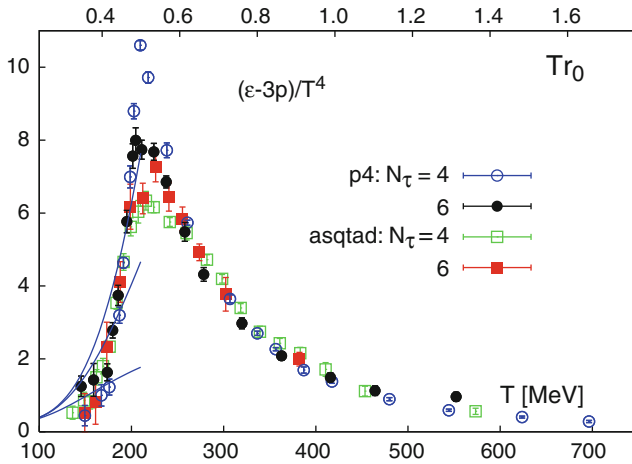


Fig. 3.12 The difference of energy density and three times the pressure in units of T^4 versus temperature obtained from calculations on lattices with temporal extent $N_\tau = 4$ and 6 [109, 179–181]. The temperature scales, Tr_0 (*upper* x-axis), and T [MeV] (*lower* x-axis), have been obtained by extracting the scale parameter r_0 from calculations of the heavy quark potential at zero temperature and by using $r_0 = 0.469$ fm. The *curves* show results for a resonance gas that includes resonances up to mass 1.0, 1.5 and 2.0 GeV, respectively (*lower to upper* curve).

$$\left(\frac{dV_{\bar{q}q}(r)}{dr} \right)_{r=r_0} = \frac{1.65}{r_0^2}. \quad (3.27)$$

Reading Fig. 3.12 with the scale Tr_0 given on the upper x-axis thus is an absolute prediction of QCD on the line of constant physics as specified above. In the continuum limit all calculations performed with different regularization schemes have to converge to a unique result for this basic observable. In a next step one has to determine r_0 in physical units. This is, at present, not without dispute. In fact, calculations performed with improved Wilson fermions tend to yield larger values for r_0 than those performed with improved staggered fermions. However, it seems that calculations with the latter are well controlled and cross-checked through the calculation of several different observables. We adopt here the value determined for r_0 from studies of level splittings in the charmonium system [182]. This yields $r_0 = 0.469$ fm, and fixes the temperature scales in units of MeV in the following figures that show lattice results in absolute units, namely Fig. 3.13 and below in Fig. 3.14. We stress that this is an absolute scale, independent of any ambiguities which may be related to extracting or defining a transition temperature in QCD.

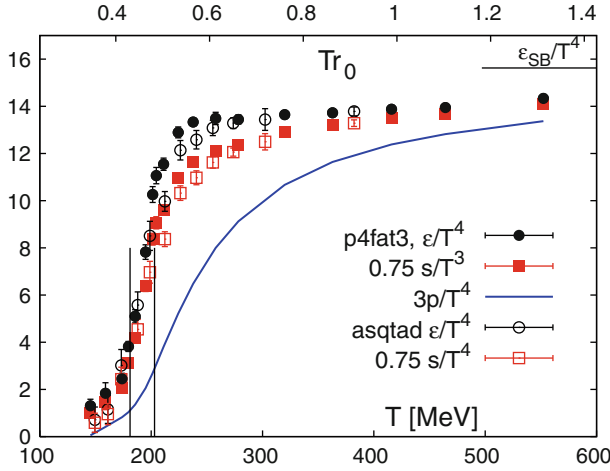


Fig. 3.13 The energy density (*circle*) and three times the pressure (*line*) in units of T^4 as well as the normalized entropy density (*squares*) in units of T^3 times 3/4 versus temperature. Shown are results from calculations obtained with two different improved staggered fermion actions for QCD with a physical value of the strange quark mass and almost physical, degenerate mass values for the up and down quarks on lattices with temporal extent $N_\tau = 6$. The temperature scales, Tr_0 (*upper x-axis*), and T [MeV] (*lower x-axis*), have been obtained by extracting the scale parameter r_0 from calculations of the heavy quark potential at zero temperature and by using $r_0 = 0.469$ fm. *Open symbols* are from calculations with the asqtad action [109, 179], *filled symbols* are from calculations with the p4fat3 action [181].

Using standard thermodynamic relations other thermodynamic observables can be extracted from $(\epsilon - 3p)/T^4$ as explained above. We show in Fig. 3.13 results for the energy and entropy densities as well as three times the pressure from calculations performed on lattices with temporal extent $N_\tau = 6$ with two different improved staggered fermion actions [109, 179, 181].

3.2.3.2 Non-zero baryon number density

Studies of the QCD equation of state have recently been extended to the case of non-zero quark chemical potential (μ_f) [155–159]. To apply such calculations to situations encountered in heavy-ion collisions, it is convenient to first consider the case of vanishing strange quark chemical potential ($\mu_s = 0$) and non-zero quark chemical potential ($\mu_q = (\mu_u + \mu_d)/2 > 0$).⁶ Calculations of bulk thermodynamic quantities for $\mu_q > 0$ based on the reweighting approach [129, 184], using the Taylor expansion of the partition function [111, 130, 138], as well as analytic continuation of calculations performed with imaginary values of the chemical potential [158] show that the μ_q -dependent contributions to energy density and pressure are dominated by the leading order $(\mu_q/T)^2$ correction for values of μ_q relevant for the description of dense matter formed at RHIC ($\mu_q/T \simeq 0.1$) as well as at the SPS ($\mu_q/T \lesssim 0.6$).

For the EoS calculation we will focus on a discussion of Taylor expansions of the partition function of 2-flavor QCD around $\mu_q = 0$. In this case the equation of state has been analyzed for the physical conditions that correspond to expanding, equilibrated matter created in a heavy-ion collision. This expansion follows lines of constant entropy per baryon.

At fixed temperature and small values of the chemical potential the pressure may be expanded in a Taylor series around $\mu_q = 0$,

$$\frac{p}{T^4} = \frac{1}{VT^3} \ln Z = \sum_{n=0}^{\infty} c_n(T, m_q) \left(\frac{\mu_q}{T} \right)^n, \quad (3.28)$$

where the expansion coefficients are given in terms of derivatives of $\ln Z$, i.e. $c_n(T, m_q) = \frac{1}{n!} \frac{\partial^n \ln Z}{\partial (\mu_q/T)^n}$. The series is even in (μ_q/T) which reflects the invariance of $Z(T, \mu_q)$ under exchange of particles and anti-particles. The quark number density is easily obtained from this expansion as a derivative with respect to the quark chemical potential,

$$\frac{n_q}{T^3} = \frac{1}{VT^3} \left. \frac{\partial \ln Z(T, \mu_q)}{\partial \mu_q/T} \right|_T = \sum_{n=2}^{\infty} n c_n(T, m_q) \left(\frac{\mu_q}{T} \right)^{n-1}. \quad (3.29)$$

⁶ At high temperature the net strange quark number vanishes for $\mu_s = 0$ up to $\mathcal{O}(g^3)$ in perturbation theory. Close to T_c and at low temperature the non-vanishing off-diagonal susceptibilities [138, 183], i.e. strangeness-quark number correlations, indicate that small but non-zero $\mu_s = 0$ may have to be considered to conserve strangeness.

Of particular importance to the physics addressed at FAIR with the CBM experiment is a detailed study of interacting dense hadronic matter. At RHIC energies it has been found that a traditional resonance gas model, constructed from a large (exponentially rising) set of non-interacting resonances provides a good approximation of the conditions met at chemical freeze out. It will be important to check how well such a model can describe properties of the QCD equation of state at non-zero density. First trials along this line were rather encouraging [107, 185] as will be discussed in detail in Sect. 4.2.

The Taylor expansion for the energy and entropy density require knowledge on the temperature dependence of the expansion coefficients of the pressure. They can then be obtained using Eq. (3.23). For the energy density one finds

$$\frac{\epsilon}{T^4} = \sum_{n=0}^{\infty} (3c_n(T, m_q) + c'_n(T, m_q)) \left(\frac{\mu_q}{T}\right)^n \quad (3.30)$$

with $c'_n(T, m_q) = T dc_n(T, m_q)/dT$. A similar relation holds for the entropy density [111],

$$\frac{s}{T^3} \equiv \frac{\epsilon + p - \mu_q n_q}{T^4} = \sum_{n=0}^{\infty} ((4-n)c_n(T, m_q) + c'_n(T, m_q)) \left(\frac{\mu_q}{T}\right)^n \quad (3.31)$$

Knowing the dependence of the energy density and the pressure on the quark chemical potential one can eliminate μ_q in favor of a variable that characterizes the thermodynamic boundary conditions for the system under consideration [111]. In the case of dense matter created in heavy-ion collisions this is a combination of entropy and baryon number. Both quantities stay constant during the expansion of the system.

It is straightforward to see that in an ideal quark-gluon gas with 2 massless flavors lines of constant S/N_B are defined by $\mu_q/T = \text{const}$,

$$\frac{S}{N_B} = 3 \frac{\frac{37\pi^2}{45} + \left(\frac{\mu_q}{T}\right)^2}{\frac{\mu_q}{T} + \frac{1}{\pi^2} \left(\frac{\mu_q}{T}\right)^3} \quad (3.32)$$

In the zero temperature limit, however, the resonance gas reduces to a degenerate Fermi gas of nucleons and the chemical potential approaches a finite value to obtain finite baryon number and entropy, i.e. $\mu_q/T \sim 1/T$.

In the left hand part of Fig. 3.14 we show the resulting isentropic lines in the $T - \mu_q$ plane on which S/N_B stays constant, together with the experimentally determined freeze-out lines for several heavy-ion experiments. The lattice results shown here are still based on calculations with only moderately light quarks on rather coarse lattices. The temperature and chemical potential scales in this figure thus are no more accurate than about (10–20)%. The isentropic lines still have to be determined with lighter quarks and a proper extrapolation to the continuum limit has to be performed. Nonetheless, it is apparent that the isentropic lines agree with the straight line, ideal gas

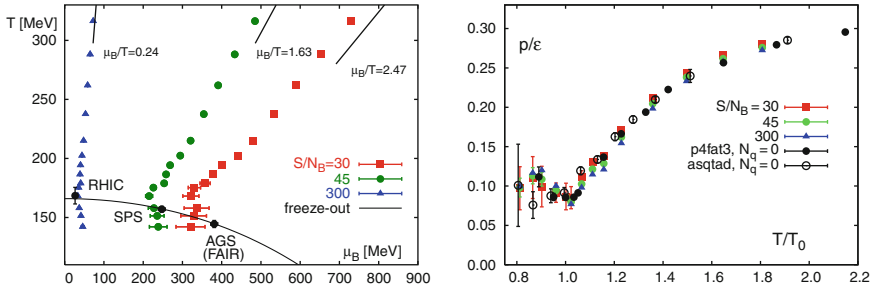


Fig. 3.14 Equation of state of 2-flavor QCD on lines of constant entropy per baryon number. The *left hand figure* shows *three lines* of constant S/N_B in the QCD phase diagram relevant for the freeze-out parameters determined in various heavy-ion experiments. Note that the baryo-chemical potential μ_B is three times the quark chemical potential, i.e. $\mu_B = 3\mu_q$. The *right hand figure* shows the equation of state on these trajectories of constant S/N_B [111].

behavior at large temperature and bend in the freeze-out region, where the physics of an (interacting) resonance gas becomes dominant.

The right hand part of Fig. 3.14 shows the isentropic equation of state as function of temperature obtained from a 6th order Taylor expansion of pressure and energy density [111]. The ratio p/ϵ is presented for three different entropy and baryon number ratios, $S/N_B = 30, 45$ and 300 , which correspond roughly to isentropic expansions of matter formed at the AGS (FAIR), SPS and RHIC, respectively. In this figure we also added results from the recent study of the thermodynamics of (2+1)-flavor QCD with an almost realistic quark mass spectrum at $\mu_q \equiv 0$. It is quite remarkable that p/ϵ is to a good approximation independent of S/N_B and also shows no significant quark mass dependence when the temperature is rescaled by the corresponding transition temperature. For temperatures larger than the transition temperature the equation of state, $p(\epsilon)$, is well described by a simple ansatz,

$$\frac{p}{\epsilon} = \frac{1}{3} \left(1 - \frac{A}{1 + B \epsilon} \right), \quad (3.33)$$

The insensitivity of the isentropic equation of state on S/N_B also implies that the velocity of sound at constant entropy,

$$v_s = \sqrt{\frac{dp}{d\epsilon}} = \sqrt{\frac{dp/dT}{d\epsilon/dT}} \quad (3.34)$$

is similar along different isentropic expansion trajectories. In fact, the parametrization given in Eq. (3.33) suggests that the velocity of sound approaches rather rapidly the ideal gas value, $v_s^2 = 1/3$. In Fig. 3.15 we summarize results for v_s^2 obtained in lattice calculations for an $SU(3)$ gauge theory

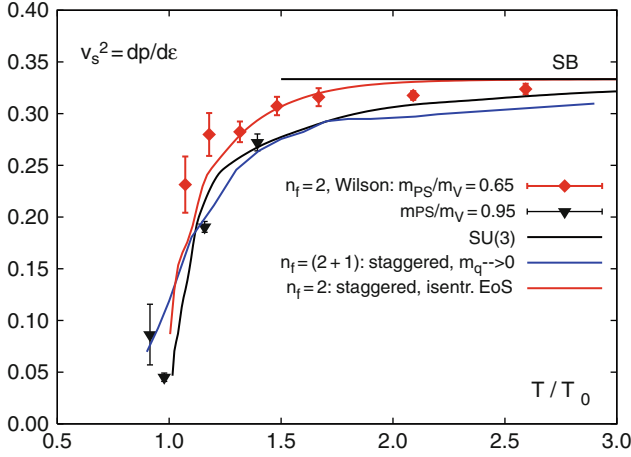


Fig. 3.15 The velocity of sound in QCD vs. temperature expressed in units of the transition temperature T_0 . Shown are results from calculations with Wilson [108] and staggered fermions [110] as well as for a pure SU(3) gauge theory [105]. Also shown is v_s^2 deduced from the isentropic equation of state [111], Eq. (3.33).

[105], for 2-flavor QCD with Wilson fermions [108], $(2+1)$ -flavor QCD with staggered fermions [110] as well as from the isentropic equation of state for 2-flavor QCD with only moderately light quarks [111].

3.2.4 The transition temperature at vanishing chemical potential

The transition from the low to the high temperature phase of QCD goes along with significant changes in thermodynamic observables. As is obvious from the discussion of the equation of state given in the previous section the transition takes place in a well defined narrow temperature interval. As the transition in QCD with physical quark mass values is a continuous crossover rather than a true phase transition accompanied by singularities in derivatives of the QCD partition, its location is usually analyzed by considering several susceptibilities that are sensitive to fluctuations in the thermal medium. The location of maxima of these observables are taken as estimates for the transition temperature. For a crossover transition this naturally involves some ambiguity. It is, however, worth noting that the temperature scale introduced, for instance, in Fig. 3.13 is independent of any convention used to define the transition temperature. Moreover, it also is helpful to realize that in simulations of QCD with varying quark masses it has been found that the

quark mass dependence of the transition temperature is weak; the transition temperature in the chiral limit sets a sensible lower limit and is close to that of QCD with its physical quark mass spectrum. Despite of this, the value of the transition temperature at vanishing chemical potential is still under intensive investigation. Calculations performed within different discretization schemes [175, 186–189] presented results between ~ 150 and $\sim 192(11)$ MeV in the years 2004–2007. The difference between these results has recently been reduced through refinements of the calculations that led to the high transition temperature ~ 190 MeV in [186]. These new calculations, performed with smaller quark masses and closer to the continuum limit, indicate a decrease of the ~ 190 MeV value to below ~ 170 MeV [190]. Calculations with a new, highly improved staggered fermion action [191] point in the same direction. This discussion will be resumed in Sect. 3.2.7.

3.2.5 Results for the location of the transition line and of the critical point

In the following we review lattice results for the transition line separating different phases and for the critical point.

3.2.5.1 Transition line

All the methods discussed in Sect. 3.2.2 have been used to give the transition line. The results are in agreement although different regularizations and quite coarse lattices were used. Up to now most results were obtained for one set of lattice spacings, namely on $N_\tau = 4$ lattices. We recall that results for the equation of state from $N_\tau = 4$ and $N_\tau = 6$ have been presented in Sect. 3.2.3. Note that different discretizations should agree only at vanishing lattice spacings, thus in the continuum limit. At non-vanishing lattice spacings one usually has different results for different lattice actions.

Using multi-parameter reweighting, the phase diagram was determined for 4 and 2+1 flavors of staggered fermions [155, 165, 192]. For the physically interesting latter case both semi-realistic and realistic quark masses were used. The phase diagram using physical quark masses is shown in Fig. 3.20 which will be discussed later in more detail.

The phase diagram obtained via Taylor expansion [156] is shown on the left panel of Fig. 3.16. Two flavors of p4 improved staggered fermions were used in this analysis. The critical point of [155] is also shown as a comparison. Note that although different lattice actions were used at a finite lattice spacing there is a good agreement.

The right panel of Fig. 3.16 shows the phase diagram obtained by analytic continuation from imaginary μ . The same method was also applied to four

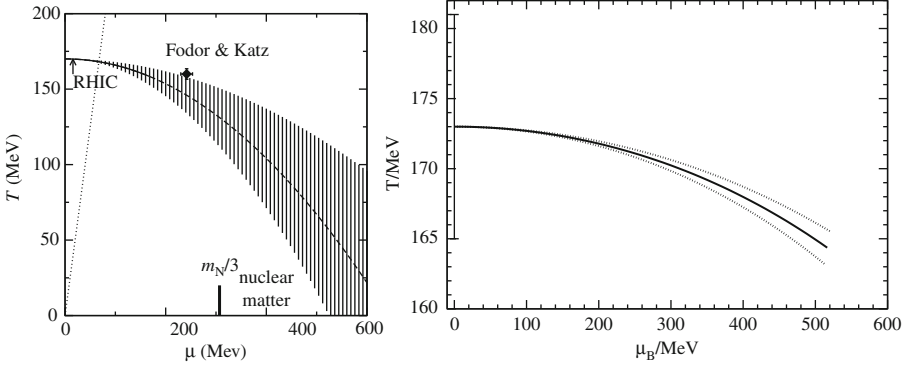


Fig. 3.16 *Left:* The phase diagram obtained from the Taylor expansion method by using two flavors of p4 improved fermions with a pion mass of ≈ 750 MeV (figure from [156]). *Right:* The phase diagram via analytic continuation from imaginary μ using two flavors of standard staggered fermions and a pion mass of ≈ 230 MeV [159].

flavors of staggered fermions in [158]. Consistent results were found with a generalization of the method which made it possible to reach somewhat larger values of μ [193].

In the case of multi-parameter reweighting the absolute temperature scale was determined by a $T = 0$ spectrum determination while in the case of the other methods only perturbative β functions were applied.

The latest result on the transition line comes from a combination of multi-parameter reweighting and the density of states method [160]. The phase diagram of four flavor staggered QCD was determined up to three times larger chemical potentials than with previous methods. A triple point was found around 900 MeV baryonic (300 MeV quark) chemical potentials (see Fig. 3.17).

Besides the transition line the equation of state can also be determined using the discussed methods. We refer to [129, 184] using multi-parameter reweighting, [111, 130] and Sect. 3.2.3 for Taylor expansion and [169] for analytic continuation from imaginary μ .

3.2.5.2 Critical point

One of the most important features of the phase diagram is the possible critical point separating a crossover region from a first-order phase transition regime. If such a point exists, its location is an unambiguous prediction of QCD.

Since phase transitions are sharp only in the thermodynamic limit of infinitely large volumes, the determination of the order of the phase transition, and the location of the associated critical point, is done by means of finite-size scaling analysis. There are different ways to locate the critical point. One

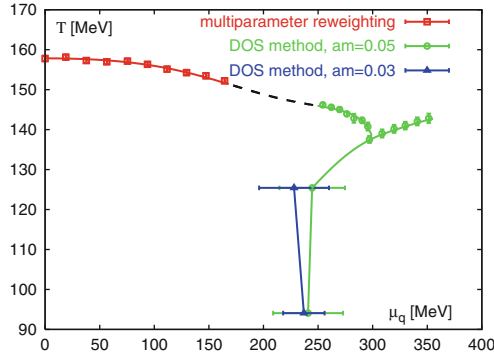


Fig. 3.17 The phase diagram of four flavor staggered QCD obtained with the density of states method on $N_\tau = 4$ lattices. A triple point was found at around 300 MeV quark chemical potential [160].

can use Lee-Yang zeroes, Binder cumulants or the convergence radius of the free energy density. These techniques will be discussed below. They can be applied directly, by determining the appropriate observables at finite μ_q using one of the methods described before. Another possibility is to start from a non-physical point (using small quark masses) where the critical point is located at zero or purely imaginary μ values and then determine the quark mass dependence of the critical point and extrapolate to the physical quark masses. The extrapolation, as usual, introduces uncontrolled errors.

At finite volumes the transition between the hadronic and quark-gluon phases is always continuous, the free energy density is analytic for all real values of the parameters of the action. Nevertheless, the partition function has zeroes even for finite volumes at complex values of the parameters. For a first-order phase transition these zeroes approach the real axis when the volume is increased – thus generating the singularity of the free energy for real parameter values. A detailed analysis shows that the imaginary part of these Lee-Yang zeroes scales as $1/V$ for large volumes. For a crossover the Lee-Yang zeroes do not approach the real axis when the volume is increased. Therefore inspecting the volume dependence of the imaginary parts of the Lee-Yang zeroes one can distinguish a first-order transition from an analytic crossover (see, however, [167] where potential problems are discussed).

Binder cumulants can also be used to locate critical points. In the infinite volume limit they converge to 1 in case of first order phase transitions and specific values (determined by the universality class) for second order phase transitions. For details see e.g. [194] where the critical point of three flavor QCD at $\mu_q = 0$ was determined using this technique.

The convergence radius of the Taylor expansion of the free energy gives the distance from the expansion point to the nearest singularity. If all expansion coefficients are positive then the singularity is at a real value of

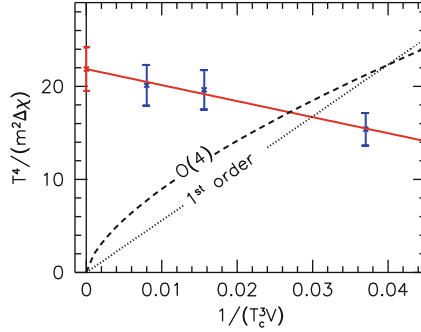


Fig. 3.18 The continuum extrapolated susceptibility $T^4/(m^2 \Delta\chi)$ as a function of $1/(T_c^3 V)$. For a true phase transition the extrapolation to infinite volume should be consistent with zero. On the other hand, for an analytic crossover the infinite volume extrapolation yields a non-vanishing value. The continuum-extrapolated susceptibility shows no volume dependence compatible with a phase transition, though the volume changes by a factor of five. For comparison, the asymptotic behavior for first-order and $O(4)$ (second-order) phase transitions is shown by *dotted* and *dashed* lines [44].

the expansion parameter which can then only be the critical point. As discussed before, this can only happen at infinite volume. The expansion coefficients have to be extrapolated to infinite volume, one has to be ensured that they are all positive and then the convergence radius can be calculated from them.

A necessary (but not sufficient) condition of the existence of the critical point is a crossover at $\mu_q = 0$. Recently it has been shown in [44] using staggered fermions that this is indeed the case (see Fig. 3.18). The transition temperature has also been determined as already discussed in Sect. 3.2.4.

It should be emphasized again that there is no fundamental reason known so far that a critical point must exist in the phase diagram of strongly interacting matter. Indeed, different lattice methods which addressed this issue have found different (preliminary) answers as will be discussed in the following. To qualitatively understand these results it is useful to extend the diagram shown in Fig. 3.8 into the region of finite chemical potentials. This is shown in Fig. 3.19 taken from [195]. Two possibilities are depicted in Fig. 3.19, namely that the region of true phase transitions located in Fig. 3.8 at (unphysically) small quark masses either is extended (left plot) at finite μ or shrinks further (right plot). Of course, even in the second case the surface might bend again, but that would happen only at rather large chemical potentials. Therefore, the curvature $dm_c/d\mu^2$ at $\mu = 0$ is an interesting quantity to study. Here m_c is the critical quark mass (e.g. in the limit of three flavors with equal mass). We will come back to this quantity below.

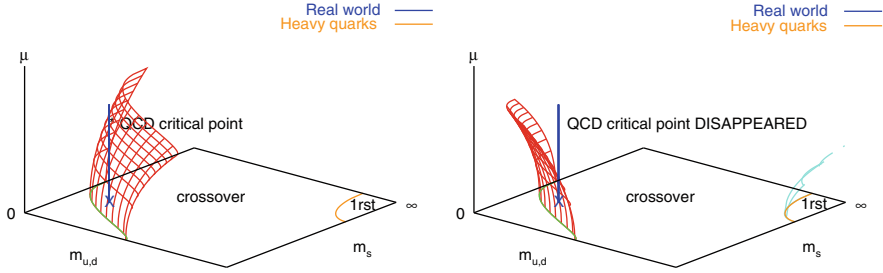


Fig. 3.19 The critical surface in the space of quark masses and chemical potential for positive (*left*) and negative (*right*) curvature, see also Fig. 3.8. For the physical point being in the crossover region for $\mu = 0$, a phase transition at finite μ will only arise in the scenario (*left*) with positive curvature, where the region of true phase transitions expands with μ . Figures taken from [195].

The multi-parameter reweighting combined with the Lee-Yang-zero analysis was used to locate the critical point. The first study was done with semi-realistic quark masses corresponding to a pion mass of ≈ 230 MeV [155]. The critical point was found at $T_E = 160 \pm 3.5$ MeV and $\mu_E = 725 \pm 35$ MeV. (Note that this is the value for the baryo-chemical potential $\mu_B = 3\mu_q$.) The whole study was repeated using larger volumes and physical quark masses in [192]. The results can be seen in Fig. 3.20. The critical point is located at $T_E = 162 \pm 2$ MeV and $\mu_E = 360 \pm 40$ MeV. One can see that the critical point moved to a smaller value of μ_q as the quark masses were decreased. This is in complete agreement with expectations. It is important to emphasize again that both of these results were obtained for one set of lattice spacings, the continuum extrapolation is still missing.

The Taylor expansion technique was used to determine the mass dependence of the critical point as discussed above. Starting from the three-flavor critical point where the phase transition is of second order at $\mu_q = 0$, the derivative $d\mu_E/dm$ was determined. A linear extrapolation to larger quark masses using only this first derivative gave $\mu_E \approx 420$ MeV for the location of the critical point for physical quark masses [196].

Another application of the Taylor expansion method was done in [137] using two flavors of staggered fermions. The convergence radius of the series was estimated using the first few coefficients. The authors claim to obtain $T_E \approx 0.95T_c$ and $\mu_E \approx 1.1T_E$ which is significantly smaller than the multi-parameter reweighting result.

For small enough quark masses the critical point can be located at a purely imaginary μ . Approaching the point where the critical point reaches $\mu = 0$ one can determine the derivative $d\mu_E^2/dm$ for negative values of μ_E^2 . This analysis was carried out in [2, 197]. For negative values of μ^2 the critical quark mass

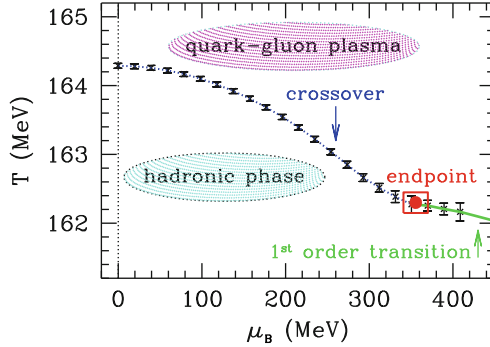


Fig. 3.20 The phase diagram obtained with multi-parameter reweighting using 2+1 flavors of standard staggered fermions corresponding to the physical pion mass [192]. The *dotted* part of the transition line is the crossover region while the *solid* line is of first order. The *box* shows the critical endpoint separating them. μ_B denotes the baryo-chemical potential: $\mu_B = 3\mu_q$.

m_c was located and the derivative $dm_c/d\mu^2$ was determined (which is just the inverse of the above quoted derivative).

In [197] $dm_c/d\mu^2$ was found rather small which by a rough, linear extrapolation would suggest a much larger value of μ_E for physical quark masses than found e.g. by multi-parameter reweighting. More surprisingly, when a similar analysis was done using an exact simulation algorithm instead of the previously applied approximate R algorithm, $dm_c/d\mu^2$ was found to be negative (but consistent with zero on the two- σ level). In other words, no critical point would exist in such a case or at least only one at very large μ . Conventionally, a positive value is expected for the derivative which was also observed with multi-parameter reweighting (larger quark masses lead to a larger value of μ_E). Effective model calculations also support the positive sign (for a recent study, see e.g. [198]). Future lattice studies on finer lattices, and eventually a continuum extrapolation will give the final answer.

3.2.6 Generalized susceptibilities and fluctuations

Derivatives of the grand canonical potential with respect to temperature and/or chemical potential define susceptibilities which experimentally become accessible through event-by-event analysis of fluctuations in observables

like baryon number, electric charge, strangeness and others. We will discuss here some observables that are generally related to density fluctuations, i.e. to derivatives of the pressure with respect to quark chemical potentials.

The expansion coefficients of the pressure with respect to quark chemical potentials are directly related to fluctuations of the quark number in a given flavor channel at vanishing chemical potential as well as correlations among these observables. One may consider the generalized susceptibilities,

$$\chi^{(i,j,k)} = \frac{1}{VT^3} \frac{\partial^i}{\partial(\mu_u/T)^i} \frac{\partial^j}{\partial(\mu_d/T)^j} \frac{\partial^k}{\partial(\mu_s/T)^k} \ln Z(T, V, z_f) \Big|_{z_f=1} . \quad (3.35)$$

In order to make contact to experimentally accessible observables it sometimes is more convenient to introduce chemical potentials for quark number (μ_q), SU(2) isospin (μ_I) and strangeness (μ_S) and rewrite the various chemical potentials for different quark flavors as,

$$\mu_u = \mu_q + \mu_I , \quad (3.36)$$

$$\mu_d = \mu_q - \mu_I , \quad (3.37)$$

$$\mu_s = \mu_q - \mu_S . \quad (3.38)$$

We will ignore in the following complications that arise with exact strangeness conservation and will approximate the zero strangeness case by setting $\mu_s = 0$ after appropriate derivatives have been taken.

3.2.6.1 Fluctuations at $\mu_f \equiv 0$

At non-zero quark number chemical potential fluctuations of e.g., quark number or electric charge are considered to be important signatures for the existence of a 2nd order phase transition point in the QCD phase diagram. These fluctuations are expected to diverge at the critical point while others, like the fluctuations of isospin are expected to stay finite. At vanishing chemical potential this behavior is anticipated already in the behavior of quartic fluctuations, i.e. the second derivative of susceptibilities such as the quark number susceptibility χ_q or the charge susceptibility χ_Q [199]. In Fig. 3.21 we show some results on quadratic and quartic fluctuations of the quark number, or more precisely,

$$\begin{aligned} d_2^q &\equiv \frac{1}{VT^3} \frac{\partial^2 \ln Z}{\partial(\mu_q/T)^2} = \frac{1}{VT^3} \langle (\delta N_q)^2 \rangle , \\ d_4^q &\equiv \frac{1}{VT^3} \frac{\partial^4 \ln Z}{\partial(\mu_q/T)^4} = \frac{1}{VT^3} \left(\langle (\delta N_q)^4 \rangle - 3 \langle (\delta N_q)^2 \rangle^2 \right) , \end{aligned} \quad (3.39)$$

with $\delta N_q \equiv N_q - \langle N_q \rangle$. Similarly one can define quadratic and quartic fluctuations of the electric charge. They are shown in Fig. 3.21 for the case of

a calculation in 2-flavor QCD still performed with rather heavy quarks. The sharp cusp developed by d_4^q at the transition temperature is quite remarkable. In fact in the chiral limit its singular behavior is expected to be identical to that of the specific heat, i.e. it is controlled by the critical exponent α ,

$$(d_4^q)_{\text{singular part}} \sim |T - T_0|^{-\alpha} \quad . \quad (3.40)$$

As this exponent is negative in 3-d, $O(N)$ symmetric spin models, d_4^q is expected to stay finite at T_0 in the chiral limit if the QCD transition belongs to this universality class.

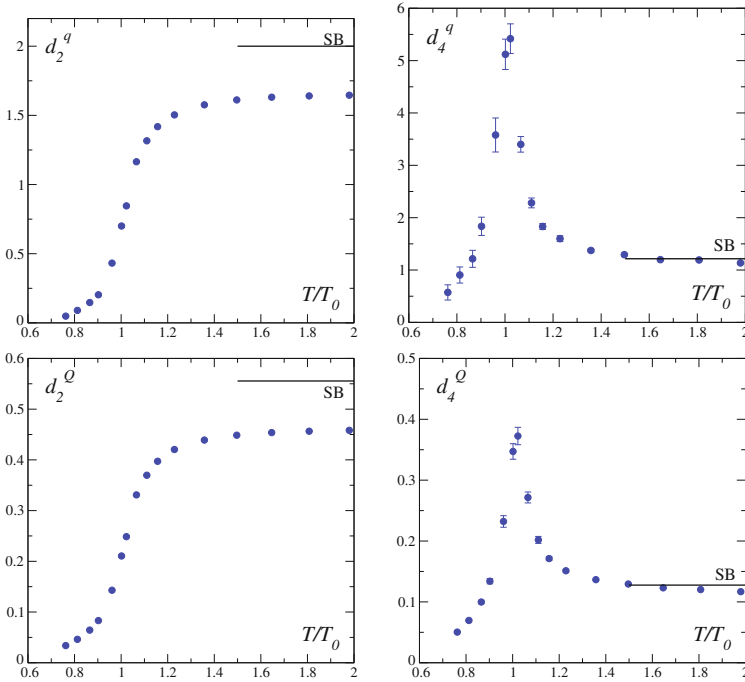


Fig. 3.21 Temperature dependence of quadratic (d_2) and quartic (d_4) fluctuations of the quark number (label “q”) and electric charge (label “Q”) calculated from the expansion coefficients for p/T^4 in 2-flavor QCD and for quark masses corresponding at T_0 to a pseudo-scalar (pion) mass of about 770 MeV [199].

Of particular interest are correlations between different conserved charges. They give insight into the structure of the thermal medium and allow to judge the nature of the dominant degrees of freedom in the low and high temperature phases, respectively. One important observable is the correlation between strangeness and e.g. baryon number or electric charges [137],

$$C_{BS} = -3 \frac{\chi_{BS}}{\chi_{SS}} = 1 + \frac{\chi_{us} + \chi_{ds}}{\chi_s} = 1 + 2 \frac{\chi_{us}}{\chi_s} , \quad (3.41)$$

$$C_{QS} = 1 - \frac{2\chi_{us} - \chi_{ds}}{\chi_s} = 1 - \frac{\chi_{us}}{\chi_s} . \quad (3.42)$$

These normalized correlations are shown in Fig. 3.22 from a calculation in 2-flavor QCD with a quenched strange quark sector (open symbols) and a preliminary result from a simulation with dynamical light and strange quark sectors (filled symbols).

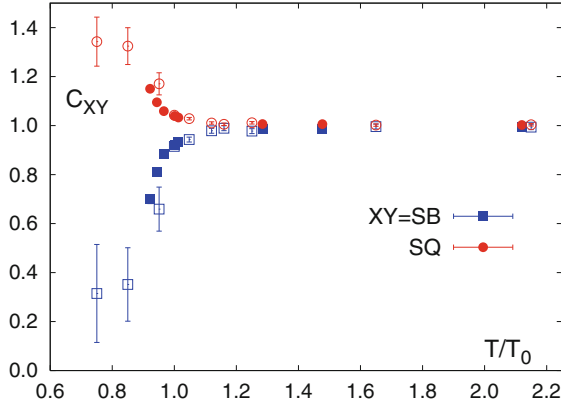


Fig. 3.22 Correlations of strangeness number with baryon number ($X = B$) and electric charge ($X = Q$). Results are obtained from simulations of QCD on lattices of size $16^3 \times 4$. *Open symbols* show data from calculations in 2-flavor QCD with a standard staggered fermion action where the strange quark sector has been dealt with in the quenched approximation. *Filled symbols* are from calculations in (2+1)-flavor QCD with improved staggered fermions [181, 200].

Figure 3.22 may be taken as evidence for strong correlations between baryon number and strangeness, i.e. both quantities fluctuate together. The simplest interpretation for this clearly is that both quantum numbers are carried by a single “particle” – quarks. As is obvious from Eq. (3.42) the proximity to unity also means that different flavor sectors are coupled only weakly and fluctuate independently.

3.2.6.2 Fluctuations at $\mu_q > 0$

The sharp peaks observed in quartic susceptibilities will contribute to quadratic susceptibilities at non-zero chemical potential. They are just the leading expansion coefficients in a Taylor expansion of quadratic susceptibilities. From such an expansion one indeed finds evidence that fluctuations in the

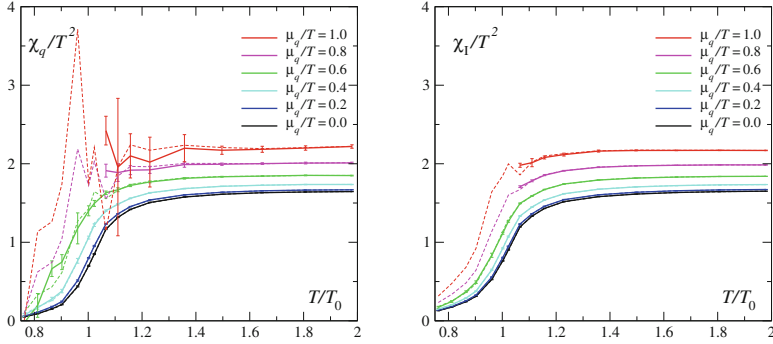


Fig. 3.23 Quark number χ_q/T^2 (left) and isospin χ_I/T^2 (right) susceptibilities for various μ_q/T ranging from $\mu_q/T = 0$ (lowest curve) to $\mu_q/T = 1$. Results are obtained by a combination of reweighting (solid lines and data points) and from a 6th-order Taylor expansion (dashed lines) [138].

quark number increase at non-zero quark chemical potential while, for instance, fluctuations of isospin seem to be insensitive to an increase in the chemical potential and show no sign for critical fluctuations. This is shown in Fig. 3.23 taken from [138].

3.2.7 Further discussion

A lattice result can be considered as a full result if two conditions are fulfilled. The first condition is related to the quark masses. We need results for physical quark masses, or in other words $m_\pi \approx 135$ MeV and $m_K \approx 500$ MeV. Controlled extrapolation in the quark masses around the transition temperature are not easy. Note, however, that today computers are quite often capable to deal with physical or almost physical quark masses. The second condition is the continuum extrapolation. It can be reached only by measuring quantities at non-vanishing lattice spacings and then extrapolating to vanishing lattice spacings. Luckily enough the choice of the action tells us what sort of functional form of the lattice spacings we expect for the deviation from the continuum limit result. If this asymptotic behavior is already present, we are in the so-called scaling region. Example for small enough lattice spacings results obtained by the standard Wilson action deviate from the continuum result by a linear term in the lattice spacing; for the staggered formalism this dependence is quadratic in the lattice spacings. Clearly, one should have an evidence that the results are already in this scaling region, which is described by the asymptotic lattice spacing dependence. For this check results at several lattice spacings are needed. Note, that thermodynamic studies are carried out on lattices, which have smaller temporal than spatial extensions. Typically

one uses $N_\tau = 4, 6, 8$ and 10 , which – as a rule of thumb – correspond to lattice spacings $\approx 0.3, 0.2, 0.15$ and 0.12 fm, respectively. (Particularly at small N_τ values, the lattice spacing in physical unit is quite ambiguous, different physical quantities give different results. This ambiguity disappears when we approach the continuum limit.)

Let us summarize what is known about our specific question, about the phase diagram of QCD. In some cases the result can be considered as a full one (at least using one specific formalism e.g. staggered one). In other cases one can estimate that the full result can be obtained in a year or two. There are however questions, which need much more time to clarify, particularly the controlled continuum limit is a difficult task.

(a) At vanishing chemical potential the nature of the $T \neq 0$ QCD transition is an analytic crossover [44]. The result was obtained with physical quark masses in the staggered formalism. This result can be considered as the full one. (As for any result of such type and huge complexity at least one independent analysis of the same depth is required to exclude any mistakes.) There are two, though unlikely possible uncertainties of this finding. One of them is a question, what happens if 2+1 flavor staggered QCD happens to be *not* in the QCD universality class. Though we do not have any theoretical proof for this universality class question, there is no sign for such a problematic scenario. Staggered lattice results for the whole spectrum and decay rates are in complete agreement with the experiments. Nevertheless it would be important to repeat the calculation with other fermion formulations (e.g. with Wilson fermions). This can be done with computer resources which are about an order of magnitude larger than the presently available ones. Since the rapid crossover is a remnant of the chiral transition of the massless theory, it would be very interesting to study the question what happens in the chiral limit. This question needs the same symmetry on the lattice as in the continuum theory. The best choice is the overlap fermion. Calculations with overlap fermions are usually two orders of magnitude more CPU-demanding than calculations with Wilson fermions. The other difficulty is related to the continuum extrapolation. It is possible – though quite unlikely – that after observing a consistent and finite continuum limit for the chiral susceptibility a completely different (phase transition-like, therefore divergent) continuum limit appears at even smaller lattice spacings. Note, that the transition turned out to be weaker and weaker as one decreased the lattice spacings. Thus, the above scenario – real phase transition in the continuum limit – would mean a completely opposite lattice spacing dependence as it was observed. This is the main reason, why one considers this possibility quite unlikely. In order to go to even smaller lattice spacings (e.g. $N_\tau = 12$ or 14) approximately 1–2 orders of magnitude more CPU capacity is needed.

(b) Due to the continuous nature of the transition at vanishing chemical potential, there is no unique transition temperature. Different observables lead to different values. According to [187] the width of the transition may be as large as ≈ 40 MeV. Depending on the definition, the transition tem-

peratures can range between ≈ 150 and 170 MeV. The actual values are still debated, since in addition to the mere definition issue, it also turned out that different groups obtained different results for the same quantity. Example for the peak in the χ/T^2 distribution (χ is the unrenormalized chiral susceptibility) [186] used two different lattice spacings, namely $N_\tau = 4$ and 6 , and obtained 192 MeV. Recent improvements in calculations with smaller lattice spacing and smaller quark masses indicate a decrease of this value to below 170 MeV [190]. For the peak in the χ_r/T^4 distribution (χ_r is the renormalized chiral susceptibility) [187] used also finer lattices with four different lattice spacings, namely $N_\tau = 4, 6, 8$ and 10 , and obtained 151 MeV (note, that for χ/T^2 the obtained value is about 10 MeV higher). Since the present CPU-capacities are enough to carry out independent lattice simulations on $N_\tau = 8$ and even on $N_\tau = 12$ lattices, the reported differences are expected to be resolved in the near future. The two (unlikely) uncertainties, mentioned in the previous paragraph, are relevant also for the transition temperature: (1) Different fermion formulations (staggered, Wilson, overlap) might yield different temperatures; (2) The observed continuum limit might be void and the real continuum limit might only appear for much finer lattices. Therefore, one should determine the $\mu = 0$ transition temperature using other formulations of lattice QCD (e.g. Wilson fermions or chiral fermions), and double check the results with even smaller lattice spacings.

(c) The curvature of the phase diagram at vanishing chemical potential is known at $a \approx 0.3$ fm lattice spacing. Results were obtained by standard and p4 improved lattice actions for 2, 2+1 and 4 flavors [156, 158, 159, 192]. Though different choices of the QCD action should not necessarily give the same result at this rather large lattice spacing, results are in good agreement. If one takes the same action, different techniques (multi-parameter reweighting with full determinant, Taylor expansion, analytic continuation) give the same result up to several digits. This nice agreement shows that the available methods are consistent. Clearly, the major drawback of these findings is the lack of the continuum extrapolation. Similarly to the determination of the crossover temperature the continuum extrapolation might change the $a \approx 0.3$ fm results quite significantly. The available computer resources allow the determination of the curvature in the continuum limit in a year or two. It is important to emphasize again, that the staggered formalism has an unclarified uncertainty, therefore the whole calculation should be repeated in the Wilson formalism, too. Such a Wilson analysis is about an order of magnitude more CPU-demanding than the staggered one.

(d) There are several results for the existence and/or location of the critical point on the temperature versus chemical potential plane. All these results were obtained at quite large lattice spacings $a \approx 0.3$ fm. We discussed in detail the difficulties and the problematic features of the available methods. Let us point out a more general difficulty, which is related to the continuum extrapolation. As one determines the nature of the transition at vanishing chemical potentials, it turns out that the transition gets weaker and weaker for smaller

and smaller lattice spacings. This feature suggests, that the critical point, if it exists, might be at larger chemical potential in the continuum limit than on $N_\tau = 4$ lattices. Unfortunately, for large chemical potentials the available methods are less reliable, which is particularly true for the staggered formalism (see [174] for a discussion on the staggered eigenvalue quartets, which suggests to use quite small lattice spacings). Searching for features at relatively large chemical potentials and at small lattice spacings is a very difficult and particularly CPU-demanding task. It is unlikely that the available methods with the present computer resources can give a continuum extrapolated staggered result in a few years. The available methods are all applicable for Wilson fermions, too. On the one hand, Wilson fermions do not have problems related to the rooting of the determinant (c.f. [174]). On the other hand, the full diagonalization of the Wilson matrix is about two orders of magnitude more CPU-consuming. Furthermore, we do not have much experience how Wilson thermodynamics approaches the continuum limit, therefore it is hard to say what temporal extensions are needed to approach the continuum limit. The overlap formalism has all the symmetries of the theory even at non-vanishing lattice spacings, which is an advantage when we look for critical behavior. Though the available methods are applicable also for overlap fermions, the CPU-costs would be very large. To summarize: the presently available resources do not allow to extrapolate into the continuum limit. Results on the critical point at one or two non-vanishing lattice spacings cannot be considered as full results (as has been emphasized e.g. in [192]).

(e) There is one exploratory lattice result on the triple point of QCD [160]. The lattice spacing is quite large, the volumes are small and four flavor is applied to avoid the rooting problem. This density of states method reached approximately three times larger chemical potentials than other methods in the literature. The CPU-costs (for this factor of three) were about two orders of magnitude larger than for the other methods. The method works, but it is clear that due to limited resources the continuum limit statement on the triple point cannot be given in the near future.

(f) Concerning the determination of the equation of state and of the susceptibilities the same remarks apply as for the nature of the phase transition, the critical temperature and the curvature of the phase diagram (cf. a–c): Clearly it would be desirable to have in the end all calculations for different fermion actions (staggered, Wilson, overlap) and for realistic quark masses and extrapolations to the continuum limit. Concerning the quark masses the calculations shown in Fig. 3.12 have been performed with almost physical masses (pion mass ≈ 210 MeV). The results shown there for $N_\tau = 6$ for different improved actions (they differ in their discretization errors) suggest that one is already close to the continuum limit. Physical quark masses and $N_\tau = 4, 6$ have been used in [110]. Clearly further studies have to be performed for different numbers of N_τ to check the appropriate scaling behavior. Concerning the extension to finite chemical potential (using the Taylor expansion method) calculations so far deal with rather coarse lattices and only

moderately light quark masses. However, as shown in Fig. 3.14 (right hand side) e.g. the ratio of pressure and energy density seems to be fairly independent of these approximations (cf. the discussion before Eq. (3.33)).

In the previous and the present section we have presented results obtained from first principle calculations, namely perturbative QCD and lattice QCD, respectively. In the following we proceed to lower temperatures and larger chemical potentials (corresponding to densities around nuclear matter saturation density and few times larger). In this region the first principle methods so far cease to work. Hence we have to rely on models which will be outlined in the next section.

3.3 The nuclear equation of state from many-body theory

In the present section theoretical studies of the nuclear equation of state in hadronic models (“hadronic many-body theory”) are reviewed.

3.3.1 Models for the nuclear equation of state

Our understanding of nuclear forces, of the structure of nuclei as well as of neutron stars and supernova explosions depends on knowledge of the nuclear equation of state (EoS) at normal and supra-normal densities as well as at extreme isospin. Nucleus–nucleus reactions provide the only possibility to explore nuclear matter densities beyond saturation density, $\rho_0 \simeq 0.16 \text{ fm}^{-3}$, in the laboratory. Consequently, the determination of the EoS has been one of the primary goals of experiments with relativistic heavy-ion beams ever since the pioneering work at the Bevalac [201]. Transport calculations indicate that in the low and intermediate energy range $E_{\text{lab}} \sim 0.1 \div 1 \text{ AGeV}$ nuclear densities between $2 \div 3\rho_0$ are accessible, while the highest baryon densities ($\sim 8\rho_0$) will probably be reached in the energy range of the future GSI facility FAIR, between $20 \div 30 \text{ AGeV}$. At higher incident energies matter becomes less baryon rich due to the dominance of meson production and, eventually, due to the onset of transparency.

Complementary information on the isospin dependence of nuclear forces and of the nuclear equation of state, which presently is not well known, is expected from the forthcoming rare isotope beam facilities at FAIR/GSI [202], SPIRAL2/GANIL and FRIB [203]. In the following we briefly discuss the present understanding of the nuclear EoS at moderate densities ($\rho \lesssim 3\rho_0$) from a theoretical point of view.

Calculations of the nuclear EoS can roughly be divided into three classes:

1. *Phenomenological approaches*: These are models based on effective density dependent interactions such as Gogny [204, 205] and Skyrme forces [206, 207] or on relativistic mean field (RMF) models [208, 209]. The number of parameters which are fine-tuned to obtain an overall fit of nuclear masses is usually in the range between 6 and 15. This type of models allows the most precise description of the properties of finite nuclei.
2. *Effective field theory approaches*: The concepts of effective field theory (EFT) have recently been applied to calculations of the nuclear EoS. These approaches involve a systematic expansion, where the small scales are the mass of the pion and the Fermi momentum. They can be based, e.g., on density functional theory [210, 211] or on chiral perturbation theory [212–217]. A major advantage of EFT approaches is the relatively small number of free parameters and a correspondingly higher predictive power. However, high precision fits to the properties of finite nuclei require the introduction and fine-tuning of additional parameters. The resulting EFT functionals then have approximately the same number of parameters as the phenomenological models.
3. *Ab initio approaches*: Based on high-precision free-space nucleon–nucleon interactions and three-nucleon forces, fitted to nucleon–nucleon scattering and the properties of three- and four-nucleon systems, the nuclear many-body problem is treated microscopically. Predictions for the nuclear EoS are essentially parameter free. Examples of such approaches are the variational calculations [218, 219], Brueckner-Hartree-Fock (BHF) [220–223] and relativistic Dirac-Brueckner-Hartree-Fock (DBHF) [224–231] calculations as well as Greens function Monte-Carlo techniques [232–234]. Recently, a novel ab initio approach to the nuclear many-body problem, based on effective low-momentum nuclear interactions [235] has been developed. The ultimate goal of this scheme is to perform systematic calculations of nuclear structure and of nuclear and neutron matter at moderate densities based on realistic two- and three-nucleon interactions [236].

Phenomenological models and effective field theories contain parameters which have to be fixed by nuclear properties around or below the saturation density. Clearly this makes a reliable extrapolation to supra-normal densities difficult. Within the EFT scheme, a controlled extrapolation to moderate densities is possible.

Microscopic many-body calculations involving a summation of relevant classes of diagrams are, at least presently, too complex for a systematic application to finite nuclei. Here the use of effective low-momentum interactions offers a promising alternative. However, systematic calculations of the properties of nuclear matter at densities beyond say three times the saturation density are not possible using presently available nuclear interactions.

3.3.1.1 Phenomenological models

To examine the structure of relativistic mean field models it is instructive to consider the simplest version of a relativistic model, i.e. the σ - ω model of Quantum Hadron Dynamics (QHD-I) [237–239]. In QHD-I the nucleon-nucleon interaction is mediated by the exchange of two effective boson fields which are attributed to a scalar (σ) and a vector (ω) meson. In the mean field approximation, the energy density in uniform, cold and isospin saturated nuclear matter reads

$$\epsilon = \frac{3}{4}E_F\varrho + \frac{1}{4}m_D^*\varrho_S + \frac{1}{2}\{\Gamma_V\varrho^2 + \Gamma_S\varrho_S^2\} \quad , \quad (3.43)$$

where the Fermi energy is given by $E_F = \sqrt{k_F^2 + m_D^{*2}}$ and the Dirac mass by $m_D^* = M - \Gamma_S\varrho_S$. In the limit $m_D^* \rightarrow M$ the first two terms in (3.43) reduce to the energy of a non-interacting relativistic Fermi gas (kinetic energy plus rest mass).

In relativistic treatments one has to distinguish between the vector density $\varrho = 2k_F^3/3\pi^2$ and the scalar density ϱ_S . The vector density is the time component of a 4-vector current j_μ , whose spatial components vanish in the nuclear matter rest frame, while ϱ_S is a Lorentz scalar. With increasing vector density, the scalar density grows and eventually saturates; an essential feature of the relativistic saturation mechanism. In QHD-I the scalar and vector field strengths are given by the coupling constants for the corresponding mesons divided by the meson masses, $\Gamma_S = g_\sigma^2/m_\sigma^2$ and $\Gamma_V = g_\omega^2/m_\omega^2$. The two parameters $\Gamma_{S,V}$ are fitted to the saturation point of nuclear matter $E/A \simeq -16$ MeV, $\varrho_0 \simeq 0.16$ fm $^{-3}$. The saturation mechanism requires that both coupling constants are large. This implies a strong cancellation between the attractive scalar field $\Sigma_S = -\Gamma_S\varrho_S$ and the repulsive vector field $\Sigma_V = \Gamma_V\varrho$. This feature of relativistic dynamics is illustrated by the single-particle potential $U = \Sigma_S(m_D^*/E^*) - \Sigma_V$, where $E^* = \sqrt{\mathbf{k}^2 + m_D^{*2}}$, which is only on the order of -50 MeV, while Σ_S and Σ_V are both on the order of several hundred MeV in magnitude.

However, with only two parameters QHD-I provides a relatively poor description of the saturation point with a too large saturation density. In order to improve upon this, higher order corrections in density have to be taken into account. This can be done in several ways. In the spirit of the Walecka model non-linear meson self-interaction terms have been introduced in the QHD Lagrangian [208, 209, 240]. Several alternative extensions of QHD-I have been discussed in the literature [210, 211, 241–246]. These models provide high quality fits to the known areas of the nuclear chart: binding energies and rms-radii are reproduced with an average relative error of about $\sim 1 - 5\%$. However, extrapolations to the unknown regions of extreme isospin or to densities beyond ρ_0 , lead to substantial differences between the models. This demonstrates the limited predictive power of these functionals.

3.3.1.2 Effective field theory

The application of effective field theory concepts to nuclear physics problems relies on a separation of scales. EFT is based on a perturbative expansion of the nucleon–nucleon (NN) interaction and the nuclear mean field within a power counting scheme. The strong short-range repulsion of some NN interactions requires a non-perturbative treatment, e.g., by means of the Brueckner ladder summation. The philosophy behind EFT is to separate the short-range correlations from the long and intermediate range parts of the NN -interaction. This assumption is motivated by the fact that the scale of the short-range correlations, i.e. the hard core, is set by the ρ and ω vector meson masses, which lie well above both the Fermi momentum and the pion mass, which in turn set the scale of the long range forces.

The density functional theory (DFT) formulation of the relativistic nuclear many-body problem [210, 211] is analogous to the Kohn–Sham DFT of condensed matter systems. An energy functional of scalar and vector densities is constructed which by minimization yields variational equations that determine the ground-state densities. The aim is to approximate the *exact* functional using an expansion in classical meson fields and their derivatives, based on the observation that these quantities are small compared to the nucleon mass, at least up to moderate densities. The DFT interpretation implies that the model parameters fitted to nuclei implicitly contain the effects of exchange correlations and all other many-body and relativistic effects, which in principle are included in the exact functional.

Recently also concepts of chiral perturbation theory (ChPT) have been applied to the nuclear many-body problem [212–217]. In this scheme, the long and intermediate-range interactions are treated explicitly within chiral pion-nucleon dynamics. This allows an expansion of the energy-density functional in powers of m_π/M and k_F/M , while the dependence on the ratio m_π/k_F should not be expanded. Like in DFT, short-range correlation are not explicitly resolved but handled by counter terms (dimensional regularization) [212] or through a cutoff regularization [216].

3.3.1.3 Ab initio calculations

The goal of ab initio approaches to the nuclear many-body problem is a systematic scheme for computing the properties of many-nucleon systems based on high-precision nuclear interactions. Such interactions provide a high-quality representation of nucleon–nucleon scattering and few-nucleon systems. A vast amount of work has been invested in the so called Brueckner-Hartree-Fock (BHF) approach to the nuclear many-body problem [248], which involves partial summations of ladder diagrams. The summation of ladder diagrams was introduced in order to deal with the strong short-range repulsion present in most high-precision nucleon–nucleon interactions. In the

late 1980s, an approximate relativistic formulation of Brueckner's approach, the Dirac-Brueckner-Hartree-Fock approach (DBHF), was proposed.

Studies for a large number of NN interactions indicate the need for a three-nucleon interaction. The saturation points obtained with different high-precision interactions are located on the so-called Coester line in the E/A - k_F plane, as shown in Fig. 3.24. Modern one-boson-exchange (OBE) potentials [249] lead to strong over-binding and a too large saturation density in non-relativistic calculations whereas relativistic calculations do a somewhat better job [225, 227]. However, in particular for the relativistic formulation, it remains unclear how to systematically improve the lowest-order two-body cluster approximation.

The saturation mechanism is quite different in relativistic and non-relativistic approaches. The magnitude of the scalar and vector DBHF self-energies is similar to that in mean-field theory, where the single-particle potential is the result of a cancellation between the large scalar and vector fields, each several hundred MeV in magnitude. In the BHF approach, on the other hand, the saturation mechanism is exclusively due to contributions of the same magnitude as the binding energy, i.e. a few tens of MeV. The tensor force, in particular the second-order one-pion-exchange contribution is large and attractive and its interplay with Pauli-blocking leads to saturation. Relativistically the tensor force is quenched and less important for the saturation mechanism [250, 251].

The role of three-body forces has been extensively studied within non-relativistic BHF [222] and variational calculations [219]. These investigations

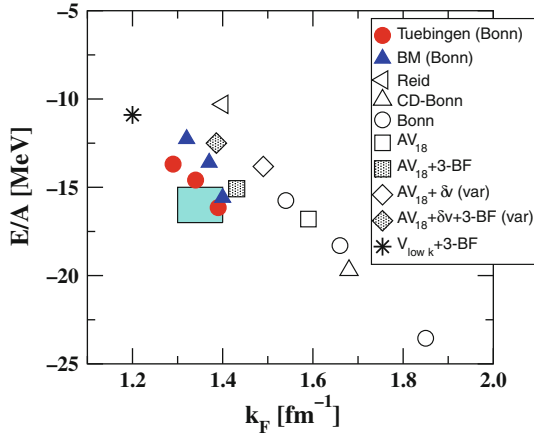


Fig. 3.24 Nuclear matter saturation points from relativistic (*full symbols*) and non-relativistic (*open symbols*) Brueckner-Hartree-Fock calculations based on different nucleon-nucleon forces. The *diamonds* show results from variational calculations. *Shaded symbols* denote calculations which include 3-body forces (3-BF). The *shaded area* is the empirical region of saturation [247].

clearly underline the importance of three-body forces for a quantitative understanding of nuclear saturation. However, the lack of a systematic framework for treating both the two- and three-nucleon forces has stymied progress on this problem. The next generation of nuclear forces, based on chiral perturbation theory [252–254], offer a perspective for a systematic treatment of two- and three-body forces.

An alternative systematic approach to nuclei and nuclear matter is based on renormalization group (RG) methods [255]. In the so-called $V_{\text{low } k}$ approach, a low-momentum effective interaction is derived from a given realistic NN potential by integrating out the model-dependent high-momentum modes using RG methods. At a cutoff $\Lambda \sim 2 \text{ fm}^{-1}$ various high-precision NN -potential models collapse to an essentially model-independent effective interaction $V_{\text{low } k}$. When applied to the nuclear many-body problem the convergence properties of the many-body perturbation theory is dramatically improved; the effective low-momentum interactions do not require a full Brueckner resummation of ladder diagrams, but may be treated perturbatively, as indicated by the exploratory calculation of [236]. The resulting equation of state is only weakly dependent on the unphysical cutoff parameter. Furthermore, by including an appropriate three-body force, fitted to reproduce the properties of three- and four-nucleon systems for a given cutoff Λ , the saturation properties of isospin symmetric nuclear matter are described on a qualitative level. The results, including three-body forces [236], are shown in Fig. 3.24.

3.3.2 Equation of state in symmetric and asymmetric nuclear matter

In Fig. 3.25 the results for nuclear and neutron matter obtained in microscopic many-body calculations – DBHF [230, 231] and variational calculation with three-body forces and boost corrections [219] – are shown together with the equation of state obtained in phenomenological approaches [245, 256] and in EFT [217]. As expected the phenomenological functionals yield more or less identical results at and below saturation density, where they are constrained by finite nuclei, but differ substantially at densities above ρ_0 . In neutron matter the situation is even worse, since the isospin dependence of the phenomenological functionals is less constrained. Ab initio calculations predict a soft EoS in the density range relevant for heavy-ion reactions at intermediate and low energies, i.e. up to about three times ρ_0 . Moreover, the microscopic calculations (BHF/DBHF, variational) agree well with each other and are consistent with Quantum-Monte-Carlo calculations [234].

In isospin asymmetric matter the binding energy is a functional of the proton and neutron densities, characterized by the asymmetry parameter $\beta = Y_n - Y_p$ which is the difference of the neutron and proton fraction

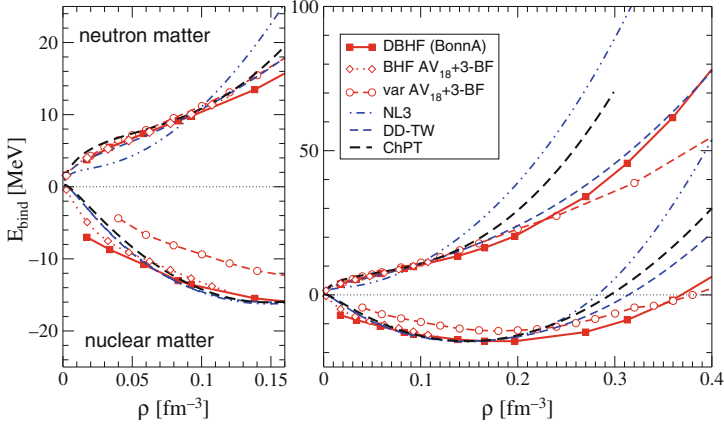


Fig. 3.25 The EoS of nuclear matter and neutron matter. BHF/DBHF and variational calculations are compared to the phenomenological density functionals NL3, DD-TW and ChPT+corr. The *left panel* shows the low-density range.

$Y_i = \rho_i/\rho$, $i = n, p$. The isospin dependence of the energy functional can be expanded in terms of β which leads to a quadratic dependence on the asymmetry parameter

$$\begin{aligned}
 E(\rho, \beta) &= E(\rho) + E_{\text{sym}}(\rho)\beta^2 + \mathcal{O}(\beta^4) + \dots, \\
 E_{\text{sym}}(\rho) &= \frac{1}{2} \frac{\partial^2 E(\rho, \beta)}{\partial \beta^2} \Big|_{\beta=0} = a_4 + \dots,
 \end{aligned}
 \tag{3.44}$$

where the ellipsis stands for terms parametrising the density dependence of the symmetry energy. In Fig. 3.26 the symmetry energy computed in DBHF [230, 231] and variational calculations are compared with those of the empirical density functionals shown in Fig. 3.25. Furthermore, the relativistic DD- $\rho\delta$ RMF functional [257] is included. Two Skyrme functionals, SkM* and the more recent Skyrme-Lyon force, SkLya, represent the non-relativistic models.

The low-density part of the symmetry energy is relatively well constrained by data. Recent NSCL-MSU heavy-ion data in combination with transport calculations are consistent with a value of $E_{\text{sym}} \approx 31$ MeV at ρ_0 and rule out extremely “stiff” and extremely “soft” density dependences of the symmetry energy [261]. The same value of the symmetry energy has been extracted [258, 259] from low-energy elastic and (p,n) charge exchange reactions on isobaric analog states, i.e. $p(^6\text{He}, ^6\text{Li}^*)n$ measured at the HMI. The data points at sub-normal densities were recently extracted from the isoscaling behavior of fragment formation in low-energy heavy-ion reactions, experimentally studied at Texas A&M and NSCL-MSU [260].

The theoretical extrapolations to supra-normal densities diverge dramatically, however. Since the structure and the stability of neutron stars are strongly influenced by the high-density behavior of E_{sym} , it is crucial to

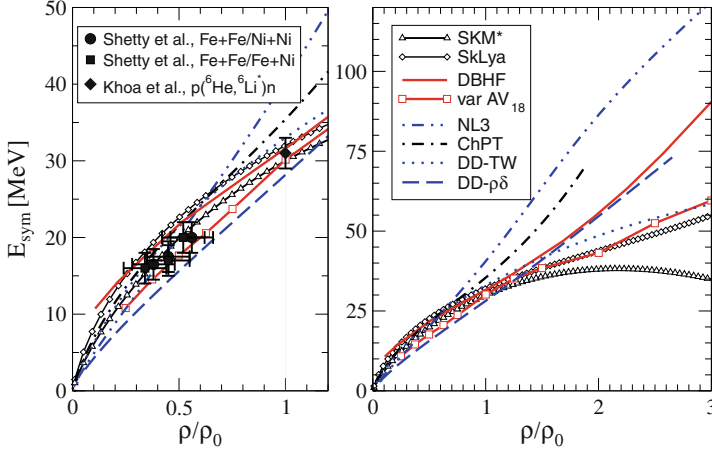


Fig. 3.26 The symmetry energy as a function of density for different models. The *left panel* shows the low-density region while the *right panel* displays the high-density range. Data are from [258–260].

constrain the symmetry energy at supra-normal densities with data from heavy-ion reactions.

3.3.2.1 Optical potentials

An important quantity related to the momentum dependence of the mean field is the optical nucleon–nucleus potential. At sub-normal densities the optical potential U_{opt} is constrained by proton-nucleus scattering data [262, 263] and at supra-normal densities by data from heavy-ion reactions [264–266]. In a relativistic framework the real part of the Schroedinger-equivalent optical nucleon potential is defined as

$$U_{\text{opt}} = -\Sigma_S + \frac{E}{M} \Sigma_V + \frac{\Sigma_S^2 - \Sigma_V^2}{2M} . \quad (3.45)$$

In a relativistic framework, momentum independent fields $\Sigma_{S,V}$ (as, e.g., in RMF theory) yield a linear energy dependence of U_{opt} . As seen from Fig. 3.27, DBHF calculations reproduce the empirical optical potential [262, 263] extracted from proton–nucleus scattering for nuclear matter at ρ_0 reasonably well up to a laboratory energy of about 0.6–0.8 GeV. However, they fail to describe the saturation at large momenta because of missing inelasticities, i.e. the excitation of isobar resonances above the pion threshold. When such continuum excitations are included, the optical model calculations are indeed able to describe nucleon–nucleus scattering data also at higher en-

ergies [267]. In the description of heavy-ion reactions at incident energies above 1 AGeV, the saturation at high momenta is required in order to reproduce transverse-flow observables [266]. In practical calculations, one has so far employed phenomenological approaches, where the strength of the vector potential is suppressed, e.g., by the introduction of form factors [266] or by energy dependent terms in the QHD Lagrangian [268] (D³C model in Fig. 3.27).

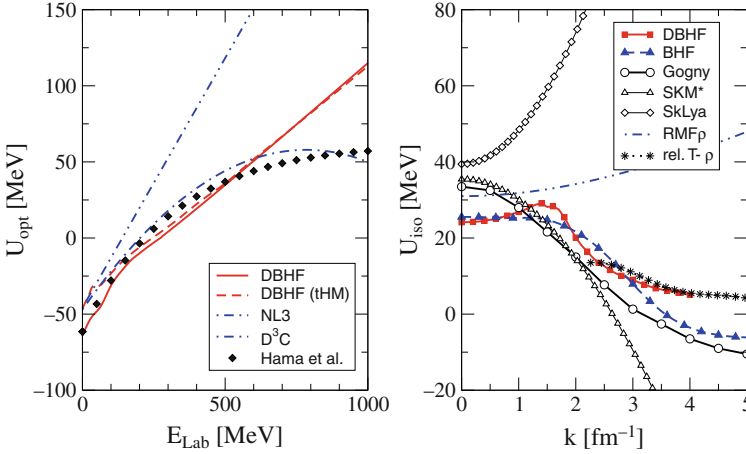


Fig. 3.27 Nucleon optical potential in nuclear matter at ρ_0 . On the *left side* DBHF calculations for symmetric nuclear matter from [224] and [227] are compared to the phenomenological models NL3 and D³C [268] and to the p-A scattering analysis of [262, 263]. The *right panel* compares the isovector optical potential from DBHF [230, 231] and BHF [269] to phenomenological RMF [270], Gogny and Skyrme (SkM* and SkLya) forces and to a relativistic T - ρ approximation [271].

The isospin dependence, expressed by the isovector optical potential $U_{\text{iso}} = (U_{\text{opt,n}} - U_{\text{opt,p}})/(2\beta)$ is much less constrained by data. The knowledge of this quantity, however, is of crucial importance for the forthcoming rare-isotope beam experiments. In the right panel of Fig. 3.27, the results of DBHF [230, 231] and BHF [269] calculations are compared with those obtained with phenomenological Gogny and Skyrme (SkM* and SkLya) forces and with the T - ρ approximation [271] based on relativistic empirical NN scattering amplitudes [272]. At large momenta DBHF agrees with the tree-level results of [271]. The energy and density dependences obtained in the various models differ substantially, in particular between the microscopic and the phenomenological approaches. The energy dependence of U_{iso} is not well constrained by data. The old optical potential analysis of scattering on charge asymmetric targets by Lane [273] is consistent with a decreasing potential as predicted by DBHF/BHF, while more recent analyses based on Dirac phenomenology [274, 275] come to the opposite conclusions. RMF models show a

linearly increasing energy dependence of U_{iso} (i.e. quadratic in k) like SkLya, however generally with a smaller slope (see discussion in [257]). To clarify this question certainly more experimental investigations are necessary.

At higher energies the knowledge on the real part of the optical potential, or equivalently the nuclear mean field, is scarce. The effective field theory schemes are limited to energies below the pion threshold ($E_{\text{lab}} \sim 300$ MeV) which also is the range where high-precision NN potentials are fitted to scattering data. Reliable many-body calculations which include effects of inelastic channels, have so far not been performed. Thus, one has to deduce the high-momentum behavior of the mean field by empirical methods. This information can be obtained, e.g., by analyzing transverse-flow observables in heavy-ion collisions (see Sect. 3.4.3, Sect. 6.4 in Part III and Chap. 6 in Part IV).

3.3.3 Connection to QCD

A connection of the empirical scalar-vector mean fields to QCD can be established by using QCD sum rules [276–278]. To leading order, the operator product expansion of the quark correlation function can be expressed in terms of scalar $\langle \bar{q}q \rangle$ and vector $\langle q^\dagger q \rangle$ condensates. The sub-leading terms, which are often neglected due to their highly non-trivial structure, involve four-quark operators and combinations of quark and gluon fields. The density dependence of higher-order contributions in the operator product expansion has been explored, e.g., in [279, 280].

The chiral condensates are modified in matter, which, to leading order in the density, gives rise to a scalar self-energy Σ_S and a vector field Σ_V . Thus, QCD sum rules predict mean fields in matter which agree both in sign and magnitude with those obtained in hadronic many-body calculations as well as in RMF fits to nuclear masses. Moreover, in [281, 282] it has been found that the structure of the nucleon–nucleon interaction enforces the existence of large scalar and vector fields as a model independent fact. This holds not only for manifestly covariant interactions, such as relativistic one-boson-exchange models (Bonn, CD-Bonn, Nijmegen), but is also obtained for non-relativistic interactions (Argonne v_{18} , Reid93, Idaho $N^3\text{LO}$, $V_{\text{low } k}$) once the symmetries of the Lorentz group are restored. From the analysis of the chiral EFT nucleon–nucleon force [253, 254, 283] it has been found that these fields are generated mainly by contact terms which occur at next-to-leading order in the chiral expansion and which are intimately connected with the short-range spin-orbit interaction [281, 282].

The connection of hadronic many-body effects to basic QCD quantities such as the chiral condensate is provided by the Hellmann-Feynman theorem, which relates $\langle \bar{q}q \rangle$ with the derivative of the QCD Hamiltonian with respect to the current quark masses. In nuclear matter the condensate is thus obtained

from the total energy density \mathcal{E} as

$$\langle \rho | \bar{q}q | \rho \rangle = \langle \bar{q}q \rangle + \frac{1}{2} \frac{d\mathcal{E}}{dm_q} \quad . \quad (3.46)$$

This relation implies a direct connection between many-body correlations, expressed in terms of hadronic degrees of freedom, and the in-medium quark condensate. The energy density \mathcal{E} can be computed within hadron effective field theories [276, 277, 284, 285], such as QHD and, more microscopically, within nuclear many-body theory. However, the unknown quark mass dependence of the corresponding model parameters, i.e. mesonic couplings and masses, introduces a large uncertainty in the resulting in-medium condensate [284, 285]. A more systematic and direct connection to QCD is provided by chiral effective field theory (EFT), where the explicit and implicit pion mass dependence – and thus the quark mass dependence – of the NN interaction has been evaluated up to next-to-leading order (NLO) [286, 287]. Hence, the Chiral EFT approach is free from ambiguities concerning the analytic and chiral structure of the potential and allows a reliable extraction of the scalar condensate at moderate densities [288, 289].

3.3.4 Summary of the present status

The status of theoretical models of the nuclear EoS can be summarized as follows: phenomenological density functionals such as Skyrme, Gogny and relativistic mean-field models provide high precision fits to nuclear masses throughout the nuclear chart. Yet extrapolations to supra-normal densities or the limits of stability are ambiguous. A more controlled approach is provided by recent developments in effective field theory. Chiral effective field theory allows a systematic generation of two- and many-body nuclear forces. However, these approaches correspond to a low-momentum expansion, and when applied to the nuclear many-body problem, to a low-density expansion. Ab initio calculations for the nuclear many-body problem such as variational or Brueckner calculations can serve as guidelines for the extrapolation to larger density and/or isospin asymmetry, while modern EFT approaches offer a perspective to achieve a consistent treatment of two- and three-nucleon forces.

Constraints on these models can be obtained from nuclear reactions, provided the reaction dynamics is accounted for by means of semi-classical transport models of the Boltzmann or molecular dynamics type (see Part III Collision Dynamics). Suitable observables, which are sensitive to the nuclear EoS, are directed and elliptic collective flow patterns and, at higher energies, particle multiplicities, in particular of kaons. Heavy-ion data suggest that the EoS of symmetric nuclear matter is relatively soft in the intermediate den-

sity regime, between one and about three times the nuclear saturation density (see, e.g., [247]), in qualitative agreement with the results of many-body calculations. Quantitative conclusions on the EoS based on heavy-ion data are, however, impeded by the interplay between the density and the momentum dependence of the nuclear mean field.

Data which constrain the isospin dependence of the mean field are still scarce. Promising observables are isospin diffusion, iso-scaling of intermediate mass fragments and particle ratios (π^+/π^- and possibly K^+/K^0). Here the situation will certainly improve, when the forthcoming rare-isotope beam facilities are in operation. This will also allow measurements of the isospin dependence of the optical potential in p+A and A+A reactions and the extraction of the symmetry energy and the proton/neutron effective masses in asymmetric matter.

On the theoretical side it will be important to invest a significant effort in the development of quantum transport models with a consistent treatment of states with a finite lifetime and three-body collisions (see also Part III Collision Dynamics).

Constraints on the equation of state can also be derived from studies of compact stars. This is reviewed in the following section.

3.4 Compact star constraints on the high-density equation of state

Compact stars are macroscopic objects ruled by the interplay of all fundamental forces in nature. Thereby the structure of the stars' interior is dominated by the strong force, which ultimately has to counter balance the gravitational attraction. Typical compact-star masses are about 1.4 solar masses, M_\odot , while the radii are in the range of 10–14 km. The central density can reach more than five times nuclear saturation density. Thus, the properties of such stars are largely determined by the equation of state (EoS) of highly compressed baryonic matter. The temperatures, which can reach a few keV in the interior, are small on nuclear scales. Therefore superfluid and/or superconductive states of matter are expected to appear inside such stars. In addition, ultrastrong magnetic fields exceeding 10^{13} Gauss and rotation periods in the millisecond regime are found. The enormous mass densities demand a general relativistic treatment. The requirement that neutron star matter be locally charge neutral and in β -equilibrium implies a high isospin asymmetry. All in all, compact stars offer the possibility to study strongly interacting matter under extreme conditions not available in the laboratory.

The existence of neutron stars as gigantic atomic nuclei was already anticipated by Landau [290] before the discovery of the neutron. Baade and Zwicky [291] regarded them as a possible result of supernova explosions. In the present picture of type II supernova explosions [292], proto-neutron stars (PNS) with radii exceeding 20 km are remnants of the collapse of massive progenitor stars ($8 < M/M_\odot < \sim 25$). In such explosions the initial collapse of the core is halted by a stiffening of the equation of state at densities beyond nuclear saturation, which generates an outward travelling shock wave. In this process temperatures of about 50 MeV can be reached. The proto-neutron star cools by first emitting copious amounts of neutrinos and in later stages by radiation of photons [293]. During this process it shrinks to its final size. The masses of neutron stars are limited by stability against gravitational collapse. Beyond a certain central density the pressure of high-density matter is not sufficient to withstand the gravitational attraction; the star collapses to a black hole. Although many details in the modelling of core-collapse supernovae are still under discussion, this dynamical process offers a further opportunity to constrain the equation of state of dense matter, provided observable signatures of a phase transition, e.g. a second neutrino burst, can be identified [294]. At present there are only two equations of state that cover the wide ranges in density, temperature and isospin asymmetry required in dynamical calculations of core collapse supernovae [295, 296]. A systematic study of the role of the equation of state in supernova explosions would be very useful. The cooling of the proto-neutron star is also strongly dependent on the properties of compressed matter as will be discussed in Sect. 3.4.2.

A comparison of model calculations with available astronomical observations offers an opportunity to study these aspects of the EoS.

The connection between properties of high-density matter and compact star phenomenology is extremely complex and multifaceted. Hence, a full discussion of this subject would by far exceed the scope of this section; for more details we refer the interested reader to excellent reviews on this topic [293, 297–306]. After a summary of the general conditions prevailing near the center of compact stars, we focus on constraints on the high-density EoS obtained from the properties of compact stars [302, 307]. Observations of compact stars, which can help to tighten the limits on the high-density EoS, will be discussed. Ultimately, such an analysis may be used to narrow down the set of acceptable equations of state.

The observation of “extreme” values of compact star properties, like masses above $2 M_{\odot}$ [308, 309],⁷ radii above 13 km [312, 313] or below 10 km [314], and rotation periods below about 1 ms [315] offer unique opportunities to gain profound insight into the properties of matter under the most extreme conditions. Modern astrophysical observations to be discussed in this section constrain the zero-temperature EoS at supersaturation densities, where data from laboratory experiments are scarce.

The structure of a compact star can be divided into three major regions – envelope, crust and core – as schematically illustrated in Fig. 3.28. The surface that encloses the star is covered by a thin atmosphere. This is of relevance for the energy transport and for the shape of the observed electromagnetic spectrum. The crust contains ionized nuclei, arranged in a lattice and embedded in a sea of electrons. At the surface of the star, nuclei with the largest binding energy per nucleon, ^{56}Fe and neighboring nuclei, are found. With increasing density, the proton number of the nuclei remains moderate, while the neutron number grows substantially, as the core-crust interface (at about $1/3$ of the nuclear saturation density, n_0) is approached. The increase of the neutron-to-proton ratio with increasing density is a consequence of β -equilibrium.

At a density of about $1.5 \cdot 10^{-3} n_0$, neutrons drip out of the nuclei and the boundary between outer and inner crust is crossed. At higher densities, approaching the interface to the core, individual nuclei are no longer stable. Here the exotic so-called nuclear “pasta” phases are expected. With increasing density, one finds a continuous change of the nuclear shapes.

Finally, the core of a compact star, with homogeneous distributions of nucleons, electrons and muons, is reached. The crust, with a thickness of 1–2 km, contributes only a few percent to the total mass of the star. Hence, the bulk properties of a compact star depend primarily on the characteristics of compressed matter at densities beyond nuclear saturation.

The transition from the outer to the inner core is specified by the appearance of a exotic phases, e.g. matter containing additional particle species such

⁷ Note that the high mass of $M = 2.1 \pm 0.2 M_{\odot}$ for PSR J0751+1807 [310] has recently been corrected to $M = 1.26 \pm 0.14 M_{\odot}$ by D. J. Nice et al. [311]

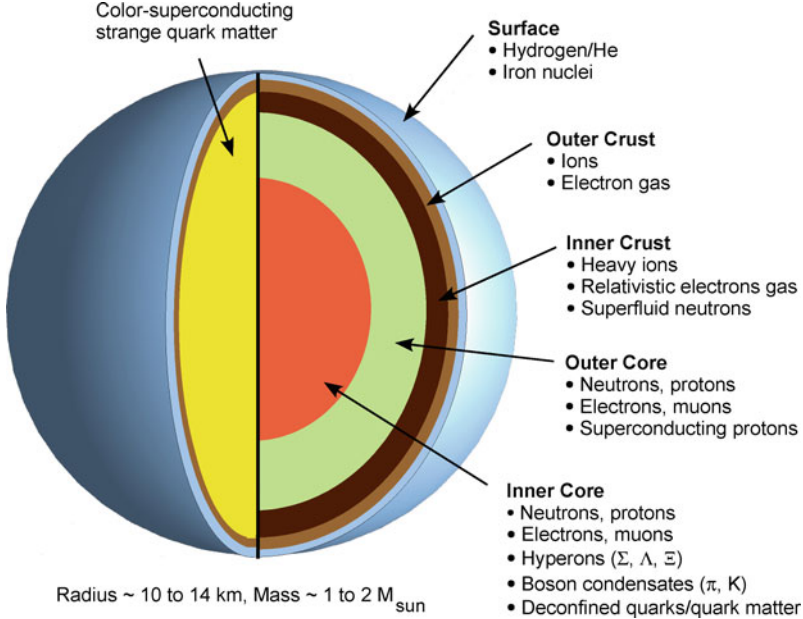


Fig. 3.28 Theoretically predicted compositions of compact stars. Novel phases of dense baryonic matter may exist in the inner cores of neutron stars (*right cross section*). If the core consists of more than one phase, e.g. an inner and an outer core with different thermodynamic phases, the compact star is called a hybrid star. There is also the theoretical possibility that compact stars consist almost entirely of absolutely stable strange quark matter, made of almost equal fractions of up, down and strange quarks (*left cross section*).

as hyperons, pion or kaon condensed matter or deconfined quark matter. The predominance of neutrons ($\gtrsim 90\%$) in the conventional picture of a compact star with a hadronic core motivated the term “neutron star”. More exotic scenarios, where a transition to quark matter takes place inside the core, or stars composed almost completely of strange quark matter, are termed “hybrid stars” and “strange stars”, respectively.

In general, the interior structure of compact stars is not well known. Astrophysical observations that are related to the total mass, the radius and possibly the moment of inertia (MoI), can only provide constraints on the high-density EoS but do not yield any information on the microscopic structure of dense matter. Hence, for the comparison of models with such data, a well chosen parametrisation of the EoS is in principle sufficient. In the present context, however, it is interesting to explore also microscopically motivated phenomenological models for the strong-interaction EoS. Here we can take advantage of a recent comparative study [307], where a broad class of rela-

tivistic nuclear matter models were confronted with the constraints deduced from observations of compact stars. All models are adjusted to reproduce structural properties of atomic nuclei and of isospin symmetric nuclear matter at saturation density $n_0 = 0.16 \text{ fm}^{-3}$ but differ in the extrapolation to isospin asymmetric matter at higher densities, appropriate for matter in the interior of compact stars. For the purposes of our discussion, only the stiffness of the equation of state at densities $n > n_0$ is relevant. Using established notation (see e.g. [307]), the equations of state used are in a sequence of increasing stiffness at high densities⁸: NL ρ , NL $\rho\delta$, KVR, DD-F, KVOR, DBHF and D³C. Some of these equations of state are discussed in Sect. 3.3.

In order to explore the interesting possibility of a phase transition to quark matter in the inner core, a set of hybrid model scenarios, based on the Nambu-Jona-Lasinio (NJL) model [317], are also studied. There a superconducting 2SC phase is considered for quark matter (cf. Sect. 3.5). The two coupling parameters of the extended NJL model, the diquark coupling η_D and the vector coupling η_V , control the density for the onset of the phase transition and the range of densities corresponding to the coexistence region. We note, however, that the hydrostatic properties of compact stars may be similar for a purely hadronic and a hybrid EoS, involving a phase transition from hadronic to quark matter. Consequently, it is possible that the corresponding mass-radius relations for compact star sequences are very similar and do not provide pertinent information on the nature of the inner core; hybrid stars “masquerade” as regular neutron stars [318].

Studies of the dynamical features of compact stars, like a statistical analysis of the cooling behavior (Sect. 3.4.2), will deliver complementary information. The cooling rates depend on the microscopic degrees of freedom as well as on the EoS. Thus, the cooling of compact stars may provide a tool to unravel the structure of their interior [319, 320]. At present there is no clear evidence for the existence of strange stars [321]. Such stars would, if they exist, form a new family of compact stars that is generally different from the equilibrium sequence that includes white dwarfs, neutron or hybrid stars [322, 323]. Due to their compactness, key observables to distinguish them from more conventional neutron stars would be, e.g., a radius below 10 km, a submillisecond rotation period and a small moment of inertia. In the discussion of the constraints derived from compact stars on the equation of state of dense matter at the onset of deconfinement, we will focus on nonstrange hybrid stars.

Gravitational-wave (GW) astronomy will open a new window for the observation of compact stars and the discussion of constraints on properties of strongly interacting matter. Remarkable progress has been made in compu-

⁸ The following notation is used: NL ρ , NL $\rho\delta$ for the non-linear σ - ω (Walecka) model with ρ and δ meson exchange; DD-F, D³C, KVR, KVOR for mean field models with density dependent nucleon-meson coupling including derivative coupling and refinements by Kolomeitsev et al. [316]; DBHF (Bonn A) for a Dirac-Bruckner-Hartree-Fock model with the Bonn A potential. For details see [307] and references therein.

tational general relativity, predicting GW signals from supernova collapse, binary mergers and rapidly spinning pulsars with ever more realistic inputs. Despite promising studies of the interrelation between GW signals and the high-density EoS, the resulting constraints for, e.g., possible quark matter phases in the Crab pulsar from LIGO observations are not yet conclusive [324]. We therefore refrain from discussing possible constraints on the EoS from GW physics here and refer to [302, 303] for further information.

3.4.1 Constraints from bulk properties

The mass, M , radius, R , and structure of a compact star are determined by the condition of hydrostatic equilibrium, treated in general relativity. The properties of spherical, nonrotating stars, are thus obtained by solving the Tolman-Oppenheimer-Volkoff (TOV) equation [325, 326]

$$\frac{dP(r)}{dr} = - \frac{G[\varepsilon(r) + P(r)][m(r)c^2 + 4\pi r^3 P(r)]}{c^4 r^2 \left[1 - \frac{2Gm(r)}{c^2 r}\right]}, \quad (3.47)$$

$$m(r) = \frac{4\pi}{c^2} \int_0^r dr' r'^2 \varepsilon(r'), \quad (3.48)$$

where $m(r)$ is the gravitational mass enclosed by a sphere of radius r , including the gravitational binding energy. Furthermore, G is the gravitational constant and c the speed of light. The baryon number inside a sphere of radius r is given by

$$N(r) = 4\pi \int_0^r \frac{dr' r'^2 n(r')}{\sqrt{1 - \frac{2Gm(r')}{c^2 r'}}}, \quad (3.49)$$

where $n(r)$ is the baryon density profile of the star. Given an equation of state, which provides the relation between pressure P and energy density ε , the solution of the TOV equation yields the pressure and energy-density profiles of a non-rotating star.

The surface of the star is defined by vanishing pressure. Thus the stellar radius R is obtained by the condition $P(R) = 0$. The total gravitational mass of the star is then given by $M = m(R)$ and its baryon number by $N = N(R)$. There are a few general constraints on the relation between mass and radius of a compact star. The Schwarzschild condition $R \geq 2GM/c^2$ follows from general relativity, while causality requires $R \geq 3GM/c^2$.

For a given EoS, the solution of the TOV equation yields a unique relation between the mass, M , and the central density, $n(r=0)$. In order to assess the limits on the bulk properties of neutron stars, the TOV equation has been

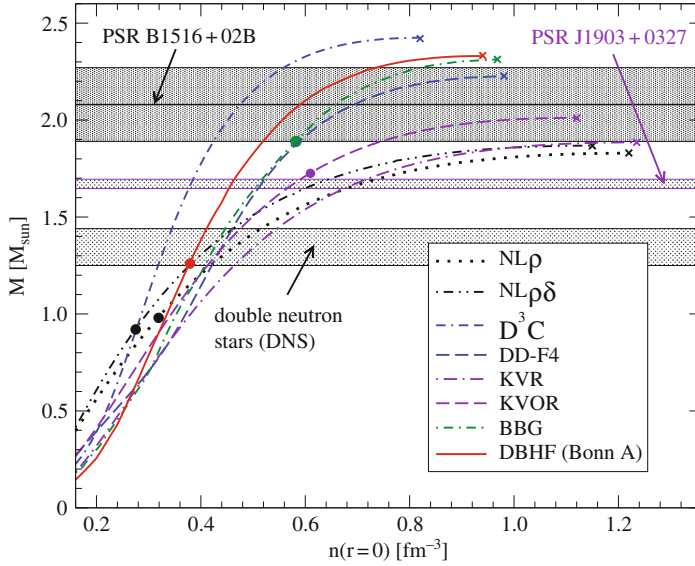


Fig. 3.29 Mass vs. central density for compact star configurations obtained by solving the TOV equations (3.47) and (3.48) for different EoS (for details see [307] and references within). *Crosses* denote the maximum mass configurations, *filled dots* mark the critical mass and central density values beyond which the direct neutrino cooling process (direct Urca, cf. Sect. 3.4.2) becomes possible.

solved for a broad range of causality constrained equations of state [302]. On the other hand, the increasing amount of direct and indirect observations of neutron star properties provide constraints on the EoS. We note that the equation of state for the interior of a star must be supplemented by a model for the crust, e.g. the BPS EoS [327]. Although uncertainties in the crust models remain, they lead to only small differences in the resulting bulk properties.

In Fig. 3.29 we show the mass versus central density relation for the set of hadronic EoS listed above. In this and in subsequent plots of this type, a point on a curve of a given EoS represents a stable star configuration. The maximum mass is primarily controlled by the stiffness of the EoS at several times the saturation density of nuclear matter. With increasing stiffness the maximum mass and the overall size of the compact star grows, while the central densities decreases. Beyond a certain central density, the star is unstable with respect to collapse into a black hole. Thus for each EoS, there is a maximum mass of a stable neutron star. If non-nucleonic degrees of freedom appear at high densities, a softening of the EoS and a corresponding reduction of the maximum mass are generally expected.

3.4.1.1 Masses of compact stars

The mass of a compact star in a binary stellar system can in principle be determined from astronomical observations. The most accurate values are obtained from observations of Doppler shifts and of relativistic effects in binary radio pulsars ($M_{BRP} = 1.35 \pm 0.04 M_{\odot}$ [328]). Less precise data are available from binary systems consisting of an accreting neutron star emitting X-rays and a companion being, e.g., a white dwarf or a main sequence star. In Fig. 3.30 a synopsis of measured neutron star masses is presented. Most mass determinations, in particular those with small errors, fall into a fairly narrow range around $1.3M_{\odot}$. Nevertheless, in spite of the large error bars, the very high and very low masses preclude definite conclusions at this point.

Recent timing measurements for PSR B1516+02B, located in the globular cluster M5, imply that the pulsar mass is $2.08 \pm 0.19 M_{\odot}$ with 1σ error; its mass is above $1.72 M_{\odot}$ with 95% probability and above $1.82 M_{\odot}$ with 90% probability [309]. Thus, if confirmed, this mass is clearly above the typical masses M_{BRP} of binary radio pulsars found in most earlier observations [328]. A lower limit on the maximum mass of a neutron star in this range is also supported by the recent precise mass measurement [330] of the eccentric binary millisecond pulsar PSR J1903+0327 [331], $M = 1.67 \pm 0.01 M_{\odot}$.

As shown in Fig. 3.29, none of the maximum masses predicted by the model calculations fall below the 2σ mass limit of $1.70 M_{\odot}$ for PSR B1516+02B, and even at the 1σ mass limit of $1.89 M_{\odot}$ the softest EoS (NL ρ and NL $\rho\delta$) cannot be definitely excluded. We point out that the observation of a pulsar with a mass exceeding 1.8 – $1.9 M_{\odot}$ at the 2σ level would significantly constrain the viable EoS (see Fig. 3.29). Within the set tested here, only the stiffest ones (D³C, DD-F4, BBG and DBHF) would then survive.

3.4.1.2 Gravitational mass – baryon mass relation

The total baryon number $N(R)$, Eq. (3.49), can be converted to the baryon mass M_N of the compact star by multiplying with the nucleon mass. The difference of the gravitational mass $M_G = M$ and M_N is a measure of the binding energy of the star.

Recently, it was speculated that pulsar B in the double pulsar system J0737–3039 may serve as a test of the gravitational mass – baryon mass relation [332]. One of the interesting characteristics of this system, is that the mass of pulsar B is only $1.249 \pm 0.001 M_{\odot}$ [333]. This fairly low value of the mass may be an indication that pulsar B was formed in an electron-capture supernova, rather than in a regular type-II supernova, triggered by a collapsing iron core. In a supernova of the former type, the O-Ne-Mg core of an 8 – $10 M_{\odot}$ star or a white dwarf of the same composition [332], develops a hydrostatic instability due to electron capture onto Mg and Ne. The critical density, at which the collapse of such stars sets in, is well established,

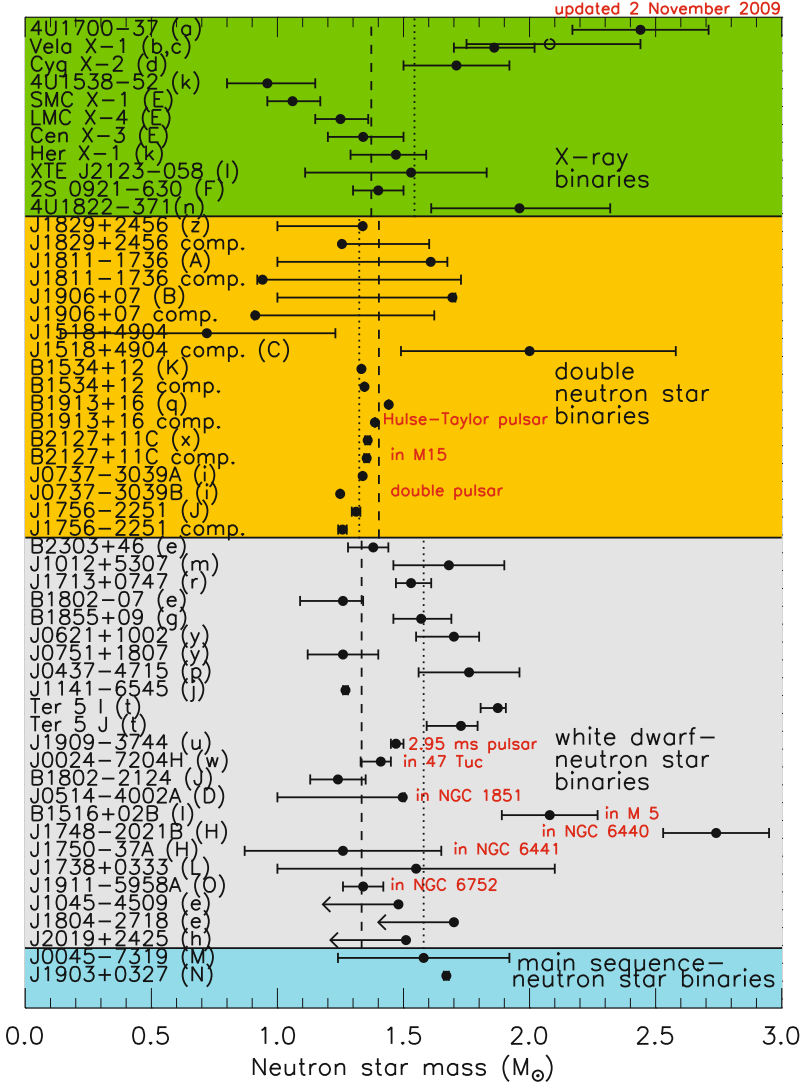


Fig. 3.30 Measured neutron star masses from [329].

$4.5 \times 10^9 \text{ g/cm}^3$. Calculations indicate that the mass loss of the core during the supernova explosion is small [334]; the resulting baryon mass of the neutron star is in the range $M_N = 1.36\text{--}1.375 M_\odot$ [332, 334]. Together with the star's observed gravitational mass of $M = 1.249 \pm 0.001 M_\odot$, the inferred baryon number sets a constraint on the EoS [332], provided the assumption on the formation mechanism of pulsar B is correct. Various caveats to this argument, such as baryon loss and variations of the critical mass due to carbon flashes during the collapse, are discussed in [332]. In Fig. 3.31, the effect of 1 and 2% mass loss on this constraint is illustrated. The baryon mass obtained in [334], $M_N = 1.360 \pm 0.002 M_\odot$, is also shown.

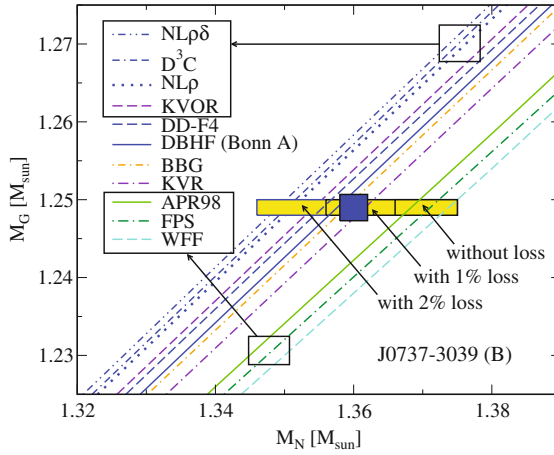


Fig. 3.31 Gravitational mass – baryon mass relation derived in [332] for PSR J0737-3039 (B) compared to a set of relativistic EoS [307] and four nonrelativistic EoS (BBG, APR, FPS and WFF). The rectangles show the experimental limits for a mass loss in the range 0–2%, while the blue rectangle shows the result of [334].

Clearly the usefulness of this criterion depends crucially on an accurate determination of the pulsar's baryon number and on the correct identification of its formation mechanism. Hence, progress in the simulation of e-capture supernovae and in the evolution of their progenitors are needed to put this type of constraint on the equation of state on a more solid basis.

3.4.1.3 Mass – radius relation

Closely linked to the relation between the mass and the central density for a given EoS, there is also a relation between the mass and the radius of a neutron star. While the maximum mass is determined mainly by the high density part of the EoS, the radius primarily depends on the properties of

neutron-rich nuclear matter near the nuclear saturation density (more precisely on the density dependence of the nuclear symmetry energy) [302]. In Fig. 3.32 the correlation between M and R is shown for a set of hadronic EoS (left panel) and for hybrid star models with a transition to a quark matter core in the superconducting 2SC phase (right panel). For neutron stars with a mass of $M = 1.5M_\odot$, one finds radii in the range 12–14 km.

Radii of compact stars are known with considerably less accuracy than the masses. Often a value for the radius can be determined only by indirect means; in some cases one cannot even obtain a value for the radius, but only a correlation between the radius and the mass. In the following three examples are discussed: the determination of the radii of low-mass X-ray binaries (LMXBs) from quasi-periodic brightness oscillations (QPOs), the observation of the thermal emission spectrum of an isolated neutron star and the surface redshift constraint. The resulting constraints are compiled in Fig. 3.32.

Radii from quasi-periodic brightness oscillations (QPO)

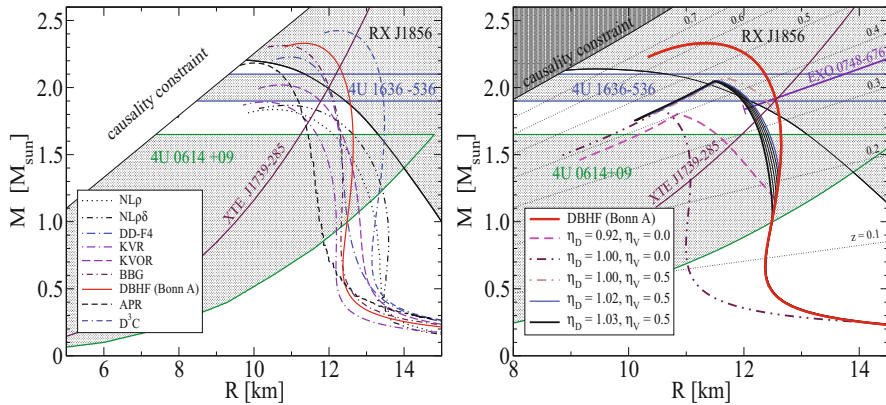


Fig. 3.32 Mass-radius relations resulting from a set of hadronic EoS (*left panel*) and for a neutron star model based on a DBHF EoS compared to a set of hybrid model stars consisting of an outer DBHF hadronic shell and an inner NJL quark matter core (*right panel*). The diquark coupling strength η_D regulates the transition density while the vector one η_V determines the stiffness and thus the maximum mass. In both panels the model EoS are confronted with the constraints resulting: **a** from QPOs in the LMXBs 4U 0614+09 (*lower left hatched area*, the “wedge”), as well as from 4U 1636-536 (the strip around $2 M_\odot$), which are regarded as separate conditions on the EoS and **b** from thermal radiation of the isolated neutron star RX J1856.5-3754 (*upper right hatched region*). The weak 2σ QPO constraint would exclude the NL ρ and NL $\rho\delta$ EoS, whereas the strong one on the 1σ level would leave only the stiffest equations of state: D ρ C, DD-F4, BBG and DBHF. The *right panel* is further supplemented by the *lines* of given surface redshifts in the range $z \in [0.1, 0.7]$. The constraints are discussed in the subsequent paragraphs.

The kilohertz QPOs seen from more than 25 neutron star in LMXBs constrain the high-density part of the equation of state because there are fundamental limits on the highest frequency of such oscillations. A pair of oscillation peaks is often found in the spectrum of such objects (see [335] for a general review). In all currently viable models of QPOs, it is assumed that the brightness modulations are caused by an object or a gas cloud orbiting the compact star; the higher of the two frequencies is then close to the orbital frequency at some particular radius. The observed lifetime of such oscillations is fairly large, up to ~ 100 cycles for some sources. Clearly this can be understood only if the orbit is outside the star. Moreover, in general relativity the orbit must be outside the innermost stable circular orbit (ISCO) of radius $R_{\text{ISCO}} = 6GM/c^2$. Matter inside the ISCO would rapidly spiral into the star, leading to a rapid damping of the QPOs. Within the models considered at present, this implies that for a given source, the mass and radius must fall inside an allowed “wedge” determined by the observed ν_{max} [336–338], see Fig. 3.32. Thus, the mass-radius relation of a viable EoS must traverse this wedge. The wedge becomes smaller for higher ν_{max} . Therefore the highest frequency QPO places the strongest constraint on the EoS. Note that a wedge derived from an observed maximal QPO frequency does not exclude neutron star masses and radii outside the wedge, corresponding to a smaller ν_{max} . On the other hand, an EoS ruled out by one star is definitely excluded, since all neutron stars have the same EoS. As shown in Fig. 3.32, the current QPO constraints do not rule out any of the EoS considered. However, because higher frequencies imply smaller wedges, a future observation of a QPO with a frequency $\sim 1,500\text{--}1,600$ Hz would rule out the stiffest equations of state. This would be a restriction complementary to those posed by RX J1856.5-3754 (discussed below) and the implied high masses for some specific neutron stars, which both favor a stiff EoS. Further information on the EoS might be provided by the observation of large radii; it is expected that the radius is determined primarily by the density dependence of the symmetry energy [302].

If it could be shown that, for a particular source, a given frequency is actually close to the orbital frequency at the ISCO, then the mass would be known to good accuracy, with uncertainties arising only from effects related to the rotation of the star. Such evidence was first claimed for 4U 1820-30 [339], but the conclusions are controversial due to the complex source phenomenology. More recently, a careful analysis of *Rossi* X-ray Timing Explorer data for 4U 1636-536 and other sources [308] suggest that sharp and reproducible changes in QPO properties are related to the ISCO. If so, this implies that several neutron stars in low-mass X-ray binaries have gravitational masses between $1.9 M_{\odot}$ and possibly $2.1 M_{\odot}$ [308]. In Fig. 3.32 we show the conjectured mass $2.0 \pm 0.1 M_{\odot}$ for 4U 1636-536.

Radii from thermal emission spectra

The nearby isolated neutron star RX J1856.5-3754 (hereafter RX J1856 for short) belongs to a group of seven objects which show a purely thermal spectrum in X-rays and in optical-UV. This allows the determination of R_∞/d , the ratio of the photospheric (or radiation) radius

$$R_\infty = \frac{R}{\sqrt{1 - 2GM/(Rc^2)}} \quad (3.50)$$

to the distance d of the object, if the radiative properties of its photosphere are known. Given an observational value for R_∞ , the actual radius of the compact star is a function of the gravitational mass according to the mass-radius relationship $M(R)$, which follows from Eq. (3.50). RX J1856 is the only object of this group which has a measured distance obtained by Hubble Space Telescope (HST) astrometry. After the distance of 117 pc [340] became known, several groups pointed out that the blackbody radius of this star is as large as 15–17 km. Although both, the X-ray and the optical-UV spectra, are extremely well represented by blackbody functions, they require different emission areas, a smaller hot spot and a larger cooler region. The overall spectrum could also be fitted by blackbody emission from a surface showing a continuous temperature distribution between a hot pole and a cool equator as expected for a magnetized neutron star. The resulting blackbody radii are 17 km (two blackbodies) and 16.8 km (continuous temperature distribution) [312]. Recently, the inclusion of more HST sightings indicated even larger distances up to 178 pc, while 140 pc is considered to be a conservative lower limit [341]. The latter is still consistent with a radius of 17 km [342, 343]. Although some questions, in particular that of the distance, are not yet finally settled, the recent data point to a large radius of the RX J1856.

Mass – radius correlation from surface redshifts

An additional test to the mass-radius relationship is provided by a measurement of the gravitational redshift of line emissions from the compact star surface given by

$$z = 1/\sqrt{1 - 2GM/(Rc^2)} - 1. \quad (3.51)$$

In the right panel of Fig. 3.33 we show the redshift z as a function of the mass of a representative pure neutron star (with DBHF EoS) and the hybrid star models [317, 344] shown in the right panel of Fig. 3.32. The controversial measurement of $z = 0.35$ for EXO 0748-676 [345, 346] would be in agreement with both hadronic and, despite claims to the contrary [346], also quark-core star models [347]. However, a redshift of $z \geq 0.5$ could not be accommodated by the hybrid star models suggested here, while hadronic models would not be invalidated by redshifts up to $z = 0.6$.

Note that once the threshold for the occurrence of strange quark matter is reached in the core of a hybrid star, the color-flavor-locking (CFL) phase [32, 37] shall be realized which softens the quark matter and leads to

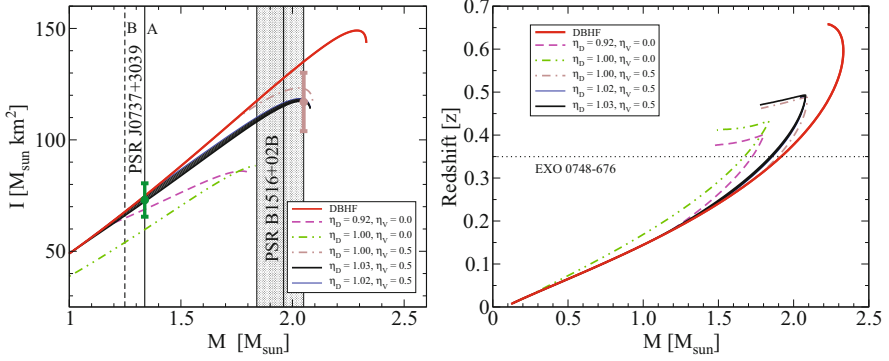


Fig. 3.33 *Left:* Moment of inertia I vs. the gravitational mass for the compact star equations of state discussed in the text. The *highlighted* mass regions correspond to the double pulsar J0737+3039 A+B and the pulsar B1516+02BA. Also shown is an anticipated data point with an error bar corresponding to a measurement with a 10% error at the 1σ level. *Right:* Surface redshift vs. gravitational mass for purely hadronic stars (DBHF) and hybrid stars with 2SC color superconducting NJL quark matter core (see text for details). For comparison the controversial result $z = 0.35$ [345, 346] for EXO 0748-676 is shown.

a gravitational instability [317, 348, 349], unless stability is enforced by a modification of the quark matter EoS [350, 351]. We exclude the CFL phase from the present discussion of compact star phenomenology and focus on the discussion of two-flavor quark matter phases, such as the color superconducting 2SC phase. A sufficient stiffness of the hybrid EoS is achieved, when a repulsive vector-meson mean field is taken into account, see [317, 344] for details. The corresponding isospin-symmetric EoS has a weak first order phase transition at 3–3.5 times the nuclear saturation density. The “masquerade” effect may indicate an artifact of the usual two-phase approach to the deconfinement phase transition and underline the necessity to develop a unified treatment of quark-hadron matter on the quark level, where the hadrons appear as bound states of quarks to be dissolved into their constituents under high pressure in analogy to the Mott transition in solid state physics [352].

3.4.1.4 Moments of inertia

The discovery of the relativistic double pulsar PSR J0737+3039 opened the possibility to measure the moment of inertia (MoI) of compact stars. This has recently been proposed as a further constraint on the EoS, assuming that the error can be reduced to about 10% in future measurements [353, 354].

Following the definition of the MoI given in [297] we show the results for a hadronic and several hybrid EoS in Fig. 3.33, left panel. For these models the observed mass of $1.338 M_{\odot}$ of PSR J0737+3039 A is rather close to the onset of the transition to a hybrid star. Hence, the quark matter fraction of

the hybrid star is expected to be small and the MoI to be practically indistinguishable from that of a pure hadronic star. The situation would improve if the MoI could be measured for more massive objects, e.g. for masses as high as $2 M_{\odot}$, where the difference in the MoI of the two models can exceed 10%. Indeed strong first order phase transitions with strong changes of the density from the outer to the inner core can significantly reduce the pulsar's MoI, and thus lead to changes in the temporal evolution of its rotational period [355].

3.4.1.5 Rotational frequencies

An absolute upper limit for the spin frequency of a pulsar is given by the mass shedding limit, at which the velocity of the stellar surface equals that of an orbiting particle suspended just above the surface. For a rigid Newtonian sphere this frequency is given by the Keplerian rate [293]

$$\nu_K = (2\pi)^{-1} \sqrt{GM/R^3} = 1833 (M/M_{\odot})^{1/2} (R/10 \text{ km})^{-3/2} \text{ Hz} . \quad (3.52)$$

However, since both deformation and general relativity effects are important, the rigid rotor relationship (3.52) has to be modified. It has been found [293] that with the empirical coefficient of 1,045 Hz in Eq. (3.52) the maximum rotation rate for a star of mass M and non-rotating radius R is very well approximated independently of the EoS [293, 356]. The observation of rapidly rotating pulsars can therefore constrain the compactness and might eventually lead to the elimination of very stiff equations of state which would result in too large radii. If the recent discovery of burst oscillations with a frequency of 1,122 Hz in the X-ray binary XTE J1739-285 [315] and their identification with the compact star spin frequency proves to be correct, this would serve as an additional constraint with far-reaching implications for the high-density nuclear EoS. The boundary for the mass-radius relationship reads in this case [357]

$$R < 9.52 (M/M_{\odot})^{1/3} \text{ km} . \quad (3.53)$$

As can be seen from the left panel of Fig. 3.32, this constraint would rule out all low-mass configurations, $M < 1.75 M_{\odot}$.

In passing we mention that rotational instabilities in rotating stars, known as gravitational radiation driven instabilities, appear to set a more stringent limit on rapid stellar rotation than mass shedding from the equator [297]. These instabilities originate from counter-rotating surface vibrational modes which at sufficiently high rotational star frequencies are dragged forward. In this case gravitational radiation, which inevitably accompanies the aspherical transport of matter, does not damp the instability modes but rather drives them. Viscosity plays an important role in damping these instabilities. The most unstable modes are the f -modes and the recently discovered r -modes

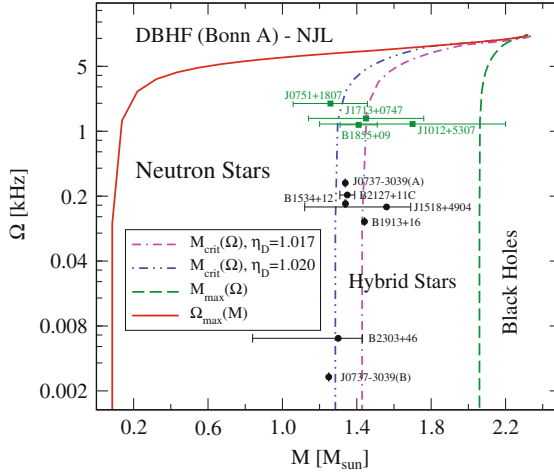


Fig. 3.34 Mass clustering observed for binary radio pulsars (*black dots*) and neutron stars with a white dwarf binary (*green squares*) in the plane of rotation frequency Ω vs. mass M . The data are compared to model calculations based on the hybrid star scenario discussed above (cf. Fig. 3.32). The mass distribution of objects is roughly correlated with a line representing the onset of deconfinement (see text).

[358]. The latter may severely constrain the composition of compact stars that would rotate at sub-millisecond periods [297, 359].

3.4.1.6 Mass clustering

Compact stars in binary systems generally undergo a stage with disc accretion during their evolution. This leads to both, spin-up and mass increase. Initial indications for a spin frequency clustering in low-mass X-ray binary systems were reported by measurements with *Rossi-XTE*. A speculative interpretation of such a correlation as a waiting-point phenomenon, where star configurations cross the border between pure neutron stars and hybrid stars in the spin frequency-mass plane, was put forward in [360]. A systematic analysis of the population distribution of accreting compact stars, in the context of the deconfinement phase transition, was performed in [361]. This revealed a mass clustering effect. For strange stars, however, such an effect is not expected [360, 362].

In Fig. 3.34 we show the masses and spin frequencies of compact stars in binary radio pulsars and neutron star-white dwarf binaries. Stable stars are found in the region bounded by the maximum rotation frequency $\Omega_{\max}(M)$ for which mass-shedding from the star equator occurs and the maximum mass $M_{\max}(\Omega)$ for which the gravitational instability against collapse to a black

hole sets in. The corresponding curves are shown for the hybrid star model discussed above. Moreover, we show the lines that mark the onset of a quark matter core. One observes an interesting correlation between the data points and the almost vertical part of these lines (for details see [361, 363]). The two choices of the diquark coupling η_D illustrate the general trend that a smaller transition density leads to clustering at a smaller mass M . There might, however, be other reasons for the mass clustering of spinning pulsars [364], but the relation to a phase transition in the interior can at present not be excluded. If this interpretation is correct, it would provide a strong constraint on the hybrid EoS. In this context a critical density for deconfinement in compact stars of about 0.4 fm^{-3} is favored.

3.4.2 Constraints from compact star cooling

The cooling behavior of compact stars belongs to the most complex phenomena in astrophysics [365]. Shortly after the formation of a proto-neutron star in a core-collapse supernova the mean free path of neutrinos becomes large enough such that they are no longer trapped inside the core and leave the star, radiating a huge amount of energy. The core of a young neutron star is cooled very efficiently by neutrino emission and a cooling front forms at the crust-core boundary. After the heat transport time scale of about 100 years the neutron star reaches an isothermal state. Its cooling is dominated by the emission of neutrinos from the interior for times $t \lesssim 10^5$ year and after that thermal photon radiation from the surface becomes dominant. The surface temperature is typically of the order of $T \sim 0.1 \text{ keV}$, while the temperature of the dense interior is two orders of magnitude higher. This value is below the critical temperatures for superconductivity in nuclear ($T_c \sim 1 \text{ MeV}$) or quark matter ($T_c \sim 1 - 100 \text{ MeV}$). Therefore, the theory of the compact star cooling evolution requires the formulation of neutrino emissivities as well as thermal and transport properties for matter in a superconducting/superfluid environment.

The most efficient cooling process in hadronic matter is the in-medium β decay of neutrons (and its inverse), known as direct Urca (DU) process. Due to conservation laws this process requires a sufficiently large proton Fermi momentum; this implies a threshold for the proton fraction, which depends on the EoS. This in turn implies a minimum mass for the compact star (the full dots in Fig. 3.29), beyond which the DU sets in. Absence of a full dot (e.g. for D³C, DD-F4, KVR) indicates that for the corresponding EoS, the DU process is strongly suppressed. Further cooling processes are the medium modified Urca (MMU) and the pair breaking and formation (PBF) processes. In quark matter the main processes are the quark direct Urca (QDU), quark modified Urca (QMU), quark bremsstrahlung (QB) and quark pair formation and

breaking (QPFB) [366]. Also electron bremsstrahlung (EB) and the massive gluon-photon decay (see [367]) have to be considered.

Codes for the numerical simulation of compact star cooling were developed by several groups. Inputs (cooling regulators) of rather different kinds are required (see, e.g., [368–372]). Attempts to develop a *Minimal Cooling Paradigm* [369] by omitting important medium effects on cooling regulators [371, 373] unfortunately can result in inconsistencies and unreliable predictions. Further uncertainties are due to anisotropies generated by the magnetic field [368] and special processes in the neutron star crust and at the surface of the star. Therefore, it is still premature to attempt a reliable identification of the neutron star interior from the cooling behavior. Nevertheless, we present some general considerations, which illustrate the relevance of key ingredients in cooling scenarios presently under discussion.

In the following, three tests are considered that show a dependence of the compact star cooling process on the assumptions for the core composition. Two purely hadronic models are compared to a class of hybrid models with superconducting quark matter phases. In order to circumvent the dependence on the cooling model a given cooling code developed in [370, 374] is employed and the matter properties such as EoS, superconductivity and star crust model are varied such as to fulfill all constraints known up to now (mass, mass-radius, temperature-age, brightness, etc.). A critical issue is the occurrence of the DU process in both phases, the hadronic and the 2SC quark-matter phase. According to the present understanding of the cooling mechanism and its observable consequences, the DU process generally leads to a too fast cooling in disagreement with some of the constraints discussed below [307, 316, 370]. In the following a few microscopic ingredients of both model phases, namely their pairing properties are listed, since they sensitively influence the cooling mechanism. For systematic field theoretic approaches to the neutrino cooling problem in neutron stars see, e.g., [304, 371, 375].

For the hadronic part of the core the $1S_0$ neutron and proton gaps are taken according to the calculations by [376] corresponding to the thick lines in Fig. 5 of [370]. However, the $3P_2$ gap is suppressed by a factor 10 compared to the BCS model calculation of [376], consistent with arguments from a renormalization group treatment of nuclear pairing [377]. Without such a suppression of the $3P_2$ gap the hadronic cooling scenario would not fulfill the temperature-age constraint, see [373].

The possibilities of pion condensation and of other so called exotic phases are included in the calculations for purely hadronic stars but not in the hybrid ones [370]. While the hadronic DU process occurs in the DBHF model EoS for all neutron stars with masses above $1.27 M_\odot$, see Fig. 3.29, it is not present at all in the DD-F4 model. This difference is caused by the much softer density dependence of the nuclear symmetry energy in the DD-F4 model [307]. The calculations account for the specific heat and the heat conductivity of all existing particle species contributing with fractions

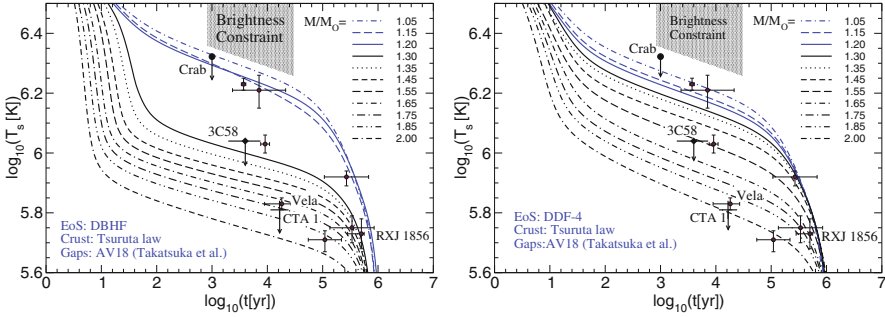


Fig. 3.35 Hadronic star cooling curves for the DBHF (*left*, with DU process occurring for $M > 1.27M_\odot$) and for the DDF-4 (*right*, with DU process absent for all masses) model equation of states. The *lines* correspond to compact star mass values indicated in the legend (in units of M_\odot); data points with error bars are from [369]. The *hatched* trapeze-like area represents the region excluded by the brightness constraint (BC) [381].

determined by the β -equilibrium conditions. Additionally, in quark matter the massless and massive gluon-photon modes also contribute.

For the hybrid star case, the assumed 2SC quark matter phase of the inner core leaves one quark color unpaired, for which the very effective quark DU process works and leads to a too fast cooling. In [378] a special mechanism in form of a density-dependent gap for the unpaired color (called X-gap) is introduced in order to moderate and tune the strength of the QDU process. The physical origin of the gap is still unclear. Nonetheless we present some results for this scenario in the subsequent discussion, in order to illustrate its effect on cooling. For further details on hybrid models, relevant color superconducting phases and sizes of the pairing gaps, we refer the reader to [378–380].

3.4.2.1 Temperature – age test

The temperature and age of a number of compact stars is known from observation. Each data point should be reproduced by a cooling curve belonging to an admissible configuration. In Fig. 3.35 we present temperature-age (TA) diagrams for two different hadronic models and in Fig. 3.36 for a special choice of the hybrid star cooling models presented in [378]. The TA data points are from [369]. No cooling curve should pass the hatched trapezoidal region due to the brightness constraint (BC) derived in [381] valid for neutron stars with not too strong magnetic fields ($B < 10^{13}$ G).⁹ For each model several cooling curves with different mass values are shown. Clearly the cooling scenario crit-

⁹ For neutron stars with strong magnetic fields (magnetars, $B > 10^{13}$ G), Joule heating in the crust leads to higher surface temperatures [382] limiting the applicability of the brightness constraint (BC) to compact stars with $B < 10^{13}$ G.

ically depends on the compact star mass and on the EoS. More massive stars cool faster. In particular the left part of Fig. 3.35 clearly shows the onset of the fast DU cooling process for masses beyond the critical mass of $1.27 M_\odot$ for the DBHF EoS. For the hybrid star models discussed above [378], it was shown that an excessive suppression of the quark DU process implies a too slow cooling, incompatible with the lowest T-A data points (e.g. from Vela). In Fig. 3.36 the results are shown for a particular model (Model IV), adjusted as to optimally fulfil the $\log N - \log S$ test (right panel) and to reproduce the mass distribution of the population synthesis (Fig. 3.37) discussed below.

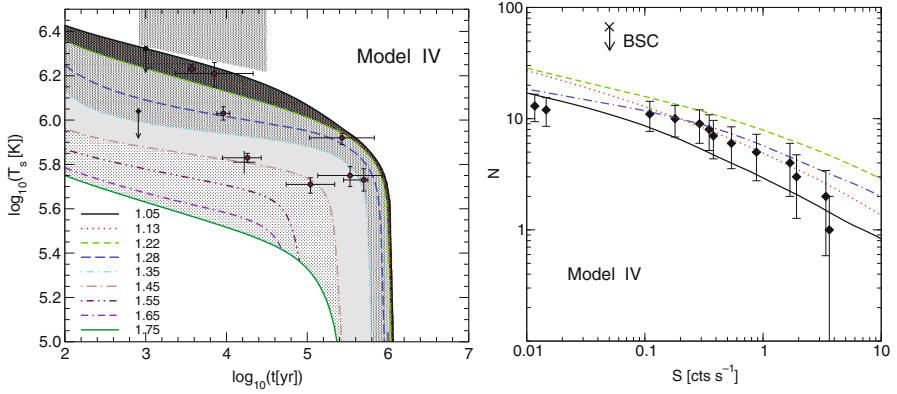


Fig. 3.36 Cooling curves (*left*) and $\log N - \log S$ distribution (*right*) for a hybrid star configuration, which is optimized to fulfil all cooling constraints within the 2SC+X pairing models, as discussed in [378]. *Left part:* The mass band with the darkest grey shading corresponds to the mass bin around $1.4 M_\odot$ which has the highest population, cf. Fig. 3.37, in the population synthesis model of [383]. *Right part:* The curves correspond to different parameters of the population synthesis model. For details see [383].

3.4.2.2 $\log N - \log S$ test

Further constraints can be obtained from statistical considerations concerning the compact-star abundance distributions in brightness and mass. The $\log N - \log S$ distribution is a widely used tool in many branches of astronomy. Here one determines the cumulative distribution of the number of sources N brighter than a given flux density S from astronomical surveys. Such an approach has already been used in [384] and [385] to investigate the origin of isolated neutron stars in the solar proximity. One immediate advantage of the $\log N - \log S$ test is that, at variance with the temperature-age test, no degree of arbitrariness is introduced through the data analysis: both the fluxes S and the number of sources N are well measured by ROSAT.

Since the method can be applied to objects with unknown age, one can include, e.g., all the ROSAT X-ray dim neutron stars, and 3EG J1835+5918 (the Geminga twin) in the testing sample. The $\log N - \log S$ test is mostly sensitive to neutron stars older than $\sim 10^5$ years, since older sources dominate in number. In the solar proximity there are about a dozen of them in comparison to very few with $t \lesssim 10^5$ years.

Nevertheless there are also significant limitations. One source of uncertainty is the incomplete knowledge of important ingredients of the population synthesis model. They concern the spatial distribution of the neutron star progenitors, the neutron star mass and velocity spectrum, and their emission properties. A more severe problem arises in connection with the low statistics of the sample, since there are only about 20 thermally emitting neutron stars known to date. This implies that the bright end of the $\log N - \log S$ relation comprises very few objects. The analysis therefore suffers from statistical fluctuations. A more detailed discussion of the method can be found in [383].

The $\log N - \log S$ test has been applied to the neutron star cooling problem for hadronic EoS in [383] and for the hybrid EoS and pairing gaps defined above in [378]. This test is sensitive to the choice of the smallest gap parameter (the X-gap) determining the cooling behavior of the superconducting quark matter core. While a larger gap with the slower drop at increasing density predicts too many sources, the results for the smaller X-gap with a somewhat faster drop Fig. 3.36 (right panel) are in accordance with the $\log N - \log S$ data.

3.4.2.3 Mass distribution from population synthesis

In order to reach the goal of unmasking the neutron star interior a new method for the quantitative analysis of the cooling behavior has been suggested in [319]. It consists in the extraction of a neutron star mass distribution from the (yet sparse) temperature-age data and its comparison with the (most likely) mass distribution from population synthesis models of neutron star evolution in the galaxy [383].

This method has been applied to the cooling models for hadronic and hybrid stars described previously. The results for the extracted mass distributions are normalized to 100 objects and shown in Fig. 3.37. The results are very sensitive to the chosen cooling model. In the hadronic scenario the onset of the DU cooling mechanism drastically narrows the mass distribution around the critical mass for the DU onset, see Fig. 3.35. On the other hand a slow cooling model without hadronic DU process predicts more massive objects than could be justified from the independent population analysis. Thus, a quantitative characterization of the cooling behavior through the mass population provides a complementary handle on the DU cooling problem [307, 316, 370]. Moreover, when comparing the density dependence of the pairing gaps with the extracted mass distributions for the corresponding

hybrid models in the right panel of Fig. 3.37, a direct relationship between the superconductivity and the mass distribution becomes obvious.

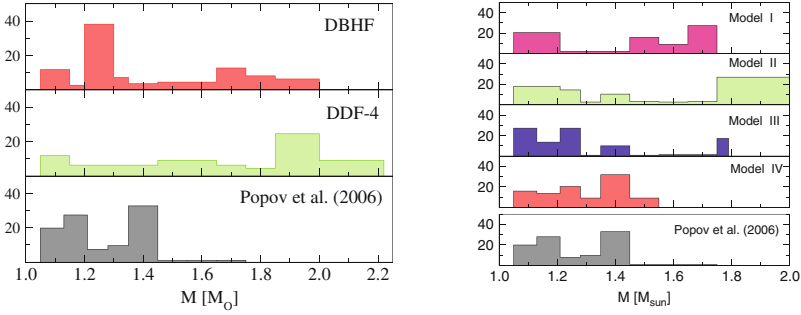


Fig. 3.37 Neutron star mass spectra extracted from the distribution of cooling data for both hadronic EoS models (*left panel*) and for hybrid stars with X-gap models I–IV (*right panel*). For comparison, the mass distribution of young, nearby neutron stars from the population synthesis of Popov et al. [378] is shown at the *bottom* of the panels.

3.4.3 Relation to nuclear collisions

In Sect. 3.4.1.1 the strong correlation between the stiffness of the equation of state and the maximum mass of a compact star was discussed. This was demonstrated for a collection of relativistic models in Fig. 3.29. As shown in [307], it is essentially the stiffness of the equation of state of symmetric matter that determines the maximum mass, in spite of the large isospin asymmetry of neutron star matter. The observation of a compact star with masses beyond $2 M_{\odot}$ would require a rather stiff EoS and the question arises, if this constraint on the high-density behavior is compatible with constraints from nuclear collisions, obtained from the analysis of flow data, cf. Sect. 3.2.5 in Part IV.

An analysis of elliptic flow data, which depends primarily on the isospin independent part of the EoS, was carried out for a specific model in [386]. In particular the range of parameters compatible with the flow data was determined. The region thus determined is shown in Fig. 3.38 by the shaded region. Danielewicz et al. [386] asserts that this region limits the range of accessible pressure values at a given density. Thus the area of allowed values does not represent experimental values itself, but results from transport calculations for the motion of nucleons in a collision [386], cf. Sect. 6.4, Fig. 6.13 in Part III. Although, it would be preferable to repeat these calculations for each specific EoS, this would not be a manageable testing tool. Therefore we adopt the results of [386] as a reasonable estimate of the preferable pressure-

density domain in SNM. Its upper boundary is expected to be stable against temperature variations [387]. An important fact is that the flow constraint probes essentially only the symmetric part of the binding energy function $E_0(n)$.

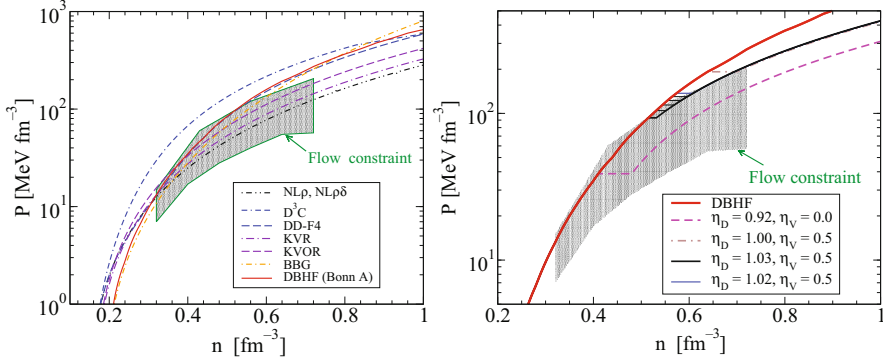


Fig. 3.38 Pressure vs. density of the isospin symmetric EoS for the set of hadronic EoS (*left panel*) and for hybrid EoS where the hadronic part is given by the DBHF EoS and the quark matter by a NJL model with 2SC color superconductivity and a vector mean field (*right panel*). The *hatched region* has been deduced from analyses of the elliptic flow in nuclear collisions [386].

Following [386] the constraint arises for a density window between 2 and 4.5 times saturation density n_0 . One has, however, to keep in mind that at high densities this constraint is based on flow data from the AGS energy regime ($E_{\text{lab}} \sim 4 - 11$ AGeV). At these energies a large amount of the initial bombarding energy is converted into new degrees of freedom, i.e., excitations of higher lying baryon resonances and mesons, which makes conclusions on the nuclear EoS more ambiguous than at low energies. Nevertheless, the analysis of [386] provides a guideline for the high density regime which we believe to be reasonable.

As can be seen from the left panel in Fig. 3.38, the flow constraint is well fulfilled by the KVOR, NLρ and NLρδ models. For the latter two models this is rather obvious since they have already been tested to reproduce flow data. For the stiffer equations of state (DD-F4, BBG and DBHF) the constraint is satisfied only for densities below $3 n_0$.

Next we discuss the hadron-to-quark matter phase transition in the context of the flow constraint. As a result of the phase transition the pressure stays constant across the coexistence phase, as shown in the right panel of Fig. 3.38. While in nuclear collisions the density changes continuously in space-time, in the hybrid star case the density jumps at the phase boundary, since gravity separates phases of different density. As illustrated in Fig. 3.38, slight variations of the quark matter model parameters η_D and η_V induce considerable changes of the critical density for the phase transition and the behavior

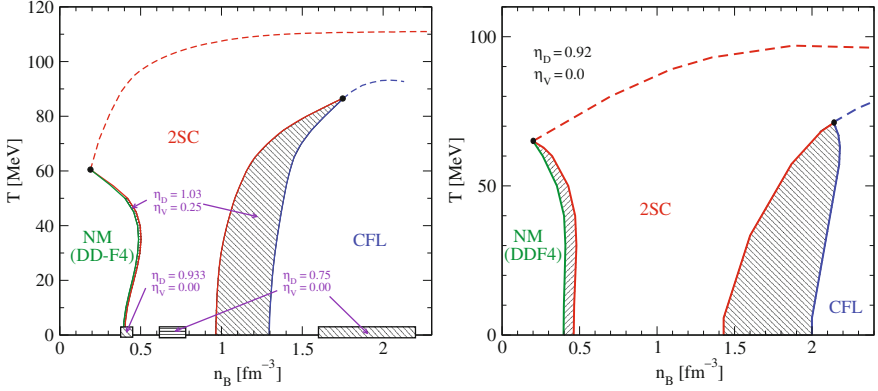


Fig. 3.39 Phase diagram for isospin symmetric matter when for neutron star matter EoS a maximum mass constraint of $2.1 M_{\odot}$ (left) or $1.7 M_{\odot}$ (right) is required. The NM-2SC phase transition is almost a crossover. The model DD-F4 has been developed as a finite-temperature extension of DBHF for applications in the supersaturation region. For the parameter set ($\eta_D = 0.75$, $\eta_V = 0.0$) the flow constraint is fulfilled but no stable hybrid stars are obtained.

of the pressure (stiffness) at high densities. We suggest that a proper choice of these parameters can be obtained by utilizing the flow constraints. At first we fix the vector coupling by demanding that the high density behavior of the hybrid EoS should be as stiff as possible but still in accordance with the flow constraint. We obtain $\eta_V = 0.50$, fairly independently of the scalar diquark coupling η_D . The latter is chosen such that the problem of the violation of the flow constraint for the DBHF EoS in symmetric nuclear matter at high densities is resolved by the phase transition to quark matter. The optimal choice for η_D is thus between 1.02 and 1.03. We point out that by this choice the hybrid EoS fulfills a wider range of astrophysical constraints than the purely hadronic DBHF EoS [317].

In a next step we extend the description to finite temperatures focusing on the behavior at the transition line. For this purpose we apply a relativistic mean-field model with density-dependent masses and couplings ([268]) adapted to mimic the DBHF-EoS and generalized to finite temperatures (DD-F4). In Fig. 3.39 we show the resulting phase diagrams including the transition from nuclear to quark matter when in the neutron star matter case a maximum mass of $2.1 M_{\odot}$ (left panel: $\eta_D = 1.030$, $\eta_V = 0.50$) or $1.7 M_{\odot}$ (left panel: $\eta_D = 0.92$, $\eta_V = 0.0$) is required. A very small coexistence region and a tiny density jump is obtained almost independently of the stiffness of the quark matter EoS and thus of the maximum neutron star mass. At temperatures beyond $T \sim 45$ MeV the present nuclear matter description is not reliable, since contributions from mesons, hyperons and nuclear resonances are missing. This will be amended in future studies.

3.4.4 Summary

To summarize the present Sect. 3.4, we note that we have discussed the constraints on the EoS of hadronic matter at high densities. There are mostly bulk properties of a compact star, such as the mass, radius, rotational frequency, momentum of inertia and their mutual relations, that can be used to select a suitable equation of state. Accordingly, powerful testing schemes were introduced in [307] and [320].

Dynamical processes like compact star cooling or supernovae explosions do not only depend on the underlying EoS but to a large extent also on the microscopic dynamics on the nuclear level. Therefore such processes are a very important testing ground for the microscopic input of theoretical models. It is clear from the discussion that there is no EoS available so far that can fulfill all constraints from astrophysical observations and nuclear collisions simultaneously.

New observations of compact star properties with unprecedented accuracy will tighten the constraints even further. In particular the high masses for PSR B1516+02B and 4U 1636-536, the large radius for RX J1856 and the submillisecond spin period for XTE J1739-285 reduce the window for extrapolations from well studied nuclear matter at subsaturation and saturation density to the densities beyond $\sim 3 n_0$, where the CBM experiment at FAIR will operate.

If quark matter occurs in compact stars, it needs to be stiff enough to support the high mass constraint. Color superconductivity, lowering the deconfinement threshold, and a repulsive vector mean field are required for the description of stable hybrid stars. Quark stars “masquerade” as hadronic stars, since their mass-radius relationship and other observables related to the compactness are similar. To unmask the compact star interior, new detailed analyses of the cooling behavior have been suggested which presently seem to favor a color superconducting quark matter interior.

The resulting EoS for isospin symmetric matter has a very weak first order deconfinement phase transition to superconducting quark matter at $\sim 3 - 3.5 n_0$. This statement, however, is based on the two-phase approach to the phase transition. Much more work needs to be done to derive the characteristics of the high density phase transition within a unified approach to dense matter on the basis of a properly defined chiral quark model.

The next section is devoted to the color superconducting phases of QCD which, as discussed above, appear at large densities and small temperatures.

3.5 Color superconducting phases of QCD matter

At sufficiently large baryon number densities and sufficiently small temperatures, quark matter is a color superconductor [26–28]. In this chapter, we shall try to quantify what “sufficiently dense” and “sufficiently cold” means in terms of physical units. This is important in order to answer the question whether color-superconducting phases of quark matter can be created (and – possibly – observed) in heavy-ion collisions at FAIR energies and whether they have an influence on the properties of compact stellar objects.

Superconductivity can be microscopically understood as the condensation of fermion pairs, so-called Cooper pairs, which form at the Fermi surface on account of an attractive interaction [388]. Depending on the color-flavor-spin structure of the order parameter for quark Cooper-pair condensation, Φ , there are many different color-superconducting phases of quark matter, similarly to the many phases of superfluid He-3 [389].

At asymptotically large densities, the QCD coupling constant, g , becomes small due to asymptotic freedom [390, 391]. This implies that color superconductivity can be analyzed rigorously in the framework of QCD, using resummation techniques based on perturbative methods and power counting [392–395]. The main result of this analysis is the color-superconducting gap parameter at zero temperature, ϕ_0 , evaluated to subleading order in the QCD coupling constant, and the transition temperature to the normal-conducting phase, T_c [396–399]. We shall summarize the current knowledge about these quantities, including the effect of gluon fluctuations on the transition temperature [400–402]. We shall also present an argument how to decide which color-superconducting phase forms the ground state for a given quark chemical potential at zero temperature.

At intermediate densities of relevance for heavy-ion collisions and compact stellar objects, the QCD coupling constant is of order one. In the absence of a small parameter, perturbative methods and power counting become inapplicable. In this situation, one has to resort to non-perturbative methods such as Schwinger-Dyson equations [403] or to phenomenological models for quark matter such as the Nambu–Jona-Lasinio (NJL) model [404–409]. Both approaches are less well controlled, and thus allow only for qualitative estimates of the gap parameter and the transition temperature. We shall summarize our current knowledge for conditions of relevance for compact stellar objects, namely β -equilibrium, as well as color and electric neutrality. New phases emerge which feature gapless quasiparticle excitations [410, 411]. Gapless color-superconducting phases may be chromomagnetically unstable [412]. The question which phase replaces them and is the true ground state of the system for given quark chemical potential and temperature is not settled up to this date.

In weak coupling, the size of the quark Cooper pair is parametrically larger than the interparticle distance, just like for electron Cooper pairs in the framework of BCS theory of ordinary superconductors [388]. As the density

decreases, however, the coupling constant becomes larger and the Cooper-pair size shrinks [413]. At some point, the pair size is of the order or smaller than the interparticle distance. Cooper pairs look like diquark molecules which, under certain circumstances, may undergo Bose-Einstein condensation (BEC). This implies an exciting analogy between quark matter and the physics of trapped ultracold fermionic atoms [414], where the BCS-BEC crossover can be studied varying the effective coupling strength (the scattering length) via tuning an external magnetic field through a Feshbach resonance. We shall report results of a recent study in the quark matter context.

3.5.1 Color superconductivity at asymptotically large densities

The argument that quark matter is color-superconducting goes as follows. Consider quark matter at zero temperature, $T = 0$, and asymptotically large density or, since density is proportional to (the third power of) Fermi momentum, $n_q \sim k_F^3$, at a Fermi momentum $k_F \gg \Lambda_{\text{QCD}} \sim 200$ MeV. In this case, due to asymptotic freedom of QCD [390, 391], quarks become weakly interacting for momentum exchanges of the order of k_F , i.e., the strong coupling constant at this momentum scale becomes small, $g(k_F/\Lambda_{\text{QCD}}) \ll 1$. Thus, the dominant interaction between quarks is single-gluon exchange. The scattering amplitude corresponding to single-gluon exchange in an $SU(N_c)$ gauge theory is proportional to

$$(T_a)_{ki} (T_a)_{lj} = -\frac{N_c + 1}{4N_c} (\delta_{jk} \delta_{il} - \delta_{ik} \delta_{jl}) + \frac{N_c - 1}{4N_c} (\delta_{jk} \delta_{il} + \delta_{ik} \delta_{jl}) , \quad (3.54)$$

where i, j are the fundamental colors of the two quarks in the incoming channel, and k, l their respective colors in the outgoing channel. Under the exchange of the color indices of either the incoming or the outgoing quarks the first term is antisymmetric, while the second term is symmetric. In group-theoretical language, for $SU(3)_c$ Eq. (3.54) represents the coupling of two fundamental color triplets to an (antisymmetric) color antitriplet and a (symmetric) color sextet, $[\mathbf{3}]_c \times [\mathbf{3}]_c = [\bar{\mathbf{3}}]_c^a + [\mathbf{6}]_c^s$. The minus sign in front of the antitriplet contribution in Eq. (3.54) signifies the fact that this channel is attractive, while the sextet channel is repulsive.

According to Cooper's theorem [388], even an arbitrarily weak attractive interaction will lead to condensation of Cooper pairs at the Fermi surface and thus destabilize the latter. The new ground state of the system is a condensate of Cooper pairs. In QCD, the attractive channel is the color-antitriplet channel, and thus the quark Cooper pair condensate carries color-antitriplet quantum numbers,

$$\langle \psi_f^i \Gamma \psi_g^j \rangle \sim \Phi_{fg}^{ij} \equiv \epsilon^{ij}_k \Phi_{k,fg} . \quad (3.55)$$

Here, $k = \bar{r}, \bar{g}, \bar{b}$ denotes anticolor indices, and f, g are flavor indices. Γ is a matrix in Dirac space. It depends on the spin representation of the Cooper pair condensate. The totally antisymmetric rank-3 tensor ϵ^{ij}_k on the right-hand side of Eq. (3.55) signifies the fact that condensation occurs in the color-antitriplet channel.

Color superconductivity of quarks is a much more natural phenomenon than ordinary superconductivity of electrons in condensed matter. While the primary interaction between electrons, photon exchange, is repulsive, electronic superconductivity arises from a secondary attractive interaction, phonon exchange. In quark matter, the primary interaction between quarks, gluon exchange, is already attractive.

On the other hand, color superconductivity is also much more complex than ordinary superconductivity. From a very qualitative point of view, in comparison to the electrons, quarks carry additional quantum numbers such as color and flavor. The Pauli principle requires that the wave function of a Cooper pair has to be antisymmetric under the exchange of the two fermions forming the pair. Consequently, the possible Dirac, color, and flavor representations of the two-fermion state have to be chosen in a way which respects this antisymmetry. This requirement helps to classify all possible color-superconducting condensates [415].

Let us discuss a few examples. Suppose the quark Cooper pairs have total spin $J = 0$. A spin singlet $[1]_J^a$ is a totally antisymmetric representation of the spin group $SU(2)_J$. Consequently, the Cooper pair has to be in a totally symmetric representation with respect to color and flavor space in order to fulfill the requirement of overall antisymmetry. If we assume the color representation to be the (attractive and antisymmetric) color-antitriplet, we can only choose an antisymmetric representation of the flavor symmetry group.

For $N_f = 1$ flavor, this is not possible, because there simply is no flavor symmetry for a single quark flavor. Condensation in the spin-zero, color-antitriplet channel thus does not occur and we either have to choose a representation for higher spin, for instance the symmetric spin-one triplet $[3]_J^s$, or the (symmetric, but repulsive) color-sextet representation $[6]_c^s$. At asymptotically large density, due to the above arguments only the former should be considered a realistic possibility. In this case, the Dirac matrix Γ in Eq. (3.55) carries a (spatial) Lorentz index $\alpha = x, y, z$ and the condensate is $\Phi^{ij,\alpha} = \epsilon^{ij}_k \Phi_k^\alpha$. The order parameter for condensation, Φ_k^α , can be viewed as a 3×3 matrix in the combined space of color and orbital angular momentum. This is similar to superfluid He-3, where the order parameter is a matrix in the combined space of spin and orbital angular momentum [389]. Consequently, like in superfluid He-3, depending on the detailed structure of the order parameter, many different phases may arise. The one with the lowest free energy or, equivalently, the highest pressure is the so-called “color-spin-locking” (CSL) phase, where $\Phi_k^\alpha \equiv \delta_k^\alpha \Phi$. The original $SU(3)_c \times SU(2)_J \times U(1)_B$ symme-

try is broken to the diagonal subgroup $SU(2)_{c+J}$. According to the Goldstone theorem, the pattern of symmetry breaking leads to the appearance of nine Goldstone bosons, eight of which are eaten by the gluons which become massive by the Anderson-Higgs mechanism [416, 417].

For $N_f = 2$ flavors, we can only choose the antisymmetric flavor singlet $[1]_f^a$ of the $SU(2)_f$ flavor group, $\Phi_{fg}^{ij} = \epsilon^{ij}_k \Phi_{k,fg} = \epsilon^{ij}_k \epsilon_{fg} \Phi_k$. The order parameter for condensation, Φ_k , has an anticolor index which, by a global color rotation, can be oriented into the $k = \bar{b} \equiv 3$ direction. This means that only quarks of colors $i, j = r, g \equiv 1, 2$ participate in forming Cooper pairs, blue quarks remain unpaired. The associated color-superconducting phase is termed “two-flavor superconducting” (2SC). Condensation breaks the original $SU(3)_c \times SU(2)_f \times U(1)_B$ symmetry to $SU(2)_c \times SU(2)_f \times \tilde{U}(1)_B$. The remaining $SU(2)_c$ symmetry resides in the color space of red and green quarks participating in Cooper pairing. $SU(2)_f$ is not broken, as the order parameter is a flavor singlet. A rotated baryon number symmetry formed from generators of the original $U(1)_B$ and T_8 from the color $SU(3)_c$ survives. The pattern of symmetry breaking leads to three massless gluons (the gauge bosons of the remaining $SU(2)_c$ symmetry) and five massive gluons.

For $N_f = 3$ flavors, we have to choose the antisymmetric flavor-antitriplet $[\bar{3}]_f^a$ of $SU(3)_f$ and $\Phi_{fg}^{ij} = \epsilon^{ij}_k \Phi_{k,fg} = \epsilon^{ij}_k \epsilon_{fg}^h \Phi_k^h$. The order parameter for condensation, Φ_k^h , can be viewed as a 3×3 matrix in the combined space of color and flavor. This is similar to superfluid He-3 and the CSL phase discussed above. Among the many possible phases the one with the highest pressure is the so-called “color-flavor-locking”(CFL) phase [32], where $\Phi_k^h \equiv \delta_k^h \Phi$. The original $SU(3)_c \times SU(3)_f \times U(1)_B$ symmetry is broken to the diagonal subgroup $SU(3)_{c+f}$. Similarly to the CSL phase, but in contrast to the 2SC phase, there is no residual (rotated) baryon number symmetry. Again, all eight gluons will become massive due to the Anderson-Higgs mechanism. An extended discussion of the order parameters and symmetry breaking patterns in other color-superconducting phases can be found in [418].

As mentioned above, at asymptotically large densities, i.e., in weak coupling, one can use resummation techniques based on perturbation theory and power counting to compute the color-superconducting gap parameter and the transition temperature to the normal-conducting phase in a controlled manner. In the computation of these quantities, power counting is only slightly modified as compared to ordinary perturbation theory: terms are ordered according to powers of $g^n \ln^m(\mu/k_0)$, where k_0 is a typical energy scale relative to the Fermi energy $\mu = \sqrt{k_F^2 + m_f^2}$ (m_f is the mass of quark flavor f , which we can safely set to zero for asymptotically large densities). For energy scales $k_0 \sim \mu$, we have $\ln(\mu/k_0) \sim 1$, and terms are ordered according to powers of g . However, for energy scales close to the Fermi surface, say, of order ϕ_0 , we have on account of the weak-coupling result $\phi_0 \sim \mu e^{-1/g}$, see Eq. (3.56) below, that $\ln(\mu/k_0) \sim 1/g \gg 1$, so that large logarithms may compensate powers of g and $g^n \ln^m(\mu/k_0) \sim g^{n-m} \gg g^n$. A more careful analysis [419]

shows that for $\phi_0 < k_0 < g\mu$ terms can be sorted in powers of $(k_0/g\mu)^{1/3}$, possibly multiplied by powers of $\ln(\mu/k_0)$.

To subleading order in g , the result for the gap parameter at zero temperature reads

$$\phi_0 = 512 \pi^4 \left(\frac{2}{N_f g^2} \right)^{5/2} \mu \exp \left(-\frac{3\pi^2}{\sqrt{2}g} - \frac{\pi^2 + 4}{8} - d - \zeta \right) [1 + O(g)] . \quad (3.56)$$

Here, the leading term is the first term $\sim 1/g$ in the exponential. It arises from almost static magnetic gluon exchange and was first computed by Son [392]. Subleading terms arise from static electric and nonstatic magnetic gluon exchange and determine the prefactor of the exponential [393–395]. Another subleading term, the second term in the exponential, reduces the magnitude by a factor $\exp[-(\pi^2 + 4)/8] \sim 1/6$. It arises from the quark self-energy [396–398]. The spin of the Cooper pair gives rise to a subleading correction parametrized by a number $d \sim O(1)$. For condensation in the spin-zero channel, $d = 0$, while for the spin-one CSL phase we have $d = 5$, suppressing the gap by a factor $\sim 1/150$. Finally, $\zeta \sim O(1)$ is determined by the eigenvalues of the order parameter in Dirac-color-flavor space. For the 2SC phase, $e^\zeta = 1$, while for the CFL phase, $e^\zeta = 2^{1/3}$. For more details and other phases, see [418, 420].

In the left panel of Fig. 3.40, we show an extrapolation of the weak-coupling result (3.56) to realistically large values of quark chemical potential μ . We used the three-loop running formula for $\alpha_S \equiv g^2/(4\pi)$ [10] in order to fix the value of $g = g(\mu/\Lambda_{\text{QCD}})$ at a given quark chemical potential. We included $N_f = 3$ flavors in the running of α_S , since at $T = 0$, only the three lightest quark flavors are present for $\mu \leq m_c \sim 1,500$ MeV. In order to obtain the correct value of α_S at the scale of the Z mass, we choose $\Lambda_{\text{QCD}} = 364$ MeV. The gap parameter is fairly constant in the range $\mu \gtrsim 1$ GeV and drops rapidly when $\mu \lesssim 500$ MeV. The reason for this suppression is the increase of the coupling constant g at smaller densities and the associated decrease of the prefactor g^{-5} of the exponential in Eq. (3.56). Note that the maximum value for spin-zero gaps is of order 10 MeV; spin-one gaps (like the one for the CSL phase) are smaller by about two orders of magnitude.

In weak coupling, one can also compute the transition temperature T_c to the normal-conducting phase by means of resummation techniques and power counting. In mean-field approximation, one obtains to subleading order [398, 399]

$$T_c = \frac{e^\gamma}{\pi} \phi_0 e^\zeta \simeq 0.57 \phi_0 e^\zeta , \quad (3.57)$$

where $\gamma \simeq 0.577$ is the Euler-Mascheroni constant. The factor e^ζ cancels the factor $e^{-\zeta}$ in the expression for the zero-temperature gap (3.56), so that the transition temperature in physical units does not depend on the detailed eigenvalue spectrum of the order parameter. Therefore, T_c assumes the same value for the 2SC and the CFL phase, cf. right panel of Fig. 3.40.

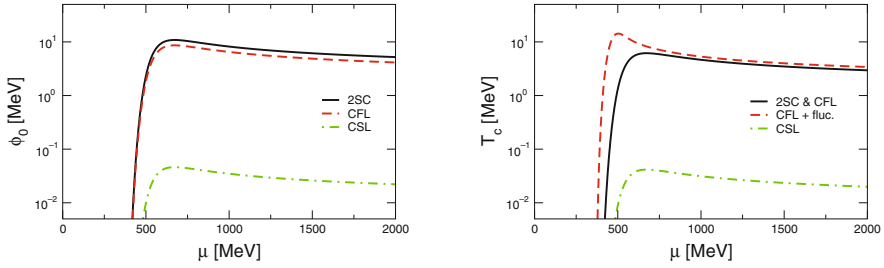


Fig. 3.40 *Left:* The zero-temperature gap for the 2SC (solid black), the CFL (dashed red), and the CSL phase (dash-dotted green) as a function of the quark chemical potential. *Right:* The transition temperature as a function of the quark chemical potential. Solid black curve: mean-field transition temperature T_c of the 2SC and CFL phases, dashed red curve: first-order transition temperature T_c^* for the CFL phase, dash-dotted green curve: mean-field transition temperature for the CSL phase.

One can also go beyond the mean-field approximation by including gluon fluctuations. These fluctuations drive the transition to first order [400–402]. Since all eight gluons become massive in the CFL phase, they fluctuate less than in the normal-conducting phase. Therefore, the difference of the fluctuation contributions in the CFL and normal-conducting phases is negative, or in other words, the free energy of the CFL phase is lowered as compared to that of the normal-conducting phase. This increases the temperature T_c^* for the first-order transition between the CFL and normal phases. In weak coupling one finds [401]

$$T_c^* = T_c \left[1 + \frac{\pi^2}{12\sqrt{2}} g + O(g^2) \right] > T_c. \quad (3.58)$$

In the right panel of Fig. 3.40 we show T_c^* for the CFL phase in comparison to the mean-field transition temperature T_c given by Eq. (3.57). Also shown is the (mean-field) transition temperature for the CSL phase. Note that the increase in the critical temperature can be quite substantial, stabilizing color-superconducting quark matter in a range of temperatures up to values $\sim \phi_0$, which is well above the canonical value $0.57 \phi_0$ for the mean-field transition temperature of BCS theory. Due to the smallness of ϕ_0 , the absolute values for T_c^* are only of order 10 MeV. However, if ϕ_0 were of the order of 100 MeV, like in Dyson-Schwinger calculations or phenomenological models for quark matter (see next section), a value for $T_c^* \sim \phi_0$ could have potential implications for the detection of color-superconducting quark matter in heavy-ion collision experiments at FAIR energies.

At asymptotically large densities, i.e., in weak coupling, one can also analytically compute the contribution of Cooper pairing to the pressure. To leading order one obtains [421]

$$\Delta p = \frac{\mu^2}{4\pi^2} \phi_0^2 \sum_r n_r \lambda_r + O(\phi_0^4), \quad (3.59)$$

where the sum over r runs over all (different) eigenvalues of the order parameter, λ_r is the r th eigenvalue and n_r its degeneracy. This formula nicely shows that the energetically most favored phase is, in principle, the one where as many quark colors and flavors as possible participate in Cooper pairing and where the gap parameter is as large as possible. (Modifications of this rule may enter through the detailed eigenvalue spectrum of the order parameter.) Thus, although the gap parameter in the 2SC phase is larger than the one in the CFL phase by a factor $e^\zeta = 2^{1/3}$, cf. Eq. (3.56), since only four quark colors and flavors participate in pairing in the 2SC phase as compared to nine in the CFL phase, the CFL phase is energetically favored. (Moreover, while eight of the nine eigenvalues in the CFL phase have $\lambda_1 = 1$, one has $\lambda_2 = 4$, leading to an additional large contribution to the pressure of the CFL phase.) It can be shown that the CFL phase wins also over all other so-called inert phases in three-flavor, spin-zero color-superconducting quark matter [422].

3.5.2 Color superconductivity at intermediate densities

While the results obtained via weak-coupling methods at asymptotically large densities are in principle exact order by order in powers of $g^n \ln^m(\mu/k_0)$, the extrapolation of these results to realistic densities, where the QCD coupling constant is large, is no longer well-controlled. At present, there are several different approaches to investigate the regime of intermediate densities. One is the “brute-force” numerical solution of the Schwinger-Dyson equation for the QCD gap function [403]. Including hard-dense-loop (HDL) resummed gluon propagators and quark self-energies, this approach reproduces by construction the subleading-order weak-coupling result (3.56) at asymptotically large densities. However, also some (but not all) contributions beyond subleading order are taken into account, which may be of sizable magnitude at intermediate densities. Results for the gap parameter are shown in Fig. 3.41.

Note that the gaps from a numerical solution of the QCD gap equation are about a factor of three larger than the weak-coupling result (3.56). The reason is the following: at asymptotically large densities, the gap function is strongly peaked at the Fermi surface (cf. discussion in [403, 413]). At this point, the quark self-energy has a logarithmic singularity [423], suppressing the density of states and inducing non-Fermi-liquid behavior in normal-conducting quark matter. In a color superconductor, on the other hand, the effect is a suppression of the gap parameter by a factor $\exp[-(\pi^2 + 4)/8] \sim 1/6$, see Eq. (3.56). However, at intermediate densities the gap function is strongly smeared around the Fermi surface [403, 413]. Then, the suppression of the

density of states around the Fermi surface induced by the quark self-energy is less important, partially compensating the factor $\exp[-(\pi^2 + 4)/8]$.

The numerical solution of the QCD gap equation leads to values for ϕ_0 which are of order ~ 70 MeV. As discussed in the previous section, gluonic fluctuations may lead to transition temperatures $T_c^* \sim \phi_0$. Then, the region of color-superconducting quark matter extends to temperatures that could potentially be explored in heavy-ion collisions at FAIR energies (see also [424, 425] for even higher values of the gap).

Finally, note that the weak-coupling results in Fig. 3.41 differ by some factor of order $O(1)$ from those shown in Fig. 3.40. The reason is a different choice for the running of α_S with μ .

Another approach to obtain results for color-superconducting quark matter at intermediate densities is the use of phenomenological NJL-type models. In the following, we report on studies performed in the framework of such models, for quark matter under the conditions of electric and color neutrality as well as β -equilibrium. This case is of relevance for compact stellar objects where quark matter is expected to occur if the core density is sufficiently large. It is, however, not of immediate relevance for heavy-ion collisions where there is no time to establish β -equilibrium and where the colliding ions are not electrically neutral. Our presentation will therefore be somewhat cursory; for more details see, e.g., the review [426].

At asymptotically large densities, we may neglect the quark masses compared to the quark chemical potential. Then, all quark flavors and colors occur in equal numbers and the system is automatically electrically and color neutral, and in β -equilibrium. As the CFL phase involves pairing of all quark colors and flavors, these conditions are maintained even in the paired state. However, as one moves towards smaller densities, the strange quark mass can

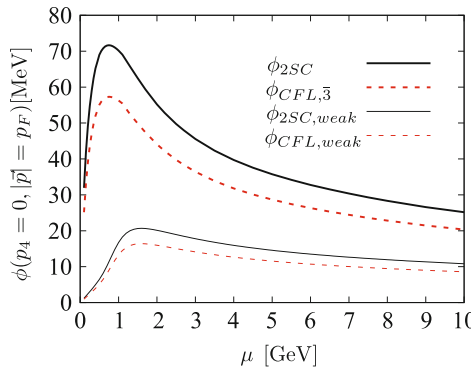


Fig. 3.41 The zero-temperature gap as a function of the quark chemical potential, for the 2SC phase (solid black curves) and the CFL phase (dashed red curves), from [403]. Thick curves are the numerical solution of the QCD gap equation, thin curves are the weak-coupling result (3.56).

no longer be neglected compared to the quark chemical potential. This, as well as the conditions of color and electric neutrality, forces the Fermi surfaces of quarks of different flavor and color apart and thus creates a difference in the numbers of the respective quarks. This exerts stress on the pairing mechanism. The system has a variety of choices to cope with this stress. In the following, we briefly list four alternatives extensively discussed in the literature. The possibility finally realized in nature will be the one with lowest free energy (highest pressure). An exhaustive comparison of the free energies (pressures) of all choices listed below has not yet been done.

1. Crystalline color superconductivity [427–431]. The underlying mechanism is analogous to the one suggested by Fulde and Ferrell [432] and, independently, Larkin and Ovchinnikov [433] in the condensed-matter context for a superconductor with magnetic impurities. Therefore, the associated color-superconducting phase is often called FFLO (or LOFF) phase. The idea is the following: the overlap between the Fermi surfaces which are forced apart by the conditions of electric and color charge neutrality and β -equilibrium can be re-established by shifting them relative to each other by a fixed momentum \mathbf{q} . The precise value of \mathbf{q} is determined from minimizing the condensation energy. Quarks which form Cooper pairs no longer have equal and opposite momenta: Cooper pairs attain a non-zero momentum. This leads to a spatial modulation of the gap parameter in the form of a plane wave, $\Phi(\mathbf{r}; \mathbf{q}) = \Phi \exp(2i\mathbf{q} \cdot \mathbf{r})$. Superimposing several such plane waves one can build crystalline structures [428]. The one with the lowest free energy is a candidate for the ground state in quark matter at intermediate densities.
2. Deformed Fermi surface (DFS) superfluidity [434]. Instead of shifting the Fermi surfaces like in the FFLO phase, one deforms them such that their overlap is increased. A simple possibility is an elliptic deformation. For a two-flavor system of up and down quarks, $\mu_{d,u} = \bar{\mu} [1 \pm \epsilon \cos^2 \theta]$, where $\epsilon \geq 0$ is a parameter that provides a prolate (oblate) deformation for the down (up) quark Fermi surface. For more details, see [434].
3. Mixed phase. In this case, quarks of that color and flavor with the smaller Fermi surface pair up completely with those of the other quark species, and the excess of the latter simply remains unpaired, i.e., forms a normal-conducting phase. The phases separate, creating a phase mixture [435]. This situation might be realized if the surface tension between normal- and superconducting phase is sufficiently small [436].
4. Gapless (breached pairing) superconductivity [410, 411, 437]. No extra mechanism like a shift or deformation of the Fermi surfaces or a formation of a mixed phase is invoked. We shall consider this case in somewhat more detail in the following.

Consider the 2SC phase where red up-quarks pair with green down-quarks. Electric neutrality forces the number of down-quarks (with an electric charge $-1/3$) to increase relative to that of up-quarks in order to balance the larger

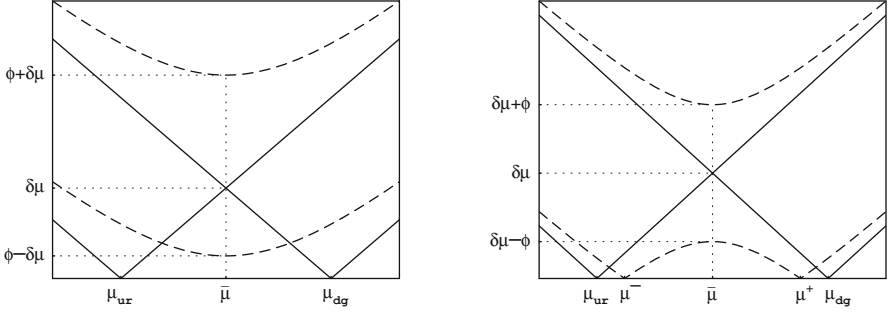


Fig. 3.42 Quasiparticle dispersion relations given by Eq. (3.60) for $\delta\mu < \phi$ (left panel) and $\delta\mu > \phi$ (right panel). Figure adapted from [411].

positive electric charge $+2/3$ of the latter. The resulting difference in particle numbers results in a mismatch of Fermi surfaces or, equivalently, in a mismatch of chemical potentials, $\mu_{dg,ur} = \bar{\mu} \pm \delta\mu$, where $\bar{\mu}$ is the average of the quark chemical potentials and $\delta\mu \geq 0$ half of their difference. The quasiparticle dispersion relations in the superconducting phase are given by

$$\epsilon_k^{\pm} = \sqrt{(k - \bar{\mu})^2 + \phi^2} \pm \delta\mu. \quad (3.60)$$

These are shown in Fig. 3.42. For $\delta\mu < \phi$, both excitation branches exhibit a gap at the “common” Fermi surface $\bar{\mu}$ (left panel). However, once the mismatch $\delta\mu$ increases beyond ϕ (right panel), the excitation branch ϵ_k^- “dips” below zero, creating two “nodes” where the excitation of quasiparticles does not cost any energy; therefore the name “gapless superconductivity”. The region between the nodes contains unpaired particles of the species with the larger Fermi surface (in this case, green down-quarks). This inspired the notion of “breached pairing superconductivity” [437]. The existence of gapless superconductivity is known for quite a while [438]. However, without the additional neutrality constraints, this state does not correspond to a minimum of the free energy but to a maximum, and is thus unstable.

In the following, we show results obtained within NJL-type models to study the phase structure of strongly interacting matter at intermediate densities. In NJL-type models, the interaction strength between quark currents is assumed to be constant; the strength between two quark-antiquark currents with scalar quantum numbers is denoted as G_S , while that between a diquark and an anti-diquark current with antitriplet quantum numbers in both flavor and color space is denoted as G_D . The latter interaction gives rise to Cooper pairing and, thus, color superconductivity. Both types of interaction are related by a Fierz transformation which yields $G_D = \frac{3}{4} G_S$ [439]. However, since the model is of phenomenological nature, it is also possible to study the influence of varying the value of G_D . Several groups have analyzed the thermodynamic properties of NJL-type models in the mean-field

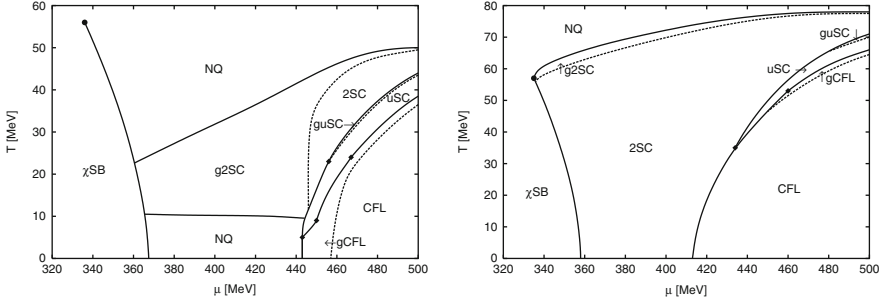


Fig. 3.43 The phase diagram of color and electrically neutral quark matter for $G_D = 0.75 G_S$ (left panel) and $G_D = G_S$ (right panel), from [408]. μ denotes quark chemical potential.

approximation [404–409]. For the sake of brevity we only report results from [408].

In Fig. 3.43 we show results for the phase diagram for the standard value $G_D = \frac{3}{4} G_S$ (left panel) and for the larger value $G_D = G_S$ (right panel). Let us first focus on the left panel and the region of small temperatures. At large values of μ , quark matter is in the CFL phase. With decreasing μ , the stress exerted on Cooper pairing by a non-zero strange quark mass and by the conditions of electric and color neutrality increases. The CFL phase gives way to the so-called gapless CFL (gCFL) phase. Here, as discussed above, some quasiparticle excitation branches feature nodes. For even smaller values of μ , the stress is too large to maintain Cooper pairs; we obtain a phase of normal, i.e., unpaired, quark matter. This phase borders the phase where chiral symmetry is spontaneously broken.

At non-zero temperature, a variety of other phases appears: next to the gCFL phase we find the so-called uSC phase, i.e., a phase where up-quarks pair with down- and with strange-quarks, but where down- and strange-quarks do not pair with each other. There is also a gapless version of this phase (guSC phase). At smaller values of μ , up-strange pairing is suppressed and we obtain the 2SC phase where only up- and down-quarks pair with each other. This phase is bordered by its gapless version (g2SC phase). At intermediate values of μ and when increasing the temperature from zero, normal quark matter first gives way to the g2SC phase and is re-established at larger temperatures. The curious fact of a color-superconducting region at intermediate, but not at zero, temperature can be explained by the observation that temperature smears out the Fermi surface and thus facilitates pairing of fermions with different Fermi surfaces. Eventually, though, increasing the temperature will destroy the Cooper pairs, and the system again enters a phase of normal quark matter.

When increasing the diquark coupling strength, the phase diagram looks qualitatively similar in the sense that the same kind of phases appear, but it differs quantitatively in the location of these phases. For $G_D = G_S$, we

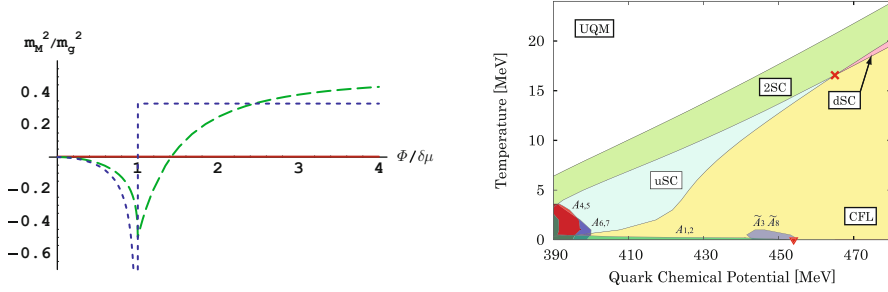


Fig. 3.44 *Left:* The gluonic Meissner masses (squared) in units of the gluon mass parameter $m_g^2 = g^2 \bar{\mu}^2 / (3\pi^2)$ as a function of $\phi/\delta\mu$ for the 2SC phase [412]. *Full red line:* gluons of adjoint color $a = 1, 2, 3$, *long-dashed green line:* $a = 4, 5, 6, 7$, *short-dashed blue line:* $a = 8$. *Right:* The phase diagram of dense quark matter. Regions where quark matter is chromomagnetically unstable are labelled by the respective gluon fields the Meissner masses of which become imaginary [441].

observe in the right panel of Fig. 3.43 that the 2SC phase occupies a larger region; it replaces the normal quark matter phase at intermediate values of μ and small temperatures. Also, the regions of the gapless phases shrink in size. The latter is naturally explained by the fact that a stronger diquark coupling increases the value of the gap, such that it remains larger than the difference in chemical potential required to neutralize the system. From Fig. 3.42 we see that this effectively prevents the formation of nodes in the dispersion relations.

It should be mentioned that the gapless phases are prone to so-called chromomagnetic instabilities [412, 440]. This means that, for decreasing values of $\phi/\delta\mu$, the gluonic Meissner masses become imaginary. The (squared) Meissner mass for gluons of adjoint color a is defined as $m_{M,a}^2 = \lim_{\omega=0, p \rightarrow 0} \Pi_{aa}^{ii}(\omega, \mathbf{p})$, where Π_{aa}^{ii} is the component of the gluon polarization tensor diagonal in color $a = 1, \dots, 8$ and spatial indices $i = x, y, z$.

For the 2SC phase, the behaviour of the (squared) Meissner masses is shown in the left panel of Fig. 3.44. For gluons of color $a = 1, 2, 3$, the Meissner masses must remain zero, since these are the gauge bosons of the residual $SU(2)_c$ symmetry in the 2SC and also the g2SC phase. However, the gluons corresponding to the broken generators of $SU(3)_c$ attain a mass. For small values of the mismatch $\delta\mu$, these are real, but become imaginary as $\delta\mu$ increases relative to the gap. Gapless quark excitations appear when $\phi = \delta\mu$. At this point, the Meissner mass of the 8th gluon becomes imaginary. However, for gluons of colors 4–7, this happens even earlier, i.e., already in the 2SC phase when $\phi = \sqrt{2} \delta\mu$. This means that the presence of gapless excitations is not a necessary condition for the appearance of the chromomagnetic instability. Vice versa, it is also not a sufficient condition: there can be gapless excitations without inducing a chromomagnetic instability [442]. This leads

to the question where in the phase diagram chromomagnetic instabilities actually occur. This has been investigated in [443–446]. One may summarize the results by stating that only the low-temperature regime of gapless phases (or of phases close to gapless phases) are subject to the chromomagnetic instability, cf. right panel of Fig. 3.44.

Nevertheless, the chromomagnetic instability poses a principle problem in the sense that negative squared Meissner masses indicate that the system is not in an absolute minimum of the free energy, i.e., not in the true ground state. Candidates for the true ground state could be either one of the possibilities 1.–3. discussed above, or some other phase, such as the at presently intensely debated gluonic phase which resolves the chromomagnetic instability of the 2SC phase [447]. In the gluonic phase, the spatial components of gluon fields corresponding to broken generators of $SU(3)_c$ condense, breaking the rotational symmetry and the residual $SU(2)_c$ gauge symmetry of the system. The analogue of the gluonic phase for the three-flavor case has not yet been studied, but it certainly bears a relationship to a phase with spontaneous creation of meson supercurrents suggested in [448, 449], which was shown to resolve the chromomagnetic instability of the gCFL phase. The true ground state of the system must be identified by comparing the free energies of all possible states. This is an ambitious project which has up to date not been concluded. We mention in passing that a (not entirely approximation-free) comparison of the free energies of the g2SC, FFLO, and gluonic phase has been made in [450].

3.5.3 Color superconductivity at low densities: *Bose-Einstein condensation of diquark molecules*

As mentioned in the introductory section, in the low-density region where the strong coupling constant becomes large, quark Cooper pairs shrink in size. Once the size becomes of the order of the interparticle distance, one may regard them as diquark molecules. Under certain conditions, these molecules may undergo Bose-Einstein condensation (BEC). Note that the situation is closely related to condensation of ultracold fermionic atoms intensely studied in atomic physics [414]. There, the coupling strength can be varied experimentally by tuning an external magnetic field through a Feshbach resonance. Note that the density still has to be above the critical value for deconfinement; below that, any quark molecule must be colorless, which a diquark is not.

Diquark molecules can be investigated in the framework of NJL-type models, but that requires to go beyond the mean-field approximation by including correlations of the diquark fields, see [451–454] for technical details. In this way, one can study where diquark molecule exist in the $(T\mu)$ -diagram, where they dissociate, and under which conditions they possibly form a Bose-

Einstein condensate. In the following we report results from an independent study [455] which comes to the same conclusion as [452].

In the left panel of Fig. 3.45 we show the phase diagram of quark matter for the case $G_D = \frac{3}{4} G_S$. To get a feeling for the densities related to the relevant quark chemical potentials we display in Fig. 3.46 for vanishing temperature the relation between quark chemical potential and baryon density. Full lines in the left panel of Fig. 3.45 show the phase boundaries of the 2SC and CFL phases, respectively. The dashed lines labelled T_{diss}^3 and $T_{\text{diss}}^{1,2}$ show the dissociation temperatures for diquark molecules made exclusively from light quarks and from a light and a strange quark, respectively. The thin dotted lines marked $\mu = M_3$ and $\mu = M_{1,2}$ show where the diquark mass equals the diquark chemical potential; to the left of these lines, BEC is possible, provided one is in the superconducting phase. This condition is not fulfilled for $G_D = \frac{3}{4} G_S$.

When increasing the diquark coupling strength, the picture changes, cf. the right panel of Fig. 3.45. As expected, the region where quark matter is a color superconductor becomes larger. Moreover, the curve where $\mu = M_3$ now extends into the 2SC phase. In the shaded region the conditions for the formation of a Bose-Einstein condensate of light diquark molecules are fulfilled. Although the line $\mu = M_{1,2}$ also extends into the 2SC phase, there is no condensate of qs diquarks, as one is not in the CFL phase. We conclude that BEC of diquark molecules is possible only if the diquark coupling strength becomes substantially larger than the standard value $G_D = \frac{3}{4} G_S$. Finally, let us note that BEC of diquark molecules has also been studied in [456, 457] in a simpler, effective field-theoretical description for the diquark fields. Further studies are certainly needed to clarify under which conditions diquark molecules may undergo BEC and whether these conditions are met in situations that can be explored in heavy-ion collisions or are of relevance for the physics of compact stellar objects.

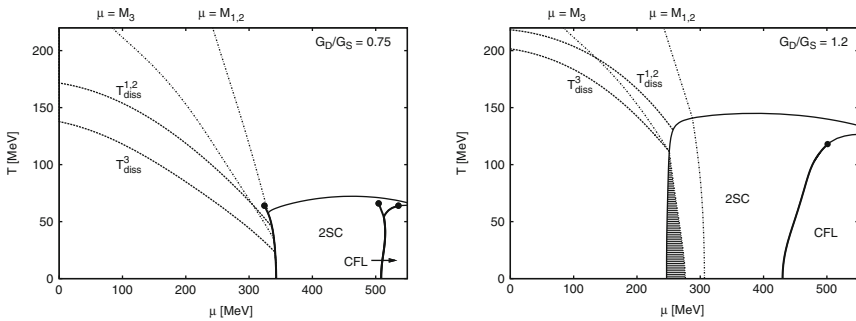


Fig. 3.45 The quark matter phase diagram for $G_D = \frac{3}{4} G_S$ (left) and for $G_D = 1.2 G_S$ (right). For an explanation of the various lines see text. μ denotes the quark chemical potential.

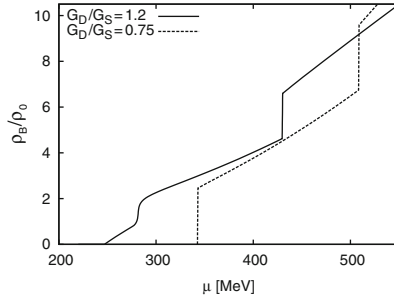


Fig. 3.46 Relation between quark chemical potential μ and baryon density for vanishing temperature in the NJL model for different ratios of G_D/G_S . ρ_0 denotes nuclear saturation density.

With this review of color superconducting phases we have finished our scan through the QCD phase diagram. In the next chapter we shall focus on the transition region from hadronic matter to the quark-gluon plasma and present several models designed to describe various aspects of this particular part of the phase diagram of QCD.

Chapter 4

Model descriptions of strongly interacting matter near deconfinement

In the present chapter various models are presented which were designed to describe the region around the transition from hadronic to quark-gluon matter.

4.1 Statistical model and particle production in heavy-ion collisions

The Statistical Thermal Model is an alternative approach to dynamical transport calculations to describe particle production yields in heavy-ion collisions [458, 459]. (For a recent analysis see also [460, 461] and the Part IV of the present book.) The main assumption of thermal models is that the fireball created in heavy-ion collisions is of thermal origin. At chemical freezeout one expects that particles are produced from a thermal source that is characterized by its volume and temperature. In addition this fireball is constrained by the conservation laws of all relevant quantum numbers that are carried by hadrons. In nucleus–nucleus collisions one needs to implement the conservation of baryon number, electric charge and strangeness. One also assumes that with respect to conservation laws the collision fireball appears at, or very near, chemical equilibrium.

In statistical physics the conservation laws can be implemented in the grand canonical or canonical ensemble [458]. From the model comparison with experimental data obtained in heavy-ion collisions it will be clear that the electric charge and baryon number conservation can be included on the grand canonical level where they are controlled in the statistical operator through the corresponding chemical potentials [458, 459]. Strangeness conservation must be, however, introduced exactly within the canonical ensemble [458]. This is particularly the case if one considers strangeness production in heavy-ion collisions at SIS up to AGS energies [462, 463]. There, strange particles and antiparticles are very rarely produced and are strongly correlated

to preserve strangeness conservation. Consequently, the thermal phase space available for strangeness production is suppressed [458, 462–471]. This suppression is effectively described by the exact strangeness conservation through the canonical formulation of the partition function [458].

In the following we will summarize the basic concepts in the formulation of the Statistical Thermal Model with strangeness conservation implemented in the grand canonical and canonical ensemble. Then, we will discuss a model comparison with experimental data for particle production yields in heavy-ion collisions in a broad energy range from SIS up to RHIC. We will show the systematics in the energy dependence of the model parameters and discuss the properties of different particle excitation functions. It will turn out that the Statistical Thermal Model provides an excellent description of particle production in heavy-ion collisions.

4.1.1 Statistical approach – grand canonical formalism

In the Statistical Thermal Model the basic quantity that describes thermodynamic properties of a medium is the partition function $Z(T, V)$. In the Grand Canonical (GC) ensemble

$$Z^{GC}(T, V, \mu_Q) = \text{Tr}[e^{-\beta(H - \sum_i \mu_{Q_i} Q_i)}], \quad (4.1)$$

where H is the Hamiltonian of the system, Q_i are the conserved charges and μ_{Q_i} are the chemical potentials that are introduced to guarantee conservation of all charges in a system. Finally $\beta = 1/T$ is the inverse temperature.

In the application of the Statistical Thermal Model to particle production in heavy-ion collisions the Hamiltonian is taken such as to describe a non-interacting hadron resonance gas. In this case H is just the sum of kinetic energies of relativistic Fermi and Bose particles of mass m_i . The main motivation of using such a Hamiltonian is that it contains all relevant degrees of freedom of the confined phase of strongly interacting matter and implicitly includes interactions that result in resonance formation [464]. In high density medium a possible repulsion between hadrons is modelled as the Van der Waals-type interaction. Details of such implementation can be found in [472, 473].

In a strongly interacting medium, one includes the conservation of electric charge, baryon number and strangeness. The GC partition function (4.1) of a hadron resonance gas can then be written as the sum of partition functions $\ln Z_i$ of all known hadrons and resonances

$$\ln Z(T, V, \boldsymbol{\mu}) = \sum_i \ln Z_i(T, V, \boldsymbol{\mu}), \quad (4.2)$$

where $\epsilon_i = \sqrt{p^2 + m_i^2}$ and $\boldsymbol{\mu} = (\mu_b, \mu_S, \mu_Q)$ with the chemical potentials μ_i related to baryon number, strangeness and electric charge, respectively.

For particle i of strangeness S_i , baryon number B_i , electric charge Q_i and spin-isospin degeneracy factor g_i , one gets for a single-particle contribution

$$\ln Z_i(T, V, \boldsymbol{\mu}) = \frac{V g_i}{2\pi^2} \int_0^\infty \pm p^2 dp \ln[1 \pm \lambda_i \exp(-\beta \epsilon_i)], \quad (4.3)$$

with $(+)$ for fermions, $(-)$ for bosons and fugacity

$$\lambda_i(T, \boldsymbol{\mu}) = \exp\left(\frac{B_i \mu_b + S_i \mu_S + Q_i \mu_Q}{T}\right). \quad (4.4)$$

Expanding the logarithm and performing the momentum integration in Eq. (4.3) we obtain

$$\ln Z_i(T, V, \boldsymbol{\mu}) = \frac{V T g_i}{2\pi^2} \sum_{k=1}^{\infty} \frac{(\pm 1)^{k+1}}{k^2} \lambda_i^k m_i^2 K_2\left(\frac{k m_i}{T}\right), \quad (4.5)$$

where K_2 is the modified Bessel function and the upper sign is for bosons and lower for fermions. The first term in Eq. (4.5) corresponds to the Boltzmann approximation. The density of particle i is given by

$$n_i(T, \boldsymbol{\mu}) = \frac{\langle N_i \rangle}{V} = \frac{T g_i}{2\pi^2} \sum_{k=1}^{\infty} \frac{(\pm 1)^{k+1}}{k} \lambda_i^k m_i^2 K_2\left(\frac{k m_i}{T}\right). \quad (4.6)$$

The partition function (4.2) together with (4.3) is the basic quantity that describes thermodynamic properties of a fireball composed of hadrons and resonances being in thermal and chemical equilibrium. In view of further application of this statistical operator to particle productions in heavy-ion collisions it is of particular importance to account for resonance contributions through the decays into lighter particles. The average number $\langle N_i \rangle$ of particles i in volume V and temperature T , that carries strangeness S_i , baryon number B_i , and electric charge Q_i , is obtained from Eq. (4.2) as

$$\langle N_i \rangle(T, \boldsymbol{\mu}) = \langle N_i \rangle^{th}(T, \boldsymbol{\mu}) + \sum_j \Gamma_{j \rightarrow i} \langle N_j \rangle^{th,R}(T, \boldsymbol{\mu}) \quad (4.7)$$

where the first term is the thermal average number of particle i and the second term describes overall resonance contributions to the particle multiplicity of species i . This term is taken as a sum of all resonances that decay into particle i . The $\Gamma_{j \rightarrow i}$ is the corresponding decay branching ratio of $j \rightarrow i$. The thermal yields of particles $\langle N_i \rangle^{th}$ and resonances $\langle N_i \rangle^{th,R}$ in Eq. (4.7) are obtained from Eq. (4.6).

In the high-density regime, that is for large T and/or μ_b , the repulsive interactions of hadrons should be included in the partition function (4.2). To incorporate the repulsion at short distances one usually uses a hard-core

description by implementing excluded-volume corrections. In a thermodynamically consistent approach [472, 473] these corrections lead to a shift of the baryo-chemical potential. The repulsive interactions are particularly important when discussing observables of density type. Particle density ratios, however, are only weakly affected by these repulsive corrections.

At lower energies, in practice for $T < 100$ MeV, also the widths of the resonances have to be included [458] in Eq. (4.7). Assuming the Boltzmann statistics and the Breit-Wigner resonance distribution one replaces the partition function in Eq. (4.5) by

$$\ln Z_R = N \frac{V d_R}{2\pi^2} T \exp[(B_R \mu_b + Q_R \mu_Q + S_R \mu_S)/T] \int_{s_{min}}^{s_{max}} ds s K_2(\sqrt{s}/T) \frac{1}{\pi} \frac{m_R \Gamma_R}{(s - m_R^2)^2 + m_R^2 \Gamma_R^2}, \quad (4.8)$$

where s_{min} is chosen to be the threshold value for the resonance decay and $\sqrt{s_{max}} \sim m_R + 2\Gamma_R$. The normalization constant N is adjusted such that the integral over the Breit-Wigner factor gives 1.

The partition function (4.2) depends in general on five parameters. However, only three are independent, since the isospin asymmetry in the initial state fixes the charge chemical potential and the strangeness neutrality condition eliminates the strange chemical potential. Thus, in the GC formulation of charge conservation and on the level of particle multiplicity *ratios* we are only left with temperature T and baryo-chemical potential μ_b as independent parameters.

4.1.2 Canonical formulation of strangeness conservation

If in the collision fireball the number of strange–antistrange particle pairs is small, then the implementation of strangeness conservation in the statistical operator has to be done exactly, implying the use of the canonical ensemble.

The canonical partition function of a hadron resonance gas in a thermal system with total strangeness S is obtained by the projection method [458] from the generating function

$$Z_S = \frac{1}{2\pi} \int_0^{2\pi} d\phi e^{-iS\phi} \tilde{Z}(T, V, \phi). \quad (4.9)$$

The generating function \tilde{Z} is connected with the grand canonical partition function (GC) through the Wick rotation of the strange chemical potential [458]

$$\tilde{Z}(T, V, \mu_b, \mu_Q, \phi) := Z^{GC}(T, V, \mu_b, \mu_Q, e^{\mu_S/T} \rightarrow e^{i\phi}) \quad (4.10)$$

For the sake of simplicity, we use the classical statistics, i.e. we assume a temperature and density regime where all particles can be treated using Boltzmann statistics. In this case

$$\frac{1}{V} \ln Z^{GC} = \sum_k Z_k^1 \exp(S_k \mu_S) \quad (4.11)$$

with the one-particle partition function

$$Z_k^1 = \frac{g_k}{2\pi^2} m_k^2 T K_2(m_k/T) \exp(B_k \mu_b + Q_k \mu_Q) \quad (4.12)$$

where the sum in Eq. (4.11) is taken over all particles and resonances of mass m_k , spin-isospin degeneracy factor g_k , baryon number B_k , electric charge Q_k and strangeness S_k .

The partition function (4.10) together with (4.11) describes the thermodynamic properties of the hadron resonance gas with strangeness conservation implemented exactly in the canonical ensemble. To calculate the density n_k of particle species k from this partition function is quite straightforward. It amounts to the replacement

$$Z_k^1 \mapsto \lambda_k Z_k^1 \quad (4.13)$$

of the corresponding one-particle partition function in the Eq. (4.11) and taking the derivative with respect to the particle fugacity λ_k as

$$n_k^C := \lambda_k \left. \frac{\partial}{\partial \lambda_k} \ln Z_S(\lambda_k) \right|_{\lambda_k=1}. \quad (4.14)$$

The integral representation of the partition function (4.9) is not convenient for the numerical analysis as the integrand is a strongly oscillating function. It was shown, however, that the integration in Eq. (4.9) can be done exactly leading to the following result for the partition function [474]

$$Z_{S=0}^C = e^{S_0} \sum_{n=-\infty}^{\infty} \sum_{p=-\infty}^{\infty} a_3^p a_2^n a_1^{-2n-3p} I_n(x_2) I_p(x_3) I_{-2n-3p}(x_1), \quad (4.15)$$

where

$$a_i = \sqrt{S_i/S_{-i}}, \quad x_i = 2V \sqrt{S_i S_{-i}}, \quad (4.16)$$

and S_i is the sum of all Z_k^1 partition functions (4.12) for particle species k carrying strangeness $S_k = i$. The $I_n(x)$ in (4.15) are the modified Bessel functions. The resulting particle densities n_i are obtained from Eqs. (4.14) and (4.15). For a particle k having the strangeness s

$$n_k^s = \frac{Z_k^1}{Z_{S=0}^C} \sum_{n=-\infty}^{\infty} \sum_{p=-\infty}^{\infty} a_3^p a_2^n a_1^{-2n-3p-s} I_n(x_2) I_p(x_3) I_{-2n-3p-s}(x_1). \quad (4.17)$$

In the canonical formulation of strangeness conservation the density of strange particles is explicitly volume dependent through the arguments x_i of the Bessel functions in Eq. (4.17). In the application of Eq. (4.17) to the description of particle production in heavy-ion collisions this volume parameter was interpreted as the strangeness correlation volume which depends on the number of participants [468–471]. For large V and for high enough temperature such that all $x_i \gg 1$ the canonical result (4.17) is converging to its GC value where strangeness conservation is controlled by the corresponding chemical potential [458]. Obviously, in the GC limit particle densities are not any more dependent on the volume parameter. In heavy-ion collisions the GC approximation was found to be adequate for energies beyond AGS [458]. For lower collision energies, in particular for SIS, the suppression due to canonical effects can even exceed an order of magnitude for the yields of $S = \pm 1$ strange particles.

The Statistical Thermal Model, outlined above, was applied to describe particle yields in heavy ion collisions. The model was compared with all available experimental data obtained in the energy range from SIS up to LHC energy. Hadron multiplicities ranging from pions to omega baryons and their ratios were used to verify that there is a set of thermal parameters (T, μ_b) which simultaneously reproduces all measured yields. In the following section we present the most recent analysis of particle production in central nucleus–nucleus collisions at SIS, AGS, SPS and RHIC energies.

4.1.3 Model description of experimental data

The Statistical Thermal Model is a unique tool in the attempt to quantify from the experimental point of view the features of the phase diagram of hadronic matter [475, 476]. An analysis of the energy dependence of the thermal parameters extracted from fits of the experimental data [477–480], temperature (T) and baryo-chemical potential (μ_b), established the “line of chemical freeze-out” [481]. These data were subsequently interpreted in terms of an universal condition for chemical freeze-out [482, 483].

The values of T and μ_b obtained from the most comprehensive thermal fits of the experimental data [459, 460] are shown in a phase diagram of hadronic and quark-gluon matter in Fig. 4.1. Full points are from fits of yields at midrapidity, open points are from fits of 4π yields. An important observation about the phase diagram is that, for beam energies larger than 30–40 AGeV, the thermal parameters are in the vicinity of the phase boundary as calculated using lattice QCD (LQCD) [192]. However, it is important to notice that the critical temperature at $\mu_b=0$ from LQCD calculations is presently

subject to serious disagreements between various approaches [186, 187]. The disagreement in the quoted values of 151 and 192 MeV [186, 187] is well beyond the overall errors of the calculations (see also the discussion in Sect. 3.2).

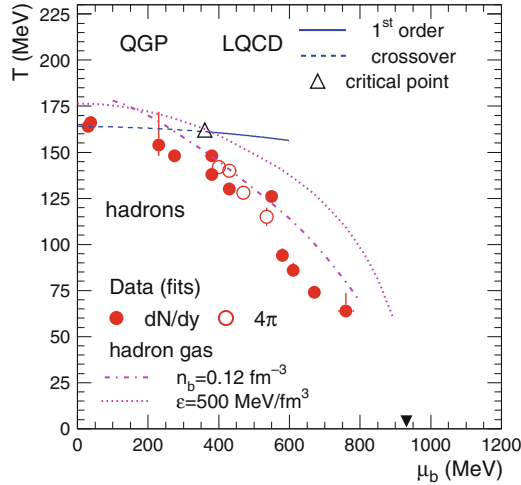


Fig. 4.1 The phase diagram of hadronic and quark-gluon matter in the T - μ_b plane. The experimental values for the chemical freeze-out are shown together with results of lattice QCD calculations [192]. The predicted [192] critical point is marked by the *open triangle*. Also included are calculations of freeze-out curves for a hadron gas at constant energy density ($\varepsilon=500$ MeV/fm³) and at constant total baryon density ($n_b=0.12$ fm⁻³). The *full triangle* indicates the location of ground state nuclear matter (atomic nuclei).

Based on the LQCD results of Fodor and Katz [192] shown in Fig. 4.1, the experimental freeze-out points are located in the vicinity of the critical point [475]. It was pointed out recently [476] that the existence of a critical point for $\mu_b < 500$ MeV requires a fine tuning of the (light) quarks masses within 5%. However, it is important to recognize that serious open problems of LQCD [476] need to be solved before one could address quantitatively such a delicate possibility. Nevertheless, it is interesting to speculate whether the deviations from the thermal model (including rather poor-quality fits) which we have encountered for the SPS energies are a hint for the critical point. It is expected that, in the (broad) vicinity of the critical (end)point the thermal model would not work [484, 485]. Thermal fits including fluctuations have been already performed [486]. Unfortunately, the present experimental situation, namely the level of disagreement between data, does not allow any firm conclusion on the interesting issue of the critical point.

Also included in Fig. 4.1 are calculations of freeze-out curves for a hadron gas at constant energy density ($\varepsilon = 500$ MeV/fm³) and at constant total baryon density ($n_b = 0.12$ fm⁻³) [487, 488]. The freeze-out points which are

departing from the LQCD phase boundary are approximately described by the curve of a hadron gas at constant baryon density. An earlier proposed freeze-out criterion corresponds to an average energy per average number of hadrons of approximately 1 GeV [482, 483]. A comparison of various freeze-out criteria was recently done in [489], which showed that all are identical except for large and small μ_b values. All are smooth curves and consequently not consistent with the new results presented here, which exhibit a rather steep trend at intermediate μ_b values. However, the errors need to be improved before one can confidently rule out any (smooth) universal freeze-out criterion. An exciting possibility is that the rather abrupt turn-over in the freeze-out points near $\mu_b=400$ MeV is caused by the approach to the QCD phase boundary.

The underlying assumption of the thermal model used to extract the (T, μ_b) values is equilibrium at chemical freeze-out. A natural question then is how the equilibrium is achieved? The answer obviously cannot come from within the framework of the thermal model. It has been argued that the QGP itself and the “deus ex machina” of phase space filling during hadronization are playing the crucial roles in achieving thermalization in high-energy nucleus–nucleus collisions [490]. More recently it was demonstrated that passing through the phase transition leads to multiparticle scattering of Goldstone bosons which drives even (multi)strange baryons rapidly into equilibration [491], providing a natural explanation for the observation that the chemical freeze-out line reaches the phase boundary for small values of μ_b . The situation is less well understood for $\mu_b > 400$ MeV and needs further investigation.

In Fig. 4.2 we show the energy dependence of T and μ_b values from the thermal fits of various groups [459, 462, 463, 486, 492–494]. The temperature T exhibits a sharp rise up to $\sqrt{s_{NN}} \simeq 7\text{--}8$ GeV, while μ_b sharply decreases all the way up to RHIC energies. In general, all results agree, with one notable exception, the results of Letessier and Rafelski [494]. The observed difference may arise from the usage in their work of seven free parameters, including, besides strangeness fugacity and suppression factor (γ_S), a light-quark occupancy factor (γ_q) and an isospin fugacity. The non-monotonic change in γ_q and γ_S as a function of energy determines the temperature extracted in [494]. To alleviate the poor quality of the fits at SPS energies, the model of Dumitru et al. [486], introducing an inhomogeneous freeze-out scenario, goes beyond other thermal models.

We have parametrized the results from the fits of mid-rapidity data [460] as a function of $\sqrt{s_{NN}}$ (in GeV) with the following expressions:

$$T[\text{MeV}] = T_{lim} \frac{1}{1 + \exp(2.60 - \ln(\sqrt{s_{NN}}(\text{GeV}))/0.45)}, \quad (4.18)$$

$$\mu_b[\text{MeV}] = \frac{a}{1 + b\sqrt{s_{NN}}(\text{GeV})}, \quad (4.19)$$

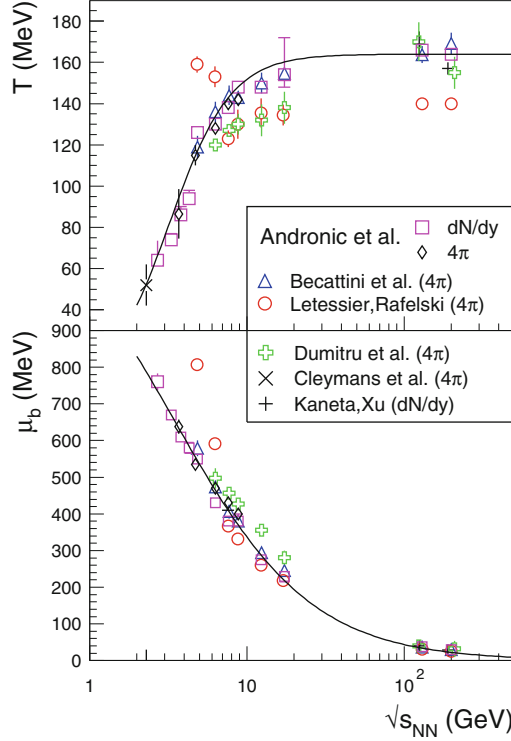


Fig. 4.2 The energy dependence of temperature and baryo-chemical potential. The *lines* are parametrizations for T and μ_b (see text).

where $T_{lim} = 164 \pm 4$ MeV and the parameters $a = 1,307 \pm 120$ MeV and $b = 0.288 \pm 0.049$ GeV $^{-1}$ are the results of a fit ($\chi^2/N_{df} = 0.48/8$). The μ_b parametrization is the one proposed in [474], but with different parameters to better fit the newly obtained μ_b values [459].

We now briefly turn to another interesting parameter which is (either implicitly or explicitly) determined in the course of thermal-model analyses. The volume at chemical freeze-out (corresponding to a slice of one unit of rapidity, dV/dy) is shown in Fig. 4.3 as a function of energy. The values extracted directly from the fits of particle yields are compared to the values obtained by dividing measured charged particle yields with calculated densities (based on the above parametrization of T and μ_b ; note that for the AGS energies of 2–8 AGeV the values of T corresponding to the upper limit of the systematic error were used instead). As expected, the two methods give identical results, with the exception of a small discrepancy for the lowest energies. The chemical freeze-out volume is compared to the kinetic freeze-out volume extracted from Hanbury Brown and Twiss (HBT) measurements, V_{HBT} [495, 496]. While the bias towards unphysically large volumes seen at

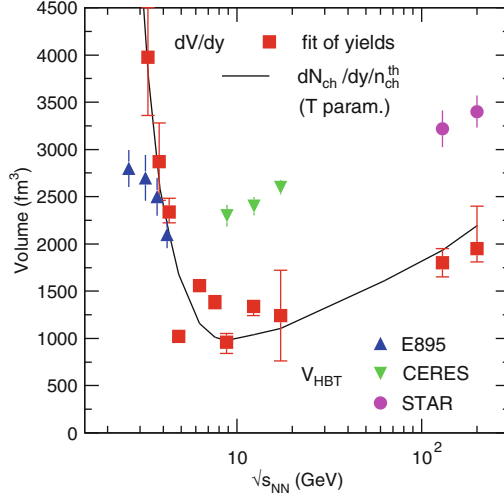


Fig. 4.3 Energy dependence of the volume for central collisions ($N_{part}=350$). The chemical freeze-out volume for one unit of rapidity, dV/dy [461], is compared to the kinetic freeze-out volume from HBT measurements, V_{HBT} [495, 496].

the energies of 2–8 AGeV is not completely understood, it is clear that the volume at kinetic freeze-out should not be exceeded. It appears that the volume at chemical freeze-out does exhibit a similar non-monotonic behavior [497] as the volume at kinetic freeze-out, a remarkable result considering that the latter is determined by a completely different procedure. A minimum is observed around $\sqrt{s_{NN}} \simeq 6$ GeV, followed by a logarithmic increase as a function of $\sqrt{s_{NN}}$.

Using the parametrizations of the chemical freeze-out parameters derived from the fits of experimental data at mid-rapidity, Eqs. (4.18) and (4.19), we calculate the energy dependence of various hadron ratios. No contribution from weak decay feed-down is included in the model calculations as well as in the data. Within the smoothing hypothesis implied by the parametrizations, the model has interpolative and extrapolative predictive power.

The comparison of the measured and calculated excitation functions for hadron abundances with respect to pions is shown in Fig. 4.4. The ratios shown in Fig. 4.4 reflect the evolution of the fireball composition at freeze-out as a function of energy. The steep decrease of the p/π^+ ratio directly reflects the decrease as a function of energy of stopping of the incoming protons, implying a decrease of μ_b . The increase of pion production also plays a role in this ratio. Beyond $\sqrt{s_{NN}} \simeq 100$ GeV, the flattening is a consequence of the dominance of newly created baryons. The steep variation of the K^+/π^+ and K^-/π^- ratios at the lowest energies reflects the threshold for strangeness production, determined in the model by the steep increase of

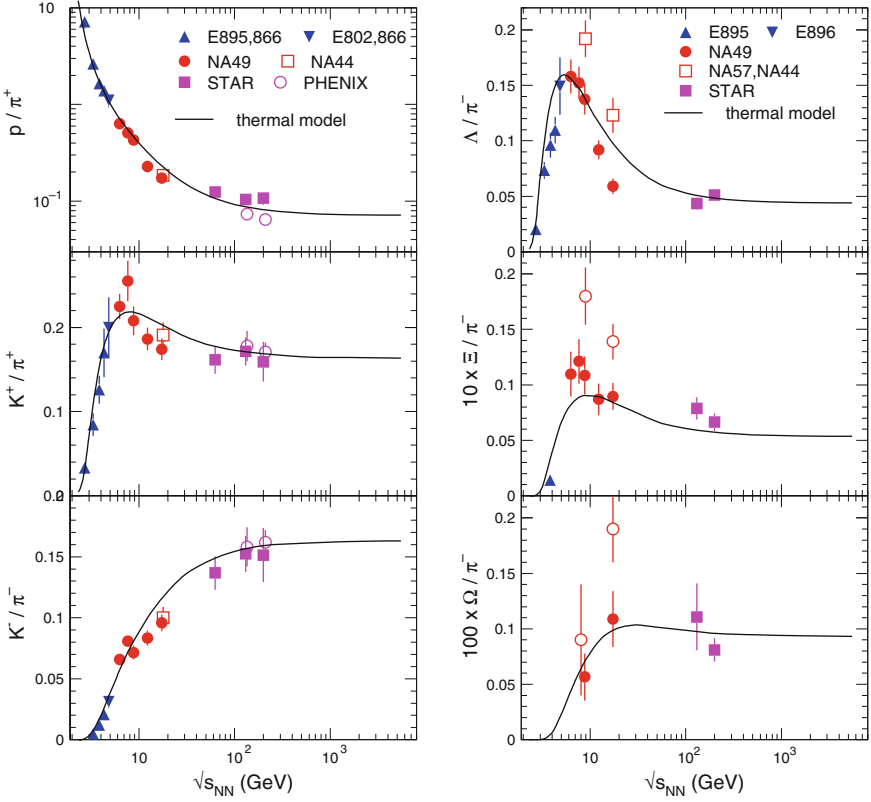


Fig. 4.4 The energy dependence of hadron yields relative to pions. In the *right panel*, note the scaling factors of 10 and 100 for the Ξ^-/π^- and Ω^-/π^- ratios, respectively. The measured yields at midrapidity are compared to the thermal-model calculations of [461].

the temperature. The canonical suppression plays an important role as well. While the ratio K^-/π^- shows a monotonic increase with energy, followed by a saturation, essentially determined by the temperature (as both particles are newly created), the ratio K^+/π^+ shows a characteristic broad peak around $\sqrt{s_{NN}} \simeq 8$ GeV, which is much discussed as a signature for the onset of QGP [498–500]. Recently, as a consequence of a more complete mass spectrum employed in the model calculations, the agreement between the data and model was substantially improved [460], as seen in Fig. 4.4. As the K^+ contains a u valence quark, which may come from the initial nucleons, its yield is the convolution of two competing contributions as a function of energy: (i) the decreasing net light quark content and (ii) the increasing production of quark-antiquark pairs. The peak in the K^+/π^+ ratio occurs naturally in the thermal model [474, 501], but is broader and has to be seen in the context

of other strange-hadron yields [501] (right panel of Fig. 4.4). It appears that, at the SPS energies of 80 and 158 AGeV, the yields of kaons and protons relative to pions are systematically below the thermal model predictions.

The energy dependence of the relative hyperon yields, Λ/π^- , Ξ^-/π^- and Ω^-/π^- , shown in the right panel of Fig. 4.4, reveals the presence of characteristic peak structures, already noted in [474]. Their strength and location follows a mass hierarchy, recently discussed by Cleymans et al. [501]. The peaks are less pronounced and located at larger energies ($\sqrt{s_{NN}} \simeq 5, 10$ and 20 GeV) the more massive the hyperon species. This results from an interplay between the baryo-chemical potential (presence of the light quarks from the initial nucleons) and temperature. The agreement between the model and the data is good at AGS and RHIC energies, while at SPS the situation is more complex.

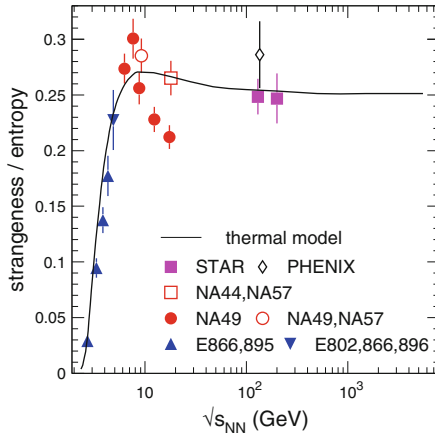


Fig. 4.5 Energy dependence of strangeness to entropy ratio (see text).

A more global way to represent the ratio of strange to non-strange hadrons is the strangeness (σ) to entropy (S) ratio. Its excitation function is presented in Fig. 4.5. We adopt an experiment-oriented construction of the two quantities [459], which we consistently employ for the model as well, calculated from the yields at mid-rapidity as:

$$\sigma = 2 \times (K^+ + K^-) + 1.54 \times (\Lambda + \bar{\Lambda}), \quad S = 1.5 \times (\pi^+ + \pi^-) + 2 \times \bar{p}. \quad (4.20)$$

The strangeness has in principle to be complemented with the yields of ϕ , Ξ and Ω (and $\bar{\Xi}$ and $\bar{\Omega}$), but, since the measurements for these yields are scarce (as seen in Fig. 4.4), we have chosen to leave them out for the

strangeness count. The ratio strangeness/entropy is well reproduced by the model, with the exception of the data at SPS, where the NA49 data exhibit a sharper peak than predicted by the model. This feature is not supported by the NA57 and NA44 combined data, which are in agreement with the model.

The parametrizations of T and μ_b as a function of energy allow to assess and understand trends visible in the experimental data. In particular, we have discussed for the yields of strange and multi-strange hadrons relative to pions the resulting non-monotonic energy dependence, where the thermal model describes the main features observed in the data, but not the details. It has been pointed out within a thermal-model analysis that scanning the energy one encounters a transition from baryon- to meson-dominated freeze-out [501], with its associated fingerprint on the characteristics of hadron yields, also evidenced earlier [474]. This transition, as manifested in the peaks observed in Figs. 4.4 and 4.5, appears to take place in the energy range of the CBM experiment.

4.2 Hadronic resonances – important degrees of freedom below deconfinement

In Sect. 3.2 the lattice gauge theory (LGT) approach was shown to be a powerful method to describe thermodynamics of QCD at finite temperature and density. It is today the only approach that can give quantitative information on the phase structure and the critical properties of the QCD medium in a broad range of thermal parameters. The LGT results are also the basis for modelling the QCD thermodynamics.

There are approaches to understand the thermodynamics of strongly interacting matter in terms of low energy effective theories, i.e. chiral perturbation theory and effective chiral models (see Sects. 2.1, 4.5). The strength of these approaches is that they incorporate the correct symmetries of the QCD Lagrangian and thus have a chance to predict the universal properties, e.g. the order of the phase transition or the value of the critical exponents, in the chiral limit of QCD. They, however, generally ignore the contributions of heavier resonances to the QCD thermodynamics which might be crucial to quantify the equation of state in confined phase of QCD.

Recently, progress has been made to develop and link an improved perturbation theory of QCD with lattice data on the equation of state in the deconfined phase (see Sect. 3.1). In addition different phenomenological models have been proposed to describe thermodynamics of QGP on the basis of actual LGT findings (see Sect. 4.3).

In this section we discuss in how far the equation of state obtained on the lattice and restricted to confined phase can be understood within hadron resonance gas thermodynamics. In this context we first formulate the hadron resonance gas model with particular emphases to fluctuations of conserved

charges. We will then compare the model predictions [107, 185, 199, 502] with lattice results [130, 138, 156] on the equation of state and different susceptibilities obtained at finite chemical potential. We show that the LGT results are quite well consistent with the hadron resonance gas model expectations.

4.2.1 Charge density fluctuations in a hadronic medium

To describe thermodynamic properties and thermal fluctuations related with conserved charges in hadronic medium at finite chemical potential we apply the partition function of hadron resonance gas (HRG).

At finite quark chemical potential the HRG-pressure P is expressed as the sum of all known mesons and baryons

$$P(T, \mu_u, \mu_d) = P^M(T, \mu_u, \mu_d) + P^B(T, \mu_u, \mu_d) \quad (4.21)$$

where μ_u and μ_d are the up and down quark chemical potentials.

Introducing the quark number μ_q and isovector μ_I chemical potentials

$$\mu_q = \frac{\mu_u + \mu_d}{2} \quad , \quad \mu_I = \frac{\mu_u - \mu_d}{2} \quad (4.22)$$

the contribution of mesons, baryons and their resonances in Eq. (4.21) is obtained in the compact form. For the Boltzmann thermal particle momentum distribution

$$\frac{P^M(T, \mu_I)}{T^4} = \sum_i F(T, m_i) \cosh \frac{2I_i^{(3)} \mu_I}{T} \quad (4.23)$$

where the sum is taken over all non-strange mesons¹ with $I_i^{(3)}$ being the third component of the isospin of the species i . Neglecting the mass difference among isospin partners the meson contribution is due to isosinglet $G^{(1)}$ ($I_i^{(3)} = 0$) and isotriplet $G^{(3)}$ ($I_i^{(3)} = \pm 1$) mesons. Thus,

$$\frac{P^M(T, \mu_I)}{T^4} = G^{(1)}(T) + \frac{1}{3} G^{(3)}(2 \cosh(\frac{2\mu_I}{T}) + 1). \quad (4.24)$$

For non-strange baryons and their resonances

¹ We have neglected the contribution of strange particles to hadronic pressure. This should be considered as an approximation of the two flavor QCD thermodynamics in a confined phase.

$$\frac{P^B(T, \mu_q, \mu_I)}{T^4} = \sum_i F(T, m_i) \cosh \frac{3\mu_q + 2I_i^{(3)}\mu_I}{T}. \quad (4.25)$$

The above pressure gets the contributions from isodoublet $F^{(2)}$ ($I_i^{(3)} = \pm 1/2$) and isoquartet $F^{(4)}$ ($I_i^{(3)} = (\pm 1/2, \pm 3/2)$) baryons. Therefore the total baryonic pressure

$$\begin{aligned} \frac{P^B(T, \mu_I)}{T^4} &= F^{(2)} \cosh\left(\frac{3\mu_q}{T}\right) \cosh\left(\frac{\mu_I}{T}\right) \\ &+ \frac{1}{2} F^{(4)} \cosh\left(\frac{3\mu_q}{T}\right) [\cosh\left(\frac{\mu_I}{T}\right) + \cosh\left(\frac{3\mu_I}{T}\right)]. \end{aligned} \quad (4.26)$$

The function $F(T, m_i)$ in Eqs. (4.23), (4.24), (4.25), and (4.26) describes the thermal occupancy of particles of mass m_i and spin degeneracy factor d_i

$$F(T, m_i) = \frac{d_i}{\pi^2} \left(\frac{m_i}{T}\right)^2 K_2\left(\frac{m_i}{T}\right) \quad . \quad (4.27)$$

The fluctuations of the globally conserved charges can be expressed through derivative of pressure with respect to the associated chemical potentials. In particular, the quark number χ_q , the isovector χ_I , and the electric charge χ^C susceptibilities, related with the baryon number, isospin and charge conservation are obtained from

$$\chi_q \equiv \frac{\partial^2 P}{\partial \mu_q^2}, \quad \chi_I \equiv \frac{\partial^2 P}{\partial \mu_I^2}, \quad \chi^C = \frac{1}{36} \chi_q + \frac{1}{4} \chi_I + \frac{1}{6} \frac{\partial^2 P}{\partial \mu_q \partial \mu_I}. \quad (4.28)$$

In the confined phase of QCD and with a particular form of the HRG pressure (4.21) one finds

$$\frac{\chi_q}{T^2} = \sum_{i \in \text{baryons}} 9F(T, m_i) \cosh \frac{3\mu_q}{T} = 9(F^{(2)} + F^{(4)}) \cosh \frac{3\mu_q}{T}, \quad (4.29)$$

and

$$\begin{aligned} \frac{\chi_I}{T^2} &= \sum_{i \in \text{mesons}} (2I_i^{(3)})^2 F(T, m_i) + \sum_{i \in \text{baryons}} (2I_i^{(3)})^2 F(T, m_i) \cosh(3\mu_q/T) \\ &= \frac{8}{3} G^{(3)} + (F^{(2)} + 5F^{(4)}) \cosh \frac{3\mu_q}{T} \end{aligned} \quad (4.30)$$

The Eqs. (4.29) and (4.30) are valid for the isospin symmetric system.

4.2.2 Charge density fluctuations in lattice gauge theory

The QCD thermodynamics and charge fluctuations have been recently calculated on the lattice in 2-flavor QCD at finite temperature and chemical potential. The essential progress in the recent lattice simulations [138] was due to first result on the sixth order coefficient in the Taylor expansion in terms of the quark chemical potential of thermodynamic pressure and different susceptibilities.

The lattice Monte-Carlo simulations of two-flavor QCD provided results for the net baryonic pressure $\Delta P(T, \mu_q) \equiv P(T, \mu_q) - P(T, \mu_q = 0)$ up to order $O((\mu_q/T)^6)$ (cf. (3.28)):

$$\frac{\Delta p(T, \mu_q)}{T^4} \simeq \sum_{n=1}^{n=3} c_{2n}(T) \left(\frac{\mu_q}{T} \right)^{2n}. \quad (4.31)$$

The basic observables characterizing baryonic contribution to QCD thermodynamics are the net quark density n_q and susceptibility χ_q . These are obtained as the first and the second order derivatives of a pressure with respect to the quark chemical potential μ_q . For the isospin symmetric system

$$\frac{n_q}{T^3} = \frac{\partial \Delta P(T, \mu_q)/T^4}{\partial \mu_q/T} \simeq 2 c_2(T) \left(\frac{\mu_q}{T} \right) + 4 c_4(T) \left(\frac{\mu_q}{T} \right)^3 + 6 c_6(T) \left(\frac{\mu_q}{T} \right)^5, \quad (4.32)$$

$$\frac{\chi_q}{T^2} = \frac{\partial^2 \Delta p(T, \mu_q)/T^4}{\partial (\mu_q/T)^2} \simeq 2 c_2(T) + 12 c_4(T) \left(\frac{\mu_q}{T} \right)^2 + 30 c_6(T) \left(\frac{\mu_q}{T} \right)^4.$$

The coefficients $c_i(T)$ in the Taylor expansion (4.31) and (4.32), calculated through the Monte-Carlo simulations of 2-flavor QCD [130, 138, 156], determine entirely the (T, μ_q) -dependence of baryonic observables in a medium.

4.2.3 Lattice gauge theory results and hadron resonance gas predictions

The lattice results (4.31) and (4.32) restricted to confined phase of QCD can be directly compared with the predictions of the hadron resonance gas model. However, such comparisons require particular care since the LGT calculations are usually performed with have quarks that leads to modification of hadronic mass spectrum. In addition the LGT results are not free from finite size effects. In order to avoid any ambiguity on models dependence describing the above required modifications of the hadronic spectrum we restrict our discussion to test only particular features of the resonance gas thermodynamics with the recent LGT results.

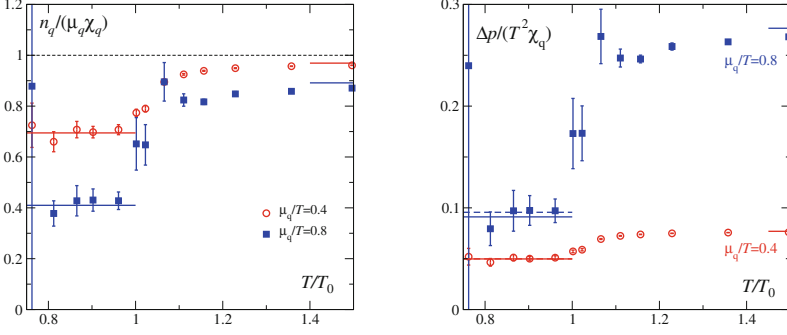


Fig. 4.6 The temperature dependence of the baryon density to net quark number fluctuations (left hand figure) and effective baryonic pressure to net quark number fluctuations (right hand figure) for $\mu_q/T = 0.4$ and $\mu_q/T = 0.8$ respectively. The points are the LGT results [138] in 2-flavor QCD obtained in the Taylor expansion up to $O(\mu_q^6)$ order. The lines are the hadron resonance gas model results.

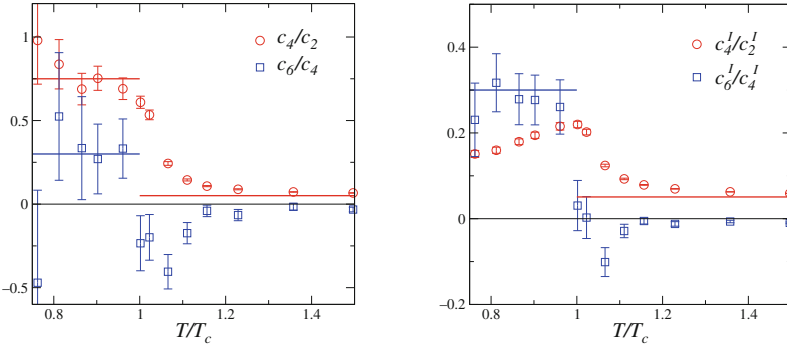


Fig. 4.7 The temperature dependence of the ratios of the Taylor coefficients in the quark chemical potential expansion of thermodynamic pressure c_i (left figure) and isovector susceptibility c_i^I (right figure). The points are the LGT results [130, 138, 156] the lines are the hadron resonance gas model predictions from Eqs. (4.33) and (4.36).

First, as seen from Eqs. (4.21) and (4.25) there is a factorization of T and (μ_q/T) dependence in the thermodynamic pressure and associated baryonic observables n_q and χ_q . Thus, in the resonance gas model any ratios of these observables, calculated at fixed quark chemical potential (μ_q/T) , should be independent of temperature [185, 502]. This property of the HRG-model is shown in Fig. 4.6 for two ratios; the net quark density to net quark fluctuations $(n_q/\mu_q \chi_q)$ and for the effective baryonic pressure per quark fluctuations $(\Delta p/T^2 \chi_q)$. The results for these ratios are illustrated in Fig. 4.6 for two values of $\mu_q/T = 0.4$ and 0.8 respectively.

Second, the (μ_q/T) -dependence in the HRG-model is described by the (cosh)-function. Thus, performing the Taylor expansion of the pressure (4.25) in (μ_q/T) at $\mu_I = 0$,

$$\frac{\Delta P(T, \mu_q, \mu_I = 0)}{T^4} \simeq \sum_i F(T, m_i) \left(\frac{9}{2} \left(\frac{\mu_q}{T} \right)^2 + \frac{81}{4!} \left(\frac{\mu_q}{T} \right)^4 + \frac{3^6}{6!} \left(\frac{\mu_q}{T} \right)^6 \right), \quad (4.33)$$

one gets the predictions on the values of the coefficients c_i in (4.32) from the HRG-model

$$c_2(T) = \frac{9}{2} F^B(T), \quad c_4 = \frac{81}{4!} F^B(T), \quad c_6 = \frac{3^6}{6!} F^B(T) \quad (4.34)$$

where from Eqs. (4.26) and (4.33), $F^B(T) = F^{(2)} + F^{(4)}$.

In Fig. 4.7, left we show the ratios c_4/c_2 and c_6/c_4 obtained on the lattice in 2-flavour QCD and the corresponding results of the HRG-model from Eq. (4.34): $c_4/c_2 = 3/4$ and $c_6/c_4 = 0.3$. The temperature dependence of the Taylor coefficients in Eqs. (4.33) and (4.34) is controlled by a common function. Thus, in HRG-model, the ratios of different c_i are independent of T . The lattice results for $T < T_c$ are, within statistical errors, consistent with HRG model prediction. Clear deviations seen at $T \simeq T_c$ are to be expected as at the critical temperature deconfinement releases the color degrees of freedom which are obviously not present in the statistical operator of hadron resonance gas.

An interesting physical observable that characterizes thermal fluctuations related with isospin conservation is the isovector susceptibility χ_I (4.28). Recently, χ_I was calculated on the lattice in 2-flavor QCD both for net-baryon free system [130] as well as for finite baryon number density [138] using the Taylor expansion approach in μ_q . The Taylor series of χ_I were calculated up to $O(\mu_q^4)$ order

$$\frac{\chi_I}{T^2} |_{\mu_I=0} \simeq 2 c_2^I(T) + 12 c_4^I(T) \left(\frac{\mu_q}{T} \right)^2 + 30 c_6^I(T) \left(\frac{\mu_q}{T} \right)^4. \quad (4.35)$$

The isovector, contrary to the baryon number susceptibility, is not directly obtained as derivative of pressure (4.31). Thus, in lattice Monte-Carlo calculations the coefficients in the Taylor expansion in Eq. (4.35) are not necessarily related with those appearing in Eq. (4.31). There is also a contribution of mesonic degrees of freedom to the isovector susceptibility which explicitly is not there in the baryon susceptibility. In view of the above the c_i^I coefficients in (4.35) required extended Monte-Carlo simulations [138, 156].

Carrying out the Taylor expansion in Eq. (4.30) up to $O(\mu_q^4)$ order the HRG-model suggests that the coefficients c_i^I in (4.35) are as follows:

$$c_2^I = \frac{F_I^M + F_I^B}{2}, \quad c_4^I = \frac{1}{12} \times \frac{9}{2} F_I^B, \quad c_6^I = \frac{1}{30} \times \frac{81}{24} F_I^B, \quad (4.36)$$

where $F_I^M = \frac{8}{3}G^{(3)}$ and $F_I^B = F^{(2)} + 5F^{(4)}$, with G and F defined as in Eqs. (4.24) and (4.26).

From Eqs. (4.35) and (4.36) the contribution of different isospin multi-plets to the overall pressure can be also expressed by the appropriate Taylor coefficients calculated on the lattice

$$G^{(3)} = \frac{3}{4}c_2^I - c_4^I, \quad F^{(2)} = \frac{5}{18}c_2 - \frac{2}{3}c_4^I, \quad F^{(4)} = \frac{2}{3}c_4^I - \frac{1}{18}c_2. \quad (4.37)$$

The above results of HRG-model can be compared with the LGT findings. In particular in the HRG the ratio of c_6^I/c_4^I is temperature independent and takes the value 0.3. Figure 4.7, right compares recent LGT results [138] for the c_6^I/c_4^I ratio with the HRG-model. It is clear from Fig. 4.7, right that for $T < T_c$ the temperature dependence and the magnitude of the above ratio calculated in LGT is, within statistical errors, well consistent with the resonance gas model results. Also, temperature dependence of the c_4^I/c_2^I ratio found in LGT is qualitatively expected from Eq. (4.36).

We have illustrated on few examples that the LGT results on the QCD thermodynamics, restricted to confined phase, are consistent with the hadron resonance gas model expectations. These examples indicate that the hadronic resonances are essential degrees of freedom in confined phase. In addition, the hadron resonance gas partition function should be considered as a good approximation of the QCD thermodynamics in the confined phase.

A more detailed quantitative comparisons of model predictions with LGT findings would require a detailed lattice calculations with physical quark masses as well as the extrapolation of LGT results to the continuum limit. Recently, such LGT studies were undertaken for vanishing chemical potential [181] and are in progress for the finite baryon number density [503].

In the present section it has been shown how the region just below the transition from hadronic to quark-gluon matter can be described within the hadron resonance gas model. In the next section we turn to a model description for the region just above the transition, the quark-gluon quasi-particle model.

4.3 The QCD equation of state near the transition line within a quasi-particle model

It is the aim of the present section to compare in detail the Rossendorf quasi-particle model [504–507] with recent lattice QCD data [130, 138] in the region around T_c with focus on finite baryon densities. After introducing the concept of quasi-particles as a successful tool for describing strongly interacting systems, various phenomenological approaches incorporating quasi-particle excitations will be introduced. We then present our quasi-particle model de-

scribing the pressure $p(T, \mu_q = 0)$ and the Taylor expansion coefficients of the excess pressure for the strongly coupled quark-gluon fluid by extending the model to finite μ_q . A family of equations of state in agreement with lattice QCD results [107, 131, 185, 508] is constructed and its impact on hydrodynamic observables in heavy-ion experiments such as the azimuthal anisotropy coefficient v_2 is studied. Finally, we apply our quasi-particle model to larger baryon densities and analyze the impact of a CEP inclusion on the EoS and, in particular, on the isentropic trajectories of the hydrodynamically evolving system.

4.3.1 Basic relations

The equation of state (EoS) of strongly interacting matter can be formulated in the form $p(T, \{\mu_f\})$. Here the pressure p as a function of temperature T and a set of chemical potentials $\{\mu_f\}$ of different quark flavors is a primary thermodynamic potential following e.g. from the partition function Z through (cf. Sect. 2.2, Eq. (2.39))

$$p(T, \{\mu_f\}) = \frac{T}{V} \ln Z(T, \{\mu_f\}). \quad (4.38)$$

We also recall the fundamental thermodynamic relations in the case of one independent chemical potential:

$$s = \frac{\partial p}{\partial T}, \quad n_q = \frac{\partial p}{\partial \mu_q}, \quad e + p - Ts = n_q \mu_q \quad (4.39)$$

with entropy density s , net baryon number density $n_B = \frac{1}{3}n_q$, energy density e and quark chemical potential μ_q . In the case of $N_f = 2$ quark flavors, p can be written as a function of a combination of up and down quark chemical potentials $\mu_q = (\mu_u + \mu_d)/2$. The second-order derivative of p with respect to μ_q defines the quark number susceptibility $\chi_q = \partial^2 p / \partial \mu_q^2$ being a measure of baryon number fluctuations, $\chi_B = \frac{1}{9}\chi_q$. The latter are, in principle, measurable via event-by-event fluctuations in heavy-ion experiments. Apart from the thermodynamic consistency conditions denoted in (4.39), thermodynamic stability conditions must be fulfilled [484, 509].

4.3.2 Concept of quasi-particles

The notion of quasi-particles (QP) has proven to be a powerful and useful concept for the understanding of the properties of strongly correlated systems (cf. [510] for an overview).

The existence of quasi-stationary collective modes allows for an efficient description of the system in terms of single-particle characteristics with approximately additive energies and momenta. Accumulating collective phenomena in such a way leads to a simplification in the description of the many-particle system. The one-particle states in strongly correlated systems are themselves quasi-stationary. The interaction among the modes limits the life-time of these one-particle states. In summary, the elementary motions in a system of strongly interacting particles being collectively carried by all particles display a single-particle character. This makes a description in terms of single quantum particles suitable. These quasi-particles cannot be described without referring to the system under consideration as a whole.

An important question concerns the weak coupling among the quasi-particles. Naively, one would expect large transport coefficients (e.g. shear viscosity) due to the long free mean path. However, an extension of the quasi-particle model including finite widths of the excitations delivers a small shear viscosity [511], in agreement with expectations extracted from experiments at RHIC [512].

4.3.3 The Rossendorf quasi-particle model at vanishing chemical potential

The Rossendorf quasi-particle model (QPM) was inspired by the work of Biro et al. [513] in which quark and gluon quasi-particles are the basic ingredients. Medium-dependent self-energies are approximated in the thermodynamically relevant momentum range as effective quasi-particle masses which are generated dynamically and are thought to parameterize in an appropriate way all the complexity of strong interactions. The employed ansatz follows the

Hard Thermal Loop/Hard Dense Loop (HTL/HDL) self-energies by using the leading-order thermal masses of hard excitations and thus makes contact with resummed perturbative QCD. However, the model goes beyond perturbation theory by using an effective coupling, which in turn approaches the perturbative coupling in the high-temperature region. Even an expansion in powers of the effective coupling gives an infinite series of terms, thus highlighting the non-perturbative character of the model. A strict perturbation expansion recovers the first two terms² of the perturbative potential of QCD [12, 516].

In the case of vanishing quark chemical potential, our ansatz for the pressure of light quarks (q) and gluons (g) reads [504–507]

² The third term $\sim g^3$ is only partially included. Its completion requires next-to-leading order contributions to the HTL dispersion laws [82, 83, 85–88, 125, 127, 514], which has recently been achieved in the solvable large- N_f limit of QCD [515], with results that provide some legitimation for a quasi-particle approach that goes beyond strict perturbation theory.

$$p = \sum_{a=q,g} p_a - B(T), \quad p_a = \frac{d_a}{3\pi^2} \int dk \frac{k^4}{\omega_a (e^{\omega_a/T} + S_a)} \quad (4.40)$$

where

$$B(T) = - \sum_{a=q,g} \frac{d_a}{4\pi^2} \int_{T_c}^T \frac{dm_a^2(T')}{dT'} \left(\int dk \frac{k^2}{\omega_a (e^{\omega_a/T'} + S_a)} \right) dT' + B(T_c) \quad (4.41)$$

with integration constant $B(T_c)$ ensures thermodynamic self-consistency [504–507], in addition to the stationarity conditions $\delta p / \delta m_a^2 = 0$ [517]. The k integrals here and below run from 0 to ∞ , $S_q = 1$, $S_g = -1$ and d_a denote the degeneracies of the quasi-particles, i.e. $d_q = 12$ and $d_g = 8$ as for free partons. The quasi-particle dispersion relations are approximated by the asymptotic mass shell expressions near the light cone

$$\omega_a = \sqrt{k^2 + m_a^2}, \quad m_a^2(T) = \Pi_a(k; T) + (x_a T)^2. \quad (4.42)$$

The essential part is the self-energy Π_a ; the last term in (4.42) accounts for the masses used in the lattice calculations [107, 130, 131, 138, 185, 508], i.e., $x_q = 0.4$ and $x_g = 0$.

A first determination of the dispersion relation within lattice QCD has been reported in [518] and made the authors of [519, 520] argue that additional degrees of freedom are required to saturate the pressure observed in the lattice results. It should be noticed, however, that relevant for the EoS are the excitations at momenta $k \sim T$, for which more accurate measurements are needed. In fact, one could easily deduce smaller quasi-particle masses, in particular for smaller temperatures, from the lattice results [518] when focusing on the relevant k region. Taking, in contrast, the large quasi-particle mass values deduced in [518] one achieves, indeed, a smaller pressure.

As suitable parametrization of Π_a , we employ the HTL self-energies with given explicit T dependence as in [504–507]. Here, the rest mass contribution stemming from the masses employed in the lattice performance is approximated following [521]. The essential point is to replace the running coupling g^2 entering Π_a by an effective coupling, $G^2(T)$.³ In this way, non-perturbative effects are thought to be accommodated in G^2 . Clearly, this assumption needs detailed tests which are presented below.

A reasoning for the strong assumptions made in such an ansatz can be described as follows. From (4.39), the entropy density is given through

$$s = \sum_{a=q,g} s_a, \quad s_a = \frac{d_a}{\pi^2 T} \int dk k^2 \frac{(\frac{4}{3}k^2 + m_a^2)}{\omega_a} \frac{1}{(e^{\omega_a/T} + S_a)}. \quad (4.43)$$

³ As shown in [522], it is the introduced $G^2(T)$ which allows to describe lattice QCD data near T_c , while the use of the pure 1-loop or 2-loop perturbative coupling together with a more complete description of the plasmon term and Landau damping restricts the approach to $T > 2T_c$ [82, 83, 85–88, 125, 127, 514].

In massless φ^4 theory this structure of the entropy density emerges by re-summing the super-daisy diagrams in tadpole topology [523]. Peshier [524] argues that such an ansatz is also valid for QCD. Although [82, 83, 85–88, 125, 127, 514] point to more complex structures, we find Eqs. (4.40), (4.41), and (4.43) flexible enough to accommodate the lattice data. Within the Φ functional approach starting from the thermodynamic potential, the expression (4.43) for the entropy density can be recovered by performing the following chain of approximations [525–527]. The Φ functional which is given by the series over all two particle irreducible skeleton diagrams is approximated by its two-loop truncation. The integral expression of s containing derivatives of the statistical distribution functions for gluons and quarks with respect to T is manifestly ultra-violet finite. Lost gauge invariance caused by the truncation in Φ is restored by arming the self-energies with HTL re-summed expressions which show the correct limiting behavior at the relevant momenta $k \sim T$. Furthermore, longitudinal gluon modes and the plasmino branch, which are both exponentially suppressed, can be neglected. Neglecting, in addition, imaginary parts in the self-energies as well as Landau damping contributions and approximating dispersion relations and self-energies suitably (cf. [504–507]) expression (4.43) is found. The pressure (4.40) follows by an integration.

As a convenient parametrization of the effective coupling we employ

$$G^2(T) = \begin{cases} G_{2\text{-loop}}^2(T), & T \geq T_c, \\ G_{2\text{-loop}}^2(T_c) + b(1 - T/T_c), & T < T_c. \end{cases} \quad (4.44)$$

Here $G_{2\text{-loop}}^2$ is the relevant part of the 2-loop coupling

$$G_{2\text{-loop}}^2(T) = \frac{16\pi^2}{\beta_0 \log \xi^2} \left[1 - \frac{2\beta_1}{\beta_0^2} \frac{\log(\log \xi^2)}{\log \xi^2} \right] \quad (4.45)$$

with $\beta_0 = (11N_c - 2N_f)/3$, $\beta_1 = (34N_c^2 - 13N_fN_c + 3N_f/N_c)/6$ and $\xi = \lambda(T - T_s)/T_c$. In (4.45) two parameters enter, being adjusted in order to describe lattice QCD results: a scale parameter λ , and T_s which regulates infrared divergencies at T_c . We choose $T_c = 170$ MeV in the following. The model has been successfully applied in the pure gauge sector [504–507] and for various numbers of quark flavors [504–507, 525–529]. Examples are exhibited in Fig. 4.8. The parameters for $N_f = 2$ are $\lambda = 7.4$, $T_s = 0.81T_c$, $b = 329.9$ and $B(T_c) = 0.24T_c^4$ and for $N_f = 2 + 1$ they read $\lambda = 7.6$, $T_s = 0.8T_c$, $b = 324.8$ and $B(T_c) = 0.5T_c^4$ with $N_c = 3$.

Note that we have also parameterized the region below T_c in (4.44). This should be regarded as just a parameterization without any microscopic meaning. Of course, hadrons are the relevant degrees of freedom below T_c and not quarks and gluons. Nonetheless, from a technical point of view and for later use it is advantageous to have a complete parameterization of the thermodynamic quantities for all values of the temperature.

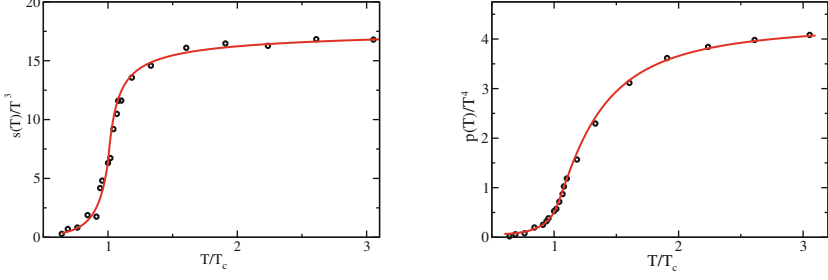


Fig. 4.8 Comparison of our model with lattice QCD results (*symbols*) for $\mu_q = 0$. Entropy density s/T^3 (*left panel*) and pressure p/T^4 (*right panel*) as functions of T/T_c for $N_f = 2+1$ quark flavors. Lattice data from [107, 131, 185, 508].

4.3.4 Baryon density effects and susceptibilities

One way to decompose the pressure is (cf. (3.28))

$$p(T, \mu_q) = p(T, \mu_q = 0) + \Delta p(T, \mu_q), \quad \Delta p(T, \mu_q) = T^4 \sum_{n=1}^{\infty} c_{2n}(T) \left(\frac{\mu_q}{T} \right)^{2n}, \quad (4.46)$$

where the excess pressure $\Delta p(T, \mu_q)$ became accessible only recently [130, 138]. In (4.46), Δp is given as Taylor series expansion in powers of μ_q/T with expansion coefficients $c_n(T)$ denoted as susceptibilities [130, 138]. Lattice QCD calculations focus on these susceptibilities instead of delivering $p(T, \mu_q)$ because they are easier calculable. In contrast, our model equally covers $p(T, \mu_q = 0)$ and $\Delta p(T, \mu_q)$ providing therefore the complete thermodynamic potential (4.46).

Extending the quasi-particle model to finite μ_q , the pressure renders to

$$p = \sum_{a=q,g} p_a - B(T, \mu_q), \quad p_a = \frac{d_a}{6\pi^2} \int dk \frac{k^4}{\omega_a} (f_a^+ + f_a^-), \quad (4.47)$$

where $B(T, \mu_q)$ is evaluated by performing an appropriate line integral in the $T - \mu_q$ plane [504–507, 525–527]. Here, the statistical distribution functions are $f_a^\pm = (\exp([\omega_a \mp \mu_a]/T) + S_a)^{-1}$ with chemical potential μ_q for light quarks and $\mu_g = 0$ for gluons. From (4.39), the entropy density explicitly reads $s = \sum_{a=q,g} s_a$ with

$$s_a = \frac{d_a}{2\pi^2 T} \int dk k^2 \left(\frac{(\frac{4}{3}k^2 + m_a^2)}{\omega_a} (f_a^+ + f_a^-) - \mu_a (f_a^+ - f_a^-) \right) \quad (4.48)$$

and the net quark number density is

$$n_q = \frac{d_q}{2\pi^2} \int dk k^2 (f_q^+ - f_q^-). \quad (4.49)$$

The quasi-particle self-energies $\Pi_a(T, \mu_q)$ in the dispersion relations now explicitly depend on T and μ_q as in [504–507].

When evaluating the thermodynamic observables in (4.47 – 4.49), the effective coupling $G^2(T, \mu_q)$ at non-vanishing μ_q has to be known. This can be achieved by imposing Maxwell’s relation onto p which results in a quasi-linear partial differential equation for $G^2(T, \mu_q)$ [504–507]

$$a_{\mu_q} \frac{\partial G^2}{\partial \mu_q} + a_T \frac{\partial G^2}{\partial T} = b. \quad (4.50)$$

The lengthy coefficients $a_{T, \mu_q}(T, \mu_q)$ and $b(T, \mu_q)$ [526, 527] obey $a_T(T, \mu_q = 0) = 0$ and $b(T, \mu_q = 0) = 0$ whereas a_{μ_q} does not vanish at $\mu_q = 0$. Peshier’s flow equation (4.50) can be solved as a Cauchy problem by knowing G^2 on an arbitrary curve in the $T - \mu_q$ plane. One possibility is to adjust $G^2(T)$ in (4.44) to lattice QCD data at vanishing μ_q which then allows for a mapping into the finite quark chemical potential region via (4.50).

In order to compare directly the quasi-particle model with the lattice results in [130, 138], the $c_n(T)$ have to be computed. The expansion coefficients in Eq. (4.46) follow from (4.47) as

$$c_n(T) = \frac{1}{n!} \left. \frac{\partial^n (p/T^4)}{\partial (\mu_q/T)^n} \right|_{\mu_q=0}. \quad (4.51)$$

For the explicit expressions cf. [530]. Due to CP invariance of the QCD partition function (4.38), c_j with odd j vanish. We adjust $G^2(T)$ to $c_2(T)$ from [130, 138] for $N_f = 2$. Figure 4.9 exhibits the comparison of Δp and n_q calculated via Eqs. (4.47) and (4.49) (dashed curves) or by using the expansion coefficients $c_{2,4}$ evaluated from (4.51) (solid curves) with the lattice QCD data [130, 138] based on the coefficients $c_{2,4}$ (symbols). One observes an astonishingly good description of the data, even slightly below T_c , where the resonance gas model [107, 185] (cf. Sect. 4.2) is appropriate.⁴ Interesting is the deviation of the full model from the results based on the truncated expansion in a small interval around T_c .

Since for small values of μ_q the higher order coefficients c_4 and in particular c_6 are less important for Δp and n_q , a more stringent test of the model

⁴ Some reasoning why the model may be applicable also slightly below T_c emerges from duality [528], similar to the application of a hadronic model slightly above T_c [531]. We do not claim the applicability of a model of quasi-gluons and quasi-quarks below T_c , but consider the extension to smaller values of T as a convenient parametrization, maybe by a numeric accident, at least for describing the present lattice data with large lattice masses for quarks being employed.

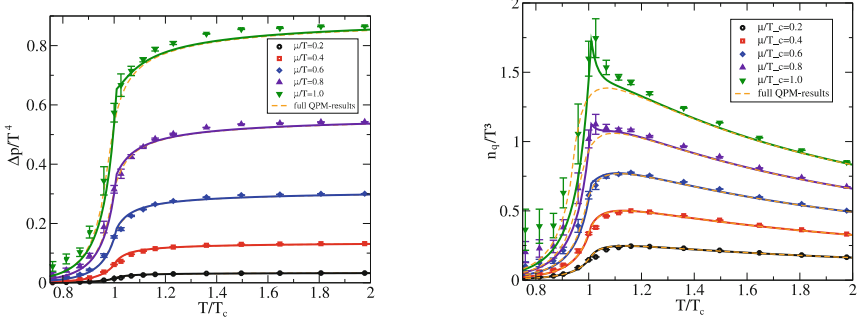


Fig. 4.9 Comparison of the quasi-particle model with lattice QCD results [130, 138] for the excess pressure (*left panel*, for constant μ_q/T) and net quark number density (*right panel*, for constant μ_q/T_c). As for the lattice QCD data (*symbols*) the quasi-particle model results (*solid curves*) are based on the expansion coefficients $c_{2,4}$, i.e. $\Delta p/T^4 = c_2(T)(\mu_q/T)^2 + c_4(T)(\mu_q/T)^4$ and $n_q/T^3 = 2c_2(T)(\mu_q/T) + 4c_4(T)(\mu_q/T)^3$. For comparison, the full quasi-particle model results (*dashed curves*) derived from (4.47) and (4.49) are exhibited. The parameters for $N_c = 3$ are $\lambda = 12$, $T_s = 0.87T_c$, and $b = 426.1$.

is accomplished by a direct comparison of the individual Taylor expansion coefficients c_i with the corresponding lattice QCD results. Straightforward evaluation of $c_{2,4,6}$ delivers the results exhibited in Fig. 4.10. Since $G^2(T)$ was already adjusted to $c_2(T)$ the agreement is good. It should be emphasized that all coefficients $c_i(T)$ are determined by $G^2(T)$. That means the same $G^2(T)$ describes also the features of c_4 and c_6 without requiring any further assumptions. Particularly interesting are the peak of c_4 (left panel of Fig. 4.10) and the double-peak of c_6 (right panel of Fig. 4.10) at T_c . Numerically, these pronounced structures stem from the change of the curvature behavior of $G^2(T)$ at T_c which determines the derivative terms of G^2 in $c_{4,6}$ obtained by employing Eq. (4.50). Neglecting these terms would completely alter the shape of $c_{4,6}$. In other words, via $c_{4,6}$ the flow equation (4.50) is probed, which is the key for extrapolating to large values of μ_q . Similar to [130, 138], we interpret the peak in c_4 as an indicator of some critical behavior, while the pressure itself is smoothly but rapidly varying at T_c .

Note that the results exhibited in Fig. 4.10 are robust with respect to the chosen form of the effective coupling (4.44). Testing the 1-loop coupling of G^2 above T_c or a quadratic function in T/T_c below T_c or both, e.g., the higher order coefficients and in particular their pronounced behavior about T_c are quantitatively reproduced when adjusting $G^2(T)$ to describe $c_2(T)$. Having the first Taylor expansion coefficients $c_{2,4,6}$ at our disposal, the baryon number susceptibility

$$\frac{\chi_B}{T^2} = \frac{2}{9}c_2 + \frac{12}{9}c_4\left(\frac{\mu_B}{3T}\right)^2 + \frac{10}{3}c_6\left(\frac{\mu_B}{3T}\right)^4 \quad (4.52)$$

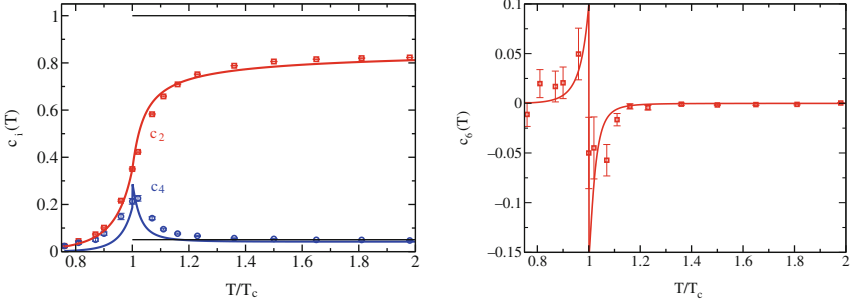


Fig. 4.10 The expansion coefficients $c_{2,4}$ (left panel, horizontal lines depict the Stefan-Boltzmann limits usually employed in bag model like equation of state approaches) and c_6 (right panel) as a function of the scaled temperature T/T_c . Symbols represent lattice data from [130, 138].

follows directly as truncated expansion in μ_B/T , where $\mu_B = 3\mu_q$ is the baryo-chemical potential.

4.3.5 A family of equations of state

Having tested these details of the quasi-particle model, we can directly apply the found parametrization and calculate the total pressure at arbitrary baryon densities, while lattice QCD calculations are yet constrained to small baryon densities. This application is of interest for the CBM project at FAIR and for studying hot proto-neutron stars and cold neutron stars with quark cores. Another application to cosmic confinement dynamics is reported in [532]. These applications, however, need a controlled chiral extrapolation which must base on improved lattice QCD data. Here, we consider first the case of small baryon densities relevant for RHIC and LHC.

It is expected that lattice QCD data at high temperature are realistic, as improved actions have been used. At low temperature, the employed quark masses are too large to give realistic results. These, however, agree with the resonance gas model once analogous assumptions are implemented [107, 185]. It is therefore reasonable to use the resonance gas model at low T (see Sect. 4.2) and employ our quasi-particle model to extrapolate lattice QCD results both to larger μ_B and smaller T as long as a systematic chiral extrapolation cannot be done safely due to lacking lattice QCD input.

Ideal (non-viscous) hydrodynamics requires the knowledge of the EoS in the form $p(e, n_B)$. Only at freeze-out $T(e, n_B)$ and $\mu_B(e, n_B)$ are needed to calculate particle spectra via the Cooper-Frye formalism. We use p in Eq. (4.47), n_B related to Eq. (4.49) and e from Eqs. (4.47), (4.48), (4.49)

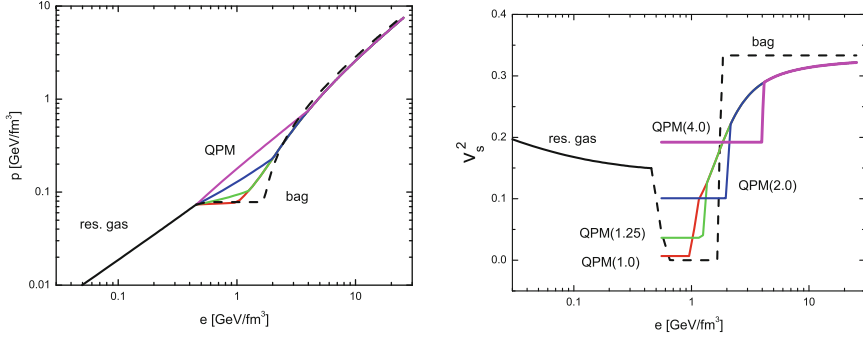


Fig. 4.11 A family of equations of state by combining our quasi-particle model in the high energy density region with the resonance gas model at low energy densities for baryon densities relevant for top RHIC energies: pressure (*left*, $\text{QPM}(e_m)$ with $e_m = 4.0, 2.0, 1.25, 1.0 \text{ GeV fm}^{-3}$ serving as label from top to bottom) and squared sound velocity (*right*) as a function of energy density. Bag model results are depicted by *dashed curves*. Effects of variations in n_B of 0.33 fm^{-3} are not visible on the given scale.

and (4.39) to obtain this information from our thermodynamically consistent QPM. G^2 is adjusted to lattice data either by $p(T, \mu_q = 0)$ or by $c_2(T)$.

We generate a family of equations of state by keeping the matching point to the resonance gas EoS fixed and interpolate linearly $p(e)$, $T(e)$ and $\mu_B(e)$ at fixed n_B to a given matching point of the quasi-particle model given by the energy density e_m which serves as label. Such a family is exhibited in Fig. 4.11. Surprising is the similarity of QPM(1.0) and the bag model EoS used in [533]. Equipped with such a QCD based EoS one can compare results of hydrodynamical calculations with data, e.g., for the azimuthal anisotropy v_2 . Examples are exhibited in Fig. 4.12 for Λ, Ξ, Ω [534].

4.3.6 The critical end point

As discussed in previous sections, a prominent feature of QCD is the appearance of a critical end point belonging to the universality class of the three-dimensional Ising model [22, 475]. In the chiral limit, the CEP converts into a tricritical end point [49, 475] (cf. Chap. 1 and Sects. 2.2, 3.2). At the CEP, a line of first order phase transitions terminates. According to [129, 155, 192, 197] the location of the critical end point in 2 or 3 flavor QCD is at $(T, \mu_B) = (162, 360) \text{ MeV}$. Our above presented formulation of a QPM does obviously not include phase transition effects. The mentioned structures in $c_{4,6}$ (cf. Fig. 4.10) result from a change in the curvature behavior of $G^2(T)$ as dictated by lattice QCD data and parametrized conveniently by Eq. (4.44).

A phenomenological procedure for including CEP effects is to combine the above regular part of the EoS with a singular part. The latter includes

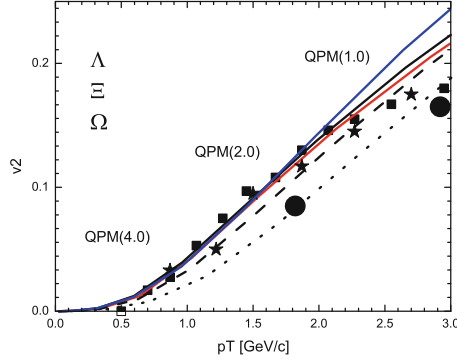


Fig. 4.12 Azimuthal anisotropy coefficient v_2 as a function of transverse momentum for strange baryons (*solid curves* QPM(1.0), QPM(2.0), QPM(4.0) [from top to bottom, with decoupling temperatures adjusted to data up to 2.5 GeV/c] compared with *squares* for Λ , *dashed curve* QPM(2.0) compared with *stars* for Ξ , *dotted curve* QPM(2.0) compared with *circles* for Ω , data from [535]). Impact parameter $b = 5.2$ fm, initial conditions $e_0 = 30$ GeV fm $^{-3}$, $n_0 = 0.4$ fm $^{-3}$, $\tau_0 = 0.6$ fm/c being the initial time when matter is thermalized and the hydrodynamical era starts. These parameters are appropriate for RHIC-200.

the proper critical exponents of the three-dimensional Ising model [536]. One possibility of combining regular and singular parts has been explored in [484] by combining a bag model EoS and a resonance gas EoS. By construction, both parts are intermixed via the singular contribution to the EoS.

Here, we would like to keep our QPM parametrization, which is already adjusted to lattice QCD data, and arm the model with a proper singular part [537, 538]. To be specific, starting from a thermodynamic potential, e.g. Gibbs free enthalpy, it can be decomposed into an analytic and a non-analytic part where the latter is related to phase transitions and critical phenomena [539]. Accordingly, the EoS formulated in terms of the entropy density is given through $s = s_a + s_n$. Here, the analytic contribution s_a has to be adjusted to the known EoS outside of the critical region. The non-analytic part s_n should embody the feature of being continuous left to the CEP (i.e. at small chemical potentials) whereas on the right (at large chemical potentials) it generates a first order phase transition. A convenient parametrization of s_n for the 3D Ising model characterized by a set of critical exponents is given in [536]. Still, the corresponding variables employed usually in condensed matter physics including the order parameter need to be mapped into the $T - \mu_B$ plane in the vicinity of the CEP. Details of this mapping and a useful formulation of the entropy density contribution can be found in the pioneering work [484] we rely on. In the following, we estimate the phase border line to be given by $T_c(\mu_B) = T_c \left(1 + \frac{1}{2}d(\mu_B/3T_c)^2\right)$ with $d = -0.122$ according to [129, 155, 156, 159, 192, 197] and locate the CEP at $\mu_{B,c} = 360$ MeV in agreement with [129, 155, 192, 197].

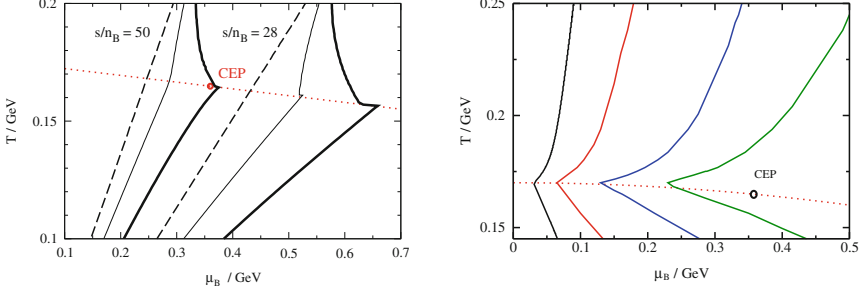


Fig. 4.13 Isentropic trajectories (Left: toy model (4.53) depending on the strength parameter A for $s/n_B = 50, 28$; dashed, thin and solid lines exhibit results for $A = 0, 0.5, 1.0$ respectively. Right: truncated quasi-particle model adjusted to lattice QCD [130, 131, 138, 508] with CEP effects included, parametrized by $D = 0.06$ and $A = 0.5$ for $s/n_B = 200, 100, 50, 33$ (from left to right).) Dotted lines represent the estimated phase border line. For $\Delta T = 10$ MeV, $\Delta\mu_B = 10$ MeV.

As a *simple toy model*, let us employ the first terms in (4.46), however, with constant expansion coefficients. The entropy density contributions are given by

$$\begin{aligned} s_a(T, \mu_B) &= 4\bar{c}_0 T^3 + \frac{2}{9}\bar{c}_2 \mu_B^2 T, \\ s_n(T, \mu_B) &= \frac{2}{9}\bar{c}_2 \mu_B^2 T A \tanh(S_c(T, \mu_B)) \end{aligned} \quad (4.53)$$

with $\bar{c}_0 = (32 + 21N_f)\pi^2/180$, $\bar{c}_2 = N_f/2$ and $N_f = 2$. n_B follows from (4.53) via standard thermodynamic relations (cf. [484]) with integration constant $n_B(0, \mu_B) = \frac{4}{3}\bar{c}_4(\mu_B/3)^3$ where $\bar{c}_4 = N_f/4\pi^2$. The ansatz for s_n has been chosen such that $s_n \rightarrow 0$ for $T \rightarrow 0$ and the net baryon density vanishes at $\mu_B = 0$. The parameter A describes the strength of the non-analytic contribution in the EoS. We apply the same $S_c(T, \mu_B)$ as in [484] assuming a fairly large critical region parametrized by $\Delta T = 100$ MeV, $\Delta\mu_B = 200$ MeV and a stretch factor $D = 0.15$. Hence, CEP effects on the EoS and in particular on isentropic trajectories $s/n_B = \text{const}$ in the $T - \mu_B$ plane can be demonstrated. In Fig. 4.13, the influence of the strength parameter A on the behavior of isentropic trajectories is exhibited. For increasing $A > 0$, the trajectories for large s/n_B tend to be attracted towards larger μ_B due to the presence of the CEP. In fact, the CEP acts as an attractor on trajectories on the left whereas on the right a repulsive impact is found. Evidently, the curves on the right hand side of the CEP display the existence of the first order phase transition. By shrinking the critical region to $\Delta T = 10$ MeV, $\Delta\mu_B = 10$ MeV and $D = 0.06$, the influence of the CEP decreases (left panel of Fig. 4.13) in comparison with the results obtained for a large critical region.

In particular, the sections on the hadronic side become less affected by CEP when decreasing the extension of the critical region.

The parameters in the non-analytic entropy density contribution and in particular A have to be chosen such that standard thermodynamic consistency conditions are satisfied [484]. Accordingly, during the adiabatic expansion of the system and its related cooling, both n_B and s must decrease. For $A < 0$ with trajectories for large s/n_B bent to smaller μ_B due to the CEP inclusion, however, these conditions are violated in the vicinity of the first order transition line. Clearly, this statement decisively depends on s in the hadronic phase where the simple toy model cannot account for QCD.

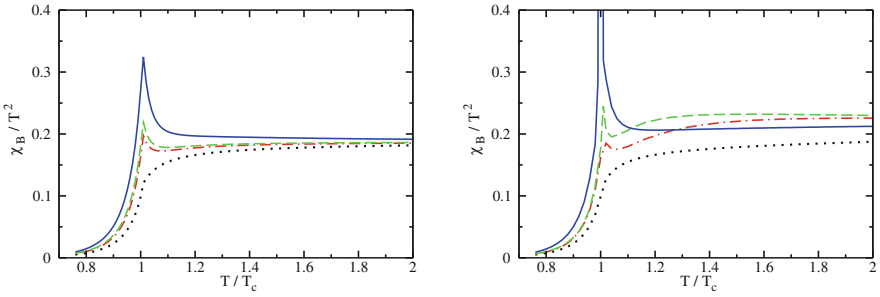


Fig. 4.14 Scaled baryon number susceptibility of the quasi-particle model neglecting $c_6(T)$ without CEP (*left panel*) and with CEP inclusion (*right panel*) as function of T/T_c for $\mu_B = 450, 330, 300, 150$ MeV (*solid, dashed, dash-dotted and dotted curves respectively*).

In contrast, basing on lattice QCD we construct the EoS as truncated Taylor series expansion including the coefficients $c_{0,2,4,6}(T)$ in Eq. (4.46) where $c_0(T) = p(T, \mu_q = 0)/T^4$. These lattice based trajectories are shown in Fig. 4.13 (right panel) where the pattern differs notably from the observations made in the above toy model. Although first principle evaluations still suffer from too heavy quark masses and deviate consequently from the resonance gas trajectories in the low-temperature phase, the values s/n_B on these lattice QCD deduced curves agree with the values at the according nearby chemical freeze-out points inferred from data [492]. Furthermore, in the deconfined phase lattice results are trustable due to convergence radius studies [130, 138] at least up to $\mu_B = 300$ MeV. Therefore, adjusting the analytic contribution of the EoS known from the lattice data by our quasi-particle model, critical end point effects should become visible only for larger μ_B implying a small critical region. We include the CEP in line with the procedure outlined above in our quasi-particle model replacing \bar{c}_2 by $c_2(T)$ in s_n and considering a small critical region characterized by $\Delta T = 10$ MeV, $\Delta\mu_B = 10$ MeV and $D = 0.06$ with strength parameter $A = 0.5$. As exhibited in Fig. 4.13 (right panel), CEP effects on isentropic trajectories are significant only for large μ_B

with negligible impact on the hadronic sections. Therefore, the pattern of the isentropic trajectories as exhibited seems to be generic (cf. [484]). Nonetheless, the baryon number susceptibility $\chi_B = \partial^2 p / \partial \mu_B^2$ being a measure of baryon number fluctuations diverges for $\mu_B > \mu_{B,c}$ (Fig. 4.14 right panel) due to the discontinuity evolving in n_B in contrast to the analytic behavior (Fig. 4.14 left panel) stemming from the quasi-particle model not containing CEP effects.

The issue of susceptibilities and fluctuations will be taken up again in Sect. 4.6. In the next sections further models are reviewed which use quark and/or gluon related degrees of freedom.

4.4 Wilson line degrees of freedom and deconfinement

We recall from Sect. 2.1 that at infinitely high temperature, by asymptotic freedom QCD is an ideal gas of massless quarks and gluons: the plasma screens electric fields, so quarks are unconfined [69]. Effective theories suggest that from infinite temperature, on down to perhaps a few hundred MeV, it really stays a plasma of weakly interacting new degrees of freedom, which are quasi-particle quarks and gluons with thermal masses (and vertices); for recent reviews see, for example, [118, 540] and references therein. However, $SU(N)$ (or QCD) thermodynamics does not evolve smoothly to low temperatures. Rather, at a temperature around ≈ 200 MeV⁵, the pressure and energy density change drastically. Thermodynamically, this indicates a rapid decrease in the effective number of degrees of freedom as the temperature is reduced below the above-mentioned “transition temperature” T_c . In a pure gauge theory, where matter fields are infinitely heavy and decouple, it would be natural to interpret this transition as “freezing-in” of the N^2-1 color degrees of freedom into colorless hadrons (glueballs in this case). This is the so-called confinement phase transition. By now, it is known to be of second order for $N = 2$ [18], and of first order for $N = 3$ [541] and $N = 4$ [542, 543] (and presumably also for all $N > 4$ [544, 545]). We shall discuss this in more detail in the next section, where we introduce the thermal Wilson line and its trace, the so-called Polyakov loop, which is an order parameter for the deconfining phase transition of $SU(N)$ gauge theory.

In reality, quarks are not infinitely heavy, of course, since $m_\pi = 138$ MeV $< \infty$. In Sect. 4.4.2 we shall attempt to incorporate quark effects a posteriori. Having done so, we can see what happens when the net density (quarks minus antiquarks) is non-zero, which is of course the case of interest for the planned “Compressed Baryonic Matter” (CBM) experiment at GSI-FAIR.

This brief review focuses on an elementary introduction into the role of Wilson lines and Polyakov loops for the deconfining phase transition. It is not

⁵ The precise value depends on the number of quark flavors and their masses, as well as on the baryon-chemical potential etc., see below.

a review of finite-temperature QCD or of perturbative resummation strategies [118, 540] (Sect. 3.1) nor of numerical lattice approaches [546, 547] (Sect. 3.2).

4.4.1 Pure Yang-Mills $SU(N)$ gauge theory

4.4.1.1 The Polyakov loop as order parameter for deconfinement

In this section, we consider a gauge theory without quarks, where N is the number of colors. Experimentally, $N = 3$. However, it will prove useful to consider N to be an arbitrary integer ≥ 2 . For large N , the free energy itself is an order parameter for the deconfining phase transition [548, 549]: below T_c , the free energy is due exclusively to glueballs. As color singlets, glueballs only contribute of order one to the free energy. In contrast, above T_c , gluons contribute $\sim N^2$ to the free energy. At very high temperature, by asymptotic freedom the behavior of the free energy can be computed perturbatively.

There is a puzzle, however. The free energy is a gauge invariant quantity, and so should be due to gauge invariant degrees of freedom. While glueball properties (masses etc.) change with temperature, they remain the dominant color-singlet excitations. If glueballs contribute of order one, what is the term $\sim N^2$ in the free energy due to?

The only quantity which can provide such a contribution is an expectation value for the Polyakov loop:

$$\ell(x) = \frac{1}{N} \text{tr } \mathbf{L} \quad , \quad \mathbf{L}(x) = \mathcal{P} \exp \left(ig \int_0^{1/T} A_0(x, \tau) d\tau \right) . \quad (4.54)$$

Here, tr denotes the trace in color space, \mathcal{P} is path ordering, and g is the gauge coupling constant; $A_0(x, \tau)$ is the time component of the vector potential in the fundamental representation, at a spatial position x and euclidean time τ . \mathbf{L} is the so-called Wilson line (here in the fundamental representation) and ℓ is its trace, normalized by the dimension of the representation. The Wilson line can be viewed as $SU(3)$ color Aharonov-Bohm phase factor for an infinitely heavy test particle (which therefore stays put at its position \mathbf{x}) in the fundamental representation. Thus the term $\sim N^2$ in the free energy is due exclusively to the potential for the Polyakov loop, $\mathcal{V}(\ell)$. Glueballs contribute ~ 1 .

The expectation value of the Polyakov loop, $\ell_0 = \langle \ell \rangle$, vanishes in the confined phase because of the global $Z(N)$ symmetry noted by 't Hooft [550–553]: besides local gauge transformations, which are periodic in time, the pure-gauge theory is also symmetric under gauge transformations which are only periodic up to an element of the center of the gauge group, which is $Z(N) = \{e^{2\pi i j/N} | j = 1 \cdots N\}$. In the fundamental representation, the simplest global $Z(N)$ transformation is

$$\Omega(\tau = 1/T) = e^{2\pi i/N} \Omega(\tau = 0) . \quad (4.55)$$

Under such transformations,

$$\ell \rightarrow e^{2\pi i e/N} \ell , \quad (4.56)$$

with $e = 1$ the $Z(N)$ “charge” of the fundamental loop. Note that the restored $Z(N)$ symmetry of the confined phase does not guarantee that expectation values of $Z(N)$ -neutral loops, such as the adjoint loop, vanish. Loops in arbitrary irreducible representations \mathcal{R} are defined as

$$\ell_{\mathcal{R}} = \frac{1}{d_{\mathcal{R}}} \text{tr } \mathbf{L}_{\mathcal{R}} \quad , \quad \mathbf{L}_{\mathcal{R}} = \mathcal{P} \exp \left(ig \int_0^{1/T} A_0^a(x, \tau) \mathbf{t}_{\mathcal{R}}^a d\tau \right) , \quad (4.57)$$

where $\mathbf{t}_{\mathcal{R}}^a$ are the generators of \mathcal{R} and $d_{\mathcal{R}}$ is its dimension. At infinite temperature, by asymptotic freedom we can ignore fluctuations in the gauge field, and $\langle \ell \rangle \rightarrow 1$ (for any representation). Hence, the $Z(N)$ center symmetry is broken spontaneously.

Assuming dominance of the fundamental loop, Svetitsky and Yaffe noticed that the global $Z(N)$ symmetry predicts the order of the $SU(N)$ phase transition (and critical properties, by universality) [554–556]. For $N = 2$, it is of second order, i.e. the expectation value of ℓ is continuous and the effective mass (inverse correlation length) of the order parameter vanishes at the transition point.

On the other hand, for $N \geq 3$ the fundamental loop is a complex valued field. Powers of $\ell \ell^*$ are invariant under $U(1)$; the symmetry is reduced to $Z(3)$ by terms such as $-\kappa_3 (\ell_N^3 + \ell_N^{*3})$ [557]. Now the phase transition is of first order because ℓ_0 jumps at T_c .

The condensation of the fundamental loop at high temperature was first observed in lattice Monte-Carlo simulations of the $SU(2)$ theory by McLerran and Svetitsky [558] and Kuti et al. [559]. They found a phase transition of second order, where the condensation of the order parameter is continuous. It should be noted that those early studies computed the expectation value of the *bare* loop. It is an order parameter only in the lattice theory with a finite lattice spacing but vanishes (even above T_c) in the continuum limit. To define an order parameter in the continuum one needs to determine renormalized loops [560–563].

Aside from the fact that the symmetry properties of the Polyakov loop determine the order of the $SU(N)$ deconfining phase transition, what else is it good for? Pisarski went a step further and suggested an effective theory where all other degrees of freedom have been integrated out, and the free energy is exclusively due to a condensate for the (fundamental) Polyakov loop [564], which is where this section started from. The potential for ℓ is then multiplied by a factor of T^4 (in four dimensions). The pressure is then given by $p = -\mathcal{V}(\ell_0)$, the energy density by $e = Tdp/dT - p$ etc.

In [565, 566] such an *Ansatz* was matched to lattice data for the $SU(3)$ pressure and energy density, thereby extracting the potential for the (renormalized) fundamental loop. It exhibits several interesting features. First, near T_c the potential changes very rapidly, and true metastable vacua (where \mathcal{V} has positive curvature) can exist only within a very narrow interval $\Delta T \approx 1\%$ around T_c . For this type of first-order phase transition, deep super-cooling or super-heating is not possible, and hysteresis effects [567] are expected to be much smaller than for more “typical” first-order transitions (which permit deep super-cooling and super-heating). On the other hand, $\mathcal{V}' = 0$ at $\ell = 0$ holds even above T_c , and so the confined phase is metastable at all $T > T_c$. This will lead to the presence of unstable modes if the system is quenched from $T < T_c$ to a temperature $T > T_c$ such that $\mathcal{V}''(0) < 0$, which will then grow exponentially (“spinodal decomposition”). This has been observed in simulations on the lattice [567–572]. Note that this behavior follows also from the global $Z(N)$ symmetry,⁶ which can therefore provide information not only about the order of the phase transition but also about its *dynamics*.

Secondly, there is a very small “nucleation barrier” between the confined and deconfined phases at T_c , i.e. that the potential is very flat. This implies a small interface tension between those phases at the transition temperature, and a small string tension and screening mass $m_{\text{eff}}(T_c+)$. Indeed, $SU(3)$ lattice results find that $\sigma(T_c)/\sigma(0) \approx 0.1$, and that the screening mass obtained from the two-point function of Polyakov loops decreases sharply as $T \rightarrow T_c+$ [573]. For lattice measurements of the tension of interfaces between confined and deconfined vacua, which indeed is rather small, see [574, 575]. It seems likely that the real-time dynamics of phase conversion for such a potential should be very different from that of ordinary, strongly first-order transitions, which proceed through nucleation. Some aspects of possible real-time dynamics in this potential were studied in [576, 577], where a Lorentz-invariant kinetic term for the Polyakov loop in Minkowski time was assumed.

4.4.1.2 Matrix models of Polyakov loops

In the previous section, we have integrated out all degrees of freedom except for the loop in the fundamental representation, thereby generating an effective scalar field theory for the order parameter which is globally invariant under the center symmetry. Such a model, however, doesn’t tell us how loops in other representations behave and how factorization arises at large N . One way out is to simply extend the effective theory to include loops in higher representations as independent scalar degrees of freedom [578]. However, even then, the factorization property is not reproduced in general. Also, lattice measurements of the $SU(3)$ renormalized adjoint loop in the confined phase [560] find that its expectation value is zero to within the numerical

⁶ Which prohibits terms $\sim \ell$, hence $\mathcal{V}'(0) = 0$ for any T is implied.

accuracy. This observation is not explained by $Z(N)$ symmetry since the adjoint loop is neutral. It is also not explained naturally by factorization alone, which would allow an expectation value on the order of $1/N^2 \sim 10\%$.

A natural solution for these questions is offered by matrix models. Here, the basic degrees of freedom are the $SU(3)$ Wilson line matrices \mathbf{L} . Damgaard et al. [579–585] showed that when fluctuations in the matrix model are neglected, the expectation value of *any* loop, including those with vanishing $Z(N)$ charge, vanish in the confined phase. If the Wilson line is constant in space, $\mathbf{L}(\mathbf{x}) = \mathbf{L}$, the functional integral reduces to a single integral over \mathbf{L} ,

$$\mathcal{Z} = \int d\mathbf{L} \exp(-N^2 \mathcal{V}(\mathbf{L})) . \quad (4.58)$$

Kinetic terms have been constructed in [586] but shall be ignored here (we consider just the matrix-valued mean-field theory). To be invariant both under $SU(N)$ gauge and global $Z(N)$ transformations, the potential must be a sum of $Z(N)$ neutral loops:

$$\mathcal{V}(\mathbf{L}) = -m^2 \ell_{ad} + \sum_{e_{\mathcal{R}}=0} \kappa_{\mathcal{R}} \operatorname{Re} \ell_{\mathcal{R}} , \quad (4.59)$$

where the adjoint loop has been pulled out of the sum. Note that, by group theory, higher powers of any loop can be reexpressed as a linear sum over loops in other representations, so this is the most general potential possible.

Since $\ell_{ad} = |\ell_N|^2 + \mathcal{O}(1/N^2)$, at large N the adjoint loop is simply a mass term for the fundamental loop, while loops in higher representations look like interactions of the fundamental loop (plus new terms, such as $\operatorname{tr} \mathbf{L}^2/N$, etc.) [586–589]:

$$\mathcal{V}(\mathbf{L}) = -m^2 |\ell_N|^2 + \kappa_4 (|\ell_N|^2)^2 + \kappa_6 (|\ell_N|^2)^3 + \dots . \quad (4.60)$$

The couplings $\kappa_{\mathcal{R}}$ in (4.59) have been relabeled as κ_{2n} , where the subscript now denotes the power of ℓ_N . As before, the $U(1)$ symmetry is broken to $Z(N)$ by a term $\sim \kappa_N \operatorname{Re} (\ell_N)^N$, but this is negligible at large N .

We can now return to the question as to why the expectation values of all loops, even of $Z(N)$ neutral ones, vanish in the confined phase. On physical grounds, it appears rather obvious that the confined phase corresponds to zero potential (mathematically more precise arguments are given in Sect. IV A of [586]). If the potential vanishes, though, the expectation value of any loop is simply an integral over the invariant group measure. For any (nontrivial) representation, however, whatever the $Z(N)$ charge of the loop, its integral over the measure vanishes,

$$\int \ell_{\mathcal{R}} d\mathbf{L} = 0 . \quad (4.61)$$

4.4.2 QCD: finite pion masses

4.4.2.1 Explicit breaking of $Z(N)$ by quarks

Pure $SU(N)$ is, of course, only interesting in theory. In reality, the dynamics is also affected by the presence of dynamical fermions in the fundamental representation (quarks). For example, the critical temperature in physical units decreases from $T_c/\sqrt{\sigma_0} \simeq 0.63$ for infinitely heavy quarks (pure gauge theory) to $T_c/\sqrt{\sigma_0} \simeq 0.41$ for massless quarks [546]. The scale is set by the $T = 0$ string tension of $SU(3)$: $\sqrt{\sigma_0} \simeq 425$ MeV.

On the other hand, the lattice also finds approximate “flavor independence” of the pressure [131]. That is, p/p_{SB} , where p_{SB} is the Stefan-Boltzmann ideal-gas pressure, is a nearly *universal* function of T/T_c . Also, near T_c , the temperature-susceptibility for the Polyakov loop peaks strongly [590] even in full QCD with dynamical fermions. Such observations suggest that perhaps fermions do not change the picture fundamentally.

The simplest way to incorporate fermion effects into the effective theory of Polyakov loops is through a “background magnetic field” term $\sim -h \ell_N$ [556, 591–594]. Such a term tilts the potential towards positive, real values of ℓ_N , which now acquires an expectation value even at low temperatures. If h is not too large though, $\langle \ell_N \rangle$ remains an approximate order parameter for deconfinement, in the sense that it changes rapidly within a small interval of temperature. For h larger than some critical value h_c , the phase transition ceases to exist in the strict sense (for example, $h_c = 0$ for a second-order phase transition but $h_c > 0$ for an ordinary first-order transition with finite correlation lengths); we shall nevertheless continue to use the term “critical temperature T_c ” in a more loose sense, namely for the temperature where the derivative of the order parameter $\partial \langle \ell_N \rangle / \partial T$ peaks.

In general, we expect that $h \rightarrow 0$ as the quark masses are sent to infinity since this limit brings us back to the pure gauge theory. On the other hand, if the quarks are made lighter and lighter, h should grow.⁷ At some point, it might not suffice any more to “integrate out” the quarks and represent them by a term $h \ell_N$. For very light quarks (and/or for large $q - \bar{q}$ asymmetry) one would then need to study quark effects *dynamically* (in particular, chiral symmetry restoration), which will likely couple to that of Polyakov loops [595–602]. The following sections attempt to shed some light on these issues.

⁷ Also, we expect that h is proportional to the number of quark flavors but inversely proportional to the number of colors since the number of gluons $\sim N^2$, while the number of quarks $\sim N_f N$: $h \sim N_f/N$.

4.4.2.2 Quark mass dependence of the QCD transition temperature

In QCD, T_c depends on the mass of the quarks [508], while in the effective Lagrangian for Polyakov loops, it depends on the strength of the “background magnetic field” h . By matching, one can extract the function $h(m_q)$, which gives us an idea of the typical magnitude of the symmetry breaking term both for heavy and (by naive extrapolation) light quarks. It also allows us to estimate the deconfining critical endpoint h_c for three colors [603].

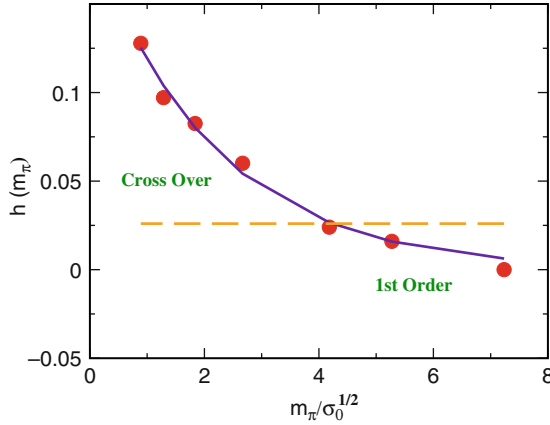


Fig. 4.15 h as a function of m_π , obtained by matching to three flavor lattice data for $T_c(m_\pi)$. The solid line corresponds to an exponential increase of h with decreasing m_π . The broken horizontal line displays the endpoint of the line of first-order phase transitions, $h = h_c$; the intersection with the $h(m_\pi)$ curve then gives the corresponding pion mass. Figure from [603].

From Fig. 4.15, the reduction of T_c by $\approx 33\%$ as $m_\pi : \infty \rightarrow \sqrt{\sigma_0}$ requires only small explicit breaking of the $Z(3)$ symmetry for the Polyakov loop. $h \leq 0.15$ even for the smallest pion masses studied in [508]. This is due to the rather small masses (or interface tension) for the first-order phase transition of the $SU(3)$ gauge theory. Also, $h(m_\pi)$ appears to follow the expected behavior $\sim \exp(-m_\pi)$. The exponential fit shown by the solid line corresponds to $h(m_\pi) = a \exp(-b m_\pi / \sqrt{\sigma_0})$, with $a = 0.19$ and $b = 0.47$. Surprisingly, by naive extrapolation one obtains a pretty small explicit symmetry breaking even in the chiral limit, $h \approx 0.2$.

The endpoint of the line of first-order transitions at $h_c = 0.026$ (indicated by the dashed horizontal line) intersects the curve $h(m_\pi)$ at $m_\pi / \sqrt{\sigma_0} \approx 4.2$. For heavier pions the theory exhibits a first-order deconfining phase transition, which then turns into a cross over for $m_\pi \lesssim 4.2 \sqrt{\sigma_0} \approx 1.8 \text{ GeV}$. This

is compatible with the estimates from [593] which span the range $m_\pi^{\text{crit}} = 1.4\text{--}2.5$ GeV, depending on N_f .

A direct confirmation of such large values of m_π^{crit} from the lattice would be useful to test whether indeed $SU(3)$ is close to the Gross-Witten point [586], where the first-order transition disappears right away, for any nonzero background field. This could perhaps be done by following the ratio of screening masses for the imaginary and real parts of the fundamental loop as a function of m_π . Perturbatively (to leading order), in the pure gauge theory this ratio is $3/2$ since $\text{Im } \ell \sim \text{tr } A_0^3$, while $\text{Re } \ell \sim \text{tr } A_0^2$. At T_c+ , from a $Z(3)$ symmetric loop potential m_i/m_r is ~ 3 [557, 604]. For finite quark masses this ratio should increase and finally diverge at the deconfinement critical endpoint [605]: while $\text{Re } \ell$ is critical, $\text{Im } \ell$ is not.

There is no phase transition for intermediate quark masses, with a first order chiral transition appearing for three flavors of *light* quark masses, near the chiral limit [42]. The first-order chiral phase transition itself ends in a critical point when the quarks are too heavy. Given that the explicit symmetry breaking term for the Polyakov loop appears to remain rather small even when extrapolated to $m_\pi = 0$ (namely $h \rightarrow 0.19$), the *chiral* critical endpoint might be located rather close to the chiral limit. Lattice estimates for $N_f = 3$ range from $m_\pi^{\text{crit},\chi} \simeq 290$ MeV [194] for standard staggered fermion action and $N_t = 4$ lattices; improved p4-actions predict values as low as $\simeq 67$ MeV [606].

Hence, although in terms of m_π the endpoint of first-order deconfinement phase transitions appears to be far from the physical point, this could very well originate in the rather unusual properties of the three-color gauge theory, and of the Gross-Witten point. Polyakov loops should then remain important degrees of freedom in QCD with physical pion and kaon masses.

4.4.2.3 Nonzero quark-antiquark asymmetry

We finally proceed to include effects from a nonzero excess of quarks over antiquarks, represented by a quark-chemical potential $\mu > 0$. The potential is given by the sum of contributions of gluons and quarks, $\mathcal{V}_{gl}(\mathbf{L}) + \mathcal{V}_{qk}(\mathbf{L})$, which are (gauge invariant) functions of the Wilson line. The gluonic contribution is constructed as before, Sect. 4.4.1. Here, we will restrict the analysis to the Gross-Witten point, or the $N = 3$ analogy thereof, and only include a mass term: $\mathcal{V}_{gl}(\mathbf{L}) = -m^2 \ell_{\bar{N}} \ell_N$, $\ell_N = \text{tr } \mathbf{L}/N$, $\ell_{\bar{N}} = \ell_N^*$. Under charge conjugation, the Wilson line transforms into its complex conjugate, and the chemical potential changes sign. In general, \mathcal{V}_{qk} involves all possible traces of $e^\mu \mathbf{L}$ and $e^{-\mu} \mathbf{L}^*$ in such combinations which are invariant under charge conjugation. These two matrices represent, respectively, the propagation of a particle forward in imaginary time, and of an anti-particle backward in time. The simplest possible contribution to the quark loop potential is then [591–593, 607–610]

$$\begin{aligned}\mathcal{V}_{qk}(\mathbf{L}) &= -\frac{h}{2} (e^{\mu} \ell_N + e^{-\mu} \ell_{\overline{N}}) \\ &= -h (\cosh(\mu) \operatorname{Re} \ell_N + i \sinh(\mu) \operatorname{Im} \ell_N) \quad ,\end{aligned}\quad (4.62)$$

(The parameter μ is the quark chemical potential divided by temperature).

At zero chemical potential, quarks generate a real background $Z(N)$ field for the real component of the loop, $\sim \operatorname{Re} \ell_N$, see the discussion at the beginning of the present Sect. 4.4.2. When the chemical potential is nonzero, however, the background $Z(N)$ field not only contains a piece proportional to the imaginary part of the loop, $\sim \operatorname{Im} \ell_N$, but with a coefficient which is itself imaginary. (Unless $N = 2$, where $\operatorname{Im} \ell_N \equiv 0$; this case will not be discussed here further.) Hence, the potential generated by quarks is complex, (4.62). This is how the fermion sign problem appears in a matrix model.

In this case, though, it is easy to show that the partition function is manifestly real. If a given matrix, \mathbf{L} , contributes, then so does its charge conjugate, \mathbf{L}^* . Adding the contributions of \mathbf{L} and \mathbf{L}^* we can write $\mathcal{Z} = \int d\mathbf{L} \exp(-\tilde{\mathcal{V}}(\mathbf{L})) \cos(\tilde{h} \operatorname{Im} \ell_N)$, where $\tilde{h} = (N^2 - 1) h \sinh(\mu)$ and $\tilde{\mathcal{V}}(\mathbf{L}) = (N^2 - 1) (\mathcal{V}_{gl}(\mathbf{L}) - h \cosh(\mu) \operatorname{Re} \ell_N)$. It should be noted that $\mu > 0$ effectively *increases* the background $Z(N)$ -breaking field; its strength is now given by $h \cosh \mu$. Turning on the chemical potential therefore corresponds to moving *away* from the deconfining critical endpoint at h_c [611]. If correlations are dominated by the Polyakov loop even for physical quark masses, then correlation lengths should decrease as μ increases. At fixed temperature, in an expansion about $\mu = 0$, a decrease of the screening masses with μ was indeed observed in [612], see also [197].

We also note that at large N (but with h fixed), effects due to a nonzero quark-chemical potential appear only in subleading terms [611]. This is because at large N , the difference between the measure for $SU(N)$ and that for $U(N)$ is of order $\mathcal{O}(1/N)$, and because terms which break $U(1)$ invariance of \mathcal{V}_{gl} are negligible. Letting $e^{\mu} \ell_N \rightarrow \ell_N$ and $e^{-\mu} \ell_{\overline{N}} \rightarrow \ell_{\overline{N}}$, one can then “rotate” the quark-chemical potential away. The very weak dependence of the (pseudo-) critical temperature on the chemical potential at small μ [155, 156, 159] might find a natural explanation.

To describe both the deconfining *and* the chiral transitions in the region of small quark masses, it is necessary to introduce a chiral order parameter, and couple that to the Wilson line [595–602]. First attempts to do this within a matrix model have been undertaken by Chen and deTar [599]. In the plane of μ and T , there may be a critical end point at large μ , where the correlation length for the sigma meson diverges; that for the Polyakov loop will remain finite, except from its coupling to the sigma. It is possible that for three colors, the coincidence of the chiral and deconfining “transitions” at $\mu = 0$ breaks down at some finite value of μ [611].

The mentioned coupling of the Wilson line to a chiral order parameter is modeled in the next section on the mean field level within Polyakov-loop-extended quark models.

4.5 Phase diagram and thermodynamics of the PNJL and PQM models

The present section is devoted to a review of quark models which, on the one hand side, describe chiral symmetry and its spontaneous breaking (on the mean field level) and, on the other hand side, incorporate aspects of the Polyakov loop discussed in the previous Sect. 4.4.

4.5.1 The NJL model

Models of the Nambu and Jona-Lasinio (NJL) type [613] have a long history and have been used extensively to describe the dynamics and thermodynamics of the lightest hadrons [39, 614–616], including investigations of phase diagrams [349, 617]. Such schematic models offer a simple and practical illustration of the basic mechanisms that drive spontaneous chiral symmetry breaking, a key feature of QCD in its low-temperature, low-density phase.

The NJL model is based on an effective Lagrangian of relativistic fermions (quarks) which interact through local current–current couplings, assuming that gluonic degrees of freedom can be frozen into pointlike effective interactions between quarks. Lattice QCD results for the gluonic field strength correlation function [618] demonstrate that the colour correlation length, i.e. the distance over which colour fields propagate in the QCD vacuum, is small, of order 0.2 fm corresponding to a characteristic momentum scale Λ of order 1 GeV. Consider now the basic non-local interaction between two quark colour currents, $J_i^\mu = \bar{\psi} \gamma^\mu t_i \psi$, where t_i are the generators of the $SU(N_c)$ colour gauge group. The contribution of this current–current coupling to the action is:

$$S_{int} = -\frac{1}{2} \int d^4x d^4y J_i^\mu(x) g^2 D_{\mu\nu}^{ij}(x, y) J_j^\nu(y) \quad , \quad (4.63)$$

where $D_{\mu\nu}^{ij}$ is the full gluon propagator and g is the QCD coupling. In perturbative QCD this S_{int} generates the familiar one-gluon exchange interaction between quarks and maintains its non-local structure. That is the situation realised in the quark-gluon phase at extremely high temperatures. As one approaches the hadronic phase around a critical temperature of about 0.2 GeV, the propagating gluons experience strong screening effects which cannot be handled perturbatively. If the range over which colour can be transported is now restricted to the short distance scale Λ^{-1} , while typical momentum scales (Fermi momenta) of the quarks are small compared to Λ , then the quarks experience an interaction which can be approximated by a local coupling between their colour currents:

$$\mathcal{L}_{int} = -G_c J_\mu^i(x) J_i^\mu(x) \quad , \quad (4.64)$$

where $G_c \sim \bar{g}^2 \Lambda^{-2}$ is an effective coupling strength of dimension *length*² which encodes the QCD coupling, averaged over the relevant distance scales, in combination with the squared correlation length, Λ^{-2} . In essence, by “integrating out” gluon degrees of freedom and absorbing them in the four-fermion interaction \mathcal{L}_{int} , the local $SU(N_c)$ gauge symmetry of QCD is now replaced by a global $SU(N_c)$ symmetry of the NJL model. Apart from this step, the interaction Lagrangian (4.64) evidently preserves the chiral $SU(N_f) \times SU(N_f)$ symmetry that it shares with the original QCD Lagrangian for N_f massless quark flavours.

A Fierz transform of the colour current–current interaction (4.64) produces a set of exchange terms acting in quark–antiquark channels. For the $N_f = 2$ case:

$$\mathcal{L}_{int} \rightarrow \frac{G}{2} [(\bar{\psi}\psi)^2 + (\bar{\psi}i\gamma_5\tau\psi)^2] + \dots, \quad (4.65)$$

where $\tau = (\tau_1, \tau_2, \tau_3)$ are the isospin $SU(2)$ Pauli matrices. Not shown for brevity is a series of terms with combinations of vector and axial vector currents, both in colour singlet and colour octet channels. The constant G is proportional to the colour coupling strength G_c . Their ratio is uniquely determined by N_c and N_f .

Equation (4.65) is the starting point of the standard NJL model. In the mean field (Hartree) approximation, the NJL equation of motion leads to the gap equation

$$m = m_0 - G\langle\bar{\psi}\psi\rangle. \quad (4.66)$$

With a small bare (current) quark mass m_0 as input, this equation links the dynamical generation of a large constituent quark mass m to spontaneous chiral symmetry breaking and the appearance of the quark condensate

$$\langle\bar{\psi}\psi\rangle = -Tr \lim_{x \rightarrow 0^+} \langle\mathcal{T}\psi(0)\bar{\psi}(x)\rangle = -2iN_fN_c \int \frac{d^4p}{(2\pi)^4} \frac{m \theta(\Lambda^2 - \mathbf{p}^2)}{p^2 - m^2 + i\varepsilon}. \quad (4.67)$$

For $m_0 = 0$ a non-zero quasiparticle mass develops dynamically, together with a non-vanishing chiral condensate, once G exceeds a critical value. The procedure requires a momentum cutoff $\Lambda \simeq 2m$ beyond which the interaction is “turned off”. Note that the strong interaction, by polarizing the vacuum and turning it into a condensate of quark–antiquark pairs, transforms an initially pointlike quark with its small bare mass m_0 into a massive quasiparticle with a finite size. (Such an NJL-type mechanism is commonly thought to be at the origin of the phenomenological constituent quark masses $m \sim 0.3\text{--}0.4$ GeV).

While the NJL model illustrates the transmutation of originally light (or even massless) quarks and antiquarks into massive quasiparticles, it generates at the same time pions as Goldstone bosons of spontaneously broken chiral symmetry. NJL type approaches have also been used extensively to explore colour superconducting phases at high densities through the formation of various sorts of diquark condensates [27, 28, 349].

4.5.2 Introducing the PNJL model

Despite their widespread use, NJL models have a principal deficiency. The reduction to global (rather than local) colour symmetry has the consequence that quark confinement is missing. Confinement is the second key feature of low-energy QCD besides spontaneous chiral symmetry breaking. While confinement is a less significant aspect for $N_c = 2$ thermodynamics which can be described quite successfully using the simplest NJL approach [619], it figures prominently for $N_c = 3$ QCD. There have been ongoing discussions whether deconfinement and the restoration of chiral symmetry are directly connected in the sense that they appear at the same transition temperature T_c , as suggested by earlier lattice computations. In any case, as one approaches T_c from above, all versions of the “classic” NJL model encounter the problem that they operate with the “wrong” degrees of freedom. Quarks as coloured quasiparticles are incorrectly permitted to propagate over large distances even in the hadronic sector of the phase diagram. In contrast, confinement and spontaneous chiral symmetry breaking imply that QCD below T_c turns into a low-energy effective theory of weakly interacting Goldstone bosons (pions) with derivative couplings to colour-singlet hadrons (rather than quarks).

As discussed in Sects. 2.1 and 4.4, in the limit of infinitely heavy quarks, the deconfinement phase transition is characterized by spontaneous breaking of the $Z(3)$ center symmetry of QCD. The corresponding order parameter is the thermal Wilson line, or Polyakov loop, winding around the imaginary time direction with periodic boundary conditions:

$$\phi(\mathbf{x}) = N_c^{-1} \text{Tr} \mathcal{P} \exp \left[i \int_0^\beta d\tau A_4(\mathbf{x}, \tau) \right], \quad (4.68)$$

with $\beta = 1/T$ the inverse temperature. Here $A_4 = iA^0$ is the temporal component of the Euclidean gauge field (\mathbf{A}, A_4) and \mathcal{P} denotes path ordering. In the presence of dynamical quarks the $Z(3)$ symmetry is explicitly broken. The Polyakov loop ceases to be a rigorous order parameter but still serves as an indicator of a rapid crossover towards deconfinement.

Recent developments have aimed at a synthesis of the NJL model with Polyakov loop dynamics. The principal idea is to introduce both the chiral condensate $\langle \bar{\psi}\psi \rangle$ and the Polyakov loop ϕ as classical, homogeneous fields which couple to the quarks according to rules dictated by the symmetries and symmetry breaking patterns of QCD, thus unifying aspects of confinement and chiral symmetry breaking. We refer to this combined scheme as the PNJL (Polyakov-loop-extended NJL) model (see also [620, 621]).

Throughout this presentation we work with two flavours ($N_f = 2$) and specify the PNJL Lagrangian [620] as follows. Its basic ingredients are the Nambu and Jona-Lasinio type four-fermion contact term and the coupling to a (spatially constant) temporal background gauge field representing Polyakov

loop dynamics:

$$\begin{aligned} \mathcal{L}_{PNJL} = & \bar{\psi} (i\gamma_\mu D^\mu - \hat{m}_0) \psi + \frac{G}{2} \left[(\bar{\psi}\psi)^2 + (\bar{\psi}i\gamma_5\boldsymbol{\tau}\psi)^2 \right] \\ & - \mathcal{U}(\phi[A], \phi^*[A]; T) , \end{aligned} \quad (4.69)$$

where $\psi = (\psi_u, \psi_d)^T$ is the quark field,

$$D^\mu = \partial^\mu - iA^\mu \quad \text{and} \quad A^\mu = \delta_0^\mu A^0 , \quad (4.70)$$

with $A^0 = -iA_4$. The gauge coupling g is conveniently absorbed in the definition of $A^\mu(x) = g\mathcal{A}_a^\mu(x)\frac{\lambda_a}{2}$ where \mathcal{A}_a^μ is the SU(3) gauge field and λ_a are the Gell-Mann matrices. The two-flavour current quark mass matrix is $\hat{m}_0 = \text{diag}(m_u, m_d)$ and we shall work in the isospin symmetric limit with $m_u = m_d \equiv m_0$. As previously mentioned, G is the coupling strength of the chirally symmetric four-fermion interaction.

The effective potential $\mathcal{U}(\phi, \phi^*; T)$ is expressed in terms of the traced Polyakov loop (4.68), reduced to our case of a constant Euclidean field A_4 :

$$\phi = \frac{1}{3} \text{Tr}_c \exp \left[\frac{iA_4}{T} \right] . \quad (4.71)$$

In a convenient gauge (the so-called Polyakov gauge), the Polyakov loop matrix can be given a diagonal representation [601].

The effective potential \mathcal{U} has the following general features. It must satisfy the $Z(3)$ center symmetry just like the pure gauge QCD Lagrangian. Furthermore, in accordance with lattice results for the behaviour of the Polyakov loop as a function of temperature T , the potential \mathcal{U} must have a single minimum at $\phi = 0$ at small T , while at high T it develops a second minimum which becomes the absolute minimum above a critical temperature T_0 . In the limit $T \rightarrow \infty$ we have $\phi \rightarrow 1$. The following general form is chosen for \mathcal{U} , including a ϕ^3 term which reflects the underlying $Z(3)$ symmetry:

$$\frac{\mathcal{U}(\phi, \phi^*; T)}{T^4} = -\frac{b_2(T)}{2} \phi^* \phi - \frac{b_3}{6} (\phi^3 + \phi^{*3}) + \frac{b_4}{4} (\phi^* \phi)^2 \quad (4.72)$$

with

$$b_2(T) = a_0 + a_1 \left(\frac{T_0}{T} \right) + a_2 \left(\frac{T_0}{T} \right)^2 + a_3 \left(\frac{T_0}{T} \right)^3 . \quad (4.73)$$

A precision fit of the coefficients a_i , b_i is performed to reproduce the pure-gauge lattice data.

There is a subtlety about the Polyakov loop field, ϕ , and its conjugate, ϕ^* , in the presence of quarks. At zero chemical potential we have $\phi = \phi^*$, i.e. the field ϕ is real, it serves as an order parameter for deconfinement and a mean-field calculation is straightforward. At non-zero quark chemical potential, $Z(3)$ symmetry is explicitly broken and ϕ differs from ϕ^* while their

thermal expectation values $\langle\phi\rangle$ and $\langle\phi^*\rangle$ remain real [611]. A detailed analysis of the stationary points of the action under these conditions requires calculations beyond mean field which will be reported elsewhere [622]. We proceed here, as in [620], by introducing $\Phi \equiv \langle\phi\rangle$ and $\bar{\Phi} \equiv \langle\phi^*\rangle$ as new independent field variables which replace ϕ and ϕ^* in Eq. (4.72). This approximate prescription corresponds to a modified mean-field scheme which can account for the difference between Φ and $\bar{\Phi}$ in the presence of quarks. The more accurate treatment is under way.

Using standard bosonization techniques, we introduce the auxiliary bosonic fields σ and π for the scalar-isoscalar and pseudoscalar-isovector quark bilinears in Eq. (4.69). The expectation value of the σ field is directly related to the chiral condensate by $\langle\sigma\rangle = G\langle\bar{\psi}\psi\rangle$ and the gap equation becomes

$$m = m_0 - \langle\sigma\rangle . \quad (4.74)$$

Note that $\langle\sigma\rangle$ is negative in our representation, and the chiral (quark) condensate is $\langle\bar{\psi}\psi\rangle = \langle\bar{\psi}_u\psi_u + \bar{\psi}_d\psi_d\rangle$.

Before passing to the actual calculations, we summarize basic assumptions behind Eq. (4.69) and comment on limitations to be kept in mind. The PNJL model reduces gluon dynamics to (a) chiral point couplings between quarks, and (b) a simple static background field representing the Polyakov loop. This picture can be expected to work only within a limited range of temperatures. At large T , transverse gluons are known to be thermodynamically active degrees of freedom, but they are ignored in the PNJL model. To what extent this model can reproduce lattice QCD thermodynamics is nonetheless a relevant question. We can assume that its range of applicability is, roughly, $T \leq (2-3)T_c$, based on the conclusion drawn in [623] that transverse gluons start to contribute significantly for $T > 2.5 T_c$.

4.5.3 Parameter fixing

The parameters of the Polyakov loop potential \mathcal{U} are fitted to reproduce the lattice data [105] for QCD thermodynamics in the pure gauge sector. Minimizing $\mathcal{U}(\Phi, \bar{\Phi}, T)$ one has $\Phi = \bar{\Phi}$ and the pressure of the pure-gauge system is evaluated as $p(T) = -\mathcal{U}(T)$ with $\Phi(T)$ determined at the minimum. The entropy and energy density are then obtained by means of the standard thermodynamic relations. Figure 4.16a shows the behaviour of the Polyakov loop as a function of temperature, while Fig. 4.16b displays the corresponding (scaled) pressure, energy density and entropy density. The lattice data are reproduced extremely well using the ansatz (4.72) and (4.73), with parameters summarized in Table 4.1. The critical temperature T_0 for deconfinement appearing in Eq. (4.73) is fixed at $T_0 = 270$ MeV in the pure gauge sector.

Table 4.1 Parameter set used in [620] for the Polyakov loop potential (4.72) and (4.73).

a_0	a_1	a_2	a_3	b_3	b_4
6.75	-1.95	2.625	-7.44	0.75	7.5

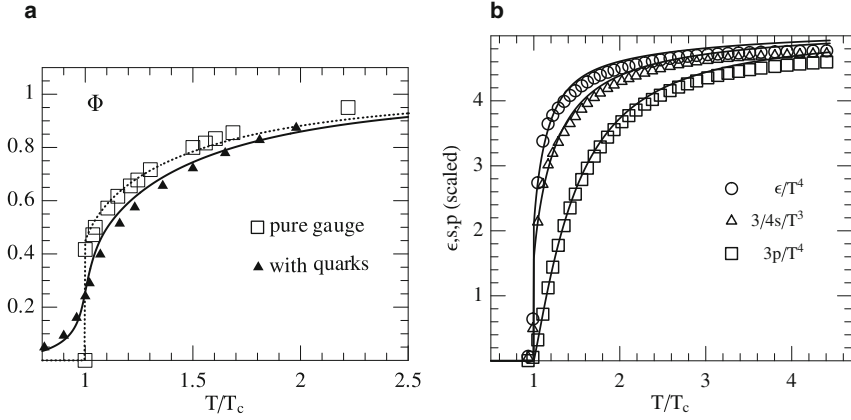


Fig. 4.16 **a** Using the fit of the Polyakov loop (*dotted line*) to lattice results taken from [561] in the pure gauge sector (*empty symbols*), the PNJL model predicts the Polyakov loop behaviour as a function of temperature in the presence of dynamical quarks (*solid line*). This prediction is compared to lattice data in two flavours (*full symbols*) taken from [176]. **b** Scaled pressure, entropy density and energy density as functions of the temperature in the pure gauge sector, compared to the corresponding lattice data taken from [105].

The pure NJL model part of the Lagrangian (4.69) has the following parameters: the “bare” quark mass m_0 , a three-momentum cutoff Λ and the coupling strength G . We fix them by reproducing the known chiral physics in the hadronic sector at $T = 0$: the pion decay constant f_π , the chiral condensate $|\langle\bar{\psi}_u\psi_u\rangle|^{1/3}$ and the pion mass m_π are evaluated in the model and adjusted at their empirical values. The results are shown in Table 4.2.

Table 4.2 Parameter set used for the NJL model part of the effective Lagrangian (4.69), and the resulting physical quantities. These values of the parameters yield a constituent quark mass $m = 325$ MeV.

Λ [GeV]	G [GeV ⁻²]	m_0 [MeV]
0.651	10.08	5.5
$ \langle\bar{\psi}_u\psi_u\rangle ^{1/3}$ [MeV]	f_π [MeV]	m_π [MeV]
251	92.3	139.3

4.5.4 Thermodynamics at finite chemical potential

4.5.4.1 General features

We now extend the model to finite temperature and chemical potentials using the Matsubara formalism. We consider the isospin symmetric case, with an equal number of u and d quarks (and therefore a single quark chemical potential μ). The quantity to be minimized at finite temperature is the thermodynamic potential per unit volume:

$$\begin{aligned} \Omega = & \mathcal{U}(\Phi, \bar{\Phi}, T) + \frac{\sigma^2}{2G} \\ & - 2N_f T \int \frac{d^3p}{(2\pi)^3} \left\{ \text{Tr}_c \ln \left[1 + e^{-(E_p - \tilde{\mu})/T} \right] + \text{Tr}_c \ln \left[1 + e^{-(E_p + \tilde{\mu})/T} \right] \right\} \\ & - 6N_f \int \frac{d^3p}{(2\pi)^3} E_p \theta(\Lambda^2 - \mathbf{p}^2) \quad , \end{aligned} \quad (4.75)$$

where $\tilde{\mu} = \mu + iA_4$ and $E_p = \sqrt{\mathbf{p}^2 + m^2}$ is the quark quasiparticle energy. The last term involves the NJL three-momentum cutoff Λ . The second (finite) term does not require any cutoff.

Notice that the coupling of the Polyakov loop to quarks effectively reduces the residues at the quark quasiparticle poles as the critical temperature is approached from $T > T_c$: expanding the logarithms in the second line of (4.75) one finds $\text{Tr}_c \ln(1 + \exp[-(E_p - \mu - iA_4)/T]) = 3\phi \exp[-(E_p - \mu)/T] + \dots$, with ϕ then to be replaced by $\langle \phi \rangle \equiv \bar{\Phi}$ which tends to zero as $T \rightarrow T_c$.

From the thermodynamic potential (4.75) the equations of motion for the mean fields σ, Φ and $\bar{\Phi}$ are determined through

$$\frac{\partial \Omega}{\partial \sigma} = 0 \quad , \quad \frac{\partial \Omega}{\partial \Phi} = 0 \quad , \quad \frac{\partial \Omega}{\partial \bar{\Phi}} = 0 \quad . \quad (4.76)$$

This set of coupled equations is then solved for the fields as functions of temperature T and quark chemical potential μ . Figure 4.17a shows the chiral condensate together with the Polyakov loop $\bar{\Phi}$ as functions of temperature at $\mu = 0$ where we find $\Phi = \bar{\Phi}$. One observes that the introduction of quarks coupled to the σ and Φ fields turns the first-order transition seen in pure-gauge lattice QCD into a continuous crossover. The crossover transitions for the chiral condensate $\langle \bar{\psi}\psi \rangle$ and for the Polyakov loop almost coincide at a critical temperature $T_c \simeq 220$ MeV (see Fig. 4.17b). We point out that this feature is obtained without changing a single parameter with respect to the pure gauge case. The value of the critical temperature found here is a little high if compared to the available data for two-flavour Lattice QCD [58, 508] which give $T_c = (173 \pm 8)$ MeV. For quantitative comparison with existing lattice results we choose to reduce T_c by rescaling the parameter T_0 from 270 to 190 MeV. In this case we loose the perfect coincidence of the chiral

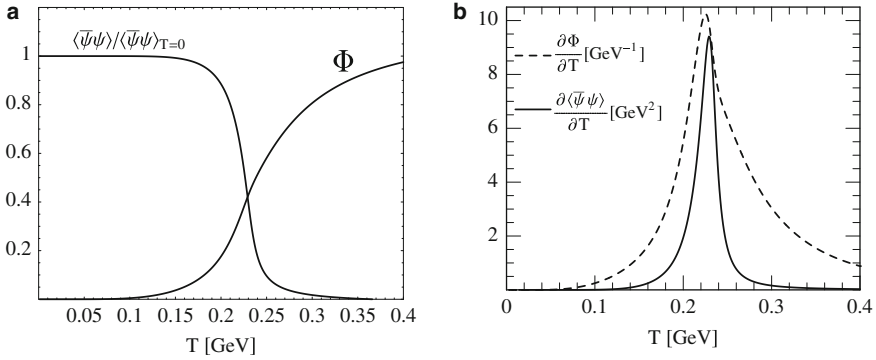


Fig. 4.17 *Left:* Scaled chiral condensate and Polyakov loop $\Phi(T)$ as functions of temperature at zero chemical potential. *Right:* Plots of $\partial\langle\bar{\psi}\psi\rangle/\partial T$ and $\partial\Phi/\partial T$.

and deconfinement transitions, but they are shifted relative to each other by less than 20 MeV. When defining T_c in this case as the average of the two transition temperatures we find $T_c = 180$ MeV.

4.5.4.2 Detailed comparison with lattice data

The primary aim is now to compare predictions of the PNJL model with the lattice data available for full QCD thermodynamics (with quarks included) at zero and finite chemical potential μ . Consider first the pressure $p(T, \mu = 0) = -\Omega(T, \mu = 0)$ of the quark-gluon system at zero chemical potential. Results are presented in Fig. 4.18 in comparison with corresponding lattice data. We point out that the input parameters of the PNJL model have been fixed independently in the pure gauge and hadronic sectors, so that the calculated pressure is a prediction of the model, without any further tuning of parameters. With this in mind, the agreement with lattice results is quite satisfactory. As a word of caution it is noted that the shown lattice results are obtained with rather large quark masses whereas physical quark masses are used in the PNJL model. Also shown in Fig. 4.18 is the result obtained in the standard NJL model. Its deficiencies are evident. At low temperatures the pressure comes out incorrect. The missing confinement permits quarks to be active degrees of freedom even in the forbidden region $T < T_c$. At high temperatures, the standard NJL result for the pressure is significantly lower than the one seen in the lattice data. The gluonic thermodynamics is missing altogether in the NJL model, whereas in the PNJL model it is partially taken into account by means of the Polyakov loop effective potential $\mathcal{U}(\Phi, \bar{\Phi}, T)$. As stated previously, the range of validity of this approach is limited, however, to temperatures smaller than $2.5 T_c$, beyond which transverse gluon degrees of freedom become important.

The introduction of the Polyakov loop within the PNJL quasiparticle model leads to a remarkable improvement in basically all thermodynamic quantities. The coupling of the quark quasiparticles to the field Φ reduces their weight as thermodynamically active degrees of freedom when the critical temperature T_c is approached from above. The quasiparticle exponentials $\exp[-(E_p \pm \mu)/T]$ are progressively suppressed in the thermodynamic potential as $T \rightarrow T_c$. This is what can be interpreted as the effect of confinement in the context of the PNJL model.

One must note that the lattice data are grouped in different sets obtained on lattices with temporal extent $N_t = 4$ and $N_t = 6$, both of which are not continuum extrapolated. In contrast, our calculation should, strictly speaking, be compared to the continuum limit. In order to perform meaningful comparisons, the pressure is divided by its asymptotic high-temperature (Stefan-Boltzmann) limit for each given case. At high temperatures the predicted curve should be located closer to the $N_t = 6$ set than to the one with $N_t = 4$. This is indeed the case.

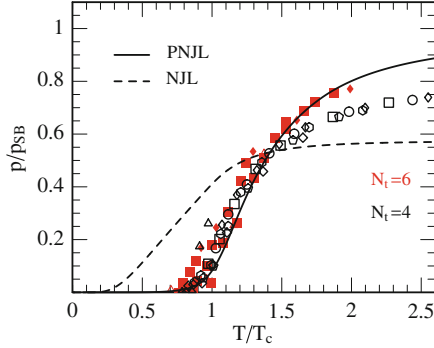


Fig. 4.18 Scaled pressure divided by the Stefan-Boltzmann (ideal gas) limit as a function of temperature at zero chemical potential: comparison between the PNJL model prediction [620] (*full line*), the standard NJL model result (*dashed*) and lattice results corresponding to $N_t = 4$ (*open symbols*) and $N_t = 6$ (*full symbols*). Lattice data are taken from [108].

At non-zero chemical potential, quantities of interest that have become accessible in lattice QCD are the “pressure difference” and the quark number density. The (scaled) pressure difference is defined as:

$$\frac{\Delta p(T, \mu)}{T^4} = \frac{p(T, \mu) - p(T, \mu = 0)}{T^4}. \quad (4.77)$$

A comparison of Δp , calculated in the PNJL model, with two-flavour lattice results is presented in Fig. 4.19. This figure shows the scaled pressure difference as a function of the temperature for a series of chemical potentials, with values ranging between $\mu = 0.2 T_c^{(0)}$ and $\mu \simeq T_c^{(0)}$ where $T_c^{(0)} \equiv T_c(\mu = 0)$.

The agreement between the PNJL model results [620] and the lattice data is quite satisfactory.

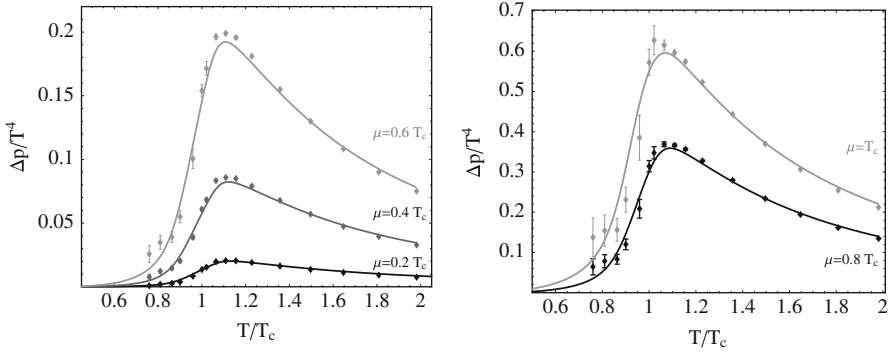


Fig. 4.19 Scaled pressure difference as a function of temperature at different values of the quark chemical potential (results from [620]), compared to lattice data taken from [130].

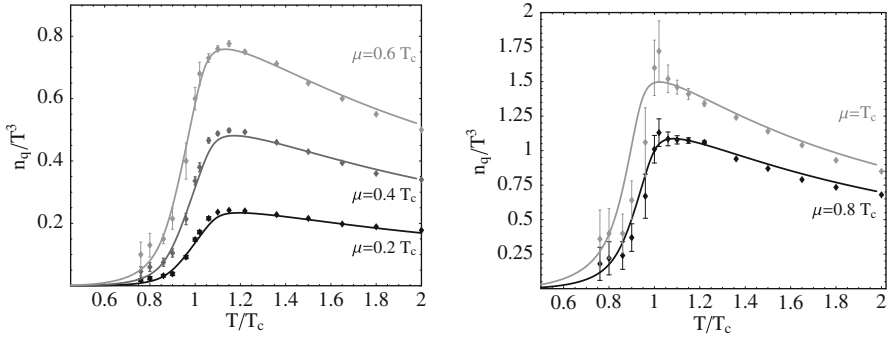


Fig. 4.20 Scaled quark number densities [620] as a function of temperature at different values of the chemical potential, compared to lattice data taken from [130].

A related quantity for which lattice results at finite μ exist, is the scaled quark number density, defined as:

$$\frac{n_q(T, \mu)}{T^3} = -\frac{1}{T^3} \frac{\partial \Omega(T, \mu)}{\partial \mu}. \quad (4.78)$$

Results [620] for n_q as a function of the temperature, for different values of the quark chemical potential, are shown in Fig. 4.20 in comparison with corresponding lattice data [130]. Also in this case, the agreement between the PNJL model and the corresponding lattice data is surprisingly good.

It is a remarkable feature that the quark densities and the pressure difference at finite μ are so well reproduced even though the lattice “data” have been obtained by a Taylor expansion up to fourth order in μ , whereas the PNJL thermodynamical potential is used with its full functional dependence on μ . We have examined the convergence in powers of μ by expanding Eq. (4.75). It turns out that the Taylor expansion to order μ^2 deviates from the full result by less than 10 % even at a chemical potential as large as $\mu \sim T_c$. When expanded to $\mathcal{O}(\mu^4)$, no visible difference is left between the approximate and full calculations for all cases shown in Figs. 4.19 and 4.20.

An exact copy of the PNJL model [620] has recently been employed in [624] to calculate susceptibilities and higher order derivatives in the expansion of the pressure $p(T, \mu) = -\Omega(T, \mu)$ around $\mu = 0$ (cf. (3.28)):

$$\frac{p(T, \mu)}{T^4} = \sum_{n \text{ even}} c_n(T) \left(\frac{\mu}{T}\right)^n. \quad (4.79)$$

The resulting quark number susceptibility

$$c_2(T) = \frac{1}{2T^2} \left(\frac{\partial^2 p}{\partial \mu^2} \right)_{\mu=0} \quad (4.80)$$

compares well with lattice QCD computations. The higher-order coefficients $c_{4,6}$ reproduce the corresponding lattice data around T_c very well, but c_4 as obtained in the PNJL calculation tends to be too large at higher temperatures. For a more quantitative understanding, further steps are yet necessary towards a consistent treatment beyond the mean-field level [622].

4.5.5 Phase diagram

Lattice data for the QCD phase diagram exist up to relatively high temperatures, but extrapolations to non-zero chemical potential are still subject to large uncertainties. It is nonetheless instructive to explore the phase diagram as calculated in the PNJL model [620] in comparison with present lattice QCD results. In particular, questions about the sensitivity of this phase diagram with respect to changes of the input quark masses will be addressed. This is an important issue, given the fact that most lattice QCD computations so far encounter technical limitations which restrict the input bare quark masses to relatively large values. The PNJL approach permits to vary the bare quark mass in a controlled way compatible with explicit chiral symmetry breaking in QCD. One can therefore interpolate between large quark masses presently accessible in lattice simulations, the physically relevant range of light quark masses around 5 MeV and further down to the chiral limit.

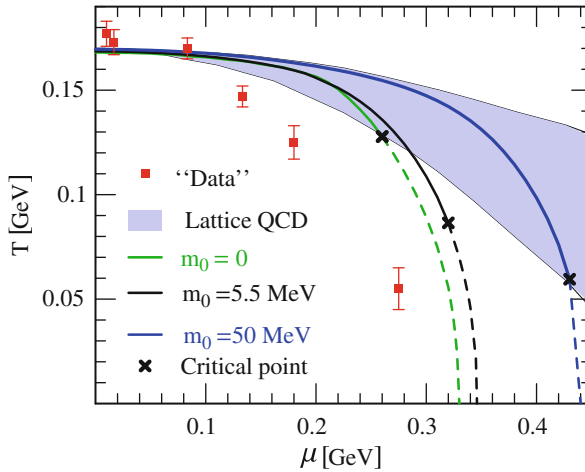


Fig. 4.21 Phase diagram of the PNJL model for different values of the bare quark mass m_0 . *Dashed lines* correspond to a first order phase transition, *full lines* to a crossover (or second order phase transition, respectively, for the case $m_0 = 0$). The band represents the extrapolation from lattice QCD results [156]. Also shown for orientation are the chemical freezeout “data” obtained through a thermal fit [625].

Figure 4.21 presents the two-flavour PNJL results of the phase boundaries in the (T, μ) plane. These calculations should still be considered as an exploratory study since they do not yet include explicit diquark degrees of freedom, an important ingredient when turning to large chemical potentials, and the Polyakov loop fields are still treated in an approximate mean-field framework. Some interesting tendencies are, however, already apparent at the present stage.

Curves are shown for three different values of the bare quark mass. For $m_0 = 50$ MeV the PNJL result falls within the broad band of lattice extrapolations using an expansion in powers of the quark chemical potential. Reducing the bare quark mass toward physically realistic values leaves the phase diagram at small chemical potentials basically unchanged. However, the phase boundary is shifted quite significantly to lower temperatures at increasing chemical potentials when m_0 is lowered. Also shown in the figure is the position of the critical point separating crossover from first order phase transition. The existence of a tricritical point was suggested many years ago within the framework of the effective potential for composite operator approach to the study of dynamical symmetry breaking [626–628]. We confirm its existence also in the PNJL model. In fact, examining the chiral condensate and the Polyakov loop as functions of temperature for a broad range of chemical potentials (see Fig. 4.22), one observes that there is a critical chemical potential above which these two quantities indicate a discontinuous jump from the confined (chirally broken) to the deconfined (chirally restored)

phase. While a more precise location of this critical point is subject to further refined calculations [622], the qualitative features outlined here are expected to remain, such as the observation that the position of the critical point depends sensitively on the input quark mass.

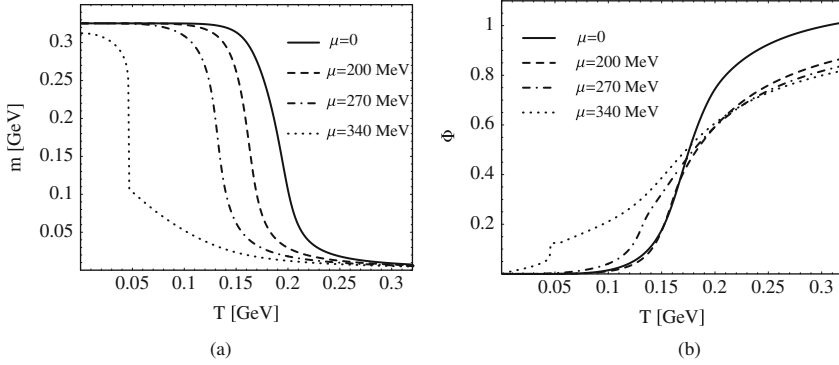


Fig. 4.22 Constituent quark mass (a) and Polyakov loop (b) as functions of temperature for different values of the chemical potential. In both figures, $m_0 = 5.5$ MeV.

4.5.6 The Polyakov–quark-meson model

The quark-meson (QM) model is another variant of an effective field theory which includes the chiral aspects of QCD. For two flavors the elementary fields are up and down quarks, pions and σ mesons. In a certain sense the QM model can be viewed as a partially bosonized version of the NJL model which has the advantage that no cut-off is needed since the model is renormalizable. The Lagrangian reads

$$\mathcal{L}_{QM} = \bar{q}(i\not{D} - g(\sigma + i\gamma_5 \boldsymbol{\tau} \boldsymbol{\pi}))q + \frac{1}{2}(\partial_\mu \sigma)^2 + \frac{1}{2}(\partial_\mu \boldsymbol{\pi})^2 - U(\sigma, \boldsymbol{\pi}) \quad (4.81)$$

where the mesonic potential is defined as

$$U(\sigma, \boldsymbol{\pi}) = \frac{\lambda}{4}(\sigma^2 + \boldsymbol{\pi}^2 - v^2)^2 - c\sigma. \quad (4.82)$$

Without the explicit symmetry breaking term c in the mesonic potential the Lagrangian is invariant under global chiral $SU(2)_L \times SU(2)_R$ rotations. The quarks receive their dynamical masses through the Yukawa coupling to the σ -field, which has a non-vanishing vacuum expectation value in the spontaneously broken phase.

As the NJL model, the QM model shows a chiral phase transition at realistic temperatures and similar characteristics, cf. e.g. [629–632]. Due to the lack of confinement also in this model single quark states are already excited at low temperatures in the chirally broken phase, see e.g. [633], resulting in an unrealistic EoS near the phase transition. Since the constituent quark masses are much larger than that of the pion, the meson dynamics dominates at low temperatures and the predictions from chiral perturbation theory are reproduced.

As described in Sect. 4.5.2 aspects of confinement can be incorporated by coupling quark degrees of freedom to the Polyakov loop. One proceeds in the same way as for the NJL model, by replacing \not{D} with the covariant derivative

$$(\partial^\mu \rho_s) = \not{D} - i\gamma_0 A^0, \quad (4.83)$$

where A^0 denotes the (spatially constant) temporal gauge field, and adding the effective Polyakov-loop potential $\mathcal{U}(\phi, \bar{\phi})$ to obtain the “Polyakov–Quark–Meson” (PQM) Lagrangian

$$\begin{aligned} \mathcal{L}_{PQM} = & \bar{q}(i(\partial^\mu \rho_s) - g(\sigma + i\gamma_5 \boldsymbol{\tau} \boldsymbol{\pi}))q + \frac{1}{2}(\partial_\mu \sigma)^2 + \frac{1}{2}(\partial_\mu \boldsymbol{\pi})^2 \\ & - U(\sigma, \boldsymbol{\pi}) - \mathcal{U}(\phi, \bar{\phi}). \end{aligned} \quad (4.84)$$

In the mean-field approximation the grand potential is given by

$$\Omega = \mathcal{U}(\phi, \bar{\phi}) + U(\sigma) + \Omega_{\bar{q}q}(\phi, \bar{\phi}, \sigma) \quad (4.85)$$

with the quark/antiquark contribution

$$\begin{aligned} \Omega_{\bar{q}q} = & \\ & -2N_f T \int \frac{d^3 p}{(2\pi)^3} \text{Tr}_c \left\{ \ln(1 + \mathcal{P} e^{-(E_p - \mu)/T}) + \ln(1 + \mathcal{P}^\dagger e^{-(E_p + \mu)/T}) \right\} \end{aligned} \quad (4.86)$$

and the purely mesonic potential

$$U(\sigma) = \frac{\lambda}{4}(\sigma^2 - v^2)^2 - c\sigma. \quad (4.87)$$

In the quark/antiquark contribution $\mathcal{P}(\mathbf{x})$ denotes the Polyakov-loop operator in the temporal direction (cf. (4.68))

$$\mathcal{P}(\mathbf{x}) = \mathcal{P} \exp \left(i \int_0^\beta d\tau A_0(\mathbf{x}, \tau) \right). \quad (4.88)$$

Furthermore, the divergent vacuum part in this contribution is absorbed in the renormalization which is done in the vacuum. The quark/antiquark single-quasiparticle energy is given by

$$E_p = \sqrt{\mathbf{p}^2 + M_q^2} \quad (4.89)$$

with the constituent quark mass $M_q = g\sigma$. The remaining color trace in the quark/antiquark contribution (4.86) is evaluated by using the identity $\text{Tr} \ln A = \ln \det A$ and yields

$$\begin{aligned} \Omega_{\bar{q}q} = -2N_f T \int \frac{d^3 p}{(2\pi)^3} \left\{ \ln \left[1 + 3(\phi + \bar{\phi} e^{-(E_p - \mu)/T}) e^{-(E_p - \mu)/T} + e^{-3(E_p - \mu)/T} \right] \right. \\ \left. + \ln \left[1 + 3(\bar{\phi} + \phi e^{-(E_p + \mu)/T}) e^{-(E_p + \mu)/T} + e^{-3(E_p + \mu)/T} \right] \right\}. \end{aligned} \quad (4.90)$$

It should be stressed again, that no ultraviolet cutoff is necessary because the PQM model is renormalizable in contrast to the PNJL model.

The equations of motion are obtained by minimizing the thermodynamic potential (4.85) w.r.t. the three constant mean fields σ , ϕ and $\bar{\phi}$:

$$\frac{\partial \Omega}{\partial \sigma} = \frac{\partial \Omega}{\partial \phi} = \frac{\partial \Omega}{\partial \bar{\phi}} \bigg|_{\sigma=\langle\sigma\rangle, \phi=\langle\phi\rangle, \bar{\phi}=\langle\bar{\phi}\rangle} = 0. \quad (4.91)$$

The solutions of these coupled equations determine the behavior of the chiral order parameter $\langle\sigma\rangle$ and the Polyakov-loop expectation values $\langle\phi\rangle$ and $\langle\bar{\phi}\rangle$ as a function of T and μ .

4.5.7 Quark-meson parameters

The four parameters of the QM model, i.e. g , λ , v and c , are chosen such that chiral symmetry is spontaneously broken in the vacuum and the σ -field develops a finite expectation value $\langle\sigma\rangle \equiv f_\pi$, where $f_\pi = 93$ MeV is set to the pion decay constant. Due to the pseudoscalar character of the pions the corresponding expectation values vanish, $\langle\pi\rangle = 0$. The Yukawa coupling constant g is fixed by the constituent quark mass in the vacuum $g = M_q/f_\pi$. Using the partially conserved axial vector current (PCAC) relation the explicit symmetry breaking parameter c is determined by $c = m_\pi^2 f_\pi$, where m_π is the pion mass. The quartic coupling constant λ is given by the sigma mass m_σ via the relation $\lambda = (m_\sigma^2 - m_\pi^2)/(2f_\pi^2)$. Finally, the parameter v^2 is found by minimizing the potential in radial direction, yielding $v^2 = \langle\sigma\rangle^2 - c/(\lambda\langle\sigma\rangle)$. For the ground state where $\langle\sigma\rangle = f_\pi$ this expression can be rewritten as $v^2 = f_\pi^2 - m_\pi^2/\lambda$. It is positive in the Nambu-Goldstone phase. In the vacuum the model parameters are fixed to $m_\pi = 138$ MeV, $m_\sigma = 600$ MeV, $f_\pi = 93$ MeV and $M_q = 300$ MeV which result in $c \sim 1.77 \cdot 10^6$ MeV³, $v \sim 87.6$ MeV, $\lambda \sim 19.7$ and $g \sim 3.2$.

4.5.8 Polyakov-loop potential parameters

The choice of parameters for the Polyakov-loop potential have been discussed in Sect. 4.5.2 and are the same for the PQM model, except for the expansion coefficient b_2 , where T_0 should be made N_f - and μ -dependent. The argument goes as follows. In the presence of dynamical quarks, the running coupling α is changed due to fermionic contributions. The size of this effect can be estimated within perturbation theory, see e.g. [634–638]. At zero temperature it leads to an N_f -dependent decrease of Λ_{QCD} , which translates into an N_f -dependent decrease of the critical temperature T_0 at finite temperature. The two-loop β -function of QCD with massless quarks is given by

$$\beta(\alpha) = -b\alpha^2 - c\alpha^3, \quad (4.92)$$

with the coefficients

$$b = \frac{1}{6\pi}(11N_c - 2N_f), \quad (4.93)$$

$$c = \frac{1}{24\pi^2} \left(34N_c^2 - 10N_cN_f - 3\frac{N_c^2 - 1}{N_c}N_f \right). \quad (4.94)$$

Here, an RG scheme is assumed that minimizes (part of) the higher-order effects. This is an appropriate scheme for the mean-field analysis. At leading order the corresponding gauge coupling is given by

$$\alpha(p) = \frac{\alpha_0}{1 + \alpha_0 b \ln(p/\Lambda)} + O(\alpha_0^2), \quad (4.95)$$

with $\alpha_0 = \alpha(\Lambda)$ at some UV-scale Λ , and $\Lambda_{\text{QCD}} = \Lambda \exp(-1/(\alpha_0 b))$. At $p = \Lambda_{\text{QCD}}$ the coupling (4.95) exhibits a Landau pole. At finite temperature the relation (4.95) allows to determine the N_f -dependence of the critical temperature $T_0(N_f)$. For $N_f = 0$ it is given by $T_0 = 270$ MeV which corresponds to fixing the coupling α_0 at the τ -scale $T_\tau = 1.770$ GeV and a running coupling of $\alpha_0 = 0.304$ accordingly. If one keeps the coupling α_0 at T_τ fixed, this identification yields the relation

$$T_0(N_f) = T_\tau e^{-1/(\alpha_0 b)}, \quad (4.96)$$

and Table 4.3 for the N_f -dependent critical temperature T_0 in the Polyakov-loop potential for massless flavors:

Table 4.3 The critical Polyakov-loop temperature T_0 for N_f massless flavors.

N_f	0	1	2	2+1	3
T_0 [MeV]	270	240	208	187	178

Massive flavors lead to suppression factors of the order $T_0^2/(T_0^2 + m^2)$ in the β -function. For $2 + 1$ flavors and a current strange quark mass $m_s \approx 150$ MeV one obtains $T_0(2 + 1) = 187$ MeV. We remark that the estimates for $T_0(N_f)$ have an uncertainty at least of the order ± 30 MeV. This uncertainty comes from the perturbative one-loop nature of the estimate and the poor accounting for the temperature effects. For example, with the two-loop coefficient (4.94) and restricting on $N_f = 2$ yields $T_0(2) = 192$ MeV. Fortunately, the results only show a mild T_0 dependence.

There are no double counting effects due to the inclusion of the Dirac determinant in the PQM and the independent adjustment of the Polyakov-loop model parameters: the Polyakov-loop potential parameters, in particular b_2 , genuinely depend on the running coupling, which is changed in the presence of quarks. This effect is modeled by changing $T_0 \rightarrow T_0(N_f)$ as defined in (4.96). The direct contributions to the grand potential which originate from the fermionic determinant $\Omega_{\bar{q}q}$, (4.86), are not governed by this redefinition, and have to be added separately.

A second step implements a μ -dependent running coupling in the b_2 coefficient, analogous to the N_f -dependence discussed above. Indeed, one can argue that this is a minimal necessary generalization: without a μ -dependent b_2 the confinement-deconfinement phase-transition has a higher critical temperature than the chiral phase transition at vanishing chemical potential. This is an unphysical scenario because QCD with dynamical massless quarks in the chirally restored phase cannot be confining since the string breaking scale would be zero.

As for the N_f -dependence one can resort to perturbative estimates, by allowing for an additional μ -dependent term in the one-loop coefficient b ,

$$b(\mu) = \frac{1}{6\pi}(11N_c - 2N_f) - b_\mu \frac{\mu^2}{T_\tau^2}. \quad (4.97)$$

This simple choice of the μ -dependent part can be motivated by using HDL/HTL results on the effective charge [516]

$$\alpha(p, T, \mu) = \frac{\alpha(p)}{1 + m_D^2/p^2}, \quad (4.98)$$

with the Debye mass $m_D^2 = (N_c/3 + N_f/6)g^2T^2 + N_f/(2\pi^2)g^2\mu^2$. The μ -derivative of the modified coupling, $\mu\partial_\mu\alpha = b_\mu\mu^2/p^2$, can be related to a momentum derivative $p\partial_p\alpha = -b(p, \mu)\alpha^2$. Within the simple approach based on a μ -dependence, that is strictly only valid in the perturbative regime, one can estimate the momentum-dependent coefficient $b(p, \mu)$ by $b(\mu) = b(\gamma T_\tau, \mu)$ at an (average) momentum scale γT_τ with $\gamma \leq 1$.

The coefficient b_μ can be fixed such that the chiral transition temperature and the confinement-deconfinement transition agree at some arbitrary non-vanishing μ . Interestingly, it turns out that then the transition temperatures agree for all values of μ . The related value of b_μ is provided by $\gamma \simeq 1/4$ and

$$b_\mu \simeq \frac{16}{\pi} N_f. \quad (4.99)$$

Inserting the μ -dependent coefficient $b(\mu)$ into (4.96) then leads to a T_0 with additional μ -dependence, such that

$$T_0(\mu, N_f) = T_\tau e^{-1/(\alpha_0 b(\mu))}. \quad (4.100)$$

(4.100) together with (4.99) should be viewed as a rough estimate of the μ -dependence of T_0 . For more quantitative results the non-perturbative running of the coupling in the presence of finite temperature and quark density has to be considered. This can be incorporated in a self-consistent RG-setting.

4.5.9 Phase structure and thermodynamic variables

The phase structure of the PQM model is determined by the behavior of the order parameters σ , ϕ and $\bar{\phi}$ and the grand canonical potential as a function of temperature and quark chemical potential. All numerical results have been obtained for $N_f = 2$. Then $T_0 = 208$ MeV in agreement with Table 4.3. This value is different from that taken in [620, 639] where $T_0 = 270$ MeV, the value of $N_f = 0$. In these works $T_0 = 210$ MeV has been fixed in order to compare with lattice results. The N_f - and μ -dependence suggested above offers a qualitative explanation for this choice.

In the left panel of Fig. 4.23 the temperature dependence of the chiral condensate $\langle \bar{q}q \rangle$ and the Polyakov-loop expectation value ϕ at $\mu = 0$ is shown in relative units. These results can be directly compared to those of the PNJL model in Fig. 4.17. They are qualitatively similar.

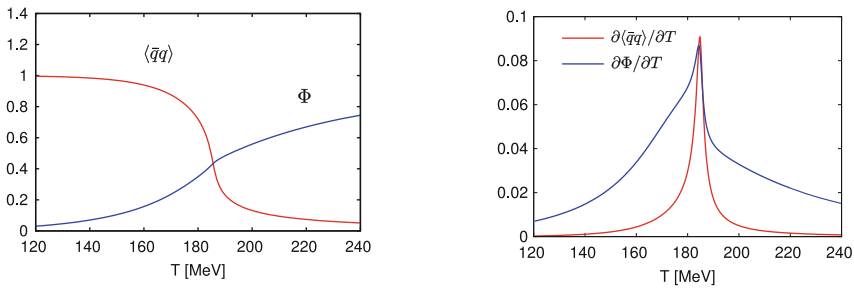


Fig. 4.23 *Left:* The normalized chiral condensate $\langle \bar{q}q \rangle$ and the Polyakov loop ϕ as a function of temperature for $\mu = 0$. *Right:* The temperature dependence of $\partial \langle \bar{q}q \rangle / \partial T$ and $\partial \phi / \partial T$ for $\mu = 0$. The Polyakov variable is scaled by a factor of 5. A chiral crossover is found at $T \sim 180$ MeV and a deconfinement crossover at a similar temperature.

At $\mu = 0$ a chiral crossover temperature $T_c = 184$ MeV is found with an uncertainty of $\sim \pm 14$ MeV originating in the error estimate ± 30 MeV for T_0 . For example, using the two-loop running of the coupling (4.94), and hence $T_0(N_f) = 192$ MeV yields $T_c \sim 177$ MeV. In the presence of dynamical quarks the Polyakov loop shows also a crossover at the same pseudo-critical temperature. This can be read off from the peak position of $\partial\langle\bar{q}q\rangle/\partial T$ and $\partial\phi/\partial T$, shown in the right panel of Fig. 4.23.

In two-flavor lattice simulations extrapolated to the chiral limit a pseudo-critical temperature $T_c = 173 \pm 8$ MeV is found using improved staggered fermions [58]. Recently, a recalculation of the transition temperature with staggered fermions for two light and one heavier quark mass close to their physical values yields a $T_c = 192 \pm 7$ MeV using the Sommer parameter r_0 for the continuum extrapolation [186]. This result has to be contrasted with another recent lattice analysis with staggered fermions but using four different sets of lattice sizes $N_\tau = 4, 6, 8$ and 10 to perform the continuum extrapolation [187]. From the same physical observable this group finds a critical temperature $T_c = 151 \pm 3$ MeV. Functional RG studies yield a critical value of $T_c = 172^{+40}_{-34}$ MeV [637, 638], where the error originates in an estimate of the uncertainty similar to the considerations put forward here. On the other hand, using the same parameters for the quark-meson model without the Polyakov-loop modifications a crossover temperature of $T_c \sim 150$ MeV emerges [640]. This situation calls for refined studies both on the lattice as well as within functional methods to resolve the apparent quantitative inaccuracies.

The phase diagram in the (T, μ) -plane resulting from the PQM model with the parameter set discussed above is shown in Fig. 4.24. Two choices for the variation of T_0 are given, ignoring or including the μ -dependence. In

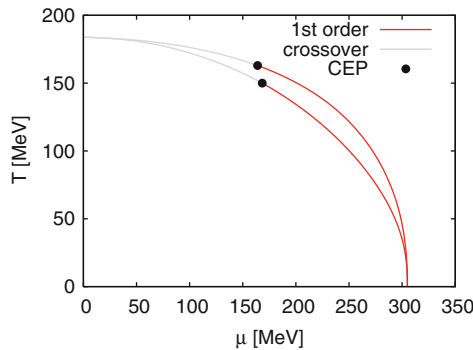


Fig. 4.24 Chiral phase diagrams for the PQM model. *Upper lines* for a μ -independent Polyakov-loop potential and *lower lines* with μ -dependent corrections. The corresponding CEP's are approximately located at $(T_c, \mu_c) = (163, 164)$ MeV (*upper case*) and at $(150, 168)$ MeV (*lower case*).

both cases the phase diagram features a critical endpoint (CEP), where the line of first-order transitions terminates in a second-order transition. Lattice simulations are not conclusive concerning the existence and location of the CEP [2, 58, 156, 159, 197].

There are indications from lattice simulations at small chemical potentials that deconfinement and chiral symmetry restoration appear along the same critical line in the phase diagram. For the PQM model and μ -independent $T_0(N_f)$ the coincidence of deconfinement and chiral transition at $\mu = 0$ disappears for finite μ . The deconfinement temperature is larger than the corresponding chiral transition temperature. This is an unphysical scenario because the deconfinement temperature should be smaller or equal to the chiral transition temperature. When resorting to the μ -dependent $T_0(\mu, N_f)$, (4.100), coinciding transition lines for the entire phase diagram within an accuracy of ± 5 MeV are found.

The corresponding order parameters as function of temperature for several chemical potentials are collected in Fig. 4.25 with N_f - and μ -dependent T_0 . The values of the chemical potential are chosen such that one curve runs through the CEP ($\mu_c = 168$ MeV) and the other through a first-order phase transition ($\mu = 270$ MeV).

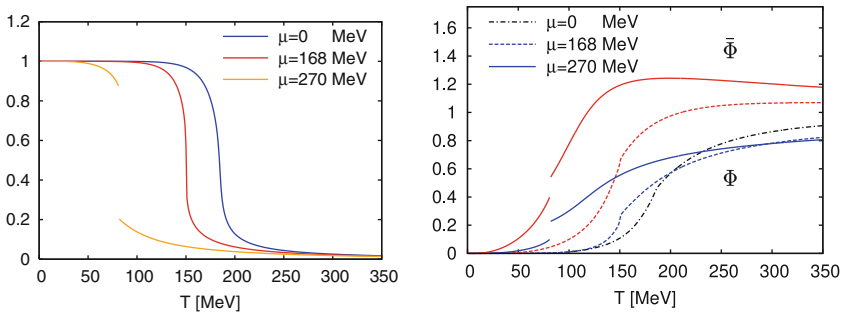


Fig. 4.25 *Left:* The normalized chiral quark condensate $\langle \bar{q}q \rangle$ as a function of temperature for three different chemical potentials $\mu = 0, 168, 270$ MeV. For $\mu = 270$ MeV a first-order transition is found at $T_c \sim 81$ MeV. *Right:* Same as left panel for the normalized Polyakov loops $\bar{\phi}$ and ϕ .

A prime thermodynamic state variable is the pressure. It is usually normalized to the QCD pressure in the Stephan-Boltzmann (SB) limit for non-interacting N_f massless quarks and $(N_c^2 - 1)$ massless gluons

$$\frac{p_{\text{SB}}}{T^4} = (N_c^2 - 1) \frac{\pi^2}{45} + N_c N_f \left[\frac{7\pi^2}{180} + \frac{1}{6} \left(\frac{\mu}{T} \right)^2 + \frac{1}{12\pi^2} \left(\frac{\mu}{T} \right)^4 \right], \quad (4.101)$$

where the first term denotes the gluonic contribution and the rest involves the fermions.

The PQM results are displayed in Fig. 4.26. For all values of T and μ the pressure p/T^4 stays below the QCD SB limit, a feature that is also observed in lattice calculations and other non-perturbative approaches. For vanishing chemical potential the pressure is a smooth function of the temperature consistent with a crossover transition. At temperatures of twice the critical temperature it reaches approximately 80% of the SB limit (left panel of Fig. 4.26). On the lattice two classes of data for the pressure obtained with a temporal extent $N_\tau = 4$ and $N_\tau = 6$ at $\mu = 0$ are currently available both of which are not extrapolated to the continuum [108, 138]. The results are in agreement with lattice simulations with a temporal extent of $N_\tau = 6$ which is also closer to the continuum limit.

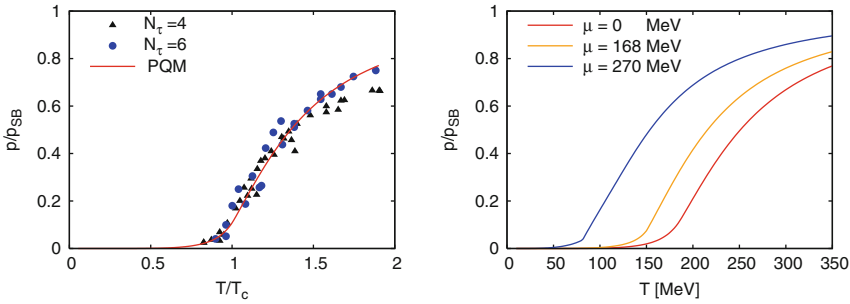


Fig. 4.26 *Left:* Scaled pressure p/p_{SB} for $\mu = 0$. The PQM model prediction (solid line) is compared to lattice results for $N_\tau = 4$ and $N_\tau = 6$. Lattice data taken from [108]. *Right:* Scaled pressure p/p_{SB} for three different quark chemical potentials, $\mu = 0, 168, 270$ MeV. $T_c(\mu = 0) = 184$ MeV.

In the right panel of Fig. 4.26 the scaled pressure is shown as function of the temperature for three different quark chemical potentials. An increase of the chemical potential leads to an increase of the pressure as more quark degrees of freedom are active. For a certain chemical potential the crossover transition changes to a first-order phase transition. In this case the pressure has a kink at the transition point but remains a continuous function. The kink at $T \sim 81$ MeV for the $\mu = 270$ MeV curve is clearly visible.

Another interesting observable is the net quark density. It is obtained from the thermodynamic potential via $n_q = -\partial\Omega(T, \mu)/\partial\mu$. The quark density, normalized to $1/T^3$, is displayed as a function of the temperature in the left panel of Fig. 4.27 for three different chemical potentials $\mu = 100, 168$ and 270 MeV. In comparison to the pure quark-meson model without the Polyakov loop, the quark density in the confined phase is much more suppressed when the interaction of quarks with the Polyakov loop is added [633, 640]. A similar effect is seen in the PNJL model. Above the phase transition, the quark density of the pure quark-meson model approaches the Stefan-Boltzmann limit $n_q = N_f \mu (T^2 + (\mu/\pi)^2)$ immediately. With the Polyakov-loop dynamics this

behavior is changed drastically. The quark densities increase slightly above the corresponding SB limits and decrease again with growing temperature. For high temperatures the SB limit of the quark density is always reached from above. At a first-order phase transition n_q jumps and drops immediately after the transition for increasing temperatures.

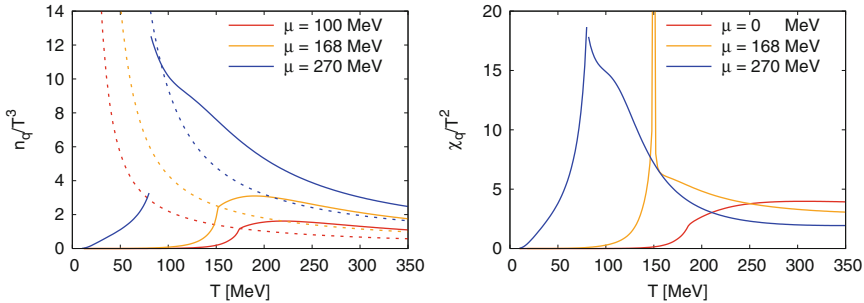


Fig. 4.27 *Left:* The quark number density n_q/T^3 for various values of μ . The *dashed lines* denote the corresponding Stefan-Boltzmann limits. *Right:* The scaled quark-number susceptibility χ_q/T^2 as a function of temperature for three different quark chemical potentials, $\mu = 0, 168, 270$ MeV.

The quark-number susceptibility measures the static response of the quark number density to an infinitesimal variation of the quark chemical potential and is given by $\chi_q = \partial n_q / \partial \mu$. It is shown in the right panel of Fig. 4.27 as a function of temperature for several values of μ . This observable can be used to identify the existence and location of the critical endpoint in the phase diagram. At a first-order phase transition this quantity has a discontinuity and in equilibrium only at a second-order critical endpoint it is divergent. Even for finite pion masses the critical endpoint is of second-order and induces a divergent quark-number susceptibility. For $\mu = 168$ MeV, close to the critical chemical potential of the CEP, χ_q diverges at the critical temperature.

The modifications caused by the quark-gluon interaction on the quark number susceptibility, are similar as those already discussed in the context of the quark-number density. Compared to the pure quark-meson model χ_q is again more suppressed below the chiral phase transition. Above the transition χ_q lies above the corresponding SB limit $\chi_q/T^2 = N_f(1 + 3/\pi^2(\mu/T)^2)$. At high temperatures the SB limit (not shown in the figure) is again reached from above.

4.5.10 Summary of the present status

The PNJL and the PQM approaches represent a minimal synthesis of the two basic principles that govern QCD at low temperatures: spontaneous chi-

ral symmetry breaking and confinement. The respective order parameters (the chiral quark condensate and the Polyakov loop) are given the meaning of collective degrees of freedom. Quarks couple to these collective fields according to the symmetry rules dictated by QCD itself.

A limited set of input parameters is adjusted to reproduce lattice QCD results in the pure gauge sector and pion properties in the hadron sector. Then the quark-gluon thermodynamics above T_c up to about twice the critical temperature is well reproduced, including quark densities up to chemical potentials of about 0.2 GeV. In particular, the PNJL and the PQM models correctly describe the step from the first-order deconfinement transition observed in pure-gauge lattice QCD (with $T_c \simeq 270$ MeV) to the crossover transition (with T_c around 200 MeV) when $N_f = 2$ light quark flavors are added. The non-trivial result is that the crossovers for chiral symmetry restoration and deconfinement almost coincide at small μ , as found in lattice simulations. It is interesting to consider a possible N_f - and μ -dependence in the parameters of the Polyakov-loop potential via the running coupling α . A qualitative estimate is provided by the one-loop β -function for α as well as using the hard dense loop approximation. This leads to an N_f - and μ -dependent T_0 , the critical temperature of the Polyakov-loop model, which decreases with increasing N_f and μ . These modifications yield coinciding peaks in the temperature derivative of the Polyakov-loop expectation value and the chiral condensate at $\mu = 0$, in agreement with the lattice findings of [156, 641]. Interestingly this coincidence of the deconfinement and chiral symmetry restoration persists at finite μ .

The models also reproduce the quark number densities and pressure difference at various chemical potentials surprisingly well when confronted with corresponding lattice data. Considering that the lattice results have been found by a Taylor expansion in powers of the chemical potential, this agreement indicates rapid convergence of the power series in μ .

The phase diagram predicted in these models has interesting implications. Starting from large quark masses an extrapolation to realistic small quark masses can be performed. The location of the critical point turns out to be sensitive to the input value of the bare (current) quark mass.

The conclusion to be drawn at this point is as follows. A quasiparticle approach, with its dynamics rooted in spontaneous chiral symmetry breaking and confinement and with parameters controlled by a few known properties of the gluonic and hadronic sectors of the QCD phase diagram, can account for essential observations from two-flavor $N_c = 3$ lattice QCD thermodynamics up to about twice the critical temperature of about 0.2 GeV. Presently ongoing further developments include:

- systematic steps beyond the mean-field approximation;
- extensions to 2+1 flavors;
- inclusion of explicit diquark degrees of freedom and investigations of color superconductivity in the high density domain;

- detailed evaluations of susceptibilities and transport properties at finite chemical potential.

Concerning the first item in the above list it is important to note that especially the description of phase transitions (order, universality class) might not come out correctly in pure mean-field approaches (cf. also Sect. 2.2). Here the renormalization group method is superior. This method is reviewed below in Sect. 4.7. In the next section, fluctuations in the presence of phase transitions are studied, using as an illustrative example the NJL model which has been introduced in the present section.

4.6 Probing the QCD phase boundary with fluctuations

The effective chiral models, e.g. the ones discussed in the last section, describe generic and universal properties of the QCD phase diagram related with the chiral phase transition [27, 50, 642]. In particular, the PNL model exhibits a critical end point (CEP) as the matching point of the first order and cross-over transition. Clearly, the position of the CEP and the properties of any physical observable outside the critical region are model dependent. However, the critical behavior of physical observables at the transition line should be universal and model independent. In particular, based on the universal properties of the QCD chiral phase transition it is rather clear that if the CEP exist then it belongs to the 3-dimensional Ising model universality class [22, 42, 49, 199, 640, 643]. This implies, that the CEP is a particular point on the QCD phase diagram where the fluctuations of the net quark and electric charge densities are diverging [52, 644, 645].

One of the objectives of the CBM experiment with ultra-relativistic heavy ion collisions is to map the QCD phase diagram and study the properties of high density strongly interacting medium. Of particular importance would be here to find the CEP and to identify the first order phase transition.

In this section, based on the NJL model calculations we argue, that by measuring the charge density fluctuations for different collision energies one can, in principle, identify the chiral phase transition experimentally.

4.6.1 *Charge density fluctuations near the critical end point*

In heavy ion phenomenology the fluctuations of conserved charges are directly accessible experimentally. Since these are also observable that are sensitive to critical properties related with chiral phase transition, thus they can give a direct access to probe the QCD phase diagram. In statistical physics fluc-

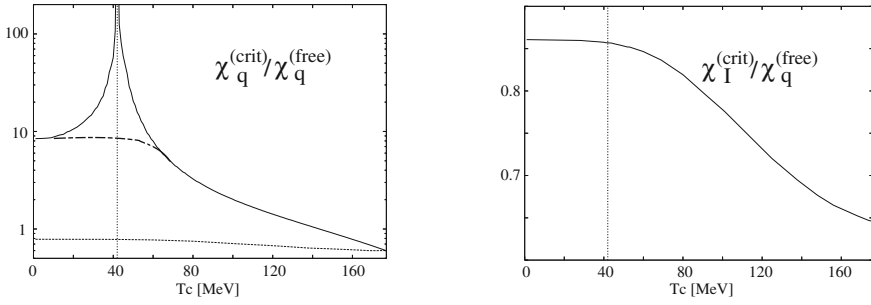


Fig. 4.28 The quark number (*left*) and isovector (*right*) susceptibilities χ_q and χ_I as functions of the temperature along the phase boundary. In the *left panel* the *solid* (*dashed*) *line* denotes χ_q in the chirally broken (symmetric) phase. The *vertical dotted-line* indicates the position of the tricritical point TCP. The calculations were done in the chiral limit in an isospin symmetric system with the vector coupling constant $G_V^{(S)} = 0.3 G_S$.

tuations of conserved charges Q_i are quantified by the corresponding susceptibilities, χ_{Q_i} . Of particular importance are susceptibilities related with the net-quark number χ_q , the electric charge χ_Q and the isospin χ_I conservation.

The susceptibilities describe the response of charge densities n_{Q_i} to any change in the corresponding chemical potentials μ_{Q_i} . Thus, in heavy ion collisions the relevant susceptibilities are defined as:

$$\chi_q = \frac{\partial n_q}{\partial \mu_q}, \quad \chi_I = \frac{\partial n_I}{\partial \mu_I}, \quad \chi_Q = \frac{\partial n_Q}{\partial \mu_Q}. \quad (4.102)$$

In isospin symmetric medium they are linearly related

$$\chi_Q = \frac{1}{36} \chi_q + \frac{1}{4} \chi_I \quad (4.103)$$

Figure 4.28 shows the NJL model results [643] on the net-quark and isovector susceptibilities along the phase boundary as a function of the transition temperature $T_c(\mu_c)$. The calculations were done in the chiral limit and under the mean field approximation of the NJL model thermodynamics [643].

The properties of the critical fluctuations shown in Fig. 4.28 are quite interesting. There is an increase of χ_q with decreasing transition temperature when approaching towards the TCP. The position of the TCP is signaled by the singularity of the net quark susceptibility χ_q and its non monotonic behavior. In the absence of TCP, the net quark susceptibility would be a monotonic function of T_c along the phase boundary, as illustrated by the dashed-dotted line in Fig. 4.28. Such a monotonic change along the transition line is seen in the behavior of the isovector susceptibility. There is also a region of $\Delta T \simeq 30$ MeV around T_{TCP} where the χ_q fluctuations are enhanced due to appearance of the critical point on the phase diagram.

The qualitative behavior of χ_q and χ_I seen in Fig. 4.28 is consistent with the results of the Landau theory discussed in Sect. 2.2 and universality arguments. First, the discontinuity across the phase boundary vanishes at $\mu_q = 0$. Second, the singularity of χ_q shows up only in the chirally broken phase, while the susceptibility in the symmetric phase is monotonous along the phase boundary and shows no singular behavior. In addition the non-singular behavior of χ_I at TCP is to be expected since there is no mixing of isospin density with the sigma field due to $SU(2)_V$ isospin symmetry [52].

In heavy ion collisions the change in temperature T_c corresponds to change in the c.m.s collision energy. An increase of \sqrt{s} results in an increase of T_c and decrease in μ_c . Thus, the critical region around tricritical point ($\Delta T, \Delta\mu$) can be (approximately) converted to a range of center-of-mass energies in A–A collisions. Assuming for simplicity that the relation of T_c and \sqrt{s} is the same as for the chemical freezeout parameters extracted from data [458], we find in the actual calculations that $\Delta T \simeq 30$ MeV would corresponds to $\Delta\sqrt{s} \sim 1$ AGeV.

From the results shown in Fig. 4.28 it is clear that the non-monotonic behavior of the baryon density fluctuations with increasing beam energy may give rise to observable effects in heavy-ion collisions to identify the critical end point TCP/CEP. Due to linear relation between different susceptibilities (4.103) it is clear that the electric charge density fluctuations should show a non-monotonic behavior as well. In addition, a non-monotonic behavior is expected for any observable that directly related to the net quark number density-density correlator. Thus, measurements of the corresponding non-monotonic structure in the baryon number or electric charge density, net-proton number density or in the mean transverse momentum would be an excellent experimental probe of CEP/TCP.

In heavy ion collision an additional complication to explore and map the QCD phase diagram experimentally appears due to finite size and live-time, the secondary hadronic rescatterings, in-medium effects and possible deviations from thermal and/or chemical equilibrium. All these effects can dilute observation of the critical fluctuations along the chiral phase transition [642]. In the next section we will discuss how deviation from equilibrium could influence the critical behavior of charge density fluctuations.

4.6.2 Charge density fluctuations in the presence of spinodal phase separation

We have argued that the non-monotonic behavior of charge fluctuations in the c.m.s collision energy in heavy ion experiments would be an ideal and transparent signal for the CEP. However, such conclusion is based on the assumption that the first order phase transition appears in equilibrium. In

heavy ion collisions, we are dealing with quickly expanding dynamical system, such that, deviations from equilibrium are not excluded.

A first-order phase transition is known to exhibit a convex anomaly in the thermodynamic pressure [500, 646–653]. There is an interval of energy density or baryon number density where the derivative of pressure is positive. This anomalous behavior characterizes a region of instability in the temperature and baryon density, (T, n_q) -plane. This region is bounded by the spinodal lines, where the pressure derivative with respect to volume vanishes. The above anomalous properties of the first order transition could be possibly uncovered in non-equilibrium system.

In the following, we will discuss what is the influence of the spinodal phase separation on the baryon number density fluctuations. We show that spinodal instabilities result in divergence of the electric and the baryon number density fluctuations. Consequently, a critical behavior of charge fluctuations is not necessarily attributed to the CEP but is also there along the first order transition if spinodal phase separation appears in a medium.

Our discussion is based on the NJL model calculations, however our main conclusion on the properties of charge fluctuations in the presence of spinodal instability is quite general and is independent on the particular choice of the effective chiral Lagrangian.

In the NJL model the dynamical quark mass M places the role of an order parameter for chiral phase transition. It is obtained as the solution of the gap equation:

$$M = m + 24G_S \int \frac{d^3p}{(2\pi)^3} \frac{M}{E} \left[1 - n^{(+)}(M, T, \mu_q) - n^{(-)}(M, T, \mu_q) \right], \quad (4.104)$$

where n^\pm are the quark and antiquark momentum density functions.

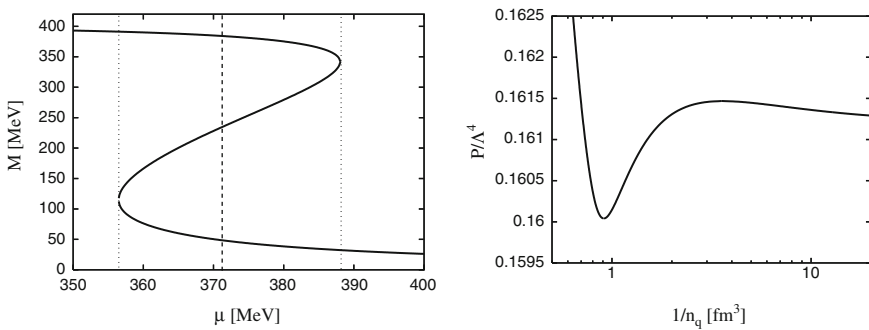


Fig. 4.29 *Left:* The dynamical quark mass at fixed temperature as a function of quark chemical potential. The *broken line* indicates an equilibrium first order phase transition. The *dotted lines* constrain the isothermal spinodal points. *Right:* The pressure as a function of inverse quark number density for fixed temperature $T = 30$ MeV [652, 653].

The left panel of Fig. 4.29 shows the solutions of the above gap equation for the constituent quark mass M at fixed temperature $T = 30$ MeV and for different values of the quark chemical potential. The behavior of M , seen in Fig. 4.29, is typical for systems that exhibit a first order phase transition: There is no unique solution of the gap equation, instead, there are metastable solutions that correspond to the local minima of thermodynamic potential. For finite current quark masses in the NJL Lagrangian, consider here, the chiral symmetry is explicitly broken. Consequently, M is not any more an order parameter and is never zero as seen in Fig. 4.29.

To identify the equilibrium transition from chirally broken to approximately symmetric phase one usually performs the Maxwell construction. In this case the chiral phase transition parameters are fixed such that the three extrema of the thermodynamic potential are degenerate. The location of an equilibrium transition from massive quasiparticles to almost massless quarks, calculate at fixed $T = 30$ MeV, is shown as dashed line in Fig. 4.29.

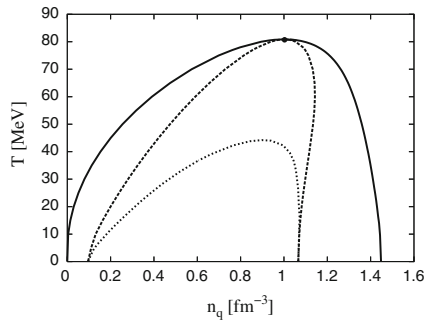


Fig. 4.30 The phase diagram in the temperature T and quark number density n_q plane in the NJL model. The *filled point* indicates the CEP. The *full lines* starting at the CEP represent boundary of the mixed phase in equilibrium. The *broken-curves* are the isothermal whereas the dotted ones are the isentropic spinodal lines.

The non-monotonic behavior of the dynamical quark mass M seen in Fig. 4.29 should affect any thermodynamic observable since $M(T, \mu_q)$ determines the properties of medium constituents. The right panel of Fig. 4.29 shows the inverse density dependence of thermodynamic pressure at fixed temperature. The pressure exhibits a non-monotonic structure as a consequence of the behavior of the dynamical quark mass seen in Fig. 4.29, left panel. The unstable solution of the gap equation leads to mechanical instabilities in the thermodynamic pressure where its volume derivative is positive. This region appears between spinodal points characterized by the minimum and the maximum of the pressure. Outside of this region the system is mechanically stable. The volume dependence of the pressure can be studied at fixed temperature or at fixed entropy. In the first case the spinodal points are isothermal whereas in the second they are isentropic. Changing the temperature or entropy re-

sults as the isothermal or isentropic spinodal lines in (T, n_q) -plane. If the volume derivative of P exists then the spinodal lines are defined through the conditions:

$$\left(\frac{\partial P}{\partial V}\right)_T = 0 \quad \text{or} \quad \left(\frac{\partial P}{\partial V}\right)_S = 0. \quad (4.105)$$

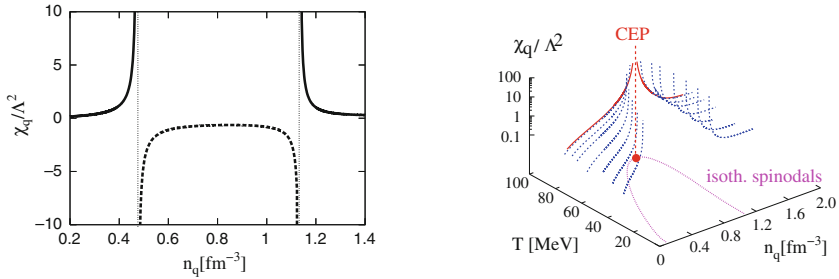


Fig. 4.31 *Left:* The net quark number susceptibility at $T = 50$ MeV as a function of the quark number density across the first order phase transition. *Right:* The net quark number susceptibility in the stable and meta-stable regions [652, 653].

Considering the properties of dynamical quark mass and thermodynamic pressure for different T and μ_q one finds the phase diagram for the chiral phase transition. Figure 4.30 shows the resulting diagram in the NJL model in the (T, n_q) -plane that accounts for spinodal instabilities. For finite current quark mass the CEP separates cross over from the first order chiral phase transition.

Assuming equilibrium transition there is a coexistence phase that ends at the CEP. However, accounting for expected instabilities due to a convex anomaly one can distinguish the metastable from mechanically unstable regions that are separated by the spinodal lines.

Figure 4.31, left panel, shows the evolution of the net quark number fluctuations along a path of fixed $T = 50$ MeV in the (T, n_q) -plane across the 1st order transition. Within coexistence region, there is a singularity in χ_q that appears when crossing the isothermal spinodal lines. There, the fluctuations diverge and the susceptibility changes its sign. Between the spinodal lines, the susceptibility is negative. This implies instabilities in baryon number fluctuations when crossing the transition between the chirally symmetric and broken phases.

The behavior of χ_q seen in Fig. 4.31 is a direct consequence of the thermodynamic relation

$$\left(\frac{\partial P}{\partial V}\right)_T = -\frac{n_q^2}{V} \frac{1}{\chi_q}, \quad (4.106)$$

which connects the pressure derivative with the net-quark susceptibility. Along the isothermal spinodal lines the pressure derivative in (4.106) van-

ishes. Thus, for non-vanishing density n_q , the χ_q must diverge to satisfy (4.106). Furthermore, since the pressure derivative $\partial P/\partial V|_T$ changes sign when crossing the spinodal line, there must be a corresponding sign change in χ_q , as seen in Fig. 4.31, left panel.

In equilibrium first order phase transition, the density fluctuations are finite. The fluctuations increase as one approaches the CEP along the first order transition and decrease again in the cross over region. This led to the prediction of a non-monotonous behavior of the fluctuations with increasing beam energy as a signal for the existence of CEP as discussed in the last section. We stress that strictly speaking this is valid only for the idealized situation where the first order phase transition takes place in equilibrium. In a more realistic, non-equilibrium system, one expects to observe large fluctuations in a broad region of the phase diagram, i.e., over a broader range of beam energies, due to the spinodal instabilities as seen in Fig. 4.31, right panel [652, 653]. Consequently, large fluctuations observed in heavy ion experiment and their drop at sufficiently high collision energy could be considered as a signal of the first order chiral phase transition.

4.7 The renormalization group method and the critical structure of QCD medium

As the underlying microscopic theory of the strong interaction, QCD describes qualitatively different physics at different length or momentum scales. QCD belongs to the class of non-Abelian Yang-Mills theories and has the important property that the strength of the strong gauge coupling varies with the size of the characteristic momentum transfer in a physical scattering process. Because QCD is an asymptotically free theory, the coupling runs in such a way that it is large for small momentum and small for large momentum transfers. Thus, at large momenta or equivalently at small distances, perturbative methods for the computation of physical observables can be used reliably because the applicability of perturbation theory is based on small couplings. An example of the applicability of perturbative methods is the successful description of jet physics at high momenta.

The situation becomes significantly more complicated at smaller momentum scales or larger distances. Perturbation theory breaks down and non-perturbative methods become indispensable. Analytical methods starting from first principles that allow to treat QCD at low-energies are only beginning to emerge. In fact, some success in the calculation of low-energy physics has been achieved with Schwinger-Dyson and functional renormalization group techniques and by numerical methods using Monte Carlo simulations, but physical mechanisms can best be analyzed in effective model calculations when detailed descriptions for this momentum regime are needed.

The situation is further complicated at finite temperature and/or baryon density. For instance, at very high temperatures perturbative calculations of the pressure in terms of the coupling constant are plagued by serious infrared divergences. This aspect is described in Sect. 3.1. Furthermore, it is generally expected that, at high enough temperature and densities, hadronic matter attains a state in which broken chiral symmetry is restored and the fundamental degrees of freedom, quarks and gluons, are no longer confined. The system undergoes a phase transition from the ordinary hadronic phase to a chirally restored and deconfined quark gluon plasma (QGP). Moreover, recent theoretical studies reveal an increasing richness in the structure of the phase diagram of strongly interacting matter. An overview over the different phases of QCD is given in Sect. 2.2.

As is well known from condensed matter physics, a viable non-perturbative method is the renormalization group (RG) [654]. The terminology renormalization group is rather unfortunate because the mathematical structure of the method is not that of a group. Neither is there one universal method which immediately may be applied to a given problem without care. In general, the RG is a framework, a certain set of ideas which has to be adapted to the nature of the problem at hand. All RG approaches have in common the idea of re-expressing the parameters, which define a given problem in terms of some other ones while keeping the interesting physical aspects of the underlying problem unchanged. Thus, the RG method has a wide range of applicability not only to equilibrium statistical physics or quantum field theory. In the context of equilibrium critical behavior, it represents a very efficient way to describe critical phenomena and in particular phase transitions. It can be used to characterize universal and non-universal aspects of second-order as well as first-order phase transitions and is thus well adapted to reveal the full phase diagram of strongly interacting matter. Applications of the RG method to the phase diagram in the framework of an effective two-flavor quark-meson model, which captures essential chiral aspects of QCD, can be found for example in [633, 640, 655, 656].

In the following the concept of the effective average action and its associated renormalization group equation will be introduced. Since it is clearly impossible to review the many facets of RG formulations here, we will concentrate on the so-called Wilsonian RG approach.

4.7.1 Renormalization group methods

The renormalization group deals with the effect of scale changes in a given theory. The central issue is the understanding of the macroscopic physics at large distances or low momenta in terms of the underlying fundamental microscopic interaction. In order to understand the evolution from the microscopic to the macroscopic scales one has to consider the quantum or

statistical fluctuations on all scales in between. The general RG idea is to treat the fluctuations not all at once but successively from scale to scale [654].

This idea combined with functional methods leads to the so-called “functional” RG. By means of functional methods, the computation of generating functionals of correlation functions becomes feasible. All important physical information is contained in the correlation functions as soon as the fluctuations have been integrated out. Instead of evaluating correlation functions by averaging over all fluctuations at once, only the change of the correlation functions induced by an infinitesimal momentum shell of fluctuations is considered. This goes along Wilson’s philosophy of integrating out modes momentum shell by momentum shell.

From a technical point of view this means one has to work with functional differential equations – the so-called RG or flow equations – instead of functional path integrals which is usually the case in standard quantum field theory. The differential structure of the RG equations has a larger versatility and offers several advantages compared to an integral formulation. Analytically and numerically it is better accessible and more stable. This is of great interest in non-Abelian gauge theories such as QCD. During the evolution from microscopic to macroscopic scales these theories turn from weak to a strong coupling and thus they become non-perturbative at macroscopic scales. In this sense RG methods provide a powerful tool to investigate non-perturbative phenomena of quantum field theories and statistical physics.

4.7.1.1 The effective average action

There are various RG methods known in the literature [629, 657–663]. One particular formulation of RG flows is based on the concept of the effective average action Γ_k , which is a simple generalization of the standard effective action Γ , the generating functional of the one-particle irreducible (1PI) Green’s functions [664]. It therefore contains all information about masses, couplings, form factors etc. and furthermore, it incorporates all quantum effects and thermal fluctuations in equilibrium matter. In the later case, the effective action represents a thermodynamic potential, which is related to the free energy, the logarithm of the grand canonical partition function, $W[J] = \ln Z[J]$ with a scalar source J , by a Legendre transform

$$\Gamma[\Phi] = -W[J] + \int d^d x J(x) \Phi(x) \quad (4.107)$$

with the so-called classical field $\Phi = \delta W[J] / \delta J$. A consequence of this transformation is that the full Γ has to be a convex functional. The generating functional $W[J]$ generates all connected Green’s functions and is defined by

$$W[J] = \ln \int \mathcal{D}\chi \exp \left\{ -S[\chi] + \int d^d x J(x)\chi(x) \right\} \quad (4.108)$$

where $S[\chi]$ represents the classical action for a real scalar field χ in d Euclidean dimensions.

The generalization of the effective action to the effective average action is achieved by implementing an infrared (IR) cutoff scale k in the functional integral for $W[J]$, (4.108). This is accomplished by adding an IR cutoff term $\Delta S_k[\chi]$ to the classical action $S[\chi]$. In this way, $W[J]$ is turned into a scale dependent functional $W_k[J]$. The IR cutoff is quadratic in the fields χ and is best formulated in momentum space as

$$\Delta_k S[\chi] = \frac{1}{2} \int \frac{d^d q}{(2\pi)^2} R_k(q) \chi(-q) \chi(q) , \quad (4.109)$$

where $R_k(q)$ denotes an appropriately chosen IR cutoff function. The regulator function is not completely arbitrary but has to satisfy certain conditions. It formally acts as a momentum-dependent mass term, which vanishes rapidly for $q^2 \gg k^2$. On the one hand, it suppresses the IR cutoff ΔS_k for large momenta q in a smooth manner. As an example a typical choice of the IR cutoff function is shown in the left panel of Fig. 4.32. The choice of a smooth cutoff function has also the advantage that no non-analytic momentum dependence is introduced as would be the case for a sharp cutoff. Thus, the functional integration of the high momentum modes in (4.108) is not disturbed. On the other hand, for momenta much smaller than the IR scale k , $q^2 \ll k^2$, the IR cutoff function behaves as $R_k(q) \simeq k^2$. This implies that all field components of χ with momenta smaller than the IR cutoff scale k acquire an effective mass proportional to k and decouple from the dynamics as a consequence of the decoupling theorem by Appelquist and Carrazone [665].

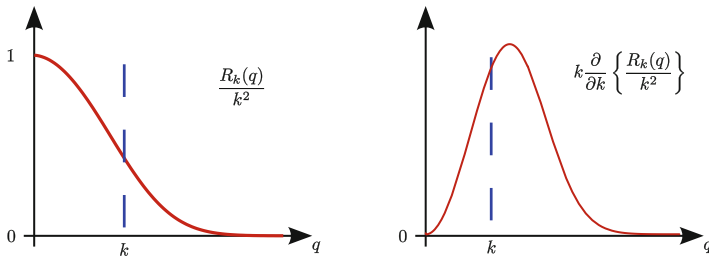


Fig. 4.32 A typical IR cutoff function $R_k(q)/k^2$ (left panel) and its scale derivative $k \frac{\partial}{\partial k} \{R_k(q)/k^2\}$ (right panel).

Finally, in terms of $W_k[J]$ the effective average action Γ_k is obtained by a modified Legendre transform similar to (4.107)

$$\Gamma_k[\Phi] = -W_k[J] + \int d^d x J(x)\Phi(x) - \Delta_k S[\Phi] \quad (4.110)$$

where the IR cutoff ΔS_k has been subtracted. This modified transformation destroys the convexity of Γ_k for any finite scale k . Only in the limit $k \rightarrow 0$, Γ_k becomes a convex functional again because the modified Legendre transformation tends back towards the pure Legendre transformation, (4.107). However, all symmetries of the system that are respected also by the IR cutoff $\Delta_k S$, are symmetries of Γ_k as well. This property concerns not only translation and rotation invariance but also chiral symmetry because a chirally invariant form for R_k can be found. Furthermore, an effective average action for gauge theories can also be formulated even though the IR cutoff $\Delta_k S$ may not be gauge invariant. Accordingly, the usual Ward identities receive further corrections for finite k which vanish in the limit $k \rightarrow 0$. For RG reviews with a focus on gauge theories, see for example [661, 662].

The average action Γ_k corresponds to an integration over all modes of the quantum fields with Euclidean momenta larger than the infrared cutoff scale, i.e., $q^2 > k^2$. The modified Legendre transform guarantees that the only difference between Γ_k and Γ is the effective IR cutoff $\Delta_k S$ and thus only quantum fluctuations with momenta larger than k are included.

In the limit $k \rightarrow 0$, the infrared cutoff is removed and the effective average action becomes the full quantum effective action Γ containing all quantum fluctuations. Thus, for any finite infrared cutoff k the integration of quantum fluctuations is only partially done. The influence of modes with momenta $q^2 < k^2$ is not considered. This scenario is visualized in Fig. 4.33 where the k -dependent effective average action Γ_k as an interpolation between the bare action in the ultraviolet and the full effective action in the infrared is shown.

In the limit $k \rightarrow \infty$ the effective average action matches the bare or classical action. In a theory with a physical UV cutoff Λ , we therefore associate $\Gamma_{k=\Lambda}$ with the bare action because no fluctuations are effectively taken into

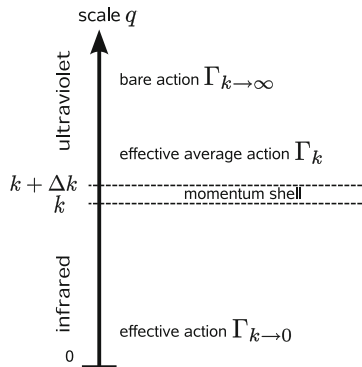


Fig. 4.33 The effective average action Γ_k as an interpolation between the bare action in the UV and the full effective action Γ in the IR.

account. As the scale k is lowered, more and more quantum fluctuations are taken into account. As a consequence, Γ_k can be viewed as a microscope with a varying resolution whose length scale is proportional to $1/k$. It averages the pertinent fields over a d -dimensional volume with size $1/k^d$ and permits to explore the system on larger and larger length scales. In this sense, it is closely related to an effective action for averages of fields, hence its denotation as effective average action becomes manifest. Thus, for large scale k one has a very precise spatial resolution, but one also investigates effectively only a small volume $1/k^d$. For lower k the resolution is smeared out and the detailed information of the short distance physics is lost. However, since the observable volume is increased, long distance effects such as collective phenomena which play an important role in statistical physics become more and more visible.

The momentum-shell idea, presented above, is in close analogy to a repeated application of the so-called block-spin transformation on a lattice invented by Kadanoff et al. [666]. This transformation is based on integrating out the fluctuations with short wavelengths and a subsequent rescaling of the parameters which govern the remaining long-range fluctuations such as the mass, coupling constant etc. On the sites of a coarse lattice more and more spin-blocks are averaged over. Hence, in the language of statistical physics, the effective average action can also be interpreted as a coarse grained free energy with a coarse graining scale k .

4.7.1.2 Functional flow equation

As already mentioned, the dependence of the effective average action Γ_k on the scale k is governed by a functional differential equation or flow equation. Its derivation is straightforward from (4.110): by calculating its k -derivative and reexpressing the emerging two-point function $W_k^{(2)}$ by $\Gamma_k^{(2)}$ the flow equation follows

$$\partial_t \Gamma_k[\Phi] = \frac{1}{2} \text{Tr} \left(\frac{\partial_t R_k}{\Gamma_k^{(2)}[\Phi] + R_k} \right). \quad (4.111)$$

Here, $\Gamma_k^{(2)}[\Phi]$ stands for the second functional derivative with respect to the field Φ

$$\Gamma_k^{(2)}[\Phi] = \frac{\delta^2 \Gamma_k}{\delta \Phi \delta \Phi} \quad (4.112)$$

and denotes the exact inverse average propagator. The trace involves a d -dimensional integration over momenta (or coordinates) as well as a summation over internal indices (e.g. flavor, color and/or Dirac indices). It is convenient to introduce the logarithmic variable $t = \ln(k/\Lambda)$ with some arbitrary momentum scale Λ with the total derivatives $\partial_t \equiv k d/dk$.

The right hand side of the flow equation (4.111) is both infrared and ultra-violet finite. The regulator R_k in the denominator (in the propagator) ensures the infrared finiteness. Its derivative, $\partial_t R_k$, in the numerator expresses the fact that only a narrow range of the whole momentum integration, hidden in the trace, effectively contributes to the flow. This is visualized in the right panel of Fig. 4.32: the function $\partial_t R_k$ has a peak for momenta around $q^2 \sim k^2$ and decays rapidly. Thus, only momenta around this peak in the momentum trace of (4.111) are taken effectively into account. In other words this is also equivalent to an integration of a smeared momentum shell around a given scale k . The addition of many momentum shells, starting deep in the ultraviolet, up to a certain infrared scale k is shown in Fig. 4.33.

The flow equation (4.111) is often labeled as functional or Exact RG (fRG). It is an exact non-perturbative functional equation in the sense that it can be derived from first principles. It has a simple graphical one-loop structure but is not of perturbative one-loop order. Because it depends on the full field-dependent inverse average propagator, $\Gamma_k^{(2)}[\phi] + R_k$, arbitrarily higher loop orders are incorporated. Thus, the flow equation includes generally the effects from all orders of a perturbative expansion. In addition, the one-loop structure has some advantages because technical complications due to overlapping loop integrations do not arise. One can thus use standard one-loop Feynman diagrams and perturbative techniques for practical calculations which establishes a direct connection between perturbation theory and solutions of RG equations. Furthermore, RG equations for any n -point functions can be derived by taking appropriate functional derivatives of (4.111) with respect to the fields. These equations have a similar structure as an analogous derivation of n -point functions in a Schwinger-Dyson framework.

4.7.1.3 Truncations

Unfortunately, general methods for the solution of partial functional differential equations are not known. Strategies to find their solutions are mainly restricted to iterative procedures that can be applied once some small parameters are identified. In the absence of a clearly identified small expansion parameter, a useful strategy to find a solution is to make an Ansatz for the effective average action Γ_k which is based on a certain expansion pattern.

The idea is that an expansion of Γ_k in terms of some invariants turns the functional differential equation into a coupled system of non-linear ordinary or partial differential equations for infinitely many couplings or vertices. In order to reduce the infinite system to a numerically manageable size one needs to truncate the most general expansion pattern of Γ_k . So far, several complementary systematic expansion schemes have been explored in the literature. One such systematic scheme is the “derivative expansion” where Γ_k is expanded in powers of derivatives. An example for this type of truncation for a one-component scalar field theory is the expression

$$\Gamma_k[\phi] = \int d^d x \left\{ V_k(\phi) + \frac{1}{2} Z_k(\phi) (\partial_\mu \phi)^2 + \mathcal{O}(\partial^4) \right\}. \quad (4.113)$$

The first term of this expansion, V_k , corresponds to the scale-dependent scalar effective potential and contains no derivatives. The first correction includes the field-dependent wave function renormalization $Z_k(\phi)$ in front of the standard kinetic term. Higher corrections of this expansion of the order $\mathcal{O}(\partial^4)$ are suppressed. Note, that this does not necessarily mean that the corresponding higher-order corrections are small. Furthermore, it is not even guaranteed that the chosen truncation scheme converges because the scale-dependent effective potential and also $Z_k(\phi)$ are often non-analytic functions of the fields. Nevertheless, one hopes that these expansions are asymptotic, similar to ordinary perturbation theory, and the calculation of physical quantities of interest are feasible at least to a certain degree of accuracy. What is important to require here, is that the influence of the neglected higher order terms on the evolution of those terms, kept in the expansion, is small. As for all non-perturbative analytical methods the truncation error has to be controlled separately which is often not an easy task.

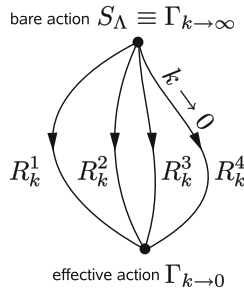


Fig. 4.34 Different trajectories in the “theory space” for different choices of the regulator R_k^i , $i = 1, \dots, 4$. The end point of all trajectories is independent of the explicit form of the regulator and represents the full effective action $\Gamma_{k \rightarrow 0}$ in the infrared.

Another point one should mention in this context is the dependence of the results on the choice of the regulator function R_k . For an exact solution without any truncations the infrared physics for $k \rightarrow 0$ does not depend on a particular choice of R_k . As already mentioned, the explicit form of the regulator function R_k is not fixed uniquely. Thus, different choices of R_k correspond to different trajectories in the space of all possible action functionals, the so-called “theory space”. It is spanned by all possible invariant field operators. The common starting point of each trajectory in this theory space is the bare action S_Λ and the end point in the infrared is the full

effective action $\Gamma_{k \rightarrow 0}$. It is unique only if no truncations are made, see Fig. 4.34. Once approximations are made, the dimension of the space becomes finite and the trajectories as well as their endpoints will depend on the choice of R_k . In this way an artificial scheme dependence is introduced similar to the scheme dependence in the perturbative renormalization theory. One may use this scheme dependence as an additional tool to study the quality of a given approximation scheme.

4.7.1.4 Proper-time flow equation

The flow equation, Eq. (4.111), is not the only exact renormalization group equation. Several other equivalent formulations, e.g. Polchinski's flow equations, are known in the literature which are also exact. Another class of RG flow equations can be obtained by approximations to the exact RG flows. An example of such an approximation is the so-called proper-time RG (PTRG) which is based on a Schwinger proper-time regularization of the one-loop effective action [633, 656, 667]. As opposed to the ERG flow equation, the PTRG has no first principle derivation. The final PTRG flow equation can be motivated by a one-loop improvement and is governed by

$$\partial_t \Gamma_k[\Phi] = -\frac{1}{2} \int_0^\infty \frac{d\tau}{\tau} [\partial_t f_k(\tau k^2)] \text{Tr} \exp \left(-\tau \Gamma_k^{(2)}[\Phi] \right) , \quad (4.114)$$

where the regulator function $f_k(\tau k^2)$ plays a similar role as the R_k in the ERG flow equation [668–671]. Similar to the ERG flow (4.111), the trace involves momentum integrations and a summation over internal spaces depending on the symmetries of the underlying theory. On the rhs of (4.114) the primary second derivative of the classical action $S^{(2)}$ has been replaced by the corresponding derivative of the scale-dependent effective action, $\Gamma_k^{(2)}$. This replacement represents the one-loop improvement. Without this replacement, an ordinary one-loop effective action would be reproduced after the evolution towards the IR.

Due to the proper-time integral the PTRG flow (4.114) does not depend linearly on the full field-dependent propagator in contrast to the ERG flow (4.111). As a consequence the PTRG cannot be an exact flow as already mentioned and shown in [672, 673]. Nevertheless, by adding further more complicated terms to (4.114) it is possible to obtain a generalized proper-time flow which is again an exact flow [674] but much more difficult to solve. However, there are arguments that these corrections must be negligible around criticality.

In summary, the standard PTRG flow is a well-defined approximation to a first-principles flow like the ERG flow [675]. So far, applications of the PTRG flow are typically based on flows of the form of (4.114) and further approx-

imations thereof. It is amazing how precisely for instance critical exponents can be calculated within this standard PTRG approach. In addition, compared to the ERG flow, the proper-time flow has a numerically simpler and physically more intuitive representation. The RG method, in general, is a non-perturbative technique and is definitely superior to mean-field approximations. It is therefore very appealing to apply RG methods to QCD.

In the following the PTRG flow will be used to investigate strongly interacting matter. We start with a brief review of some IR features of QCD and focus on the formation of light mesonic bound states and their effective chiral description. Semi-quantitative considerations using the presented RG technique naturally lead to a chiral quark-meson model as an effective description for scales below the mesonic “compositeness” scales which is presented in the next subsection.

4.7.2 QCD in an RG framework

In QCD quarks and gluons represent the microscopic degrees of freedom, whereas the macroscopic degrees of freedom are the observed color neutral particles like the mesons, baryons and/or glueballs. Hence there must be a transition from the microscopic to the macroscopic degrees of freedom and the relevant degrees of freedom change with the scale k . Such a scale dependence can be treated via the RG. In order to apply RG techniques to QCD an initial starting effective action has to be formulated.

When constructing effective models for the macroscopic degrees of freedom one usually relies on the guiding symmetries of QCD because a first-principle derivation from QCD is still missing. One important symmetry of QCD is the local $SU(N_c)$ color invariance which is related to confinement. This symmetry cannot be used here since the observed hadronic spectrum consists of color blind states. This is the reason why we will concentrate on the chiral aspects of QCD. The current masses of the two light quark flavors are much smaller compared to those of other quark flavors. This justifies to consider QCD with only two light quark flavors as a realistic starting point. For vanishing current quark masses the classical QCD Lagrangian does not couple left- and right-handed quarks. Ignoring for the moment the axial anomaly and baryon number conservation it exhibits a global chiral $SU_L(N_f) \times SU_R(N_f)$ invariance where N_f denotes the number of quark flavors. In the observed hadron spectrum, however, only the vector-like subgroup $SU_V(N_f)$ is realized which implies a spontaneous symmetry breaking of the chiral $SU_L(N_f) \times SU_R(N_f)$ symmetry down to the $SU_V(N_f)$ symmetry. For two quark flavors this breaking pattern predicts the existence of three massless parity-odd Goldstone bosons, the three pions π . The observed finite but small masses are a consequence of the additional explicit chiral symmetry breaking due to the finite current quark masses.

4.7.2.1 Hierarchy of momentum scales

At scales above ~ 2 GeV the dynamics of the relevant quark and gluonic degrees of freedom appear to be well described by perturbative QCD. Due to the running of the QCD gauge coupling the quark–gluon interaction strength will change with respect to a change of the momentum scale. Thus at lower scales bound states of quarks and gluons, quark condensates etc. emerge and confinement sets in.

To each such non-perturbative phenomenon one can associate an appropriate scale. Focusing on the physics of scalar and pseudoscalar mesons and assuming that all other bound states are integrated out it appears that all these scales are rather well separated from each other. An overview of the possible hierarchy of the different momentum scales is given in Fig. 4.35.

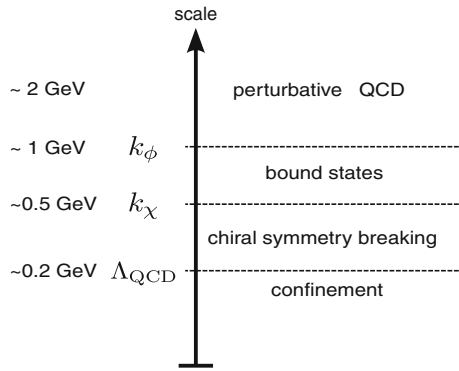


Fig. 4.35 Hierarchy of momentum scales: different non-perturbative phenomena and their approximate scales.

Somewhere around 1 GeV the so-called “compositeness” scale k_ϕ arises. Around these scales mesonic bound states are formed. Below the compositeness scale, typically around 500 MeV, the chiral symmetry breaking scale k_χ appears at which the chiral quark condensate develops a non-vanishing value. Finally, the last scale where confinement sets in, is related to the Landau pole in the perturbative evolution of the strong coupling constant and it is of the order of $\Lambda_{\text{QCD}} \sim 200$ MeV.

Thus, for scales $k_\chi \leq k \leq k_\phi$ the most relevant degrees of freedom are quarks and mesons and their dynamics is dominated by a strong Yukawa coupling g between them. This picture legitimates the use of a quark-meson model but only if one assumes that the dominant QCD effects are included in the meson physics. Below the scale k_χ the strong coupling α_s increases further and quark degrees of freedom will confine. Getting closer to Λ_{QCD} it is not justified to neglect those QCD effects which certainly go beyond the meson dynamics. Of course, gluonic interactions are expected to be crucial

for an understanding of the confinement phenomenon. However, due to the increase of the constituent quark masses towards the IR the quarks decouple from the further evolution of the mesonic degrees of freedom. As long as one is only interested in the dynamics of the mesons one expects that the confinement on the mesonic evolution has only little influence even for scales below Λ_{QCD} . Hence there are good prospects that the meson physics can be described by an effective quark-meson model [630, 632, 676]. However, it is possible to incorporate explicit gluonic degrees of freedom into this model, for instance, by coupling quark degrees of freedom to the Polyakov loop. This is explained in Sect. 4.5 and is neglected in the following.

4.7.2.2 The quark-meson model as initial effective action

As motivated above, a good ansatz for the initial starting effective action at the compositeness scale k_ϕ for the RG evolution is given by the two flavor quark-meson model

$$\Gamma_{k=k_\phi} = \int d^4x \left\{ \bar{q} (i \not{\partial} + g(\sigma + i\gamma_5 \boldsymbol{\tau} \boldsymbol{\pi})) q + \frac{1}{2} (\partial_\mu \sigma)^2 + (\partial_\mu \boldsymbol{\pi})^2 - U(\sigma, \boldsymbol{\pi}) \right\} \quad (4.115)$$

with the purely mesonic potential

$$U(\sigma, \boldsymbol{\pi}) = \frac{\lambda}{4} (\sigma^2 + \boldsymbol{\pi}^2 - v^2)^2 - c\sigma .$$

The quark fields are denoted by q and the Yukawa coupling g describes the common interaction strength of the σ and the three pion fields $\boldsymbol{\pi} = (\pi_1, \pi_2, \pi_3)$ with the quarks and antiquarks. The isoscalar-scalar σ field and the three isovector-pseudoscalar pion fields $\boldsymbol{\pi}$ together form a chiral 4-component field $\boldsymbol{\phi} = (\sigma, \boldsymbol{\pi})$ whose squared field $\boldsymbol{\phi}^2$ is also invariant under $O(4)$ -rotations. Without the explicit symmetry breaking term c the effective action is invariant under global chiral $SU(2)_L \times SU(2)_R$ symmetry transformations which are also isomorphic to $O(4)$ -transformations.

The physical picture underlying this ansatz is the following: the effective action of the quark-meson model at the compositeness scale k_ϕ , (4.115), emerges from short distance QCD in basically two steps. Starting from QCD in the UV one first computes an effective action which only involves quarks. This corresponds to an integration over the gluonic degrees of freedom in a quenched approximation. This will generate many effective nonlocal four and higher quark vertices and a nontrivial momentum dependence of the quark propagator. In the second step decreasing the scale further these four and higher quark interactions will cause the formation of mesonic bound states. Thus, at the compositeness scale not only quarks but also composite fields, the mesons, are present and interact with each other. The four quark interactions have been replaced by mesonic fields and for the higher interactions

a certain truncation has to be performed. It is obvious that for scales below the compositeness scale a description of strongly interacting matter in terms of quark degrees of freedom alone would be rather inefficient.

Thus, the ansatz for the effective action (4.115) at the compositeness scale corresponds to a gradient expansion to lowest order (cf. (4.113)) where wave-function renormalization corrections are neglected. It also incorporates a truncation to four quark interactions and higher quark interactions have been suppressed. This is then translated into a purely quadratic mesonic potential at k_ϕ with a positive mass term. Consequently, the chiral order parameter represented by the minimum of the mesonic potential vanishes. This implies that chiral symmetry is restored at the compositeness scale and the scalar expectation value $\langle\sigma\rangle$ will vanish [633]. For lower scales, chiral symmetry is spontaneously broken and the expectation value increases for decreasing scales.

4.7.2.3 Flow equation for the grand canonical potential

The phenomenological scenario, introduced above, is described by a flow equation. In order to derive this flow equation the ansatz for the effective action is plugged into the PTRG (4.114). In the following we omit the discussion of the solution of the flow equation for the vacuum and generalize the investigation to a system in thermal equilibrium with finite net-baryon or net-quark number density. This generalization of the PTRG to thermal equilibrium can be done straightforwardly: the temperature T is introduced by means of the Matsubara formalism where the zeroth component of the momentum integration in the trace of (4.114) is replaced with a summation over temperature-dependent, discrete Matsubara frequencies. A quark chemical potential μ_q is introduced by adding a term proportional to $i\mu_q \int d^4x \bar{q}\gamma_0 q$ in the action (4.115). In such systems the effective average action plays the role of the grand canonical potential Ω and depends on the temperature T and a single averaged quark chemical potential μ_q if isospin symmetry is assumed i.e. if the difference between the up-quark and the down-quark mass is neglected.

This then leads to the following flow equation, which describes the scale-dependent grand canonical potential Ω_k [640, 655]:

$$\begin{aligned} \partial_t \Omega_k(T, \mu; \phi^2) = & \frac{k^4}{12\pi^2} \left[\frac{3}{E_\pi} \coth\left(\frac{E_\pi}{2T}\right) + \frac{1}{E_\sigma} \coth\left(\frac{E_\sigma}{2T}\right) \right. \\ & \left. - \frac{2N_c N_f}{E_q} \left\{ \tanh\left(\frac{E_q - \mu_q}{2T}\right) + \tanh\left(\frac{E_q + \mu_q}{2T}\right) \right\} \right], \end{aligned} \quad (4.116)$$

with the quasi-particle energies $E_q = \sqrt{1 + g^2 \phi^2 / k^2}$ for the (anti-)quarks, $E_\pi = \sqrt{1 + 2\Omega'_k / k^2}$ for the pions and $E_\sigma = \sqrt{1 + 2\Omega'_k / k^2 + 4\phi^2 \Omega''_k / k^2}$ for

the σ meson. The grand canonical potential also depends on the expectation value of the square of the chiral 4-component field $\phi^2 = \langle \phi \rangle^2$ which coincides with $\langle \sigma \rangle^2$ since $\langle \boldsymbol{\pi} \rangle^2 = 0$. As a function of ϕ^2 the potential Ω_k can have certain minima. The global minimum of Ω_k corresponds to the chiral order parameter and is itself a function of the scale k . The primed (or double-primed etc.) potential in the flow equation denotes the ϕ^2 -derivative (or higher derivatives etc.) of the potential, e.g., $\Omega'_k := \partial \Omega_k / \partial \phi^2$.

The flow equation in this truncation has a very simple and intuitive physical interpretation: at first, the flow equation has an overall scale factor k^4 which reflects the correct dimension of the effective potential in $d = 4$ space-time dimensions. The different degrees of freedom contribute in an additive way to the flow. In the square brackets one recognizes the three degenerate pion, one sigma and the quark/antiquark contributions which are proportional to N_f . The fermionic contributions enter with a negative sign due to the fermion loop and have a degeneracy factor of $(2s+1)N_c N_f$ with $s = 1/2$. The quark chemical potential enters only in the quark/antiquark part with the appropriate sign as it should be. It influences the bosonic part of the flow equation only implicitly through the quasi-particle energies of the mesons which are functions of the potential derivatives (Ω' , Ω''). For comparison, one obtains standard mean-field theory results for the grand canonical potential if the bosonic fluctuations are neglected, i.e. if the first two terms of the flow equation (4.116) are ignored. On the other hand, including these terms, the RG results are much better than that obtained in mean-field theory, $1/N$ -expansions or ladder resummations. Finally, the vacuum flow equation can be deduced analytically by examining the limits $T \rightarrow 0$ and $\mu_q \rightarrow 0$ of this equation.

The flow equation (4.116) constitutes a set of coupled, highly non-linear, partial differential equations which cannot be solved with analytical methods: the unknown quantity, the potential Ω_k , appears also as derivatives on the rhs of this equation. One can now proceed in principle in two ways in order to integrate this equation numerically: either one discretizes the unknown potential Ω_k on a ϕ^2 -grid or one expands the potential in powers of ϕ^2 around its minimum ϕ_0^2 up to a certain order. On the one hand, the advantage of the potential expansion is that only a finite set of coupled flow equations has to be solved, depending on the chosen expansion order. For each higher order of the potential expansion, however, a new coupled flow equation is generated which increases the numerical effort drastically. On the other hand, a drawback of this expansion method is that finally the potential is only known around the minimum ϕ_0^2 , once the system has been solved [668, 671].

This is different for the grid solution: here, the potential is not only known around the minimum but also for arbitrary ϕ^2 . This is of importance, for example, in a first-order phase transition around the critical temperature (or quark chemical potential) where two degenerate minima of the potential emerge. In this case the knowledge of all local minima is required to describe the phase transition correctly. This is cumbersome in a potential

expansion, except for some simple potentials. Thus, a precise determination of the critical temperature of a first-order transition is very difficult within an expansion scheme around only one potential minimum. Another important advantage of the grid solution is that the potential is not fixed to a certain truncation. During the evolution, arbitrary higher mesonic $O(4)$ -symmetric self-interactions in the potential are allowed to be generated numerically by the RG evolution. By calculating higher potential derivatives it is possible to extract and investigate the flow of these higher contributions. For these reasons the grid solution is favored. For each grid point a flow equation is obtained, which finally leads to a coupled closed system and can be solved with standard numerical methods.

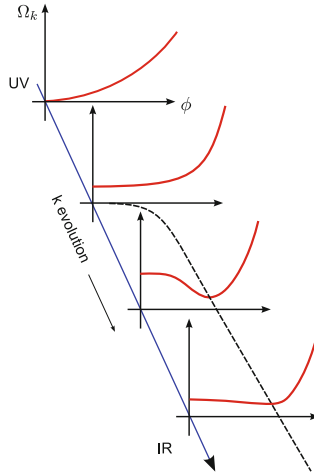


Fig. 4.36 Scale evolution of the grand canonical potential Ω_k towards the infrared starting at k_ϕ . The *dashed line* shows the scale evolution of the nontrivial minimum of the potential starting at k_χ . For small values of k , the potential becomes more and more convex and the minimum becomes scale-independent.

4.7.2.4 RG evolution towards the infrared

The RG evolution is started at the compositeness scale k_ϕ and is displayed in Fig. 4.36 where the k -evolution of the potential as a function of (positive) ϕ and its minimum ϕ_0 (dashed line), starting at k_χ , is visualized. The dynamics at the beginning of the scale evolution just below the compositeness scale is almost entirely driven by quark fluctuations. These fluctuations rapidly drive the squared scalar mass term in the action to negative values. This then immediately leads to a potential minimum away from the origin

such that the vacuum expectation value ϕ_0 becomes finite. This happens at the chiral symmetry breaking scale $k_\chi < k_\phi$, not far below k_ϕ . The reason for this behavior lies in the suppression of the meson contributions. All meson masses are much larger than the constituent quark masses around these scales and are therefore further suppressed during the evolution. Below k_χ the system stays in the regime with spontaneous chiral symmetry breaking (see dashed line). Around scales of the order of the pion mass the potential minimum becomes scale-independent. The reason for this stability of the vacuum expectation value is that the quarks acquire a relatively large constituent mass M_q . These heavy modes will decouple from the further evolution once the scale drops below M_q . The evolution is then essentially driven by the massless Goldstone bosons in the chiral limit. Of course, for non-vanishing pion masses the evolution of the model is effectively terminated around scales $k \sim m_\pi$. Quarks below such scales appear to be no longer important for the further evolution of the mesonic system. Due to confinement quarks should anyhow no longer be included for scales below Λ_{QCD} . As already mentioned, the final goal of such an evolution is to extract experimental quantities such as meson (pole) masses, decay constants etc. in the IR. These are also used to fix the initially unknown model parameters at the UV scale for the vacuum. They are adjusted in such a way that chiral symmetry is spontaneously broken in the IR (see also discussion in Sect. 4.5.6). This means for example that the minimum ϕ_0 is set to the pion decay constant $f_\pi = 93$ MeV in the IR. Finally, once the parameters for the vacuum are fixed, the finite temperature and density behavior of the system can then be predicted without further adjustments.

4.7.3 The phase diagram of the quark-meson model

The knowledge of the thermodynamic potential Ω as a function of its natural variables T and μ_q in the IR completely specifies the equilibrium thermodynamics of the system. Other quantities of interest can then be expressed as derivatives in the usual way. For example, the net quark number density and the chiral quark number susceptibility are given by

$$n_q(T, \mu_q) = -\frac{\partial \Omega(T, \mu_q)}{\partial \mu_q} \quad \text{and} \quad \chi_q(T, \mu_q) = -\frac{\partial^2 \Omega(T, \mu_q)}{\partial \mu_q^2}. \quad (4.117)$$

In general, any phase transition is characterized by an order parameter. It is finite in the broken symmetry phase and vanishes in the restored phase. For the chiral phase transition the order parameter is identified with the expectation value of the sigma field, namely the minimum ϕ_0 of the potential. Its thermodynamic behavior is determined by the corresponding equation of motion that is obtained by minimizing the potential Ω in radial σ -direction. This

leads to the so-called gap equation whose solution determines the behavior of the order parameter as a function of T and μ_q .

The resulting phase diagrams in the (T, μ_q) -plane for the chiral limit and for physical pion masses are both shown in Fig. 4.37, left panel. For a physical pion mass $M_\pi = 138$ MeV in the vacuum the two-flavor quark-meson model exhibits a smooth crossover on the T axis (not visible in the figure) and a first-order chiral phase transition on the μ_q axis. For increasing temperatures this first-order phase transition (solid line) persists up to a critical endpoint (CEP) where the chiral transition becomes second order. The critical behavior of this point falls into the universality class of the Ising model in three dimensions which can be modeled by a one-component scalar ϕ^4 theory in three dimensions. Typical for the RG treatment is the bending of the first-order transition lines for smaller temperatures. But very close to the μ_q axis the slope of the first-order line $dT_c/d\mu_q$ diverges. This feature is in agreement with the Clausius-Clapeyron relation. For temperatures above the CEP the phase transition is washed out and a smooth crossover takes place which is not shown in the figure.

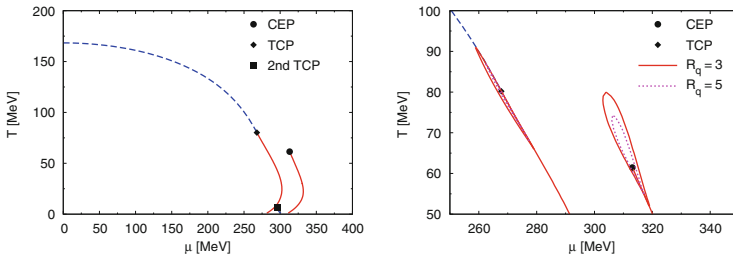


Fig. 4.37 *Left panel:* Two phase diagrams of the linear two-flavor quark-meson model obtained with the RG method: One for physical pion masses (*right solid line* which ends in the CEP) and another one for the chiral limit. *Solid lines* are first-order and *dashed lines* second-order transition lines. *Right panel:* Contour regions for two different ratios of the quark number susceptibilities R_q around the CEP and TCP.

In the chiral limit a second-order phase transition (dashed line) belonging to the $O(4)$ universality class is found on the T axis [42]. A critical temperature $T_c \sim 170$ MeV is obtained for two massless quark flavors which is in good agreement with lattice simulations. But note, that the value for the critical temperature is a non-universal quantity and depends on the used input parameters. For increasing μ_q the second-order transition line ends in a tricritical endpoint (TCP) which is a critical point where three phases coexist. This point has a so-called trivial Gaussian fixed point structure meaning that the universal critical exponents are those of the trivial Gaussian model, i.e. mean-field theory. The location of the TCP in the phase diagram is not universal and depends on the choice of parameters [677]. Thus, the existence

of this point, the shape of the transition line and its universality class are predictions within the underlying quark-meson model.

For temperatures below ~ 15 MeV two phase transitions with a further critical point (labeled as “2nd TCP” in the figure) emerges. The left transition line represents a first-order transition down to the $T = 0$ axis. At this transition the order parameter jumps not to zero but to a finite value. The chiral symmetry remains spontaneously broken and is only restored for higher μ_q ’s which then produce the second (right) transition line. At this right transition line we initially find a first-order transition where the order parameter jumps to zero and chiral symmetry is restored. But for smaller temperatures close the μ axis the order parameter tends smoothly to zero. It seems that this transition is again of second order. If this is true we infer that there must be a second tricritical point in the phase diagram in the chiral limit. For finite pion masses the right second-order transition turns into a crossover and is again not visible in the phase diagram anymore. Analogously, the second tricritical point, if it exists, should turn into a critical point. Some remnants of this critical point can indeed be seen in the vacuum expectation value and in the behavior of the meson masses.

4.7.3.1 The size of the critical region around the TCP and CEP

In Fig. 4.37, right panel, a contour plot for two fixed ratios of the chiral quark number susceptibility and its massless free quark gas limit, $R_q(T, \mu_q) = \chi_q(T, \mu_q)/\chi_q^{\text{free}}(T, \mu_q)$, is shown in the phase diagram near the TCP and CEP. This ratio is used here as an estimate for the size of the critical region around a critical endpoint. In general, the size of a critical region is defined through the breakdown of the mean-field theory and the emergence of nontrivial critical exponents. Usually, this size can be determined by the well-known Ginzburg criterion which is based on an expansion of the singular part of the free energy for a second-order phase transition. However, since the expansion coefficients are not known for the strong interaction the Ginzburg criterion is only of limited use in the present context.

An alternative estimate for the size of the critical region for hadronic matter, which is pursued here, can also be defined by calculating susceptibilities such as χ_q and using their enhancement as the criterion. The susceptibility has the following thermodynamic features: in the chiral limit, the susceptibility always jumps across the first- or the second-order transition and is suppressed far below the chiral phase transition. In the restored phase χ_q tends towards the value of the massless free quark gas, χ_q^{free} . Only at the TCP the susceptibility diverges when this point is approached from the broken phase. When the chiral limit is left, the critical behavior of the transition around the CEP changes. For temperatures above the CEP the discontinuity vanishes across the transition and the quark number susceptibility changes gradually due to the smooth crossover. This also leads to a finite height of

χ_q . The height decreases for decreasing chemical potentials towards the T axis. For temperatures below the CEP it is discontinuous and jumps across the first-order line. Hence, χ_q is finite everywhere else and diverges in equilibrium only at the CEP. Thus, the divergence of χ_q survives even at finite pion masses. Below the chiral transition, the susceptibility is again suppressed and in the restored phase it tends towards χ_q^{free} of a massless free quark gas. Only at the first-order transition there is a discontinuity. In contrast to the chiral limit, χ_q is a smooth continuous function for temperatures above the CEP.

A comparison of the critical region around the CEP with the one around the TCP, obtained with two dimensionless ratios R_q , is shown in Fig. 4.37, right panel, in a larger sector of the phase diagram containing both critical points. The CEP is far away from the TCP at larger values of the chemical potential and smaller temperature as expected. Because of the sharp transition lines in the chiral limit the critical region around the TCP is chopped off in the chirally symmetric phase. The region of enhanced χ_q around the CEP is elongated in the direction of the extrapolated first-order transition line. The deeper reason for this shape can be understood by a study of the critical exponents of the susceptibility which specify its power-law behavior in the vicinity of the critical point. In the case of the susceptibility the form of this divergence depends on the path by which one approaches the critical point. For the path asymptotically parallel to the first-order transition line the divergence scales with an critical exponent γ which e.g. in mean field is $\gamma = 1$. For any other path, not parallel to the first-order line, the divergence scales with another critical exponent ϵ which in mean-field theory is equal to $2/3$. Since $\gamma > \epsilon$ the susceptibility is enhanced in the direction parallel to the first-order transition line. This is the reason for the elongated shape of the critical region in the phase diagram since the inequality of the critical exponents remains valid within the RG treatment.

It is instructive to compare these findings with those obtained in mean-field theory. In general, fluctuations are neglected in mean-field theory. Thus, the impact of the quantum and thermal fluctuations on the shape of the region around the critical points in the phase diagram can be investigated. Repeating a similar calculation of the contour plot of Fig. 4.37 now for the scalar susceptibility in mean-field approximation an elongated region in the direction of the first-order transition line is again found. The results for three different ratios of the scalar susceptibilities around the CEP in reduced units are collected in Fig. 4.38. The light curves are the mean-field and the other ones the RG results. The region obtained with the RG is much more compressed. While the interval in the temperature direction is comparable in both cases, the effect in the chemical potential direction is enormous. In the RG calculation the interval is shrunk by almost one order of magnitude, despite the fact that the corresponding critical exponents are quite similar. A similar result is obtained for the critical region of the quark number susceptibility.

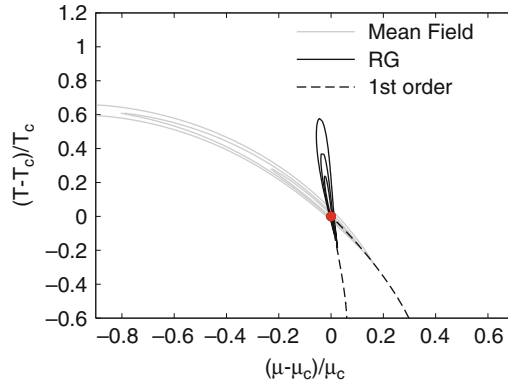


Fig. 4.38 Contour regions in the phase diagram for different ratios of the scalar susceptibilities around the CEP in reduced units. *Dark lines:* RG result, *light lines:* mean-field approximation.

4.7.4 Summary of the present status

A brief introduction to the functional renormalization group methods with a focus on the flow equation for the effective average action is presented. The class of the proper-time flow is introduced and its relation to the effective average action is discussed. QCD in an RG framework is exposed and the hierarchy of different momentum scales presented. Within the presented Wilsonian RG approach the phase structure of hadronic matter in the context of a two-flavor quark-meson model is analyzed. This effective model captures essential features of QCD such as the spontaneous breaking of chiral symmetry in the vacuum. It can therefore yield valuable insights into the critical behavior which is associated with chiral symmetry. Of special importance is the emergence of a CEP in the phase diagram which is intensely discussed at present in connection with fluctuation signals in heavy-ion collisions (cf. Sect. 4.6). Here the size of the critical region around the CEP is of special importance. So far, most studies of this issue which are available in the literature, have been performed in the mean-field approximation which neglects thermal and quantum fluctuations. As is also well known from condensed matter physics, fluctuations in the vicinity of a phase transition are important. These can be assessed in the RG approach which is able to correctly predict critical exponents in the vicinity of critical points of the phase diagram.

From universality arguments it is expected that the quark-meson model (and most likely QCD) has a TCP in the chiral limit. For the parameter set chosen a mean-field calculation is not able to find such a point, while the RG predicts its existence. The expected critical behavior at the TCP which has a Gaussian fixed-point structure with mean-field critical exponents is verified. When effects of finite pion masses are included, a CEP emerges in both

the mean-field and the RG calculation. By analyzing susceptibilities close to the CEP nontrivial critical exponents consistent with the expected 3D Ising universality class are found. As a consequence of quantum and thermal fluctuations, the size of the critical region around the CEP is substantially reduced, as compared to mean-field results. This is particularly true in the μ_q -direction where a shrinking by almost one order of magnitude is observed. This effect may have consequences for the experimental localization of the CEP in the phase diagram since it further complicates its detection through event-by-event fluctuations.

4.8 Strongly coupled quark gluon plasma

4.8.1 *Why is it strongly coupled?*

The finding [519, 678, 679] that QGP at RHIC is not a weakly coupled gas but rather a strongly coupled liquid has led to a paradigm shift in the field. It was extensively debated at the “discovery” BNL workshop in 2004 [512, 678, 680] (at which the abbreviation sQGP was established) and multiple other meetings since. The experimental situation was then summarized by “white papers” of four RHIC experiments. During few intervening years theorists had to learn a lot, some of which is new physics and some borrowed from other fields which happened to have experience with strongly coupled systems. Those range from ultracold trapped quantum gases to classical plasmas to string theory.

In short, we are facing *two* fundamental issues: (i) One is to understand dynamics of strongly coupled gauge plasmas, and explain *why* QGP at RHIC ($T = (1-2)T_c$) is strongly coupled, and what exactly it means in quantitative terms. (ii) The second is the huge old problem of understanding confinement, and what exactly happens near the *deconfinement*/chiral restoration, at $|T - T_c| \ll T_c$.

As usual, progress proceeds from catching/formulating the main concepts and qualitative pictures, to mastering some technical tools, doing some toy calculations which finally lead to quantitative predictions: now we are somewhere in the middle of this process. The work is going on at many fronts and at different level of sophistication.

At the *classical* level, treating medium as ensemble of interacting classical (quasi)particles, we learned that transport properties are quite different for gases and liquids. It is very valuable, since our main tool – lattice gauge theories – have great difficulties in deriving transport parameters like viscosity. We also learned how one can treat color degrees of freedom in strongly coupled *non – Abelian* plasmas. Recently those were generalized to a plasma with both *electrically* (gluons and quarks) and *magnetically* (monopoles and

dyons) charged quasiparticles. Such novel plasmas were never studied before, and we will discuss below how mixture of both types of particles helps reduce diffusion and viscosity.

Quantum-mechanical studies of sQGP are more difficult. With quasiparticle masses and forces derived from lattice, one may study various bound states above T_c and their dissolution. There is evidence that s-wave mesons and basic baryons may survive up to $(1 - 2)T_c$. Unusual many-body states seem to be also bound, including “gluonic polymeric chains”. However truly many-body studies at quantum level are still ahead of us.

The ultimate level of *quantum field/string* theory is even more difficult than quantum many-body one: and yet a spectacular progress in this direction has been made due to a remarkable new tool – the AdS/CFT correspondence, which we will try to introduce below. Paying a price of shifting from QCD to its cousin and to working in the limit of infinite number of colors, one can make use of profoundly consistent math and rich black hole physics. It provided concrete answers to viscosity, diffusion constant and jet quenching, and even “holograms” with complete description of conical flow. Work in progress is to provide a detailed picture of complete evolution, from collision point to hydrodynamical evolution. And yet, to be honest, while intuition “on gravity side” is being built, deep microscopic understanding of these results from “the gauge side” is still missing and is put aside for later.

A bit more concrete list of arguments explaining *why* we think QGP is strongly coupled at $T > T_c$ is constantly growing: here is its current version:

1. *Heavy Ion Phenomenology*: Collective flows observed at RHIC are explained by hydrodynamics so well, that sQGP seems to be “the most perfect liquid” ever known, with unusually small *viscosity-to-entropy ratio* $\eta/s \sim 0.1 \ll 1$ [46]. Gluon/quark jets are strongly quenched, including heavy (charmed) ones. Single electron data on charm quenching and elliptic flow can be described by charm diffusion constant D_c which is remarkably small, an order of magnitude below the pQCD estimates.
2. *Lattice quasiparticles and potentials*. Combining data on quasiparticle masses and inter-particle potentials, one finds that sQGP quasiparticle are not at all free to move but should form bound states [681]: that was one of the departures from “weakly coupled” ideology. In particular, lowest charmonia $\eta_c, J/\psi$ remains bound till near $T \approx 2T_c$, as was observed on the lattice [682, 683]. Perhaps experimental observation that J/ψ suppression at RHIC is no stronger than at SPS hints in the same direction. Heavy-light resonances enhance transport cross sections [684] and may help to explain charm quenching, cf. also Part II. (Note that it is the same mechanism as the one used to make ultracold trapped atoms strongly coupled, going by the name of “Feshbach resonances” and allowing the scattering length to be large $a \rightarrow \infty$.)
3. *Classical plasmas*: The parameter characterizing interaction strength used in this field is $\Gamma \sim \langle \text{potential energy} \rangle / \langle \text{kinetic energy} \rangle$. When it is small we deal with a gas, at $\Gamma \sim 1 - 10$ such plasmas are good liquids, becoming glassy

and eventually solid at $T > 300$. This key parameter in sQGP is certainly above one [685–687]. Molecular dynamics simulations to be described below give the first glimpse of its properties for non-Abelian plasmas [686, 687], as well as plasmas containing magnetic monopoles [688].

4. *AdS/CFT correspondence*: Exact correspondence between a conformal (CFT) $\mathcal{N}=4$ supersymmetric Yang-Mills theory at strong coupling and string theory in Anti-de-Sitter space (AdS) in classical SUGRA regime was conjectured by Maldacena [689]. The results obtained this way on the $g^2 N_c \rightarrow \infty$ regime of the CFT plasma are all in qualitative agreement to what we know about sQGP. Indeed, it has a very similar thermodynamics, it is equally good liquid with record low viscosity, there is very strong jet quenching and small diffusion constant for heavy quarks. We will present these results below: but a real intellectual challenge to theorists lies in their interpretation, as well as in understanding deep new insights into the origin of dissipation/equilibration offered by physics of black holes involved in it.

5. *Electric-Magnetic duality and confinement* is last but not least in this list. In a way, it was on the mind of theorists from Maxwell to Dirac, to 't Hooft and Polyakov, who discovered monopoles in gauge theories. We long viewed confinement as a dual superconductivity, and the famous Seiberg-Witten solution of the $\mathcal{N}=2$ supersymmetric Yang-Mills (SYM) theory is an example how confinement can be induced by condensed monopoles [690]. If so, at $T \approx T_c$ one expects [688] a high density of magnetic monopoles. They provide a substantial part of sQGP. As we will discuss below, electric and magnetic charge must run in the opposite directions: this offers a completely new view at the phase diagram, as an arena at which the electric-magnetic fight/competition takes place.

4.8.2 Radial, elliptic and conical flows

Phenomenology of heavy ion collisions and their macroscopic description via hydrodynamics is too large subject to be discussed here. Let me just remind here that the amount of data involved is quite extensive. The flow affects different secondaries differently, yet their spectra are in quantitative agreement with the data for all of them, from π to Ω^- . At non-zero impact parameter the original excited system has a deformed almond-like shape: thus its expansion in the transverse plane leads to the so called elliptic flow described by the (Fourier) parameter

$$v_2(s, p_t, M_i, y, b, A) = \langle \cos(2\phi) \rangle$$

where ϕ is the azimuthal angle. Multiple arguments stand for the collision energy s , transverse momentum p_t , particle mass/type M_i , rapidity y , centrality b or number of participants, and the atomic number A characterizing

the absolute system size. Hydrodynamics of QGP appended in a hadronic phase by hadronic cascade [691–693] explains all of those dependences in details for about 99% of the particles. Only at the large $p_t > 2$ GeV an ideal hydro fails: here a different regime starts. Viscous effects [46, 694, 695] extend the agreement even further and provide an estimate of the viscosity.

New hydrodynamical phenomenon⁸ suggested in [696–698], is the so called *conical* flow which is induced by jets quenched in sQGP. Although the QCD Lagrangian tells us that charges are coupled to gluons and thus it is gluons which are to be radiated, at strong coupling those are rapidly quenched themselves. Effectively the jet energy is dumped into the medium and then it transformed into coherent cone of sound waves, which remarkably survive till freezeout. They are detected by observed peaks in angular correlations with the trigger jets, at the Mach cone direction.

Figure 4.39 explains a view of the process, in a plane transverse to the beam. Two oppositely moving jets originate from the hard collision point B. Due to strong quenching, the survival of the trigger jet biases it to be produced close to the surface and to move outward. This forces its companion to move inward through matter and to be maximally quenched. The energy deposition starts at point B, thus a spherical sound wave appears (the dashed circle in Fig. 4.39). Further energy deposition is along the jet line, and is propagating with a speed of light, till the leading parton is found at point A at the moment of the snapshot.

The main prediction is that the shape of the jet passing through sQGP drastically changes: most of associated secondaries fly preferentially to a very large angle with jet direction, $\approx 70^\circ$ consistent with the Mach angle for (a time-averaged) speed of sound. Data on 3-particle correlations from STAR, PHENIX and even CERES at SPS (see QM08) confirmed conical interpretation of this signal.

Casalderrey and Shuryak [699] have shown, using conservation of adiabatic invariants, that fireball expansion should in fact greatly enhance the sonic boom: the reason is similar to enhancement of a sea wave (such as tsunami) as it goes onshore. They also showed that data exclude 1-st order phase transition, because in this case conical flow would stop and split into two, which is not observed. Antinori and Shuryak [700] suggested a decisive test by b-quark jets. Those can be tagged experimentally even when semi-relativistic: the Mach cone should then shrink, till its opening angle goes to zero at the critical velocity $v = c_s = 1/\sqrt{3}$. (Gluon radiation behaves oppositely, expanding with *decreasing* v .) A number of authors have reproduced conical flow in hydro, see e.g. [701]: but really quantitative study of it is still to be done.

⁸ In the field of heavy ion collisions Mach cone emission was actively discussed in 1970s: but it turned out not to work. The reason: nuclear matter, unlike sQGP, is not a particularly good liquid.

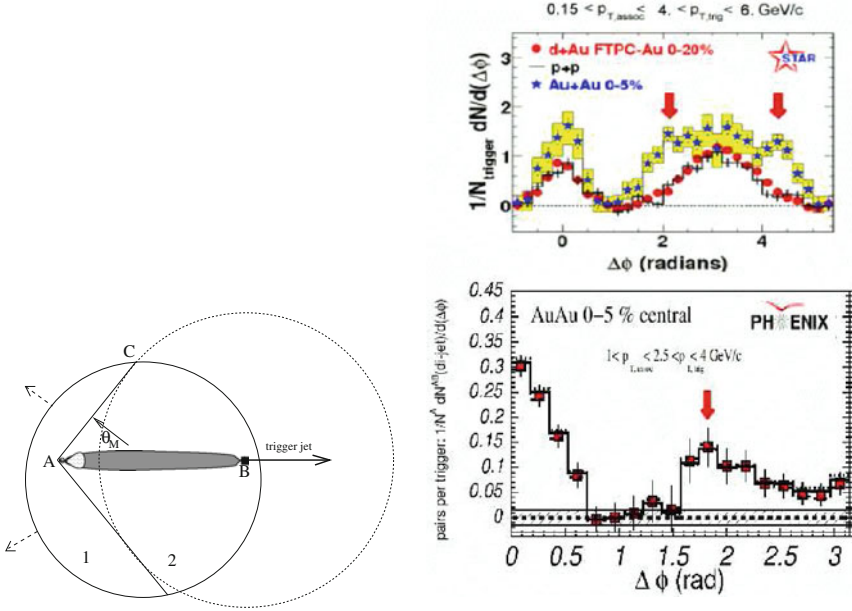


Fig. 4.39 *Left:* A schematic picture of flow created by a jet going through the fireball. The trigger jet is going to the right from the origination point B. The companion quenched jet is moving to the left, heating the matter (in *shadowed area*) and producing a shock cone with a flow normal to it, at the Mach angle $\cos\theta_M = v/c_s$, where v, c_s are jet and sound velocities. *Right:* The background subtracted correlation functions from STAR and PHENIX experiments, a distribution in azimuthal angle $\Delta\phi$ between the trigger jet and associated particle. Unlike in pp and dAu collisions where the decay of the companion jet create a peak at $\Delta\phi = \pi$ (STAR plot), central AuAu collisions show a minimum at that angle and a maximum corresponding to the Mach angle (*downward arrows*).

4.8.3 Classical strongly coupled non-Abelian plasmas

In the electromagnetic plasmas the term “strongly coupled” is expressed via dimensionless parameter $\Gamma = (Ze)^2/(a_{WS}T)$ characterizing the strength of the inter-particle interaction. Ze, a_{WS}, T are respectively the ion charge, the Wigner-Seitz radius $a_{WT} = (3/4\pi n)^{1/3}$ and the temperature. Only in the case of small Γ one can use Boltzmann equation, cascades and other simple tools appropriate for a gas: otherwise it is not possible because particles are strongly correlated.

Gelman et al. [686, 687] proposed a classical model for the description of strongly interacting colored quasiparticles as a nonrelativistic Non-Abelian Coulomb gas. The sign and strength of the inter-particle interactions are fixed by the scalar product of their classical *color vectors* subject to Wong’s equations [702]. Details should be looked up in the papers: let us just explain here its physical meaning. For SU(2) color group a color vector rotates around the

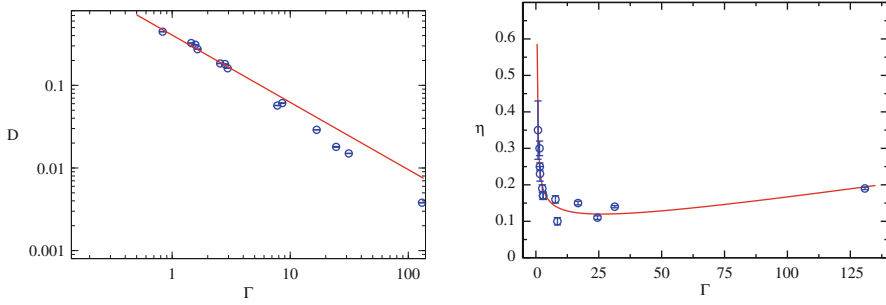


Fig. 4.40 The diffusion constant (*left*) and shear viscosity (*right*) of a one species cQGP as a function of the dimensionless coupling Γ . *Blue points* are the MD simulations; the *red curve* is the fit.

direction of the total color field induced by all other particles at its position: same as magnetic moments would do in a magnetic field. For arbitrary group precession on a group is determined by the Poisson brackets of color vectors: $\{Q^a, Q^b\} = f^{abc} Q^c$ which are classical analogue of the $SU(N_c)$ color commutators: thus one should use f^{abc} , the structure constants of the appropriate group. For the non-Abelian group $SU(2)$ the adjoint color vectors reside on a 3-dimensional unit sphere: with one conserved quantity ($(Q^a)^2$) it makes 2 d.o.f. The $SU(3)$ group has 8 dimensions: with two conserved combinations $(Q^a)^2, d^{abc} Q^a Q^b Q^c$ it is 6 d.o.f. Although color precession equations do not look like the usual canonical equations of motion for pairs of coordinates and momenta, they actually can be rewritten as pairs of conjugated variables, as can be shown via the so called Darboux parameterization. Thus one can define the phase space and use all theorems related to it for this system.

The model can be studied using Molecular Dynamics (MD), which means solving numerically equations of motion for 10^2 – 10^3 particles. It displays strong correlations and various phases, as the Coulomb coupling is increased ranging from a gas, to a liquid, to a crystal with anti-ferromagnetic-like color ordering. Skipping the details, we jump to the results on transport properties. In Fig. 4.40 one can see the result for diffusion and viscosity vs coupling: note how different and nontrivial they are. When extrapolated to the sQGP they suggest that the phase is liquid-like, with a diffusion constant $D \approx 0.1/T$ and a bulk viscosity to entropy density ratio $\eta/s \approx 1/3$.

Next step in studies of classical molecular dynamics included magnetic quasiparticles (monopoles) of QGP: we will discuss those in Sect. 4.8.5.

4.8.4 Quantum mechanics of the quasiparticles

In the deconfined phase, at $T > T_c$, the basic objects are quasiparticles, or “dressed” quarks and gluons. Perturbatively they get masses of the order $M_{eff} \sim gT$ and a dispersion curve, which is close to that of a massive particle. It follows from lattice measurements [518] (admittedly, with still poor accuracy) that in the T domain $(1-3)T_c$ (i) these masses are very large, about $M_{eff} \approx (3-4)T$; and (ii) quarks and gluons have very close masses, in contrast to pQCD. Thus quasiparticles are rather heavy (non-relativistic).

Furthermore, lattice data on the interaction (deduced for static quarks) plus quantum mechanics leads to existence of quasiparticle bound states. The most obvious state to think of is charmonium, which had a long story of a debate whether J/ψ survives in QGP or not. The answer depends on which effective potential is used. In contrast to earlier works, Shuryak and Zahed argued [519] that one has to remove the entropy term and use the “energy” potentials $U(T, r) = F - TdF/dT$ rather than the free energy $F(T, r)$. The argument is based on relatively short time of charm quark motion in charmonium relative to that of heat transfer (level crossings). If so, it leads to deeper potentials and better binding, so J/ψ survives till $T = (2-3)T_c$. This was confirmed by direct calculation of spectral densities by the maximal entropy method [682, 683]. It also nicely correlates well with surprisingly small J/ψ suppression observed at RHIC, where $T < 2T_c$.

It was then pointed out in [681] that also multiple binary *colored* bound states should exist in the same T domain. Since QGP is a deconfined phase, there is nothing wrong with that, and the forces between say singlet $\bar{q}q$ and octet qg quasiparticle pairs are about the same. Liao and Shuryak [520, 703] have also found evidence for survival of the s-wave baryons ($N, \Delta \dots$) at $T < 1.6T_c$.

A particularly interesting objects are *multibody* [703] bound states, such as “polymer chains”. Those can be “open strings” $\bar{q}gg \dots gq$ or closed chains of gluons (e.g. very robust ggg state we studied). Their binding *per bond* was proved to be the same as for light-quark mesons, and both are bound till about $1.5T_c$ or so. They have interesting AdS/CFT analogs (see below) and they also can be viewed as precursor to the formation of the QCD strings from the deconfined phases.

A curve of marginal stability (CMS) is not a thermodynamic singularity but it often indicates a change of physics. Zahed and Shuryak [519] argued that resonances can strongly enhance transport cross section near multiple CMS’s and thus explain small viscosity. Rapp et al. [684] studied $\bar{q}c$ resonances, and found that they can significantly enhance charm stopping.

Similar phenomenon does happen for ultracold trapped atoms, which are extremely dilute but due to Feshbach-type resonances at which the scattering length $a \rightarrow \infty$ they behave like very good liquids with very small viscosity, see [704, 705]. In fact they are “second best” liquids after the QGP.

Unfortunately, quantum many-body theory of strongly coupled gases is quite involved, and so neither for ultracold trapped atoms nor for sQGP quasiparticles we do not have at the moment any realistic simulations good enough to estimate the role of quantum corrections to MD results.

4.8.5 *The magnetic side of sQGP and confinement*

One of the oldest and most fundamental question of QCD is understanding confinement, as well as the deconfinement transition region at $T \approx T_c$. Since SPS-RHIC experiments are done in this temperature region, the answer should obviously be important for understanding sQGP. Recently there was a significant paradigm shift in relation to this question as well, which regards deconfinement and phenomena close to it as a result of a struggle between electric and magnetic objects for dominance.

One important element of the story are magnetic excitations – the monopoles. According to 't Hooft-Mandelstam scenario, confinement of electric objects (quarks) is due to monopole condensate – “dual superconductor” – expelling electric field into the flux tubes. Monopoles themselves were first found by 't Hooft and Polyakov, as solutions in gauge theories with (adjoint color) scalars, having non-zero vacuum expectations in the “Higgs phase”. Seiberg and Witten found famous solution [690] for one of them, the N=2 SYM, providing explicit example of how dual superconductor and electric-magnetic duality should work. Here there is no place to explain those in any detail: however some important features found in that context are generic, not only they persist in QCD and other gauge theories, but they provide a clue to what is happening.

But first some brief explanations are in order. Although QCD does not have explicit Higgs scalar, its role is taken by a nonzero mean $\langle A_0 \rangle$ related to the so called Polyakov loop

$$L = \exp\left(ig \int_0^\beta A_0 d\tau\right)$$

where $\beta = 1/T$ is the so called Matsubara time, the time extension of finite-T lattices. The mean value $\langle L \rangle$ as a function of T is known from lattice works.

A nonzero mean $\langle A_0^a T^a \rangle$ is a color matrix, which can be diagonalized: such “adjoint Higgsing” makes some gluons massive but leaves $(N_c - 1)$ gluons (which commute with it) massless. Thus the SU(3) color group contains 2 different U(1) “electrodynamics” with massless “photons”: those correspond to two magnetic charges which monopoles may have.

Electric-magnetic duality is an idea which is alive since the time of Maxwell: and in a theory with magnetic objects one may naturally ask why do we formulate gauge theory putting electric objects – quarks – into the La-

grangian, while insisting that monopoles are found only as some composites (solutions). Can it be formulated differently, interchanging their roles?

For gauge fields it simply means rewriting B as gradient and E as a curl of another “dual” potential. For monopoles that means including them into the action, as new source fields. This can be done: but since *both description should describe the same theory* serious issues of consistency appear. At the quantum mechanics level the famous Dirac [706] condition must be held, demanding basically that the product of two couplings is fixed

$$\alpha_{electric} \cdot \alpha_{magnetic} = 1$$

This requires that while one of them may be small, the other must necessarily be large!

At the quantum field theory level the Dirac condition elevates into a requirement that two couplings *must run into the opposite directions!* And indeed, the electric (usual) $\alpha_s = e^2/4\pi$ has asymptotic freedom and gets small at large momenta (UV), while magnetic is U(1) with Landau pole, running into zero at IR.

What does it mean for QGP? At *high* T the usual electric description is the perturbative one. One can calculate e.g. quark and gluon masses and find them to be light $M/T \sim \sqrt{\alpha_{electric}} \ll 1$. The monopoles are heavy and strongly interacting, thus they can be considered composites which play a minor role. However as T goes down and one approaches the deconfinement transition, the inverse is happening. Electrically charged particles – quarks and gluons – are getting heavier, while monopoles get lighter and more important. At some point their masses and roles get comparable, and then tables are turned and their fortunes reversed. Electric objects get strongly coupled and complicated while monopoles get lighter, proliferate and take over the heat bath. In Seiberg-Witten theory all of it can be analytically traced in great detail, but, as emphasized by Liao and Shuryak [688] the same qualitative features are there in QCD as well.

New phase diagram proposed focuses on the competition of electric and magnetic quasiparticles (EQPs and MQPs). It is divided into (i) the “magnetically dominated” region at $T < T_{E=M}$ and (ii) “electrically dominated” one at $T > T_{E=M}$. In our opinion, the key aspect of the physics involved is the *coupling strength* of both interactions. So, a divider is some *E-M equilibrium* region at intermediate $T-\mu$. Since it is *not* a singular line, one can define it in various ways, e.g. by a condition that electric and magnetic couplings are just equal

$$\alpha_{electric} = \alpha_{magnetic} = 1 \tag{4.118}$$

Besides equal couplings, the “E-M equilibrium” region should also have comparable densities as well as masses of both electric and magnetic quasiparticles.

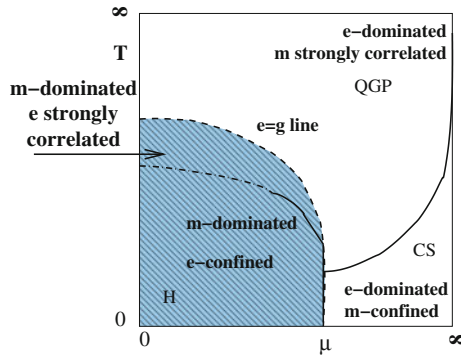


Fig. 4.41 A schematic phase diagram on a (“compactified”) plane of temperature and baryonic chemical potential $T - \mu$. The shaded region shows “magnetically dominated” region $g < e$, which includes the e-confined hadronic phase as well as “postconfined” part of the QGP domain. Light region includes “electrically dominated” part of QGP and also color superconductivity (CS) region, which has e-charged diquark condensates and therefore obviously m-confined. The dashed line called “e=g line” is the line of electric-magnetic equilibrium. The solid lines indicate true phase transitions, while the dash-dotted line is a deconfinement cross-over line.

The “magnetic-dominated” low- T (and low- μ) region (i) can in turn be subdivided into the *confining* part (i-a) in which electric field is confined into quantized flux tubes surrounded by the condensate of MQPs, forming ‘t Hooft-Mandelstam “dual superconductor” [707, 708], and a new “*postconfinement*” region (i-b) at $T_c < T < T_{E=M}$ in which EQPs are still strongly coupled (correlated). Increasing T and/or μ one enters either the high- T “electric-dominated” perturbative wQGP, or color-electric superconductor at high- μ , with electrically charged diquark condensate taking over the monopole condensate; here there is magnetic confinement of the monopoles. A phase diagram explaining this viewpoint pictorially is shown in Fig. 4.41.

After we presented the picture, let us provide some illustrations in its favor, from lattice works. The T -dependence of the electric and magnetic screening masses calculated by Nakamura et al. [709], are shown in Fig. 4.42, left panel. Note that electric mass is larger than magnetic one at high T , but drops steeply towards zero at T_c (because here electric objects gets too heavy and effectively disappear). The magnetic screening mass however grows toward T_c and the point at which electric and magnetic masses are equal (the E - M equilibrium point we emphasized above) is thus in the region of

$$T_{E=M} \approx (1.2 - 1.5)T_c = 250 - 300 \text{ MeV} \quad (4.119)$$

The second example (so far unpublished picture courtesy of D’Alessandro and D’Elia related to paper [710]) in Fig. 4.42, right panel, is the correlation function of monopole with antimonopole, traced on the lattice. Note that

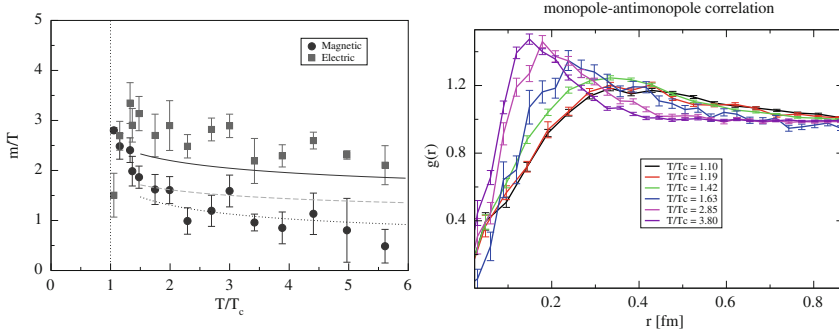


Fig. 4.42 *Left*: Temperature dependence of electric and magnetic screening masses according to Nakamura et al. [709]. The *dotted line* is fitted by Polyakov assumption, $m_g \sim g^2 T$. For the electric mass, the *dashed and solid lines* represent LOP and HTL resummation results, respectively. *Right*: Spatial correlation function for monopole-antimonopole, at different temperatures [710].

it develops a characteristic liquid-phase peak, which gets more visible at *higher* T . This is the first direct confirmation of Liao-Shuryak scenario, with a magnetic coupling running upward at higher T .

The third lattice example is related to a puzzling behavior of static $\bar{Q}Q$ potentials close to T_c . At $T = 0$ we all know that a potential between heavy quarks is a sum of the Coulomb and linear terms

$$V = -(4/3)\alpha_s/r + \sigma(T=0)r \quad (4.120)$$

At deconfinement $T > T_c$ the linear term $\sigma_F = 0$ has vanishing string tension, for *free energy* $F(T, r) = -T \log \langle W \rangle$ related to Wilson line W . However if one calculates the *energy* or *entropy* separately, by

$$F(T, r) = U(T, r) - TS(T, r), \quad S = -\partial F / \partial T \quad (4.121)$$

one still finds [562] a linear growing energy with nonzero tension: in fact at $T = T_c$ σ_U is several times that in vacuum. The total energy added to a pair is surprisingly large reaches about $E(T = T_c, r \rightarrow \infty) = 3 - 4 \text{ GeV}$, and the entropy as large as $S(T = T_c, r \rightarrow \infty) \sim 20$. Where all this energy and entropy may come from in the deconfined phase? Liao and Shuryak [711] found that a sufficiently dense gas of monopoles leads to electric flux tubes, even in the plasma phase. Indeed: the monopoles scatter from the electric flux tube back into plasma, compressing it. Whether they are Bose condensed (in dual superconductor) or not is *not* crucial for mechanical stability of the flux tubes, but the absence of supercurrents induces thermal losses and thus plasma tubes are metastable. (Metastable magnetic flux tubes – dual to what we now discuss – are well known e.g. in solar plasmas.)

Plasma with magnetic charges was studied in [688] by molecular dynamics. Simulations included transport properties such as diffusion coefficients and viscosity. A number of collective modes have been discovered, and their oscillation frequencies and damping parameters calculated.

The results will be shown together with those from AdS/CFT correspondence and also compared with empirical data from RHIC experiments. Those are summarized in Fig. 4.43, as a log–log plot of properly normalized dimensionless (heavy quark) diffusion constant and viscosity.

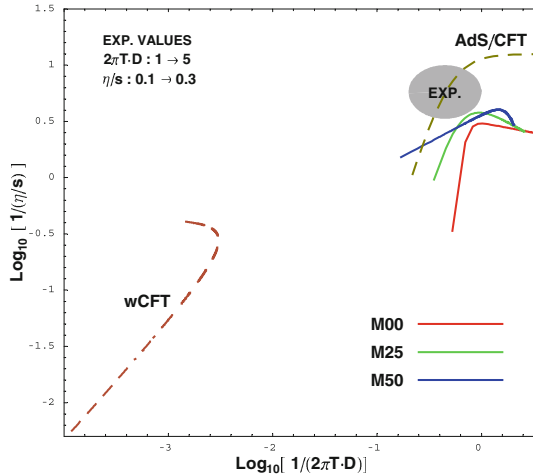


Fig. 4.43 Plots of $\text{Log}[1/(\eta/s)]$ v.s. $\text{Log}[1/(2\pi TD)]$ including results from our MD simulations, the AdS/CFT calculations, the weakly coupled CFT calculations, as compared with experimental values, see text.

The dashed curve in the left lower corner is for $\mathcal{N}=4$ SUSY YM theory in weak coupling, where viscosity is from [712] and diffusion constant from [713]. The curve has a slope of one on this plot, as in weak coupling both quantities are proportional to the same mean free path. As one can easily see, weak coupling results are quite far from empirical data from RHIC, shown by a gray oval in the right upper corner. Viscosity estimates follow from deviations of the elliptic flow at large p_t from hydro predictions [46], and diffusion constants are estimated from R_{AA} and elliptic flow of charm [714].

The curve for strong-coupling AdS/CFT results (viscosity according to [715] with $O(\lambda^{-3/2})$ correction, diffusion constant from [716]), shown by upper dashed line, is on the other hand going right through the empirical region. At infinite coupling this curve reaches $s/\eta = 4\pi$ which is conjectured to be the ever possible upper bound.

The MD results – three solid lines on the right – correspond to our calculations with different EQPs/MQPs ratio. They are close to the empirical

region, especially the optimal version, with the equal mixture of EQPs and MQPs.

4.8.6 *AdS/CFT correspondence and conformal sQGP*

AdS/CFT correspondence [689] is a duality between specific gauge theory known as $\mathcal{N}=4$ super-Yang-Mills theory (SYM) in 4 dimensions and (10-dimensional) superstring theory in a specific setting. Before we describe the results obtained, here is a brief introduction, explaining its logic and what all these words mean.

The $\mathcal{N}=4$ SYM theory is a cousin of QCD: it also has gauge fields with $SU(N_c)$ color symmetry, but instead of quarks it has four “flavors” of fermions called gluinos, as their adjoint colors are the same as for gluons. There are also 6 adjoint scalars: with 2 polarizations of gluons it makes 8 bosonic modes, same as 2×4 fermions. This makes supersymmetry possible and leads to cancellations of power divergences. This theory is the most symmetric theory possible in 4 dimensions: its *coupling does not run*!

(How do we know this? One may calculate the first coefficient of the beta function, and indeed see that negative gauge contribution is nicely canceled by fermions and scalars. But there are infinitely many coefficients, and one has to check them all! An elegant way to prove the case is based on another outstanding feature of the $\mathcal{N}=4$ SYM: this theory is *self-dual* under electric-magnetic duality. As we discussed above, the Dirac condition requires the product of electric and magnetic couplings to be constant: and so in QCD and other gauge theories they indeed run in the opposite directions, electric becoming weak in ultraviolet and magnetic weak in infrared. But the multiplet of (lowest) magnetic objects of the $\mathcal{N}=4$ SYM theory include 6 scalars (the monopoles), plus 4 fermions (monopoles plus one gluino zero mode occupied), plus 2 spin-1 (monopoles with 2 gluinos): this turns out to be exactly the same set of states as the original electric degrees of freedom (gluons-gluinos-Higgses). That means that an effective magnetic theory has the *same* Lagrangian as the original electric formulation: thus it must have the same beta function. Since two couplings cannot run in the opposite direction following the same beta function, they cannot run at all!)

If the coupling constant does not run, it means that there is no analog of Λ_{QCD} in this theory, and since all the fields are massless and all the coupling dimensionless, the $\mathcal{N}=4$ SYM theory knows no scales at all. It is thus a conformal field theory – the CFT in the AdS/CFT correspondence. One consequence is that the finite-T version of this theory (we will be mostly interested in) is the same whether T is large or small, since there is no other scale to compare with! This is similar to QCD plasma in “quasi-conformal regime”: at high enough $T > 3T_c$ all dimensionless ratios like (energy density)/ T^4 are practically T -independent.

Weakly coupled $\mathcal{N}=4$ SYM theory can be studied perturbatively, like any other gauge theory. What makes it unique is that AdS/CFT correspondence allows also to study it in the *strong coupling* limit, defined by a large value of the so called 't Hooft coupling, a combination of gauge coupling and number of colors which go together

$$\lambda = g^2 N_c \gg 1 \quad (4.122)$$

Now is the time to explain what AdS stands for. String theory is a large subject to explain in few words: let me just mention that one of the discoveries of 1990s was realization that it has solitonic objects of (nearly) any dimensions p called D_p branes. Think of them as some p -dimensional membranes, embedded in $9+1$ dimensions of space-time. For example D_3 branes have infinite extension in 3 coordinates x_1, x_2, x_3 , while being are just points in the remaining 6 coordinates $x_4 \dots x_9$. Since branes are material objects with some mass and charge, they create gravity/Coulomb field around them. Large ($N_c \rightarrow \infty$) number of branes put into the same point, create strong gravity field, described by classical Einstein/Maxwell equations. The solution is just a specific (6-dimensional) charged black hole: in fact it turns out the so called extremal black hole which has the lowest possible mass for a given charge. It is spherically symmetric, so one can separate the 5 angles (making the 5-dim sphere S_5) from the radius r in 6-dimensions, on which metrics depends

$$ds^2 = \frac{-dt^2 + dx_1^2 + dx_2^2 + dx_3^2}{\sqrt{1 + L^4/r^4}} + \sqrt{1 + L^4/r^4}(dr^2 + r^2 d\Omega_5^2) \quad (4.123)$$

Approximate form of this metric, at $r \ll L$ when 1 in the root can be ignored, is further simplified: in the last term r^2 cancels out and 5-dimensional sphere gets decoupled (and ignored). What is left is quite simple Anti-de-Sitter 5-dimensional metric, which we rewrite in a new coordinate $z = L^2/r$ as “standard AdS metric”:

$$ds^2 = \frac{-dt^2 + dx_1^2 + dx_2^2 + dx_3^2 + dz^2}{z^2} \quad (4.124)$$

Note that z counts the distance from “the AdS boundary” $z = 0$, where the 4-d gauge theory is located.

So far nothing unusual happened: all formulae come straight from string and general relativity textbooks. A truly remarkable theoretical discovery is the so called “holography”: the exact duality (one-to-one correspondence) between the 5-dim “bulk” effective theory in AdS_5 to 4-dim “boundary” ($r \rightarrow \infty$) gauge theory. There is a dictionary, relating any observable in the gauge theory to another one in string theory: the duality means the answers are the same in both formulations.

The last step, which makes it so useful, is the relation between the gauge coupling, the AdS radius L and the string tension α' (which comes from the

total mass of the brane set):

$$L^4 = g^2 N_c (\alpha')^2 = \lambda (\alpha')^2 \quad (4.125)$$

It tells us that large gauge coupling $\lambda \gg 1$ corresponds to large AdS radius (in string units) and one can use classical (rather than quantum) gravity. At the same time the string and gravity couplings $g_s \sim g^2$ may remain small: so one may do perturbative calculations in the bulk!

At this point many readers are probably very confused by the new 5-th dimension of space. One possible approach is to think of it as just a mathematical trick, somewhat analogous to more familiar introduction of the complex variables. Suppose an Experimentalist measured some complicated cross section which is approximately a sum of Breit-Wigner resonances. His friend Phenomenologist may be able to write the answer as an analytic function with certain pole singularities in the complex energy plane, which will help for fitting and for evaluating integrals. Even better, their other friend Theorist cleverly developed a “bulk theory”, deriving the pole positions from some interaction laws on the complex plane.

The truth is that there is a perfectly physical meaning of the 5-th coordinate. A hint is provided by the fact that distance along it $\int_a^b dl = \int_a^b dz/z = \log(b/a)$ is the logarithm of the ratio. Thus its meaning is the “scale”, the argument of the renormalization group. If one takes a bulk object and move it into larger z , its hologram at the boundary ($z=0$) grows in size: this direction thus corresponds to the infrared direction.

The running coupling constant would thus be a z -dependent field called “dilaton”. Indeed, there are theories with gravity dual, in which this field (the coupling) does run: unfortunately, known examples do not (yet?) include QCD! In spite of that, there are efforts to build its gravity dual “bottom-up”, introducing weak coupling at ultraviolet (small z) [717] and confinement in infrared (large z) [718] by certain modification of the rules: these approaches are known as AdS/QCD, but we will not discuss them here.

Completing this introduction, let us briefly consider one of the first examples of “AdS/CFT at work”: the strong-coupling Coulomb law calculated via AdS/CFT [719, 720]. The setting, shown in Fig. 4.44, includes two static charges (heavy fundamental quarks) separated by the distance R . Their electric flux in the bulk forms a singular object – the string (shown by the solid curve) – which pends by gravity force into the 5-th dimension. Simple calculation – minimization of the Nambu-Goto action or the invariant length of the string – produces a particular shape and also gives the total string energy

$$E = -\frac{4\pi^2\sqrt{\lambda}}{\Gamma(1/4)^4 R} \quad (4.126)$$

which has (now famous) $\sqrt{\lambda}$, instead of λ in the usual (weak coupling) result, and a fancy constant including the Euler Gamma function.

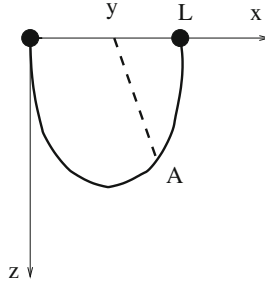


Fig. 4.44 Setting of the Maldacena dipole: two charges at the boundary (*black dots*) are connected by the string (shown by *solid curve*) pending under gravity toward the AdS center $z \rightarrow \infty$. Classical graviton propagator (the *dashed line*) should be used to calculate the “hologram” – the stress tensor at the observation point y . The string is the gravity source; the point A has to be integrated over.

One may think that strongly coupled vacuum acts like some kind of a dielectric constant, modifying only the coefficient of the Coulomb law and fields. In order to test that one has to perform more involved calculation, finding the *hologram* of this pending string. This can be done by solving the linearized Einstein equation for the gravity propagator (the dashed line in Fig. 4.44) and find (by the AdS/CFT rules) the induced stress tensor of matter at point y in the gauge theory. Done only recently in [721], the resulting stress tensor displays no visible trace of the flux string in the hologram (although there is one in the “bulk”). This happens because the most remote part of the string (in its middle) is far in infrared and thus get projected on a larger area. However the stress-energy distribution is not like in the perturbative (zero coupling) case either. In particular, the energy density at large distances from the dipole $r \gg R$ is not $T_{00} \sim R^2/r^6$ as in weak coupling, but is $\sim R^3/r^7$ instead, with a different angular distribution. This feature, as well as $\sqrt{\lambda}$ dependence on coupling, was in fact understood: the clue is short color correlation time of two charges pointed out in [679, 722].

4.8.7 AdS/CFT correspondence predictions for sQGP

Finite-T CFT plasma is studied following Witten’s proposal to upgrade the AdS_5 metric discussed above to that of non-extremal AdS-black hole⁹:

$$ds^2 = \frac{-[1 - (z/z_0)^4]dt^2 + dx_1^2 + dx_2^2 + dx_3^2 + dz^2/[1 - (z/z_0)^4]}{z^2}. \quad (4.127)$$

⁹ The power of the distance in the bracket is 4 and not 1, as for Schwarzschild, because it should correspond to the 6-dim, not 3-dim, Newton law.

Now it has a horizon (the zero of the time component g_{00}) at $z = z_0$, generating both the Hawking temperature $T = 1/\pi z_0$ and the Bekenstein entropy. To find the entropy one has to calculate the horizon area (see [723]): the result (in Stephan-Boltzmann units) is surprisingly simple

$$S(g^2 N_c \rightarrow \infty, T)/S(g = 0, T) = [(3/4) + O((g^2 N_c)^{-3/2})]. \quad (4.128)$$

The authors first thought the factor $(3/4)$ is wrong, but then it was clarified that it is indeed a limit at strong coupling. In fact it compares well with the lattice measurements in the “conformal domain” of $T = \text{few } T_c$ where this constant is about 0.8, with or without quarks.

Heavy-quark potentials at finite T were calculated [719, 720] by calculating the energy of the static pending string as explained in the previous subsection, but in a modified (thermal) metric. The Debye screening is now happening when a string touches the horizon and breaks into two parts: the screening radius is finite $O(1/T)$ at strong coupling $g^2 N_c \rightarrow \infty$.

This feature was explained by Zahed and Shuryak [679], who used lattice diagram resummation. In another work [724] they had discussed the velocity-dependent forces as well as spin–spin and spin–orbit interaction: ladder resummation predicts that all of them join into one common square root

$$V(T, r, g) \sim \sqrt{(g^2 N_c)[1 - \mathbf{v}_1 \cdot \mathbf{v}_2 + (\text{spin-spin}) + (\text{spin-orbit})]}/r \quad (4.129)$$

where $\mathbf{v}_1, \mathbf{v}_2$ are velocities of the quarks. If so, the $(\mathbf{v}_1 \cdot \mathbf{v}_2)$ term – the strong coupling version of Ampere’s interaction between two currents – should have extra $1/2$ at small velocity. Lin and Shuryak [725, 726] solved for a string with two quarks moving away from each other: their answer in the small-velocity limit is $\sim (1 + 0.68 v^2 + \dots)$, close to $1/2$ but not exactly.

Bound states of quarks at strong coupling is a very difficult but crucial issue. Naively, one may simply take a modified (Maldacena) Coulombic potential and plug it into Klein-Gordon/Dirac equations. As discussed in [679], there is no problem with states at large orbital momentum $J \gg \sqrt{g^2 N_c}$, but others famously “fall onto the center”. From gauge side nothing we know seems to be able to stop this falling.

And yet, studies based on the AdS/CFT gravity side [727] found that there is no falling at all! The Coulombic states at large J are supplemented by two more families: “Regge states” with masses $M \sim M_{HQ}/(g^2 N_c)^{1/4}$ and even lighter s -wave states (one may call them $\eta_c, J/\psi$) with masses $M \sim M_{HQ}/\sqrt{g^2 N_c}$. The issue of “falling” was further discussed by Klebanov, Maldacena and Thorn [722]. There are also multi-body heavy-quark+scalar states similar to “polymeric chains” $\bar{q}.g.g\dots q$ discussed in QGP context: see more on that in Hong, Yoon and Strassler [728]. And yet – as for sQGP – the microscopic structure of the CFT plasma remains unknown.

Transport properties of the CFT plasma was a subject of significant studies and breakthroughs. One famous work is that by Policastro, Son and Starinets

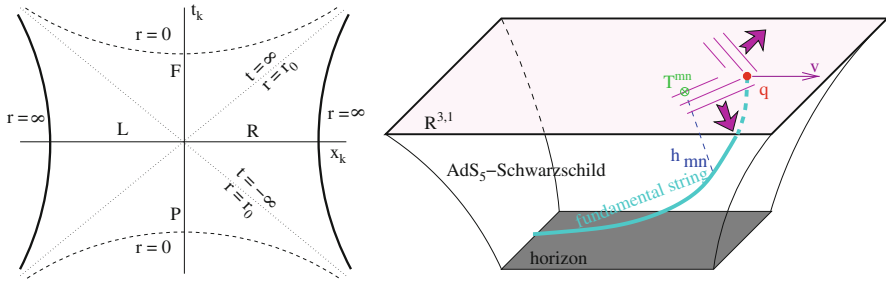


Fig. 4.45 *Left* (from [716]): In Kruskal coordinates one can study two Universes at the same time, shown *right* and *left*, and the evaluated Wilson line contains static quarks on their boundaries. *Right* (from [729]): The dragged quark trails a string into the five-dimensional AdS bulk, representing color fields sourced by the quark’s fundamental charge and interacting with the thermal medium. The back reaction on gravity describes how matter flows on the boundary.

[715] who have calculated viscosity-to-entropy ratio, finding that at infinite coupling it has a finite limit $\eta/s = 1/4\pi$, right in the ballpark of the empirical RHIC value. Deep reasons for this simple answer go back to the so called “membrane paradigm” of the black hole physics, which ascribes certain dissipative properties to its horizon.

Heavy quark diffusion constant has been calculated by Casalderrey-Solana and Teaney [716] who found that

$$D_{HQ} = \frac{2}{\pi T \sqrt{g^2 N_c}}. \quad (4.130)$$

Note that it contains large coupling in denominator and thus is parametrically smaller than an expression for the momentum diffusion $D_p = \eta/(\epsilon+p) \sim 1/4\pi T$. This work is methodically quite different from others: global Kruskal coordinates are used (see Fig. 4.45, left panel) which allows to consider propagation of the perturbation *through* the black hole into another “Universe”, with the opposite time direction. This corresponds to Keldysh-Schwinger rules for calculating *probabilities* involving both an amplitude and a conjugated amplitude together.

Jet quenching studies [730–734] have used the so called “trailing string” solution, see Fig. 4.45, right panel. It predicts the drag force

$$\frac{dP}{dt} = -\frac{\pi T^2 \sqrt{g^2 N_c} v}{2\sqrt{1-v^2}}. \quad (4.131)$$

Quite remarkably, the Einstein relation (which in equilibrium relates the heavy quark diffusion constant to the drag force) is fulfilled, although it is not easy to see how those two quite different gravity settings know about it.

The magnitude of this drag force qualitatively agrees with observed single electrons from heavy quark decays at RHIC, as was demonstrated in the AdS/CFT line in Fig. 4.43. Right now those are seen up to $p_t \sim 5 \text{ GeV}$ at which c,b quarks contribute comparably: a challenging task would be to test this drag prediction for charm and bottom quarks separately and see if it does or does not work.

Two examples of holograms provide much more detailed microscopic pictures of complicated processes in real time, showing what AdS/CFT correspondence can in principle do. Figure 4.46, left panel from Lin and Shuryak [725, 726] shows a snapshot of the distribution and direction of a Poynting vector of matter corresponding to two heavy quarks moving *away* from each other. The string now is no longer stationary and is stretching and simultaneously falling into the 5-th direction as a function of time. Time-dependent picture is clearly an explosion: but it is a non-hydrodynamical one, a AdS/CFT analog of a pair of jets.

Stationary holograms from a trailing string has been calculated by Gubser et al. [729] as well as Chesler and Yaffe [735], from whom we took Fig. 4.46, right panel. It shows remarkable picture of the conical flow: note e.g. a surplus of energy in front of the quark and a deficit behind it. A Mach cone, with opening half angle $\theta_M \approx 50^\circ$ is clearly visible in both the energy density and the Poynting vector.

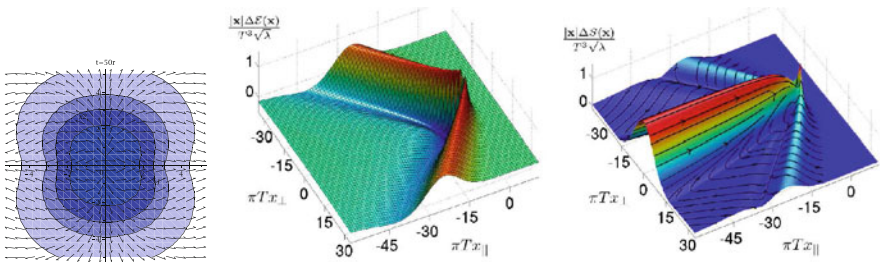


Fig. 4.46 *Left* (from [725, 726]): The contours of Poynting vector T^{0i} in transverse plane, induced by two quarks moving away from each other. The magnitude is represented by color, with darker color corresponding to greater magnitude. The direction of the momentum flow is indicated by *arrows*. *Middle and right* (from [735]): Plot of the normalized energy density (*middle*) and Poynting vector (*right*) for one quark (supersonic jet) with $v = 3/4$ at nonzero T .

“Gravity duals” to heavy ion collisions is the ultimate AdS/CFT application, aiming to reproduce the whole collision process, including equilibration, entropy production and hydrodynamical explosion. This should be described via a *dynamically generated* black hole (BH). Sin, Zahed and Shuryak [736] argued that exploding/cooling fireball on the brane is dual to departing black hole, formed by the collision debris and then falling toward the AdS center. A specific solution they discussed in the paper was a brane departing from a

static black hole, which generated a “spherical” solution (no dependence on all 3 spatial coordinates) with a time-dependent T (which however is more appropriate for cosmology but not heavy ion applications). These authors also discussed other idealized settings, with d -dimensional stretching, corresponding for $d=1$ to a collision of two infinite thin walls and subsequent Bjorken rapidity-independent expansion, with $2d$ and $3d$ corresponding to cylindrical and spherical relativistic collapsing walls.

Janik and Peschanski [737, 738], found asymptotic (late-time) solution corresponding to 1- d rapidity-independent Bjorken expansion. It indeed has a departing *horizon* $z \sim \tau^{1/3}$ (z, τ are the distance from our brane in 5-th coordinate and the proper time). A very important feature of the Janik-Peschanski solution is that while the horizon is stretching in one direction and contracting in others, two effects compensate each other and keep the *total horizon area constant*: this corresponds to entropy conservation on the boundary, in ideal hydrodynamic expansion. Further discussion of the first subleading terms $O(\tau^{-2/3})$ correcting the JP solution has been made by Sin and Nakamura [739] who identified them with the viscosity effects, but they do not find any preference for a particular value of the viscosity. Janik [740] was able to derive sub-sub-leading term in the metric $O(\tau^{-4/3})$ and provide an argument why viscosity should be what was found in equilibrium.

Recently, Princeton group (Friess et al. [741]) pointed out very nice analytic solution to a problem of departing point-like black hole. It produces at the boundary violent spherically symmetric explosion, in which matter is expanding in a form of a spherical shell. This solution explicitly conserves entropy so one may call it a “reversible” explosion. Further work towards identifying the “gravity dual” to the heavy-ion fireball is actively pursued by all those groups.

Chapter 5

Summary

The main purpose of the preceding Chaps. 2, 3 and 4 has been to review our present understanding of the bulk properties of strongly interacting matter, especially of the equation of state and the location of transition lines, crossovers and critical points. In the present section we will not summarize all findings of these previous chapters. Instead, we will focus here on issues which are potentially related to experiments at high baryon densities. This concerns possible predictions as well as future work which has to be performed on the theory side to decrease the uncertainties and develop new concepts. We shall concentrate on four points, namely (1) the quest to identify and model the relevant degrees of freedom, especially in the transition region, (2) the determination of the equation of state of dense and especially baryon-rich strongly interacting matter, (3) color superconductivity and (4) the transition region between hadronic and quark-gluon matter and the possible critical point.

1. Modeling the relevant degrees of freedom:

As has already been stressed, first principle calculations are so far not applicable in the region of high net baryon densities and moderate temperatures, in particular close to the transition region. Here various models have been developed which compete with or complement each other. An important point is that these models can not only be constrained by data, but also by comparison to lattice QCD results for the region where the latter works reasonably well. This has been utilized, e.g. by the models presented in Sects. 4.2, 4.3, 4.4, 4.5, and 4.8. One phenomenological model which is appealing due to its simplicity is the statistical model reviewed in Sect. 4.1 which can be used to predict particle production yields. Still one would like to understand from a microscopic point of view why it works so well and where its limitations show up. The hadron resonance gas model of Sect. 4.2 rests on a vast amount of measurements of hadron properties as summarized by the Particle Data Group [10] and on the assumption that the main interactions between hadrons are covered by

resonance production. Naturally, the hadron resonance gas model is restricted to the region below the transition to the quark-gluon plasma where the relevant degrees of freedom change. A complementary model for the region above the transition is the one presented in Sect. 4.3 using quark and gluon quasi-particles. These models are of phenomenological nature by resting either on experimental results or on fits to lattice calculations. There is another class of models which put their prime attention to the underlying symmetry aspects, cf. Sects. 4.4, 4.5, 4.7.

At present, it is rather unclear, whether the models presented in the previous chapter just exclude each other or whether they highlight different aspects of one complex picture. For example, it appears very natural to describe the region below the transition by a gas of resonances. Indeed, their appearance can explain the drastic rise in the pressure as a function of the temperature when approaching the transition. On the other hand, it is also natural to assume that the deconfinement transition is connected to the underlying symmetry, the center symmetry, and therefore to the Wilson line degrees of freedom discussed in Sect. 4.4. However, the connection between the hadronic resonances and the Wilson lines is completely unclear. The same holds true for the possible connection between chiral symmetry restoration and the hadronic resonances. And exactly the same statement also applies to the situation above the transition: Also here there are no obvious links between Wilson lines, chiral symmetry and quasi-particles (for some recent ideas see [590, 596, 742]). Without a deeper understanding of such possible connections it is not clear whether an extrapolation of the discussed models to other (less constrained) regions of the phase diagram will yield reliable results. Here more work on the theory side is clearly required. Improved models which take into account both phenomenological constraints as well as the underlying symmetries and their changes will be an important tool to understand the physics of strongly interacting matter at high baryon densities.

2. Equation of state:

The quest for the nuclear equation of state at high densities and/or extreme isospin is one of the longstanding problems of nuclear physics. Models applicable in a density range where nucleons, or hadrons in general, can be considered as the relevant degrees of freedom, are either based on empirical density functionals, effective field theory or ab initio approaches to the nuclear many-body problem (cf. Sect. 3.3). While being well constrained at sub-nuclear densities by data, empirical functionals diverge dramatically when extrapolated to high densities and/or extreme isospin. The ab initio approaches differ in detail, i.e. the particular approximation schemes and the usage of nucleon–nucleon forces, but they show a fair agreement up to two to three times saturation density. They predict an equation of state which is soft for symmetric nuclear matter but relatively stiff what concerns the isospin dependence. A more systematic treatment of many-body forces and a closer connection to QCD

will in future be achieved by a further development of chirally invariant theories.

Constraints obtained from studying neutron stars also come into play here (cf. Sect. 3.4): Observational evidence for masses of neutron stars above 1.7 times the solar mass also favors a stiff equation of state for isospin asymmetric nuclear matter at high densities, i.e. for three to five times saturation density. Such studies can be used to tighten the constraints for the equation of state in nuclear collisions provided, e.g., by the analysis of flow data. Concerning the transition to quark matter one obtains the following constraint from neutron star studies: If quark matter is invoked to explain the properties of compact stars with typical masses of 1.25–1.45 solar masses, then the phase transition to deconfined quark matter is expected to occur at densities below 3.5 times saturation density, i.e. below 0.55 fm^{-3} .

As already pointed out, lattice QCD cannot be used at present to determine the equation of state for large net baryon densities. In principle, perturbative QCD (cf. Sect. 3.1) is applicable at finite chemical potentials, but only for situations where the temperature or the chemical potential or both are very high (compared, e.g., to Λ_{QCD}). At present, resummation techniques are developed to extend the region of applicability of perturbative QCD down to smaller values of temperature and/or chemical potential. In addition, the results of both first principle approaches, lattice and perturbative QCD, can be used to inspire or constrain quark model approaches. One example has been presented in Sect. 4.3, the quark-gluon quasi-particle model. It describes the available lattice QCD results, e.g., the equation of state and the susceptibilities as a measure for fluctuations from high temperatures down to the transition point. The qualitative dependence of the masses of the quasi-particles on the temperature and the chemical potential is inspired by (resummed) QCD perturbation theory. In that way, one can extrapolate the equation of state known for small baryon densities from ab initio lattice calculations towards large baryon densities relevant for CBM in a thermodynamically consistent way. In addition, features of the QCD critical point can be included phenomenologically into the model in order to study the behavior of fluctuations in the vicinity of such an exceptional point.

3. Color superconductivity:

Whether one can get some glimpse of a color superconducting phase in a nuclear-collision experiment is very speculative. Clearly, this possibility hinges on the size of the gap for diquark condensation (cf. Sect. 3.5). In perturbative QCD one obtains rather small gaps, but it is not so clear down to which values of the chemical potential this method is applicable (cf. e.g. the discussion in [743]). There are model calculations which predict sizable gaps which in turn would lead to transition temperatures not far below the ones reachable in nuclear collisions with large net baryon densities. Hence, it might be possible to see precursor phenomena

of a color superconducting phase or the possible crossover between Bose-Einstein condensation of diquark molecules and a homogeneous color superconducting phase.

4. Transition region and critical point:

At present, lattice QCD as a first principle method is the most promising tool to determine the transition region from hadronic matter to the quark-gluon plasma (cf. Sect. 3.2). There are two symmetry aspects which separate these two states of matter, namely chiral symmetry and the center symmetry connected to confinement. However, both symmetries are only approximately realized in nature. Hence, there is no strict reason why hadronic and quark-gluon matter should be separated by a true phase transition. Indeed, lattice results indicate that at low baryo-chemical potentials there is a crossover between these two states of matter, i.e. no real phase transition. One also infers from lattice calculations that the order parameters of both considered symmetries drastically change at the very same temperature. These findings concern the case of vanishing chemical potential. For large chemical potentials one might resort to effective models. There is no general proof (and indeed, in models one can construct counterexamples), but most models seem to predict a first order transition. In particular, these are models which focus on the chiral symmetry aspect of the transition (cf. e.g. Sect. 4.5). On the other hand, if one studies the deconfinement transition using Wilson line degrees of freedom (cf. Sect. 4.4) one also finds that the transition at finite temperature, but vanishing chemical potential, is a crossover for realistic quark masses. Only for much higher quark masses one finds a first order transition (cf. Fig. 3.19). However, the presence of a chemical potential now weakens this first order transition. This would suggest that decreasing the quark mass or increasing the chemical potential both work against a first order phase transition. It should be stressed, however, that it is not clear whether the deconfinement and the chiral restoration transition also coincide at non-vanishing chemical potential.

If there is a crossover at low and a true phase transition at high chemical potentials, then there must be a critical point, where the first order transition line starts. At this particular point the transition is of second order which leads to large correlation lengths and allows for large fluctuations. Unfortunately, it is very difficult to perform reliable lattice calculations at finite chemical potentials. Recently, calculational techniques have been developed to scan deeper into this region using lattice QCD. However, at present, predictions for the location of the critical point vary strongly, and even the existence of the critical point is not fully settled.

From the experimental side, it clearly would be a very spectacular result to find an indication for the critical point. Here, fluctuations seem to be the most promising tool. From the theoretical point of view, fluctuations are intimately connected to the (charge and baryon number) susceptibilities. The latter diverge at the critical point leading to large

fluctuations. The determination of susceptibilities from lattice QCD is also under current investigation. So far, however, one also has to rely on models to get a qualitative and semi-quantitative picture of the critical point and the susceptibilities connected to it. In that context there is an interesting finding from the renormalization group approach (cf. Sect. 4.7): If one improves on a quark model mean field result using the renormalization group method, it turns out that the critical region appreciably shrinks – as compared to the pure mean field result. The critical region is the area around the critical point where the susceptibilities are still sizable. This finding seems to indicate that it might be difficult to actually detect the critical point. On the other hand, these considerations concern thermal equilibrium. As has been shown in Sect. 4.6, susceptibilities can also diverge in the region of spinodal instabilities which accompany a first order transition. Indeed, in an off-equilibrium situation – which typically would appear, if the state of matter traversed a first order phase transition – the instability region is accessible. Therefore an experimental verification of huge fluctuations might point towards a first order phase transition and not directly towards a critical point. On the other hand, this makes it more likely that such a phenomenon is observed at all. In addition, the theoretical finding of lattice QCD that there is a crossover at low chemical potentials together with an experimental finding of a true phase transition at large net baryon densities would also indicate that there is a critical point in between. Of course, an experimental indication of a first order phase transition would be as spectacular as the discovery of a critical point.

References

1. M. D'Elia, A. Di Giacomo, C. Pica, Phys. Rev. D **72**, 114510 (2005) [41](#), [116](#)
2. P. de Forcrand, O. Philipsen, JHEP **01**, 077 (2007) [41](#), [116](#), [137](#), [256](#)
3. D.J. Schwarz, Mod. Phys. Lett. A **13**, 2771 (1998) [42](#)
4. L.A. Boyle, P.J. Steinhardt, Phys. Rev. D **77**, 063504 (2008) [42](#)
5. K. Jedamzik, Phys. Rev. D **55**, 5871 (1997) [42](#)
6. C. Schmid, D.J. Schwarz, P. Widerin, Phys. Rev. Lett. **78**, 791 (1997)
7. C. Schmid, D.J. Schwarz, P. Widerin, Phys. Rev. D **59**, 043517 (1999)
8. K.N. Abazajian, G.M. Fuller, Phys. Rev. D **66**, 023526 (2002)
9. M. Hindmarsh, O. Philipsen, Phys. Rev. D **71**, 087302 (2005) [42](#)
10. W.M. Yao, et al., J. Phys. G **33**, 1 (2006) [47](#), [48](#), [52](#), [53](#), [101](#), [106](#), [186](#), [307](#)
11. M.E. Peskin, D.V. Schroeder, *An Introduction to Quantum Field Theory* (Perseus, Cambridge, MA, 1995) [50](#), [51](#), [53](#)
12. J.I. Kapusta, *Finite-Temperature Field Theory*. Cambridge Monographs on Mathematical Physics (Cambridge University Press, Cambridge, UK, 1989) [51](#), [217](#)
13. S. Weinberg, Physica A **96**, 327 (1979) [54](#)
14. J. Gasser, H. Leutwyler, Ann. Phys. **158**, 142 (1984)
15. J. Gasser, H. Leutwyler, Nucl. Phys. B **250**, 465 (1985)
16. S. Scherer, Adv. Nucl. Phys. **27**, 277 (2003) [54](#)
17. M. Creutz, *Quarks, Gluons and Lattices*. Cambridge Monographs On Mathematical Physics (Cambridge University Press, Cambridge, UK, 1983) [54](#)
18. J. Engels, J. Fingberg, M. Weber, Nucl. Phys. B **332**, 737 (1990) [54](#), [228](#)
19. K. Holland, U.J. Wiese, (2000). hep-ph/0011193 [58](#)
20. S. Schael, et al., Phys. Rep. **421**, 191 (2005) [64](#)
21. U.G. Meissner, Phys. Rep. **161**, 213 (1988) [65](#)
22. A.M. Halasz, A.D. Jackson, R.E. Shrock, M.A. Stephanov, J.J.M. Verbaarschot, Phys. Rev. D **58**, 096007 (1998) [82](#), [224](#), [260](#)
23. A.B. Migdal, E.E. Saperstein, M.A. Troitsky, D.N. Voskresensky, Phys. Rep. **192**, 179 (1990) [82](#)
24. I.R. Klebanov, Nucl. Phys. B **262**, 133 (1985) [82](#)

25. B.C. Barrois, Nucl. Phys. B **129**, 390 (1977) [82](#)
26. D. Bailin, A. Love, Phys. Rep. **107**, 325 (1984) [182](#)
27. M.G. Alford, K. Rajagopal, F. Wilczek, Phys. Lett. B **422**, 247 (1998) [238](#), [260](#)
28. R. Rapp, T. Schafer, E.V. Shuryak, M. Velkovsky, Phys. Rev. Lett. **81**, 53 (1998) [82](#), [182](#), [238](#)
29. D.B. Kaplan, A.E. Nelson, Phys. Lett. B **175**, 57 (1986) [82](#)
30. E. Witten, Phys. Rev. D **30**, 272 (1984) [82](#), [83](#)
31. E. Farhi, R.L. Jaffe, Phys. Rev. D **30**, 2379 (1984) [82](#), [83](#)
32. M.G. Alford, K. Rajagopal, F. Wilczek, Nucl. Phys. B **537**, 443 (1999) [83](#), [89](#), [169](#)
33. K. Rajagopal, F. Wilczek, (2000). hep-ph/0011333 [83](#), [87](#), [89](#)
34. T. Schafer, (2003). hep-ph/0304281
35. M.G. Alford, Ann. Rev. Nucl. Part Sci. **51**, 131 (2001) [89](#)
36. M.G. Alford, PoS **LAT2006**, 001 (2006) [83](#), [87](#), [89](#)
37. T. Schäfer, F. Wilczek, Phys. Rev. Lett. **82**, 3956 (1999) [83](#), [169](#)
38. L.P. Csernai, J.I. Kapusta, Phys. Rep. **131**, 223 (1986) [83](#), [84](#)
39. S.P. Klevansky, Rev. Mod. Phys. **64**, 649 (1992) [83](#), [84](#), [237](#)
40. M.A. Stephanov, Phys. Rev. Lett. **76**, 4472 (1996) [84](#)
41. W. Trautmann, (1996). nucl-ex/9611002 [84](#)
42. R.D. Pisarski, F. Wilczek, Phys. Rev. D **29**, 338 (1984) [86](#), [235](#), [260](#), [282](#)
43. U.M. Heller, PoS **LAT2006**, 011 (2006) [87](#), [88](#)
44. Y. Aoki, G. Endrodi, Z. Fodor, S.D. Katz, K.K. Szabo, Nature **443**, 675 (2006) [88](#), [136](#), [143](#)
45. L.P. Csernai, J.I. Kapusta, L.D. McLerran, Phys. Rev. Lett. **97**, 152303 (2006) [88](#)
46. D. Teaney, Phys. Rev. C **68**, 034913 (2003) [88](#), [287](#), [289](#), [297](#)
47. P. Kovtun, D.T. Son, A.O. Starinets, Phys. Rev. Lett. **94**, 111601 (2005) [88](#)
48. I.D. Lawrie, S. Sarbach, *Phase Transitions*, vol. 9 (Academic Press, London, 1984) [91](#)
49. Y. Hatta, T. Ikeda, Phys. Rev. D **67**, 014028 (2003) [92](#), [224](#), [260](#)
50. M.A. Stephanov, K. Rajagopal, E.V. Shuryak, Phys. Rev. Lett. **81**, 4816 (1998) [92](#), [116](#), [260](#)
51. M.A. Stephanov, K. Rajagopal, E.V. Shuryak, Phys. Rev. D **60**, 114028 (1999)
52. Y. Hatta, M.A. Stephanov, Phys. Rev. Lett. **91**, 102003 (2003) [92](#), [260](#), [262](#)
53. U.G. Meissner, J.A. Oller, A. Wirzba, Ann. Phys. **297**, 27 (2002) [93](#), [95](#)
54. M. Gell-Mann, R.J. Oakes, B. Renner, Phys. Rev. **175**, 2195 (1968) [93](#)
55. M.C. Birse, Phys. Rev. C **53**, 2048 (1996) [93](#)
56. J.I. Kapusta, E.V. Shuryak, Phys. Rev. D **49**, 4694 (1994) [93](#)
57. C.A. Dominguez, K. Schilcher, Phys. Lett. B **581**, 193 (2004) [93](#)
58. F. Karsch, Lect. Notes Phys. **583**, 209 (2002) [94](#), [116](#), [118](#), [243](#), [255](#), [256](#)
59. J. Gasser, H. Leutwyler, Phys. Lett. B **184**, 83 (1987) [95](#)
60. J. Gasser, H. Leutwyler, Nucl. Phys. B **307**, 763 (1988) [95](#)
61. P. Gerber, H. Leutwyler, Nucl. Phys. B **321**, 387 (1989) [96](#), [97](#), [98](#)
62. J.R. Pelaez, Phys. Rev. D **66**, 096007 (2002) [96](#), [97](#)
63. S. Leupold, J. Phys. G **32**, 2199 (2006) [97](#), [98](#)

64. V.L. Eletsky, Phys. Lett. B **299**, 111 (1993) [97](#)
65. S. Leupold, Phys. Lett. B **616**, 203 (2005) [97](#)
66. B.J. Schaefer, J. Wambach, Work in progress [98](#)
67. A. Tawfik, D. Toublan, Phys. Lett. B **623**, 48 (2005) [98](#)
68. A.D. Linde, Phys. Lett. B **96**, 289 (1980) [101](#), [103](#), [112](#), [115](#)
69. D.J. Gross, R.D. Pisarski, L.G. Yaffe, Rev. Mod. Phys. **53**, 43 (1981) [101](#), [103](#), [228](#)
70. K. Kajantie, M. Laine, K. Rummukainen, Y. Schroder, Phys. Rev. D **67**, 105008 (2003) [101](#), [103](#), [104](#), [114](#)
71. A. Vuorinen, Phys. Rev. D **67**, 074032 (2003) [101](#)
72. A. Vuorinen, Phys. Rev. D **68**, 054017 (2003) [101](#), [111](#), [112](#)
73. A. Ipp, K. Kajantie, A. Rebhan, A. Vuorinen, Phys. Rev. D **74**, 045016 (2006) [101](#), [113](#)
74. J.I. Kapusta, Nucl. Phys. B **148**, 461 (1979) [102](#), [103](#), [104](#)
75. M. Laine, Y. Schroder, Phys. Rev. D **73**, 085009 (2006) [102](#), [104](#), [105](#), [106](#), [114](#), [115](#)
76. K. Kajantie, M. Laine, K. Rummukainen, Y. Schroder, Phys. Rev. Lett. **86**, 10 (2001) [102](#), [108](#), [110](#)
77. A. Hietanen, K. Kajantie, M. Laine, K. Rummukainen, Y. Schroder, JHEP **01**, 013 (2005) [108](#)
78. A. Hietanen, K. Kajantie, M. Laine, K. Rummukainen, Y. Schroder, PoS **LAT2005**, 174 (2006) [102](#), [108](#)
79. F. Karsch, A. Patkos, P. Petreczky, Phys. Lett. B **401**, 69 (1997) [102](#), [108](#), [109](#)
80. S. Chiku, T. Hatsuda, Phys. Rev. D **58**, 076001 (1998) [108](#)
81. A. Peshier, (1999). hep-ph/9910451 [108](#), [110](#)
82. J.O. Andersen, E. Braaten, M. Strickland, Phys. Rev. Lett. **83**, 2139 (1999) [108](#), [217](#), [218](#), [219](#)
83. J.O. Andersen, E. Braaten, M. Strickland, Phys. Rev. D **61**, 014017 (2000) [217](#), [218](#), [219](#)
84. J.O. Andersen, E. Braaten, M. Strickland, Phys. Rev. D **61**, 074016 (2000)
85. J.P. Blaizot, E. Iancu, A. Rebhan, Phys. Rev. Lett. **83**, 2906 (1999) [108](#), [110](#), [217](#)
86. J.P. Blaizot, E. Iancu, A. Rebhan, Phys. Lett. B **470**, 181 (1999)
87. J.P. Blaizot, E. Iancu, A. Rebhan, Phys. Rev. D **63**, 065003 (2001) [108](#), [110](#)
88. J.O. Andersen, E. Braaten, M. Strickland, Phys. Rev. D **63**, 105008 (2001) [108](#), [109](#), [217](#), [218](#), [219](#)
89. J.O. Andersen, M. Strickland, Phys. Rev. D **64**, 105012 (2001) [108](#)
90. J.O. Andersen, E. Braaten, E. Petitgirard, M. Strickland, Phys. Rev. D **66**, 085016 (2002) [108](#), [109](#), [110](#)
91. J.O. Andersen, E. Petitgirard, M. Strickland, Phys. Rev. D **70**, 045001 (2004) [102](#), [108](#)
92. E.V. Shuryak, Sov. Phys. JETP **47**, 212 (1978) [103](#)
93. S.A. Chin, Phys. Lett. B **78**, 552 (1978) [103](#)
94. T. Toimela, Phys. Lett. B **124**, 407 (1983) [103](#)
95. P. Arnold, C.X. Zhai, Phys. Rev. D **50**, 7603 (1994) [103](#)
96. P. Arnold, C.X. Zhai, Phys. Rev. D **51**, 1906 (1995) [103](#)
97. C.X. Zhai, B.M. Kastening, Phys. Rev. D **52**, 7232 (1995) [103](#)

98. F. Di Renzo, M. Laine, V. Miccio, Y. Schroder, C. Torrero, JHEP **07**, 026 (2006) [103](#)
99. A. Gynther, M. Vepsalainen, JHEP **03**, 011 (2006) [103](#)
100. A. Gynther, M. Vepsalainen, JHEP **01**, 060 (2006) [103](#)
101. G.D. Moore, JHEP **10**, 055 (2002) [103](#)
102. A. Ipp, G.D. Moore, A. Rebhan, JHEP **01**, 037 (2003)
103. A. Ipp, A. Rebhan, JHEP **06**, 032 (2003)
104. A. Ipp, A. Rebhan, A. Vuorinen, Phys. Rev. D **69**, 077901 (2004) [103](#), [111](#)
105. G. Boyd, et al., Nucl. Phys. B **469**, 419 (1996) [103](#), [104](#), [105](#), [132](#), [241](#), [242](#)
106. B. Beinlich, F. Karsch, E. Laermann, A. Peikert, Eur. Phys. J. C **6**, 133 (1999) [103](#), [104](#), [105](#)
107. F. Karsch, K. Redlich, A. Tawfik, Eur. Phys. J. C **29**, 549 (2003) [106](#), [130](#), [210](#)
108. A. Ali Khan, et al., Phys. Rev. D **64**, 074510 (2001) [107](#), [132](#), [245](#), [257](#)
109. C. Bernard, et al., Phys. Rev. D **75**, 094505 (2007) [127](#), [128](#), [129](#)
110. Y. Aoki, Z. Fodor, S.D. Katz, K.K. Szabo, JHEP **01**, 089 (2006) [127](#), [132](#), [145](#)
111. S. Ejiri, F. Karsch, E. Laermann, C. Schmidt, Phys. Rev. D **73**, 054506 (2006) [107](#), [129](#), [130](#), [131](#), [132](#), [134](#)
112. E. Braaten, A. Nieto, Phys. Rev. D **53**, 3421 (1996) [107](#)
113. K. Kajantie, M. Laine, K. Rummukainen, M.E. Shaposhnikov, Nucl. Phys. B **458**, 90 (1996)
114. K. Kajantie, M. Laine, K. Rummukainen, M.E. Shaposhnikov, Nucl. Phys. B **503**, 357 (1997)
115. K. Kajantie, M. Laine, A. Rajantie, K. Rummukainen, M. Tsypin, JHEP **11**, 011 (1998) [107](#)
116. A. Gynther, M. Laine, Y. Schroder, C. Torrero, A. Vuorinen, JHEP **04**, 094 (2007) [108](#)
117. G. Baym, Phys. Rev. **127**, 1391 (1962) [108](#), [110](#)
118. J.O. Andersen, M. Strickland, Ann. Phys. **317**, 281 (2005) [108](#), [110](#), [228](#), [229](#)
119. J.P. Blaizot, E. Iancu, A. Rebhan, (2003). hep-ph/0303185 [108](#)
120. B.M. Kastening, Phys. Rev. D **56**, 8107 (1997) [109](#)
121. T. Hatsuda, Phys. Rev. D **56**, 8111 (1997)
122. G. Cvetic, R. Kogerler, Phys. Rev. D **66**, 105009 (2002) [109](#)
123. R.R. Parwani, Phys. Rev. D **64**, 025002 (2001) [109](#)
124. R.R. Parwani, Phys. Rev. D **63**, 054014 (2001) [109](#)
125. J.P. Blaizot, E. Iancu, A. Rebhan, Phys. Rev. D **68**, 025011 (2003) [110](#), [217](#), [218](#)
126. J.M. Luttinger, J.C. Ward, Phys. Rev. **118**, 1417 (1960) [110](#)
127. J.P. Blaizot, E. Iancu, A. Rebhan, Phys. Lett. B **523**, 143 (2001) [111](#), [112](#), [217](#)
128. J.P. Blaizot, E. Iancu, A. Rebhan, Eur. Phys. J. C **27**, 433 (2003) [111](#)
129. Z. Fodor, S.D. Katz, K.K. Szabo, Phys. Lett. B **568**, 73 (2003) [111](#), [129](#), [134](#), [224](#)
130. C.R. Allton, et al., Phys. Rev. D **68**, 014507 (2003) [111](#), [129](#), [134](#), [210](#), [212](#), [213](#)
131. F. Karsch, E. Laermann, A. Peikert, Phys. Lett. B **478**, 447 (2000) [111](#), [126](#), [216](#)
132. S. Gupta, Phys. Rev. D **64**, 034507 (2001) [111](#)
133. C.P. Korthals Altes, R.D. Pisarski, A. Sinkovics, Phys. Rev. D **61**, 056007 (2000) [112](#)
134. A. Hart, M. Laine, O. Philipsen, Nucl. Phys. B **586**, 443 (2000)

- 135. D. Bodeker, M. Laine, JHEP **09**, 029 (2001) [112](#)
- 136. R.V. Gavai, S. Gupta, P. Majumdar, Phys. Rev. D **65**, 054506 (2002) [112](#)
- 137. R.V. Gavai, S. Gupta, Phys. Rev. D **71**, 114014 (2005) [112](#), [137](#), [140](#)
- 138. C.R. Allton, et al., Phys. Rev. D **71**, 054508 (2005) [112](#), [129](#), [142](#), [210](#), [212](#), [213](#)
- 139. A. Hietanen, K. Rummukainen, JHEP **04**, 078 (2008) [112](#)
- 140. J. Frenkel, J.C. Taylor, Nucl. Phys. B **334**, 199 (1990) [112](#)
- 141. E. Braaten, R.D. Pisarski, Nucl. Phys. B **337**, 569 (1990)
- 142. T. Altherr, U. Kraemmer, Astropart. Phys. **1**, 133 (1992)
- 143. C. Manuel, Phys. Rev. D **53**, 5866 (1996) [112](#)
- 144. B.A. Freedman, L.D. McLerran, Phys. Rev. D **16**, 1130 (1977) [112](#)
- 145. B.A. Freedman, L.D. McLerran, Phys. Rev. D **16**, 1147 (1977)
- 146. B.A. Freedman, L.D. McLerran, Phys. Rev. D **16**, 1169 (1977) [112](#)
- 147. V. Baluni, Phys. Rev. D **17**, 2092 (1978) [112](#)
- 148. T. Holstein, R.E. Norton, P. Pincus, Phys. Rev. B **8**, 2649 (1973) [112](#)
- 149. S. Chakravarty, R.E. Norton, O.F. Syljuåsen, Phys. Rev. Lett. **74**, 1423 (1995) [112](#)
- 150. T. Schafer, K. Schwenzer, Phys. Rev. D **70**, 054007 (2004) [112](#)
- 151. A. Ipp, A. Gerhold, A. Rebhan, Phys. Rev. D **69**, 011901 (2004) [113](#)
- 152. A. Gerhold, A. Ipp, A. Rebhan, Phys. Rev. D **70**, 105015 (2004) [113](#)
- 153. A. Gerhold, A. Rebhan, Phys. Rev. D **71**, 085010 (2005) [113](#), [114](#)
- 154. T. Schafer, K. Schwenzer, Phys. Rev. D **70**, 114037 (2004) [113](#)
- 155. Z. Fodor, S.D. Katz, JHEP **03**, 014 (2002) [116](#), [124](#), [129](#), [133](#), [137](#), [224](#), [225](#), [236](#)
- 156. C.R. Allton, et al., Phys. Rev. D **66**, 074507 (2002) [121](#), [133](#), [134](#), [144](#), [210](#), [212](#)
- 157. R.V. Gavai, S. Gupta, Phys. Rev. D **64**, 074506 (2001)
- 158. M. D'Elia, M.P. Lombardo, Phys. Rev. D **67**, 014505 (2003) [122](#), [129](#), [134](#), [144](#)
- 159. P. de Forcrand, O. Philipsen, Nucl. Phys. B **642**, 290 (2002) [116](#), [120](#), [122](#), [123](#), [129](#)
- 160. Z. Fodor, S.D. Katz, C. Schmidt, JHEP **03**, 121 (2007) [116](#), [134](#), [135](#), [145](#)
- 161. C. Bernard, M. Golterman, Y. Shamir, Phys. Rev. D **73**, 114511 (2006) [118](#)
- 162. M. Creutz, PoS **LAT2007**, 007 (2007)
- 163. A.S. Kronfeld, PoS **LAT2007**, 016 (2007) [118](#)
- 164. I.M. Barbour, S.E. Morrison, E.G. Klepfish, J.B. Kogut, M.P. Lombardo, Nucl. Phys. Proc. Suppl. **60A**, 220 (1998) [120](#)
- 165. Z. Fodor, S.D. Katz, Phys. Lett. B **534**, 87 (2002) [120](#), [133](#)
- 166. S. Ejiri, Phys. Rev. D **69**, 094506 (2004) [120](#)
- 167. S. Ejiri, Phys. Rev. D **73**, 054502 (2006) [120](#), [135](#)
- 168. P. de Forcrand, S. Kim, T. Takaishi, Nucl. Phys. Proc. Suppl. **119**, 541 (2003) [122](#)
- 169. M. D'Elia, M.P. Lombardo, Phys. Rev. D **70**, 074509 (2004) [122](#), [134](#)
- 170. V. Azcoiti, G. Di Carlo, A. Galante, V. Laliena, JHEP **12**, 010 (2004) [122](#)
- 171. S. Kratochvila, P. de Forcrand, Nucl. Phys. Proc. Suppl. **140**, 514 (2005) [122](#)
- 172. A. Alexandru, M. Faber, I. Horvath, K.F. Liu, Phys. Rev. D **72**, 114513 (2005) [122](#)
- 173. Z. Fodor, S.D. Katz, arXiv:0908.3341 [hep-ph] [123](#), [124](#)
- 174. M. Golterman, Y. Shamir, B. Svetitsky, Phys. Rev. D **74**, 071501 (2006) [124](#), [145](#)
- 175. C. Bernard, et al., Phys. Rev. D **71**, 034504 (2005) [126](#), [133](#)

176. O. Kaczmarek, F. Zantow, Phys. Rev. D **71**, 114510 (2005) [126](#), [242](#)
177. T. Blum, L. Karkkainen, D. Toussaint, S.A. Gottlieb, Phys. Rev. D **51**, 5153 (1995) [126](#)
178. C.W. Bernard, et al., Phys. Rev. D **55**, 6861 (1997) [126](#)
179. C. Bernard, et al., PoS **LAT2005**, 156 (2006) [127](#), [128](#), [129](#)
180. F. Karsch, (2007). hep-ph/0701210 [127](#)
181. M. Cheng, et al., Phys. Rev. D **77**, 014511 (2008) [127](#), [128](#), [129](#), [141](#), [215](#)
182. A. Gray, et al., Phys. Rev. D **72**, 094507 (2005) [128](#)
183. R.V. Gavai, S. Gupta, Phys. Rev. D **68**, 034506 (2003) [129](#)
184. F. Csikor, et al., JHEP **05**, 046 (2004) [129](#), [134](#)
185. F. Karsch, K. Redlich, A. Tawfik, Phys. Lett. B **571**, 67 (2003) [130](#), [210](#), [213](#), [216](#)
186. M. Cheng, et al., Phys. Rev. D **74**, 054507 (2006) [133](#), [144](#), [203](#), [255](#)
187. Y. Aoki, Z. Fodor, S.D. Katz, K.K. Szabo, Phys. Lett. B **643**, 46 (2006) [143](#), [144](#)
188. V.G. Bornyakov, et al., PoS **LAT2005**, 157 (2006)
189. Y. Maezawa, et al., J. Phys. G **34**, S651 (2007) [133](#)
190. E. Laermann, Presented at the workshop ‘FAIR Lattice QCD Days’, GSI-Darmstadt, Nov. 2009; <http://www-aix.gsi.de/conferences/lattice09/> [133](#), [144](#)
191. A. Bazavov, P. Petreczky, PoS **LAT2009**, 163 (2009) [133](#)
192. Z. Fodor, S.D. Katz, JHEP **04**, 050 (2004) [133](#), [137](#), [138](#), [144](#), [145](#), [202](#), [203](#), [224](#)
193. V. Azcoiti, G. Di Carlo, A. Galante, V. Laliena, Nucl. Phys. B **723**, 77 (2005) [134](#)
194. F. Karsch, E. Laermann, C. Schmidt, Phys. Lett. B **520**, 41 (2001) [135](#), [235](#)
195. O. Philipsen, PoS **CPOD07**, 028 (2007) [136](#), [137](#)
196. S. Ejiri, et al., Prog. Theor. Phys. Suppl. **153**, 118 (2004) [137](#)
197. P. de Forcrand, O. Philipsen, Nucl. Phys. B **673**, 170 (2003) [137](#), [138](#), [224](#), [225](#), [236](#)
198. P. Kovacs, Z. Szep, Phys. Rev. D **75**, 025015 (2007) [138](#)
199. S. Ejiri, F. Karsch, K. Redlich, Phys. Lett. B **633**, 275 (2006) [139](#), [140](#), [210](#), [260](#)
200. C. Miao, C. Schmidt, PoS **LAT2007**, 175 (2007) [141](#)
201. H.A. Gustafsson, et al., Phys. Rev. Lett. **52**, 1590 (1984) [146](#)
202. <http://www.gsi.de/GSI-Future>, GSI Conceptual Design Report [146](#)
203. <http://www.frib.msu.edu>, Facility for rare isotope beams (FRIB) homepage [146](#)
204. J. Decharge, D. Gogny, Phys. Rev. C **21**, 1568 (1980) [147](#)
205. M. Kleban, B. Nerlo-Pomorska, J.F. Berger, J. Decharge, M. Girod, S. Hilaire, Phys. Rev. C **65**, 024309 (2002) [147](#)
206. B. Cochet, K. Bennaceur, J. Meyer, P. Bonche, T. Duguet, Int. J. Mod. Phys. E **13**, 187 (2004) [147](#)
207. P.G. Reinhard, M. Bender, Lect. Notes Phys. **641**, 249 (2004) [147](#)
208. P. Ring, Prog. Part. Nucl. Phys. **37**, 193 (1996) [147](#), [148](#)
209. P. Ring, Prog. Part. Nucl. Phys. **641**, 175 (2004) [147](#), [148](#)
210. B.D. Serot, J.D. Walecka, Int. J. Mod. Phys. E **6**, 515 (1997) [147](#), [148](#), [149](#)
211. R.J. Furnstahl, Lect. Notes Phys. **641**, 1 (2004) [147](#), [148](#), [149](#)
212. M. Lutz, B. Friman, C. Appel, Phys. Lett. B **474**, 7 (2000) [147](#), [149](#)
213. N. Kaiser, S. Fritsch, W. Weise, Nucl. Phys. A **697**, 255 (2002)

- 214. P. Finelli, N. Kaiser, D. Vretenar, W. Weise, Eur. Phys. J. A **17**, 573 (2003)
- 215. P. Finelli, N. Kaiser, D. Vretenar, W. Weise, Nucl. Phys. A **735**, 449 (2004)
- 216. D. Vretenar, W. Weise, Lect. Notes Phys. **641**, 65 (2004) [149](#)
- 217. S. Fritsch, N. Kaiser, W. Weise, Nucl. Phys. A **750**, 259 (2005) [147](#), [149](#), [151](#)
- 218. V.R. Pandharipande, R.B. Wiringa, Rev. Mod. Phys. **51**, 821 (1979) [147](#)
- 219. A. Akmal, V.R. Pandharipande, D.G. Ravenhall, Phys. Rev. C **58**, 1804 (1998) [147](#), [150](#), [151](#)
- 220. K.A. Brueckner, J.L. Gammel, Phys. Rev. **107**, 1023 (1958) [147](#)
- 221. M. Jaminon, C. Mahaux, Phys. Rev. C **40**, 354 (1989)
- 222. W. Zuo, A. Lejeune, U. Lombardo, J.F. Mathiot, Nucl. Phys. A **706**, 418 (2002) [150](#)
- 223. X.R. Zhou, G.F. Burgio, U. Lombardo, H.J. Schulze, W. Zuo, Phys. Rev. C **69**, 018801 (2004) [147](#)
- 224. B. ter Haar, R. Malfliet, Phys. Rep. **149**, 207 (1987) [147](#), [154](#)
- 225. R. Brockmann, R. Machleidt, Phys. Rev. C **42**, 1965 (1990) [150](#)
- 226. F. de Jong, H. Lenske, Phys. Rev. C **58**, 890 (1998)
- 227. T. Gross-Boelting, C. Fuchs, A. Faessler, Nucl. Phys. A **648**, 105 (1999) [150](#), [154](#)
- 228. E. Schiller, H. Mütter, Eur. Phys. J. A **11**, 15 (2001)
- 229. C. Fuchs, Lect. Notes Phys. **641**, 119 (2004)
- 230. E.N.E. van Dalen, C. Fuchs, A. Faessler, Nucl. Phys. A **744**, 227 (2004) [151](#), [152](#)
- 231. E.N.E. van Dalen, C. Fuchs, A. Faessler, Phys. Rev. C **72**, 065803 (2005) [147](#), [151](#)
- 232. H. Mütter, A. Polls, Prog. Part. Nucl. Phys. **45**, 243 (2000) [147](#)
- 233. W.H. Dickhoff, C. Barbieri, Prog. Part. Nucl. Phys. **52**, 377 (2004)
- 234. J. Carlson, J. Morales, V.R. Pandharipande, D.G. Ravenhall, Phys. Rev. C **68**, 025802 (2003) [147](#), [151](#)
- 235. S.K. Bogner, T.T.S. Kuo, A. Schwenk, Phys. Rep. **386**, 1 (2003) [147](#)
- 236. S.K. Bogner, A. Schwenk, R.J. Furnstahl, A. Nogga, Nucl. Phys. A **763**, 59 (2005) [147](#), [151](#)
- 237. B.D. Serot, J.D. Walecka, Adv. Nucl. Phys. **16**, 1 (1986) [148](#)
- 238. H.P. Duerr, E. Teller, Phys. Rev. **101**, 494 (1956)
- 239. H.P. Duerr, Phys. Rev. **103**, 469 (1956) [148](#)
- 240. J. Boguta, Phys. Lett. B **109**, 251 (1982) [148](#)
- 241. C. Fuchs, H. Lenske, H.H. Wolter, Phys. Rev. C **52**, 3043 (1995) [148](#)
- 242. H. Lenske, C. Fuchs, Phys. Lett. B **345**, 355 (1995)
- 243. F. Hofmann, C.M. Keil, H. Lenske, Phys. Rev. C **64**, 034314 (2001)
- 244. C.M. Keil, F. Hofmann, H. Lenske, Phys. Rev. C **61**, 064309 (2000)
- 245. S. Typel, H.H. Wolter, Nucl. Phys. A **656**, 331 (1999) [151](#)
- 246. T. Niksic, D. Vretenar, P. Ring, Phys. Rev. C **66**, 064302 (2002) [148](#)
- 247. C. Fuchs, Prog. Part. Nucl. Phys. **56**, 1 (2006) [150](#), [157](#)
- 248. H. Bethe, Ann. Rev. Nucl. Sci. **21**, 93 (1971) [149](#)
- 249. R. Machleidt, K. Holinde, C. Elster, Phys. Rep. **149**, 1 (1987) [150](#)
- 250. M.K. Banerjee, J.A. Tjon, Phys. Rev. C **58**, 2120 (1998) [150](#)
- 251. M.K. Banerjee, J.A. Tjon, Nucl. Phys. A **708**, 303 (2002) [150](#)

- 252. U. van Klock, Phys. Rev. C **49**, 2932 (1994) [151](#)
- 253. D.R. Entem, R. Machleidt, Phys. Rev. C **66**, 014002 (2002) [155](#)
- 254. D.R. Entem, R. Machleidt, Phys. Rev. C **68**, 041001 (2003) [151](#), [155](#)
- 255. S.K. Bogner, T.T.S. Kuo, A. Schwenk, Phys. Rep. **386**, 1 (2003) [151](#)
- 256. G.A. Lalazissis, J. König, P. Ring, Phys. Rev. C **55**, 540 (1997) [151](#)
- 257. V. Baran, M. Colonna, V. Greco, M.D. Toro, Phys. Rep. **410**, 335 (2005) [152](#), [155](#)
- 258. D.T. Khoa, et al., Nucl. Phys. A **759**, 3 (2005) [152](#), [153](#)
- 259. D.T. Khoa, W. von Oertzen, H.G. Bohlen, S. Ohkubo, J. Phys. G **33**, R111 (2007) [152](#)
- 260. D.V. Shetty, S.J. Yennello, G.A. Souliotis, Phys. Rev. C **76**, 024606 (2007) [152](#), [153](#)
- 261. D.V. Shetty, S.J. Yennello, G.A. Souliotis, Phys. Rev. C **75**, 034602 (2007) [152](#)
- 262. S. Hama, B.C. Clark, E.D. Cooper, H.S. Sherif, R.L. Mercer, Phys. Rev. C **41**, 2737 (1990) [153](#), [154](#)
- 263. E.D. Cooper, S. Hama, B.C. Clark, R.L. Mercer, Phys. Rev. C **47**, 297 (1993) [153](#), [154](#)
- 264. P. Danielewicz, Nucl. Phys. A **673**, 375 (2000) [153](#)
- 265. T. Gaitanos, C. Fuchs, H.H. Wolter, A. Faessler, Eur. Phys. J. A **12**, 421 (2001)
- 266. P.K. Sahu, W. Cassing, U. Mosel, A. Ohnishi, Nucl. Phys. A **672**, 376 (2000) [153](#), [154](#)
- 267. H.F. Arellano, H.V. von Geramb, Phys. Rev. C **66**, 024602 (2002) [154](#)
- 268. S. Typel, Phys. Rev. C **71**, 064301 (2005) [154](#), [180](#)
- 269. W. Zuo, L.G. Cao, B.A. Li, U. Lombardo, C.W. Shen, Phys. Rev. C **72**, 014005 (2005) [154](#)
- 270. T. Gaitanos, M.D. Toro, S. Typel, V. Baran, C. Fuchs, V. Greco, H.H. Wolter, Nucl. Phys. A **732**, 24 (2004) [154](#)
- 271. L.W. Chen, C.M. Ko, B.A. Li, Phys. Rev. C **72**, 064606 (2005) [154](#)
- 272. J.A. McNeil, J.R. Shepard, S.J. Wallace, Phys. Rev. C **27**, 2123 (1983) [154](#)
- 273. A.M. Lane, Nucl. Phys. **35**, 676 (1962) [154](#)
- 274. R. Kozack, D.G. Madland, Phys. Rev. C **39**, 1461 (1989) [154](#)
- 275. R. Kozack, D.G. Madland, Nucl. Phys. A **509**, 664 (1990) [154](#)
- 276. T.D. Cohen, R.J. Furnstahl, D.K. Griegel, Phys. Rev. C **45**, 1881 (1992) [155](#), [156](#)
- 277. T.D. Cohen, R.J. Furnstahl, D.K. Griegel, Phys. Rev. Lett. **67**, 961 (1991) [156](#)
- 278. E.G. Drukarev, E.M. Levin, Prog. Part. Nucl. Phys. **27**, 77 (1991) [155](#)
- 279. R. Thomas, S. Zschocke, B. Kampfer, Phys. Rev. Lett. **95**, 232301 (2005) [155](#), [356](#)
- 280. R. Thomas, T. Hilger, B. Kampfer, Nucl. Phys. A **795**, 19 (2007) [155](#)
- 281. O. Plohl, C. Fuchs, E.N.E. van Dalen, Phys. Rev. C **73**, 014003 (2006) [155](#)
- 282. O. Plohl, C. Fuchs, Phys. Rev. C **74**, 034325 (2006) [155](#)
- 283. E. Epelbaum, W. Glöckle, U.G. Meissner, Nucl. Phys. A **747**, 362 (2005) [155](#)
- 284. R. Brockmann, W. Weise, Phys. Lett. B **367**, 40 (1996) [156](#)
- 285. G.Q. Li, C.M. Ko, Phys. Lett. B **338**, 118 (1994) [156](#)

- 286. E. Epelbaum, U.G. Meissner, W. Gloeckle, Nucl. Phys. A **714**, 535 (2003) [156](#)
- 287. S.R. Beane, M.J. Savage, Nucl. Phys. A **717**, 91 (2003) [156](#)
- 288. O. Plohl, C. Fuchs, Nucl. Phys. A **798**, 75 (2008) [156](#)
- 289. N. Kaiser, P. de Homont, W. Weise, Phys. Rev. C **77**, 025204 (2008) [156](#)
- 290. L.D. Landau, Physikalische Zeitschrift der Sowjetunion **1**, 285 (1932) [158](#)
- 291. W. Baade, F. Zwicky, Phys. Rev. **46**, 76 (1934) [158](#)
- 292. H.T. Janka, K. Langanke, A. Marek, G. Martinez-Pinedo, B. Müller, Phys. Rep. **442**, 38 (2007) [158](#)
- 293. J.M. Lattimer, M. Prakash, Science **304**, 536 (2004) [158](#), [159](#), [171](#)
- 294. I. Sagert, et al., Phys. Rev. Lett. **102**, 081101 (2009) [158](#)
- 295. J.M. Lattimer, F.D. Swesty, Nucl. Phys. A **535**, 331 (1991) [158](#)
- 296. H. Shen, H. Toki, K. Oyamatsu, K. Sumiyoshi, Nucl. Phys. A **637**, 435 (1998) [158](#)
- 297. F. Weber, *Pulsars as Astrophysical Laboratories for Nuclear and Particle Physics* (IOP, Bristol, UK, 1999) [159](#), [170](#), [171](#), [172](#)
- 298. D. Blaschke, N.K. Glendenning, A. Sedrakian (eds.), *Physics of Neutron Star Interiors*. Lect. Notes Phys., **578**. Springer, Berlin (2001)
- 299. F. Weber, Prog. Nucl. Part. Phys. **54**, 193 (2005)
- 300. D. Page, S. Reddy, Ann. Rev. Nucl. Part. Sci. **56**, 327 (2006)
- 301. F. Weber, R. Negreiros, P. Rosenfield, M. Stejner, Prog. Nucl. Part. Phys. **59**, 94 (2007)
- 302. J.M. Lattimer, M. Prakash, Phys. Rep. **442**, 109 (2007) [159](#), [162](#), [163](#), [167](#), [168](#)
- 303. J. Schaffner-Bielich, PoS **CPOD07**, 062 (2007) [162](#)
- 304. A. Sedrakian, Prog. Part. Nucl. Phys. **58**, 168 (2007) [174](#)
- 305. H. Heiselberg, V. Pandharipande, Ann. Rev. Nucl. Part. Sci. **50**, 481 (2000)
- 306. J. Piekarewicz, AIP Conf. Proc. **1128**, 144 (2009) [159](#)
- 307. T. Klähn, et al., Phys. Rev. C **74**, 035802 (2006) [159](#), [160](#), [161](#), [163](#), [166](#), [174](#), [177](#)
- 308. D. Barret, J.F. Olive, M.C. Miller, Mon. Not. R. Astron. Soc. **361**, 855 (2005) [159](#), [168](#)
- 309. P.C.C. Freire, A. Wolszczan, M.V.D. Berg, J.W.T. Hessels, Astrophys. J. **679**, 1433 (2008) [159](#), [164](#)
- 310. D.J. Nice, E.M. Splaver, I.H. Stairs, O. Löhmer, A. Jessner, M. Kramer, J.M. Cordes, Astrophys. J. **634**, 1242 (2005) [159](#)
- 311. D.J. Nice, I.H. Stairs, L. Kasian, Bull. Am. Astron. Soc. **39**, 918 (2007) [159](#)
- 312. J.E. Trümper, V. Burwitz, F. Haberl, V.E. Zavlin, Nucl. Phys. Proc. Suppl. **132**, 560 (2004) [159](#), [169](#)
- 313. Heinke, et al., Astrophys. J. **644**, 1090 (2006) [159](#)
- 314. B. Gendre, D. Barret, N.A. Webb, Astron. Astrophys. **403**, L11 (2003) [159](#)
- 315. P. Kaaret, et al., Astrophys. J. **657**, L97 (2007) [159](#), [171](#)
- 316. E.E. Kolomeitsev, D.N. Voskresensky, Nucl. Phys. A **759**, 373 (2005) [161](#), [174](#), [177](#)
- 317. T. Klähn, et al., Phys. Lett. B **654**, 170 (2007) [161](#), [169](#), [170](#), [180](#)
- 318. M. Alford, M. Braby, M.W. Paris, S. Reddy, Astrophys. J. **629**, 969 (2005) [161](#)

319. D. Blaschke, H. Grigorian, *Prog. Part. Nucl. Phys.* **59**, 139 (2007) [161](#), [177](#)
320. H. Grigorian, *Phys. Part. Nucl.* **39**, 1143 (2008) [161](#), [181](#)
321. P. Haensel, A.Y. Potekhin, D.G. Yakovlev, *Neutron Stars I* (Springer, 2007) [161](#)
322. N.K. Glendenning, C. Kettner, F. Weber, *Astrophys. J.* **450**, 253 (1995) [161](#)
323. N.K. Glendenning, C. Kettner, F. Weber, *Phys. Rev. Lett.* **74**, 3519 (1995) [161](#)
324. B. Abbott, et al., *Astrophys. J.* **683**, L45 (2008) [162](#)
325. R.C. Tolman, *Phys. Rev.* **55**, 364 (1939) [162](#)
326. J.R. Oppenheimer, G.M. Volkoff, *Phys. Rev.* **55**, 374 (1939) [162](#)
327. G. Baym, C. Pethick, P. Sutherland, *Astrophys. J.* **170**, 299 (1971) [163](#)
328. S.E. Thorsett, D. Chakrabarty, *Astrophys. J.* **512**, 288 (1999) [164](#)
329. J.M. Lattimer, M. Prakash, *Phys. Rev. Lett.* **94**, 111101 (2005) [165](#)
330. P.C.C. Freire, arXiv:0907.3219 [164](#)
331. D.J. Champion, et al., *Science* **320**, 1309 (2008) [164](#)
332. P. Podsiadlowski, J.D.M. Dewi, P. Lesaffre, J.C. Miller, W.G. Newton, J.R. Stone, *Mon. Not. R. Astron. Soc.* **361**, 1243 (2005) [164](#), [166](#)
333. M. Kramer, et al., *ECONF C041213*, 0038 (2004). astro-ph/0503386 [164](#)
334. F.S. Kitaura, H.T. Janka, W. Hillebrandt, *Astron. Astrophys.* **450**, 345 (2006) [166](#)
335. M. van der Klis, *Ann. Rev. Astron. Astrophys.* **38**, 717 (2000) [168](#)
336. M.C. Miller, *AIP Conf. Proc.* **714**, 365 (2004) [168](#)
337. M.C. Miller, F.K. Lamb, D. Psaltis, *Astrophys. J.* **508**, 791 (1998)
338. F.K. Lamb, M.C. Miller, D. Psaltis, arXiv:astro-ph/9802348 [168](#)
339. W. Zhang, A.P. Smale, T.E. Strohmayer, J.H. Swank, *Astrophys. J.* **503**, L147 (1998) [168](#)
340. F.M. Walter, J. Lattimer, *Astrophys. J.* **576**, L145 (2002) [169](#)
341. D.L. Kaplan, *AIP Conf. Proc.* **968**, 129 (2008) [169](#)
342. W.C.G. Ho, D.L. Kaplan, P. Chang, M. van Adelsberg, A.Y. Potekhin, *Mon. Not. R. Astron. Soc.* **375**, 821 (2007) [169](#)
343. W.C.G. Ho, K. Mori, *AIP Conf. Proc.* **983**, 340 (2008) [169](#)
344. D.B. Blaschke, D. Gomez Dumm, A.G. Grunfeld, T. Klähn, N.N. Scoccola, *Phys. Rev. C* **75**, 065804 (2007) [169](#), [170](#)
345. J. Cottam, F. Paerels, M. Mendez, *Nature* **420**, 51 (2002) [169](#), [170](#)
346. F. Özel, *Nature* **441**, 1115 (2006) [169](#), [170](#)
347. M. Alford, D. Blaschke, A. Drago, T. Klähn, G. Pagliara, J. Schaffner-Bielich, *Nature* **445**, E7 (2007) [169](#)
348. M. Baldo, et al., *Phys. Lett. B* **562**, 153 (2003) [170](#)
349. M. Buballa, *Phys. Rep.* **407**, 205 (2005) [170](#), [237](#), [238](#)
350. G. Pagliara, J. Schaffner-Bielich, *Phys. Rev. D* **77**, 063004 (2008) [170](#)
351. B. Agrawal, *Phys. Rev. D* **81**, 023009 (2010) [170](#)
352. N.F. Mott, *Rev. Mod. Phys.* **40**, 677 (1968) [170](#)
353. M. Bejger, T. Bulik, P. Haensel, *Mon. Not. R. Astron. Soc.* **364**, 635 (2005) [170](#)
354. J.M. Lattimer, B.F. Schutz, *Astrophys. J.* **629**, 979 (2005) [170](#)

355. N.K. Glendenning, S. Pei, F. Weber, *Phys. Rev. Lett.* **79**, 1603 (1997) [171](#)
356. M. Bejger, P. Haensel, J.L. Zdunik, *Astron. Astrophys.* **464**, L49 (2007) [171](#)
357. G. Lavagetto, I. Bombaci, A. D’Ai’, I. Vidana, N.R. Robba, (2006). [astro-ph/0612061](#) [171](#)
358. N. Andersson, K. Kokkotas, *Int. J. Mod. Phys. D* **10**, 381 (2001) [172](#)
359. A. Drago, G. Pagliara, I. Parenti, *Astrophys. J.* **678**, L117 (2008) [172](#)
360. N.K. Glendenning, F. Weber, *Astrophys. J.* **559**, L119 (2001) [172](#)
361. G.S. Poghosyan, H. Grigorian, D. Blaschke, *Astrophys. J.* **551**, L73 (2001) [172](#), [173](#)
362. D. Blaschke, I. Bombaci, H. Grigorian, G.S. Poghosyan, *New Astron.* **7**, 107 (2002) [172](#)
363. D. Blaschke, G. Poghosyan, H. Grigorian, *AIP Conf. Proc.* **1068**, 191 (2008) [173](#)
364. E.P.J. van den Heuvel, (2007). 0704.1215 [[astro-ph](#)] [173](#)
365. D.G. Yakovlev, C.J. Pethick, *Ann. Rev. Astron. Astrophys.* **42**, 169 (2004) [173](#)
366. P. Jaikumar, M. Prakash, *Phys. Lett. B* **516**, 345 (2001) [174](#)
367. D. Blaschke, T. Klähn, D.N. Voskresensky, *Astrophys. J.* **533**, 406 (2000) [174](#)
368. D. Page, U. Geppert, F. Weber, *Nucl. Phys. A* **777**, 497 (2006) [174](#)
369. D. Page, J.M. Lattimer, M. Prakash, A.W. Steiner, *Astrophys. J. Suppl.* **155**, 623 (2004) [174](#), [175](#)
370. D. Blaschke, H. Grigorian, D.N. Voskresensky, *Astron. Astrophys.* **424**, 979 (2004) [174](#), [177](#)
371. D.N. Voskresensky, *Lect. Notes Phys.* **578**, 467 (2001) [174](#)
372. D.G. Yakovlev, A.D. Kaminker, O.Y. Gnedin, P. Haensel, *Phys. Rep.* **354**, 1 (2001) [174](#)
373. H. Grigorian, D.N. Voskresensky, *Astron. Astrophys.* **444**, 913 (2005) [174](#)
374. D. Blaschke, H. Grigorian, D.N. Voskresensky, *Astron. Astrophys.* **368**, 561 (2001) [174](#)
375. A. Sedrakian, *Phys. Part. Nucl.* **39**, 1155 (2008) [174](#)
376. T. Takatsuka, R. Tamagaki, *Prog. Theor. Phys.* **112**, 37 (2004) [174](#)
377. A. Schwenk, B. Friman, *Phys. Rev. Lett.* **92**, 082501 (2004) [174](#)
378. S. Popov, H. Grigorian, D. Blaschke, *Phys. Rev. C* **74**, 025803 (2006) [175](#), [176](#), [177](#)
379. H. Grigorian, D. Blaschke, D. Voskresensky, *Phys. Rev. C* **71**, 045801 (2005)
380. D. Blaschke, D.N. Voskresensky, H. Grigorian, (2004). [astro-ph/0403171](#) [175](#)
381. H. Grigorian, *Phys. Rev. C* **74**, 025801 (2006) [175](#)
382. D.N. Aguilera, J.A. Pons, J.A. Miralles, *Astrophys. J.* **673**, L167 (2008) [175](#)
383. S. Popov, H. Grigorian, R. Turolla, D. Blaschke, *Astron. Astrophys.* **448**, 327 (2006) [176](#), [177](#)
384. R. Neuhäuser, J. Trümper, *Astron. Astrophys.* **343**, 151 (1999) [176](#)
385. S.B. Popov, M. Colpi, M.E. Prokhorov, et al., *Astrophys. J.* **544**, L53 (2000) [176](#)
386. P. Danielewicz, R. Lacey, W.G. Lynch, *Science* **298**, 1592 (2002) [178](#), [179](#)

387. P. Danielewicz, private communication [179](#)
388. J. Bardeen, L.N. Cooper, J.R. Schrieffer, Phys. Rev. **108**, 1175 (1957) [182](#), [183](#)
389. A.J. Leggett, Rev. Mod. Phys. **47**, 331 (1975) [182](#), [184](#)
390. D.J. Gross, F. Wilczek, Phys. Rev. Lett. **30**, 1343 (1973) [182](#), [183](#)
391. H.D. Politzer, Phys. Rev. Lett. **30**, 1346 (1973) [182](#), [183](#)
392. D.T. Son, Phys. Rev. D **59**, 094019 (1999) [182](#), [186](#)
393. T. Schäfer, F. Wilczek, Phys. Rev. D **60**, 114033 (1999) [186](#)
394. R.D. Pisarski, D.H. Rischke, Phys. Rev. D **61**, 074017 (2000)
395. D.K. Hong, V.A. Miransky, I.A. Shovkovy, L.C.R. Wijewardhana, Phys. Rev. D **61**, 056001 (2000) [182](#), [186](#)
396. W.E. Brown, J.T. Liu, H.C. Ren, Phys. Rev. D **61**, 114012 (2000) [182](#), [186](#)
397. W.E. Brown, J.T. Liu, H.C. Ren, Phys. Rev. D **62**, 054016 (2000)
398. Q. Wang, D.H. Rischke, Phys. Rev. D **65**, 054005 (2002) [186](#)
399. A. Schmitt, Q. Wang, D.H. Rischke, Phys. Rev. D **66**, 114010 (2002) [182](#), [186](#)
400. T. Matsuura, K. Iida, T. Hatsuda, G. Baym, Phys. Rev. D **69**, 074012 (2004) [182](#), [187](#)
401. I. Giannakis, D.F. Hou, H.C. Ren, D.H. Rischke, Phys. Rev. Lett. **93**, 232301 (2004) [187](#)
402. J.L. Noronha, H.C. Ren, I. Giannakis, D. Hou, D.H. Rischke, Phys. Rev. D **73**, 094009 (2006) [182](#), [187](#)
403. D. Nickel, J. Wambach, R. Alkofer, Phys. Rev. D **73**, 114028 (2006) [182](#), [188](#), [189](#)
404. M. Alford, C. Kouvaris, K. Rajagopal, Phys. Rev. Lett. **92**, 222001 (2004) [182](#), [192](#)
405. M. Alford, C. Kouvaris, K. Rajagopal, Phys. Rev. D **71**, 054009 (2005)
406. S.B. Ruester, I.A. Shovkovy, D.H. Rischke, Nucl. Phys. A **743**, 127 (2004)
407. K. Iida, T. Matsuura, M. Tachibana, T. Hatsuda, Phys. Rev. D **71**, 054003 (2005)
408. S.B. Ruester, V. Werth, M. Buballa, I.A. Shovkovy, D.H. Rischke, Phys. Rev. D **72**, 034004 (2005) [192](#)
409. D. Blaschke, S. Fredriksson, H. Grigorian, A.M. Oztas, F. Sandin, Phys. Rev. D **72**, 065020 (2005) [182](#), [192](#)
410. I. Shovkovy, M. Huang, Phys. Lett. B **564**, 205 (2003) [182](#), [190](#)
411. M. Huang, I. Shovkovy, Nucl. Phys. A **729**, 835 (2003) [182](#), [190](#), [191](#)
412. M. Huang, I.A. Shovkovy, Phys. Rev. D **70**, 051501 (2004) [182](#), [193](#)
413. H. Abuki, T. Hatsuda, K. Itakura, Phys. Rev. D **65**, 074014 (2002) [183](#), [188](#)
414. M.W. Zwiernik, C.H. Schunck, A. Schirotzek, W. Ketterle, Nature **442**, 54 (2006) [183](#), [194](#)
415. R.D. Pisarski, D.H. Rischke, Phys. Rev. Lett. **83**, 37 (1999) [184](#)
416. A. Schmitt, Q. Wang, D.H. Rischke, Phys. Rev. Lett. **91**, 242301 (2003) [185](#)
417. A. Schmitt, Q. Wang, D.H. Rischke, Phys. Rev. D **69**, 094017 (2004) [185](#)
418. A. Schmitt, (2004). nucl-th/0405076 [185](#), [186](#)
419. T. Schafer, K. Schwenzer, Phys. Rev. Lett. **97**, 092301 (2006) [185](#)
420. D.H. Rischke, Prog. Part. Nucl. Phys. **52**, 197 (2004) [186](#)
421. A. Schmitt, Phys. Rev. D **71**, 054016 (2005) [187](#)

- 422. H. Malekzadeh, Phys. Rev. D **74**, 065011 (2006) [188](#)
- 423. C. Manuel, Phys. Rev. D **62**, 076009 (2000) [188](#)
- 424. G.W. Carter, D. Diakonov, Phys. Rev. D **60**, 016004 (1999) [189](#)
- 425. R. Rapp, T. Schafer, E.V. Shuryak, M. Velkovsky, Ann. Phys. **280**, 35 (2000) [189](#)
- 426. A. Sedrakian, J.W. Clark, M. Alford (eds.), *Pairing in Fermionic Systems, Series on Advances in Quantum Many-Body Theory*, vol. 8 (World Scientific, Singapore, 2006) [189](#)
- 427. M.G. Alford, J.A. Bowers, K. Rajagopal, Phys. Rev. D **63**, 074016 (2001) [190](#)
- 428. J.A. Bowers, K. Rajagopal, Phys. Rev. D **66**, 065002 (2002) [190](#)
- 429. R. Casalbuoni, R. Gatto, M. Mannarelli, G. Nardulli, Phys. Lett. B **511**, 218 (2001)
- 430. R. Casalbuoni, R. Gatto, N. Ippolito, G. Nardulli, M. Ruggieri, Phys. Lett. B **627**, 89 (2005)
- 431. K. Rajagopal, R. Sharma, Phys. Rev. D **74**, 094019 (2006) [190](#)
- 432. P. Fulde, R.A. Ferrell, Phys. Rev. A **135**, 550 (1964) [190](#)
- 433. A.I. Larkin, Y.N. Ovchinnikov, Sov. Phys. JETP **20**, 762 (1965) [190](#)
- 434. H. Muther, A. Sedrakian, Phys. Rev. D **67**, 085024 (2003) [190](#)
- 435. P.F. Bedaque, H. Caldas, G. Rupak, Phys. Rev. Lett. **91**, 247002 (2003) [190](#)
- 436. S. Reddy, G. Rupak, Phys. Rev. C **71**, 025201 (2005) [190](#)
- 437. E. Gubankova, W.V. Liu, F. Wilczek, Phys. Rev. Lett. **91**, 032001 (2003) [190](#), [191](#)
- 438. G. Sarma, Phys. Chem. Solids **24**, 1029 (1963) [191](#)
- 439. B. Vanderheyden, A.D. Jackson, Phys. Rev. D **61**, 076004 (2000) [191](#)
- 440. R. Casalbuoni, R. Gatto, M. Mannarelli, G. Nardulli, M. Ruggieri, Phys. Lett. B **605**, 362 (2005) [193](#)
- 441. K. Fukushima, (2005). hep-ph/0510299 [193](#)
- 442. M. Kitazawa, D.H. Rischke, I.A. Shovkovy, Phys. Lett. B **637**, 367 (2006) [193](#)
- 443. K. Fukushima, Phys. Rev. D **72**, 074002 (2005) [194](#)
- 444. O. Kiriyaama, Phys. Rev. D **74**, 074019 (2006)
- 445. O. Kiriyaama, Phys. Rev. D **74**, 114011 (2006)
- 446. L. He, M. Jin, P. Zhuang, Phys. Rev. D **75**, 036003 (2007) [194](#)
- 447. E.V. Gorbar, M. Hashimoto, V.A. Miransky, Phys. Lett. B **632**, 305 (2006) [194](#)
- 448. T. Schafer, Phys. Rev. Lett. **96**, 012305 (2006) [194](#)
- 449. A. Kryjevski, Phys. Rev. D **77**, 014018 (2008) [194](#)
- 450. O. Kiriyaama, D.H. Rischke, I.A. Shovkovy, Phys. Lett. B **643**, 331 (2006) [194](#)
- 451. L. He, M. Jin, P. Zhuang, (2005). hep-ph/0511300 [194](#)
- 452. H. Abuki, Nucl. Phys. A **791**, 117 (2007) [195](#)
- 453. L. He, P. Zhuang, Phys. Rev. D **75**, 096003 (2007)
- 454. G.F. Sun, L. He, P. Zhuang, Phys. Rev. D **75**, 096004 (2007) [194](#)

455. M. Kitazawa, I.A. Shovkovy, D.H. Rischke, Prog. Theor. Phys. Suppl. **168**, 389 (2007) [195](#)
456. A.H. Rezaeian, H.J. Pirner, Nucl. Phys. A **779**, 197 (2006) [195](#)
457. J. Deng, A. Schmitt, Q. Wang, Phys. Rev. D **76**, 034013 (2007) [195](#)
458. P. Braun-Munzinger, K. Redlich, J. Stachel, in *Quark Gluon Plasma 3*, (R. Hwa, X.N. Wang (Eds.), World Scientific, Singapore, 2004), p. 491 [197](#), [198](#)
459. A. Andronic, P. Braun-Munzinger, J. Stachel, Nucl. Phys. A **772**, 167 (2006) [197](#), [202](#), [204](#), [205](#), [208](#)
460. A. Andronic, P. Braun-Munzinger, J. Stachel, **673**, 142 (2009). Erratum-ibid. B **678**, 516 (2009) [197](#), [202](#), [204](#), [207](#)
461. A. Andronic, P. Braun-Munzinger, J. Stachel, **40**, 1005 (2009) [197](#), [206](#), [207](#)
462. J. Cleymans, D. Elliott, A. Keranen, E. Suhonen, Phys. Rev. C **57**, 3319 (1998) [197](#), [198](#), [204](#)
463. J. Cleymans, H. Oeschler, K. Redlich, Phys. Rev. C **59**, 1663 (1999) [197](#), [204](#)
464. R. Hagedorn, CERN Report **71-12** (1971) [198](#)
465. E.V. Shuryak, Phys. Lett. B **42**, 357 (1972)
466. J. Rafelski, M. Danos, Phys. Lett. B **97**, 279 (1980)
467. R. Hagedorn, K. Redlich, Z. Phys. C **27**, 541 (1985)
468. K. Redlich, A. Tounsi, Eur. Phys. J. C **24**, 589 (2002) [202](#)
469. A. Tounsi, K. Redlich, J. Phys. G **28**, 2095 (2002)
470. S. Hamieh, K. Redlich, A. Tounsi, Phys. Lett. B **486**, 61 (2000)
471. K. Redlich, S. Hamieh, A. Tounsi, J. Phys. G **27**, 413 (2001) [198](#), [202](#)
472. E. Suhonen, S. Sohlo, J. Phys. G **13**, 1487 (1987) [198](#), [200](#)
473. D.H. Rischke, M.I. Gorenstein, H. Stoecker, W. Greiner, Z. Phys. C **51**, 485 (1991) [198](#), [200](#)
474. P. Braun-Munzinger, J. Cleymans, H. Oeschler, K. Redlich, Nucl. Phys. A **697**, 902 (2002) [201](#), [205](#), [207](#), [208](#), [209](#)
475. M.A. Stephanov, Prog. Theor. Phys. Suppl. **153**, 139 (2004) [202](#), [203](#), [224](#)
476. O. Philipsen, PoS **LAT2005**, 016 (2006) [202](#), [203](#)
477. P. Braun-Munzinger, J. Stachel, J.P. Wessels, N. Xu, Phys. Lett. B **344**, 43 (1995) [202](#)
478. P. Braun-Munzinger, J. Stachel, J.P. Wessels, N. Xu, Phys. Lett. B **365**, 1 (1996)
479. P. Braun-Munzinger, I. Heppe, J. Stachel, Phys. Lett. B **465**, 15 (1999)
480. R. Averbeck, R. Holzmann, V. Metag, R.S. Simon, Phys. Rev. C **67**, 024903 (2003) [202](#)
481. P. Braun-Munzinger, J. Stachel, Nucl. Phys. A **638**, 3 (1998) [202](#)
482. J. Cleymans, K. Redlich, Phys. Rev. Lett. **81**, 5284 (1998) [202](#), [204](#)
483. J. Cleymans, K. Redlich, Phys. Rev. C **60**, 054908 (1999) [202](#), [204](#)
484. C. Nonaka, M. Asakawa, Phys. Rev. C **71**, 044904 (2005) [203](#), [216](#), [225](#), [226](#), [227](#)
485. M. Asakawa, C. Nonaka, Nucl. Phys. A **774**, 753 (2006) [203](#)
486. A. Dumitru, L. Portugal, D. Zschesche, Phys. Rev. C **73**, 024902 (2006) [203](#), [204](#)
487. P. Braun-Munzinger, J. Stachel, J. Phys. G **28**, 1971 (2002) [203](#)
488. P. Braun-Munzinger, J. Phys. Conf. Ser. **50**, 238 (2006) [203](#)

489. J. Cleymans, H. Oeschler, K. Redlich, S. Wheaton, Phys. Rev. C **73**, 034905 (2006) [204](#)
490. R. Stock, Phys. Lett. B **456**, 277 (1999) [204](#)
491. P. Braun-Munzinger, J. Stachel, C. Wetterich, Phys. Lett. B **596**, 61 (2004) [204](#)
492. F. Becattini, M. Gazdzicki, A. Keranen, J. Manninen, R. Stock, Phys. Rev. C **69**, 024905 (2004) [204](#), [227](#)
493. F. Becattini, J. Manninen, M. Gazdzicki, Phys. Rev. C **73**, 044905 (2006)
494. J. Letessier, J. Rafelski, Eur. Phys. J. A **35**, 221 (2008) [204](#)
495. D. Adamova, et al., Phys. Rev. Lett. **90**, 022301 (2003) [205](#), [206](#)
496. M.A. Lisa, S. Pratt, R. Soltz, U. Wiedemann, Ann. Rev. Nucl. Part. Sci. **55**, 357 (2005) [205](#), [206](#)
497. V.D. Toneev, A.S. Parvan, J. Phys. G **31**, 583 (2005) [206](#)
498. M. Gazdzicki, M.I. Gorenstein, Acta Physiol. Pol. B **30**, 2705 (1999) [207](#)
499. M. Gazdzicki, J. Phys. G **30**, S161 (2004)
500. V. Koch, A. Majumder, J. Randrup, Phys. Rev. C **72**, 064903 (2005) [207](#), [263](#)
501. J. Cleymans, H. Oeschler, K. Redlich, S. Wheaton, Phys. Lett. B **615**, 50 (2005) [207](#), [208](#), [209](#)
502. K. Redlich, F. Karsch, A. Tawfik, J. Phys. G **30**, S1271 (2004) [210](#), [213](#)
503. C. Schmidt, PoS **CPOD2006**, 002 (2006) [215](#)
504. A. Peshier, B. Kampfer, O.P. Pavlenko, G. Soff, Phys. Lett. B **337**, 235 (1994) [215](#), [217](#), [218](#), [219](#), [220](#), [221](#)
505. A. Peshier, B. Kampfer, O.P. Pavlenko, G. Soff, Phys. Rev. D **54**, 2399 (1996)
506. A. Peshier, B. Kampfer, G. Soff, Phys. Rev. C **61**, 045203 (2000)
507. A. Peshier, B. Kampfer, G. Soff, Phys. Rev. D **66**, 094003 (2002) [215](#), [217](#), [218](#)
508. F. Karsch, E. Laermann, A. Peikert, Nucl. Phys. B **605**, 579 (2001) [216](#), [218](#), [220](#)
509. L.D. Landau, E.M. Lifshitz, *Statistical Physics, Course of Theoretical Physics*, vol. 5 (Butterworth-Heinemann, Oxford, 1980) [216](#)
510. H. Eschrig, The Particle World of Condensed Matter - An Introduction to the Notion of Quasi-Particle (Edition am Gutenbergplatz Leipzig, Leipzig, 2005) [216](#)
511. A. Peshier, W. Cassing, Phys. Rev. Lett. **94**, 172301 (2005) [217](#)
512. E.V. Shuryak, Nucl. Phys. A **750**, 64 (2005) [217](#), [286](#)
513. T.S. Biro, P. Levai, B. Müller, Phys. Rev. D **42**, 3078 (1990) [217](#)
514. A. Rebhan, P. Romatschke, Phys. Rev. D **68**, 025022 (2003) [217](#), [218](#), [219](#)
515. J.P. Blaizot, A. Ipp, A. Rebhan, U. Reinosa, Phys. Rev. D **72**, 125005 (2005) [217](#)
516. M.L. Bellac, *Thermal Field Theory* (Cambridge University Press, Cambridge, 1996) [217](#), [253](#)
517. M.I. Gorenstein, S.N. Yang, Phys. Rev. D **52**, 5206 (1995) [218](#)
518. P. Petreczky, F. Karsch, E. Laermann, S. Stickan, I. Wetzorke, Nucl. Phys. Proc. Suppl. **106**, 513 (2002) [218](#), [292](#)
519. E.V. Shuryak, I. Zahed, Phys. Rev. C **70**, 021901 (2004) [218](#), [286](#), [292](#)

520. J. Liao, E.V. Shuryak, Phys. Rev. D **73**, 014509 (2006) [218](#), [292](#)
521. R.D. Pisarski, Nucl. Phys. A **498**, 423c (1989) [218](#)
522. A. Peshier, B. Kampfer, G. Soff, (2003). hep-ph/0312080 [218](#)
523. A. Peshier, B. Kämpfer, O.P. Pavlenko, G. Soff, Eur. Phys. Lett. **43**, 381 (1998) [219](#)
524. A. Peshier, Phys. Rev. D **63**, 105004 (2001) [219](#)
525. M. Bluhm, B. Kampfer, G. Soff, J. Phys. G **31**, S1151 (2005) [219](#), [220](#)
526. M. Bluhm. Diploma Thesis, Technische Universität Dresden (2004) [221](#)
527. M. Bluhm, B. Kampfer, R. Schulze, D. Seipt, Eur. Phys. J. C **49**, 205 (2007) [219](#), [220](#), [221](#)
528. M. Bluhm, B. Kampfer, G. Soff, (2004). hep-ph/0402252 [221](#)
529. K.K. Szabo, A.I. Toth, JHEP **06**, 008 (2003) [219](#)
530. M. Bluhm, B. Kämpfer, G. Soff, Phys. Lett. B **620**, 131 (2005) [221](#)
531. D. Blaschke, K.A. Bugaev, Fizika B **13**, 491 (2004) [221](#)
532. B. Kämpfer, M. Bluhm, J. Phys. G **31**, 1151 (2005) [223](#)
533. P.F. Kolb, U. Heinz, in *Quark Gluon Plasma* (R. Hwa, X.N. Wang (Eds.), World Scientific, Singapore, 2004), p. 634 [224](#)
534. M. Bluhm, B. Kämpfer, R. Schulze, D. Seipt, U. Heinz, Phys. Rev. C **76**, 034901 (2007) [224](#)
535. J. Adams, et al., Phys. Rev. Lett. **95**, 122301 (2005) [225](#)
536. R. Guida, J. Zinn-Justin, Nucl. Phys. B **489**, 626 (1997) [225](#)
537. B. Kampfer, M. Bluhm, R. Schulze, D. Seipt, U. Heinz, Nucl. Phys. A **774**, 757 (2006) [225](#)
538. M. Bluhm, B. Kampfer (2005). hep-ph/0511015 [225](#)
539. W. Gebhardt, U. Krey, *Phasenübergänge und kritische Phänomene* (Vieweg, Braunschweig/Wiesbaden, 1980) [225](#)
540. U. Kraemmer, A. Rebhan, Rep. Prog. Phys. **67**, 351 (2004) [228](#), [229](#)
541. M. Fukugita, M. Okawa, A. Ukawa, Phys. Rev. Lett. **63**, 1768 (1989) [228](#)
542. M. Wingate, S. Ohta, Phys. Rev. D **63**, 094502 (2001) [228](#)
543. R.V. Gavai, Nucl. Phys. Proc. Suppl. **106**, 480 (2002) [228](#)
544. B. Lucini, M. Teper, U. Wenger, Phys. Lett. B **545**, 197 (2002) [228](#)
545. B. Lucini, M. Teper, U. Wenger, JHEP **01**, 061 (2004) [228](#)
546. E. Laermann, O. Philipsen, Ann. Rev. Nucl. Part. Sci. **53**, 163 (2003) [229](#), [233](#)
547. P. Petreczky, Nucl. Phys. Proc. Suppl. **140**, 78 (2005) [229](#)
548. C.B. Thorn, Phys. Lett. B **99**, 458 (1981) [229](#)
549. R.D. Pisarski, Phys. Rev. D **29**, 1222 (1984) [229](#)
550. G. 't Hooft, Nucl. Phys. B **138**, 1 (1978) [229](#)
551. G. 't Hooft, Nucl. Phys. B **153**, 141 (1979)
552. A.M. Polyakov, Phys. Lett. B **72**, 477 (1978)
553. L. Susskind, Phys. Rev. D **20**, 2610 (1979) [229](#)
554. B. Svetitsky, L.G. Yaffe, Nucl. Phys. B **210**, 423 (1982) [230](#)
555. L.G. Yaffe, B. Svetitsky, Phys. Rev. D **26**, 963 (1982)
556. B. Svetitsky, Phys. Rep. **132**, 1 (1986) [230](#), [233](#)
557. A. Dumitru, R.D. Pisarski, Phys. Rev. D **66**, 096003 (2002) [230](#), [235](#)
558. L.D. McLerran, B. Svetitsky, Phys. Rev. D **24**, 450 (1981) [230](#)

559. J. Kuti, J. Polonyi, K. Szlachanyi, Phys. Lett. B **98**, 199 (1981) [230](#)
560. A. Dumitru, Y. Hatta, J. Lenaghan, K. Orginos, R.D. Pisarski, Phys. Rev. D **70**, 034511 (2004) [230](#), [231](#)
561. O. Kaczmarek, F. Karsch, P. Petreczky, F. Zantow, Phys. Lett. B **543**, 41 (2002) [242](#)
562. O. Kaczmarek, S. Ejiri, F. Karsch, E. Laermann, F. Zantow, Prog. Theor. Phys. Suppl. **153**, 287 (2004) [296](#)
563. P. Petreczky, K. Petrov, Phys. Rev. D **70**, 054503 (2004) [230](#)
564. R.D. Pisarski, Phys. Rev. D **62**, 111501 (2000) [230](#)
565. A. Dumitru, R.D. Pisarski, Phys. Lett. B **504**, 282 (2001) [231](#)
566. O. Scavenius, A. Dumitru, J.T. Lenaghan, Phys. Rev. C **66**, 034903 (2002) [231](#)
567. B.A. Berg, U.M. Heller, H. Meyer-Ortmanns, A. Velytsky, Phys. Rev. D **69**, 034501 (2004) [231](#)
568. T.R. Miller, M.C. Ogilvie, Phys. Lett. B **488**, 313 (2000)
569. B.A. Berg, U.M. Heller, H. Meyer-Ortmanns, A. Velytsky, Nucl. Phys. Proc. Suppl. **129**, 587 (2004)
570. A. Bazavov, B.A. Berg, A. Velytsky, Nucl. Phys. Proc. Suppl. **140**, 574 (2005)
571. A. Bazavov, B.A. Berg, A. Velytsky, Int. J. Mod. Phys. A **20**, 3459 (2005)
572. E.T. Tomboulis, A. Velytsky, Phys. Rev. D **72**, 074509 (2005) [231](#)
573. O. Kaczmarek, F. Karsch, E. Laermann, M. Lutgemeier, Phys. Rev. D **62**, 034021 (2000) [231](#)
574. Y. Iwasaki, K. Kanaya, L. Karkkainen, K. Rummukainen, T. Yoshie, Phys. Rev. D **49**, 3540 (1994) [231](#)
575. B. Beinlich, F. Karsch, A. Peikert, Phys. Lett. B **390**, 268 (1997) [231](#)
576. O. Scavenius, A. Dumitru, A.D. Jackson, Phys. Rev. Lett. **87**, 182302 (2001) [231](#)
577. A. Dumitru, R.D. Pisarski, Nucl. Phys. A **698**, 444 (2002) [231](#)
578. R.D. Pisarski, Nucl. Phys. A **702**, 151 (2002) [231](#)
579. P.H. Damgaard, Phys. Lett. B **194**, 107 (1987) [232](#)
580. J. Christensen, P.H. Damgaard, Phys. Rev. Lett. **65**, 2495 (1990)
581. J. Christensen, P.H. Damgaard, Nucl. Phys. B **348**, 226 (1991)
582. J. Christensen, P.H. Damgaard, Nucl. Phys. B **354**, 339 (1991)
583. J. Christensen, G. Thorleifsson, P.H. Damgaard, J.F. Wheeler, Phys. Lett. B **276**, 472 (1992)
584. J. Christensen, G. Thorleifsson, P.H. Damgaard, J.F. Wheeler, Nucl. Phys. B **374**, 225 (1992)
585. P.H. Damgaard, M. Hasenbusch, Phys. Lett. B **331**, 400 (1994) [232](#)
586. A. Dumitru, J. Lenaghan, R.D. Pisarski, Phys. Rev. D **71**, 074004 (2005) [232](#), [235](#)
587. E. Brezin, C. Itzykson, G. Parisi, J.B. Zuber, Commun. Math. Phys. **59**, 35 (1978)
588. D.J. Gross, E. Witten, Phys. Rev. D **21**, 446 (1980)

589. O. Aharony, J. Marsano, S. Minwalla, K. Papadodimas, M.V. Raamsdonk, *Adv. Theor. Math. Phys.* **8**, 603 (2004) [232](#)
590. S. Digal, E. Laermann, H. Satz, *Eur. Phys. J. C* **18**, 583 (2001) [233](#), [308](#)
591. T. Banks, A. Ukawa, *Nucl. Phys. B* **225**, 145 (1983) [233](#), [235](#)
592. P.N. Meisinger, M.C. Ogilvie, *Phys. Rev. D* **52**, 3024 (1995)
593. C. Alexandrou, A. Borici, A. Feo, P. de Forcrand, A. Galli, F. Jegerlehner, T. Takaishi, *Phys. Rev. D* **60**, 034504 (1999) [235](#)
594. F. Green, F. Karsch, *Nucl. Phys. B* **238**, 297 (1984) [233](#)
595. A. Mocsy, F. Sannino, K. Tuominen, *JHEP* **03**, 044 (2004) [233](#), [236](#)
596. A. Mocsy, F. Sannino, K. Tuominen, *Phys. Rev. Lett.* **92**, 182302 (2004) [308](#)
597. F. Sannino, K. Tuominen, *Phys. Rev. D* **70**, 034019 (2004)
598. F. Sannino, *Phys. Rev. D* **72**, 125006 (2005)
599. C.X. Chen, C. DeTar, *Phys. Rev. D* **35**, 3963 (1987) [236](#)
600. K. Fukushima, *Phys. Rev. D* **68**, 045004 (2003)
601. K. Fukushima, *Phys. Lett. B* **591**, 277 (2004) [240](#)
602. E. Megias, E. Ruiz Arriola, L.L. Salcedo, *Phys. Rev. D* **74**, 065005 (2006) [233](#), [236](#)
603. A. Dumitru, D. Röder, J. Ruppert, *Phys. Rev. D* **70**, 074001 (2004) [234](#)
604. S. Datta, S. Gupta, *Phys. Rev. D* **67**, 054503 (2003) [235](#)
605. A. Mocsy, *J. Phys. G* **31**, S1203 (2005) [235](#)
606. F. Karsch, et al., *Nucl. Phys. Proc. Suppl.* **129**, 614 (2004) [235](#)
607. S.I. Azakov, P. Salomonson, B.S. Skagerstam, *Phys. Rev. D* **36**, 2137 (1987) [235](#)
608. D.E. Miller, K. Redlich, *Phys. Rev. D* **37**, 3716 (1988)
609. J. Condella, C.E. Detar, *Phys. Rev. D* **61**, 074023 (2000)
610. M.G. Alford, S. Chandrasekharan, J. Cox, U.J. Wiese, *Nucl. Phys. B* **602**, 61 (2001) [235](#)
611. A. Dumitru, R.D. Pisarski, D. Zschiesche, *Phys. Rev. D* **72**, 065008 (2005) [236](#), [241](#)
612. M. Doring, S. Ejiri, O. Kaczmarek, F. Karsch, E. Laermann, *Eur. Phys. J. C* **46**, 179 (2006) [236](#)
613. Y. Nambu, G. Jona-Lasinio, *Phys. Rev.* **122**, 345 (1961) [237](#)
614. U. Vogl, W. Weise, *Prog. Part. Nucl. Phys.* **27**, 195 (1991) [237](#)
615. T. Hatsuda, T. Kunihiro, *Phys. Rep.* **247**, 221 (1994)
616. G. Ripka, *Quarks Bound by Chiral Fields* (Clarendon, Oxford, 1997) [237](#)
617. A. Barducci, R. Casalbuoni, G. Pettini, L. Ravagli, *Phys. Rev. D* **72**, 056002 (2005) [237](#)
618. A. Di Giacomo, H.G. Dosch, V.I. Shevchenko, Y.A. Simonov, *Phys. Rep.* **372**, 319 (2002) [237](#)
619. C. Ratti, W. Weise, *Phys. Rev. D* **70**, 054013 (2004) [239](#)
620. C. Ratti, M.A. Thaler, W. Weise, *Phys. Rev. D* **73**, 014019 (2006) [239](#), [241](#), [242](#)
621. S. Roessner, C. Ratti, W. Weise, *Phys. Rev. D* **75**, 034007 (2007) [239](#)
622. S. Roessner, T. Hell, C. Ratti, W. Weise, *Nucl. Phys. A* **814**, 118 (2008) [241](#), [247](#), [249](#)
623. P.N. Meisinger, M.C. Ogilvie, T.R. Miller, *Phys. Lett. B* **585**, 149 (2004) [241](#)

624. S.K. Ghosh, T.K. Mukherjee, M.G. Mustafa, R. Ray, Phys. Rev. D **73**, 114007 (2006) [247](#)
625. A. Andronic, P. Braun-Munzinger, Lect. Notes Phys. **652**, 35 (2004) [248](#)
626. A. Barducci, R. Casalbuoni, S. De Curtis, R. Gatto, G. Pettini, Phys. Lett. B **231**, 463 (1989) [248](#)
627. A. Barducci, R. Casalbuoni, S. De Curtis, R. Gatto, G. Pettini, Phys. Rev. D **41**, 1610 (1990)
628. A. Barducci, R. Casalbuoni, G. Pettini, R. Gatto, Phys. Rev. D **49**, 426 (1994) [248](#)
629. B.J. Schaefer, J. Wambach, Phys. Part. Nucl. **39**, 1025 (2008) [250](#), [268](#)
630. D.U. Jungnickel, C. Wetterich, Phys. Rev. D **53**, 5142 (1996) [277](#)
631. J. Berges, D.U. Jungnickel, C. Wetterich, Int. J. Mod. Phys. A **18**, 3189 (2003)
632. N. Tetradis, Nucl. Phys. A **726**, 93 (2003) [250](#), [277](#)
633. B.J. Schaefer, H.J. Pirner, Nucl. Phys. A **660**, 439 (1999) [250](#), [257](#), [267](#), [274](#), [278](#)
634. T. Banks, A. Zaks, Nucl. Phys. B **196**, 189 (1982) [252](#)
635. V.A. Miransky, K. Yamawaki, Phys. Rev. D **55**, 5051 (1997)
636. T. Appelquist, J. Terning, L.C.R. Wijewardhana, Phys. Rev. Lett. **77**, 1214 (1996)
637. J. Braun, H. Gies, JHEP **06**, 024 (2006) [255](#)
638. J. Braun, H. Gies, Phys. Lett. B **645**, 53 (2007) [252](#), [255](#)
639. C. Sasaki, B. Friman, K. Redlich, (2007). hep-ph/0702025 [254](#)
640. B.J. Schaefer, J. Wambach, Phys. Rev. D **75**, 085015 (2007) [255](#), [257](#), [260](#), [267](#), [278](#)
641. F. Karsch, E. Laermann, Phys. Rev. D **50**, 6954 (1994) [259](#)
642. J. Berges, K. Rajagopal, Nucl. Phys. B **538**, 215 (1999) [260](#), [262](#)
643. C. Sasaki, B. Friman, K. Redlich, Phys. Rev. D **75**, 074013 (2007) [260](#), [261](#)
644. H. Fujii, M. Ohtani, Phys. Rev. D **70**, 014016 (2004) [260](#)
645. T. Kunihiro, Phys. Lett. B **271**, 395 (1991) [260](#)
646. P. Chomaz, M. Colonna, J. Randrup, Phys. Rep. **389**, 263 (2004) [263](#)
647. D. Bower, S. Gavin, Heavy Ion Phys. **15**, 269 (2002)
648. J. Randrup, Acta Phys. Hung. A **22**, 69 (2005)
649. J. Randrup, Phys. Rev. Lett. **92**, 122301 (2004)
650. H. Heiselberg, C.J. Pethick, D.G. Ravenhall, Phys. Rev. Lett. **61**(7), 818 (1988)
651. H. Heiselberg, C.J. Pethick, D.G. Ravenhall, Ann. Phys. **223**, 37 (1993)
652. C. Sasaki, B. Friman, K. Redlich, Phys. Rev. Lett. **99**, 232301 (2007) [263](#), [265](#), [266](#)
653. K. Redlich, B. Friman, C. Sasaki, J. Phys. G **34**, S437 (2007) [263](#), [265](#), [266](#)
654. K.G. Wilson, J.B. Kogut, Phys. Rep. **12**, 75 (1974) [267](#), [268](#)
655. B.J. Schaefer, J. Wambach, Nucl. Phys. A **757**, 479 (2005) [267](#), [278](#)
656. B.J. Schaefer, H.J. Pirner, (1997). hep-ph/9712413 [267](#), [274](#)
657. D.F. Litim, J.M. Pawłowski, (1998). hep-th/9901063 [268](#)
658. K. Aoki, Int. J. Mod. Phys. B **14**, 1249 (2000)
659. J. Polonyi, Cent. Eur. J. Phys. **1**, 1 (2003)
660. J. Berges, N. Tetradis, C. Wetterich, Phys. Rep. **363**, 223 (2002)
661. J.M. Pawłowski, Ann. Phys. **322**, 2831 (2007) [270](#)

662. H. Gies, (2006). hep-ph/0611146 [270](#)
663. C. Bagnuls, C. Bervillier, Phys. Rep. **348**, 91 (2001) [268](#)
664. C. Wetterich, Phys. Lett. B **301**, 90 (1993) [268](#)
665. T. Appelquist, J. Carazzone, Phys. Rev. D **11**, 2856 (1975) [269](#)
666. L. Kadanoff, W. Goetz, D. Hamblen, R. Hecht, E. Lewis, V. Palciauskas, M. Rayl, J. Swift, Rev. Mod. Phys. **39**, 395 (1967) [271](#)
667. S.B. Liao, Phys. Rev. D **53**, 2020 (1996) [274](#)
668. B.J. Schaefer, O. Bohr, J. Wambach, Phys. Rev. D **65**, 105008 (2002) [274](#), [279](#)
669. B.J. Schaefer, O. Bohr, J. Wambach, Int. J. Mod. Phys. A **16**, 2119 (2001)
670. O. Bohr, B.J. Schaefer, J. Wambach, Int. J. Mod. Phys. A **16**, 3823 (2001)
671. G. Papp, B.J. Schaefer, H.J. Pirner, J. Wambach, Phys. Rev. D **61**, 096002 (2000) [274](#), [279](#)
672. D.F. Litim, J.M. Pawłowski, Phys. Rev. D **66**, 025030 (2002) [274](#)
673. D.F. Litim, J.M. Pawłowski, Phys. Rev. D **65**, 081701 (2002) [274](#)
674. D.F. Litim, J.M. Pawłowski, Phys. Lett. B **546**, 279 (2002) [274](#)
675. D.F. Litim, J.M. Pawłowski, L. Vergara, (2006). hep-th/0602140 [274](#)
676. D.U. Jungnickel, C. Wetterich, Eur. Phys. J. C **2**, 557 (1998) [277](#)
677. N. Brouzakis, N. Tetradis, Nucl. Phys. A **742**, 144 (2004) [282](#)
678. E. Shuryak, Prog. Part. Nucl. Phys. **53**, 273 (2004) [286](#)
679. E. Shuryak, I. Zahed, Phys. Rev. D **69**, 046005 (2004) [286](#), [301](#), [302](#)
680. M. Gyulassy, L. McLerran, Nucl. Phys. A **750**, 30 (2005) [286](#)
681. E.V. Shuryak, I. Zahed, Phys. Rev. D **70**, 054507 (2004) [287](#), [292](#)
682. M. Asakawa, T. Hatsuda, Phys. Rev. Lett. **92**, 012001 (2004) [287](#), [292](#)
683. S. Datta, F. Karsch, P. Petreczky, I. Wetzorke, Nucl. Phys. Proc. Suppl. **119**, 487 (2003) [287](#), [292](#)
684. H. van Hees, V. Greco, R. Rapp, AIP Conf. Proc. **842**, 77 (2006) [287](#), [292](#)
685. M.H. Thoma, Nucl. Phys. A **774**, 307 (2006) [288](#)
686. B.A. Gelman, E.V. Shuryak, I. Zahed, Phys. Rev. C **74**, 044909 (2006) [288](#), [290](#)
687. B.A. Gelman, E.V. Shuryak, I. Zahed, Phys. Rev. C **74**, 044908 (2006) [288](#), [290](#)
688. J. Liao, E. Shuryak, Phys. Rev. C **75**, 054907 (2007) [288](#), [294](#), [297](#)
689. J.M. Maldacena, Adv. Theor. Math. Phys. **2**, 231 (1998) [288](#), [298](#)
690. N. Seiberg, E. Witten, Nucl. Phys. B **426**, 19 (1994) [288](#), [293](#)
691. T. Hirano, Acta Physiol. Pol. B **36**, 187 (2005) [289](#)
692. D. Teaney, J. Lauret, E.V. Shuryak, (2001). nucl-th/0110037
693. C. Nonaka, S.A. Bass, Phys. Rev. C **75**, 014902 (2007) [289](#)
694. P. Romatschke, U. Romatschke, Phys. Rev. Lett. **99**, 172301 (2007) [289](#)
695. D. Molnar, (2007). 0707.1251 [nucl-th] [289](#)
696. H. Stoecker, Nucl. Phys. A **750**, 121 (2005) [289](#)
697. J. Casalderrey-Solana, E.V. Shuryak, D. Teaney, J. Phys. Conf. Ser. **27**, 22 (2005)
698. J. Casalderrey-Solana, E.V. Shuryak, D. Teaney, (2006). hep-ph/0602183 [289](#)
699. J. Casalderrey-Solana, E.V. Shuryak, (2005). hep-ph/0511263 [289](#)

700. F. Antinori, E.V. Shuryak, J. Phys. G **31**, L19 (2005) [289](#)
701. B. Bauchle, L. Csernai, H. Stocker, (2007). 0710.1476 [nucl-th] [289](#)
702. S.K. Wong, Nuovo Cim. A **65S10**, 689 (1970) [290](#)
703. J. Liao, E.V. Shuryak, Nucl. Phys. A **775**, 224 (2006) [292](#)
704. B.A. Gelman, E.V. Shuryak, I. Zahed, Phys. Rev. A **72**, 043601 (2005) [292](#)
705. A. Turlapov, J. Kinast, B. Clancy, L. Luo, J. Joseph, J. of Low Temp. Phys., **150**, 567 (2008) [292](#)
706. P.A.M. Dirac, Proc. R. Soc. Lond. A **133**, 60 (1931) [294](#)
707. G. 't Hooft, Nucl. Phys. B **190**, 455 (1981) [295](#)
708. S. Mandelstam, Phys. Rep. **23**, 245 (1976) [295](#)
709. A. Nakamura, T. Saito, S. Sakai, Phys. Rev. D **69**, 014506 (2004) [295](#), [296](#)
710. A. D'Alessandro, M. D'Elia, Nucl. Phys. B **799**, 241 (2008) [295](#), [296](#)
711. J. Liao, E. Shuryak, Phys. Rev. C **77**, 064905 (2008) [296](#)
712. S.C. Huot, S. Jeon, G.D. Moore, Phys. Rev. Lett. **98**, 172303 (2007) [297](#)
713. P.M. Chesler, A. Vuorinen, JHEP **11**, 037 (2006) [297](#)
714. G.D. Moore, D. Teaney, Phys. Rev. C **71**, 064904 (2005) [297](#)
715. G. Policastro, D.T. Son, A.O. Starinets, Phys. Rev. Lett. **87**, 081601 (2001) [297](#), [303](#)
716. J. Casalderrey-Solana, D. Teaney, Phys. Rev. D **74**, 085012 (2006) [297](#), [303](#)
717. E. Shuryak, (2007). 0711.0004 [hep-ph] [300](#)
718. A. Karch, E. Katz, D.T. Son, M.A. Stephanov, Phys. Rev. D **74**, 015005 (2006) [300](#)
719. J.M. Maldacena, Phys. Rev. Lett. **80**, 4859 (1998) [300](#), [302](#)
720. S.J. Rey, J.T. Yee, Eur. Phys. J. C **22**, 379 (2001) [300](#), [302](#)
721. S. Lin, E. Shuryak, Phys. Rev. D **76**, 085014 (2007) [301](#)
722. I.R. Klebanov, J.M. Maldacena, I. Thorn, Charles B., JHEP **04**, 024 (2006) [301](#), [302](#)
723. S.S. Gubser, I.R. Klebanov, A.A. Tseytlin, Nucl. Phys. B **534**, 202 (1998) [302](#)
724. E.V. Shuryak, I. Zahed, Phys. Lett. B **608**, 258 (2005) [302](#)
725. S. Lin, E. Shuryak, Phys. Rev. D **77**, 085013 (2008) [302](#), [304](#)
726. S. Lin, E. Shuryak, Phys. Rev. D **77**, 085014 (2008) [302](#), [304](#)
727. M. Kruczenski, D. Mateos, R.C. Myers, D.J. Winters, JHEP **07**, 049 (2003) [302](#)
728. S. Hong, S. Yoon, M.J. Strassler, JHEP **03**, 012 (2006) [302](#)
729. J.J. Friess, S.S. Gubser, G. Michalogiorgakis, JHEP **09**, 072 (2006) [303](#), [304](#)
730. S.J. Sin, I. Zahed, Phys. Lett. B **608**, 265 (2005) [303](#)
731. C.P. Herzog, A. Karch, P. Kovtun, C. Kozcaz, L.G. Yaffe, JHEP **07**, 013 (2006)
732. S.S. Gubser, Phys. Rev. D **74**, 126005 (2006)
733. A. Buchel, Phys. Rev. D **74**, 046006 (2006)
734. S.J. Sin, I. Zahed, Phys. Lett. B **648**, 318 (2007) [303](#)
735. P.M. Chesler, L.G. Yaffe, Phys. Rev. D **78**, 045013 (2008) [304](#)
736. E. Shuryak, S.J. Sin, I. Zahed, J. Korean, Phys. Soc. **50**, 384 (2007) [304](#)
737. R.A. Janik, R.B. Peschanski, Phys. Rev. D **74**, 046007 (2006) [305](#)

- 738. R.A. Janik, R.B. Peschanski, Phys. Rev. D **73**, 045013 (2006) [305](#)
- 739. S. Nakamura, S.J. Sin, JHEP **09**, 020 (2006) [305](#)
- 740. R.A. Janik, Phys. Rev. Lett. **98**, 022302 (2007) [305](#)
- 741. J.J. Friess, S.S. Gubser, G. Michalogiorgakis, S.S. Pufu, JHEP **04**, 080 (2007) [305](#)
- 742. Y. Hatta, K. Fukushima, Phys. Rev. D **69**, 097502 (2004) [308](#)
- 743. M.G. Alford, A. Schmitt, K. Rajagopal, T. Schafer, Rev. Mod. Phys. **80**, 1455 (2008) [309](#)

Part II

In-Medium Excitations

Conveners: R. Rapp^{1,a,b} and B. Kämpfer^{2,3,c,d,e}

Authors, who contributed to the various chapters or sections given in brackets:

A. Andronic⁴ [6.2]; D. Blaschke^{5,15,f} [2.6.2, 7.1, 7.2]; C. Fuchs^{6,g} [4.1]; M. Harada^{7,h} [2.4.1.5, 2.5.3]; T. Hilger^{2,c} [5.4]; B. Kämpfer^{2,3,c,d,e} [2.3.1, 3.2.1, 3.2.2, 4.2, 5.2.1, 5.4]; M. Kitazawa⁸ [7.3]; T. Kunihiro⁸ [7.3]; P. Petreczky^{9,i} [2.5.1, 6.1]; R. Rapp^{1,a,b} [1, 2.1, 2.2, 2.3.2, 2.4.1.1–2.4.1.4, 2.4.1.6, 2.4.2, 2.4.3, 2.5.1, 2.5.2, 2.6.1, 3.1, 3.2.3, 5.2.1, 5.2.2, 5.2.3, 5.3, 8]; F. Riek^{1,4,a} [2.4.1.1]; C. Sasaki¹⁰ [2.4.1.5, 2.5.3]; R. Thomas^{2,3,e} [5.2.1]; L. Tolos^{11,j} [5.5]; P. Zhuang^{12,k} [6.3]; H. van Hees^{1,a,b} [5.2.2]; R. Vogt^{13,14,l} [5.1]; S. Zschocke^{2,3,c,e} [5.4].

Affiliations:

¹Texas A&M University, College Station, TX, USA; ²Technical University of Dresden, Dresden, Germany; ³Forschungszentrum Dresden-Rossendorf, Dresden, Germany; ⁴GSi Helmholtzzentrum für Schwerionenforschung, Darmstadt, Germany; ⁵University of Wrocław, Wrocław, Poland; ⁶Martin-Gerbert-Gymnasium, Horb am Neckar, Germany; ⁷Nagoya University, Nagoya, Japan; ⁸Kyoto University, Kyoto, Japan; ⁹Brookhaven National Laboratory, Upton, NY, USA; ¹⁰Technical University of Munich, Munich, Germany; ¹¹University of Frankfurt, Frankfurt, Germany; ¹²Tsinghua University Beijing, Beijing, China; ¹³Lawrence Livermore National Laboratory, Livermore, CA, USA; ¹⁴University of California at Davis, Davis, CA, USA; ¹⁵Joint Institute of Nuclear Research (JINR), Dubna, Russia

Support:

^aU.S. National Science Foundation CAREER grant no. PHY-0449489; ^bAlexander von Humboldt Foundation; ^cBMBF 06DR136; ^dEU I3HP; ^eGSi Darmstadt; ^fPolish Ministry for Research and Higher Education grant No. N N 202 0953 33 (DBB) and CompStar - an ESF Research Networking Programme; ^gGSi-F&E; ^hJSPS Grant-in-Aid for Scientific Research (c) 20540262, Global COE Program “Quest for Fundamental Principles in the Universe” of Nagoya University provided by Japan Society for the Promotion of Science (G07); ⁱU.S. Department of Energy under Contract No. DE-AC02-98CH10886; ^jRosalind Franklin Programme of the University of Groningen (RFF-Open and hidden charm at PANDA), Helmholtz International Center for FAIR (LOEWE program), European Community-Research Infrastructure Integrating Activity HadronPhysics2 (Grant Agreement n. 227431, FP7); ^kNational Science Foundation of China grants no. 10575058 and 10735040; ^lU.S. Department of Energy under Contract No. DE-AC52-07NA27344, National Science Foundation Grant NSF PHY-0555660

Rapp, R. et al.: *Part II In-Medium Excitations*.

Lect. Notes Phys. **814**, 335–529 (2011)

DOI 10.1007/978-3-642-13293-3_4

© Springer-Verlag Berlin Heidelberg 2011

Spectral properties of hadronic excitations are direct probes of the strongly interacting medium as created in energetic collisions of heavy nuclei. In this part of the book we discuss the pertinent theoretical background, recent developments and perspectives for using electromagnetic radiation, as well as strange and charm hadrons, to infer microscopic properties of QCD matter. In the electromagnetic emission sector, our focus is on thermal dileptons and the in-medium modifications of the light vector mesons. We outline their potential for characterizing the QCD phase transition by establishing connections of the electromagnetic correlation function to order parameters of chiral symmetry restoration. Complementary information can be obtained from hadronic decays of resonances probing the more dilute stage of a heavy-ion collision. We then turn to in-medium properties of strange and charm quarks and hadrons, which includes charm-quark diffusion in the QGP as well as spectral functions of K and D mesons in hadronic matter. While these quantities are not directly accessible in experiment, a careful study of their production systematics in terms of total abundance, chemistry and collective flow patterns will lead to key insights into the relevant interactions in high-density matter. Finally, we discuss medium effects on charmonia in both the QGP and hadronic matter, and how these could manifest themselves in observables.

Chapter 1

Introduction

The vacuum of strong interactions is of a rather complex nature giving rise to several fundamental phenomena, most notably the confinement of quarks and the generation of (the major part of) hadronic masses. The nontrivial vacuum structure is associated with the formation of quark and gluon condensates, which are intimately related to the spontaneous breaking of chiral symmetry and the breaking of scale invariance of Quantum Chromodynamics (QCD). The condensates are, however, not directly observable, and therefore information has to be obtained from excitations of the ground state. At zero temperature and density, the physical excitations are colorless hadrons, whose spin and flavor structure provide a rich laboratory for spectroscopy.

At sufficiently high temperature (T) and/or baryon density, ϱ_B (or baryon chemical potential, μ_B), asymptotic freedom of QCD predicts the existence of new phases of matter, in particular the Quark-Gluon Plasma (QGP) at high T and the Color-Superconductor (CSC) at high μ_B and low T . It is expected that the bulk excitation of the QCD vacuum (thermal or density) induces a “melting” of the condensate structures, accompanied by the restoration of chiral symmetry and deconfinement of color charges. At finite temperature (and vanishing μ_B) this transition is fairly well established by lattice QCD (lQCD) computations, with a (pseudo-) critical temperature of $T_c = 180 \pm 20$ MeV. While this is presumably not a phase transition in the strict sense, lQCD clearly reveals a rapid change in the thermodynamic properties of the system (most notably energy density) over a rather small interval in temperature. The properties of the equation of state and their possible signals in heavy-ion reactions are discussed in detail in Parts I and IV of this book.

The phase transformation, in turn, implies dramatic changes in the underlying microscopic properties of the strongly interacting medium. Naively, this is realized by a conversion of the degrees of freedom, i.e., from hadrons to quarks and gluons, as roughly reflected in the (degeneracy) coefficient of the equation of state. However, this notion is far from providing an understanding of the mechanisms inducing deconfinement and chiral symmetry restoration in the medium. More precisely, the microscopic matter properties

are characterized by density and temperature dependent changes in hadronic spectral functions.¹ While medium modifications of hadrons in strongly interacting matter are an interesting and important subject in itself, connections to the underlying condensate structure(s) are essential to meet the challenge of conducting fundamental studies of the QCD phase diagram. Indeed, (approximate) chiral symmetry alone predicts that (the spectral functions of) chiral partners (i.e. hadronic multiplets that transform into each other under chiral transformations) become (nearly) degenerate in the symmetric phase. The degeneracy of π and σ channels, ρ and a_1 , or N and $N^*(1,535)$, obviously implies major changes of the pertinent spectral functions toward the chiral transition. To detect such modifications in heavy-ion experiments, one needs access to the hot and dense phases of the fireball, leading to the notion of “penetrating probes”. In general, the latter encompass electromagnetic (photons and dileptons), heavy-quark and high transverse-momentum observables. In the present part, we will focus on the former two due to their potential of characterizing the matter at relatively soft energy/momentum scales, $\sim T, \Lambda_{\text{QCD}}, 4\pi f_\pi$ ($f_\pi=92$ MeV: pion decay constant). The modes representing the prevalent degrees of freedom and encoding phase transition properties are expected to operate at these scales. Our goal is to provide a comprehensive presentation of theoretical tools and approaches (with emphasis on recent developments) which are currently available to convert experimental data into meaningful information on spectral and phase-transition properties of QCD matter.

The inherently non-perturbative nature of this problem renders a direct solution from first principles difficult. While lattice QCD is well suited to compute the equation of state, its formulation in euclidean space-time makes the evaluation of spectral functions much more demanding. It is for this reason that effective hadronic (and quark) models are an indispensable tool to provide quantitative predictions that can be tested in experiment. No less important, hadronic models can serve as the main bridge between first principles and experiment, if the following program can be carried out: (a) The interaction Lagrangian is constructed based on essential symmetry principles (chiral, gauge). (b) The Lagrangian parameters (masses, coupling constants etc.) are constrained by a wide range of empirical information in the vacuum (decay widths, scattering data). (c) The in-medium spectral functions (as calculated, e.g., within finite- T field theory) are checked against lattice QCD predictions for euclidean correlation functions, susceptibilities, and even order parameters (using, e.g., sum rules). (d) The in-medium spectral functions are applied to and tested against varying matter environments (ground-state nuclei or the medium in heavy-ion collisions). Throughout the discussion in

¹ Note that the (gauge-invariant) concept of a hadronic spectral function is equally valid in the hadronic and QGP phases.

this part of the book, we will take recourse to these criteria as guiding principles.²

Concerning electromagnetic probes (Chap. 2), dilepton invariant-mass spectra in heavy-ion collisions offer the unique opportunity to directly monitor the in-medium electromagnetic spectral function. In the vacuum, and at low masses ($M_{ll} \leq 1$ GeV), the latter is essentially saturated by the light vector mesons $V = \rho, \omega, \phi$ (via exclusive decays $V \rightarrow l^+ l^-$, $l = e, \mu$), giving rise to the vector dominance model (VDM). To the extent that this holds up in the medium, dilepton spectra directly probe the in-medium V spectral functions (experiments support this notion). As a further benefit, it turns out that the dominant contribution to the experimental spectra in the low-mass regime (LMR) originates from the hot and dense hadronic phase (not from the QGP). A key issue is thus a reliable calculation of the vector-meson properties in the medium. Low-mass thermal dilepton emission is dominated by the ρ meson, which has received most of the attention in this context. However, ω and ϕ contributions are more localized in invariant mass, and are being studied rather intensely in production reactions off nuclei, which provides important complementary information on their in-medium properties. Some of the core questions may be summarized as follows [1]:

- (1) Do ρ , ω and ϕ mesons behave alike in different regimes of the phase diagram?
- (2) Do hadronic many-body effects account for a realistic evaluation of medium modifications in hadronic matter? What role do intrinsic T - and μ_B -dependencies of the parameters of the effective Lagrangian play?
- (3) How do vector-meson spectral functions change in different regimes of the phase diagram (i.e., baryon- vs. meson-driven modifications)?
- (4) What is the impact of medium-modified hadronic spectral functions on the EoS and its chemical composition?
- (5) What are the connections between vector spectral functions and (chiral) order parameters (quark and gluon condensates, f_π , susceptibilities, ...), and how can they be exploited?
- (6) What is the fate of the vector dominance model in the medium?

Item (5) is pivotal for extracting signatures of chiral symmetry restoration from dilepton spectra. We will outline a scheme in which hadronic model calculations of in-medium vector *and* axialvector spectral functions can be exploited to (a) compute the temperature and density dependence of chiral order parameters (using chiral and QCD sum rules), and (b) perform detailed comparisons to dilepton spectra (vs. collision energy, centrality, mass and 3-momentum). This provides a direct link between experiment and chiral order parameters, especially if the latter can be quantified by first principle, unquenched lattice QCD computations below T_c . The study of in-medium spec-

² The missing link in realizing point (d) is a realistic space-time evolution of a heavy-ion collision, as well as a reliable assessment of non-thermal sources. These issues are discussed in Parts III and IV of this compendium.

tral functions might be further supplemented with “hadronic spectroscopy” via strong decay of short-lived resonances, e.g., $\rho \rightarrow \pi\pi$ or $\Delta \rightarrow \pi N$ (Chap. 3). While the detectable decays will mostly arise from dilute matter close to thermal freeze-out of the fireball, the benefit is that channels other than the vector one are, in principle, accessible.

The heavy-quark complex divides into open-charm (Chap. 5) and charmonium (Chap. 6) properties (bottom production is not feasible at the energies envisaged at FAIR). An important feature here is that the charm-quark mass is large enough for $c\bar{c}$ production to be restricted to initial (hard) N – N collisions. This implies that c -quarks do not “change their identity” during the fireball evolution, and therefore changes in their momentum distribution as they traverse the fireball can serve as quantitative measures of their interactions in the medium, even at low p_T ; the relatively large mass further increases their value as a probe of transport properties of the medium, since more (or stronger) interactions are required to thermalize c -quarks compared to light partons (once thermalized, light partons have lost their virtue as a probe).

A similar situation applies to charmonia (J/ψ , χ_c , ψ'): after primordial production, their survival critically depends on their (inelastic) interaction rate within the hot and dense medium, while regeneration (via c – \bar{c} coalescence) is presumably suppressed at CBM energies. In particular, Debye screening is expected to reduce binding energies of charmonia, eventually leading to their dissolution, or at least an increase in the dissociation rate. Charmonia have the additional benefit that they appear well suited for lattice QCD studies: both (Euclidean) correlation functions and (static) c – \bar{c} free energies have recently been computed with good precision; effective quark models can thus be used to check the notion of in-medium potential approaches, as well as to improve on phenomenological applications in heavy-ion reactions. Some of the important questions in the heavy-flavor context include:

- (1) What are the prevalent c -quark interactions around and above T_c , and what is the charm diffusion constant in the medium?
- (2) Do \bar{c} quarks behave differently from c quarks in baryon-rich matter?
- (3) What are the charmonium spectral functions in hot and dense matter, and what is their sensitivity to open-charm properties (threshold effects, spectral functions)?
- (4) Are charmonium spectral properties related to deconfinement, and if so, how?

We will also address the role of strange hadrons (Chap. 4). The current strange-quark mass is intermediate between those of light ($q=u, d$) and charm quarks, but the physics questions pertaining to the strange sector probably more closely relate to the light sector. Indeed, subthreshold kaon production in intermediate-energy heavy-ion reactions has been intensely studied to infer spectral properties of kaons in hot/dense matter with possible relations to chiral symmetry restoration. At ultrarelativistic energies, this question merges into the one of chemical strangeness equilibration, one of the early suggestions as a QGP signature (due to a much reduced mass threshold as a

consequence of the s -quark shedding off its constituent mass). Again, as for the electromagnetic (vector meson) and charmonium complex, the issue of reliable calculations of hadronic medium effects is essential to (i) quantify the impact of dilute stages in the reaction, and (ii) establish relations between “hadronic” effects and quark/gluon condensates.

An important aspect that we will return to throughout this part is the significance of high baryon density effects, which is one of the major objectives of the CBM experiment. In a larger context, this connects to the physics of (the interior) of neutron (quark) stars, even though those objects are comparatively cold (possibly up to tens of MeV following a core collapse in a supernova explosion). While the increasing particle and entropy production in heavy-ion reactions necessarily implies an increase of temperature with collision energy, one might entertain the possibility of precursor phenomena of color superconductivity in the transient (early) stages (provided the critical temperatures are large, say ~ 100 MeV). We will briefly allude to such possibilities (Chap. 7).

Part II is organized as follows: Chap. 2 is devoted to electromagnetic probes, starting with a brief overview of the current phenomenological state-of-affairs (Sect. 2.1), followed by introducing the electromagnetic correlation function (Sect. 2.2), its connection to condensates and order parameters as provided by chiral and QCD sum rules (Sect. 2.3), hadronic model calculations of light vector-meson spectral functions (ρ , ω , ϕ) in hot and/or dense matter (Sect. 2.4), pertinent thermal dilepton (Sect. 2.5) and photon (Sect. 2.6) emission rates. Chapter 3 discusses possibilities for obtaining supplementary information on hadronic spectral functions via spectroscopy of strongly decaying meson (Sect. 3.1) and baryon (Sect. 3.2) resonances. Chapter 4 addresses medium modifications of strange hadrons, i.e., anti-/kaons (Sect. 4.1) and strange baryons (Sect. 4.2). Chapter 5 concerns our current understanding of open charm in the medium, starting with Sect. 5.1 on perturbative QCD calculations of open-charm production cross sections close to the kinematic threshold and the specific problems and uncertainties involved. Section 5.2 elaborates on the problem of c -quark interactions and diffusion in the QGP, with emphasis on nonperturbative approaches, followed by Sect. 5.3 on the chemistry of charmed hadrons within the thermal model, Sect. 5.4 on QCD sum rules for D mesons, and Sect. 5.5 on hadronic model calculations of charmed hadrons in hot/dense hadronic matter. Chapter 6 contains our discussion of charmonia in medium; it is organized into Sect. 6.1 on charmonium equilibrium properties as inferred from lattice QCD and potential models and Sect. 6.3 on kinetic/transport approaches to describe the space-time evolution of charmonium yields and transverse-momentum spectra in heavy-ion collisions. Chapter 7 briefly discusses excitations of the color superconducting phases in the QCD phase diagram (Sect. 7.1), with emphasis on meson correlation functions (Sect. 7.2) and precritical phenomena above

the critical temperature (Sect. 7.3). Finally, Chap. 8 contains an executive-type summary, where we recall what we deem are the most important conclusions from this part along with consequences for observables in the CBM context.

Chapter 2

Electromagnetic probes and light vector mesons

The virtue of electromagnetic (EM) radiation as a probe of strongly interacting matter in heavy-ion collisions resides in the fact that once the (real or virtual) photon is produced, it escapes the medium essentially undistorted, since its mean free path is much larger than the typical system size. While the production of real photons is suppressed relative to hadrons by one power of the electromagnetic coupling constant, $\alpha_{\text{em}} = 1/137$, dilepton emission (i.e., virtual photons with subsequent decay $\gamma^* \rightarrow l^+l^-$ with $l=e$ or μ) is further suppressed by an additional power of α_{em} . However, dileptons carry invaluable extra information in terms of their invariant mass (which they inherit from their parent particle), which renders them *the* prime observable to search for in-medium modifications of hadrons. The latter are restricted to vector mesons, which are the only ones that directly couple to the EM current. It turns out that only the light vector mesons ρ , ω and ϕ are expected to contribute with a significant fraction of in-medium decays to the finally observed dilepton spectrum. For example, for the J/ψ , its vacuum lifetime of about $\tau_\psi=2,000$ fm/c implies that the observed signal will overwhelmingly contain decays after the fireball freeze-out, with a ratio of $\sim \tau_\psi/\tau_{FB} \approx 100$ (assuming a fireball lifetime of $\tau_{FB} \approx 20$ fm/c). In this section we therefore focus on the medium modifications of the light vector mesons in connection with EM thermal emission rates, primarily dileptons but with a short digression to photon spectra. In Sect. 2.2, we introduce the EM current–current correlation function which is the key quantity figuring into both dilepton and photon production rates. We discuss its main features in the vacuum along with model independent evaluations of medium effects in low-density expansion schemes. In Sect. 2.3 we discuss how (model-independent) QCD and chiral sum rules provide us with: (i) constraints on models of vector-meson spectral functions; (ii) links between correlation functions and chiral order parameters. In Sect. 2.4 we turn to a detailed discussion of hadronic approaches to assess the properties of ρ , ω and ϕ mesons in hot and/or dense matter, including up-to-date information from experiment. In Sects. 2.5 and 2.6 a survey of

thermal dilepton and photon production rates is given including temperature and density regimes appropriate for heavy-ion collisions at CBM.

2.1 Brief overview of experimental status and interpretation

Measurements of EM probes in heavy-ion collisions have thus far consistently provided exciting data with vigorous subsequent theoretical activity, interpretations and insights.

At relativistic bombarding energies at the BEVALAC ($E_{lab} \simeq 1\text{--}5$ AGeV), the DLS collaboration performed a systematic measurement of low-mass ($M \leq 1$ GeV) dilepton spectra in various combinations of light and medium heavy nuclei (from $p\text{--}p$ to Ca–Ca) [2, 3]. A large (up to 6-fold) enhancement over final state decays (“hadronic cocktail”) has been observed in $^{12}\text{C}+^{12}\text{C}$ and $^{40}\text{Ca}+^{40}\text{Ca}$ systems at $E_{lab} \simeq 1$ AGeV, which to date cannot be satisfactorily explained theoretical models [4–7].¹ A clarification of the situation in this energy regime is expected by upcoming precision data from the HADES experiment [8], and first results have confirmed the DLS data [9, 10].

At ultrarelativistic lab energies at the CERN-SPS, $E_{lab}=158\text{--}200$ AGeV for lead and sulfur projectiles, respectively, low-mass dilepton spectra have been measured by the HELIOS-3 [11], NA50 [12] and CERES/NA45 [13, 14] collaborations. The CERES dielectron data consistently exhibit a substantial enhancement over the hadronic cocktail as well, of about a factor of 3, while the excess in the NA50 and HELIOS-3 dimuon data is much smaller (this has been attributed to the rather high cut on transverse pair momentum, $q_t \geq 1$ GeV, in the latter two experiments; indeed, the CERES enhancement is concentrated at low q_t). Various theoretical models can explain the SPS data reasonably well provided that substantial medium effects on primarily the ρ meson spectral function are included in the description, cf. [15–19] for reviews. However, a definite discrimination between, e.g., a strong broadening of the ρ with essentially no mass shift (“melting”) and a “dropping-mass” scenario could not be achieved [20].² With baryon-induced medium effects playing a major role in both approaches, and in view of the large DLS enhancement, the question arises how the excess radiation develops with collision energy. Maximal baryon densities are expected below maximal SPS energy [22]. Indeed, a CERES run with 40 AGeV projectiles resulted in a

¹ Recent developments point at the importance of nucleon–nucleon Bremsstrahlung for explaining (part of) the discrepancy.

² Recent dimuon data from the NA60 experiment [21] in In(158 AGeV)+In collisions have overcome the hampering high- q_t cut of its NA50 predecessor, and in this way one can take full advantage of much improved statistics and mass resolution over previous dielectron results. This allows for major advances in the theoretical interpretation as will be discussed in more detail below.

substantially larger enhancement factor, but with limited statistical significance [23]. Thus, two natural questions arise in this context: (i) Is there a regime of maximal dilepton enhancement which is possibly connected to maximal baryon densities achieved in the collisions (as expected from current theory)? (ii) Somewhat more speculatively, is there a connection between a maximal excess and the putative critical endpoint in the QCD phase diagram (in this case, prolonged fireball lifetimes could further stipulate the effects, including an increase of the total yield)?

As emphasized below, (low-mass) dilepton production is intimately related to the emission of real photons, as these quantities represent different kinematic realizations of the same underlying emission function, i.e., the EM current correlation function. Thus, a simultaneous investigation of photon observables is very desirable. The WA98 collaboration has measured direct photons (i.e., photons that are not due to final-state hadron decays but directly from the source, including primordial N - N collisions and thermal radiation) [24, 25] which provides valuable complementary information on temperature, lifetime, the relevant microscopic mechanism of photon production as well as consistency checks with dilepton observables (both in terms of the EM correlator and source properties). When combining photon and dilepton measurements at the SPS, the observed excess radiation in (semi-) central Pb-Au/Pb can essentially be explained by a common thermal source with initial temperature $T_0 \simeq 210 \pm 30$ MeV and a lifetime of around 10–14 fm/c. The baryonic medium effects required to account for the low-mass dilepton excess are prevalent in the photon transverse-momentum spectra in the $q_t \simeq 0.2$ –1 GeV regime [26].

To conclude these introductory notes, one may state that the current situation rather distinctly calls for accurate measurements of EM probes in the beam energy regime of 10–50 AGeV (the regime accessible with FAIR). Except for a short CERES run at 40 AGeV, no such measurements have been performed to date. Dilepton experiments in this regime are also planned at collider machines, within a systematic energy scan down to $\sqrt{s} = 6$ AGeV (corresponding to $E_{lab} \simeq 20$ AGeV) as part of the (near-) future RHIC program [27], as well as at the Nuclotron facility in Dubna [28].³

2.2 Emissivity of strongly interacting matter

2.2.1 *Electromagnetic correlation function and thermal emission rates*

The general framework for calculating thermal EM emission rates from a strongly interacting medium in thermal equilibrium is provided by the

³ This should be viewed as a great opportunity rather than a drawback, as experimental redundancy and competition have proved to be very fruitful in the RHIC campaign to date.

(retarded) EM current–current correlation function. The latter is defined as the thermal expectation value of the retarded (hadronic) EM current operator

$$\Pi_{\text{em}}^{\mu\nu}(q_0, q) = -i \int d^4x \, e^{iq \cdot x} \, \Theta(x^0) \, \langle\langle [j^\mu(x), j^\nu(0)] \rangle\rangle, \quad (2.1)$$

where $\langle\langle \dots \rangle\rangle$ denotes the ensemble average encoding the dependence on temperature T and chemical potential μ_B , and q_0 and q are the photon energy and magnitude of its 3-momentum, respectively. To lowest order in the EM coupling, α_{em} , (to which we will restrict ourselves here) $\Pi_{\text{em}}^{\mu\nu}$ corresponds to the retarded photon self-energy. Its imaginary part, $\text{Im}\Pi_{\text{em}}$ (which we will refer to as EM spectral function), directly determines thermal photon (γ) and dilepton (l^+l^-) rates according to [29]

$$q_0 \frac{dN_\gamma}{d^4x d^3q} = -\frac{\alpha_{\text{em}}}{\pi^2} f^B(q \cdot u; T) \, \text{Im}\Pi_{\text{em}}(q_0 = q; \mu_B, T), \quad (2.2)$$

$$\frac{dN_{ll}}{d^4x d^4q} = -\frac{\alpha_{\text{em}}^2}{M^2 \pi^3} L(M^2) f^B(q \cdot u; T) \, \text{Im}\Pi_{\text{em}}(M, q; \mu_B, T), \quad (2.3)$$

where $M^2 = q_0^2 - q^2$ is the photon's invariant mass squared, f^B the Jüttner function (which recovers the Bose distribution function in the local rest frame of matter), and $L(M^2)$ a lepton phase space factor involving the mass, m_l , of the outgoing leptons. The medium's four-velocity is denoted by $u^\mu = \gamma(1, \boldsymbol{\beta})$, and $\Pi_{\text{em}} = \frac{1}{3} \Pi_{\text{em}}^{\mu\nu} g_{\mu\nu}$. While the dilepton rate involves an average of longitudinal and transverse polarizations, $\Pi_{\text{em}} = \frac{1}{3}(\Pi_{\text{em}}^L + 2\Pi_{\text{em}}^T)$, only the transverse part contributes to real photons. We emphasize again that dilepton and photon rates are governed by the same underlying spectral function, albeit in different kinematic regimes (timelike vs. lightlike, respectively). To leading order in the strong coupling constant, α_s , the photon rate is $\mathcal{O}(\alpha_s)$ while the dilepton rate is $\mathcal{O}(\alpha_s^0)$. Thus, each process that contributes to photon production will also produce dileptons (the reverse statement excludes $\mathcal{O}(\alpha_s^0)$ annihilation reactions such as $q\bar{q} \rightarrow e^+e^-$ or $\pi^+\pi^- \rightarrow e^+e^-$). Thus model calculations for dilepton production can and should be tested in photon production (and vice versa). This not only provides consistency constraints on the EM spectral functions, but, when applied to experimental spectra in heavy-ion reactions, also on the underlying space-time (temperature-density) evolution.

2.2.2 Electromagnetic spectral function in vacuum

In the vacuum, $\text{Im}\Pi_{\text{em}}$ can be measured in e^+e^- annihilation as it is directly proportional to the corresponding cross section into hadronic final states,

$$\sigma(e^+e^- \rightarrow \text{hadrons}) = \sigma(e^+e^- \rightarrow \mu^+\mu^-) \frac{(-12\pi)}{s} \text{Im} \Pi_{\text{em}}^{\text{vac}}(s), \quad (2.4)$$

where $\sigma(e^+e^- \rightarrow \mu^+\mu^-) = 4\pi\alpha^2/3s$ (Lorentz invariance implies that $\Pi_{\text{em}}^{\text{vac}} = \Pi_{\text{em}}(T=0, \mu_B=0)$ depends on $s \equiv M^2$ only and that longitudinal and transverse parts are identical; both features are broken in the medium). The intimate relation between dilepton production, Eq. (2.3), and e^+e^- annihilation, Eq. (2.4), is of course a consequence of time-reversal invariance of the strong and electromagnetic interactions. e^+e^- annihilation has a well-known cross section which has been measured over more than thirty years with increasing accuracy, cf. the upper panel of Fig. 2.1. In the low-mass region, $M \lesssim 1.1 \text{ GeV}$, the EM spectral function is dominated by the low-mass vector mesons ρ , ω and ϕ (cf. the lower panel in Fig. 2.1), giving rise to the vector-dominance model (VDM). At higher masses, $M \geq 1.5 \text{ GeV}$, one enters a perturbative regime where the annihilation occurs at short distance implying that the strength of the total cross section is essentially given by a $q\bar{q}$ final state with negligible impact of the subsequent hadronization,

$$\sigma(e^+e^- \rightarrow \text{hadrons}) = N_c \frac{4\pi\alpha_{\text{em}}^2}{3s} \sum_q e_q^2 \left(1 + \frac{\alpha_s}{\pi} + 1.411 \left(\frac{\alpha_s}{\pi} \right)^2 - 12.8 \left(\frac{\alpha_s}{\pi} \right)^3 + \dots \right) \quad (2.5)$$

with $N_c = 3$ the number of colors and e_q the charge of the active quark flavors (in units of the electron charge). Nonperturbative effects (resonance formation) become important again in the vicinity of the heavy-quark thresholds (charm and bottom). However, for thermal dilepton emission in heavy-ion reactions only the mass region below the charmonium resonances is of importance [32] (above, the contributions from primordial Drell-Yan annihilation and/or final-state charm and bottom decays dominate the invariant-mass spectrum). Thus, the following decomposition of the EM spectral function emerges:

$$\text{Im} \Pi_{\text{em}}^{\text{vac}}(M) = \begin{cases} \sum_{V=\rho,\omega,\phi} \left(\frac{m_V^2}{g_V} \right)^2 \text{Im} D_V^{\text{vac}}(M) & , \quad M < M_{\text{dual}}, \\ -\frac{M^2}{12\pi} \left(1 + \frac{\alpha_s(M)}{\pi} + \dots \right) N_c \sum_{q=u,d,s} (e_q)^2 & , \quad M > M_{\text{dual}}, \end{cases} \quad (2.6)$$

with $M_{\text{dual}} \simeq 1.5 - 2 \text{ GeV}$, and $\text{Im} D_V(M)$ denoting the imaginary parts of the vector-meson propagators (spectral functions). Without any medium modifications, dilepton experiments would measure the spectral shape of the (time-reversed) $e^+e^- \rightarrow \text{hadrons}$ cross section, folded with the temperature evolution of the system. Indeed, for high masses $M > M_{\text{dual}}$, where the vacuum spectrum is rather structureless and medium effects are expected to be small, this can be exploited to perform a measurement of the (highest) temperature of the system (much like for photons) [32]. At low masses, however,

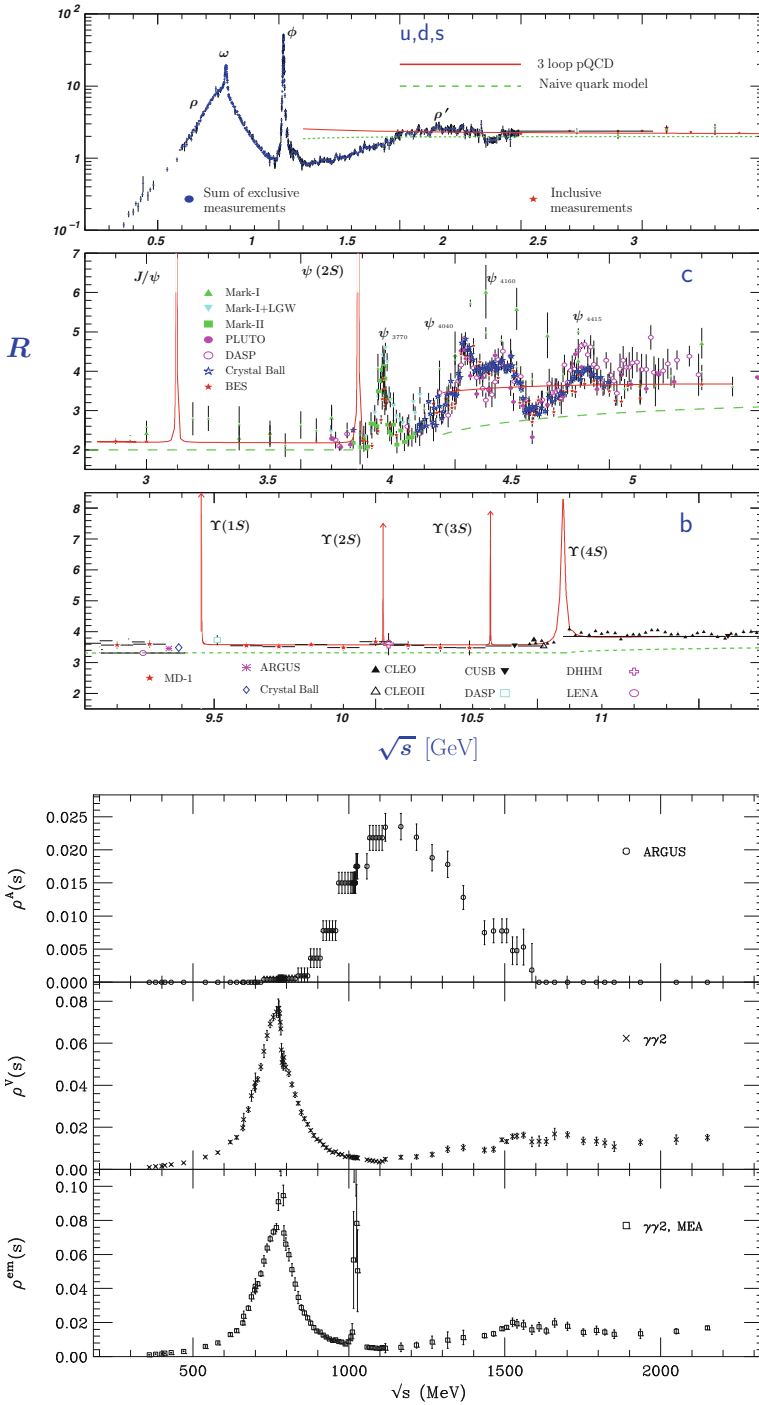


Fig. 2.1 (continued)

the key issue is to search for medium modifications in the (nonperturbative) resonance spectrum in order to probe the spectral properties of the matter in connection with possible phase changes.

The low-mass strength of the correlator is largely dominated by the isovector ρ^0 meson, with a relative strength of 10:1:2 for $\rho : \omega : \phi$, as encoded in the VDM couplings (or electromagnetic decay widths, $\Gamma_{V \rightarrow ee}$). Therefore, most of the efforts in evaluating medium effects in dilepton rates to date have focused on the ρ . We will discuss these in detail in Sect. 2.4. In the following subsection we briefly review model-independent approaches in terms of low-density expansions coupled with current algebra.

2.2.3 Low-density expansions and chiral mixing

The leading temperature dependence of the isovector part of the EM correlator (ρ channel) has been first elaborated in [33]. Using chiral reduction formulae to evaluate the matrix elements of the isovector-vector (V) correlator between thermal one-pion states, the results naturally involve its chiral partner, the isovector-axialvector correlator (A), i.e., the a_1 channel. In the chiral ($m_\pi=0$) and soft-pion limit (i.e., neglecting the thermal motion of the heat-bath pions in the arguments of the correlators), one finds the so-called chiral mixing formula,

$$\Pi_{V,A}(q) = (1 - \varepsilon) \Pi_{V,A}^0(q) + \varepsilon \Pi_{A,V}^0(q) \quad (2.7)$$

with the mixing parameter $\varepsilon = T^2/6f_\pi^2$. Thus, to leading order in T , the axial-/vector correlator does neither experience a broadening nor a mass shift, but a mere admixture of its chiral partner. Recalling the spectral densities of the free V and A correlators in the right upper two panels of Fig. 2.1, an immediate prediction of the chiral mixing would be an enhancement of the dilepton production rate in the region between the ρ and the duality threshold, M_{dual} . Such an effect might have been observed in the recent NA60 data [34], cf. the discussion in [35, 36]. In cold nuclear matter, chiral mixing has been worked out in [37, 38], while more advanced studies at finite temperature can be found in [39, 40]

An implementation of the mixing theorem into the dilepton rate based on experimental input for the EM spectral function has been given [31], yielding

Fig. 2.1 (continued) *Upper panel:* data compilation [30] of the ratio $R=\sigma(e^+e^- \rightarrow \text{hadrons})/\sigma(e^+e^- \rightarrow \mu^+\mu^-)$ for energy regimes covering the light-flavor (*top*), charm (*middle*) and bottom (*bottom*) sectors. *Dashed and dotted lines* depict the leading-order and 3-loop pQCD results, respectively, describing the nonresonant part of the ratio fairly well. *Lower panel:* Magnification of the vacuum isovector-axialvector (*top*), isovector-vector (*middle*), and EM spectral functions (*bottom*) in the regime relevant for thermal dilepton emission. Figure taken from [31].

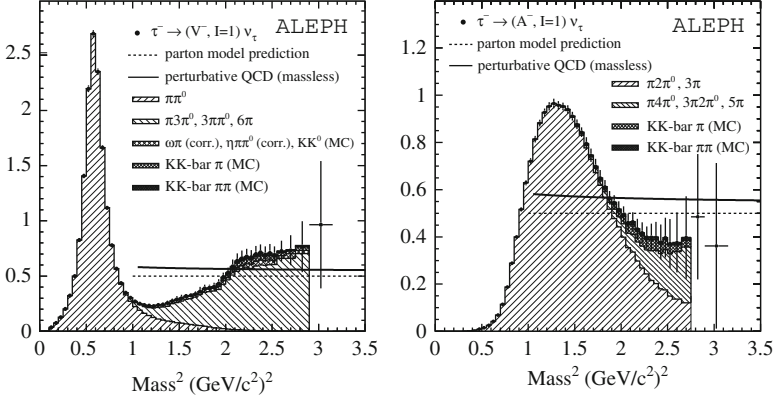


Fig. 2.2 Experimental data of the isovector-vector ($IJ^P = 11^-$, *left panel*) and isovector-axialvector ($IJ^P = 11^+$, *right panel*) spectral functions via hadronic decays of τ leptons (produced in $\sqrt{s}=91$ GeV e^+e^- annihilation at LEP) into even and odd numbers of pions/kaons, respectively. The *lines* indicate theoretical calculations using pQCD.

$$\frac{dN_{ll}}{d^4x d^4q} = \frac{4\alpha_{\text{em}}^2 f^B}{(2\pi)^2} \left\{ \rho_{\text{em}} - \left(\varepsilon - \frac{\varepsilon^2}{2} \right) (\rho_V - \rho_A) \right\}. \quad (2.8)$$

The inclusive EM spectral function, $\rho_{\text{em}} = -\text{Im} \Pi_{\text{em}}/(\pi s)$, as well as pertinent vector and axialvector spectral functions (corresponding to even- and odd-numbered pion states) are compiled in the lower panel of Fig. 2.1. Updated measurements with much improved precision and a more detailed decomposition of the hadronic final states have been performed through hadronic τ decays by the ALEPH [41] and OPAL [42] collaborations at LEP, cf. Fig. 2.2.

A more elaborate application of the virial expansion, coupled with chiral reduction techniques, has been carried out in [43], including contributions from a nucleonic medium [44, 45]. The calculations have been performed including the proper kinematics beyond the soft-pion and the chiral limit, which entails a reduction of the medium effects compared to the simple mixing formula, Eq. (2.7). However, the more elaborate treatment of medium effects, in particular those induced by nucleons (both resonant and nonresonant) leads to an appreciable increase of low-mass enhancement in the dilepton rate. While the resonance peaks are somewhat quenched, their width is not affected owing to the nature of the low-density expansion.

2.3 Sum rules

The generic idea of sum rules (SR's) in the QCD context is to establish a relation between (energy-) integrals (“sums”) over hadronic spectral func-

tions and the nonperturbative ground-state structure encoded in expectation values of pertinent correlators. The latter are then expanded in a series of more elementary quark and gluon condensates (plus perturbative terms to account for the high-energy behavior) and, therefore, provide a link between spectral properties and (chiral) order parameters. While it has been realized that SR's do not provide definite predictions for masses and widths of hadrons, they nevertheless constitute powerful constraints on model spectral functions, especially when applied at finite baryon density and temperature, where the condensates are expected to change appreciably. Ideally, the in-medium condensates are evaluated in lattice QCD, but in practice one often takes recourse to low- ρ_B - T expansions. In the following, we will distinguish and discuss two classes of SRs: QCD Sum Rules (QCDSRs) [46] (Sect. 2.3.1) and Chiral Sum Rules (CSRs) [47] (Sect. 2.3.2).

2.3.1 QCD sum rules

In this subsection, we first recall the general setup of the QCD sum rule approach, followed by a discussion of its main input, i.e., quark and gluon condensates and their modifications in matter. We then focus on applications to vector mesons, in particular ρ and ω .

2.3.1.1 General setup

QCDSRs have been devised by Shifman et al. [46] as a nonperturbative method to evaluate empirical properties of hadronic current correlation functions in QCD, generically written via expectation values of the type

$$\Pi_X(q) = \int d^4x e^{iqx} \langle \Omega | T j_X(x) j_X(0) | \Omega \rangle, \quad (2.9)$$

where $|\Omega\rangle$ denotes the ground state of the system (either in vacuum or at finite temperature/density) and X the (hadronic) quantum numbers of the current under consideration (at $T > 0$, the time-ordered correlator should be replaced by the retarded one). Exploiting analyticity one can formulate a (suitably subtracted) dispersion relation,⁴

⁴ The notion “sum rule” is actually related to the dispersion integral, not the sum on the r.h.s. of Eq. (2.11). The spirit of the SR is as usual: the integral over excitation strength (r.h.s.) is related to a model independent quantity (l.h.s.). For instance, the famous Thomas-Reiche-Kuhn SR for dipole strength of a nucleus with Z protons and N neutrons reads $\sum_{\beta} \int dE_{\beta} \sigma_{abs} = \frac{2\pi^2 \hbar}{Mc} \frac{NZ}{A} (1 + \mathcal{V})$, where \mathcal{V} accounts for exchange forces among nucleons, and the l.h.s. is the absorption cross section integrated over all $E1$ transitions from the ground state to excited states labelled by β , cf., e.g., [48].

$$\frac{\Pi(Q^2)}{Q^2} = \frac{\Pi(0)}{Q^2} - \Pi'(0) + Q^2 \frac{1}{\pi} \int_0^\infty ds \frac{\text{Im}\Pi(s)}{s^2(s+Q^2)}, \quad (2.10)$$

where $Q^2 \equiv -q^2 > 0$ denotes a spacelike four-momentum q , and $\Pi(0)$ and $\Pi'(0)$ are subtraction constants. The basic idea of the QCDSR approach is to evaluate both sides of Eq. (2.10) using different techniques thereby establishing a link between empirical information (spectral functions) and ground-state properties (condensates). For sufficiently large momenta, the left-hand-side (l.h.s.) of Eq. (2.10) can be expanded in inverse powers of Q^2 according to Wilson's operator-product expansion (OPE),

$$\frac{\Pi(Q^2)}{Q^2} = -c_0 \log \frac{Q^2}{\mu^2} + \sum_{j=1}^{\infty} \frac{c_j}{Q^{2j}}, \quad (2.11)$$

where the coefficients c_j are composed of perturbatively calculable (Wilson) coefficients and Q^2 -independent expectation values of matrix elements of quark and gluon field operators, the so-called condensates. The latter encode all the nonperturbative physics and represent a series of power corrections to the perturbative coefficient c_0 . The right-hand-side (r.h.s.) of Eq. (2.10) involves timelike spectral functions which can either be taken directly from experiment (as, e.g., in Eq. (2.4), where $\text{Im}\Pi_{\text{em}} \propto \sigma_{e^+e^- \rightarrow \text{hadrons}}$) or calculated in a hadronic model approach (as is typically the case for in-medium applications). To improve the convergence of the dispersion integral one usually applies a so-called Borel transformation [49] which converts the Q^2 variable into the Borel mass \mathcal{M} ; the sum rule then takes the form

$$\Pi(0) - \frac{1}{\pi} \int_0^\infty ds \frac{\text{Im}\Pi(s)}{s} e^{-s/\mathcal{M}^2} = c_0 \mathcal{M}^2 + \sum_{j=1}^{\infty} \frac{c_j}{(j-1)! \mathcal{M}^{2j}}. \quad (2.12)$$

For a reliable evaluation of the sum rule a reasonably large range in \mathcal{M} needs to be established over which the result is stable, i.e. independent of \mathcal{M} within a ‘‘Borel window’’. Besides the spectral function, a key ingredient are the coefficients c_j , especially their quark- and gluon-condensate dependence. In practice, the OPE is truncated after a few terms keeping the lowest-dimension condensates including the chiral condensate $\langle\langle \bar{q}q \rangle\rangle$, 4-quark condensates $\langle\langle \bar{q}\Gamma q \bar{q}\Gamma' q \rangle\rangle$ (with Γ, Γ' Dirac-color-flavor matrices), the gluon condensate $\langle\langle \frac{\alpha_s}{\pi} G^2 \rangle\rangle$ (signifying the breaking of scale invariance), and mixed quark-gluon condensates, e.g., $\langle\langle \bar{q}g_s \sigma_{\mu\nu} G^{\mu\nu} q \rangle\rangle$. The condensates therefore represent order parameters of different symmetry breakings.

Historically, QCDSRs have been first applied to the vacuum meson spectrum [50], in particular light vector mesons, and subsequently extended to baryons [51]. The first in-medium application was conducted at finite temperature in [52], and for a cold nuclear medium in [53], both focusing on the changes in the pole masses of vector mesons. More recent applications includ-

ing medium effects on the widths in the vector-meson spectral functions can be found in [54–58].

2.3.1.2 In-medium condensates

When applying QCD sum rules to in-medium correlators, the key role on the OPE side is attached to the temperature and density dependence of the condensates. Ideally, these would be taken from lattice QCD calculations, but currently the latter are not easily applied to both higher dimension condensates as well as finite baryon (or quark) chemical potential. Therefore, one usually takes recourse to low-temperature and -density expansions. For a given (quark-/gluon-) operator \mathcal{O} , the leading terms are given in the dilute gas approximation for non-interacting pions and nucleons as

$$\langle\langle\mathcal{O}\rangle\rangle = \langle\mathcal{O}\rangle_0 + \frac{\varrho_N}{2m_N} \langle N|\mathcal{O}|N\rangle + \frac{T^2}{8} \langle\pi|\mathcal{O}|\pi\rangle + \cdots, \quad (2.13)$$

where $\langle\mathcal{O}\rangle_0$ denotes the vacuum expectation value. The (scalar) pion density has been expressed in terms of the temperature T in (2.13) which is valid for massless pions. While the pion matrix elements $\langle\pi|\mathcal{O}|\pi\rangle$ can be evaluated in a model-independent way using soft pion theorems (in analogy to the low-density expansions discussed in Sect. 2.2.3), first principle information on the nucleon matrix elements $\langle N|\mathcal{O}|N\rangle$ is more difficult to obtain and often substituted by empirical information (cf. also [59] for an alternative approach). For analyses going beyond the leading terms see, e.g., [60–62]. For finite density the leading terms for the chiral condensate and for the gluon condensate are given model independently by the Hellmann-Feynman theorem and by the trace anomaly, respectively [63, 64]. Numerically, these leading terms can be estimated as

$$\langle\langle\bar{q}q\rangle\rangle \simeq \langle\bar{q}q\rangle_0 \left(1 - 0.33 \frac{\varrho_N}{\varrho_0}\right), \quad (2.14)$$

$$\langle\langle\frac{\alpha_s}{\pi}G^2\rangle\rangle \simeq \langle\frac{\alpha_s}{\pi}G^2\rangle_0 \left(1 - 0.077 \frac{\varrho_N}{\varrho_0}\right). \quad (2.15)$$

Temperature effects in the gluon condensate are presumably small below $T \simeq 100$ MeV, but significant for the quark condensate (cf. Eq. (2.16) below). Following [65], both condensates are displayed in Fig. 2.3, where especially the strong density dependence of the chiral condensate $\langle\langle\bar{q}q\rangle\rangle$ is noteworthy.

The leading terms for the quark condensate in Eq. (2.13) can also be formulated in terms of the hadronic “ σ ” terms and the pertinent scalar densities, ϱ_h^s , as [66, 67]

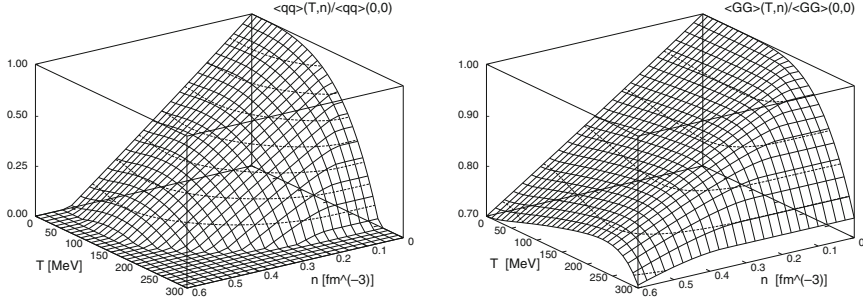


Fig. 2.3 Density and temperature dependence of the chiral condensate (*left panel*) and the gluon condensate (*right panel*) normalized to their vacuum values [65]. The calculation is based on a low-temperature and low-density expansion and therefore only qualitative for larger values of T and ϱ_N ($=n$).

$$\begin{aligned} \frac{\langle \bar{q}q \rangle}{\langle \bar{q}q \rangle_0} &\simeq 1 - \sum_h \frac{\Sigma_h \varrho_h^s}{f_\pi^2 m_\pi^2} \\ &\simeq 1 - \frac{T^2}{8f_\pi^2} - 0.33 \frac{\varrho_N}{\varrho_0} , \end{aligned} \quad (2.16)$$

where the last expression holds only for massless pions (and with a $\sim 20\%$ uncertainty on the density coefficient induced by the nucleon σ -term, $\Sigma_N = 45 \pm 15$ MeV).

The rather poorly known higher order condensates and their density dependence constitute some of the current limitations of the QCDSR approach (as well as practical problems with a unique definition of the Borel window). We also recall that sum rules do not directly determine the properties of a specific hadronic state (such as its mass or width), but a weighted integral over the spectral function, i.e., a strength distribution.

2.3.1.3 QCD sum rules for vector mesons in medium

In the following we will concentrate on light vector-meson currents, $j_X = j_V^\mu$, which in quark basis decomposes into isospin-0 (ω) and isospin-1 (ρ) channels according to

$$j_\mu^\omega = \frac{1}{6} (\bar{u}\gamma_\mu u + \bar{d}\gamma_\mu d) , \quad (2.17)$$

$$j_\mu^\rho = \frac{1}{2} (\bar{u}\gamma_\mu u - \bar{d}\gamma_\mu d) . \quad (2.18)$$

We will restrict ourselves to mesons at rest in the thermal rest frame, i.e., $\mathbf{q} = 0$, which implies degeneracy of transverse and longitudinal components, and

therefore it is sufficient to consider $\Pi_V = g_{\mu\nu} \Pi_V^{\mu\nu} / 3$. The explicit form of the coefficients c_j up to order α_s , up to mass dimension 6 for scalar condensates and up to twist 2 for non-scalar condensates, can be found, e.g. in [68]. Note that for vector mesons the Landau damping corresponds to subtraction constants like $\text{Im}\Pi(0)$ which are related to the forward scattering amplitude in the Thomson limit [69]. The quark currents of the ρ and ω mesons only differ by the relative sign of the two contributions. Correspondingly, the sum rule for the ρ meson is very similar to that of the ω meson, except for some sign changes in the four-quark condensates. If one uses factorization for the four-quark condensates even this difference vanishes (this explains, e.g., the near degeneracy of ρ and ω mesons in vacuum; even though their widths differ by a factor of almost 20; the ρ width appears to be still narrow enough to not affect the dispersion integral appreciably). In medium further terms arise which have different signs. It is, however, the different Landau damping term causing the main difference of ρ and ω in a medium.

Two further approximations are commonly applied, especially in earlier works. First, the spectral function is decomposed into a resonance part with a single state characterized by the pole position and its residue, and a perturbative continuum part, represented by the ansatz

$$\frac{1}{\pi} \text{Im}\Pi_V(s) = F_V \delta(s - m_V^2) + \frac{1}{\pi} \text{Im}\Pi_V^{\text{cont}}(s) \Theta(s - s_{th}) \quad (2.19)$$

(s_{th} : continuum threshold). Upon replacing $\text{Im}\Pi_V^{\text{cont}}(s)$ by the corresponding expression in the perturbative part, c_0 , of the OPE, the sum rule Eq. (2.12) turns into a relation for the pole mass m_V and its residue F_V . This procedure is called “narrow (zero) width approximation”. However, the ansatz Eq. (2.19) may no longer be justified if large widths and/or multiple structures arise in the spectral function (as borne out of hadronic many-body calculations discussed in Sect. 2.4), and consequently has been improved upon. Second, the higher order condensates are used within an factorization assumption which also has given rise to concerns.

2.3.1.4 Survey of approaches

A compilation of QCD sum rule applications to in-medium vector mesons is given in Table 2.1. The main differences between the approaches lie in the treatment of (i) the hadronic spectral function (e.g. zero-width approximation vs. detailed hadronic models), (ii) the Landau damping term, and, (iii) approximations to the condensates on the OPE side (truncation of the expansion at a given mass-dimension d , factorization of higher-order condensates). In the following, we discuss separately the cases of ρ and ω mesons, as well as their relation.

Table 2.1 Examples of in-medium QCD sum rules applications to light vector (and axial-vector) mesons (only first authors are quoted). “ κ values” concern the evaluation of four-quark condensates, “zero-width”, “Breit-Wigner” and “res.-hole” concern the modeling of the low-energy spectral functions, “V-A mix” denotes mixing of vector and axial-vector spectra, “factor.” indicates factorization of four-quark condensates, “current alg.” indicates the evaluation of four-quark condensates with respect to soft pions, “VDM” denotes vector dominance models.

	Hadron	Range	Hadronic model	OPE side	κ values
Dey [33]	ρ, a_1	$T \neq 0$	Zero width, V-A mix	None	
Hatsuda [53]	ρ, ω, ϕ	$\varrho_N \neq 0$	Zero-width	$d \leq 6$	Factor.
Hatsuda [70]	ρ, ω, a_1	$T \neq 0$	Zero-width	$d \leq 6$	Current alg.
Asakawa [54]	ρ	$\varrho_N \neq 0$	VDM	$d \leq 6$	Factor.
Eletsky [71]	ρ, a_1	$T \neq 0$	Zero-width	$d \leq 6$	Current alg.
Hatsuda [72]	ρ, ω	$\varrho_N \neq 0$	Zero-width	$d \leq 6$	Factor.
Jin [73]	ρ, ω, ϕ	$\varrho_N \neq 0$	Zero-width	$d \leq 6$	Factor.
Koike [74]	ρ, ω, ϕ	$\varrho_N \neq 0$	Zero-width	$d \leq 6$	Factor.
Klingl [55]	ρ, ω, ϕ	$\varrho_N \neq 0$	Chiral SU(3) VDM	$d \leq 6$	Admitted
Lee [75]	ρ, ω, ϕ	$\varrho_N \neq 0$	$\mathbf{q} \neq 0$	$d \leq 6$	Factor.
Leupold [56]	ρ	$\varrho_N \neq 0$	Breit-Wigner	$d \leq 6$	Admitted
Leupold [76]	ρ	$\varrho_N \neq 0$	$\mathbf{q} \neq 0$	$d \leq 6$	Admitted
Hofmann [77]	ρ	$T \neq 0$	Zero-width	$d \leq 6$	Dim. scal.
Marco [78]	ρ, a_1	$T \neq 0$	V-A mix	$d \leq 4$	
Zschocke [57]	ρ, ω, ϕ	$T, \varrho_N \neq 0$	Zero-width	$d \leq 6$	Admitted
Zschocke [79]	ρ, ω	$\varrho_N \neq 0$	In-med. propag.	$d \leq 6$	Admitted
Thomas [279]	ω	$\varrho_N \neq 0$	Normal. moment	$d \leq 8$	Adjusted
Ruppert [58]	ρ	$\varrho_N \neq 0$	Breit-Wigner	$d \leq 6$	Adjusted
Steinmüller [81]	ω	$\varrho_N \neq 0$	Breit-Wigner, res.-hole	$d \leq 6$	Admitted

2.3.1.5 ρ meson

A generic feature of QCDSR’s for the ρ is that the in-medium reduction of the condensates typically requires a softening of the hadronic spectral density. In early works [53, 70], based on the narrow width approximation (and for nuclear densities on the factorization of the 4-quark condensates), it was thus predicted that the ρ meson mass drops with increasing temperature and density. In [54] effects of the $\Delta(1, 232)$ -nucleon-hole polarization on the pion were included in the ρ spectral function, but its mass was still found to drop. In [55] a more elaborate treatment of the finite-density effects on the pion cloud of the ρ was carried out, and the QCDSR was found to be satisfied without invoking additional mass shifts. In [56] a more general analysis was performed based on Breit-Wigner parametrizations with variable width and mass. It was found that the sum rules only constrain a correlation of the resonance parameters, i.e., the softening dictated by the reduced condensates can be saturated by either a reduction in mass or an increase in width, or a combination of both, see Fig. 2.4. This clearly illustrates the point that QCDSR’s are not able to *predict* spectral shapes, but rather provide *constraints*.

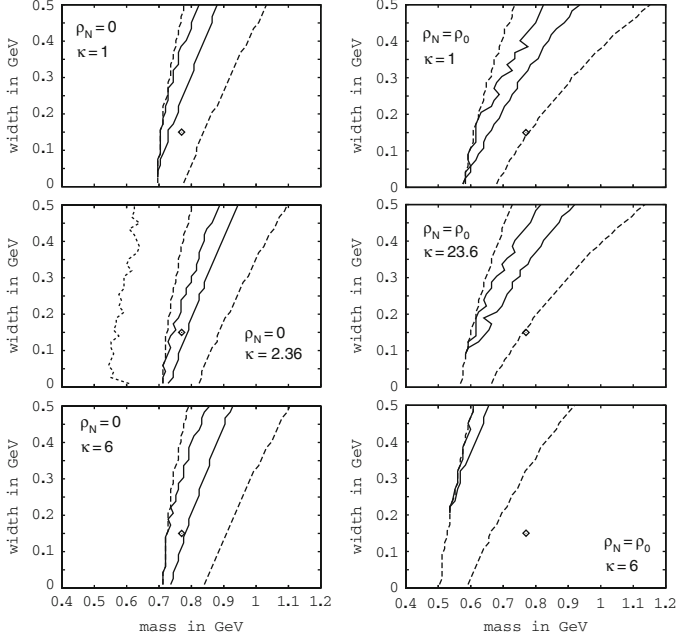


Fig. 2.4 QCD sum rule constraints on ρ meson mass and width as inferred from Breit-Wigner parameterizations of its spectral function [56] (*left panel*: vacuum, *right panel*: cold nuclear matter at saturation density). “Allowed” regions of mass and width are indicated by the bands between *solid* and *dashed curves*, corresponding to maximal deviations between the l.h.s and r.h.s. of the SR of 0.2 and 1%, respectively. The *diamond* depicts the corresponding vacuum parameters. The *upper*, *middle* and *lower panels* illustrate the uncertainty induced by the parameter κ used in the factorization of the 4-quark condensates, $\langle\langle\bar{q}\Gamma q\bar{q}\Gamma'q\rangle\rangle \rightarrow \langle\langle(\bar{q}q)^2\rangle\rangle \rightarrow \kappa\langle\langle\bar{q}q\rangle\rangle^2$.

2.3.1.6 ω meson

Similar to the ρ meson, the narrow width approximation for the ω (which, after all, may be better justified) leads to the prediction [53] that its mass drops with increasing nuclear density. However, at finite temperature the ω mass seems to stay essentially constant [70]. According to [55] the dropping mass at finite nuclear densities persists when finite-density effects on the pion cloud are incorporated in the ω spectral function, although this finding has been challenged in later, more elaborate, calculations [81–83].

Let us be more specific and focus on density effects. The integral in Eq. (2.12) can be decomposed into a low-lying resonance part, namely $\int_0^{s_\omega} ds \text{Im} \Pi_\omega(s, \varrho_N) s^{-1} e^{-s/\mathcal{M}^2}$, and a continuum part,

$$\int_{s_\omega}^{\infty} ds \text{Im} \Pi_\omega(s, \varrho_N) s^{-1} e^{-s/\mathcal{M}^2} \equiv -\pi \mathcal{M}^2 c_0 e^{-s_\omega/\mathcal{M}^2}, \quad (2.20)$$

both depending on the continuum threshold s_ω . The quantity

$$m_\omega^2(\varrho_N, \mathcal{M}^2, s_\omega) \equiv \frac{\int_0^{s_\omega} ds \operatorname{Im} \Pi_\omega(s, \varrho_N) e^{-s/\mathcal{M}^2}}{\int_0^{s_\omega} ds \operatorname{Im} \Pi_\omega(s, \varrho_N) s^{-1} e^{-s/\mathcal{M}^2}} \quad (2.21)$$

is a normalized moment which characterizes the center of gravity of the weighted spectral function, $\operatorname{Im} \Pi_\omega(s, \varrho_N) e^{-s/\mathcal{M}^2}/s$, in the interval $s = 0 \cdots s_\omega$. Clearly, when additional strength of $\operatorname{Im} \Pi_\omega$ at lower values of s is caused by in-medium effects (as, e.g., suggested by recent experiments [84, 85]), the above defined value of m_ω is diminished. Truncating Eq. (2.12) at $j = 4$, Eq. (2.21) for the ω meson can be arranged as

$$m_\omega^2(\varrho_N, \mathcal{M}^2, s_\omega) = \frac{c_0 \mathcal{M}^2 \left[1 - \left(1 + \frac{s_\omega}{\mathcal{M}^2} \right) e^{-s_\omega/\mathcal{M}^2} \right] - \frac{c_2}{\mathcal{M}^2} - \frac{c_3}{\mathcal{M}^4} - \frac{c_4}{2\mathcal{M}^6}}{c_0 \left(1 - e^{-s_\omega/\mathcal{M}^2} \right) + \frac{c_1}{\mathcal{M}^2} + \frac{c_2}{\mathcal{M}^4} + \frac{c_3}{2\mathcal{M}^6} + \frac{c_4}{6\mathcal{M}^8} - \frac{\Pi^\omega(0, \varrho_N)}{\mathcal{M}^2}}. \quad (2.22)$$

Following [57, 68], the sum rule is handled as usual by determining the sliding Borel window requiring that (1) the sum of the $c_{3,4}$ terms in Eq. (2.12) does not contribute more than 10% to the r.h.s., (2) the continuum part defined above does not exceed 50% of the integral on the l.h.s. of (2.12) to ensure sufficient sensitivity to the resonance part, (3) the continuum threshold satisfies maximum flatness of $m_\omega^2(\varrho_N, \mathcal{M}^2, s_\omega)$ within the Borel window, (4) a sensible value of m_ω^2 follows as average with respect to \mathcal{M}^2 .

It turns out that the chiral condensate enters the SR for the light vector mesons only in the renormalization invariant combination $m_q \langle \bar{q}q \rangle$. Numerically, this term is negligible, i.e. this order parameter of chiral symmetry breaking does practically not influence the SR for ρ and ω mesons.⁵ In contrast, the 4-quark condensates have a strong impact. As pointed out in [80], from the experimental data in [85] one can deduce that a certain combination of 4-quark condensates must undergo a strong density dependence, see Fig. 2.5. This is in line with arguments based on a large- N_c expansion according to which the 4-quark condensates have often been factorized into squares of the chiral condensate. The occasionally quoted dependence on the chiral condensate is in fact a dependence on various 4-quark condensates.

As an example, let us briefly sketch the procedure adopted in [80]. The 4-quark condensates that enter in the ω sum rule are

⁵ Another connection to an order parameter of chiral symmetry breaking, namely to the pion decay constant f_π , is suggested in [86] based on the hypothesis of identifying the continuum threshold with the chiral gap, i.e., $s_\rho \equiv 4\pi f_\pi$. In a hierarchy of moments of the spectral integrals, the lowest moments avoid higher-order condensates. For example, for the in-medium ρ spectral function of [55], the moment corresponding to the in-medium ρ mass (in cold nuclear matter) resembles Brown-Scaling, while for the ρ spectral function of [87, 88] the pertinent moment exhibits little density dependence.

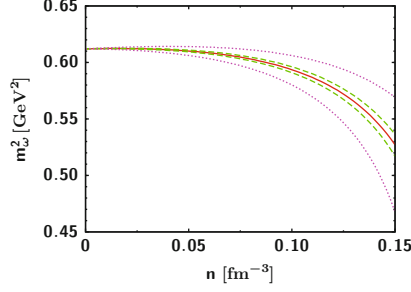


Fig. 2.5 The mass parameter m_ω^2 defined in Eq. (2.21) and averaged within the Borel window as a function of the baryon density ($n \equiv \varrho_N$) for $\kappa_N=4$ and $c_4=0$ (solid curve). m_ω^2 coincides with the ω pole mass squared only in zero-width approximation; in general it is a normalized moment of $\text{Im}\Pi^\omega$ to be calculated from data or models. The sum rule Eq. (2.22) is evaluated as described in the text with appropriately adjusted κ_0 . Inclusion of $c_4^{(0)} = \mathcal{O}(\pm 10^{-3})$ GeV⁸ requires a readjustment of κ_0 in the range $1 \dots 5$ to $m_\omega^{(0)2}$. A simultaneous change of κ_N of $\sim 20\%$ is needed to recover the same density dependence as given by the solid curve at small values of ϱ_N . The effect of a $c_4^{(1)}$ term is exhibited using $c_4^{(1)} = \pm 10^{-5} n_0^{-1}$ GeV⁸: dashed curves, $c_4^{(1)} = \pm 5 \cdot 10^{-5} n_0^{-1}$ GeV⁸; dotted curves; the upper (lower) curves are for negative (positive) signs.

$$\langle \langle \bar{u}\gamma^\mu \lambda_A u \bar{d}\gamma_\mu \lambda_A d \rangle \rangle = -\kappa_1 \frac{4}{9\pi^2} \frac{Q_0^2}{f_\pi^2} \langle \langle \bar{q}q \rangle \rangle^2 \quad (2.23)$$

$$\langle \langle \bar{u}\gamma_5\gamma^\mu \lambda_A u \bar{d}\gamma_5\gamma_\mu \lambda_A d \rangle \rangle = \kappa_2 \frac{4}{9\pi^2} \frac{Q_0^2}{f_\pi^2} \langle \langle \bar{q}q \rangle \rangle^2, \quad (2.24)$$

$$\langle \langle \bar{q}\gamma^\mu \lambda_A q \bar{q}\gamma_\mu \lambda_A q \rangle \rangle = -\frac{16}{9} \kappa_3 \langle \langle \bar{q}q \rangle \rangle^2, \quad (2.25)$$

$$\langle \langle \bar{q}\gamma_5\gamma^\mu \lambda_A q \bar{q}\gamma_5\gamma_\mu \lambda_A q \rangle \rangle = \frac{16}{9} \kappa_4 \langle \langle \bar{q}q \rangle \rangle^2, \quad (2.26)$$

where Q_0 is a cutoff related to the ρ - ω mass splitting. All expressions go beyond the ground state saturation (factorization approximation) which is recovered for $\kappa_{1,2} = 0$ and $\kappa_{3,4} = 1$. Following [80] we proceed as follows: expand κ_Ω in density, i.e., $\kappa_\Omega = \kappa_\Omega^{(0)} + \kappa_\Omega^{(1)} \varrho_N$, use the known sigma term σ_N in $\langle \langle \bar{q}q \rangle \rangle = \langle \bar{q}q \rangle_0 + \xi \varrho_N$ with $\xi = \sigma_N/(2m_q)$, linearize the resulting expressions, add up all contributions with their corresponding pre-factors to get a common factor $\kappa_0 = \frac{9}{28\pi^2} \frac{-Q_0^2}{f_\pi^2} (\frac{2}{9}\kappa_1^{(0)} - \kappa_2^{(0)}) - \frac{2}{7}\kappa_3^{(0)} + \frac{9}{7}\kappa_4^{(0)}$ for the vacuum contribution, $-\frac{112}{81}\pi\alpha_s\kappa_0\langle \bar{q}q \rangle_0^2$, and a common factor $\kappa_N = \kappa_0 + \frac{\langle \bar{q}q \rangle_0}{2\xi} \left(\frac{9}{28\pi^2} \frac{-Q_0^2}{f_\pi^2} (\frac{2}{9}\kappa_1^{(1)} - \kappa_2^{(1)}) - \frac{2}{7}\kappa_3^{(1)} + \frac{9}{7}\kappa_4^{(1)} \right)$ for the density dependent medium contribution of the above four-quark condensates. κ_0 figures into the vacuum sum rule and has to be adjusted properly together with other quantities to recover the empirical vacuum ω mass, while κ_N is discussed furtherin

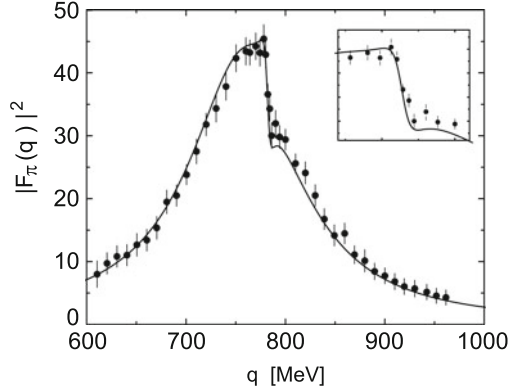


Fig. 2.6 The pion form factor exhibiting ρ - ω mixing. Data are from [89] and the curves from a QCD sum rule evaluation [68].

connection with Fig. 2.5; due to the mixing of density dependencies of κ_Ω and $\langle\bar{q}q\rangle$ even an accurate knowledge of κ_0 does not fix κ_N .

Given the above empirical constraints on the 4-quark condensates the in-medium behavior of the OPE side is largely determined also for the ρ meson. However, the Landau damping term for the ρ meson is by a factor $1/9$ smaller, which implies that the softening of the ρ spectral function is much more pronounced (in agreement with previous analyses [53]). In addition, the ω decay to $\pi^+\pi^-$ (with a small branching ratio of $BR = 2.21 \pm 0.3\%$ [30]) gives rise to ρ - ω mixing as seen experimentally in the deformation of the pion form factor, cf. Fig. 2.6. In fact, this interference might play an important role in the interpretation of medium effects in the ρ - ω region in situations where the ω contribution is large, e.g., in proton-induced production off nuclei, $p + A \rightarrow e^+e^-X$ [84, 90].

2.3.2 Chiral sum rules and axialvector spectral function

The closest connection between the (in-medium) vector-isovector spectral function (which can be probed by dilepton observables) and chiral restoration is probably given by Weinberg sum rules which have been derived prior to QCD based on current algebra [47]. As a brief reminder, we recall that the QCD Lagrangian is, up to order $\mathcal{O}(m_q)$, invariant under chiral rotations $R(\alpha_{L,R}) \equiv \exp[-i\alpha_{L,R} \cdot \boldsymbol{\tau} \gamma_\pm]$ of the (light) quark fields, where $\boldsymbol{\tau}$ are the standard Pauli matrices in isospin space and $\gamma_\pm = 1/2(1 \pm \gamma_5)$ are the left-/right-handed projection operators ($q_{L,R} = \gamma_\mp q$). The ground state of QCD, however, is characterized by a complicated (quark- and gluon-) con-

densate structure (the Nambu Goldstone phase, as opposed to the “trivial” Wigner-Weyl phase). Most notably, the scalar quark condensate, $\langle 0|\bar{q}q|0\rangle = \langle 0|\bar{q}_L q_R + \bar{q}_R q_L|0\rangle$, exhibits a maximal violation of chiral symmetry, and is intimately related to the generation of constituent quark masses, $m_q^* \simeq -G\langle 0|\bar{q}q|0\rangle \simeq 0.35 - 0.4$ GeV, and thus of more than 95% of the visible mass in the Universe. Neither condensates nor the quark mass are directly accessible in experiment. However, observable consequences of the spontaneous breaking of chiral symmetry can be found in the physical excitations of the ground state, i.e., in the (low-lying) hadron spectrum. The (almost) massless pions are believed to be the Goldstone bosons of the unbroken directions of the chiral group, i.e., pions emerge as a chiral rotation of the scalar-isoscalar σ (the condensate channel). More generally, the hadron spectrum is characterized by non-degenerate chiral partners (hadronic multiplets transforming into each other under chiral rotations), split in mass by typically $\Delta M = 0.5$ GeV, e.g., $\pi(140) - \sigma(400-1,200)$, $\rho(770) - a_1(1260)$ and $N-N^*(1,535)$, see also Sects. 3.2.1 and 4.1.5.

Weinberg sum rules precisely quantify the relation between chiral order parameters (e.g., quark condensates or the pion “pole strength” (decay constant), f_π) and differences of (moments of) vector-isovector (“ ρ ”) and axialvector-isovector (“ a_1 ”) spectral functions. As such, they are more directly related to chiral symmetry and its spontaneous breaking than QCD sum rules, and thus are ideally suited to connect (the approach) to chiral restoration (vanishing of order parameters) to in-medium vector spectral functions (and eventually to dilepton observables). In vacuum they read⁶

$$-\int_0^\infty \frac{ds}{\pi s^2} [\text{Im} \Pi_V^{\text{vac}}(s) - \text{Im} \Pi_A^{\text{vac}}(s)] = f_\pi^2 \frac{\langle r_\pi^2 \rangle}{3} - F_A, \quad (2.27)$$

$$-\int_0^\infty \frac{ds}{\pi s} [\text{Im} \Pi_V^{\text{vac}}(s) - \text{Im} \Pi_A^{\text{vac}}(s)] = f_\pi^2, \quad (2.28)$$

$$-\int_0^\infty \frac{ds}{\pi} [\text{Im} \Pi_V^{\text{vac}}(s) - \text{Im} \Pi_A^{\text{vac}}(s)] = 0, \quad (2.29)$$

$$-\int_0^\infty s \frac{ds}{\pi} [\text{Im} \Pi_V^{\text{vac}}(s) - \text{Im} \Pi_A^{\text{vac}}(s)] = -2\pi\alpha_s \langle \langle \mathcal{O}_4 \rangle \rangle. \quad (2.30)$$

Equations (2.28) and (2.29) are the famous sum rules derived by Weinberg [47] based on chiral Ward identities (i.e., conserved vector and axi-

⁶ The form of the sum rules as written above applies to the chiral limit (vanishing current light-quark and pion masses). Corrections to the second Weinberg Sum Rule (WSR), Eq. (2.29), have been discussed, e.g., in [91–93], while the first WSR, Eq. (2.28), seems not to be affected.

axialvector currents in the chiral limit) and the assumption of free fields at high momenta (in the language of QCD, these would correspond to the perturbative limit where V and A correlators degenerate); $f_\pi=92$ MeV is the pion decay constant. In Eq. (2.27) [94], $\langle r_\pi^2 \rangle$ denotes the pion charge radius squared, and F_A the pion axialvector form factor. In Eq. (2.30), which was obtained well after the invention of QCD [95], $\langle \langle \mathcal{O}_4 \rangle \rangle$ denotes a combination of 4-quark condensates; e.g., in the factorization (or ground state) approximation it is given by $(16/9)\langle \langle \bar{q}q \rangle \rangle^2$. The direct connection of the chiral sum rules to the vector correlator renders them particularly valuable in the context of dilepton production. The assessment of in-medium effects requires their extension to finite temperature which has been elaborated in [95]. Due to loss of Lorentz-invariance, the original vacuum results become energy sum rules at fixed 3-momentum and split into longitudinal (L) and transverse (T) components of the correlators,

$$-\int_0^\infty \frac{dq_0^2}{\pi(q_0^2 - q^2)} [\text{Im}\Pi_V^L(q_0, q) - \text{Im}\Pi_A^L(q_0, q)] = 0, \quad (2.31)$$

$$-\int_0^\infty \frac{dq_0^2}{\pi} [\text{Im}\Pi_V^{L,T}(q_0, q) - \text{Im}\Pi_A^{L,T}(q_0, q)] = 0, \quad (2.32)$$

$$-\int_0^\infty q_0^2 \frac{dq_0^2}{\pi} [\text{Im}\Pi_V^{L,T}(q_0, q) - \text{Im}\Pi_A^{L,T}(q_0, q)] = -2\pi\alpha_s \langle \langle \mathcal{O}_4 \rangle \rangle. \quad (2.33)$$

The transverse and longitudinal components of the spectral functions are given in terms of standard projection operators,

$$\Pi_V^{\mu\nu} = \Pi_{V,A}^T P_T^{\mu\nu} + \Pi_{V,A}^L P_L^{\mu\nu}, \quad (2.34)$$

and we have absorbed the pionic piece of the (longitudinal) axialvector correlator (which in the vacuum reads $\text{Im}\Pi_\pi^{\mu\nu} = f_\pi^2 q^2 \delta(q^2) P_L^{\mu\nu}$) into the definition of the in-medium spectral function, $\text{Im}\Pi_A^L(q_0, q)$. This is motivated by the expectation that the pion itself will be subject to medium effects and thus its spectral function will no longer be represented by a δ -function.

The chiral sum rules clearly emphasize the necessity of incorporating the axialvector channel into the discussion of medium effects in dilepton production if firm conclusions about the nature of chiral restoration are to be drawn. In the vacuum, both V and A correlators have been measured with excellent precision up to $M \simeq 1.5$ GeV in τ -lepton decays at LEP by both the ALEPH [41] and OPAL [42] experiments, cf. left panel of Fig. 2.7. These data alone provide a rich testing ground for low-energy (“strong”) QCD. In particular, they very nicely illustrate spontaneous chiral symmetry breaking in the (nonstrange) $I = J = 1$ multiplet.

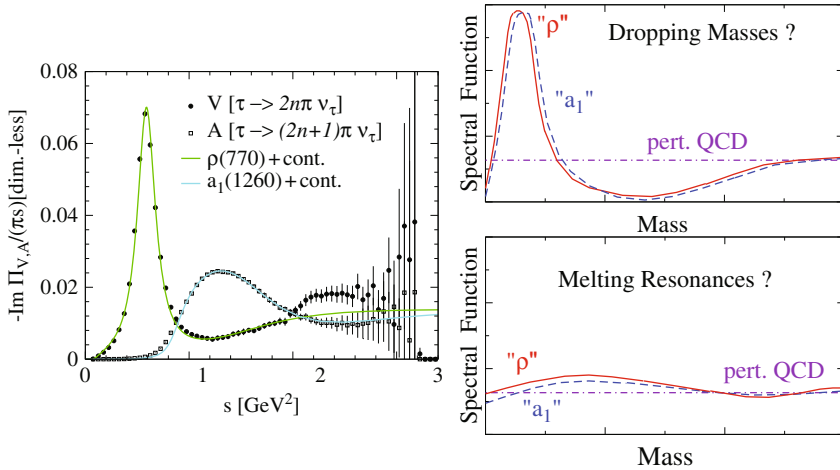


Fig. 2.7 *Left panel:* vector and axialvector spectral functions as measured in hadronic τ decays [41] with model fits using vacuum ρ and a_1 spectral functions plus perturbative continua [96]; *right panel:* schematic scenarios for chiral symmetry restoration in matter.

Chiral symmetry restoration at T_c requires that the V and A spectral functions become degenerate (up to corrections in the current up- and down-quark masses), which obviously requires a dramatic reshaping of either of the spectral functions, or (more likely) both. How this happens is one of the major objectives using dilepton measurements in heavy-ion collisions, and it will also illuminate the nature of mass generation as the strongly interacting matter of a fireball cools down below T_c . A direct experimental approach would be the simultaneous measurement of the axialvector spectral function (in addition to dileptons for the vector spectral function); in [97] it has been suggested to measure $\pi^\pm \gamma$ invariant mass spectra, as triggered by recent successes of measuring $\pi^+ \pi^-$ invariant mass spectra in Au–Au collisions at RHIC, with interesting results [98]. Nonetheless, the rather broad structures in the A channel, together with the large expected background, render a practical realization rather challenging (as a first step, and a proof of principle, such a measurement should be performed in more elementary systems, e.g., with pion beams at HADES; here, even 3-pion invariant mass spectra have been raised as a feasible option). The $\pi\gamma$ spectra have the additional disadvantage compared to dileptons that the emitted pion undergoes final-state absorption which will bias the emission of undistorted pairs toward the later (less hot and dense) stages of a heavy-ion collisions (however, it has one pion-absorption factor less than $\pi\pi$ spectra). The uncertainties in the experimental approach to extract the A spectral function mandate the theoretical tools to be sharpened to deduce chiral symmetry restoration from the dilepton spectra alone. We envisage the following 3-step strategy [27]:

- (1) Calculate vector (V) and axialvector (A) spectral functions as a function of invariant mass, 3-momentum, temperature and density (including phenomenological and theoretical constraints) in a chiral model (which gives, of course, a realistic description of vacuum data).
- (2) Insert the results into Weinberg sum rules to calculate the temperature dependence of pion decay constant and 4-quark condensate, and compare to results from lattice QCD (note that $f_\pi(T)$ and $\langle\langle(\bar{q}q)^2\rangle\rangle(T)$ are presumably more easily evaluated in lQCD than spectral functions; however, at finite densities lQCD results for these quantities may not become available in the near future).
- (3) Perform detailed comparisons of the in-medium effects on the vector correlator with dilepton data (centrality, excitation function, mass and q_t -spectra); this requires additional input from realistic model for the expansion dynamics (e.g. hydrodynamical and transport simulations), which, however, are/can be thoroughly tested against the large body of hadronic observables.

Consistency between (2) and (3) will provide rather direct evidence for chiral restoration (note that (2) involves several energy-moments of the V - A spectral functions and various chiral order parameters).

2.4 Vector mesons in medium: hadronic models

As elaborated above, dilepton production in the low-mass region is governed by the spectral functions of light vector meson, ρ , ω and ϕ . Since the ρ meson dominates the overall yield, many analyses have been performed to address its in-medium properties, cf. [15–19] for rather recent reviews. Consequently, our main emphasis will be on the ρ meson. With increasingly accurate information from experiment, however, both in reactions on cold nuclei [84, 85, 99] and in heavy-ion collisions [21], in-medium properties of ω and ϕ mesons are becoming accessible, especially since their contributions are rather localized in invariant mass. In addition to being interesting in their own right, it is obviously desirable to provide a unified theoretical description of the in-medium properties of light vector mesons.

Calculations of in-medium vector-meson properties have also been conducted in quark-based approaches, e.g., chiral quark models with Nambu–Jona-Lasinio [100, 101] or instanton-induced interactions [102]. In these approaches the medium effects are mainly induced by modifications of the quark-antiquark interaction within the meson, as well as condensate-driven changes of the constituent quark mass. Generically, it turns out that the modifications of the ρ meson mass are rather moderate (width effects are difficult to assess if quark confinement is not accounted for). However, as we will see below, the interactions of the vector mesons with surrounding hadrons in the heat bath are very important, typically leading to a substantial increase

Table 2.2 Survey of approaches to calculate light vector-meson spectral functions in a hot and/or dense hadronic medium. For details, see text.

Author(s)	Medium effects	Method	Vertex corrections
Asakawa [54] Chanfray [103] Herrmann [104]	Finite ϱ_N , 3-momentum $q=0$ pisobar $\pi\Delta N^{-1}$	Perturbative	Yes
Chanfray [105]	Finite ϱ_N and T , $q=0$ pisobars $\pi[N, \Delta]N^{-1}$	Perturbative	Yes
Friman [106]	Finite ϱ_N , $q \neq 0$ rhosobars $\rho[N(1,720), \Delta(1,905)]N^{-1}$	Perturbative	No
Rapp [87]	Finite ϱ_B and T $\pi[N, \Delta]N^{-1}$, $\pi[N, \Delta]\Delta^{-1}$ ($q=0$) $\rho[N, \Delta, N(1,720), \Delta(1,905)]N^{-1}$ + conjugate ($q \neq 0$)	Perturbative	Yes No
Klingl [55]	Finite ϱ_N and T , $q=0$ $\pi[N, \Delta]N^{-1}$	Perturbative	Yes
Peters [107]	Finite ϱ_N , $q \neq 0$ $\rho[N(1,520, 1,650, 1,720), \Delta(1,620, 1,700, 1,905)]N^{-1}$	Selfconsistent mass feedback	No
Rapp [88, 108] Urban [109]	Finite ϱ_B and T $\pi[N, \Delta]N^{-1}$ + conjugate ($q \neq 0$); $\rho[N, N(1,440, 1,520, 1,720, 2,000), \Delta, \Delta(1,620, 1,700, 1,905)]N^{-1}$, $\rho[A(1,520, 1,690, 1,820, 1,890), \Sigma(1,670, 1,915)]Y^{-1}$ + conj ($q \neq 0$); $\rho\pi[\omega, h_1, a_1, \pi', a_2, \omega(1,420, 1,650)]$, $\rho K[K^*, K_1]$, $\rho\rho f_1$ ($q \neq 0$)	Perturbative	Yes No No
van Hees [110]	Finite T $\rho\pi\pi$	Selfconsistent	Ps-1
Post [111]	Finite ϱ_N $\rho[N(1,520, 1,650, 1,720), \Delta, \Delta(1,620, 1,700, 1,905)]N^{-1}$ ($q \neq 0$)	Modified low density approx.	No
Cabrera [112]	Finite ϱ_N $\pi[N, \Delta]N^{-1}$ $\rho N(1520)N^{-1}$	Perturbative	Yes No
Riek [113]	Finite ϱ_N and T $\pi\rho\omega + \pi N\Delta$	Selfconsistent in two subsystems	Ps-1
Ruppert [114]	Finite T $\pi\rho$	Selfconsistent	Ps-1 Ps-2
Santini [115]	Finite ϱ_N $\rho[N(1,440, 1,520, 1,535, 1,650, 1,680, 1,720), \Delta, \Delta(1,620, 1,700, 1,905, 1,950)]N^{-1}$	Selfconsistent	No

in the vector meson's width. In this section, we therefore focus on hadronic model calculations, attempting a systematic discussion by confronting a selection of representative results of different approaches to extract common (robust) features. An initial overview of the considered approaches and some of their main features are compiled in Table 2.2. Predictions and/or con-

straints from QCD sum rules and lattice QCD are discussed separately in Sects. 2.3 and 2.5.1, respectively. We will classify the hadronic approaches for each of the three light vector mesons according to the different input assumptions and calculational techniques (e.g., perturbative evaluation of loops vs. selfconsistent schemes). Concerning input assumptions, we distinguish between approaches where the underlying parameters of the effective Lagrangian are kept constant (“hadronic many-body theory”) vs. those where the bare parameters are subjected to so-called “intrinsic” temperature and/or density dependencies, as e.g. in the works of Brown and Rho [116] or the more recent renormalization-group (RG) approach by Harada and Yamawaki [18]. To further facilitate the comparison, we will organize the discussion according to the type of medium: cold nuclear matter, hot meson gas and (combined) hot hadronic matter. For the CBM experiment, baryon effects are expected to dominate, but with anticipated temperatures well in excess of 100 MeV, thermal effects need to be addressed as well.

2.4.1 ρ meson

In this subsection we discuss medium modifications of the ρ propagator as obtained by hadronic many-body theory in cold nuclear matter (induced by a renormalization of its pion cloud (2.4.1.1) and by direct ρ - N resonance interactions (2.4.1.2)), in a hot meson gas (2.4.1.3), as well as in hot hadronic matter (2.4.1.4). We also present a renormalization group approach to evaluate ρ properties at finite temperature and density within a Hidden Local Symmetry model based on the “vector manifestation” of chiral symmetry. The latter, in particular, addresses medium effects on the bare parameters in the effective hadronic Lagrangian.

2.4.1.1 Cold nuclear matter I: pion cloud

Early investigations of ρ properties in nuclear matter have focussed on medium effects on its pion cloud via the rather well-known renormalization of the pion propagators via delta-nucleon-hole (ΔN^{-1}) [54, 103, 104] and nucleon-nucleon-hole (NN^{-1}) [55, 105, 112] excitations, as obtained in nuclear many-body theory. The generic result, obtained for vanishing 3-momentum of the ρ in the nuclear matter rest frame, is a substantial broadening of the ρ spectral function accompanied by a slight upward mass-shift of the peak position. A collective ΔN^{-1} mode induces additional strength (or even a peak structure) around $M = 0.4 - 0.5$ GeV, while NN^{-1} modes are found to be instrumental in shifting additional strength to low mass including below the 2π threshold. Quantitatively, these effects depend on the cutoff parameter of the πNN and $\pi N\Delta$ vertex formfactor. With $\Lambda_{\pi NN} = \Lambda_{\pi N\Delta} = 1-$

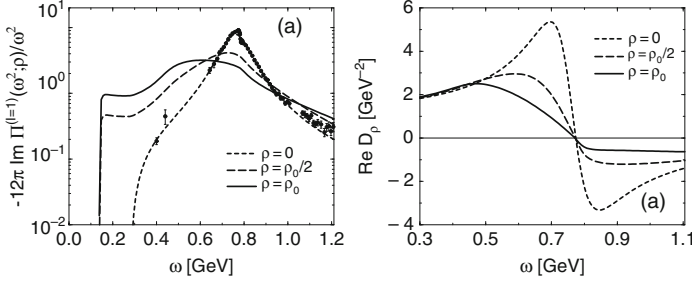


Fig. 2.8 Isovector-vector spectral function (ρ channel), divided by energy squared, (*left panel*) and pertinent real part of the ρ meson propagator (*right panel*) in cold nuclear matter ($\varrho_N = \varrho_0$) when dressing the pion cloud with ΔN^{-1} and NN^{-1} using hard formfactors, $\Lambda_{\pi NN, \Delta} \simeq 1$ GeV [55]. A substantial broadening is accompanied by a small (if any) mass shift.

1.2 GeV, as required in one-pion exchange potentials to fit N - N scattering, the ρ broadening at nuclear saturation density amounts to a total width of ~ 400 MeV [55, 87, 105], see, e.g., Fig. 2.8.

The calculations have been generalized to finite 3-momentum in [117], which is not only necessary for quantitative applications to dilepton and photon experiments, but also enables an important consistency check against nuclear photoabsorption data [118]. One finds that much softer πNN and $\pi N \Delta$ formfactor cutoffs are required ($\Lambda_{\pi NN} \simeq 0.3$ – 0.5 GeV) than implemented in the earlier works [54, 55, 103–105], and consequently the medium effects due to the dressing of the pion cloud are reduced (analogous conclusions have been drawn from the analysis of $\pi N \rightarrow \rho N$ scattering data, although here the experimental procedure of accounting for finite-width effects on the final-state ρ mesons has not been fully clarified yet), cf. Fig. 2.9.

All the above calculations are not self-consistent in the sense that the intermediate nucleon and Δ propagators are not dressed with in-medium pions (and vice versa; the calculations of [117], however, have been constrained to photo-absorption data on nucleons and nuclei [118], where the description of the latter requires in-medium widths for baryons; selfconsistent effects are thus implicit in a phenomenological way). The selfconsistent problem has recently been addressed within a ϕ -derivable approach in [113], where also the $\pi\rho\omega$ coupling has been included. A major problem in this context is to maintain the 4-dimensional transversality of the ρ selfenergy, $q_\mu \Sigma_\rho^{\mu\nu} = 0$, as required by the conservation of the vector current (or gauge invariance). In the “perturbative” implementation of the in-medium pion propagators, this can be kept track of by appropriate vertex corrections, but these no longer suffice if fully dressed propagators are implemented. Therefore, several projector techniques have been suggested to maintain 4-dimensional transversality of the ρ self-energy. Since the results can be quite sensitive to the applied

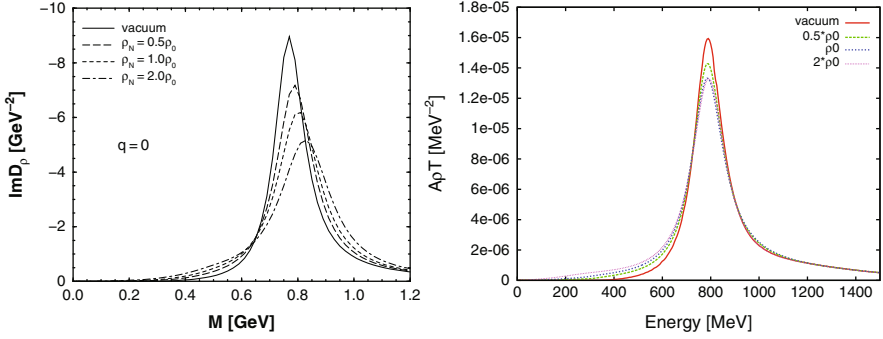


Fig. 2.9 ρ meson spectral functions in cold nuclear matter when dressing the pion cloud with ΔN^{-1} and NN^{-1} . In the *left panel*, the corresponding loops have been evaluated with baryon propagators with in-medium widths estimated from nuclear photoabsorption [117], while the *right panel* shows a selfconsistent calculation with iterated imaginary parts of the selfenergies [113]. Both calculations indicate significantly reduced widths compared to Fig. 2.8 due to softer πNN , $\pi N \Delta$ formfactors.

procedure, we will discuss in the following the inherent problems in some detail.

If one goes beyond perturbation theory the Dyson resummation generally violates Ward identities on the correlator level. Thus the polarization tensor (or selfenergy) may contain four-longitudinal components $\Sigma_l^{\mu\nu}(q)$, which may lead to the propagation of unphysical degrees of freedom and therefore have to be removed. In principle, this deficiency can be cured by corresponding vertex corrections. Without further approximations, however, this leads to a presently intractable scheme of Bethe-Salpeter equations including t -channel exchanges required by crossing symmetry. To date, two schemes have been proposed [110, 114] to deal with this problem (cf. also [119, 120]). Both schemes lead to somewhat different predictions for the spectral function of the ρ meson at finite temperature (as presented in [114]). In order to understand possible reasons for these differences we have to compare the schemes for reconstructing the four-transversality; both calculations used the ϕ functional so that one can exclude effects from other parts of the models. The idea of the scheme introduced by van Hees and Knoll (denoted by Ps-1 in Table 2.2) is to obtain a much better approximation of the spatial components using a Dyson scheme that one can expect for the time component. This is due to the fact that such a tensor has effectively two relaxation times. The spatial correlations will always have a finite relaxation time and can therefore be better approximated in a Dyson scheme where due to the finite damping of the propagators in the loops one can only have finite relaxation times in the final result. On the contrary, the time components have infinite relaxation time due the conservation law which can never be reached within a simple Dyson resummation. So the idea is to take only information from the spatial part and then to reconstruct the time components such as to fulfill the

requirements of four transversality. However the construction of the tensor according this description is still beset with problems since the longitudinal part has a kinematical singularity at zero energy which artificially enhances the strength in the spectral function. In contrast to this, the approach by Ruppert and Renk (denoted by Ps-2 in Table 2.2) employs the R_ξ gauge with $\xi \rightarrow \infty$, where the longitudinal components decouple from the system and one ends up with only the transversal structure of the tensor,

$$\Sigma^{\mu\nu}(q) = \Sigma_L^{\mu\nu}(q) + \Sigma_T^{\mu\nu}(q). \quad (2.35)$$

This however also suffers from an artifact. The problem is that calculated tensor is actually not four transversal on the light cone meaning:

$$q_\mu q_\nu \Sigma^{\mu\nu}(q^2 = 0) \sim N. \quad (2.36)$$

On the other hand, the longitudinal projector $\Sigma_L^{\mu\nu}(q)$ has a singularity at the light cone which requires this trace to vanish. This leads to a selfenergy tensor that has a quadratic singularity at the light cone and accumulates even more strength than with the linear singularity in the van Hees-Knoll scheme. In the selfconsistent calculation this turns out to be a quite unfortunate situation because the artificial strength at the light cone offers the pion a new but completely unphysical decay mode which renders the pion broad and in turn, due to the selfconsistency, also enhances the width of the ρ meson. In the scheme by van Hees and Knoll the situation is a bit better because the artifacts are located in a region where the influence on the ρ selfenergy is not so large.

In the right panel of Fig. 2.9 we show a selfconsistent calculation of the rho spectral function based on an in-medium pion cloud according to [113], using the van Hees-Knoll projector scheme. The $\pi N \Delta$ vertex has been constrained by πN scattering phase shifts using a Gaussian ansatz for the formfactor resulting in a rather soft cutoff $\Lambda=440$ MeV, quite reminiscent to [117, 118]. The resulting spectral functions exhibit somewhat smaller medium effects compared to the ones in the left panel [117, 118]; e.g., the slight mass shift in the latter is absent in the self-consistent calculations since the in-medium real parts have not been included in the iteration procedure. Whether the smaller width is due to the self-consistency, due to the lack of in-medium real parts, due to the different modeling of the in-medium pions or due to another reason, remains to be investigated.

2.4.1.2 Cold nuclear matter II: ρ - N resonances

In addition to medium effects in the pion cloud, it has been realized that the ρ meson can be modified due to direct coupling to nucleons via resonance excitations ($\rho B N^{-1}$ -“rhosobars”, in analogy to $\pi \Delta N^{-1}$ “pisobars”) [87, 106, 107, 111]. An indication of the importance of a given baryon resonance, B ,

follows from its decay branching into ρ - N final states. In non-relativistic approximation, these excitations can be classified via S - and P -wave ρ - N interaction Lagrangians,

$$\mathcal{L}_{\rho BN}^{S\text{-wave}} = \frac{f_{\rho BN}}{m_\rho} \Psi_B^\dagger (q_0 \mathbf{s} \cdot \boldsymbol{\rho}_a - \rho_a^0 \mathbf{s} \cdot \mathbf{q}) t_a \Psi_N + \text{h.c.} , \quad (2.37)$$

$$\mathcal{L}_{\rho BN}^{P\text{-wave}} = \frac{f_{\rho BN}}{m_\rho} \Psi_B^\dagger (\mathbf{s} \times \mathbf{q}) \cdot \boldsymbol{\rho}_a t_a \Psi_N + \text{h.c.} . \quad (2.38)$$

The summation over a is in isospin space with isospin matrices $\mathbf{t} = \boldsymbol{\tau}$, \mathbf{T} depending on whether the resonance B carries $I=1/2$ or $3/2$, respectively. Analogously, the various vector/scalar products act in spin-momentum space with spin operators $\mathbf{s} = \boldsymbol{\sigma}$, \mathbf{S} corresponding to $J=1/2$ - or $J=3/2$ -resonances. P -wave interactions have first been suggested in [106], where the $J^P = 3/2^+$ $N(1,720)$ and $J^P = 5/2^+$ $\Delta(1,905)$ were identified as important states. For ρ - N S -wave scattering, $N(1,520)$ and $\Delta(1,700)$ are important [107], which both are located below the naive ρ - N threshold. This renders the experimental determination of the coupling constants rather challenging [121–123]. While the decay branchings can be used for first estimates, a more quantitative description requires comprehensive fits to $\pi N \rightarrow \rho N$ scattering data [111], or photoabsorption spectra on nucleons and nuclei [45, 118], cf. Fig. 2.10 for two examples.

In addition to providing a more reliable (combined) determination of the coupling strengths it also enables, to a certain extent, a better handle on 3-momentum dependencies which are not only governed by the interaction Lagrangians but also encoded in hadronic formfactors.

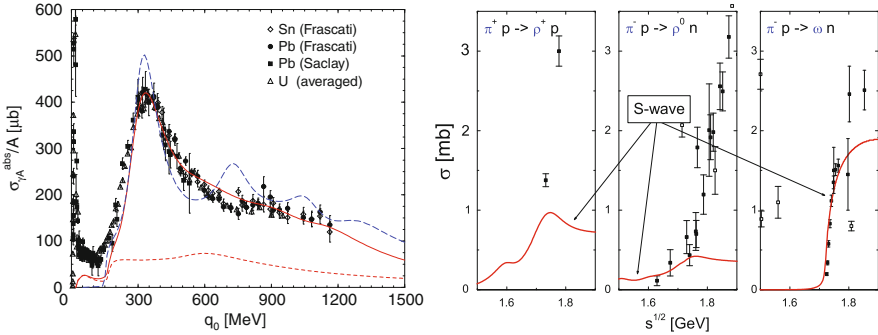


Fig. 2.10 Constraints on ρ meson interactions with nucleons from photoabsorption on nuclei (left panel) [118, 124] or $\pi N \rightarrow \rho N$ scattering (right panel) [82]. In the left panel, the long-dashed line represents the fit on the nucleon, the solid line the total result including broadened resonances in nuclear matter at $\varrho_N = 0.8\varrho_0$, and the short-dashed line the non-resonant background associated with pion-cloud modifications of the ρ .

With the effective vertices fixed in this way, one proceeds to calculate the corresponding ρ selfenergy, either to leading order in the density (T - ρ approximation) [45, 55, 106, 111], or using Lindhard functions which allow for modifications of the intermediate baryon propagators [107, 112, 118]. The consistent use of (relativistic) kinematics in both formfactors and vertices to evaluate the coupling strengths has been emphasized in [111].

Figure 2.11 illustrates several calculations for ρ spectral functions in cold nuclear matter. The upper left panel shows a coupled-channel resonance-model where baryon and meson selfenergies have been calculated selfconsistently [125]. The coupling parameters, taken from fits to ρ - N amplitudes, are based on comprehensive analyses of $\pi N \rightarrow \pi\pi N$ scattering data [121, 126]. As in the case of the pion cloud effects, the implementation of selfconsistency was found to have a moderate impact on the in-medium ρ spectral function. The variation due to different data sets in constraining the interaction parameters is somewhat larger, but still very moderate as seen from the figure: the largest uncertainty resides in the ρ - N coupling to the $N(1,520)$ (causing the peak at $q^2 \simeq 0.3 \text{ GeV}^2$), while the location and width of the ρ peak varies much less.

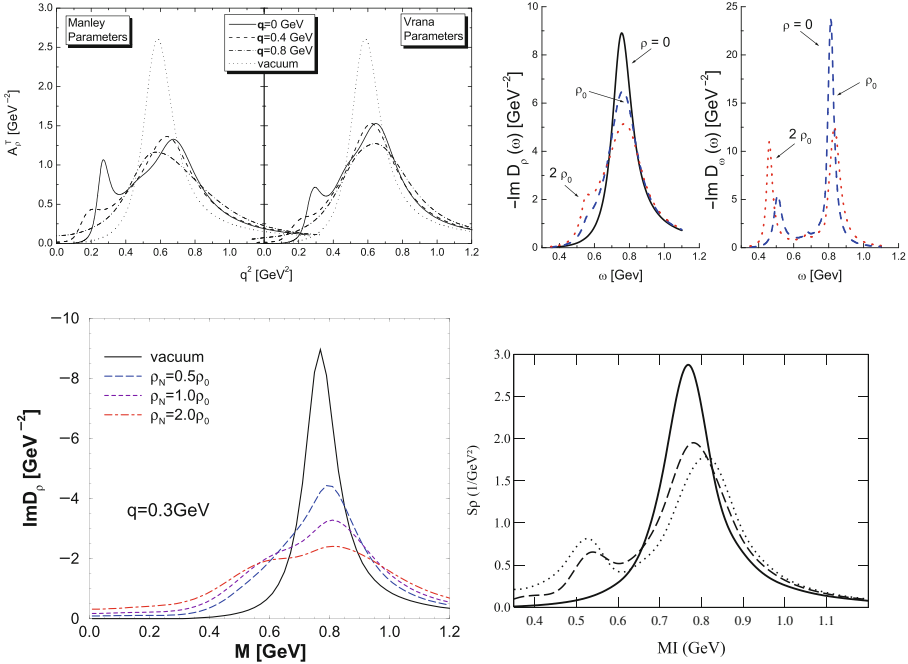


Fig. 2.11 Comparison of ρ meson spectral functions in cold nuclear matter within the hadronic many-body approaches of [125] (upper left panel) [82] (upper right panel) [88, 109] (lower left panel) and [112] (lower right panel) .

The upper right panel of Fig. 2.11 corresponds to a relativistic coupled-channel approach using ρ - N point vertices to dynamically generate the relevant S -wave resonance. The amplitudes are then constrained by an extensive set of πN and γN scattering data (cf. right panel of Fig. 2.10), and the resulting amplitudes are implemented to leading order in density (T - ϱ approximation) into ρ and ω propagators. In this approach, the medium modifications of the ρ are significantly less pronounced due to a reduced coupling to the $N(1,520)$ (as emerging from the best overall fit), as well as the neglect of ρ - N P -wave interactions.

In the lower left panel, the ρ spectral function includes medium effects due to both the pion cloud and (S - and P -wave) rhosobars (with non-relativistic form factors) [117]; the interaction Lagrangians have been comprehensively constrained by photoabsorption cross sections on nucleons and nuclei [118] (cf. left panel of Fig. 2.10), as well as total $\pi N \rightarrow \rho N$ cross sections. The resulting medium effects are quite comparable to the selfconsistent results of Post et al. [125]; the most notable difference is the absence of a peak structure around $M \simeq 0.55$ GeV, although a pronounced shoulder is still visible. This is due to the implementation of an empirical in-medium width of ~ 250 MeV (at $\varrho_N = \varrho_0$) for the $N(1,520)$ resonance deduced from the photo-nuclear data (similarly for other baryon resonances). Also note that the density effects build up rather quickly for moderate densities (as low as $\varrho_N = 0.5\varrho_0$) and show less variation at higher densities. This is compatible with the empirical finding in photoabsorption that the modifications have an early onset for small nuclear mass number (as low as $A=4$, i.e. ${}^4\text{He}$), with rather little additional effects even for ${}^{238}\text{U}$. Since the spectral shape does not follow a simple Breit-Wigner form, one should define the centroid mass via the lowest energy (-squared) moment of the spectral function,

$$(m_\rho^*)^2 = \int_0^\infty \frac{q_0 dq_0}{\pi} q_0^2 [-2\text{Im}D_\rho(q_0, q=0)] . \quad (2.39)$$

For the spectral function of [117] one obtains $m_\rho^* \simeq 0.83$ GeV at normal nuclear density. Together with an approximate full-width at half maximum of $\Gamma_\rho \simeq 0.42$ GeV, one finds remarkable agreement with the constraints set by QCD sum rules in [56], recall the middle right panel in Fig. 2.4.

Finally the lower right panel shows a calculation of Cabrera et al. [112], where pion cloud modifications are supplemented with the leading S -wave rhosobar excitation, $N(1,520)N^{-1}$. Again, in agreement with all other calculations above, one finds a substantial broadening accompanied by a slight upward mass shift and extra rhosobar-strength around $M \simeq 0.5$ GeV (obviously the medium effects will be stronger if a more complete set of ρ - BN^{-1} excitations is included).

To summarize this section, it seems fair to conclude that reasonable agreement (on the 30% level) is established between spectral function calculations

once a comprehensive and complete inclusion of empirical constraints. Differences in whether the medium effects are solely ascribed to rho-sobar excitations, point interactions, or evaluated in combination with pion cloud effects, seem to be the reason for current discrepancies. Another open issue in this context is the relation of the ρ -baryon coupling to chiral symmetry which must be answered before definite conclusion on the nature of (the approach to) chiral symmetry restoration in cold nuclear matter can be drawn.

2.4.1.3 Hot meson gas

Investigations of the ρ properties in a hot pion gas have been initiated in the early eighties and developed thereafter in various aspects. While in mean-field theories one usually finds a decrease of the ρ mass with increasing temperature (and density), due to the built-up of an attractive scalar field, it has been realized early on that width effects may play an important role [127, 128]. An explicit finite- T field theoretic calculation, however, found rather moderate effects induced by the Bose enhancement in the pion cloud of the ρ [129]. The (selfconsistent) inclusion of a rather complete set of $\pi\pi$ interactions [130] did not affect this conclusion substantially, see also [131] or an evaluation within finite- T chiral perturbation theory [132].

The selfconsistency problem has been revisited in [110], with special attention to maintaining a 4-dimensionally transverse ρ -selfenergy; the technical aspects of that have been sketched in Sect. 2.4.1.1 above. With the van Hees-Knoll projector method, the broadening effects on the ρ are again moderate (at least at small ρ meson 3-momenta), while the alternative method employed in [114] induces stronger effects which, however, are probably spurious, as discussed above. General arguments based on the Goldstone nature of pions suggest that their modifications in a pion gas should be small.

Much like in the baryon case, the ρ meson can directly interact with mesons from the heat bath to form resonances (which usually dominate over non-resonant interactions). These have been investigated, e.g., in [108, 133], an example of which is shown in Fig. 2.12. For a rough reference relative to the cold nuclear matter case, we note that the thermal $\pi+K+\bar{K}+\rho$ density at $T=150$ MeV amounts to about normal nuclear matter density, $\varrho_0=0.16\text{ fm}^{-3}$. Comparing the ρ spectral function in mesonic matter at $T=150$ MeV to the one in cold nuclear matter at $\varrho_N = \varrho_0$ (lower left panel in Fig. 2.11) reveals substantially stronger medium effects for the latter, especially in terms of the enhancement below the free ρ mass.

2.4.1.4 Hot hadronic matter

In (ultra-) relativistic heavy-ion collisions at AGS energies ($E_{lab} \simeq 10$ AGeV) and upward, the created (hadronic) medium consists of comparable concen-

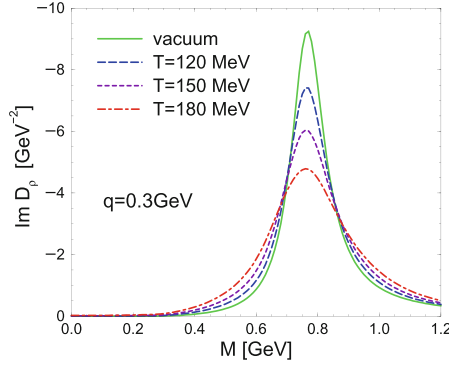


Fig. 2.12 ρ meson spectral functions [108] in hot meson matter when accounting for thermal Bose enhancement and a rather complete set of resonant $\rho + M \rightarrow R$ interactions ($M = \pi, K, \rho$, $R = \omega(782), h_1(1, 170), a_1(1, 260), K_1(1, 270), f_1(185)\pi'(1, 300)$); nonresonant interactions, as well as a dressing of the pion cloud have been neglected.

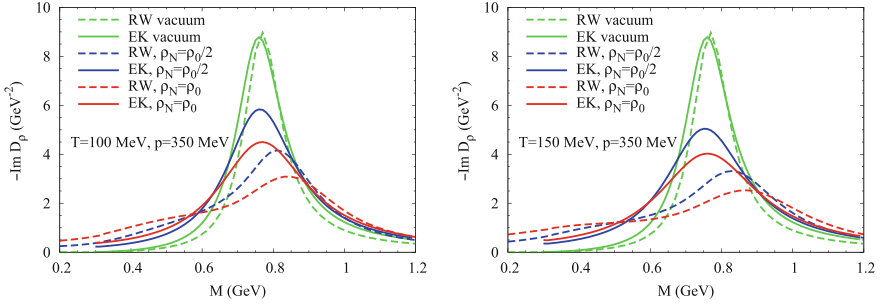


Fig. 2.13 Comparison of ρ meson spectral functions in hot and dense hadronic matter from [88] (dashed lines) and [133] (solid lines) at temperatures of $T=100$ MeV (left panel) and $T=150$ MeV (right panel) for nucleon densities of $\varrho_N=0.5, 1.0 \varrho_0$ (the corresponding nucleon chemical potentials are $\mu_N=673,745$ MeV for $T=100$ MeV and $\mu_N=436,542$ MeV for $T=150$ MeV, respectively).

trations of mesons and baryons, and therefore realistic applications of spectral functions should include medium effects of both type (even at RHIC energies, with a proton-to-pion ratio of about 1/10, the combined effects of baryons and anti-baryons has been shown to be substantial [134]). However, rather few calculations of ρ spectral functions have simultaneously accounted for both baryon density and temperature. Two such calculations are compared in Fig. 2.13. While the hadronic-many body calculation of [88] has been discussed above (cf. lower left panel in Figs. 2.11 and 2.12), the spectral function of [133] has been constructed rather differently using empirical ρ - N and ρ - π scattering amplitudes. The imaginary parts of the latter have been saturated by resonances (plus a background Pomeron term) at low energies, and based on a Regge parametrization at high energies; the real parts

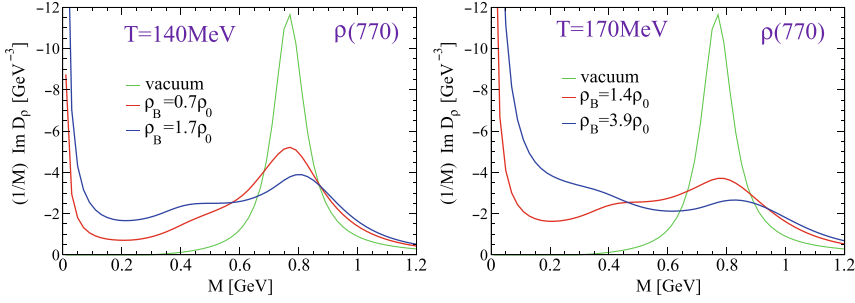


Fig. 2.14 ρ meson spectral functions, weighted by a factor $1/M$ (as figuring into the dilepton rate) under SPS (red lines) and FAIR (blue lines) conditions, as well as in vacuum (green lines), in the hadronic many-body approach of [88].

have been recovered by a dispersion integral. While there is qualitative agreement between this approach and the hadronic many-body calculations, the most significant difference appears to be a stronger broadening and the extra low-energy strength in the $M \simeq 0.4$ GeV region of the hadronic many-body spectral function which is caused by off-shell (“subthreshold”) ρ - N resonances (most notably the $N(1,520)$). The latter do not explicitly appear in the on-shell scattering approach of [133] (but are subsumed in the Regge term). Furthermore, in the many-body framework, the level repulsion between the resonance-hole loop and the elementary ρ peak causes the latter to shift up in mass. In both approaches, the 3-momentum dependence of the ρ spectral function is rather moderate.

To illustrate again the sensitivity to the modifications caused by the baryonic component of the medium, we compare in Fig. 2.14 the hadronic many-body ρ meson spectral function [88] for conditions expected at FAIR and SPS for an “intermediate” (left panel) and a high temperature. An additional factor of $1/M$ has been introduced to resemble the dilepton rate after transformation from q_0 to M (the Bose factor will further amplify the low-mass region). The plots suggest that the largest sensitivity is residing in the mass region below ~ 0.4 GeV.

2.4.1.5 Renormalization group approach and vector manifestation of chiral symmetry

In all approaches discussed thus far, the parameters in the (free) lagrangian (masses, coupling constants and formfactor cutoffs) have been kept fixed in the medium. Since hadrons are composite objects, the question arises whether this is justified. Recent work by Harada et al. [18] addresses this problem in a renormalization group approach as will be elaborated in more detail in the following.

The vector manifestation (VM) [135] was proposed as a novel pattern of the Wigner realization of chiral symmetry in which the ρ meson becomes massless degenerate with the pion at the chiral phase transition point. The VM is formulated [18, 136, 137] in the effective field theory (EFT) based on the hidden local symmetry (HLS) [138, 139]. The VM gives a theoretical description of the dropping ρ mass, which is protected by the existence of the fixed point (VM fixed point) of the renormalization group equations (RGEs). In the formulation of the VM, an essential role is played by the *intrinsic temperature/density effects* of the parameters which are introduced through the matching to QCD in the Wilsonian sense combined with the RGEs. The intrinsic effect produces the violation of vector dominance (VD) near the chiral restoration point.

Hidden Local Symmetry and Wilsonian Matching

The HLS Lagrangian is based on the $G_{\text{global}} \times H_{\text{local}}$ symmetry, where $G = SU(N_f)_L \times SU(N_f)_R$ is the chiral symmetry and $H = SU(N_f)_V$ is the HLS. Within the HLS framework, it is possible to perform a systematic derivative expansion including the vector mesons as the HLS gauge boson in addition to the pseudoscalar mesons as the NG bosons [18, 140–142]. In this chiral perturbation theory (ChPT) with the HLS, the Lagrangian with lowest derivative terms is counted as $\mathcal{O}(p^2)$, which in the chiral limit is given by [138, 139]

$$\mathcal{L}_{(2)} = F_\pi^2 \text{tr}[\hat{\alpha}_{\perp\mu} \hat{\alpha}_{\perp}^\mu] + F_\sigma^2 \text{tr}[\hat{\alpha}_{\parallel\mu} \hat{\alpha}_{\parallel}^\mu] - \frac{1}{2g^2} \text{tr}[V_{\mu\nu} V^{\mu\nu}], \quad (2.40)$$

where g is the HLS gauge coupling, $V_{\mu\nu}$ is the field strength of V_μ and

$$\hat{\alpha}_{\perp,\parallel}^\mu = \frac{1}{2i} [D^\mu \xi_R \cdot \xi_R^\dagger \mp D^\mu \xi_L \cdot \xi_L^\dagger]. \quad (2.41)$$

Here two variables ξ_L and ξ_R are parameterized as

$$\xi_{L,R}(x) = e^{i\sigma(x)/F_\sigma} e^{\mp i\pi(x)/F_\pi}, \quad (2.42)$$

where $\pi = \pi^a T_a$ denotes the pseudoscalar Nambu-Goldstone (NG) bosons associated with the spontaneous symmetry breaking of G_{global} chiral symmetry, and $\sigma = \sigma^a T_a$ denotes the NG bosons associated with the spontaneous breaking of H_{local} . F_π and F_σ are the decay constants of associated particles.

At the leading order of the chiral perturbation with HLS the Lagrangian includes three parameters: the pion decay constant F_π ; the HLS gauge coupling g ; and a parameter a defined as $a = F_\sigma^2/F_\pi^2$. Using these three parameters, the ρ meson mass m_ρ , the ρ - γ mixing strength g_ρ , the ρ - π - π coupling strength $g_{\rho\pi\pi}$ and the direct γ - π - π coupling strength $g_{\gamma\pi\pi}$ are expressed as

$$m_\rho^2 = g^2 a F_\pi^2, \quad g_\rho = g a F_\pi^2, \quad g_{\rho\pi\pi} = \frac{a}{2} g, \quad g_{\gamma\pi\pi} = 1 - \frac{a}{2}. \quad (2.43)$$

From these expressions, one can easily see that vector dominance of the electromagnetic form factor of the pion, i.e. $g_{\gamma\pi\pi} = 0$, is satisfied for $a = 2$. We would like to stress that VD at zero temperature and density is accidentally satisfied: The parameter a is $4/3$ at the bare level and it becomes 2 in the low-energy region by including the quantum correction [143]. This can be rephrased in the following way: the parameter a in the large N_c limit is $4/3$ and it becomes 2 when the $1/N_c$ corrections are included [144].

The Wilsonian matching is a novel manner to determine the parameters of EFTs from the underlying QCD in the vacuum [18, 145]. It has been applied to study the chiral phase transition at a large number of flavor [18, 135] and at finite temperature/density [136, 137]. The matching in the Wilsonian sense is based on the following idea: The bare Lagrangian of an EFT is defined at a suitable high energy scale Λ and the generating functional derived from the bare Lagrangian leads to the same Green's function as that derived from original QCD Lagrangian at Λ . The *bare* parameters of the EFT are determined through the matching of the Green's functions. In other words, one obtains the bare Lagrangian of the EFT after integrating out high energy modes, i.e., quarks and gluons above Λ . The information of the high energy modes is involved in the parameters of the EFT. Once the bare parameters are determined through the matching, quantum corrections are incorporated into the parameters through the RGEs.

Extension to hot/dense matter

Now we apply the above procedure to the study of hot/dense matter. As noted, the bare parameters are determined by integrating out high frequency modes above the matching scale. Thus when we integrate out those degrees of freedom in hot/dense matter, the bare parameters are dependent on temperature/density. We shall refer to them as the *intrinsic temperature/density effects* [136, 137]. The intrinsic dependences are nothing but the signature that the hadron has an internal structure constructed from quarks and gluons. This is similar to the situation where the coupling constants among hadrons are replaced with momentum-dependent form factors in the high-energy region. Thus the intrinsic temperature/density effect plays an important role in the higher temperature/density region, especially near the phase transition point.

Vector manifestation in hot/dense matter

As emphasized above, the VM was proposed in [135] as a novel pattern of the Wigner realization of chiral symmetry with a large number of massless quark flavors, in which the vector meson becomes massless at the restoration point and belongs to the same chiral multiplet as the pion, i.e., *the massless vector meson is the chiral partner of the pion*. The studies of the VM in hot/dense matter have been carried out in [136, 137, 146–150] and

the VM was also applied to construct an effective Lagrangian for the heavy-light mesons which can describe the recent experimental observation on the $D(0^+, 1^+)$ mesons [151].

The most important ingredient in the formulation of the VM in hot/dense matter is the intrinsic temperature/density dependence of the parameters of the HLS Lagrangian [136, 137] introduced through the Wilsonian matching between the HLS and QCD: The Wilsonian matching near the critical point T_c/μ_c yields the following behavior for the bare parameters a and g :

$$g(\Lambda; T, \mu_q) \sim \langle \bar{q}q \rangle \rightarrow 0, \quad a(\Lambda; T, \mu_q) - 1 \sim \langle \bar{q}q \rangle^2 \rightarrow 0, \quad \text{for } (T, \mu_q) \rightarrow (T_c, \mu_c). \quad (2.44)$$

It was shown [18, 136, 137] that these conditions are protected by the fixed point of the RGEs and do not acquire quantum corrections at the critical point. Thus the parametric vector meson mass determined for the on-shell vector meson also vanishes since it is proportional to the vanishing gauge coupling constant. The vector meson mass m_ρ defined as a pole position of the full vector meson propagator has hadronic corrections through thermal loops, which are proportional to the gauge coupling constant [136, 137, 146]. Consequently the vector meson pole mass also goes to zero for $(T, \mu_q) \rightarrow (T_c, \mu_c)$:

$$m_\rho(T, \mu_q) \sim \langle \bar{q}q \rangle \rightarrow 0. \quad (2.45)$$

We would like to stress that VD is strongly violated near the critical point associated with the dropping ρ in the VM in hot/dense matter [137, 146]:

$$a(T, \mu_q) \rightarrow 1, \quad \text{for } (T, \mu_q) \rightarrow (T_c, \mu_c). \quad (2.46)$$

Temperature dependence of parameters

In the present framework, the physical quantities in the low-energy region have two kinds of temperature/density dependences, one is the intrinsic effect while the other is due to ordinary hadronic corrections included through the thermal/dense loops. In the following analysis to determine both effects, we study the system at finite temperature and zero density [152].

We consider how the intrinsic temperature dependence of the bare parameters is introduced. As the temperature approaches the critical temperature from below, the difference of the two current correlators approaches zero. On the HLS side near the critical point, the bare g and $a - 1$ are both proportional to the quark condensate, determined by the Wilsonian matching near T_c [136]:

$$g^2(\Lambda; T) \propto \langle \bar{q}q \rangle_T^2 \quad \text{and} \quad a(\Lambda; T) - 1 \propto \langle \bar{q}q \rangle_T^2 \quad \text{for } T \simeq T_c. \quad (2.47)$$

This implies that the bare parameters are thermally evolved following the temperature dependence of the quark condensate, which is precisely the intrinsic temperature effect.

It should be stressed that the above matching conditions hold *only in the vicinity of T_c* : Eq. (2.47) is not valid any more far away from T_c where ordinary hadronic corrections are dominant. The temperature above which the intrinsic effect becomes important we shall denote by T_{flash} , the so-called flash temperature [153, 154]. The VM and therefore the dropping ρ mass become transparent for $T > T_{flash}$.⁷ On the other hand, we expect that the intrinsic effects are negligible in the low-temperature region below T_{flash} : only hadronic thermal corrections are considered for $T < T_{flash}$. For making a numerical analysis including hadronic corrections in addition to the intrinsic effects determined above, we take $T_c = 170$ MeV as a typical example and $T_{flash} = 0.7 T_c$ as proposed in [153, 154]. Here we would like to remark that the BR scaling deals with the quantity directly locked to the quark condensate and hence *the scaling masses are achieved exclusively by the intrinsic effect in the present framework*.

Physical quantities are obtained by including the hadronic corrections generated through thermal loop diagrams at one loop order. We show the temperature dependences of the ρ meson mass $m_\rho(T)$ defined in its rest frame and the ρ - γ mixing strength in Fig. 2.15. Figure 2.15a shows that the vector

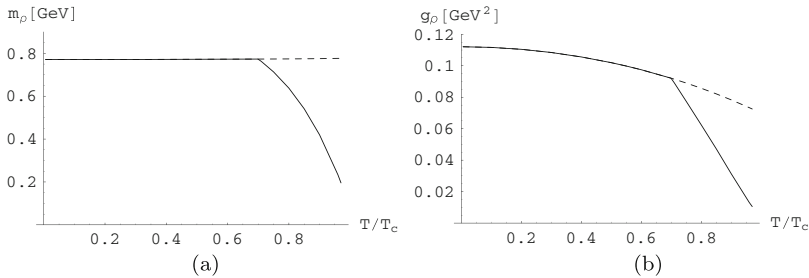


Fig. 2.15 Temperature dependences of **a** the vector meson mass m_ρ , **b** the ρ - γ mixing strength g_ρ [152]. The *solid curves* denote the full (both intrinsic and hadronic) temperature dependences. The *curves with the dashed lines* include only the hadronic temperature effects.

meson mass including only the hadronic correction changes little with temperature and that the hadronic correction yields a positive contribution to m_ρ , $\delta^{(\text{had})} \simeq 5$ MeV. In the temperature region above the flash temperature, $T/T_c > T_{flash}/T_c = 0.7$, the ρ mass with the intrinsic effect drops rapidly corresponding to a rapid decrease of the gauge coupling. In Fig. 2.15b we can see that the hadronic effect yields a negative correction to the ρ - γ mixing strength. Above the flash temperature, the intrinsic effect causes a rapid decrease of the gauge coupling g , which leads to a further drop of g_ρ towards zero.

⁷ As was stressed in [18, 155], the VM should be considered only as a limit. So we include the temperature dependence of the parameters only for $T_{flash} < T < T_c - \epsilon$.

Electromagnetic form factor

Using the in-medium parameters obtained in the previous section, the thermal width of the ρ meson is calculated as shown in Fig. 2.16. Since m_ρ slightly

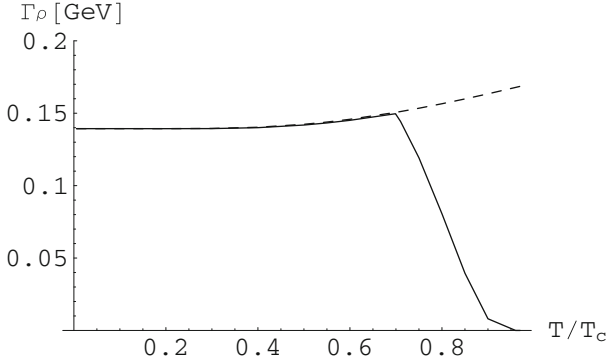


Fig. 2.16 Decay width of the ρ meson as a function of T/T_c [152]. The curve with the dashed line includes only the hadronic temperature effects. The solid curve denotes the full (both intrinsic and hadronic) temperature dependences.

increases with T as shown in Fig. 2.15a (dashed line) for $T < T_{flash}$, Γ_ρ increases with T . This implies that the hadronic effect causes a broadening of the ρ width. When the intrinsic effect is included for $T > T_{flash}$, $g_{\rho\pi\pi}$ as well as m_ρ decrease with T in the VM, and the width Γ_ρ decreases as $\Gamma_\rho \sim g^3 \rightarrow 0$.

Figure 2.17 shows the electromagnetic form factor \mathcal{F} for several temperatures. In Fig. 2.17a there is no remarkable shift of the ρ meson mass but

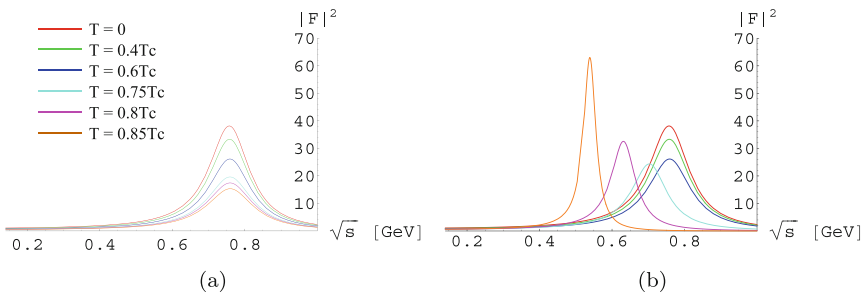


Fig. 2.17 Electromagnetic form factor of the pion as a function of the invariant mass \sqrt{s} for several temperatures [152]. The curves in the left panel **a** include only the hadronic temperature effects and those in the right panel **b** include both intrinsic and hadronic temperature effects.

the width becomes broader with increasing temperature, which is consistent with the previous study [131]. In Fig. 2.17b the intrinsic temperature effects are also included into all the parameters of the form factor. At a temperature below T_{flash} , the hadronic effect dominates the form factor, so that the curves for $T = 0, 0.4T_c$ and $0.6T_c$ agree with the corresponding ones in Fig. 2.17a. At $T = T_{flash}$ the intrinsic effect starts to contribute and thus in the temperature region above T_{flash} the peak position of the form factor moves as $m_\rho(T) \rightarrow 0$ as the temperature approaches T_c . Associated with this dropping ρ mass, the width becomes narrow, and the value of the form factor at the peak grows as $\sim g^{-2}$ [136].

As noted, vector dominance is controlled by the parameter a in the HLS theory. The VM leads to the strong violation of VD (denoted by “ $\nabla\mathbb{D}$ ”) near the chiral symmetry restoration point, which can be traced through the Wilsonian matching and the RG evolutions. We compare the dilepton spectra predicted in the VM (including the effect of $\nabla\mathbb{D}$) with those obtained by assuming VD, i.e. taking $g_{\gamma\pi\pi} = 0$. Figure 2.18 shows the temperature dependence of the ρ - γ mixing strength g_ρ with VD (dash-dotted line) and $\nabla\mathbb{D}$ (solid line). In the low-temperature region, $T < T_{flash}$, the hadronic

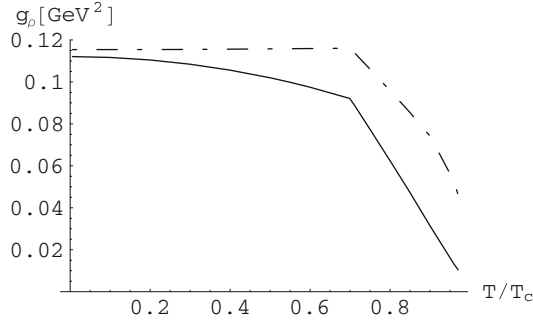


Fig. 2.18 Temperature dependence of the ρ - γ mixing strength g_ρ for $\sqrt{s} = m_\rho$ [152]. The dash-dotted curve corresponds to the case with the VD assumption. The solid one includes the effect of the VD violation due to the VM.

corrections to m_ρ and $g_{\rho\pi\pi}$ are small, so that the ρ - γ mixing strength with VD, $g_\rho^{(VD)}$, is almost independent of temperature (see the dash-dotted line). On the other hand, the hadronic correction to g_ρ with $\nabla\mathbb{D}$ is non-negligible in the HLS, which leads to a decrease with temperature (see the solid line). Near the critical temperature, $T > T_{flash}$, both m_ρ and $g_{\rho\pi\pi}$ drop due to the VM and the above ratio also decreases since $m_\rho^2/g_{\rho\pi\pi} \propto g$. However compared to g_ρ with $\nabla\mathbb{D}$, the decreasing of $g_\rho^{(VD)}$ (dash-dotted line) is much more gentle. This affects the pion form factor which exhibits a strong suppression provided by decreasing g_ρ in the VM.

Our analysis can be applied to a study at finite density. Especially a study of the conditions of the future GSI/FAIR would be important. In such a dense environment, the particle-hole configurations with the quantum numbers of pions and ρ mesons are important, as discussed extensively above. The violation of VD at finite density has also been discussed in the HLS theory [137]. It was found that the dilepton rate as well as the form factor are strongly affected by the intrinsic density effects and reduced above the “flash density”.

2.4.1.6 Final remarks on the ρ meson

Hadronic many-body approaches largely coincide on a strong broadening of the ρ spectral function in hot hadronic matter, possibly accompanied by a slight upward mass shift. While quantitative agreement remains to be established, empirical constraints on the effective Lagrangians from free scattering data are mandatory for reliable predictions. The role of full selfconsistency needs to be addressed in a more complete fashion. It has become clear, though, that the medium effects induced by baryons are more important than those induced by mesons at comparable densities, rendering the maximal baryon densities envisaged in the CBM context a promising environment. An important open question concerns the medium dependence of the bare parameters in the effective Lagrangian. Intrinsic medium dependencies (*i.e.*, dropping mass and coupling constants) are predicted by the vector manifestation scenario in connection with a QCD sum-rule type matching to (perturbative) QCD correlators. On the one hand, the many-body effects included in these calculations are not yet complete (*e.g.*, in the medium, additional low-energy degrees of freedom appear in form of resonance-hole loops), and the notion of the “flash” temperature needs to be clarified. On the other hand, vector dominance is found to be violated, which is not accounted for in most of the many-body approaches. Clearly, further theoretical investigations are necessary to progress on these issues.

2.4.2 ω meson

In the thermal dilepton rate the contribution of ω mesons is suppressed by a about a factor 10 compared to the ρ and therefore has (until very recently) received rather little attention. However, in photon- and proton-induced production, the ω contribution is relatively less suppressed and has been subject of recent experiments using nuclear targets [84, 85, 156], cf. Fig. 2.19. Even in heavy-ion reactions, the new level of precision reached by NA60 dimuon spectra in In-In collisions at SPS [34] has indicated the possibility to study in-medium effects on the ω [35].

2.4.2.1 Cold nuclear matter

Similar to the case of the ρ , early calculations of the in-medium ω spectral function have focussed on dressing its pion cloud, cf. left panel of Fig. 2.20 [157]; here an attractive ω - N amplitude (which was not directly confronted with data) has been found to reduce the ω mass at normal nuclear density to ~ 600 MeV, together with a broadening by ~ 80 MeV. Subsequently, it has been realized that the ω should also couple to resonance-hole excitations, which are, however, more difficult to infer from experiment than for the ρ . Indirect methods have been applied taking recourse to comprehensive coupled channel analysis of πN and γN scattering data [82, 83], cf. upper right panel in Figs. 2.11 and 2.20. These updated analyses lead to somewhat smaller in-medium widths, $\Gamma_{\omega}^{tot}(\rho_0) \simeq 40 - 60$ MeV with little (if any) mass shift but significant strengths in resonance-hole excitations at $M \simeq 500$ MeV.

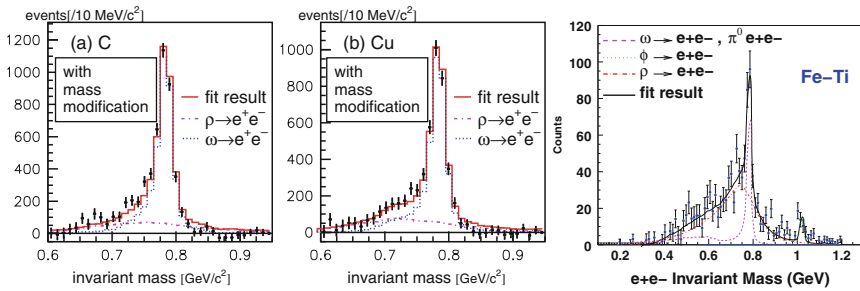


Fig. 2.19 Background-subtracted e^+e^- invariant-mass spectra in proton- (left) and photon-induced (right) reactions off nuclear targets. The E325 collaboration [84] (left panels) reports a significant drop of ω and ρ masses, while the CLAS collaboration [156] (right panel) reports a broadening of the ρ line shape without significant mass shift. The results of $\pi^0\gamma$ spectra of [85], which reported an in-medium mass reduction of low-momentum ω mesons, are currently being revisited.

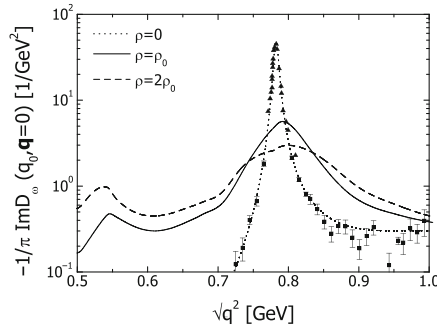


Fig. 2.20 ω meson spectral function in cold nuclear matter implementing coupled channel ω - N resonance interactions [83]. These results may be compared to the upper right panel in Fig. 2.11.

In [82] the latter is mostly due to the $N(1,520)N^{-1}$ and $N(1,535)N^{-1}$, while in [83] it is attributed to the $N(1,535)N^{-1}$ with smaller strength. The discrepancy with the early calculations in [157] has recently been scrutinized in [158] where it is argued that the heavy-baryon approximation employed in [157] does not apply and therefore does not produce reliable results.

2.4.2.2 Hot meson gas

Finite-temperature calculations of the ω meson width have been conducted, e.g., in [159] in terms of elastic and inelastic collisions rates with pions; at $T = 150$ MeV, a broadening of ~ 30 MeV, dominated by the (elastic) resonance scattering $\omega + \pi \rightarrow b_1(1,235)$, was found. In [160] a finite- T calculation of the $\omega \rightarrow 3\pi$ width was carried out including Bose enhancement factors as well as the $\omega + \pi \rightarrow \pi + \pi$ channel. The latter exhibits a rather sharp increase for $T > 100$ MeV and is the dominant contribution to a ~ 55 MeV broadening at $T = 150$ MeV, see upper left panel of Fig. 2.21. This is roughly consistent with the results of [133, 134] as well.

2.4.2.3 Hot and dense hadronic matter

When combining pion- and baryon-induced effects, the ω broadens further. In the hadronic many-body framework, the inclusion of anti-/nucleons, even under RHIC conditions, increases the ω width to 80–150 MeV for $T = 150$ –180 MeV (upper right panel of Fig. 2.21) [134]. This is again quite consistent with the empirical scattering-amplitude based approach of [133, 161] (lower right panel of Fig. 2.21). The calculations for a selfconsistent $\pi\rho\omega$ system with dressed pions indicate that the pion and ρ broadening further accelerate the ω melting close to the expected phase transition (lower left panel of Fig. 2.21).

2.4.3 ϕ meson

Recent data on photon- [99] and proton-induced [162] ϕ production off nuclei, as well as in heavy-ion collisions [34], have revived the interest on medium effects on the ϕ meson.

The expected lack of ϕ - N resonances renders a dressing of the kaon cloud as the prime candidate for modifications in the nuclear medium. Hadronic many-body calculations with in-medium anti-kaons predict ϕ widths of around 20 MeV at normal nuclear matter density [163], which, however, appear to underestimate the observed ϕ absorption by about a factor of 2.

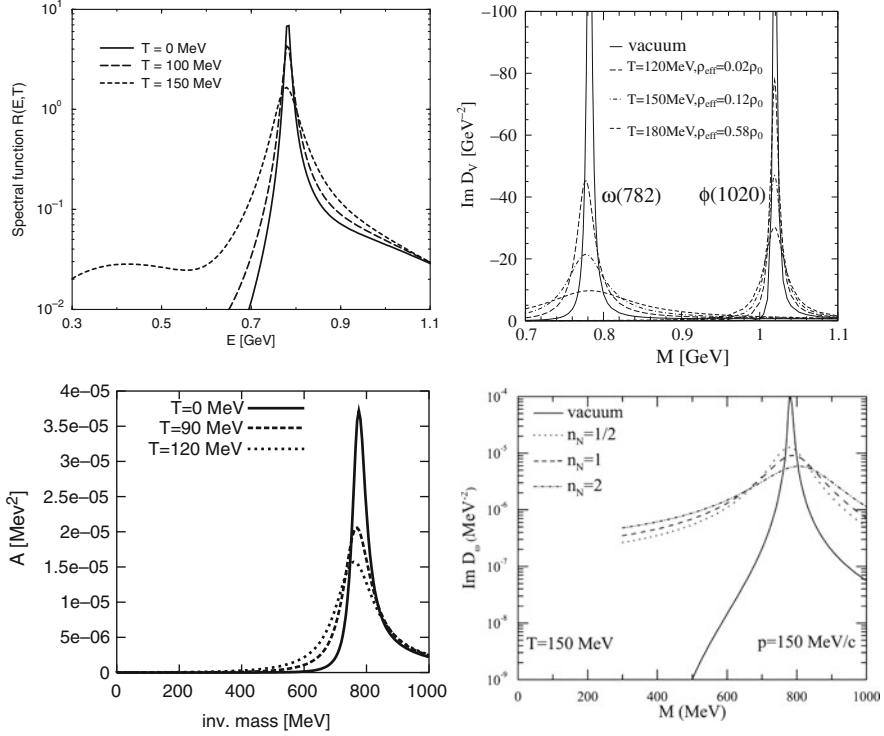


Fig. 2.21 In-medium ω meson spectral functions in: (i) a hot pion gas based on $\omega \rightarrow 3\pi$ and $\omega\pi \rightarrow 2\pi$ channels including Bose enhancement [160] (upper left panel), (ii) hot hadronic matter appropriate for RHIC conditions, including $\omega \rightarrow \rho\pi$, 3π (with in-medium ρ spectral function), $\omega\pi \rightarrow b_1(1, 235), 2\pi$ and $N(1, 520)N^{-1}$, $N(1, 650)N^{-1}$ excitations [134] (upper right panel), (iii) hot nuclear matter for a selfconsistent $\pi\rho\omega$ system including with NN^{-1} and ΔN^{-1} dressing of the pion clouds [113] (lower left panel); (iv) hot hadronic matter using the approach of [133] based on empirical $\omega\pi$ and (updated) ωN scattering amplitudes [161] (lower right panel).

Calculations of collision rates in a meson gas at $T = 150$ MeV indicate a broadening by about 20 MeV [164]. Including a moderate baryon component at finite temperature does not increase this value by much [134]. Thus, hadronic calculations suggest that the ϕ remains a well-defined resonance structure even close to the expected critical temperature. This makes it a good object for precision spectroscopy in heavy-ion reactions.

2.5 Thermal dilepton rates

In this section, we compile and discuss thermal dilepton production rates as following from the hadronic approaches discussed above, complemented by results from perturbative and lattice QCD above T_c , including a brief digression to the recent NA60 dimuon data.

2.5.1 Lattice QCD

First principle results for thermal EM emission rates can be obtained from numerical solutions of lattice-discretized QCD (lQCD). However, the extraction of finite-temperature spectral functions in the time-like regime is hampered by the finite extent of the (Euclidean) time component due to (anti-) periodic boundary conditions. The vector spectral function, which is directly proportional to the thermal emission rate, is related to the Euclidean time current-current correlation function via the integral representation

$$G(\tau, T) = \int_0^\infty dq_0 \sigma(q_0, T) \frac{\cosh(q_0(\tau - 1/(2T)))}{\sinh(q_0/(2T))}. \quad (2.48)$$

In lattice calculations there is only a finite number of points in the (Euclidean) time direction. The extraction of the spectral functions from the Euclidean time correlation functions is usually performed using probabilistic method, the so-called Maximum Entropy Method (MEM) [165]. Furthermore, dynamical quark loops are currently too CPU-time intensive to be included in spectral function computations. Notwithstanding these limitations, the left panel of Fig. 2.22 shows thermal dilepton rates from quenched lQCD for 2 temperatures above T_c [166], compared to expectations from pQCD, either in the simplest $\mathcal{O}(\alpha_s^0)$ approximation (corresponding to naive $q\bar{q} \rightarrow e^+e^-$ annihilation) or within the Hard-Thermal-Loop formalism [167]. While all rates agree at large invariant mass, the lQCD rates exhibit up to a factor 2 enhancement at intermediate mass (possibly reflecting a broad resonance structure) and, more notably, a sharp decrease in the low-mass region which is in marked contrast to the pQCD rates.

The low-mass region is problematic both for perturbative approach and the (nonperturbative) lattice approach. The HTL calculations of [167] imply that the spectral function behaves like $1/q_0$ for $q_0 < gT$. This behavior has been confirmed by recent analysis of [168], where it was also pointed out that the previous calculations [167] are incomplete. The $1/q_0$ -behavior of the spectral functions would imply infinite electric conductivity, however its has been shown in [168] that at very small energies ($q_0 \ll g^4T$) the spectral functions can be approximated by a Lorentzian, i.e., for $q_0 \ll g^4T$ it is proportional to q_0 , while for $q_0 > g^4T$ it behaves like $1/q_0$. The spectral function integrated

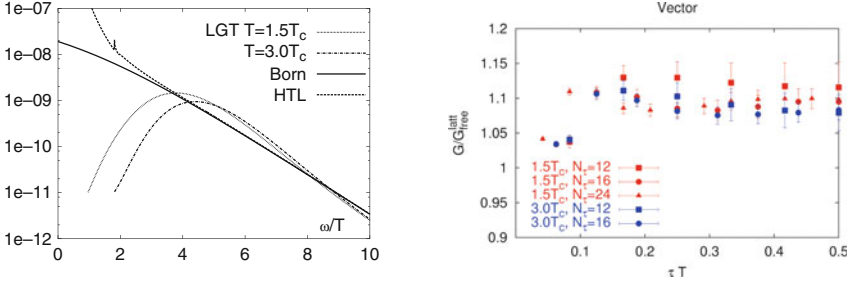


Fig. 2.22 *Left panel:* Thermal dilepton rates, $dN/(d^4q d^4x)$, extracted from quenched lattice QCD above the critical temperature [166] compared to calculations in perturbation theory, either to leading order ($\mathcal{O}(\alpha_s^0)$) $q\bar{q}$ annihilation (solid line) or within the hard-thermal-loop (HTL) framework [167]. All rates are calculated at a total pair momentum of $\mathbf{q}=0$, i.e., the dilepton energy $\omega = q_0$ equals its invariant mass, M . *Right panel:* the ratio of the underlying vector correlation function computed in lattice QCD to the free correlation function.

up to energy $\sim g^4 T$ gives the quark number susceptibility [168], $\chi(T)$. Although the above considerations, strictly speaking, hold in the weak coupling regime $g \ll 1$, the transport peak associated with electric conductivity may be present also for realistic couplings (e.g., $\alpha_s = 0.3$, i.e., $g = 1.94$) [168]. This would pose a problem for lattice calculations of the spectral functions as a narrow peak at $q_0 = 0$ is difficult to reconstruct using MEM. For this reason, lattice calculations have considered the sum over all four (Lorentz) components of the spectral function [166]. For the temporal component of the vector correlation function, one has $G_{00} = -T\chi(T)$. Therefore, if the weak coupling arguments apply, the contribution from the transport peak drops out in this sum.

Although the reconstruction of the spectral functions using MEM is problematic the lattice data on Euclidean time correlators can be calculated reliably and provide useful information about the spectral functions. The ratio of the correlation function calculated on lattice to the free correlation function is shown in the right panel of Fig. 2.22, where the sum over all four components has been taken. As one can see from the figure the calculations performed on different lattices agree well with each other, indicating that lattice artifacts are under control and that the correlation function deviates from the free one only by about 10%. This provides stringent constraints on the spectral functions at low energies which cannot be reliably calculated in perturbation theory (cf. Eq. (2.48)).

Attempts to calculate the spectral function at very low energies, $q_0 \simeq 0$, in lattice QCD have been presented in [169, 170] in terms of the electric conductivity, defined by the time-like limit of the energy-derivative of the EM correlator,

$$\sigma_{\text{el}}(T) = \frac{1}{6} \frac{\partial}{\partial q_0} \rho_{\text{em}i}^i(q_0, q = 0; T)|_{q_0=0}, \quad (2.49)$$

with $\rho_{\text{em}i}^i = -24\pi\alpha_{\text{em}} \text{Im } \Pi_{\text{em}}$. These studies indicated that the electric conductivity at temperatures not too far from the transition temperature is significantly smaller than the prediction of perturbation theory. However, because of the use of the so-called staggered fermion formulation, the number of data points of the correlation functions was quite small (between 7 and 12). It remains to be seen if these results can be confirmed in lattice calculations using larger number of data points.

It would be most interesting to confront model predictions from in-medium hadronic approaches with lattice computations at the level of correlation functions. Results for a hot pion gas based on unitarized chiral perturbation theory have been obtained in [171, 172], where, in particular, the close relation of the EM conductivity to (very) soft photon emission has been emphasized (see also [173]).

2.5.2 Hadronic approaches

The in-medium vector-meson spectral functions discussed in Sect. 2.4 directly figure into the (low-mass) dilepton rates. The most common assumption to do so is by employing the vector-dominance model which works well in the vacuum (at least in the purely mesonic sector), recall Eq. (2.6). In the baryonic sector, modified versions of VDM [174] are suitable to describe photo-absorption reactions on the nucleon and on nuclei, i.e., up to at least nuclear saturation density [118]. Thus it appears reasonable to assume VDM to hold also in mesonic matter; however, its ultimate fate in the medium, especially when approaching the phase transition, is not settled (cf., e.g., Sect. 2.5.3 below).

Rather than choosing a particular 3-momentum, it is more convenient (and more closely related to mass spectra as observed in experiment) to display the rates in momentum integrated form,

$$\frac{dR_{ll}}{dM^2} = \int \frac{d^3q}{2q_0} \frac{dR_{ll}}{d^4q}. \quad (2.50)$$

In the left panel of Fig. 2.23 in-medium hadronic many-body emission rates in the isovector (ρ) channel are confronted with results of the chiral virial expansion. Below the free ρ mass, both approaches predict a large enhancement over the free emission rates (based on the vacuum EM correlator); the agreement becomes even closer if resonance-hole contributions are implemented in the virial expansion [45]. However, at the free ρ mass, the hadronic many-body calculations lead to a substantial suppression (broadening) of the peak due to the resummation of selfenergy insertions in the ρ propagator, which is not present in the virial expansion. This difference remains evident when convoluting the rates over (central) In-In collisions at SPS energies [35, 176] and

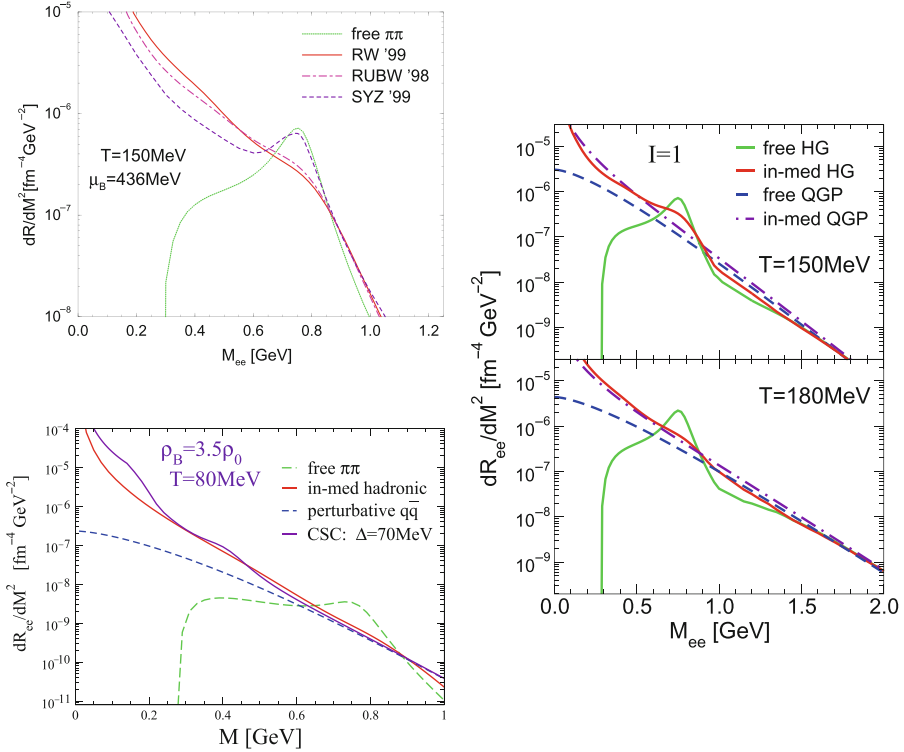


Fig. 2.23 *Upper left panel:* 3-momentum integrated thermal hadronic dilepton rates for the vacuum ρ spectral function (dotted line), within the many-body approach of [88, 118] (dashed-dotted and solid line, the latter additionally including ρ interactions with thermally excited baryons) and from the chiral virial expansion of [44] (dashed line); *right panel:* comparison of hadronic many-body calculations (solid line) [88] to QGP emission for either free $q\bar{q}$ annihilation (dashed line) or hard-thermal loop improved rates [167] (dashed-dotted line); *lower left panel:* dilepton rates at high baryon density and low temperature, comparing in medium hadronic emission (red solid line) [88] with that from a color-superconductor (CSC) using effective hadronic theory on the CSC ground state (purple solid line) [175]. Free QGP and hadron gas rates are shown as a reference (dashed lines).

comparing to NA60 data, cf. Fig. 2.24. The latter apparently favor the broadening (peak suppression) in the many-body calculations, which, in fact, give a very good description of the data. Since in the underlying time evolutions, the initial phases are around (and beyond) the expected phase boundary to the QGP, it is of interest to compare the (bottom-up and top-down) extrapolation of hadronic and QGP rates close to T_c , as done in the right panel of Fig. 2.23. The general trend in these comparisons is that whereas the free emission rates in QGP and hadron gas are very different from each other, the in-medium rates in both phase show a remarkable tendency of approaching each other

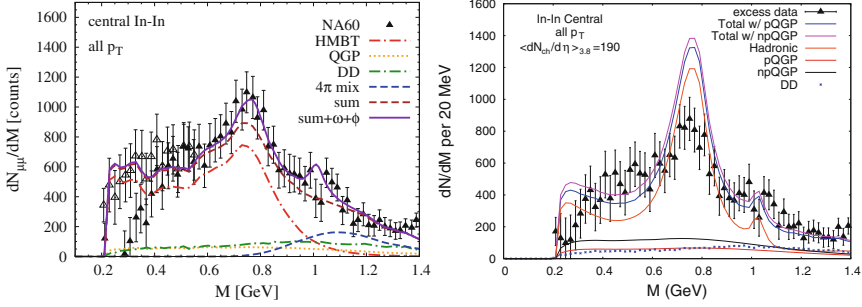


Fig. 2.24 NA60 dilepton excess spectra in central *In-In* [34] compared to calculations using **a** vector-meson spectral functions from hadronic many-body theory [88] within an expanding fireball (*left*) [35], **b** a chiral virial expansion within a hydrodynamic simulation (*right*) [176].

when extrapolated into the expected phase transition region. A deeper understanding of this feature (or whether it is just a coincidence) is currently lacking. Note, however, that the requirement of having a non-vanishing photon emission rate implies a divergence of the dilepton rates toward $M = 0$, and in this sense is a generic feature of many-body calculations. Furthermore, the broadening of excitations is also a quite general phenomenon; the non-trivial behavior here is that the ρ meson broadening is so pronounced that it leads to a complete melting of the resonance structure, as seems to be required by the NA60 data. Another intriguing consequence of a degeneracy of the top-down and bottom-up extrapolated pQCD and hadronic many-body calculations, respectively, is that it indirectly implies chiral symmetry restoration, since, in pQCD, vector and axialvector channels are automatically degenerate.

We finally compare in-medium hadronic rates at rather low temperatures but high baryon density to calculations within a color-superconductor in the so-called Color-Flavor-Locked (CFL) phase (lower left panel of Fig. 2.23). The latter is characterized by a broken chiral symmetry that allows the formulation of a chiral effective theory with vector mesons implemented via a Hidden Local Symmetry, much like in the normal vacuum. The corresponding in-medium dilepton rates again show a surprising agreement with the hadronic-many body calculations [88]. It seems that for $M > 1$ GeV the rate is fairly robust and insensitive to the microscopic matter state.

2.5.3 RG approach: vector manifestation

Within the vector manifestation (VM) scenario of the Hidden Local Symmetry (HLS) framework, dilepton rates have been evaluated in [152]. Following the approach outlined in Sect. 2.4.1.5, Fig. 2.25 shows the form factor and

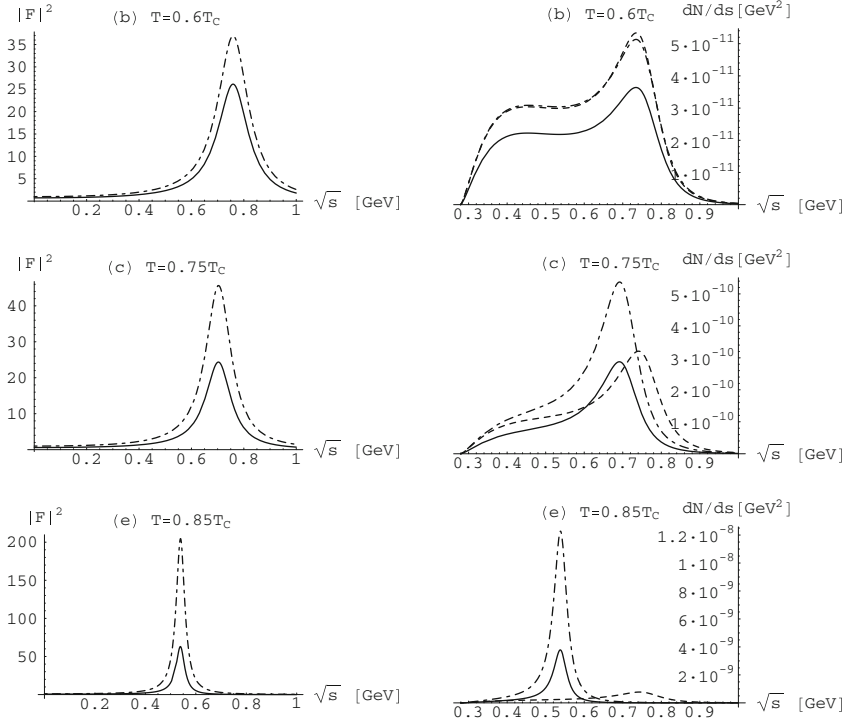


Fig. 2.25 Electromagnetic form factor of the pion (*left*) and dilepton production rate (*right*) as a function of the invariant mass \sqrt{s} for various temperatures [152]. The *solid lines* include the effects of the violation of VD. The *dashed-dotted lines* correspond to the analysis assuming VD. In the *dashed curves* in the right-hand figures, the parameters at zero temperature were used.

the dilepton production rate integrated over three-momentum, Eq. (2.50), confronting the VD and $\mathbb{V}\mathbb{D}$ scenarios presented in Sect. 2.4.1.5. It can be easily seen that the $\mathbb{V}\mathbb{D}$ gives a reduction compared to the VD case. The features of the form factor as well as the dilepton production rate coming from two-pion annihilation shown in Fig. 2.25 are summarized below for each temperature:

Below $T_{flash} = 0.7 T_c$: The form factor is slightly suppressed with increasing temperature. The suppression with $\mathbb{V}\mathbb{D}$ is greater than with VD. This is due to the decrease of the ρ - γ mixing strength g_ρ at finite temperature (see Fig. 2.18). For $T < T_f$, g_ρ decreases mainly due to hadronic corrections. The decrease of g_ρ implies a reduction of the dilepton rate in the $\mathbb{V}\mathbb{D}$ scenario.

Above $T_{flash} = 0.7 T_c$: Once the intrinsic temperature effects are turned on, a shift of the ρ meson mass to lower values can be seen. g_ρ is further reduced by the intrinsic effects and decreases much more rapidly than $g_\rho^{(\text{VD})}$.

Thus the form factor, which becomes narrower with increasing temperature due to the dropping m_ρ , exhibits an obvious difference between the cases with VD and $\overline{\text{V}}\overline{\text{D}}$. The production rate based on the VM (i.e., the case with $\overline{\text{V}}\overline{\text{D}}$) is suppressed compared to that with VD. One observes that the suppression is stronger for larger temperatures: The suppression factor is ~ 1.8 in (c) and ~ 3.3 in (e).

As one can see in (c), the peak value of the rate predicted by the VM in the temperature region slightly above the flash temperature is even smaller than the one obtained with vacuum parameters, while the shapes are quite similar. This indicates that it might be difficult to measure the signal of the dropping ρ experimentally, if this temperature region is dominant in the evolution of the fireball. In the case shown in (e), on the other hand, the VM rate is substantially enhanced compared with the one obtained with the vacuum ρ . This implies that if somewhat higher temperatures are reached, we may have a chance to discriminate a dropping ρ from the vacuum ρ .

2.6 Thermal photon rates

In this section we will address two aspects of real photon observables in heavy-ion collisions. The first are the traditional single-photon transverse-momentum spectra which have been suggested long ago to give information on the (highest) temperatures of the system, as well as modifications of the spectral strength. We will in particular elaborate on connections to dileptons. The second aspect is the more speculative one of di-photon production; pertinent invariant-mass spectra have never been measured in heavy-ion collisions, but the exciting possibility of inferring medium modifications of the σ meson (with its close connection to chiral symmetry restoration) warrants at least an exploratory study of this observable.

2.6.1 *Direct single photons*

The production of thermal photons from strongly interacting matter is a vast subject that cannot be done justice to here; for recent reviews see [16, 177–179]. We will focus on emission from hadronic matter, as this is expected

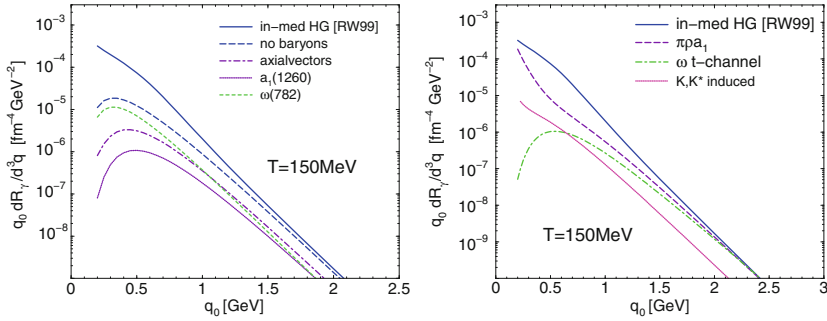


Fig. 2.26 *Left panel:* thermal hadronic photon rates following from the in-medium ρ spectral function of [88]; *right panel:* additional mesonic sources for thermal photons corresponding to non-resonant $\pi\rho \rightarrow \pi\gamma$ reactions (dashed lines) and scatterings involving K and K^* mesons [26].

to be the dominant direct photon source at CBM,⁸ and in particular on connections to dileptons.

As emphasized earlier in Sect. 2.2.1, thermal production rates of dileptons and photons are intimately related since they are governed by the same function (EM current correlator), albeit in different kinematic regimes, recall Eqs. (2.2) and (2.3). Any calculation of dilepton rates to nontrivial order in α_s encodes real photon production. For hadronic production rates this connection has been exploited in [26] in an attempt to establish consistency between low-mass dilepton [23, 34, 180] and direct photon [24, 25] measurements in heavy-ion reactions at CERN-SPS energies.

In the left panel of Fig. 2.26 [26] results are shown for photon rates when the isovector EM correlator (ρ spectral function) of the hadronic many-body approach of [88] is carried to the light-like limit ($q_0 = q$); temperature ($T = 150 \text{ MeV}$) and chemical potential ($\mu_B = 340 \text{ MeV}$) roughly correspond to bombarding energies in the SPS energy regime. The decomposition into various channels, and especially into baryon- and meson-induced processes, shows that for SPS energies the baryonic part of the medium is the prevalent photon source for energies $q_0 \simeq 0.2\text{--}1 \text{ GeV}$. This reflects that baryon effects are the main source of medium effects in low-mass dilepton production. Above $q_0 \simeq 1 \text{ GeV}$, meson-resonance formation makes up the major part of the strength in the lightlike ρ spectral function. However, the latter does not reproduce photon sources corresponding to t -channel meson exchange (π, ω, a_1) in the $\pi\rho \rightarrow \pi\gamma$ reaction. An evaluation of these reactions within the Massive-Yang-Mills approach, taking special care of formfactor effects and extended

⁸ We adopt the nomenclature defined in [178]; “direct” photons are to be distinguished from “decay photons”: the former encompass emission from initial hard pQCD scattering and pre-equilibrium phases, as well as thermal radiation, while the latter are from decays after freezeout, mostly from π^0 and η mesons (commonly referred to as “cocktail” in the dilepton context).

to strangeness-bearing channels, indicates that t -channel exchanges become competitive above $q_0 \simeq 1$ GeV, and dominant above ~ 2.5 GeV, cf. right panel of Fig. 2.26. At temperatures above $T = 150$ MeV, or baryon chemical potentials below $\mu_B = 340$ MeV (as shown in the figure), the mesonic reactions take over at lower energies [26]. Thus, in the CBM energy regime, direct photons of energies up to $\simeq 1$ GeV would provide a valuable cross check on model interpretations of low-mass dilepton observables. At the SPS, this check has been performed [26] by applying the pertinent photon rates to WA98 data [24], employing the same fireball model for the space-time evolution as underlying, e.g., the left panel in Fig. 2.24. The theoretical spectra agree with the data, cf. left panel of Fig. 2.27. Unfortunately, the subtraction method of the (large) background from decay photons limits the experimental direct photon signal to transverse momenta above $q_t > 1.5$ GeV, where the (Cronin-enhanced) primordial pQCD contribution becomes the leading source (the QGP contribution is moderate throughout). More recently, using two-photon interferometry methods, the WA98 collaboration extracted a direct photon signal for small $q_t \simeq 0.1 - 0.3$ GeV [25]. Even though the uncertainty is appreciable, the theoretical predictions of [26] fall short of the yield. Subsequent inclusion of $\pi\pi \rightarrow \pi\pi\gamma$ Bremsstrahlung, while adding $\sim 30\%$ to the yield at $q_t = 0.2$ GeV, could not resolve this discrepancy [32, 181, 182]. In [173] a more precise evaluation of the Bremsstrahlung's contribution, going beyond the soft-photon approximation and including final-state Bose enhancement factors in the multi-dimensional phase space integrals, leads to a 60–70% enhancement over the previous Bremsstrahlung's rate (plus another 20% contribution from $\pi K \rightarrow \pi K\gamma$ Bremsstrahlung), reducing the discrepancy with

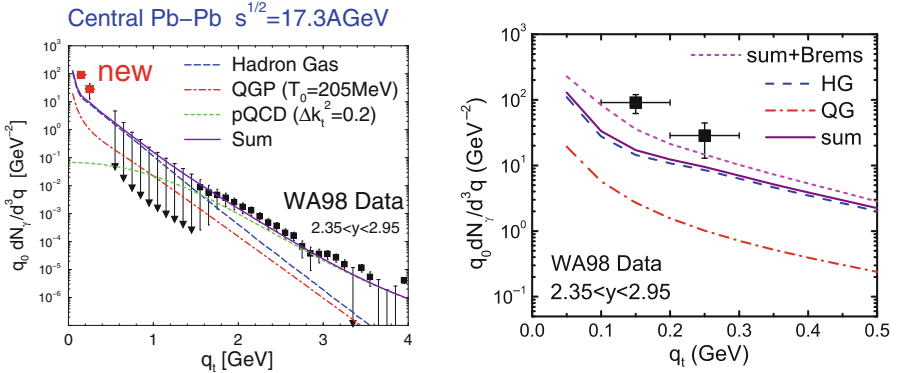


Fig. 2.27 *Left panel:* expanding fireball calculations for thermal photon spectra supplemented with primordial pQCD yields including an estimate of the Cronin effect [26], compared to direct photon spectra in central Pb–Pb collisions at SPS [24]. The underlying hadronic emission rates correspond to the ones displayed in the *right panel* of Fig. 2.26. *Right panel:* the same calculation (*solid line*) compared to low-momentum WA98 data [25] in the same reaction; the addition of improved Bremsstrahlung's rates from $\pi\pi$ and πK scattering (*upper dotted line*) [173] significantly reduces the discrepancy with the data.

the low- q_t data, cf. right panel of Fig. 2.27 (the suppression of the yield due to Landau-Pomeranchuk-Migdal interference has not been included but was estimated to be a factor of ~ 0.8 at $q_t = 0.2$ GeV). Also note that the Bremsstrahlungs spectrum has a significantly steeper slope than the previously calculated photon sources, thus not compromising the compatibility with the WA98 data (and upper limits) at larger momentum.

It is highly desirable to clarify the situation of the possibly very large enhancement at (very) low photon momenta. In particular, a reasonably accurate measurement of low- q_t photons within CBM would be valuable, providing additional clues on the origin of the WA98 enhancement, e.g., whether the source is of baryonic or mesonic origin.

2.6.2 Diphotons and in-medium “ σ ”

According to a suggestion by Hatsuda and Kunihiro [183] the light sigma-meson $\sigma(600)$ can serve as an indicator for the chiral phase transition. In the vacuum, the $\sigma(600)$ is a very broad resonance in the $\pi\pi$ scattering amplitude with a width $\Gamma_\sigma = 600 - 1,000$ MeV [30] due to $\sigma \rightarrow \pi\pi$. According to the standard representation, the σ and the π are chiral partners so that at the chiral restoration transition their masses become degenerate. Consequently, the channel $\sigma \rightarrow \pi\pi$ shuts off already at temperatures and chemical potentials where the condition $m_\sigma = 2m_\pi$ is reached, and the σ width could become relatively small until at the deconfinement transition the channel for decays in quark-antiquark states opens. Experimental signatures might be expected in the channel $\sigma \rightarrow \gamma\gamma$, where a resonance structure or at least a shoulder should be observable at the two-pion threshold, $M_{\gamma\gamma} \sim 2m_\pi \sim 300$ MeV.

2.6.2.1 Estimates for the $\sigma \rightarrow 2\gamma$ production rate

In [184], an estimate of diphoton production via $\pi\pi \rightarrow \gamma\gamma$ annihilation has been conducted within a Nambu-Jona-Lasinio (NJL) model. In the vacuum, the pion exchange Born diagram dominates this process, but when approaching the critical temperature, quark-exchange substructure effects lead to a substantial enhancement of the pertinent cross section, which develops a rather pronounced maximum structure in the T - μ phase diagram as shown in the left panel of Fig. 2.28. The pertinent diphoton production rate is displayed in the right panel of Fig. 2.28 for different temperatures at fixed quark chemical potential [184].

The optimal conditions for observing a soft- σ induced enhancement in heavy-ion reactions occur if the latter can reach into the realm of a first order transition and create a mixed phase with extended lifetime. In this case one can hope for the formation of an extended region of matter at constant

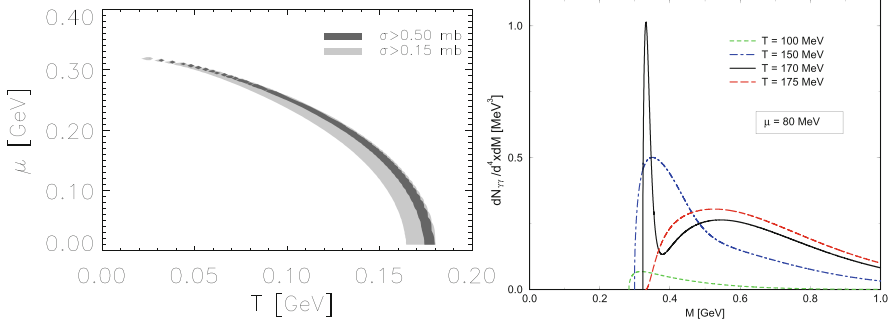


Fig. 2.28 Diphotons from “sigma” decays within a schematic NJL calculation neglecting pion width effects [184]. *Left panel:* regions of maximal cross section for the process $\sigma \rightarrow \gamma\gamma$ in the phase diagram of quark chemical potential vs. temperature; *right panel:* corresponding thermal production rate of photon pairs vs. their invariant mass for different temperatures at $\mu_B/3 = \mu = 80$ MeV.

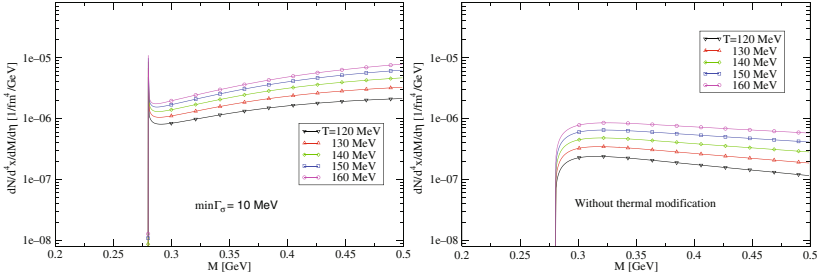


Fig. 2.29 Diphoton production rate per 4-volume and invariant mass at the critical temperature for a first order chiral transition produced in a nucleus–nucleus collision. The width of σ is 10 MeV (*left*) and at its vacuum value (*right*).

temperature thus generating a diphoton mass spectrum which resembles the emission rate at fixed temperature.

A schematic study of the width effect on the 2γ production rate, $dN^{\gamma\gamma}/d^4x dM$, is summarized in Fig. 2.29. For definiteness, the mass of the pion is taken at its vacuum value, $m_\pi = 140$ MeV, and the mass of σ as $m_\sigma = 2m_\pi$. Within the NJL model the quark mass then follows $m_q = \sqrt{3}m_\pi/2$. We assume that the ratio $m/f_\pi \approx 4$ does not change in the range of temperatures we are interested in. Remaining details are also taken from the NJL model. As the temperature of the phase transition is not well known and will probably vary with μ_B , we choose a range from 120 to 160 MeV. The σ meson spectral function is assumed to be narrow (with a width parameter of 10 MeV), as well in its vacuum form. To estimate the maximum effect, additional broadening of the meson spectral functions in a hot/dense medium is neglected. It

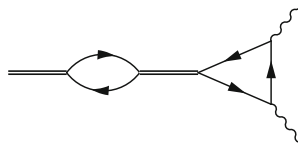


Fig. 2.30 Feynman diagram for the $\rho(\omega, \phi) \rightarrow \gamma\gamma$ decay. The crossed diagram is not shown.

appears that for σ widths above 10 MeV, it will be very hard to discriminate the threshold enhancement against an expected large combinatorial background of both decay and direct photons. Such widths, are, however, easily generated if realistic in-medium spectral functions of pions are accounted for both in nuclear and/or hot meson matter, see, *e.g.*, [185, 186]. Thus, the feasibility of detecting a “ σ ” signal in the diphoton spectrum appears rather questionable.

2.6.2.2 Other anomalous channels: $\rho \rightarrow \gamma\gamma$, $\sigma \rightarrow e^+e^-$

The medium-induced breaking of Lorentz symmetry for ground state matter can facilitate processes that are forbidden in free space. Typical examples are the mixing of scalar and vector mesons such as σ - ω , ρ - a_0 and ϕ - $f_0(980)$. The role of the σ - γ transition in the enhancement of e^+e^- production due to the (in vacuum forbidden) decay $\sigma \rightarrow e^+e^-$ near the two-pion threshold was discussed by Weldon [187]. (According to the vector dominance model, all electromagnetic interactions of mesons should be mediated by vector mesons: a scalar transforms to a vector which then transforms to a photon.) The effect of σ - ω and ρ - a_0 mixing on the pion-pion annihilation in dilepton production was investigated in [188], where it was shown that additional peaks appear in the dilepton spectrum in sufficiently dense baryonic matter. On the other hand, the scalar-vector mixing can trigger two-photon decays of vector mesons, where a vector meson first transforms to a neutral scalar meson which then produces two correlated photons. In the case of ρ - a_0 mixing, an additional (resonant) amplification can occur because of the degeneration of the ρ and a_0 meson masses under particular conditions in dense matter [189]. Moreover, the enhancement in two-photon or dilepton production from the processes with σ - ω , ρ - a_0 and ϕ - f_0 mixing can be observed in a wide range of temperature and baryon density [190]. Earlier estimates of “anomalous” dilepton production from $q\bar{q}$ annihilation in deconfined quark matter have been performed in [191]. The pertinent results for scalar-vector mixing have been used by the authors of [189].

The process is represented by the diagram drawn in Fig. 2.30. First, a quark loop mediates vector-scalar mixing, followed by an intermediate scalar

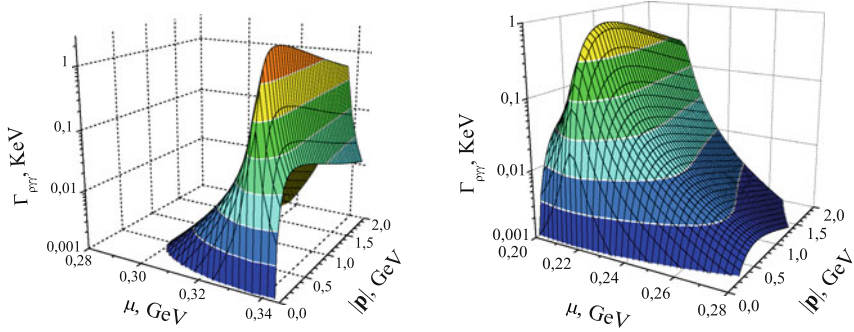


Fig. 2.31 Two-photon decay width of ρ meson as a function of μ and $|\mathbf{p}|$ for $T = 20$ MeV (left panel) and 120 MeV (right panel).

resonance and completed by the triangular quark loop describing a decay of the scalar meson to photons. For rough estimates we will assume that the ρ meson mass is constant in the hadron phase, while the σ meson mass drops significantly with growing temperature and chemical potential, until it becomes almost degenerate with the pion mass close to chiral symmetry restoration. The same is expected for the a_0 meson.

Since the decay $\rho \rightarrow \gamma\gamma$ involves the a_0 meson the corresponding amplitude is proportional to the a_0 propagator,

$$D_{a_0} = \frac{1}{M_{a_0}^2 - M_\rho^2 - i\Gamma_{a_0}(M_\rho)M_{a_0}}, \quad (2.51)$$

which is of the Breit-Wigner form; M_{a_0} and M_ρ are masses of a_0 and ρ , respectively, while Γ_{a_0} is the width of a_0 (it depends on the mass of the decaying particle, M_ρ). Here, it must be pointed out that due to the degeneration of a_0 and ρ masses at a certain temperature and chemical potential, an additional enhancement can arise from D_{a_0} . This enhancement is similar to that in the process $\pi\pi \rightarrow \gamma\gamma$ [184, 192] and $\pi\pi \rightarrow \pi\pi$ [193]. Numerical estimates for the width of the process $\rho \rightarrow \gamma\gamma$ at various values of chemical potential and 3-momentum \mathbf{p} of the ρ meson are given in Fig. 2.31 for two temperatures, 20 and 120 MeV.

One can perform similar calculations for the decays $\omega \rightarrow \gamma\gamma$ and $\phi \rightarrow \gamma\gamma$. The characteristic order of magnitude for rate of such processes is a few keV. The maximal effect is reached near the phase transition and for momenta near the maximum in the momentum distribution for the decaying particle.

A peculiarity of the decay $\rho \rightarrow \gamma\gamma$ is that the a_0 meson mass is larger than the ρ meson mass in vacuum, but may drop significantly when approaching the transition to the phase with restored chiral symmetry. One can envisage that under particular conditions the masses of a_0 and ρ become degenerate, which is followed by a resonant amplification of the decay $\rho \rightarrow \gamma\gamma$ and no-

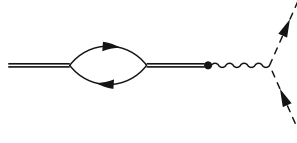


Fig. 2.32 The diagram that describes dilepton decays of the scalar meson in medium via scalar-vector mixing.

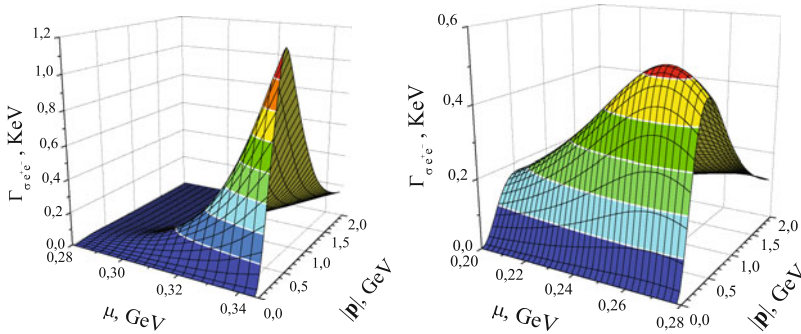


Fig. 2.33 Decay rate for $\sigma \rightarrow e^+e^-$ at $T = 20$ MeV (*left panel*) and 120 MeV (*right panel*).

ticeable enhancement near the ρ meson mass in the two-photon spectrum. As for the σ - ω mixing, their mass difference is expected to grow with μ , and, as a consequence, no resonant phenomenon occurs in this decay. Therefore, the number of two-photon events related to decays of vector mesons will be dominated by $\rho \rightarrow \gamma\gamma$ rather than $\omega \rightarrow \gamma\gamma$.

The direct decay of the σ meson to dileptons is also forbidden in vacuum and is allowed in dense medium due to σ - ω mixing. After the transition of σ to ω , the latter transforms to a photon (according to VDM) which then produces an electron and a positron (see the diagram in Fig. 2.32). Numerically, the decay $\sigma \rightarrow e^+e^-$ rate reaches about 1.5 keV at $T \sim 20$ MeV, Fig. 2.33. One can estimate the decays $a_0 \rightarrow e^+e^-$ and $f_0(980) \rightarrow e^+e^-$ in the same manner.

Both the two-photon decays of vector mesons and dilepton decays of scalar mesons have common peculiarities: they are forbidden in the vacuum and open up only in the medium. The effect is maximized near the phase transition and is more pronounced for smaller temperature and larger chemical potential. However, for practical purposes the decays widths seem to be rather small unless anomalously small total widths or particular resonance degeneration phenomena occur.

Chapter 3

Hadronic resonance spectroscopy

The use of dilepton invariant-mass spectra to obtain direct spectral information on hadronic properties in medium is limited to mesons in the vector channel. In addition, the measured spectra (after background and “cocktail” subtraction) are composed of a superposition of spectral functions at varying temperatures and densities (which, of course, provides unique access to the hot and dense phases). The situation changes for invariant-mass spectra of strongly decaying resonances: due to final-state absorption, undistorted emission is mostly emanating from temperatures and densities at the late stages of a heavy-ion collision, but a large variety of hadronic states is, in principle, available with comparatively high rates (not being penalized by α_{em}^2). The drawbacks are, of course, severe: one is only probing low densities/temperatures, the system is about to break up rendering the notion of equilibrium questionable, and the backgrounds are large. Nevertheless, an appreciable number of resonances and associated spectral modifications have been studied in both hadronic and heavy-ion collisions (even e^+e^- annihilation), e.g., $\Delta \rightarrow \pi N$ at BEVALAC, SIS [194, 195] and RHIC [196], $\phi \rightarrow KK$ at AGS [197], SPS [198] and RHIC [199], strange baryon resonances [200] and $\rho \rightarrow \pi\pi$, $K^* \rightarrow K\pi$ at RHIC [98, 201]. We emphasize again the importance of assessing the in-medium $a_1(1,260)$ spectral function, possibly via $\pi^\pm\gamma$ spectra [97], which would constitute a major milestone towards establishing the connection to its chiral partner, the ρ meson, which is the main contributor to low-mass dileptons.

In the following we discuss selected examples for resonances in the light-quark sector where previous measurements have provided promising results. The method also applies to strange and possibly charmed resonances, whose medium effects are addressed in Chaps. 4 and 5.

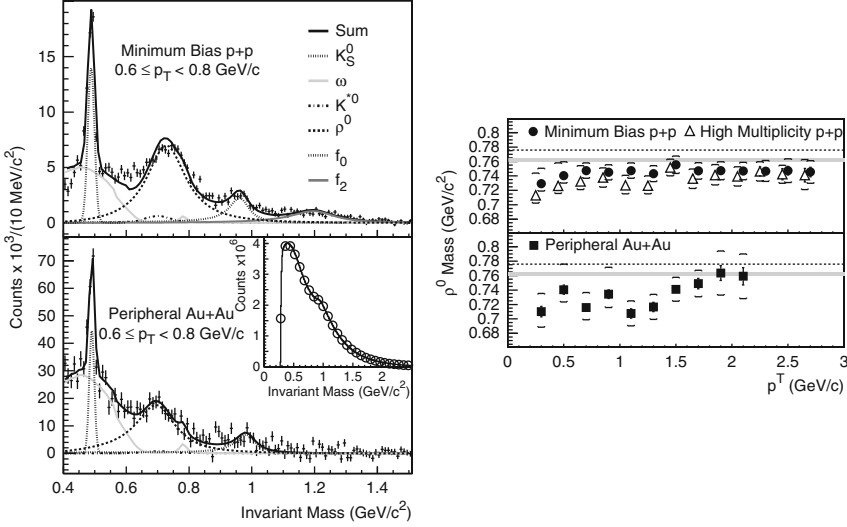


Fig. 3.1 STAR results [98] for $\pi^+\pi^-$ invariant-mass spectra in $\sqrt{s_{NN}} = 200$ GeV p - p (upper left panel) and peripheral Au–Au (lower left panel) collisions at RHIC. The right panel displays extracted ρ -mass values as a function of transverse momentum based on fits to the mass spectra using a relativistic Breit-Wigner spectral function and appropriate phase-space for background subtraction; the horizontal lines (bands) represent the average ρ -mass values extracted from e^+e^- annihilation (hadronic collisions) at lower energies.

3.1 Meson resonances

The most prominent resonance in the $\pi\pi$ channel is the (P -wave) vector-isovector $\rho(770)$ meson. Measurements of $\pi^+\pi^-$ invariant-mass spectra in $\sqrt{s_{NN}} = 200$ GeV p - p and peripheral Au–Au collisions by the STAR collaboration at RHIC have found rather large downward mass shifts of the ρ resonance peak by about -40 and -70 MeV, respectively, cf. Fig. 3.1. The effect is most pronounced at low transverse momenta, and has triggered a number of theoretical works to investigate its origin [97, 202–206]. In [202], contributions to the ρ mass were estimated from the real part of resonant scattering amplitudes on pions and nucleons in the heat bath. The net effect under the expected thermal freezeout conditions at RHIC was rather moderate; using a rate equation framework for the spectra, an additional attractive mass shift of about -50 MeV was inferred. Since the contributions from resonances can be both attractive and repulsive, they tend to cancel each other. The main effect was, in fact, from a scalar mean field which has been identified with a “dropping mass”. A rate-equation approach was also employed in [97, 203]. The former study [203] confirmed the need for an attractive mass shift of the ρ of at least -50 MeV in Au–Au, on top of thermal phase space effects [207]. In the latter study [97], an in-medium spectral function

as calculated from hadronic many-body theory was implemented (which is consistent with dilepton measurements at the CERN-SPS [35, 88]). Under conditions resembling thermal freezeout in Au–Au at RHIC, a factor of ~ 2 broadening renders the spectral shape more susceptible for modulations due to thermal phase space. Bose-Einstein enhancement on the outgoing pions, as well as an underlying (falling) “background” from scalar $\pi^+\pi^-$ correlations combines to a total mass shift of -30 MeV relative to conditions expected in p – p collisions, in line with experiment. However, the -40 MeV shift in p – p collisions is not reproduced (in [208], e.g., this effect has been largely attributed to an interference between direct ρ decays and rescattered pions).

In [204], the single-freezeout model has been applied to $\pi\pi$ spectra. This approach assumes a sudden decoupling at a thermal freezeout temperature that coincides with chemical freezeout at $T_{ch} \simeq 165$ MeV. In such a setting, resonant correlations can be implemented using a virial expansion via vacuum (two-body) scattering phase shifts, or, more precisely, their derivatives [205, 209, 210]. This, in particular, implies, that the contribution of broad resonances is suppressed (while in the rate-equation approach, this is compensated by the increase in emission rate). Again, if the width of the ρ is not modified, a thermal mass shift of -50 MeV has been inferred to be compatible with the STAR $\pi\pi$ data.

More information can be obtained from the *number* of detected ρ^0 mesons. For p – p and peripheral Au–Au collisions, the measured ρ^0/π^- ratios are 0.183 ± 0.027 and 0.169 ± 0.037 , respectively (dominated by systematic errors) [98]. Both values tend to be larger than predictions from thermal models at chemical freezeout, yielding $\sim 0.11 \pm 0.02$ [97, 211], which is the more surprising as $\rho^0 \rightarrow \pi^+\pi^-$ is expected to be emitted at thermal freezeout, where the thermal ρ^0/π^- ratio is further reduced, to about 0.06 – 0.08 [97]. The emission of 2 generations of $\rho^0 \rightarrow \pi^+\pi^-$ in a rate-equation picture could be a possibility to resolve the discrepancies [97], even in p – p collisions [208].¹ Additional information on the question of rescattering and possible modifications in line shapes due to phase space effects may be obtained from transport simulations [213].

Further indications for modifications in π – π invariant mass spectra can be found from the pair- p_T spectra, cf. Fig. 3.2 [98]. One recognizes a significant change in shape, from power-law in p – p to exponential in Au–Au, which corroborates that the emission environment in heavy-ion collisions is quite different, indicative for the final stages of a thermalized medium.

$\pi\pi$ invariant mass spectra contain, in principle, information on isoscalar channels as well. In p – p collisions, one finds a clear signal of the $f_0(980)$ (and possibly of the tensor $f_2(1, 270)$) meson, see upper left panel of Fig. 3.1. The $f_0(980)$ is also visible in the Au–Au spectra. The low-lying “ $\sigma(500)$ ” (listed as $f_0(600)$ in recent editions of the review of particle physics [30]) is more diffi-

¹ Evidence for $\pi\pi$ rescattering in peripheral In – In has recently been reported in dimuon spectra by NA60 [34]; the secondary production is concentrated at low p_T [212] and may be quite consistent with the analysis of [208] at RHIC energy.

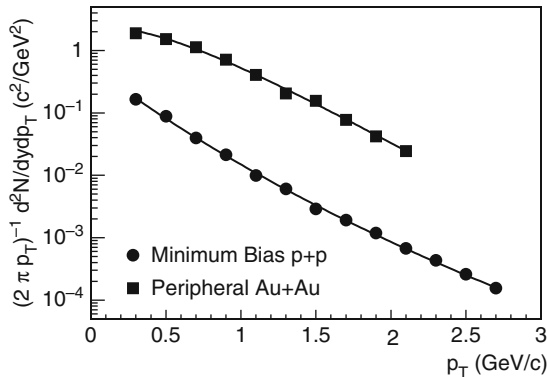


Fig. 3.2 STAR results [98] for transverse-momentum spectra of $\pi^+\pi^-$ pairs in the ρ -mass region in $\sqrt{s_{NN}} = 200$ GeV p - p (circles) and peripheral Au-Au (squares) collisions at RHIC.

cult to identify, mainly due to its broad structure. Pion- and photon-induced two-pion production experiments off nuclei, $\pi(\gamma)A \rightarrow \pi\pi A$, have found intriguing evidence for medium effects in terms of a substantial enhancement of strength close to the two-pion threshold [214–216]. Whether this is due to nuclear many-body effects [185, 217] or a “genuine” dropping σ mass [218], and in how far it is related to partial chiral symmetry restoration, is not clear at present. In [219, 220] final-state interactions of the individual outgoing pions were found to largely account for the observed enhancement. The final-state interactions in the nuclear medium are based on the same physics as the nuclear many-body effects evaluated in [185, 217], and therefore both effects do not mutually exclude each other (on the contrary, both should be included). It would be very interesting to investigate the invariant-mass region close to the two-pion threshold in heavy-ion reactions [97, 202], preferably at high baryon density where the predicted medium effects are large [130, 221].

3.2 Baryon resonances

Before turning to the baryon spectroscopy in hadronic models with applications to heavy-ion collisions, let us make a few general remarks including aspects of chiral symmetry and QCD sum rules.

The excitation spectrum in the baryon sector is characterized by an extraordinary richness: the nucleon can be excited in both isospin and spin quantum numbers, while each IJ^P state itself maybe considered as a base for building another tower of (mass) excitations. For example, quark models on various levels of sophistication have been employed to compute these

excitation spectra, resulting in a large number of states, not all of which have been experimentally identified. This constitutes the well-known “missing resonance problem”; part of this problem are the often rather large decay widths of several hundred MeV. The situation becomes even more complicated in hot and dense hadronic matter where one generally expects further broadening.² In-medium properties of baryon resonances are also important to evaluate medium effects in the meson sector. As discussed in the previous section, the medium modifications of the light vector mesons ρ and ω (including their pion cloud) are largely driven by the coupling to the baryonic component of the matter. These interactions, in turn, are often dominated by resonant meson-nucleon scattering, rendering a quantitative (selfconsistent) determination of the medium modifications of the intermediate baryon resonance mandatory (e.g., whether it is dynamically generated or a genuine state).

3.2.1 Chiral symmetry of baryons

As in the meson sector, a key issue concerns how (the approach toward) chiral symmetry restoration manifests itself in the in-medium spectrum of baryons. In a first step, one has to identify the chiral structure of the baryon spectrum in the vacuum, i.e., the chiral partners, e.g., N – $N(1,535)$ and Δ –($N(1,520)$, $\Delta(1,700)$), see, e.g., [222–226]. Since chiral symmetry breaking is a low-energy phenomenon, its effects should cease at sufficiently large excitation energies. In particular, Glozman [223, 227] advanced the view that chiral symmetry, in the sense of degeneracy of chiral partners, is restored for high-lying baryon resonances, cf. Fig. 3.3. In [224, 225] chiral representations for baryons have been elaborated within a linear sigma model, arriving at a quartet scheme where N_+^* , N_-^* , Δ_+^* and Δ_-^* with given spin form a chiral multiplet. Empirical mass orderings and pion decay branchings seem to support this identification.

3.2.2 Baryon masses and QCD condensates

In a chiral expansion, the nucleon mass in the vacuum takes the form [228]

$$M_N = M_N^{(0)} + A_1 m_\pi^2 + A_2 m_\pi^3 + A_3 m_\pi^4 \log(m_\pi/M_N) + A_4 m_\pi^4 + \dots \quad (3.1)$$

² This applies, for instance, for the so-called second resonance group (including $N(1,440)P_{11}$, $N(1,520)D_{13}$, $N(1,535)S_{11}$) as observed in photo-absorption or electro-excitation of mesons on the nucleon; even for light nuclear targets ($A \geq 4$), these resonances are strongly broadened converging to an essentially structureless “universal curve”, independent of atomic mass number (upon scaling by A), recall left panel of Fig. 2.10.

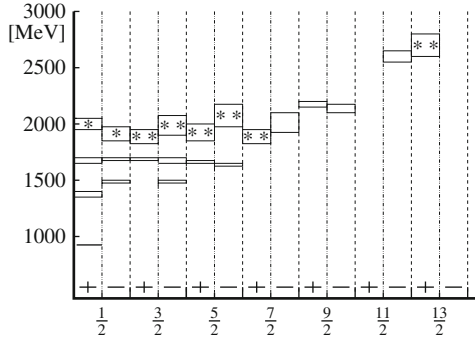


Fig. 3.3 Parity partners for nucleons of various spins. According to [223], a degeneracy of parity partners sets in at masses above ~ 1.7 GeV (similarly for Δ states).

Note that, in the chiral limit ($m_\pi = m_{u,d} = 0$), the nucleon mass is still fairly heavy, $M_N^{(0)} = 770$ MeV.³ the nucleon remains fairly heavy; explicit symmetry breaking shifts the nucleon mass by 20% upwards. This might be contrasted with the celebrated Ioffe formula (cf. [229])

$$M_N = -\frac{8\pi^2}{\mathcal{M}^2} \langle \bar{q}q \rangle, \quad (3.2)$$

which ascribes the nucleon mass entirely to the formation of the chiral condensate ($\mathcal{M} \simeq 1$ GeV is the so-called Borel mass). One should, however, keep in mind that the Ioffe formula is a somewhat simplistic approximation to rather complex QCD sum rules for the nucleon, where, similar to the meson case, a variety of quark and gluon condensates (including quark-gluon and higher-order quark condensates, in particular, 4-quark ones) play an important role (or, in the medium, moments of parton distributions). Nevertheless, the Ioffe formula is very suggestive to expose the relation of in-medium properties and QCD vacuum properties as encoded in the chiral condensate. A recent analysis [230] confirms that, within the conventional sum rule approach, a freezing of all QCD parameters other than the chiral condensate leads to an in-medium nucleon that decreases linearly with $\langle \bar{q}q \rangle$ to leading order in density.

The QCD sum rule approach to baryon masses is as for mesons: define a phenomenological current with suitable interpolating fields (which is subject of ongoing trials [51, 231, 232]), perform the Operator Product Expansion (here the condensates come into play) and equate it to the moments of the baryon spectral function. The latter step is hampered in a similar way as for mesons: baryon and anti-baryons mix (or need to be disentangled), and

³ Instead of quark mass one often refers to the pion mass, cf. [228] for the definition of the A_i and further details.

Baryon	N	Λ	$\Sigma^{\pm,0}$	$\Xi^{-,0}$
Shift (MeV)	-154	-152	-18	0

Table 3.1 Shift of mass parameters of baryon octet ground states following from lowest-order chiral perturbation theory in isospin-symmetric nuclear matter [240].

only integrals over spectral functions are subject of the sum rules. Even the usual decomposition into a ground-state (g.s.) pole + continuum faces problems [233].

The pioneering works [234] found a sizeable influence of the poorly known four-quark condensates. Revisiting such approaches evidence that three different combinations of four-quark condensates determine the in-medium spectral properties of the nucleon [235]. However, a stable result is the large (order of a few hundred MeV) and nearly compensating scalar and vector self-energy contributions, analog to advanced Brueckner calculations [236].

The extension to other baryons is essentially straightforward. In [237] the Δ has been analyzed within the QCD sum rule approach. In [238] coupled positive and negative parity flavor-octet baryons have been studied in vacuum, in particular with the assignments of $\Lambda(1,670)$ and $\Sigma(1,620)$ as chiral partners of g.s. Λ and Σ ; the $\Lambda(1,405)$ is conjectured as flavor singlet or exotic state. In [239] the mass spectrum in the baryon decuplet sector has been considered, again focussing on the vacuum case.

An alternative, model-independent, approach to assess in-medium changes in baryon masses is provided by chiral perturbation theory, as has been carried out in [240] for nuclear matter to leading order in density; the resulting mass shifts are summarized in Table 3.1.

Finally, let us briefly discuss effective hadronic model approaches. Here, the model parameters are typically fixed in the vacuum by reproducing a large set of scattering data. This allows for a more complete account of the interactions in the vacuum, and thus more realistic applications to in-medium properties, at least for small and moderate densities. In a unitary coupled-channel approach the Giessen group [125] has computed in-medium spectral functions of the low-lying baryons, see Fig. 3.4. Note that the π , η and ρ mesons are accounted for within the same framework, thus representing a step towards a consistent treatment of hadronic complexity.

3.2.3 Baryon resonance decays in heavy-ion collisions

The most prominent baryon resonance, $\Delta(1,232)$, predominantly couples to the P -wave πN channel, much like the ρ to the $\pi\pi$ channel. Its properties in cold nuclear matter have been extensively studied in both photon and hadron-induced reactions on nucleons and nuclei, indicating a moderate broadening

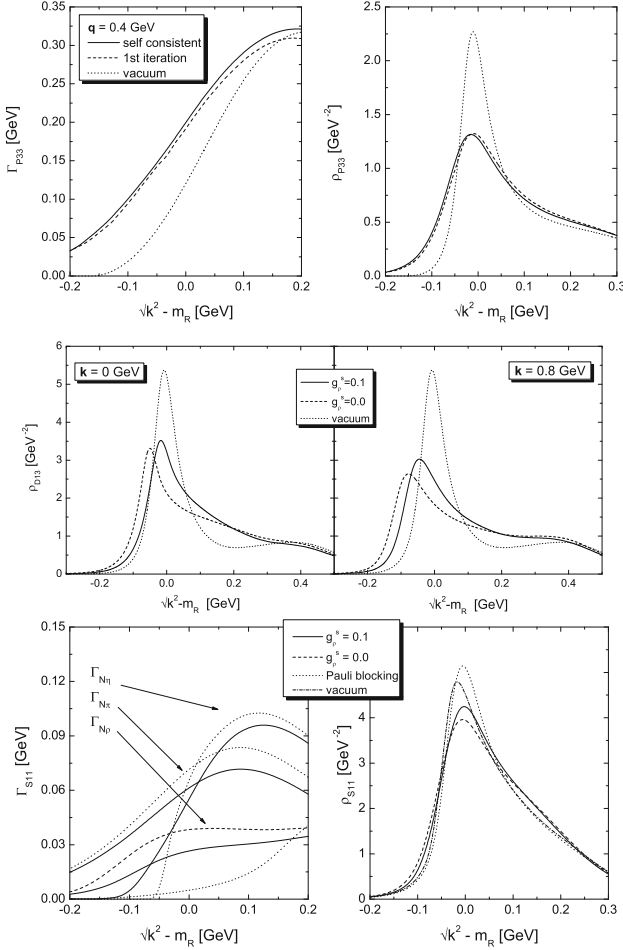


Fig. 3.4 Baryon spectral functions from [125]. *Top row*: Width (*left panel*) and spectral function (*right panel*) of $\Delta(1,232)P_{33}$ at momentum 0.4 GeV/c; *middle row*: $N(1,520)D_{13}$ for momenta 0 (*left panel*) and 0.8 GeV/c (*right panel*); *bottom row*: partial widths (*left panel*) and spectral function (*right panel*) of $N(1,535)S_{11}$ at momentum of 0.8 GeV/c. *Dotted curves* are for vacuum, while *solid* and *dashed curves* are for two coupling parameters in nuclear matter.

(presumably stabilized by Fermi blocking of the nucleon) and possibly a small mass shift, see, e.g., [241–244].

$\pi^\pm p$ invariant mass spectra in heavy-ion collisions have been measured at BEVALAC/SIS [194, 195] as well as at RHIC energies [201]. In the former, i.e., for bombarding energies of 1–2 AGeV, significant reductions in the Δ peak position of -50 to -100 MeV have been reported. Thermal phase space at

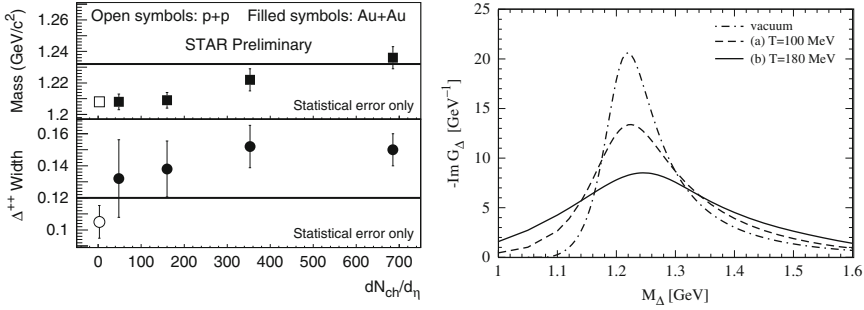


Fig. 3.5 *Left panel:* mass and width of the $\Delta(1,232)$ as extracted from πp invariant mass spectra at RHIC as a function of collision centrality (characterized by the charged particle multiplicity) [201]. *Right panel:* hadronic many-body calculations of the in-medium Δ spectral function under RHIC conditions, including both a renormalization of the πN cloud and direct $\Delta + \pi \rightarrow B^*$ interactions (B^* : baryon resonances) [244].

typical freezeout temperatures of $T_{fo} \simeq 70$ MeV seems insufficient to account for these results, while transport simulations [245, 246] are in reasonable agreement with data without invoking a reduced in-medium Δ mass.

In $\sqrt{s_{NN}} = 200$ GeV Au–Au collisions at RHIC, both mass and width of the Δ were found to increase with increasing collision centrality by about 20–30 MeV and ~ 40 MeV, respectively, from the values measured in p – p collisions, cf. left panel of Fig. 3.5. This is in rough agreement with the Δ spectral function calculated in [244], which includes both the medium modifications of the π – N cloud and direct $\Delta + \pi \rightarrow B^*$ resonance scattering. These calculations further imply that the Δ resonance essentially melts when approaching the expected phase boundary, both under RHIC and CBM conditions.

A reliable calculation of in-medium spectral functions of baryon resonances requires as input in-medium π and N spectral functions. The former has been discussed in some detail in the previous section. The nucleon mass is expected to be reduced in cold nuclear matter due to the scalar mean field, while at finite temperatures a substantial collisional broadening has been predicted [244, 247]. This raises the interesting question how the N spectral function develops toward chiral symmetry restoration, in particular how it degenerates with its chiral partner, the $N^*(1,535)$. An ambitious goal would therefore be to measure $N^*(1,535)$ decays, e.g., in the $N\eta$ channel. In Sects. 4.2 and 5.5.4 we will briefly return to baryon spectroscopy including strangeness and charm.

Chapter 4

Strangeness

The strange quark is significantly heavier than the light up and down quarks, with a current mass parameter of $m_s \approx \mathcal{O}(\Lambda_{\text{QCD}})$. However, it is still small compared to the typical hadronic scale of 1 GeV and thus rather considered as (and treated in analogy to) a light quark than a heavy quark (the charm-, bottom- and top-quark masses are (well) above 1 GeV). The quantum number “strangeness”, S , is conserved in strong interaction processes, implying associated strangeness production in such processes. Strangeness-changing weak interactions couple strange quarks or hadrons to other flavor sectors. The quark structure of hadrons with strange quark constituents can be read off from Fig. 5.1 in the zero-charm planes.

Historically, an important motivation for considering strangeness as a probe of hot and dense matter was the suggestion by Müller and Rafelski [248] that enhanced strangeness production could be an indicator for creating deconfined matter in ultrarelativistic heavy-ion collisions. Indeed, at SPS energies and above, chemical equilibration of strangeness production has been identified as a key difference in the hadro-chemistry of (central) A – A compared to p – p collisions [211, 249]. At lower energies, in particular around the strangeness production threshold, kaon production has been widely utilized to study modifications of kaon masses (or, more generally, their spectral functions) in hot hadronic matter. Section 4.1 will discuss this topic which comprises the main part of this chapter. Less attention has been paid thus far to in-medium modifications of strange baryons, which will be briefly addressed in Sect. 4.2.

4.1 Kaons in dense matter

The natural starting point to study the interaction of pseudoscalar mesons and baryons at low energies is the chiral Lagrangian. Kaplan and Nelson were the first to apply the chiral Lagrangian to the properties of kaons in nuclear matter at the mean field level [250, 251]. The chiral Lagrangian has been applied extensively to derive the in-medium properties of kaons [252–265]. Applications of various approaches to heavy-ion collisions can be found in [266].

We first discuss the chiral Lagrangian used at the mean-field level and then turn to its more realistic coupled-channel applications. The leading order terms that are relevant for a mean field evaluation of the kaon self energy are

$$\mathcal{L} = \bar{N}(i\gamma^\mu\partial_\mu - m_N)N + \partial^\mu \bar{K}\partial_\mu K - (m_K^2 - \frac{\Sigma_{KN}}{f^2}\bar{N}N)\bar{K}K - \frac{3i}{8f^2}\bar{N}\gamma^\mu N \bar{K} \overleftrightarrow{\partial}_\mu K, \quad (4.1)$$

where the parameter $f \simeq f_\pi \simeq f_K$ may be identified with the pion or kaon decay constant at leading order. It contains a vector interaction, the Weinberg-Tomozawa term, which is repulsive for kaons and attractive for antikaons due to G -parity. It constitutes the leading order term. The attractive scalar interaction, the Kaplan-Nelson term, is equal for kaons and antikaons and enters at subleading order. The strength of the Kaplan-Nelson term is controlled by the magnitude of the kaon-nucleon sigma term Σ_{KN} .

In contrast to the pion-nucleon-sigma term which is experimentally well determined from pion-nucleon scattering ($\Sigma_{\pi N} \simeq 45$ MeV), the kaon-nucleon-sigma term is poorly known. It is related to the strangeness content of the nucleon. Quenched lattice QCD simulations suggest values between 300 and 450 MeV [252, 267, 268]. However, at present there is no unquenched three-flavor QCD lattice simulation available that is extrapolated to the continuum limit and down to physical quark masses. Thus a reliable value for the kaon-nucleon sigma term is not yet available. While heavy-baryon Chiral Perturbation Theory (ChPT) [269] predicts the range $\Sigma_{KN} = 380 \pm 40$ MeV ($I=1$) a chiral quark model calculation finds $\Sigma_{KN} = 386$ MeV [270]. Significantly smaller values, compatible with zero, have been obtained in a recent self-consistent one-loop computation that for the first time considered the effect of intermediate states of a Goldstone boson and a baryon octet or baryon decuplet based on the chiral Lagrangian [271]. Thus the current theoretical range for Σ_{KN} extends from ~ 0 up to 450 MeV.

4.1.1 Mean field dynamics

For estimates of kaon mass shifts in nuclear matter and kaon dynamics in heavy ion reactions the above Lagrangian (4.1) was frequently applied in the

mean field ansatz. Already in the early 1990s corresponding calculations were carried out in the Nambu-Jona-Lasinio (NJL) model [272]. The in-medium Klein-Gordon equation for the kaons follows from Eq. (4.1) via the Euler-Lagrange equations

$$\left[\partial_\mu \partial^\mu \pm \frac{3i}{4f^2} j_\mu \partial^\mu + \left(m_K^2 - \frac{\Sigma_{KN}}{f^2} \varrho_N^s \right) \right] \phi_{K^\pm}(x) = 0 \quad . \quad (4.2)$$

Here $j_\mu = \langle \bar{N} \gamma_\mu N \rangle$ is the nucleon four-vector current and $\varrho_N^s = \langle \bar{N} N \rangle$ the scalar baryon density. With the vector potential

$$V_\mu = \frac{3}{8f^2} j_\mu \quad (4.3)$$

and an effective kaon mass m_K^* defined as [273]

$$m_K^* = \sqrt{m_K^2 - \frac{\Sigma_{KN}}{f^2} \varrho_N^s + V_\mu V^\mu} \quad (4.4)$$

the Klein-Gordon equation (4.2) can be written as

$$\left[(\partial_\mu \pm iV_\mu)^2 + m_K^{*2} \right] \phi_{K^\pm}(x) = 0 \quad . \quad (4.5)$$

Thus the vector field is introduced by minimal coupling into the Klein-Gordon equation with opposite signs for K^+ and K^- while the effective mass m_K^* is equal for both. The space-like components of the vector potential vanish in nuclear matter at rest. They, however, come into play when heavy-ion collisions are considered. One has to transform between different reference frames, the center-of-mass frame of the colliding nuclei and the frame where a kaon is created. Like in electrodynamics the spatial components of the vector field give rise to a Lorentz force [273]. The in-medium dispersion relation can also be expressed in terms of an optical potential,

$$0 = k_\mu^2 - m_K^2 - 2m_K U_{\text{opt}} \quad . \quad (4.6)$$

4.1.2 Effects non-linear in density

To lowest order in density the energy or mass shift of a meson, ΔE , is determined by the scattering length of the considered meson and the nucleon. In the case of kaons one has

$$\Delta E_K^2(\mathbf{k}=0) = \Delta m_K^2 = -\pi \left(1 + \frac{m_K}{m_N} \right) \left(a_{KN}^{(I=0)} + 3a_{KN}^{(I=1)} \right) \varrho_N + \mathcal{O}(k_F^4), \quad (4.7)$$

where the correction terms start at order k_F^4 (k_F : Fermi momentum of nuclear matter). The empirical values of the isospin $I=0$ and $I=1$ K^+ -nucleon scattering lengths are $a_{K^+N}^{(I=0)} \simeq 0.02$ fm and $a_{K^+N}^{(I=1)} \simeq -0.32$ fm [274] which leads to a repulsive mass shift of about 28 MeV at nuclear saturation density ($k_F \simeq 265$ MeV). Higher order corrections in the density expansion of Eq. (4.7) were found to be small for K^+ . The k_F^4 correction was found to increase the repulsive K^+ -mass shift by about 20% [261] compared to expression (4.7). This suggests that the density expansion is applicable in the K^+ sector. The empirical scattering lengths can now be compared to the tree level Weinberg-Tomozawa interaction which yields $a_{K^+N}^{(I=0)} = 0$ fm and $a_{K^+N}^{(I=1)} \simeq -0.585$ fm [256]. Thus current algebra and the corresponding effective KN Lagrangian, Eq. (4.1), are in rough qualitative agreement with the constraints from low energy K^+ nucleon scattering. The large vector repulsion, Eq. (4.3), may be compensated by an attractive scalar Kaplan-Nelson potential.

Next we turn to the antikaon. Again one can use the low density theorem to estimate the medium effects to leading order in density. Utilizing Eq. (4.7), the empirical scattering lengths, $a_{K^-N}^{(I=0)} \simeq (-1.70 + i0.68)$ fm and $a_{K^-N}^{(I=1)} \simeq (0.37 + i0.60)$ fm [274, 275], lead to a repulsive mass shift of 23 MeV and a width of $\Gamma_{K^-} \simeq 147$ MeV at saturation density. In contrast to the K^+ , the next order correction to the density expansion of Eq. (4.7) is large, resulting in a total repulsive mass shift of 55 MeV and a width of $\Gamma_{K^-} \simeq 195$ MeV [261]. First of all, this questions the convergence of a density expansion for the K^- -mode. Moreover, the leading terms suggest a repulsive K^- potential. Finally, the empirical K^-N scattering lengths are in disagreement with the Weinberg-Tomozawa term which predicts an attractive mass shift. These facts imply that perturbation theory is not applicable in the K^- sector. The reason lies in the existence of a resonance, the $\Lambda(1,405)$ close to the K^-p threshold which makes the K^-p interaction repulsive at threshold. The presence of resonances generally requires a non-perturbative treatment of two-body scattering processes. We will return to this issue below.

It has been suggested by Brown and Rho [257] to model non-linear terms in the density by using a medium dependent parameter $f \simeq f_\pi$. Assuming the Gell-Mann-Oakes-Renner relation to be approximatively valid in the medium, one obtains the following relation for the in-medium pion decay constant f_π^*

$$\frac{f_\pi^{*2}}{f_\pi^2} = \frac{m_\pi^2}{m_\pi^{*2}} \frac{\langle \Omega | \bar{q}q | \Omega \rangle}{\langle \bar{q}q \rangle}. \quad (4.8)$$

According to ChPT [276] and π -mesic atoms [277], S -wave interactions induce only a small change of the pion mass with nuclear density. Using the empirical values of $m_\pi^*(\varrho_0)/m_\pi \approx 1.05$, one obtains

$$f_\pi^{*2}(\varrho_0)/f_\pi^2 \approx 0.6 \quad (4.9)$$

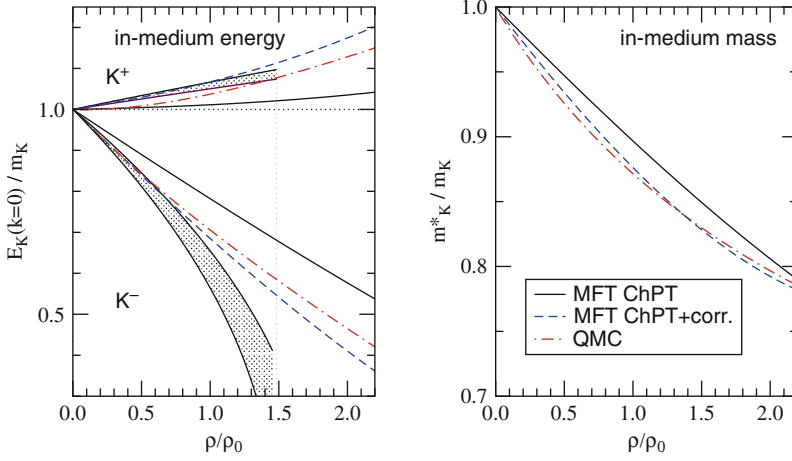


Fig. 4.1 In-medium kaon energy (*left*) and quasi-particle mass (*right*) in the chiral mean field theory (MFT ChPT) and including higher order corrections (MFT ChPT+corr.) [257]. Results from the mean field quark-meson-coupling (QMC) model [283] are shown as well. The bands represent the values extracted from empirical K^+N scattering and K^- atoms [282]. Figure taken from [266].

at nuclear saturation density, $\rho_0 \simeq 0.16 \text{ fm}^{-3}$. A dropping pion decay constant enhances both the vector repulsion and the scalar attraction. Such a dropping of the pion decay constant seems to be supported by the potentials extracted from pionic atoms [278, 279]. At the mean field level these results can be incorporated by replacing $f^2 \mapsto f_\pi^{*2}$ only in the vector potential, Eq. (4.3).

Figure 4.1 shows the in-medium energy shift of K^+ and K^- and the in-medium mass defined by Eq. (4.4) in nuclear matter. The label MFT corresponds to the Lagrangian (4.1) with a value of $\Sigma_{KN} = 350 \text{ MeV}$ which has originally been used by Li and Ko [280, 281]. MFT+corr. denotes the mean field model proposed by Brown et al. [257] including the above mentioned higher order corrections with a value of $\Sigma_{KN} = 450 \text{ MeV}$. The MFT and MFT+corr. curves shown in Fig. 4.1 are obtained by Eq. (4.4) with the corresponding values for Σ_{KN} , with the additional replacement of f^2 by f_π^{*2} in the vector field, Eq. (4.3), in the MFT+corr. case. The empirical energy shifts are shown as well in Fig. 4.1. For the K^+ the value is obtained by Eq. (4.7) from the empirical K^+N scattering length. The K^- band corresponds to the effective isospin averaged K^-N scattering length of $\bar{a}_{K^-N} = 0.62 \pm 0.5 \text{ fm}$ suggested by kaonic atom data [282].

Similar results have been obtained with slightly modified versions of the effective chiral Lagrangian [262], in the quark-meson-coupling (QMC) model [283] shown in Fig. 4.1 and in relativistic mean field calculations where kaons are coupled to static σ, ω, ρ and δ meson background fields [284].

In this context it is worth mentioning that the philosophy underlying KN mean field models is similar to that of effective relativistic nucleon-meson

Lagrangians of Quantum Hadro Dynamics for nucleons [285, 286]. Both are designed to describe in-medium properties, in the latter case nuclear matter and finite nuclei. The models do not pretend to give a description of free scattering data.

4.1.3 Coupled channel dynamics

A unitary approximation to the two-body scattering amplitude T is obtained by solving the Lippmann-Schwinger equation, or its relativistic counterpart, the Bethe-Salpeter equation. For kaon-nucleon scattering the Bethe-Salpeter equation reads schematically

$$T_{KN \rightarrow KN} = V_{KN \rightarrow KN} + \sum_{MB} V_{KN \rightarrow MB} \cdot G_{MB} \cdot T_{MB \rightarrow KN} \quad (4.10)$$

where $G_{MB} = -i D_M \cdot S_B$ is the two-particle propagator given by the meson and baryon propagators

$$D_M(k) = \frac{1}{k^2 - m_M^2 + i\epsilon} \quad , \quad S_B(p) = \frac{1}{\not{p} - m_B + i\epsilon} \quad , \quad (4.11)$$

respectively. The Bethe-Salpeter integral equation (4.10) iterates the KN interaction kernel V to infinite order. It is a coupled-channel equation since it contains not only kaon and nucleon degrees of freedom but involves the complete baryon ($B = N, \Lambda, \Sigma, \Xi$) and pseudoscalar meson ($M = \pi, K, \eta$) octet of the chiral Lagrangian. The integral equation (4.10) involves a sum over all possible intermediate states MB . A solution requires the consideration of additional but analogous equations for the amplitudes $T_{MB \rightarrow M'B'}$. The coupling to Ξ 's and η 's can be neglected. The Λ , Σ and π degrees of freedom are, however, essential for KN scattering.

While a perturbative expansion for the $T_{\pi N \rightarrow \pi N}$ amplitude proved quite successful [287] close to threshold a corresponding attempt fails in the strangeness sector. As already pointed out above the leading order Weinberg-Tomozawa term is in striking conflict with the empirical K^-p scattering lengths. In applications of the chiral $SU(3)$ Lagrangian it is advantageous to change the strategy and expand the interaction kernel V , rather than directly the scattering amplitude. This kernel is then iterated to all orders in the Bethe-Salpeter equation and scattering amplitudes are obtained that comply with coupled-channel unitarity. The leading order in the expansion of the KN interaction represents current algebra, i.e. the Weinberg-Tomozawa term which is of chiral order Q (denoting a small momentum or energy scale). Figure 4.2 shows the real and imaginary part of the isospin zero S -wave K^- -nucleon scattering amplitude from the iterated Weinberg-Tomozawa interaction in the coupled-channel calculation from [264]. It is nicely demonstrated

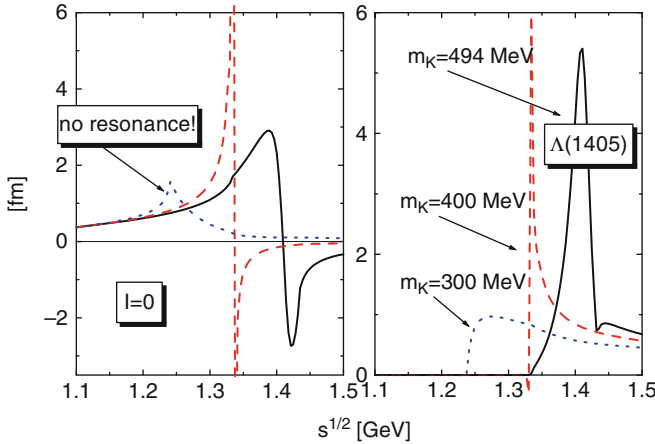


Fig. 4.2 Real (*left*) and imaginary (*right*) part of the isospin zero S -wave K^- -nucleon scattering amplitude from the iterated Weinberg-Tomozawa interaction in a coupled channel calculation. Figure taken from [264].

that using the physical kaon mass the $\Lambda(1,405)$ resonance is dynamically generated as a pole in the K^- -proton scattering amplitude. A decrease of the K^- mass leads to a disappearance of the $\Lambda(1,405)$ which will be crucial for the discussion of in-medium effects.

Expanding V beyond current algebra the corresponding coefficients have to be fixed by KN scattering data. Coupled-channel calculations for S -wave scattering with the interaction kernel truncated at chiral order Q^2 were first carried out by Kaiser et al. [256]. Lutz and Kolomeitsev [263] took into account P -wave and D -wave contributions in a coupled-channel calculation that considered Q^2 and Q^3 counter terms. In this work a simultaneous description of the available low-energy pion-, kaon- and antikaon-nucleon scattering data has been achieved for the first time. The resulting dynamics was used to study antikaon propagation in nuclear matter in [264, 265] based on a fully self-consistent and covariant many-body approach. Based on the Jülich meson-exchange potential [288] Tolos et al. [289, 290] performed G-Matrix calculations, which relied on a quasi-particle ansatz for the antikaon spectral distribution. As pointed out in [265] the higher partial-wave contributions of the Jülich meson-exchange potential [288] have not been tested against available K^-p differential cross section data. Two phenomenological works by Oset et al. [291, 292] were based on the leading order chiral Lagrangian. A partially self-consistent approximation that relied on an angle-average assumption was suggested. The possible effects of an in-medium change of pion properties were emphasized.

After fixing the model parameters from free NK scattering one is now able to systematically incorporate medium effects and thus to determine in-

medium scattering amplitudes, mass shifts and spectral functions. Medium modifications of the Bethe-Salpeter-equation (4.10) are the following:

- *Pauli-blocking* of intermediate nucleon states: The Pauli principle is of course not active for hyperons and suppresses NK excitations compared to $Y\pi$ excitations.
- *Self-consistency*: This means a self-consistent dressing of the K^- propagator

$$D_{K^-}(k) \mapsto D_{K^-}^*(k) = \frac{1}{k^2 - m_K^2 - \Pi_{K^-} + i\epsilon} \quad (4.12)$$

by the in-medium kaon self-energy Π_{K^-} . Since K^- mesons receive a substantial width in the medium Π_{K^-} is generally complex

$$\begin{aligned} \text{Re}\Pi_{K^-}(k) &= 2E(\mathbf{k})\text{Re}U_{\text{opt}}(E, \mathbf{k}), \\ \text{Im}\Pi_{K^-}(k) &= -E(\mathbf{k})\Gamma_{K^-}(E, \mathbf{k}) \end{aligned} \quad (4.13)$$

- *Dressing of the nucleon propagator*: At finite nuclear density the nucleon propagator is dressed by the nucleon self-energy Σ_N due to the interaction with the surrounding nucleons

$$S_N^*(p) = \frac{1}{\not{p} - m_N + \Sigma_N + i\epsilon} \quad (4.14)$$

Nucleons are still good quasi-particles and thus $\Sigma_N = \Sigma_S + \gamma_\mu \Sigma_V^\mu$ is real. Scalar and vector contributions of Σ_N can e.g. be taken from the Walecka model of nuclear matter [285]. The same holds for the other baryons of the baryon octet where self-energy contributions can, e.g., be estimated from simple counting of non-strange quarks, e.g., $\Sigma_\Lambda = 2/3\Sigma_N$.

- *Dressing of the pion propagator*: Analogous to the kaons the intermediate pion propagator $D_\pi \mapsto D_\pi^*$ is dressed by a pion self-energy Π_π due to Δ -hole or N -hole excitations in the nuclear medium.

The effect of Pauli blocking was first pointed out by Koch [293] and later on studied in detail by Waas et al. [259, 260]. Pauli blocking effects were found to play a dominant role since the attractive K^-N interaction is reduced at finite densities. This acts effectively as a repulsive force which shifts the $\Lambda(1,405)$ resonance above the K^-p threshold and leads to a dissolution of this resonance at densities above 2–3 ϱ_0 . Since the existence of the $\Lambda(1,405)$ was, on the other hand, the origin of the repulsive K^-N scattering length at threshold, a shift or a dissolution of this resonance causes an in-medium K^- potential which may be now close to the tree-level result predicted by the attractive Weinberg-Tomozawa term. However, self-consistency, i.e. the dressing of the K^- propagator by the attractive potential counteracts the Pauli effect. As pointed out by Lutz [261] a decreasing K^- mass results in a negative shift of the $\Lambda(1,405)$ and compensates the positive Pauli shift to a large extent. The position of the $\Lambda(1,405)$ pole stays fairly constant in [291, 292] but in more sophisticated studies [264, 265] is even pushed down to lower mass. In both cases the resonance is substantially broadened

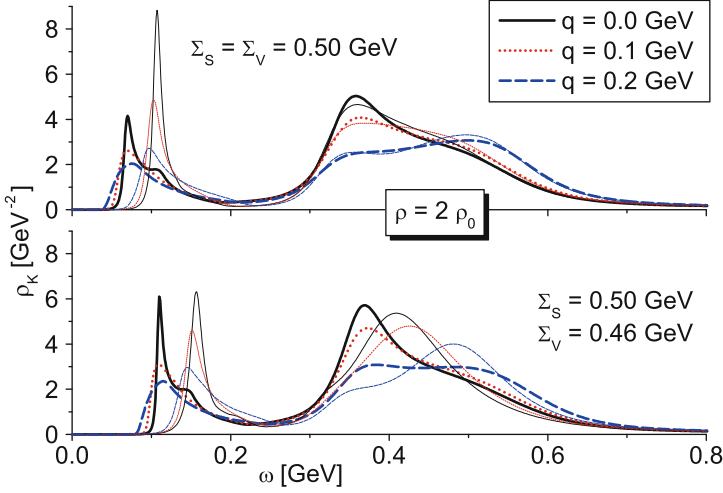


Fig. 4.3 Antikaon spectral distribution as a function of energy ω and momentum \mathbf{q} at twice nuclear saturation density. The *thin* and *thick lines* show the results with and without angle-average approximation. Two large-mean field scenarios are shown.

and dissolves at high densities (as can be anticipated from the schematic calculation shown in Fig. 4.2.)

The influence of dressing of nucleon and hyperon propagator due to short-range NN and NY correlations has been investigated in [294] at the one-loop level with particular emphasis on the role of P -wave channels. The dressing of nucleon and hyperon propagators is generally included in such type of calculations but the effects are of minor importance if implemented in a non-relativistic framework. Contrasting results were obtained recently by Lutz and Korpa [265], who for the first time set up a self-consistent and covariant many-body approach for the nuclear antikaon dynamics that incorporated the effect of scalar and vector mean fields for the nucleon. The actual computation presented in [265] uses the chiral dynamics as developed in [263], which considers S -, P - and D -wave channels. Though at nuclear saturation density the results of such a scheme confirm almost quantitatively the previous study [264], at larger nuclear densities significant differences arise.

In Fig. 4.3 the antikaon spectral distributions from [265] are shown at twice nuclear saturation density. A striking effect is revealed. At small antikaon energies the spectral distributions develop significant strength in a narrow peak at around 70 or 110 MeV, depending on the choice of the mean fields. The peak remains narrow and pronounced for finite antikaon momenta $0 < |\mathbf{q}| < 200$ MeV. This is in contrast to the antikaon spectral distribution

at saturation density. The corresponding structure has very little weight and is dissolved much more quickly as the antikaon starts to move through the bulk matter. The peak reflects the coupling of the antikaon to a $\Lambda(1,115)$ nucleon-hole state. The soft antikaon mode is located at 70(110) MeV, even though the $\Lambda(1,115)$ effective mass is reduced by 25(23) MeV below its free-space limit at the considered density of $2 \varrho_0$. In the low-density limit the soft mode has energy $m_\Lambda - m_N \simeq 175$ MeV, a value significantly larger than the peak positions at 70(110) MeV in Fig. 4.3. This illustrates that the $\Lambda(1,115)$ nucleon-hole state becomes highly collective. The peak positions at $\mathbf{q} = 0$ follow quite accurately the difference of the $\Lambda(1,115)$ quasi-particle energy and the nucleon hole-energy at maximum momentum, $|\mathbf{p}| = k_F = 340$ MeV. The complicated antikaon nuclear dynamics appears to collect maximum strength at the Fermi surface. It is speculated in [265] that this may lead to the formation of exotic nuclear systems with strangeness and antikaon condensation in compact stars at moderate densities.

4.1.3.1 In-medium potentials

Figure 4.4 shows the single particle energy or “in-medium mass shift” $E(\mathbf{k} = 0) = m_K + \Re U_{\text{opt}}(E, \mathbf{k} = 0)$ for antikaons obtained in various coupled-channel calculations. This quantity can be compared to the mean field picture although such a comparison has to be taken with care. At finite densities the antikaons acquire a substantial in-medium width and do no longer behave like quasi-particles, as assumed in a mean field picture. In particular at low momenta the spectral functions can be of complex structure without a well defined quasi-particle pole which makes the interpretation of the in-medium

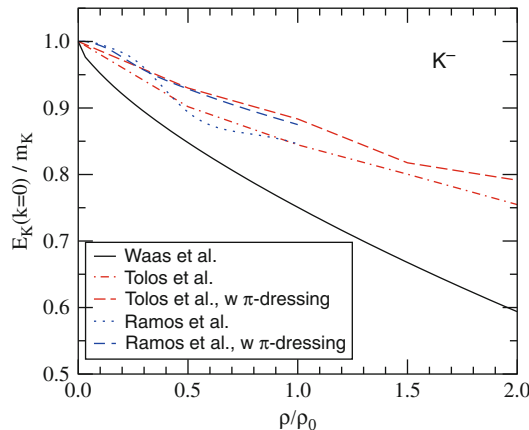


Fig. 4.4 In-medium K^- energy obtained in coupled channel calculations which includes Pauli-blocking (Waas et al. [259]), kaon dressing (Ramos et al. [291]) and pion dressing (Ramos et al. [291], Tolos et al. [289]). Figure taken from [266].

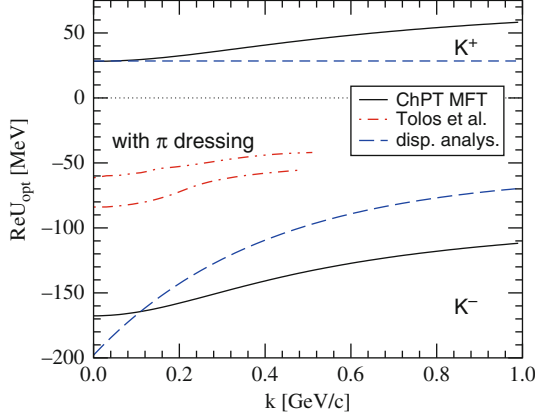


Fig. 4.5 Optical kaon potentials at nuclear saturation density. Results from the chiral mean field approach (ChPT MFT) [257], coupled channel calculations [289] and dispersion analyses [298] are compared. Figure taken from [266].

self-energy Π_K in terms of on-shell potentials highly questionable. However, transport models are usually formulated in terms of quasi-particles. Hence, we do not want to refrain from this comparison. The microscopic coupled-channel calculations deliver an attractive in-medium potential which is significantly smaller than in the mean field approaches, in particular when a self-consistent dressing of the kaon propagator is taken into account, and even smaller when pion dressing is included. Ramos and Oset [291] and also Tolos et al. [289] claim that the dressing of the pion propagator by nucleon- and Δ -hole excitations in the medium leads to significant effects for the in-medium K^- potential. However, contrasting results were obtained by Korpa and Lutz [295], Cieply et al. [296] and Roth et al. [297]. As pointed out in [265] the influence of pion dressing depends on the details of the production amplitude $T_{KN \rightarrow \pi\Sigma}$ at subthreshold energies, but also on the amount of softening assumed for the in-medium pion modes.

This fact is also reflected in the optical potential (real part) shown in Fig. 4.5. We compare the momentum dependence of $\Re U_{\text{opt}}$ at saturation density obtained in various approaches. Results are taken from the chiral mean field approach [257], denoted in Fig. 4.1 as MFT ChPT+corr., the coupled-channel calculations of Tolos et al. [289], with and without pion dressing, and a dispersion analysis of K^+N and K^-N scattering amplitudes by Sibirtsev and Cassing [298]. The definition used to extract the optical potential from the self-energy Π varies in the literature. For instance the relation (4.13) has been used in [289]. For K^+ the magnitudes of the potential are consistent, i.e. the dispersion analysis agrees with the mean field approach at zero momentum. It predicts an almost momentum independent potential while U_{opt} is slightly rising as a function of momentum in mean field models. For K^- all models predict a considerably reduced attraction at high kaon momenta,

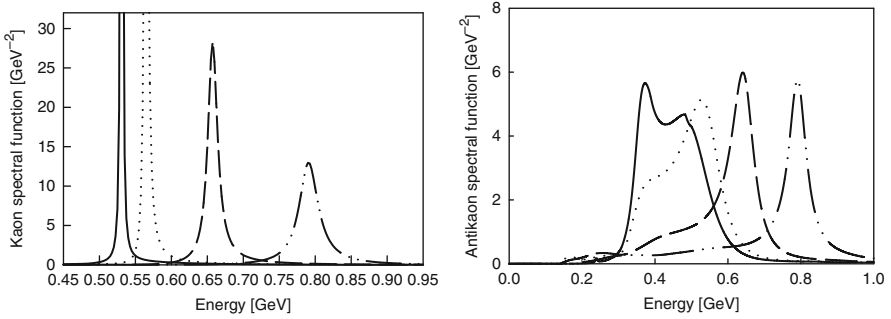


Fig. 4.6 In-medium kaon (*left*) and antikaon (*right*) spectral functions from coupled channel calculations of [295] at saturation density. Results are shown for different kaon momenta: $p_K = 0$ (solid line), 200 MeV (dotted line), 400 MeV (dashed line), and 600 MeV (dash-dot-dotted line).

however, the potential depths strongly deviate. The partially self-consistent coupled channel calculations from Schaffner et al. [299], which rely on an angle average ansatz, predict an even smaller potential which is of the size of -32 MeV at saturation density.

The dispersion analysis of [298] comes close to the mean field result which is, however, not astonishing since the authors disregarded the repulsive contributions from the $\Sigma(1,385)$ and $\Lambda(1,405)$ resonances according to the argument that these resonances should dissolve at finite density. They claim their parameterizations of the K^- potential consistent with data from $p + A$ reactions [298].

All the microscopic approaches predict K^- potentials of only moderate attraction and are thus in stark contrast to the mean field picture. It is an interesting question to what extent such findings are compatible with the analysis of kaonic atoms [300]. The latter suggests a strongly attractive on-shell K^- potential of about 200 MeV at ϱ_0 . There are indications, however, that existing kaonic atom data probe the antikaon potential only at the nuclear surface [301] and weak K^- potentials describe the available data reasonably well [302]. A final answer would require to account for the full off-shell behavior of the self energy and the spectral properties of a bound K^- state. However, such calculations have not yet been performed.

Figure 4.6 finally addresses the validity of the quasi-particle picture for the K^+ . It shows the kaon and antikaon spectral functions at saturation density obtained from coupled channel calculations from [295] (including pion dressing) for different momenta. The kaons have still a clear quasi-particle peak which in the medium acquires a finite width. The latter is, however, quite small (less than 5 MeV) for small momenta and increases up to 15 MeV at a momentum above 400 MeV which is still moderate. Hence the quasi-particle picture and the mean field approximation are well justified. As al-

ready stressed several times, the situation for K^- mesons is quite different. In particular at low momenta the spectral functions are broad and of complex structure. At larger momenta a quasi-particle peak may still be visible but also here substantial strength is shifted to lower momenta. Thus the mean field approximation is highly questionable for the antikaons.

4.1.3.2 In-medium cross sections

Coupled-channel calculations typically predict sizeable in-medium modifications of the pion-induced K^- production cross sections and the corresponding absorption cross sections for $\pi Y \longleftrightarrow NK^-$. The fact that the S -wave $\Lambda(1,405)$ resonance lies only 27 MeV below the K^-p threshold implies a strong coupling to this state and requires a non-perturbative treatment. The melting of the $\Lambda(1,405)$ and $\Sigma(1,385)$ bound states due to Pauli blocking of the intermediate states in the BS-equation (4.10) leads to a dramatic increase in particular of the $\pi\Sigma \longrightarrow NK^-$ cross section at threshold. In [299] the enhancement factor was found to be more than one order of magnitude at ϱ_0 . However, self-consistency shifts the K^- mass below threshold and decreases the available phase space which counteracts the enhancement due to a melting $\Lambda(1,405)$. In the calculations of Schaffner et al. [299] the $\pi\Sigma \longrightarrow NK^-$ is then only enhanced by a factor of two and the $\pi\Lambda \longrightarrow NK^-$ is hardly affected at all. In the self-consistent calculations of Lutz and Korpa [263] the predicted in-medium modifications of these cross sections are practically opposite. They additionally account for the full in-medium modifications of the K^- spectral distributions and obtain a strong enhancement of the $\pi\Lambda \longrightarrow NK^-$ cross section due to the coupling to the $\Sigma(1,385)$ but almost no changes for the $\pi\Sigma \longrightarrow NK^-$ channel. The G-matrix calculations of Tolos et al. [289] came to opposite conclusions, namely an almost complete suppression of the pion-induced reactions in the nuclear environment. Such strong modifications of the K^- production cross sections and the corresponding absorption cross sections would have severe consequences for the K^- dynamics in heavy-ion reactions.

4.1.4 Kaons in pion matter

Whereas in heavy-ion reactions at intermediate energies the matter is baryon dominated, at ultra-relativistic energies (e.g., at CERN-SPS or at RHIC) the matter is characterized by a larger meson content. For completeness it is thus instructive to consider this case as well. The problem of medium modifications experienced by kaons in a hot pion gas has been evaluated in the early 1990s in [303, 304] where the authors came, however, to differing conclusions concerning the kaon mass shifts. Recently this problem

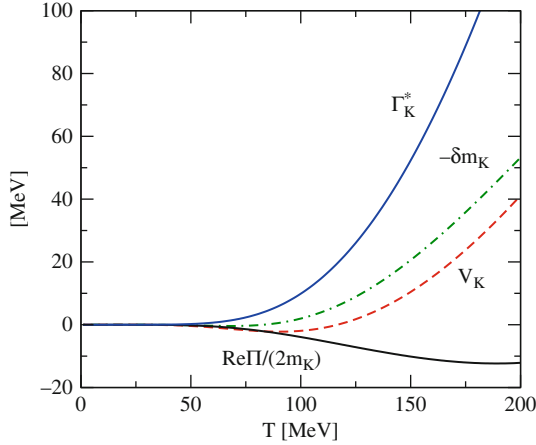


Fig. 4.7 Medium modifications of kaons in an isospin-symmetric hot pion gas: self-energy $\Re\Pi_K/(2m_K)$, mass shift $-\delta m_K$, vector potential V_K , and kaon collision width Γ_K^* versus temperature T . Results are taken from [305].

has been revisited by Martemyanov et al. [305]. In [305] the kaon self-energy has been determined in a model independent way to leading order in pion density, based on ChPT at low temperatures and experimental phase shifts at high temperatures.

Analogous to nuclear matter, Eq. (4.7), the kaon self-energy $\Pi_K(k^2, E)$ can be expressed in terms of the πK forward scattering amplitudes for on-shell pions and off-shell kaons. The necessary on-shell πK amplitudes have been evaluated in ChPT to order p^4 by several authors (see e.g. [306] and references therein). Near the threshold, the isospin-even (+) and odd (−) πK scattering amplitudes can be expressed in terms of scattering lengths and effective ranges $a_\ell^{(\pm)}$ and $b_\ell^{(\pm)}$. To lowest order ChPT isospin symmetric pion matter does not change the kaon dispersion law. The leading order effect appears at the one loop level. The mean field, i.e. the scalar mass shift δm_K and the vector potential V_K follow from the self-energy $\Pi_K(m_K^2, m_K)$ at the on-shell point which can be expressed in terms of s - and p -wave scattering lengths and s -wave effective ranges. Since ChPT is only valid at temperatures well below the pion mass in [305] the high temperature behavior has been based on a more phenomenological approach which parameterizes the experimental phase shifts and matches smoothly with the one-loop ChPT low-temperature limit. The corresponding kaon self-energy at threshold, the mass shift and the vector potential are shown in Fig. 4.7 as a function of temperature. At $T = 170$ MeV one obtains a negative mass shift $\delta M_K = -33$ MeV and a repulsive vector potential of $V_K = 21$ MeV. There exists a remarkable analogy to the nuclear matter case: the kaon mass shift at high temperatures is large and negative, the vector potential is large and positive, their sum is relatively small and negative. Kaons are therefore bound in pion matter similar to nucleons or antikaons in nuclear matter. The vector potential is, however,

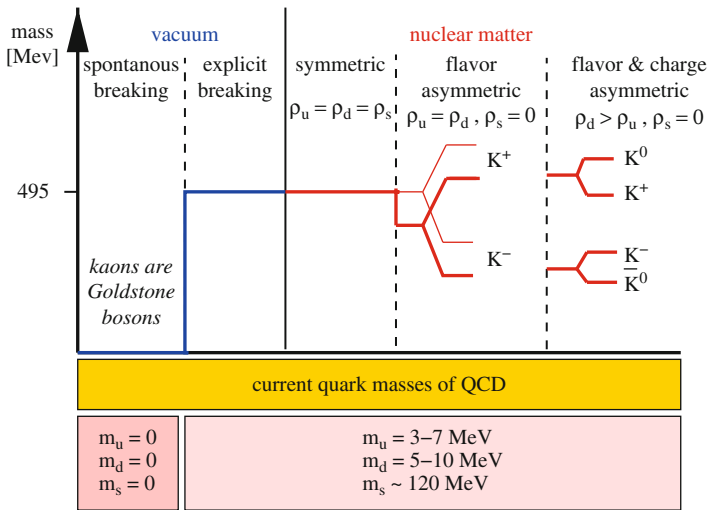


Fig. 4.8 Schematic representation of kaon and antikaon energy shifts in dense nuclear matter due to SU(3) symmetry breaking ($\varrho_u = \varrho_d, \varrho_s = 0$). The Weinberg-Tomozawa term leads to the K^+ / K^- mass splitting (*thin line*) while the Kaplan-Nelson term is responsible for the common mass shift (*thick line*). Figure taken from [266].

C -even, distinct from the case of nuclear matter. In addition both, kaons and antikaons acquire a substantial in-medium width Γ_K^* at finite temperature [305].

We recall that in-medium modifications of the kaons have direct impact on the properties of the ϕ meson, see Sect. 2.4.3.

4.1.5 Chiral symmetry restoration

At the end of this section we briefly address connections of in-medium kaon dynamics to chiral symmetry restoration. The spontaneously broken chiral symmetry of QCD manifests itself in the large vacuum expectation value of the scalar quark condensate, $\langle \bar{q}q \rangle$. The small but finite current quark masses are responsible for the explicit chiral symmetry breaking of QCD. In the chiral limit of vanishing current quark masses, the Goldstone bosons of spontaneous chiral symmetry breaking, the pion (or the full pseudo-scalar octet) become massless. This fact is described by the Gell-Mann-Oakes-Renner (GOR) relation. Through the GOR relation the pseudoscalar meson masses are directly proportional to products of the scalar quark condensates and the current quark masses.

Nevertheless, it remains unclear how and to what extent the in-medium changes of the antikaon mass distribution is related to the (partial) restoration of spontaneously broken chiral symmetry at finite density and/or temperature. In a mean field ansatz the Weinberg-Tomozawa term is responsible for the splitting of the energy levels between the degenerate flavor eigenstates $K^+(u\bar{s})$ and $K^-(\bar{u}s)$. As indicated in Fig. 4.8, $SU(3)$ flavor symmetry is broken by non-vanishing up and down quark densities $\varrho_{u/d} \neq \varrho_s = 0$ while the strange quark density, ϱ_s is still zero. In contrast, in isospin symmetric pion matter no mass splitting occurs between kaons and antikaons. Charge symmetry breaking which occurs in isospin asymmetric nuclear matter leads to an additional mass splitting of the different isospin states, i.e., between K^+ and $K^0(d\bar{s})$ as well as between K^- and $\bar{K}^0(\bar{d}s)$.

In chiral coupled-channel dynamics the leading order Weinberg-Tomozawa kaon-nucleon interaction is iterated to infinite order. The kaons are subject to medium modifications, i.e. mass shifts and changes of their spectral distributions. However, in this framework their origin can not easily be traced back to a restoration of chiral symmetry.

4.2 Strange baryons

Strangeness transfer reactions, e.g., $\pi\Lambda \leftrightarrow NK^-(\bar{K}^0)$, induce a coupling of kaon and hyperon channels [307]; some of the (coupled-channel) models for in-medium kaon dynamics discussed in the previous section include such a coupling. Analogous effects are present in the non-strange sector as implicit in the discussion of Chap. 3, as well as in the charm sector, cf. Sect. 5.5.

4.2.1 QCD sum rules

The in-medium properties of the Λ have been considered in [308, 309] within the QCD sum rule approach. Here, the poorly known strange-quark condensate $\langle\bar{s}s\rangle$ enters, among other condensate terms. A conclusion of [309] is that the vector self-energy is only 1/3 of the corresponding nucleon self-energy, while the scalar part is sensitive to the four-quark condensates. Phenomenological implications have not been addressed in this paper, except for the Λ spin-orbit potential.

The Λ - Σ^0 mixing in nuclear matter has also been found to sensitively depend on higher-order condensates [310]. This reiterates the urgent need to have better control over these condensates of mass dimension larger than 4 to establish a firm relation of baryon properties in dense matter and QCD vacuum parameters.

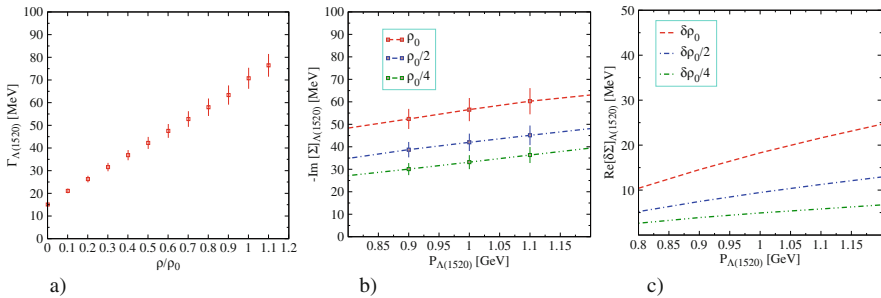
Table 4.1 Changes of mass parameters and decay widths for strange baryons in nuclear matter at saturation density as predicted in [263].

Baryon	$\Lambda(1, 405)$	$\Sigma(1, 385)$	$\Lambda(1, 520)$
Shift [MeV]	-60	-60	-100
Width [MeV]	120	70	90

4.2.2 Hadronic models

A comprehensive approach including the evaluation of strange-baryon properties has been constructed in [263] based on chiral coupled-channel dynamics. Part of the known baryons emerge as dynamically generated resonances, while others are required as genuine resonance states, encompassing both strange and charm [311] sectors. In the strangeness sector [263] anti-kaons and hyperons are coupled. Corresponding in-medium properties of a few selected hyperons are listed in Table 4.1. Further properties of $\Lambda(1, 115)$, $\Lambda(1, 405)$, $\Lambda(1, 520)$, $\Sigma(1, 195)$, $\Sigma(1, 385)$ and $\Sigma(1, 690)$ can be found in [263].

In another variant of chiral meson and baryon dynamics [312] the resonance states $\Lambda(1, 405)$ and $\Lambda(1, 520)$ are dynamically generated with the interpretation that the constituents qqs of strange baryons are carried by the meson-baryon cloud. An example is exhibited in Fig. 4.9 for the in-medium modifications of $\Lambda(1, 520)$. Most notably, the in-medium width may reach up to 100 MeV at normal nuclear matter density.

**Fig. 4.9** Density and momentum dependence of the self-energies of $\Lambda(1, 520)$ as computed in [312]. *Left panel:* width as a function of density; *middle and right panels:* imaginary part (half width) and real part of the self-energy as a function of 3-momentum at various densities.

4.2.3 *Exotica*

The experimental situation of the penta-quark state Θ^+ , proposed as a novel baryon in [313], is still controversial. Due to the conjectured quark structure $uud(d\bar{s})$ the coupling to strangeness channels is important. For an attempt to reconcile the current experimental (non-) evidences, i.e., why a Θ^+ signal is seen in some experiments but not in others, see [314] Under the assumption that the Θ^+ can be considered as a hadronic state in hadronic matter, its production rate in heavy-ion collisions has been estimated in thermal [315], transport [316, 317] and quark-recombination models [318].

Chapter 5

Open charm probes

Hadrons containing charm quarks are particularly valuable probes of the medium formed in ultra-/relativistic heavy-ion collisions. Contrary to u , d and s quarks, the (bare) charm-quark mass, $m_c \simeq 1.3$ GeV, provides a scale which is much larger than $\Lambda_{QCD} \simeq 0.2$ GeV and the QCD transition temperature, $T_c \simeq 0.18$ GeV. In addition, m_c is significantly larger than typical temperatures in the early stages of heavy-collisions, even at the highest currently available collision energies, $T_0 \simeq 0.3 - 0.4$ GeV at maximum RHIC energy. Consequently, charm-quark production is expected to be dominated by primordial $N-N$ collisions, and thus can be benchmarked rather reliably via binary scaling from $p-p$ reactions (recent RHIC data support this notion, and even at LHC secondary production of $c\bar{c}$ pairs is expected to be small); this will be discussed in Sect. 5.1. At the same time, m_c is small enough for charm quarks to be sensitive to reinteractions within the hot and dense medium, and therefore provide valuable information about medium properties. On the one hand, this applies at the partonic level in the Quark-Gluon Plasma, where recent RHIC data have given intriguing insights on charm- (and possibly bottom-) quark energy loss and collective motion [319, 320]. The latter, in particular, indicates strong, presumably nonperturbative, interactions of charm quarks in a (strongly interacting) QGP, and allows to put constraints on pertinent diffusion coefficients. These questions will be discussed in Sect. 5.2. An approximate thermalization (kinetic equilibration) of c -quarks further opens the door to study the chemistry of charmed hadrons with potential insights on hadronization mechanisms (e.g., quark coalescence vs. fragmentation), which is addressed in Sect. 5.3. On the other hand, D meson spectral functions are expected to be modified in a hot and dense hadronic medium. This will be discussed within the QCD sum rule approach in Sect. 5.4, and within a hadronic many-body framework in Sect. 5.5. In analogy to the kaon case, it has been argued that a reduced mass and/or increased width of in-medium D meson spectral functions could lead to an increase of the total charm production cross section in $A-A$ collisions, especially for energies close to the $D\bar{D}$ production threshold (as discussed in

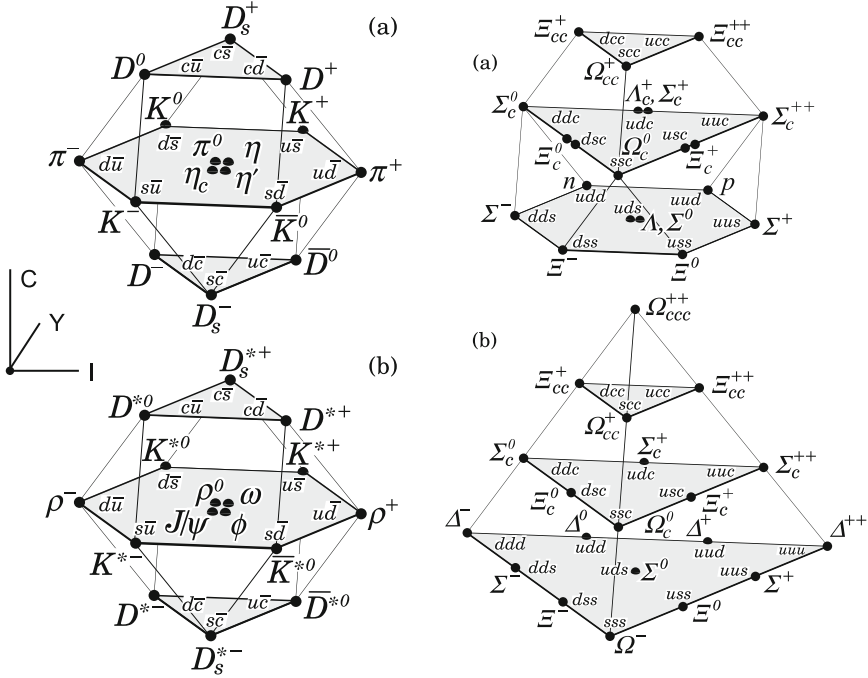


Fig. 5.1 $SU(4)_f$ multiplets of mesons (left) panel and baryons (right), taken from [30].

Part IV on “Observables”). We note, however, that charm production and medium effects on charmed hadrons presumably operate on rather different time scales. To the extent that $c\bar{c}$ production is a perturbative process its characteristic time scale is $\tau_{\text{prod}} \simeq 1/2m_c \leq 0.1 \text{ fm}/c$, while the typical formation time of a hadron wave function is roughly determined by the hadron’s binding energy, $\tau_{\text{form}} \simeq 0.5 - 1 \text{ fm}/c$. A possible caveat is that, to date, the description of the total charm production cross section within perturbative QCD is still beset with rather large uncertainties, leaving room for the relevance of additional time scales larger than the naive expectation.

The basic $SU(4)$ (flavor) multiplet classification of charmed hadrons in the vacuum is depicted in $C - Y - I_3$ space in Fig. 5.1 (using the quantum numbers C : charm, Y : hypercharge and I_3 : third component of isospin). Note that some of the multiple-charm baryons have not been discovered (yet). The comparatively large charm-quark mass strongly breaks $SU(4)$ flavor symmetry, implying substantial mass splittings within a multiplet. A quantitative level scheme of D mesons in the vacuum is displayed in Fig. 5.2, where angular momentum and spin quantum numbers have been assigned according to the constituent quark model.

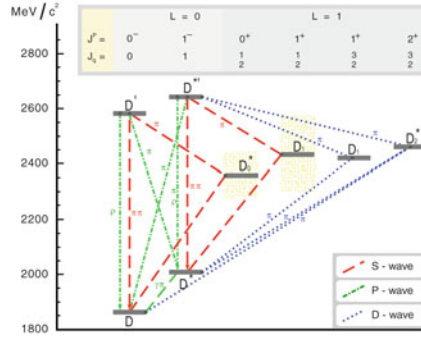


Fig. 5.2 Excitation spectrum of D mesons in vacuum [321].

5.1 Perturbative calculation of charm-quark production near threshold

Calculations of charm production are still not under solid theoretical control. A good understanding of the charm cross section is of interest for heavy ion physics. Charm production is an important contribution to the dilepton continuum at low masses. In particular, the total charm rate is a useful reference for J/ψ production in heavy ion collisions. The FAIR facility is the only modern heavy ion experiment that can measure charm in the near-threshold region with $p_{\text{lab}} \sim 25$ GeV ($\sqrt{s_{NN}} \approx 6.98$ GeV), a region that is only marginally explored in pp collisions.

Because the charm quark mass is a few times Λ_{QCD} , it is generally treated as a heavy quark in perturbative QCD calculations. However, its relative lightness results in a rather strong dependence of the total cross section on mass and scale, with up to a factor of 100 between the lowest and highest next-to-leading order (NLO) results [322]. There is also a rather broad spread in the measured charm production cross section data at fixed target energies. Much of this uncertainty arises from low statistics in the early experiments, assumptions of how much of the total charm yield results in final-state D mesons, and how the measured data are extrapolated to full phase space. The more recent data have improved considerably with new detection techniques and higher statistics.

Improvements in the calculation of the charm cross section are difficult at all energies, but are perhaps possible when the $c\bar{c}$ pair is produced close to threshold, as we now describe. Factorization properties of QCD separate cross sections into universal, nonperturbative parton densities and a perturbatively calculable hard scattering function, the partonic cross section. Remnants of long-distance dynamics in the hard scattering function can dominate corrections at higher orders near production threshold. These Sudakov corrections have the form of distributions singular at partonic threshold. Threshold re-

summation techniques organize these singular distributions to all orders, presumably extending the reach of QCD into near-threshold production.

Resummed cross sections are useful as generating functions for approximate finite-order corrections to the cross section when expanded in powers of the strong coupling constant α_s , as we describe here. The resummed cross sections may also be evaluated numerically. The charm fixed-target data were first compared to a leading log (LL) resummed calculation of the total cross section in [323]. Because the ratio m/Λ_3 is quite small, the expansion parameter, α_s , is not and the LL resummation began to fail at $\sqrt{S} \approx 20$ GeV. A NLL resummed evaluation in [324] found significant threshold corrections, albeit with a reduction in scale dependence.

We work at finite order to avoid artificial cutoffs, using our results of [325–329]. The soft corrections that we calculate take the form of logarithms, $[\ln^l(x_{\text{th}})/x_{\text{th}}]_+$, also called plus distributions, with $l \leq 2n - 1$ for the order α_s^n corrections, where x_{th} is a kinematical variable that measures distance from threshold and goes to zero at threshold. We have calculated the double-differential heavy quark hadroproduction cross sections up to next-to-next-to-leading order (NNLO), $\mathcal{O}(\alpha_s^4)$, at leading logarithm (LL) with $l = 3$, next-to-leading logarithm (NLL) with $l = 2$, next-to-next-to-leading logarithm with $l = 1$ and next-to-next-to-next-to-leading logarithm (NNNLL) with $l = 0$ and some virtual terms (NNNLL+ ζ). We only discuss $Q\bar{Q}$ production in the $ij = q\bar{q}$ and gg channels since qg scattering first appears at NLO.

We first briefly describe our NNLO-NNNLL calculations. We show results for several values of the charm quark mass, $m = 1.2, 1.5$ and 1.8 GeV and for scales $\mu = m$ and $2m$. We compare our results for the NNLO-NNNLL inclusive $c\bar{c}$ cross section to charm production data and to the NLO cross sections in the relevant energy regime.

5.1.1 Resummation

In our approach, the distance from partonic threshold in the plus distributions depends on how the cross section is calculated. We either integrate over the momentum of the unobserved heavy quark or antiquark and determine the one-particle inclusive (1PI) cross section for the detected quark or treat the Q and \bar{Q} as a pair in the integration, in pair invariant mass (PIM) kinematics.

In 1PI kinematics, a single quark is identified, so that

$$i(p_a) + j(p_b) \longrightarrow Q(p_1) + X[\bar{Q}](p_2) \quad (5.1)$$

where Q is the identified heavy quark of mass m and $X[\bar{Q}]$ is the remaining final state that contains the \bar{Q} . We define the kinematical invariants $s =$

$(p_a + p_b)^2$, $t_1 = (p_b - p_1)^2 - m^2$, $u_1 = (p_a - p_1)^2 - m^2$ and $s_4 = s + t_1 + u_1$. At threshold, $s_4 \rightarrow 0$, and the soft corrections appear as $[\ln^l(s_4/m^2)/s_4]_+$.

In PIM kinematics, we have instead

$$i(p_a) + j(p_b) \longrightarrow Q\bar{Q}(p) + X(k). \quad (5.2)$$

At partonic threshold, $s = M^2$, M^2 is the pair mass squared, $t_1 = -(M^2/2)(1 - \beta_M \cos \theta)$, and $u_1 = -(M^2/2)(1 + \beta_M \cos \theta)$ where $\beta_M = \sqrt{1 - 4m^2/M^2}$ and θ is the scattering angle in the parton-parton center-of-mass frame. The soft corrections appear as $[\ln^l(1 - z)/(1 - z)]_+$ with $z = M^2/s \rightarrow 1$ at threshold.

Any difference in the integrated cross sections due to kinematics choice arises from the ambiguity of the estimates. At leading order the threshold condition is exact and there is no difference between the total cross sections in the two kinematic schemes. However, beyond LO additional soft partons are produced and there is a difference. To simplify the argument, the total partonic cross section may be expressed in terms of dimensionless scaling functions $f_{ij}^{(k,l)}$ that depend only on $\eta = s/4m^2 - 1$ [326],

$$\sigma_{ij}(s, m^2, \mu^2) = \frac{\alpha_s^2(\mu)}{m^2} \sum_{k=0}^{\infty} (4\pi\alpha_s(\mu))^k \sum_{l=0}^k f_{ij}^{(k,l)}(\eta) \ln^l \left(\frac{\mu^2}{m^2} \right). \quad (5.3)$$

We have constructed LL, NLL, NNLL and NNNLL+ ζ approximations to $f_{ij}^{(k,l)}$ in the $q\bar{q}$ and gg channels for $k \leq 2$, $l \leq k$. Exact results are known for $k = 1$ and can be derived using renormalization group methods for $k = 2$, $l = 1, 2$ [326]. Our calculations use the exact LO and NLO cross sections with the approximate NNLO-NNNLL+ ζ corrections.

The inclusive hadronic cross section is obtained by convoluting the inclusive partonic cross sections with the parton luminosity Φ_{ij} ,

$$\Phi_{ij}(\tau, \mu^2) = \tau \int_0^1 dx_1 \int_0^1 dx_2 \delta(x_1 x_2 - \tau) \phi_{i/h_1}(x_1, \mu^2) \phi_{j/h_2}(x_2, \mu^2), \quad (5.4)$$

where $\phi_{i/h}(x, \mu^2)$ is the density of partons of flavor i in hadron h carrying a fraction x of the initial hadron momentum, at factorization scale μ . Then

$$\begin{aligned} \sigma_{h_1 h_2}(S, m^2) &= \sum_{i,j=q,\bar{q},g} \int_{4m^2/S}^1 \frac{d\tau}{\tau} \Phi_{ij}(\tau, \mu^2) \sigma_{ij}(\tau S, m^2, \mu^2) \\ &= \sum_{i,j=q,\bar{q},g} \int_{-\infty}^{\log_{10}(S/4m^2-1)} d \log_{10} \eta \frac{\eta}{1+\eta} \ln(10) \\ &\quad \times \Phi_{ij}(\eta, \mu^2) \sigma_{ij}(\eta, m^2, \mu^2), \end{aligned} \quad (5.5)$$

where

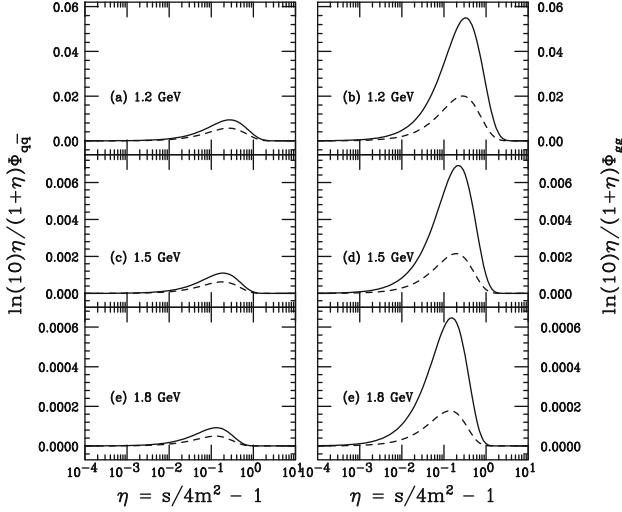


Fig. 5.3 The parton luminosity for pp interactions at $\sqrt{S} = 6.98$ GeV as a function of η using the GRV 98 HO densities. The *left-hand side* gives the $q\bar{q}$ luminosity, the right-hand side the gg luminosity. From *top to bottom*, the charm quark mass is 1.2 GeV in (a) and (b), 1.5 GeV in (c) and (d), and 1.8 GeV in (e) and (f). The *solid curves* are with $\mu = m$ and the *dashed*, $\mu = 2m$.

$$\eta = \frac{s}{4m^2} - 1 = \frac{\tau S}{4m^2} - 1. \quad (5.6)$$

Our investigations in [326] showed that the approximation should hold if the convolution of the parton densities is not very sensitive to the high η region. The GRV98 parton luminosities are shown in Fig. 5.3. We focus our calculations on the 1PI kinematics because these kinematics are more compatible with $c\bar{c}$ production through the gg channel.

5.1.2 Charm-quark production in pp collisions

We compare our results to the pp data tabulated in [322, 330]. These data are the most recent and incorporate the newest measurements of branching ratios. The pp data at $\sqrt{S} \leq 30$ GeV are given in [331–333].

How the $c\bar{c}$ pairs hadronize is a particularly important question for energies near threshold where some channels may be energetically disfavored. We follow [322] and assume that $\sigma(D_s)/\sigma(D^0 + D^+) \simeq 0.2$ and $\sigma(\Lambda_c)/\sigma(D^0 + D^+) \simeq 0.3$, independent of energy, so that the total $c\bar{c}$ cross section is obtained from $\approx 1.5\sigma(D\bar{D})$. This assumption could have a strong energy dependence near threshold. Thus as many charm hadrons (mesons and baryons) as possible should be measured to better understand fragmentation and hadronization.

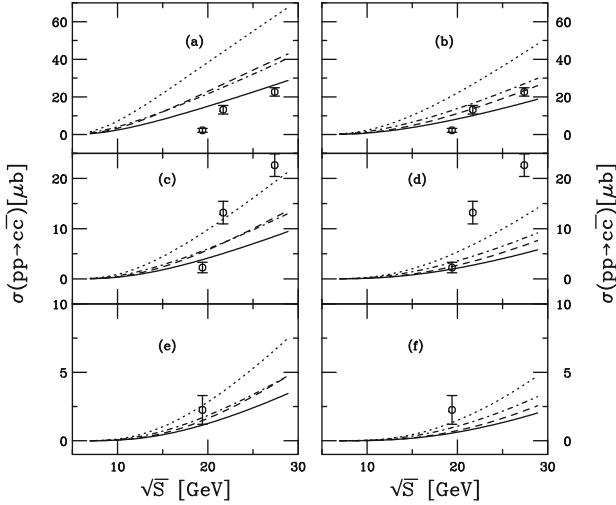


Fig. 5.4 The energy dependence of $c\bar{c}$ production in pp collisions with, (a) and (b), $m = 1.2$, (c) and (d), $m = 1.5$, and, (e) and (f), $m = 1.8$ GeV. We show the NLO (solid – GRV98, dashed – MRST2002), and 1PI NNLO-NNLL+ ζ (dot-dashed – GRV98, dotted – MRST2002) results. On the left-hand side, $\mu = m$ while on the right-hand side, $\mu = 2m$.

Finally, some of the data are taken on nuclear targets and then extrapolated to pp assuming a linear A dependence [334, 335].

Recent comparisons of the full $pp \rightarrow c\bar{c}$ data set with exact NLO cross sections were made to determine the best mass and scale choices for extrapolation to higher energies [336]. Rough agreement with the data up to the top ISR energy, $\sqrt{S} = 63$ GeV, was found for $m = 1.2$ GeV and $\mu = 2m$ for the MRST densities and $m = 1.3$ GeV with $\mu = m$ for the GRV98 densities [336]. These values of m are rather small compared to the typical value of 1.5 GeV. Thus, as in our previous paper [327], we calculate the NLO, 1PI NNLO-NNLL and, in addition here, the 1PI NNLO-NNLL+ ζ cross sections using $m = 1.2, 1.5$ and 1.8 GeV as well as $\mu = m$ and $2m$. We can then test whether the NNLO+NNLL+ ζ cross sections might favor a higher charm quark mass. Our charm calculations employ the GRV98 HO and MRST2002 NNLO proton parton densities.

In Fig. 5.4, we compare the exact NLO and 1PI NNLO-NNLL+ ζ cross sections calculated with the GRV98 HO and MRST2002 NNLO proton parton densities. At NLO, the best agreement is with $m = 1.2$ GeV and $\mu = 2m$, seen in Fig. 5.4b.

The MRST2002 NNLO parton densities generally give larger cross sections, even for the exact NLO result, since the value of A_3 is larger than that of the GRV98 HO set. Also due to the larger A_3 , the NNLO corrections are significantly larger.

The exact NLO cross sections calculated with $m = 1.2$ GeV and $\mu = 2m$ are relatively compatible with the data. Note that in Fig. 5.4b, the 1PI NNLO-NNLL+ ζ result is in somewhat better agreement with the two highest energy data points than the exact NLO. The 1PI NNLO cross sections are in rather good agreement with the data when $m = \mu = 1.5$ GeV is used with the MRST2002 NNLO parton densities. Indeed, the 1PI NNLO-NNLL+ ζ result in Fig. 5.4c agrees rather well with the two higher energy data points. Thus, we can conclude that the full NNLO result can likely describe the charm data well with $m = \mu = 1.5$ GeV whereas the lower mass is needed with an NLO calculation alone.

Table 5.1 gives the charm cross sections in pp collisions at $\sqrt{S} = 6.98$ GeV. The results are based on a central value of $m = \mu = 1.5$ GeV. (The choice of mass and scale used for our central value is for better illustration of the uncertainties rather than any fit to data.) The first uncertainty is due the the scale choice. Since we do not calculate the result for $\mu = m/2$ here, we show only the difference between the values of $\mu = m$ and $2m$. The second uncertainty is that due to the charm quark mass. The exact NLO and the 1PI NNLO-NNLL+ ζ cross sections are shown. The NNLO-NNLL+ ζ cross section is larger than the NLO result by a factor of 2.6 for the MRST densities and 2.2 for the GRV98.

Table 5.1 The $c\bar{c}$ production cross sections in pp collisions at $\sqrt{S} = 6.98$ GeV. The exact NLO results and the approximate NNLO-NNLL+ ζ results, based on $m = \mu = 1.5$ GeV, are shown. The first uncertainty is due to the scale choice, the second, the charm quark mass.

σ (μb)						
Order	MRST2002 NNLO			GRV98		
NLO	0.034	- 0.027	$\begin{smallmatrix} +0.56 \\ -0.032 \end{smallmatrix}$	0.028	- 0.022	$\begin{smallmatrix} +0.42 \\ -0.026 \end{smallmatrix}$
NNLO-NNLL+ ζ	0.09	- 0.07	$\begin{smallmatrix} +1.4 \\ -0.085 \end{smallmatrix}$	0.061	- 0.05	$\begin{smallmatrix} +0.9 \\ -0.057 \end{smallmatrix}$

In Fig. 5.5, we compare the pp theoretical K factors for GRV98 HO and MRST2002 NNLO. We show both $K_0^{(1)}$, the NLO to LO cross section ratios and $K_{\text{sub}}^{(2)}$, the NNLO-NNLL+ ζ to NLO cross section ratios. The K factors are not strong functions of mass, scale or parton density. Note that $K_{\text{sub}}^{(2)}$ varies between 1.3 and 1.7 for GRV98 HO and 1.5 to 1.9 for MRST2002 NNLO when $\sqrt{S} \geq 15$ GeV and $K_{\text{sub}}^{(2)} < K_0^{(1)}$ for all cases considered.

Finally, we compare the scale dependence of the cross sections in Fig. 5.6. The GRV98 HO cross section ratios on the left-hand side are compared to the MRST2002 NNLO ratios on the right-hand side. The scale dependence is similar for the two sets of parton densities although the MRST scale dependence is lower than the NLO scale dependence for all masses. These calculations are thus more stable with respect to scale than the LO and NLO cross sections.

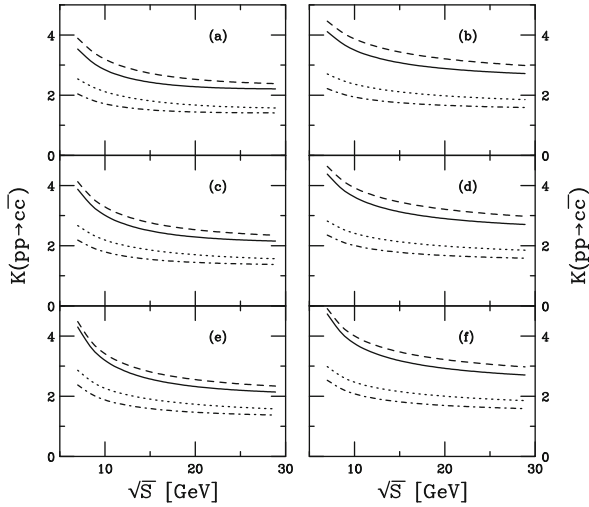


Fig. 5.5 The K -factors for $c\bar{c}$ production in pp collisions with, (a) and (b), $m = 1.2$, (c) and (d), $m = 1.5$, and, (e) and (f), $m = 1.8$ GeV. We present $K_0^{(1)}$ (solid – GRV98 and dashed – MRST2002) and $K_0^{(2)}$ (dot-dashed – GRV98 and dotted – MRST2002) for $\mu = m$ (left-hand side) and $\mu = 2m$ (right-hand side).

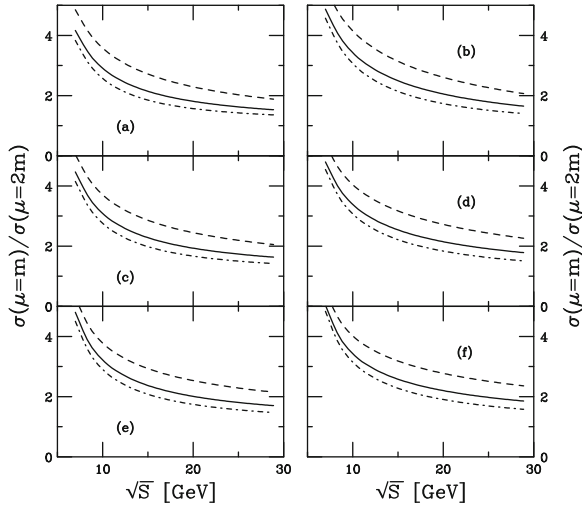


Fig. 5.6 The scale dependence of $c\bar{c}$ production in pp collisions with, (a) and (b), $m = 1.2$, (c) and (d), $m = 1.5$, and, (e) and (f), $m = 1.8$ GeV. We give the ratios $\sigma(\mu = m)/\sigma(\mu = 2m)$ for the LO (dashed), NLO (solid), and 1PI NNLO-NNLL+ ζ (dot-dashed) cross sections. Results with the GRV98 HO densities are given on the left-hand side while the MRST2002 NNLO results are shown on the right-hand side.

These pQCD calculations of the approximate NNLO cross section, while not exact, show that the total charm cross section may be considerably larger

than predicted by leading order calculations. Thus a large charm cross section may not be a result of in-medium effects but of an incomplete calculation. The perturbative cross section should thus be checked against at least pA collisions with light ions if pp is not possible.

We note again that the charm cross section is strongly dependent on the charm quark mass and scale, making it doubly important to check the results with pA interactions, particularly with light nuclei, as a means of restricting the parameter space.

With this cautionary note, we remark that while these calculations are all for near-threshold production in pp collisions, the results are relevant for AA collisions. If the time scale of the collision is such that the D mesons are produced in the medium, then predicted mass shifts could have an appreciable effect on the total $c\bar{c}$ cross section that should be observable at FAIR.

5.2 Charm-quark interactions in the QGP

As indicated in the Introduction to this chapter, charm (and, in principle, also bottom) quarks are valuable probes of the transport properties of the medium formed in high-energy heavy-ion collisions: it turns out that their mass of $m_c=1.2\text{--}1.5$ GeV implies that their thermal relaxation time is long enough to not fully thermalize, but short enough to undergo significant reinteractions which reflect on their coupling to the medium. A quantitative understanding of those interactions is thus the key to utilizing charm-hadron spectra in heavy-ion reactions. In this section we focus on the QGP, starting from the high-momentum side, where energy loss is the prevalent concept, turning to intermediate and small momenta, where charm-quark diffusion has proved a fruitful concept.

5.2.1 Energy loss of charm quarks at high momentum

One of the major new findings in the first years of operation at RHIC was a strong suppression of light hadron spectra in central $Au\text{--}Au$ collisions at high transverse momentum, $p_T \gtrsim 6$ GeV, by about a factor of 4–5 relative to $p\text{--}p$ collisions (as characterized by the so-called nuclear modification factor, $R_{AA} \equiv dN/dp_T / (N_{\text{coll}} dN/dp_T) \simeq 0.2 - 0.25$, where N_{coll} denotes the number of primordial $N\text{--}N$ collisions in $Au\text{--}Au$ at given centrality). This observation, including the rather flat dependence of $R_{AA}(p_T)$ up to currently accessible momenta of $p_T \simeq 20$ GeV, has been successfully described by energy loss of high-energy partons via induced gluon radiation when traversing a (gluon-dominated) QGP. The application of the radiative energy-loss picture to heavy quarks ($Q = b, c$) leads to significantly less energy loss. In [337],

it has been pointed out that gluon radiation off fast moving heavy quarks is suppressed in forward direction, the so called “dead-cone” effect. Employing perturbation theory with exact kinematics, it was confirmed in Ref. [338] that, at sufficiently large energy E , the radiation suppression occurs within the forward cone

$$\Theta < \Theta_0 = \frac{m_c}{E}. \quad (5.7)$$

Consequently, the suppression of charm quarks (and much more so for bottom quarks) has been predicted to be less pronounced, at least for momenta up to ~ 10 GeV [339, 340]. Around the same time, the importance of elastic scattering for heavy-quark energy loss has been pointed out, both for perturbative [341, 342] and nonperturbative [343, 344] interactions. Elastic energy loss becomes parametrically dominant over the radiative one toward low momenta; within the currently accessible momentum range at RHIC, both contributions are comparable when evaluated within pQCD. However, the nonperturbative elastic resonance interactions introduced in [343] have been found to be significantly stronger.

In heavy-ion collisions at RHIC, p_T spectra of charm and bottom hadrons have thus far been measured indirectly via their semi-leptonic decay channel, $D, B \rightarrow e^\pm X$ [319, 345, 346]. The signal, also called “non-photonic” electrons, is extracted after subtraction of all other “photonic” sources, e.g. π^0 , η Dalitz decays and photon conversions in the detector material. It turns out that the momenta of a parent D meson and decay e^\pm are reasonably well correlated: the e^\pm momentum is about half of the D ’s and also the directional information is largely conserved (which is essential for elliptic flow measurements) [347].

First (low-statistics) nonphotonic e^\pm spectra in $Au+Au$ at $\sqrt{s_{NN}} = 130$ and 200 GeV did not reveal large differences between peripheral and more central collisions [351], and initial semi-quantitative analyses [352, 353] suggested rather limited room for large energy loss. However, more recent data with improved statistics and explicit baseline spectra from $p-p$ and $d-Au$ collisions [319, 345, 346] exhibit a large suppression with an $R_{AA}(p_T \gtrsim 3 \text{ GeV}) \simeq 0.2 - 0.3$, quite comparable to the high- p_T light hadron suppression. pQCD-based radiative energy loss calculations cannot account for this finding, even after inclusion of pQCD elastic energy loss [350] or when upscaling the underlying transport coefficient by a large factor of 3–5 [340]. Thus, nonperturbative interactions seem to be required. This conclusion is further corroborated by the elliptic flow data which indicate much larger collectivity than provided by the geometric effects accounted for in energy-loss calculations (longer path length and thus more suppression out-of-plane, i.e., along the “long” axis of the ellipse), at least in the momentum range up to $p_T^e \lesssim 5$ GeV. A collective motion of charm quarks as part of the hydrodynamically expanding medium furthermore requires the inclusion of energy-gain processes. These issues will be discussed in more detail in Sect. 5.2.2 below.

Part of the difficulty in generating the observed suppression in the single- e^\pm spectra is due to significant contributions from B meson decays, in con-

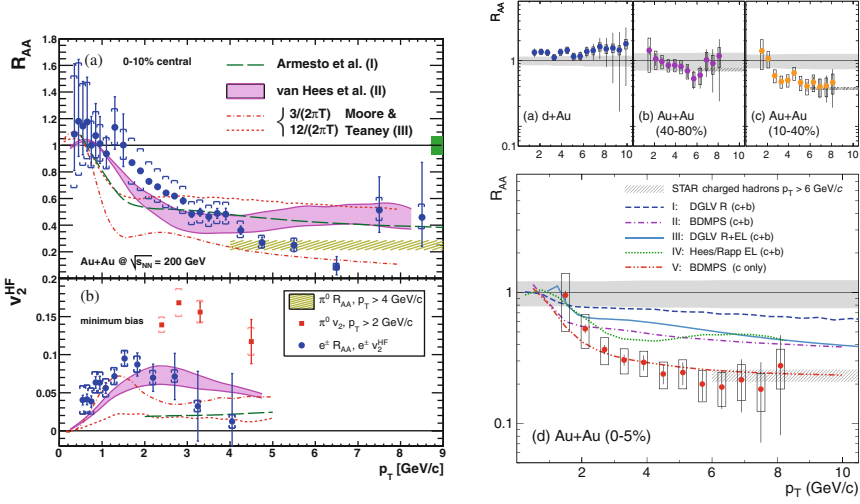


Fig. 5.7 Nuclear modification factor of nonphotonic electron spectra (attributed to semileptonic decays of open-charm and -bottom hadrons) in central $\sqrt{s_{NN}} = 200$ A GeV Au–Au collisions at RHIC. *Left panel:* PHENIX data (*upper panel:* R_{AA} , *lower panel:* elliptic flow coefficient v_2) [319] compared to theory predictions using radiative energy loss (I) [348], and Langevin simulations using elastic HQ scattering based on either pQCD+resonance scattering (II) [344] or pQCD only with upscaled friction coefficient (III) [342]. *Right panel:* STAR data [346] for R_{AA} in d -Au, peripheral (40–80%) and semi-central (10–40%) Au–Au (*upper panels*), as well as central (0–5%) Au–Au collisions, compared to theory predictions from pQCD radiative [348, 349] and radiative+elastic [350] energy-loss, as well as Langevin simulations using elastic HQ pQCD+resonance interactions [344].

nection with a smaller energy loss of b quarks. For p - p collisions, fixed-order next-to-leading logarithm (FONLL) pQCD calculations predict the transition from D to B -decay electrons around $p_T^e \simeq 4 - 5$ GeV (as used in the theoretical predictions depicted in Fig. 5.7). Rather large and possibly different K -factors for charm and bottom production render the transition momentum quite uncertain, between ca. 3 and 10 GeV [354]. This uncertainty can be resolved with explicit D meson measurements. First data from STAR for D and D^* production in d -Au are, in fact, available [355]. When using these to determine the D contribution to single- e^\pm in p - p collisions, and attributing the missing yield to B decays, the crossing between charm- and bottom-decay electrons occurs at $p_T^e \simeq 5$ GeV [356], in good agreement with the FONLL pQCD predictions.

In a recent work [357] it has been pointed out that the larger mass of heavy quarks implies a reduction in the heavy-meson formation time and therefore, for not too high momentum, the hadronization process will occur inside the medium (in standard jet quenching calculations, partons are assumed to fragment into hadrons subsequent to the energy loss processes).

Employing a light-cone model for B and D meson wave functions, and including transverse-momentum broadening due to interactions with the medium, the suppression of B mesons was found to be appreciably larger than in previous calculations. This approach presumably bears some resemblance to the resonant interactions introduced in [343], but more work is required to better understand possible connections.

5.2.2 Charm diffusion and nonperturbative correlations in the QGP

As first suggested in [358], the problem of heavy-quark (HQ) propagation in a thermal medium of (light) partons is well suited for a Brownian motion approach. If the momentum transfers are sufficiently small, the collision term of the Boltzmann equation for the HQ distribution function, f_Q , can be expanded leading to a Fokker-Planck equation,

$$\frac{\partial f_Q}{\partial t} = \gamma \frac{\partial(p f_Q)}{\partial p} + D \frac{\partial^2 f_Q}{\partial p^2}, \quad (5.8)$$

where γ and D are the (momentum-space) drag and diffusion coefficients, respectively (the former is directly related to the thermal relaxation time of a heavy quark, $\tau_Q = \gamma^{-1}$).¹ They are, in fact, related through the Einstein relation, $\gamma = D/Tm_Q$ (T : temperature, m_Q : HQ mass), and thus the approach to equilibrium is, in principle, fully characterized by the diffusion coefficient. Employing elastic $Q + p \rightarrow Q + p$ scattering ($p = q, \bar{q}, g$ with $q = u, d, s$), Langevin simulations of the Fokker-Planck equation have recently been performed to calculate heavy-quark [342, 343] and nonphotonic electron spectra [344, 359] at RHIC. In the following, we will discuss these in more detail.

In LO pQCD, elastic two-body scattering is dominated by t -channel gluon-exchange, with a total cross section $\sigma_{\text{el}} \propto \alpha_s^2/m_D^2$ where $m_D \propto gT$ is the Debye screening mass. For example, at a temperature $T=300$ MeV, and for a strong coupling constant $\alpha_s=0.4$, the thermal relaxation time is $\tau_Q \simeq 15$ fm/c [358], well above expected QGP lifetimes of $\tau_{\text{QGP}} \lesssim 5$ fm/c at RHIC. In [342], drag and diffusion coefficients for charm quarks (assuming $m_c=1.4$ GeV) have been evaluated in hard-thermal-loop improved perturbation theory, and implemented into a relativistic Langevin simulation of the Fokker-Planck equation within a hydrodynamic evolution of the (thermal) bulk matter for Au - Au collisions at full RHIC energy. The simulations have

¹ For momentum dependent coefficients, and in more than 1 spatial dimension, Eq. (5.8) takes the form

$$\frac{\partial f_Q}{\partial t} = \frac{\partial}{\partial p_i} (p_i \gamma f_Q) + \frac{\partial^2}{\partial p_i \partial p_j} (B_{ij} f_Q).$$

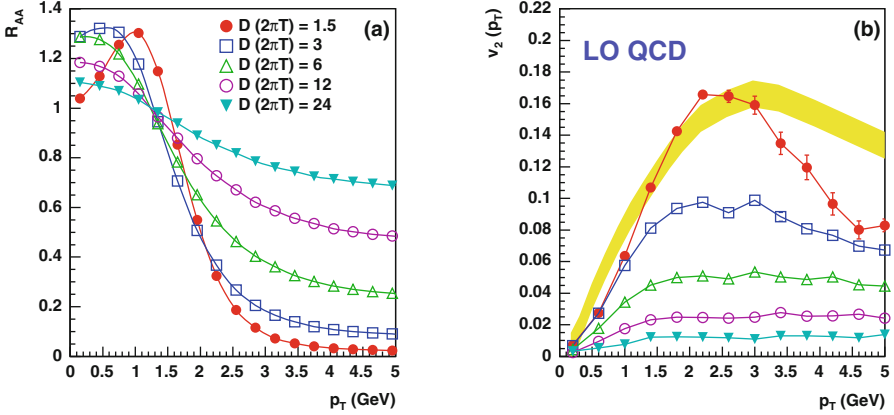


Fig. 5.8 HQ nuclear suppression factor (*left panel*) and elliptic flow (*right panel*) following from relativistic Langevin simulations for an expanding QGP in a hydrodynamic calculation for $Au-Au$ at RHIC [342]; pQCD elastic scattering has been employed for a fixed Debye mass ($m_D = gT$ with $g=1.5$, i.e., $g^2/4\pi=0.179$) and variable $\alpha_s \simeq 0.25 - 1$ corresponding to the diffusion coefficients quoted in the legend (*bottom-up*) based on the LO QCD relation $D \times 2\pi T \simeq 6/(0.5/\alpha_s)^2$.

been carried out for semicentral collisions (impact parameter $b=6.5$ fm) with an initial QGP temperature of $T_0 \simeq 265$ MeV and a transition temperature of $T_f = 165$ MeV, amounting to a QGP fireball lifetime of about 6 fm/c. The initial conditions for the c -quark spectrum were fixed from the LO parton model assuming binary scaling. The resulting nuclear modification factor and elliptic flow parameter as a function of p_T are summarized in Fig. 5.8. One finds a strong dependence of both suppression and collective flow on the (spatial) charm diffusion coefficient, along with a marked correlation between these two quantities. Also note the leveling off of $v_2(p_T)$ for $p_T \gtrsim 2$ GeV, characteristic for the transition from a thermal to a kinetic regime, which is naturally borne out of the Langevin process (and has been observed at RHIC for light hadrons).

In [343] heavy-light quark *resonances* have been introduced to calculate drag and diffusion coefficients in a strongly interacting QGP (sQGP). This is motivated by lattice QCD computations which found hadronic resonance states above T_c in both light-light ($q\bar{q}$) and heavy-heavy ($Q\bar{Q}$) channels [360, 361]. The $Q\text{-}\bar{q}\text{-}\Phi$ vertex ($\Phi=D$ or B resonance) has been constructed in accordance with HQ symmetry as

$$\mathcal{L} = G_\Phi \bar{Q} \frac{1 + \not{v}}{2} \Phi \Gamma q + \text{h.c.} , \quad (5.9)$$

where \not{v} denotes the HQ four velocity operator and G_Φ the effective (unknown) coupling constant. Assuming the existence of one state, say, in the pseudoscalar channel ($J^P = 0^-$), HQ (spin) symmetry implies degeneracy with the vector state ($J^P = 1^-$). In addition, chiral restoration in the QGP

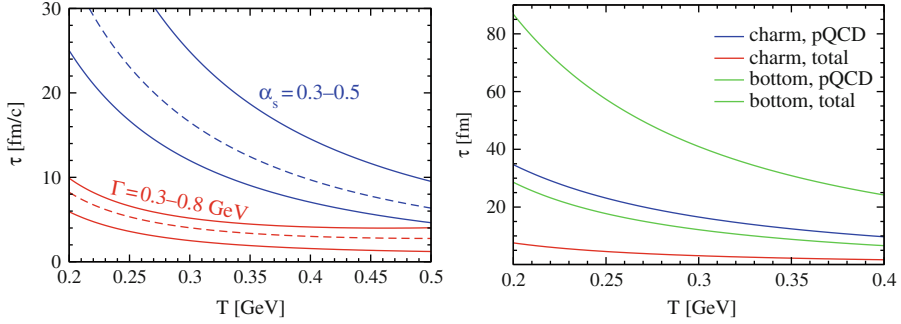


Fig. 5.9 *Left panel:* thermalization times of c quarks based on elastic interactions with thermal partons in a QGP using either LO pQCD (*upper band*) or resonance interactions (*lower band*) [343], at quark momentum $p=0$; *right panel:* c - and b -quark thermalization times at $p=0$ for LO pQCD interactions ($\alpha_s=0.4$, *upper green and blue curve*) and when adding resonance interactions ($\Gamma_\Phi=0.5$ GeV, *lower green and red curve*).

leads to degeneracy of chiral partners, i.e., scalar with pseudoscalar and vector with axialvector Φ mesons. Thus, the Dirac-matrix part of the coupling Γ in Eq. (5.9) takes on the values 1, γ_5 , γ^μ and $\gamma_5\gamma^\mu$, leading to a total of 16 spin-isospin states for both D and \bar{D} mesons with a single coupling constant G_Φ .² The latter has been varied to cover a range of decay widths for $\Phi \rightarrow c + \bar{q}$ of 0.3–0.8 GeV, as calculated from the 1-loop selfenergy which, in turn, figures into the Φ propagators. When evaluating the charm-quark thermalization time using s - and u -channel D meson exchange one finds a factor of ~ 3 reduction compared to elastic pQCD scattering at temperatures typical for the first few fm/c in Au – Au collisions at RHIC, cf. left panel of Fig. 5.9. The resulting total thermal relaxation times for elastic c -quark rescattering in an sQGP are around 5–7 fm/c (right panel of Fig. 5.9) and thus comparable to the expected duration of the QGP phase at RHIC. B meson resonances similarly reduce the thermalization times of b -quarks by a factor of ~ 3 relative to pQCD scattering. However, the absolute value is significantly larger than for c -quarks, $\tau_b \simeq 10 - 30$ fm/c in the temperature range $T \simeq 1 - 2T_c$, rendering (the approach to) b -quark thermalization much delayed.

The corresponding drag and diffusion coefficients have been implemented into a relativistic Langevin simulation using an expanding elliptic fireball model for the thermal background medium (with expansion parameters adjusted to hydrodynamic calculations [362]) [344]. The initial temperature in (semi-)central $\sqrt{s_{NN}} = 200$ GeV Au – Au collisions amounts to $T_0 = 370(340)$ MeV, with an assumed $T_c = 180$ MeV, resulting in a total QGP lifetime of ~ 7 (5) fm/c (at the end of the QGP-hadron gas mixed phase). When employing elastic pQCD rescattering alone, the results for the c -quark v_2 and R_{AA} , displayed in Fig. 5.10, approximately agree with the

² For HQ interactions with strange quarks, only HQ symmetry for D_s resonances has been assumed.

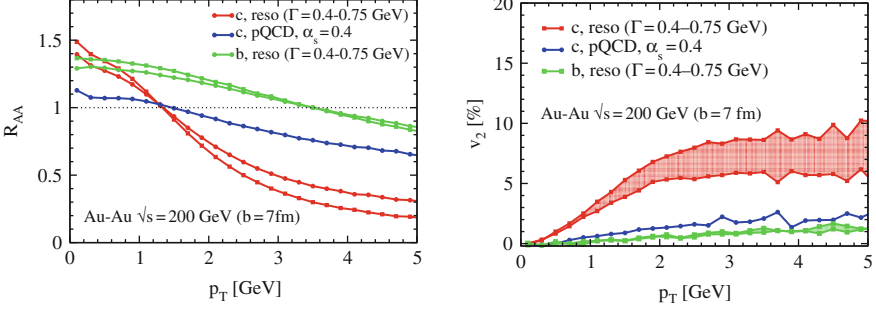


Fig. 5.10 HQ nuclear suppression factor (*left panel*) and elliptic flow (*right panel*) following from relativistic Langevin simulations for an expanding QGP in Au–Au at RHIC; *red (green) lines* R_{AA} at large p_T : c (b) quarks using resonance+pQCD interactions; *blue lines*: c quarks with LO pQCD scattering only. In the right panel the order of the lines is reversed.

hydrodynamic Langevin simulations of Moore and Teaney [342], cf. Fig. 5.8.³ As to be expected from the thermal relaxation times, resonance interactions lead to a substantial (factor of ~ 3) increase of the c -quark suppression and elliptic flow. At the same time, the b -quark spectra are still rather little affected. Also note that the sensitivity to the (unknown) resonance coupling strength at the Q - q - Φ vertex is quite moderate. One of the features in the efficacy of the resonant interactions in accelerating the approach to thermalization is their isotropic angular distribution in the center-of-mass system of the quarks; pQCD scattering, on the other hand, occurs mostly at forward angles.

To compare to experimental e^\pm spectra, the HQ output spectra from the Langevin simulation have to be hadronized and decayed. In [344], the former has been carried out in a combined coalescence and fragmentation approach: using the model of Greco et al. [347], the HQ spectra are first subjected to coalescence with light quarks (with radial and elliptic flow distributions as used in the description of light hadron data); left-over c and b quarks are fragmented into D and B mesons assuming no momentum loss (δ -function fragmentation, providing a conservative estimate of the suppression effect). After 3-body decays into electrons, the resulting spectra agree reasonably well with PHENIX [345, 364] and STAR data [346], cf. lower panels in Fig. 5.11 and left panels in Fig. 5.7. The upper panel of Fig. 5.11 shows the e^\pm spectra if all c and b quarks are hadronized with δ -function fragmentation, i.e. if no coalescence is implemented. One sees that coalescence leads to a significant increase of *both* v_2^2 and R_{AA}^2 , introducing an “anti”-correlation of the two quantities (usually a stronger coupling to the medium implies stronger elliptic flow and suppression, i.e. an increase in v_2 along with a reduction in

³ Recalling the form of the dominant pQCD c - g cross section, $\sigma_{el} \propto \alpha_s^2/m_D^2$, a coupling constant of $\alpha_s = 0.4$, together with a Debye mass $m_D = gT$ with $g = (4\pi\alpha_s)^{1/2} = 2.23$ (implying $\alpha_s^2/g^2 = 0.032$) as used in [344], corresponds to a diffusion constant of close to $D(2\pi T) = 24$ in Fig. 5.8 [342] (implying $\alpha_s^2/g^2 \simeq 0.25^2/1.5^2 = 0.028$).

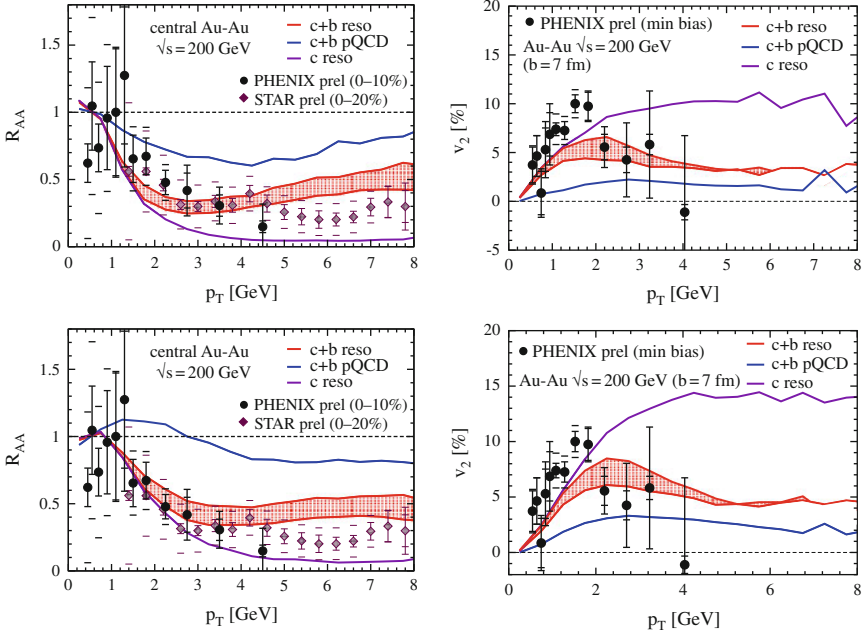


Fig. 5.11 Nuclear suppression factor (*left panels*) and elliptic flow (*right panels*) of single electrons emerging from the decay of D and B mesons based on relativistic Langevin simulations for heavy quarks at RHIC [344, 363]. The upper panels represent calculations where the final heavy-quark distributions have been hadronized using δ -function fragmentation only, while the results in the *lower panels* are based on a coalescence+fragmentation approach [347], i.e., include coalescence of heavy quarks with light quarks from the heat bath. The calculations are compared to PHENIX [345] and STAR [346] data for R_{AA} , and PHENIX data [364] for v_2 .

R_{AA}). Both features improve the description of the experimental data, i.e., the large v_2 and the shape of R_{AA} (in particular the “delayed” decrease up to $p_T^e \simeq 3$ GeV). The e^\pm suppression and elliptic flow of the charm contribution alone is displayed by the purple lines in Fig. 5.11, exhibiting stronger effects compared to the total at e^\pm momenta $p_T^e \gtrsim 3$ GeV. This shows that the bottom decay contributions become appreciable (and eventually dominant) at rather low e^\pm momenta, but it also means that an explicit D meson measurement is a key to resolving the question of the bottom contribution, to either refute or confirm the large effects on the charm quarks.

Due to the discriminative power of the recent e^\pm spectra it is possible to estimate the charm diffusion constant in the sQGP. Given a fair agreement with the Langevin simulations including resonance interactions plus coalescence, the range of diffusion constants corresponding to the uncertainty in the interaction strength in the approach of [343, 344] is plotted in Fig. 5.12. One finds a spatial diffusion constant of about $D_s \simeq 5/2\pi T$. This can be compared to the pQCD inspired approach of Moore and Teaney [342]: recalling

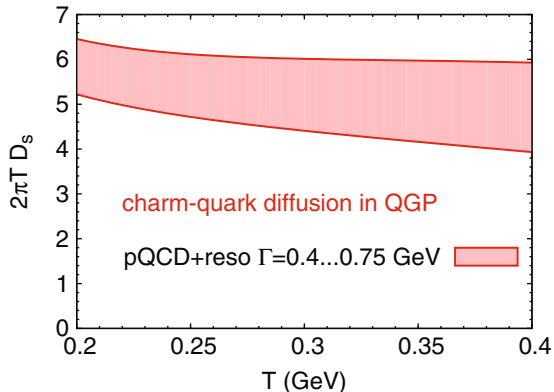


Fig. 5.12 Heavy-quark (spatial) diffusion constant underlying the Langevin simulations with quark coalescence corresponding to the bands in the *left panel* of Fig. 5.7 and *lower panels* in Fig. 5.11 [343, 344].

Fig. 5.8, a comparable value of D_s leads to an R_{AA} and v_2 at the c -quark level which is roughly consistent with that following from the pQCD+resonance interactions as shown in Fig. 5.11.

HQ spectra at RHIC have also been investigated in transport calculations [365, 366], with conclusions quite similar to the Langevin approaches: a substantial upscaling of elastic pQCD cross sections for c -parton scattering is required to obtain a suppression and flow reminiscent to what is observed in the data (including effects of coalescence with light quarks), corroborating the notion of a strongly interacting QGP.

It seems inevitable to conclude that pQCD interactions are not strong enough to account for the modifications of HQ spectra at RHIC, thus requiring the presence of substantial nonperturbative effects. Remaining challenges toward a deeper understanding of HQ interactions in the sQGP include: (i) The assumption of resonance interactions should be scrutinized by employing a more microscopic description of Q - \bar{q} scattering using input from finite-temperature lattice QCD (lQCD). One could adopt, e.g., the T -matrix approach as recently constructed to evaluate Q - \bar{Q} (as well as q - \bar{q}) interactions in the sQGP [367, 368] based on heavy-quark potentials extracted from the lQCD HQ free energy above T_c . The pertinent T -matrices show a large non-perturbative enhancement close to and above the quark-antiquark thresholds; it would be very interesting to compute pertinent friction and diffusion coefficients in the heavy-light sector. (ii) Radiative processes, which are expected to become the dominant source of energy loss in the high-momentum limit, should be implemented into the Fokker-Planck framework. One of the problems is a proper treatment of interference (Landau-Pomeranchuk-Migdal) effects for radiated gluons, which, however, is presumably less pronounced for heavy quarks. First estimates for $2 \rightarrow 3$ processes in the HQ sector have been

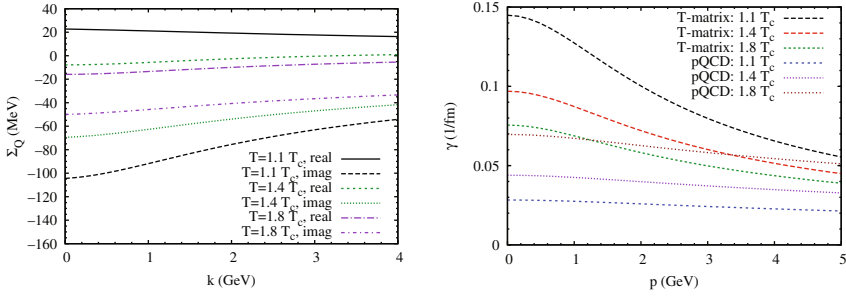


Fig. 5.13 Charm-quark selfenergies (*left panel*) and friction coefficients (*right panel*) based on a T -matrix approach for heavy-light quark scattering in a QGP [370] with interaction potentials estimated from finite-temperature lattice QCD.

performed in [369]. (iii) A systematic study should be performed with respect to the chemical composition of the QGP: current radiative energy-loss models as discussed in the previous section routinely assume the early matter to be a gluon-dominated plasma (as a natural result of a color-glass initial state of the colliding nuclei), which maximizes the radiative interaction strength (induced gluon radiation). If, however, the QGP quickly reaches chemically equilibrium, about 60% of the partons are anti-/quarks. The latter are, in turn, the key mediator for the resonance interactions (or, more generally, color-neutral channels). The chemical composition of the QGP thus has important impact on the evaluation of HQ interactions (and, possibly, also for light partons).

Item (i) has been addressed in a recent paper by van Hees et al. [370]: based on potentials extracted from lQCD computations of the heavy-quark free energy at finite temperature, heavy-light quark T -matrices have been calculated in both quark-antiquark ($c\bar{q}$) and quark-quark (cq) channels, accounting for both S - and P -wave scattering. It has been found that the dominant contributions to the in-medium HQ selfenergy are due to the attractive color-singlet (meson) and color-antitriplet (diquark) channels. These are precisely the channels that are present in mesons and baryons, i.e., relevant for hadronization. This approach therefore provides a natural link between a strongly interacting QGP and hadronization via constituent-quark recombination, and thus between the phenomenological successes of ideal hydrodynamic and quark-coalescence models at RHIC. The resulting c -quark widths in the QGP are large (up to ~ 300 MeV), and the transport (friction) coefficients are quite similar to the effective resonance model, cf. Fig. 5.13. However, while in the resonance model most of the interaction strength for c -quarks is due to scattering off antiquarks from the heat bath, in the T -matrix approach the contributions from meson and diquark channels are about equal (the latter carry less interaction strength but a larger (color-)degeneracy). Consequently, the resonance model would predict a rather different behavior of c and \bar{c} quarks in baryon-rich matter as expected in heavy-ion collisions

at the future CBM experiment (a potentially formed QGP should have an appreciable excess of quarks over antiquarks). This effect is not present in the microscopic T -matrix approach. However, the dominance of interactions with anti-/quarks over gluons from the heat bath in both approaches might help to distinguish between “pre-hadronic” correlations and an sQGP which is driven by interactions with gluons. In the former case, the observable effects on D mesons at CBM (i.e., elliptic flow and suppression) should be larger than in the latter case. These effects could receive additional contributions from the hadronic phase, where D^+ and D^0 can undergo charm-exchange reactions with baryons (e.g., $DN \rightarrow \pi\Lambda_c$) which are not available to D^- and \bar{D}^0 mesons (antibaryons are much less abundant) [371]. Thus, the importance of reactions in the hadronic phase would be signaled by stronger modifications of D meson spectra relative to \bar{D} spectra.

5.2.3 Charm dilepton decays

Since parton fusion in primordial N - N collisions is expected to be the dominant source of charm in heavy-ion collisions, c and \bar{c} are produced pairwise. If both c and \bar{c} within a correlated pair eventually decay semileptonically,

$$\bar{c}c \rightarrow D\bar{D} \rightarrow e^+e^-X, \quad (5.10)$$

one ends up with a correlated source of dileptons that cannot be subtracted by standard combinatorial methods (such as mixed event techniques), see also [372].

At maximum SPS energy, the correlated-charm contribution to the dilepton spectrum in p - p (or p - A) collisions is comparable to Drell-Yan annihilation in the invariant mass range up to $M \simeq 3$ GeV. When these two sources are extrapolated to central Pb - Pb (using binary collision scaling), the experimental dimuon spectra in the intermediate-mass region (IMR, $1 \text{ GeV} \lesssim M \lesssim 3 \text{ GeV}$) as measured by NA38/NA50 [373] are underpredicted by about a factor of 2. Originally, this has been taken as an indication of a factor of ~ 3 enhancement of open-charm production in central Pb - Pb . However, it has been shown that the presence of a rather standard thermal fireball (with initial temperature of $T_0 \simeq 200$ MeV and total lifetime of 12–15 fm/c) leads to thermal dilepton radiation that essentially accounts for the observed excess [374], cf. also [375, 376]. Di-muon spectra from open charm decays and thermal spectra have indeed a very similar shape at SPS energies [377].⁴ Recent data from the NA60 collaboration in In - In collisions at full SPS energy [379] have reconfirmed the presence of an excess and, using

⁴ In principle, there could be charm energy loss and diffusion, even though theoretical analysis does not indicate large effects [378]. However, more definite conclusions require more precise data and more elaborate calculations.

displaced decay vertices, have shown that this excess is not due to open-charm decays. At beam energies envisaged in the CBM experiment one is significantly closer to the open-charm threshold, implying that the relative magnitude of the charm component in the dilepton spectra is reduced. However, if charm quarks undergo significant rescattering in a putative sQGP, and if their dilepton signal can be separated from the prompt yield (e.g., using displaced vertices), possible medium modifications (most notably a softening of the invariant mass distribution) could provide a valuable complement to the single-charm observables discussed in Sect. 5.2.2.

Finally we note that the in-medium properties of open-charm states have important consequences on the in-medium spectral properties of charmonia, and thus on their suppression pattern in heavy-ion collisions. If, in addition, regeneration of charmonia via $c\bar{c}$ coalescence becomes important, charmonium production also becomes sensitive to both the total number of $c\bar{c}$ pairs and their p_T spectra (however, this is only expected for ultrarelativistic heavy-ion collisions at center-of-mass energies above 20 GeV, i.e., above the SPS energy range) [380, 381]. These points are to be discussed in relation with charmonium physics.

5.3 Charm chemistry and thermal models

Thermal models are successful in reproducing ratios of produced light hadrons in heavy-ion collisions in terms of just two parameters, the baryon chemical potential and temperature, (μ_B^{ch}, T_{ch}) (in addition, one introduces chemical potentials for conserved charges, such as isospin, strangeness or charm in strong interactions), cf. Braun-Munzinger et al. [211] for a recent review. These quantities have been interpreted in terms of a chemical freezeout of the interacting system, characterizing the stage of the evolution where *inelastic* reactions cease and the abundancies of stable hadrons (with respect to strong interactions) are frozen. This is to be distinguished from thermal freezeout (at temperature T_{fo}), which occurs when *elastic* interactions, such as $\pi N \rightarrow \Delta \rightarrow \pi N$ or $\pi\pi \rightarrow \rho \rightarrow \pi\pi$, cease (at which point the momentum distributions are frozen). Since elastic reactions usually have much larger cross sections than inelastic ones, such as $\pi N \rightarrow K\Lambda$ or $\pi\pi \rightarrow K\bar{K}$, one expects $T_{ch} > T_{fo}$.⁵ In elementary p - p / A (as well as π - p / A) collisions, chemical and thermal freezeout temperatures essentially coincide, consistent with the notion of little, if any, final-state interactions. Even though in elementary reactions the nonstrange particle ratios also follow chemical freezeout systematics (interpreted as “statistical hadronization”), strangeness production is suppressed, i.e., chemically not equilibrated. It is then natural to ask how the situation develops for the substantially heavier charm quarks and

⁵ Note that this does not apply to strongly decaying resonances which are rather the main mediators of elastic interactions, such as Δ and ρ , cf. Sect. 3.

Table 5.2 Compilation of D meson flavor ratios evaluated for elementary p - N collisions in a recombination approach based on parton distribution functions [389] (lines 2 and 3, corresponding to rapidity integrated yields) and within the statistical recombination approach for central A - A collisions based on thermal equilibrium [391] (lines 2 and 3, corresponding to midrapidity yields, dN_D/dy).

system (\sqrt{s} energy)	$(D^++D^-)/(D^0+\bar{D}^0)$	D^-/D^+	\bar{D}^0/D^0	D_s/D
p - N (20-40 GeV)	0.40 ± 0.05	1.3 ± 0.1	1.4 ± 0.1	0.13 ± 0.01
p - N (200 GeV)	0.40 ± 0.05	1.24 ± 0.1	1.35 ± 0.1	0.23 ± 0.02
A - A (17.3 GeV)	0.46	1.6	1.59	0.25
A - A (200 GeV)	0.45	1.04	1.05	0.26

hadrons. As briefly alluded to in Sect. 5.2.3, the *number* of produced $c\bar{c}$ pairs is most likely *not* enhanced in A - A collisions, i.e., it follows the expected binary collisions scaling, both at SPS [379] and at the much higher RHIC energies [382] (this is corroborated by theoretical estimates [383]). The off-chemical-equilibrium for charm quarks can be accommodated by introducing a charm-quark fugacity factor, γ_c , which is equal for c and \bar{c} quarks. The key question then is how the c and \bar{c} quarks distribute themselves among the produced charm hadrons, i.e., the *relative* charm chemistry, and what one can learn from it (the rich information encoded in momentum spectra has been discussed in some detail in Sects. 5.2.1 and 5.2.2).

Flavor asymmetries are a well-established phenomenon in hadronic collisions (p - p , π - N etc.). Especially at forward rapidities, marked enhancements of antiparticle-to-particle ratios of produced strange and charm hadrons have been observed, e.g. for K^+/K^- or D^-/D^+ [384, 385]. This has been successfully attributed to quark recombination processes, where a strange or charm antiquark, produced in forward direction, coalesces with a valence quark from the projectile [386–388]. An extension of these ideas to central rapidities has been discussed, e.g., in [389] by generalizing the approach to include coalescence with sea quarks (cf. also [390]). This enables the investigation of *inclusive* particle production asymmetries for charmed hadrons; the fraction of D mesons produced via recombination amounts to 50–80%, and fair overall agreement with available data for the x_F -dependent and inclusive flavor asymmetries in elementary collisions has been found. Typical results for D meson flavor ratios for fixed target (RHIC) energies, \sqrt{s} =20–40 GeV (200 GeV) are summarized in the upper two lines of Table 5.2 [389]. These values for elementary collision can then be used as a baseline for charm-hadrochemical analysis in heavy-ion reactions.

Hadrochemical analysis of open-charm hadron production have been conducted in the statistical hadronization model, e.g., in [381, 391, 392], see also Sect. 6.2 including charmonia. While the number of charm quarks is routinely assumed to be fixed by hard production as discussed above, the notion of temperature in a statistical hadronization approach still requires the c -quark momentum distributions to kinetically equilibrate (which seems to be a good

assumption at least for RHIC energies, cf. Sect. 5.2.2). The charged-to-neutral D meson ratio appears to be rather stable, but the antiparticle-to-particle ratios vary much stronger with collisions energy in central A – A compared to elementary collisions, reflecting the variation in chemistry with \sqrt{s} (essentially the decrease in baryon chemical potential; note, however, that the values quoted for A – A correspond to midrapidity, while the p – N ones refer to inclusive yields). Also note that at lower energies, strangeness equilibration reflects itself by a factor of 2 increase in the D_s/D ratio, which could be a promising signal at CBM energies.

5.4 QCD sum rules

Given a current with the quantum numbers of a hadron with open or hidden charm one can evaluate, along the strategy outlined in Sect. 2.3.1, the current–current correlator with an Operator Product Expansion (OPE) to relate the hadronic properties to various condensate terms. The advantage of QCD sum rules is the use of universal condensates which are estimates at finite baryon density and temperature utilizing leading terms in the corresponding expansion, in connection with pertinent nucleon and pion matrix elements.

5.4.1 Open charm mesons

In the light quark sector, the vector mesons ρ and ω depend only weakly on the genuine chiral condensate $\langle \bar{q}q \rangle$ but sizeably on 4-quark condensates [80] which often are factorized in squares of the chiral condensate. The reason for this weak dependance is that the renormalization group invariant combination $m_q \langle \bar{q}q \rangle$ enters sum rules for ρ and ω mesons; due to the smallness of the u , d quark masses, m_q , the impact of $\langle \bar{q}q \rangle$ is strongly suppressed. In the light-heavy quark sector, say for D mesons, the combination $m_c \langle \bar{q}q \rangle$ enters and one anticipates that the large charm mass m_c amplifies the role of the chiral condensate $\langle \bar{q}q \rangle$.

With respect to the quark structures $D^+ = \bar{d}c$ and $D^- = \bar{c}d$ one further expects [393] a pattern of in-medium modifications as known from K^- and K^+ mesons [394], *i.e.*, a downward shift of excitation strength with quantum numbers of K^- or D^+ , D^0 and a tiny upward shift for K^+ or D^- , \bar{D}^0 . Purely hadronic model calculations (cf. Sect. 5.5) indeed qualitatively support this pattern in the open charm sector.

Most QCD sum rule evaluations for open-charm mesons focus on vacuum properties (see [395, 396] and references therein). The in-medium study in [397] has considered the isospin average of D^\pm . In [393] both the isospin average and a D^\pm mass splitting in the nuclear medium are evaluated based

on a pole ansatz. While the latter is appropriate in vacuum, it may not be accurate in medium in view of recent hadronic model calculations [311, 398] (also discussed in Sect. 5.5). Therefore, one should rather evaluate QCD sum rules by considering appropriate moments of the spectral distributions of D^\pm (as well as D^0 and \bar{D}^0).

The Wilson coefficients are calculated up to mass dimension 6 and listed in various papers, both for vacuum [395, 396] and in medium [397, 399]. The literature on the medium modifications of D mesons within the QCD sum rule approach is poor, cf. [397, 399]. Reference [397] claims an isospin averaged D^\pm downward mass shift of ~ 50 MeV at nuclear saturation density, while [399, 400] favor a mass splitting of about 40 MeV.

The pseudo-scalar current $j_{D^+} = i\bar{d}\gamma_5 c$ for the D^+ meson results in the correlator

$$\Pi_{D^+}(q) = i \int d^4x e^{iq \cdot x} \langle \mathcal{T} j_{D^+}(x) j_{D^+}^\dagger(0) \rangle, \quad (5.11)$$

where $\langle \dots \rangle$ means Gibbs average and \mathcal{T} time ordering. A similar correlator may be defined for the D^- meson with current $j_{D^-} = i\bar{c}\gamma_5 d$. (D^0 and \bar{D}^0 follow by the replacement $d \rightarrow u$.) The occurrence of positive and negative frequency contributions lead to the decomposition $\Pi_{D^+} = \Pi_{D^+}^+ + \Pi_{D^+}^-$ and a further decomposition into parts which are even or odd, respectively, with respect to $q \rightarrow -q$. In total: $\Pi_{D^+} = \Pi_{D^+}^{+e} + \Pi_{D^+}^{-e} + \Pi_{D^+}^{+o} + \Pi_{D^+}^{-o}$.

Twice subtracted dispersion relations for the correlator of D^+ mesons at rest, $q = (\omega, \mathbf{0})$, read

$$\text{Re}\Pi_{D^+}^e(\omega^2) = \frac{\omega^4}{\pi} \int_0^\infty \frac{ds}{s^2} \frac{1}{s - \omega^2} (\text{Im}\Pi_{D^+}^{+e}(s) + \text{Im}\Pi_{D^+}^{-e}(s)) + \text{subtractions} \quad (5.12)$$

$$\frac{1}{\omega} \text{Re}\Pi_{D^+}^o(\omega) = \frac{\omega^4}{\pi} \int_0^\infty \frac{ds}{s^{5/2}} \frac{1}{s - \omega^2} (\text{Im}\Pi_{D^+}^{+e}(s) - \text{Im}\Pi_{D^+}^{-e}(s)) + \text{subtractions} \quad (5.13)$$

The subtraction terms vanish after a Borel transformation $\mathcal{B}_{\omega \rightarrow \mathcal{M}}$ [49]. A subtle issue in medium is a possible Landau term emerging from contributions at $s \rightarrow 0$. It corresponds to the Thomson limit of the forward DN scattering amplitude, which, however, vanishes in leading order in a medium without charm content.

For large space-like momenta, $-\omega^2 \gg \Lambda_{QCD}^2$, the OPE for the left-hand-side of Eqs. (5.12) and (5.13) is used:

$$\text{Re}\Pi_{OPE}^e(\omega^2) = c_0 + \sum_{j=1}^{\infty} c_j(\omega^2) \langle \mathcal{O}_j \rangle \quad (5.14)$$

and an analogous expansion for the odd part. Here, c_0 denotes the perturbative contribution and is given explicitly in [401]. Condensates are encoded

in the expectation values $\langle \mathcal{O}_j \rangle$ and are ordered according to their dimensionality. Condensates of high dimensionality are accompanied by high powers of $1/\omega^2$ and/or $1/m_c^2$ encoded in the Wilson coefficients c_j . In the region of applicability of the OPE ω and m_c are large. Consequently, condensates of high dimensionality are suppressed and therefore neglected. Typically one considers in Eq. (5.14) condensates up to dimension 6 (not explicitly given here).

For the right-hand-side of Eqs. (5.12, 5.13) one might use the standard pole + continuum ansatz (assuming equal continua for $\text{Im}\Pi_{D+}^{\pm e}$)

$$\frac{1}{\pi} \text{Im}\Pi_{D+}^{\pm e}(s) = F_{\pm} \delta(s - m_{\pm}^2) + \frac{1}{2\pi} \text{Im}\Pi^{\text{per}}(s) \Theta(s - s_{\pm}).$$

The perturbative contribution $\text{Im}\Pi^{\text{per}}$ corresponds to c_0 on the OPE side, and we have defined $F_{\pm} = F \pm \Delta F$, $m_{\pm} = m \pm \Delta m$ and $s_{\pm} = s_0 \pm \Delta s$. The residues F_{\pm} and masses m_{\pm} can be determined from the sum rules (5.12) and (5.13). To leading order in ΔF , Δs and Δm , one obtains the mass splitting Δm and the residue F

$$F = \frac{1}{2} e^{m^2/\mathcal{M}^2} \mathcal{B}_{\omega \rightarrow \mathcal{M}} (\text{Re}\Pi_{OPE}^e(\omega^2)) - \frac{1}{2\pi} \int_{s_0}^{\infty} ds e^{(m^2-s)/\mathcal{M}^2} \text{Im}\Pi^{\text{per}}(s) \quad (5.15)$$

$$\Delta m = -\frac{1}{4F(s_0 - m^2)} e^{m^2/\mathcal{M}^2} \mathcal{B}_{\omega \rightarrow \mathcal{M}} \left(\frac{1}{\omega} \text{Re}\Pi_{OPE}^o(\omega)(m^2 - \omega^2)(s_0 - \omega^2) \right), \quad (5.16)$$

where the logarithmic derivative of Eq. (5.15) is used to determine m as average in the Borel window with adjustment of s_0 to achieve maximum flatness, and Eq. (5.15) itself to determine afterwards F . The mass splitting Δm follows then from (5.16).

The quantities defined in Eqs. (5.15) and (5.16) depend on the Borel mass \mathcal{M} . They have to be averaged within the sliding Borel window from \mathcal{M}_{\min} to \mathcal{M}_{\max} which is determined by the requirements of not more than 10% contribution of the mass dimension 6 condensates to the total OPE (\mathcal{M}_{\min}) and equality of the low-lying resonance contribution and the perturbative continuum contribution (\mathcal{M}_{\max}). The continuum threshold s_0 is determined by the requirement of maximum flatness within the Borel window.

The above sum rule considerations provide robust results for the mass splitting $m_{D^+} - m_{D^-} = 2\Delta m$ of the charged D mesons. Using standard values for the involved vacuum and in-medium condensates the mass splitting grows almost linear with increasing density, as shown in Fig. 5.14. At nuclear saturation density $n_0 = 0.16 \text{ fm}^{-3}$ a value of $\sim 60 \text{ MeV}$ is reached, where the D^+ is below the D^- mass, as expected. We note in this context that the density dependence of the centroid of the D meson mass doublet cannot appropriately be determined by the above sum rules. For further discussions we refer to [402].

Several issues remain to be clarified, including: (i) the Landau term beyond leading order, (ii) the symmetric continuum [393], (iii) moments when

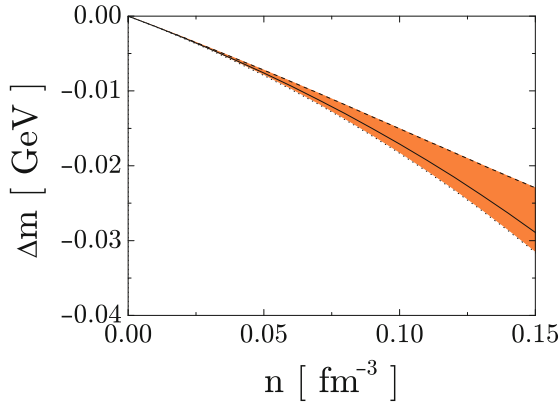


Fig. 5.14 Mass splitting $\Delta m = \frac{1}{2}(m_{D^+} - m_{D^-})$ in cold nuclear matter as a function of density within the QCD sum rule calculations of Hilger et al. [402].

going beyond the zero-width approximation, (iv) the influence of density dependence of genuine chiral condensate.

5.4.2 Remarks on J/ψ

In the QCD sum rule for the J/ψ , a term $m_c \langle \bar{c}c \rangle$ appears, which for the heavy quark can be expanded as [403]

$$m_Q \langle \bar{Q}Q \rangle = -\frac{1}{12\pi} \langle \frac{\alpha_s}{\pi} G^2 \rangle - \frac{1}{1440\pi^2 m_Q^2} \langle g_s^3 G^3 \rangle - \frac{1}{120\pi^2 m_Q^2} \langle (DG)^2 \rangle + \mathcal{O}(m_Q^{-5}, \alpha_s). \quad (5.17)$$

This implies that in the heavy-quark limit, $m_Q \rightarrow \infty$, the 2-quark condensate is to be substituted by the gluon condensate $\langle \frac{\alpha_s}{\pi} G^2 \rangle$. The latter, in turn, is rather inert against density and temperature changes far enough from the deconfinement boundary in the hadronic phase. Since this is the only dependence on quark condensates of low mass dimension, it is expected that medium modifications of J/ψ are tiny (< 10 MeV), as more complete evaluations of the sum rules confirm [400].

5.5 Charm hadrons in medium

In the following we explore medium modifications of D mesons along the strategy employed for K^\pm mesons, see Sect. 4.1.

5.5.1 Cold nuclear matter

In [404], the spectral density of the D meson in cold nuclear matter is studied within a microscopic self-consistent coupled-channel approach using a separable potential for the S -wave DN interaction. This bare interaction allows for the transition from DN to $\pi\Lambda_c$, $\pi\Sigma_c$, $\eta\Lambda_c$ and $\eta\Sigma_c$ channels, all carrying charm $c = 1$. We only consider channels with up, down and charm-quark content keeping the $SU(3)$ symmetry. This approach is similar to using $SU(4)$ symmetry and ignore the channels with strangeness which are higher in mass and well above the DN threshold. The parameters of this model, i.e. coupling constant g and cutoff Λ , are determined by generating dynamically the $\Lambda_c(2593)$ resonance, which is the counterpart of the $\Lambda(1405)$ in the charm sector.

The medium effects on the $\Lambda_c(2593)$ resonance and, hence on the D meson potential, due to the Pauli blocking of the intermediate nucleonic states as well as due to the dressing of nucleons and pions are analyzed. In Fig. 5.15, the D meson optical potential is obtained for different approaches: self-consistent calculation for the D meson potential and self-consistent calculation for the

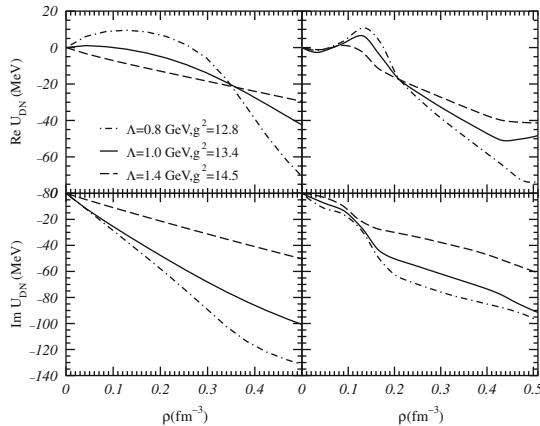


Fig. 5.15 Real and imaginary parts of the D meson potential at $k_D=0$ as a function of the density for different sets of coupling constants and cutoffs, that generate dynamically the $\Lambda_c(2593)$ resonance, and for two approaches: self-consistent calculation for the D meson potential (*left panels*) and self-consistent calculation for the D meson potential including the dressing of nucleons and the pion self-energy in the intermediate states (*right panels*).

D meson potential including the dressing of nucleons and the pion self-energy in the intermediate states. The D meson potential at zero momentum and nuclear matter saturation density, $\rho_0=0.17 \text{ fm}^{-3}$, stays between 8.6 MeV for $\Lambda = 0.8 \text{ GeV}$ and -11.2 MeV for $\Lambda = 1.4 \text{ GeV}$ when only the D meson is dressed (upper left panel). For the full self-consistent calculation (upper right panel), the value of the D meson potential lies in between 2.6 MeV for $\Lambda = 0.8 \text{ GeV}$ and -12.3 MeV for $\Lambda = 1.4 \text{ GeV}$. Previous works based on QCD sum-rules [397, 400], quark-meson coupling (QMC) models [405, 406] or chiral effective Lagrangians [407] predict an attractive D -nucleus potential with depths ranging from -50 to -200 MeV . We therefore conclude that the coupled-channel effects result in an overall reduction of the in-medium effects independent of the set of parameters (g, Λ) and the in-medium properties of the intermediate states. On the other hand, the self-consistent coupled-channel calculation allows for the determination of the imaginary part of the D meson potential, which was not obtained in the previous works. The imaginary part turns out to be quite important ranging from -51.6 MeV for $\Lambda = 0.8 \text{ GeV}$ to -27.9 MeV for $\Lambda = 1.4 \text{ GeV}$ when only the D meson is dressed (lower left panel) while it changes from -49 MeV for $\Lambda = 0.8 \text{ GeV}$ to -18.2 MeV for $\Lambda = 1.4 \text{ GeV}$ in the full self-consistent calculation (lower right panel). A later coupled-channel calculation [311], which includes channels with strangeness saturating the interaction by t -channel vector-meson exchange [408], substantiates our findings obtaining a repulsive D meson mass shift and a considerable imaginary part for the D meson potential.

The D meson spectral density at zero momentum is shown in Fig. 5.16 for $\Lambda = 1 \text{ GeV}$ and $g^2 = 13.4$, and for several densities in the two self-consistent approaches considered before. When only the D meson is dressed self-consistently (left panel), the quasi-particle peak slightly moves to lower

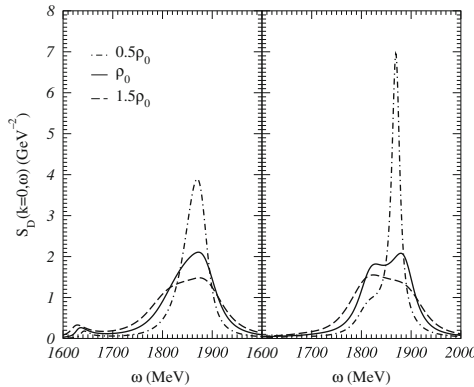


Fig. 5.16 D meson spectral density at $k_D = 0$ as a function of energy with $\Lambda = 1 \text{ GeV}$ and $g^2 = 13.4$ for different densities and for two approaches: self-consistent calculation for the D meson potential (left panel) and self-consistent calculation for the D meson potential including the dressing of nucleons and the pion self-energy in the intermediate states (right panel).

energies as density increases since the D meson potential becomes more attractive (see upper left panel of Fig. 5.15). The $\Lambda_c(2593)$ resonance is seen for energies around 1.63–1.65 GeV as a second peak on the left-hand side of the quasi-particle peak. For the second approach when nucleons and pions are dressed in the intermediate states (right panel), a structure around 1.8 GeV mixes with the quasi-particle peak which translates into a broadening of the spectral density at the quasi-particle energy. This structure corresponds to a resonance below the DN threshold with the Λ_c -like quantum numbers and, as reported in [404], appears together with another structure below the $\pi\Sigma_c$ threshold, which is not noticeable in the figure. The nature of these two structures deserves further studies. In both cases we conclude that the quasi-particle peak stays close to its free position. However, the features of the low-energy region on the left-hand side of the quasi-particle peak are different according to the different in-medium behavior of the $\Lambda_c(2593)$ resonance in both approaches.

Table 5.3 Mass shifts of peaks (in MeV) in D^\pm spectral functions at nuclear saturation density.

	D^+	D^-
Lutz and Korpa [311]	−250, +32	+18
Tolos et al. [398]	Small	Small mainly widths effects

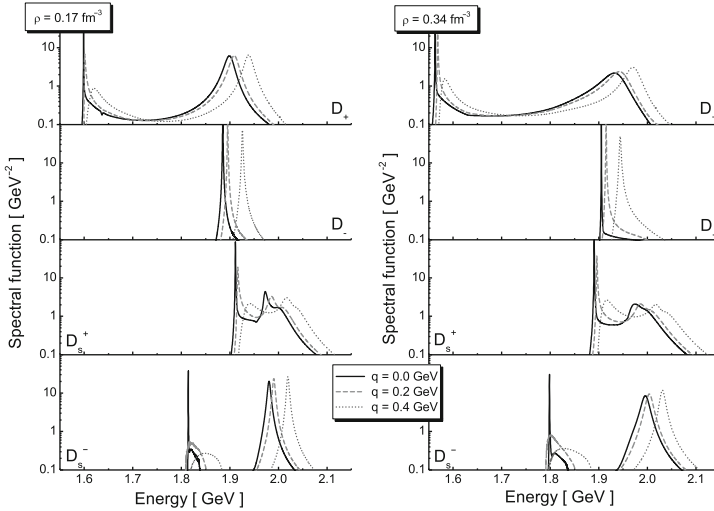


Fig. 5.17 Spectral distributions of D^\pm and D_s^\pm at nuclear saturation density according to [311].

The calculation of D meson spectral distributions in cold nuclear matter of Lutz and Korpa [311] results in an up-shifted (18 MeV) D^- peak, while the D^+ develops strongly down-shifted (250 MeV) strength due to resonance-hole states with $\Lambda_c(1594)$ and $\Sigma_c(2620)$ and an up-shift (30 MeV) of the original D^+ peak. The spectral distributions are exhibited in Fig. 5.17, where also the D_s^\pm is included. The above results of in-medium effects are summarized in Table 5.3.

5.5.2 Hot pion gas

Fuchs et al. [409] considered open and hidden charm hadrons in a hot pion gas. They find sizeable effects at temperatures above 100 MeV: at $T = 150$ MeV the mass shift is about -40 MeV for D mesons and the J/ψ width is increased to 10 MeV. Their results are summarized in Fig. 5.18. Due to reactions $J/\psi \leftrightarrow D\bar{D}, D^*\bar{D}^*, D^+\bar{D}^+$ a shift of the effective in-medium D, D^+ masses can open these channels.

The behavior of D mesons was also addressed in a linear sigma model near the chiral symmetry restoration transition in [410].

5.5.3 Hot and dense nuclear matter

Evaluations of D meson spectral densities under conditions resembling those expected at FAIR have recently been performed in [398]. The D meson spectral density under such conditions can be obtained by extending the microscopic self-consistent coupled-channel calculation in dense nuclear matter of

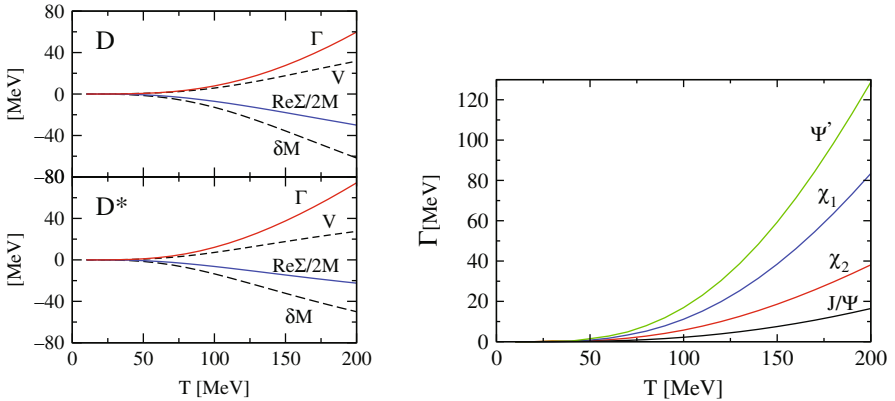


Fig. 5.18 Temperature dependence of D, D^+ and J/ψ states in a hot pion medium. Results are from [409].

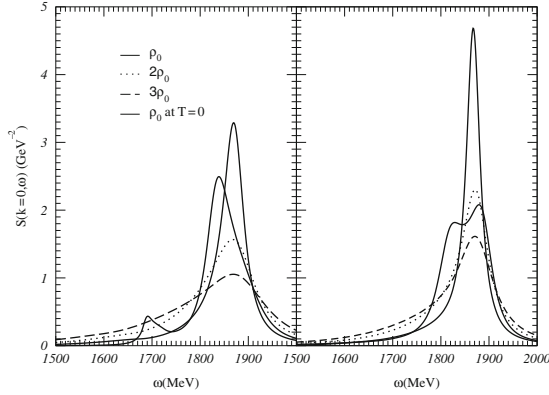


Fig. 5.19 D meson spectral density at $k_D = 0$ and $T = 120$ MeV as a function of energy for different densities together with the D meson spectral density at $k_D = 0$ and $T = 0$ MeV for normal nuclear matter density ρ_0 in the two approaches considered: self-consistent calculation of the D meson self-energy including the dressing of the nucleons in the intermediate states (*left panel*) and including not only the dressing of nucleons but also the self-energy of pions (*right panel*).

Tolees et al. [404] to finite temperature [398]. The introduction of temperature in the in-medium DN interaction affects the intermediate channels (DN , $\pi\Lambda_c$, $\pi\Sigma_c$, $\eta\Lambda_c$ and $\eta\Sigma_c$) by modifying the Pauli blocking of the nucleons, the Bose distribution on the pionic intermediate states and the dressing of D mesons, nucleons and pions, as reported for the $\bar{K}N$ case in [290].

In Fig. 5.19 the D meson spectral density at zero momentum and $T = 120$ MeV is shown for different densities and for a cutoff $\Lambda = 1$ GeV and a coupling constant $g^2 = 13.4$. This is one of the sets of parameters that reproduce the position and width of the $\Lambda_c(2593)$ resonance (see [404]). The temperature is chosen in accord with the expected temperatures for which D mesons will be produced at FAIR. The spectral density is displayed for the two approaches considered [398]: self-consistent calculation of the D meson self-energy including the dressing of the nucleons in the intermediate states (left panel) and the self-consistent calculation including not only the dressing of nucleons but also the self-energy of pions (right panel). The spectral density at $T = 0$ for nuclear matter saturation density, $\rho_0 = 0.17 \text{ fm}^{-3}$, is also included. Compared to the zero temperature case, the quasi-particle peak at finite temperature stays closer to its free position for the range of densities analyzed (from ρ_0 up to $3\rho_0$). This is due to the fact the Pauli blocking is reduced with increasing temperature. Furthermore, structures present in the spectral distribution at $T = 0$ are washed out [290]. However, the D meson spectral density still shows a considerable width.

In order to better study the evolution of the spectral density with temperature, Fig. 5.20 displays the quasi-particle energy together with the width of the D meson spectral density at zero momentum as a function of the tem-

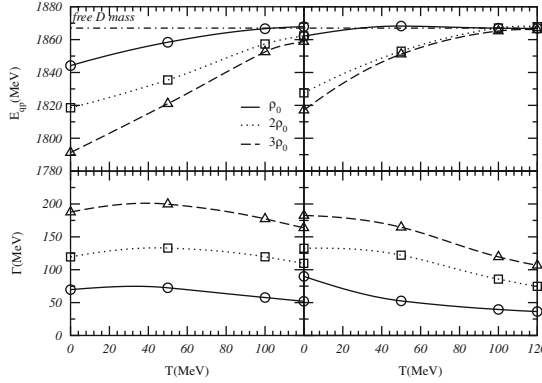


Fig. 5.20 Quasi-particle energy and width of the D meson spectral density at $k_D = 0$ as a function of temperature for different densities and the two approaches considered: self-consistent calculation of the D meson self-energy including the dressing of the nucleons in the intermediate states (*left panels*) and including not only the dressing of nucleons but also the self-energy of pions (*right panels*).

perature for the previous densities and for the approaches considered before. For $T = 0$ we observe a change of the D meson mass with respect to its free value between -23 MeV for ρ_0 and -76 MeV for $3\rho_0$ when D mesons and nucleons are dressed in the intermediate states (upper left panel). For the full self-consistent calculation (upper right panel), the D meson potential lies between -5 MeV for ρ_0 and -48 MeV for $3\rho_0$. For higher temperatures, the quasi-particle peak is close to the free D meson mass (at $T = 120$ MeV and ρ_0 , the D meson potential is -1 MeV for the first approach and -0.1 MeV for the second one). With regards to the width of the D meson spectral density, we observe a slight dependence on the temperature. At $T = 120$ MeV the width increases from 52 to 163 MeV for ρ_0 to $3\rho_0$ when D mesons and nucleons are dressed in the intermediate channels (lower left panel). The increment goes from 36 MeV at ρ_0 to 107 MeV at $3\rho_0$ for the full self-consistent calculation (lower right panel).

Similar finite-temperature results have been obtained recently within a self-consistent coupled-channel approach for the D meson selfenergy taking, as a bare interaction, a type of broken $SU(4)$ S -wave Weimberg-Tomozawa term supplemented by an attractive scalar-isoscalar interaction [411]. Within this model, at finite temperature the D meson spectral density shows a single pronounced peak for energies close to the D meson free-space mass that broadens with increasing density with an extended tail towards lower energies [412], as seen in Fig. 5.21.

As already reported for the case of cold nuclear matter, the small shift of the D meson mass in the nuclear medium is contrary to the large changes (-50 to -200 MeV) reported in previous mean-field calculations [397, 400, 405–407]. Based on these results, an enhancement of open charm in

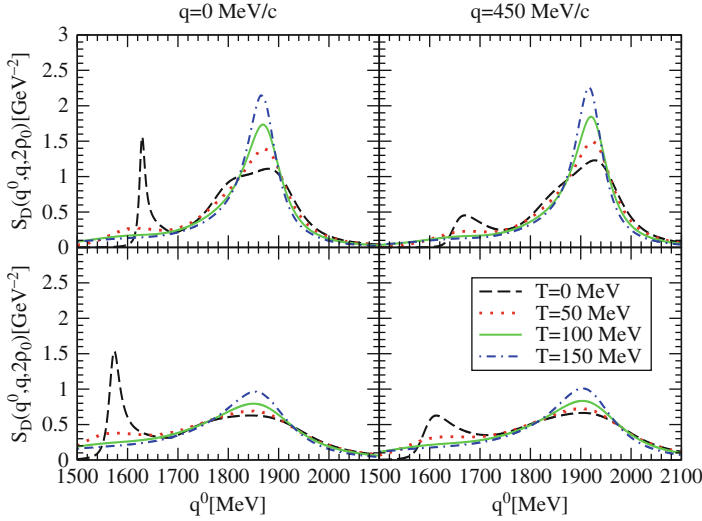


Fig. 5.21 The D meson spectral function for $q = 0$ MeV/c and $q = 450$ MeV/c at ρ_0 and $2\rho_0$ as a function of the D meson energy for different temperatures from a self-consistent coupled-channel calculation, which takes, as a bare interaction, a type of broken $SU(4)$ S -wave Weimberg-Tomozawa term supplemented by an attractive scalar-isoscalar interaction.

nucleus-nucleus collisions was suggested to understand the enhancement of “intermediate-mass dileptons” in Pb+Pb collisions at the SPS energies [413] (however, more recent NA60 data [379] have shown that this enhancement is due to “prompt” dileptons, presumably thermal radiation [374]). According to the previous self-consistent models, the inclusion of a considerable width of the D meson in the medium is the only source which could lead to an enhanced in-medium D meson production, as studied for kaons in [414].

As a consequence, an off-shell transport theory is needed to describe D meson production. For that purpose, not only the D meson spectral density but also in-medium D meson cross sections are required. Fig. 5.22 shows the elastic in-medium transition rates for D^+n (D^0p) at $T = 120$ MeV for the two approaches considered. For the self-consistent calculation including the dressing of D mesons and nucleons in the intermediate states (left panel), we observe an enhanced transition rate for energies around the $\Lambda_c(2593)$ resonance mass. However, when pions are also dressed in the self-consistent process (right panel), the enhanced transition rate is reduced drastically according to the different in-medium behavior of the $\Lambda_c(2593)$ resonance (see previous discussion in Sect. 5.5.1). The cross sections at threshold are expected on the order of 1–20 mb for the range of densities studied in both approaches.

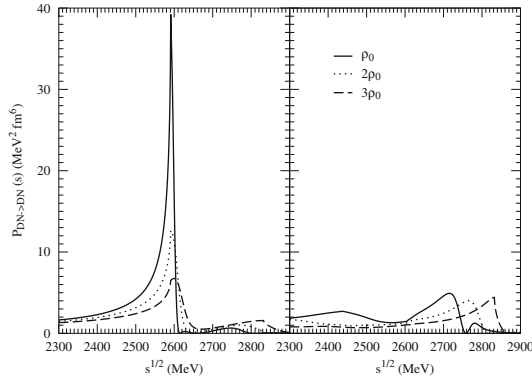


Fig. 5.22 In-medium transition rates for D^+n (D^0p) at $T = 120$ MeV as a function of the center-of-mass energy for different densities and the two approaches considered: self-consistent calculation of the D meson self-energy including the dressing of the nucleons in the intermediate states (*left panel*) and including not only the dressing of nucleons but also the self-energy of pions (*right panel*).

The in-medium effects discussed here may be relevant for heavy-ion experiments at the future International FAIR project at GSI. The CBM experiment will address, among others, the investigation of open charm. Our results imply that the effective mass of D mesons, however, may not be drastically modified in dense matter at finite temperature, but D mesons develop an appreciable width in the hot and dense environment. Therefore, the abundance of D mesons in nucleus-nucleus collisions should be calculated in off-shell transport theory. Our calculation indicates that the medium modifications to the D mesons in nucleus-nucleus collisions will be dominantly on the width and not on the mass.

5.5.4 Charm baryons

In-medium properties of open-charm baryon resonances have also been studied in [311], extending the approach of Lutz et al. [263] based on non-linear chiral SU(3) dynamics into the charm sector. Similar to strangeness exchange reactions, which couple K^- and Λ production in intermediate-energy heavy-ion reactions, one accounts for charm exchange reactions coupling open-charm mesons and baryons [311]. The baryonic counter parts to the open charm meson dynamics are displayed in Fig. 5.23.

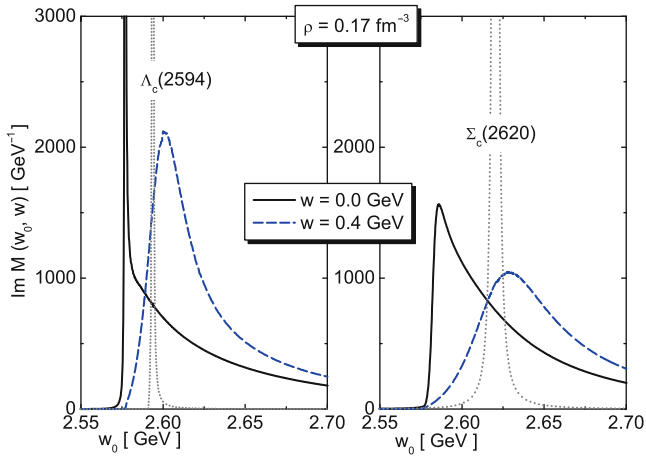


Fig. 5.23 Imaginary part of scattering amplitudes for D^+N scattering in the isospin-0 ($\Lambda_c(2594)$, left panel) and isospin-1 ($\Sigma_c(2620)$, right panel) channels for vacuum (dotted curves) and normal nuclear matter density (solid and dashed curves for momenta of 0 and 400 MeV/c). Figure taken from [311].

Chapter 6

Charmonium

As discussed in the preceding chapter, the charm-quark mass introduces an additional *large* scale into the problem of studying hot and dense QCD matter in the vicinity of phase changes, $m_c \gg T_c, \Lambda_{\text{QCD}}$. While *open*-charm probes are an ideal tool to assess the transport properties of the medium at the interface of the kinetic and thermal regimes, the investigations of *hidden*-charm bound states (charmonia) allows, in principle, a unique access to the QCD potential between two heavy (quasistatic) color charges. Charmonium (and bottomonium) spectroscopy in the vacuum has been widely and successfully used to infer the properties of the strong force in the vacuum, see, e.g., [415] for a comprehensive survey. The challenge in the present context is to transfer these (and develop new) concepts to the study of charmonia in medium and connect these to the properties of the medium. The “holy grail” of this enterprise is the discovery of the deconfinement transition. Indeed, in a seminal paper [416], Matsui and Satz suggested that the suppression of J/ψ ’s in heavy-ion collisions could be used as a direct indicator of deconfinement, and NA50 data from Pb–Pb collisions at the SPS apparently confirm this effect. However, recent developments have revealed that the problem of charmonium production in heavy-ion collisions is substantially more complex: lattice QCD computations indicate that ground-state charmonia (and bottomonia) may survive as bound states well into the Quark-Gluon Plasma, and observations at RHIC found the same level of J/ψ suppression as at the SPS, despite the unequivocally larger energy densities (temperatures) reached at $\sqrt{s_{NN}} = 200$ A GeV as compared to 17.3 GeV. This, e.g., immediately prompts the question of how the (absence of a) trend will continue at higher (LHC) and lower (FAIR) energies. Does, e.g., secondary charmonium production via $c\bar{c}$ (or $D\bar{D}$) coalescence solve the puzzles?

The following sections will be devoted to short up-to-date reviews of equilibrium properties of charmonia as inferred from lattice QCD and potential models (Sect. 6.1), as well as of applications to heavy-ion collisions within the statistical hadronization model (Sect. 6.3) and charmonium transport approaches (Sect. 6.3).

6.1 Charmonium in equilibrium

6.1.1 Color screening and quarkonium

The Matsui and Satz suggestion referred to above [416] is based on the notion that, at high temperatures, color screening will lead to melting of heavy-quark bound states. While early lattice calculations confirmed the presence of strong color screening at high temperature [417] it was not until recently that lattice studies of color screening have been related to quarkonium properties at finite temperature. The reason for this is the fact that on the lattice color screening is studied in terms of the free energy of a static quark-antiquark pair, and its relation to the potential used in the Schrödinger equation is not clear. In the next section we will discuss the properties of the heavy quark-antiquark free energy calculated in lattice QCD.

6.1.2 Free energy of static quarks in lattice QCD

Following McLerran and Svetitsky [417] the partition function of a system with a static quark-antiquark ($Q\bar{Q}$) pair at finite temperature T can be written as

$$Z_{Q\bar{Q}}(r, T) = \langle W(\mathbf{r}) W^\dagger(0) \rangle Z(T) , \quad (6.1)$$

with $Z(T)$ being the partition function of the system without static charges and

$$W(\mathbf{x}) = \mathcal{P} \exp \left(ig \int_0^{1/T} d\tau A_0(\tau, \mathbf{x}) \right) \quad (6.2)$$

the temporal Wilson line. $L(\mathbf{x}) = \text{Tr} W(\mathbf{x})$ is also known as Polyakov loop, and in the case of pure gauge theory it is an order parameter of the deconfinement transition. As the $Q\bar{Q}$ pair can be either in color singlet or octet state one should separate these irreducible contributions to the partition function. This can be done using the projection operators P_1 and P_8 onto color singlet and octet states introduced in [418, 419]. Applying P_1 and P_8 to $Z_{Q\bar{Q}}(r, T)$ we obtain the following expressions for the singlet and octet free energies of the static $Q\bar{Q}$ pair

$$\exp(-F_1(r, T)/T) = \frac{1}{Z(T)} \frac{\text{Tr} P_1 Z_{Q\bar{Q}}(r, T)}{\text{Tr} P_1} = \frac{1}{3} \text{Tr} \langle W(\mathbf{r}) W^\dagger(0) \rangle \quad (6.3)$$

$$\begin{aligned} \exp(-F_8(r, T)/T) &= \frac{1}{Z(T)} \frac{\text{Tr} P_8 Z_{Q\bar{Q}}(r, T)}{\text{Tr} P_8} \\ &= \frac{1}{8} \langle \text{Tr} W(\mathbf{r}) \text{Tr} W^\dagger(0) \rangle - \frac{1}{24} \text{Tr} \langle W(\mathbf{r}) W^\dagger(0) \rangle. \end{aligned} \quad (6.4)$$

Although usually $F_{1,8}$ is referred to as the free energy of the static $Q\bar{Q}$ pair, it is important to keep in mind that it refers to the difference between the free

energy of the system with static quark-antiquark pair and the free energy of the system without static charges.

As $W(\mathbf{x})$ is a not gauge invariant operator we have to fix a gauge in order to define F_1 and F_8 . To ensure F_1 and F_8 to have a meaningful zero temperature limit we better fix the Coulomb gauge because in this gauge a transfer matrix can be defined and the free energy difference can be related to the interaction energy of a static $Q\bar{Q}$ pair at zero temperature ($T = 0$). Another possibility discussed in [420] is to replace the Wilson line by a gauge invariant Wilson line using the eigenvector of the spatial covariant Laplacian. For the singlet free energy both methods were tested and they were shown to give numerically indistinguishable results, which in the zero temperature limit are the same as the canonical results obtained from Wilson loops. One can also define the color-averaged free energy,

$$e^{-F_{av}(r,T)/T} = \frac{1}{Z(T)} \frac{\text{Tr}(P_1 + P_8) Z_{Q\bar{Q}}(r, T)}{\text{Tr}(P_1 + P_8)} = \frac{1}{9} \langle \text{Tr} W(\mathbf{r}) \text{Tr} W^\dagger(0) \rangle, \quad (6.5)$$

which is expressed entirely in terms of gauge invariant Polyakov loops. This is the reason why it was extensively studied on the lattice during the last two decades. The color-averaged free energy is a thermal average over the free energies in color-singlet and color-octet states

$$e^{-F_{av}(r,T)/T} = \frac{1}{9} e^{-F_1(r,T)/T} + \frac{8}{9} e^{-F_8(r,T)/T}. \quad (6.6)$$

Therefore it gives less direct information about medium modifications of inter-quark forces. Given the partition function $Z_{Q\bar{Q}}(r, T)$, we can calculate not only the free energy but also the entropy as well as the internal energy of the static charges

$$S_i(r, T) = \frac{\partial}{\partial T} \ln \left(T \frac{Z_{Q\bar{Q}}^i(r, T)}{Z(T)} \right) = - \frac{\partial F_i(r, T)}{\partial T} \quad (6.7)$$

$$U_i(r, T) = T^2 \frac{\partial}{\partial T} \ln \left(\frac{Z_{Q\bar{Q}}^i(r, T)}{Z(T)} \right) = F_i(r, T) + T S_i(r, T) \quad (6.8)$$

with $i = 1, 8, av$. For the discussion of the in-medium properties of quarkonium the color-singlet free energy as well as the internal energy are the most appropriate quantities. The color-singlet free energy, $F_1(r, T)$, has been calculated in quenched ($N_f = 0$) [421–423], 2-flavor ($N_f = 2$) [424] and 3-flavor [425], as well as most recently in 2+1-flavor QCD with realistic quark masses [426–428]. Evaluating the temperature derivative of $F_1(r, T)$ numerically one can estimate the corresponding internal energy. Lattice calculations of the singlet free energy in quenched QCD are shown in Fig. 6.1. At short distances the free energy is temperature independent and coincides with the zero temperature potential (shown by the black line). The temperature dependence of the singlet free energy becomes significant at distances larger than

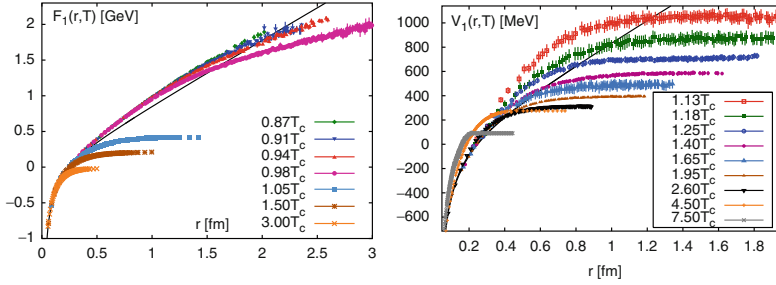


Fig. 6.1 The color-singlet free energy in quenched QCD (*left*) and the corresponding internal energy (*right*) [421–423]. The *black line* shows the parametrization of the zero temperature potential calculated on the lattice.

$0.4 \text{ fm}/(T/T_c)$ [423]. Furthermore, at distances larger than $(1 - 1.2)/T$, the singlet free energy is exponentially screened [423]. This exponential screening is governed by the Debye mass m_D . However, for quarkonium physics the behavior of the free energy at short distances $r < T$ is more relevant. Note that the free energy above T_c is monotonically decreasing, and, at sufficiently high temperatures, is negative at all separations. The internal energy is larger than the free energy and is even larger than the zero temperature potential at intermediate distances. At small distances it agrees, of course, with the zero temperature potential as expected. If used as a potential in the Schrödinger equation it will give significantly larger binding energy than the free energy.

The free energy of static quark-antiquark pair calculated in full QCD shares most of the properties of the free energy calculated in quenched QCD discussed above. In Fig. 6.2 we show the result of calculations in 2+1-flavor QCD with physical strange quark mass and light quark masses corresponding to a pion mass of about 200 MeV. The most significant difference to quenched calculations is the presence of string breaking: the free energy approaches a constant at large distances instead of linearly rising. The internal energy calculated in full QCD is also very large in the vicinity of the transition. In Fig. 6.2 we also show the asymptotic value of the internal energy, $U_\infty(T) = U_1(r \rightarrow \infty, T)$, in full QCD at high temperatures. If $U_\infty(T)/2$ is interpreted as a thermal correction to the heavy quark mass increase implies that close to T_c the effective charm quark mass is larger by a factor of two!

The free energy of a static quark-antiquark pair has been also studied at finite baryon density using the Taylor expansion method [429]. At finite baryon density screening effects become stronger, as expected [429]. At high temperatures the dependence of the screening mass on the baryon chemical potential can be described by perturbation theory [429].

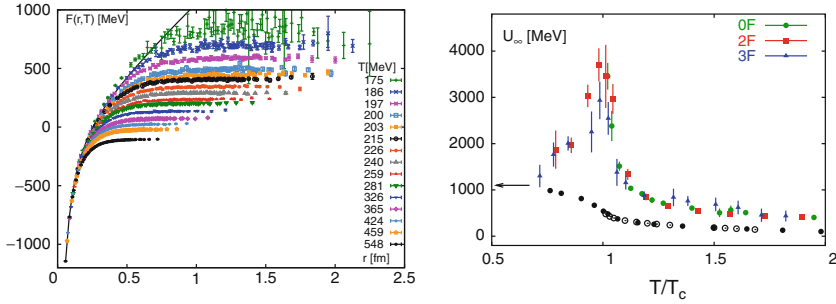


Fig. 6.2 The free energy of a static quark-antiquark pair calculated in 2+1 flavor QCD on a $24^3 \times 6$ lattice [427, 428] (left), and the internal energy $U_{\infty}(T)$ in quenched [422], 2-flavor [424] and 3-flavor [425] QCD as a function of the temperature (right).

6.1.3 Spectral functions and Euclidean correlators

Spectral functions offer the most suitable way to study in-medium properties and/or the dissolution of charmonium states at high temperature and density. The spectral functions are related to the Euclidean-time correlation functions, $G(\tau, T)$, by the integral relation

$$G(\tau, T) = \int_0^{\infty} d\omega \sigma(\omega, T) \frac{\cosh(\omega(\tau - 1/2T))}{\sinh(\omega/2T)}. \quad (6.9)$$

Euclidean time correlation functions can be calculated in lattice QCD. There have been several attempts to extract the charmonium spectral functions from lattice correlators using the Maximum Entropy Method (MEM) [361, 430–432]. For the light quark sector this has been already discussed in Sect. 2.5. The studies of charmonium spectral functions have indicated that quarkonium states can survive up to temperatures as high as $1.6 T_c$, contradicting earlier expectations based on potential models with screening (see, e.g., [433–436]). At low temperatures, spectral functions can be reliably calculated using MEM. However, at high temperatures the reconstruction of the spectral functions becomes more difficult as the extent of the Euclidean time direction, $\tau_{\max} = 1/(2T)$, becomes smaller (see, e.g., the discussion in [432]). Therefore, it has been suggested to study in detail the temperature dependence of the correlation function $G(\tau, T)$. This can be done most effectively by studying the temperature dependence of the ratio $G(\tau, T)/G_{rec}(\tau, T)$ [430], where

$$G_{rec}(\tau, T) = \int_0^{\infty} d\omega \sigma(\omega, T=0) \frac{\cosh(\omega(\tau - 1/2T))}{\sinh(\omega/2T)}. \quad (6.10)$$

The trivial temperature dependence due to the integration kernel is eliminated in this ratio. If the spectral function does not change above the deconfinement transition, one has $G(\tau, T)/G_{rec}(\tau, T) = 1$. Deviations of this ratio

from unity thus indicate changes in the spectral functions. It has been found that in the pseudo-scalar channel this ratio shows little temperature dependence, remaining close to unity well into the QGP [430, 432]. In the scalar and axial-vector channels, on the other hand, this ratio is temperature dependent and changes by a factor of two across the deconfinement transition [430, 432]. This seems to suggest that the $1S$ charmonium state survives in the deconfined medium up to quite high temperatures, while P -wave charmonium (χ_c) melts close to the transition temperature, in agreement with expectations based on a sequential suppression pattern [436]. It has been realized, however, that zero-mode contributions could be the dominant source of the temperature dependence of the Euclidean correlators [437, 438]. This contribution arises because in the deconfined phase charmonium spectral functions contain information not only about quark-antiquark pairs (bound or un-bound) but also about scattering states of single heavy quarks in the plasma, i.e., heavy-quark transport (see e.g., [439]; this topic is discussed in some detail in Sect. 5.2). When the zero-mode contribution is subtracted the temperature dependence of charmonium correlators turns out to be very small even in the case of the P -waves [437, 438]. In the next subsection we will discuss how this can be understood in terms of potential models.

6.1.4 Charmonium spectral functions and potential models

Traditionally, charmonium properties at finite temperature have been studied using potential model with some phenomenological version of a screened potential [433–436, 440–442]. In more recent studies the free or internal energy of the static quark-antiquark pair calculated on the lattice, or the combination of the two, has been used as a potential in a Schrödinger equation (see, e.g., [440–442]). At zero temperature, the potential is well defined in terms of an effective theory, potential Non-Relativistic QCD (pNRQCD) [415, 443]. In the absence of the corresponding effective field theory approach at finite temperature (see, however, [444] for recent progress in this direction), the definition of the potential is somewhat ambiguous. The free energy and the internal energy provide lower and upper bounds on the potential. Typically, the dissociation temperatures have been defined as the point of zero binding. Clearly, such a definition overestimates the dissociation temperatures, and their precise value depends on the choice of the potential. However, for any choice of the potential consistent with lattice data the binding energy of charmonium states will decrease with the temperature (see, e.g., [440]).

A more consistent approach to the problem of quarkonium melting relies on the calculation of *spectral functions* in potential models. For sufficiently heavy quarks the spectral function can be related to the non-relativistic Green functions [445–447] or to the T -matrix [368]. One can study the spectral functions

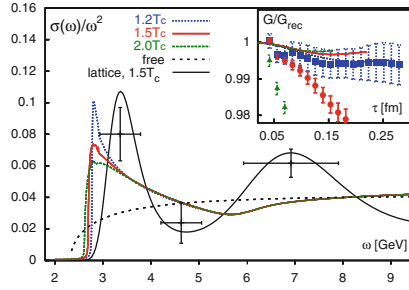


Fig. 6.3 The S -wave charmonium spectral functions at different temperatures as calculated in the potential model of [445, 446]. The inset shows the comparison of the corresponding Euclidean correlators to the results of lattice calculations.

at different temperatures and the absence of a resonance peak in the spectral function will determine more precisely the dissolution temperatures of different charmonium states. From the spectral functions the Euclidean time correlation functions can be straightforwardly calculated using Eq. (6.9), which, in turn, can be compared to the correlation functions calculated directly in lattice QCD. Such comparisons provide valuable checks for potential models. In Fig. 6.3 the spectral function calculated in a potential model is shown for S -wave charmonia together with the corresponding Euclidean time correlation functions [445]. The $1S$ charmonium state melts at temperatures around $1.2T_c$, but this does not lead to large changes in the correlation functions which agree well with the results of the lattice calculations. The situation is similar in the case of the P -wave charmonia (see discussion in [445]). The analyses of the spectral functions and the corresponding Euclidean time correlators have been performed for other choices of potential and temperature dependent quark masses and lead to similar findings [368, 448], albeit with quantitatively varying conclusions. Of course, the precise shape of the spectral functions as well as the values of the dissociation temperatures depend on the assumed potential and are somewhat different in different studies.

6.2 Charm(onium) production within the statistical hadronization model

6.2.1 Introduction

In a recent series of publications [391, 449, 450] it has been demonstrated that data on J/ψ and ψ' production in nucleus-nucleus collisions, in the energy range from top SPS energy ($\sqrt{s_{NN}} \approx 17$ GeV) on, can be interpreted within the statistical hadronization model proposed in [451, 452].

This includes the centrality and rapidity dependence of recent data at RHIC ($\sqrt{s_{NN}}=200$ GeV) [453], as shown in Fig. 6.4 [450]. The extrapolation of these results to LHC energy ($\sqrt{s_{NN}}=5.5$ TeV) yields a rather striking centrality dependence [449, 450], also shown in Fig. 6.4. Depending on the magnitude of the $\bar{c}c$ cross section in central Pb–Pb collisions [454], even an enhancement of J/ψ production compared to pp collisions ($R_{AA}^{J/\psi} > 1$) is expected due to hadronization (at chemical freeze-out) of uncorrelated (at these high energies) charm quarks thermalized in QGP.

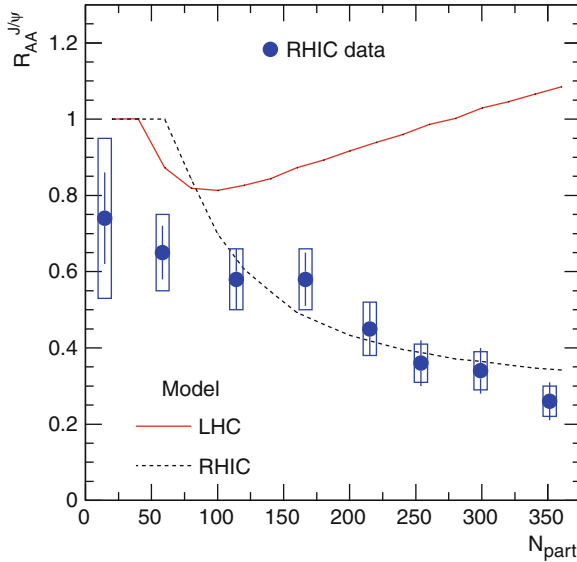


Fig. 6.4 Centrality dependence of the relative J/ψ yield $R_{AA}^{J/\psi}$ at midrapidity [450].

In this section results of the statistical model for charm are presented for the energy range from near threshold ($\sqrt{s_{NN}} \approx 6$ GeV) to RHIC [381]. The lower end of this range is relevant for the CBM experiment [455] at the future FAIR facility. One of the motivations for such studies was the expectation [398, 455] to provide, by a measurement of D meson production near threshold, information on their possible in-medium modification near the phase boundary. However, the cross section $\sigma_{c\bar{c}}$ is governed by the mass of the charm quark $m_c \approx 1.3$ GeV, which is much larger than any soft Quantum Chromodynamics (QCD) scale such as Λ_{QCD} . Therefore we expect no medium effects on this quantity.¹ The much later formed D mesons, or other charmed hadrons, may well change their mass in the hot medium. The results of various studies on in-medium modification of charmed hadrons masses

¹ Such a separation of scales is not possible for strangeness production, and the situation there is not easily comparable.

[311, 397, 398, 405, 406, 413, 456–458] are sometimes contradictory. Whatever the medium effects may be, they can, because of the charm conservation, $\sigma_{c\bar{c}} = \frac{1}{2}(\sigma_D + \sigma_{A_c} + \sigma_{\Xi_c} + \dots) + (\sigma_{\eta_c} + \sigma_{J/\psi} + \sigma_{\chi_c} + \dots)$, only lead to a redistribution of charm quarks [381]. This argument is essentially model-independent and applies equally well at all energies. Here we will consider various types of scenarios for medium modifications and study their effect within the statistical hadronization framework in the energy range from charm threshold to collider energies. In this context, we note that excellent fits of the common (non-charmed) hadrons to predictions of the thermal model have been obtained using vacuum masses (see [459] and references therein). An attempt to use modified masses for the RHIC energy [460] has not produced a conclusive preference for any mass or width modifications of hadrons in medium. On the other hand, some evidence for possible mass modifications was presented in the chiral model of [461].

6.2.2 Assumptions and ingredients of the statistical hadronization model

The statistical hadronization model (SHM) [449, 451, 452] assumes that the charm quarks are produced in primary hard collisions and that their total number stays constant until hadronization. Another important factor is thermal equilibration in the QGP, at least near the critical temperature, T_c . We neglect charmonium production in the nuclear corona [449], since we focus in the following on central collisions ($N_{part}=350$), where such effects are small.

In the following we briefly outline the calculation steps in our model [449, 451, 452]. The model has the following input parameters: (i) charm production cross section in pp collisions; (ii) characteristics at chemical freeze-out: temperature, T , baryochemical potential, μ_b , and volume corresponding to one unit of rapidity $V_{\Delta y=1}$ (our calculations are for midrapidity). Since, in the end, our main results will be ratios of hadrons with charm quarks normalized to the $c\bar{c}$ yield, the detailed magnitude of the open charm cross section and whether to use integrated yield or midrapidity yields is not crucial.

The charm balance equation [451, 452], which has to include canonical suppression factors [465] whenever the number of charm pairs is not much larger than 1, is used to determine a fugacity factor g_c via:

$$N_{c\bar{c}}^{dir} = \frac{1}{2} g_c N_{oc}^{th} \frac{I_1(g_c N_{oc}^{th})}{I_0(g_c N_{oc}^{th})} + g_c^2 N_{c\bar{c}}^{th}. \quad (6.11)$$

Here $N_{c\bar{c}}^{dir}$ is the number of initially produced $c\bar{c}$ pairs and I_n are modified Bessel functions. In the fireball of volume V the total number of open ($N_{oc}^{th} = n_{oc}^{th} V$) and hidden ($N_{c\bar{c}}^{th} = n_{c\bar{c}}^{th} V$) charm hadrons is computed from their grand-canonical densities n_{oc}^{th} and $n_{c\bar{c}}^{th}$, respectively. This charm balance

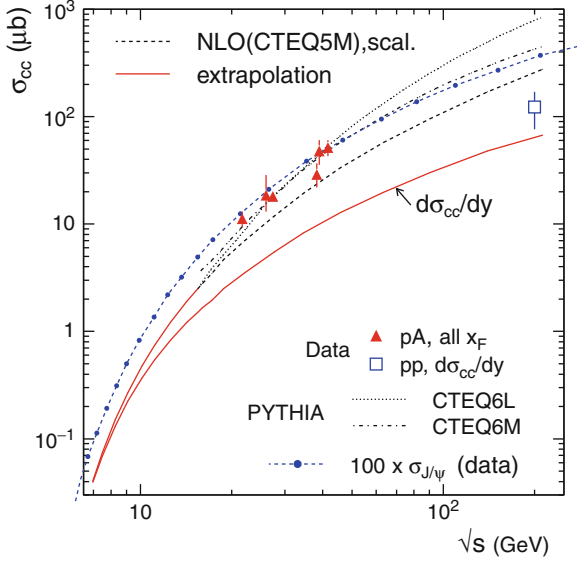


Fig. 6.5 Energy dependence of the charm production cross section in pp collisions. The NLO pQCD values [336] are compared to calculations using PYTHIA and to data in pA collisions, taken from [462]. Our extrapolations for low energies are shown with continuous lines, for total and midrapidity ($d\sigma_{cc}/dy$) cross section. The open square is a midrapidity measurement in pp collisions [463]. The dashed line with dots indicates a parameterization of the measured energy dependence of the J/ψ production cross section [464].

equation is the implementation within our model of the charm conservation constraint. The densities of different particle species in the grand canonical ensemble are calculated following the statistical model [459]. The balance equation (6.11) defines the fugacity parameter g_c that accounts for deviations of heavy quark multiplicity from the value that is expected in complete chemical equilibrium. The yield of charmonia of type j is obtained as: $N_j = g_c^2 N_j^{th}$, while the yield of open charm hadrons is: $N_i = g_c N_i^{th} I_1(g_c N_{oc}^{th}) / I_0(g_c N_{oc}^{th})$.

As no information on the charm production cross section is available for energies below $\sqrt{s}=15$ GeV, we have to rely on extrapolation. The basis for this extrapolation is the energy dependence of the total charm production cross section calculated in [336] for the CTEQ5M parton distribution functions in next-to-leading order (NLO), as shown in Fig. 6.5. We have scaled these calculations to match the more recent values calculated at $\sqrt{s}=200$ GeV in [354]. We employ a threshold-based extrapolation using the following expression:

$$\sigma_{cc} = k(1 - \sqrt{s_{thr}}/\sqrt{s})^a (\sqrt{s_{thr}}/\sqrt{s})^b \quad (6.12)$$

with $k=1.85 \mu\text{b}$, $\sqrt{s_{thr}}=4.5$ GeV (calculated assuming a charm quark mass $m_c=1.3$ GeV [30]), $a=4.3$, and $b=-1.44$. The parameters a , b , k were tuned to reproduce the low-energy part of the (scaled) NLO curve. The extrapolated

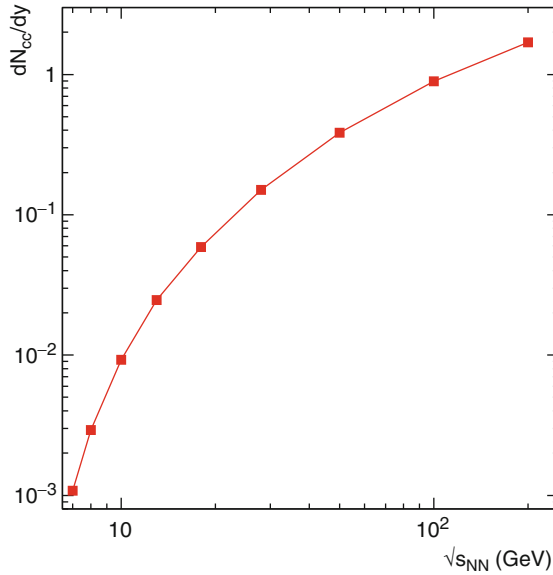


Fig. 6.6 Energy dependence of the number of initially produced charm quark pairs ($N_{part} = 350$).

curves for charm production cross section are shown with continuous lines in Fig. 6.5. Also shown for comparison are calculations with PYTHIA [462]. To obtain the values at midrapidity we have extrapolated to lower energies the rapidity widths (FWHM) of the charm cross section known to be about 4 units at RHIC [354] and about 2 units at SPS [466].

With these cross section values, the rapidity density of initially produced charm quark pairs, shown in Fig. 6.6 strongly rises from $1.1 \cdot 10^{-3}$ to 1.7 for the energy range $\sqrt{s_{NN}} = 7$ –200 GeV. We note that the so-obtained charm production cross section has an energy dependence similar to that measured for J/ψ production, recently compiled and parametrized by the HERA-B collaboration [464]. For comparison, this is also shown in Fig. 6.5. The extrapolation procedure for the low-energy part of the cross section obviously implies significant uncertainties. We emphasize, however, that the most robust predictions of our model, i.e. the yields of charmed hadrons and charmonia relative to the initially produced $c\bar{c}$ pair yield are not influenced by the details of this extrapolation.

For the studied energy range, $\sqrt{s_{NN}} = 7$ –200 GeV, T rises from 151 to 161 MeV from $\sqrt{s_{NN}} = 7$ to 12 GeV and stays constant for higher energies, while μ_b decreases from 434 to 22 MeV [459]. The volume $V_{\Delta y=1}$ at midrapidity, shown in Fig. 6.7 [459] continuously rises from 760 to 2,400 fm³. Due to the strong energy dependence of charm production, Fig. 6.6, the canonical suppression factor (I_1/I_0) varies from 1/30 to 1/1.2. Correspondingly, the charm fugacity g_c increases from 0.96 to 8.9, see Fig. 6.8.

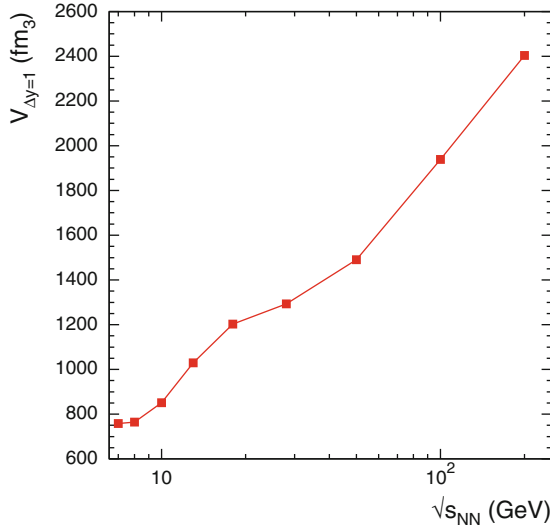


Fig. 6.7 Energy dependence of the volume at midrapidity, $V_{\Delta y=1}$, for central collisions [459].

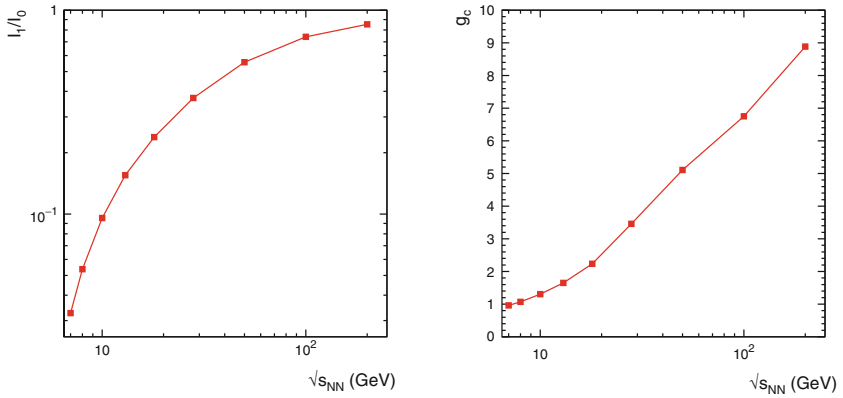


Fig. 6.8 Energy dependence of the canonical suppression for charm, I_1/I_0 (left panel) and of the charm quark fugacity, g_c (right panel).

Before proceeding to discuss our results, we would like to emphasize some peculiar aspects of charm at low energies. First, the assumption of charm equilibration can be questionable. In this exploratory study we have nevertheless assumed full thermalization. At SPS and lower energies collision time, plasma formation time, and charmonium (or open charm hadrons) formation time are all of the same order [467, 468]. Furthermore, the maximum plasma temperature may not exceed the J/ψ dissociation temperature, T_D , although recent results [445] indicate that T_D can be very close to T_c . Char-

monia may be broken up by gluons and by high energy nucleons still passing by from the collision. In this latter case cold nuclear suppression needs to be carefully considered (as discussed, e.g., in [469, 470]). Consequently, our calculations, in which both charmonium formation before QGP production and cold nuclear suppression are neglected, may somewhat underestimate the charmonium production yield at SPS energies [449] and below.

We note that models that combine the “melting scenario” with statistical hadronization have been proposed [380, 471]. Alternatively, a kinetic description of charmonium formation by coalescence in the plasma [472–475] as well as within transport models [476, 477] has been considered.

6.2.3 Energy dependence of charmed hadrons yield

Our main results are presented in Fig. 6.9. The left panel shows our predictions for the energy dependence of midrapidity yields for various charmed hadrons. Beyond the generally decreasing trend towards low energies for all yields one notices first a striking behavior of the production of Λ_c^+ baryons: their yield exhibits a weaker energy dependence than observed for other charmed hadrons. In our approach this is caused by the increase in baryochemical potential towards lower energies (coupled with the charm neutrality condition). A similar behavior is seen for the Ξ_c^+ baryon. These results emphasize the importance of measuring, in addition to D meson production, also the yield of charmed baryons to get a good measure of the total charm production cross section. In detail, the production yields of D mesons depend also on their quark content.

The differing energy dependences of the yields of charmed hadrons are even more evident in the right panel of Fig. 6.9, where we show the predicted yields normalized to the number of initially produced $c\bar{c}$ pairs. Except very near threshold, the J/ψ production yield per $c\bar{c}$ pair exhibits a slow increase with increasing energy. This increase is a consequence of the quadratic term in the J/ψ yield equation discussed above. At LHC energy, the yield ratio $J/\psi/c\bar{c}$ approaches 1% [449], scaling linearly with $\sigma_{c\bar{c}}$ (for details see [381]). The ψ' yield shows a similar energy dependence as the J/ψ , except for our lowest energies, where the difference is due to the decrease of temperature (see above). We emphasize again that this model prediction, namely yields relative to $c\bar{c}$ pairs, is a robust result, as it is in the first order independent on the charm production cross section. Due to the expected similar temperature, the relative abundance of open charm hadrons at LHC is predicted [454] to be similar to that at RHIC energies.

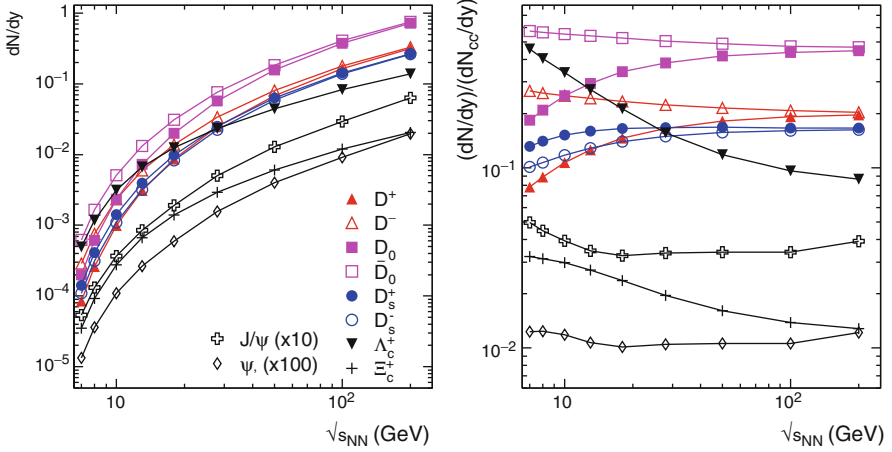


Fig. 6.9 Energy dependence of charmed hadron production at midrapidity. *Left panel:* absolute yields, *right panel:* yields relative to the number of $c\bar{c}$ pairs. Note, in both panels, the scale factors of 10 and 100 for J/ψ and ψ mesons, respectively [381].

6.2.4 Effects of in-medium modification of charmed hadrons masses

We consider two scenarios² for a possible mass change Δm of open charm hadrons containing light, u or d , quarks: (i) a common decrease of 50 MeV for all charmed mesons and their antiparticles and a decrease of 100 MeV for the Λ_c and Σ_c baryons (50 MeV decrease for Ξ_c); (ii) a decrease of 100 MeV for all charmed mesons and a 50 MeV increase for their antiparticles, with the same (scaled with the number of light quarks) scenario as in (i) for the baryons. Scenario (i) is more suited for an isospin-symmetric fireball produced in high-energy collisions and was used in [413], while scenario (ii) may be realized at low energies. In both scenarios, the masses of the D_s mesons and of the charmonia are the vacuum masses. We also note that if one leaves all D meson masses unchanged but allows their widths to increase, the resulting yields will increase by 11% (2.7%) for a width of 100 MeV (50 MeV). If the in-medium widths exhibit tails towards low masses, as has been suggested by [398], to first order the effect on thermal densities is quantitatively comparable with that from a decrease in the pole mass.

The results for the two cases are presented in Fig. 6.10 as yields relative to the number of initially-produced $c\bar{c}$ pairs. As a result of the redistribution of the charm quarks over the various species, the relative yields of charmed

² The scenarios are constructed by modification of the constituent quark masses of light (u and d) quarks in the charmed hadrons by fixed amounts. Reducing, for example, the light quark masses by 50 MeV will lower D meson masses by 50 MeV and the $\Lambda_c(\Xi_c)$ mass by 100 (50) MeV.

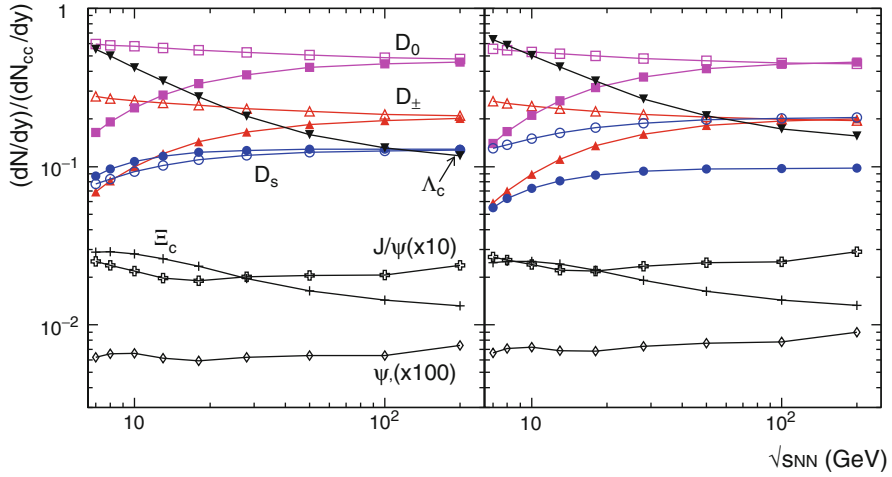


Fig. 6.10 Energy dependence of the yield of charmed hadrons relative to the charm quark pair yield for two scenarios of the mass change (*left panel* for scenario i), *right panel* for scenario (ii), see text. For the D mesons, the full and open symbols are for particles and antiparticles, respectively. Note the factors 10 and 100 for the J/ψ and ψ' mesons, respectively [381].

hadrons may change. For example, in scenario (i) the ratios of D mesons are all close to those computed for vacuum masses (Fig. 6.9), while for scenario (ii) the changes in the relative abundances of the D and \bar{D} mesons are obvious. In both cases the Λ_c/D ratio is increased.

As a result of the asymmetry in the mass shifts for particles and antiparticles assumed in scenario (ii), coupled with the charm neutrality condition, the production yields of D_s^+ and D_s^- mesons are very different compared to vacuum masses. Overall, however, charm conservation leads to rather small changes in the total yields. We emphasize that, although the charm conservation equation is strictly correct only for the total cross section we expect within the framework of the statistical hadronization model, also little influence due to medium effects on distributions in rapidity and transverse momentum. This is due to the fact that the crucial input into our model is $dN_{c\bar{c}}^{AuAu}/dy$ and there is no substantial D meson rescattering after formation at the phase boundary.

In Fig. 6.11 we demonstrate that the total open charm yield (sum over all charmed hadrons) exhibits essentially no change if one considers mass shifts, while the effect is large on charmonia. This is to be expected from Eq. (6.11): as the masses of open charm mesons and baryons are reduced, the charm fugacity g_c is changed accordingly to conserve charm. Consequently, since the open charm yields vary linearly with g_c , one expects little change with medium effects in this case. In contrast, the yields of charmonia vary strongly, since they are proportional to g_c^2 . To demonstrate this we plot, in Fig. 6.11,

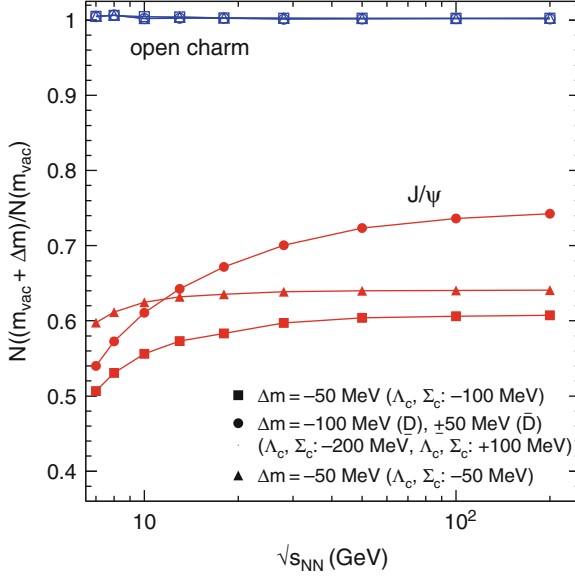


Fig. 6.11 Energy dependence of the relative change in the production yield of open charm hadrons and of J/ψ meson considering different scenarios for in-medium mass modifications (see text) [381].

the relative change of the yields with in-medium masses compared to the case of vacuum masses. For this comparison, we have added a third case, namely considering that the mass change of charmed baryons is the same as for the mesons. Because of total charm conservation, with lowering of their masses the open charm hadrons eat away some of the charm quarks of the charmonia but, since the open charm hadrons are much more abundant, their own yield will hardly change.

Note that the reduction of the J/ψ yield in our model is quite different from that assumed in [397, 456, 457, 474, 476], where a reduction in D meson masses leads to the opening up of the decay of ψ' and χ_c into $D\bar{D}$ and subsequently to a smaller J/ψ yield from feed-down from ψ' and χ_c . In all the previous work the in-medium masses are considered in a hadronic stage, while our model is a pure QGP model, with in-medium mass modifications considered at the phase boundary.

6.2.5 Conclusions

We have investigated charmonium production in the statistical hadronization model at lower energies. An interesting result is that the yield of charmed baryons (Λ_c , Ξ_c) relative to the total $c\bar{c}$ yield increases strongly with decreas-

ing energy. Below $\sqrt{s_{NN}}=10$ GeV, the relative yield of Λ_c exceeds that of any D meson except \bar{D}_0 , implying that an investigation of open charm production at low energies needs to include careful measurements of charmed baryons, a difficult experimental task. The charmonium/open charm yield rises only slowly from energies near threshold to reach $\sim 1\%$ at LHC energy. Note that this ratio depends on the magnitude of the charm cross section, further underlining the importance to measure this quantity with precision. We have also investigated the effect of possible medium modifications of the masses of charmed hadrons. Because of a separation of time scales for charm quark and charmed hadron production, the overall charmed meson and baryon cross section is very little affected by in-medium mass changes, if charm conservation is taken into account. Measurable effects are predicted for the yields of charmonia. These effects are visible at all beam energies and are more pronounced towards threshold.

6.3 Charmonium transport in hot and dense medium

6.3.1 Introduction

The J/ψ suppression signature in nuclear collisions (possibly indicating deconfinement [416]) is defined as a reduced J/ψ yield per binary nucleon-nucleon collision in a heavy-ion reaction, relative to elementary $p+p$ reactions at the same energy. This is quantified by the so-called nuclear modification factor (sometimes also referred to as suppression factor, $S_{J/\psi}$),

$$R_{AA}^{J/\psi} = \frac{dN_{J/\psi}^{AA}/dy}{N_{coll} \cdot dN_{J/\psi}^{pp}/dy}, \quad (6.13)$$

where N_{coll} denotes the number of binary collisions for a given centrality class, and $dN_{J/\psi}/dy$ the rapidity density of the J/ψ yield integrated over transverse momentum. J/ψ suppression is characterized by $R_{AA}^{J/\psi}$ being less than one. Since the mass of heavy quarks (charm and bottom) is much larger than typical secondary (thermal) excitations of the system created in nuclear collisions, $m_{c,b} \gg T$, they are mainly produced through initial hard processes. Therefore, the background for theoretically calculating heavy-flavor production is rather solid and the study of J/ψ production can yield important information on the properties of the quark-gluon plasma (QGP) formed in the early stage of nuclear collisions.

Charmonia are bound states of charm and anti-charm quarks (recall Fig. 5.1), and J/ψ is the ground ($1S$) state of charmonia with spin 1 found by Richter and Ting in 1974. The $1P$ and $2S$ states with spin 1 are χ_c and ψ' . The $J^P=1^-$ vector mesons J/ψ and ψ' can decay into a pair of leptons

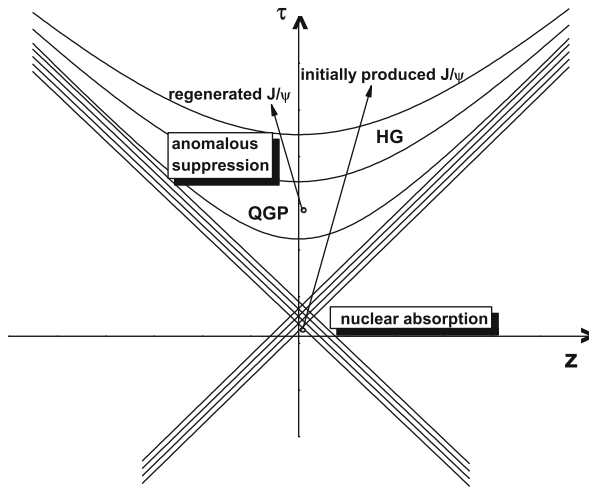


Fig. 6.12 A schematic illustration of J/ψ production and suppression in relativistic heavy ion collisions.

($\mu^+\mu^-$ or e^+e^-) and are thus directly measurable in experiment, while it is more difficult to detect χ_c 's. In $p+p$ collisions, the contribution from χ_c decays to the final-state J/ψ yield ("feeddown") is about 30% at SPS energy, but it is less than 10% for the ψ decay [478].

The formation time of a $c\bar{c}$ pair produced through hard interactions (e.g., gluon fusion) is about $1/m_c \sim 0.1$ fm/c, and only a small fraction of the $c\bar{c}$ pairs ($\sim O(10^{-2})$) eventually form charmonia in a color-singlet state. Since charmonium formation is a non-perturbative process, it is difficult to directly apply QCD in the study of the formation processes. Effective methods include the color-evaporation, color-singlet and color-octet models.

Since $c\bar{c}$ pairs are created via hard processes, the J/ψ yield in $p+A$ collisions should be proportional to the number of binary nucleon-nucleon interactions. However, from the experimental findings in $p+A$ collisions (as well as for light nuclear projectiles), there exists already a J/ψ suppression, the so-called "normal" nuclear suppression induced by multiple scattering between J/ψ (or its pre-resonance state) and spectator nucleons [479]. In addition to nuclear absorption, the primordially produced charmonia suffer "anomalous" suppression when they pass through the hot and dense medium created in heavy-ion collisions [480, 481].

The number of charm quarks created in the initial stage of heavy-ion collisions increases substantially with collision energy. While a small production of charm quarks at SPS energy is expected (about ~ 0.2 in central Pb-Pb), there are more than 10 $c\bar{c}$ pairs produced in a central Au+Au collision at RHIC (at $\sqrt{s_{NN}} = 0.2$ TeV) [382], and the number is probably over 200 in heavy-ion collisions at LHC (at $\sqrt{s_{NN}} = 5.4$ TeV) [482]. The large number of uncorrelated $c\bar{c}$ pairs in the QGP can recombine to form charmonia (primarily

J/ψ s). Obviously, this regeneration will enhance the J/ψ yield, and the momentum spectra of the final-state J/ψ 's may be quite different from the one with only initial production. The time evolution of J/ψ initial production, nuclear absorption, anomalous suppression and continuous regeneration in the course of a heavy-ion reactions are schematically illustrated in Fig. 6.12.

6.3.2 Normal and anomalous J/ψ suppression

Proton-nucleus ($p+A$) collisions are believed to be a good measure of normal (nuclear) J/ψ suppression. Suppose the projectile proton collides with a nucleon at (\mathbf{b}, z) (characterizing the transverse and longitudinal positions) in the target nucleus and produces a J/ψ or its pre-resonant state on a very short time scale. On its way out of the nucleus, the produced J/ψ collides inelastically with spectators which can be expressed via an absorption factor (or survival probability) as

$$\begin{aligned} S_{J/\psi}^{\text{nuc}} &= \frac{1}{A} \int d^2\mathbf{b} dz \rho(\mathbf{b}, z) e^{-\int_z^\infty dz' \sigma_{\text{abs}} \rho(\mathbf{b}, z')} \\ &= \frac{1}{A\sigma_{\text{abs}}} \int d^2\mathbf{b} \left(1 - e^{-\sigma_{\text{abs}} T(\mathbf{b})}\right), \end{aligned} \quad (6.14)$$

where ρ is the nucleon density distribution function, σ_{abs} the J/ψ absorption cross section, and $T(\mathbf{b}) = \int dz \rho(\mathbf{b}, z)$ is the thickness function. Strictly speaking, there should be a factor of $(A-1)/A$ in the exponential, which, however, can be neglected for sufficiently large A . For small absorption cross sections, the survival probability can be simplified as

$$S_{J/\psi}^{\text{nuc}} = e^{-\sigma_{\text{abs}} \langle T \rangle / 2}, \quad (6.15)$$

where $\langle T \rangle = \frac{1}{A} \int d^2\mathbf{b} [T(\mathbf{b})]^2$ is the average thickness of the nucleus A . From the comparison with the SPS data [483] (see Fig. 6.13), the average nuclear absorption cross section at SPS energy is extracted as $\sigma_{\text{abs}} = 6.5 \pm 1.0$ mb, similar for both J/ψ and ψ' . Early photon production experiments [484] suggest that the inelastic J/ψ +nucleon cross section (3.5 ± 0.8 mb) is significantly less than the above value, and the inelastic cross section for ψ' is almost four times the value for J/ψ . The most recent analysis of NA50 data [485], which features an increased sensitivity to ψ' production, exhibits some of this trend, with $\sigma_{\text{abs}} = 4.1 \pm 0.5$ and 8.2 ± 1.0 mb for the J/ψ and ψ' , respectively. This indicates that the $c\bar{c}$ states suffering from nuclear absorption have already (at least partially) evolved into their final states, even though the role of pre-resonant states could still be present.

Note that the effect of nuclear absorption depends strongly on the passing time $d_t = 2R_A / \sinh Y_B$ of the two colliding nuclei, where R_A is the nuclear

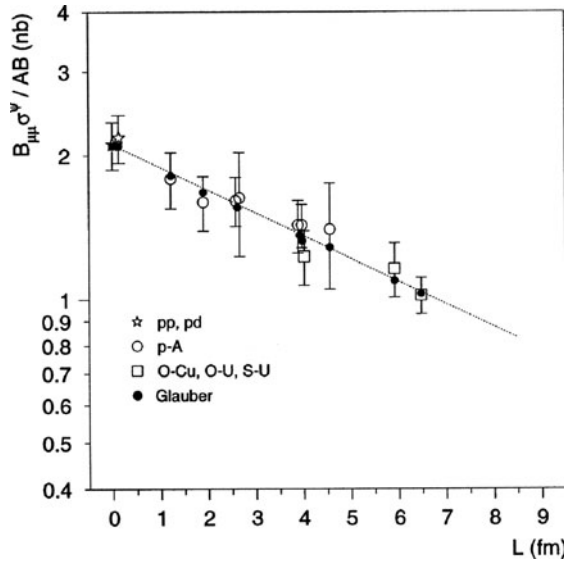


Fig. 6.13 Normal nuclear suppression of the J/ψ at SPS energy. The y -coordinate is proportional to the suppression factor $S_{J/\psi}$ and the x -coordinate is the effective nuclear path length, $L = \langle T \rangle / 2\rho_0$, with ρ_0 being normal nuclear density. The dashed line represents a fit using the expression (6.15). The figure is taken from [483].

radius and Y_B is their rapidity in the center-of-mass frame. While at SPS energy the collision time is about 1 fm/c and normal suppression is large, the cold nuclear matter effect in extremely energetic nuclear collisions should be small, due to the small collision time, e.g., $d_t \sim 0.1$ fm/c at RHIC and 1/200 fm/c at LHC.

While Fig. 6.13 illustrates that the nuclear absorption mechanism can well account for the experimental data in $p+A$ and light nuclear collision systems at SPS energy, the experiments with heavy nuclear projectile and target (Pb-Pb and In-In) show that the suppression of J/ψ (and ψ') in semi-/central collisions goes well beyond normal nuclear absorption [486–488], see Fig. 6.14. This phenomenon, called “anomalous” J/ψ suppression, is considered as one of the most important experimental results in relativistic heavy-ion collisions at SPS [489]. Various theoretical approaches have been put forward to explain the anomalous suppression [480, 481, 490, 491].

The first mechanism is based on the original prediction of Matsui and Satz [416]: the Debye screening effect in the QCD medium created in the early stage of nuclear collisions leads to J/ψ melting. The properties of the charmonium states in QGP and in vacuum are presumably quite different. In the vacuum, the effective static potential between a c and a \bar{c} can be written as

$$V(r) = -\frac{4}{3} \frac{\alpha_s(r)}{r} + \sigma r, \quad (6.16)$$

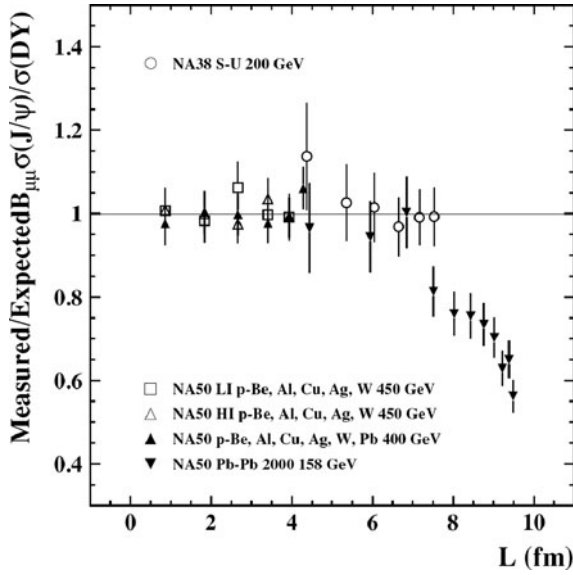


Fig. 6.14 Anomalous J/ψ suppression at SPS energy. The figure is taken from [486].

as recently confirmed in lattice QCD computations, see, e.g., [424]. The first and the second term in Eq. (6.16) are associated with one-gluon exchange and a linear confinement potential, respectively. At finite temperature, the potential is modified due to color screening, which can be implemented in a phenomenological way as [433]

$$V_{\text{med}}(r) = -\frac{4}{3} \frac{\alpha_s(r)}{r} e^{-m_D r} + \sigma r \left(\frac{1 - e^{-m_D r}}{m_D r} \right), \quad (6.17)$$

where $1/m_D(T)$ is called Debye screening length. The heavy-quark free energies computed in lattice QCD [492] at different temperatures are, however, more involved, cf. Fig. 6.1. In particular, as discussed in the preceding Sect. 6.1, it is currently an open question whether the free energy, $F = U - TS$, or the internal energy, U , is the appropriate quantity to be identified with a heavy-quark potential suitable for use in Schrödinger or Lippmann-Schwinger equation [368, 446, 447, 493–495]. In any case, due to the weakening of the potential with increasing temperature, the resonant states of $c\bar{c}$ dissociate at some Mott temperature T_d [416]. If the maximum temperature of the medium produced in heavy-ion collisions reaches the Mott temperature, the Debye screening effect results in anomalous charmonium suppression. Recent lattice calculations of charmonium spectral functions in the deconfined phase suggest that the J/ψ can survive up to temperatures of $T_d \simeq 1.6 - 2 T_c$ [430, 496, 497] (T_c : (pseudo-)critical temperature of the deconfined phase transition), while the excited states ψ' and χ_c disappear

around T_c [430], see also Sect. 6.1. Employing the heavy-quark potential extracted from the lattice calculation, the potential models generally support the results from the spectral function analyses [368, 446, 447, 493–495], even though no quantitative conclusions on the dissociation temperatures have been reached yet. A common conclusion from the lattice-based calculations is that different charmonium states correspond to different dissociation temperatures. This leads to the sequential dissociation model [498, 499] of describing anomalous charmonium suppression: With continuously increasing temperature of the fireball, ψ' will melt first, then χ_c dissociates, and finally J/ψ disappears. Considering the fact that about 40% of the final state J/ψ 's originate from the decay of ψ' and χ_c in $p+p$ and $p+A$ collisions, the anomalous J/ψ suppression in Pb+Pb collisions at SPS is associated with the dissociation of ψ' and χ_c in the produced fireball. A precise measurement on ψ' and especially on χ_c yield in the future can help to check the sequential model. Along similar lines, J/ψ suppression in hot and dense medium has been described in a general threshold model without considering microscopic dynamics [500]. In this model the J/ψ suppression function is written as

$$S_{J/\psi}(b) = \int d^2\mathbf{s} S_{J/\psi}^{nuc l}(b, \mathbf{s}) \Theta(n_c - n_p(b, \mathbf{s})) , \quad (6.18)$$

where $S_{J/\psi}^{nuc l}(b, \mathbf{s})$ is the J/ψ survival probability after nuclear absorption, b is the impact parameter, and \mathbf{s} is the transverse coordinate of J/ψ . The density $n_p(b, \mathbf{s})$ in the step function is proportional to the energy density of the matter at position (b, \mathbf{s}) . In the hot and dense part of the fireball, where n_p is larger than a critical value n_c , all the J/ψ 's are absorbed by the matter, and those J/ψ 's outside this region only suffer normal suppression. The threshold density n_c in this model is a parameter, taken, e.g., as the maximum n_p in S+U collisions at SPS (where no anomalous J/ψ suppression is observed). If the matter with $n_p > n_c$ is QGP, the critical density n_c can be considered as the threshold value to create QGP. Despite its simplicity, the threshold explains well the anomalous suppression in Pb–Pb collisions at SPS [501], see Fig. 6.15.

The above analyses utilizing the Debye screening effect is typically based on the simplifying assumption of a constant temperature in connection with a sharp transition of the inelastic charmonium widths from zero (stable below T_d) to infinity (dissolved above T_d). However, the volume of the produced fireball in relativistic heavy-ion collisions is relatively small and expands rapidly, implying rather fast temperature changes and short fireball lifetimes. In this case, the conclusion from the static Debye screening effect may deviate from the real system, and it becomes essential to include the concrete interactions between partons and charmonia, leading to sizable inelastic reaction rates comparable to the fireball expansion (or cooling) rate. In particular, the charmonia can be destroyed below the dissociation temperature. Debye screening is still operative, by controlling the binding energy

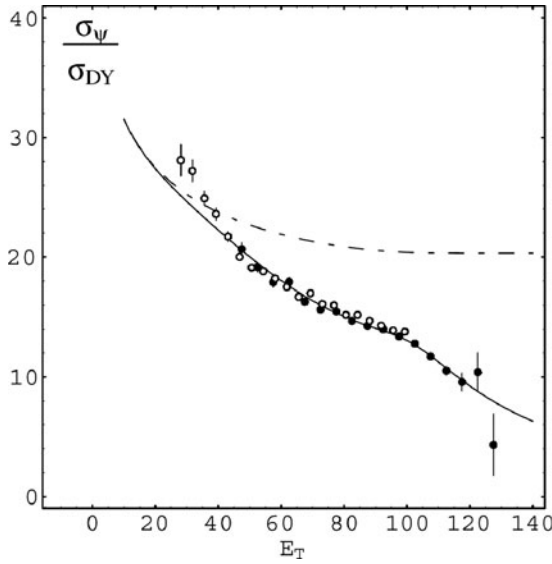


Fig. 6.15 The J/ψ suppression at SPS energy. The *solid line* is the calculation in the threshold model and the *dashed line* is the result with only nuclear absorption. The figure is taken from [501].

which in turn determines the phase space (and thus the width) of the dynamic dissociation reactions [380]. An important such process in the QGP is the (leading-order) gluon dissociation process [502] $g + J/\psi \rightarrow c + \bar{c}$, in analogy to the photon dissociation process of electromagnetic bound states [503]. For small binding energies (i.e., when approaching the dissociation temperature), the phase space for gluon dissociation shrinks and next-to-leading order (NLO) processes take over [380, 504], most notably inelastic parton scattering $g(q, \bar{q}) + J/\psi \rightarrow g(q, \bar{q}) + c + \bar{c}$. Not only partons in the deconfined phase can induce anomalous suppression, but also the secondary particles like π , ρ and ω (so-called comovers) in a hot and dense hadron gas can interact with charmonia inelastically and cause J/ψ suppression [505–508]. The suppression due to the comover effect can be schematically expressed as

$$S_{J/\psi}^{co} = e^{-\int d\tau \langle v \sigma_{co} \rangle \rho_{co}(\tau)}, \quad (6.19)$$

where $\rho_{co}(\tau)$ is the comover density at proper time τ at the J/ψ 's position, and the inelastic cross section (multiplied by the relative velocity) is averaged over different kinds of comovers and the interaction energy. The comover density, $\rho_{co}(\tau)$, is normally obtained through some kind of evolution mechanism of the matter (generally assumed to be of Bjorken-type, i.e., proportional to the inverse of the proper time, $1/\tau$), and is fitted to the measured final-state hadron yield dN_h/dy . The cross section σ_{co} is an adjustable parameter in the calculation. In some calculations the comover densities turn out to be rather

high, corresponding to energy densities well above the critical one computed in lattice QCD. Consequently, the pertinent comover-interaction cross section assumes rather small values, e.g., $\sigma_{co} = 0.65$ mb in [508], which are more suitably interpreted as partonic comover interactions.

A more detailed description of the matter evolution together with a dynamical treatment of the interactions between charmonia and comovers has been carried out in the hadronic transport models UrQMD [509] and HSD [477] where the J/ψ motion is traced microscopically throughout the medium. The charmonium-hadron cross sections, however, remain input parameters to these models. Alternatively, one may employ theoretical calculations of charmonium dissociation cross sections with light mesons, as computed in either quark [510] or hadronic models [511, 512]. By adjusting the comover cross sections (and possibly other parameters, such as formation times), interactions at the hadron level can reproduce the SPS data of J/ψ suppression [477, 508], see Fig. 6.16.

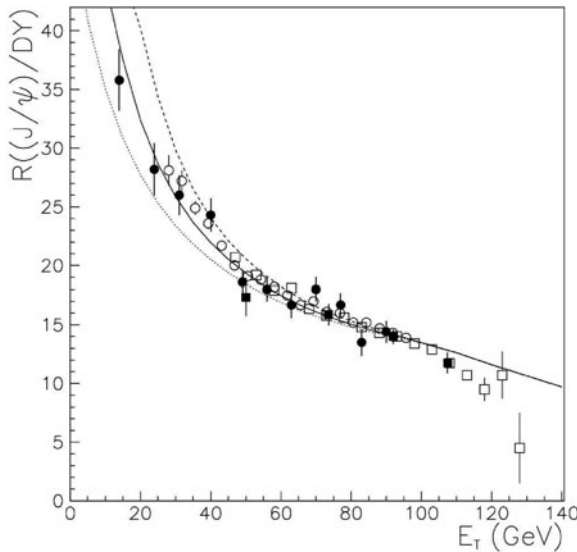


Fig. 6.16 The J/ψ suppression at SPS energy. The *lines* represent calculations in the comover model. The figure is taken from [508].

Motivated by the lattice QCD findings of surviving J/ψ bound states well above T_c , recent work in [513] has treated the formation and evolution of $c\bar{c}$ correlations more microscopically. In a weakly coupled QGP (wQGP), charm quarks would fly away from each other as soon as enough energy is available, while in a strongly coupled QGP (sQGP), the strong attraction between quarks (see Fig. 6.1), as well as their small diffusion constant in the sQGP, opens the possibility of returning to the J/ψ ground state, leading to a substantial increase in survival probability [513]. The charm-quark motion

in the medium is described by a Langevin equation,

$$\frac{d\mathbf{p}}{dt} = -\gamma\mathbf{p} + \boldsymbol{\eta} - \nabla V, \quad (6.20)$$

where $\boldsymbol{\eta}$ is a Gaussian noise variable, normalized such that $\langle \eta_i(t)\eta_j(t') \rangle = 2m_c T$ with i, j indexing transverse coordinates (m_c : charm quark mass). For strongly coupled matter, the drag coefficient characterizing the thermalization of charm quarks in the medium is large, $\gamma \simeq (2 - 4) \frac{\pi T^2}{1.5m_c}$. Taking the internal energy as the heavy-quark potential (extracted from a lattice-QCD computed free energy, see Fig. 6.1) the survival probability of charmonia in sQGP is larger than that in wQGP. This qualitatively explains why there is no large difference between suppressions at SPS and RHIC. When using effective potentials which are identified with the free energy, F , or a linear combination the internal energy U and F , the charmonium binding is less pronounced leading to dissociation temperatures (i.e., zero binding) below $1.5 T_c$ even for the J/ψ , as compared to above $2 T_c$ when employing U [368, 493]. We also recall that a small charm diffusion constant can be obtained from elastic c -quark interactions based on the internal energy as a potential, cf. Sect. 5.2.2.

6.3.3 Regeneration

The normal and anomalous suppressions discussed above apply to initially produced charmonia. In $A+A$ collisions at SPS energy and below, there is typically no more than one $c\bar{c}$ pair produced per central Pb–Pb collision ($N_{c\bar{c}} \simeq 0.2$ at $E_{\text{lab}}=158$ A GeV). Thus, if the two quarks can not form a (pre-resonant) charmonium bound state close to their creation point, the probability to recombine in the medium and form a resonant state is small and can probably be neglected. However, for nuclear collisions at collider energies (RHIC and LHC), the situation becomes quite different. In a central Au+Au collision at the maximum RHIC energy, about 10–20 $c\bar{c}$ pairs are produced [382, 482], and the uncorrelated c and \bar{c} from different pairs have a significant probability (proportional to square of the number of $c\bar{c}$ pairs) to meet and form a charmonium bound state in the medium. The J/ψ regeneration in partonic and hadronic (or mixed) phases arises as a possible new mechanism for charmonium production in heavy-ion collisions at RHIC and LHC.

Within the statistical hadronization model, charm quarks are assumed to equilibrate kinetically and secondary charmonium production entirely occurs at the hadronization transition, as discussed in Sect. 6.2.

Recent lattice calculation of charmonium spectral functions [430, 496, 497] (see also Sect. 6.1) suggest that J/ψ can exist in a thermal environment at temperatures well above the deconfinement phase transition. Therefore,

unlike in the statistical model, charmonia in the kinetic formation model [472–475, 514, 515] can be regenerated continuously throughout the QGP region, and the formed J/ψ 's reflect the initially produced charm-quark spectra and their modification due to the interaction with the medium. In the kinetic approach of [472, 473, 514], J/ψ production during the entire lifetime of the deconfined phase is dynamically calculated through (related) formation and dissociation processes at finite temperature and density. The simplest dissociation reaction utilizes absorption of individual (deconfined) gluons in the medium to “ionize” the color-singlet J/ψ , $g + J/\psi \rightarrow c + \bar{c}$, resulting in a $c\bar{c}$ pair in a color-octet state. The inverse of this process serves as the corresponding formation reaction, in which a $c\bar{c}$ pair in a color-octet state emits a color-octet gluon and falls into the color-singlet J/ψ bound state. The dissociation cross section σ_D has been calculated in the OPE-based model of gluon dissociation of a deeply bound heavy quarkonium [516, 517], and the formation cross section is obtained through detailed balance. The competition between the J/ψ formation and suppression is characterized by the kinetic equation [473]

$$\frac{dN_{J/\psi}}{d\tau} = \lambda_F N_c N_{\bar{c}} / V_{FB}(\tau) - \lambda_D N_{J/\psi} \rho_g, \quad (6.21)$$

where ρ_g is the gluon density in the thermalized medium, and $\lambda = \langle \sigma v_{\text{rel}} \rangle$ the reactivity determined by the inelastic cross section (σ) and initial relative velocity (v_{rel}), averaged over the momentum distribution of the initial particles. The fireball volume, V_{FB} , is modeled according to the expansion and cooling profiles of the heavy-ion reaction zone. The first term on the right hand side of Eq. (6.21) represents formation, and the second term accounts for anomalous suppression of the produced charmonia in the medium. Due to the quadratic behavior of the formation rate on the charm-quark number, one expects an increase with centrality of formed J/ψ per binary collision. The medium is usually considered as an ideal gas of quarks and gluons, described by perfect Bjorken (1+1 dimensional) hydrodynamics. Integrating (6.21) over the QGP lifetime, one obtains the final J/ψ yield [472]. When investigating charmonium 3-momentum spectra [473] even the use of pQCD calculated charm-quark distributions leads to rapidity and transverse-momentum spectra of the formed quarkonia which are narrower than those expected from diagonal pairs (initially created together) in the absence of a deconfined medium. For thermalized charm quarks with collective flow controlled by hydrodynamics, the J/ψ spectra are substantially narrower and contain information on those of the underlying heavy quarks.

A common assumption of the statistical hadronization model [451] and the above kinetic model [472] is that the initially produced charmonia are entirely destroyed (or not formed) in the (early) QCD medium. This is probably a good approximation for central heavy-ion collisions at RHIC and LHC energies, but for nuclear collisions at SPS and lower energies, as well as for peripheral collisions and light ions (even at higher energies), one needs to

include initial production together with normal and anomalous suppressions. This was first done in the two-component model of [380, 471], where the final yield of charmonia is the sum of “direct” and “thermal” production,

$$N_{J/\psi} = N_{J/\psi}^{dir} + N_{J/\psi}^{th} . \quad (6.22)$$

The direct component are charmonia initially produced via hard processes with subsequent nuclear absorption and anomalous suppression in the QGP [380, 471]. Regeneration in this model is restricted to statistical hadronization at the boundary of the confinement phase transition, as in the statistical hadronization model. Both direct and thermal components are subsequently subject to hadronic dissociation processes. The two-component model has been further developed into a kinetic rate-equation approach in [474], where a differential equation similar to Eq. (6.21) has been solved in an expanding thermal fireball background,

$$\frac{dN_\Psi}{d\tau} = -\Gamma_\Psi(N_\Psi - N_\Psi^{eq}) , \quad (6.23)$$

formulated in terms of the charmonium equilibrium limits, N_Ψ^{eq} , and inelastic dissociation rates, Γ_Ψ . The former have been evaluated including in-medium masses of charm quarks and open-charm hadrons in the QGP and hadron gas (HG), respectively, as well as a schematic correction for incomplete thermalization (determined by a charm-quark relaxation time, τ_c^{eq}); the inelastic reaction rates account for in-medium binding energies of charmonia. The above form of the rate equation allows to incorporate inelastic processes beyond $2 \leftrightarrow 2$ scattering, which is particularly important for small charmonium binding energies where inelastic $2 \leftrightarrow 3$ processes, $g(q, \bar{q}) + J/\psi \rightarrow g(q, \bar{q}) + c + \bar{c}$, become important (instead of gluo-dissociation used in the kinetic model of [472]). In the HG, inelastic interactions with pions ($\pi + J/\psi \rightarrow D + \bar{D}^*, \bar{D} + D^*$) and ρ mesons ($\rho + J/\psi \rightarrow D + \bar{D}, D^* + \bar{D}^*$) are accounted for, which mostly affect the ψ abundance. This approach has largely confirmed the results of the 2-component model and can describe well the J/ψ production from SPS to RHIC energy. At SPS energy, the direct production prevails over the thermal component for S+U ($E_{lab} = 200$ A GeV) and Pb+Pb ($E_{lab} = 158$ A GeV) collisions at any centrality [471]. The thermal contribution sets in when the temperature of the system reaches the critical value for deconfinement phase transition and grows with increasing open-charm production. At RHIC energy, the J/ψ yield is still dominated by initial production for peripheral collisions, but regeneration becomes comparable (or even exceeds) direct production for semi-/central collisions, albeit a significant uncertainty due to incomplete charm-quark thermalization remains [518, 519], see Fig. 6.17.

In the above kinetic rate equation approaches, charmonia are essentially regenerated at or before the hadronization transition. J/ψ regeneration may also occur in hadron matter by considering the backward channels

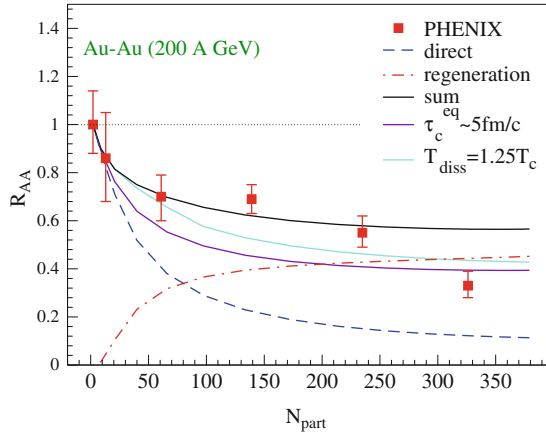


Fig. 6.17 The centrality dependence of the nuclear modification factor $R_{AA}^{J/\psi}$ calculated in the thermal rate-equation approach of [474] at RHIC energy. The figure is taken from [518].

$D + \bar{D} \rightarrow J/\psi +$ mesons through detailed balance [477]. While the regeneration is negligible at SPS energy, its contribution to the final J/ψ yield is essential and comparable to the dissociation by the comoving mesons at extremely relativistic energies (note, however, that the comover densities may be of the same magnitude as the critical energy density, $\epsilon_c \simeq 1 \text{ GeV/fm}^3$). Also in this approach, regeneration explains why the total J/ψ suppression at RHIC energy as a function of centrality is similar to the suppression at SPS energy [520].

Recent RHIC data on the rapidity dependence of the nuclear modification factor [453] show that the J/ψ yield in the forward rapidity region ($|y| \in [1.2, 2.2]$) is smaller than that in the central rapidity region ($|y| < 0.35$). This phenomenon is hard to explain in models with only initial production mechanisms, since the anomalous suppression in the central region, where the highest temperatures are expected, should be stronger than that at forward/backward rapidities. Considering that the regeneration occurs mainly in the central region, this J/ψ rapidity dependence is probably an evidence for charmonium regeneration in heavy ion collisions at RHIC [449, 521].

6.3.4 Transverse-momentum distributions

All models for inclusive J/ψ yields – with and without the assumption of a QGP and with and without regeneration mechanism – describe the observed suppression after at least one parameter is adjusted. Transverse-momentum distribution may depend more directly on the production and regeneration

mechanisms and, therefore, contain additional information about the nature of the medium and J/ψ , thus helping to distinguish between different scenarios.

Anomalous suppression is not an instantaneous process, but takes a certain time depending on the mechanism. During this time the produced charmonia with high transverse momentum may “leak” out the parton/hadron plasma and escape suppression [416]. As a consequence, low- p_t charmonia are more likely to be absorbed, and consequently the average transverse momentum of the observed charmonia will show an increase which grows monotonically with the average lifetime of the plasma. A self-consistent way to incorporate the effect of leakage into the various models is through charmonium transport equation in phase space [522–524].

The medium created in high-energy nuclear collisions evolves dynamically. In order to extract information about the medium by analyzing the J/ψ distributions, both the hot and dense medium and the J/ψ production processes must be treated dynamically. Due to its large mass, the J/ψ is unlikely fully thermalized with the medium. Thus its phase space distribution should be governed by transport equation including both initial production (incl. anomalous suppression) as well as regeneration. The charmonium distribution function, $f_\Psi(\mathbf{p}_t, \mathbf{x}_t, \tau|\mathbf{b})$ ($\Psi = J/\psi, \psi', \chi_c$), in the central rapidity region and in the transverse phase space, $(\mathbf{p}_t, \mathbf{x}_t)$, at fixed impact parameter \mathbf{b} is controlled by the classical Boltzmann transport equation [475]

$$\frac{\partial f_\Psi}{\partial \tau} + \mathbf{v}_\Psi \cdot \nabla f_\Psi = -\alpha_\Psi f_\Psi + \beta_\Psi. \quad (6.24)$$

The second term on the left-hand side arises from free streaming of Ψ with transverse velocity $\mathbf{v}_\Psi = \mathbf{p}_t / \sqrt{\mathbf{p}_t^2 + m_\Psi^2}$ which leads to the leakage effect. The anomalous suppression and regeneration mechanisms are reflected in the loss term α_Ψ and gain term β_Ψ , respectively. It is assumed that the medium locally equilibrates at time τ_0 , after nuclear absorption of the initially produced J/ψ 's has ceased. The latter effect can be included in the initial distribution, $f_\Psi(\mathbf{p}_t, \mathbf{x}_t, \tau_0|\mathbf{b})$, of the transport equation.

When the loss and gain terms are known, the transport equation can be solved analytically with the result

$$f_\Psi(\mathbf{p}_t, \mathbf{x}_t, \tau|\mathbf{b}) = f_\Psi(\mathbf{p}_t, \mathbf{x}_t - \mathbf{v}_\Psi(\tau - \tau_0), \tau_0|\mathbf{b}) e^{-\int_{\tau_0}^{\tau} d\tau' \alpha_\Psi(\mathbf{p}_t, \mathbf{x}_t - \mathbf{v}_\Psi(\tau - \tau'), \tau'|\mathbf{b})} + \int_{\tau_0}^{\tau} d\tau' \beta_\Psi(\mathbf{p}_t, \mathbf{x}_t - \mathbf{v}_\Psi(\tau - \tau'), \tau'|\mathbf{b}) e^{-\int_{\tau'}^{\tau} d\tau'' \alpha_\Psi(\mathbf{p}_t, \mathbf{x}_t - \mathbf{v}_\Psi(\tau - \tau''), \tau''|\mathbf{b})}. \quad (6.25)$$

The first and second terms on the right-hand side indicate the contribution from initial production and continuous regeneration, respectively. Both suffer anomalous suppression. The coordinate shift $\mathbf{x}_t \rightarrow \mathbf{x}_t - \mathbf{v}_\Psi \Delta\tau$ reflects the leakage effect during the time period $\Delta\tau$.

At SPS energy [522, 523] regeneration can be neglected by setting $\beta_\Psi = 0$. In the comover-interaction model [508] for the suppression mechanism,

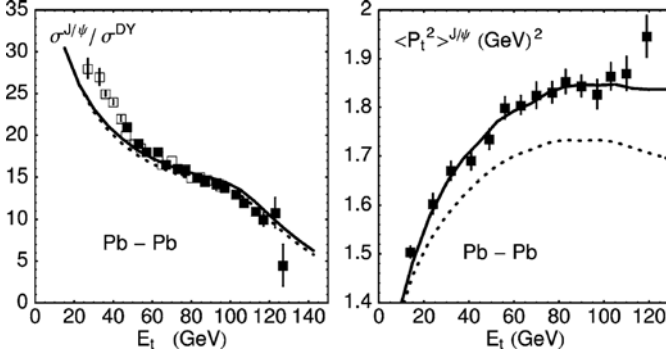


Fig. 6.18 The suppression factor and $\langle p_t^2 \rangle$ for J/ψ in Pb+Pb collisions at SPS as a function of transverse energy E_t . The *dotted* and *solid* lines are calculated with the comover model without and with considering the leakage effect, respectively. The figure is taken from [523].

the J/ψ suppression and averaged transverse momentum $\langle p_t^2 \rangle$ are shown in Fig. 6.18. The calculation without leakage, obtained by setting $\mathbf{v}_\psi = 0$, does not fit the data for $\langle p_t^2 \rangle$, even in the domain of low transverse energy, E_t (which in the NA50 experiment is used as a measure of centrality). Only when the leakage effect is taken into account, the calculation agrees well with the data. Since only high- \mathbf{p}_t charmonia are sensitive to the leakage effect, and since they are only a small fraction of the inclusive yield, both calculations with and without leakage can fit the J/ψ yield very well. The leakage effect on the transverse-momentum distribution is not sensitive to the underlying mechanism; the calculation [523] with the threshold model [501] as the suppression mechanism gives a similar structure of $\langle p_t^2 \rangle$ for J/ψ .

At RHIC energy [475, 524] we should include the contribution from the continuous regeneration in QGP (see also [449, 473, 519]). Since the hadronic phase occurs later in the evolution of heavy ion collisions when the density of the system is lower compared to the early hot and dense period, the hadronic dissociation can, as a first approximation, be neglected. Considering only the gluon dissociation process for the loss term α_ψ and its inverse process for the gain term β_ψ , and determining the thermal gluon distribution and the QGP space-time region by solving the ideal hydrodynamic equations, the $\langle p_t^2 \rangle$ of the J/ψ is shown in Fig. 6.19 as a function of the number of binary collisions, N_{coll} . For both the pQCD calculated (left panel) and thermalized (right panel) charm-quark distributions, the momentum spectra are indeed more sensitive to the production mechanism than the integral yield. For the initially produced J/ψ 's, the multiple gluon scattering in the initial state and the leakage effect due to the anomalous suppression lead to a $\langle p_t^2 \rangle$ broadening. For the regenerated J/ψ 's, the charm quarks in the pQCD scenario undergo no rescattering in the initial state nor in the QGP, and they are similar to the statistical distribution in the thermal scenario. The $\langle p_t^2 \rangle$ of the regenerated

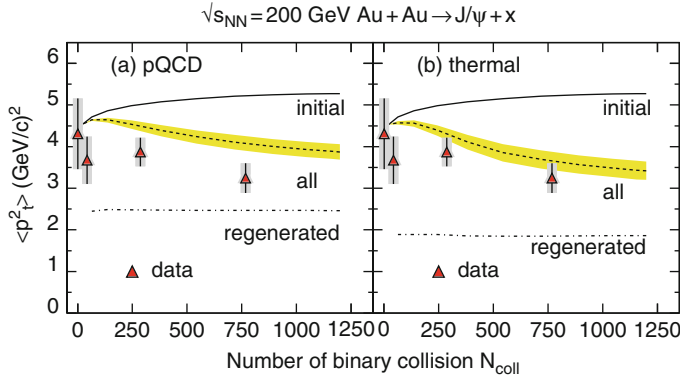


Fig. 6.19 The $\langle p_t^2 \rangle$ for J/ψ at RHIC energy as a function of number of binary collisions. The left and right panel correspond to pQCD calculated and thermalized charm-quark distributions, respectively. The figure is taken from [475].

J/ψ 's is much smaller than that of the initially produced J/ψ 's. In both scenarios, only the full calculation with both production mechanisms can fit the experimental data reasonable well. Since the collective flow develops with time, the $\langle p_t^2 \rangle$ for the suddenly produced J/ψ 's on the hadronization hypersurface should be larger than the result for continuously regenerated J/ψ 's in the whole volume of QGP.

6.3.5 Charmonia in heavy-ion collisions at low energies

While in heavy-ion collisions at RHIC and LHC the formed medium is characterized by high temperatures and low net baryon densities, at relatively low energies, such as at FAIR, highly compressed baryon matter at low temperature is anticipated. Monte Carlo simulations [525] indicate the maximum energy and baryon density in a central Au+Au collision at FAIR energy to reach $\epsilon \sim 6 \text{ GeV}/\text{fm}^3$ and $\rho/\rho_0 \sim 10$, see the detailed discussion in Part III of this book. In the following, we will give a qualitative discussion of some of the trends one might expect in the FAIR energy regime, based on the experimental and theoretical lessons at higher energies as discussed above.

Normal vs. Anomalous Suppression. At low energies, regeneration in both the partonic and hadronic medium is expected to be small and the initial production will dominate the charmonium yield. Normal nuclear absorption of the directly produced charmonia is in the time period $t < t_d$. At RHIC and LHC energies, where the collision time t_d is small and the lifetime of the partonic medium large, nuclear absorption is not a dominant factor, compared to anomalous suppression. However, at low energies, where the collision time

t_d is much longer and the lifetime of partonic medium is much shorter, nuclear absorption becomes important, possibly the dominant effect. It has even been argued [526] that heavy quark re-scattering in a cold nuclear medium can fully account for the observed J/ψ suppression in Pb+Pb collisions at SPS energy, without considering further suppression in the hot medium created in the later expansion stages.

Transverse-Momentum Spectra. In comparison with the regenerated charmonia in the medium, the initially produced charmonia through hard processes have larger transverse momentum. At RHIC, the superposition of initial production and regeneration for J/ψ 's leads to a roughly constant (or even slightly decreasing) average transverse momentum squared, $\langle p_t^2 \rangle$, with centrality [475, 519, 527]. However, at FAIR energy, the $\langle p_t^2 \rangle$ of the J/ψ 's (dominated by initial production) should increase with centrality, due to the Cronin effect, i.e., the initial multiple scattering of gluons with nucleons (prior to the hard scattering leading to charmonium production).

Formation Time Effects. The time for the medium created in heavy ion collisions to reach thermal equilibrium is short at high energies, about 0.5 fm/c at RHIC and 0.1 fm/c at LHC, and long at low energies, at least 1 fm/c at FAIR (the time interval between first contact and full nuclear overlap is already ~ 1.5 fm/c). Considering a finite formation time of charmonia, about 0.5 fm/c, J/ψ 's are easily dissociated in the hot medium at RHIC and LHC, but might survive in the medium at low energies. Since charmonia are difficult to be thermalized at low energies, their elliptic flow at FAIR will be smaller than that at RHIC and LHC. Charmonia studies at FAIR may also present a possible way to distinguish different scenarios of J/ψ suppression [528]. For instance, when after adjusting the suppression at SPS energy, the suppression at FAIR by comovers will be stronger than that by threshold melting; in addition, for the ψ'/ψ ratio, the comover scenario predicts a smooth excitation function, contrary to a step-like structure for threshold melting. See [Part IV](#) of this book for more details.

Medium Effects. It is widely believed that chiral symmetry governs the low-energy properties and dynamics of hadrons in the vacuum and at finite temperature and density. The chiral symmetry restoration transition at high temperature (small baryon density) is a crossover, while it presumably becomes a first order phase transition at high density. Both the QCD sum rule analysis [157] and the LO perturbative QCD calculations [516] suggest that the J/ψ mass is reduced in nuclear matter due to the reduction of the gluon condensate. At SPS energy, chiral symmetry restoration reduces the threshold for charmonium break-up and could lead to a step-like behavior of the reaction rate, as suggested to account for the anomalous J/ψ suppression [529]. The study of the ratio ψ'/ψ at SPS shows the importance of the hadronic phase for ψ' interactions, possibly related to the effect of chiral symmetry

restoration [474]. Another high density effect is the Friedel oscillation in the single-particle potential induced by a sharp Fermi surface at low temperature, which is widely discussed in nuclear matter and quark matter [530–533]. The heavy-quark potential at zero baryon density, shown in Fig. 6.1, decreases monotonously with increasing temperature. In compressed baryon matter, however, the potential may oscillate and approach the weak coupling limit very slowly. This could imply that J/ψ 's survive in a wide region of high densities.

Charmed Baryons. The importance of charmed baryons at low energies has been recently discussed in [381] within the statistical hadronization model. While the J/ψ and ψ' yields relative to the total number of $c\bar{c}$ pairs are roughly independent of collision energy over a wide region from FAIR to RHIC, the relative yield for charmed baryon Λ_c decreases strongly with increasing energy, exceeding the yield of D mesons at the low-energy end. This indicates that the investigation of open-charm production at low energies mandates the inclusion of charmed baryons.

Chapter 7

Excitations of color-superconducting matter

7.1 Color superconductivity in the QCD phase diagram

Color-superconducting quark matter phases play an important role in the discussion of the QCD phase diagram at low temperatures and intermediate to high densities. Predictions in the vicinity of the deconfinement phase transitions rely on effective models since systematic methods (lattice QCD, perturbative QCD, Hard Dense Loop approximation) do not apply. The status of the field is summarized in recent reports, e.g. [536–538] and useful references are found therein. Out of the many phases discussed the phase eventually relevant for heavy-ion collisions at high baryon densities is the two-flavor superconducting (2SC) phase where the scalar diquark field develops a non-vanishing mean value, the corresponding energy gap is of the order of 100–200 MeV leading to estimates for the critical temperature in a large range between 20 and 100 MeV. Most of the microscopic model calculations of the phase diagram and properties of in-medium fluctuations are performed in NJL-type models [538]; promising approaches, closer to QCD, with

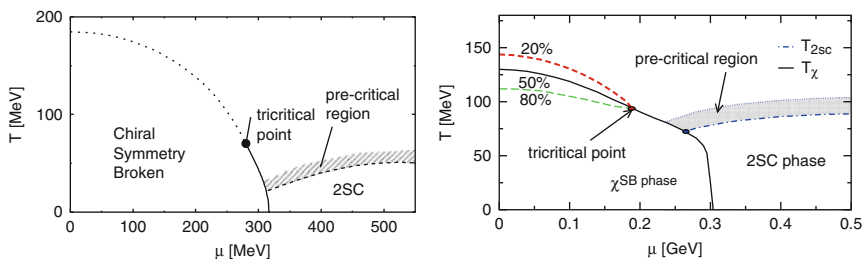


Fig. 7.1 Phase diagram for isospin-symmetric two-flavor quark matter from NJL-type modelling [534] (*left*) and for a covariant, nonlocal quark model [535] (*right*). The critical temperatures for the 2SC phase transition and the occurrence of the pseudo-gap phase can be very model dependent (μ : quark chemical potential).

dynamical quark self energies are covariant nonlocal approaches [535, 539]. We give examples for the 2SC phase boundaries of these two types of models in Fig. 7.1.

7.2 Strong decays of mesonic resonances

In the mean-field approximation, the ground state of the color-neutral quark matter with 2 flavors corresponds to the minimum of the zero-temperature thermodynamic potential density, Ω , which in a four-quark model of the NJL type looks as

$$\begin{aligned} \Omega(m, \Delta) = & \frac{(m - m_0)^2}{4G} + \frac{|\Delta|^2}{4H_s} - 4 \sum_{\pm} \int \frac{d^3q}{(2\pi)^3} |E_{\Delta}^{\pm}| \\ & - 2 \sum_{\pm} \int \frac{d^3q}{(2\pi)^3} |\check{E}^{\pm}|, \end{aligned} \quad (7.1)$$

where $E_{\Delta}^{\pm} = \sqrt{(E^{\pm})^2 + |\Delta|^2}$, $E^{\pm} = E \pm \bar{\mu}$ and $\check{E}^{\pm} = E \pm \check{\mu}$ are dispersion laws of quarks and antiquarks in the 2SC phase, with $E = \sqrt{\mathbf{q}^2 + m^2}$ being the quark dispersion law in vacuum, m the constituent quark mass and $\bar{\mu} = \mu + \mu_8$, $\check{\mu} = \mu - 2\mu_8$, with μ and μ_8 being the quark baryonic chemical potentials (the main and the one related to the color-charge Q_8 , respectively). The interaction strength of the standard and diquark channels is described by constants G and H_s . In the 2SC phase, there is a gap, Δ , in the dispersion law of quarks.

To find the minimum of Ω , one should solve the gap equations

$$\frac{\partial \Omega(m, \Delta; \mu, \mu)}{\partial m} = \frac{\partial \Omega(m, \Delta; \mu, \mu_8)}{\Delta} = 0, \quad (7.2)$$

while keeping the quark matter color-neutral:

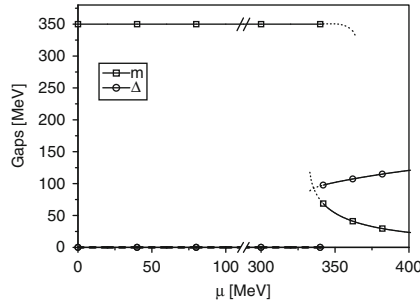


Fig. 7.2 The constituent quark mass m vs. μ and color gap Δ vs. μ under local color neutrality constraint.

$$\langle Q_8 \rangle = -\frac{\partial \Omega(m, \Delta; \mu, \mu_8)}{\partial \mu_8} = 0. \quad (7.3)$$

Solving these equation, one obtains values of the gaps, as shown in Fig. 7.2.

The calculation of masses of meson and diquark states requires two-point correlators of related quark currents. The masses are found as the values of energy at zero-valued 3-momentum that correspond to the poles of the correlators. Results of numerical calculations performed in [540] are presented in Figs. 7.3 and 7.4.

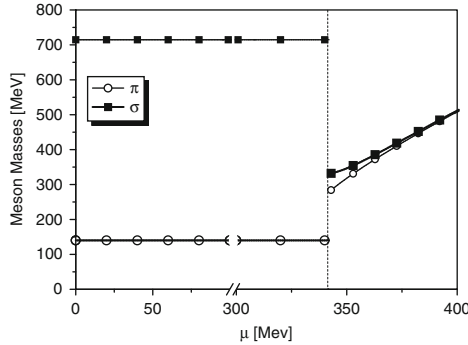


Fig. 7.3 The masses of the σ meson and pion as functions of μ , when mixing of σ and Δ_2^s is neglected.

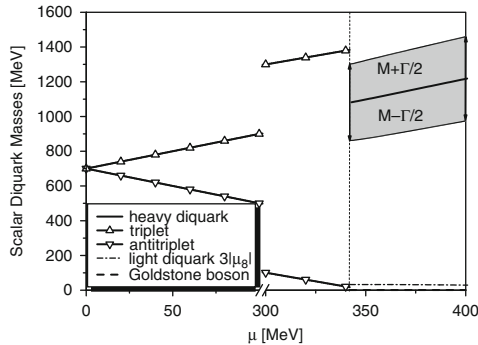


Fig. 7.4 The masses of diquarks. At $\mu < \mu_c = 342$ MeV, six diquark states are splitted into a (color)triplet of heavy states and an anti-triplet of light states. In the 2SC phase ($\mu > \mu_c$), one observes the Nambu–Goldstone boson, four light diquarks with the mass $3|\mu_8|$, and a heavy singlet state with the mass M (solid line). The shaded rectangular displays the width Γ of the heavy singlet resonance; its upper border is half-width higher than the mass and the bottom border is half-width lower.

In the phase with color superconducting quark matter, mesons can, in principle, decay to free quarks. However, there is some reason for decays of the σ and π mesons to be suppressed in these conditions. As it has been discussed in [540, 541], in the 2SC phase the σ and π mesons turn to be quasi-particles with quantum numbers of a scalar isoscalar and a pseudoscalar isovector meson, respectively. These quasi-particles have almost degenerate masses because chiral symmetry is almost restored in these conditions, and the pion is as heavy as the σ meson with the mass about 300 MeV. Nevertheless, a direct decay of a pion to free quarks is forbidden at zero temperature. Moreover, it turns out that the σ meson is also stable if its mixing with diquarks is neglected (numerically, it is very small). As a consequence, one should observe a narrow state with vacuum quantum numbers and with the mass near 300 MeV.

The reason for the mesons stability comes from the following: A decay of a meson means that its constituents become free and move with four-momenta satisfying their dispersion laws. In the 2SC phase, the quark and antiquark have gaps in the dispersion laws that push up their energy so high that their total energy should have at least ~ 700 MeV to move freely. But there are poles in the propagators of the σ meson and pion at the energy about 300 MeV just a little above the phase transition. This means that the paired quarks cannot take there places on the mass-shell to begin their free motion and have to remain bound inside the meson. As there are unpaired quarks in the 2SC phase, one can think that they could contribute to the decay. In fact, insofar as free quarks appear in pairs (a quark and an antiquark), the total energy that is necessary to create such a pair is the sum of the creation energies both of the quark and the antiquark. It turns out that the energy is enough to produce a free pair because there is no gap in the dispersion law for unpaired quarks. Nevertheless, it turns out that at zero temperature their energy levels are already occupied by other quarks from the medium; as there cannot be two fermions with the same quantum numbers at the same time and place, such decay is suppressed, according to the Pauli blocking principle.

One should note here that once the mixing of σ meson with the scalar diquarks is taken into account the σ meson can decay to quarks via the diquark channel. In this case, the rate of σ decay depends on the mixing and is numerically very small.

In order to illustrate the explanations above, it is instructive to display the part of the two-point correlator of pseudoscalar isovector currents that determines the inverse pion propagator. The calculations carried out by authors in [540] give the following result:

$$\begin{aligned} \Pi_{ab}(p_0) = & \frac{\delta_{ab}}{2G} - 8\delta_{ab} \int \frac{d^3q}{(2\pi)^3} \frac{E_{\Delta}^+ E_{\Delta}^- + E^+ E^- + \Delta^2}{E_{\Delta}^+ E_{\Delta}^-} \frac{E_{\Delta}^+ + E_{\Delta}^-}{(E_{\Delta}^+ + E_{\Delta}^-)^2 - p_0^2} \\ & - 16\delta_{ab} \int \frac{d^3q}{(2\pi)^3} \frac{\theta(E - \check{\mu})E}{4E^2 - p_0^2} \equiv \delta_{ab}\Pi(p_0), \end{aligned} \quad (7.4)$$

One can see from (7.4) that the inverse propagator of the pion can acquire an imaginary part (which represents its decay rate and is proportional to the pion width) only if the denominators of the integrand can be equal zero somewhere in the integration region. In fact, the integrands are not singular if the parameters correspond to on-shell pions in the 2SC phase. Look, the quantity $(E_{\Delta}^+ + E_{\Delta}^-)^2$ is an increasing function of 3-momentum and has the minimal value $\sqrt{(\bar{\mu} - m)^2 + |\Delta|^2} + \sqrt{(\bar{\mu} + m)^2 + |\Delta|^2}$ which is larger than 700 MeV. The second singularity (see the last integral in (7.4) is disabled because it is cut out by the θ -function that determines the energy spectrum of fermion states which are allowed, according to the Pauli blocking principle.

7.3 Pre-critical phenomena of color superconductivity

So far, we have discussed possible experimental signatures of the creation of the color-superconducting quark matter. In this section, we shall consider quark matter *in the normal phase* but near the critical temperature T_c of the color superconductivity and discuss the possibility to observe pre-critical phenomena of color superconductivity by the heavy-ion collisions. Our discussions are based on the observation that there can exist a rather wide pre-critical region of the color superconductivity in the T - μ plane at moderate density, as shown in Fig. 7.1: The large fluctuations of the diquark-Cooper pair field can survive even well above T_c owing to the strong coupling nature of the quark matter [542, 543]. The large diquark pair fluctuations may affect various observables leading to distinct *precursory phenomena* of the color superconductivity [542], and one may think of the possibility to see precursory phenomena of color superconductivity in the quark matter possibly created by the heavy-ion collisions *even if* the created matter is not cold enough to realize the color superconductivity.

In the extremely high-density region, the perturbative calculation should be valid and it shows that the quark matter in this region is the color superconductor of a strong type-I in which the fluctuations of the gauge fields dominate those of the diquark-pair field [544, 545]. The phase transition to the color-superconducting phase is a first order due to the gauge fluctuations in this region. On the other hand, the color superconductivity is expected to turn to a type-II at lower density [546]. Therefore, it should be appropriate to consider only the effect of the pair fluctuations at moderate density which is relevant to heavy-ion collisions.

The low energy effective models yield a large diquark gap $\Delta \sim 100$ MeV at moderate densities and vanishing temperature [538]. This implies that the ratio of the diquark coherence length to the average inter-quark length, which is proportional to E_F/Δ with E_F being the Fermi energy, can be as small as ~ 10 . This value is more than two or three order smaller than those of the metal superconductors; the stronger the interaction between the quarks, the

shorter the coherence length, which can be as small as almost the same order of the inter-quark distance [547, 548]. The short coherence length implies that the fluctuation of the pair field is significant and the mean-field approximation loses its validity.

It is known that the large fluctuations cause an excess of the specific heat, which eventually diverges at T_c owing to the critical fluctuations for the second order transition [534, 543]; such an anomalous increase of the specific heat may affect the cooling of the proto-compact stars. Here one should, however, notice that the critical divergence of the specific heat is essentially due to the static fluctuations of the pair field [549]. The analysis of the static fluctuations around the critical temperature as seen in the specific heat leads to the notion of the Ginzburg-Levanyuk region where the fluctuation overwhelms the mean-field [534, 543].

In the following, we turn to the discussions on the dynamical fluctuations of the diquark pair field. At finite temperature, the dynamical fluctuations of the pair field become also significant and develop a well-defined collective mode as the temperature is lowered toward T_c if the color superconducting phase transition is of second order or of weak first order. A calculation using the Nambu-Jona-Lasinio model shows that it is the case: The spectral function of the diquark fluctuations gets to have a sharp peak in the low-energy region at about $T = 1.2T_c$, and the peak position decreases as the temperature is lowered toward the critical temperature [542]. The collective mode associated with the fluctuations of the order parameter is called the soft mode of the phase transition.

Are there interesting phenomena owing to the existence of the soft mode of the color superconductivity in the heated quark matter at moderate densities? One of them is the formation of a pseudo-gap in the density of states (DOS) of quarks, i.e., an anomalous depression in the DOS around the Fermi surface [534, 550]: The DOS of the quark matter is calculated in [550] in the low-energy effective model: Here, the quark propagator is modified due to the coupling with the fluctuating pair-field or the pairing soft mode, as shown in Fig. 7.5. The resulting DOS above T_c is shown in Fig. 7.6 for several values of the quark chemical potential $\mu = 350, 400, 500$ MeV. One clearly sees that there appears a depression in the DOS around the Fermi energy for each μ

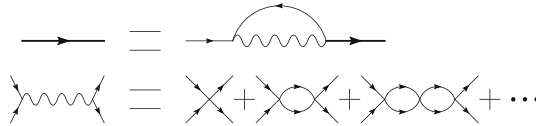


Fig. 7.5 The Feynman diagrams representing the quark Green function in the T-matrix approximation employed in [534]. The *thin (bold) lines* represent the free (full) propagator and the *wavy line* denotes the pairing soft mode.

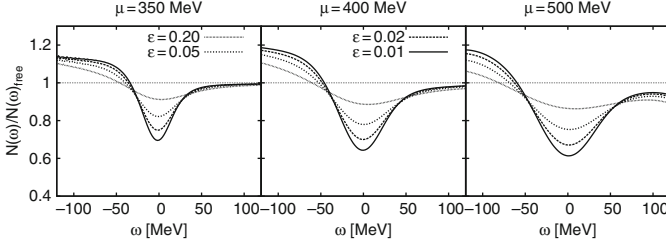


Fig. 7.6 Density of states for quark matter near but *above* T_c with several reduced temperatures $\varepsilon \equiv (T - T_c)/T_c$ and quark chemical potentials μ [550]. One sees a clear pseudogap phenomenon irrespective of μ near T_c .

near T_c , and they survive up to $\varepsilon \equiv (T - T_c)/T_c \approx 0.1$ irrespective of μ [534, 550]. In other words, there is a “pseudo-gap region” within the QGP phase above T_c up to $T^* = 1.1T_c$ at moderate densities. One should notice that the pseudo-gap in the DOS is a reflection that the quarks around the Fermi surface have a short life time owing to the decay process $q \rightarrow \text{hole} + (qq)_{\text{soft}}$ emitting the soft mode like Cherenkov process. This short-livedness of the quarks around the Fermi surface means that the heated quark matter at moderate densities can not be a Fermi liquid [534, 551]. It is noteworthy that the pseudo-gap formation is known as a characteristic behavior of the materials which become the high- T_c superconductors (HTSC) [552, 553]. Thus heated quark matter at moderate densities is similar to the HTSC materials rather than the usual superconductors of metals.

What observables are most favorable to see the effect of the existence of the soft mode composed of the fluctuations of the pair field in the quark matter? It is known in the condensed matter physics that pair fluctuations above T_c cause a large excess of the electric conductivity, which is called the para-conductivity. Two microscopic mechanisms that give rise to such an anomalous conductivity are identified and called Aslamazov-Larkin and Maki-Thompson terms [554–556], both of which are depicted in Fig. 7.7: The dotted lines in the figure denote the gauge field, i.e., the electro-magnetic field (or the photon) in this case. The *color-conductivity* would be also enhanced by the similar mechanisms near T_c of the color superconductivity, although it would be difficult to detect the conductivities directly in experiments. However, an idea is that the diagrams shown in Fig. 7.7 can be interpreted as modifications of the self-energy of the gauge fields, i.e., $\Pi^{\mu\nu}(Q) = \mathcal{F}[i\theta(t)\langle j^\mu(x), j^\nu(0) \rangle]$, where \mathcal{F} denotes the Fourier transformation. That is, the external photon or gluon fields can couple to the soft mode of the color superconductivity with the pairing soft mode in the diagrams being replaced by the diquark pair fields. Thus one sees that the *photon* self-energy $\Pi^{\mu\nu}(Q)$ in the quark matter at $T > T_c$ can be modified due to the fluctuations of the diquark pair field as well as inside the color superconducting phase [175]. This is interesting, because modifications of the photon

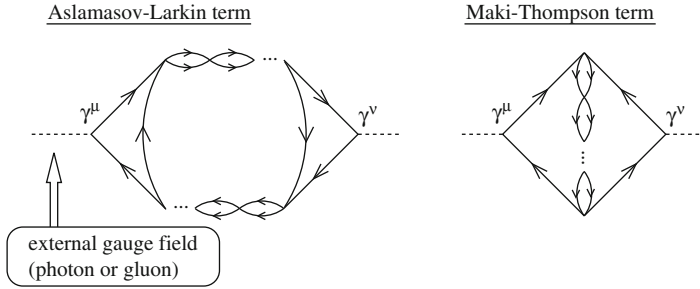


Fig. 7.7 The diagrams that contribute to the photon (or gluon) self-energy representing the Aslamasov-Larkin (*left*) and the Maki-Thompson (*right*) terms[534]. The wavy lines denote the soft mode.

self-energy due to the soft mode may be detected as an enhancement of the invariant-mass distribution of dileptons emitted from the created matter, as represented by the well-known formula (2.3), cf., e.g., [557]. The typical observable in experiment is the invariant-mass spectrum of dilepton production rate, which is given in terms of dR_{ee}/d^4q as

$$\frac{dR_{ee}}{dM^2} = \int \frac{d^3q}{2q^0} \frac{dR_{ee}}{d^4q}. \quad (7.5)$$

Figure 7.8 shows a preliminary result [558, 559] of dR_{ee}/dM^2 obtained from the $\Pi_{\mu\nu}(Q)$ with the AL term, which is evaluated in an approximate form. The solid lines denote the contributions of the AL term to the production rate for reduced temperatures $\varepsilon \equiv (T - T_c)/T_c$ at $\mu = 400$ MeV, while the dashed lines show the production rate from the free quark system for $T = T_c$ and $1.5 T_c$ at $\mu = 400$ MeV. The figure shows that the contribution of the AL term causes a large enhancement with a sharp peak structure in the production rate at very low masses, and the peak becomes larger and sharper as the temperature approaches T_c . Such a low-mass region is, however, where a large contribution due to π^0 Dalitz decays occurs. Therefore, these processes have to be disentangled to identify the AL process due to the precursory diquark pairing fluctuations, which might be, unfortunately, difficult to perform [559].¹ One should also estimate the contribution from the Maki-Tompson term as well as check the present estimate of the AL term.

Another open question is the relative magnitude of these processes compared to emission from the color-superconducting quark matter phase, if the latter is realized in experiment. In [175] dilepton production from the three-flavor color-flavor locked phase has been estimated, expected to be realized at extremely high densities; a similar behavior of dR_{ee}/dM^2 as that in Fig. 7.8

¹ We remark that the soft modes associated with the *chiral phase transition* at finite temperature can also cause an anomalous enhancement of the dilepton production rate [559]

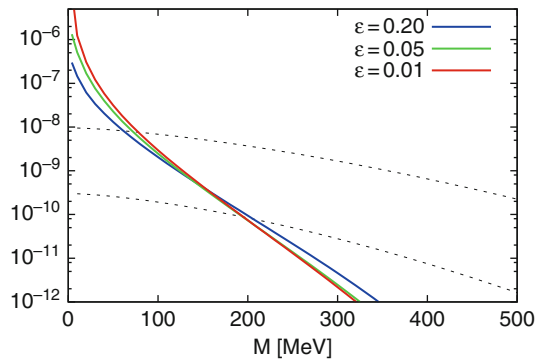


Fig. 7.8 A preliminary result for the dilepton production rates, Eq. (7.5), for several reduced temperatures $\varepsilon \equiv (T - T_c)/T_c$ near but above T_c with $\mu = 400$ MeV [558, 559]. The *solid lines* denote the contributions of the Aslamazov-Larkin term, while the *dashed lines* represent the dilepton rate from the free quark matter at $T = T_c$ (*below*) and $T = 1.5 T_c$ (*above*).

is observed, recall lower left panel in Fig. 2.23. A corresponding calculation of dilepton production rates from the 2SC phase has not yet been performed. If it turns out that a peak in the spectrum at not too small invariant masses can be identified, then one would possibly have an observational signal for the color-superconducting phase. This would be quite a unique characteristics of the CBM experiment, if CSC (or their precursor) phases are at all accessible in terrestrial heavy-ion collisions.

Chapter 8

Summary and relations to observables

Based on our discussion of excitations of strongly interacting matter in this part, let us reassess what we deem the most promising avenues for further progress in understanding the fundamental (microscopic) structure of QCD matter. Rather than aiming for completeness, we will focus in this summary on a few central points that relate to the questions posed in the introduction. Concerning the consequences for observables we will restrict ourselves to heavy-ion collisions and not allude to more elementary reactions (such as pA or πA).

A central issue is to find unambiguous signatures of chiral symmetry restoration, requiring a connection between observables and chiral order parameters. In Sect. 2.3.2 we have outlined a systematic approach that we believe can deliver this connection: Based on chiral model calculations of both in-medium (isovector) vector and axialvector correlators on the one hand, and on accurate (dilepton) measurements to constrain the vector spectral function on the other hand, one evaluates Weinberg sum rules that relate energy moments of “vector-minus-axialvector” spectral functions to chiral order parameters (pion radius and decay constants, 4-quark condensates). The four sum rules provide four moments which significantly constrain the energy, momentum and temperature dependence of any (experimentally) viable effective model for axial-/vector correlators. This connection is further strengthened if the order parameters are evaluated model-independently within lattice QCD. An additional, but not required, bonus would be experimental information on the in-medium axialvector spectral function, maybe in the $\pi^\pm\gamma$ channel. Especially the first two sum rules, Eqs. (2.31) and (2.32), which are moments in $1/s^2$ and $1/s$, emphasize the soft parts of the spectral functions. In light of model calculations which predict baryonic effects (a central point of CBM) to be most significant at masses below $M \simeq 0.4$ GeV (recall Fig. 2.14), the need for experimental access to this regime is compelling. From this perspective, dielectrons are preferable over dimuons.

The importance of soft electromagnetic (EM) observables is further amplified by the connection to susceptibilities and conductivities. These quantities

follow from spacelike zero-momentum and timelike zero-energy limits of vector and EM correlators, and have already been computed in lattice QCD. Experimentally, valuable information should be encoded in comparisons of ρ vs. ω spectral functions to study isovector vs. isoscalar susceptibilities; in this context an accurate excitation function of dilepton spectra is particularly important to possibly identify a regime of a large enhancement of the isoscalar susceptibility. Here an experimental bonus could come in form of the prolonged lifetime of a (pseudo-) mixed phase in the first-order regime which would naturally enhance pertinent dilepton emission. The EM conductivity, on the other hand, can be directly related to the (very) soft photon production rate, suggesting that a soft-photon measurement via HBT correlation methods (à la WA98) should be conducted.

In the open-charm sector we have identified transport properties of charm quarks and/or hadrons as promising quantities to connect matter properties with observables, in particular the pertinent charm diffusion coefficient(s). At RHIC, the observed suppression of primordial charm spectra (currently measured via semileptonic electron decays), and especially their collective behavior as reflected in the elliptic flow, $v_2(p_T)$, are instrumental in characterizing the produced strongly coupled medium. A key question is the microscopic origin of the underlying charm-quark interactions with the medium, e.g., whether they are driven by the quark or gluon component of the heat bath. Here, the baryon-rich matter in the CBM experiment might provide an improved discriminatory power, especially if nonperturbative effects in the vicinity of T_c play an important role (initial temperatures at CBM are not expected to significantly exceed $T_c \simeq 180$ MeV, in contrast to the early stages at RHIC). Arguments based on perturbative QCD suggest that in-medium properties of D mesons (or c -quarks) do not affect the total charm production cross section (being determined in hard N - N collisions, i.e., on a much shorter time scale than the formation of a D meson wave function). The relevance of hadronic medium effects on D meson spectral properties most likely resides in their transport properties as discussed above, as well as in their impact on charmonium decays (reduced thresholds). In fact, the conditions at CBM could facilitate the discrimination of hadronic from partonic effects: if hadronic reinteractions of D mesons are prevalent, the baryon-dominated matter should result in an asymmetry in D and \bar{D} (or e^+ and e^-) spectra, since the former (but not the latter) can interact via charm-exchange reactions ($D + N \rightarrow \pi + \Lambda_c$) or particle-hole excitations ($D \rightarrow \Lambda_c N^{-1}$). The asymmetry should manifest itself in stronger modifications (e.g., larger elliptic flow) of D mesons relative to \bar{D} 's. If the opposite is observed, it would be indicative for mesonic resonance interactions in the partonic stage ($\bar{c} + q \rightarrow \bar{D} \rightarrow \bar{c} + q$), which affect \bar{c} quarks stronger than c 's. If the modifications are about equal, it would still be indicative for QGP-driven reinteractions, since (i) even at CBM energies the quark-antiquark asymmetry in the QGP is moderate, and (ii) recent microscopic computations of charm transport in the QGP suggest an approximate balance between mesonic ($c\bar{q}$, $\bar{c}q$)

and diquark (c - q , \bar{c} - \bar{q}) interaction strengths. Measurements of charm baryons would further clarify these systematics.

Another fundamental aspect of the QCD phase diagram is the de-/confinement transition. Here, it is notoriously difficult to establish a close connection between observables and order parameters. The most promising one is probably the expectation value of the Polyakov loop which characterizes the (exponent of the) large-distance limit of the free energy of a heavy-quark pair, and thus relates to in-medium charmonium properties. Whether in practice this corresponds to a dissolution of (certain) charmonium bound states, or rather a (possibly sharp) increase in their width across T_c , remains an open problem at present. Also here it will be essential to quantify the strength of the hadronic dissociation rates of charmonia, especially for ψ' and χ_c states which are rather close to the $D\bar{D}$ threshold and are therefore expected to be particularly sensitive to in-medium modifications of D mesons (possibly related to chiral symmetry restoration). Since the suppression of direct J/ψ 's in the QGP could be rather small, an accurate assessment of the χ_c feeddown will be mandatory (as well as a precise determination of (primordial) nuclear absorption effects in p - A reactions; primordial ψ' production is expected to be small).

With the tools and strategies utilizing electromagnetic and charm probes as described above, we believe that we can significantly advance our understanding of a fundamental form of matter that under laboratory conditions is only accessible in energetic collisions of heavy nuclei. A close collaboration between theory and experiment will be mandatory in this endeavor.

References

1. R. Rapp, J. Phys. G **34**, S405 (2007) [339](#)
2. R.J. Porter, et al. [DLS Collaboration], Phys. Rev. Lett. **79**, 1229 (1997) [344](#)
3. W.K. Wilson, et al. [DLS Collaboration], Phys. Rev. C **57**, 1865 (1998) [344](#)
4. E.L. Bratkovskaya, W. Cassing, R. Rapp, J. Wambach, Nucl. Phys. A **634**, 168 (1998) [344](#)
5. C. Ernst, S.A. Bass, M. Belkacem, H. Stöcker, W. Greiner, Phys. Rev. C **58**, 447 (1998)
6. E.L. Bratkovskaya, C.M. Ko, Phys. Lett. B **445**, 265 (1999)
7. K. Shekhter, C. Fuchs, A. Faessler, M. Krivoruchenko, B. Martemyanov, Phys. Rev. C **68**, 014904 (2003) [344](#)
8. P. Salabura, et al. [HADES Collaboration], Nucl. Phys. A **749**, 150 (2005) [344](#)
9. T. Christ, et al. [HADES Collaboration], Int. J. Mod. Phys. A **22**, 600 (2007) [344](#)
10. G. Agakishiev, et al. [HADES Collaboration], Phys. Lett. B **663**, 43 (2008) [344](#)
11. A.L.S. Angelis, et al. [HELIOS/3 Collaboration], Eur. Phys. J. C **13**, 433 (2000) [344](#)
12. M.C. Abreu, et al. [NA38 and NA50 Collaborations], Eur. Phys. J. C **13**, 69 (2000) [344](#)
13. G. Agakishiev, et al. [CERES Collaboration], Phys. Rev. Lett. **75**, 1272 (1995) [344](#)
14. G. Agakishiev, et al. [CERES/NA45 Collaboration], Phys. Lett. B **422**, 405 (1998) [344](#)
15. R. Rapp, J. Wambach, Adv. Nucl. Phys. **25**, 1 (2000) [344](#), [364](#)
16. J. Alam, S. Sarkar, P. Roy, T. Hatsuda, B. Sinha, Annals Phys. **286**, 159 (2001) [392](#)
17. C. Gale, K. Haglin, *Quark gluon plasma 3* (R.C. Hwa, X.-N. Wang (Eds.), 2003). [arXiv:hep-ph/0306098]
18. M. Harada, K. Yamawaki, Phys. Rept. **381**, 1 (2003) [366](#), [375](#), [376](#), [377](#), [378](#), [379](#)
19. G.E. Brown, M. Rho, Phys. Rep. **396**, 1 (2004) [344](#), [364](#)

20. R. Rapp, arXiv:nucl-th/0502020 [344](#)
21. S. Damjanovic, et al. [NA60 Collaboration], Nucl. Phys. A **774**, 715 (2006) [344](#), [364](#)
22. E.L. Bratkovskaya, W. Cassing, Nucl. Phys. A **619**, 413 (1997) [344](#)
23. D. Adamova, et al. [CERES/NA45 Collaboration], Phys. Rev. Lett. **91**, 042301 (2003) [345](#), [393](#)
24. M.M. Aggarwal, et al. [WA98 Collaboration], Phys. Rev. Lett. **85**, 3595 (2000) [345](#), [393](#), [394](#)
25. M.M. Aggarwal, et al. [WA98 Collaboration], Phys. Rev. Lett. **93**, 022301 (2004) [345](#), [393](#), [394](#)
26. S. Turbide, R. Rapp, C. Gale, Phys. Rev. C **69**, 014903 (2004) [345](#), [393](#), [394](#)
27. G. David, R. Rapp, Z. Xu, Phys. Rep. **462**, 176 (2008) [345](#), [363](#)
28. A.N. Sissakian, A.S. Sorin, M.K. Suleymanov, V.D. Toneev, G.M. Zinovjev, Phys. Part. Nucl. Lett. **5**, 1 (2008) [345](#)
29. L.D. McLerran, T. Toimela, Phys. Rev. D **31**, 545 (1985) [346](#)
30. W.M. Yao, et al., J. Phys. G **33**, 1 (2006). [<http://pdg.lbl.gov/>] [349](#), [360](#), [395](#), [403](#)
31. Z. Huang, Phys. Lett. B **361**, 131 (1995) [349](#)
32. R. Rapp, J. Phys. G **31**, S217 (2005) [347](#), [394](#)
33. M. Dey, V.L. Eletsky, B.L. Ioffe, Phys. Lett. B **252**, 620 (1990) [349](#), [356](#)
34. R. Arnaldi, et al. [NA60 Collaboration], Phys. Rev. Lett. **96**, 162302 (2006) [349](#), [382](#), [384](#), [390](#), [393](#), [403](#)
35. H. van Hees, R. Rapp, Phys. Rev. Lett. **97**, 102301 (2006) [349](#), [382](#), [388](#), [390](#), [403](#)
36. H. van Hees, R. Rapp, arXiv:hep-ph/0604269 [349](#)
37. B. Krippa, Phys. Lett. B **427**, 13 (1998) [349](#)
38. G. Chanfray, J. Delorme, M. Ericson, M. Rosa-Clot, Phys. Lett. B **455**, 39 (1999) [349](#)
39. M. Urban, M. Buballa, J. Wambach, Phys. Rev. Lett. **88**, 042002 (2002) [349](#)
40. M. Harada, C. Sasaki, W. Weise, Phys. Rev. D **78**, 114003 (2008) [349](#)
41. R. Barate, et al. [ALEPH Collaboration], Eur. Phys. J. C **4**, 409 (1998) [350](#), [362](#)
42. K. Ackerstaff, et al. [OPAL Collaboration], Eur. Phys. J. C **7**, 571 (1999) [350](#), [362](#)
43. J.V. Steele, H. Yamagishi, I. Zahed, Phys. Lett. B **384**, 255 (1996) [350](#)
44. J.V. Steele, H. Yamagishi, I. Zahed, Phys. Rev. D **56**, 5605 (1997) [350](#), [389](#)
45. J.V. Steele, I. Zahed, Phys. Rev. D **60**, 037502 (1999) [350](#), [370](#), [371](#), [388](#)
46. M.A. Shifman, A.I. Vainshtein, V.I. Zakharov, Nucl. Phys. B **147**, 385 (1979) [351](#)
47. S. Weinberg, Phys. Rev. Lett. **18**, 507 (1967) [351](#), [360](#), [361](#)
48. J.M. Eisenberg, W. Greiner, *Nuclear Theory*, vol. 2 (North-Holland Publishing Company Amsterdam, 1970) [351](#)
49. S. Narison, *QCD as Theory of Hadrons* (Cambridge University Press, Cambridge, 2004) [352](#), [452](#)
50. M.A. Shifman, A.I. Vainshtein, V.I. Zakharov, Nucl. Phys. B **147**, 448 (1979) [352](#)
51. B.L. Ioffe, Nucl. Phys. B **188**, 317 (1981). [Erratum-ibid. B **191**, 591 (1981)] [352](#), [406](#)
52. A.I. Bochkarev, M.E. Shaposhnikov, Nucl. Phys. B **268**, 220 (1986) [352](#)

53. T. Hatsuda, S.H. Lee, Phys. Rev. C **46**, 34 (1992) [352](#), [356](#), [357](#), [360](#)
54. M. Asakawa, C.M. Ko, Phys. Rev. C **48**, 526 (1993) [353](#), [356](#), [365](#), [366](#), [367](#)
55. F. Klingl, N. Kaiser, W. Weise, Nucl. Phys. A **624**, 527 (1997) [356](#), [357](#), [358](#), [365](#)
56. S. Leupold, W. Peters, U. Mosel, Nucl. Phys. A **628**, 311 (1998) [356](#), [357](#), [372](#)
57. S. Zschocke, O.P. Pavlenko, B. Kämpfer, Eur. Phys. J. A **15**, 529 (2002) [356](#), [358](#)
58. J. Ruppert, T. Renk, B. Müller, Phys. Rev. C **73**, 034907 (2006) [353](#), [356](#)
59. S. Zschocke, B. Kämpfer, G. Plunien, Phys. Rev. D **72**, 014005 (2005) [353](#)
60. R. Brockmann, W. Weise, Phys. Lett. B **367**, 40 (1996) [353](#)
61. J.R. Pelaez, Phys. Rev. D **59**, 014002 (1999)
62. G.X. Peng, U. Lombardo, M. Loewe, H.C. Chiang, P.Z. Ning, Int. J. Mod. Phys. A **18**, 3151 (2003) [353](#)
63. E.G. Drukarev, E.M. Levin, Prog. Part. Nucl. Phys. **27**, 77 (1991) [353](#)
64. T.D. Cohen, R.J. Furnstahl, D.K. Griegel, Phys. Rev. C **45**, 1881 (1992) [353](#)
65. R. Thomas, S. Zschocke, T. Hilger, B. Kämpfer, arXiv:hep-ph/0602163 [353](#), [354](#)
66. G. Chanfray, M. Ericson, J. Wambach, Phys. Lett. B **388**, 673 (1996) [353](#)
67. M.C. Birse, Acta Phys. Polon. B **29**, 2357 (1998) [353](#)
68. S. Zschocke, B. Kämpfer, Phys. Rev. C **70**, 035207 (2004) [355](#), [358](#), [360](#)
69. W. Florkowski, W. Broniowski, Nucl. Phys. A **651**, 397 (1999) [355](#)
70. T. Hatsuda, Y. Koike, S.H. Lee, Nucl. Phys. B **394**, 221 (1993) [356](#), [357](#)
71. V.L. Eletsky, B.L. Ioffe, Phys. Rev. D **51**, 2371 (1995) [356](#)
72. T. Hatsuda, S.H. Lee, H. Shiomi, Phys. Rev. C **52**, 3364 (1995) [356](#)
73. X. m. Jin, D.B. Leinweber, Phys. Rev. C **52**, 3344 (1995) [356](#)
74. Y. Koike, A. Hayashigaki, Prog. Theor. Phys. **98**, 631 (1997) [356](#)
75. S.H. Lee, Phys. Rev. C **57**, 927 (1998). [Erratum-ibid. C **58**, 3771 (1998)] [356](#)
76. S. Leupold, U. Mosel, Phys. Rev. C **58**, 2939 (1998) [356](#)
77. R. Hofmann, T. Gutsche, A. Faessler, Eur. Phys. J. C **17**, 651 (2000) [356](#)
78. E. Marco, R. Hofmann, W. Weise, Phys. Lett. B **530**, 88 (2002) [356](#)
79. S. Zschocke, O.P. Pavlenko, B. Kämpfer, Prog. Part. Nucl. Phys. **53**, 317 (2004) [356](#)
80. R. Thomas, S. Zschocke, B. Kämpfer, Phys. Rev. Lett. **95**, 232301 (2005) [358](#), [359](#)
81. B. Steinmueller, S. Leupold, Nucl. Phys. A **778**, 195 (2006) [356](#), [357](#)
82. M.F.M. Lutz, G. Wolf, B. Friman, Nucl. Phys. A **706**, 431 (2002). [Erratum-ibid. A **765**, 431 (2006)] [370](#), [371](#), [383](#), [384](#)
83. P. Muehlich, V. Shklyar, S. Leupold, U. Mosel, M. Post, Nucl. Phys. A **780**, 187 (2006) [357](#), [383](#), [384](#)
84. M. Naruki, et al. [E325 Collaboration], Phys. Rev. Lett. **96**, 092301 (2006) [358](#), [360](#), [364](#), [382](#), [383](#)
85. D. Trnka, et al. [CBELSA/TAPS Collaboration], Phys. Rev. Lett. **94**, 192303 (2005) [358](#), [364](#), [382](#), [383](#)
86. Y. Kwon, M. Procura, W. Weise, Phys. Rev. C **78**, 055203 (2008) [358](#)
87. R. Rapp, G. Chanfray, J. Wambach, Nucl. Phys. A **617**, 472 (1997) [358](#), [365](#), [367](#)
88. R. Rapp, J. Wambach, Eur. Phys. J. A **6**, 415 (1999) [358](#), [365](#), [371](#), [374](#), [375](#), [389](#)
89. R.R. Akhmetshin, et al. [CMD-2 Collaboration], Phys. Lett. B **527**, 161 (2002) [360](#)

90. R. Veenhof, *Proc. of the 21. Winter Workshop on Nuclear Dynamics and Breckenridge, Co and USA* (Feb. 05-12, 2005) [360](#)
91. E.G. Floratos, S. Narison, E. de Rafael, Nucl. Phys. B **155**, 115 (1979) [361](#)
92. S. Narison, Z. Phys. C **14**, 263 (1982)
93. V. Dmitrasinovic, Phys. Rev. D **57**, 7019 (1998) [361](#)
94. T. Das, V.S. Mathur, S. Okubo, Phys. Rev. Lett. **19**, 859 (1967) [362](#)
95. J.I. Kapusta, E.V. Shuryak, Phys. Rev. D **49**, 4694 (1994) [362](#)
96. R. Rapp, Pramana **60**, 675 (2003) [363](#)
97. R. Rapp, Nucl. Phys. A **725**, 254 (2003) [363](#), [401](#), [402](#), [403](#), [404](#)
98. J. Adams, et al. [STAR Collaboration], Phys. Rev. Lett. **92**, 092301 (2004) [363](#), [401](#), [402](#), [403](#), [404](#)
99. J.K. Ahn, et al., Phys. Lett. B **608**, 215 (2005) [364](#), [384](#)
100. V. Bernard, U.G. Meissner, Nucl. Phys. A **489**, 647 (1988) [364](#)
101. M. Oertel, M. Buballa, J. Wambach, Phys. Atom. Nucl. **64**, 698 (2001) [364](#)
102. M. Velkovsky, E.V. Shuryak, Phys. Rev. D **56**, 2766 (1997) [364](#)
103. G. Chanfray, P. Schuck, Nucl. Phys. A **555**, 329 (1993) [365](#), [366](#), [367](#)
104. M. Herrmann, B.L. Friman, W. Nörenberg, Nucl. Phys. A **560**, 411 (1993) [365](#), [366](#)
105. R. Rapp, G. Chanfray, J. Wambach, Phys. Rev. Lett. **76**, 368 (1996) [365](#), [366](#), [367](#)
106. B. Friman, H.J. Pirner, Nucl. Phys. A **617**, 496 (1997) [365](#), [369](#), [370](#), [371](#)
107. W. Peters, M. Post, H. Lenske, S. Leupold, U. Mosel, Nucl. Phys. A **632**, 109 (1998) [365](#), [369](#), [370](#), [371](#)
108. R. Rapp, C. Gale, Phys. Rev. C **60**, 024903 (1999) [365](#), [373](#), [374](#)
109. M. Urban, M. Buballa, R. Rapp, J. Wambach, Nucl. Phys. A **673**, 357 (2000) [365](#), [371](#)
110. H. van Hees, J. Knoll, Nucl. Phys. A **683**, 369 (2000) [365](#), [368](#), [373](#)
111. M. Post, S. Leupold, U. Mosel, Nucl. Phys. A **689**, 753 (2001) [365](#), [369](#), [370](#), [371](#)
112. D. Cabrera, E. Oset, M.J.V. Vacas, Nucl. Phys. A **705**, 90 (2002) [365](#), [366](#), [371](#)
113. F. Riek, J. Knoll, Nucl. Phys. A **740**, 287 (2004) [365](#), [367](#), [368](#), [369](#), [385](#)
114. J. Ruppert, T. Renk, Phys. Rev. C **71**, 064903 (2005). [Erratum-ibid. C **75**, 059901(E) (2007)] [365](#), [368](#), [373](#)
115. E. Santini, M.D. Cozma, A. Faessler, C. Fuchs, M.I. Krivoruchenko, B. Martemyanov, Phys. Rev. C **78**, 034910 (2008) [365](#)
116. G.E. Brown, M. Rho, Phys. Rept. **363**, 85 (2002) [366](#)
117. M. Urban, M. Buballa, R. Rapp, J. Wambach, Nucl. Phys. A **641**, 433 (1998) [367](#), [368](#), [369](#), [372](#)
118. R. Rapp, M. Urban, M. Buballa, J. Wambach, Phys. Lett. B **417**, 1 (1998) [367](#), [369](#), [370](#), [371](#), [372](#), [388](#), [389](#)
119. F. Riek, H. van Hees, J. Knoll, Phys. Rev. C **75**, 059801 (2007) [368](#)
120. S. Leupold, Phys. Lett. B **646**, 155 (2007) [368](#)
121. D.M. Manley, R.A. Arndt, Y. Goradia, V.L. Teplitz, Phys. Rev. D **30**, 904 (1984) [370](#), [371](#)
122. A. Zabrodin, et al., Phys. Rev. C **60**, 055201 (1999)
123. W. Langgärtner, et al., Phys. Rev. Lett. **87**, 052001 (2001) [370](#)
124. R. Rapp, arXiv:nucl-th/9804065 [370](#)

125. M. Post, S. Leupold, U. Mosel, Nucl. Phys. A **741**, 81 (2004) [371](#), [372](#), [407](#), [408](#)
126. T.P. Vrana, S.A. Dytman, T.S.H. Lee, Phys. Rept. **328**, 181 (2000) [371](#)
127. R.D. Pisarski, Phys. Lett. B **110**, 155 (1982) [373](#)
128. C.A. Dominguez, M. Loewe, J.C. Rojas, Z. Phys. C **59**, 63 (1993) [373](#)
129. C. Gale, J.I. Kapusta, Nucl. Phys. B **357**, 65 (1991) [373](#)
130. R. Rapp, J. Wambach, Phys. Lett. B **351**, 50 (1995) [373](#), [404](#)
131. C. Song, V. Koch, Phys. Rev. C **54**, 3218 (1996) [373](#), [381](#)
132. A.G. Nicola, F.J. Llanes-Estrada, J.R. Pelaez, Phys. Lett. B **606**, 351 (2005) [373](#)
133. V.L. Eletsky, M. Belkacem, P.J. Ellis, J.I. Kapusta, Phys. Rev. C **64**, 035202 (2001) [373](#), [374](#), [375](#), [384](#), [385](#)
134. R. Rapp, Phys. Rev. C **63**, 054907 (2001) [374](#), [384](#), [385](#)
135. M. Harada, K. Yamawaki, Phys. Rev. Lett. **86**, 757 (2001) [376](#), [377](#)
136. M. Harada, C. Sasaki, Phys. Lett. B **537**, 280 (2002) [376](#), [377](#), [378](#), [381](#)
137. M. Harada, Y. Kim, M. Rho, Phys. Rev. D **66**, 016003 (2002) [376](#), [377](#), [378](#), [382](#)
138. M. Bando, T. Kugo, S. Uehara, K. Yamawaki, T. Yanagida, Phys. Rev. Lett. **54**, 1215 (1985) [376](#)
139. M. Bando, T. Kugo, K. Yamawaki, Phys. Rept. **164**, 217 (1988) [376](#)
140. H. Georgi, Phys. Rev. Lett. **331**, 311 (1989) [376](#)
141. M. Harada, K. Yamawaki, Phys. Lett. B **297**, 151 (1992)
142. M. Tanabashi, Phys. Lett. B **316**, 534 (1993) [376](#)
143. M. Harada, K. Yamawaki, Phys. Rev. Lett. **87**, 152001 (2001) [377](#)
144. M. Harada, S. Matsuzaki, K. Yamawaki, Phys. Rev. D **74**, 076004 (2006) [377](#)
145. M. Harada, K. Yamawaki, Phys. Rev. D **64**, 014023 (2001) [377](#)
146. M. Harada, C. Sasaki, Nucl. Phys. A **736**, 300 (2004) [377](#), [378](#)
147. M. Harada, Y. Kim, M. Rho, C. Sasaki, Nucl. Phys. A **727**, 437 (2003)
148. C. Sasaki, Nucl. Phys. A **739**, 151 (2004)
149. M. Harada, Y. Kim, M. Rho, C. Sasaki, Nucl. Phys. A **730**, 379 (2004)
150. M. Harada, M. Rho, C. Sasaki, arXiv:hep-ph/0506092 [377](#)
151. M. Harada, M. Rho, C. Sasaki, Phys. Rev. D **70**, 074002 (2004) [378](#)
152. M. Harada, C. Sasaki, Phys. Rev. D **74**, 114006 (2006) [378](#), [379](#), [380](#), [381](#), [390](#), [391](#)
153. G.E. Brown, C.H. Lee, M. Rho, Nucl. Phys. A **747**, 530 (2005) [379](#)
154. G.E. Brown, C.H. Lee, M. Rho, Phys. Rev. C **74**, 024906 (2006) [379](#)
155. C. Sasaki, PhD thesis, Nagoya University (2005), arXiv:hep-ph/0504073 [379](#)
156. R. Nasseripour, et al. [CLAS Collaboration], Phys. Rev. Lett. **99**, 262302 (2007) [382](#), [383](#)
157. F. Klingl, S. Kim, S.H. Lee, P. Morath, Phys. Rev. Lett. **82**, 3396 (1999). [Erratum-ibid. **83**, 4224 (1999)] [383](#), [384](#), [496](#)
158. F. Eichstaedt, S. Leupold, U. Mosel, arXiv:hep-ph/0703170 [384](#)
159. K. Haglin, Nucl. Phys. A **584**, 719 (1995) [384](#)
160. R.A. Schneider, W. Weise, Phys. Lett. B **515**, 89 (2001) [384](#), [385](#)
161. A.T. Martell, P.J. Ellis, Phys. Rev. C **69**, 065206 (2004) [384](#), [385](#)
162. R. Muto, et al., Phys. Rev. Lett. **98**, 042501 (2007) [384](#)
163. D. Cabrera, et al., Nucl. Phys. A **733**, 130 (2004) [384](#)

164. L. Alvarez-Ruso, V. Koch, Phys. Rev. C **65**, 054901 (2002) [385](#)
165. M. Asakawa, T. Hatsuda, Y. Nakahara, Prog. Part. Nucl. Phys. **46**, 459 (2001) [386](#)
166. F. Karsch, E. Laermann, P. Petreczky, S. Stickan, I. Wetzorke, Phys. Lett. B **530**, 147 (2002) [386](#), [387](#)
167. E. Braaten, R.D. Pisarski, T.C. Yuan, Phys. Rev. Lett. **64**, 2242 (1990) [386](#), [387](#)
168. G.D. Moore, J.M. Robert, arXiv:hep-ph/0607172 [386](#), [387](#)
169. S. Gupta, Phys. Lett. B **597**, 57 (2004) [387](#)
170. G. Aarts, C. Allton, J. Foley, S. Hands, S. Kim, Phys. Rev. Lett. **99**, 022002 (2007) [387](#)
171. D. Fernandez-Fraile, A.G. Nicola, Phys. Rev. D **73**, 045025 (2006) [388](#)
172. D. Fernandez-Fraile, A.G. Nicola, Eur. Phys. J. A **31**, 848 (2007) [388](#)
173. W. Liu, R. Rapp, Nucl. Phys. A **796**, 101 (2007) [388](#), [394](#)
174. N.M. Kroll, T.D. Lee, B. Zumino, Phys. Rev. **157**, 1376 (1967) [388](#)
175. P. Jaikumar, R. Rapp, I. Zahed, Phys. Rev. C **65**, 055205 (2002) [389](#), [505](#), [506](#)
176. K. Dusling, D. Teaney, I. Zahed, Phys. Rev. C **75**, 024908 (2007) [388](#), [390](#)
177. T. Peitzmann, M.H. Thoma, Phys. Rep. **364**, 175 (2002) [392](#)
178. F. Arleo et al., arXiv:hep-ph/0311131 [393](#)
179. R. Rapp, Mod. Phys. Lett. A **19**, 1717 (2004) [392](#)
180. G. Agakichiev, et al. [CERES Collaboration], Eur. Phys. J. C **41**, 475 (2005) [393](#)
181. S. Turbide, private communication (2004) [394](#)
182. D.K. Srivastava, Phys. Rev. C **71**, 034905 (2005) [394](#)
183. T. Hatsuda, T. Kunihiro, Phys. Lett. B **185**, 304 (1987) [395](#)
184. M.K. Volkov, E.A. Kuraev, D. Blaschke, G. Röpke, S.M. Schmidt, Phys. Lett. B **424**, 235 (1998) [395](#), [396](#), [398](#)
185. R. Rapp, et al., Phys. Rev. C **59**, 1237 (1999) [397](#), [404](#)
186. Y. Hidaka, O. Morimatsu, T. Nishikawa, M. Ohtani, Phys. Rev. D **68**, 111901 (2003) [397](#)
187. H.A. Weldon, Phys. Lett. B **274**, 133 (1992) [397](#)
188. O. Teodorescu, A.K. Dutt-Mazumder, C. Gale, Phys. Rev. C **63**, 034903 (2001) [397](#)
189. A.E. Radzhabov, M.K. Volkov, arXiv:hep-ph/0509288 [397](#)
190. A.E. Radzhabov, M.K. Volkov, V.L. Yudichev, J. Phys. G **32**, 111 (2006) [397](#)
191. D. Blaschke, Y.L. Kalinovsky, S.M. Schmidt, H.J. Schulze, Phys. Rev. C **57**, 438 (1998) [397](#)
192. M.K. Volkov, A.E. Radzhabov, N.L. Russakovich, Phys. Atom. Nucl. **66**, 997 (2003) [398](#)
193. T. Hatsuda, T. Kunihiro, arXiv:nucl-th/0112027 [398](#)
194. E.L. Hjort, et al., Phys. Rev. Lett. **79**, 4345 (1997) [401](#), [408](#)
195. M. Eskef, et al. [FOPI Collaboration], Eur. Phys. J. A **3**, 335 (1998) [401](#), [408](#)
196. H.B. Zhang, et al. [STAR Collaboration], arXiv:nucl-ex/0403010 [401](#)
197. B.B. Back, et al. [E917 Collaboration], Phys. Rev. C **69**, 054901 (2004) [401](#)
198. D. Adamova, et al. [CERES Collaboration], Phys. Rev. Lett. **96**, 152301 (2006) [401](#)

- 199. S.S. Adler, et al. [PHENIX Collaboration], Phys. Rev. C **72**, 014903 (2005) [401](#)
- 200. C. Markert, et al. [STAR Collaboration], J. Phys. G **30**, S1313 (2004) [401](#)
- 201. P. Fachini, J. Phys. G **30**, S735 (2004) [401](#), [408](#), [409](#)
- 202. E.V. Shuryak, G.E. Brown, Nucl. Phys. A **717**, 322 (2003) [402](#), [404](#)
- 203. P.F. Kolb, M. Prakash, Phys. Rev. C **67**, 044902 (2003) [402](#)
- 204. W. Broniowski, W. Florkowski, B. Hiller, Phys. Rev. C **68**, 034911 (2003) [403](#)
- 205. S. Pratt, W. Bauer, Phys. Rev. C **68**, 064905 (2003) [403](#)
- 206. A. Ayala, J.G. Contreras, J. Magnin, Phys. Lett. B **603**, 165 (2004) [402](#)
- 207. H.W. Barz, G. Bertsch, B.L. Friman, H. Schulz, S. Boggs, Phys. Lett. B **265**, 219 (1991) [402](#)
- 208. P. Fachini, R.S. Longacre, Z. Xu, H. Zhang, J. Phys. G **33**, 431 (2007) [403](#)
- 209. R. Dashen, S.K. Ma, H.J. Bernstein, Phys. Rev. **187**, 345 (1969) [403](#)
- 210. W. Weinhold, B. Friman, W. Nörenberg, Phys. Lett. B **433**, 236 (1998) [403](#)
- 211. P. Braun-Munzinger, K. Redlich, J. Stachel, arXiv:nucl-th/0304013 [403](#), [411](#), [449](#)
- 212. S. Damjanovic, Eur. Phys. J. C **49**, 235 (2007) [403](#)
- 213. M. Bleicher, H. Stoecker, J. Phys. G **30**, S111 (2004) [403](#)
- 214. N. Grion, et al. [CHAOS Collaboration], Nucl. Phys. A **763**, 80 (2005) [404](#)
- 215. A. Starostin, et al. [Crystal Ball Collaboration], Phys. Rev. Lett. **85**, 5539 (2000)
- 216. J.G. Messchendorp, et al., Phys. Rev. Lett. **89**, 222302 (2002) [404](#)
- 217. M.J.V. Vacas, E. Oset, Phys. Rev. C **60**, 064621 (1999) [404](#)
- 218. T. Hatsuda, T. Kunihiro, H. Shimizu, Phys. Rev. Lett. **82**, 2840 (1999) [404](#)
- 219. O. Buss, L. Alvarez-Ruso, A.B. Larionov, U. Mosel, Phys. Rev. C **74**, 044610 (2006) [404](#)
- 220. F. Bloch, et al., Eur. Phys. J. A **32**, 219 (2007) [404](#)
- 221. Z. Aouissat, R. Rapp, G. Chanfray, P. Schuck, J. Wambach, Nucl. Phys. A **581**, 471 (1995) [404](#)
- 222. V.L. Eletsky, B.L. Ioffe, Phys. Rev. D **47**, 3083 (1993) [405](#)
- 223. L.Y. Glozman, Phys. Lett. B **475**, 329 (2000) [405](#), [406](#)
- 224. D. Jido, T. Hatsuda, T. Kunihiro, Phys. Rev. Lett. **84**, 3252 (2000) [405](#)
- 225. D. Jido, M. Oka, A. Hosaka, Prog. Theor. Phys. **106**, 873 (2001) [405](#)
- 226. E.E. Kolomeitsev, M.F.M. Lutz, Phys. Lett. B **585**, 243 (2004) [405](#)
- 227. L.Y. Glozman, Phys. Rep. **444**, 1 (2007) [405](#)
- 228. U.G. Meissner, PoS **LAT2005**, 009 (2006) [405](#), [406](#)
- 229. A.W. Thomas, W. Weise, *The Structure of the Nucleon* (Wiley-VCH, 2001) [406](#)
- 230. R. Thomas, T. Hilger, B. Kämpfer, Nucl. Phys. A **795**, 19 (2007) [406](#)
- 231. V.M. Braun, P. Gornicki, L. Mankiewicz, A. Schäfer, Phys. Lett. B **302**, 291 (1993) [406](#)
- 232. R.J. Furnstahl, X. Jin, D.B. Leinweber, Phys. Lett. B **387**, 253 (1996) [406](#)
- 233. M.C. Birse, B. Krippa, Phys. Lett. B **381**, 397 (1996) [407](#)
- 234. T.D. Cohen, R.J. Furnstahl, D.K. Griegel, X. Jin, Prog. Part. Nucl. Phys. **35**, 221 (1995) [407](#)

235. R. Thomas, T. Hilger, B. Kämpfer, Phys. Rev. C **79**, 025202 (2009) [407](#)
236. O. Plohl, C. Fuchs, Phys. Rev. C **74**, 034325 (2006) [407](#)
237. M.B. Johnson, L.S. Kisslinger, Phys. Rev. C **52**, 1022 (1995) [407](#)
238. Y. Kondo, O. Morimatsu, T. Nishikawa, Y. Kanada-En'yo, Phys. Rev. D **75**, 034010 (2007) [407](#)
239. F.X. Lee, Nucl. Phys. A **791**, 352 (2007) [407](#)
240. M.J. Savage, M.B. Wise, Phys. Rev. D **53**, 349 (1996) [407](#)
241. E. Oset, L.L. Salcedo, Nucl. Phys. A **468**, 631 (1987) [408](#)
242. A.B. Migdal, E.E. Saperstein, M.A. Troitsky, D.N. Voskresensky, Phys. Rep. **192**, 179 (1990)
243. C.L. Korpa, M.F.M. Lutz, Nucl. Phys. A **742**, 305 (2004)
244. H. van Hees, R. Rapp, Phys. Lett. B **606**, 59 (2005) [408](#), [409](#)
245. Y. Pang, T.J. Schlagel, S.H. Kahana, Phys. Rev. Lett. **68**, 2743 (1992) [409](#)
246. A.B. Larionov, W. Cassing, M. Effenberger, U. Mosel, Eur. Phys. J. A **7**, 507 (2000) [409](#)
247. H. Leutwyler, A.V. Smilga, Nucl. Phys. B **342**, 302 (1990) [409](#)
248. J. Rafelski, B. Muller, Phys. Rev. Lett. **48**, 1066 (1982). [Erratum-ibid. **56**, 2334 (1986)] [411](#)
249. J. Rafelski, Eur. Phys. J. ST **155**, 139 (2008) [411](#)
250. D.B. Kaplan, A.E. Nelson, Phys. Lett. B **175**, 57 (1986) [412](#)
251. A.E. Nelson, D.B. Kaplan, Phys. Lett. B **192**, 193 (1987) [412](#)
252. G.E. Brown, M. Rho, Phys. Rep. **269**, 333 (1996) [412](#)
253. G.E. Brown, C.H. Lee, M. Rho, V. Thorsson, Nucl. Phys. A **567**, 937 (1994)
254. G.E. Brown, K. Kubodera, M. Rho, V. Thorsson, Phys. Lett. B **291**, 355 (1992)
255. E.E. Kolomeitsev, D.N. Voskresensky, B. Kämpfer, Nucl. Phys. A **588**, 889 (1995)
256. N. Kaiser, P.B. Siegel, W. Weise, Nucl. Phys. A **594**, 325 (1995) [414](#), [417](#)
257. G.E. Brown, M. Rho, Nucl. Phys. A **596**, 503 (1996) [414](#), [415](#), [421](#)
258. T. Waas, N. Kaiser, W. Weise, Phys. Lett. B **379**, 34 (1996)
259. T. Waas, M. Rho, W. Weise, Nucl. Phys. A **617**, 449 (1996) [418](#), [420](#)
260. N. Kaiser, T. Waas, W. Weise, Nucl. Phys. A **612**, 297 (1997) [418](#)
261. M. Lutz, Phys. Lett. B **426**, 12 (1998) [414](#), [418](#)
262. G. Mao, P. Papazoglou, S. Hofmann, S. Schramm, H. Stöcker, W. Greiner, Phys. Rev. C **59**, 3381 (1999) [415](#)
263. M.F.M. Lutz, C.L. Korpa, Nucl. Phys. A **700**, 309 (2002) [417](#), [419](#), [423](#), [427](#), [462](#)
264. M.F.M. Lutz, E.E. Kolomeitsev, Nucl. Phys. A **700**, 193 (2002) [416](#), [417](#), [418](#), [419](#)
265. M.F.M. Lutz, C.L. Korpa, M. Möller, Nucl. Phys. A **808**, 124 (2008) [412](#), [417](#), [418](#)
266. C. Fuchs, Prog. Part. Nucl. Phys. **56**, 1 (2006) [412](#), [415](#), [420](#), [421](#), [425](#)
267. S.J. Dong, J.F. Lagae, K.F. Liu, Phys. Rev. D **54**, 5496 (1996) [412](#)
268. B. Borasoy, R. Lewis, P.P. Ouimet, Phys. Rev. D **65**, 114023 (2002) [412](#)
269. B. Borasoy, Eur. Phys. J. C **8**, 121 (1999) [412](#)
270. T. Inoue, V.E. Lyubovitskij, T. Gutsche, A. Faessler, Phys. Rev. C **69**, 035207 (2004) [412](#)

- 271. A. Semke, M. Lutz, Nucl. Phys. A **778**, 153 (2007) [412](#)
- 272. M. Lutz, A. Steiner, W. Weise, Nucl. Phys. A **574**, 755 (1994) [413](#)
- 273. C. Fuchs, D. Kosov, A. Faessler, Z.S. Wang, T. Waindzocho, Phys. Lett. B **434**, 254 (1998) [413](#)
- 274. A.D. Martin, Nucl. Phys. B **179**, 33 (1981) [414](#)
- 275. M. Iwasaki, et al., Phys. Rev. Lett. **78**, 3067 (1997) [414](#)
- 276. T. Waas, R. Brockmann, W. Weise, Phys. Lett. B **405**, 215 (1997) [414](#)
- 277. P. Kienle, T. Yamazaki, Prog. Part. Nucl. Phys. **52**, 85 (2004) [414](#)
- 278. J. Delorme, M. Ericson, T.E.O. Ericson, Phys. Lett. B **295**, 379 (1992) [415](#)
- 279. E. Friedman, A. Gal, Phys. Lett. B **578**, 85 (2004) [415](#)
- 280. G.Q. Li, C.M. Ko, B.A. Li, Phys. Rev. Lett. **74**, 235 (1995) [415](#)
- 281. G.Q. Li, C.M. Ko, Nucl. Phys. A **594**, 460 (1995) [415](#)
- 282. C.J. Batty, E. Friedmann, A. Gal, Nucl. Rep. **287**, 385 (1997) [415](#)
- 283. K. Tsushima, K. Saito, A.W. Thomas, S.V. Wright, Phys. Lett. B **429**, 239 (1998) [415](#)
- 284. J. Schaffner, J. Bondorf, I.N. Mishustin, Nucl. Phys. A **625**, 325 (1997) [415](#)
- 285. B.D. Serot, J.D. Walecka, Adv. Nucl. Phys. **16**, 1 (1988) [416](#), [418](#)
- 286. P. Ring, Prog. Part. Nucl. Phys. **641**, 175 (1996) [416](#)
- 287. V. Bernard, N. Kaiser, U.G. Meissner, Nucl. Phys. A **615**, 483 (1997) [416](#)
- 288. A. Müller-Groeling, K. Holinde, J. Speth, Nucl. Phys. A **513**, 557 (1990) [417](#)
- 289. L. Tolos, A. Ramos, A. Polls, T.T.S. Kuo, Nucl. Phys. A **690**, 547 (2001) [417](#), [420](#)
- 290. L. Tolos, A. Ramos, A. Polls, Phys. Rev. C **65**, 054907 (2002) [417](#), [459](#)
- 291. A. Ramos, E. Oset, Nucl. Phys. A **671**, 481 (2000) [417](#), [418](#), [420](#), [421](#)
- 292. L. Tolos, E. Oset, A. Ramos, Phys. Rev. C **74**, 015203 (2006) [417](#), [418](#)
- 293. V. Koch, Phys. Lett. B **337**, 7 (1994) [418](#)
- 294. E.E. Kolomeitsev, D.N. Voskresensky, Phys. Rev. C **68**, 015803 (2003) [419](#)
- 295. C.L. Korpa, M.F.M. Lutz, Acta Phys. Hung. A **22**, 21 (2005) [421](#), [422](#)
- 296. A. Cieply, E. Friedman, A. Gal, J. Mares, Nucl. Phys. A **696**, 17 (2001) [421](#)
- 297. T. Roth, M. Buballa, J. Wambach, arXiv:nucl-th/0504056 [421](#)
- 298. A. Sibirtsev, W. Cassing, Nucl. Phys. A **641**, 476 (1999) [421](#), [422](#)
- 299. J. Schaffner-Bielich, V. Koch, M. Effenberger, Nucl. Phys. A **669**, 153 (2000) [422](#), [423](#)
- 300. E. Friedmann, A. Gal, C.J. Batty, Nucl. Phys. A **579**, 518 (1994) [422](#)
- 301. A. Baca, C. Garcia-Recio, J. Nieves, Nucl. Phys. A **673**, 335 (2000) [422](#)
- 302. A. Ramos, S. Hirenzaki, S.S. Kamalov, T.T.S. Kuo, Y. Okumura, E. Oset, A. Polls, H. Toki, L. Tolos, Nucl. Phys. A **691**, 258 (2001) [422](#)
- 303. D. Lissauer, E.V. Shuryak, Phys. Lett. B **253**, 15 (1991) [423](#)
- 304. J.P. Blaizot, R.M. Galain, Phys. Lett. B **271**, 32 (1991) [423](#)
- 305. B.V. Martemyanov, A. Faessler, C. Fuchs, M.I. Krivoruchenko, Phys. Rev. Lett. **93**, 052301 (2004) [424](#), [425](#)
- 306. A.G. Nicola, J.R. Peláez, Phys. Rev. D **65**, 054009 (2002) [424](#)
- 307. C. Hartnack, H. Oeschler, J. Aichelin, Phys. Rev. Lett. **90**, 102302 (2003) [426](#)
- 308. V.M. Belyaev, B.L. Ioffe, Sov. Phys. JETP **57**, 716 (1983). [Zh. Eksp. Teor. Fiz. **84**, 1236 (1983)] [426](#)

- 309. X. Jin, R.J. Furnstahl, Phys. Rev. C **49**, 1190 (1994) [426](#)
- 310. N. Yagisawa, T. Hatsuda, A. Hayashigaki, Nucl. Phys. A **699**, 665 (2002) [426](#)
- 311. M.F.M. Lutz, C.L. Korpa, Phys. Lett. B **633**, 43 (2006) [427](#), [452](#), [456](#), [457](#), [458](#)
- 312. E. Oset et al., Nucl. Phys. A **782**, 259 (2007) [427](#)
- 313. D. Diakonov, V. Petrov, M. Polyakov, Z. Phys. A **359**, 305 (1997) [428](#)
- 314. A.I. Titov, B. Kämpfer, S. Date, Y. Ohashi, Phys. Rev. C **74**, 055206 (2006) [428](#)
- 315. J. Randrup, Phys. Rev. C **68**, 031903 (2003) [428](#)
- 316. L.W. Chen, V. Greco, C.M. Ko, S.H. Lee, W. Liu, Phys. Lett. B **601**, 34 (2004) [428](#)
- 317. S. Scherer, M. Bleicher, S. Haussler, H. Stocker, Int. J. Mod. Phys. E **17**, 965 (2008) [428](#)
- 318. F. L. Shao, Q. B. Xie, Q. Wang, Phys. Rev. C **71**, 044903 (2005) [428](#)
- 319. A. Adare, et al. [PHENIX Collaboration], Phys. Rev. Lett. **98**, 172301 (2007) [429](#), [439](#), [440](#)
- 320. R. Rapp, H. van Hees, arXiv:0803.0901 [429](#)
- 321. S. Bianco, AIP Conf. Proc. **814**, 24 (2006) [431](#)
- 322. S. Frixione, M.L. Mangano, P. Nason, G. Ridolfi, Nucl. Phys. B **431**, 453 (1994) [431](#), [434](#)
- 323. J. Smith, R. Vogt, Z. Phys. C **75**, 271 (1997) [432](#)
- 324. R. Bonciani, S. Catani, M.L. Mangano, P. Nason, Nucl. Phys. B **529**, 424 (1998) [432](#)
- 325. N. Kidonakis, Phys. Rev. D **64**, 014009 (2001) [432](#)
- 326. N. Kidonakis, E. Laenen, S. Moch, R. Vogt, Phys. Rev. D **64**, 114001 (2001) [433](#), [434](#)
- 327. N. Kidonakis, E. Laenen, S. Moch, R. Vogt, Phys. Rev. D **67**, 074037 (2003) [435](#)
- 328. N. Kidonakis, R. Vogt, Phys. Rev. D **68**, 114014 (2003)
- 329. N. Kidonakis, R. Vogt, Eur. Phys. J. C **36**, 201 (2004) [432](#)
- 330. S. Frixione, M.L. Mangano, P. Nason, G. Ridolfi, Adv. Ser. Direct High Energy Phys. **15**, 609 (1998) [434](#)
- 331. S. Barlag, et al. [ACCMOR Collaboration], Z. Phys. C **39**, 451 (1988) [434](#)
- 332. G.A. Alves, et al. [E769 Collaboration], Phys. Rev. Lett. **77**, 2388 (1996)
- 333. M. Aguilar-Benitez, et al. [LEBC-EHS Collaboration], Z. Phys. C **40**, 321 (1988) [434](#)
- 334. G.A. Alves, et al. [E769 Collaboration], Phys. Rev. Lett. **70**, 722 (1993) [435](#)
- 335. M.J. Leitch, et al. [E789 Collaboration], Phys. Rev. Lett. **72**, 2542 (1994) [435](#)
- 336. R. Vogt, Int. J. Mod. Phys. E **12**, 211 (2003) [435](#), [474](#)
- 337. Y.L. Dokshitzer, D.E. Kharzeev, Phys. Lett. B **519**, 199 (2001) [438](#)
- 338. R. Thomas, B. Kämpfer, G. Soff, Heavy Ion Phys. A **22**, 83 (2005) [439](#)
- 339. M. Djordjevic, M. Gyulassy, Nucl. Phys. A **733**, 265 (2004) [439](#)
- 340. N. Armesto, A. Dainese, C.A. Salgado, U.A. Wiedemann, Phys. Rev. D **71**, 054027 (2005) [439](#)
- 341. M.G. Mustafa, Phys. Rev. C **72**, 014905 (2005) [439](#)
- 342. G.D. Moore, D. Teaney, Phys. Rev. C **71**, 064904 (2005) [439](#), [440](#), [441](#), [442](#), [444](#)

- 343. H. van Hees, R. Rapp, Phys. Rev. C **71**, 034907 (2005) [439](#), [441](#), [442](#), [443](#), [445](#), [446](#)
- 344. H. van Hees, V. Greco, R. Rapp, Phys. Rev. C **73**, 034913 (2006) [439](#), [440](#), [441](#)
- 345. S.S. Adler, et al. [PHENIX Collaboration], Phys. Rev. Lett. **96**, 032301 (2006) [439](#), [444](#), [445](#)
- 346. B.I. Abelev, et al. [STAR Collaboration], Phys. Rev. Lett. **98**, 192301 (2007) [439](#), [440](#), [444](#), [445](#)
- 347. V. Greco, R. Rapp, C.M. Ko, Phys. Lett B B **595**, 202 (2004) [439](#), [444](#), [445](#)
- 348. N. Armesto, M. Cacciari, A. Dainese, C.A. Salgado, U.A. Wiedemann, Phys. Lett. B **637**, 362 (2006) [440](#)
- 349. M. Djordjevic, M. Gyulassy, R. Vogt, S. Wicks, Phys. Lett. B **632**, 81 (2006) [440](#)
- 350. S. Wicks, W. Horowitz, M. Djordjevic, M. Gyulassy, Nucl. Phys. A **784**, 426 (2007) [439](#), [440](#)
- 351. R. Averbeck, et al. [PHENIX Collaboration], Nucl. Phys. A **715**, 695 (2003) [439](#)
- 352. K. Gallmeister, B. Kämpfer, O.P. Pavlenko, Nucl. Phys. A **715**, 705 (2003) [439](#)
- 353. K. Gallmeister, B. Kämpfer, O.P. Pavlenko, Phys. Rev. C **66**, 014908 (2002) [439](#)
- 354. M. Cacciari, P. Nason, R. Vogt, Phys. Rev. Lett. **95**, 122001 (2005) [440](#), [474](#), [475](#)
- 355. J. Adams, et al. [STAR Collaboration], Phys. Rev. Lett. **94**, 062301 (2005) [440](#)
- 356. R. Rapp, V. Greco, H. van Hees, Nucl. Phys. A **774**, 685 (2006) [440](#)
- 357. A. Adil, I. Vitev, Phys. Lett. B **649**, 139 (2007) [440](#)
- 358. B. Svetitsky, Phys. Rev. D **37**, 2484 (1988) [441](#)
- 359. P.B. Gossiaux, V. Guiho, J. Aichelin, J. Phys. G **32**, S359 (2006) [441](#)
- 360. F. Karsch, E. Laermann, *Quark Gluon Plasma 1* (R.C. Hwa, X.-N. Wang (Eds.), 2003). arXiv:hep-lat/0305025 [442](#)
- 361. M. Asakawa, T. Hatsuda, Phys. Rev. Lett. **92**, 012001 (2004) [442](#), [469](#)
- 362. P.F. Kolb, J. Sollfrank, U.W. Heinz, Phys. Rev. C **62**, 054909 (2000) [443](#)
- 363. R. Rapp, H. van Hees, J. Phys. G **32**, S351 (2006) [445](#)
- 364. Y. Akiba, et al. [PHENIX Collaboration], Nucl. Phys. A **774**, 403 (2006) [444](#), [445](#)
- 365. B. Zhang, L.W. Chen, C.M. Ko, Phys. Rev. C **72**, 024906 (2005) [446](#)
- 366. D. Molnar, Eur. Phys. J. C **49**, 181 (2007) [446](#)
- 367. M. Mannarelli, R. Rapp, Phys. Rev. C **72**, 064905 (2005) [446](#)
- 368. D. Cabrera, R. Rapp, Phys. Rev. D **76**, 114506 (2007) [446](#), [470](#), [471](#), [485](#), [486](#), [489](#)
- 369. W. Liu, C.M. Ko, arXiv:nucl-th/0603004 [447](#)
- 370. H. van Hees, M. Mannarelli, V. Greco, R. Rapp, Phys. Rev. Lett. **100**, 192301 (2008) [447](#)
- 371. W. Cassing, private communication (2006) [448](#)
- 372. K. Gallmeister, B. Kämpfer, O.P. Pavlenko, Eur. Phys. J. C **6**, 473 (1999) [448](#)
- 373. M.C. Abreu, et al. [NA38 Collaboration], Eur. Phys. J. C **14**, 443 (2000) [448](#)
- 374. R. Rapp, E.V. Shuryak, Phys. Lett. B **473**, 13 (2000) [448](#), [461](#)

375. K. Gallmeister, O.P. Pavlenko, B. Kämpfer, Phys. Lett. B **473**, 20 (2000) [448](#)
376. I. Kvasnikova, C. Gale, D.K. Srivastava, Phys. Rev. C **65**, 064903 (2002) [448](#)
377. B. Kämpfer, J. Cleymans, K. Gallmeister, S.M. Wheaton, Heavy Ion Phys. **18**, 1 (2003) [448](#)
378. X.N. Wang, Phys. Rev. Lett. **81**, 2655 (1998) [448](#)
379. R. Shahoyan, et al. [NA60 Collaboration], Nucl. Phys. A **774**, 677 (2006) [448](#), [450](#)
380. L. Grandchamp, R. Rapp, Phys. Lett. B **523**, 60 (2001) [449](#), [477](#), [487](#), [491](#)
381. A. Andronic, P. Braun-Munzinger, K. Redlich, J. Stachel, Phys. Lett. B **659**, 149 (2008) [449](#), [450](#), [472](#), [473](#), [477](#), [478](#), [479](#), [480](#), [497](#)
382. S.S. Adler, et al. [PHENIX Collaboration], Phys. Rev. Lett. **94**, 082301 (2005) [450](#), [482](#), [489](#)
383. P. Levai, B. Müller, X.N. Wang, Phys. Rev. C **51**, 3326 (1995) [450](#)
384. E.M. Aitala, et al. [E791 Collaboration], Phys. Lett. B **371**, 157 (1996) [450](#)
385. M. Adamovich, et al. [Beatrice Collaboration], Nucl. Phys. B **495**, 3 (1997) [450](#)
386. V.G. Kartvelishvili, A.K. Likhoded, S.R. Slabospitsky, Sov. J. Nucl. Phys. **33**, 434 (1981) [450](#)
387. R. Vogt, S.J. Brodsky, P. Hoyer, Nucl. Phys. B **383**, 643 (1992)
388. R. Hwa, Phys. Rev. D **51**, 85 (1995) [450](#)
389. R. Rapp, E.V. Shuryak, Phys. Rev. D **67**, 074036 (2003) [450](#)
390. E. Braaten, Y. Jia, T. Mehen, Phys. Rev. Lett. **89**, 122002 (2002) [450](#)
391. A. Andronic, P. Braun-Munzinger, K. Redlich, J. Stachel, Phys. Lett. B **571**, 36 (2003) [450](#), [471](#)
392. F. Becattini, Phys. Rev. Lett. **95**, 022301 (2005) [450](#)
393. P. Morath, Ph. D. thesis, Technische Universität, München (2001). W. Weise in “Structure of Hadrons”, Proc. Int. Workshop XXIX, Hirschegg, Austria, Jan 14–20, 2001 (H. Feldmeier et al. (Eds.)) [451](#), [453](#)
394. W. Scheinast, et al. [KaoS Collaboration], Phys. Rev. Lett. **96**, 072301 (2006) [451](#)
395. A. Hayashigaki, K. Terasaki, arXiv:hep-ph/0411285 [451](#), [452](#)
396. S. Narison, Phys. Lett. B **605**, 319 (2005) [451](#), [452](#)
397. A. Hayashigaki, Phys. Lett. B **487**, 96 (2000) [451](#), [452](#), [456](#), [460](#), [473](#), [480](#)
398. L. Tolos, J. Schaffner-Bielich, H. Stöcker, Phys. Lett. B **635**, 85 (2006) [452](#), [457](#)
399. P. Morath, PhD thesis, Technische Universität, München (2001) [452](#)
400. P. Morath, W. Weise, S.H. Lee, Proceedings of the 17th Autumn School: “QCD: Perturbative or Nonperturbative?”, Lisbon and Portugal, 29 Sep–4 Oct 1999 [452](#), [454](#), [456](#), [460](#)
401. D.J. Broadhurst, Phys. Lett. B **101**, 423 (1981) [452](#)
402. T. Hilger, R. Thomas, B. Kämpfer, Phys. Rev. C **79**, 025202 (2009) [453](#), [454](#)
403. S.C. Generalis, D.J. Broadhurst, Phys. Lett. B **139**, 85 (1984) [454](#)
404. L. Tolos, J. Schaffner-Bielich, A. Mishra, Phys. Rev. C **70**, 025203 (2004) [455](#), [457](#)
405. K. Tsushima, D.H. Lu, A.W. Thomas, K. Saito, R.H. Landau, Phys. Rev. C **59**, 2824 (1999) [456](#), [460](#), [473](#)
406. A. Sibirtsev, K. Tsushima, A.W. Thomas, Eur. Phys. J. A **6**, 351 (1999) [456](#), [473](#)

- 407. A. Mishra, E.L. Bratkovskaya, J. Schaffner-Bielich, S. Schramm, H. Stöcker, Phys. Rev. C **69**, 015202 (2004) [456](#), [460](#)
- 408. J. Hofmann, M.F.M. Lutz, Nucl. Phys. A **763**, 90 (2005) [456](#)
- 409. C. Fuchs, B.V. Martemyanov, A. Faessler, M.I. Krivoruchenko, Phys. Rev. C **73**, 035204 (2006) [458](#)
- 410. D. Röder, J. Ruppert, D. Rischke, Phys. Rev. D **68**, 016003 (2003) [458](#)
- 411. T. Mizutani, A. Ramos, Phys. Rev. C **74**, 065201 (2006) [460](#)
- 412. L. Tolos, A. Ramos, T. Mizutani, Phys. Rev. C **77**, 015207 (2008) [460](#)
- 413. W. Cassing, E.L. Bratkovskaya, A. Sibirtsev, Nucl. Phys. A **691**, 753 (2001) [461](#), [473](#), [478](#)
- 414. L. Tolos, A. Polls, A. Ramos, J. Schaffner-Bielich, Phys. Rev. C **68**, 024903 (2003) [461](#)
- 415. N. Brambilla et al., arXiv:hep-ph/0412158 [465](#), [470](#)
- 416. T. Matsui, H. Satz, Phys. Lett. B **178**, 416 (1986) [465](#), [466](#), [481](#), [484](#), [485](#), [493](#)
- 417. L.D. McLerran, B. Svetitsky, Phys. Rev. D **24**, 450 (1981) [466](#)
- 418. L.S. Brown, W.I. Weisberger, Phys. Rev. D **20**, 3239 (1979) [466](#)
- 419. S. Nadkarni, Phys. Rev. D **33**, 3738 (1986) [466](#)
- 420. O. Philipsen, Phys. Lett. B **535**, 138 (2002) [467](#)
- 421. O. Kaczmarek, F. Karsch, P. Petreczky, F. Zantow, Phys. Lett. B **543**, 41 (2002) [467](#), [468](#)
- 422. O. Kaczmarek, F. Karsch, P. Petreczky, F. Zantow, Nucl. Phys. Proc. Suppl. **129**, 560 (2004) [469](#)
- 423. O. Kaczmarek, F. Karsch, F. Zantow, P. Petreczky, Phys. Rev. D **70**, 074505 (2004) [467](#), [468](#)
- 424. O. Kaczmarek, F. Zantow, Phys. Rev. D **71**, 114510 (2005) [467](#), [469](#), [485](#)
- 425. P. Petreczky, K. Petrov, Phys. Rev. D **70**, 054503 (2004) [467](#), [469](#)
- 426. K. Petrov, et al. [RBC-Bielefeld Collaboration], PoS **LAT2006**, 144 (2006) [467](#)
- 427. K. Petrov, et al. [RBC-Bielefeld Collaboration], PoS **LAT2007**, 217 (2007) [469](#)
- 428. O. Kaczmarek, PoS C **POD07**, 043 (2007) [467](#), [469](#)
- 429. M. Doring, S. Ejiri, O. Kaczmarek, F. Karsch, E. Laermann, Eur. Phys. J. C **46**, 179 (2006) [468](#)
- 430. S. Datta, et al., Phys. Rev. D **69**, 094507 (2004) [469](#), [470](#), [485](#), [486](#), [489](#)
- 431. T. Umeda, et al., Eur. Phys. J. C **39S1**, 9 (2005)
- 432. A. Jakovác, et al., Phys. Rev. D **75**, 014506 (2007) [469](#), [470](#)
- 433. F. Karsch, M.T. Mehr, H. Satz, Z. Phys. C **37**, 617 (1988) [469](#), [470](#), [485](#)
- 434. G. Röpke, D. Blaschke, H. Schulz, Phys. Rev. D **38**, 3589 (1988)
- 435. T. Hashimoto, et al., Z. Phys. C **38**, 251 (1988)
- 436. S. Digal, et al., Phys. Lett. B **514**, 57 (2001) [469](#), [470](#)
- 437. T. Umeda, Phys. Rev. D **75**, 094502 (2007) [470](#)
- 438. S. Datta, P. Petreczky, J. Phys. G **35**, 104114 (2008) [470](#)
- 439. P. Petreczky, D. Teaney, Phys. Rev. D **73**, 014508 (2006) [470](#)
- 440. C.Y. Wong, Phys. Rev. C **72**, 034906 (2005) [470](#)
- 441. W.M. Alberico, A. Beraudo, A.D. Pace, A. Molinari, Phys. Rev. D **72**, 114011 (2005)

442. A. Mócsy, P. Petreczky, Phys. Rev. D **73**, 074007 (2006) [470](#)
443. N. Brambilla, A. Pineda, J. Soto, A. Vairo, Rev. Mod. Phys. **77**, 1423 (2005) [470](#)
444. N. Brambilla, J. Ghiglieri, A. Vairo, P. Petreczky, Phys. Rev. D **78**, 014017 (2008) [470](#)
445. A. Mócsy, P. Petreczky, Phys. Rev. Lett. **99**, 211602 (2007) [470](#), [471](#), [476](#)
446. A. Mócsy, P. Petreczky, Phys. Rev. D **77**, 014501 (2008) [471](#), [485](#), [486](#)
447. W.M. Alberico, A. Beraudo, A.D. Pace, A. Molinari, Phys. Rev. D **77**, 017502 (2008) [470](#), [485](#), [486](#)
448. W.M. Alberico, et al., Phys. Rev. D **77**, 017502 (2008) [471](#)
449. A. Andronic, P. Braun-Munzinger, K. Redlich, J. Stachel, Nucl. Phys. A **789**, 334 (2007) [471](#), [472](#), [473](#), [477](#), [492](#), [494](#)
450. A. Andronic, P. Braun-Munzinger, K. Redlich, J. Stachel, Phys. Lett. B **652**, 259 (2007) [471](#), [472](#)
451. P. Braun-Munzinger, J. Stachel, Phys. Lett. B **490**, 196 (2000) [471](#), [473](#), [490](#)
452. P. Braun-Munzinger, J. Stachel, Nucl. Phys. A **690**, 119c (2001) [471](#), [473](#)
453. A. Adare, et al. [PHENIX Collaboration], Phys. Rev. Lett. **98**, 232301 (2007) [472](#), [492](#)
454. A. Andronic, P. Braun-Munzinger, K. Redlich, J. Stachel, arXiv:0707.4075 [472](#), [477](#)
455. P. Senger, J. Phys. Conf. Ser. **50**, 357 (2006) [472](#)
456. A. Sibirtsev, K. Tsushima, K. Saito, A.W. Thomas, Phys. Lett. B **484**, 23 (2000) [473](#), [480](#)
457. B. Friman, S.H. Lee, T. Song, Phys. Lett. B **548**, 153 (2002) [480](#)
458. K. Morita, S.H. Lee, Phys. Rev. Lett. **100**, 022301 (2008) [473](#)
459. A. Andronic, P. Braun-Munzinger, J. Stachel, Nucl. Phys. A **772**, 167 (2006) [473](#), [474](#), [475](#), [476](#)
460. M. Michalec, W. Florkowski, W. Broniowski, Phys. Lett. B **520**, 213 (2001) [473](#)
461. D. Zschesche, S. Schramm, J. Schaffner-Bielich, H. Stöcker, W. Greiner, Phys. Lett. B **547**, 7 (2002) [473](#)
462. C. Lourenço, H. Wöhri, Phys. Rep. **433**, 127 (2006) [474](#), [475](#)
463. A. Adare, et al. [PHENIX Collaboration], Phys. Rev. Lett. **97**, 252002 (2006) [474](#)
464. I. Abt, et al. [HERA-B Collaboration], Phys. Lett. B **638**, 407 (2006) [474](#), [475](#)
465. M.I. Gorenstein, A.P. Kostyuk, H. Stoecker, W. Greiner, Phys. Lett. B **509**, 277 (2001) [473](#)
466. P. Braun-Munzinger, D. Miśkowiec, A. Drees, C. Lourenco, Eur. Phys. J. C **1**, 123 (1998) [475](#)
467. F. Karsch, R. Petronzio, Phys. Lett. B **39**, 232 (1987) [476](#)
468. J.P. Blaizot, J.Y. Ollitrault, Phys. Rev. D **39**, 232 (1989) [476](#)
469. H. Satz, J. Phys. G **32**, R25 (2006) [477](#)
470. F. Arleo, V. Tram, Eur. Phys. J. C **55**, 449 (2008) [477](#)
471. L. Grandchamp, R. Rapp, Nucl. Phys. A **709**, 415 (2002) [477](#), [491](#)
472. R.L. Thews, M. Schroedter, J. Rafelski, Phys. Rev. C **63**, 054905 (2001) [477](#), [490](#), [491](#)

473. R.L. Thews, M.L. Mangano, Phys. Rev. C **73**, 014904 (2006) [490](#), [494](#)
474. L. Grandchamp, R. Rapp, G.E. Brown, Phys. Rev. Lett. **92**, 212301 (2004) [480](#), [491](#), [492](#), [497](#)
475. L. Yan, P. Zhuang, N. Xu, Phys. Rev. Lett. **97**, 232301 (2006) [477](#), [490](#), [493](#), [494](#)
476. B. Zhang, C.M. Ko, B.A. Li, Z.W. Lin, S. Pal, Phys. Rev. C **65**, 054909 (2002) [477](#), [480](#)
477. E.L. Bratkovskaya, W. Cassing, H. Stöcker, Phys. Rev. C **67**, 054905 (2003) [477](#), [488](#), [492](#)
478. A. Zoccoli, et al. [HERA-B Collaboration], Eur. Phys. J. C **43**, 179 (2005) [482](#)
479. C. Gerschel, J. Hufner, Phys. Lett. B **207**, 253 (1988) [482](#)
480. R. Vogt, Phys. Rep. **310**, 197 (1999) [482](#), [484](#)
481. C. Gerschel, J. Hüfner, Annu. Rev. Nucl. Part. Sci. **49**, 255 (1999) [482](#), [484](#)
482. R.V. Gavai, et al., Int. J. Mod. Phys. A **10**, 2999 (1995) [482](#), [489](#)
483. M.C. Abreu, et al. [NA38 Collaboration], Phys. Lett. B **466**, 408 (1999) [483](#), [484](#)
484. R.L. Anderson, et al., Phys. Rev. Lett. **38**, 263 (1977) [483](#)
485. B. Alessandro, et al. [NA50 Collaboration], Eur. Phys. J. C **48**, 329 (2006) [483](#)
486. P. Cortese, et al. [NA50 Collaboration], J. Phys. G **31**, S809 (2005) [484](#), [485](#)
487. M. Gonin, et al. [NA50 Collaboration], Nucl. Phys. A **610**, 404c (1996)
488. L. Ramello, et al. [NA50 Collaboration], Nucl. Phys. A **774**, 59 (2006) [484](#)
489. U.W. Heinz, M. Jacob, arXiv:nucl-th/0002042 [484](#)
490. R. Rapp, L. Grandchamp, J. Phys. G **30**, S305 (2004) [484](#)
491. D.E. Kharzeev, J. Phys. G **34**, S445 (2007) [484](#)
492. F. Karsch, E. Laermann, A. Peikert, Nucl. Phys. B **605**, 579 (2001) [485](#)
493. E.V. Shuryak, I. Zahed, Phys. Rev. D **70**, 054507 (2004) [485](#), [486](#), [489](#)
494. C.Y. Wong, H.W. Crater, Phys. Rev. D **75**, 034505 (2007)
495. M. Laine, O. Philipsen, M. Tassler, JHEP **0709**, 066 (2007) [485](#), [486](#)
496. H. Matsufuru, T. Onogi, T. Umeda, Phys. Rev. D **64**, 114503 (2001) [485](#), [489](#)
497. M. Asakawa, T. Hatsuda, Nucl. Phys. A **738**, 249 (2004) [485](#), [489](#)
498. F. Karsch, D. Kharzeev, H. Satz, Phys. Lett. B **637**, 75 (2006) [486](#)
499. H. Satz, Nucl. Phys. A **783**, 249 (2007) [486](#)
500. J.P. Blaizot, J.Y. Ollitrault, Phys. Rev. Lett. **77**, 1703 (1996) [486](#)
501. J.P. Blaizot, P.M. Dinh, J.Y. Ollitrault, Phys. Rev. Lett. **85**, 4010 (2000) [486](#), [487](#)
502. H. Satz, arXiv:hep-ph/9711289 [487](#)
503. D. Kharzeev, H. Satz, Phys. Lett. B **334**, 155 (1994) [487](#)
504. Y. Park, K.I. Kim, T. Song, S.H. Lee, C.Y. Wong, Phys. Rev. C **76**, 044907 (2007) [487](#)
505. J. Ftacnik, P. Lichard, J. Pisut, Phys. Lett. B **207**, 194 (1988) [487](#)
506. S. Gavin, M. Gyulassy, A. Jackson, Phys. Lett. B **207**, 257 (1988)
507. R. Vogt, M. Prakash, P. Koch, Phys. Lett. B **207**, 263 (1988)
508. A. Capella, E.J. Feireiro, A.B. Kaidalov, Phys. Rev. Lett. **85**, 2080 (2000) [487](#), [488](#), [493](#)
509. C. Spieles, et al., J. Phys. G **25**, 2351 (1999) [488](#)
510. T. Barnes, E.S. Swanson, C.Y. Wong, Phys. Rev. C **68**, 014903 (2003) [488](#)

- 511. F.O. Duraes, H.C. Kim, S.H. Lee, F.S. Navarra, M. Nielsen, *Phys. Rev. C* **68**, 035208 (2003) [488](#)
- 512. A. Bourque, C. Gale, *Phys. Rev. C* **78**, 035206 (2008) [488](#)
- 513. C. Young, E. Shuryak, *Phys. Rev. C* **79**, 034907 (2009) [488](#)
- 514. R.L. Thews, *Nucl. Phys. A* **702**, 341 (2002) [490](#)
- 515. A. Polleri, et al., *Phys. Rev. C* **70**, 044906 (2004) [490](#)
- 516. M.E. Peskin, *Nucl. Phys. B* **156**, 365 (1979) [490](#), [496](#)
- 517. G. Bhanot, M.E. Peskin, *Nucl. Phys. B* **156**, 391 (1979) [490](#)
- 518. R. Rapp, D. Cabrera, H. van Hees, *arXiv:nucl-th/0608033* [491](#), [492](#)
- 519. X. Zhao, R. Rapp, *Phys. Lett. B* **664**, 253 (2008) [491](#), [494](#), [496](#)
- 520. O. Linnyk, E.L. Bratkovskaya, W. Cassing, H. Stoecker, *Phys. Rev. C* **76**, 041901 (2007) [492](#)
- 521. A. Capella, L. Bravina, E.G. Ferreira, A.B. Kaidalov, K. Tywoniuk, E. Zabrodin, *Eur. Phys. J. C* **58**, 437 (2008) [492](#)
- 522. J. Hüfner, P. Zhuang, *Phys. Lett. B* **515**, 115 (2001) [493](#)
- 523. J. Hüfner, P. Zhuang, *Phys. Lett. B* **559**, 193 (2003) [493](#), [494](#)
- 524. X. Zhu, P. Zhuang, N. Xu, *Phys. Lett. B* **607**, 107 (2005) [493](#), [494](#)
- 525. I.C. Arsene, et al., *Phys. Rev. C* **75**, 034902 (2007) [495](#)
- 526. J. Qiu, J.P. Vary, X. Zhang, *Phys. Rev. Lett.* **88**, 232301 (2002) [496](#)
- 527. H.P.D. Costa, et al. [PHENIX Collaboration], *Nucl. Phys. A* **774**, 747 (2006) [496](#)
- 528. O. Linnyk, E.L. Bratkovskaya, W. Cassing, H. Stoecker, *Nucl. Phys. A* **786**, 183 (2007) [496](#)
- 529. D. Blaschke, G. Burau, Y.L. Kalinovsky, V.L. Yudichev, *Prog. Theo. Phys. Supp.* **149**, 182 (2003) [496](#)
- 530. J. Kapusta, T. Toimela, *Phys. Rev. D* **37**, 3731 (1988) [497](#)
- 531. J. Diaz-Alosa, A.P. Canyellas, H. Sivak, *Nucl. Phys. A* **505**, 695 (1989)
- 532. J. Durso, H. Kim, J. Wambach, *Phys. Lett. B* **298**, 267 (1993)
- 533. J. Diaz-Alosa, E. Gallego, A. Perez, *Phys. Rev. Lett.* **73**, 2536 (1994) [497](#)
- 534. M. Kitazawa, T. Koide, T. Kunihiro, Y. Nemoto, *Prog. Theor. Phys.* **114**, 117 (2005) [499](#), [504](#), [505](#), [506](#)
- 535. D. Blaschke, H. Grigorian, A. Khalatyan, D.N. Voskresensky, *Nucl. Phys. Proc. Suppl.* **141**, 137 (2005) [499](#), [500](#)
- 536. R. Rapp, T. Schafer, E.V. Shuryak, M. Velkovsky, *Ann. Phys.* **280**, 35 (2000) [499](#)
- 537. K. Rajagopal, F. Wilczek, *arXiv:hep-ph/0011333*
- 538. M. Buballa, *Phys. Rept.* **407**, 205 (2005) [499](#), [503](#)
- 539. R.S. Duhau, A.G. Grunfeld, N.N. Scoccola, *Phys. Rev. D* **70**, 074026 (2004) [500](#)
- 540. D. Ebert, K.G. Klimenko, V.L. Yudichev, *Phys. Rev. D* **72**, 056007 (2005) [501](#), [502](#)
- 541. D. Ebert, K.G. Klimenko, V.L. Yudichev, *Phys. Rev. C* **72**, 015201 (2005) [502](#)
- 542. M. Kitazawa, T. Koide, T. Kunihiro, Y. Nemoto, *Phys. Rev. D* **65**, 091504 (2002) [503](#), [504](#)

- 543. D.N. Voskresensky, Phys. Rev. C **69**, 065209 (2004) [503](#), [504](#)
- 544. T. Matsuura, K. Iida, T. Hatsuda, G. Baym, Phys. Rev. D **69**, 074012 (2004) [503](#)
- 545. I. Giannakis, D.F. Hou, H.c. Ren, D.H. Rischke, Phys. Rev. Lett. **93**, 232301 (2004) [503](#)
- 546. I. Giannakis, H.C. Ren, Nucl. Phys. B **669**, 462 (2003) [503](#)
- 547. M. Matsuzaki, Phys. Rev. D **62**, 017501 (2000) [504](#)
- 548. H. Abuki, T. Hatsuda, K. Itakura, Phys. Rev. D **65**, 074014 (2002) [504](#)
- 549. L.D. Landau, E.M. Lifshiz, *Statistical Physics* (Pergamon, New York, NY, 1958) [504](#)
- 550. M. Kitazawa, T. Koide, T. Kunihiro, Y. Nemoto, Phys. Rev. D **70**, 056003 (2004) [504](#), [505](#)
- 551. M. Kitazawa, T. Kunihiro, Y. Nemoto, Phys. Lett. B **631**, 157 (2005) [505](#)
- 552. T. Timusk, B. Statt, Rep. Progr. Phys. **62**, 61 (1999) [505](#)
- 553. Y. Yanase, T. Jujo, T. Nomura, H. Ikeda, T. Hotta, K. Yamada, Phys. Rep. **387**, 1 (2003) [505](#)
- 554. L.G. Aslamazov, A.I. Larkin, Sov. Phys. Solid State **10**, 875 (1968) [505](#)
- 555. K. Maki, Prog. Theor. Phys. **40**, 193 (1968)
- 556. R.S. Thompson, Phys. Rev. B **1**, 327 (1970) [505](#)
- 557. M.L. Bellac, *Thermal Field Theory* (Cambridge University Press, England, 1996) [506](#)
- 558. K. Mitsutani, M. Kitazawa, T. Kunihiro, Y. Nemoto, Prog. Theor. Phys. Suppl. **174**, 262 (2008) [506](#), [507](#)
- 559. T. Kunihiro, M. Kitazawa, Y. Nemoto, PoS (CPOD07) 041 (2007) [506](#), [507](#)

Part III

Collision Dynamics

Conveners: J. Knoll^{1,2}, J. Randrup³, and C. Fuchs⁴

Authors, who contributed to the various chapters or sections given in brackets:

J. Aichelin⁵ [3.5, 4.1], M. Bleicher⁶ [4.1, 5.6], E. Bratkovskaya⁶ [3.5], W. Cassing⁷ [3.4.6, 3.5], P. Danielewicz⁸ [1.2, 3.5], C. Fuchs^{4,a} [3.5, 4.1, 6.2, 6.3, 7.2], Y. Ivanov^{12,1,b,c} [5.3.1] B. Kämpfer¹⁰ [3.5], J. Knoll^{1,2} [1, 2, 3.3, 3.4, 5.2, 5.5–5.9, 6.4, 7], C.-M. Ko¹¹ [3.5], A. Larionov^{12,13} [3.5], H. Petersen⁶ [5.6], J. Randrup³ [1, 2, 3.1, 3.2, 4.2, 5.1, 5.4, 6.1, 6.5, 7.4], V. Toneev^{14,1,a,b} [3.5]

Affiliations:

¹GSI Helmholtzzentrum für Schwerionenforschung, Darmstadt, Germany; ²University of Heidelberg, Heidelberg, Germany; ³Lawrence Berkeley National Laboratory, Berkeley, CA, USA; ⁴Martin-Gerbert-Gymnasium, Horb am Neckar, Germany; ⁵SUBATEC Nantes, Nantes, France; ⁶University of Frankfurt, Frankfurt, Germany; ⁷University of Gießen, Gießen, Germany; ⁸Michigan State University, East Lansing, MI, USA; ⁹Technical University of Darmstadt, Darmstadt, Germany; ¹⁰Technical University of Munich, Munich, Germany; ¹¹Texas A&M, College Station, TX, USA; ¹²Kurchatov Institute Moscow, Moscow, Russia; ¹³Frankfurt Institute for Advanced Studies (FIAS), Frankfurt, Germany; ¹⁴Joint Institute of Nuclear Research (JINR), Dubna, Russia

Support:

^aGSI-F&E

^bDeutsche Forschungsgemeinschaft (DFG project 436 RUS 113/558/0-2)

^cRussian Minpromnauki (grant NS-1885.2003.2)

Chapter 1

Introduction

This Part presents the various conceptual schemes and computational models that are employed for the dynamical description of high-energy nuclear collisions. The focus will be on the energy range where one expects large enhancements of both the net baryon density and the energy density, relative to the values characteristic of ordinary nuclear matter. As quantitatively illustrated in Fig. 1.1, such collisions are utilised as a tool for exploring the properties of hot and baryon-dense matter.

However, this task is not straightforward. Nuclear systems are relatively small even on the scale of the strong-interaction range. Indeed, even the largest available nuclei have about half of their nucleons situated in the surface region.¹ Further complication arises from the long-range Coulomb interaction which, together with the surface energy, reduces the nuclear binding energy by typically about a factor of two, relative to the value of a corresponding piece of bulk matter. Thus the physical environments produced in nuclear collisions are far from those of idealised uniform matter and it is therefore essential to take proper account of the significant variation of the local conditions throughout the system probed.

Moreover, the time window during which the densities are significantly enhanced is often so short that local equilibrium may not be established. Consequently, it is generally not straightforward to extract the statistical equilibrium quantities of primary interest, such as temperature and chemical potentials, from the collision data.

Thus, while thermodynamics describes bulk matter in statistical equilibrium, which may be characterised as being *large* and *stationary*, the available collision systems are neither. They may rather be characterised as being *small* and *transient*. Because these problems are inherent to heavy-ion physics, it is necessary to rely extensively on dynamical transport treatments. Unfortu-

¹ The total number of nucleons in a nucleus is $A = \frac{4}{3}\pi R^3 \rho_0$, where $R = r_0 A^{1/3}$ is the nuclear radius, while the number of nucleons within a distance a from the surface is $A_{\text{surf}} = 4\pi R^2 a \rho_0$, so the ratio is $A_{\text{surf}}/A = 3a/r_0 A^{1/3} \approx a/2r_0$ for lead, which amounts to about one half for $a \approx r_0 \approx 1.2$ fm.

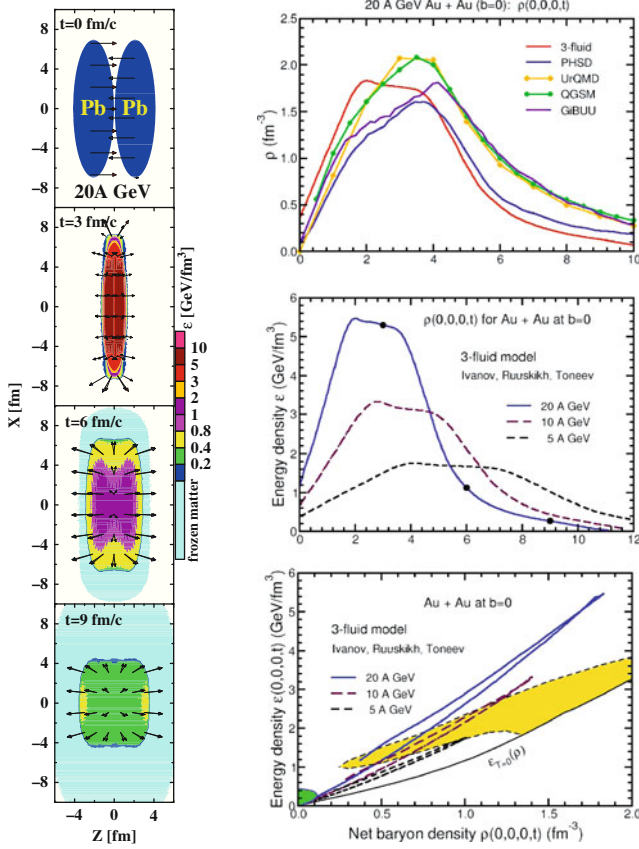


Fig. 1.1 Time evolution of a central gold–gold collision as obtained with the 3-fluid model [1] (Sect. 5.3.1). *Left*: Contours of the total energy density in the reaction plane, for a bombarding energy of 20 A GeV. The light coloured outer halo indicates the matter that has already undergone chemical freeze-out. The flow velocities of the baryon-rich projectile-like and target-like fluids are indicated by the *arrows* (*open and solid*, respectively). *Right*: The associated time evolution of the net baryon density $\rho(0,0,0,t)$ and the total energy density $\varepsilon(0,0,0,t)$ in the centre of the system, as well as the corresponding trajectory in the $\rho - \varepsilon$ phase plane, with results for bombarding energies of 10 and 5 A GeV also shown [2]. The expected phase coexistence region is indicated schematically (*yellow*), while the chemical freeze-out (*green*) is based on fits to data [3].

nately, as of yet, it has not been possible to derive such treatments directly from the underlying QCD quantum field theory. Extensive phenomenological modelling is therefore required.

After an introductory discussion of the general physical features of the nuclear collision dynamics, we discuss the range of conceptual approaches. Starting with cascade models (Chap. 2), we continue with treatments building on the one-body approximation level that have been so successful for nuclear dynamics at lower energies (Chap. 3). Besides kinetic transport, detailed conceptual developments in the treatment of “unstable” particles such as res-

onances are reviewed. This is followed by various microscopic many-body models (Chap. 4), before finally macroscopic concepts such as fluid-dynamic treatments are presented (Chap. 5). Subsequently, we discuss a number of illustrative applications (Chap. 6) and then close with an exposition of the main challenges still facing us in the area of collision dynamics modelling (Chap. 7). For an introduction and survey about the various concepts in physical kinetics and fluid mechanics we refer to the corresponding text books in the Landau-Lifshitz series [4, 5].

1.1 General features

The strength of elementary interactions and their uncertainties due to the composite nature of hadrons, together with the mesoscopic nature of the interacting systems, make nuclear and hadron physics essentially a phenomenological science. Nuclear reactions, particularly central collisions of heavier nuclei, bring in a complexity above that present for nuclear structure and are best discussed within the framework of transport concepts. While such transport description should ideally be derived from the basic physics, it is in practice necessary to significantly rely on phenomenology. But even though, transport models can provide valuable insight and help to guide both, theory and experiment.

Derived or based on physically sound assumptions, the many-particle reaction models have a number of common features. The most important is an element of information reduction (“coarse graining”). Attempts to follow the detailed many-body evolution of the evolving system are neither practical nor desirable. In practice, the most important information is expressible in terms of the one-body phase-space densities for the various particle species in a given event.

The transport descriptions generally rest on a separation of the space-time scales that characterise the microscopic interactions between individual hadrons from the scales characteristic of the macroscopic dynamics. In the absence of short encounters between individual hadrons, the changes within a reacting system are gradual. This invites a classical description and, in fact, the majority of transport approaches in our context rely on the classical dynamics as long as hadrons are well separated. On the other hand, basic considerations demonstrate that a classical description cannot apply to the collisions between individual hadrons at short distances. In such collisions, quantum numbers change abruptly. Since details of the initial conditions of short-range encounters between hadrons are essentially wiped out by the coarse-graining, the outcome can normally be predicted only probabilistically. The combination of a probabilistic treatment of the short-range encounters between the particles and a classical deterministic treatment of motion in-between the close encounters is characteristic for most of the transport approaches employed for reactions. Even if the dynamics in-between collisions

is not treated classically, given the gradual changes a primarily deterministic treatment can be employed e.g. in form of a wave function dynamics which most likely captures most changes of interest during a limited evolution time.

At the high hadron densities of interest, the separation between the various times scales become blurred. Thus the typical travel time between successive hadron-hadron encounters shrinks and becomes comparable to the duration of the encounters themselves. Furthermore, the macroscopic evolution grows relatively rapid and can no longer be clearly separated from the microscopic time scales. On the other hand, the high-density parts of the system tend to fairly quickly reach local thermal equilibrium. Therefore, even in the absence of a clear separation of the relevant scales invalidates the standard justification for a transport treatment, such a framework may still produce the correct macroscopic properties of the system and hence yield a quantitatively useful dynamical description. However, there is no similar mitigating factor apparent when the separation between the scales is blurred due to Lorentz effects in highly relativistic collisions. The identity of individual hadrons is then brought into question and a description in terms of constituent partons may be more appropriate.

1.2 Collision geometry and dynamical scales

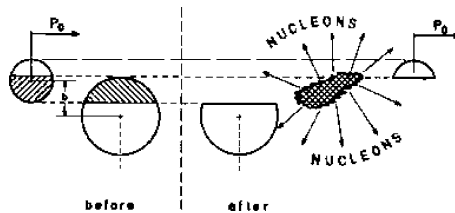


Fig. 1.2 Participant-spectator picture of a nucleus-nucleus collision [6].

The gross features of the collision dynamics can simply be estimated assuming that irrespective of scatterings to finite angles the nucleons keep their original straight-line trajectories on their way through the opposing nucleus, Fig. 1.2, defining the separation into *participants* and *spectators*. These two notions refer to nucleons that do collide at least once and to those that continue their original motion in the respective projectile or target fragments. In the following A and B denote the mass numbers of projectile and target nucleus, respectively. With nuclear radii and a total nucleon-nucleon cross section of the order of

$$R_A \approx r_0 A^{1/3}, \quad R_B \approx r_0 B^{1/3},$$

$$\sigma_{tot}^{NN} \approx \pi r_0^2 \approx 40 \text{ mb}; \quad r_0 = 1.12 \text{ fm} \quad (1.1)$$

a projectile nucleon hitting centrally a lead nucleus with a diameter of 13 fm experiences collisions with about $\bar{N} \approx B^{1/3} \approx 7$ target nucleons on its way.

The straight-line collision geometry considerations discussed in Sect. 2.2 lead to very simple geometrical estimates for the mean number of participants and mean number of NN-collisions. Impact parameter averaged (i.e. for minimum bias events) they become [6]

$$\begin{aligned} \langle N_{\text{part}} \rangle &= \frac{A\sigma_B + B\sigma_A}{\sigma_{AB}} \approx \frac{AB^{2/3} + BA^{2/3}}{(A^{1/3} + B^{1/3})^2}, \\ \langle N_{\text{coll}} \rangle &= AB \frac{\sigma_{tot}^{NN}}{\sigma_{AB}} \approx \frac{AB}{(A^{1/3} + B^{1/3})^2}. \end{aligned} \quad (1.2)$$

Here $\sigma_A \approx \pi r_0 A^{2/3}$, $\sigma_B \approx \pi r_0 B^{2/3}$ and, $\sigma_{AB} \approx \pi r_0 (A^{1/3} + B^{1/3})^2$ are the corresponding nuclear reaction cross sections. In central collisions the above averages roughly change to

$$\begin{aligned} \langle N_{\text{part}} \rangle &\approx \begin{cases} A + \frac{3}{2}A^{2/3}B^{1/3} & \text{for } A \ll B \\ A + B & \text{for } A \approx B \end{cases} \\ \langle N_{\text{coll}} \rangle &\approx \begin{cases} AB^{1/3} & \text{for } A \ll B \\ \frac{1}{2}A^{4/3} & \text{for } A \approx B \end{cases} \end{aligned} \quad (1.3)$$

assuming for simplicity a cylindrical target participant zone for the asymmetric case $A \ll B$.

While signals arising from equilibrated matter (such as the multiplicity of pions) tend to scale with the number of participants, $\langle N_{\text{part}} \rangle$, processes that can be treated perturbatively (such as hard electromagnetic probes or near-threshold kaons) scale with the number of collisions, $\langle N_{\text{coll}} \rangle$.

The geometrical scales are to be compared with the typical dynamical scales. These concern the interaction ranges and for the application of classical dynamics the typical de Broglie wavelength.

The long range part of the strong interaction between two hadrons is limited by inverse mass of the lightest exchanged meson, mostly the pion, yielding $r_{\text{int}} \lesssim \hbar/(m_\pi c) \sim 1.4 \text{ fm}$. At short distances typically at a size $\sim 0.5 \text{ fm}$ the repulsive core of the NN interaction and sub-hadron structure effects come into play. Since the dynamics at short inter-particle distances is quite quantal, the actual distances explored in the interactions may be characterised by the inverse momentum transfer, $r \sim \hbar/q$.

In the classical collision regime the average distance between the elementary collisions, i.e. the mean free path, can be estimated as $\lambda \approx 1/(\rho\sigma)$, where ρ is the hadron density and σ is a representative cross section for the interaction in free space. With an NN cross section of $\sigma = 40 \text{ mb} = 4 \text{ fm}^2$ this yields $\lambda \sim 1.6 \text{ fm}$ at normal nuclear density of $\rho_0 = 0.16 \text{ fm}^{-3}$. The effec-

tive in-medium cross section may differ from its free-space value for various reasons. In particular, quantum-statistical effects such as the Pauli principle and changes in the single-particle dispersion relations may suppress the cross sections or induce a resonance behaviour [7, 8]. Moreover, at high densities only lower angular momenta can be attributed to the microscopic collision of two hadrons, while the higher angular momenta still contribute to the mean field. Such suppression effects were observed in the calculations of [9–12].

A semi-classical description requires that the reduced de Broglie's wavelength, $\lambda_B = \hbar/p$, where p is the characteristic particle momentum, is small relative to the characteristic scales for spatial changes $\min(\lambda, R)$. From the low side, the typical momenta are limited by the Fermi momentum in the initial nuclei, yielding $\lambda_B \lesssim 1$ fm. Towards the end of a collision, some degree of local equilibration is usually established, with temperatures that depend on the collision energy and usually do not exceed $T \sim 150$ MeV. For nucleons, this yields $\lambda_B \gtrsim \hbar/\sqrt{3m_N T} \sim 0.3$ fm. On the other hand, the characteristic scales for the spatial variation are of the order of the nuclear radius, $R \simeq 1.12 \text{ fm } A^{1/3}$ which amounts to $3 - 7$ fm, for $A = 20 - 240$.

Characteristic temporal scales for collisions are generally related to the spatial scales through the characteristic particle velocities v . Thus, the mean time between collisions is $\tau \simeq \lambda/v$, while the interaction time is $t_{int} \sim r_{int}/v$ (in the absence of a resonance). The mean free-flight time τ generally determines the rate of equilibration for the single-particle phase-space density. On the other hand, the duration of an interaction t_{int} , determines the rate at which the two-particle density equilibrates at short inter-particle distances.

Kinetic transport theories normally require $\lambda > r_{int}$ and $\min(\lambda, R) > \lambda_B$ with analogous inequalities for the respective times. When important, relativistic effects complicate the relations between the scales, since different results are obtained in different frames, elongated or shortened. As an example, consider a nucleon excited into a resonance with a half life t_{int}^* of the order of $(1 - 2)$ fm/c. When that resonance moves at a non-relativistic speed in its host nucleus, the corresponding interaction distance is relatively short as compared to the mean free path or the nuclear size, $r_{int} \approx v t_{int}^* < \lambda < R$. However, when the Lorentz factor γ of the relative nuclear motion is large, the interaction range seen from the collision partner is $r'_{int} = v \gamma t_{int}^*$ which may exceed the interaction mean free path in that nucleus or even its radius. When such apparent transient times acquire macroscopic size, the validity of transport theory may be extended by explicitly incorporating degrees of freedom for the long-lived states, be that baryon resonances, nuclear clusters, or strings. A byproduct of such an explicit treatment of transient states may be practical simplifications in dealing with interaction processes involving more than two particles in the initial or final states. As an example consider the pion absorption process on two nucleons: $\pi NN \rightarrow NN$. Process of such type are complicated to handle as it involves a three-body initial state. Employing an intermediate resonance picture as provided by the Δ isobar resonance in this case, the process may then be accommodated as a sequence of two-body

precesses: $\pi N \rightarrow \Delta$ and $\Delta N \rightarrow NN$, though for the price that possible interference effects are ignored. That latter strategy is followed in many kinetic applications.

1.3 Degrees of freedom

Nuclear collisions in the addressed energy range experience quite rapidly changing physical environments (see Fig. 1.1). Therefore it is a significant challenge to encompass all of those within a single microscopic model. In the approach phase the dominant processes may already be direct interactions between partonic degrees of freedom, quarks and gluons, whereas the late stage is well described in terms of a hadron resonance gas. The explicit reference to the microscopic degrees of freedom is avoided in macroscopic treatments such as fluid dynamics, see Chap. 5.

The inclusion of the partonic degrees of freedom is not yet at a satisfactory level, although a number of practical prescriptions were devised, as will be described in connection with the specific models. By comparison, the treatment of the hadronic gas is rather well developed. The most important hadronic states are shown in Figs. 1.3 and 1.4. When the models are extended to the charm sector the SU(3) multiplets have to be extended to the corresponding SU(4) multiplets [13].

A specific production process is denoted as *subthreshold* if the threshold rapidity difference for its occurrence in an elementary NN collision exceeds that of the nuclear collision. The most important production thresholds at both SIS-18 and SIS-300 are shown in Fig. 1.5. Particle production in the vicinity of the corresponding threshold leads to particular physical insight in many cases. The reason is simply that these particles carry special quantum numbers and may not reach chemical equilibrium with the surrounding medium. Under such circumstances, their detection provides specific information on the conditions prevailing at their production stage.

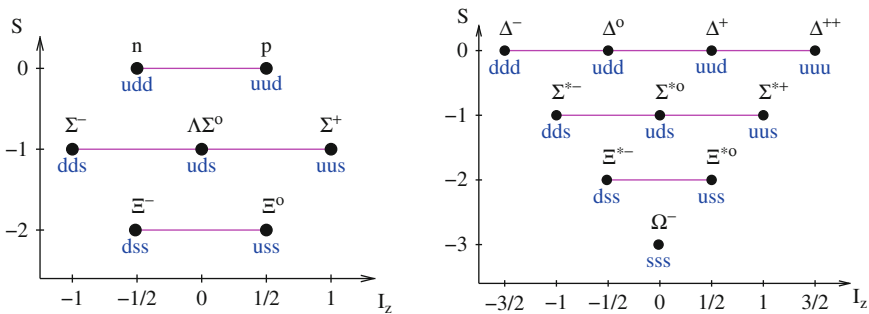


Fig. 1.3 The lowest SU(3) baryon multiplets: the octet (*left*) and the decuplet (*right*).

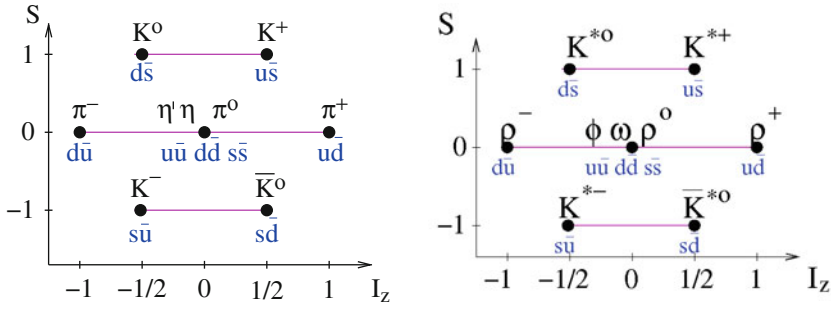


Fig. 1.4 The lowest SU(3) meson multiplets: the pseudo-scalar nonet (*left*) and the vector nonet (*right*).

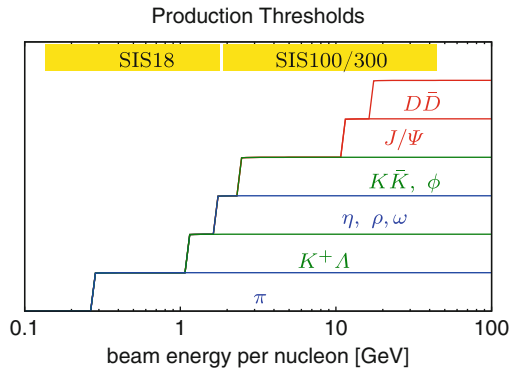


Fig. 1.5 Threshold beam energies for the production of various hadrons in elementary reactions $NN \rightarrow X$ compared to the energy ranges available at the existing SIS18 at GSI and the future SIS100/300 at FAIR/GSI.

Rare production processes are of particular interest, since they may serve as probes of the high-density collision stage. An instructive example is the production of K^+ mesons near the threshold (which is ≈ 1.6 GeV in NN collisions), which was studied extensively first at the Bevalac and subsequently at SIS and has provided valuable information on the nuclear equation of state [14] (see also the section on strangeness in the Part “Observables”). Due to the absence of other low-mass hadrons with positive strangeness, the kaons are not absorbed in the medium, although they may experience some elastic scattering [15, 16]. (It should be noted, though, that the same is not true for antikaons, such as the K^- , which react strongly with baryons to form Λ hyperons; this illustrates that not all rare particles are suitable in the same way.)

The energy range where a given model is applicable is essentially determined by the degrees of freedom included. Thus, if the abundance of strangeness-carrying particles is sufficient to influence the overall dynamics then strangeness must be included explicitly. On the other hand, if the colli-

sion energy lies just in the vicinity of the threshold of a particular mesonic or baryonic production then such a process is relatively rare and does not influence the overall reaction dynamics. In this situation, it need not be treated dynamically but can be calculated by perturbative means [15].

Indeed, from the calculational point of view, the small kaon production cross section at BEVALAC and SIS18 energies invites for *perturbative* schemes, in which the individual production events can be treated as additive, with no effect on the overall dynamics [15]. This method can then also be employed for rare processes at higher collision energies, such as charm production at CBM energies (see Fig. 1.5) which is somewhat analogous to strangeness production at the Bevalac and the SIS18. It reduces the computational requirements by orders of magnitude, thus making otherwise prohibitively rare processes readily calculable.

1.4 Relation to the equation of state

A dynamical transport model should describe not only the temporal evolution of the system away from equilibrium but it should also account for the equilibrium state itself. The latter can, ideally, be obtained by propagating the equations of motion while imposing spatial periodic boundary conditions, i.e. “putting the system into a box and letting it settle”. In this manner, the statistical properties of the system can be extracted. Of particular interest is the *equation of state*, the pressure of uniform matter as a function the controllable state variables, namely the energy density and the net densities associated with each of the conserved “charges” (baryon number, electric charge, strangeness, etc.).

Obviously, when a particular dynamical model is employed as a tool for exploring the equation of state it is important to know the equation of state implied by the model itself. While this information can in principle be obtained by the equilibration procedure sketched above, it is quite problematic in practice. In particular, some dynamical models violate detailed balance because certain reverse processes are not included. (Typically, many-body decays, such as $\omega \rightarrow 3\pi$, may readily be included while the reverse many-body fusion processes are difficult to treat.) Fortunately, in the context of nuclear collisions, such reverse processes may often be safely neglected because the dynamics is completed before they can play a role. But in the context of the (artificially imposed) equilibration process, the absence of reverse processes distorts the resulting stationary state away from the proper equilibrium. This inherent feature makes it especially challenging to probe the equation of state with dynamical transport models.

It is important in this connection to recognise that the *actual* equation of state of a given dynamical model, as discussed above, generally differs from the equation of state specified as a model ingredient. For example, in

one-body models (Chap. 3) the Boltzmann collision integral is (usually) local and so it does not contribute to the pressure. The equation of state implied by the model is then identical to the one specified in the effective one-body Hamiltonian. However, this simple feature holds only if the actual numerical implementation of the collision integral is effectively local. While this would be true in the limit of infinitely many test particles per physical particle, it is not true in the most often employed implementations, such as those using parallel ensembles (see Sect. 3.5.2). As a result, there is usually an additional (but most often unknown) contribution to the pressure from the residual scatterings. This practical problem underscores the subtlety of the relationship between simulation models and the equation of state.

Another inherent problem of particular relevance to the CBM experiment arises from the (presumed) presence of a first-order phase transition. Dynamical simulations with a variety of transport models (Sect. 6.1) suggest that over a wide range of energies the expansion stage of nuclear collisions drives the bulk of the system into the region of phase coexistence. Such matter is thermodynamically unstable against a spatial separation into the two coexisting phases, a deconfined baryon-rich quark-gluon plasma and a gas of hadron resonances. This phase-separation process is a key companion to the occurrence of a first-order phase transition and may form the basis for developing suitable signals of this central feature of the phase diagram. It is therefore essential to develop transport treatments that have the ability to encompass this phenomenon.

This problem was faced during an earlier epoch of the field when the focus was on the nuclear liquid-gas phase transition, cf. Sect. 2.2.3.4 in Part I. This resulted in the development of the Boltzmann-Langevin model in which the inherent randomness of the residual collisions provides the physical trigger of the instabilities accompanying the phase transition. The self-consistent mean field then amplifies the instabilities and thus leads the system towards a phase separation. Such an approach describes the system as an ensemble of individual many-body systems, each described within the one-body approximation, that develop independently into spatially different geometric configurations.

Unfortunately, it has not yet been possible to develop a transport model capable of treating the confinement transition. This would be no easy task, since such a model would not only have to deal with trajectory branchings, as the system is faced with a choice of a multitude of different phase separation “channels” but it must also be capable of changing its effective degrees of freedom (quarks and gluons in one phase and hadron resonances in the other). The first problem is similar to that occurring in nuclear multi-fragmentation caused by the liquid-gas phase transition and it could perhaps be treated in a manner analogous to the Boltzmann-Langevin treatment developed for nuclear dynamics at intermediate energies (Sect. 3.2). But the second problem would presumably require the development of an explicit description of hadrons in terms of the basic chromodynamic degrees of freedom, a feat that has not yet been accomplished. We shall return to this challenge in Sect. 7.4.

Chapter 2

Cascade models

Cascade models provide the simplest microscopic transport descriptions of high-energy nuclear collisions. They are best justified when the early violent part of the collision event occurs so fast that only direct hard interactions play a role and mean-field effects can be neglected.

At centre-of-mass energies of about $\sqrt{s} \geq 3$ GeV, corresponding roughly to the AGS regime of about 6 AGeV laboratory energy, strings-like modes start to be excited. This is also the energy range where the nuclear mean field becomes less important as direct elastic and inelastic collisions start to dominate the reaction dynamics. Then a pure cascade treatment may be applicable. However, even when applied to the ultra-relativistic regime, where the initial collision stage is dominated by binary collisions, a cascade description relies on the assumption that the system is already sufficiently dilute and, furthermore, it still needs to incorporate various subtle effects such as off-shell transport of broad resonances. Finally, apart from collisional encounters a pure cascade treatment suffers from the neglect of interactions such as given by mean-fields or of correlations resulting from final-state interactions.

2.1 Intra-nuclear cascade models

The cascade description of nuclear collisions builds on the intranuclear cascade model VEGAS initially developed for proton (or pion) induced nuclear reactions [17] and a similar code developed in Dubna [18, 19]. It represents the nucleus as a collection of A spatially fixed individual nucleons distributed within the nuclear volume. The incoming hadron then interacts sequentially with those target nucleons that are encountered along its path through random momentum changes in accordance with the free elementary cross sections. Between the scattering events all particles move classically on straight lines. With the event of high-energy nucleus–nucleus collisions such models were correspondingly generalised [20–23]. They were found to be fairly suc-

cessful in reproducing the then available data in the range of bombarding energies up to 1 AGeV. A more refined intranuclear cascade model developed by Cugnon et al. [24, 25] was employed extensively in the Bevalac era.

Different scattering prescriptions were used [23]. The most common one is to decide on the scattering event by means of an impact parameter criterium related to the total cross section and to randomly change the particles' momenta independent of their relative positions, however in accordance with the differential cross section. The other extreme is to use a deterministic classical prescription which relates the scattering angle to the impact parameter, e.g. such as a hard sphere (Billiard ball) dynamics. While the former has a trivial equation of state (EoS), namely that of a gas of non-interacting particles, the latter implies a highly non-trivial EoS, namely that of a hard-sphere gas (which is conceptually complicated to analytically be formulated, but easily simulated through classical Newtonian dynamics).

The early treatments included nucleons and Δ resonances which were allowed to scatter both elastically ($NN \leftrightarrow NN$, $N\Delta \leftrightarrow N\Delta$, $\Delta\Delta \leftrightarrow \Delta\Delta$) and inelastically ($NN \leftrightarrow N\Delta$, $N\Delta \leftrightarrow \Delta\Delta$), while the Δ resonances were allowed to decay only after all interactions had ceased. This picture had the initial difficulty that “cross sections” had to be guessed for the Δ resonance which is an unstable particle with a broad spectral mass width. Initial attempts indeed failed to respect detailed balance across the spectral width of the Δ . The pion (and other hadronic states) were explicitly included in later extensions. The Fermi momenta of the initial nucleons were usually included in the kinematics which was particularly important for production processes near or below threshold.

Hadronic cascade treatments have provided a very useful framework for understanding the dynamics of relativistic nuclear collisions. However, the relevance of these models to the CBM energy domain is limited. The collision energy is sufficiently high to bring the underlying partonic degrees of freedom into play early on and, moreover, the subsequent hadronic stage can now be treated with more refined models.

2.2 The linear cascade model (rows-on-rows)

A simplified cascade treatment called the linear cascade (or rows-on-rows) model¹ was developed by Hüfner and Knoll [6]. It used the straight line dynamics depicted in Fig. 2.1 which leads to a decoupling of the spatial dynamics from that of the particle's momenta. Therefore the co-linear collision dynamics can entirely be formulated as a sequence of processes in momentum space describing the evolution of the momentum distribution in the course of a relativistic nucleus–nucleus collision.

¹ The model rests on the multiple scattering theory developed by Glauber [26–28].

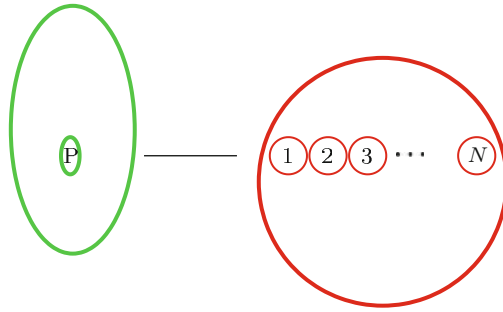


Fig. 2.1 Illustration of the *straight line* collision concept. A particular nucleon P from the Lorentz contracted projectile (*green*) hits N target nucleons on its way through the target (*red*).

Ignoring spatial correlations, the probability $P_B(N)$ that a given projectile nucleon P hits N nucleons on its way through the target B is most often assumed to be Poisson distributed with a mean value \bar{N} given by the integrated nuclear density within a transverse area of the total nucleon–nucleon cross section σ_{tot}^{NN} , i.e. ²

$$P_B(N, \mathbf{s}_B) = \frac{1}{N!} (\bar{N}_B(\mathbf{s}_B))^N e^{-\bar{N}_B(\mathbf{s}_B)} \quad \text{with} \quad (2.1)$$

$$\bar{N}_B(\mathbf{s}_B) = \sigma_{tot}^{NN} \int dz \rho_B(\mathbf{s}_B, z) .$$

Here \mathbf{s}_B is the impact parameter relative to the centre of the target nucleus B . It should be noted that \bar{N} is a Lorentz invariant quantity. The corresponding relations obtained by replacing B by A hold for a target nucleon being struck by M projectile nucleons. With σ_{tot}^{NN} in the range of 40–50 mb, the mean free path has about the same size as the inter-nucleon distance of 1.8 fm in the nuclear bulk region. The total cross section for a nucleon to react with the nucleus A can be obtained by integrating over those impact parameters for which at least one collision occurs,

$$\sigma_A = \int d^2\mathbf{s} \left[1 - e^{-\bar{N}_A(\mathbf{s})} \right] \approx \pi r_0^2 A^{2/3} , \quad (2.2)$$

with $r_0 = 1.12$ fm and similarly for σ_B . Nucleons that suffer at least one collision are called *participants*, the others are quoted as *spectators*. With $\sigma_{AB} \approx \pi r_0^2 (A^{1/3} + B^{1/3})^2$ for the nucleus–nucleus reaction cross section, the impact-parameter averaged number of participants [6] and number of collisions result to the simple expressions given in (1.2).

² Processes arising from Coulomb interactions are ignored here.

The rows-on-rows approach was subsequently refined [29] and used in a variety of studies [30–32], including in particular kaon production [15, 16]. Equilibration in uniform matter consisting of nucleons, pions, and Δ resonances was studied in a treatment that included the quantum-statistical suppression and enhancement factors in the collision sequences [33]. Alternative extensions successfully assumed a kind of statistical equilibration within each rows-on-rows ensemble treating it as a micro-canonical ensemble. The required total energy and momentum results from the Fermi motion averaged energies and momenta of the colliding nucleons [34]. Successful applications were reported for the production of pions and hard photons in nucleus–nucleus collisions [35–37].

In high energy physics, the concept of wounded nucleons [38] was introduced along similar lines. Since these studies concentrated on production processes, which produce at least one extra hadron, such as a pion, it is the inelastic nucleon–nucleon cross section σ_{inel}^{NN} that should enter in the above expressions, rather than σ_{tot}^{NN} . Typically half of all collisions are of production type, though this fraction depends on the energy.

By construction the linear cascade picture is not able to deal with compression effects arising from the equation of state. Therefore it rather serves as a background reference supplying the trivial collision dynamics. As such this concept was revived years later under the term LEXUS³ [39] for the interpretation of the CERN SPS data.

2.3 Parton cascades

Parton cascade models seek to treat the very early and most violent stage of ultra-relativistic nuclear collisions by evolving explicitly the partonic degrees of freedom. They are therefore mostly applied to study the initial compressional and thus high density phase of ultra-relativistic heavy ion collisions (collider energies, $\sqrt{s} \geq 200$ GeV).

The parton cascade description is founded on the field-theoretic parton picture of hadronic interactions within the established framework of perturbative QCD. The colliding nuclei are visualised as clouds of quasi-real quarks and gluons whose mutual inter-penetration causes a rapid materialisation. Multiple short-range scatterings between the partons (minijet production) together with associated QCD radiation (gluon bremsstrahlung) produce the major part of the entropy and transverse energy. The approach is designed for high energy collisions. Hence long-range colour forces and associated non-perturbative effects are assumed to be negligible. The treatment becomes increasingly ill-justified at lower energies where most parton scatterings involve momentum transfers that are too small to be described

³ LEXUS: Linear extrapolation of ultra-relativistic nucleon–nucleon scattering to nucleus–nucleus collisions.

perturbatively. An excellent review of this class of treatment was given by Geiger [40].

The parton cascade models have the following general structure:

1. Initialisation: The initial parton distributions are obtained on the basis of the measured nucleon structure functions.
2. Interaction: Perturbative QCD provides the parton interactions that in turn evolve the ensemble of partons during the violent collision stage. This includes multiple scatterings together with associated space-like and time-like parton emission processes before and after each scattering. However, the scatterings are incoherent with no possibility for quantum interference effects.
3. Propagation: The partons are propagated freely on straight trajectories between interactions, without any non-perturbative effects.
4. Hadronization: Towards the end of the violent stage the partons are recombined or converted via string fragmentation into hadrons that may or may not interact further among themselves.

In the present applications, hadronization is not implemented as a transport process with proper forward and backward reactions between the two phases (which should be governed by corresponding driving potentials). Rather, the partons are instantaneously converted into hadrons according to a certain criterion for the onset of hadronization. Thus, such descriptions of the hadronization process violate detailed balance requirements, see Sect. 5.8.

2.4 String models

The majority of the dynamical models being used in energy ranges where the partonic degrees of freedom can be excited do not explicitly treat the partonic degrees of freedom. Rather, they invoke concepts developed for the description of elementary collisions, such as pp , $\bar{p}p$, or e^+e^- . The basic picture is that of a color exchange between the virtual partons associated with the fast-moving collision partners. So, as a result, colour charges become spatially separated and energy is being stored into the resulting chromo-electric field between the receding colour charges. This situation is phenomenologically described by a string, cf. e.g. the Lund string model [41]. The energy stored in the string may then subsequently create $q\bar{q}$ pairs that locally neutralise the field and thus fragment the string. Strings below a certain threshold energy are then considered as hadrons. In this manner, a high-energy elementary collision leads to a many-hadron final state.

Thus, phenomenological strings present a tool for taking account of the fact that an increase in the collision energy leads to the activation of ever more partonic degrees of freedom (quarks and gluons), without a need for

explicitly treating the partonic phase. Optionally the models include collective string effects such as the color-rope picture [42, 43]. They normally ignore the associated space-time evolution and operate solely in momentum space. Possible space-time coherence effects for the reaction are usually mocked up by a phenomenological formation time that prevents created particles from immediate interactions with other ones. Up to now, the string models contain no fields and reverse reactions are ignored as well. This inherent lack of detailed balance prevent the system from equilibrating and may lead to an over-population of phase space. Further details can be found in the model descriptions in Sect. 3.5.

Chapter 3

Kinetic transport models

The above cascade models treat the collisions among the constituents on a very simplistic level that ignores both mean fields and correlations. Thus refined treatments are needed. On the other hand, an exact many-body treatment of the complex collision process is neither possible nor desirable. Therefore one still must develop a suitably reduced level of description. The dynamics of the system will then be described in terms of certain well chosen relevant observables that are supposed to contain the most relevant information. Then only these are treated explicitly by the dynamics, while the irrelevant degrees of freedom generally provide a stochastic background for the retained variables. Typically such procedures imply a separation of scales, mostly time scales, where the modes with fast relaxation times generally resulting from higher-order correlations provide the coupling and stochastic terms for the explicitly treated slow modes of the dynamics. Such reductions in information generally imply a growth in an appropriately defined entropy.

Nuclear collisions are mostly described by simply retaining the single-particle information. In its simplest still non-dissipative form in terms of single-particle wave functions it leads to the time-dependent (Brueckner) Hartree-Fock picture. The step forward towards a density-matrix description permits the inclusion of dissipative effects. In the semi-classical limit, the latter take the form of a collision term expressed in terms of the single particle distribution functions in phase-space $\{f_a(x, p)\}$ of the various hadronic species $\{a\}$. In the following we shall consider just one generic nucleon specie. The extension to several hadronic species is straightforward and yields a set of coupled but similar equations.

Notationally we use the relativistically covariant form with the metric $g^{\mu\nu} = \text{diag}(1, -1, -1, -1)$ with the convention for the units that $\hbar = c = 1$, if not explicitly stated differently. The four-coordinates and four-momenta are $x = (t, \mathbf{x})$, $p = (p^0, \mathbf{p})$, etc., where p^0 is the energy including the rest mass m of the particles.

3.1 Potentials and mean fields

Within one-body approaches the nucleons are assumed to move in an effective one-body field. Given a two-body interaction, the effective one-body potential or self-energy of a given particle results from the coherent effect on its forward motion due to its interaction with all the other particles in the medium. Again tractable truncation schemes are to be used. The simplest is the Hartree-Fock (HF) approximation which ignores all higher order correlations and thus explores the interaction proportional to the density ρ of the medium. In a relativistic formulation the interaction can be provided by an exchange of a meson with mass m_s . For example the exchange of a scalar boson leads a scalar two-body potential which in its four momentum representation becomes $\tilde{V}_{NN}(p) \propto 1/(p^2 - m_s^2)$. In HF approximation the many-body wave function is given by a Slater determinant of single particle states which are propagated in the self-consistent mean field Σ_N . The latter consists of a direct and an exchange potential, both given by the self-consistent densities of the system. The classical analogue to the HF approximation is the Vlasov treatment (which can be characterised as the Boltzmann equation (3.4) without the collision term). In the non-relativistic limit the interaction is considered instantaneously and the meson-exchange potential simply becomes a function of three momentum, hence $\tilde{V}_{NN}(q) \propto 1/(\mathbf{q}^2 + m_s^2)$. The exchange of other bosons such as vector bosons would imply corresponding tensor structures.

In the nuclear case particular complications arise from the fact that realistic NN potentials have a strong repulsive core at short distances r , which lead to non meaningful expressions for the HF approximation. This can be cured by using an effective interaction instead of the bare two-body interaction V , either fitted to a wide body of nuclear structure data or microscopically derived from V . The latter derivation includes the T - ρ approximation, where the two-body potential V is replaced by the corresponding vacuum two-body scattering matrix T , or its in-medium improvement, the Brückner G matrix [44]. Modern renormalisation group approaches (RG) [45–47] construct effective interactions through a separation in momentum scale: the high momentum sector is eliminated by the RG method leading to a correspondingly tamed two-body potential called $V_{\text{low}k}$ for the dynamics in the low momentum sector. Alternatively the unitary correlation operator method (UCOM) [48–50] explicitly treats the short range correlations arising from the short range sector of the interaction by a unitary transformation and arrives at very similar tamed potentials.

Already through the exchange Fock-term but also due to the use of effective interactions the so derived mean field potentials become momentum dependent. The non-relativistic single particle Hamiltonian then reads

$$h = \frac{\mathbf{p}^2}{2m} + \Sigma(\mathbf{p}, \rho(\mathbf{x})). \quad (3.1)$$

For iso-symmetric matter the relativistic Dirac mean-field Hamiltonian can only contain two fields, a scalar and a vector field,

$$h_{\text{Dirac}} = \boldsymbol{\alpha} \cdot \mathbf{p} + \beta(m - \Sigma_S) + \Sigma_V^0, \quad (3.2)$$

with Dirac matrices $\boldsymbol{\alpha}, \beta$, for the nuclear problem first investigated by Dürr in 1956 [51] almost two decades prior to Walecka [52]. It should be noted that in the relativistic case a momentum dependence arises due to Lorentz forces generated by the vector component of the self-energy, even if the self-energies $\Sigma_{S,V}$ do not explicitly depend on momentum. In semi-classical treatments one alternatively uses the quasi-relativistic “Hamiltonian”

$$h = \sqrt{\mathbf{p}^2 + m^2 + \Pi(\mathbf{p}, \rho(\mathbf{x}))} \quad (3.3)$$

with the Schrödinger-equivalent optical potential

$$U_{\text{opt}}(\mathbf{p}, \rho) = \frac{1}{2m} \Pi(\mathbf{p}, \rho) = -\Sigma_S + \frac{p_\mu \Sigma_V^\mu}{m} + \frac{\Sigma_S^2 - \Sigma_{V\mu} \Sigma_V^\mu}{2m}.$$

Here we introduced the Lorentz-scalar (polarisation) function Π to be added to the m^2 term in (3.3).

The momentum dependence of the effective interaction causes some extra complications for the interpretation of the calculated results. The UCOM method for example directly explains that along with the unitary transformation of the Hamiltonian also all other operators have to be transformed likewise to corresponding effective operators. This is particularly visible for conserved currents. The simplest consequence of momentum-dependent interactions is that the mass of a particle changes to an effective mass m^* in the medium. A naive interpretation would imply that the entire body of A particles would respond to a boost with a mass Am^* which is of course false. Rather the elementary expressions for the conserved currents, as derived from a microscopic Lagrangian are only valid for the full configuration space. For the reduced description in terms of effective interactions they are to be readjusted accordingly, e.g. by direct derivation or in case of phenomenological interactions minimum substitution methods are of help. In semi-classical descriptions the corresponding back-flow term can be furnished by extra Poisson bracket terms beyond the ones appearing in the Boltzmann equation (3.4), see details given in Sect. 3.3.4.

Through the optical theorem the imaginary part of the mean potential or self-energy Σ is related to the total cross section, *i.e.* to all processes leading to non-forward scattering or to inelastic processes. The latter will explicitly be treated by the loss term of the collision term in the Boltzmann equation (3.4). Genuine mean-field schemes, which are entirely governed by *hermitian* one-body Hamiltonians such as time-dependent Hartree-Fock (TDHF), are non-dissipative and conserve the entropy exactly already at the one-body level. (This holds both for quantum and classical mean-field dynamics with

zero collision term.) Nonetheless, by considering a certain limited set of observables or by performing a coarse graining in conjunction with a suitable limit procedure, also such mean-field evolutions (for example for nuclear collisions) display relaxation features.

3.2 Two-body collisions (Boltzmann equation)

The residual interaction omitted in the mean-field description may be accommodated into a one-body description by means of the *Stoßzahlansatz* which approximates the two-body density as a product of one-body densities, $f^{(2)}(i, j) \approx f^{(1)}(i)f^{(1)}(j)$ (also known as “molecular chaos”), along the line laid out by Boltzmann. (As above, we still assume that the interaction is of two-body form; suitable generalisations are needed for multi-particle interactions.) By this device, the dynamical information about the system, at any time, is given solely in terms of the one-body density, from which most of the quantities of interest can be obtained. This continual reduction of information generates entropy.

Conceptually, the natural implementation of this program within the quantum framework is *Stochastic TDHF* [53], in which the residual interaction causes the system to continually jump from one Slater determinant to another. Though considerable work has been devoted to this type of model, its practical use has been rather limited so far [54].

By contrast, the (semi-)classical framework of the Vlasov model provided a very useful and practical calculational tool that has led to numerous simulation codes. We therefore describe this approach briefly. In this physical picture, individual hadrons (here nucleons) move in the self-consistent effective one-body field while experiencing direct (here Pauli-suppressed) residual scatterings that are governed by the effective differential cross section $d\sigma/d\Omega$. The combined time evolution of the phase-space density $f(x, \mathbf{p})$ is then described by the following equation of motion,

$$\dot{f}(x, \mathbf{p}) \equiv \frac{\partial f}{\partial t} + \{h[f], f\} = C[f](x, \mathbf{p}) = \bar{C}[f] + \delta C[f], \quad (3.4)$$

here and in the next subsection using three-momentum notation in the sense of the l.h.s. of (3.6). The left-hand side gives the collision-less (Vlasov) evolution in the self-consistent effective field,¹ while the effect of the residual (two-body) interaction is given by the collision term on the right.

Since the individual collisions are stochastic, the collision term C can be decomposed into its average and fluctuating parts, \bar{C} and δC , respectively.

¹ In case of momentum dependent potentials the Poisson-bracket term in the equation of motion (3.4) is insufficient, since further gradient terms have to appear in order to recover its Galilei (Lorentz) invariance through a corresponding back-flow term. Thus the treatment of momentum dependent forces is nontrivial, see also Sect. 3.3.4.

In most applications, however, only the average effect of the collisions is considered. Relative to the original treatment by Boltzmann, which was aimed at dilute classical gases, suitable Pauli blocking or Bose enhancement factors are added for applications to nuclear systems. Thus, for a gas of nucleons, the effect of the average collision term \bar{C} is

$$\bar{C}[f](x, \mathbf{p}_1) = \int \frac{d^3 \mathbf{p}_2}{(2\pi)^3} \int d\Omega' v_{12} \frac{d\sigma_{12 \rightarrow 1'2'}}{d\Omega'} \times \underbrace{[(1-f_1)(1-f_2)f_{1'}f_{2'}]}_{\text{gain}} - \underbrace{f_1 f_2 (1-f_{1'})(1-f_{2'})}_{\text{loss}}. \quad (3.5)$$

where $f_1 \equiv f(x, \mathbf{p}_1)$ etc. are the local phase-space occupancies and $v_{12} \equiv |\mathbf{v}_1 - \mathbf{v}_2|$ is the relative speed of the two colliding nucleons. Thus the net effect on the phase-space density at (x, \mathbf{p}_1) is obtained by subtracting the loss from scatterings with partners at x having momentum \mathbf{p}_2 from the gain resulting from the reverse reactions, $\mathbf{p}_1' \mathbf{p}_2' \rightarrow \mathbf{p}_1 \mathbf{p}_2$. (The loss term can directly be associated with the imaginary part of the optical potential mentioned above.)

The quantum refinement of the collision term (3.5) was first made for electron gases by Nordheim [55] and Uehling and Uhlenbeck [56]. It was adapted to uniform gases of nucleons, pions, and Δ resonances about 30 years ago [33] and was subsequently augmented by the mean field [57] to provide a description of collisions between finite nuclei. The resulting *nuclear Boltzmann-Uehling-Uhlenbeck (BUU) equation* exists in many implementations that differ with respect to both the physics input (such as the types of hadrons included, the form of their effective Hamiltonian, and their differential interaction cross sections, including inelastic reactions and particle production) and the numerical methods employed (see Sect. 3.5.2 below). Mostly the particles were assumed to be on-shell. Furthermore, in most applications to nuclear collisions, the collision term (3.5) was taken to be local in both, space and time, a simplification that is not generally justified. The extension to the corresponding non-Markovian evolution was pioneered by Ayik [58] and has been shown to play a significant role for nuclear dynamics in the presence of instabilities [59]. Alternatively Morawetz et al. [60] proposed a space-time nonlocal collision term with first applications to nuclear collisions. Besides the mean field part such nonlocal collision terms lead to supplementary contributions to the equation of state due to the finite virial.

3.2.1 Boltzmann-Langevin dynamics

It is important to recognise that the standard nuclear Boltzmann equation includes only the average effect \bar{C} of the residual collisions and therefore leads to a deterministic time evolution of $f(\mathbf{r}, \mathbf{p}, t)$ (although ensembles of final states, $\{f(\mathbf{r}, \mathbf{p}, t \rightarrow \infty)\}$ may be obtained by propagating suitable ensem-

bles of initial configurations, $\{f(\mathbf{r}, \mathbf{p}, t_i)\}$). By contrast, when the fluctuating term δC is included in (3.4) the stochastic character of the individual collisions leads to a diffusive time evolution such that a single initial phase-space density $f(\mathbf{r}, \mathbf{p}, t_i)$ develops into an entire ensemble of phase-space densities, $\{f(\mathbf{r}, \mathbf{p}, t)\}$. Viewed in the abstract space of one-body densities, the evolution resembles a random walk, as each distinct collision event causes a given one-body density to branch into an entire family of densities, each one reachable from the given density as one particular outcome of the collision event in play. Each of these systems then undergoes its own self-consistent mean-field evolution until its next two-body collision occurs. The resulting transport description is referred to as the nuclear Boltzmann-Langevin model [61–64].

When the global dynamics is stable, the effect of these trajectory branchings generates the appropriate statistical fluctuations around the average trajectory approximately given by the standard evolution obtained without the fluctuating collision term. While conceptually gratifying, these fluctuations are usually not essential.

However, the situation is radically changed when the system encounters instabilities, such as when a phase transition is present. The different trajectory branches may then evolve into configurations that are macroscopically quite different from one another. (For example, the number of final nuclear fragments may differ from one dynamical history to another, as typically happens in nuclear multi-fragmentation.) In such a situation, the single trajectory $f(\mathbf{r}, \mathbf{p}, t)$ generated by the mean Boltzmann equation becomes meaningless and may not even resemble any of the members of the ensemble resulting when the fluctuating term is included. (For example, if one were to simulate thermal fission of a spherical nucleus by the standard Boltzmann approach, the system would remain strictly spherical at all times and might not even be energetically able to disintegrate, whereas the Boltzmann-Langevin equation would yield an ensemble of regular binary events, each one displaying its own fission direction.) It is thus evident that the Boltzmann-Langevin model may be particularly well-suited for studies of phase transition dynamics.

However, it is technically rather demanding to treat the Boltzmann-Langevin model and this has limited its practical utility. Fortunately, though, various adequate approximate treatments were developed for nuclear dynamics. In particular, the Brownian One-Body (BOB) model replaces the effect of the stochastic part of the collision term by a Brownian one-body force wherever the local conditions are inside the spinodal phase region of instability [65]. This one-body force is designed so as to emulate the growth of the most unstable spinodal mode, which tends to become dominant, and the resulting dynamics therefore provides a quantitative approximation to the full Boltzmann-Langevin dynamics. The Brownian One-Body treatment has proven particularly powerful for the understanding of the nuclear liquid-gas phase transition and the associated multi-fragmentation phenomenon [66].

Such a refinement level was so far achieved only for nuclear dynamics at intermediate energies. However, nuclear collisions in the FAIR energy

range may generate environments that are situated inside the thermodynamic phase-coexistence region and, therefore, are inherently unstable against a phase separation. For the corresponding dynamical treatment it is essential to develop the transport models in a manner that is conceptually similar to what was done at medium energies as described above. (A comprehensive review of stochastic approaches to nuclear dynamics was given in [67].)

3.3 Transport theory with dynamical spectral functions

Already in the early days of kinetic transport descriptions of nuclear collisions one had to deal with a problem that definitely lied beyond the applicability of the standard Boltzmann equation. Namely one had to deal with broad resonances such as the Delta-isobar resonance. Its decay width of 120 MeV exceeds by far the mean kinetic energies of the particles in the collision system. In order to circumvent this deficiency recipes were invented, such as to represent the resonances by a bunch of appropriately weighted on-shell particles with masses distributed across the mass spectrum of the resonance. This permitted to define proper creation cross sections, while the decay of all the mass components was treated by an exponential law in time in accordance with the nominal decay rate. It took more than a decade, namely until the seminal work of Danielewicz and Bertsch [68], before it was realized that this prescription violates detailed balance. Thus in the event of equilibration the system would be driven towards the wrong occupations for the resonance. The improved formulation [68] still relied on the concept of cross sections, since this was the main input to determine the collision rates. However such strategies based on asymptotic scattering state concepts loose their sense for short lived “particle states”. This includes resonances which attain their width through decays already in vacuum but also particles which through collisions acquire a corresponding damping width (collision broadening). With mean-free collision times typically below 5 fm/c, the damping widths become comparable with the mean kinetic energies of the particles. Thus most particles in the collision system cannot appropriately be described by a quasi-particle ansatz of infinite lifetime.

The basic concepts for a proper transport treatment of particles with broad spectral widths were already laid out in the book by Kadanoff and Baym (1962) [69]. In principle, the Kadanoff-Baym (KB) equations – e.g. derived in lowest order from a two-particle irreducible (2PI) action as described below – provide a convenient starting point. First discussions on quantum effects for the collision rates evaluated in the context of the KB equations date back to the pioneering work by Danielewicz in 1984 [7, 8]. However enormous demands on computational resources deferred further progress for long time. The KB equations may directly be solved including also non-locality in space-time. This is a formidable task and presently intractable in its full

scale.² Most attempts dealt with very simple theories and in simplifying geometry, such as spatial homogeneity, cf. e.g. [73]. But rarely the special issue of broad spectral functions was addressed so far. The question arises, if further approximations to the KB equations – like the gradient expansion – which lead to a generalized transport treatment do perform well enough in case of inhomogeneous systems with strong coupling. In this respect serious progress was achieved only rather recently [74–84].

In this section we try to outline the main steps towards a transport treatment with dynamical spectral functions. Since most of the published presentations are rather technical we try to be more pedagogical. We shall outline the basic steps in simple physical terms. We start from known grounds, as the Golden Rule, in order to motivate the general form of the driving terms, namely current–current correlation functions. The latter drive the quantum Kadanoff-Baym equations which are the basis for the derivation of the generalised kinetic transport equations. In subsequent sections we further address important special features which arise in the context of unstable particles with broad spectral functions.

Conceptual wise one has to switch from distributions in spatial momentum to distributions in four momentum permitting that particles can have a spectral width. The link between distributions in spatial momenta \mathbf{p} of on-shell particles and the corresponding four-momentum expression results from

$$f_{(3)}(x, \mathbf{p}) \frac{d^3 p}{(2\pi)^3} = f_{(4)}(x, p) \underbrace{\frac{2\pi\delta(p^2 - m^2)}{A(x, p)}}_{F(x, p)} \Theta(p^0) 2p^0 \frac{d^4 p}{(2\pi)^4}. \quad (3.6)$$

Here the Θ -function permits only positive energies p^0 . This already allows to introduce two quantities of central importance. On the one hand the spectral function $A(x, p)$, which here takes the trivial relativistic form for on-shell particles, and secondly the four-momentum distribution function $F(x, p)$. In expression (3.6) the on-shell character of the spectral function will convert the four-phase-space distribution function $f_{(4)}(x, p)$ on the r.h.s. to the three-momentum distribution on the l.h.s. $f_{(3)}(x, \mathbf{p})$ (below we'll drop the subscripts (3) or (4)). The interaction with other particles will modify the spectral function $A(x, p)$, both due to the real part of the mean field potential or self energy $\Sigma(x, p)$, but also due to dissipative processes that contribute to the imaginary part of the self energy in form of a damping width $\Gamma(x, p) = -2\text{Im } \Sigma(x, p)$ for fermions or $\Gamma(x, p) = -\text{Im } \Pi(x, p)/p^0$ for relativistic bosons. In the latter case the polarisation function Π replaces the self-energy. The discussion of these dynamical quantities will be the central issues of this chapter.

² Recent progress in this context with applications to various branches in physics can be found in the proceedings of workshops on the KB equations and non-equilibrium Green's function methods [70–72].

3.3.1 From the golden rule to the Kadanoff-Baym equations

The standard text-book transition rate e.g. for the radiation from some initial state $|i\rangle$ with occupation n_i to final states $|f\rangle$ given per 3-momentum \mathbf{p} of the emitted boson (e.g. a photon emitted through an orbital transition of an electron in an atom, or a nucleon in a nucleus) is given by Fermi's golden rule³

$$\begin{aligned}
 (2\pi)^3 \frac{W_{if}(\mathbf{p})}{d^3k dt} &= \sum_{i f} n_i (1 - n_f) \left| \int d^3x \langle f | \phi_{\mathbf{p}}(\mathbf{x}) j(\mathbf{x}) | i \rangle \right|^2 2\pi \delta(E_i - E_f - \omega_{\mathbf{p}}) \\
 &= \sum_{i f} n_i (1 - n_f) \left| \begin{array}{c} f \\ \uparrow \\ \vdots \\ \uparrow \\ i \end{array} \right|_{\mathbf{p} \in}^2 2\pi \delta(E_i - E_f - \omega_{\mathbf{p}}). \quad (3.7)
 \end{aligned}$$

Here $j(x)$ is the current operator that couples to the emitted boson with the wave function $\phi_{\mathbf{p}}(x) = \phi_0 e^{i\mathbf{p}\mathbf{x}}$ where \mathbf{p} is the boson momentum. This formulation is limited to the concept of asymptotic states and therefore inappropriate for problems which deal with particles of finite life time. One rather has to go from the level of absolute squares of tree-level diagrams to a two-point description. Then the very same rate can be separated into a part that encodes the source properties times that describing the produced boson

$$\begin{aligned}
 (2\pi)^3 \frac{W_{if}(\mathbf{p})}{d^3k dt} &= \int d^3x d^3y \frac{d\omega}{2\pi} \times \overbrace{\sum_{i f} n_i (1 - n_f) \langle i | j^\dagger(\mathbf{x}) | f \rangle \langle f | j(\mathbf{y}) | i \rangle 2\pi \delta(\omega + E_i - E_f)}^{-i\Pi(\mathbf{x}, \mathbf{y}; \omega)} \\
 &\quad \times \underbrace{\phi_{\mathbf{p}}(\mathbf{x}) \phi_{\mathbf{p}}^\dagger(\mathbf{y}) 2\pi \delta(\omega - \omega_{\mathbf{p}})}_{A_{\mathbf{p}}(\mathbf{y}, \mathbf{x}; \omega)}. \quad (3.8)
 \end{aligned}$$

On the two-point level it specifies the corresponding spectral function $A_{\mathbf{p}}(\mathbf{x}, \mathbf{y}; \omega)$ of the boson (here given in a mixed energy-spatial-coordinate representation). The source properties are given by the polarisation function which results from the current-current correlator

³ This was first derived by Dirac [85] in 1927. The “golden” part of the rule is that coming from time-dependent perturbation theory one of the time integrations occurring in the square of the amplitude conspires to a delta-function in energy. Similar considerations lead to a delta-function in 3-momentum for homogeneous systems in the infinite volume limit. All these “tricks” are resolved by the Wigner transformation which is discussed below.

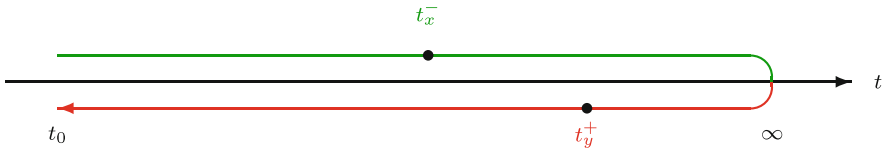


Fig. 3.1 Closed real-time contour \mathcal{C} with two external points x, y on the contour.

Indeed non-equilibrium many-body or field theory is based on the strategy to marry the time-ordered evolution inherent in the *amplitude* with the anti-time ordered evolution pertaining to the *conjugate complex amplitude*. Thus, rather than only considering the time-ordered products of operators as in standard (zero temperature) many-body or scattering theory one generalises the concept to a so called time contour \mathcal{C} , cf. Fig. 3.1. It joins the time evolution with vertices marked by a $-$ sign with a subsequent anti-time evolution with vertices marked by a $+$ sign.

The Dyson equation for the two-point Green's functions can then accordingly be formulated as time contour functions. This was the conceptual starting point used by Kadanoff and Baym [69]. They reformulated the non-equilibrium Dyson equations in such a form that amends to describe the evolution of the special $\{-+\}$ and $\{-+\}$ components of the propagators. This way one comes to equations that directly determine the space-time changes of occupied states as just discussed. For relativistic bosons the Kadanoff-Baym (KB) equations then read⁵

$$\begin{aligned} (G_0^{-1}(-i\partial_x) - G_0^{-1}(-i\partial_y)) G(x^-, y^+) \\ = \int_{\mathcal{C}} dz (\Pi(x^-, z) G(z, y^+) - G(x^-, z) \Pi(z, y^+)) \end{aligned} \quad (3.11)$$

$$\text{where } G_0^{-1}(p) = p^2 - m^2 \text{ for relativistic bosons.} \quad (3.12)$$

Thereby the time-part of the folding integral on the r.h.s goes over the time-contour \mathcal{C} given in Fig. 3.1. Interchange of x^- with y^+ gives the equation for G^{+-} , i.e. for the “density” of available states. Thereby the driving kernel of these dynamical equations of motion as given by the current-current correlation function Π , cf. Eq. (3.9), is restricted to *one-particle irreducible* (1PI) diagrams,⁶ since the KB (or Dyson) equations of motion generate the reducible pieces. These KB equations constitute the basis for all transport theory formulations on the one-particle distribution level.

For slightly inhomogeneous and slowly evolving systems, the degrees of freedom can be subdivided into rapid and slow ones. Any kinetic approxi-

⁵ Notation wise using synonymously $F^{ij}(x, y) = F(x^i, y^j)$ where with $i, j \in \{-+\}$ the x^i, y^j are the space-time contour coordinates on \mathcal{C} , while x, y are the corresponding physical coordinates.

⁶ These are diagrams that upon cutting a single propagator line do not split into two disconnected pieces.

mation is essentially based on this assumption. Then for any two-point function $F(x_1, x_2)$, one separates the variable $\xi = (t_1 - t_2, \mathbf{x}_1 - \mathbf{x}_2)$, which relates to the rapid and short-ranged microscopic processes, and the variable $x = \frac{1}{2}(t_1 + t_2, \mathbf{x}_1 + \mathbf{x}_2)$, which refers to the slow and long-ranged collective motions. The Wigner transformation, i.e. the Fourier transformation in four-space difference $\xi = x_1 - x_2$ to four-momentum p of the components of any two-point function

$$F^{ij}(x, p) = \int d\xi e^{ip\xi} F^{ij}(x + \xi/2, x - \xi/2), \quad \text{where } i, j \in \{-+\} \quad (3.13)$$

leads to a (co-variant) four phase-space formulation of two-point functions.

It is helpful to avoid cumbersome notations in terms of Green's functions and use quantities which have a straight physical interpretation analogously to the terms in the Boltzmann equation. As already suggested in (3.6) we define the four-phase space distribution functions (4 dim. Wigner functions) as

$$\begin{aligned} F(x, p) &= f(x, p)A(x, p) = \mp iG^{-+}(x, p) \\ \tilde{F}(x, p) &= [1 \mp f(x, p)]A(x, p) = iG^{+-}(x, p) \end{aligned} \quad (3.14)$$

with the corresponding Fermi/Bose occupation functions $f(x, p)$ and $[1 \mp f(x, p)]$. Here and below upper signs factors relate to fermion quantities, whereas lower signs refer to boson quantities.

The key quantity that contains the spectral mass distributions is the spectral function $A(x, p)$. Formally it relates to the imaginary part of the retarded Green's function

$$A(x, p) \equiv -2\text{Im } G^R(x, p) = \tilde{F} \pm F. \quad (3.15)$$

According to the retarded relations between Green's functions G^{ij} , *only two real functions, e.g. f and A , are required for a complete dynamical description*. Basically the spectral function A contains the information on how the single particle modes with a given momentum are distributed in energy, while f determine the actual occupation of these modes. As the dimension of the field operators and likewise the propagators depends on the type of particle, the physical meaning of the distribution and spectral functions, F and A , changes depending on, whether one deals with non-relativistic Schrödinger or relativistic Dirac particles on the one side or relativistic Klein-Gordon bosons which have second order time derivatives in the field equations of motion. For instance the vector current densities are alternatively given as

$$j^\mu(x) = \int \frac{d^4p}{(2\pi)^4} v^\mu F_{\text{non-rel}}(x, p) \quad \begin{cases} \text{for non-rel. particles} \\ \text{where } v = (1, \mathbf{v}) \end{cases} \quad (3.16)$$

$$j^\mu(x) = \int \frac{d^4p}{(2\pi)^4} 2p^\mu F_{\text{rel}}(x, p) \quad \text{for relativistic bosons.} \quad (3.17)$$

Correspondingly the Kadanoff-Baym and retarded equations given below take different forms.

The steps towards a derivation of general transport equations is to describe the dynamics by a set of coupled Dyson equations which one then uses in its Kadanoff–Baym (KB) form (3.11). Through the Wigner transformation one directly obtains the space-time changes of the distribution functions F

$$v^\mu \partial_\mu \underbrace{i G^{-+}(x, p)}_{F(x, p)} = \{G \otimes \Sigma\}_{(x, p)}^{-+} - \{\Sigma \otimes G\}_{(x, p)}^{-+} \quad (\text{non-rel.}) \quad (3.18)$$

$$2p^\mu \partial_\mu \underbrace{i G^{-+}(x, p)}_{F(x, p)} = \{G \otimes \Pi\}_{(x, p)}^{-+} - \{\Pi \otimes G\}_{(x, p)}^{-+} \quad (\text{rel. bosons}) \quad (3.19)$$

and similar equations for $\tilde{F} = iG^{+-}$. On the r.h.s. the Wigner transformed contour convolutions (abbreviated by \otimes) is a-priori a complicated formal expression. However, in the limit of negligible space-time variations it becomes a simple product of the corresponding Wigner-transformed quantities. Formally these steps are still exact, provided one uses the exact set of Dyson equations.

Practical applications do require a truncation of the hierarchy which implies to work with approximate correlations functions Σ or Π which are then self-consistently expressed through the propagators G . Such truncations should be done in such a way that they assure conservation laws, detailed balance for the rates and thermodynamic consistence for the equilibrium limit [86]. In order to approximate the r.h.s. the standard steps towards a derivation of transport equations then usually involve two further approximations: (i) the gradient expansion for the slow degrees of freedom, as well as (ii) the quasi-particle approximation for the rapid ones. We intend to avoid the latter approximation and will solely deal with the gradient approximation for slow collective motions by performing a systematic gradient expansion of the coupled Kadanoff–Baym equations (3.18). Its r.h.s. then conspires to a collision term containing gain and loss parts and 1st-order gradient corrections, cf. Sect. 3.3.2. For a detailed derivation and the extensions to include the coupling to classical field equations we further refer to [77, 80, 87].

In the limit of smooth space-time behaviours the retarded propagator and thus the spectral function can be obtained simply algebraically from the self-energies or the polarisation functions. For non-relativistic particles (bosons or fermions) one obtains

$$\begin{aligned} G^R(x, p) &= \frac{1}{p_0 - m - \mathbf{p}^2/(2m) - \Sigma_R(x, p)} \quad \text{for non-rel. particles, where} \\ A(x, p) &= \frac{\Gamma(x, p)}{(p_0 - m - \mathbf{p}^2/(2m) - \text{Re } \Sigma_R(x, p))^2 + \Gamma(x, p)^2/4} \quad \text{and} \\ \Gamma(x, p) &= -2\text{Im } \Sigma_R(x, p). \end{aligned} \quad (3.20)$$

Here A is the spectral function with local damping width Γ at four momentum p . Accounting for intrinsic quantum numbers such as spin or iso-spin or in the relativistic Dirac case these relations are corresponding matrix relations. In the case of relativistic bosons the corresponding relations read

$$G^R(x, p) = \frac{1}{p^2 - m^2 - \Pi_R(x, p)} \quad \text{for relativistic bosons, where}$$

$$A(x, p) = \frac{2p_0 \Gamma(x, p)}{(p^2 - m^2 - \text{Re } \Pi_R(x, p))^2 + p_0^2 \Gamma^2(x, p)} \quad \text{and} \quad (3.21)$$

$$\Gamma(x, p) = -\text{Im } \Pi_R(x, p)/p_0. \quad (3.22)$$

For vector mesons these forms become corresponding Lorentz-tensor relations. According to (3.22) all rates become Lorentz time-delayed by a factor \sqrt{s}/p_0 . Though generally valid also for particles with broad damping width, this fact is immediately obvious in vacuum where the polarisation function Π is solely a function of the invariant mass $s = p^2 = p_0^2 - \mathbf{p}^2$.

As further shown in [87] mean fields and condensates, i.e. non-vanishing expectation values of one-point functions can also be included.

In local thermal equilibrium quite some simplifications among the kinetic quantities result. The Kubo–Martin–Schwinger condition determines the distribution functions to be of Fermi–Dirac or Bose–Einstein type, respectively, known as Jüttner functions. They are then simply a function of energy with respect to the co-moving fluid cell

$$f_{\text{loc-eq}}(x, p) = 1 / (\exp((p_\mu u^\mu(x) - \mu(x))/T(x)) \pm 1). \quad (3.23)$$

Here $u^\mu(x)$ is the local fluid velocity, while $\mu(x)$ and $T(x)$ are the local chemical potential and temperature, respectively. The corresponding forms of the spectral functions (3.20) and (3.21) are rigorous through the four-momentum $p = (p_0, \mathbf{p})$ dependence of the retarded self-energy or polarisation function. In the non-equilibrium case all quantities become functions of the space-time coordinates x and, of course, the distribution functions $f(x, p)$ generally also depend on the four momentum p .

3.3.2 Generalised transport equations with dynamical spectral functions

From now on we confine the presentation to the case of relativistic bosons in order to also discuss dilatation effects arising from relativistic kinematics. A systematic first order gradient approximation [75, 77, 78, 80] to the corresponding Kadanoff–Baym Equations [69], cf. Eq. (3.19), provides a generalised transport equation which determines the space-time changes of the

four-phase-space distribution function $F(x, p) = f(x, p)A(x, p)$ for relativistic bosons⁷ as

$$2p^\mu \partial_\mu F(x, p) - \{\text{Re } \Pi^R, F\} + \{\Pi^{\text{gain}}, \text{Re } G^R\} = C_{\text{loc}} \quad (3.24)$$

with $\Pi^{\text{gain}} = \pm i\Pi^{-+}$ plus a similar equation for $\tilde{F} = (1 \mp f(x, p))A(x, p)$. The local collision term C_{loc} will be explained below. In first order gradient approximation the spectral function is given by the imaginary part of the retarded propagator, according to the algebraic expressions (3.20) or (3.21).

The simultaneous adjustment of the spectral function to the local real and imaginary parts of the polarisation function, i.e. mass shift and total width, among others restores unitarity as will be discussed below in Sect. 3.3.6. The above set of equations generalises the on-shell scheme of the standard Boltzmann equation (3.4).

In thermal equilibrium $f(x, p)$ becomes a Fermi-Dirac or Bose-Einstein distribution (3.23) in the particles' energy p_0 . The evolution of F is governed by the generalised transport Eq. (3.24). Together with the retarded equation (3.20) or (3.21) this defines a generalised quantum transport scheme which is void of the usual quasi-particle assumption. The space-time evolution is completely determined by the initial values of the Green's functions at an initial time for each space point. Thus the evolution is “*Markovian*”. Within its validity range this transport scheme is capable to describe slow space-time evolutions of particles with broad damping width, such as resonances, within a transport dynamics, now necessarily formulated in the four-dimensional phase-space.

3.3.3 Generalised collision term C_{loc}

Coming from the usual on-shell Boltzmann or Boltzmann-Uehling-Uhlenbeck collision term (3.5), each occurring three-momentum distribution function together with its momentum integration is simply to be replaced by its four-momentum analogue in the sense of Eq. (3.6). Thus

$$f(x, \mathbf{p}) \frac{d^3 \mathbf{p}}{(2\pi)^3} \implies F(x, p) \frac{d^4 p}{(2\pi)^4} = f(x, p) A(x, p) \frac{d^4 p}{(2\pi)^4}. \quad (3.25)$$

Alongside the normally occurring two-body cross-sections have to be replaced by the corresponding T -matrix expressions providing proper off-shell extensions. For genuine momentum dependent T -matrices the collision term has a finite virial (Sect. 3.3.5) due to the interactions at finite distances and

⁷ The non-relativistic generalised transport equation can simply be obtained by replacing everywhere $\Pi(x, p)$ by $2m\Sigma(x, p)$ in (3.24) and on the l.h.s p_0 by the mass m , and switching to the proper non-relativistic determination, cf. (3.20) of the retarded propagator and the spectral function.

therefore the collision term contributes to the conservation laws and therefore to the EoS in a non-trivial fashion (cf. the discussion in Sect. 1.4). Within field theory or many-body theory one has to evaluate the corresponding self-energies or polarisation functions for the collision term, which then reads

$$C_{\text{loc}} = \underbrace{\Pi^{\text{gain}}(x, p)(A(x, p) \mp F(x, p))}_{\text{gain}} - \underbrace{F(x, p)\Pi^{\text{loss}}(x, p)}_{\text{loss}} \quad (3.26)$$

$$= \Pi^{\text{gain}}(x, p)A(x, p) - 2p^0 \Gamma(x, p) F(x, p). \quad (3.27)$$

Here form (3.26) generalises the standard Boltzmann collision term, while form (3.27) display its damping properties with the local damping rate given by $\Gamma = (\Pi^{\text{loss}} \pm \Pi^{\text{gain}})/(2p^0)$. Thereby the $\Pi^{\text{gain,loss}}(x, p)$ (alias $-i\Pi^{\pm\mp}(x, p) = -i\Pi^{><}(x, p)$) are the current-current correlation functions, cf. (3.9), which determine the gain and loss rates. In case of local couplings the local collision term does not contribute to the conservation laws.

In local equilibrium the collision term vanishes and one infers from (3.23) the standard Kubo–Martin–Schwinger relations for the gain and loss rates

$$\Pi^{\text{gain}}(x, p) = \pm i\Pi^{-+}(x, p) = f_{\text{loc-eq}}(x, p)2p^0 \Gamma(x, p) \quad (3.28)$$

$$\Pi^{\text{loss}}(x, p) = -i\Pi^{+-}(x, p) = (1 \mp f_{\text{loc-eq}}(x, p))2p^0 \Gamma(x, p). \quad (3.29)$$

3.3.4 Gradient terms

More subtle than the collision term are the first order gradient terms encoded in the two Poisson brackets of the quantum kinetic Eq. (3.24). Indeed both contribute to the conservation laws, and this way also define the underlying equation of state (EoS). Thereby the first Poisson bracket furnishes the so-called drag-flow. In the quasi-particle limit it accounts for the dressing of the particles by the dragged matter cloud as to form a quasi-particle with a non-trivial dispersion relation with a corresponding in-medium group velocity that can be expressed by an effective mass. This change in flow is just compensated by the second Poisson bracket through the polarisation of the medium. The latter therefore forms a back-flow component. Only the coherent play of both Poisson brackets restores the conserved Noether currents and thus recovers e.g. Galilei (Lorentz) invariance [80]. Thus for a uniform boost of a system of N particles it acquires a total mass of $M = Nm$ rather than N times the effective mass!

Since the first Poisson bracket involves space-time and momentum gradients directly acting on the distribution function F this term has an easy classical interpretation, where the motion of the corresponding (quasi-)particle is

subjected to a force which generally is momentum dependent. It generalises the Vlasov or Hartree-Fock term discussed in Sect. 3.1. A generalisation of this concept to the four-momentum picture is straight forward, since it just amounts to establish the corresponding characteristic curves of the homogeneous first-order partial differential equation. For the second Poisson bracket term on the other hand the derivatives of the distribution function appear only implicitly through the self-energy with the result that they affect momenta other than the momentum externally entering the l.h.s. of the transport equation (3.24). This has to be such, since the discussed term describes the reaction of the surrounding matter on the particle moving through the matter. However this term escapes an immediate description in terms of test particles (cf. Sect. 3.5.2), such that an appropriate simulation algorithm could not yet be established for the exact quantum kinetic equation (3.24).

Guided by equilibrium relations Botermans and Malfliet [88] suggested a simplification of this second Poisson term, cf. [75, 77, 78]

$$\{\Pi^{\text{gain}}, \text{Re } G^R\} \underset{\text{BM}}{\Longrightarrow} \{f(x, p) 2p_0 \Gamma(x, p), \text{Re } G^R\} \quad (3.30)$$

with $\Gamma = -\text{Im } \Pi^R/p_0$, formally valid up to second order gradient terms. Here the distribution function $f(x, p)$ directly appears, while Γ is the damping width. The advantage of this substitution is that now the Poisson-bracket derivatives directly act on the distribution function f and the term amends a test-particle simulation [75, 78]. The price to be payed is that then the conservation laws are modified, since instead of the spectral function A rather the entropy-spectral function $A_s = \frac{1}{2}A\Gamma^2$, as introduced in [89], enters the conserved current expression

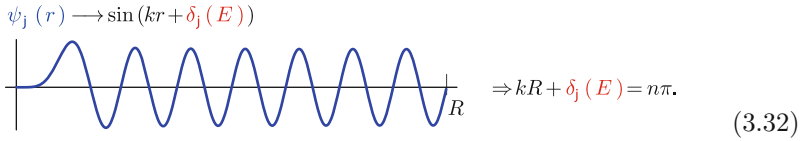
$$J_{\text{BM}}^\mu(x) = e \int \frac{d^4p}{(2\pi)^4} 2p^\mu f(x, p) A_s(x, p)(x, p). \quad (3.31)$$

The BM substitution accounts for part of the back flow. In the quasi-particle limit both spectral functions converge to the same δ -function at the quasi-particle energy [77, 89]. A further merit of the BM-substitution is that for certain collision terms an entropy current can be derived which fulfils an exact H-theorem, for details see [77]. Recent first numerical applications with this substitution [75, 78, 82, 83] were performed.

Once one starts to include the real part of the self-energies in particular beyond mean-field approximations, one has to face the problem of renormalisation in the context of self-consistent schemes. This was an unsettled problem for decades. Recent progress in this context was achieved by the work of van Hees and Knoll [90–92] and follow-up work by Blaizot et al. [93].

3.3.5 The virial limit

An interesting simplifying case is provided by the low density limit, i.e. the virial limit. Since Beth-Uhlenbeck (1937) [94] it is known that the corrections to the level density are given by the asymptotic properties of binary scattering processes, i.e. in a partial wave decomposition by means of phase shifts, see also [95–97]. The reasoning can be summarised as follows. While for any pair the c.m. motion remains unaltered the relative motion is affected by the mutual two-body interaction. Considering a large quantisation volume of radius R and a partial wave of angular momentum j , the levels follow the quantisation condition

$$\psi_j(r) \longrightarrow \sin(kr + \delta_j(E)) \quad \Rightarrow kR + \delta_j(E) = n\pi. \quad (3.32)$$


Here $\delta_j(E)$ is the phase shift of this partial wave at invariant c.m. energy $E = \sqrt{s}$, while n is an integer counting the levels. Thereby the kR term accounts for the free part of the relative motion. The corresponding corrections to both, to the level density and thermodynamic partition sum, in this partial wave are then given by

$$\rho_j = (2j+1) \frac{dn}{dE} = \frac{d\rho^{\text{free}}}{dE} + \frac{2j+1}{\pi} \frac{d\delta_j}{dE} \quad (3.33)$$

$$Z_j = \sum_i e^{-E_i/T} = \int dE \frac{d\rho_j}{dE} e^{-E/T}. \quad (3.34)$$

Since Z determines the equation of state (EoS), its low density limit is uniquely given by the scattering phase shifts. The phase shifts of resonance scattering, cf. Fig. 3.2 for the Δ^{33} resonance in πN scattering, behave exactly as in the case of a driven harmonic oscillator with damping: at low or high frequencies, respectively, oscillator and external frequency are in phase or opposite (180°) phase, while at resonance condition the phase is 90° . The advance of a phase shift by a value range of π across a certain energy window adds one state to the level density and points towards an s -channel resonance. The energy derivative of the phase shifts has a dimension of a time and indeed defines the extra time, called delay time,

$$B(E) = \frac{1}{\hbar} \tau_{\text{delay}} = 2 \frac{\partial \delta(E)}{\partial E}, \quad (3.35)$$

spent in the interaction region compared to the free motion case [100]. The function $B(E)$ related to the time delays has similar but not quite the same properties as the spectral function of the resonance, Fig. 3.2. Attractive po-

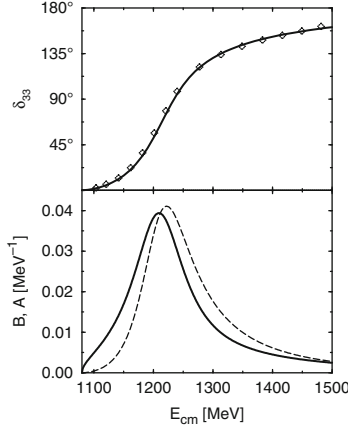


Fig. 3.2 *Top:* Model fit [98] to the πN scattering phase shifts in the 33 channel from [99]; *bottom:* Resulting level density function $B(E_{cm})$ (full line) compared to the corresponding spectral function $A(E_{cm})$ of the Δ^{33} resonance (dashed line). Figure from [98].

tentials and resonance scattering lead to positive delay times, whereas repulsive potentials generally shorten the scattering path and thus lead to negative delay times. Due to such delays the scattered particle reaches less or more frequently the borders e.g. of a confining vessel, implying the pressure to decrease or increase with the above discussed consequence for the level densities. While transition rates are given by the absolute square of the transition matrix element, the delay times result from the energy behaviour of the complex phase of the amplitude. For resonances the time delay culminates at resonance condition to $\tau_{\text{delay}}(E_{\text{res}} \approx 4\hbar/\Gamma(E_{\text{res}}) = 4\tau_{\text{damping}}$ and drops to zero far away from resonance. One recognises the significantly different threshold behaviour of the level density function $B(E) = \partial\delta(E)/\partial E$ compared to spectral function $A(E)$, Fig. 3.2. This difference is discussed in detail by Weinhold and Friman [98] within a thermal freeze-out model applied to pion production data of the TAPS collaboration [101], Fig. 3.4. The difference between the virial treatment of the level density and the simple resonance recipe, where a gas of free pions is supplemented by those pions resulting from incoherent Δ decays, results from πN correlations.

Alternatively, Ivanov et al. [87] discussed this effect in terms of the pion optical potential, Fig. 3.3, resulting to lowest virial order in the nucleon density ρ_N from the scattering phase shifts δ^{33} as

$$U_{\text{opt}}(x, p) = \Pi^R(x, p)/(2p^0)$$

$$\Pi^R(x, p) = -4\pi F_{\pi N}(0)\rho_N(x) = -\frac{4}{3} \frac{2\pi}{|\mathbf{p}|} \rho_N(x) 2e^{i\delta^{33}} \sin \delta^{33}. \quad (3.36)$$

Here $F_{\pi N}(0)$ is the zero degree πN scattering amplitude. The real part of the resulting optical potential is attractive below resonance shifting the levels

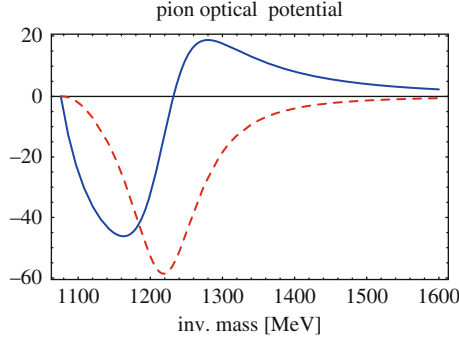


Fig. 3.3 Real (*full line*) and imaginary part (*dashed*) of the pion optical potential U_{opt} (3.36) arising from the $\pi N \Delta$ interaction at a density of $\rho_N = 0.4\rho_0$ used in the fit of Fig. 3.4, where $\rho_0 = 0.16 \text{ fm}^{-3}$ is the nuclear saturation density.

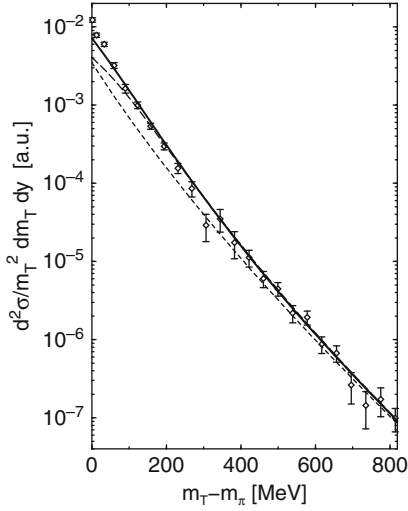


Fig. 3.4 π^0 spectrum of Au+Au collisions at 1 A GeV [101] compared to the thermal pion spectrum (*short dashes*), the thermal pions plus pions from Δ decays (*long dashes*) and the pion spectrum (*full line*) arising from the level density correction (3.33); calculations from [98].

downwards and repulsive above the resonance energy. For a detailed discussion of freeze-out concepts we refer to Sect. 5.8 on decoupling and freeze-out.

In cases, where the resonance solely couples to one asymptotic channel, the corresponding phase shifts relate to the vacuum spectral function $A_j(s)$ of that resonance via

$$4|T_{\text{in,out}}|^2 = \begin{cases} \frac{\Gamma_{\text{in}}(s)\Gamma_{\text{out}}(s)}{(\sqrt{s} - m_R(s))^2 + \Gamma_{\text{tot}}^2(s)/4} & \text{non-relativistic} \\ \frac{4s\Gamma_{\text{in}}(s)\Gamma_{\text{out}}(s)}{(s - m_R^2(s))^2 + s\Gamma_{\text{tot}}^2(s)} & \text{relativistic bosons} \end{cases} \quad (3.37)$$

$$= 4 \sin^2 \delta_j(s) = A_j(s, \mathbf{p} = 0) \times \begin{cases} \Gamma_{\text{tot}}(s) & \text{non-rel.} \\ 2\sqrt{s}\Gamma_{\text{tot}}(s) & \text{rel. bosons} \end{cases} \quad (3.38)$$

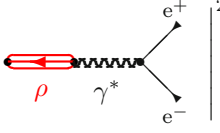
the latter valid for a single channel. In the virial limit only vacuum properties enter which are solely a function of the invariant Mandelstamm-variable $s = (p_{\pi^+} + p_{\pi^+})^2$. Thus partial and total decay rates entering the relativistic boson case in (3.37) are the intrinsic decay rates of the resonance, i.e. at vanishing total momentum \mathbf{p} . If the resonance is moving the rates transform according to $p_0\Gamma(s, \mathbf{p}) = \sqrt{s} \Gamma(s, \mathbf{p} = 0)$. In (3.37) $T_{\text{in,out}}$ is the corresponding T -matrix element. While this relation is correct also in the case where many channels couple to the same resonance, relation (3.38) only holds for the single channel case, where $\Gamma_{\text{in}} = \Gamma_{\text{out}} = \Gamma_{\text{tot}}$. Relation (3.38) illustrates that in the single channel case the vacuum spectral functions of resonances can almost model-independently be deduced from phase-shift information. In the case of the ρ meson additional information is provided by the pion form factor. Also in the case of two channels coupling to a resonance the energy dependence of phase shifts of the two scattering channels together with the inelasticity coefficient provide stringent constraints for the spectral function of the resonance.

The above discussed time delays can also explicitly be treated by finite space-time corrections to the Boltzmann collision term as proposed in [102], where then the non-local collision term leads to the corresponding virial corrections of the underlying EoS.

3.3.6 Non-additivity of perturbative rates

In the case of broad spectral functions the treatment of partial rates is subtle. As an example let us discuss the properties of the ρ meson and the consequences for the decay into dileptons. The exact dielectron production rate at total four-momentum P can be obtained by the corresponding golden rule expression⁸

⁸ Here keeping explicitly the \hbar dependences; further $L(M) = (1 + 2m^2/M^2)\sqrt{1 - 4m^2/M^2}$ denotes the lepton factor at invariant mass $M^2 = P^2$ resulting from the integration over the final state momenta of electron and positron under the assumption that $\Pi_{\text{el}}^{\mu\nu}$ is transversal, i.e. $P_\mu \Pi_{\text{el}}^{\mu\nu} = 0$, while M_ρ , m , and $\alpha = e^2/(4\pi)$ denote the masses of ρ meson, electron or positron, and the fine-structure constant, respectively.

$$\begin{aligned}
\frac{dN^{e^+e^-}}{d^4P dtd^3x} &= \int \frac{d^4p_+}{(2\pi)^4} \frac{d^4p_-}{(2\pi)^4} \left| \text{Diagram} \right|^2 \delta^4(P - p_+ - p_-) \\
&= -\frac{1}{6\pi^3} \alpha^2 \frac{L(M)}{M^2} i\Pi_{\text{el}}^{-+\mu}{}_\mu(x, P) \quad (\text{McLerran-Toimela}). \quad (3.39)
\end{aligned}$$


The latter known as the McLerran-Toimela formula [103] results from the integration over the lepton momenta p_+, p_- , keeping their total four-momentum P fixed. In straight analogy to the photon case, discussed around Eq. (3.9) in Sect. 3.3.1, also here $\Pi_{\text{el}}^{-+\mu\nu}$ is the electromagnetic current-current correlator of the source. In the vector dominance picture it directly relates to the phase-space abundance F_ρ of the ρ meson via [104, 105]

$$-i\Pi_{\text{el}}^{-+\mu\nu}(x, P) = \left(\frac{m_\rho^2}{g_\rho} \right)^2 F_\rho^{\mu\nu}(x, P) \quad (3.40)$$

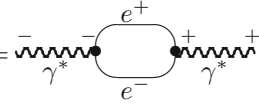
such that

$$(2\pi)^4 \frac{dN^{e^+e^-}}{d^4P dtd^3x} = \underbrace{\frac{8\pi}{3} \alpha^2 \frac{L(M)}{M^2}}_{-i\Pi_{\rho \rightarrow e^+e^-}^{+-}(M^2)} \underbrace{\frac{m_\rho^4}{g_\rho^2}}_{-i\Pi_{\text{el}}^{-+\mu\nu}(x, P)} F_\rho^{\mu\nu}(x, P). \quad (3.41)$$

The under-braced part of this formula permits an alternative interpretation. Namely from detailed balance arguments this rate is identical to the partial lepton-pair decay rate of the ρ meson as given by the Kadanoff-Baym rate (3.19) in the quasi homogeneous limit, where (omitting the tensor indices $\mu\nu$)

$$(2\pi)^4 \frac{dN^{e^+e^-}}{d^4P dtd^3x} = -2P^\mu \partial_\mu \delta F_\rho(x, P) = \underbrace{-i\Pi_{\rho \rightarrow e^+e^-}^{+-}(M^2)}_{2P_0 \Gamma_{\rho \rightarrow e^+e^-}(P)} \underbrace{F_\rho(x, P)}_{f(x, P) A_\rho(x, P)} \quad (3.42)$$

Here $\delta F_\rho(x, P)$ specifies that partial fraction of $F_\rho(x, P)$ which decays into electron pairs. Given by vacuum properties

$$\begin{aligned}
-i\Pi_{\rho \rightarrow e^+e^-}^{+-}(M^2) &= -2\text{Im} \Pi_{\rho \rightarrow e^+e^-}^R(M^2) = \text{Diagram} \\
&= \frac{8\pi}{3} \alpha^2 \frac{L(M)}{M^2} \frac{m_\rho^4}{g_\rho^2} = 2 M \Gamma_{\rho \rightarrow e^+e^-}^{\text{proper}}(M) \\
&= 2P_0 \Gamma_{\rho \rightarrow e^+e^-}(P)
\end{aligned} \quad (3.43)$$


determines the mass-dependent electromagnetic decay rate $\Gamma_{\rho \rightarrow e^+e^-}(P)$ of the ρ meson via the virtual photon into the di-electron channel. As usual this rate is time dilated by a factor M/P_0 compared to the proper decay rate $\Gamma^{\text{proper}}(M)$ defined with respect to the ρ meson rest frame. The phase-space distribution $f_\rho(x, P)$ and the spectral function $A_\rho(x, P)$ define the properties of the ρ meson at space-time point $x = (t, \mathbf{x})$. Both quantities are in principle to be determined dynamically by an appropriate transport model. For simplicity the subsequent discussion refers to the equilibrium situation. In this context it is not aimed to compete with by far more sophisticated equilibrium calculations such as those discussed in e.g. [106–110] and also presented in detail in Part II of this book on “In-medium Effects”. Rather we try to give a clarifying analysis in simple terms with the aim to discuss the consequences for the implementation of such resonance processes into dynamical transport simulation codes.

As an illustration we present the model case discussed in Knoll’s Erice lectures [74]. There it is assumed that the ρ meson just strongly couples to two channels: naturally to the $\pi^+\pi^-$ channel which determines the vacuum decay properties and secondly to the $\pi N \leftrightarrow \rho N$ channel relevant at finite nuclear densities. The latter component is representative for all channels contributing to the so-called *direct* ρ in transport codes.

Both considered processes add to the total width of the ρ meson

$$\Gamma_{\text{tot}}(m, \mathbf{p}) = \Gamma_{\rho \rightarrow \pi^+\pi^-}(m, \mathbf{p}) + \Gamma_{\rho \rightarrow \pi N N^{-1}}(m, \mathbf{p}). \quad (3.44)$$

The equilibrium spectral function then results from the cuts⁹ of the two diagrams

$$A_\rho(m, \mathbf{p}) = \text{diagram 1} + \text{diagram 2} \quad (3.45)$$

$$= \frac{2p_0 (\Gamma_\rho \pi^+\pi^- + \Gamma_\rho \pi N N^{-1})}{(m^2 - m_\rho^2 - \text{Re}\Pi)^2 + p_0^2 \Gamma_{\text{tot}}^2}.$$

In principle both diagrams have to be calculated by fully self consistent propagators, i.e. with corresponding widths for all particles involved. This formidable task has not been done yet. Using micro-reversibility and the properties of thermal distributions the two terms in (3.45) contributing to the di-lepton yield (3.39) can indeed approximately be reformulated as the thermal average of a $\pi^+\pi^- \rightarrow \rho \rightarrow e^+e^-$ -annihilation process and a $\pi N \rightarrow \rho N \rightarrow e^+e^-N$ -scattering process, i.e.

⁹ The cut here meant in separating time ordered (–) from anti-time ordered (+) vertices in the context of the time-contour in Fig. 3.1.

$$\frac{dn^{e^+e^-}}{dm dt} \propto \langle f_{\pi^+} f_{\pi^-} v_{\pi\pi} \sigma(\pi^+\pi^- \rightarrow \rho \rightarrow e^+e^-) + f_{\pi} f_N v_{\pi N} \sigma(\pi N \rightarrow \rho N \rightarrow e^+e^- N) \rangle_T \quad (3.46)$$

with partial cross sections resulting from (3.37). However, the important fact to be noticed is that in order to preserve unitarity the corresponding cross sections are no longer the free ones, as given by the vacuum decay width in the denominator, but rather involve the *medium dependent total width* (3.44). This illustrates in simple terms that rates of broad resonances can *not* simply be added in a perturbative way. Since it concerns a coupled channel problem there is a cross talk between the different channels to the extent that the common resonance propagator attains the total width arising from all partial widths feeding and depopulating the resonance. While a perturbative treatment with free cross sections in (3.46) would enhance the yield at resonance, $p^2 = m_\rho^2$, if a channel is added, cf. Fig. 3.5 left part, the correct treatment (3.45) even inverts the trend and indeed depletes the yield at resonance, right part in Fig. 3.5. Furthermore one sees that only the total yield involves the spectral function, while any partial cross section only refers to that partial term with the corresponding partial width in the numerator. All these effects are accounted for in the presented resonance transport scheme.

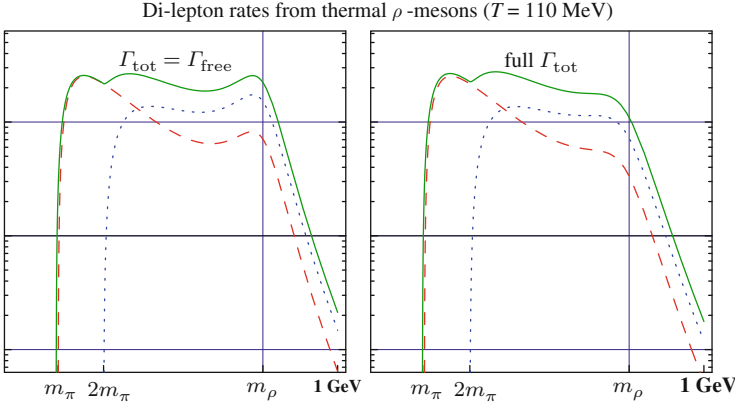


Fig. 3.5 e^+e^- rates (arb. units) as a function of the invariant pair mass m at $T = 110$ MeV from $\pi^+\pi^-$ annihilation (dotted line) and direct ρ meson contribution (dashed line), the full line gives the sum of both contributions. *Left part:* using the free cross section recipe, i.e. with $\Gamma_{\text{tot}} = \Gamma_{\rho \pi^+\pi^-}$; *right part:* for the correct partial rates (3.45). The calculation are done with $\Gamma_{\rho \leftrightarrow \pi\pi}(m_\rho) = 150$ MeV and $\Gamma_{\rho \leftrightarrow \pi N N^{-1}}(m_\rho) = 70$ MeV. Figure taken from [74].

Compared to the spectral function which is relatively symmetric around the nominal resonance mass m_ρ the di-lepton rates in Fig. 3.5 show a significant enhancement on the low mass side and a strong depletion at high masses due to the statistical weight $f \propto \exp(-p_0/T)$ in the rate (3.39). Similar ef-

fects also arise in genuine non-equilibrium processes due to the truncation of phase space at increasing energy.

3.3.7 Physical processes in dense matter

The extension towards a dynamical treatment of the spectral functions in transport implies to deal with “dressed” propagators. Many processes which in a quasi-particle picture appear only at higher orders are then already implicitly included at a lower order (loop) level. This has a couple of physical and conceptual consequences.

While the processes discussed in Fig. 3.5 were still calculated with on-shell particles in the loops and therefore show a threshold behaviour, for loops with dressed propagators all thresholds disappear. Thus, each particle in the dense environment has non vanishing spectral strength for all four momenta p . This also includes spectral strength in the space-like region, where $p^2 < 0$. While strength localises in the time-like region describes propagating “broadened” particles or resonances, strength in the space-like region is associated with a virtual particle exchanged through scattering processes. Permitting particles and anti-particles in the loop, a single loop contribution to the self-energy or polarisation function implies three different processes. This explained in the left part of Fig. 3.6 for the processes obtained from cutting the $\pi\pi$ loop

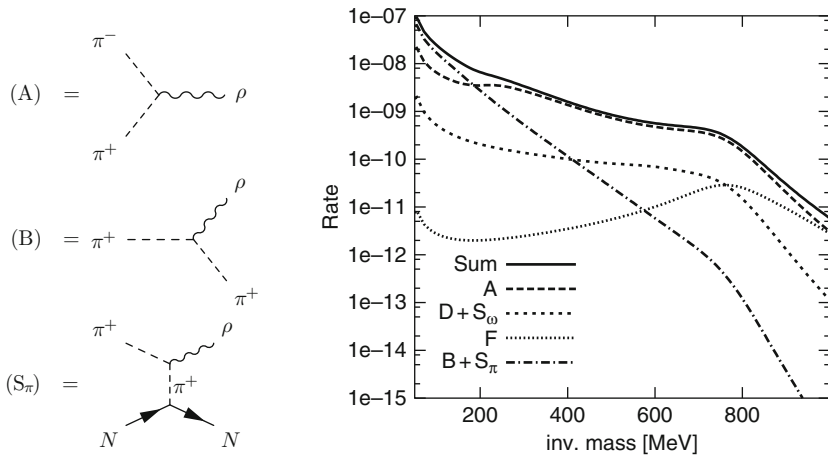


Fig. 3.6 *Left panel:* different physical processes contributing to the $\pi\pi$ loop of Π_ρ . *Right panel:* di-electron spectrum resulting from the ρ meson spectral function decomposed with respect to the different physical process arising from the $\pi\pi$ loop (*left panel*) and the corresponding process from the $\pi\omega$ loop. Thereby (D) denote the ω Dalitz decay: $\omega \rightarrow \pi\rho \rightarrow \pi e^+e^-$, while (F) denotes the fusion: $\pi\omega \rightarrow \rho$. Figure taken from the self-consistent calculations at $T = 120$ MeV and normal nuclear density given in [111].

of Π_ρ . Process (A) is the standard $\pi^+\pi^-$ annihilation process, which exists already in vacuum. The Bremsstrahlung process (B) contributes only in matter, and there in the one-loop calculations only, if the particles in the loop have spectral width. For scattering process (S_π) the vertical pion line represents a space-like (virtual) pion induced through the scattering e.g. on a nucleon.

The r.h. part of Fig. 3.6 shows a typical di-electron spectrum resulting from the ρ meson decay in a self-consistent equilibrium calculation [111] of an interacting $\{N, \Delta, \pi, \rho, \omega\}$ system. Thereby it was assumed that the ρ solely couples to mesonic currents. The quantitative level of the different contribution may vary depending on the model assumptions, the general features are essentially generic. The resulting total spectrum emerges pretty featureless, namely steeply falling with the invariant pair mass, the signal of the ρ solely appearing as a knee in the curve. Above 200 MeV it is essentially coined by the annihilation process (A), while below 200 MeV the main contribution results from Bremsstrahlung (B).

The collision rate of production Γ (or absorption) processes sets a scale which divides soft from hard processes. While hard processes proceed relatively unaltered in dense matter compared to the quasi-free scatter prescription, soft processes are significantly affected by the presence of a dense medium [112]. The latter, known as the Landau-Pomeranchuk-Migdal effect (LPM) [113, 114], essentially arises from the fact that soft processes coherently watch the collision system during a time $\tau \approx 1/\omega$, where ω is the typical energy scale, which is much longer than the time $\tau_{\text{coll}} \approx 1/\Gamma$ between collisions. Thus individual collisions are not resolved and the net result is that generally the rates are reduced compared to the quasi-free prescription [112]. In part the here discussed dynamical spectral function picture accounts for the LPM effect, as the spectral functions know about the damping width. However, coherence effects between successive collisions, as discussed in the context of the LPM effect and which modify the suppression, are largely ignored. For a detailed discussion in this context involving ladder resummation techniques we refer to [112]. In transport codes the LPM effect is mostly accommodated by the concept of a “formation time”, which has the effect that the created particles only appear after a certain time typically chosen to be of the order of 1 fm/c. This however is a very crude mock-up and work around for the subtle destructive interference phenomenon.

3.3.8 Detailed balance and two-particle irreducible (2PI) method

Detailed balance is guaranteed if all self-energies and polarisation functions of the different particles are generated from a given set of so called closed or vacuum diagrams. These are diagrams expressed in terms of bare vertices

and “full” propagators, where all extremities of each vertex are either linked to a propagator line or to a classical field. The exact generating functional is then build up by the sum over all closed diagrams which are two-particle irreducible (2PI). The latter property implies, that these diagrams still remain connected if two different propagator lines are cut. According to the name given by Baym [86] in his pioneering work the so constructed generating function is called Φ -functional or in field theory CJT-functional following the initials of the authors of [115] who reformulated the original approach by [116] in terms of path integrals. By opening a single propagator line of the closed Φ diagrams produces diagrams with two open legs, i.e. with the topology of proper self-energy or polarisation diagrams. Since the Dyson or Kadanoff-Baym equations iterate each self-energy insertion to infinite order the 2PI property of Φ precisely prevents double counting. The Φ -functional further permits truncations at any level, e.g. by considering only a few or even only one diagram, without loosing a number of desired properties for the so defined self-consistent approximation schemes of coupled Dyson equations [86, 87]. Such Φ -derivable approximations then guarantee

- a. detailed balance for the collision term
- b. thermodynamic consistence
- c. conserved currents arising from the gradient terms (see below)
- d. to avoid double counting for multi-particle processes (see below).

These properties even hold after the gradient approximation [80] which defines the quantum transport equations (3.24) discussed above.

As an illustrative example [87, 98] we discuss the scattering of pions (blue dotted line) on nucleons (full black line) through an intermediate Delta (1232) resonance (double line). Here the scattering amplitude

$$T_{\pi N} = \text{diagram} \quad (3.47)$$

is formulated by a phenomenological $\pi N \Delta$ vertex. To lowest order the corresponding closed 2PI diagram defining the Φ -functional is given by

$$\Phi = \frac{1}{2} \text{diagram} \quad (3.48)$$

Here all three lines denote full self-consistent propagators. The respective self-energies of nucleon and Delta resonance and polarisation functions of the pion are obtained by opening a corresponding propagator line, i.e.

$$-i\Sigma_\Delta = \text{diagram}; \quad -i\Sigma_N = \text{diagram}; \quad -i\Pi_\pi = \text{diagram}. \quad (3.49)$$

The example is non-trivial with respect to the on-shell Boltzmann concept as it replaces the binary πN -scattering by creation and decay of an intermediate resonance, which itself is treated dynamically within the generalised transport equation (3.24). Cutting these diagrams vertically visualises the squares of the corresponding tree-level transition amplitudes entering the collision terms for the three species.

The concept to deal with dynamical, i.e. non-on-shell spectral functions, further avoids singular or even mathematically pathological terms which notoriously appear in higher order perturbative expressions (cf. Sect. 3.4).

3.4 Beyond binary collisions

With increasing energy inelastic processes open which lead to the creation of new particles, either through a kind of bremsstrahlung process, like $NN \rightarrow NN\gamma$ or $NN \rightarrow NN\pi$ or other production mechanisms, like $\bar{p}p \rightarrow 5\pi$. Such processes were phenomenologically introduced into transport schemes on the basis of measured cross-sections. However the inclusion of the appropriate backward reaction caused problems and they were commonly neglected. Recently arguments were given in the context of anti-particle production [117, 118] which indeed date back to the time of Planck, when he wrote down his radiation law. They state that the equilibration rate is determined by the fastest rate. Hence, if the forward rate is strong also the backward rates should become strong as to furnish the proper equilibrium within the equilibration time set by the forward rate. Thus processes of the type “3 to 2” or even “5 to 2” particles can become important and have to be included [117–120].

There are several suggestions to properly include such “beyond binary” processes. Not all of them lead to a consistent picture.

3.4.1 Phenomenological quasi-free ansatz for multi-particle processes

One option is to ignore the internal dynamics of the multi-particle production process itself and to assume that it happens at space-time scales shorter than relevant for the description of the dynamics. Thus, the multi-particle interaction vertex is assumed to be essentially point-like and the picture is that of a quasi-free collision process. Then the multi-particle process rate

can be described by Fermi's golden rule with a transition-matrix T for the process, e.g. extracted from a measured cross-section for a binary entrance channel, or given by the point-like transition vertex from the corresponding lowest order self-energy diagram [68, 118–121]. Detailed balance can then be enforced by the 2PI-method described above in Sect. 3.3.8, just by closing the self-energy diagram with the external line this way producing a diagram of the Φ -functional. Upon opening any other particle's line one obtains the self-energies for the other particles involved in the process.

This method

- (a) rests on measured cross-section which in part are scarcely available or based on theoretical guesses;
- (b) obeys detailed balance by construction;
- (c) enables the calculation of composite particle production [68];
- (d) is mostly limited to on-shell particles;
- (e) cannot properly describe the production of soft particles, particles that are soft on the scale of the collision rate, where the Landau-Pommeranchuk effect suppresses the particle production compared to the quasi-free production prescription [112].

3.4.2 Intermediate resonances

A further option is to describe multi-particle process in a sequential scheme where in a first step an intermediate resonance is formed which then subsequently decays. This is for instances used in most treatments of pion production which essentially runs across the Δ^{33} resonance: $NN \leftrightarrow N\Delta$; $\Delta \leftrightarrow N\pi$.

This makes the following improvements possible:

- (a) treatment of broad resonances in a dynamical way;
- (b) inclusion of decay processes ("1 to 2") of otherwise on-shell particles even if they are kinematically forbidden under on-shell conditions as well as their inverse fusion processes ("2 to 1");
- (c) fitting to measured cross-sections within this picture.

Such strategies obey detailed balance, if all processes are described by self-energies derived from closed diagrams within the 2PI method.

3.4.3 Transport with dynamical spectral functions

The intermediate resonance picture can directly be generalised to a general transport with dynamical spectral functions concept. This has the advantage that through the off-shellness of normally stable particles the bremsstrahlung (and its inverse) are automatically included (e.g. through a $N \rightarrow N\gamma$ process).

This strategy approximately also accounts for the Landau-Pomeranchuk suppression which in this picture arises from the damping widths (e.g. collision rate) of the particles.

3.4.4 Inclusion of many-body collisions in transport simulations

At the densities reached in nuclear collisions at high energies, the standard assumption of isolated two-body collisions is not well justified. To remedy this problem, Batko et al. [122] developed a general model for inclusion of multi-particle scattering within the framework of BUU transport simulations. In that model, the occurrence of a collision is determined as usual on the basis of the energy-dependent binary cross section but the particular collision is assumed to involve all those particles that happen to be situated within the associated interaction range at the time of the collision. The combined energy of these participating particles is then shared micro-canonically among the resulting particles. This procedure provides a general treatment of both elastic and inelastic many-body scattering that can be easily incorporated into standard BUU-type transport codes.

The model was applied to symmetric nuclear collisions at bombarding energies of 200–1,000 MeV per nucleon and a variety of observables were studied, including anisotropy, flow angle, sideways momentum, and backwards yield, as well as certain particle production processes. Generally, the results of the standard BUU dynamical simulations are not appreciably affected by this incorporation of many-body collisions. While this feature lends support to the use of the BUU model as a quantitative tool for relativistic nuclear collisions, it should be emphasised that those studies were based on the assumption of perfect equipartition within each collision cluster.

In order to elucidate the importance of the equipartition approximation, the same authors made a detailed study of the simplest many-body case, namely elastic scattering of three nucleons by means of pion exchange, with an off-shell intermediate baryon between the two pion exchanges [122]. At all energies, the resulting angular distribution is always anisotropic, in contrast to the two-body scattering which remains isotropic up to about 400 MeV per nucleon. The associated evolution in momentum was studied in uniform matter starting from two interstreaming Fermi distributions having a velocity separation given by the collision energy of interest. As one might expect, scattering to the backward direction is enhanced in the three-body scenario, but only at early times; subsequent collisions quickly drive the momentum distribution towards the associated equilibrium, which is independent of the specific collision mechanism employed. But equilibrium is reached much faster with three-body scattering, particularly at higher energies. This result pro-

vides some support for the adopted equipartition assumption for the general treatment of many-body scattering.

Subsequently, the model was further developed for the calculation of the energy spectra of kaons produced in relativistic nuclear collisions and the effect of many-body collisions on subthreshold kaon production was studied especially [123]. Generally speaking, the kaon yields are enhanced only rather little which is understood as a result of the statistical sharing of the energy between the produced kaon and the baryons involved in its productions. However, as one would expect, the enhancement grows with the kaon energy and becomes relatively significant in the regions of very small yields.

3.4.5 Higher-order processes within the quasi-particle picture

Attempts to construct higher order collision terms within the quasi-particle approximation merely by adding some perturbative diagrams of higher order for the self-energies run into serious conceptual difficulties. The problem is very subtle and plagued with mathematically ill defined singular expressions which notoriously appear in perturbation theory at higher orders.

To be specific: For the construction of the collision term the imaginary parts of the self-energies are the key quantities. If a higher-order diagram has genuine lower-order self-energy insertions, one definitely encounters expressions containing the absolute square(!) of the retarded quasi-particle propagators (i.e. propagators with zero damping width). If then the corresponding self-energy insertion does not vanish at that on-shell condition, the expression contains squares of singular distribution functions (i.e. squares of delta- and principle-value-functions) which are mathematically ill defined and which through the integration within the collision term thus lead to diverging collision rates! A well known example case is the “scattering” process of a $N\Delta \rightarrow \Delta N$ (u -channel) via the exchange of a pion. This pion can be on-shell, which provides an infinite “cross section” in such descriptions. It is well known that (a) such problems cannot be solved within perturbation theory, but (b) rather require special partial resummation techniques to infinite order, in order to come to regular and physically meaningful expressions. One then has to deal with *rates* rather than with the limited concept of scattering cross sections.

Indeed the problem is tightly connected with the *irreducibility* features required for the *kernel* or driving term of a dynamical equation of motion. The transport equations are self-consistent dynamical equations to the extent that the dynamical quantities calculated in one time step enter as input for the next time step. Thus, the solution of such equations generates higher order terms out of its kernel, namely the collision term (and also the driving self-energies in the Poisson brackets). Therefore the collision term by itself

has to obey specific irreducibility criteria: it has to be void of any process that can implicitly be generated through the solution of the transport equation! Restricted to the quasi-particle limit these are precisely the processes, namely intermediate on-shell propagations, that lead to the above stated mathematical difficulties.

Let us add a general note on the irreducibility concept. It is readily through the formulation of equations of motion with *irreducible* kernels that one avoids such singular structures. Therefore this issue is indeed completely settled for the case of the self-consistent solutions of the Dyson (or Kadanoff-Baym) equations, when the proper self-energy is entirely a functional of the self-consistent propagator. There the precise rule is that the kernel of the Dyson equation, i.e. the self-energy, has to be derived from a 2-particle irreducible (2PI) functional [86, 116], i.e. it has to be void of any self-energy insertion. The step towards transport is achieved by a consistent gradient approximation of the Kadanoff-Baym equations, cf. [80]. Still then the 2PI-rule applies.

If, however, as frequently addressed, one tries to restrict the dynamical description to *on-shell* (or better *quasi*-)particles, one may seriously spoil the 2PI irreducibility concept. Then one carefully has to separate self-energy terms that are treated explicitly from those implicitly generated by the kernel through terms of lower order. This implies the necessity of so-called z -factors for the quasi-particle strength on the one hand and an implicit treatment of the complementary background terms. As yet there is no formulation in the literature where such a separation was thoroughly addressed for the higher order terms such that (a) the irreducibility properties are appropriately formulated for the quasi-particle picture, while (b) at the same time physically meaningful and non-singular expressions emerge.

3.4.6 Recent progress and challenges

In principle, the Kadanoff-Baym equations – derived in lowest order from the two-particle irreducible (2PI) action – provide a convenient starting point to treat particles with broad spectral distributions. However they are presently only tractable in very simplified cases. The question arises, if further approximations to these equations – like the gradient expansion – do perform well enough in case of inhomogeneous systems with strong coupling. Furthermore, is the Botermans-Malfliet (BM) substitution [88] for the backflow-term accurate enough to allow for a convenient test-particle simulation of the transport equations?

Some of these questions were already addressed in [82–84] for the case of a scalar relativistic field theory with strong coupling. Here the numerical studies on a fixed momentum grid have shown that the gradient expansion in time is a “reasonable” approximation even for large coupling. This goes in line with the experience in transport studies in the quasi-particle limit which

involves also a first order gradient expansion in space-time. Furthermore, the BM approximation for the backflow-term was found to hold very well in case of the scalar Φ^4 -theory [83]. Consequently, the Φ^4 model example allows for a convenient test-particle solution – including dynamical spectral functions – when allowing for $1 \leftrightarrow 3$ transition rates (cf. [119]) apart from the conventional $2 \leftrightarrow 2$ scattering processes to achieve proper chemical equilibrium [84].

This progress on the frontier should not hide the fact that most of the transport models still treat broad resonances rather crude. On the collision term level the resonance rates are mostly implemented in some approximate way, either indirectly through resonance cross sections excluding the explicit dynamics of resonances or approximately in some perturbative way. Also the propagation in between collisions (or decays) is then dealt with as if each mass component is an on-shell particle. Furthermore many particles which are known to suffer strong changes in their spectral behaviour in dense matter such as e.g. the pion are still treated as on-shell particles with nominal masses. Improvements in this respect are vital though admittedly very tedious and in part beyond present compute capabilities.

And there are further challenges. The 2PI Φ -functional provides an exact approach of the field theoretical equations of motion and the thermodynamic potential. However, on the truncated level of self consistent Dyson schemes – limited to two-point functions – certain conceptual difficulties arise. While as a positive achievement Noether currents are conserved on the expectation value level, such currents are no longer conserved on the higher order correlator level [124, 125]. This comes about due to the partial resummation implied by solving the dynamical equations of motion, be it on the Schwinger-Dyson or Kadanoff-Baym level or the here discussed transport scheme with dynamical spectral functions, which lead to a violation of Ward-Takahashi identities. A famous example is the violation of the Goldstone theorem in the spontaneously broken phase, where the self-consistent Hartree-Fock approximation leads to propagators for the Goldstone-bosons which have a non-vanishing mass! Other problems concern the polarisation tensor of vector mesons, which, if coupled to conserved currents, should be four-transverse. However the self-consistent 2PI scheme violates this condition. Cure can be obtained from higher order vertex equations such as the Bethe-Salpeter ladder resummations. Such extensions are (i) numerically such demanding that they are presently intractable and (ii) they spoil the self-consistent concept, where one expects *all* dynamical quantities to be determined self-consistently. Indeed the symmetry preserving self-energies resulting from higher order vertex equations do not influence the self-consistent Dyson scheme. Partial cure can come from symmetry restoring correction terms to the Φ -functional recently suggested in the context of Nambu-Goldstone modes [126, 127] or from projection methods [124, 128] for restoring the four-transversality of vector mesons. The latter, however, led to other difficulties in form of kinematical singularities, either at energy zero or on the light cone [111]. These led to spurious (infra-red) modes which seriously corrupt the self-consistent dynamics.

The tensor representation of vector bosons discussed in [129] though provides an alternative option to maintain their four-transversality throughout the self-consistent scheme. Thus, the treatment of vector mesons or even gauge bosons in self-consistent schemes is still relatively unsettled and requires serious conceptual efforts before one comes to reliable schemes.

For test-particle implementations a further problem arises in case of low-mass quanta with a large spectral width. This comes about as follows: The energy integral of the spectral function is normalised, since it is directly connected to the equal-time commutator of the fields which provides the quantisation of the theory and the particle interpretation accordingly. In case of a large spectral width the spectral function $A(p)$ is non-vanishing also for space-like invariant mass squared ($p^2 < 0$); this fraction of the spectral function physically describes t -channel scattering processes whereas the time-like sector corresponds to s -channel particle propagation processes. Thereby space-like parts of the spectral function do not violate micro-causality for the exact KB equations while they partially do in first order gradient approximation. Consequently a particle interpretation has to be attributed to “field quanta” that (depending on the environment (e.g. temperature)) may change from t - to s -channel processes, cf. the discussion of time and space-like processes given in [130]. So far it is not known how to realize this in transport descriptions with dynamical spectral functions, where presently [82, 83] only s -channel processes, i.e. the time-like parts of the spectral function are treated dynamically. However, promising progress concerning these issues has recently been reported by Cassing [84].

Also the production of soft quanta cannot appropriately be described by incoherent quasi-free scattering processes (the standard concept in transport treatments). This comes about due to destructive coherence effects which essentially lead to a suppression of the production rates of soft quanta known as the Landau-Pomeranchuk-Migdal (LPM) effect [113, 114], cf. in the context of transport [112, 131]. In dealing with dynamical spectral functions the singular behaviour in the soft limit is cured and part of the LPM effect is properly accounted for due to the finite life time of the particles. However the coherent action of many successive scatterings as discussed in [112] is still lacking.

There is growing evidence from lattice QCD calculations [132] that the flavors in the deconfined phase are carried by independent (but possibly medium-modified) quarks, thus giving the system the character of a gas of weakly interacting quasi-particles in a mean field. This important insight was first gained from consideration of the correlations between baryon number B (or charge Q) and strangeness S , $\sigma_{BS} = \langle BS \rangle - \langle B \rangle \langle S \rangle$ and $\sigma_{QS} = \langle QS \rangle - \langle Q \rangle \langle S \rangle$ which are simply related to the mixed-flavor susceptibilities χ_{us} and χ_{ds} [133]. The system is more complicated in the transition region, where it appears more as a strongly coupled liquid (sQGP). There a finite spectral function might not necessarily arise from a well-defined pole structure. Apart from the gauge-fixing problem it is also not clear how to

deal with partially confined quanta, i.e. with “parton propagators” which do not necessarily possess a positive definite spectral function [134].

3.5 Specific implementations

In this section we collect brief descriptions of different one-body models that have extensively been applied to high-energy nuclear collisions. These descriptions provided by the main developers and/or practitioners summarise those features that they deem to be special and noteworthy about their numerical scheme. Before that we start with some general features.

3.5.1 Initialization

In one-body simulations of nuclear collisions, the nuclei are generally prepared in their respective rest frames and then boosted to the calculational frame, usually the centre-of-mass frame. The lower the collision energy is the more care must be taken with the initialisation. In its rest frame, an initial nucleus is represented as a collection of individual nucleons (or test particles) that are distributed in space according to a realistic density profile, such as a Saxon-Woods distribution, while the momenta are sampled from within the associated Fermi sphere. It should be noted that these samplings are performed in an uncorrelated manner and, consequently, the resulting phase-space distribution is endowed with an unrealistic degree of irregularity.

3.5.2 Solution methods

A large number of codes have been developed for the solution of the nuclear Boltzmann equation. They differ in many details of the physical input as well as with regard to the basic numerical technique employed. We describe below the most common classes of solution methods.

- *Phase-space lattice:* The conceptually most straightforward method consists in representing $f(x, \mathbf{p})$ on a lattice in phase space. The collision term can then be calculated at each spatial location separately, leading to a modification in the local momentum distribution, and the collisionless propagation can be performed by standard methods (for example a simple leap-frog propagation which also works even when the interaction is momentum dependent). Obviously, this discretization method yields an ever more accurate solution as the lattice is made ever finer. However, the number of

lattice points required is prohibitively large for most realistic applications and this method has so far been most useful for lower-dimensional studies.

- *Pseudo-particles*: In the pseudo-particle method, the phase-space density of each physical particle is represented by a large number of pseudo- or test-particles, \mathcal{N} , each carrying a correspondingly reduced weight of $1/\mathcal{N}$. Furthermore, their interaction cross sections are scaled by the factor $1/\sqrt{\mathcal{N}}$ in order to leave the transport properties unchanged. An advantage of this method is that it converges towards the exact solution of the Boltzmann equation as $\mathcal{N} \rightarrow \infty$. But the computational effort scales as \mathcal{N}^2 , although this problem can be largely mitigated by use of suitable indexing.

The residual interactions are usually limited to binary scatterings, but the pseudo-particle method makes it readily possible to make scatterings according to the local phase-space occupations, thus allowing the inclusion of non-trivial effects, such as finite spectral widths and multi-particle collisions (see below).

- *Parallel ensembles*: The parallel-ensemble method was developed in order to ensure that the numerical effort scales only linearly with \mathcal{N} . For this purpose, the system is represented by an ensemble of \mathcal{N} separate systems. The particles in a given system scatter only with particles from that system, but the effective one-body field is obtained by averaging over all these \mathcal{N} individual systems in the ensemble. This method is very convenient, both numerically and for the purpose of generating a sample of events. But, although it also converges as $\mathcal{N} \rightarrow \infty$, the limit is generally *not* identical to the solution of the Boltzmann equation. This is related to the fact that the residual interaction has a finite range proportional to the square root of the cross section. Thus, depending on the scattering prescription the collision term may contribute to the pressure contrary to the two methods above.

On the other hand, the method goes beyond the one-body level of the Boltzmann treatment and makes it readily possible to calculate also correlation quantities. In fact, the parallel-ensemble method is practically very similar to N -body molecular dynamics (see Sect. 4), the only difference being that the mean field is averaged at each time step.

- *Treatment of rare processes*: The numerical treatment of processes that occur only rarely presents a special computational problem, since their direct simulation is highly inefficient. A familiar example is the production of particles at collision energies near the production threshold. A general and efficient technique for treating such processes was developed in connection with kaon production in relativistic nuclear collisions [15]. The method utilizes the fact that the small production cross section permits a perturbative treatment in which numerous potential production processes may be followed in parallel.

For example, for the original case of near-threshold kaon production, each baryon-baryon encounter may produce a kaon with a small probability given by the appropriate partial cross section. These probabilities may

then be accumulated in the course of the entire collision process without modifying the original collision dynamics. Thus, rather than producing a large number of simulations to obtain just a single kaon, one obtains many kaons from each individual nuclear collision event. Consequently, this perturbative technique provides a very powerful way to access rare processes in dynamical simulation.

Furthermore, since the production of the particle is so rare, one may study its dynamical fate by actually introducing it into the system where it then propagates in the unmodified collision environment [16]. In this manner, it is possible not only to obtain the total production cross section but also the effects of residual collisions on the produced particle through rescattering or secondary production processes.

3.5.3 Boltzmann-equation model BEM (MSU)

Simulations of nuclear reactions within the MSU Boltzmann-Equation Model (BEM) [68, 121] are based on solving a set of Boltzmann equations for the quasiparticle phase-space distributions, within a relativistic version of the Landau theory. The quasiparticles in BEM include nucleons, light nuclei up to mass 3, pions, Δ and N^* resonances. Their quasiparticle energies are given in terms of functional derivatives of an energy functional with respect to the phase-space distributions. The nuclear part of this functional is constructed [121] in the local rest frame of matter, with the main part of the energy density taken in a local form and with range effects accounted for in terms of gradient corrections. The functional is constrained by the established nuclear properties, thereby in particular accounting for the momentum dependence of nucleonic optical potentials at normal density.

Composite-particle production in BEM takes place in few-nucleon collisions, in processes that are inverse to composite-particle break-up. The break-up cross-sections, and the corresponding formation rates are constrained using available data on composite break-up. For the dynamics of broad baryon resonances within BEM, the adiabatic limit is adopted [68], where within the mean-field dynamics the quasiparticles representing a resonance retain the mass difference relative to centroid of the resonance. Compared to preceding approaches, a detailed balance relation has been introduced in BEM [68]. It links the cross sections for resonance production to the absorption rate, such that they are balanced in equilibrium. This improved the transport schemes such that e.g. for pion yields they produce results that are compatible with requirements from thermodynamic and with the observed reaction data.

The phase-space distributions are represented in BEM in terms of test-particles. For integrating the mean-field part of the Boltzmann equation, the conserving lattice Hamiltonian method of Lenk and Pandharipande [135] is used. For the collision integral the traditional method combining cross-

section size and distance of closest approach is replaced by a novel method [68], where collision partners are randomly chosen from within lattice cells. That new method is instrumental for the feasibility of integrating the contributions of few-nucleon collisions to the collision integral. The configurations of the incident nuclei are consistently prepared by solving the corresponding Thomas-Fermi equations that produce phase-space distributions which minimize the assumed energy functional for the BEM dynamics. Among others this prevents otherwise occurring giant monopole oscillations during the approach phase of the two nuclei.

3.5.4 *GiBUU (Giessen)*

The Giessen BUU model (GiBUU) [136–139] explicitly propagates 9 N^* and 9 Δ resonances with mass below 2 GeV. Apart from that, the model propagates the $S = -1$ baryons $Y = \Lambda, \Sigma$ and 19 Y^* resonances. Also the cascades and charmed baryons are included. In the mesonic sector, the following particles are propagated: $\pi, \eta, \rho, \sigma, \omega, \eta', \phi, \eta_c, J/\psi, K, \bar{K}, K^*, \bar{K}^*$. The baryon–baryon (meson–baryon) collisions below $\sqrt{s} = 2.6$ (2) GeV are treated within the resonance scenario, while at higher invariant energies the string model is applied. The model includes optionally (at SIS energies) the nucleon and kaon mean fields. In the local rest frame (l.r.f.) of nuclear matter the nucleon potential has a Skyrme-like form with a momentum dependent part added separately. The nucleon energy in the l.r.f. is then represented in the Lorentz invariant way by keeping only the scalar potential. The actual calculation of the scalar potential is performed self-consistently, since the nucleon potential in the l.r.f. depends on its momentum. The mean field potentials of the nonstrange baryonic resonances are put equal to the nucleon mean field, while the hyperonic potentials are rescaled by a factor of 2/3 according to the fraction of the nonstrange quarks. The GiBUU model contains a larger set of the baryonic resonances than other transport models (excepting the Tübingen QMD model) and consequently leads to higher pion numbers in vacuum. Medium corrections to the cross sections $NN \leftrightarrow NR$ and $NN \leftrightarrow NN\pi$ reduce the pion number in medium. The in-medium reduced cross sections are implemented (optionally) in GiBUU. They are computed with the Dirac masses from the NL2 model [140]. In particular, the $NN \leftrightarrow N\Delta$ matrix element is given by the one-pion exchange model – same as in the calculations of Dmitriev et al. [141], but with replacement of the vacuum Δ and nucleon masses by the Dirac ones. This leads to a strong in-medium reduction of the cross section [138]. The GiBUU model is suitable not only for heavy-ion collisions and hadron-nucleus reactions, but also for photon-, electron- and neutrino-induced reactions. This gives the possibility to test the same dynamical part of the model with various physical initial conditions. A new

numerical realization of the model [142] is currently being tested. The results presented here are based on the old version described in [136–139].

3.5.5 BRoBUU (*Budapest/Rosendorf*)

The BRoBUU computer code [143] for heavy-ion collisions is developed in a Budapest-Rosendorf cooperation. This code solves the Boltzmann-Ühling-Uhlenbeck equation in the quasi-particle limit [144],

$$\frac{\partial f}{\partial t} + \frac{\partial H}{\partial \mathbf{p}} \frac{\partial f}{\partial \mathbf{x}} - \frac{\partial H}{\partial \mathbf{x}} \frac{\partial f}{\partial \mathbf{p}} = C, \quad H = \sqrt{(m_0 + U_s(\mathbf{p}, \mathbf{x}))^2 + p^2},$$

for the one-body distribution function $f(\mathbf{x}, \mathbf{p}, t)$ of a certain hadron species. This equation is applied to the motion of the different hadrons, each with mass m_0 in a momentum and density dependent mean field U . This scalar mean field U_s is chosen in such away that the Hamiltonian H equals $H = \sqrt{m_0^2 + p^2} + U^{nr}$ with the potential U^{nr} calculated in the usual non-relativistic manner (see Eq. 3.1). Different particles species (each described by a corresponding distribution F) are coupled by the collision integral C which also contains the Ühling-Uhlenbeck terms responsible for Pauli blocking and Bose enhancement in the collision and particle creation and annihilation processes. The coupled set of Boltzmann-Ühling-Uhlenbeck equations is solved by using the parallel-ensemble test-particle method. This method transforms the partial differential-integro equations into a set of ordinary differential equations for a large number of test particles simulating the ensemble averaging process for the respective function f .

Recently theoretical progress has been made in describing the in-medium properties of particles. In the medium particles have a finite life time which is described by the width Γ in the spectral function of the particles. The spectral function can significantly change during the heavy-ion collision process and can be simulated by an ensemble of test particles with different masses. The change of the spectral function is given by time variation of the test particle mass m [75, 78]. For bosons this additional equation reads

$$\frac{dm^2}{dt} \approx \frac{\delta}{\delta t} Re\Sigma^{ret} + \frac{m^2 - m_0^2 - Re\Sigma^{ret}}{\Gamma} \frac{\delta}{\delta t} \Gamma,$$

where $Re\Sigma$ is related to the mean field U , and $\delta/\delta t$ stands for the comoving time derivation. This equation ensures that resonances are propagated towards their vacuum spectral functions at freeze-out. In particular, this technique, allowing for a consistent propagation of broad resonances, is applied in the BRoBUU code for calculating the di-electron emission of ω and ρ mesons in the 1 GeV region.

The BRoBUU code propagates 24 Δ and N^* resonances in the baryon sector together with the $\pi, \eta, \sigma, \omega$ and ρ mesons. In addition, the strange particles Λ, Σ and K^\pm are propagated, however their production processes are treated by a perturbative method so that they do not effect the dynamics of the collision. Baryons propagate in the mean field. Strange baryons feel 2/3 of the baryon field. Nonstrange mesons are not effected by a potential, but a potential may be easily added if needed. Various sets of mean fields for kaons are available [145]. The nonstrange mesons are produced via resonance decays. This means that the reactions $NN \leftrightarrow NR$ and $mN \leftrightarrow R$ are implemented in the code (with R denoting any baryon resonance and m denoting any meson). Parameters are best fitted to available data [146]. For K^+ production and ϕ meson production cross sections parameters are taken from [147] and [148], respectively. Production and absorption cross section of K^- mesons are measured to a large extent, but for $NY \leftrightarrow NNK^-$ processes one has to rely on theoretical predictions [149].

3.5.6 Relativistic BUU (Texas A&M/Stony Brook)

The Relativistic Boltzmann-Uehling-Uhlenbeck (RBUU) approach has been used by several groups to develop transport models for the intermediate relativistic energy regime.

The RBUU model developed by the Texas A&M and Stony Brook groups is a covariant microscopic transport model for heavy ion collisions at SIS/GSI energies [150–157]. This model includes simultaneously the effects of mean field, two-body collisions, and the Pauli blocking for fermions. The covariant RBUU transport equation is solved by the test-particle method and the one-body phase space distributions are represented by point-like test-particles. In this model, only the nucleon, $\Delta(1232)$ resonance, and pion are treated explicitly and the isospin dependence is neglected. Besides undergoing elastic and inelastic two-body scatterings, these particles also propagate in mean-field potentials. For nucleons, their potential is taken from the nonlinear Walecka model used in [150] or the effective chiral Lagrangian of [158]. The Δ resonance is assumed to have the same mean-field potential as the nucleon, while the mean-field potential for the pion is neglected.

This RBUU model allows to consistently investigate the medium effects on hadron properties through the change of the scalar and vector potential. Kaons together with its partners (hyperons or antikaons) are produced in this model from pion-baryon and baryon-baryon reactions, i.e., $\pi B \rightarrow KY$ and $BB \rightarrow BYK$. Antikaons are produced not only from pion-baryon and baryon-baryon reactions, i.e., $\pi B \rightarrow K\bar{K}B$ and $BB \rightarrow BBK\bar{K}$, but also from the pion-hyperon reactions $\pi Y \rightarrow \bar{K}N$ [159], where Y denotes either Λ or Σ . Their cross sections are taken either from predictions of the boson-exchange model or from the empirical values as given in [155]. Annihilation of produced

antikaons is included via the inverse reactions of pion-hyperon reactions, i.e., $\bar{K}N \rightarrow \pi Y$, as other absorption reactions involve the rarely produced kaons and are thus unimportant. However, the annihilation of kaons is neglected as it has little effect on kaon production [160]. Because of the small production probabilities of kaons, hyperons, and antikaons in heavy-ion collisions at SIS energies, the above discussed reactions are treated perturbatively. For Λ and Σ , their mean-field potentials are taken to be 2/3 of the nucleon potential according to their light quark content. For kaon and antikaon, their mean-field potentials are obtained from a chiral Lagrangian including both scalar and vector interactions [155]. Recently, this perturbative method was extended to also investigate the subthreshold production of the multistrange baryon Ξ [161].

3.5.7 Relativistic BUU (Catania/Munich/Tübingen)

The RBUU model developed by the Catania-Munich-Tübingen groups is a fully covariant transport model for heavy ion collisions at SIS/GSI energies. In contrast to most other BUU models this model is based on a representation of the one-body phase space distributions by covariant Gaussian distributions [162] instead of point-like test-particles. The collision integral incorporates elastic and inelastic channels (Δ and N^* resonance production with 1- and 2-pion final channels). The baryon resonances feel the same mean field potential as the nucleons, while the pions are propagated under the influence of the Coulomb potential and they also strongly interact with the hadronic environment via re-absorption processes. In the strangeness sector, only the positively charged (K^+) kaons were considered in the same way as given in [14]. The RBUU approach was recently extended towards an appropriate description of the isovector part of the nuclear equation of state [163, 164]. Thereby the fully covariant formulation is essential for the understanding of the Lorentz structure of the symmetry energy at supra-normal densities [163–166]. In particular one can directly probe the interplay of different isovector mesons such as the competition between an isovector, vector repulsive ρ and an isovector, scalar attractive δ field, as recently suggested [167, 168]. Compared to other transport codes where only the relativistic kinematics is included, this code cares about the following genuine relativistic effects:

- It accounts for new structures due to the contributions of the vector and scalar Lorentz components to the self-energies of protons, neutrons and of the various isospin states of other baryons such as ($\Delta^{\pm,0,++}$, $N^{+,0}$, Λ , $\Sigma^{\pm,0}$). This implies an important modification of the standard numerical treatment of the collision term when inelastic processes are included, in particular with respect to the energy conservation. A detailed discussion is given in [166].

- The Lorentz effect of the vector field contributes to the “magnetic force” acting on the baryons. In [163] it was clearly shown that in neutron-rich systems this effect will lead to large differences in neutron/proton flows at high transverse momenta.

3.5.8 A Relativistic Transport ART (Texas A&M)

ART is a hadronic transport model which was particularly designed for the AGS energy range [169, 170]. It consists of a hadronic cascade supplemented by a Skyrme type mean field. Particle production is not described via string excitations but by an explicit treatment of the various hadronic reaction channels. Cross sections are based on parametrisations of available data or determined within a resonance production model.

The ART model includes baryon–baryon, baryon–meson, and meson–meson elastic and inelastic scatterings. It treats explicitly the isospin degrees of freedom for most particle species and their interactions, which permits to study isospin effects in heavy ion collisions [171]. Since it includes mean-field potentials for nucleons and kaons, the ART model can also be used to investigate effects arising from the hadronic equation of state. Resonances such as ρ and Δ are formed from pion–pion and pion–nucleon scattering, respectively, with cross sections given by the standard Breit-Wigner form with mass dependent width which also govern their decays. The masses and widths of resonances are taken to be their values in the vacuum, i.e., effects due to possible modifications in dense hadronic matter are neglected.

For baryon–baryon scatterings, the ART model includes the following inelastic channels: $NN \leftrightarrow N(\Delta N^*)$, $NN \leftrightarrow \Delta(\Delta N^*(1440))$, $NN \leftrightarrow NN(\pi\rho\omega)$, $(N\Delta)\Delta \leftrightarrow NN^*$, and $\Delta N^*(1440) \leftrightarrow NN^*(1535)$. In the above, N^* denotes either $N^*(1440)$ or $N^*(1535)$, where the bracket symbol (ΔN^*) denotes a choice, here of Δ or N^* . Also included are reaction channels relevant for kaon production, i.e. $(N\Delta N^*)(N\Delta N^*) \rightarrow (N\Delta)(\Lambda\Sigma)K$. For meson–baryon scatterings, the ART model includes the following reaction channels for the formation and decay of resonances: $\pi N \leftrightarrow (\Delta N^*(1440) N^*(1535))$, and $\eta N \leftrightarrow N^*(1535)$. Furthermore it accounts for elastic scatterings such as $(\pi\rho)$ on $(N\Delta N^*)$. As an example, the cross section for the elastic scattering of $\pi^0 N$ is evaluated by including heavier baryon resonances with masses up to 2.0 GeV/ c^2 as intermediate states of Breit-Wigner form but neglecting interferences between the amplitudes from different resonances [169]. The ART model further includes inelastic reaction channels such as $\pi N \leftrightarrow (\pi\rho\eta)\Delta$ and kaon production channels such as $(\pi\rho\omega\eta)(N\Delta N^*) \leftrightarrow K(\Lambda\Sigma)$. Kaon and antikaon elastic scatterings with nucleons as well as inelastic channels for antikaons, such as $\bar{K}(N\Delta N^*) \leftrightarrow \pi(\Lambda\Sigma)$, are included [172] using parametrized experimental data [173]. Also included are kaon production channels involving three-body final states, $(\pi\rho\omega)(N\Delta N^*) \rightarrow K\bar{K}N$ [172]. Because of the

difficulty associated with the three-body kinematics, the inverse kaon annihilation reactions of the above channels are neglected.

For meson–meson interactions, the ART model includes both elastic and inelastic $\pi\pi$ interactions, with the elastic cross section consisting of ρ meson formation and the remaining part treated as elastic scattering. Kaon production from inelastic scatterings of light mesons is included via the reactions $(\pi\eta)(\pi\eta) \leftrightarrow K\bar{K}$ and $(\rho\omega)(\rho\omega) \leftrightarrow K\bar{K}$. Kaon or antikaon elastic scatterings with mesons in the SU(2) multiplets except the pion are included using a constant cross section of 10 mb [169], while the kaon-pion elastic scattering is modelled through the K^* resonance.

3.5.9 A Multi-Phase Transport AMPT (Texas A&M)

The AMPT [174] is a Monte Carlo model for heavy ion collisions at relativistic energies. It uses minijet partons from hard processes and strings from soft processes in the Heavy Ion Jet Interaction Generator (HIJING) [175] as the initial conditions. In the default version of AMPT [176, 177], time evolution of the minijet partons is described by Zhang’s Parton Cascade (ZPC) [178] with parton scattering cross sections derived from the lowest-order Born diagrams where magnitude and angular distribution are fixed by treating the gluon screening mass as a parameter. After minijet partons stop interacting, they are combined with their parent strings to fragment into hadrons using the Lund string fragmentation model as implemented in the PYTHIA program [179]. The final-state hadronic scatterings are modelled by A Relativistic Transport (ART) model [169, 170]. In the string melting version of AMPT [180], those hadrons potentially being produced from string fragmentation are rather converted to their valence quarks and/or antiquarks. Interactions among quarks and antiquarks are described by ZPC with same scattering cross sections as in the default model [178]. Once all scatterings are stopped, quarks and antiquarks are converted to hadrons via a simple coalescence model, which combines two nearest quark and antiquark into mesons and three nearest quarks or antiquarks into such baryons or anti-baryons that are close to their invariant masses. Final-state scatterings of produced hadrons are again modelled by the ART model.

The code is posted at

<http://nt3.phys.columbia.edu/people/zlin/AMPT/>

3.5.10 Hadron String Dynamics HSD

The Hadron-String Dynamics (HSD) transport approach is a covariant microscopic transport model developed to simulate relativistic heavy-ion collisions, proton-nucleus reactions and pion-nucleus reactions in the energy range from SIS to RHIC.

The HSD transport approach [181–183] provides the numerical test-particle solution of a coupled set of relativistic transport equations for particles with in-medium self-energies. It is based on quark, diquark, string and hadronic degrees of freedom. On the hadronic side it treats explicitly the familiar baryon octet and decuplet and selected higher resonances as well as their antiparticles. On the meson side it includes the pseudo-scalar and vector meson nonets as well as some higher meson states (a_1 etc.). Hadrons of even higher mass are treated as 'strings' that reflect the continuum excitation spectrum of hadrons. Dileptons (e^+e^- , $\mu^+\mu^-$), open and hidden charm mesons (D , D^* , D_s , D_s^* , J/Ψ , χ_c , Ψ') as well as high p_T hadrons are treated perturbatively [184–186]. The baryons are propagated explicitly with momentum-dependent scalar and vector self-energies [187]; baryons with a strange quark have self-energies reduced by a factor of 2/3 and baryons with two strange quarks are evolved in time with 1/3 of the scalar and vector potentials by default. All mesons can optionally be propagated with in-medium potentials, too.

High-energy inelastic hadron-hadron collisions in HSD are described by the FRITIOF string model [188] (including PYTHIA [179]) whereas low energy hadron-hadron collisions are modelled on the basis of experimental cross sections (when available) or OBE calculations whenever no data exist. The transport approach is matched to reproduce the nucleon-nucleon, meson-nucleon and meson-meson cross section data in wide kinematic ranges. HSD takes into account the formation and multiple rescattering of leading pre-hadrons and hadrons with cross sections in line with the additive quark model. Optionally multi-meson fusion channels for baryon-antibaryon production can be included as well as the off-shell propagation of particles as described by Juchem and Cassing in [78]. The major aim of HSD is - within a single transport model - to gain an understanding about the nuclear dynamics, the creation of dense and hot hadronic matter and the modification of hadron properties in a medium.

More recently an extended version of HSD was developed which is denoted as PHSD (Parton-Hadron-String Dynamics) [189]. Additionally it includes an early partonic phase. Here the equation-of-state is taken from lattice QCD and the quasi-particle properties for quarks, antiquarks and gluons are obtained from fits to lattice results [190–192]. Due to the large damping width of the partonic degrees of freedom an off-shell propagation is implemented by default. Partonic elastic and inelastic reactions are included ($qq \leftrightarrow qq$, $q\bar{q} \leftrightarrow q\bar{q}$, $gg \leftrightarrow gg$, $gg \leftrightarrow g$, $q\bar{q} \leftrightarrow g$ etc.) with non-perturbative cross sections taken

from [190] or of Breit-Wigner form which are fixed by the quasi-particle spectral functions. The transition from partonic degrees of freedom to hadronic resonant states is performed with the help of transition matrix elements that strongly peak at an energy density of about 1 GeV/fm^3 . In all reactions “detailed balance” is implemented in the partonic sector and energy-momentum conservation strictly holds in the parton-hadron transition. Furthermore, the conservation of flavor currents is exactly fulfilled. The PHSD approach is presently tested in a wide dynamical regime up to LHC energies.

The code is posted at

<http://www.th.physik.uni-frankfurt.de/~brat/hsd.html>.

3.5.11 Quark-Gluon String Model QGSM

An alternative string model realisation is the Quark-Gluon String Model (QGSM) [193–198]. It incorporates partonic and hadronic degrees of freedom and is based on Gribov-Regge theory (GRT) [199, 200] accomplished by a string phenomenology of particle production in inelastic hadron–hadron collisions. To describe hadron–hadron, hadron–nucleus and nucleus–nucleus collisions the cascade procedure of multiple secondary interactions of hadrons was implemented. The QGSM incorporates the string fragmentation, formation of resonances, and rescattering of hadrons, but simplifies the nuclear effects neglecting, e.g., the mean fields or multi-particle interactions. As independent degrees of freedom the QGSM includes octet and decuplet baryons, octet and nonet vector and pseudoscalar mesons, and their antiparticles. The momenta and positions of nucleons inside the nuclei are generated in accordance with the Fermi momentum distribution and the Woods-Saxon density distribution, respectively. Pauli blocking of occupied final states is taken into account. Strings in the QGSM can be produced as a result of the colour exchange mechanism or, like in diffractive scattering, due to momentum transfer. The Pomeron, which is a pole with an intercept $\alpha_P(0) > 1$ in the GRT, corresponds to the cylinder-type diagrams. The s -channel discontinuities of the diagrams, representing the exchange by n -Pomerons, are related to the process of $2k$ ($k \leq n$) string production. If the contributions of all n -Pomeron exchanges to the forward elastic scattering amplitude are known, the Abramovskii-Gribov-Kancheli (AGK) cutting rules [201] enable one to determine the cross sections for $2k$ -strings. Hard gluon–gluon scattering and semi-hard processes with quark and gluon interactions are also incorporated in the model [202]. The inclusive spectra in the QGSM have automatically the correct triple-Regge limit for the Feynman variable $x \rightarrow 1$, double-Regge limit for $x \rightarrow 0$, and satisfy all conservation laws. The particular stages of the collision model, namely (i) initialisation of interacting projectile and target nuclei, (ii) string formation via inelastic nucleon–nucleon (hadron–hadron) interaction, (iii) string fragmentation, i.e. hadronization, and (iv) hadron–hadron rescattering, are solved basically by Monte Carlo simulation techniques.

Chapter 4

Many-body models

Molecular dynamics is a widely applied technique for simulating many-body systems and it provides a very convenient framework for studies of nuclear dynamics.

In the simplest approach, one considers the classical evolution of A nucleons that are subject to a given two-body interaction which generally consists of a short-range repulsion and a long-range attraction so that the resulting nuclear matter equation of state has a Van der Waals form. The early work by Lenk and Pandharipande [203, 204] provides a good illustration of this type of model.

Although molecular dynamics is entirely deterministic, the evolution generally has a chaotic character so that small differences in the initial states may lead to quite different final states. Furthermore, the treatment has the virtue of retaining all the orders of many-body correlations (at the classical level), contrary to the one-body treatments discussed earlier. While many important properties of the nuclear many-body quantum system cannot be reproduced in a model based on classical particles (see below), classical molecular dynamics has nevertheless yielded useful insight into the evolution of nuclear collisions, including the general features of fragmenting finite systems, such as critical phenomena [205], phase evolution [206], the caloric curve [207] and isoscaling [208].

One of the central problems associated with attempts to describe nuclear systems in terms of classical particles is the lack of Fermi motion. Indeed, in the ground state of the classical Hamiltonian \mathcal{H} all particles have vanishing velocities. Furthermore, the absence of the Fermi pressure causes the inter-nucleon distances to be too small at low temperatures. This inherent problem makes it hard to emulate the most basic features of nuclear systems.

One partial remedy for this problem is the introduction of a so called Pauli potential, a momentum-dependent repulsion that serves to emulate the exclusion principle, as first proposed by Wilets et al. [209, 210]. This approach was pursued in more detail by Dorso et al. [211] with a Gaussian repulsion depending on the phase-space separation s_{ij} , with $s_{ij}^2 = r_{ij}^2/q_0^2 + p_{ij}^2/p_0^2$.

They first demonstrated that such a repulsion leads to a reasonable emulation of the Fermi-Dirac momentum distribution in thermal equilibrium, over a broad energy range of interest [211]. Furthermore, when augmented by a Lennard-Jones potential, the model yields a reasonable reproduction of the nuclear equation of state and hence appears to be suitable for instructive simulations of nuclear collisions [212]. Indeed, a first application to an initially compressed and heated nucleus allowed the extraction of its thermodynamic phase evolution, showing that the spinodal region was entered, and the resulting fragmentation exhibited characteristic signs of filamentation [206]. The Pauli potential was also employed for the study of clustering in nuclear matter at subsaturation densities [213].

4.1 Molecular dynamics with phase-space smearing

The most extensively employed class of many-body simulation models seeks to remedy the most basic short-comings of the classical framework by representing each particle as a Gaussian density distribution in phase space. The latter obeys the uncertainty principle and is therefore frequently referred to as a wave packet although the treatment is still entirely classical. The essential effect is the generation of an additional smearing in the calculation of the interparticle forces, resulting in a much smoother behaviour. In fact, interactions void of a repulsive core lead to forces similar to those associated with the mean fields employed in the one-body approaches. It is thus possible to effectively obtain a mean field for each individual A -body system without the use of partial (test) particles or parallel ensembles methods, as required in the Boltzmann treatment. Because the phase-space smearing effectively produces a mean field, the model is supplemented by direct collisions, representing the short-range repulsion omitted in the calculation of the field. This part is entirely similar to what is done in the Boltzmann treatments, but it has a key advantage that through the wave packets allows to calculate the required local phase-space occupancies in each individual collision event, in spite of the rather low phase-space density of physical particles. Numerically stable results can thus be obtained for the quantum-statistical (Pauli-blocking or Bose-enhancement) factors. Because of their ability to treat this basic quantum feature, these models are usually referred to as QMD: Quantum Molecular Dynamics [214–218] (even though the actual equations of motion for the centroids of the wave packets are still of purely classical form). The ability of QMD to simulate individual collision events significantly facilitates the contact with actual collision experiments and was (and still is) the main reason for its extensive usage.

Molecular dynamics can readily accommodate a variety of different species and reactions between them. Furthermore, extensions to relativistic kinematics were made, most notably Relativistic Quantum Molecular Dynamics

(RQMD) [219, 220] and further extension towards ultrarelativistic collisions (named UrQMD) have widely been applied to relativistic nuclear collisions with considerable success in reproducing many aspects of the data. To account for high energetic binary collisions strings were included into RQMD and UrQMD.

The initial A -body state is usually generated by a phase-space sampling similar to the one employed in the one-body simulations. This initialisation ensures that the initial distribution of the nucleons in the one-body phase space is realistic (i.e. it resembles results obtained with Hartree-Fock calculations, for example), whereas a minimization of the Hamiltonian would usually lead to too compact configurations and the nucleons would all be at rest, as mentioned above. Even though such initial “nuclei” are unstable against emission and collapse, the time scale for this exceeds that of interest in the context of nuclear collisions. On the other hand, the composite objects formed at the end of a collision suffer from this problem and causes the analysis of the multifragment final state to be somewhat problematic, an issue, however, of less importance in the present context.

Alternatively, one may add a suitable Pauli-potential and then perform a minimization to obtain a suitable initial nucleus. The presence of the Pauli potential has the advantage that the final composite objects have a much larger resemblance with actual nuclei, especially with regard to size and binding energy. However, while this refinement yielded some instructive results [213], it did not become part of the standard QMD treatment.

Many versions of the QMD approach have been developed, most (but far from all) of them being rooted in the code originally developed by Aichelin and coworkers [215]. Here we mention several extensions relevant in the present context. Results obtained with these models will be presented in Chap. 6.

4.1.1 IQMD: Isospin Quantum Molecular Dynamics

The Isospin Quantum Molecular Dynamics model (IQMD) [218] represents an extension of the original QMD model (or code) developed by Aichelin and coworkers [215]. The basic QMD concepts remain the same, but the treatment was somewhat refined, in particular with respect to the isospin dependence of the nuclear forces determining the mean field and the cross sections for the binary scatterings. Furthermore, in addition to the two nucleons (neutrons and protons), the four charge states of Δ resonances and the three ones of the pion are now included. Thus the model is by design suitable for an application in the SIS energy range, i.e. up to beam kinetic energies of about 2 A GeV.

The code is posted at

<http://www-subatech.in2p3.fr/theo/qmd>.

4.1.2 Relativistic Quantum Molecular Dynamics

Relativistic Quantum Molecular Dynamics (RQMD), as originally developed by Sorge et al. [219], represents a fully covariant description of a classical N -particle system based on Dirac's Constrained Hamilton Dynamics [221, 222]. The N -body Hamiltonian is thereby expressed by $2N - 1$ constraints ϕ_i ,

$$H = \sum_{i=1}^{2N-1} \lambda_i \phi_i \quad . \quad (4.1)$$

where the first N constraints are given by the mass-shell conditions $K_i = p_i^2 - m_i^2 - V_i = 0$. In contrast to the vacuum case the mass-shell constraints are now modified by the presence of a potential which is a covariant extension of the standard Skyrme interaction, $V_i = \frac{1}{2} \sum_{j \neq i} V_{ij}^{\text{Sk}}(q_{ij}^T)$, depending on the transverse relative inter-particle separation q_{ij}^T . The remaining $N - 1$ constraints serve to fix the world lines of the particles, *i.e.* to ensure world line invariance, causality, and cluster separability. Their explicit form is motivated by studies of singular Lagrangians. A final time constraint which does not enter the Hamiltonian fixes an overall evolution time of the system.

The complete set of $2N - 1$ constraints generates the equations of motions for canonically conjugate coordinates and momenta,

$$dq_i^\mu / d\tau = \{H, q_i^\mu\} \quad , \quad dp_i^\mu / d\tau = \{H, p_i^\mu\} \quad . \quad (4.2)$$

where $\{\cdot, \cdot\}$ denotes the Poisson bracket. To compute the evolution of the system, *i.e.* integrating the set of above equations of motion (4.2), one must determine the unknown Lagrange multipliers $\lambda_i(\tau)$. This difficult task is simplified when Dirac's first class condition is fulfilled, $\{K_i, K_j\} = 0$, since in that case the Hamiltonian can be reduced to the simpler form. While Hamilton Constrained Dynamics provides the most exact solution toward the relativistic N -body problem the numerical effort is prohibitively large since the computational time scales with N^3 . Thus in many cases additional approximations were introduced in order to reduce the numerical effort [219].

The Frankfurt group has extended the RQMD code developed by Sorge et al. [219] towards ultrarelativistic collisions by the inclusion of strings which account for high energetic binary collisions [223]. This model has been extensively applied to nuclear collisions from AGS up to RHIC energies [223–227]. A further development of the RQMD is UrQMD (described below). While in these versions (RQMD and UrQMD) employ nuclear forces that are solely based on Skyrme interactions, an alternative model, (R)QMD, also based on Constrained Hamiltonian Dynamics, was developed in Tübingen [220] and extended for the application to relativistic dynamics through scalar and vector type interactions [228].

The Tübingen (Relativistic) Quantum Molecular Dynamics (R)QMD transport code [229] is in principle similar to the IQMD model. It uses relativistic

kinematics (but is not formulated covariantly like the RQMD model based on Hamilton Constrained Dynamics described above). The only mesons included dynamically in the (R)QMD and IQMD models are the pions, while heavier mesons (K , η , ρ , ω , ...) are treated perturbatively. These models in particular are suited for studies of subthreshold meson production at SIS energies. They were extensively applied to kaon production at subthreshold energies [14, 230] and used for vector meson and dilepton production [231]. For the latter application, the Tübingen model was extended to include all nuclear resonances with masses below 2 GeV, in total 11 N^* and 10 Δ resonances [231].

In all cases elastic and inelastic binary collisions as well as particle production and absorption processes are accounted for in a way similar to the Cascade models, however including Pauli-blocking and Bose-enhancement factors in the collisions terms, though these are of relatively little importance at relativistic energies.

4.1.3 *UrQMD: Ultra-relativistic Quantum Molecular Dynamics*

The Ultra-relativistic Quantum Molecular Dynamics model [232, 233] developed by the Frankfurt group represents the most stringent extension of the QMD concept towards relativistic and ultra-relativistic energies. Concerning the nuclear forces, UrQMD uses the usual QMD Hamiltonian but the number of baryons and mesons included has been significantly enlarged over the last two decades. Thus the model is applicable to (ultra)relativistic nuclear collisions in the energy range from the BEVALAC and SIS up to AGS, SPS and RHIC.

The UrQMD collision term contains 55 different baryon species (including nucleon, Delta and hyperon resonances with masses up to $2.25 \text{ GeV}/c^2$) and 32 different meson species (including strange meson resonances), which are supplemented by their corresponding antiparticle and all isospin-projected states. The hadrons and hadron-resonances, which can be populated in UrQMD are listed in Table 7.1. For details see [232]. The states listed can either be produced in string decays, s-channel collisions or resonance decays. For excitations with masses higher than $2 \text{ GeV}/c^2$ a string picture is used. Full baryon/antibaryon symmetry is included with antibaryon–antibaryon interaction inferred from baryon–baryon interaction cross sections. Elementary cross sections are fitted to available proton–proton or pion–proton data. When possible isospin symmetry is used in order to reduce the number of individual cross sections to be parametrized or tabulated.

In the UrQMD model hadron–hadron collisions are performed stochastically, in a way similar to the original cascade models. Particle production in UrQMD either takes place via the decay of a meson or baryon resonance or

via a string excitation and fragmentation. Up to incident beam energies of 8–10 A GeV particle production is dominated by resonance decays. Production cross sections for the excitation of individual resonances can be calculated in the framework of OPE or OBE models [234]. Due to the large pion-nucleon cross section at low c.m. energies, resonant meson-baryon and meson-meson cross sections are among the most important in UrQMD. Up to c.m. energies of 2.2 GeV meson-baryon and meson-meson interactions in UrQMD are dominated by resonance scattering, i.e. the formation of intermediate resonances.

The hadron-hadron interactions at high energies are simulated in three stages. The type of interaction is determined according to the cross sections: elastic, inelastic, antibaryon-baryon annihilation, etc. In the case of inelastic collisions with string excitation the kinematical characteristics of strings are modelled in the following way: the hadron momentum transfer p_T is simulated according to a Gaussian distribution. The other interacting hadron gets the same momentum transfer but in the opposite direction. The excited strings have a continuous mass distribution $f(M) \propto 1/M^2$ with the masses M limited by the total collision energy \sqrt{s} : $M_1 + M_2 \leq \sqrt{s}$. The remaining energy is then equally distributed between the longitudinal momenta of two produced strings. The longitudinal momenta of the constituent quarks are chosen according to the structure functions of hadrons, $f(x_q) = f_0(x_q)^{\alpha-1}(1-x_q)^{\beta-1}$, with $\alpha = 0.5$ and $\beta = 2.5$ for valence quarks in nucleons. Their transverse distributions follow the same Gaussian distribution as for the momentum transfer, leaving the remaining diquark with a transverse momentum which is the same in magnitude, but of opposite direction. The second stage of h - h interactions is connected with string fragmentation for which UrQMD uses the Field-Feynman fragmentation procedure [235], where the strings decay independently from both ends. The procedure accounts for energy, momentum and quantum number conservation and includes the possibility of converting diquarks into mesons via diquark breaking.

The code is posted at

<http://th/physik.uni-frankfurt.de/~urqmd/>.

4.2 Quantum many-body approaches

In recent years, a variety of true quantum many-body approaches to the simulation of nuclear dynamics were developed. These all represent the state of the system as Slater determinants but differ with respect to the degrees of freedom considered and the form of their dynamical evolution. While these treatments are on much better ground from basic theory, they are relatively complicated to apply and, as a result, their applicability is considerably more limited compared to the range of observables calculated within the Boltzmann and QMD approaches.

4.2.1 Fermionic molecular dynamics

Fermionic molecular dynamics (FMD) [236–240] is a true quantum treatment that represents the many-body state as antisymmetrized Slater determinants composed of single particle wave functions of Gaussian form

$$\varphi_i(\mathbf{r}, t) \sim \exp[-\nu_i(t)[\mathbf{r} - \mathbf{Z}_i(t)]^2] |\chi_i(t)\rangle |\xi_i(t)\rangle. \quad (4.3)$$

The wave packet centroids $\{\mathbf{Z}_i\}$ and widths $\{\nu_i\}$ are complex dynamical variables (parameters) whose equations of motion are derived from the time-dependent variational principle. The concept explicitly includes spin $|\chi_i(t)\rangle$ and isospin degrees of freedom $|\xi_i(t)\rangle$. All physical observables, such as positions, momenta or the total energy, are then obtained as *expectation values* of the corresponding quantum operators with the FMD many-body wave function. The latter makes the FMD to a genuine quantum many-body approach.

If limited to a single Slater determinant, FMD is a constrained form of TDHF with nonorthogonal single-particle states for which the overlap matrix $\langle\varphi_i|\varphi_j\rangle$ should be properly considered. This non-orthogonality implies that the physical mean position and momentum of a given nucleon are not at all simply related to the associated centroid parameters, a feature also reflected by the fact that due to anti-symmetrization $\{\mathbf{Z}_i, \mathbf{Z}_i^*\}$ or $\{\nu_i, \nu_i^*\}$ are generally not canonical variables. Only for sufficiently dilute configurations the Pauli effects cease and the equations of motion take on the classical form [240].

In its original form, FMD employs just a single Slater determinant with single wave packets for each nucleon. With such a restriction it thus does not offer the possibility of *dynamical bifurcations*, an feature important in collisions already at moderate energies [240]. An important practical example is the emission of a nucleon from an excited nucleus. In the course of a given time interval this happens with a certain probability while with the complementary probability the nucleon remains in the source. In a quantum picture this process would be described by a wave function that splits in two parts, one for the emitted component which spreads in space, and one for the still bound component which remains localized within the nucleus. This phenomenon is clearly beyond the capabilities of a description with a single Slater determinant built from one Gaussian wave packet per nucleon. The example shows that this restriction leads to a severe suppression of quantum branching. The introduction of appropriate branching processes within some suitable stochasticity in the dynamics is discussed in Sects. 4.2.2 and 4.2.3).

There were several other works based on molecular dynamics with dynamical wave packet widths. It was found that the inclusion of a dynamical width improves the agreement with data in some cases, such as fusion cross section above the Coulomb barrier [241]. Kiderlen et al. [242] studied the fragmentation of excited systems. In response to the initial pressure, the excited system begins to expand but clusters were *not* produced even though Gaussian wave packets with many-body correlations were employed. When

the excited system expands, the widths of wave packets grow and then, in turn, the interaction between the packets weakens. The mean field for such a configuration is very shallow and smooth and there is then little chance for clusters to appear. This feature conflicts with the general expectation that clusters should appear in such situations. Similarly, studies of spinodal instability [243] showed that the zero sound is significantly affected when the width of the wave packets become large and this spatial spreading then inhibits the formation of clusters.

On the other hand FMD provides genuine quantum features such as the proper specific heat of a fermion system. By enclosing the system in a large harmonic oscillator potential well and coupling the system weakly to a virtual thermometer while examining its long-time behavior, it was possible to study the thermodynamic properties of FMD [244]. The model was shown to exhibit a liquid-gas phase transition (Sect. 2.2.3.4 in Part I) and the associated caloric curves were extracted. They are similar to those obtained experimentally, with a low-temperature Fermi-liquid like region ($E \propto T^2$), an intermediate plateau associated with the coexistence region, and a high-temperature gas-like region.

Originally developed as a quantum mechanically consistent molecular dynamics model [245], where quantum uncertainty and Fermi motion are treated by antisymmetrized wave packets, over the years the FMD approach has been evolved into a very successful model for nuclear structure [246–248]. As regards the nuclear Hamiltonian it should be noted that a satisfactory description of the diverse nuclear structure properties can only be achieved when using an effective Hamiltonian based on realistic NN-forces like those obtained by the Unitary Correlation Operator Method (UCOM) [48, 49]. Simplified forces without e.g. momentum dependence or spin-orbit terms are not sufficient.

Many quantal or classical molecular dynamics models that retain many-body correlations have shown that in multifragmentation the correlations leading to the formation of the final clusters can be traced back far in time even to the initial state. An obvious example for these correlations is the observed cluster structure of light nuclei, especially close to the breakup threshold. In ^{12}C or ^{16}O resonant states exist which undergo multifragmentation into α -particles. FMD describes these states in a fully microscopic quantal picture by admixing to single-particle shell-model like states antisymmetrized products of α -clusters at various relative positions [246].

Another exotic phenomenon, the formation of halos, occurs at the limit of stability, where nucleons are about to escape from the nucleus, but their energy is not quite sufficient. This corresponds to particle evaporation at higher energies. Again FMD describes this successfully by employing superpositions of narrow and broad gaussians.

These are two example cases of precursors of quantum branching or correlations which are implemented in the stationary version of FMD but still await proper treatment in the time-dependent case in order to overcome the

various spurious effects caused by the restriction to the evolution of single Slater determinants.

4.2.2 *Antisymmetrized molecular dynamics*

Antisymmetrized molecular dynamics (AMD) [249–251] is similar to FMD in that the system is represented by a Slater determinant and that a part of the equation of motion is derived from the time-dependent variational principle. An important difference to FMD is that stochastic terms were added to the equation of motion so that many configurations can appear during the course of the reaction dynamics.

On the other hand, AMD usually treats the width parameters $\{\nu_i\}$ of the single-particle wave packets as a constant parameter common to all the nucleons. This simplification reduces the computational burden but limits the flexibility of the description, compared to the FMD description, as long as the stochastic extension terms are ignored. Nevertheless, the constant width parameter guarantees that there is no spurious coupling of the internal motion and the center-of-mass motion of a cluster or a nucleus. Furthermore, the presence of trajectory branching due to the stochasticity avoids the creation of spurious correlations in the wave function. For example, for the nucleon emission process, channels with and without nucleon emission will appear as separate branches and therefore avoid to be mingled into a single Slater determinant.

Recent versions of AMD [252–254] seek to also account for the dynamics of the width and thus the shape of the wave packets by splitting them into several components. Here one uses a stochastic term derived from the single-particle motion in the mean field. It assumes that the coherence of the single-particle wave function is lost and it branches into incoherent Gaussian wave packets at a certain time due to many-body effects. This quantum branching process provides the coexistence between the single-particle dynamics in the mean field and e.g. the fragment formation, which requires spatial localization and the emergence of many configurations. The resulting extended AMD may be regarded as a specific case of the stochastic mean field equation (3.4) in Sect. 3.2 now with the fluctuations of the collision term $\delta C[f]$ designed in such a way that Gaussian wave packets appear.

When the wave packet branching is included by means of a stochastic term, the resulting state must be adjusted such as to ensure energy conservation. This is achieved by means of a dissipative term in the equation of motion. Although carefully constructed in order to obtain a reasonable time evolution, this dissipative term was not derived from a basic principle.

The implementation of two-nucleon collisions is similar to QMD (Sect. 4.1), with some differences described below. The antisymmetrization implies that the wave packet centroids $\{\mathbf{Z}_i\}$ cannot be interpreted as the positions

and momenta of nucleons. Rather, the physical coordinates are given as non-linear functions of the centroids [250] and the two-nucleon collisions are performed by using these physical coordinates. There then appear Pauli-forbidden phase-space regions into which the physical coordinates will never be able to enter. These regions are regarded as Pauli-blocked and not allowed as a final state of a collision.

With a conventional effective interaction and a reasonable choice of the width parameter AMD is capable of providing a quite good description of not only the basic properties of ground state nuclei but also of many detailed structure features. With some extensions such as the parity and angular momentum projections this includes the excitation level spectra of light nuclei [255]. The equilibrium properties of AMD were studied by solving the long time evolution of a many-nucleon system in a container in order to obtain a micro-canonical ensemble. When the liquid phase, in the form of a nucleus, is embedded in a nucleon gas of temperature T , the characteristic quantum relation $E_{\text{liq}}^* \sim T^2$ was obtained [256] and the resulting caloric curves show that AMD is consistent with the liquid-gas phase transition [257–259]. The wave packet branching plays an essential role in this respect. Although not yet studied very carefully, this success suggests that the statistical nucleon emission from an excited fragment may also be qualitatively quite well described within AMD. But a quantitative description would require the model to also give the correct value for the nuclear level density parameter a .

AMD was also successfully applied to fragmentation reactions, such as central collisions in the energy region of several tens of MeV/nucleon for light and heavy systems [252, 260]. The fragment iso-spin composition obtained in dynamical collisions is consistent with statistical predictions, such as the iso-scaling relation and the dependence on the symmetry energy term of the effective force [261, 262]. These results are consistent with the idea that the fragment iso-spin composition is determined when the density is low ($\rho \approx \frac{1}{2}\rho_0$) and reflects the symmetry energy of dilute nuclear matter. At higher energies ($E_{\text{beam}} \gtrsim 50 A \text{ MeV}$) the multiplicity of nucleons is strongly overestimated in AMD. This shows the lack of few-body correlations, which probably should be treated more quantum mechanically than by the accidental merging of randomly distributed wave packets.

4.2.3 Quantal Langevin dynamics

A more formal development of trajectory branching in wave packet dynamics has led to the Quantal Langevin (QL) model [263, 264]. The motivation for this work lies in the fact that the nuclear liquid-gas phase transition differs significantly from the usual liquid-gas phase transition in macroscopic matter primarily in the role played by quantum statistics. For usual macroscopic matter, the total energies are to a good approximation linear functions of the

temperature in both the liquid and gas phases. Thus the effective number of degrees of freedom is essentially constant in each phase. In contrast to this familiar situation, the liquid phase of a nucleus exhibits an increase in the number of activated degrees of freedom as the temperature is raised. In particular, the excitation energy of a nucleus at low temperature increases like $E^* = aT^2$ (with $a \approx A/(8 \text{ MeV})$), which is a typical quantal behavior, while the gas phase is characterized by the usual classical relation $E^*/A = \frac{3}{2}T$. The two curves intersect at $T \approx 12 \text{ MeV}$, which is much higher than the transition temperature suggested by experimental data. This indicates that the quantal statistical nature of the nuclear system plays an important role for the phase transition and, presumably, for the associated nuclear multifragmentation processes.

Part of the reason for the persistent shortcoming of wave-packet dynamics for the description of multifragmentation (see above) may be found in the fact that the equation of motion for the wave-packet centroids is not consistent with the quantal statistical nature, because quantum fluctuations inherent in the wave packets are neglected. The presence of quantum fluctuations is signalled by the fact that a given wave packet is a superposition of many energy eigenstates. Therefore the fluctuations should be taken into account in such a way that the different components are properly explored in the course of time.

This fundamental problem can be clearly brought out by making a cumulant expansion of the canonical weight of a given wave packet, at the temperature $T = 1/\beta$ [265],

$$\ln \mathcal{W}_\beta = \ln \langle \exp(-\beta \hat{H}) \rangle = -\beta \mathcal{H} + \frac{1}{2} \beta^2 \sigma_H^2 + \mathcal{O}(\beta^3) . \quad (4.4)$$

Here $\mathcal{H} \equiv \langle \hat{H} \rangle$ is the usual expectation value of the energy in the given wave packet and it is evident that the weight \mathcal{W}_β is affected by its energy spread σ_H . Truncation of the cumulant expansion at second order, corresponding to a Poisson energy distribution in each packet (as a Gaussian would have) leads to a much improved global description of the quantum-statistical properties of the many-body system.

This approach was extended to dynamical scenarios by the introduction of a Langevin force emulating the transitions between the wave packets [263, 264]. The corresponding transport process in wave packet space can be described as a Langevin process and the general form of the associated transport coefficients was derived. The ensuing diffusive wave packet evolution exhibits appealing physical properties, including relaxation towards the appropriate micro-canonical quantum-statistical equilibrium distribution in the course of the time evolution. Specific expressions for the transport coefficients were subsequently derived on the basis of Fermi's golden rule and it was verified that they satisfy the associated fluctuation-dissipation theorem.

This approach is not specific to nuclear dynamics but has general applicability. For example, it was used to study the effect of quantum fluctuations

on the critical properties of noble gases [266]. In nuclear physics it was applied to hyperfragment formation from Ξ^- absorption on ^{12}C where it was found that quantum fluctuations affect the outcome qualitatively [267, 268] and to multifragmentation [269] which is of particular interest here and will be briefly summarized below.

The Langevin force enables the wave packet system to explore its entire energy spectral distribution, rather than being restricted to its average value. This leads to a much improved description of the quantum statistical features. In particular, the resulting specific heat now exhibits the characteristic evolution from a quantum fluid towards a classical gas as a function of temperature [265], in contrast to the behavior emerging with the usual treatment. Since a change of a fragment's specific heat is associated with a change in its statistical weight, the effect is clearly relevant for the fragment production problem.

The key new features of the results obtained with the quantal Langevin model are the occurrence of larger fluctuations and an enhancement of stable configurations, such as bound fragments, as a result of the need to take account of the spectral distortion of the wave packets. The former feature arises from the fact that the wave packet parameter of each nucleon is populated according to the strength of the eigen components for the given energy expectation value, and therefore the wave packet parameter can have larger fluctuations than when the energy is fixed to the expectation value. On the other hand, in order to project out the appropriate energy component from the wave packet, it is necessary to take account of its internal distortion. The combination of these two basic features then enhances the average multiplicity of intermediate mass fragments IMF at the final stage, especially in central collisions, as was demonstrated for Au+Au at 100–400 MeV/nucleon [269]. While the larger fluctuations allow the system to explore more configurations and thus enhances the yield of primary fragments, the latter stabilizes the fragments, since the compensation for the quantum distortion effectively acts as a cooling mechanism.

These studies suggest that the underlying quantal nature of the nuclear many-body system may indeed play a significant role in fragmentation reactions.

Chapter 5

Fluid dynamics

Fluid dynamics approaches provide the most direct access to the bulk matter properties of the system. They describe the evolution of the system at a macroscopic level where only the local densities and currents enter. The microscopic structure of the underlying system is then encoded via the equation of state (EoS) and, in dissipative dynamics, appropriate transport coefficients. For a general introduction see e.g. [5] or [270].

5.1 General framework

Ideal fluid dynamics is based on the assumption of instantaneous local equilibration. The system is then characterized by its local energy density $\varepsilon(x)$, the local pressure $p(x)$, and the local flow velocity $\mathbf{v}(x)$, plus one density $\rho_a(x)$ for each conserved “charge” a , all functions of the four-coordinate $x = (t, \mathbf{x})$. The local energy-momentum tensor then takes the form

$$T^{\mu\nu}(x) = [\varepsilon(x) + p(x)] u^\mu(x) u^\nu(x) - g^{\mu\nu} p(x) \quad (5.1)$$

with four-velocity $u^\mu = \gamma(1, \mathbf{v})$ and Lorentz factor $\gamma(x) = (1 - v^2)^{-1/2}$. The equations of motion then follow from energy-momentum conservation and, when applicable, charge conservation,

$$\partial_\mu T^{\mu\nu}(x) = 0, \quad \partial_\mu j_a^\mu(x) = 0, \quad (5.2)$$

where the four-current density for the charge a is $j_a^\mu = \rho_a u^\mu = \gamma(\rho_a, \rho_a \mathbf{v})$ with $\rho_a(x)$ being the density in the rest frame of the fluid cell at x .

For N conserved charges (baryon number, electric charge, strangeness, ...) there are thus $5 + N$ dynamical variables (ε , p , \mathbf{v} , and $\{\rho_a\}$) whereas there are $4 + N$ conservation laws and, correspondingly, $4 + N$ equations of motion. Closure is obtained by the EoS $p_0(\varepsilon, \{\rho_a\})$ which gives the local pressure in terms of the local energy and charge densities, $p(x) = p_0(\varepsilon(x), \{\rho_a(x)\})$.

In the ideal fluid approximation, the EoS is the *only* input to the equations of motion that relates to the specific properties of the matter under consideration and there is thus a relatively close connection between this key quantity and the dynamical evolution of the system.

In the present context it is important to recognize that along with the conserved charges a ideal fluid dynamics also conserves entropy. Indeed, it readily follows from the above equations of motion (5.2) that the entropy density $\sigma = (p + \varepsilon - \sum_a \mu_a \rho_a)/T$ satisfies a continuity equation,

$$\partial_\mu \sigma^\mu(x) = 0, \quad (5.3)$$

where $\sigma^\mu = \sigma u^\mu$ is the entropy current density. It also follows that the local ratio between the various charge densities remains constant, $u^\mu \partial_\mu (\rho_a/\rho_b) = 0$ and that the entropy per net charge also remains constant in the local flow frame, $u^\mu \partial_\mu (\sigma/\rho_a) = 0$. Therefore ideal fluid dynamics is best suited for isentropic processes, for which $\delta\rho_a/\rho_a = \delta\varepsilon/(p + \varepsilon)$, and it may therefore be appropriate for the expansion dynamics occurring after the compression phase of a nuclear collision.

5.2 One-fluid hydrodynamics

The first suggestions and actual calculations of fluid dynamical effects [271, 272] date back to the early days of relativistic nuclear collisions and are later followed by various developments, e.g. in [273–288]. Improvements concerned the numerical algorithms, the switch from initially cylinder geometry to full 3 dimensional codes as well as the change towards a fully relativistic treatment. Due to the condition of instantaneous local equilibration and the implied zero range space-time scales there are dynamical constellations where the one-fluid picture (cf. Fig. 5.1) is less or even not at all applicable. These concern e.g.

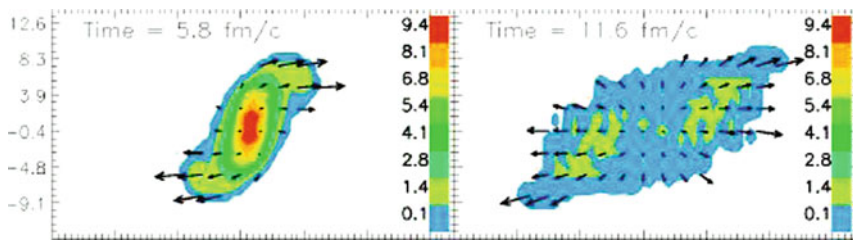


Fig. 5.1 A semi-central collision of two gold nuclei at a laboratory bombarding energy of 10 A GeV as calculated in one-fluid hydrodynamics (V.N. Russkikh, privat communication). The density contours and the local flow (*arrows*) are shown soon after the initial encounter (*left*) and somewhat later (*right*).

the initial stage as well as the final dilute stage, but also rapid processes during a phase-transition dynamics that lead to dynamical instabilities.

With the character more of two interstreaming gases the initial stage of energetic nuclear collisions cannot be well described by a single fluid. If one still would insist on keeping the one fluid picture, it would lead to the formation of discontinuities in form of shock fronts with a heated contact zone and the infalling matter at the outer side of the shock fronts. In this limit the entropy is generated through the shock fronts. While interesting as a limiting case with various physical phenomena as the formation of Mach cones [271], the true finite transport or dissipative space-time scale may significantly blur the picture and smoothen the shock fronts.

At the very late stage the system becomes so dilute, see Fig. 5.1 right frame, the microscopic collision rates so low, that local equilibrium can no longer be maintained and the particles freeze out, cf. Sect. 5.8.

The use of ideal fluid dynamics may also become questionable, when a first-order phase transition is present, since it is only applicable to adiabatic (i.e. slow) evolutions. However, a fast phase transition enforced through the expansion of the system may induce noticeable dissipative effects. Further limitations of the perfect, i.e. non-viscous fluid picture are discussed in Sect. 5.5 on viscous hydrodynamics.

To circumvent the above short comings, various strategies have been developed. For example the initial state of the fireball can be constructed from either kinetic simulations [289, 290] or from a multi-fluid scheme, cf. Sect. 5.3, or from some general (but model-dependent) assumptions (see [291–298]).

As a consequence various hybrid models, cf. Sect. 5.6, were developed, which appropriately link e.g. a microscopic kinetic transport with the macroscopic one-fluid dynamics, where the latter usually is only restricted to describe the expansion stage of the reaction after an approximately equilibrated fireball was formed.

5.3 Multi-fluid hydrodynamics

As the collision energy is raised, the assumption of instant local equilibration in the collision zone becomes increasingly unrealistic. In order to address this problem, models were developed that consider several distinct fluids that interpenetrate and exchange both four-momentum and conserved charges. In particular during the initial inter-penetrating phase of the reaction such approaches are esteemed to be much more appropriate than viscous hydrodynamics (Sect. 5.5). In such multi-fluid descriptions the above ideal conditions hold within each fluid α , while additional source terms describe the transport among the different fluids. The equations of motion then take the following form

$$\partial_\mu T_\alpha^{\mu\nu}(x) = F_\alpha^\nu(x) , \quad \partial_\mu j_{a,\alpha}^\mu = C_{a,\alpha}(x) , \quad (5.4)$$

where the friction forces F_α^μ result from the exchanges of energy and momentum between the fluid α and the other fluids, while the fluxes $C_{a,\alpha}$ describe the associated exchanges of the charge a . There is thus generally no overall local equilibrium in the multi-fluid system and so certain non-equilibrium phenomena can be described, such as partial stopping, under-cooling and super-heating associated with phase transformations, and delayed chemical reactions. Generally the different fluids attain different values of their local flow velocities, temperatures, and chemical potentials.

Already during the early days of low energy nuclear collisions the first two-fluid model calculations were performed [299] and later further developed for higher energies [274, 286]. However, towards relativistic collision energies the inclusion of a third fluid of the created particles became important.

5.3.1 Three-fluid model

In view of the two counter streaming nuclei in the initial phase and the formed fireball due to collisions a three fluid scenario seems to be the most adequate to description of the nuclear collision dynamics in macro-dynamical terms. Experimental rapidity distributions observed in nucleus–nucleus collisions between a few up to 200 A GeV support this counter-streaming behaviour.

In the following we therefore focus here on the three-fluid models as developed in [1, 286, 300–302]. They are in active use and under further development. The basic idea is that at each space-time point $x = (t, \mathbf{x})$ the baryon-rich matter, can be represented as a sum of two distinct contributions,

$$f_{\text{baryon}}(x, p) = f_{\text{p}}(x, p) + f_{\text{t}}(x, p),$$

initially associated with constituent nucleons of the projectile (p) and target (t) nuclei. In addition, newly produced particles, populating the mid-rapidity region, are associated with a fireball (f) fluid described by the distribution function $f_{\text{f}}(x, p)$. Therefore, the three-fluid approximation is a minimal way to simulate the finite stopping power at high incident energies. Note that both, the baryon-rich and fireball fluids may consist of any type of hadrons and/or partons (quarks and gluons), rather than e.g. only nucleons and pions.

To justify the term “fluids” it is assumed that constituents within each distribution are locally equilibrated, both thermodynamically and chemically. This assumption relies on the fact that intra-fluid collisions are much more efficient in driving a system to equilibrium than inter-fluid interactions. As applied to the fireball fluid, this assumption requires some additional comments, related to the concept of a finite formation time. During the proper formation time τ after production, the fireball fluid propagates freely, interacting neither with itself nor with the baryon-rich fluids. After this time

interval, the fireball matter starts to interact with both itself and the baryon-rich fluids and, as a result, thermalizes locally.

The main unknowns of the present approach can be briefly summarised as follows: the EoS and the coupling terms in (5.4). The EoS is an external input to the calculation and thus can be varied with the goal to find an EoS which in the best way reproduces *the largest body of available observables*. The coupling terms are equally important. They determine friction forces between fluids and hence the nuclear stopping power. In principle, friction forces are EoS dependent, because medium modifications, providing a nontrivial EoS, also modify cross sections, and should be externally supplied together with the EoS. However, presently there are only rough estimates of the friction forces [303] based on experimental inclusive proton–proton cross sections. Therefore the friction forces have to be fitted to the stopping power observed in proton rapidity distributions.

The hydrodynamic treatment of nuclear collisions is a promising alternative to kinetic simulations with its advantages and disadvantages. Lacking the microscopic feature of kinetic simulations, it overcomes their basic assumption, i.e. the assumption of binary collisions, which is quite unrealistic with growing matter densities. The scheme directly addresses the nuclear EoS that is of prime interest in this research. The three fluid construction accommodates the finite stopping power naturally in terms of friction coefficients such that one does not rely on some modelling for the initial phase of a single fluid approach (Sect. 5.2 above). The three-fluid initialisation is straightforward: in their respective rest frames, the colliding nuclei are represented by two spherical pieces of cold nuclear matter which are then accordingly boosted to the center-of-mass frame of the reaction. Due to the employed Maxwell construction for the phase-coexistence the model has still some deficiencies for an appropriate treatment of phase transitions.

First model results of the Moscow-GSI group were presented in [1, 301, 304–306]. See also Sect. 6.1. The code is posted at

<http://theory.gsi.de/~mfd/>.

5.3.2 Phase conversion within non-equilibrium chemistry

In this section we report on a special multi-component hydrodynamic model proposed in 1988 by Barz et al. [307, 308] under the name Flavour Kinetics. In the context of nuclear collisions for the first time and so far still unique this model deals with the phase conversion problem using driving potentials, that depending on the thermodynamic conditions drive the system towards the stable phase. Its formulation is transport theoretically sound, it provides a growing entropy and is free from such “never come back” concepts for the

hadronisation transition as e.g. implied by the string fragmentation mechanism.

The flavour kinetic model rests on a two-phase concept within a first order phase transition scenario. Each phase consists of a number of constituents, the quarks and gluons in the QGP-phase and of baryons and mesons in the hadronic phase. A bag-model EoS is assumed for the QGP, while the hadronic phase is described by free mesons and a Walecka-type EoS [51, 52] for the baryons. The resulting repulsion is important in order to furnish a proper phase transition at high baryon densities [309]. In order to simplify the dynamics global thermal and pressure equilibrium in an isotropically expanding fireball model is assumed. It accounts for radial flow with a linear (Hubble like) radial velocity profile, c.f. Sect. 5.7. The radial expansion generated self-consistently through the pressure led to a predicted flow velocity of 0.5 c [308] prior to experimental data. The core of the model are chemical rate equations which take the generic form

$$\langle \text{rate} \rangle = \langle \text{forward rate} \rangle [1 - e^{(\mu_r - \mu_l)/T}]. \quad (5.5)$$

Here μ_r and μ_l denote the sum of the chemical potentials of the particles on the right, respectively left side of a rate balance. Example for $q + \bar{q} \rightleftharpoons \pi + \pi$ one has $\mu_l = \mu_q + \mu_{\bar{q}}$ and $\mu_r = 2\mu_\pi$ (note that $\mu_q + \mu_{\bar{q}}$ vanishes only in equilibrium). These rates are generic, since they also include the standard Boltzmann collision term for free particles, if integrated over the particle momenta. The actual calculations within the Flavour Kinetic Model included close to hundred different chemical reactions.

These rates describe the density changes of the different constituents, both due to collisions and through phase-conversion rates. Within each phase standard binary collision and decay rates determine the forward rate for each process, while for the phase-transition rates assumptions lent from the string fragmentation are taken to determine the forward rates. The rate equations fully comply with detailed balance, they are generic, since the rate is determined by the off-set in chemical potentials, which for each particle follow from its density and the underlying EoS. If the chemical potentials become disfavoured in one phase relative to the other, the system is driven to the other phase. In the event of constant conditions the rates drive the system towards chemical equilibrium. Thereby it is important to use appropriate EoS for the two phases in order to comply with confinement. For example if both phases solely deal with free particles the system would rather be driven to a free gas of partons rather than hadrons in the low density limit according to the law of mass action, just like in very dilute inter stellar gases where atomic hydrogen prevails relative to hydrogen molecules. Thus the action of confinement can not be described by the mass action law, but rather requires a description in the form (5.5) with non-trivial EoS dependent chemical potentials.

The model accounts for radial flow, and permits delayed conversion rates between the two phases and this way super-cooling effects. The generic results

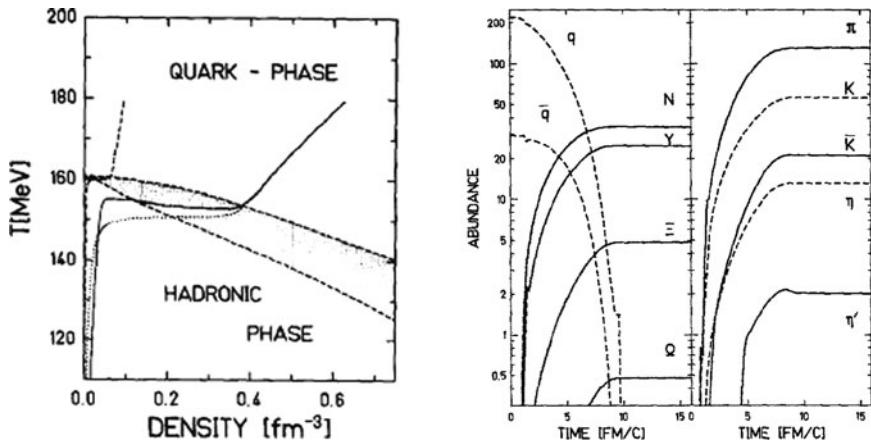


Fig. 5.2 *Left panel:* Three trajectories in the phase-diagram plane of density versus temperature. *Dashed line:* baryon poor case with initial $\mu_B = 100$ MeV; *full line:* baryon rich case with initial $\mu_B = 600$ MeV and a strong phase-conversion rate; *dotted line:* same as before for a slow phase-conversion rate. The *hashed area* shows the coexistence phase. *Right panel:* Time evolution for various species in the system for the baryon rich scenario.

of this study are the following. Due to the latent heat released during the transition and accompanying strong reduction of the specific entropy density from about 40 degrees of freedom in the QGP phase to essentially three degrees of freedom (3 pion states) in the hadron phase the following happens, cf. Fig. 5.2:

- the phase conversion takes time (about 6–10 fm/c depending on system size)
- the drop in entropy density during the transition is compensated by three means:
 - the volume increases roughly by a factor of five;
 - the system is steadily heated compensating the usual drop in temperature such that the temperature drop essentially ceases during the transition;
 - new constituents are created.

The three types of process contribute about equally to keep the entropy slightly rising during the transition. With respect to the chemical rates one finds that independent of the detailed assumptions finally the conversion rates become large during the phase transition due to the occurrence of instabilities. Thus, after phase-conversion the system finds itself in near chemical equilibrium, c.f. also the discussion on decoupling phenomena [310] in Sect. 5.8. Besides conservation law constraints the final composition is found to be blind with respect to detailed composition within the plasma phase, e.g. to the ratio of strange to non-strange quarks. These findings remain qualitatively

true also for a second order phase transition or for finite system sizes, where though more smoothly the system still exhibits significant changes in energy and entropy density over a small temperature range. In the Flavour Kinetic Model chemical freeze-out emerges automatically through the rate equations and was predicted to occur slightly below the phase-transition temperature which those days was assumed to be around 160 MeV.

The empirical results that the abundance of the different particles produced in the nuclear collisions at the CERN SPS can very precisely be explained within chemical equilibrium models, see Part I, Sect. 4.1, was one of the key arguments given that in such experiments the quark-gluon plasma was actually formed during the early phase of such reactions. Particularly for the strangeness sector it was claimed, that solely hadronic reactions do not suffice for reaching chemical equilibrium on such short time scales.

5.4 Collective modes

In the context of phase transitions and dynamical instabilities, it is of special importance to understand how fluid dynamics responds to local disturbances in the densities. To elucidate this central feature, we assume for simplicity that there are no conserved charges and consider a small disturbance away from a static uniform system with energy density $\bar{\varepsilon}$ and pressure $\bar{p} = p_0(\bar{\varepsilon})$,

$$\varepsilon(x) = \bar{\varepsilon} + \delta\varepsilon(x) , \quad p(x) = \bar{p} + \delta p(x) , \quad v(x) \ll 1 . \quad (5.6)$$

Note that the perturbative character of the disturbance implies the local flow velocity $\mathbf{v}(x)$ to be small, $v(x) \ll 1$. Therefore, to leading order, we may ignore v^2 and thus put γ to unity. The equations of motion then simplify,

$$0 = \partial_\mu T^{\mu 0} = \partial_t \delta\varepsilon + (\bar{\varepsilon} + \bar{p}) \partial_i v^i , \quad (5.7)$$

$$0 = \partial_\mu T^{\mu i} = (\bar{\varepsilon} + \bar{p}) \partial_t v^i + \partial^i \delta p . \quad (5.8)$$

Using $\delta p(x) = \partial_\varepsilon p_0(\varepsilon(x)) \delta\varepsilon(x) = v_s^2 \delta\varepsilon(x)$, where $v_s^2 \equiv \partial_\varepsilon p_0(\varepsilon)$ is the square of the sound speed, we then obtain the usual form of the equation for sound wave propagation,

$$\partial_t^2 \delta\varepsilon(x) = \partial_i \partial^i \delta p(x) = v_s^2(\bar{\varepsilon}) \partial_i \partial^i \delta\varepsilon(x) \quad \Rightarrow \quad \omega_k^2 = v_s^2 k^2 . \quad (5.9)$$

The right-hand side is the dispersion relation for disturbances of harmonic form, $\delta\varepsilon \sim \exp(i\mathbf{k} \cdot \mathbf{r} - i\omega_k t)$.

The above dispersion relation reveals a generic problem with ideal fluid dynamics: The frequency is strictly proportional to the magnitude of the wave number, $\omega_k \sim k$. Thus the shorter the spatial scale of the density disturbance, the faster the system responds. Fortunately, this problem is not essential in the mechanically stable region of the phase plane, because the rapid oscilla-

tion of the fine density ripples has negligible import on the overall dynamics. However, inside the spinodal phase region, where $v_s^2 < 0$ and uniform matter is mechanically unstable, the frequency is imaginary so the disturbance acquires an exponential time development, $\exp(-i\omega_k t) = \exp(\gamma_k t)$, where $\gamma_k \equiv \text{Im}(\omega_k)$ is the *growth rate*. This feature is disastrous, because it leads to ever faster amplification of ever shorter irregularities, thus rendering the problem mathematically meaningless as well as numerically intractable.

Because of this inherent divergence, which is due to the absence of a natural length scale in ideal fluid dynamics, this treatment is not applicable in the spinodal part of the phase coexistence region, and there is a need for developing suitable refinements. A refined treatment should lead to a dispersion relation for the unstable sound modes that has a qualitative appearance similar to what is usually found, namely a growth rate γ_k that displays a maximum value at some optimal wave number k_0 and then falls off to zero as k is increased further. For a discussion of this issue in the context of the nuclear liquid-gas phase transition, see [66], and for the QCD transition see e.g. [311].

The above analysis was carried out for the simplest case of no conserved charges. Though more complicated, similar considerations apply when conserved charges are present in the system. A further problem with ideal fluid dynamics in connection with phase transitions is related to the fact that the dynamical instability region is smaller because of the requirement of entropy conservation: the isentropic spinodal region generally lies inside the region enclosed by the isothermal spinodals.

5.5 Viscous fluid dynamics

Ideal fluid dynamics holds in the limit where the mean free path of the constituents is sufficiently small to guarantee effectively instantaneous local equilibration. (When several species are present, it is also required that the reaction rates be sufficiently fast to maintain local chemical equilibrium.) When this idealization is violated, as it usually is to some degree in nuclear collision dynamics, the local equilibrium can no longer be perfectly maintained as the constituents continually transport their momentum (and charges) to other parts of the system. To leading order, this complication can be incorporated into the fluid dynamic treatment by means of additional dissipative terms.

This can be done in a variety of ways (see for example [5, 312, 313] and references therein). The departure from the equilibrium form of the stress-energy tensor as given by the pressure p is normally formulated by the Navier-Stokes ansatz,

$$T_{ij} = \delta_{ij}(p - \zeta \nabla \mathbf{v}) - \eta(\partial_i v_j + \partial_j v_i - \frac{2}{3} \delta_{ij} \nabla \mathbf{v}), \quad (5.10)$$

where η is the shear viscosity coefficient and ζ is the bulk viscosity coefficient. Formally, these transport coefficients are given by the Kubo formulae through correlation functions of the stress-energy tensor [314],

$$\eta = -\frac{i}{20} \int d^3\mathbf{r} dt t \langle T_{ij}(\mathbf{0}, 0) T_{ij}(\mathbf{r}, t) \rangle, \quad (5.11)$$

$$\zeta = -\frac{i}{2} \int d^3\mathbf{r} dt t \langle \delta T(\mathbf{0}, 0) \delta T(\mathbf{r}, t) \rangle, \quad (5.12)$$

$$\delta T \equiv T_{ii} - p - v_s^2(T_{00} - \langle T_{00} \rangle), \quad (5.13)$$

where v_s is the speed of sound. Naturally, the presence of viscosity produces entropy, $\dot{\sigma} \equiv \partial_\mu \sigma^\mu = \partial_\mu \sigma u^\mu > 0$.

The most significant dissipative agency is usually the shear viscosity, which seeks to reduce the shear stress and thus counteracts the build-up of elliptic flow, for example. On the other hand, the spinodal phase separation process, which is primarily a local condensation, is affected by both η and ζ , $\dot{\sigma} \sim \frac{4}{3}\eta + \zeta$; the viscosity suppresses the growth rates at large wave numbers so that they approach a constant (but the region of instability is unaffected) [315]. Heat conduction and gradient effects are also important but not discussed here.

References [316, 317] list a number of physical reasons why the stress-energy tensor T_{ij} (the spatial part of $T_{\mu\nu}$ in the local rest frame) might depart from its equilibrium form in rapidly expanding systems. They are briefly as follows:

- Local kinetic distributions become anisotropic due to anisotropic flows which leads to the shear viscosity proportional to the mean free path.
- Interactions and correlations extending over a finite range lead to transport at finite distances and contribute to both shear and bulk viscosities [318].
- Near T_c , mean fields may find it difficult to adjust to rapidly changing equilibrium value, leading to peaks in the bulk viscosity near T_c [319].
- Chemical populations, especially for massive particles, fall out of equilibrium for rapidly expanding systems, resulting in fugacities. These effects can be incorporated either by explicitly treating the unequilibrated populations as dynamical charges, or as a bulk viscosity.
- The system may not have relaxed from initial conditions. Most notably, at early times the stress-energy tensor might be dominated by longitudinal colour fields [318, 320], which are characterised by large transverse components of T_{ij} and a small, perhaps even negative, longitudinal component.

The Navier-Stokes formulation is not free from conceptual difficulties. Besides a violation of causality, its time locality causes modes of short wave length to be unstable. In order to overcome these difficulties Israel and Stewart [321, 322] suggested a relaxation time concept, where the non-equilibrium part of T_{ij} will relax towards the Navier-Stokes values. Thereby two microscopically determined relaxation times govern the relaxation, both for the trace part T_{ii} responsible for the bulk viscosity and for the traceless part of

T_{ij} governing the shear viscosity. The ansatz results from a linear response derivation and ensures entropy growth.

The general difficulty for fluid dynamics to treat short spatial scales can be largely remedied by employing an EoS having a finite range [323]. In particular, such a refinement adds a quartic term in the collective dispersion relation and thus ensures that the spinodal growth rate drops to zero at a finite wave number, as occurs for other substances. This has recently been done by means of a gradient term in the energy functional [311, 315].

Viscosity has become a central issue in RHIC physics due to the success of ideal fluid dynamics in reproducing the bulk part of the flow, in particular the observed v_2 , see Fig. 6.16. The so derived very low viscosity coined the notion of a strongly coupled quark-gluon plasma (sQGP), c.f. Sect. 4.8 of Part I. An important question is how large the viscosity can be without conflicting with the data. Therefore viscous hydrodynamic approaches, in particular of the Israel-Stewart type, have recently been applied to RHIC collisions [313, 324–329]. Such approaches may also become useful for the description of the phase-transition dynamics in the CBM energy regime, since it avoids the problems associated with the change in degrees of freedom and the incorporation of driving potentials that plague the kinetic transport models.

5.6 Hybrid models

Hybrid approaches [298, 330–339] are regarded as the state-of-the-art models to describe the evolution of the nuclear collision dynamics. They combine the advantages of transport approaches that are well suited to deal with the non-equilibrium initial and final states, with those of an intermediate hydrodynamic evolution, where the equation of state (EoS) is an explicit input and phase transitions can be treated properly. Although microscopic transport approaches, cf. Sect. 3.5, provide the full space-time dynamics of all particles, it is presently not clear how to describe the phase transition and hadronization within such an approach.

In order to overcome the restrictions in each case, hybrid models generally schedule three dynamical stages: during the initial stage a microscopic transport scheme carries the incidentally colliding nuclei towards a locally equilibrated “fireball” that subsequently is followed by a hydrodynamic evolution until the description is handed over to a final-state kinetic transport description. While the first stage determines the initial conditions for the relativistic hydrodynamic equations of motion, the latter stage automatically furnishes a continuous freeze-out processes, an important improvement compared to the else wise employed prescription of an instantaneous freeze-out (see Sect. 5.8).

The hand shake between the subsequent schemes has to occur under well matched conditions such that both schemes are still applicable and do agree

in their local macro dynamical properties. This implies that near local equilibrium conditions have to be met for the first conceptual transition. Moreover the stochastic nature of the transport simulations generates initial conditions for the hydrodynamic stage that fluctuate from event to event. The latter can cause a significant spread in the subsequent hydrodynamic evolution due to the occurrence of dynamical instabilities, much as discussed in Sect. 5.4. The final conceptual transfer back to a kinetic scheme has to occur well before the hydrodynamic description ceases to be valid. As the macroscopic dynamics does not resolve the internal composition of the medium, the resulting abundances of the produced hadrons and composite nuclei have to be inferred through a well tuned thermal model from the (local) hydrodynamic fields. The so obtained phase-space distributions of the hadrons are then subsequently further propagated by the kinetic transport equations. The later then includes rescattering and final state interactions like resonance decays and provides a separation of chemical and kinetic freeze-out. The thereby resulting long freeze-out durations, cf. Fig. 5.5, p. 625, are well in line with the general freeze-out considerations presented in Sect. 5.8. They are seen to even comply with HBT observations for the “radii” of the emitting source [336, 340], for details see Sect. 5.9.

During the last years various hybrid models of the above kind have been developed. Example for the NEXSphRIO approach the initial stage is calculated within the non-equilibrium model (NEXUS) [332, 341], Toneev et al. [342] use the Quark-Gluon-String model (QGSM), cf. Sect. 3.5.11, while other groups, e.g., Teaney et al. [343], Hirano et al. [333, 344], Bass/Nonaka [334], rely on smooth Glauber or Color-Glass-Condensate initial conditions. The Frankfurt group [339] uses the Ultra-relativistic Quantum Molecular Dynamics (UrQMD) transport approach [233, 345, 346] for both kinetic regimes. The latter model is applicable to the broad energy range from $E_{\text{lab}} = 2\text{--}160$ A GeV and therefore covers well that of the planned CBM experiment at FAIR.

Compared to treatments solely throughout by kinetic transport, as e.g. by UrQMD, such hybrid strategies provide a well pronounced sensitivity of the transverse flow on the hydrodynamic part of the evolution and its EoS [337, 347–350]. Among others they further enhance the production of strange particles (by about 20% for the CERN SPS experiments) and significantly increase the elliptic flow towards collider energies [338] as indeed observed at RHIC. The latter has suggested that the created matter behaves like a perfect fluid, i.e. with very low viscosity, cf. the discussion in the context of Fig. 6.16 on p. 652.

While preserving the feature of exploring different equations of state, hybrid approaches also allow to constrain the initial and the final state prescriptions, since, besides the impact of the EoS on the collision dynamics, the treatment of the initial-state fluctuations and the final decoupling are of major importance for a sound interpretation of the experimental data.

5.7 Fluid dynamics inspired models

Already very early on the severe numerical complications associated with solving the fluid-dynamical equations of motion motivated work towards the development of simplified approximation schemes. Though inspired by hydrodynamics, they mostly rely on geometrical simplifications for the overall dynamics. Prominent examples in this respect are (a) the spherical expansion models and (b) for the application to collider energies the boost invariant scenario suggested by Bjorken [351]. For hadronic observables the details of the expansion dynamics barely matter, since up to freeze-out the system is relatively opaque for such probes, Sect. 5.8. Thus all that matters is the distribution of flow velocities and temperatures at freeze-out. There are many freeze-out studies in this respect, the blast wave model of Siemens and Rasmussen [352] assuming a spherical expansion is the earliest concept in this context. We have devoted an entire section on these matters in Part I, Sect. 4.1 of this book. For penetrating probes such as photons or dileptons the entire fireball evolution matters and one has to consider the corresponding course of the reaction.

In the spherical expansion models one assumes a radial velocity profile. Most prominent is the Hubble-like¹ scenario [353], where in a relativistic formulation the collective four velocity $\mathbf{u} = \gamma \mathbf{v}$ of a fluid cell scales with the radial distance from the origin, R , i.e. $\mathbf{u} = H \mathbf{R}$ with Hubble constant H . Note that $u^2 = 1$ and for particles with mass M one has $\langle \mathbf{p} \rangle \approx M \mathbf{u}$. Assuming a universal temperature T for the whole volume, then simply a description of the fireball radius $R(t)$ in its time evolution is required. This can either suitably be parametrised or inferred self-consistently by the averaged fluid dynamical equations of motion, i.e. by the conservation laws. For example, the flavor-kinetic model [308] described in Sect. 5.3.2 just uses such a simplification in order to leave computationally room for the complicated chemical rate equations.

For central collisions with extreme collision energies Bjorken [351] assumed that the expansion transverse to the beam direction can be neglected. Thus after collision of the extreme Lorentz contracted nuclei the system solely expands in longitudinal direction. The corresponding solution of the relativistic hydrodynamical equations of motion then become very simple. They imply boost invariance, which means the spatial rapidity η of a fluid cell at space-time position $\mathbf{x} = (t, x, y, z)$ is identical to its local flow rapidity y , i.e.

$$\eta(\mathbf{x}) = y(\mathbf{x}), \quad \text{where} \quad (5.14)$$

$$\left. \begin{aligned} \eta(\mathbf{x}) &= \frac{1}{2} \ln \frac{t+z}{t-z} \\ y(\mathbf{x}) &= \frac{1}{2} \ln \frac{u^0(\mathbf{x}) + u^z(\mathbf{x})}{u^0(\mathbf{x}) - u^z(\mathbf{x})} \end{aligned} \right\} \quad \text{or} \quad \frac{u^z}{u^0} = \frac{z}{t}, \quad (5.15)$$

¹ Such a scaling expansion is analogous to the Hubble expansion of the universe.

and $u(x)$ is the local four velocity. Boost invariance implies that fluid cells viewed from their local rest frame look the same at same proper times $\tau = \sqrt{t^2 - z^2}$. Thus, a freeze-out condition posed at a characteristic freeze-out temperature or energy density then defines a freeze-out hyperbola in the $z - t$ plane. In case of massless constituents the only scale in the system are the proper time τ and the constant transverse area S leading to a volume $V = S\tau$. Thus from entropy conservation and dimensional arguments entropy density $s(x)$ and temperature T have to scale like

$$s(x) \propto T^3 \propto S^{-2}\tau^{-1} \quad \text{for a gas of massless particles.} \quad (5.16)$$

The first proportionality coincides with the Stefan-Boltzmann law, while the last proportionality results from entropy conservation applied to the locally expanding fluid cell. With $TV^{\kappa-1}$ the corresponding adiabatic index results to $\kappa = \frac{4}{3}$. For mass dominated non-relativistic systems with particle density $\rho(x)$, on the other hand, one has

$$\left. \begin{aligned} s(x) &\propto -\rho(x) \ln(\rho(x)(MT)^{-3/2}) \propto S^{-2}\tau^{-1} \\ T &\propto \rho(x)^{2/3} \propto (S^2\tau)^{-2/3} \end{aligned} \right\} \quad (\text{for } M \gg T), \quad (5.17)$$

where the last relation results from also imposing particle number conservation, where $\rho(x) \propto S^{-2}\tau^{-1}$. Here the adiabatic index is $\kappa = \frac{5}{3}$.

5.8 Decoupling and freeze-out

Common to all fluid-dynamical approaches describing the expansion of the collision system into a very dilute gas of non-interacting (i.e. freely moving) particles is that the fluid-dynamical stage must be terminated by a decoupling or freeze-out procedure. Although such procedures were originally applied to high-energy physics already almost 50 years ago [354–356], there are still open issues under active discussion. While intuitively clear and easily applicable, the original method suffered from violation of energy conservation. To remedy the situation, Cooper and Frye [357] proposed a modified procedure, which complies with the conservation laws. The freeze-out then takes place on a specified freeze-out hypersurface. Depending on the character of its normal vector, the freeze-out hypersurface is either *time-like* or *space-like*. For time-like hypersurfaces, which describe a freeze-out due to a global dilution of the system, the Cooper-Frye formulation complies with energy-momentum and particle number conservation, i.e. $\partial_\mu j^\mu = 0$. For space-like hypersurfaces which describe the emission from a spatial surface into vacuum (such as the emission of photons from the sun), however, this recipe includes negative contributions to the particle spectrum, the latter arising from particles moving inwards. Various further remedies were then discussed in the literature

[358–361] but all suffer from certain deficiencies. Thus, the transition from the highly collisional dynamics to the collision-free stage is still challenging.

There are two main problems with the instantaneous freeze-out formulation (a recent discussion of this issue was given in [306]). First, such decoupling processes are continuous and therefore proceed during a certain time-span [310, 335, 362–365]. Second, the drain of particles and energy-momentum of the frozen out matter is mostly not coupled back to the fluid dynamic equations governing the matter in the interior [366]. Thereby the freeze-out of a certain species occurs during (or after) its last interaction with an other particle in the medium. This last interaction for example puts particles which are off-shell in the medium, e.g. due to collision broadening, asymptotically on-shell. Such processes involve certain space-time scales which in the case of strong interactions are typically quite above a few fm/c, as we shall see.

For *strongly interacting probes* one must account for the degradation of the flux of the particles on their way through the matter along with the deflections and accelerations due to the mean field of the source. In the following we follow recent considerations by Knoll [310]. Similar consideration were given by Sinyukov [365] within a gas-kinetic picture. Employing a final state Kadanof-Baym formulation which leads to distorted wave techniques (c.f. [367]) together with semi-classical approximations [368] one arrives at a microscopic derivation of the decoupling process [310, 369]. Besides a source term encoded in the corresponding current–current correlator it accounts for the flux degradation for the decoupled particles on their way out of the source. The corresponding *local off-shell* decoupling rates as a function of four-momentum p then emerge as [310]

$$(2\pi)^4 \frac{dN_a(x, p)}{d^4p d^4x} = \Pi_a^{\text{gain}}(x, p) A_a(x, p) e^{-\int_t^\infty dt' \Gamma_a(x(t'), p(t'))} \quad (5.18)$$

$$\text{with} \quad A_a(x, p) = \frac{2p^0 \Gamma_a(x, p)}{(p^2 - m_a^2 - \text{Re} \Pi_a^{\text{R}}(x, p))^2 + (p^0 \Gamma_a(x, p))^2},$$

a formula that can rigorously be derived in the small-width limit, which suggestively (but not yet proven) may also apply to cases with broader spectral widths. Here the first two factors on the r.h.s. of the rate exactly comprise the standard gain part of the four-phase-space collision term (3.26) of the gradient expanded Kadanoff-Baym equations (3.18). The corresponding loss term is integrated out and compiled into the third factor which defines the corresponding escape probability. For the latter the attenuation integral (or optical depth) in the exponent is to be integrated along the classical escape path $x(t'), p(t')$ from the space-time source point x with momentum p . As a central relation Eq. (5.18) generalises the instantaneous Cooper-Frye formula to the continuous decoupling case. It also permits applications to the case of particles with a broad spectral distribution $A(x, p)$ such as resonances which subsequently competitively decay e.g. into hadrons and dileptons [370]. The

special case of *weakly interacting and thus penetrating probes* (cf. Eq. (3.42)) is simply obtained from (5.18) in the limit of vanishing final state distortions and thus entirely given by the correlation function Π_a^{gain} , since then $\int_t dt' \Gamma(t') = 0$ together with $A = 2\pi\delta(p^2 - m^2)$ for on-shell particles.

As the escape probability involves the vision on the future, Eq. (5.18) is a retrospective relations. However, given that the $\Gamma(x, p)$ is already known in its complete space-time evolution,² this relation precisely determines the instant rates of all particles which from then can freely escape (except for mean-field accelerations). This also includes those particles which decouple *strongly*. The latter influence the fluid system due to the corresponding drains in particle number and energy and a recoil momentum via the re-coupling terms,

$$\partial_\mu j_{\alpha, \text{fluid}}^\mu(x) = - \sum_a e_{a\alpha} \int d^4p \frac{dN_a(x, p)}{d^4p dt d^3x}, \quad (5.19)$$

$$\partial_\mu T_{\text{fluid}}^{\mu\nu} = - \sum_a \int d^4p p^\nu \frac{dN_a(x, p)}{d^4p dt d^3x}, \quad (5.20)$$

in the corresponding fluid cells of the source given by the corresponding integrals over the gain part of collision term. Here α denotes a conserved current and $e_{a\alpha}$ the corresponding charge of particle a . These coupling terms have the same form as in the multi-fluid case (5.4) [306]. A complete treatment of the decoupling rates (5.18) together with the fluid drain terms (5.19) provides an overall conserving scheme. Such re-couplings, though unimportant for perturbative probes, lead to a gradual fading of the fluid phase upon creating the freely streaming particle phase.

In thermal equilibrium the source function can directly be expressed as

$$\Pi_a^{\text{gain}}(x, p) = f_{\text{th}}(p^0) \text{Im} \Pi_a^{\text{R}}(x, p) = f_{\text{th}}(p^0) 2p^0 \Gamma_a(x, p). \quad (5.21)$$

This property leads to quite some important compensation effect. Namely for large source extensions the Γ -dependent factors in (5.18) define a visibility probability P_t . It indeed integrates to unity along the classical paths leading from a completely opaque interior to the outside

$$\int_{-\infty}^{\infty} dt \underbrace{\Gamma(t) \exp\{-\int_t^{\infty} dt' \Gamma(t')\}}_{= P_t(t)} = 1. \quad (5.22)$$

Thereby $P_t(t)$ achieves its maximum at

$$\left[\dot{\Gamma}(t) + \Gamma^2(t) \right]_{t_{\text{max}}} = 0, \quad \text{with value} \quad P_t(t_{\text{max}}) \approx \frac{1}{e} \Gamma(t_{\text{max}}), \quad (5.23)$$

² This may require an iterative procedure between fluid dynamic evolution and the decoupling rates, in order to overcome the lacking vision into the future.

the dot denoting the time derivative along the corresponding classical path. The corresponding mean decoupling time approximately follows from the normalisation to

$$\Delta t_{\text{dec}} \approx \frac{1}{P_t(t_{\text{max}})} \approx \frac{e}{\Gamma(t_{\text{max}})}. \quad (5.24)$$

The importance of the above relations can be seen upon collecting all rates along the bundle of classical trajectories leading to the detector with measured three momentum \mathbf{p}_A . The corresponding detector yield then becomes

$$(2\pi)^4 \frac{dN_a(\mathbf{p}_A)}{d^3p_A} \quad (5.25)$$

$$= \int \underbrace{d^3\sigma_\mu dx^\mu}_{=d^4x} dp^0 \underbrace{2p^0 f_{\text{th}}(p^0) \Gamma_a(x, p)}_{\approx \Pi^{\text{gain}}} \mathcal{J} A_a(x, p) e^{-\int_t^\infty dt' \Gamma_a(x', p)} \\ \Rightarrow \int_{\sigma_{\text{CFP}}(p)} d^3\sigma_\mu 2p^\mu dp^0 \mathcal{J} f_{\text{th}}(p^0) A_a(x, p). \quad (5.26)$$

Here $\mathcal{J} = (\partial(\mathbf{p}_A(\mathbf{p}, x))/\partial(\mathbf{p}))^{-1}$ defines the Jacobian of the mapping of the local three-momentum to the detector momentum³ due to deflections and accelerations induced by the real part of the optical potential ($\text{Re } \Pi^{\text{R}}$). The hypersurfaces σ in (5.25) may be defined through constant values of $\Gamma_a(x, p)$. Thereby $p^0 dx^\mu = p^\mu dt$ defines the local world line direction of the path towards the detector with momentum p_A . Further $d^3\sigma_\mu$ denotes the 3-dimensional surface element of the hypersurfaces encoded as a vector “perpendicular” to the hypersurface such that the four-volume becomes the covariant scalar product $d^4x = d^3\sigma_\mu dx^\mu$.

In the *opaque* limit of the matter and as long as the matter properties such as the temperature do not significantly change across the decoupling process this permits us to replace the continuous emission formulation (5.25) by an instantaneous recipe. It provides an improved Cooper-Frye-Planck decoupling rate (5.26) now corrected for the partial escape probability given by the optical depth. The latter leads to the momentum dependence of the emitting hypersurface $\sigma_{\text{CFP}}(p)$ in (5.26) [365], which for each observed momentum \mathbf{p}_A can be determined from the space-time points of highest brilliance, c.f. Fig. 5.3, as given by (5.23) to

$$[p^\mu \partial_\mu \Gamma(x, p) + p^0 \Gamma^2(x, p)]_{x \in \sigma_{\text{CFP}}(p)} = 0. \quad (5.27)$$

³ With the understanding that $\mathcal{J} = 0$, if the detector momentum cannot be reached from that source point.

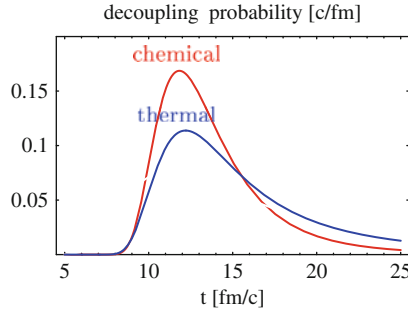


Fig. 5.3 Decoupling probability $P_t(t)$ as a function of time for chemical and thermal freeze-out for the schematic freeze-out scenarios discussed in [310].

Thus the simplistic assumption by Cooper-Frye and others [358–361] of an *overall* freeze-out for *all* particles is physically not tenable.⁴ Rather the decoupling happens only partially and individually for each particle as a function of its momentum. Thereby the process has to be balanced by the corresponding fluid loss rates (5.19) in order to preserve the over all conservation laws.

In [310] various consequences of the continuous decoupling formalism (5.25) are discussed. As an illustration we consider the competition between chemical and kinetic (thermal) freeze-out of slow particles escaping from a spherically expanding uniform fireball. The emission is than essentially from a time-like hypersurface. Both processes go with a different pace as a function of density and/or temperature during the expansion, since inelastic processes drop much faster than the elastic scattering processes, the latter essentially determining the kinetic rates.

For example a fireball evolution with a freeze-out radius of $R_{\text{dec}} \approx 6$ fm and collective velocity $\dot{R}_{\text{dec}} = 0.5$ fm/c leads to a decoupling peak at $t_{\text{dec}} = 12$ fm/c for both types of freeze-out. The damping widths at decoupling peak are as large as $\Gamma_{\text{dec}}^{\text{chem}} = \Gamma_{\text{dec}}^{\text{kin}} = 0.5$ c/fm ≈ 100 MeV. Coming from complete opaqueness the damping rate varies by more than an order of magnitude, namely by a factor $e^{-e} \approx 1/15$ between the onset and end of decoupling (full width at half maximum (FWHM)). This is a robust result (e.g. $\Gamma[\text{onset, peak, end}] = [370, 100, 24]$ MeV for the cases of Fig. 5.3). Thus, during their decoupling particles have damping width values that initially are far beyond the values of their mean kinetic energies. During decoupling the system’s volume grows by more than a factor 5. The above statements are generic and likewise, if properly scaled, apply to the microwave background radiation released during the early universe evolution. Depending on the underlying EoS the thermodynamic properties of the matter can there-

⁴ References [358–361] introduced a Θ function factor to correct for this deficiency, though still insisting on that all particles touching the freeze-out surface decouple. The enforcement of conservation laws, however, then led to readjustments of the emission spectrum and thus to deviations from Planck’s radiation law limit.

fore significantly change during the decoupling time window. For example the resulting distributions in temperature $P_T(T) = P_t(t)(dT(t)/dt)^{-1}$ as shown in Fig. 5.4 for two normally behaved example EoS show significant widths in the resulting T distributions. Remarkable is further that although both time distributions P_t peak at the same time, the slower decrease in kinetic rates leads to a considerably downward shifted and much broader T distribution for thermal freeze-out compared to that in the chemical freeze-out case.

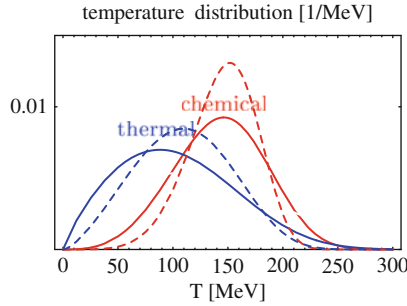


Fig. 5.4 The resulting temperature profiles $P_T(T)$ for an adiabatically expanding homogeneous fireball with adiabatic index $\kappa = 1.5$ (full lines) and $\kappa = 4/3$ (dashed lines).

The analytic considerations above are confirmed by recent calculations within hybrid scenarios [335, 336], cf. Sect. 5.6, where an initial fluid dynamic phase is sufficiently early converted to a kinetic transport scheme in order to provide a continuous freeze-out process in the late phase. Recording the instants of the last interaction of particles that reach the detector with certain momentum maps out the corresponding freeze-out zone, Fig. 5.5. The plots show the initial opaqueness of the collision zone's interior for $r_t, x < 8$ fm and τ or t below 5 fm/c. They nicely confirm that the freeze-out zones depend on the observed momentum. For a low momentum (a) the decou-

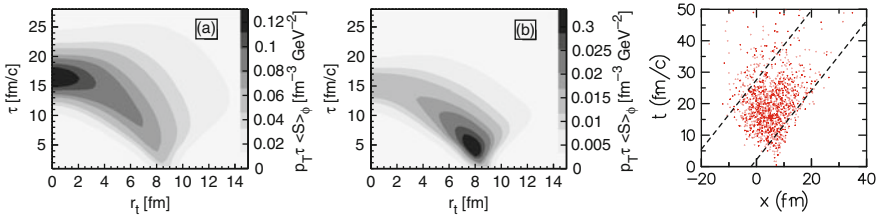


Fig. 5.5 Contour plots of the freeze-out points in transverse radius versus time ($r_t \cdot \tau$, respectively $x \cdot t$) for the emission of pions in RHIC events. Plots (a) and (b) taken from [335] show freeze-out distributions for pion momenta at 300 and 600 MeV/c, respectively. The r.h. figure shows a corresponding scatter plot from [336, 340] for a pion momentum of 300 MeV/c. The dashed lines show two representative world lines leading to the detector.

pling essentially happens as a time-like transition, i.e. at large times for low r_t values. With increasing observed momentum the emission becomes more surface dominated and develops strong space-time correlations. The latter are important in the context of HBT, see Sect. 5.9.

From all considerations presented one expects quite a spread in decoupling temperatures, unless there are processes that provide a sufficient release of latent heat and therefore induce a much weaker drop in T during the decoupling phase than with ordinary EoS. An example could be a phase transition as e.g. presented in the first order phase transition scenario [307, 308] discussed in Sect. 5.3.2, Fig. 5.2. There the latent heat caused by the phase conversion from the QCD plasma to the hadronic phase even leads to a stop in temperature drop during the phase conversion. If the chemical decoupling happens right after this phase transition this could lead to a sharp temperature deduced from the observed abundances of the various hadrons created at freeze-out.

Thermal fits to hadron abundances observed in all kinds of nuclear collision data were performed by many authors, cf. Part I, Sect. 4.1 or Part IV, Chap. 2. Such data found their place as “measured” freeze-out points in a T - μ_B phase diagram, Fig. 4.1 in Part I, p. 203 (μ_B is the baryon chemical potential) [371–374]. Fits with a common (i.e. species-independent) temperature at each collision energy determined the freeze-out temperature to a quite sharp value of e.g. $T_{\text{chem}} = 164 \pm 5$ MeV for RHIC and top SPS energies with excellent χ^2 values of 0.9. On the other hand, there is a recent analysis [375] of the similar data which permitted Gaussian fluctuations in T and baryon chemical potential μ_B . These authors arrived at improved fits with a better χ^2 at temperature fluctuations even on the order of 50 MeV. While the authors speculated on fluctuations due to the vicinity of a critical point in the phase diagram, the more natural explanation may be a spread in temperatures resulting from the finite decoupling time.

Particles with similar or even identical masses but different interactions with the source are well suited for quantifying dynamical effects. The abundances of the three charge states of the pion may serve to quantify Coulomb effects (apart from a small violation in iso-spin symmetry). This covers most of the clear two-slope behaviour e.g. seen in the π^- spectra [379]. Still a net steepening of the low-energy part of the spectrum even survives the Coulomb correction as visible in the π^0 data [101], c.f. Fig. 3.4 in Sect. 3.3.5. Probes interacting weakly with the environment essentially decouple relatively early right after creation, while strongly interacting probes decouple late with spread in decoupling times according to the above discussion. This is nicely demonstrated for the weakly interacting K^+ mesons at SIS energies and the Ω^- baryon at SPS energies compared to the strongly interacting K^- and protons, respectively, cf. Figs. 5.6 and 5.7.

The long freeze-out durations separate long-lived resonances that essentially decay far outside from the short-lived ones decaying during decoupling.

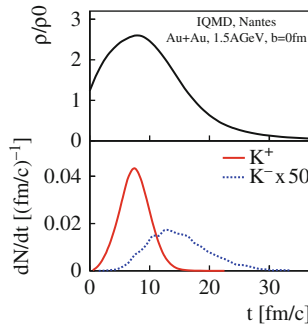


Fig. 5.6 Density $\rho(t)$ and emission source yields $dN(t)/dt$ of K^+ and K^- mesons as a function of time for central Au + Au collisions at 1.5 A GeV resulting from IQMD calculations of the Nantes group (c.f. Sect. 4.1.1) [376]; Figure from [377].

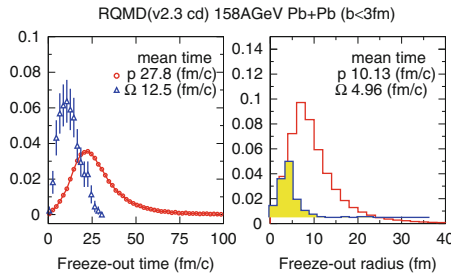


Fig. 5.7 Emission time and transverse radius distributions at freeze-out of mid-rapidity Ω^- and protons for central Pb + Pb collisions at 158 A GeV resulting from RQMD calculations [378].

As a result, kinematical finger prints of very short lived resonances such as the pions originating from the Δ^{33} resonance do not survive the relatively long decoupling times. The physical origin of this is that pions emitted in resonance have a short mean-free path, while pions emitted with energies off resonance have long mean-free paths. Thus the visible layers are different in depth such that the enhanced resonance production is essentially compensated by the corresponding reduced mean free path. The net result ultimately leads to Planck's law of black-body radiation in the opaque limit. Yet, as shown in Sect. 3.3.5, such resonances do influence the corresponding optical potential U_{opt} of the emitted particle, Fig. 3.3. In lowest order virial expansion U_{opt} is determined by the corresponding scattering phase-shifts [94], c.f. also [87, 98] for the π , N , Δ system. This implies rearrangements in the level densities and this way to some enhancement of the pion spectrum above the thermal yields towards low momenta, Fig. 3.4.

A microscopic formulation of the freeze-out process in the context of composite particle production, such as deuterons, that goes beyond the naive

coalescence picture [380], was formulated by Remler [381] in the early 1980s. Further conceptual improvements were later given by Danielewicz et al. [68, 369]. Thereby composite particles are dynamically formed by multi-particle processes in compliance with the conservation laws.

5.9 Collision source imaging (HBT) and final-state correlations

Imaging of objects is a daily experience. Exploiting the wave coherence the of photon field the lenses of our eyes project the surrounding world on their retinas. However there are objects, like distant stars, that cannot be resolved in their extensions by standard optical devices such as telescopes. It was therefore a remarkable advance when, about fifty years ago, the two astronomers Hanbury Brown and Twiss (HBT) reported about a measurement of the size of Sirius. They simply correlated the intensities of the fluctuating signals from two photo-multipliers placed only a few meters apart, rather than seeking to exploit phase coherence effects in the amplitudes, as is standard practice in optics. The effect is straightforward within classical field dynamics and known from radio astronomy, but was initially questioned to occur, if merely independent photon pairs were detected. Still, the quantum boson nature demands the two-photon wave function to be symmetric with respect to the interchange of the two photons. This leads to two options for the classical propagation of the photon pair leading to an intensity interferometry pattern known as the HBT effect, Fig. 5.8. A detailed compact historical review of this field in the context of nuclear collision was given by T. Csörgő [382], see also S. Padula's review [383], while U.A. Wiedemann and H.U. Heinz detailed the theory developments [384].

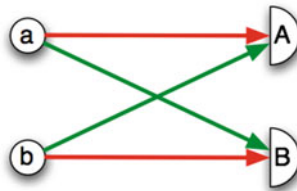


Fig. 5.8 Two classical propagation paths (*green or red*) for the emission of the two photons from the source points (a) and (b) reaching the detectors at places (A) and (B). Figure from Wikipedia.

The intensity coincidence rate of two identical bosons/fermions with mass m and asymptotic four-momenta p_A and p_B with $p_A^2 = p_B^2 = m^2$ over the product of the corresponding single rates is then given by the asymptotic

state two-body wave function over the uncorrelated single ones at the source points⁵

$$C(\mathbf{p}_A, \mathbf{p}_B) = \left| \frac{\langle \Psi_{\mathbf{p}_A \mathbf{p}_B}^{(-)}(x_a, x_b) \Psi_{\mathbf{p}_A \mathbf{p}_B}^{(+)\dagger}(y_a, y_b) \rangle}{\langle \Psi_{\mathbf{p}_A}^{(-)}(x_a) \Psi_{\mathbf{p}_A}^{(+)\dagger}(y_a) \Psi_{\mathbf{p}_B}^{(-)}(x_b) \Psi_{\mathbf{p}_B}^{(+)\dagger}(y_b) \rangle} \right| \quad (5.28)$$

$$\xrightarrow{\text{(nii)}} \frac{1}{2} \left| \left\langle e^{ip_A(r_a - r_A)} e^{ip_B(r_b - r_B)} \right. \right. \\ \left. \left. \pm e^{ip_B(r_a - r_B)} e^{ip_A(r_b - r_A)} \right\rangle \right|^2 \\ = \langle 1 \pm \cos((p_A - p_B)(r_a - r_b)) \rangle, \quad (5.29)$$

where $r_a = (x_a + y_a)/2$, $r_b = (x_b + y_b)/2$. The averages $\langle \dots \rangle$ are to be understood as integrations over all source coordinates x, y or r in the sense as explained below at Eq. (5.30) ff. Thereby the coordinate differences $\xi = x - y$ determine the four-momentum distributions via the Wigner transformation (3.13) defined in Sect. 3.3.1. Simplification (5.29) results for the case of non-interacting identical (nii) bosons/fermions. If the emission at both source points happens statistically uncorrelated with a source distribution $S(\mathbf{r}_a - \mathbf{r}_b)$ in the relative distance of the two emission points, then the measured correlation function $C(\mathbf{p}_A - \mathbf{p}_B)$ is given by the Fourier transformation of the source distribution S . Thereby the absolute position of the source cannot be determined. In compliance with the bosonic (fermionic) nature and the uncertainty principle the correlation function shows an enhancement beyond (depletion below) unity for momentum differences $|\mathbf{p}_A - \mathbf{p}_B| < 1/R$, where R is the source radius, ideally reaching a value of two (zero) at vanishing momentum difference.

Independently of the first HBT observation Goldhaber et al. [385] found related correlations in high energy experiments in observing pairs of equally charged pions in coincidence a few years later. With the advent of high-energy nuclear collisions this method then became a tool to directly measure the size of the collision zone [386, 387], thereby extending the method also to fermions. Besides the measurement of the transverse extension of the source, encoded in two transverse “radii”, also interferometry with momentum differences $\mathbf{q} = \mathbf{p}_A - \mathbf{p}_B$ parallel to the mean pair momentum $\mathbf{K} = \frac{1}{2}(\mathbf{p}_A + \mathbf{p}_B)$ can be observed. The latter is sensitive to both, the parallel extension of the source and its life time. In nuclear collision one orients oneself with respect to the beam direction and defines R_{long} as longitudinal to the beam and two

⁵ Equation (5.28) is written for the nuclear collision case, where the source size, i.e. $|\mathbf{r}_{a,b}|$, is extremely small compared to the distance between the detector positions $|\mathbf{r}_A|, |\mathbf{r}_B|$. Thus the latter define the direction of the measured momenta $\mathbf{p}_A, \mathbf{p}_B$; in astrophysics the situation is reverse: there the stellar positions define the directions of measured momenta, i.e. $\mathbf{p}_a, \mathbf{p}_b$ and the measurement done with respect to the separation distance of the detectors determines the distributions of the difference in transverse momenta, which, knowing the distance of the star, determines its size.

perpendicular radii R_{out} lying in the plane of \mathbf{K} and the beam direction, and finally R_{side} perpendicular to this plane [388]. One then generally does the analysis in a co-moving longitudinal frame where \mathbf{K} is perpendicular to the beam direction such that for the case $\mathbf{q} \parallel \mathbf{K}$ simultaneously R_{out} and the life-time of the source are measured, c.f. Eq. (5.38) below.

While a two-photon coincidence [389] would map out the entire nuclear collision zone during its entire life time, the observation of strongly interacting probes limits the observation to the corresponding freeze-out zone. Furthermore, final-state interaction (FSI) between the observed particles distorts the imaging. In particular the long-range Coulomb force has a major effect on the correlation pattern, suppressing coincidence yields at low relative momenta. Due to correlations imposed by FSI, even pairs of non-identical particles can be used. In contrast to astrophysical HBT observation, in nuclear collisions also significant space-momentum correlations can build up before freeze-out, e.g. due to collective flow as first discussed by Pratt [387]. In such cases the interferometry is not able to map out the entire collision zone but rather extracts source radii that are generally smaller than the true fireball size, c.f. Fig. 5.9. Furthermore life-time effects of resonances that decay into the observed particles can significantly blur the interferometry of the source [390]. In particular, the decay of long lived resonances creates an additional halo source which cannot be resolved by the detector resolutions and thus causes the experimentally measured values of C to show a smaller interferometry correlation (parametrised by a parameter $\lambda < 1$) than ideally expected. For recent reviews see also [384, 391].

By straightforward generalisation of the microscopic definition of the single-particle sources (3.9), the two-particle source is now given by the gain component of a double current-current correlation function of the two observed particles a and b [384]

$$S(x_a, y_a; x_b, y_b) = \left\langle J_a(x_a^-) J_a^\dagger(y_a^+) J_b(x_b^-) J_b^\dagger(y_b^+) \right\rangle,$$

where again

$$J_a(x) = \frac{\delta}{\delta \phi_a^\dagger(x)} \mathcal{L}^{\text{int}}(\phi) \quad (5.30)$$

with four-coordinates x_a , etc. The coincidence signal of (5.28) then becomes

$$I(\mathbf{p}_A, \mathbf{p}_B) = \int d^4x_a d^4y_a d^4x_b d^4y_b S(x_a, y_a; x_b, y_b) \Psi_{\mathbf{p}_A \mathbf{p}_B}^{(-)}(x_a, x_b) \Psi_{\mathbf{p}_A \mathbf{p}_B}^{(-)\dagger}(y_a, y_b). \quad (5.31)$$

In order to view only the freeze-out zone, the wave function must account for appropriate damping along the path from the source points to the detectors. Such concepts were first introduced in the context of pion interferometry by Gyulassy et al. [392] and they were recently reformulated and applied to

RHIC data by Miller and Cramer [393]. Details that also include the account of FSI will be discussed below.

Under the standard assumption of independent emissions along with that of a smooth momentum dependence the Wigner transformed two-particle source then simply factorises to

$$\begin{aligned} \frac{\langle N_a \rangle \langle N_b \rangle}{\langle N_a N_b \rangle} S(r_a, p_a; r_b, p_b) &\approx S_a(r_a, p_a) S_b(r_b, p_b) \\ &\approx S_a(r_a, K) S_b(r_b, K), \end{aligned} \quad (5.32)$$

where $S_a(r, p) = \Pi_a^{\text{gain}}(r, p)$, etc.

The N_a and N_b are the corresponding number operators.⁶ Here and in the following we use standard HBT notations

$$K = \frac{1}{2}(p_A + p_B), \quad q = p_A - p_B \quad (5.33)$$

for the mean momentum and momentum difference, respectively (the latter not to be confused with the relative momentum). Without any distortion for the outgoing waves one simply recovers the result for penetrating probes, cf. [384],

$$C(p_A, p_B) = \left[\frac{\int d^4 r_a d^4 r_b (1 \pm \cos q(r_a - r_b)) S_a(r_a, p_A) S_b(r_b, p_B)}{\int d^4 r_a d^4 r_b S_a(r_a, p_A) S_b(r_b, p_B)} \right]_{p_a^2 = p_b^2 = m^2} \quad (5.34)$$

$$\approx 1 + \left[\frac{|\int d^4 r e^{iqr} S(r, K)|^2}{\int d^4 r_a S_a(r_a, p_A) \int d^4 r_b S_b(r_b, p_B)} \right]_{p_A^2 = p_B^2 = m^2} \quad \text{for } |\mathbf{K}| \gg |\mathbf{q}|, \quad (5.35)$$

for the source integrated correlation function C . This pocket formula (5.35) assumes the smooth momentum dependence which at least requires $|\mathbf{K}| \gg |\mathbf{q}| \approx 1/R$, where R is the typical space-time extension of the source. Although in the strict sense only valid for penetrating probes, i.e. particles with mean free paths large compared to the source size, this relation was frequently used also for the HBT data analysis of strongly interacting particles such as pions. Thereby one relaxes the original definitions (5.30) and (5.32) of the source distribution S towards an effective or visible source as to e.g. effectively include the escape probability (5.25) discussed in the context of continuous freeze-out

$$S_{\text{eff}}(r, K) = \Pi^{\text{gain}}(r, K) e^{-\chi(r, K)} \quad \text{with} \quad \chi(r, K) = \int_t^\infty dt' \Gamma(t'). \quad (5.36)$$

The data are normally analysed by a parametrisation of S_{eff} , most commonly taken as a Gaussian shape in space-time [384],

⁶ For Poisson distributions of identical particles we have $\langle N^2 \rangle = \langle N \rangle (\langle N \rangle + 1)$.

$$S_{\text{eff}}(r, K) \propto \exp \left(-\frac{1}{2} r^\mu r^\nu ((B(K))^{-1})_{\mu\nu} \right). \quad (5.37)$$

This leads to a Gaussian form also for the correlated yield ratio,

$$C(p_A, p_B) = 1 \pm \exp \left(-\frac{1}{2} q^\mu q^\nu B(K)_{\mu\nu} \right), \quad (5.38)$$

$$\text{with the on-shell constraints } \begin{cases} q^0 = \sqrt{\mathbf{p}_A^2 + m^2} - \sqrt{\mathbf{p}_B^2 + m^2} \\ 2Kq = p_A^2 - p_B^2 = 0 \end{cases}.$$

Here time and spatial variances mix due to the on-shell constraint. Thereby the symmetric tensor $B(K)$ specifies the space-time covariance of the source,

$$B(K)_{\mu\nu} = \langle \tilde{r}_\mu \tilde{r}_\nu \rangle \quad \text{with} \quad \tilde{r}_\mu = r_\mu - \langle r_\mu \rangle, \quad (5.39)$$

where the average $\langle \dots \rangle$ is understood to be taken with respect to $S_{\text{eff}}(r, K)$. Besides the damping effects inherent in (5.36), cf. Fig. 5.5, the K dependence can also arise from collective-flow effects as illustrated in Fig. 5.9, c.f. Sects. 5.7 and 6.4. One commonly then condenses the information into three orthogonal “radii” [388]

$$R_{\text{out}}^2 \approx \langle (\tilde{x} - v_x \tilde{t})^2 \rangle, \quad R_{\text{side}}^2 \approx \langle \tilde{y}^2 \rangle, \quad R_{\text{long}}^2 \approx \langle \tilde{z}^2 \rangle. \quad (5.40)$$

With $\mathbf{q} \perp \mathbf{K}$ one explores the two radii, R_{long} and R_{side} , which are perpendicular to the mean pair momentum \mathbf{K} , while for $\mathbf{q} \parallel \mathbf{K}$ one simultaneously measures a combination of the depth of the visible layer and the lifetime of the source. Thus, the disentanglement of the emission time of the source from its spatial *out* extension requires additional information. Sometimes one sees the recipe

$$\langle v_x^2 \tau^2 \rangle \approx R_{\text{out}}^2 - R_{\text{side}}^2 \quad (\text{valid solely for penetrating probes}) \quad (5.41)$$

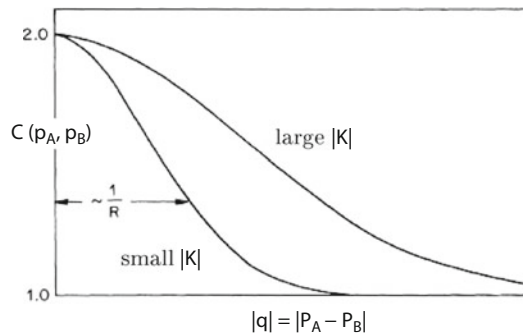


Fig. 5.9 HBT correlation from a collectively expanding source. For low pair momenta $|\mathbf{p}_{AB}|$ one approximately recovers the source size, while for large pair momenta only a smaller source region is explored by the interferometry. Figure from [387].

being applied to extract the source's life time τ . This relation ignores any type of correlations. It therefore holds only under very severe restrictions,⁷ such that it essentially never applies to strongly interaction probes, such as pions. For example the events shown in the r.h. plot of Fig. 5.5 [336] are compatible with the ratio $R_{\text{out}}/R_{\text{side}} \simeq 1.0 - 1.2$ observed at RHIC despite the fact that the freeze-out duration is above 10 fm/c. This shows that relation (5.41) is inapplicable in realistic cases. The origin are strong positive x, t correlations, in part resulting from a kind of Hubble flow [382], which through (5.40) reduce the value of R_{out} despite the long freeze-out duration. Findings of these kinds resolve the so called RHIC HBT puzzle [383, 394] which arose from earlier UrQMD, blast-wave hydrodynamic and many other dynamical model calculations (more than fifty), which throughout predicted $R_{\text{out}}/R_{\text{side}}$ values far beyond unity.

The effective source function (5.36) entering the plane wave result (5.35) may in fact become quite distorted for strongly interacting probes, such as pions or nucleons. In this case a couple of further effects appear which in their totality cannot exactly be accounted for, as it ultimately would amount to solve a three-body problem for the final-state wave functions in (5.31). Rather some further simplifications are required. The relevant effects for the HBT observation are:

- only the outer layer of the source is probed, its depth being determined by the last scattering experienced by the observed probe;
- the emitted particles feel the mean field of the source, such as the Coulomb field; and
- generally there is also a mutual interaction between the pair of emitted particles due to the mutual strong and Coulomb forces.

In transport simulations point (a) can easily be accommodated by sampling the corresponding last collisional interaction points of the observed probes, cf. Fig. 5.5. Otherwise one can exploit the semi-classical approach discussed in Sect. 5.8 [310, 369], and use the path integrated attenuation factors $e^{-\int_t dt' \Gamma(x')}$ included in S_{eff} , Eq. (5.36). Thereby Jacobian effects from the mapping of the local momenta to the detector momenta cancel out in the correlation ratio $C(\mathbf{p}_A, \mathbf{p}_B)$. As a result the free correlation ratio (5.35) can simply be used with the Fourier integrals replaced by

$$\begin{aligned} \int d^4r e^{iqr} S_{\text{eff}}(r, K) &\approx \int d^4r \Pi^{\text{gain}}(r, K) e^{iqr} e^{-\chi(r, K)}. \\ &\approx 2iK^0 \int d^4r f_{\text{th}}(K^0) \Gamma(r, K) e^{iqr} e^{-\chi(r, K)}. \end{aligned} \quad (5.42)$$

In the last line local thermal equilibrium is assumed. Thereby the detector momenta are replaced by the local momenta to take account of the real part of the optical potential. This procedure ensures that only particles out of a layer

⁷ It requires: (a) penetrating probes that have an undistorted view of the entire collision zone, (b) $K_x \gg 1/R_{\text{out}}$ as well as (c) no space-momentum and no space-time correlations.

of one mean free path depth contribute to the intensity interferometry. It is through the attenuation factor that strong space-time correlations, as seen in Fig. 5.5, build up beyond those possibly inherent in the source distribution Π^{gain} . For instance in central collisions the original source distribution Π^{gain} is cylindrically symmetric around the beam (long) axis. If both detectors watch the events from one side, this symmetry is broken for S_{eff} due to the attenuation factors. It implies that the visible space extensions in *side* and *out* direction may significantly differ. The expression (5.42) again clarifies the detailed balance relation between the source function given by the damping rate Γ times the thermal occupations and the attenuation rate along the escape paths also given by Γ leading to similar compensation effects as in the single particle yields.

Returning to the optical potential problem, for probes that escape faster than the fireball expands also the central Coulomb boost of the fireball can simply be accounted for by a corresponding rescaling of the asymptotic momenta to the local ones at the source points [392] (deflections are generally negligible and possible Jacobian determinant effects of this momentum mapping cancel out in the ratio (5.34)⁸).

The mutual interaction (c) between the interferometric partners must be evaluated wave mechanically in terms of the relative scattering two-body wave function $\Xi_{\mathbf{q}_{\text{rel}}}^{(-)}(r)$. With these preparations, a still easily tractable two-body wave function can be obtained by a separation into a centre-of-mass motion with coordinate $\mathbf{R}(t)$ and a relative wave function

$$\begin{aligned} \Psi_{\mathbf{p}_A \mathbf{p}_B}^{(-)}(\mathbf{r}_a, \mathbf{r}_b) &\propto e^{i\mathbf{P}\mathbf{R}} e^{-i(\varphi_a(t) + \varphi_b(t))} \Xi_{\mathbf{q}_{\text{rel}}}^{(-)}(\mathbf{r}) \quad \text{where} \quad (5.43) \\ \mathbf{r} &= \mathbf{r}_a - \mathbf{r}_b & \mathbf{R} &= (m_b \mathbf{r}_a + m_a \mathbf{r}_b) / (m_a + m_b) \\ \mathbf{P} &= \mathbf{p}_a + \mathbf{p}_b & \mathbf{q}_{\text{rel}} &= (m_b \mathbf{p}_A - m_a \mathbf{p}_B) / (m_a + m_b). \end{aligned}$$

It feels the mean fields of the central fireball in terms of the action phases φ_a and φ_b to be integrated along the path of the centre-of-mass coordinate $\mathbf{R}(t)$, which implies that polarisation effects due to the central mean field are ignored. The relative wave function $\Xi_{\mathbf{q}_{\text{rel}}}^{(-)}(\mathbf{r})$ is then simply determined by the corresponding two-body potential acting between the two observed particles.

⁸ In case of slow probes the account of the Coulomb boost is intractable unless one has a full many-body evolution for the expanding system.

Chapter 6

Characteristic results

In this chapter we present further characteristic results obtained by the application of dynamical transport models to nuclear collisions in the CBM energy range, concentrating on the description of physical phenomena during the collision process, such as compression and flow effects. A detailed discussion in the context of experimental observables will be given in the review section of Part [IV](#).

6.1 Gross characteristics of nucleus–nucleus collisions

We first elucidate the physical characteristics of the “matter” produced in nuclear collisions in the FAIR energy range. For simplicity, we consider head-on collisions of two heavy (gold) nuclei and then monitor the central region of the collision system where the most extreme conditions occur. We shall focus on the net baryon density, $\rho(t) \equiv \rho_B(t) - \rho_{\bar{B}}(t)$, and the (total) energy density, $\varepsilon(t)$. When expressed in the CM frame of the symmetric collision system, these quantities are particularly simple to extract since there is neither any time dilation nor any collective flow involved. Furthermore, both ρ and ε have well-defined values at all times and, in particular, their extraction does not rely on any assumptions regarding the degree of local equilibration achieved. This is one advantage of considering these particular observables for the present study.

In each specific transport model, it may be possible to also extract local thermodynamic quantities, such as temperature T , baryon chemical potential μ , and entropy density σ , but although most extraction methods can be cast in sufficiently general terms to make them applicable also to non-equilibrium scenarios, these quantities have physical meaning only in equilibrium. Furthermore, importantly, even if equilibrium is reached, identical values of ρ and ε will generally lead to different values for the thermodynamic quantities

from one model to the other, due to the difference in the degrees of freedom treated.

By contrast, ρ and ε are inherently more robust variables since they are subject to local conservation laws. For example, in fluid dynamics the conservation of four-momentum is expressed as $\partial_\mu T^{\mu\nu} = 0$, while the conservation of baryon charge is expressed by the continuity equation $\partial_\mu j^\mu = 0$. Since the various transport models generally abide by these basic conservation laws, they will have a tendency to yield similar results for the corresponding quantities. By asking about the behavior of such conserved observables we may therefore expect to obtain relatively robust answers. [Of course, for the purpose of discriminating between models (which is not our purpose here), it would be better to consider observables that are more sensitive to the specific model ingredients.]

A special advantage of employing ρ and ε rather than μ and T for the present purposes is that these act as *order parameters* in the sense that the *equation of state*, i.e. the local pressure p , is always a single-valued function of ρ and ε but not always of μ and T . Indeed, precisely when a first-order phase transition is present, the bulk pressure (i.e. the pressure in a spatially uniform system) is multi-valued throughout the region of phase coexistence when viewed as a function of the thermodynamic variables, cf. the discussion in [Part I](#) of the book dealing with the properties of the equation of state (EoS). This fundamental feature of first-order phase transitions has the consequence that the entire region of phase coexistence is invisible on a μ - T phase diagram (it is “folded under”, so to speak), and the corresponding representation of the phase trajectory, $(\mu(t), T(t))$, would exhibit a rather complex zig-zag behavior as the phase point moves through the phase-transition region. This problem is not encountered in the $(\rho(t), \varepsilon(t))$ representation, where the phase trajectory has a regular behavior throughout, making it straightforward, for example, to judge how long time will be spent in the spinodal region.

In order to get an impression of the spread in predictions, we present results from a variety of existing dynamical models that have had considerable success in accounting for a variety of existing experimental collision data: Three-Fluid Hydrodynamics (3-fluid) (Sect. [5.3.1](#)), Parton-Hadron String Dynamics (PHSD) (Sect. [3.5.10](#)), Ultrarelativistic Quantum Molecular Dynamics (UrQMD) (Sect. [4.1.3](#)), the Quark-Gluon String Model (QGSM) (Sect. [3.5.11](#)), and the Gießen Boltzmann-Ühling-Uhlenbeck model (GiBUU) (Sect. [3.5.4](#)). For each of these models, the dynamical evolution of head-on gold-gold collisions was calculated and the values of ρ and ε at the center-of-mass were extracted at consecutive points in time, t . (A report on this study was given in [\[2\]](#).) In the analysis of the results it should be kept in mind that the early part of the collision generally has a strong non-equilibrium character and the local conditions are more reminiscent of two interstreaming nuclei than of compressed matter in thermal equilibrium.

Let us first consider how the central net baryon density evolves in the course of a collision. This is illustrated in Fig. 6.1, where $\rho(t)$ is shown for four different bombarding energies: 5, 10, 20, 40 MeV/A.

In all cases, the density exhibits a relatively rapid increase followed by a slower decrease. As the collision energy is increased, the maximum compression achieved increases steadily as the characteristic time scale decreases. However, for a given energy, there is a significant spread in the calculated curves, amounting to a difference of roughly $0.5 \text{ fm}^{-3} \approx 3\rho_0$ between the lowest and the highest peak values. At all energies the smallest peak value is obtained with PHSD, while the largest peak compressions are obtained with QGSM at the lower end and with UrQMD and the 3-fluid model at the highest energy. The origin of the double-bump structure of $\rho(t)$ obtained with some of the models (3-fluid, PHSD, and GiBUU) is not yet clear and is under current investigation. On the basis of these results, we may expect that densities in excess of 1.0 fm^{-3} (corresponding to compressions ρ/ρ_0 of about 6) are maintained for about 5 fm/c at 5 AMeV, while 50% higher compressions are maintained for about half that time at 20 AMeV.

It should be noted that most of these models have yielded overall good reproduction of a variety of existing experimental data. More details about this study can be found in [2].

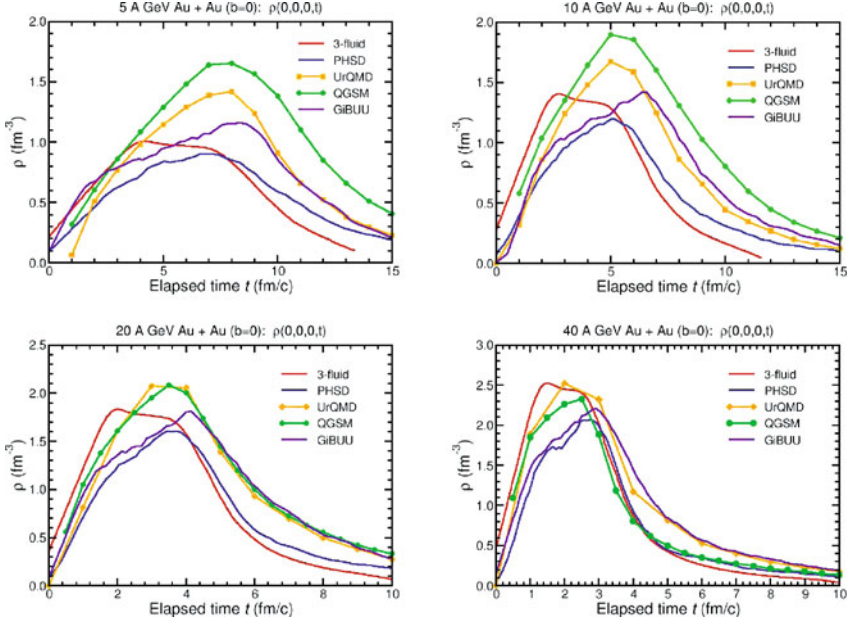


Fig. 6.1 The net baryon density $\rho(t)$ at the center of a head-on Au+Au collision for various bombarding energies as obtained with the dynamical models used in [2]. The symbols on the UrQMD and QGSM curves are separated by the indicated time intervals of $\Delta t = 1 \text{ fm}/c$. Densities and time are with respect to the c.m. frame.

The dynamical evolution of the energy density, $\varepsilon(t)$, largely follows the evolution of the baryon density, $\rho(t)$. Apart from binding effects, which are negligible in the present context, the energy density must always exceed the minimum amount dictated by the prevailing net baryon density, *i.e.* we have $\varepsilon \geq m_N \rho$, where m_N is the nucleon mass. Therefore, it may be more instructive to consider the excitation energy density $\varepsilon^* \equiv \varepsilon - m_N \rho$. Part of ε^* is due to compression, while the rest is available for particle production and motion. (While it might be preferable to also subtract the compressional energy, $\varepsilon_{T=0}^*(\rho)$, this quantity is not yet well under control theoretically and rather the objective of these investigations.)

Figure 6.2 shows $\varepsilon^*(t)$ for the scenarios considered in Fig. 6.1. These curves are qualitatively similar to those for $\rho(t)$, but while the lowest curves are again obtained with PHSD, UrQMD yields the highest at all energies. As was the case for the densities, there is a significant spread in the degrees of excitation achieved at a given collision energy, increasing from several hundred MeV/fm³ at 5 AGeV to well over 1 GeV/fm³ at 40 AGeV. Roughly, values of $\varepsilon^* > 800$ MeV/fm³ are maintained for about 5 fm/c at 5 AGeV, while $\varepsilon^* > 1.8$ GeV/fm³ is maintained for about 4 fm/c at 20 AGeV.

In order to ascertain the prospects towards probing the phase structure of hot and dense matter by high-energy nuclear collisions, it is important to

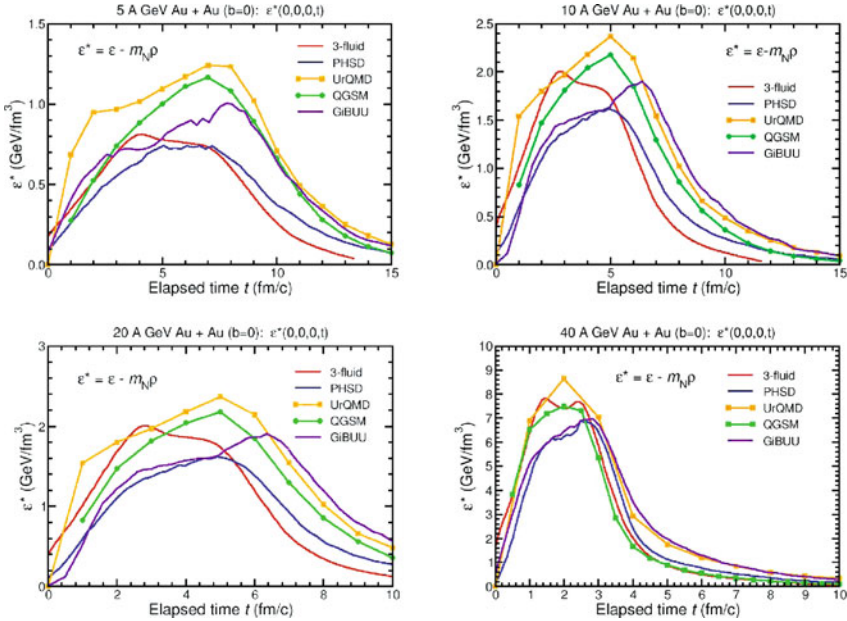


Fig. 6.2 The excitation energy $\varepsilon^* \equiv \varepsilon - m_N \rho$ at the center of a head-on Au+Au collision for various bombarding energies as obtained with the same set of models under the same conditions as used in Fig. 6.1.

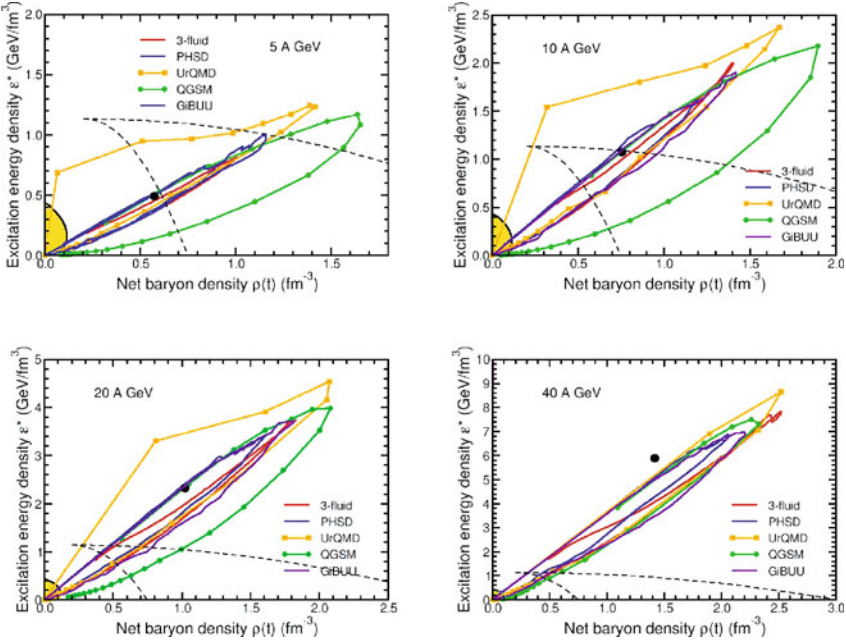


Fig. 6.3 The phase trajectories $(\rho(t), \varepsilon(t))$ of the environments at the center of a head-on Au+Au collision for various bombarding energies as obtained by combining the results in Figs. 6.1 and 6.2 (see [2]). The trajectories turn in a clockwise sense and the symbols on the UrQMD and QGSM curves are separated by steps of 1 fm/c. The phase points corresponding to idealized early interstreaming are indicated by the *solid dots*, while post-freezeout free streaming occurs in the *yellow zone*. The *dashed curves* trace out the coexisting phase points which come together at the critical point; this phase boundary is schematic and serves primarily as a reference.

determine which parts of the corresponding $\rho - \varepsilon$ phase diagram were visited during the dynamical evolutions. The resulting dynamical trajectories are shown in Fig. 6.3.

First one notes a remarkable degree of agreement between the results of the different models. The most notable exception are the QGSM expansion paths which come out significantly lower in excitation energy than those of the other models. Furthermore, the UrQMD entry trajectories differ significantly from the overall trend but, although this behavior is not quite understood, this anomaly is probably less important because the system is still far away from equilibrium during this early stage.

At early times, when the density is rapidly increasing, the different models (apart from UrQMD) yield nearly identical phase trajectories. Furthermore, this common path goes through the point corresponding to the idealized interstreaming of the two Lorentz-contracted nuclei. The latter picture would yield $\rho = 2\gamma_{\text{cm}}\rho_0$ (in the CM frame) with the CM Lorentz factor $\gamma_{\text{cm}} = \sqrt{1 + E_B/2m_N}$, where E_B is the beam kinetic energy per nucleon for

a stationary target. In the CM frame the energy per baryon is $\gamma_{\text{cm}}m_N$, so the energy density is $\varepsilon = \gamma_{\text{cm}}m_N\rho_i = 2\gamma_{\text{cm}}^2m_N\rho_0 = (2m_N + E_B)\rho_0$.

For the lowest beam energies the attained degree of compression and agitation does not suffice to explore the phase coexistence region and thus possible signals of a phase transition. However, due to their relative slowness, these collisions may achieve of high degree of local equilibration and therefore may well provide quantitative information on the equation of state at the correspondingly moderate compressions. The precise “subcoexistence” range of collision energies is naturally determined by the so far relatively unknown EoS. With the reference phase boundaries employed in [2] this subcoexistence range extends up to beam energies of 5 AGeV or so.

Above those subcoexistence energies follows a range (approximately 5 – 10 AGeV for the reference boundary adopted in [2]), across which the highest degree of compression occurs within the region of phase coexistence. As the beam energy is increased across this range, the turning point of the phase trajectory traverses the coexistence region, starting at the hadronic phase coexistence boundary and ending at the plasma boundary. Though somewhat more violent, for these trajectories the matter is generally expected to still attain a high degree of local equilibration. Furthermore, importantly, they spend the longest period of time within the phase coexistence region. Therefore, this energy range appears to be especially well suited for generating signals of the phase transition.

As the collision energy is increased further, the turning points of the phase trajectories move further inside the plasma region and, at the same time, the expansion path steepens. The time spent crossing the phase coexistence region then decreases, both in absolute terms and relative to the overall expansion time, so one would expect any phase-transition signals to gradually subside.

Ultimately, beyond a certain critical collision energy (for which the expansion path passes straight through the critical point), the phase trajectories no longer enter the coexistence region but pass entirely to the left of the critical point. Though interesting in its own right, this super-critical region of collision energy would not be expected to elucidate the character of the deconfinement phase transformation at sufficiently high baryon density, i.e. to clarify whether there is in fact a first-order transition.

Finally, we wish to emphasise that none of the dynamical models employed (except possibly PHSD) incorporate a first-order phase transition. They would therefore not be suited, in their present form, for studying actual dynamical consequences of a phase transition. However, the presence of such a phase transition is not expected to have an overwhelming effect on the gross dynamics, primarily due to the predominance of the overall expansion. [This expectation is supported by comparisons between HSD (which does not contain a partonic phase) and PHSD (which does have a partonic phase) in the energy range considered here.] Therefore, it must also be expected that

the effects of a phase transition would be relatively subtle and might best be studied with carefully designed correlation observables.

6.2 Benchmarks

This section further investigates the consistency among the various models. Differences result from different physical inputs, such as the chosen elementary cross sections employed or the included set of hadronic resonances, since these are not sufficiently constrained by experimental data. In particular for resonances one mostly relies on model-dependent assumptions.

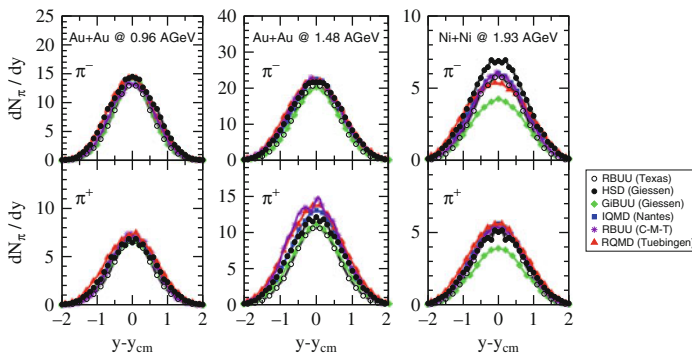


Fig. 6.4 π^\pm rapidity distributions in central ($b=1$ fm) Au+Au reactions at 0.96 and 1.48 AGeV and Ni+Ni reactions at 1.93 AGeV from various transport models: GiBUU (Giessen, *full diamonds*), RBUU (Texas, *open circles*), RBUU (Catania-Munich-Tübingen, *stars*), HSD (Giessen, *full circles*), IQMD (Nantes, *full squares*) and RQMD (Tübingen, *full triangles*). Figure taken from [395].

For the calculation of more global observables, such as e.g. rapidity distributions, one expects minor differences between the employed types of the model, be it one-body, many-body, or fluid dynamics. As the simulation codes are complicated and often based on different numerical and methodical solution techniques, the physical results are somewhat sensitive to such technical issues. Therefore it is necessary to carefully assess (and attempt to reduce) such uncertainties. This was the major goal of two workshops held in Trento 2001 and 2003, where most transport practitioners working in the Bevalac/SIS and AGS energy range met. In a first round of home works the default versions of the codes were compared. Further specifications were then suggested for a detailed comparison in the SIS energy range. The results of the second round were published in [395]. As an illustration, Fig. 6.4 shows the result of the benchmark test for pion production in central Au+Au collisions at 0.96 and 1.48 AGeV and Ni+Ni reactions at 1.93 AGeV.

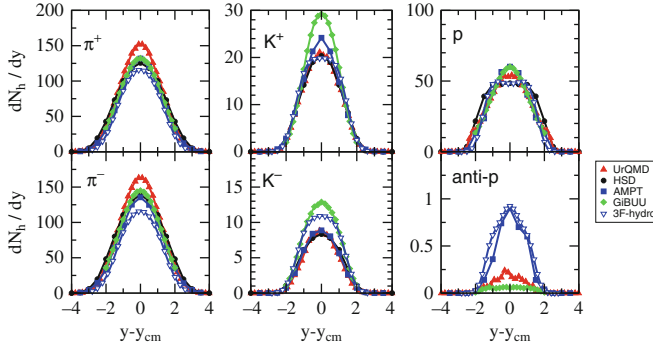


Fig. 6.5 π^\pm , K^\pm and p , \bar{p} rapidity distributions in central ($b=1$ fm) Pb+Pb reactions at 40 AGeV from various transport models: GiBUU (Giessen, *full diamonds*), HSD (*full circles*), UrQMD (*full triangles*) and AMPT (*full triangles*). Prediction from the three-fluid hydro model of [301] are shown as well.

For this comparison a nuclear mean field corresponding to a soft EoS ($K \sim 200$ MeV) was applied together with a constant Δ width, $\Gamma_\Delta = 120$ MeV, in most models, corresponding to a constant lifetime $\tau_\Delta = 1/\Gamma_\Delta$. Though unphysical and not used in the default versions of the codes, such a constant resonance life time simplifies the comparison of the pion yields. Overall agreement in the predictions on the pion rapidity distributions was obtained for beam energies around 1 AGeV, while discrepancies appeared towards higher energies. The latter partially results from differences in the number of included resonances: for this test only the $\Delta(1232)$ and $N^*(1440)$ resonances were included in RQMD and IQMD, while the Giessen HSD additionally considered the $N^*(1535)$ and GiBUU even higher-lying resonances. However, the GiBUU calculations were performed with medium-dependent $NN \leftrightarrow NR$ and $NN \leftrightarrow NN\pi$ cross sections which led to a reduction for the corresponding pion yields. Figure 6.5 shows a corresponding model comparison at 40 AGeV for the rapidity distributions of protons and produced hadrons (π^\pm , K^\pm and \bar{p}) in central Pb+Pb reactions. Predictions from various transport models (AMPT, HSD, UrQMD) and the three-fluid model [301] are compared.

6.3 Mean-field dynamics

Before discussing further dynamical effects of nuclear collisions, we wish to spend a few words on the dynamics of finite nuclei. The motivation in doing so is to recall that semi-classical approaches, such as the Boltzmann or Vlasov equations, are able to describe basic features of collective nuclear dynamics with high precision. For non-relativistic models it was found that the results

from the Vlasov equation coincide with the results from the corresponding quantum mechanical calculations, i.e. time-dependent Hartree-Fock (TDHF) to quite some acceptable accuracy [396].

Prototype examples are giant resonances in nuclear structure. They are successfully described in terms of the Random Phase Approximation (RPA), which is the small amplitude limit of TDHF. Thus the RPA and TDHF approaches also include shell effects. If only the average features are of interest, then semi-classical treatments based on the Vlasov equation may be applied, providing an accurate treatment of the nuclear mean field, including Coulomb and isospin effects. After proper initialisation the system will oscillate and the associated frequency then depends on the compression modulus implied by the mean field. In Fig. 6.6 the result of a recent relativistic RBUU transport calculation [397] for the Isoscalar Giant Monopole Resonance (ISGMR) in ^{208}Pb is shown. The resulting peak at 13.4 MeV agrees well with the experimental observation at $E = 13.7 \pm 0.3$ MeV and state-of-the-art time-dependent relativistic mean field (TDRMF) calculations [398]. Such calculations demonstrate that for one-body observables semi-classical approaches reach accuracies comparable those of the corresponding quantum mechanical calculations. In most applications, though, the effective field is not microscopically derived but approximated by a density-dependent functional, such as the Skyrme potential (or Walecka-type models in the relativistic Dirac case).

The importance of the mean-field effects depends on the energy range considered. At low energies, where binary collisions are largely Pauli blocked, the reaction dynamics is dominantly driven by the real part of the mean field [or the self-energy $\text{Re } \Sigma^R$ e.g. in (3.24)]. Models designed for low and inter-

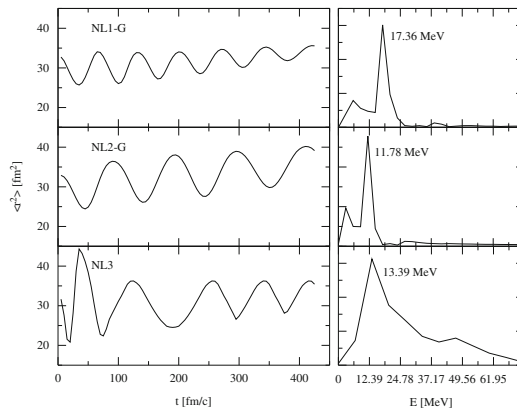


Fig. 6.6 Iso-scalar Giant Monopole Resonance (ISGMR) breathing mode for in ^{208}Pb obtained within a RBUU transport calculation for different parametrization of the nuclear mean field (from *top* to *bottom*). *Right*: density oscillations as a function of time; *left*: position of the ISGMR after Fourier transformation. From [397].

mediate relativistic energies generally contain more sophisticated treatments of the mean field than those designed for the ultra-relativistic regime. Appropriate microscopic Brueckner-Hartree-Fock (BHF) and relativistic Dirac-Brueckner-Hartree-Fock (DBHF) calculations were presented in [399, 400] and [401–404], respectively. To perform such Brueckner calculations for arbitrary non-equilibrium configurations, as they occur in nuclear reactions, is presently out of reach. One possible option is to use the BHF/DBHF results for infinite nuclear matter in a local density approximation (LDA). Attempts to go beyond the LDA and to incorporate non-equilibrium features on the level of the effective interaction were reported in [405, 406]. Since, however, the density and momentum dependence of the G -matrix is rather complex, most transport models use simpler effective interactions, such as Skyrme forces [214] or parametrisations of the non-linear Walecka model, Quantum Hadron Dynamics [407, 408].

At intermediate and relativistic energies, from Bevalac/SIS up to AGS energies, the mean field still plays a dominant (or at least an important) role. As the collision energy is further raised, the reaction dynamics is ever more dominated by direct collisions as well as particle production and absorption. Empirical studies, based e.g. on HSD or UrQMD models, suggest that the nuclear mean field becomes unimportant above about 10 AGeV laboratory energy, at least for the description of the flow data. As a consequence, many transport models are run in their cascade modes when applied to top AGS or SPS energies. Except for the PHSD approach most models specifically designed for ultra-relativistic energies do not contain a mean field at all. Likewise hadron production through string excitations is generally based on vacuum hadron masses, such that mass shifts arising through the presence of mean fields are usually ignored. Empirically this treatment is justified by the fact the particle yields are generally well described by statistical freeze-out models, c.f. the decoupling discussion in Sect. 5.8 and the model results presented in Part I, Sect. 4.1.

6.4 Collective flow

Since the early days of relativistic nuclear collisions the occurrence of flow phenomena was in the minds of the physicists as a tool for probing the nuclear equation of state (EoS). Anticipating a true hydrodynamic behavior, investigators expected the production of shock fronts that would cause the matter to be ejected in specific directions [271, 409]. These expectations were later qualitatively confirmed by transport calculations that include mean field potentials [410–412]. More modest ideas considered a radial emission of the matter in form of a blast wave due to the high compression zone formed in the centre [352]. This idea found its beautiful confirmation in the mass dependence of the mean kinetic energies $\langle E_{\text{kin}} \rangle$ of the emitted particles

observed in central gold-gold collisions at SIS energies by the FOPI collaboration [379, 413]. Overlaying the random thermal motion of temperature T with a collective radial flow $v_{\text{flow}} \sim r$ leads to a linear dependence of the average kinetic energy of a particle specie on its mass M , $\langle E_{\text{kin}} \rangle = \frac{3}{2} T + \frac{1}{2} M \langle v_{\text{flow}}^2 \rangle$, cf. Fig. 6.7. A similar phenomenon was observed in the AGS energy range. In such central collisions close to 50% of the available collision energy is converted into collective motion. At higher energies, one distinguishes between a longitudinal expansion, which at collider energies could be boost invariant as suggested by Bjorken [351], and a transverse flow. Yet, both the discussed radial or alternatively the transverse flow do not directly provide a measure of the underlying EoS of the system. Large pressures acting over a short time may produce the same net collective energy as low pressures acting over a long time. This calls for a special timer [414] of the reaction course.

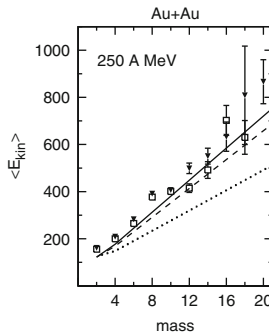


Fig. 6.7 Mean kinetic energies of fragments of different mass emitted from in a central Au+Au collisions at 250 A MeV. Lines show blast wave calculations with different velocity profiles. Figure and data extracted from [413].

Such a timer can be provided in non-central collisions at intermediate impact parameters. Here one observes a subtle interplay between the spectators and the participants. The spectator nucleons originate from the periphery of the interaction zone and are only weakly affected by the collision processes, so they proceed essentially undisturbed with their original velocity, see Fig. 6.8. By contrast, the participant nucleons originate from the interaction zone and thus experience violent collisions and are subjected to matter compression and expansion in the course of the reaction. The spectators are expected to bounce off the compressed central zone thereby through their deflection defining the reaction plane. The radially accelerated particles emitted from the central fireball zone are in part shielded by the spectators which leads to a preferred emission perpendicular to the reaction plane. This phenomenon was called “squeeze-out” [410].

In this context the role of the timer may be taken up by the spectators, cf. Fig. 6.8. As the participant zone expands, the spectators, moving at a

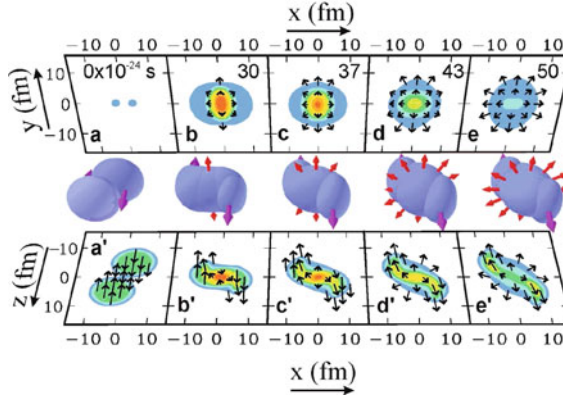


Fig. 6.8 Dynamical evolution of density and flow profiles in a semi-central ($b=6$ fm) Au+Au collisions at 2 AGeV as the result of a BUU transport simulation in time frames in units of 10^{24} s. The beam direction is given by the z axis; the x - z plane (*lower panels*) defines the reaction plane; the *upper panels* define the density contours and flow directions in a plane lying in the origin perpendicular to the beam direction. From [414].

prescribed pace, shadow the expansion. If the pressure in the central region is high and the expansion is rapid, the anisotropies generated by the presence of spectators are expected to be strong. On the other hand, if the pressure is low and, correspondingly, the expansion of the matter is slow, the shadows left by spectators will be less pronounced. Faced with this situation special observables were suggested which in each event (i.e. event by event) first determine the reaction plane from the multi-particle emission pattern and then investigate special correlations of the emitted particles relative to the so determined reaction plane. Special care must be taken to ensure that such analyses are free from spurious correlations in case of low multiplicities [411, 415]. The “flow” observables provide a direct information on the dynamical flow behavior during the collision. The oldest of this type, the “transverse momentum analysis” or “directed flow”, dates back to a suggestion of Danielewicz and Odniewicz [416], see also the review [411]. In slices of rapidity it measures the average transverse momentum within the reaction plane, c.f. Fig. 6.9. This observable is known to be sensitive on the EoS. As an example recent three-fluid dynamic (3FD) calculations [304] as presented in Sect. 5.3.1 are displayed in Fig. 6.9.

Nowadays the anisotropies in azimuthal emission pattern are characterised in terms of a Fourier series [417, 418] also to be evaluated at different slices of rapidity y ,

$$\frac{dN}{d\phi} \propto 1 + 2v_1 \cos(\phi) + 2v_2 \cos(2\phi) + \dots \quad (6.1)$$

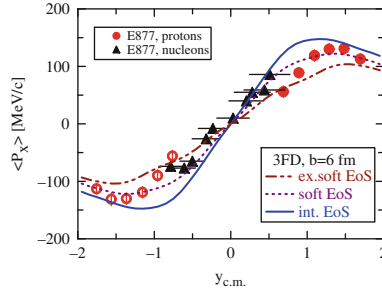


Fig. 6.9 Directed Flow of nucleons and protons as a function of rapidity for mid-central Au+Au collisions at $E_{\text{lab}} = 10.5$ AGeV from the E877 experiment [419] compared to recent 3FD calculations [304] with three types of EoS at impact parameter $b = 6$ fm. *Full symbols* correspond to measured data, the *open ones* result from a reflection at mid-rapidity.

Here ϕ denotes the angle relative to the reaction plane determined for each event. The advantage of this method is that the coefficients v_1 and v_2 can be determined fairly accurately despite the uncertainty in the determination of the reaction plane due to finite particle number fluctuations. Both coefficients have a quite transparent interpretation. The dipole term v_1 is closely related to the directed flow and arises from the collective sideward deflection of the particles within the reaction plane (x - z plane when z is chosen as the beam axis) and characterizes the transverse flow in the reaction plane. The second harmonics characterize the emission perpendicular to the reaction plane. It is called elliptic flow. For negative v_2 one has a preferential out-of-plane emission pointing towards a *squeeze-out* effect.

The two different types of anisotropic flow, sideward and elliptic, have different dynamical origin and their magnitudes depend strongly on the bombarding energy. At low and intermediate collision energy, throughout the early stages, the particles move primarily along the beam axis in the centre of mass. However, during the compression stage, the participants get locked within a channel, tilted at an angle, between the spectator pieces, cf. Fig. 6.8. As a consequence, the forward and backward emitted particles acquire an average deflection away from the beam axis, towards the channel direction. Thus the transverse or sideward flow, in particular its slope at mid-rapidity, denoted as $F_y = d\langle p_x \rangle / dy$, has its analogy in the scattering angle in elementary hadron-hadron reactions. It characterizes the sideward over the longitudinal streaming velocity (close to the centre-of-mass rapidity the proportionality $F_y \propto d\langle u_x \rangle / du_y$ holds).

However, with rising energy the characteristics of the collective motion change substantially. This feature becomes evident from the measured excitation functions shown in Fig. 6.10. The transverse anisotropy, expressed by the sideward flow parameter F , is maximal at lower energies (SIS) and drops practically down to zero at ultra-relativistic energies (SPS and RHIC). For a summary of experimental data see [420, 421].

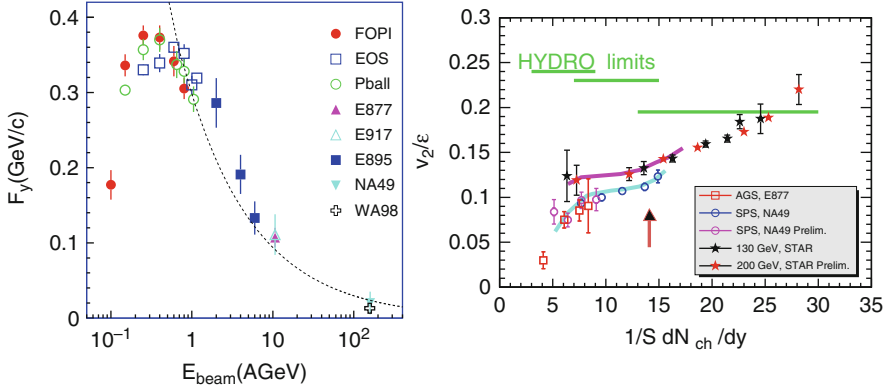


Fig. 6.10 *Left*: measured excitation function of the sideward flow parameter F . Figure from [421]; data from [419, 420, 422–427]. *Right*: measured excitation function of the elliptic flow v_2 per energy density ϵ (from [428]), here plotted versus charged particle multiplicities per rapidity y and transverse area S , latter in units of fm^2 . *Lines* link data at same beam energy and provide the correspondence to the *lines* for the hydrodynamic limit. STAR data from [429, 430].

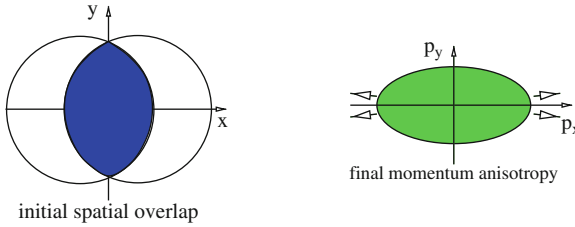


Fig. 6.11 Schematic representation of the creation of elliptic flow at RHIC. *Left*: spatial overlap in the plane perpendicular to the beam direction. The anisotropic pressure gradients translate the initial spatial anisotropy into an anisotropic transverse momentum distribution (*right figure*).

The elliptic anisotropy, expressed by the elliptic flow v_2 , shows the opposite trend of a steady increase. At RHIC energies v_2 reaches the hydrodynamical limit of an ideal fluid with zero viscosity. This indicates the transition from density-driven dynamics with non-vanishing viscosity to the geometry-driven dynamics of almost perfect hydrodynamics. It suggests that at RHIC energies particle densities are already large enough, respectively interaction lengths short enough, for the systems to reach the hydrodynamical limit.

As discussed e.g. in [298, 431–433], in the hydrodynamical limit the elliptic flow is approximately proportional to the original spatial deformation (ϵ) of the nuclear overlapping region which determines the pressure gradients of the expanding fireball, see Fig. 6.11. During the expansion the spatial anisotropy decreases and thus the flow has to built up in the very early stages of the reaction. In the opposite limit, the elliptic flow depends stronger on the particle

density in the transverse plane: $v_2 \propto \varepsilon dN/dy / S$, where ε and S are the central energy density and the area of the overlapping zone, respectively [434]. Some hadronic string-cascade models [233, 435] have problems in explaining the strong elliptic flow observed at RHIC, while for the Quark-Gluon-String models [196–198] such large elliptic flow values are shown to be well in reach.

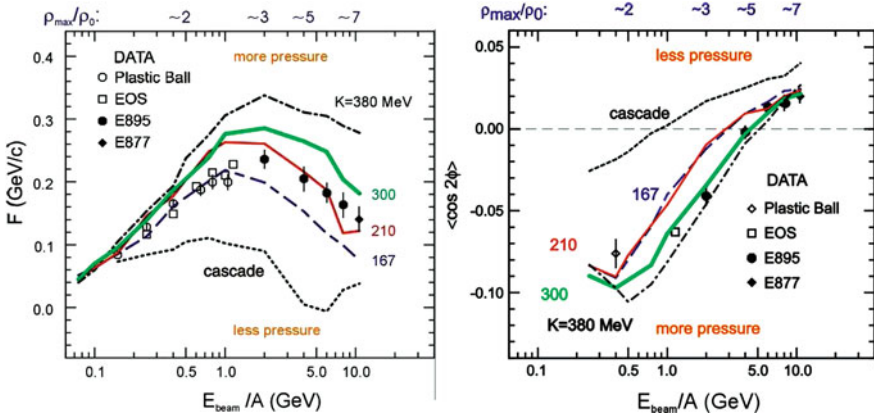


Fig. 6.12 Sideward flow (*left*) and elliptic (*right*) flow excitation function for Au + Au. Data and transport calculations are represented by *symbols* and *lines*, respectively. The different *lines* refer to different values of the incompressibility parameter K of the EoS. Here $\varepsilon = \langle y^2 - x^2 \rangle / \langle y^2 + x^2 \rangle$ denotes the initial spatial deformation. Figures and calculations are from [414]. Experimental data are from the same refs. as quoted in Fig. 6.10.

In the Bevalac/SIS and AGS domains transport models were successfully applied to explain both transverse and elliptic flow. Thereby the transverse flow was found to be sensitive to the nuclear EoS and, in particular in peripheral reactions, to the momentum dependence of the mean field [405, 414, 436, 437]. The elliptic flow v_2 , in contrast, showed a sensitivity to the maximal compression reached in the early phase of a heavy-ion reaction. The crossover from preferential out-of-plane flow ($v_2 < 0$) to preferential in-plane flow ($v_2 > 0$) around 4–6 AGeV also led to speculations about a phase transition in this energy region which goes along with a softening of the EoS [438, 439].

Figure 6.12 gives an impression on how these two types of anisotropy depend on the nuclear EoS. The figure shows results of BUU transport calculations from [414] where the underlying EoS, i.e. the corresponding nuclear mean field, was varied between super-soft ($K=167$ MeV) up to stiff ($K=380$ MeV). The stiffness of the EoS can directly be linked to the pressure built up during the collisions. The pressure is lowest in the absence of a mean field, i.e. in a pure cascade scenario. This case is clearly ruled out by data. However, the transport investigations of [414] put only weak constraints on the stiffness of the EoS, c.f. Fig. 6.13. At lower energies, corresponding to lower compres-

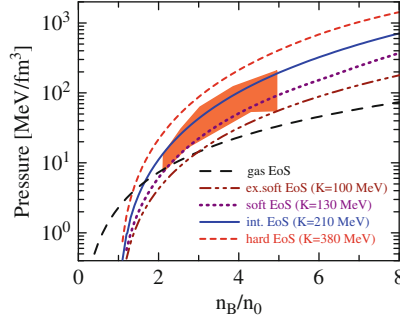


Fig. 6.13 Constraints (*hatched area*) on the EoS extracted by Danielewicz [414, 445] compared to various EoS discussed in the context of Fig. 6.9 and used in the 3FD model [304].

sions, the transverse-flow data would favour a softer EoS, while requiring a stiffer behaviour at higher densities, in accordance with the corresponding v_2 data. Such constraints from nuclear-collision data supplement corresponding EoS investigations on neutron matter resulting from observations of neutron stars. For details see Part I, Sect. 3.4.

In recent years the situation was considerably sharpened from the experimental side when the FOPI Collaboration provided a rather complete set of transverse and elliptic flow data in the SIS range [440–444]. These data favour a soft EoS ($K = 200$ MeV) in the explored density range of 2–3 ρ_0 .

The present correspondence between theory and experiment is illustrated in Fig. 6.14. The left panel compares transport model calculations to recent FOPI data [444]. The BUU studies from Danielewicz [437] and Larionov et

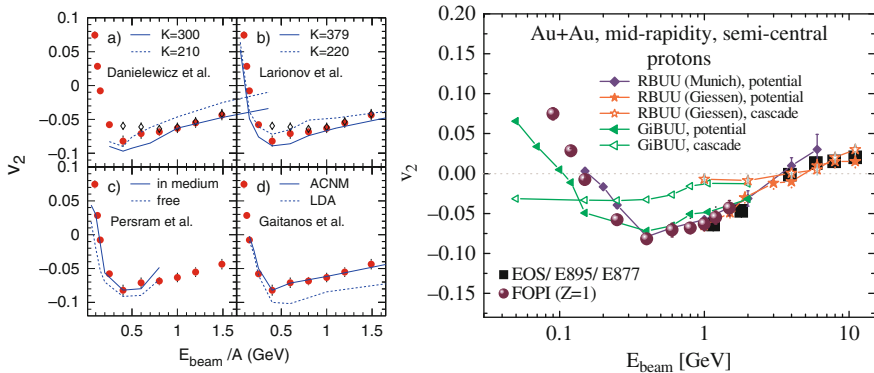


Fig. 6.14 Elliptic flow excitation function at SIS (*left*) and from SIS to AGS energies (*right*). Various theoretical studies based on transport models [405, 406, 437, 446, 447] are compared to FOPI data [444] (*left panel*, figure from [444]) and to data from the FOPI and the EOS/E877/E895 Collaborations [419, 425, 439, 448] (*right panel*).

al. [446] focussed on the EoS dependence, while Persram et al. [447] found a sensitivity of v_2 on the medium dependence of the NN cross sections. Finally, non-equilibrium effects were investigated at the level of the effective interaction based on RBUU (Munich) [405, 406]. There local phase-space anisotropies during the pre-equilibrium stage of the reaction were found to reduce the repulsion of the mean-field and to soften the corresponding EoS. Corresponding microscopic DBHF mean-field calculations by Gaitanos et al. [449] lead to a good description of the v_2 data. The right panel of Fig. 6.14 shows the excitation functions up to AGS energies comparing to FOPI and EOS, E877 and E895 data. Two of the transport models shown there are the same as in the left panel, in addition results from RBUU (Giessen) [408, 450] are shown. The theoretical calculations are in reasonable agreement amongst each other and provide a fair description of the data. The figure stresses again the importance of the nuclear mean field since pure cascade calculations completely fail to describe the excitation function. However, Fig. 6.14 also demonstrates that v_2 is generated by the interplay of the mean field and binary collisions which impedes to extract exclusive information on the EoS from the data. Here certainly further clarifying studies are required.

With increasing energy the situation changes as can be read from Fig. 6.15. Here UrQMD and HSD transport calculations as well as a 3-fluid hydrodynamical calculation [302] are compared to NA49 data [451] for v_1 and v_2 at

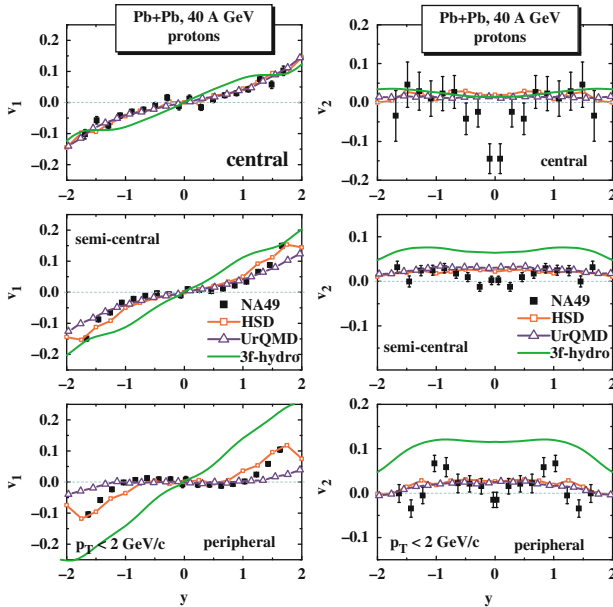


Fig. 6.15 Proton directed v_1 (left) and elliptic v_2 (right) flow for central, semi-central and peripheral Pb+Pb collisions at 40 AGeV. The *full squares* indicate NA49 data [451], the *solid lines with open squares* show the HSD results, whereas the *solid lines with open triangles* are the UrQMD results. The *green solid lines* show the results from the 3-fluid hydrodynamical model [302] with a hadronic EoS.

40 AGeV. These data indicate the occurrence of proton “anti-flow” around mid-rapidity, in contrast to the AGS data as well as to the UrQMD and HSD calculations at 40 AGeV involving no phase transition; the hadron/string transport calculations show a robust positive v_2 of about 3% (Fig. 6.15, r.h.s.). Remarkably, the three-fluid hydrodynamic model [302] with a hadronic EoS shows qualitatively similar results; however, the actual flow v_2 is even much higher in this model. The behavior of the data might be an indication for a so-called flow collapse as predicted by early hydrodynamical calculations [452] as a signature for a first order phase transition in the energy range between 10 and 40 AGeV. (For a further going discussion see Part IV.)

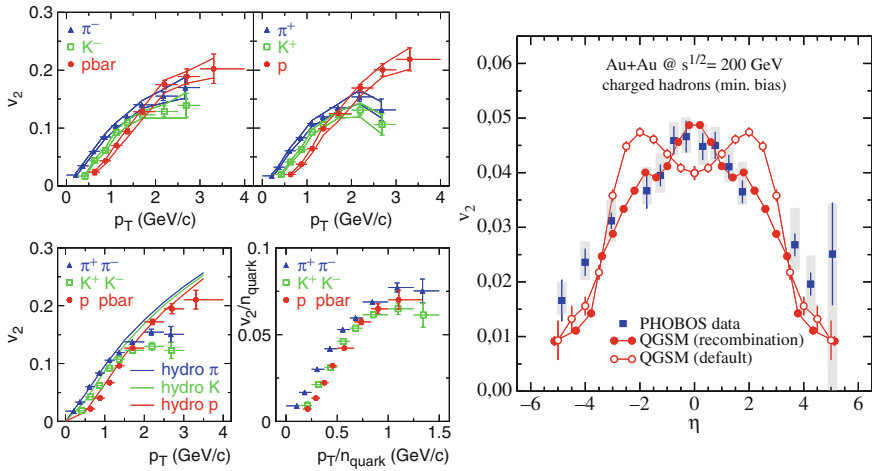


Fig. 6.16 Elliptic flow at RHIC. *Left:* Transverse momentum dependence of v_2 for identified particles. PHENIX data [453] are compared to a hydrodynamical calculation (solid lines). The *bottom-right panel* shows the quark v_2 as a function of the quark p_T by scaling both axes with the number of quarks for each particle. The figure is taken from [453]. *Right:* $v_2(\eta)$ of charged hadrons from the standard QGSM transport model (open symbols) and those obtained with parton recombination (filled symbols) are compared to PHOBOS data [454]. From [455].

The fact that the matter created at RHIC differs from pure hadronic matter is clearly reflected in the collective dynamics of the expanding source. Not only that the matter behaves like a strongly coupled liquid, corresponding data indicate the partonic nature of this liquid. Figure 6.16 shows the elliptic flow in Au+Au collisions at $\sqrt{s_{NN}} = 200$ GeV, as a function of transverse momentum p_T (left) and pseudo-rapidity (right). The results from PHENIX [453] display separately v_2 of identified particles, π^- , K^- , \bar{p} (top-left) and π^+ , K^+ , p (top-right). The combined positively and negatively charged particles are shown in the bottom-left panel and compared to the result of a hydrodynamical calculation with a first-order phase transition and a freeze-out temperature of 120 MeV for π , K and p from upper to lower curves,

respectively. Motivated by a quark coalescence model [456] the bottom-right panel shows the “quark” v_2 as a function of the quark transverse momentum p_T by scaling both axes with the number of valence quarks for each hadron specie.

The hydrodynamical calculation can reproduce the mass ordering and magnitude of v_2 for the different particles in the region up to transverse momenta of 2 GeV/c (which covers 99% of the bulk production), but overpredicts it beyond. This success led to the conjecture that the created matter behaves as a perfect fluid with extremely low viscosity [454, 457–459]. The hydrodynamical calculations require that the matter formed reaches local thermal equilibrium as early as within 1 fm/c [460] and then expands with a shear velocity $\eta \ll s$ [461], where s is the entropy density, i.e. with values reaching the lower bound of $\eta_{\min} = s/4\pi$ reached in strongly coupled supersymmetric gauge theories [462]. This raised the interest towards the application of viscous hydrodynamics to the collision dynamics [313, 316, 324–329], cf. Sect. 5.5.

Alternatively, the quark-coalescence scenario assumes that the flow is generated in a partonic medium which implies that after formation all hadrons flow with the same velocity. Thus quark coalescence predicts a simple scaling behavior between the v_2 for mesons and for (anti)baryons. When the data are presented as a function of the transverse mass m_T , the scaling behaviour is even more apparent [463].

Such a behavior is supported by the transport calculation shown in the right panel of Fig. 6.16. Here QGSM simulations are compared to minimum bias PHOBOS data [454]. The standard QGSM allows for a reasonable description of the magnitude of v_2 but clearly fails in the shape as function of rapidity. If, however, partonic recombination processes are included in the model [455] the corresponding data are almost perfectly reproduced. This result may be interpreted as follows: In contrast to a highly dissipative hadronic medium, the parton recombination processes lead to a reduction of the mean free path in the very dense stages of the collision. Accordingly, the viscosity is effectively lowered in comparison to the pure hadronic medium. Thus rearrangement processes on the partonic level reduce the amount of dissipation in the highly dense matter and therefore enhance the elliptic flow, especially in the mid-rapidity region in line with the experimental observations.

6.5 Rare probes

Rare probes may provide useful insight into the conditions and features of the matter existing during the various stages of a nucleus-nucleus collision. The small production cross sections for rare probes have two general causes:

- The particles originate from electro-weak processes whose coupling constants are inherently small. Of particular interest are electromagnetic probes, i.e. photons and dileptons (e^+e^- , $\mu^+\mu^-$).
- The large mass of the produced hadron suppresses the available phase space. As a consequence, the thermal production of heavy hadrons is suppressed by the corresponding Boltzmann factor. This suppression mechanism is particularly relevant for hadrons carrying strange or charm quarks. The most extreme case is subthreshold particle production where the incident energy (counted per nucleon) of the projectile lies below the elementary production threshold in vacuum.

Electromagnetic probes have the advantage that their interaction with the surrounding matter is negligible on the space-time scales of the nuclear collision. They thus provide direct and undistorted information on the matter or, when originating from weak decays, on the properties of their parent hadrons.

Rare hadronic probes are useful, since they can provide a sort of a timer of the reaction, in particular when produced close to threshold. The production of these particles has to happen during the very early stage of the reaction, where densities and temperature are still high and – depending on their quark content – probes like kaons or D mesons may have only little chance to reach chemical and/or kinetic equilibrium during the expansion phase. Hence, such probes carry important information on the initial stages of the reaction. It should be noted that a similar effect can be obtained by triggering on high transverse momenta p_T (or high m_T) as a substitution for a large hadron mass.

The statistical description of strange and charmed hadrons requires special care because of the requirement of flavor conservation in each event separately. Therefore the grand canonical treatment is inadequate and the rare flavors must be treated microcanonically (see, for example, [464]).

Furthermore, the transport description of such rare particles requires cross sections that are often only weakly constrained by data, in particular in the vicinity of production thresholds, and one must therefore to a large degree rely on theoretical modeling.

On the other hand, by virtue of their rareness, the production of these particles may be treated perturbatively in the transport models [15]. The nuclear collision of interest is treated with the transport model in the usual manner, without dynamical inclusion of the particular rare probe, but its small production probability is calculated in each individual binary collision and the accumulated yield thus extracted. This method was introduced for the calculation of kaon production at the Bevalac and it offers a highly efficient means for calculating the production of rare probes in nuclear collisions. [The alternative method, direct simulation with dynamical inclusion of the rare process, grows progressively more inefficient as ever rarer processes are treated. It typically requires the generation of thousands of individual collision events for the production of just a single rare particle, whereas in the perturbative method each individual binary encounter contributes an entire

differential distribution, thus making it possible to obtain rather detailed distributions from relatively few events.] The method was subsequently generalized to the study of the dynamical fate of a produced rare particle which may be inserted and propagated in the unmodified collision event [16].

A detailed discussion of the physics of rare probes, the present status as well as predictions for the CBM regime, can be found in the corresponding chapters of Parts II and IV.

Chapter 7

Status, perspectives and challenges

The theoretical description of relativistic nucleus-nucleus collisions in the addressed energy regime is a formidable task. The time evolution of a complicated many-body quantum system must be followed through several stages characterised by different physical scenarios. At the early stage of the collision the initial correlated nuclear ground states are first violently transformed into some non-equilibrated form of matter that is expected to be in a deconfined partonic stage whose properties are still poorly understood. This rather exotic system will rapidly expand, first predominantly along the original relative nuclear motion but gradually a transverse expansion builds up and, concurrently, a certain (but yet unknown) degree of local equilibration occurs. The continual expansion causes the system to transform itself into a gas of hadronic resonances whose spectral functions and interaction cross sections are complicated and largely unknown, until the gas has become sufficiently dilute. Whereas the dynamics of a low-density hadron gas with moderate collision rates and/or self energies appears to be sufficiently well understood within familiar hadronic physics, the treatment becomes ill-founded when the volume per hadron is comparable to the hadronic eigenvolume (which is about 1 fm^3 for pions and 2 fm^3 for nucleons), i.e. at densities of 3–5 times the nuclear saturation density.

Therefore the description of high-energy nuclear collisions requires a versatile arsenal of models, each of which must compromise on certain physics aspects in order to be practical. These treatments range from microscopic kinetic transport models at various levels of refinement to macroscopic approaches such as single- or multi-fluid dynamics. In this final chapter we review the status of these approaches in brief terms in order to provide the reader with a quick access to the main points. The details were given in previous chapters. We further discuss future developments needed and outline some major challenges in the context of the high densities reached in these reactions and about the instabilities and the change of degrees of freedom occurring during the confinement phase transition.

7.1 Summary of dynamical concepts

We summarise here the characteristics of the various dynamical approaches, together with their main capabilities and limitations.

7.1.1 *Micro-dynamical concepts*

The most commonly used microscopic frameworks are one-body approaches based on the Boltzmann equation and molecular-dynamics type many-body schemes.

Boltzmann dynamics (BUU): These approaches (Sect. 3.5) attempt to solve the Boltzmann equation for the reduced one-body phase-space densities for the various constituents (mostly hadrons). They move in a self-consistent effective mean field, while experiencing occasional two-body collisions that are subject to quantum-statistical Pauli suppression (for baryons) or Bose enhancement (for mesons) of the Uhling-Uhlenbeck type. Some treatments include medium-dependent masses and cross sections. The effective field frequently includes some momentum dependence which, however, can be in conflict with conservation laws due to the lack of a corresponding back flow part.¹ The required smooth phase-space densities are usually obtained through test-particle or parallel-ensemble methods (Sect. 3.5.2), although lattice methods have also been employed.

Molecular dynamics (QMD): In these approaches (Sect. 4.1) the mean-field dynamics used in BUU is replaced by a classical many-body dynamics subjected to mostly density- and momentum-dependent effective two-body forces. The latter account for the smooth part of the interactions, while the short range encounters are treated by a stochastic collision term as in BUU. The key device to generate reasonably smooth phase-space densities that can be used both for the required Pauli blocking and for the effective field is to employ a Gaussian convolution in phase space. Due to the effective fuzziness of the particles obeying the minimal uncertainty principle this class of models have been dubbed “quantum” molecular dynamics.

We wish to draw attention to a number specific aspects common two both approaches:

- *Limitations*: Both approaches require the quasi-classical approximation to be valid and are limited to small densities (i.e. long mean free paths) for a meaningful separation of the smooth part of the interaction and the

¹ Momentum-dependent forces generally lead to quasi-particles with an effective mass m^* that may deviate significantly from the free mass m . However, the total mass of the A -body system is not $\approx Am^*$ but rather $\approx Am$ and the back flow (Sect. 3.3.4) just compensates for this difference by restoring Galilei (or Lorentz) invariance to the total system.

collisions, cf. Sect. 1.1 and the discussion of the high density challenge (Sect. 7.3).

- *Equation of state:* The equation of state is primarily determined by the dependence of the mean field on the particle density in BUU or by the effective two-body potential in QMD. However, there is generally some dependence on the specific numerical procedure. Furthermore, while the residual interaction governing the collisions is assumed to have zero range in the ideal Boltzmann model, the numerical implementations use a finite range which may then contribute to the pressure, thus modifying the effective equation of state. Generally, the latter potentially important effect has mostly not been determined in the various models.
- *Composite particle formation:* For the CBM energy regime addressed here, the formation of composite particles, such as deuterons or α particles, is unimportant, unless one looks at specific channels. But it is important at low collision energies. Through the interactions QMD (and with a specific technique also BUU) are in principle able to form composite clusters.² In many cases, however, “post” transport prescriptions are employed to form clusters, such as coalescence pictures or, more advanced, as microscopic many-body scattering schemes within a final state interaction formulation.
- *Strings:* Most of the BUU and QMD models include string concepts in order to extend the range of applicability to higher energies. Strings offer an efficient phenomenological tool for parametrising multi-hadron production processes. As the strings are generally formed in binary hadron collisions, this agency violates detailed balance since the reverse processes cannot readily be included. Fortunately, in a collision setting this may not be a serious flaw, since the collisions tend to be over before the reverse processes would play a role. However, the absence of reverse processes renders the model unsuitable for equilibrium scenarios, thus deferring to assess the effective equation of state.
- *Cascade mode:* For survey studies, and in order to obtain a background reference, most codes can be run in the so-called cascade mode (Sect. 2) which ignores mean-field effects and solely treats collisions and decays on the basis of vacuum cross sections and decay rates.
- *Resonances:* The treatment of resonances (Sect. 3.3) pose a special challenge, in particular with respect to the required detailed balance between creation and decay (Sect. 3.3.8) as well as unitarity problems (Sect. 3.3.6), once several channels feed into the same resonance. Furthermore, the propagation of a resonances is mostly treated as if each mass component of the resonance spectrum is an on-shell particle with this mass. There is a great potential for improvements of the microscopic transport approaches with

² Composite particle formation requires the simultaneous interaction with a third body in order to comply with the conservation laws. This would not be possible in ideal BUU which contains only two-body scattering. However, in a special parallel ensemble treatment it is possible to build up few-body correlations and through them to form clusters.

regard to the treatment of broad spectral structures. Recent progress and further challenges are discussed in Sect. 3.4.6.

- *Boltzmann-Langevin*: The Boltzmann equation describes the average evolution of the one-body phase-space density. Thus the system is at any time described in terms of a single phase-space density whose evolution is entirely deterministic, thus preventing the system from branching into macroscopically different configurations. The Boltzmann-Langevin (BL) model reintroduces the stochastic part of the collision term and thus each individual binary collision provides an opportunity for trajectory branching (Sect. 3.2.1). Through this diffusive dynamics in the space of one-body densities the system is described by an ensemble of densities, each one giving rise to its own effective one-body field. Such a framework is particularly useful for scenarios where the system may break up into a variety of different channels, as expected to happen during a phase decomposition. It may therefore be of particular interest in the CBM context.
- *Quantum many-body approaches*: Several models seek to treat the collision system at a quantum level by describing the many-body state by means of Slater determinants (Sect. 4.2) on the basis of Gaussian single particle states. With the help of the Unitary Correlation Operator Method (UCOM) the Fermionic Molecular Dynamics (FMD) concept permits to deal with realistic nuclear forces. It developed into a quantitative tool for nuclear structure calculations, Sect. 4.2.1. The Antisymmetrised Molecular Dynamics (AMD), Sect. 4.2.2, can only deal with effective forces. It is though supplemented with a stochastic collision term similar as in QMD. Besides structure calculations it permits the description of low energy collisions.

A different refinement is presented by the Quantum-Langevin (QL) approach which takes account of the quantum fluctuations inherent in a wave-packet representation. This basic feature has significant consequences for the dynamics near a phase transition.

Though conceptually interesting, all these quantal approaches are technically extremely demanding and direct application to the CBM collisions are not foreseen.

7.1.2 Macroscopic transport dynamics

- *Ideal fluid dynamics*: This simplest macroscopic treatment (Sect. 5.2) rests on the assumption of instantaneous local equilibration. The equations of motion for the density and local temperature and flow velocity follow from the conservation laws. The sole physical input is an equation of state that determines the local energy-momentum tensor. The resulting evolution is isentropic. The implied zero space-time scales cause discontinuities, such as shock fronts. Though physically interesting as a specific limit case, such dis-

continuities are difficult to treat in the numerical codes. Due finite mean-free path effects in the true physical case such discontinuous structures may significantly be blurred. Ideal hydrodynamics can deal with phase transitions, though, solely along the equilibrium configurations e.g. across the coexistence phase.

- *Viscous fluid dynamics:* The presence of a finite mean free path causes transport over finite distances and thus distorts the local conditions away from perfect equilibrium (Sect. 5.5). Such a situation requires the introduction of transport coefficients describing shear and the bulk viscosity as well as thermal conductivity, which can, in principle, be determined from kinetic transport theory. However, these are even less known than the equation of state and, moreover, the associated numerics is fairly tedious. As a consequence, numerical treatments have appeared only very recently in the context of the conjectured low viscosity deduced from the collider events at RHIC.
- *Multi-fluid dynamics:* Since the deviations from local equilibrium can be quite large at the early collision stage, where the participant system has the character of two interstreaming media, it may be advantageous to consider the system as several interacting fluids (Sect. 5.3), rather than a single viscous fluid. The three-fluid concept is adapted to the nuclear collision scenario with two incoming fluids and a third one created through collisions. Also this approach requires additional coefficients governing the collisional transport between the fluids. The multi-fluid framework also provides a convenient framework for treating different phases that are not in mutual equilibrium and therefore offer a perspective for a dynamical treatment of phase transitions (Sect. 5.3.2).
- *Freeze-out:* Fluid-dynamic approaches must be supplemented by a freeze-out procedure describing the conversion of the macroscopic fluid into individual particles when a sufficient degree of dilution has been reached. The commonly used Cooper-Frey prescription with its globally defined freeze-out hypersurface still has conceptual problems, since the duration of the decoupling is non-negligible. It is shown to be comparable to the expansion time scale even for strongly interacting probes. Refinements towards detector-dependent formulations of the freeze-out zone, including the possibility of a continuous decoupling, were recently investigated (Sect. 5.8).

7.2 Model overview

Table 7.1 summarises the main features of the most commonly employed transport models for high-energy nuclear collisions.

The energy range of applicability is given in terms of the beam kinetic energy per nucleon for a stationary target, in GeV per nucleon. For reference, the current SIS18 at GSI delivers heavy-ion beams up to around 1.6 AGeV,

Table 7.1 Energy range, degrees of freedom (DoF) and mean-field and hadronisation concepts used and applied in the different models: the energy range coded in part by the accelerator; besides explicitly treated DoFs (*dynamical*) most codes also include [*perturbatively*] treated DoFs. The last column specifies the type of mean-field and the concepts used for the hadronisation transition. Further details are given in the text.

Model	Energy range [A GeV]	Baryonsdynamical [perturbative]	Mesonsdynamical [perturbative]	Potential/ hadronisation
QGSM	10 – RHIC	SU(3)	SU(3) (ps & v)	no/by strings
BRoBUU	0.1–4	$N^{(*)}, \Delta^{(*)}; M \leq 2.2 \text{ GeV}$ [Λ, Σ]	$\pi, \eta, \sigma, \rho, \omega$ [K^\pm, ϕ]	$U(\rho, p)/\text{no}$
GiBUU	0.1–40	$N^{(*)}, \Delta^{(*)}, Y^{(*)}, \Xi^{(*)}$ $M \leq 2 \text{ GeV}$	$\pi, \eta, \rho, \sigma, \omega, \eta', \phi,$ $\eta_c, J/\psi, K, \bar{K}, K^*, \bar{K}^*$	$U(\rho, p)/\text{by strings}$
BUU ¹	0.1–6	N, Δ, N_{1440}^*	π	$U(\rho, p)/\text{no}$
RBUU ²	0.1–2	N, Δ, N_{1440}^* [Λ, Σ]	π [K^\pm]	$\Sigma(\rho, \beta)/\text{no}$
RBUU ³	0.1–2	N, Δ [Λ, Σ, Ξ]	π [K^\pm]	$\Sigma(\rho)/\text{no}$
AMPT	10 – RHIC	SU(3)	SU(3) (ps & v)	no/by strings
HSD	0.1–RHIC	SU(3), $N^{(*)}, \Delta^{(*)}$ [high p_T]	SU(3) (ps & v), a_1 [$D, D^*, D_s, D_s^*, J/\psi, \chi_c,$ $\Psi', \text{high } p_T \text{ e}^\pm, \mu^\pm, \gamma$]	$\Sigma(\rho, p)/\text{no}$
(I)QMD	0.1–2	N, Δ [Λ, Σ]	π [K^\pm]	$U(\rho, p)/\text{no}$
RQMD	0.1–4	$N^{(*)}, \Delta^{(*)}; M \leq 2 \text{ GeV}$ [Λ, Σ]	π [$K^+, \eta, \rho, \omega, \phi e^\pm$]	$U(\rho, p)/\text{no}$
UrQMD	0.1–4	SU(3)*; $M \leq 2.2 \text{ GeV}$	$0^-, 1^-, 0^{++}, 1^{++},$ $2^{++}, 1^{+-}, 1^{--}, 1^{---}$	$U(\rho)/\text{by strings}$
1-fluid ^{4,†} (FFD)	1–SPS	N with in-med. masses quarks	σ, ω gluons	EoS/phase trans.
3-fluid ^{4,†} (FFD)	1–SPS	N with in-med. masses quarks	σ, ω gluons	EoS/phase trans.
3-fluid ^{5,†}	1–SPS	$N^{(*)}, \Delta^{(*)}; M \leq 1.9 \text{ GeV}$ $\Lambda, \Sigma^{(*)}; M \leq 1.4 \text{ GeV}$	$\pi, K, k^*, \eta, \eta', \rho, \omega$ f_0, a_0, ϕ	EoS/no

¹MSU (Danielewicz) [414, 445]

²Catania/Munich/Tübingen

³Texas A&M/Stony Brook

⁴Frankfurt Fluid Dynamics [278]

⁵3-fluid model from [1]

[†]All listed hadrons are included in the EoS)

for the heaviest species such as Uranium, the AGS at BNL goes up to about 14 AGeV, and the SPS at CERN has a top energy of about 160 AGeV for lead beams. The RHIC facility at BNL is a collider with a top energy of $\sqrt{s_{NN}} = 200 \text{ GeV}$, corresponding to about 2,200 AGeV on a fixed target.

As the collision energy is raised, various thresholds open. Important examples are the thresholds for open or hidden strangeness at SIS18 energies and for charm at AGS energies. Some of these new hadrons are very rare and may be treated perturbatively, whereas others have a significant influence on the overall evolution and must be fully included into the dynamical treatment.

The table lists the hadronic degrees of freedom that are included and indicates the type of treatment used for the mean field, whether non-relativistic (U) or relativistic (Σ). Furthermore, SU(3) refers to the flavour multiplets,

with “ps & v” denoting pseudo-scalar and vector mesons. The N , Δ_{1232} , ... baryons and their excited states are denoted by $N^{(*)}$, $\Delta^{(*)}$, ..., while the quantum numbers refer to the standard JPC classification. The models are grouped into cascade, one-body, N -body, and fluid-dynamical models. The table also indicates which models use strings to account for the fact that the appropriate degrees of freedom are no longer hadronic beyond a certain energy density.

7.3 High-density challenge

The CBM experiment explores an energy regime where the increasing abundance of particles in combination with high compressions (beyond five times the saturation density) poses a particular challenge. These conditions imply a significant increase in the inter-particle collision rates, such that

- (a) most hadrons attain a significant damping width from collisions and
- (b) multi-particle processes occur at a significant rate.

Therefore, at the microscopic level, the particles should be described with dynamical spectral functions the discussed in Sects. 3.3 and 3.4, a significant complication that may render a kinetic transport treatment impractical. Furthermore, most of the required microscopic input information is not only unavailable but in fact unobtainable from elementary collision experiments.

Fortunately some mitigation can be expected. It arises from the mere fact that due to the large collision rates the system may quickly produce local equilibrium so that the evolution is essentially as in ideal fluid dynamics. In such a situation ideal fluid dynamics would present an appropriate framework, as represented by the various hybrid models that have been developed. In such macroscopic descriptions of the high density stage, the various hadronic species appear only implicitly through the equation of state; once the interaction zone has become sufficiently dilute, one may switch to a kinetic picture with the hadrons appearing explicitly and finally decoupling, as described in Sect. 5.8.

But since fluid dynamical descriptions are also not devoid of conceptual difficulties, one might alternatively consider the high-density challenge as an opportunity: One could simply use a kinetic treatment throughout, since the high collision rates and the approximate local equilibrium would render the details about the microscopic collisions less crucial. Thus, as long as the kinetic model implements an appropriate equation of state along with proper viscosity properties, it might be perfectly suitable for exploring the high-density stage and yield reliable predictions for the kinetically driven parts of the reaction dynamics, namely the collective flow aspects and the resulting kinetic particle spectra. Thus the kinetic model would produce an initial stopping and approximate local equilibration at the early high-density

stage as well as the transport evolution during the later low-density stage, including a proper freeze-out into the asymptotically observed hadrons. Such considerations led to the constraints on the nuclear equation of state put forward by in [414, 445], cf. the discussion in Sect. 6.4 in the context of Fig. 6.13.

7.4 Phase transitions

The CBM experiment will explore hot and dense matter in a phase region where the confinement transformation is expected to be of first order. This poses several challenges to both experiment and theory.

On the experimental side, there is a need to develop robust observables that can signal the occurrence of this first-order transition, including the associated critical end point. This task is made more difficult by the dearth of transport treatments suitable for dynamical simulations in the phase transition region where the effective degrees of freedom change radically.

At the microscopic level, a proper treatment would need to represent the confined phase in terms of the degrees of freedom present in the deconfined phase, i.e. it must describe hadrons in terms of quarks and gluons. This basic problem has not yet been solved in a satisfactory manner. Furthermore, such a transport model must describe the thermodynamics correctly. This important demand requires first of all that the model satisfies detailed balance, so a proper equilibrium exists. Second, the associated equation of state must display a first-order confinement transition consistent with our theoretical expectations. Third, the associated spinodal instabilities which provide the main mechanism for the phase separation must be properly described in order for the dynamics of the phase transition to be simulated in a realistic manner. These interesting but challenging problems are all far from being solved and intensified efforts are highly desirable. From a practical perspective, what is most urgently needed is some sort of (relativistic) molecular dynamics that would provide a reasonable (semi-quantitative) description of the key physics features, particularly the occurrence of a first-order confinement transition, without necessarily yielding a quantitative reproduction of actual hadronic properties. With such a transport model in hand, it would be possible to simulate the collision dynamics and examine the suitability of various candidate signals.

One might hope to sidestep some of these difficult problems by developing instead a macroscopic treatment, in which the specific degrees of freedom do not enter explicitly but only indirectly through such properties as the equation of state and the transport coefficients. The natural starting point for such an approach is ideal fluid dynamics which has proven to be quite useful for nuclear collision simulations. However, ideal fluid dynamics conserves entropy and it therefore appears particularly unsuitable for the description of phase

separation processes, which occur because of the associated gain in entropy. Furthermore, for the same reason, its region of mechanical phase instability is not bounded the isothermal spinodal given by thermodynamics but rather by the isentropic spinodal which is more restrictive. Thus ideal fluid dynamics tends to suppress the development of phase separation relative to what would be expected on more general grounds. Finally, within its limited region of spinodal instability, ideal fluid dynamics yields a divergent dispersion relation for the unstable sound modes, thereby rendering the instability growth mathematically meaningless as well as numerically intractable. There is thus considerable work to be done before fluid dynamics is suitable for dynamical simulations involving the confinement transition. Furthermore, it should be kept in mind that such a macroscopic approach has certain general limitations. For example, the dynamical initial states need to be prepared on the basis of a more detailed dynamical treatment of the early collision stage when the local conditions are far from equilibrium. Furthermore, a suitable freeze-out procedure needs to be applied at the late stages when the expansion causes the various hadronic species to successively decouple. While this latter problem would be relatively straightforward to treat, this has in fact not yet been done (and it is perhaps less urgent).

In addition to the here discussed confinement phase transition, theoretical considerations lead to the expectation of further phases at high net baryon density but rather low temperature, such as colour superconductivity. Although there are similar challenges with regard to these phase transitions, these are less urgent from a practical point of view, because it is not expected that the relevant phase regions can be accessed in nuclear collisions. This is because a high degree of compression is invariably accompanied by a correspondingly high degree of heating, as illustrated in the dynamical phase trajectories (Fig. 6.3) that were discussed in Sect. 6.1.

References

1. Y.B. Ivanov, V.N. Ruuskikh, V.D. Toneev, Phys. Rev. C **73**, 44904 (2006) [534](#), [610](#), [611](#), [662](#)
2. I.C. Arsene, L.V. Bravina, W. Cassing, Y.B. Ivanov, A. Larionov, J. Randrup, V.N. Ruuskikh, V.D. Toneev, G. Zeeb, D. Zschesche, Phys. Rev. C **75**, 24902 (2007) [534](#), [636](#), [637](#), [639](#), [640](#)
3. J. Randrup, J. Cleymans, Phys. Rev. C **74**, 47901 (2006) [534](#)
4. E.M. Lifshitz, L.P. Pitaevskii, *Physical Kinetics* (Nauka, Moscow, 1979; Pergamon Press, Oxford, 1981) [535](#), [558](#)
5. L. Landau, E. Lifshitz, *Fluid Mechanics* (Pergamon Press, Oxford, 1963) [535](#), [607](#)
6. J. Hüfner, J. Knoll, Nucl. Phys. **290**, 460 (1977) [536](#), [537](#), [544](#), [545](#)
7. P. Danielewicz, Ann. Phys. **152**, 239 (1984) [538](#), [555](#)
8. P. Danielewicz, Ann. Phys. **152**, 305 (1984) [538](#), [555](#)
9. P. Danielewicz, Phys. Lett. B **146**, 168 (1984) [538](#)
10. B. ter Haar, R. Malfliet, Phys. Rev. C **36**, 1611 (1987)
11. T. Alm, G. Röpke, M. Schmidt, Phys. Rev. C **50**, 31 (1994)
12. C. Fuchs, A. Faessler, M. El-Shabshiry, Phys. Rev. C **64**, 024003 (2001) [538](#)
13. W.M. Yao, et al., J. Phys. G **33**, 1 (2006). [<http://pdg.lbl.gov/>] [539](#)
14. C. Fuchs, Prog. Part. Nucl. Phys. **56**, 1 (2006) [540](#), [589](#), [599](#)
15. J. Randrup, C.M. Ko, Nucl. Phys. A **343**, 519 (1980) [540](#), [541](#), [546](#), [584](#), [654](#)
16. J. Randrup, Phys. Lett. B **99**, 1981 (1981) [540](#), [546](#), [585](#), [655](#)
17. K. Chen, Z. Fraenkel, G. Friedlander, J.R. Grover, J.M. Miller, Y. Shimamoto, Phys. Rev. **166**, 949 (1969) [543](#)
18. V.S. Barashenkov, K.K. Gudima, V.D. Toneev, Acta Physiol. Pol. **36**, 457 (1969) [543](#)
19. V.S. Barashenkov, K.K. Gudima, V.D. Toneev, Acta Physiol. Pol. **36**, 887 (1969) [543](#)
20. Y. Yariv, Z. Fraenkel, Phys. Rev. **C20**, 2227 (1979) [543](#)
21. K.K. Gudima, H. Iwe, V.D. Toneev, J. Phys. G **5**, 229 (1979)
22. K.K. Gudima, V.D. Toneev, Sov. J. Nucl. Phys. **31**, 1455 (1980)
23. E.C. Halbert, Phys. Rev. C **23**, 295 (1981) [543](#), [544](#)
24. J. Cugnon, T. Mizutani, J. Vandermeulen, Nucl. Phys. **352**, 505 (1981) [544](#)

25. J. Cugnon, Nucl. Phys. A **387**, 191c (1982) [544](#)
26. R.J. Glauber, Phys. Rev. **100**, 242 (1955) [544](#)
27. R.J. Glauber, *Lectures in Theoretical Physics*, vol. I, ed. W. E. Brittin et al. (Interscience Publishers, New York, NY, 1959)
28. R.J. Glauber, G. Matthiae, Nucl. Phys. B **21**, 135 (1970) [544](#)
29. J. Knoll, J. Randrup, Nucl. Phys. **324**, 445 (1979) [546](#)
30. J. Knoll, J. Randrup, Phys. Lett. B **103**, 264 (1981) [546](#)
31. J. Cugnon, J. Knoll, J. Randrup, Nucl. Phys. A **360**, 444 (1981)
32. B. Schürmann, J. Randrup, Phys. Rev. C **23**, 2766 (1981) [546](#)
33. J. Randrup, Nucl. Phys. **314**, 429 (1979) [546](#), [553](#)
34. J. Knoll, Phys. Rev. C **20**, 773 (1979) [546](#)
35. R. Shyam, J. Knoll, Nucl. Phys. A **426**, 606 (1984) [546](#)
36. R. Shyam, J. Knoll, Phys. Lett. B **136**, 221 (1984)
37. J. Knoll, R. Shyam, Nucl. Phys. A **483**, 711 (1988) [546](#)
38. A. Bialas, M. Bleszynski, W. Czyz, Nucl. Phys. B **111**, 461 (1976) [546](#)
39. S. Jeon, J.I. Kapusta, Phys. Rev. C **56**, 468 (1997) [546](#)
40. K. Geiger, Phys. Rep. **258**, 237 (1995) [547](#)
41. B. Andersson, G. Gustafson, B. Soderberg, Z. Phys. C **20**, 317 (1983) [547](#)
42. T.S. Biro, J. Knoll, H.B. Nielsen, Nucl. Phys. B **245**, 449 (1984) [548](#)
43. J. Knoll, Z. Phys. C **38**, 187 (1988) [548](#)
44. K.A. Brueckner, et al., Phys. Rev. **95**, 217 (1954) [550](#)
45. G.P. Lepage, arXiv:nucl-th/9706029 (1997) [550](#)
46. S.R. Beane, P.F. Bedaque, W.C. Haxton, D.R. Phillips, M.J. Savage, arXiv:nucl-th/0008064 (2000)
47. S.K. Bogner, A. Schwenk, T.T.S. Kuo, G.E. Brown, arXiv:nucl-th/0111042 (2001) [550](#)
48. H. Feldmeier, T. Neff, R. Roth, J. Schnack, Nucl. Phys. A **632**, 61 (1998) [550](#), [602](#)
49. T. Neff, H. Feldmeier, Nucl. Phys. A **713**, 311 (2003) [602](#)
50. R. Roth, et al., Phys. Rev. C **73**, 044312 (2006) [550](#)
51. H.P. Duerr, Phys. Rev. **103**, 469 (1956) [551](#), [612](#)
52. J.D. Walecka, Ann. Phys. **83**, 491 (1974) [551](#), [612](#)
53. P.G. Reinhard, E. Suraud, Ann. Phys. **216**, 98 (1992) [552](#)
54. E. Suraud, P.G. Reinhard, arXiv:nucl-th/9704048 (1997) [552](#)
55. L.W. Nordheim, Proc. R. Soc. Lond. A **119**, 689 (1928) [553](#)
56. E.A. Uehling, G.E. Uhlenbeck, Phys. Rev. **43**, 552 (1933) [553](#)
57. G.F. Bertsch, H. Kruse, S.D. Gupta, Phys. Rev. C **29**, 673 (1984) [553](#)
58. S. Ayik, Z. Phys. A **350**, 45 (1994) [553](#)
59. S. Ayik, J. Randrup, Phys. Rev. **50**, 2947 (1994) [553](#)
60. K. Morawetz, P. Lipavsky, V. Spicka, Prog. Part. Nucl. Phys. **42**, 147 (1999) [553](#)
61. S. Ayik, Z. Phys. A **298**, 83 (1980) [554](#)
62. J. Randrup, B. Remaud, Nucl. Phys. A **514**, 339 (1990)
63. P. Chomaz, G.F. Burgio, J. Randrup, Phys. Lett. B **254**, 340 (1991)
64. G.F. Burgio, P. Chomaz, J. Randrup, Nucl. Phys. A **529**, 157 (1991) [554](#)

65. P. Chomaz, M. Colonna, A. Guarnera, J. Randrup, Phys. Rev. Lett. **73**, 3512 (1994) [554](#)
66. P. Chomaz, M. Colonna, J. Randrup, Phys. Rep. **389**, 263 (2004) [554](#), [615](#)
67. Y. Abe, S. Ayik, P.G. Reinhard, E. Suraud, Phys. Rep. **275**, 49 (1996) [555](#)
68. P. Danielewicz, G.F. Bertsch, Nucl. Phys. A **533**, 712 (1991) [555](#), [577](#), [585](#), [586](#)
69. L.P. Kadanoff, G. Baym, *Quantum Statistical Mechanics* (Benjamin, New York, NY, 1962) [555](#), [559](#), [562](#)
70. M. Bonitz (ed.), *Progress in Nonequilibrium Green's Functions* (World Scientific, Singapore, 1999) [556](#)
71. M. Bonitz, D. Semkat (eds.), *Progress in Nonequilibrium Green's Functions II* (World Scientific, Singapore, 2002)
72. M. Bonitz, A. Filinov (eds.), *Progress in Nonequilibrium Green's Functions III*, vol. 35 (Institute of Physics, Bristol, UK, 2006) [556](#)
73. J. Berges, S. Borsanyi, J. Serreau, Nucl. Phys. **B660**, 51 (2003) [556](#)
74. J. Knoll, Prog. Part. Nucl. Phys. **42**, 177 (1999) [556](#), [571](#), [572](#)
75. S. Leupold, Nucl. Phys. A **672**, 475 (2000) [562](#), [565](#), [587](#)
76. W. Cassing, S. Juchem, Nucl. Phys. A **665**, 377 (2000)
77. Y.B. Ivanov, J. Knoll, D.N. Voskresensky, Nucl. Phys. A **672**, 313 (2000) [561](#), [562](#)
78. W. Cassing, S. Juchem, Nucl. Phys. A **672**, 417 (2000) [562](#), [565](#), [587](#), [592](#)
79. W. Cassing, S. Juchem, Nucl. Phys. A **677**, 445 (2000)
80. J. Knoll, Y.B. Ivanov, D.N. Voskresensky, Ann. Phys.(NY) **293**, 126 (2001) [561](#), [562](#), [564](#), [575](#), [580](#)
81. S. Leupold, Nucl. Phys. A **695**, 377 (2001)
82. S. Juchem, W. Cassing, C. Greiner, Phys. Rev. D **69**, 025006 (2004) [565](#), [580](#), [582](#)
83. S. Juchem, W. Cassing, C. Greiner, Nucl. Phys. A **743**, 92 (2004) [565](#), [581](#), [582](#)
84. W. Cassing, Eur. Phys. J. ST **168**, 3 (2009). DOI 10.1140/epjst/e2009-00959-x [556](#), [580](#), [581](#), [582](#)
85. P.A.M. Dirac, Proc. Roy. Soc. **114**, 243 (Lond) [557](#)
86. G. Baym, Phys. Rev. **127**, 1391 (1962) [561](#), [575](#), [580](#)
87. Y.B. Ivanov, J. Knoll, D.N. Voskresensky, Nucl. Phys. A **657**, 413 (1999) [561](#), [562](#)
88. W. Botermans, R. Malfliet, Phys. Rep. **198**, 115 (1990) [565](#), [580](#)
89. G.M. Carneiro, C.J. Pethick, Phys. Rev. B **11**, 1106 (1975) [565](#)
90. H. van Hees, J. Knoll, Phys. Rev. D **65**, 025010 (2002) [565](#)
91. H. van Hees, J. Knoll, Phys. Rev. D **65**, 105005 (2002)
92. H. van Hees, J. Knoll, Phys. Rev. D **66**, 025028 (2002) [565](#)
93. J.P. Blaizot, E. Iancu, U. Reinosa, Nucl. Phys. A **736**, :149 (2004) [565](#)
94. E. Beth, G.E. Uhlenbeck, Physica **4**, 915 (1937) [566](#), [627](#)
95. K. Huang, *Statistical Mechanics* (Wiley, New York, NY, 1963) [566](#)
96. R. Dashen, S. Ma, H.J. Bernstein, Phys. Rev. **187**, 345 (1969)
97. A.Z. Mekjian, Phys. Rev. C **17**, 1051 (1978) [566](#)
98. W. Weinhold, B. Friman, W. Nörenberg, Phys. Lett. B **433**, 236 (1998) [567](#), [568](#)
99. R.A. Arndt, I.I. Strakovsky, R.L. Workman, Phys. Rev. C **52**, 2246 (1995) [567](#)
100. P. Danielewicz, S. Pratt, Phys. Rev. C **53**, 249 (1996) [566](#)
101. O. Schwalb, et al., Phys. Lett. B **321**, 20 (1994) [567](#), [568](#), [626](#)

102. V. Špička, P. Lipavský, K. Morawetz, Phys. Lett. A **240**, 160 (1998) [569](#)
103. L.D. McLerran, T. Toimela, Phys. Rev. D **31**, 545 (1985) [570](#)
104. C. Gale, J.I. Kapusta, Phys. Rev. C **35**, 2107 (1987) [570](#)
105. M. Herrmann, B.L. Friman, W. Norenberg, Nucl. Phys. A **560**, 411 (1993) [570](#)
106. S. Leupold, U. Mosel, Phys. Rev. C **58**, 2939 (1998) [571](#)
107. R. Rapp, G. Chanfray, J. Wambach, Nucl. Phys. A **617**, 472 (1997)
108. F. Klingl, N. Kaiser, W. Weise, Nucl. Phys. A **624**, 527 (1997)
109. B.L. Friman, H.J. Pirner, Nucl. Phys. A **617**, 496 (1997)
110. B. Friman, M. Lutz, G. Wolf, Nucl. Phys. A **661**, 526 (1999) [571](#)
111. F. Riek, H. van Hees, J. Knoll, Phys. Rev. C **75**, 059801 (2007) [573](#), [574](#), [581](#)
112. J. Knoll, D.N. Voskresensky, Ann. Phys. **249**, 532 (1996) [574](#), [577](#), [582](#)
113. L.D. Landau, I. Pomeranchuk, Dokl. Akad. Nauk Ser. Fiz. **92**, 535 (1953) [574](#), [582](#)
114. A.B. Migdal, Phys. Rev. **103**, 1811 (1956) [574](#), [582](#)
115. J.M. Cornwall, R. Jackiw, E. Tomboulis, Phys. Rev. D **10**, 2428 (1974) [575](#)
116. J.M. Luttinger, J.C. Ward, Phys. Rev. **118**, 1417 (1960) [575](#), [580](#)
117. R. Rapp, E.V. Shuryak, Phys. Rev. Lett. **86**, 2980 (2001) [576](#)
118. C. Greiner, S. Leupold, J. Phys. G **27**, L95 (2001) [576](#), [577](#)
119. Z. Xu, C. Greiner, Phys. Rev. C **71**, 064901 (2005) [581](#)
120. W. Cassing, Nucl. Phys. A **700**, 618 (2002) [576](#)
121. P. Danielewicz, Nucl. Phys. A **673**, 375 (2000) [577](#), [585](#)
122. G. Batko, J. Randrup, T. Vetter, Nucl. Phys. A **536**, 786 (1992) [578](#)
123. G. Batko, J. Randrup, T. Vetter, Nucl. Phys. A **546**, 761 (1992) [579](#)
124. H. van Hees, J. Knoll, Nucl. Phys. A **683**, 369 (2001) [581](#)
125. Y.B. Ivanov, J. Knoll, D.N. Voskresensky, Phys. Atom. Nucl. **66**, 1902 (2003) [581](#)
126. Y.B. Ivanov, F. Riek, H. van Hees, J. Knoll, Phys. Rev. D **72**, 036008 (2005) [581](#)
127. Y.B. Ivanov, F. Riek, J. Knoll, Phys. Rev. D **71**, 105016 (2005) [581](#)
128. J. Ruppert, T. Renk, Phys. Rev. C **71**, 064903 (2005) [581](#)
129. S. Leupold, Phys. Lett. B **646**, 155 (2007) [582](#)
130. F. Riek, J. Knoll, Nucl. Phys. A **740**, 287 (2004) [582](#)
131. Y.B. Ivanov, J. Knoll, H.V. Hees, D.N. Voskresensky, Phys. Atom. Nucl. **64**, 652 (2001) [582](#)
132. R.V. Gavai, S. Gupta, Phys. Rev. D **73**, 014004 (2006) [582](#)
133. V. Koch, A. Majumder, J. Randrup, Phys. Rev. Lett. **95**, 182301 (2005) [582](#)
134. C.D. Roberts, A.G. Williams, Prog. Part. Nucl. Phys. **33**, 477 (1994) [583](#)
135. R.J. Lenk, V.R. Pandharipande, Phys. Rev. C **39**, 2242 (1989) [585](#)
136. M. Effenberger, E.L. Bratkovskaya, U. Mosel, Phys. Rev. C **60**, 44614 (1999) [586](#), [587](#)
137. M. Effenberger, PhD thesis, University Giessen (1999)
138. A.B. Larionov, U. Mosel, Nucl. Phys. A **728**, 135 (2003) [586](#)
139. M. Wagner, A.B. Larionov, U. Mosel, Phys. Rev. C **71**, 034910 (2005) [586](#), [587](#)
140. S.J. Lee, et al., Phys. Rev. Lett. **57**, 2916 (1986) [586](#)

- 141. V. Dmitriev, O. Sushkov, C. Gaarde, Nucl. Phys. A **459**, 503 (1986) [586](#)
- 142. O. Buss, L. Alvarez-Ruso, P. Mühlich, U. Mosel, Eur. Phys. J. A **29**, 189 (2006) [587](#)
- 143. H.W. Barz, B. Kampfer, G. Wolf, M. Zetenyi, arXiv:nucl-th/0605036 (2006) [587](#)
- 144. G. Wolf, W. Cassing, U. Mosel, Nucl. Phys. A **552**, 549 (1993) [587](#)
- 145. H.W. Barz, M. Zétényi, Phys. Rev. C **69**, 024605 (2004) [588](#)
- 146. G. Wolf, Heavy Ion Phys. **5**, 281 (1997) [588](#)
- 147. K. Tsushima, A. Sibitsev, A.W. Thomas, G.Q. Li, Phys. Rev. C **59**, 369 (1999) [588](#)
- 148. H.W. Barz, M. Zétényi, G. Wolf, B. Kämpfer, Nucl. Phys. A **705**, 223 (2002) [588](#)
- 149. H.W. Barz, L. Naumann, Phys. Rev. C **68**, 041901 (R) (2003) [588](#)
- 150. C.M. Ko, Q. Li, R. Wang, Phys. Rev. Lett. **59**, 1084 (1987) [588](#)
- 151. C.M. Ko, Q. Li, Phys. Rev. C **37**, 2270 (1988)
- 152. Q. Li, J.Q. Wu, C.M. Ko, Phys. Rev. C **39**, 849 (1989)
- 153. C.M. Ko, Nucl. Phys. A **495**, 321 (1989)
- 154. C.M. Ko, G.Q. Li, J. Phys. G **22**, 405 (1996)
- 155. G.Q. Li, C.H. Lee, G.E. Brown, Nucl. Phys. A **625**, 372 (1997) [588](#), [589](#)
- 156. G.Q. Li, G.E. Brown, Phys. Rev. C **58**, 1698 (1998)
- 157. G.Q. Li, G.E. Brown, Nucl. Phys. A **636**, 487 (1998) [588](#)
- 158. R.J. Furnstahl, H.B. Tang, B.D. Serot, Phys. Rev. C **52**, 1368 (1995) [588](#)
- 159. C.M. Ko, Phys. Lett. B **120**, 294 (1983) [588](#)
- 160. S. Pal, C.M. Ko, Z.W. Lin, Phys. Rev. C **64**, 042201 (2001) [589](#)
- 161. L.W. Chen, C.M. Ko, Y. Tzeng, Phys. Lett. B **584**, 269 (2004) [589](#)
- 162. C. Fuchs, H.H. Wolter, Nucl. Phys. A **589**, 732 (1995) [589](#)
- 163. V. Greco, et al., Phys. Lett. B **562**, 215 (2003) [589](#), [590](#)
- 164. T. Gaitanos, et al., Nucl. Phys. A **732**, 24 (2004) [589](#)
- 165. T. Gaitanos, et al., Phys. Lett. B **595**, 209 (2004)
- 166. G. Ferini, et al., Nucl. Phys. A **762**, 147 (2005) [589](#)
- 167. B. Liu, et al., Phys. Rev. C **65**, 045201 (2002) [589](#)
- 168. V. Baran, M. Colonna, V. Greco, M.D. Toro, Phys. Rep. **410**, 335 (2005) [589](#)
- 169. B.A. Li, C.M. Ko, Phys. Rev. C **52**, 2037 (1995) [590](#), [591](#)
- 170. B. Li, A.T. Sustich, B. Zhang, C.M. Ko, Int. J. Mod. Phys. E **10**, 267 (2001) [590](#), [591](#)
- 171. B.A. Li, C.M. Ko, W. Bauer, Int. J. Mod. Phys. E **7**, 147 (1998) [590](#)
- 172. G. Song, B.A. Li, C.M. Ko, Nucl. Phys. A **646**, 481 (1999) [590](#)
- 173. J. Cugnon, P. Deneye, J. Vandermeulen, Phys. Rev. C **41**, 1701 (1990) [590](#)
- 174. Z.W. Lin, C.M. Ko, B.A. Li, B. Zhang, S. Pal, Phys. Rev. C **72**, 064901 (2005) [591](#)
- 175. X.N. Wang, M. Gyulassy, Phys. Rev. D **44**, 3501 (1991) [591](#)
- 176. B. Zhang, C.M. Ko, B.A. Li, Z.W. Lin, Phys. Rev. C **61**, 067901 (2000) [591](#)
- 177. Z.W. Lin, S. Pal, C.M. Ko, B.A. Li, B. Zhang, Phys. Rev. C **64**, 011902(R) (2001) [591](#)
- 178. B. Zhang, Comput. Phys. Commun. **109**, 193 (1998) [591](#)

179. T. Sjostrand, *Comput. Phys. Commun.* **82**, 74 (1994) [591](#), [592](#)
180. Z.W. Lin, C.M. Ko, *Phys. Rev. C* **65**, 034904 (2002) [591](#)
181. W. Ehehalt, W. Cassing, *Nucl. Phys. A* **602**, 449 (1996) [592](#)
182. J. Geiss, W. Cassing, C. Greiner, *Nucl. Phys. A* **644**, 107 (1998)
183. W. Cassing, E.L. Bratkovskaya, *Phys. Rep.* **308**, 65 (1999) [592](#)
184. E.L. Bratkovskaya, W. Cassing, *Nucl. Phys. A* **619**, 413 (1997) [592](#)
185. W. Cassing, E.L. Bratkovskaya, A. Sibirtsev, *Nucl. Phys. A* **691**, 753 (2001)
186. W. Cassing, K. Gallmeister, C. Greiner, *Nucl. Phys. A* **735**, 277 (2004) [592](#)
187. W. Cassing, E.L. Bratkovskaya, S. Juchem, *Nucl. Phys. A* **674**, 249 (2000) [592](#)
188. B. Andersson, G. Gustafson, H. Pi, *Z. Phys. C* **57**, 485 (1993) [592](#)
189. W. Cassing, (2005).
URL <http://conferences.jlab.org/ECT/program> [592](#)
190. A. Peshier, W. Cassing, *Phys. Rev. Lett.* **94**, 172301 (2005) [592](#), [593](#)
191. W. Cassing, *Nucl. Phys. A* **795**, 70 (2007)
192. W. Cassing, *Nucl. Phys. A* **791**, 365 (2007) [592](#)
193. A.B. Kaidalov, *Phys. Lett. B* **116**, 459 (1982) [593](#)
194. A.B. Kaidalov, K.A. Ter-Martirosian, *Phys. Lett. B* **117**, 247 (1982)
195. N.S. Amelin, L.V. Bravina, L.P. Csernai, V.D. Toneev, K.K. Gudima, S.Y. Sivoklokov, *Phys. Rev. C* **47**, 2299 (1993)
196. E.E. Zabrodin, C. Fuchs, L.V. Bravina, A. Faessler, *Phys. Rev. C* **63**, 034902 (2001) [649](#)
197. E.E. Zabrodin, C. Fuchs, L.V. Bravina, A. Faessler, *Phys. Lett. B* **508**, 184 (2001)
198. G. Bureau, J. Bleibel, C. Fuchs, A. Faessler, L.V. Bravina, E.E. Zabrodin, *Phys. Rev. C* **71**, 054905 (2005) [593](#), [649](#)
199. V. Gribov, *Sov. Phys. JETP* **26**, 414 (1968) [593](#)
200. L.V. Gribov, E.M. Levin, M.G. Ryskin, *Phys. Rep.* **100**, 1 (1983) [593](#)
201. V. Abramovskii, V. Gribov, O. Kancheli, *Sov. J. Nucl. Phys.* **18**, 308 (1974) [593](#)
202. N.S. Amelin, E.F. Staubo, L.P. Csernai, *Phys. Rev. D* **46**, 4873 (1992) [593](#)
203. R.J. Lenk, V.R. Pandharipande, *Phys. Rev. C* **34**, 177 (1986) [595](#)
204. R.J. Lenk, V.R. Pandharipande, *Phys. Rev. C* **36**, 162 (1987) [595](#)
205. C.O. Dorso, V.C. Latora, A. Bonasera, *Phys. Rev. C* **60**, 34606 (1999) [595](#)
206. C. Dorso, J. Randrup, *Phys. Lett. B* **232**, 29 (1989) [595](#), [596](#)
207. A. Chernomoretz, C.O. Dorso, J.A. López, *Phys. Rev. C* **64**, 044605 (2001) [595](#)
208. C.O. Dorso, C.R. Escudero, M. Ison, J.A. López, *Phys. Rev. C* **73**, 044601 (2006) [595](#)
209. L. Wilets, E.M. Henley, M. Kraft, A.D. Mackellar, *Nucl. Phys. A* **282**, 341 (1977) [595](#)
210. L. Wilets, Y. Yariv, R. Chestnut, *Nucl. Phys. A* **301**, 359 (1978) [595](#)
211. C. Dorso, S. Duarte, J. Randrup, *Phys. Lett. B* **188**, 287 (1987) [595](#), [596](#)
212. C. Dorso, J. Randrup, *Phys. Lett. B* **215**, 611 (1988) [596](#)

- 213. G. Peilert, J. Randrup, H. Stöcker, W. Greiner, Phys. Lett. B **260**, 271 (1991) [596](#), [597](#)
- 214. J. Aichelin, H. Stöcker, Phys. Lett. B **176**, 14 (1986) [596](#), [644](#)
- 215. J. Aichelin, Phys. Rep. **202**, 233 (1991) [597](#)
- 216. G. Peilert, H. Stöcker, W. Greiner, A. Rosenhauer, A. Bohnet, J. Aichelin, Phys. Rev. C **39**, 1402 (1989)
- 217. T. Maruyama, A. Ohnishi, H. Horiuchi, Phys. Rev. C **42**, 386 (1990)
- 218. C. Hartnack, R.K. Puri, J. Aichelin, J. Konopka, S.A. Bass, H. Stöcker, W. Greiner, Eur. Phys. J. A **1**, 151 (1998) [596](#), [597](#)
- 219. H. Sorge, H. Stöcker, W. Greiner, Ann. Phys. **192**, 266 (1989) [597](#), [598](#)
- 220. E. Lehmann, R.K. Puri, A. Faessler, G. Batko, S.W. Huang, Phys. Rev. C **51**, 2113 (1995) [597](#), [598](#)
- 221. P.A.M. Dirac, Rev. Mod. Phys. **21**, 392 (1949) [598](#)
- 222. J. Samuel, Phys. Rev. D **26**, 3482 (1982) [598](#)
- 223. H. Sorge, Phys. Rev. C **52**, 3291 (1995) [598](#)
- 224. H. Sorge, Phys. Lett. B **373**, 16 (1996)
- 225. G.Q. Li, C.M. Ko, G.E. Brown, H. Sorge, Nucl. Phys. A **611**, 539 (1996)
- 226. H. Sorge, Phys. Rev. Lett. **78**, 2309 (1997)
- 227. H. Sorge, Phys. Rev. Lett. **82**, 2048 (1999) [598](#)
- 228. C. Fuchs, E. Lehmann, L. Sehn, F. Scholz, T. Kubo, J. Zipprich, A. Faessler, Nucl. Phys. A **603**, 471 (1996) [598](#)
- 229. W.S.U. Maheswari, C. Fuchs, A. Faessler, L. Sehn, D. Kosov, Z. Wang, Nucl. Phys. A **628**, 669 (1998) [598](#)
- 230. C. Fuchs, A. Faessler, E. Zabrodin, Y.E. Zheng, Phys. Rev. Lett. **86**, 1974 (2001) [599](#)
- 231. K. Shekter, C. Fuchs, A. Faessler, M. Krivoruchenko, B. Martemyanov, Phys. Rev. C **68**, 014904 (2003) [599](#)
- 232. S.A. Bass, et al., Prog. Part. Nucl. Phys. **41**, 225 (1998) [599](#)
- 233. M. Bleicher, et al., J. Phys. G **25**, 1859 (1999) [599](#), [618](#), [649](#)
- 234. M. Berenguer, H. Sorge, W. Greiner, Phys. Lett. B **332**, 15 (1994) [600](#)
- 235. R.D. Field, R.P. Feynman, Nucl. Phys. B **136**, 1 (1978) [600](#)
- 236. H. Feldmeier, Nucl. Phys. A **515**, 147 (1990) [601](#)
- 237. H. Feldmeier, J. Schnack, Nucl. Phys. A **583**, 347 (1995)
- 238. H. Feldmeier, K. Bieler, J. Schnack, Nucl. Phys. A **586**, 493 (1995)
- 239. H. Feldmeier, J. Schnack, Prog. Part. Nucl. Phys. **39**, 393 (1997)
- 240. H. Feldmeier, J. Schnack, Rev. Mod. Phys. **72**, 655 (2000) [601](#)
- 241. T. Maruyama, K. Niita, A. Iwamoto, Phys. Rev. C **53**, 297 (1996) [601](#)
- 242. D. Kiderlen, P. Danielewicz, Nucl. Phys. A **620**, 346 (1997) [601](#)
- 243. M. Colonna, P. Chomaz, Phys. Lett. B **436**, 1 (1998) [602](#)
- 244. J. Schnack, H. Feldmeier, Phys. Lett. B **409**, 6 (1997) [602](#)
- 245. H. Feldmeier, *The Nuclear Equation of State, Part A*, W. Greiner and H. Stöcker (ed) (Plenum Press, New York, NY, 1989) [602](#)
- 246. M. Chernyk, H. Feldmeier, T. Neff, P. von Neumann-Cosel, A. Richter, Phys. Rev. Lett. **98**, 032501 (2007) [602](#)
- 247. T. Neff, H. Feldmeier, R. Roth, Nucl. Phys. A **752**, 321 (2005)

248. T. Neff, H. Feldmeier, Nucl. Phys. A **738**, 357 (2004) [602](#)
249. A. Ono, H. Horiuchi, T. Maruyama, A. Ohnishi, Phys. Rev. Lett. **68**, 2898 (1992) [603](#)
250. A. Ono, H. Horiuchi, T. Maruyama, A. Ohnishi, Prog. Theor. Phys. **87**, 1185 (1992) [604](#)
251. A. Ono, H. Horiuchi, Prog. Part. Nucl. Phys. **53**, 501 (2004) [603](#)
252. A. Ono, H. Horiuchi, Phys. Rev. C **53**, 2958 (1996) [603](#), [604](#)
253. A. Ono, Phys. Rev. C **59**, 853 (1999)
254. A. Ono, S. Hudan, A. Chbihi, J.D. Frankland, Phys. Rev. C **66**, 014603 (2002) [603](#)
255. Y. Kanada-En'yo, M. Kimura, H. Horiuchi, C. R. Physique **4**, 497 (2003) [604](#)
256. A. Ono, H. Horiuchi, Phys. Rev. C **53**, 2341 (1996) [604](#)
257. Y. Sugawa, H. Horiuchi, Phys. Rev. C **60**, 064607 (1999) [604](#)
258. Y. Sugawa, H. Horiuchi, Prog. Theor. Phys. **105**, 131 (2001)
259. T. Furuta, A. Ono, Phys. Rev. C **74**, 014612 (2006) [604](#)
260. R. Wada, et al., Phys. Rev. C **62**, 034601 (2000) [604](#)
261. A. Ono, P. Danielewicz, W.A. Friedman, W.G. Lynch, M.B. Tsang, Phys. Rev. C **68**, 051601(R) (2003) [604](#)
262. A. Ono, P. Danielewicz, W.A. Friedman, W.G. Lynch, M.B. Tsang, Phys. Rev. C **70**, 041604(R) (2004) [604](#)
263. A. Ohnishi, J. Randrup, Phys. Rev. Lett. **75**, 596 (1995) [604](#), [605](#)
264. A. Ohnishi, J. Randrup, Ann. Phys. **253**, 279 (1997) [604](#), [605](#)
265. A. Ohnishi, J. Randrup, Nucl. Phys. A **565**, 474 (1994) [605](#), [606](#)
266. A. Ohnishi, J. Randrup, Phys. Rev. A **55**, R3315 (1997) [606](#)
267. Y. Hirata, A. Ohnishi, Y. Nara, T. Harada, J. Randrup, Nucl. Phys. A **639**, 389 (1998) [606](#)
268. Y. Hirata, Y. Nara, A. Ohnishi, T. Harada, J. Randrup, Prog. Theor. Phys. **102**, 89 (1999) [606](#)
269. A. Ohnishi, J. Randrup, Phys. Lett. B **394**, 260 (1997) [606](#)
270. L.P. Csernai, *Introduction to Relativistic Heavy Ion Collisions* (Chichester, UK: Wiley, 310p, 1994) [607](#)
271. H.G. Baumgardt, et al., Z. Phys. A **273**, 359 (1975) [608](#), [609](#), [644](#)
272. A.A. Amsden, F.H. Harlow, J.R. Nix, Phys. Rev. C **15**, 2059 (1977) [608](#)
273. R.B. Clare, D. Strottman, Phys. Rep. **141**, 177 (1986) [608](#)
274. I.N. Mishustin, V.N. Russkikh, L.M. Satarov, Nucl. Phys. A **494**, 595 (1989) [610](#)
275. N. Amelin, E.F. Staubo, L. Csernai, V.D. Toneev, K.K. Gudima, D. Strottman, Phys. Rev. Lett. **67**, 1523 (1991)
276. B.R. Schlei, D. Strottman, Phys. Rev. C **59**, 9 (1999)
277. D.H. Rischke, Nucl. Phys. A **610**, 88c (1996)
278. D.H. Rischke, S. Bernard, J.A. Maruhn, Nucl. Phys. A **595**, 346 (1995) [662](#)
279. D.H. Rischke, Y. Pursun, J.A. Maruhn, Nucl. Phys. A **595**, 383 (1995)
280. J. Bolz, U. Ornik, R.M. Weiner, Phys. Rev. C **46**, 2047 (1992)
281. P. Huovinen, P.V. Ruuskanen, Ann. Rev. Nucl. Part. Sci. **56**, 163 (2006)
282. P. Huovinen, arXiv:nucl-th/0305064 (2003)

283. P.F. Kolb, U.W. Heinz, P. Huovinen, K.J. Eskola, K. Tuominen, Nucl. Phys. A **696**, 197 (2001)
284. P. Huovinen, P.F. Kolb, U.W. Heinz, P.V. Ruuskanen, S.A. Voloshin, Phys. Lett. B **503**, 58 (2001)
285. J. Sollfrank, et al., Phys. Rev. C **55**, 392 (1997)
286. J. Brachmann, et al., Nucl. Phys. A **619**, 391 (1997) [610](#)
287. K. Paech, H. Stoecker, A. Dumitru, Phys. Rev. C **68**, 044907 (2003)
288. L.P. Csernai, J.I. Kapusta, Phys. Rev. D **46**, 1379 (1992) [608](#)
289. Y. Hama, R. Andrade, F. Grassi, O. Socolowski, T. Kodama, B. Tavares, S.S. Padula, AIP Conf. Proc. **828**, 485 (2006) [609](#)
290. V.V. Skokov, V.D. Toneev, Phys. Rev. C **73**, 021902(R) (2006) [609](#)
291. J. Sollfrank, P. Huovinen, M. Kataja, P.V. Ruuskanen, M. Prakash, R. Venugopalan, Phys. Rev. C **55**, 392 (1997) [609](#)
292. P. Huovinen, P.V. Ruuskanen, J. Sollfrank, Nucl. Phys. A **650**, 227 (1999)
293. P.F. Kolb, J. Sollfrank, P.V. Ruuskanen, U. Heinz, Nucl. Phys. A **661**, 349 (1999)
294. C. Nonaka, S.A. Bass, Nucl. Phys. A **774**, 873 (2006)
295. C.M. Hung, E.V. Shuryak, Phys. Rev. Lett. **75**, 4003 (1995)
296. C.M. Hung, E. Shuryak, Phys. Rev. C **57**, 1891 (1998)
297. D. Teaney, J. Lauret, E.V. Shuryak, arXiv:nucl-th/0110037 (2001)
298. D. Teaney, J. Lauret, E.V. Shuryak, Phys. Rev. Lett. **86**, 4783 (2001) [609](#), [617](#)
299. A.A. Amsden, A.S. Goldhaber, F.H. Harlow, J.R. Nix, Phys. Rev. C **17**, 2080 (1978) [610](#)
300. U. Katscher, et al., Z. Phys. A **346**, 209 (1993) [610](#)
301. V.D. Toneev, Y.B. Ivanov, E.G. Nikonov, W. Norenberg, V.N. Russkikh, Phys. Part. Nucl. Lett. **2**, 288 (2005) [611](#), [642](#)
302. V.N. Russkikh, Y.B. Ivanov, E.G. Nikonov, W. Norenberg, V.D. Toneev, Phys. Atom. Nucl. **67**, 199 (2004) [610](#), [651](#), [652](#)
303. L.M. Satarov, Sov. J. Nucl. Phys. **52**, 264 (1990) [611](#)
304. V.N. Russkikh, Y.B. Ivanov, Phys. Rev. C **74**, 034904 (2006) [611](#), [646](#), [647](#), [650](#)
305. Y.B. Ivanov, V.N. Russkikh, Eur. Phys. J. A **37**, 139 (2008)
306. V.N. Russkikh, Y.B. Ivanov, Phys. Rev. C **76**, 054907 (2007) [611](#), [621](#), [622](#)
307. H.W. Barz, B.L. Friman, J. Knoll, H. Schulz, Nucl. Phys. A **484**, 661 (1988) [611](#), [626](#)
308. H.W. Barz, B.L. Friman, J. Knoll, H. Schulz, Nucl. Phys. A **519**, 831 (1990) [611](#), [612](#), [619](#), [626](#)
309. H.W. Barz, B.L. Friman, J. Knoll, H. Schulz, Phys. Rev. D **40**, 157 (1989) [612](#)
310. J. Knoll, Nucl. Phys. A **821**, 235 (2009) [613](#), [621](#), [624](#), [633](#)
311. V.V. Skokov, D.N. Voskresensky, JETP Lett. **90**, 223 (2009) [615](#), [617](#)
312. P. Danielewicz, M. Gyulassy, Phys. Rev. D **31**, 53 (1985) [615](#)
313. U.W. Heinz, H. Song, A.K. Chaudhuri, Phys. Rev. C **73**, 034904 (2006) [615](#), [617](#)
314. R. Kubo, J. Phys. Soc. Jpn. **12**, 570 (1957) [616](#)
315. J. Randrup, Phys. Rev. C **79**, 054911 (2009); C **82**, 034902 (2010) [616](#), [617](#)

- 316. K. Paech, S. Pratt, Phys. Rev. C **74**, 014901 (2006) [616](#), [653](#)
- 317. S. Pratt, arXiv:0809.0089 [nucl-th] (2008) [616](#)
- 318. S. Cheng, et al., Phys. Rev. C **65**, 024901 (2002) [616](#)
- 319. F. Karsch, D. Kharzeev, K. Tuchin, Phys. Lett. B **663**, 217 (2008) [616](#)
- 320. A. Krasnitz, Y. Nara, R. Venugopalan, Nucl. Phys. A **717**, 268 (2003) [616](#)
- 321. W. Israel, Ann. Phys. **100**, 310 (1976) [616](#)
- 322. W. Israel, J.M. Stewart, Ann. Phys. **118**, 341 (1979) [616](#)
- 323. J. Randrup, Phys. Rev. Lett. **92**, 122301 (2004) [617](#)
- 324. A. Muronga, Eur. Phys. J. ST **155**, 107 (2008) [617](#), [653](#)
- 325. A. Muronga, J. Phys. G **31**, S1035 (2005)
- 326. T. Koide, Phys. Rev. E **75**, 060103 (2007)
- 327. R. Baier, P. Romatschke, U.A. Wiedemann, Phys. Rev. C **73**, 064903 (2006)
- 328. H. Song, U.W. Heinz, Phys. Rev. C **77**, 064901 (2008)
- 329. P. Romatschke, U. Romatschke, Phys. Rev. Lett. **99**, 172301 (2007) [617](#), [653](#)
- 330. A. Dumitru, S.A. Bass, M. Bleicher, H. Stoecker, W. Greiner, Phys. Lett. B **460**, 411 (1999) [617](#)
- 331. S.A. Bass, A. Dumitru, Phys. Rev. C **61**, 064909 (2000)
- 332. R. Andrade, et al., Eur. Phys. J. A **29**, 23 (2006) [618](#)
- 333. T. Hirano, U.W. Heinz, D. Kharzeev, R. Lacey, Y. Nara, Phys. Lett. B **636**, 299 (2006) [618](#)
- 334. C. Nonaka, S.A. Bass, Phys. Rev. C **75**, 014902 (2007) [618](#)
- 335. S.V. Akkelin, Y. Hama, I.A. Karpenko, Y.M. Sinyukov, Phys. Rev. C **78**, 034906 (2008) [621](#), [625](#)
- 336. S. Pratt, J. Vredevoogd, Phys. Rev. C **78**, 054906 (2008), Erratum ibid. C **79**, 069901 (2009) [618](#), [625](#), [633](#)
- 337. Q.f. Li, J. Steinheimer, H. Petersen, M. Bleicher, H. Stoecker, Phys. Lett. B **674**, 111 (2009) [618](#)
- 338. H. Petersen, J. Steinheimer, G. Burau, M. Bleicher, Eur. Phys. J. C **62**, 31 (2009) [618](#)
- 339. H. Petersen, J. Steinheimer, G. Burau, M. Bleicher, H. Stoecker, Phys. Rev. C **78**, 044901 (2008) [617](#), [618](#)
- 340. S. Pratt, Phys. Rev. Lett. **102**, 232301 (2009) [618](#), [625](#)
- 341. F. Grassi, Y. Hama, O. Socolowski, T. Kodama, J. Phys. G **31**, S1041 (2005) [618](#)
- 342. V.V. Skokov, V.D. Toneev, Phys. Rev. C **73**, 021902 (2006) [618](#)
- 343. D. Teaney, J. Lauret, E.V. Shuryak, arXiv:nucl-th/0110037 [618](#)
- 344. T. Hirano, U.W. Heinz, D. Kharzeev, R. Lacey, Y. Nara, Phys. Rev. C **77**, 044909 (2008) [618](#)
- 345. S.A. Bass, et al., Prog. Part. Nucl. Phys. **41**, 255 (1998) [618](#)
- 346. H. Petersen, M. Bleicher, S.A. Bass, H. Stoecker, arXiv:0805.0567 [618](#)
- 347. H. Petersen, J. Steinheimer, M. Bleicher, H. Stoecker, J. Phys. G **36**, 055104 (2009) [618](#)
- 348. H. Petersen, M. Bleicher, Phys. Rev. C **79**, 054904 (2009)

349. H. Petersen, M. Mitrovski, T. Schuster, M. Bleicher, Phys. Rev. C **80**, 054910 (2009)
350. J. Steinheimer, et al., Phys. Rev. C **81**, 044913 (2010) [618](#)
351. J.D. Bjorken, Phys. Rev. D **27**, 140 (1983) [619](#), [645](#)
352. P.J. Siemens, J.O. Rasmussen, Phys. Rev. Lett. **42**, 880 (1979) [619](#), [644](#)
353. T. Biro, H.W. Barz, B. Lukacs, J. Zimanyi, Phys. Rev. C **27**, 2695 (1983) [619](#)
354. G.A. Milekhin, Zh. Eksp. Teor. Fiz. **35**, 1185 (1958) [620](#)
355. G.A. Milekhin, Sov. Phys. JETP **35**, 829 (1959)
356. G.A. Milekhin, Trudy FIAN **16**, 51 (1961) [620](#)
357. F. Cooper, G. Frye, Phys. Rev. D **10**, 186 (1974) [620](#)
358. K.A. Bugaev, Nucl. Phys. A **606**, 559 (1996) [621](#), [624](#)
359. K.A. Bugaev, M.I. Gorenstein, W. Greiner, J. Phys. G **25**, 2147 (1999)
360. C. Anderlik, et al., Phys. Rev. C **59**, 3309 (1999)
361. L.P. Csernai, Z. Lazar, D. Molnar, Heavy Ion Phys. **5**, 467 (1997) [621](#), [624](#)
362. F. Grassi, Y. Hama, T. Kodama, Z. Phys. C **73**, 153 (1996) [621](#)
363. F. Grassi, Y. Hama, T. Kodama, Phys. Lett. B **355**, 9 (1995)
364. V.K. Magas, et al., Heavy Ion Phys. **9**, 193 (1999)
365. Y.M. Sinyukov, S.V. Akkelin, Y. Hama, Phys. Rev. Lett. **89**, 052301 (2002) [621](#), [623](#)
366. J.J. Neumann, B. Lavrenchuk, G.I. Fai, Heavy Ion Phys. **5**, 27 (1997) [621](#)
367. R.G. Newton, *Scattering Theory of Waves and Particles* (Springer, New York, NY, 1982) [621](#)
368. J. Knoll, R. Schaeffer, Ann. Phys. **97**, 307 (1976) [621](#)
369. P. Danielewicz, P. Schuck, Phys. Lett. B **274**, 268 (1992) [621](#), [628](#), [633](#)
370. H. van Hees, R. Rapp, Nucl. Phys. A **806**, 339 (2008) [621](#)
371. P. Braun-Munzinger, J. Stachel, Nucl. Phys. A **606**, 320 (1996) [626](#)
372. P. Braun-Munzinger, J. Stachel, Nucl. Phys. A **638**, 3 (1998)
373. J. Cleymans, K. Redlich, Phys. Rev. Lett. **81**, 5284 (1998)
374. P. Braun-Munzinger, J. Stachel, C. Wetterich, Phys. Lett. B **596**, 61 (2004) [626](#)
375. A. Dumitru, L. Portugal, D. Zschesche, Phys. Rev. C **73**, 024902 (2006) [626](#)
376. C. Hartnack, H. Oeschler, J. Aichelin, J. Phys. G **35**, 044021 (2008) [627](#)
377. A. Forster, et al., Phys. Rev. C **75**, 024906 (2007) [627](#)
378. H. van Hecke, H. Sorge, N. Xu, Phys. Rev. Lett. **81**, 5764 (1998) [627](#)
379. B. Hong, et al. [FOPI Collaboration], Phys. Rev. C **57**, 244 (1998) [626](#), [645](#)
380. H. Sato, K. Yazaki, Phys. Lett. B **98**, 153 (1981) [628](#)
381. E.A. Remler, Ann. Phys. **136**, 293 (1981) [628](#)
382. T. Csörgő, J. Phys. Conf. Ser. **50**, 259 (2006) [628](#), [633](#)
383. S.S. Padula, Braz. J. Phys. **35**, 70 (2005) [628](#), [633](#)
384. U.A. Wiedemann, U.W. Heinz, Phys. Rep. **319**, 145 (1999) [628](#), [630](#), [631](#)
385. G. Goldhaber, et al., Phys. Rev. Lett. **3**, 181 (1959) [629](#)
386. G.I. Kopylov, Phys. Lett. B **50**, 472 (1974) [629](#)
387. S. Pratt, Phys. Rev. Lett. **53**, 1219 (1984) [629](#), [630](#), [632](#)
388. G.F. Bertsch, Nucl. Phys. A **498**, 173c (1989) [630](#), [632](#)

389. L.V. Razumov, H. Feldmeier, Phys. Lett. B **377**, 129 (1996) [630](#)
390. G.F. Bertsch, P. Danielewicz, M. Herrmann, Phys. Rev. C **49**, 442 (1994) [630](#)
391. M.A. Lisa, S. Pratt, R. Soltz, U. Wiedemann, Ann. Rev. Nucl. Part. Sci. **55**, 357 (2005) [630](#)
392. M. Gyulassy, S.K. Kauffmann, L.W. Wilson, Phys. Rev. C **20**, 2267 (1979) [630](#), [634](#)
393. G.A. Miller, J.G. Cramer, J. Phys. G **34**, 703 (2007) [631](#)
394. M. Gyulassy, Lect. Notes Phys. **583**, 37 (2002) [633](#)
395. E.E. Kolomeitsev, C. Hartnack, H.W. Barz, M. Bleicher, E. Bratkovskaya, W. Cassing, L.W. Chen, P. Danielewicz, C. Fuchs, T. Gaitanos, C.M. Ko, A. Larionov, M. Reiter, G. Wolf, J. Aichelin, J. Phys. G **31**, 741 (2005) [641](#)
396. H. Stöcker, W. Greiner, Phys. Rep. **137**, 277 (1986) [643](#)
397. S. Yildirim, T. Gaitanos, M.D. Toro, V. Greco, Phys. Rev. C **72**, 064317 (2005) [643](#)
398. P. Ring, D. Vretenar, B. Podobnik, Nucl. Phys. A **598**, 107 (1996) [643](#)
399. H. Mütter, A. Polls, Prog. Part. Nucl. Phys. **45**, 243 (2000) [644](#)
400. X.R. Zhou, G.F. Burgio, U. Lombardo, H.J. Schulze, W. Zuo, Phys. Rev. C **69**, 018801 (2004) [644](#)
401. B. ter Haar, R. Malfliet, Phys. Rep. **149**, 207 (1987) [644](#)
402. R. Brockmann, R. Machleidt, Phys. Rev. C **42**, 1965 (1990)
403. T. Gross-Boelting, C. Fuchs, A. Faessler, Nucl. Phys. A **648**, 105 (1999)
404. E. van Dalen, C. Fuchs, A. Faessler, Nucl. Phys. A **744**, 227 (2004) [644](#)
405. T. Gaitanos, C. Fuchs, H.H. Wolter, A. Faessler, Eur. Phys. J. A **12**, 421 (2001) [644](#), [649](#), [650](#), [651](#)
406. C. Fuchs, T. Gaitanos, Nucl. Phys. A **714**, 643 (2003) [644](#), [650](#), [651](#)
407. B.D. Serot, J.D. Walecka, Adv. Nucl. Phys. **16**, 1 (1988) [644](#)
408. B. Blättel, V. Koch, U. Mosel, Rep. Prog. Phys. **56**, 1 (1993) [644](#), [651](#)
409. P. Danielewicz, Nucl. Phys. A **314**, 465 (1979) [644](#)
410. H. Stoecker, W. Greiner, Phys. Rep. **137**, 277 (1986) [644](#), [645](#)
411. P. Danielewicz, et al., Phys. Rev. C **38**, 120 (1988) [646](#)
412. P. Danielewicz, Phys. Rev. C **51**, 716 (1995) [644](#)
413. W. Reisdorf, et al. [FOPI Collaboration], Nucl. Phys. A **612**, 493 (1997) [645](#)
414. P. Danielewicz, R. Lacey, W.G. Lynch, Science **298**, 1592 (2002) [645](#), [646](#), [649](#), [650](#)
415. P. Danielewicz, M. Gyulassy, Phys. Lett. B **129**, 283 (1983) [646](#)
416. P. Danielewicz, G. Odyniec, Phys. Lett. B **157**, 146 (1985) [646](#)
417. J.Y. Ollitrault, arXiv:nucl-ex/9711003 (1997) [646](#)
418. J.Y. Ollitrault, Nucl. Phys. A **638**, 195 (1998) [646](#)
419. M.D. Partlan, et al. [EOS Collaboration], Phys. Rev. Lett. **75**, 2100 (1995) [647](#), [648](#), [650](#)
420. W. Reisdorf, H.G. Ritter, Ann. Rev. Nucl. Part. Sci. **47**, 663 (1997) [647](#), [648](#)
421. N. Herrmann, J.P. Wessels, T. Wienold, Ann. Rev. Nucl. Part. Sci. **49**, 581 (1999) [647](#), [648](#)

- 422. H.H. Gutbrod, A.M. Poskanzer, H.G. Ritter, Rep. Prog. Phys. **52**, 1267 (1989) [648](#)
- 423. H.H. Gutbrod, et al., Phys. Rev. C **42**, 640 (1990)
- 424. J. Barrette, et al. [E877 Collaboration], Phys. Rev. C **55**, 1420 (1997)
- 425. H. Liu, et al. [E895 Collaboration], Phys. Rev. Lett. **84**, 5488 (2000) [650](#)
- 426. A. Wetzler, et al. [NA49 Collaboration], Nucl. Phys. A **715**, 583 (2003)
- 427. M.M. Aggarwal, et al. [WA98 Collaboration], Nucl. Phys. A **638**, 459 (1998) [648](#)
- 428. S.A. Voloshin, Nucl. Phys. A **715**, 379 (2003) [648](#)
- 429. C. Adler, et al. [STAR Collaboration], Phys. Rev. C **66**, 034904 (2002) [648](#)
- 430. J. Adams, et al. [STAR Collaboration], Phys. Rev. Lett. **92**, 112301 (2004) [648](#)
- 431. J.Y. Ollitrault, Phys. Rev. D **46**, 229 (1992) [648](#)
- 432. P. Kolb, J. Sollfrank, U. Heinz, Phys. Lett. B **459**, 667 (1999)
- 433. P. Kolb, J. Sollfrank, U. Heinz, Phys. Rev. C **62**, 054909 (2000) [648](#)
- 434. S.A. Voloshin, A.M. Poskanzer, Phys. Lett. B **474**, 27 (2000) [649](#)
- 435. H. Petersen, M. Bleicher, Eur. Phys. J. C **49**, 91 (2007) [649](#)
- 436. A. Hombach, W. Cassing, S. Teis, U. Mosel, Eur. Phys. J. A **5**, 157 (1999) [649](#)
- 437. P. Danielewicz, Nucl. Phys. A **673**, 275 (2000) [649](#), [650](#)
- 438. P. Danielewicz, et al., Phys. Rev. Lett. **81**, 2438 (1998) [649](#)
- 439. C. Pinkenburg, et al. [E895 Collaboration], Phys. Rev. Lett. **83**, 1295 (1999) [649](#), [650](#)
- 440. A. Andronic, et al. [FOPI Collaboration], Nucl. Phys. A **661**, 333 (1999) [650](#)
- 441. A. Andronic, et al. [FOPI Collaboration], Phys. Rev. C **64**, 041604 (2001)
- 442. A. Andronic, et al. [FOPI Collaboration], Phys. Rev. C **67**, 034907 (2003)
- 443. G. Stoicea, et al. [FOPI Collaboration], Phys. Rev. Lett. **92**, 072303 (2004)
- 444. A. Andronic, et al. [FOPI Collaboration], Phys. Lett. B **612**, 173 (2005) [650](#)
- 445. P. Danielewicz, arXiv:nucl-th/0512009 (2005) [650](#), [662](#), [664](#)
- 446. A.B. Larionov, W. Cassing, C. Greiner, U. Mosel, Phys. Rev. C **62**, 064611 (2000) [650](#), [651](#)
- 447. D. Persram, C. Gale, Phys. Rev. C **65**, 064611 (2002) [650](#), [651](#)
- 448. J. Barrette, et al. [E877 Collaboration], Phys. Rev. C **56**, 3254 (1997) [650](#)
- 449. T. Gaitanos, C. Fuchs, H.H. Wolter, Nucl. Phys. A **741**, 287 (2004) [651](#)
- 450. T. Maruyama, W. Cassing, U. Mosel, S. Teis, K. Weber, Nucl. Phys. A **573**, 653 (1994) [651](#)
- 451. C. Alt, et al., Phys. Rev. C **68**, 034903 (2003) [651](#)
- 452. L.P. Csernai, D. Rohrich, Phys. Lett. B **458**, 454 (1999) [652](#)
- 453. S.S. Adler, et al. [PHENIX Collaboration], Phys. Rev. Lett. **91**, 182301 (2003) [652](#)
- 454. B.B. Back, et al. [PHOBOS Collaboration], Phys. Rev. C **72**, 051901 (2005) [652](#), [653](#)

- 455. J. Bleibel, G. Bureau, A. Faessler, C. Fuchs, Phys. Rev. C **76**, 024912 (2007) [652](#), [653](#)
- 456. D. Molnar, S.A. Voloshin, Phys. Rev. Lett. **91**, 092301 (2003) [653](#)
- 457. I. Arsene, et al., Nucl. Phys. A **757**, 1 (2005) [653](#)
- 458. J. Adams, et al., Nucl. Phys. A **757**, 102 (2005)
- 459. K. Adcox, et al., Nucl. Phys. A **757**, 184 (2005) [653](#)
- 460. U.W. Heinz, P.F. Kolb, Nucl. Phys. A **702**, 269 (2002) [653](#)
- 461. D. Teaney, Phys. Rev. C **68**, 034913 (2003) [653](#)
- 462. P. Kovtun, D.T. Son, A.O. Starinets, Phys. Rev. Lett. **94**, 111601 (2005) [653](#)
- 463. B.I. Abelev, et al. [STAR Collaboration], Phys. Rev. C **75**, 054906 (2007) [653](#)
- 464. V. Koch, A. Majumder, J. Randrup, Phys. Rev. C **72**, 064903 (2005) [654](#)

Part IV

Observables and Predictions

Conveners:

P. Senger^{1,a} and E. Bratkovskaya³

Authors, who contributed to the various chapters or sections given in brackets:

A. Andronic¹ [4, 8], R. Averbeck¹ [7], R. Bellwied⁶ [3.2, 3.3], E. Bratkovskaya³ [4–9], V. Friese¹ 3.3], C. Fuchs⁵ [3.1], J. Knoll^{1,4} [9, 9.2, 9.3] J. Randrup² [9], P. Senger^{1,a} [1, 3, 4–9], J. Steinheimer³ [10]

Affiliations:

¹GSI Helmholtzzentrum für Schwerionenforschung, Darmstadt, Germany; ²Lawrence Berkeley National Laboratory, Berkeley, CA, USA; ³University of Frankfurt, Frankfurt, Germany; ⁴University of Heidelberg, Heidelberg, Germany; ⁵Martin-Gerbert-Gymnasium, Horb am Neckar, Germany; ⁶Wayne State University, Detroit, MI, USA

Support:

^aEU, FP6 Hadron Physics (I3HP) under Contract number RII3-CT-2004-506078

Chapter 1

Introduction

In the laboratory hot and dense nuclear matter can be generated in a wide range of temperatures and densities by colliding atomic nuclei at high energies. In the collision zone, the matter is heated and compressed to a "fire-ball" for a very short period of time. At moderate collision energies, nucleons are excited to short-lived states (baryonic resonances) which decay by the emission of mesons. At higher collisions energies and thus at higher temperatures, also baryon-antibaryon pairs are created. This mixture of baryons, antibaryons and mesons, all strongly interacting particles, is generally called hadronic matter, or baryonic matter if baryons prevail. At very high temperatures or densities the hadrons melt, and their constituents, the quarks and gluons, form a new phase, the Quark-Gluon Plasma. High-energy heavy-ion collision experiments provide the unique possibility to create and investigate these extreme states of matter, and, therefore, address fundamental aspects of QCD: (i) the equation-of-state of strongly interacting matter at high temperatures and high net-baryon densities, (ii) the microscopic structure of strongly interacting matter as function of temperature and baryon density, such as hadronic and partonic phases, (iii) the location of the phase transitions and critical points, and (iv) the in-medium modifications of hadrons which might be related to the restoration of chiral symmetry.

The nuclear matter equation of state plays an important role for the dynamics of core collapse supernova and for the stability of neutron stars. In type II supernova explosions, symmetric nuclear matter is compressed to 2–3 times saturation density ρ_0 . Such conditions have been realized in heavy-ion collisions at BEVALAC/GSI-SIS18 beam energies (up to about 2 AGeV), although the temperatures reached in nuclear collisions are higher than those in the core of a supernova. Heavy-ion experiments at BEVALAC/GSI-SIS18 discovered the collective flow of nucleons, and studied in detail the production of pions and strange particles. In particular the data on strangeness production obtained at SIS18 provided evidence for a soft nuclear matter equation-of-state, and for the modification of kaon properties in dense nuclear matter. Moreover, pioneering studies of electromagnetic radiation from

the fireball via the measurement of electron-positron pairs were performed at the BEVALAC in order to obtain information on the in-medium properties of vector mesons. At GSI, the 2nd generation High Acceptance Dilepton Spectrometer (HADES) has been installed and started data production.

The experiments at BNL-AGS (using gold beams of energies between 2 and 11 AGeV) measured the yields and momentum spectra of various particle species in heavy-ion collisions, and established the scenario of an expanding thermalized source with a common chemical freeze-out temperature for all particles. A major achievement of the experiments at AGS was the measurement of the excitation function of collective flow of protons as a probe of the equation-of-state of dense nuclear matter.

Experiments at CERN-SPS (using lead beams of energies between 10 and 160 AGeV) extended the list of hadrons observed in heavy-ion collisions up to multi-strange hyperons, and confirmed the picture of a chemically equilibrated fireball. The particle yields and event-wise fluctuations measured in Pb+Pb collisions exhibit intriguing features at low SPS energies, which have been interpreted as signatures for the onset of deconfinement. The observation of a strong suppression of the charmonium yield in central collisions supported the idea of Debye screening of charmonium in quark-gluon matter. Measurements of electron-positron pairs and muon pairs found an enhanced dilepton yield at invariant masses between $0.2 \text{ GeV}/c^2$ and $1 \text{ GeV}/c^2$, an effect which is interpreted as a contribution from ρ mesons with a modified in-medium mass distribution.

Experimental observations at RHIC provided strong evidence for the creation of partonic matter at the highest collision energies reached so far ($\sqrt{s_{NN}}=200 \text{ GeV}$). This interpretation is based on three major discoveries: the large azimuthal anisotropy of particle emission in noncentral collisions (elliptic flow), the scaling of this anisotropy with the number of constituent quarks (constituent quark scaling), and the suppression of high-energetic particles traversing the medium (“jet-quenching”).

According to lattice QCD calculations the critical energy densities for the formation of a quark-gluon plasma is $E_c = 1.15 \pm 0.3 \text{ GeV}/\text{fm}^3$ [1]. Estimates based on the Bjorken formula [2] for the energy density achieved in central Au+Au collisions suggest that this value of E_c is by far exceeded in the initial phase of collisions at Relativistic Heavy-Ion Collider (RHIC) energies. On the other hand, critical energy densities in the order of $E_c = 1 \text{ GeV}/\text{fm}^3$ might already be reached at beam energies of $\sim 10 \text{ AGeV}$, and thus also in heavy-ion collisions at FAIR energies [3–5].

The analysis of particle yields and their ratios measured in heavy-ion collisions from AGS to RHIC energies using a thermal (statistical) model finds a limiting chemical freeze-out temperature of about 160 MeV above a kinetic beam energy of about 30 AGeV [6]. This nontrivial observation might reflect a change in the degrees-of-freedom of the fireball at low-SPS energies. The freeze-out temperature is roughly compatible with the critical temperatures of $T_c = 150\text{--}190 \text{ MeV}$ found in lattice QCD calculations at zero quark chem-

ical potential [7, 8]. According to these calculations the phase transition at vanishing quark chemical potential is a cross over [9]. On the other hand, most models predict the transition at zero temperature and finite density to be of first order. Then, the first-order transition line has to end in a critical point (for a review see [10]). Lattice QCD calculations, however, have not yet reached conclusion on whether the QCD critical endpoint exists, and if yes, where it is located [7, 11–13]. A theoretical answer to these questions is expected from more realistic calculations based on physical quark masses and a more accurate continuum extrapolation.

Experiments at top SPS and RHIC energies so far did not find indications of the QCD critical point. Theoretical predictions suggest that the first order transition and the critical endpoint are located at large baryo chemical potentials which are well in reach for low SPS and FAIR energies. A careful beam energy scan will be required to possibly discover these most prominent landmarks of the QCD phase diagram. In order to obtain a consistent picture one has to investigate a comprehensive set of observables, and to search for a non-monotonous behaviour in the excitation functions. The challenge is to identify signatures of the partonic phase, of the coexistence phase, or of the critical point which survive hadronization. It is obvious that those observables which are generated in the early phase of the collision and which are not distorted by final-state interactions during the evolution of the fireball, are the most promising candidates in this respect.

One of the observables which develop early is the elliptic flow, as it senses the initial anisotropic fireball shape in coordinate space. An important question is whether the hadron elliptic flow still remembers its partonic origin, as it is suggested by the data obtained at RHIC: the observed elliptic flow is extremely large, and its strength scales with the number of constituent quarks, independent of the quark flavor content. Will this scaling feature disappear below a certain beam energy? The answer to this question requires a beam energy scan of the elliptic flow of pions, kaons, ϕ mesons, D mesons, charmonium, as well as of nucleons, and (multi-) strange hyperons (including the antiparticles). Particularly sensitive probes of the partonic phase are ϕ mesons and particles containing charm quarks due to their small hadronic cross sections. The experimental challenge is to measure all these particles up to high transverse momenta. This would also allow to search for the disappearance of the suppression of high energetic particles at a given beam energy as a signature for the phase transition.

The microscopic properties of QCD matter vary with temperature and density. The structure of hot and dense hadronic matter as created in energetic heavy-ion collisions is strongly related to the spectral properties of the hadrons and their interactions in the medium. Therefore, the investigation of hadronic excitations will shed light on the conditions inside the fireball. The in-medium properties of strange and charmed hadrons are not directly measurable, but might be extracted from their abundance, phase-space distributions, and flow pattern. Using electromagnetic radiation as a probe, one

can study the in-medium modifications of light vector mesons. The dilepton observable accumulates information on the entire collision history, and, thus, provides an undistorted insight into the hot and dense phase [14].

The dissociation of charmonium due to Debye-screening in the QGP has been proposed as a signature for the deconfined phase [15]. Lattice QCD calculations predict different dissociation temperatures for the various charmonium states. As a consequence, the observation of sequential melting of ψ' and J/ψ mesons has been predicted as an indication for the onset of deconfinement [16, 17].

Another sensitive probe of the structure of strongly interacting matter are the charm diffusion coefficients which differ for the QGP as compared to the hadronic phase [18]. These coefficients will affect significantly both the nuclear suppression factor and the elliptic flow of D mesons in a consistent way (see Sect. 5.2.2). Moreover, the relative yields of hadrons containing charm quarks (D^+ , D^- , D^0 , D_s , J/ψ , ψ' , Λ_c) may allow to distinguish whether the early phase is partonic or hadronic [19]. Possible in-medium effects on the D meson are expected to modify the observed ratio of ψ' to J/ψ .

Particle correlations – in particular strange particle correlations – might serve as indication for a phase coexistence which is expected to cause clustering or clumping of particles in the spinodal region. Nonstatistical fluctuations of charges, particle abundances or mean transverse momenta measured event-by-event have been proposed as a signature for critical opalescence which might occur at the critical endpoint.

The research program outlined above requires the measurement of light, strange and charmed hadrons, of vector mesons decaying into lepton pairs, of yields, momentum distributions, collective flow, correlations and fluctuations. These measurements have to be performed in nucleus–nucleus, proton–nucleus, and proton–proton collisions at different beam energies. A selection of the available experimental information, its theoretical interpretation, and predictions for FAIR energies will be presented in the following.

Chapter 2

Exploring the QCD phase diagram

High-energy heavy-ion collision experiments provide the unique opportunity to explore the QCD phase diagram, and to investigate the properties of strongly interacting matter under extreme conditions. At very high beam energies as available at RHIC and LHC the research programs concentrate on the study of the properties of deconfined QCD matter at very high temperatures and almost zero net baryon densities, whereas at moderate beam energies (SPS and FAIR) experiments focus on the search for structures in the QCD phase diagram such as the critical endpoint, the predicted first order phase transition between hadronic and partonic matter, and the chiral phase transition. The critical endpoint and the first order phase transition are expected to occur at finite baryo chemical potential and moderate temperatures. In the following we briefly review what is known from experiment about the QCD phase diagram.

The statistical model as outlined in [Part I](#) is a unique tool to relate experimental data to the phase diagram of hadronic matter [\[20–22\]](#). Particle yields or ratios measured at different beam energies and analyzed with the statistical model provide sets of thermal parameters, temperature (T) and baryo-chemical potential (μ_b), which establish a “line of chemical freeze-out” [\[23–25\]](#). The results of the fits to experimental data are shown in a phase diagram of hadronic and quark-gluon matter in [Fig. 2.1](#) [\[6\]](#) which is an updated version of the diagram shown in [\[26\]](#). Full points are from fits to particle yields observed at midrapidity, open points refer to yields measured over the full solid angle (4π). The dashed-dotted line – which roughly follows the freeze-out points – corresponds to a constant total baryon density of $n_b=0.12\text{ fm}^{-3}$. The open triangle in [Fig. 2.1](#) represents the QCD critical endpoint predicted by Fodor and Katz [\[11\]](#). According to this lattice QCD result, the experimental freeze-out points are located in the vicinity of the critical point.

The thermal model is based on the assumption of a common chemical freeze-out temperature for all particles independent of their inelastic interaction cross sections. Given the fact that the fireball expands and therefore potentially cools during the freeze-out process, cf. [Sect. 5.8](#) in [Part III](#), the

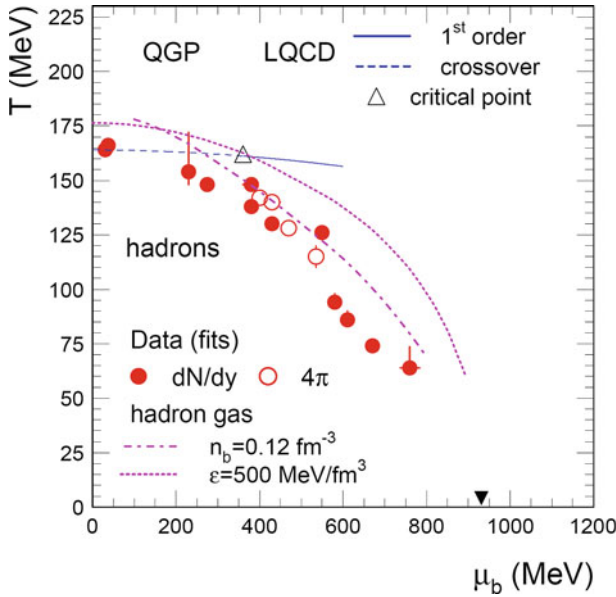


Fig. 2.1 The phase diagram of hadronic and quark-gluon matter in the T - μ_b plane. The experimental values for the chemical freeze-out are shown together with results of lattice QCD calculations, the predicted critical point is marked by the open triangle [11]. Also included are calculations of freeze-out curves for a hadron gas at constant energy density ($\varepsilon=500$ MeV/fm³) and at constant total baryon density ($n_b=0.12$ fm⁻³). The *full triangle* indicates the location of ground state nuclear matter (atomic nuclei). Taken from [6]

assumption of a common and well defined freeze-out temperature is far from being obvious and deserves justification. One possible scenario could be that the freeze-out occurs sufficiently shortly after a first-order phase transition. The latent heat released during phase coexistence can then stabilize the temperature during the subsequent freeze-out process. Moreover, there is an ongoing debate on strangeness equilibration in nuclear collisions. According to the thermal model analysis of Becattini et al. strangeness is not fully saturated at top SPS energies and below [27]. These authors also claim that, dependent on centrality, recent RHIC data on strange-particle production can be explained by a superposition of a fully equilibrated hadron gas, and particle emission from single independent nucleon-nucleon collisions in the outer corona of the collision zone. Finally, the statistical models achieve best fits ignoring effects of in-medium modifications of hadrons in the fireball. Thermal model calculations assuming mass modifications showed significant effects on the resulting yields. This finding implies that the number of frozen-out particles is practically not influenced by their properties in the dense medium.

Figure 2.2 presents a comparison of the thermodynamic parameters T and μ_B extracted from the transport models in the central overlap regime of Au+Au collisions [28–30]. The symbols represent temperatures T and

chemical potentials μ_B extracted from UrQMD 1.3 transport calculations for central Au+Au (Pb+Pb) collisions at kinetic beam energies of 11, 40, 160 AGeV and at $\sqrt{s} = 200$ AGeV at various time steps. The open symbols denote non-equilibrium configurations and correspond to T parameters extracted from the transverse momentum distributions, whereas the full symbols denote equilibrium configurations which means that the momentum distributions are isotropic. The solid line in Fig. 2.2 characterizes the universal chemical freeze-out line from Cleymans et al. [24, 25], and the full dots with error bars denote the chemical freeze-out parameters – determined from the thermal model fits to the experimental ratios – taken from [24, 25]. Figure 2.2 also contains the predictions for the location of the critical endpoint as extracted from lattice QCD calculations by Karsch et al. [7] (large open circle) and Fodor et al. [8] (large open square).

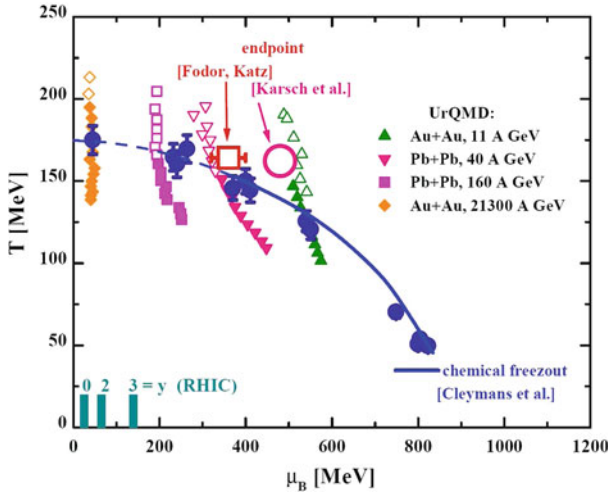


Fig. 2.2 Schematic phase diagram in the T - μ_B plane. The *solid line* characterizes the universal chemical freeze-out line from Cleymans et al. whereas the *full dots* (with *error bars*) denote the chemical freeze-out parameters from [24, 25]. The various symbols represent temperatures T and chemical potentials μ_B extracted from UrQMD 1.3 transport calculations in central Au+Au (Pb+Pb) collisions at 21.3 ATeV, 160, 40 and 11 AGeV [28, 29]. The *large open circle* and the *square* indicate the critical endpoints from lattice QCD calculations by Karsch et al. [7] and Fodor et al. [8], respectively. The picture is taken from [31]

Figure 2.3 presents dynamical trajectories in the T - μ_B plane as calculated for central Pb+Pb collisions at various beam energies with a 3-fluid hydrodynamical model [32]. The bold parts of the trajectories indicate that the system has reached approximate equilibration. The dotted line represents the freeze-out curve as determined by [24, 25] under the condition that the energy per hadron is 1 GeV. These trajectories depend strongly on the equation of state (EoS) which in this case is purely hadronic, i.e. no phase transition

is included. Therefore, the calculations only provide a rough estimate of the beam energies which are relevant for the search for the expected deconfinement phase transition, or for the QCD critical endpoint as predicted by [33] and marked by the star in Fig. 2.3.

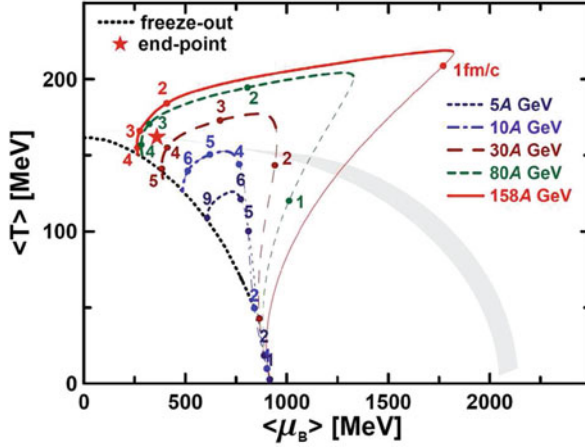


Fig. 2.3 Dynamical trajectories in the T - μ_B plane for central Pb+Pb collisions ($b = 2.5$ fm) at various incident energies calculated with a 3-fluid hydrodynamical model [32]. Numbers near the trajectories correspond to time steps (in fm/c) in the c.m. frame of the colliding nuclei. Bold parts of trajectories indicate an approximately thermalized baryon-rich subsystem. The dotted line represents the freeze-out curve determined by a thermal model [24, 25]. The critical end-point calculated in [33] is marked by the star

McLerran and Pisarski [34] have proposed the existence of a new state of matter at moderate temperatures and high net baryon density. This new phase appears due to a separation of the chiral and deconfinement phase transitions at finite baryon density, and exhibits features of both baryonic and quark matter. The phase is confined and chirally symmetric. The argument here is that at sufficiently high density and temperature one would generate a very large Fermi sea which is mostly well described as a quark sea. But when the quarks are within Λ_{QCD} of the Fermi surface confinement will force the quarks to convert to colorless states, i.e. baryons. The combination of both parts can be viewed as a “quarkyonic” system. For smaller values of the quark chemical potential which equals M/N_c the baryonic skin will increase its thickness and once the chemical potential is close to Λ_{QCD} the system freezes out into nuclear matter.

In conclusion, beam energies between 10 and 40 AGeV are expected to be well suited to produce nuclear matter under extreme conditions, and to explore the QCD phase diagram at high baryon densities. The experimental task is to systematically measure the relevant observables for various beam energies, and to search for structures in the excitation functions. First indica-

tions of a non-monotonous behaviour of particle ratios were found in central Pb+Pb collisions around 30 AGeV at the SPS by NA49 [35]. These measurements will be repeated by experiments at RHIC running at beam energies close to or even below injection energy [36]. A comprehensive experimental program – which for the first time includes measurements of very rare diagnostic probes at moderate beam energies – will be performed at FAIR with the Compressed Baryonic Matter (CBM) experiment.

Chapter 3

Review of experimental observations

3.1 Probing dense nuclear matter: results from GSI

The study of strangeness production in heavy-ion collisions addresses fundamental questions in nuclear and astrophysics such as the equation of state (EoS) at high baryon densities and the modification of hadron properties in dense and hot hadronic or baryonic matter. K^+ mesons have been proposed already many years ago as a promising diagnostic probe for the nuclear equation of state at high densities. Microscopic transport calculations indicate that the yield of kaons created in collisions between heavy nuclei at sub-threshold beam energies ($E_{beam} = 1.58$ GeV for $NN \rightarrow K^+ \Lambda N$) is sensitive to the compressibility of nuclear matter at high baryon densities [37, 38]. This sensitivity is due to the production mechanism of K^+ mesons. At subthreshold beam energies, the production of kaons requires multiple nucleon-nucleon collisions or secondary collisions such as $\pi N \rightarrow K^+ \Lambda$. These processes are expected to occur predominantly at high baryon densities, and the densities reached in the fireball depend on the nuclear EoS (For a review see [39]).

The properties of kaons and antikaons are expected to be modified in dense baryonic matter (see e.g. [40–42]). In mean-field calculations, this effect is caused by a repulsive K^+N potential and an attractive K^-N potential. As a consequence, the total energy of a kaon at rest in nuclear matter increases and the antikaon energy decreases with increasing density. It has been speculated that an attractive K^-N potential will lead to Bose condensation of K^- mesons in the core of compact stars above baryon densities of about 3 times saturation density [43]. According to G. Brown and H. Bethe this effect has dramatic consequences for the stability of neutron stars and the formation of low mass black holes [44]. This scenario is supported by recent self-consistent coupled-channel calculations which find a narrow structure in the antikaon in-medium spectral function at low energies for twice saturation density [45].

Strangeness is exactly conserved during a nuclear collision. Open strangeness can be produced by the creation of kaon ($K^+(u\bar{s}), K^0(d\bar{s})$) - antikaon ($K^-(\bar{u}s), \bar{K}^0(\bar{d}s)$) pairs or by kaon-hyperon pairs. The hyperons carrying one strange quark are $\Lambda(uds)$ and Σ ($\Sigma^-(dds), \Sigma^0(uds), \Sigma^+(uus)$) hyperons. The production of hidden strangeness through $\phi(s\bar{s})$ mesons is possible but suppressed according to the Okubo-Zweig-Iizuka selection rule. A consequence of strangeness conservation is the fact that K^+ mesons, once produced, cannot be absorbed by the surrounding nucleons. This results in a rather long mean free path of K^+ mesons of about 7 fm in nuclear matter. Therefore, K^+ mesons are a suitable “penetrating” probe for the dense fireball produced in heavy ion reactions at 1–2 A GeV where nuclear densities between 2–3 ρ_0 are reached. Antikaons, in contrast, are strongly coupled to the environment through strangeness exchange reactions (such as $\bar{K}N \longleftrightarrow \pi Y$ with $Y = \Lambda, \Sigma$) and the excitation of baryonic resonances (such as $\Lambda(1405)$). Hence, the mean free path of antikaons in nuclear matter is much shorter than the one of kaons.

3.1.1 Kaons in dense nuclear matter

Theory predicts strong modifications of the kaon and antikaon properties in a dense hadronic environment. Mean field models as well as chiral perturbation theory predict a repulsive K^+ potential of about $V_{K^+} \simeq +(20 - 30)$ MeV at nuclear saturation density ρ_0 . Such a value is in agreement with empirical kaon-nucleon scattering. The K^- -nucleon interaction, in contrast, is resonant around threshold and requires non-perturbative approaches. The strength of the K^- potential is still an open issue. The depth of the attractive antikaon-nucleon potential ranges from $V_{K^-} \simeq -(50 - 100)$ MeV, obtained within chiral coupled channel dynamics, to $V_{K^-} \simeq -(100 - 200)$ MeV predicted by mean field approaches and the analysis of kaonic atoms. Self-consistent coupled-channel calculations based on a chiral Lagrangian predict a dynamical broadening of the antikaon spectral function in dense nuclear matter [45–48]. A particularly interesting result is the prediction of a sizable population of soft antikaon modes that arise from the coupling of the antikaon to a highly collective $\Lambda(1115)$ nucleon-hole state at twice nuclear matter density [45]. To search for evidences of these medium modifications was one of the major goals of the KaoS and FOPI experiments at SIS18 where kaons and antikaons were measured below and at threshold energies.

3.1.1.1 Total yields

Various transport models meanwhile provide a relatively consistent picture concerning the net potential effect on the K^+ meson multiplicities. The

repulsive mean field leads to a reduction of the yields by 30–50%, depending on the actual strength of the potential, the system size and the energy of the reaction. The magnitude of the reduction within different transport model realizations can be read off from Figs. 3.1 and 3.5. The reduction of the K^+ yield due to the repulsive potential is, as expected, slightly larger in heavy systems than in light systems and most pronounced at energies far below threshold.

The results obtained by several independent groups, i.e. the Tübingen group (RQMD) [39, 49], the Texas and Stony Brook groups (RBUU) [43, 50], the Nantes group (IQMD) [51] and the Giessen group (HSD) [52] converged to the conclusion that the measured K^+ yield can only be reproduced when taking into account a repulsive K^+N potential. This fact is demonstrated by Fig. 3.1 which compares K^+ rapidity distributions in Ni+Ni reactions at 1.93 AGeV obtained with RQMD, IQMD, RBUU and HSD in Ni+Ni reactions at 1.93 AGeV to data from FOPI [53] and KaoS [54]. Although the theoretical descriptions show still some variance they allow to distinguish between the scenarios with and without in-medium effects. The data clearly support the calculations which include a repulsive K^+N potential.

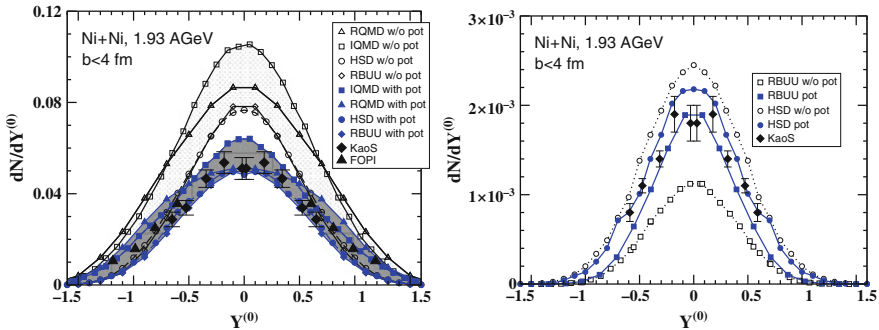


Fig. 3.1 Rapidity distributions of K^+ mesons (*left panel*) and K^- mesons (*right panel*) measured in Ni+Ni reactions at 1.93 AGeV, and compared to calculations with and without in-medium kaon and antikaon potentials: RQMD [39], IQMD [51], HSD [52] and RBUU [55]). The K^+ data have been measured by FOPI [53] and KaoS [54], the K^- data by KaoS [54]

The interpretation of K^- meson data is complicated by the fact that strangeness exchange reactions ($\pi Y \longleftrightarrow NK^-$, $Y = \Lambda, \Sigma$) play an important role in the production, propagation and freeze-out of K^- mesons. While strangeness production takes place predominantly in the early high density phase, strangeness exchange reactions are the driving processes for K^- production and absorption at later stages and at lower nuclear densities [56, 57]. In this case the attractive potential is weak, and the net effect of the in-medium potentials on the K^- yield may be small [52, 57, 58]. The same is true when less attractive K^- potentials, e.g. from coupled channel calcula-

tions, are used instead of mean fields potentials. The right panel of Fig. 3.1 depicts the rapidity distribution of K^- mesons measured by KaoS in semi-central Ni+Ni reactions at 1.93 AGeV, in comparison to results of transport calculations HSD [52] and RBUU (Texas) [55]. Both models support the K^- in-medium scenario, but on the basis of a qualitatively different behavior.

The results of the calculations depend on the density dependence of the cross section for strangeness exchange which is still a matter of investigations. The predictions obtained within coupled channel calculations range from a moderate enhancement close to threshold [59, 60] to a strong suppression [58]. A consistent treatment of these effects requires to take into account off-shell dynamics within the transport approach. First off-shell transport calculations using K^- meson spectral functions have been performed, but a satisfactory agreement with measured K^- meson spectra and angular distributions has not yet been achieved [58].

3.1.1.2 In-plane flow

Dynamical observables such as collective flow patterns are to large extent free from uncertainties in the total production rates. They depend on the phase space pattern of the primordial sources and the final state interaction. For K^+ mesons the final state interaction is well under control since only elastic (and charge exchange) reactions occur, the total elastic cross section is of the order of 10–15 mb.

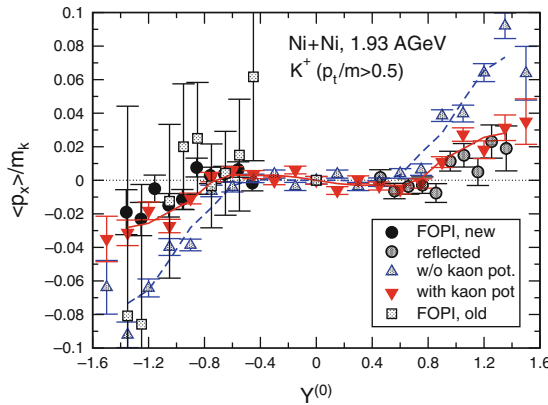


Fig. 3.2 Transverse K^+ flow in 1.93 AGeV $^{58}\text{Ni} + ^{58}\text{Ni}$ reactions at impact parameter $b \leq 4$ fm. RQMD calculations with and w/o kaon in-medium potential are compared to FOPI data [61] (old) and [62] (new). The Lorentz force is included

The transverse or in-plane flow was proposed as a promising observable to address in-medium potentials [63, 64]. A repulsive potential pushes the kaons away from the nuclear matter and produces slight anti-flow at specta-

tor rapidities and a zero flow signal around mid-rapidity. This behavior was found to be consistent with the first available flow data from FOPI [61]. Other theoretical studies predicted similar features for the kaon flow [65–68]. However, the scalar-vector type structure of the kaonic mean field implies the occurrence of a Lorentz-force [69]. The Lorentz-force from the vector field counterbalances the influence of the time-like vector potential on the K^+ in-plane flow to large extent which makes it more difficult to draw definite conclusions from transverse flow pattern. As can be seen from the flow pattern around mid-rapidity in Fig. 3.2 it is difficult to distinguish between the scenarios w/o in-medium potentials and full covariant in-medium dynamics. However, at spectator rapidities clear differences appear and the data favor again the in-medium scenario [70] with a relatively strong repulsive mean field. Similar results have been obtained in [71].

The effect of the Lorentz-force may be reduced by an explicit momentum dependence beyond mean field. Such a momentum dependence is known to reduce the nucleon flow and it is necessary in order to comply with the empirical optical nucleon-nucleus potential and nucleon flow data above 1 AGeV [72–75]. Similarly, spectra (p_{lab} , p_T and m_T) imply that the KN interaction is less repulsive at high p_T which might be an indication for an explicit momentum dependence counterbalancing the Lorentz force to some extent. Slopes obtained in central Au+Au reactions are too hard while C+C spectra are well described [71]. The FOPI Collaboration measured also the p_T dependence of v_1 in Ni+Ni and Ru+Ru reactions at spectator rapidities where a transition from anti-flow to flow with rising p_T was observed [76]. Also these data require a repulsive in-medium potential where compensation effects from Lorentz forces are necessary not to overestimate the data [71]. For a precise determination of the density *and* momentum dependence of the K^+ potential certainly more theoretical efforts are needed.

3.1.1.3 Out-of-plane flow

The phenomenon of collective flow can generally be characterized in terms of anisotropies of the azimuthal emission pattern, expressed in terms of a Fourier series

$$\frac{dN}{d\phi}(\phi) \propto 1 + 2v_1 \cos(\phi) + 2v_2 \cos(2\phi) + \dots \quad (3.1)$$

which allows a transparent interpretation of the coefficients v_1 and v_2 . The dipole term v_1 arises from a collective sideward deflection of the particles in the reaction plane and characterizes the transverse flow in the reaction plane. The second harmonic describes the emission pattern perpendicular to the reaction plane. For negative v_2 one has a preferential out-of-plane emission, called *squeeze-out*. Pions exhibit a clear out-of-plane preference [77, 78] which is due to shadowing by spectator nucleons. The short mean free path of the

pions hinders pions produced in the central reaction zone to traverse the spectator matter located in the reaction plane. Therefore it is easier for them to escape perpendicular to the reaction plane. Since the K^- mean free path is comparable to that of the pions one might expect the same phenomenon for K^- while the mean free path of K^+ mesons is large and no squeeze-out signal should be observed. These arguments hold when the final state interaction is exclusively determined by scattering and absorption processes.

First measurements of the azimuthal emission pattern of K^+ mesons [79] found that K^+ mesons are preferentially emitted perpendicular to the reaction plane, similar to the pions. In transport calculations [79–81] this effect could only be reproduced by the presence of the repulsive K^+ mean field. Elastic rescattering of K^+ mesons was found to be not sufficient to create the observed squeeze-out signal. If the repulsive potential is taken into account, the kaons are driven by potential gradients preferentially out-of-plane. Thus, the repulsive potential leads to an additional dynamical focusing out of the reaction plane.

Figure 3.3 shows the azimuthal distributions for semi-central Au+Au reactions at 1 AGeV and Ni+Ni at 1.93 AGeV [82]. In the Au+Au case we compare RQMD [39] and GiBUU [71] calculations to the KaoS data [79]. The results confirm the findings that the in-medium potential is needed in order to explain the experimental squeeze-out signal. Another interesting observation is the fact that the Lorentz force, present in covariant dynamics, has only a small influence on the out-of-plane flow, contrary to the in-plane flow discussed above [71]. The right panel of Fig. 3.3 shows also HSD results. Calculations using various transport models converge to the conclusion that the azimuthal K^+ emission pattern can be explained only by taking into account a repulsive mean field.

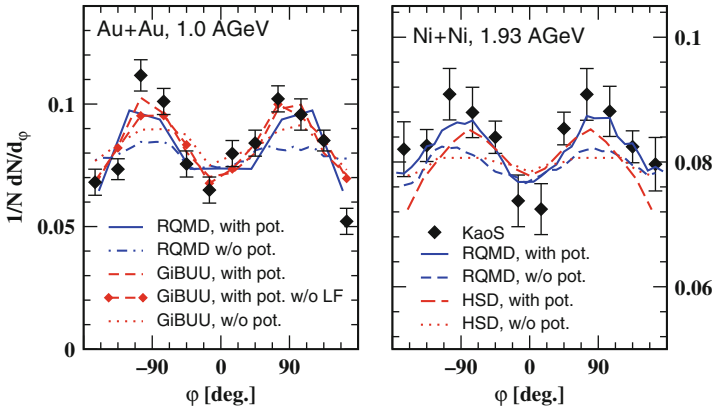


Fig. 3.3 K^+ azimuthal angular distributions in semi-central Au+Au reactions at 1.0 AGeV and Ni+Ni reactions at 1.93 AGeV. RQMD [39], GiBUU (with and without Lorentz force) [71] and HSD [83] calculations without and with in-medium potential are compared to data from KaoS [79, 82]

The interpretation of the azimuthal emission pattern of K^- mesons is less conclusive. The first predictions [81, 84] for K^- out-of-plane emission pattern exhibited an obvious scenario: due to the short mean free path K^- should behave similar like pions, i.e. they should show a clear squeeze-out signal caused by absorption and rescattering. However, the existence of an attractive K^-N potential would strongly reduce the absorption of K^- mesons, and consequently the shadowing of K^- mesons by the spectator fragments would be reduced as well. In this case the K^- mesons are expected to be emitted almost isotropically in semi-central Au+Au collisions. The observation of a flat azimuthal distribution of K^- mesons would provide strong experimental evidence for in-medium modifications of antikaons. Figure 3.4 (right panel) depicts the first data on the K^- azimuthal emission pattern measured in heavy-ion collisions which differs significantly from the corresponding K^+ pattern (left panel) [82]. The K^- data are compared to IQMD calculations without (dashed) and with (solid) K^-N -potential [51]. The attractive in-medium K^-N -potential produces an in-plane enhancement which agrees better with the data.

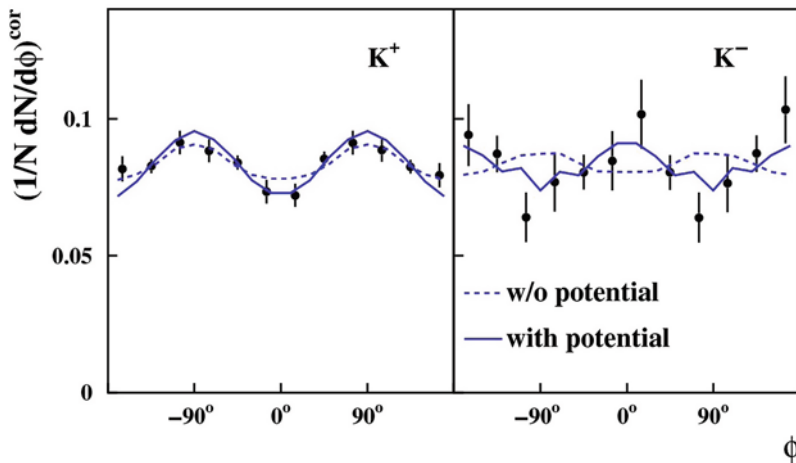


Fig. 3.4 Azimuthal distributions of K^+ and K^- mesons measured in semi-central Ni+Ni collisions at 1.93 AGeV. The data are corrected for the resolution of the reaction plane and refer to impact parameters of $3.8 \text{ fm} < b < 6.5 \text{ fm}$, rapidities of $0.3 < y/y_{\text{beam}} < 0.7$ and momenta of $0.2 \text{ GeV}/c < p_t < 0.8 \text{ GeV}/c$. The *lines* represent results of IQMD transport calculations with and without KN potential (see [85])

The flow pattern of K^- mesons is determined by the interplay between mean field and absorption. However, inside the medium the theoretical knowledge of the absorption rates is very uncertain since the corresponding absorption cross sections are predicted to have an extremely pronounced density dependence. This is due to the strong – and theoretically not well controlled – density dependency and off-shell behavior of the hyperon resonances which

govern the K^-N interaction at threshold. As shown e.g. within the HSD model [83] the emission pattern of K^- mesons depends strongly on model uncertainties concerning the in-medium K^-N cross sections. The observed emission pattern of K^- mesons is at present not fully understood, and further experimental and theoretical efforts are needed to clarify the picture.

Experiments on strangeness production in proton-nucleus collisions provide important information complementary to heavy ion reactions. Although proton-nucleus reactions only explore normal and subnormal nuclear densities, they are easier to interpret than heavy-ion collisions with their complicated dynamical evolution. Measurements of the K^+ cross section in p+Au and p+C reactions [86, 87] support the existence of a repulsive kaon potential of $V_{K^+} \sim 20 \pm 5$ MeV at the saturation density ρ_0 which is consistent with the conclusions from heavy ion reactions. Such a potential was also found to be consistent with the measured K^+ spectra in p+A reactions at subthreshold energies [88, 89].

Both K^+ and K^- meson differential cross sections have been measured in p+C and p+Au reactions at several beam energies and emission angles at SIS18/GSI [90]. The data are consistent with the assumption of a repulsive K^+N potential of $V_{K^+} = 25 \pm 5$ MeV, and an attractive K^-N potential of $V_{K^-} = -80 \pm 20$ MeV at ρ_0 .

3.1.2 Probing the nuclear equation-of-state with subthreshold kaon production

The most intriguing motivation for the first heavy-ion experiments at relativistic energies was to obtain information on the nuclear matter equation-of-state (EoS) [91]. At twice the saturation density – which should be reached in the fireball at BEVALAC/SIS energies – the difference in binding energy per nucleon between a soft and a hard Skyrme EoS is about 13 MeV. If the matter is compressed up to $3\rho_0$ the difference is already ~ 55 MeV. It was expected that the compressional energy should be released into the creation of new particles, primarily pions, when the matter expands [91]. However, pions have large inelastic cross sections, they undergo several absorption cycles through nucleon resonances [92–94], and freeze out at final stages of the reaction and at low densities. Hence, pions lose most of their sensitivity on the compression phase, and turned out not to be very suitable probes for the stiffness of the EoS.

In contrast to pions, K^+ mesons have a long mean free path in nuclear matter due to the absence of absorption reactions. Moreover, at BEVALAC/SIS energies K^+ mesons are produced preferentially in the high density phase by multiple scattering processes which are required to accumulate energy, and to overcome the energy threshold for kaon production. Therefore, K^+ mesons have been suggested as promising tools to probe the nuclear EoS [37]. This scenario was supported by the results of the first theoretical investigations

using transport models which found a strong dependence of the K^+ yield on the nuclear compressibility [38, 95–97]. On the experimental side the KaoS Collaboration performed systematic measurements of the K^+ meson yields and phase-space distributions in heavy-ion collisions at GSI/SIS18 [98–102]. These data triggered a major theoretical activity in the field of transport calculations in order to improve our understanding of K^+ meson production mechanisms in heavy-ion collisions, and to extract reliable information on the nuclear matter EoS from the data [49, 51]. Subsequent investigations of kaon production in heavy-ion collisions confirmed the robust dependence of the K^+ meson yield on the nuclear matter EoS [39, 103, 104].

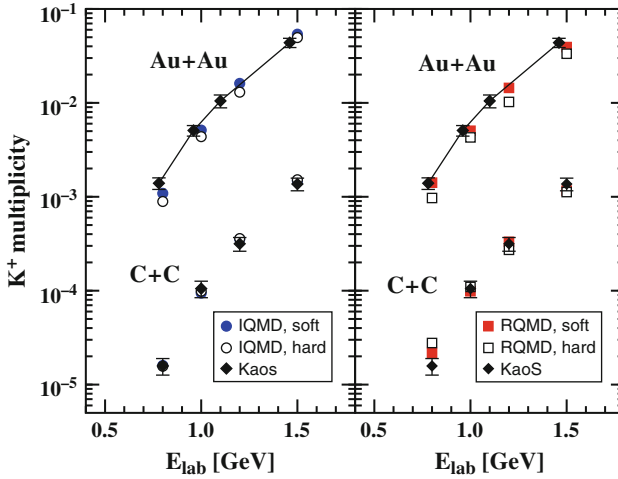


Fig. 3.5 Excitation function of the K^+ multiplicities in Au + Au and C + C reactions. RQMD [49] and IQMD [104] with in-medium kaon potential and using a hard/soft nuclear EoS are compared to data from the KaoS Collaboration [102]

Excitation functions of K^+ meson production in inclusive Au+Au and C+C collisions measured by the KaoS collaboration [100, 102] are shown in Fig. 3.5 in comparison to RQMD [39, 49] and IQMD [104] transport calculations. The kaon yield from C+C collision does not depend on the nuclear EoS, but rather on the in-medium K^+N potential. Only when taking into account a repulsive kaon-nucleon potential the calculations are able to reproduce the data. The Au+Au data are in agreement with the assumption of a nuclear matter compression modulus of $\kappa = 200$ MeV. The calculations use a momentum-dependent Skyrme interaction to determine the binding energy per nucleon.

In order to reduce systematic uncertainties both in experiment (normalization, efficiencies, acceptances) and theory (elementary cross sections) the K^+ multiplicities are plotted as ratios $(K^+/A)_{\text{Au+Au}} / (K^+/A)_{\text{C+C}}$ in the right panel of Fig. 3.6 [102]. In this representation also the in-medium effects

cancel to a large extent. The data are compared to results of different transport model calculations [39, 49, 104] which are performed with a compression modulus of $\kappa = 380$ MeV (corresponding to a “hard” EoS) and with $\kappa = 200$ MeV (corresponding to a “soft” EoS). The shaded area in Fig. 3.6 represents the range of theoretical uncertainties. The data clearly favor a soft EoS.

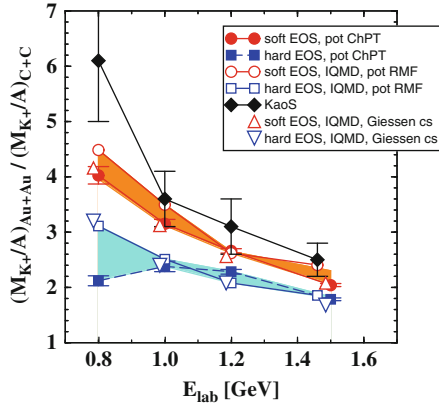


Fig. 3.6 Excitation function of the ratio R of K^+ multiplicities obtained in inclusive Au+Au over C+C reactions. RQMD [49] and IQMD [104] calculations are compared to KaoS data [102]. The shaded area indicates thereby the range of uncertainty in the theoretical models. In addition IQMD results based on an alternative set of elementary K^+ production cross sections are shown

The ratio of K^+ production excitation functions shown in Fig. 3.6 has been proven to be a very robust observable which does not depend significantly on the theoretical uncertainties of the input to the transport models such as the elementary production cross sections $N\Delta; \Delta\Delta \mapsto NYK^+$ [104]. These cross sections are not constrained by data, and their parameterizations vary by almost one order of magnitude in the different models [42, 105]. Nevertheless, the ratio R – and the conclusions drawn from it – are practically independent of the variation of the elementary cross sections, even when taking into account an additional medium dependence [104].

Figure 3.7 depicts different versions of the equation of state as predicted by different calculations [39]. The figure illustrates that it is not sufficient to determine the nuclear compressibility (which is determined by the curvature of $E/A(\rho)$ at saturation density ρ_0), but rather one has to study the response of nuclear matter at different densities, which means one has to perform nucleus-nucleus collisions at different beam energies.

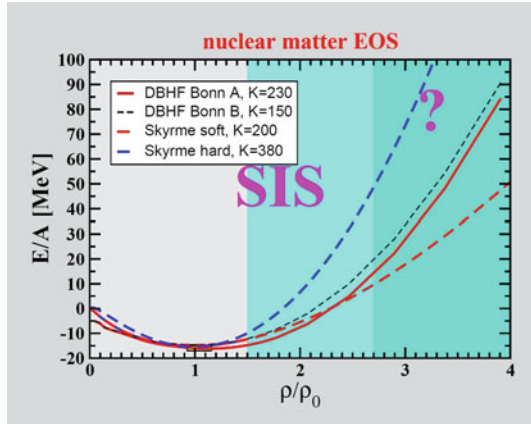


Fig. 3.7 Binding energy per nucleon as a function of the nuclear density obtained from relativistic Dirac-Brueckner Hartree-Fock calculations and from a phenomenological model based on Skyrme forces. Both approaches assume different values for the compressibility as indicated (taken from [39])

3.1.3 Conclusions

The experiments on strangeness production at GSI demonstrated how kaons can be used as diagnostic probes both for the properties of compressed nuclear matter and for the modifications of hadrons inside the dense medium. It turned out that the sensitivity of the kaon probe to medium properties is strongly enhanced if the beam energy is below the kaon production threshold energy in nucleon-nucleon collisions. We have also learned that dynamical transport models play a crucial role in the extraction of the relevant physics information from the heavy-ion data. State of the art transport calculations have reached a reasonable degree of consistency concerning K^+ meson production and dynamics. The comparison of theory to experiment concerning total yields, momentum distributions, and the collective flow pattern supports the existence of a slightly repulsive in-medium K^+N potential of $V_{K^+} = 25 \pm 5$ MeV at nuclear saturation density as predicted by chiral dynamics. This result is supported by data on K^+ meson production in proton-nucleus collisions [86–90]. A very important result of the strangeness experiments at GSI is that K^+ mesons have been proven to provide information on the compressibility of nuclear matter at densities up to twice or three times saturation density.

Due to the in-medium strangeness exchange reactions it is complicated to extract information on the K^-N potential from the measured K^- yield in heavy-ion collision at SIS18 energies. In proton-nucleus collisions – where the strangeness exchange process $\pi Y \rightarrow K^-N$ is strongly reduced – it was found that the measured K^-/K^+ ratio can be reproduced with an attractive in-medium K^-N potential of $V_{K^-} = -80 \pm 20$ MeV at saturation density

[90, 106]. However, the quasi-particle picture which underlies most of the semi-classical transport approaches, is much better justified for the kaons than for the antikaons. Microscopic coupled-channel calculations based on a chiral Lagrangian predict a dynamical broadening of the K^- meson spectral function in dense nuclear matter [45, 47, 48, 107, 108]. First off-shell transport calculations using K^- meson spectral functions have been performed [58]. The ultimate goal of the calculations is to relate the in-medium spectral function of K^- mesons to the anticipated chiral symmetry restoration at high baryon density.

3.2 Probing hot and dense hadronic matter: results from AGS

The Alternating Gradient Synchrotron (AGS) at BNL was home of a dedicated fixed target relativistic heavy-ion program from 1988 through 1999. During this decade of data taking a variety of experiments were performed. Each experiment had to re-apply for beam time when one of their programs was completed, therefore certain long standing collaborations were re-numbered several times. The two main collaborations were E802/E866/E910/E917 and E814/E877. In addition the first generation of experiments also included the initial usage of a Time Projection Chamber (TPC) by E810. The second generation featured a dedicated strangelet search experiment in E864, which also made substantial measurements in light nuclei production. The third generation featured a dedicated H-dibaryon experiment in E896, and this experiment also made substantial measurements in mid-rapidity strangeness production, in light nuclei production and in strange particle polarization. The program was rounded out by E895, an experiment which performed the only AGS energy scan measurements and utilized the EOS-TPC to obtain a multitude of measurements relevant to the CBM program. The program was performed using either Si or Au beams and using Si, Al or Au targets. The collision energies ranged from 2 to 14.5 AGeV. This is an interesting energy region because it is expected that the underlying reactions will change from being baryon dominated at the lower energies to meson dominated at the highest energies. It was also believed that these collision energies could generate the necessary conditions for a phase transition from hadronic to partonic matter. Unfortunately none of the anticipated signatures were found. The program can be considered exhaustive in terms of global observables, basic hadronic spectra, strange particle (kaon and Lambda) formation, and correlation measurements such as collective flow and Hanbury Brown-Twiss (HBT) correlations. Measurements of rare probes such as hadronic resonances, multi-strange hyperons (except for one Ξ data point at 6 AGeV), lepton pairs and charmed particles have not been performed. Also fluctuations were not addressed in depth.

In the following we will highlight the main AGS physics results that pertain to the future measurements at FAIR.

3.2.1 Identified particle spectra

Identified particle spectra have been measured extensively at the AGS by various experiments. These spectra formed the basis of initial applications of thermal model calculations to experimental spectra. It was concluded that a thermal system was reached that had a freeze-out temperature of $T = 90\text{--}130$ MeV and a baryo-chemical potential of $\mu_B = 500\text{--}600$ MeV. The system expands out radially with a mean transverse expansion velocity of $0.3\text{--}0.5c$ [23]. The rapidity distributions of pions, kaons, protons and Lambdas measured for central Au+Au collisions at 10.7 AGeV are presented in Fig. 3.8 [109]. Based on the extracted baryo-chemical potential, which is considerably higher than at SPS and RHIC one can deduce that there is a substantial amount of baryon stopping at AGS energies. The rapidity distribution of protons by E917 at a variety of energies and centralities is shown in Fig. 3.9 [110]. The plateau signals a considerable amount of stopping, however the stopping is not complete. When applying a Bjorken estimate to the boost-invariant mid-rapidity part of the spectrum we can deduce an energy density of 1.4 GeV/fm³ for the highest AGS energies, which is just above the critical energy density estimate from lattice QCD [111].

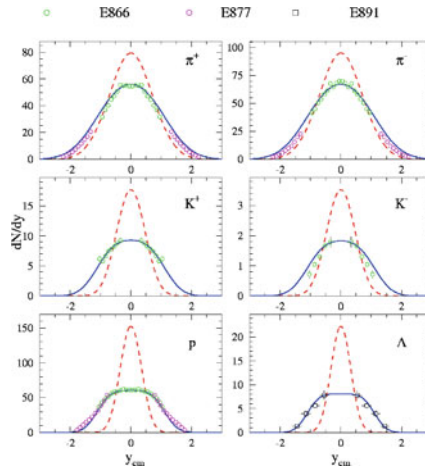


Fig. 3.8 Pion, kaon, proton, and Lambda rapidity distributions measured in central Au+Au collisions at 10.7 AGeV by different experiments. *Dashed line*: isotropic, thermal source ($T=130$ MeV). *Solid line*: longitudinally expanding source ($T=130$ MeV, $\beta_t=0.5$) (from [109])

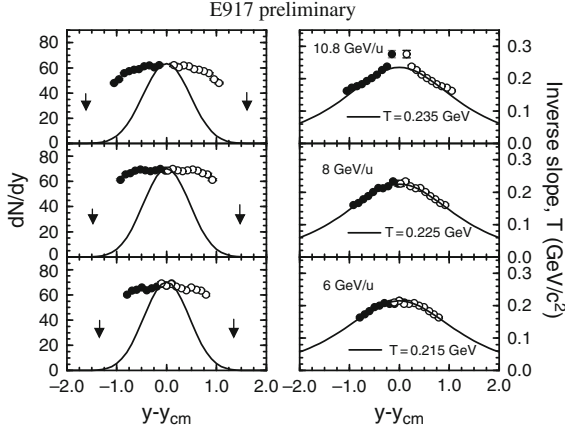


Fig. 3.9 Proton rapidity and inverse slope distributions compared to simple thermal source predictions for Au+Au collisions at three different beam energies (from [110])

3.2.2 Strange particle measurements

The excitation function of kaon production as measured by E866/E917 and its very good agreement with hadronic transport models, as shown in Fig. 3.10, indicates that the strangeness enhancement at the AGS may still be a purely hadronic effect, i.e. its cause is predominantly hadronic rescattering [112].

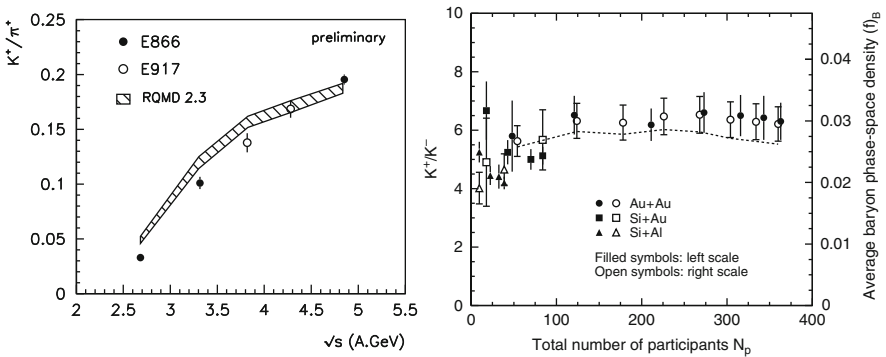


Fig. 3.10 (a) Excitation function of mid-rapidity K^+/π^+ ratio in central Au+Au collisions (from [112], b) centrality dependence of the K^+/K^- ratio (left scale and data points) as well as the average baryon phase space density at kinetic freeze-out (right scale and dashed curve) for various collision systems at the AGS (from [113])

The K^+/K^- ratio stays constant over all centralities and system sizes as is shown in Fig. 3.10. The ratio can be related to a baryon phase-space density and therefore one can conclude that the baryon phase-space density is constant at a given collision energy at the AGS. When relating these results to similar measurements at the SPS we find that the charged kaon ratio is highly correlated with the baryon phase-space density and drops with increasing collision energy [113].

E896 has also performed the only strange particle polarization measurement in a relativistic heavy ion system (Au+Au) prior to RHIC [114]. The results are shown in Fig. 3.11. It shows a Λ polarization level, as a function of x_F , that is comparable to the level measured in elementary collisions [115, 116]. The disappearance of the strange particle polarization is considered a QGP signature [117], yet these measurements indicate that strangeness hadronization in heavy ion collisions at AGS energies proceeds according to the mechanisms deduced from elementary particle collisions.

Another important strangeness measurement from the AGS is the quantitative mapping of anti-flow of neutral kaons. Figure 3.12 shows the directed sideward flow measurements by E895 at 6 A GeV collision energy [118]. This effect is likely due to a large repulsive interaction (mean field) between baryons and kaons. At lower energies FOPI measured a directed flow consistent with zero.

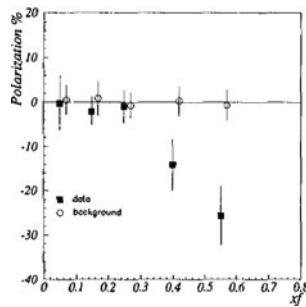


Fig. 3.11 Λ polarization as a function of x_F as measured by E896 in central Au+Au collisions at 11.6 A GeV (from [118])

Finally, multi-strange baryons (Ξ) have been successfully reconstructed at the AGS in 6 A GeV Au+Au collisions and 14.5 A GeV Si+Au Collisions by E895 and E810, respectively [119]. The results can be seen in Fig. 3.13. In both cases the yields and their centrality dependence are again well described by hadronic transport and thermal models, which seems to indicate strangeness saturation of the available phase space even at low AGS energies.

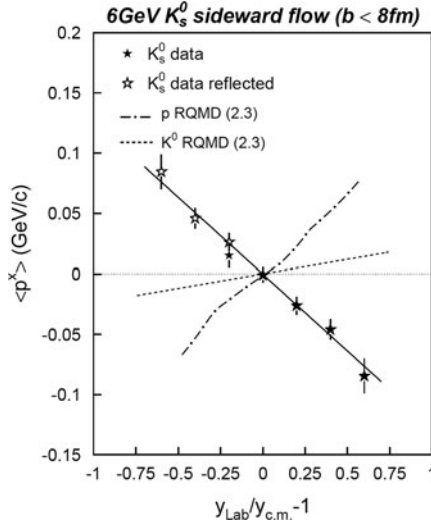


Fig. 3.12 Directed K_s^0 antiproton flow measured in 6 A GeV Au+Au collisions (from [118])

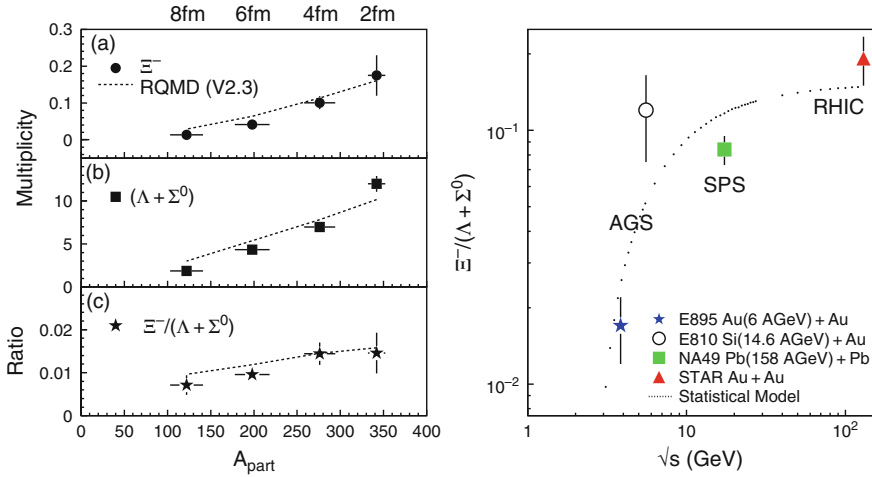


Fig. 3.13 (a) Centrality dependence of Ξ^- and $\Lambda + \Sigma$ yields, as well as $\Xi^-/(\Lambda + \Sigma)$ ratio for 6 A GeV Au+Au collisions in comparison to RQMD calculations, (b) Excitation function of $\Xi^-/(\Lambda + \Sigma)$ ratio based on E810, E895, NA49 and RHIC data (from [119])

3.2.3 Antibaryon production

One of the remaining puzzles of the AGS program is the unusually large $\bar{\Lambda}/\bar{p}$ ratio which was first measured by E878 and then confirmed subsequently by E864, E917 and the SPS experiments [120–122]. The ratio seems to exceed 3 in central Au+Au collisions at the highest AGS energies as shown in Fig. 3.14.

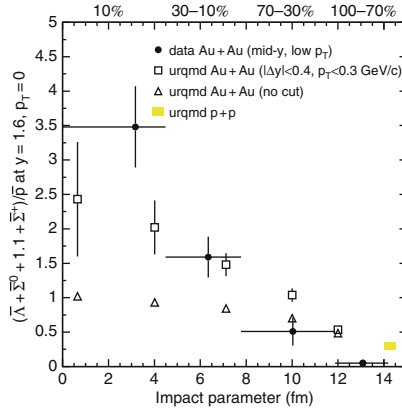


Fig. 3.14 Measurements of the $\bar{\Lambda}/\bar{p}$ ratio at mid-rapidity and low p_T as a function of impact parameter compared to UrQMD calculations (from [113])

The interpretation is complex because at these energies two competing effects, namely enhanced production and large annihilation (absorption) cross sections compete. Strange antibaryons are furthermore unique by being sensitive to deconfinement based on an enhanced probability for strangeness enhancement, although the equally sensitive multi-strange baryons do not indicate any partonically driven strangeness production as shown in the previous chapter. The dramatic ratio increase as a function of centrality from 0.2 in peripheral collisions to 3.5 in central collisions has never been properly modelled. Thermal models, constrained by the detailed K/π measurements, fail completely, and transport models which allow the variation of annihilation cross section and antiparticle formation time get closer to the central data, but fail to describe the centrality dependence [123]. The closest theory calculation, based on UrQMD, is shown in Fig. 3.14 [124]. Many additional measurements have been performed in order to further constrain the problem. E941 measured the antiproton production in p+Be [125] and E877 measured the anti-flow of antiprotons [126]. Both measurements underline the importance of absorption and hint at a scaling of the ratio with the number of first collisions. But even with this additional input a complete explanation of the very unusual ratio has not been found.

3.2.4 HBT studies

Detailed and extensive Hanbury Brown-Twiss (HBT) measurements, cf. Part III, Sect. 5.9, were at the center of the physics program of many AGS experiments from E802 [128] to E895 [129]. Figures 3.15 and 3.16 show the present knowledge of the basic HBT parameters for energies ranging

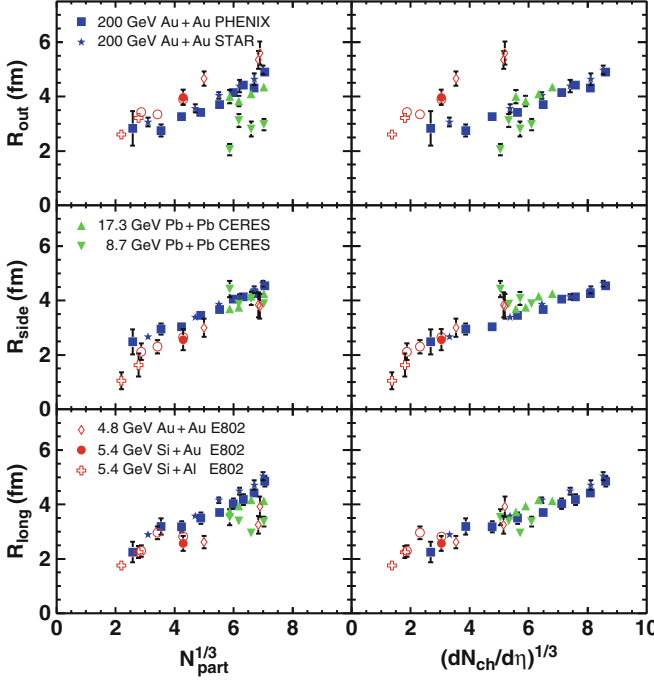


Fig. 3.15 Pion source radii scaling for AGS, SPS and RHIC data (from [127])

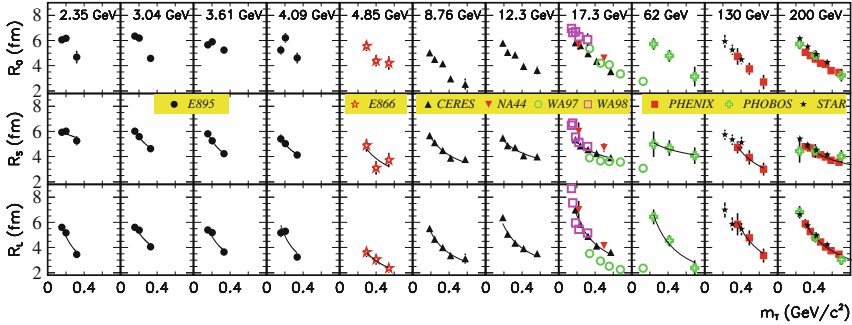


Fig. 3.16 Pion source radii as a function of m_T from Au+Au (Pb+Pb) collisions at AGS, SPS and RHIC energies (from [127])

from AGS to RHIC [127]. Ultimately no substantial change in the HBT parameters, which is expected in the case of a long-lived fireball including substantial partonic and hadronic phases, has been observed. Recent, more detailed results based on 3-d imaging indicate that the distributions at RHIC might have a substantial non-Gaussian tail [130] which could explain at least part of the lack of differences in the Gaussian fit parameters from AGS to RHIC as shown here. Overall the AGS HBT results are well within

expectations and should be treated as a reference for future measurements at comparable energies.

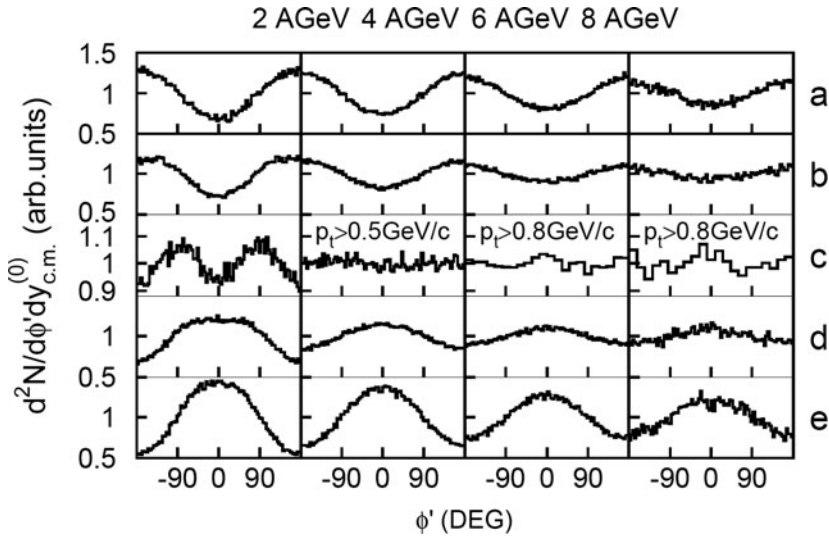


Fig. 3.17 Azimuthal distributions (with respect to the reconstructed reaction plane) for 2, 4, 6, and 8 AGeV Au + Au collisions. Distributions are shown for different rapidity bins: (a) $-0.7 < y_{cm} < -0.5$, (b) $-0.5 < y_{cm} < -0.3$, (c) $-0.1 < y_{cm} < 0.1$, (d) $0.3 < y_{cm} < 0.5$, and (e) $0.5 < y_{cm} < 0.7$. The mid-rapidity selections for 4–8 AGeV also include a transverse momentum selection as indicated (from [131])

3.2.5 Elliptic and directed flow studies

A very important measurement performed at AGS was the excitation function of collective flow [131]. The azimuthal angle distributions of protons measured in Au+Au collisions from 2 to 8 AGeV are presented in Fig. 3.17 for different bins in rapidity. A dramatic result from this energy scan was the discovery of the transition from out-of-plane to in-plane emission based on the measurement of proton elliptic flow. The $\cos 2\phi$ component switches from negative to positive values at $E_{beam}=4$ AGeV as shown in Fig. 3.18. Early interpretations suggest a softening of the equation of state from a high compressibility factor ($\kappa \approx 380$ MeV) below 4 AGeV to a low compressibility factor ($\kappa \approx 210$ MeV) above 4 AGeV (see Fig. 3.18). This could potentially signal a phase transition in the mapped out energy regime. More recent transport model calculations, however, which take into account in-medium cross sections and momentum dependent interactions, find a reduced sensitivity of the proton flow data to the nuclear equation-of-state [132].

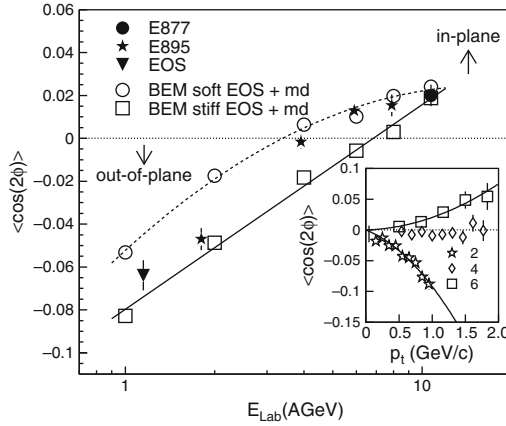


Fig. 3.18 Elliptic flow excitation function for Au+Au measured by E895. The *curves* and *open symbols* represent calculated excitation functions with different equations of state. The insert shows the transverse momentum dependence of the elliptic flow for collision energies of 2, 4, and 6 AGeV (from [131])

Directed sideward flow (v_1) measurements of the protons are shown in Fig. 3.19 [133]. The data do not exhibit a pronounced dip or shape change in the energy range where the v_2 changes its sign. Therefore the v_1 data do not seem sensitive to a sudden change in reaction dynamics, but again transport models fail to consistently reproduce the data.

3.2.6 Conclusions and perspectives for FAIR

The physics of dense baryonic matter has been pioneered with heavy-ion collision experiments at AGS. The measurements provided information on global observables such as the yields and phase space distributions of hadrons including strange particles (kaons and lambdas). Measurements of hadronic resonances, multi-strange hyperons (except one Ξ point at 6 AGeV), lepton pairs and charmed particles have not been performed. The detailed investigation of these rare probes as function of beam energy and system size will be a central part of the heavy-ion research program at FAIR.

One of the most intriguing results obtained at AGS was the excitation function of proton collective flow. It was observed that the elliptic flow of protons changes its pattern from preferential out-of-plane to in-plane emission at a beam energy around 4 AGeV. These data have been interpreted using microscopic transport models in order to extract information on the nuclear equation-of-state at baryonic densities above 3 times saturation density [132, 134]. It turned out that the strength of the collective flow of protons or fragments in nucleus-nucleus collisions depends not only on the nuclear

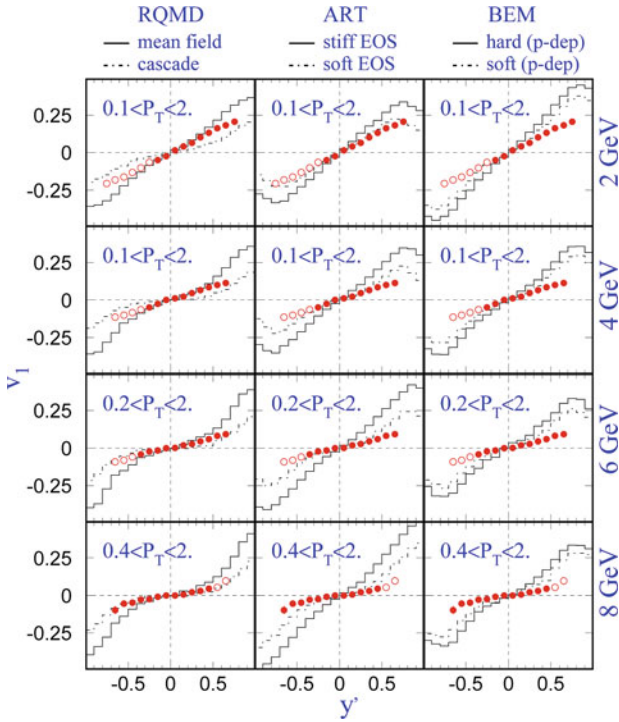


Fig. 3.19 The Fourier coefficient (v_1) as a function of the normalized rapidity for Au+Au collisions at different beam energies. The *symbols* are the data (*solid*=direct, *open*=mirrored), the *curves* are transport models under different assumptions, see labels (from [133])

equation-of-state, but also on the assumptions on the in-medium nucleon-nucleon cross sections, and on momentum-dependent interactions. Therefore, the analysis and interpretation of data on proton collective flow measured at AGS energies (2–10 AGeV) provided only limits on the nuclear compressibility (see Chap. 6).

Novel observables are required in order to obtain more detailed information on the nuclear equation-of-state at densities from 3 to $7 \rho_0$. One promising experimental approach would be the measurement of the excitation function of multi-strange hyperon production in heavy-ion collisions in the energy range between about 2 and 15 AGeV. The threshold beam energies for the processes $pp \rightarrow \Lambda \bar{\Lambda} pp$, $pp \rightarrow \Xi^+ \Xi^- pp$, and $pp \rightarrow \Omega^+ \Omega^- pp$ are 7, 1, 9.0 and 12.7 GeV, respectively. However, multi-strange hyperons can also be created via strangeness exchange reactions in multi-step collisions involving processes like $pp \rightarrow K^+ \Lambda p$, $pp \rightarrow K^+ K^- pp$, $\Lambda K^- \rightarrow \Xi^- \pi^0$, $\Xi^- K^- \rightarrow \Omega^- \pi^-$ [135]. In this case the minimum energy required in a single NN collision corresponds to the production of a $K^+ K^-$ pair. The yield of anti-hyperons is suppressed because the sequential production chain starts with anti-Lambdas, and con-

tinues with $\bar{\Lambda} \rightarrow \Xi^+\pi^0$, and $\Xi^+K^+ \rightarrow \Omega^+\pi^+$. The “cooking” of particles containing 2 or 3 strange quarks (or antiquarks) is favored at high densities where the mean free path between consecutive collisions is short. Therefore, the yield of multi-strange hyperons depends very much on the density, and, hence on the compressibility of baryonic matter at these particular densities. In summary, the detailed measurement of the excitation function of the multiplicities and the collective flow of multi-strange hyperons in heavy-ion collisions at beam energies between 2 and about 15 AGeV will provide new information on the high density nuclear EoS. Such an experiment has a high discovery potential as no multi-strange hyperons have been measured at AGS beam energies, except for a total Ξ yield at 6 AGeV [119].

3.3 Searching for the phase transition: results from SPS

At the CERN SPS the first heavy ion induced reactions were studied already in 1986. At that time oxygen (and shortly afterwards sulphur) ions were available. Two experiments, WA80 and NA35 with strong participation from GSI and LBL, were among the first to take data. Both were designed to cover a large fraction of charged particle phase space. WA85/94 was designed to measure baryons and antibaryons with emphasis on hyperons. Other experiments concentrated on rare probes like muon pairs (NA38) or on spectrometer techniques (NA44). The experiment NA36 pioneered the use of the “Time Projection Chamber” technique in the field, which was the prerequisite of the successes of the later EOS experiment at the AGS (see previous section) and of NA49 at the SPS, although the latter was a direct follow-up of NA35 with its own TPC upgrade [136]. The most important results of the early SPS experiments with ^{16}O and ^{32}S beams, which are still valid today, were the first estimates of the large energy density obtained in nuclear collisions, the approximate scaling of the number of produced pions with the number of wounded nucleons as suggested by Bialas [137, 138], and strong deviations of the wounded nucleon scaling for strange particle production, at that time dubbed as strangeness enhancement. After the first heavy-ion experiments had confirmed the expectation of large energy densities and the failure of the trivial superposition picture in the SPS energy range, ^{208}Pb beams became available in 1994, and an extensive scientific programme at the beam energy of 158 AGeV was established. The experiments and their main features and goals are described next.

Most experimental groups which had used the ^{16}O and ^{32}S beams proposed a continuation of their research programme with Pb ions. WA98 became the successor of WA80 with increased photon detection capabilities and a new large acceptance charged hadron spectrometer. WA85/94 became WA97 and later on NA57 still concentrating on hyperon decays this time by means of small acceptance high resolution Silicon hodoscopes. NA49 evolved from

NA35 by replacing the visual device (streamer chamber) by four large volume TPCs covering the c.m.-forward hemisphere both in tracking as well as in particle identification via high resolution dE/dx measurement in the relativistic rise region. The Di-muon spectrometer NA38 became NA50 and needed only little modification to run with Pb-beams. Since 2002, NA50 was equipped with silicon tracking detectors placed in a dipole field close to the target. With this setup (named NA60) high quality data on the production of both charmonium and low-mass muon pairs have been measured. The Dilepton study with electrons was taken over by the new experiment NA45 (CERES), a novel large acceptance hadron blind spectrometer consisting of RICH detectors in a magnetic field. The second new and large experiment was NA52 which searched for new particles with unusual mass and/or charge at small transverse momenta using a modified beam line as spectrometer.

The first results from 158 A GeV Pb+Pb collisions at the SPS were the “horse back” shapes of the transverse energy spectra [139] which quantified the energy deposited in those interactions. Assumptions about the transverse and longitudinal size of the interaction zone allowed to infer the size of this zone and thus a range of energy densities between 1 and 3 GeV/fm³. This size and the lifetime of the zone was later deduced from two pion correlation studies [140]. No results on estimates of the energy density at low SPS and AGS energies have been reported so far, probably since Bjorken scaling is no longer a valid assumption. It will be a challenge for the CBM physics program to come up with new methods and results on the energy density reached in A+A collisions in the SIS300 regime.

The field of high energy nuclear collisions is based on the assumption that the produced particles constitute a reaction volume (“fireball”) in which equilibrium conditions prevail for finite periods of time. Only then the concepts of statistical mechanics or thermodynamics are appropriate. Such an assumption seems reasonable in view of the success of the Hagedorn fireball model [141] to explain the bulk kinematical properties of the final state in hadronic interactions. Early concepts of extending the thermal/statistical picture to particle yields [142, 143] were soon probed experimentally. These studies revealed an astonishing approach to equipartition of (energy among) essentially all particle species [144, 145]. The success of the underlying chemical equilibration picture apparently applies to heavy ion collisions at all energies. It justifies the use of bulk property observables in the description of the reaction zone in high energy nuclear collisions.

Further important observations made at the SPS are the strong J/ψ suppression [146], the intermediate mass di-electron enhancement [147, 148] and the enhanced yield ratio of strange to non strange particles in Pb+Pb versus p+p collisions [149]. The interpretation of the observed J/ψ suppression was and still is controversial, since the original prediction of J/ψ dissolution in deconfined matter (or Quark-Gluon-Plasma, QGP) [15] turned out to be more difficult to describe theoretically than anticipated. The surplus of di-electrons on top of the expected cocktail of known hadronic sources,

as observed by CERES may have various medium induced origins: two-pion interactions, multi-hadron interactions and vector meson mass modifications. The third finding confirmed an early prediction of strangeness enhancement in a QGP [150], however, such an enhancement is also expected as the result of multiple hadron interactions in the reaction zone in any high energy nucleus-nucleus collision. So far microscopic transport models cannot reproduce the experimental results on strangeness enhancement quantitatively at the highest SPS energy in contrast to the situation at AGS. The implications of all three experimental results for the nature of the produced fireball are thus not yet fully understood. On the other hand they suggest that interactions and degrees of freedom are important which go beyond those established in hadronic physics.

Although matter properties had been established for the fireball created in ultra-relativistic heavy ion collisions, and the prospects for new physics beyond the hadronic “world” were favorable, unequivocal signatures for a new state of matter were still missing. Instead CERN officially announced “compelling evidence ... for the formation of a new state of matter ... in which quarks and gluons no longer feel the constraints of color confinement” [151]. The main observations supporting such a conclusion were charmonium suppression, strangeness enhancement and the initial energy density.

At about the same time the idea was realized to measure the excitation function of many hadronic observables with the aim to identify possible threshold phenomena which would signal the onset of new phenomena. Beams of 80, 40, 30, and 20 AGeV beams were used to study the energy dependence of hadronic particle production in Pb+Pb collisions. This energy scan program provided two intriguing results. The pion source size parameters turned out to be approximately energy independent (even when including AGS and RHIC data [152]). The non-monotonic behavior of the K^+/π ratio, and a step-like behavior of transverse mass slopes as function of \sqrt{s} (or of m_T) hint at a threshold phenomena at around 30 AGeV which cannot be explained by hadronic phenomena. On the contrary, models which include both hadronic and partonic matter phases can reproduce the experimental findings qualitatively.

In the following, we will briefly outline the main physics results of the CERN-SPS heavy-ion programme.

3.3.1 Initial energy density

The initial density of the produced energy can be estimated from the measurement of the total transverse energy E_T using Bjorken’s formula [2]

$$\epsilon(\tau_0) = \frac{1}{2\tau_0\pi R^2} \frac{dE_T}{d\eta} \quad (3.2)$$

which assumes a boost-invariant longitudinal expansion. Evidence that the Bjorken scenario holds in the midrapidity region at SPS exists from HBT measurements [140].

The transverse energy at midrapidity in central Pb+Pb collisions was measured by the experiments NA49 and WA98 and found to be around 400 GeV [139, 153]. The NA49 data are presented in Fig. 3.20. Using Eq. (3.2) with $\tau_0 = 1$ fm, this translates to an initial energy density of about 3 GeV/fm³, to be compared to the 600 MeV/fm³ which are, according to lattice QCD calculations, required for the transition to deconfined matter. This result demonstrates that the initial conditions reached in central collisions of heavy ions at the SPS are likely to be suitable for the creation of quark-gluon matter.

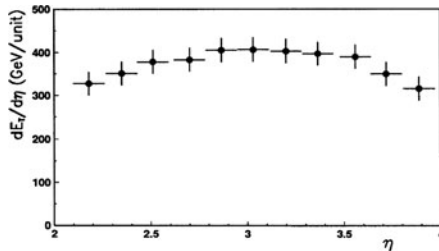


Fig. 3.20 Pseudorapidity distribution of transverse energy for central Pb+Pb collisions at 158 AGeV [139]

3.3.2 Hadronic expansion

The transverse momentum spectra of the produced particles provide information on the hadronic final state after thermal freeze-out, i.e. after inelastic collisions cease. Assuming local thermalization at this stage, the spectra reflect both the thermal conditions and the collective motion (“transverse flow”). Figure 3.21 shows a simultaneous blast-wave parameterization of transverse mass spectra for different particle species measured by the NA49 experiment [154]. The model reproduces the measured spectra well, possibly with the exception of multi-strange hyperons (Ξ and Ω), for which NA57 claims to see deviations from the blast wave model fitted to the bulk hadrons [155]. This would signify an earlier decoupling of the hyperons due to their low scattering cross section.

The fact that the transverse mass spectra are well described by the blast wave model suggests that the fireball is thermalized and expands explosively with a velocity of about half the speed of light. It finally decouples when the temperature has dropped to about 120 MeV. These freeze-out conditions agree with the analysis of the k_T dependence of the transverse HBT radius

R_T measured in two-pion interferometry [140]. Hadronic transport models (e.g. UrQMD) failed to reproduce the observed spectra, demonstrating that hadronic scattering cannot generate sufficient pressure to drive the collective expansion.

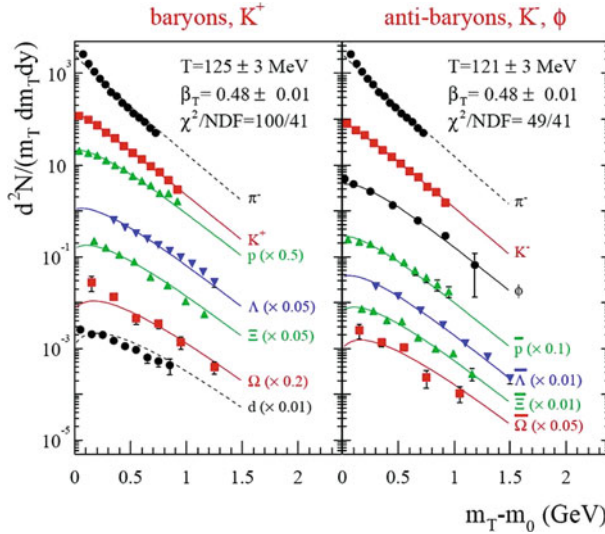


Fig. 3.21 Blastwave fit to the transverse mass spectra measured in central Pb+Pb collisions at 158 AGeV [154]

3.3.3 Strangeness enhancement and chemical equilibrium

Enhanced strangeness production with respect to p+p interactions was proposed as a messenger of the deconfined state since strangeness is more effectively produced in parton-parton interactions than in hadronic reaction scenarios [156]. Indeed, it was observed that all strange particles are enhanced in Pb+Pb collision [157–159]; the enhancement grows with the number of strange valence quarks and reaches up to 15 for Ω baryons (see Fig. 3.22). A study of smaller colliding nuclei revealed that it is also present in relatively small systems (C+C, S+S) and rises quickly to a saturation value [160].

Enhanced strangeness production in nuclear collisions arises naturally in the framework of statistical models as a consequence of the increased reaction volume, which relaxes the impact of exact strangeness conservation on the strange particle yields [161]. In fact, all measured hadron abundances measured at midrapidity at SPS are well described by a hadron resonance

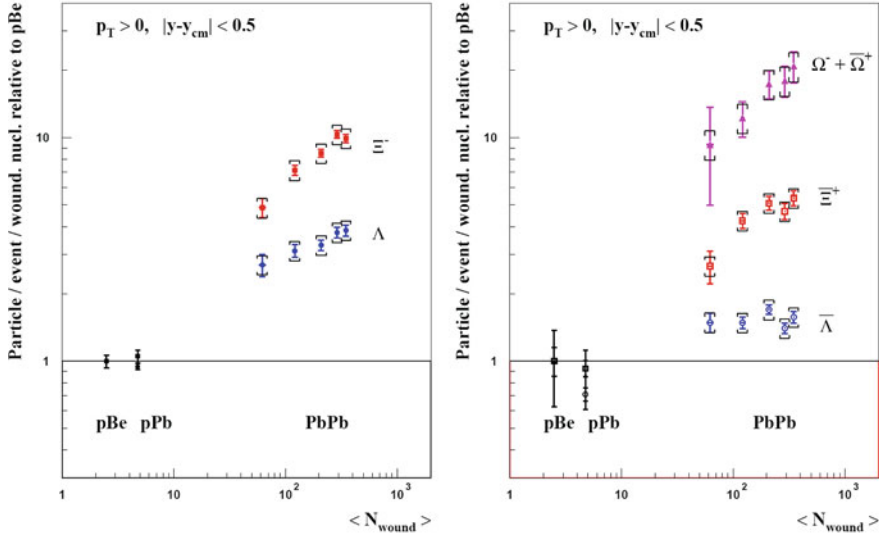


Fig. 3.22 Enhancement of hyperons in Pb+Pb collisions at the SPS with respect to p+p collisions [157]

gas in chemical equilibrium as shown in Fig. 3.23. The temperature T_{chem} is obtained to be about 170 MeV, thus coinciding with the critical temperature for color deconfinement as deduced from lattice QCD calculations. The fact that the hadronic final state resembles a hadron gas in or close to equilibrium

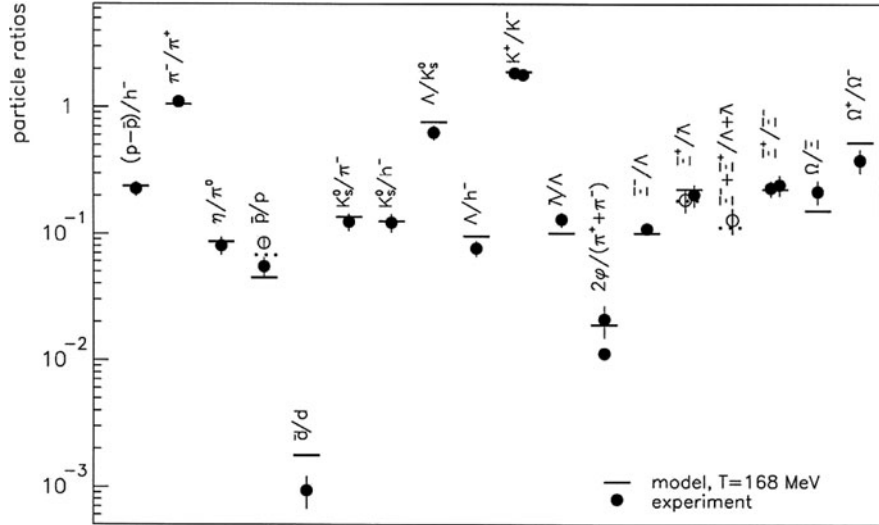


Fig. 3.23 Particle ratios measured in central Pb+Pb collisions at 158 AGeV compared to the prediction of a hadron resonance gas in full equilibrium [144]

was attributed to a hadronisation process from colored quarks to hadrons, because microscopic simulations using hadron-string degrees of freedom fail to create an equilibrium out of the non-equilibrium initial state [162].

When considering particle multiplicities in full phase space instead of midrapidity yields, the agreement of data and hadron-gas model is less good, in particular for strange hadrons. This led to the introduction of a strangeness undersaturation parameter γ_s , which parameterises the deviation from strangeness equilibrium [145]. As by definition, this parameter acts on the number of strange valence quarks of the hadron species, its successful application suggests that the final state strangeness content is determined in a partonic stage of the collision.

3.3.4 J/ψ suppression

The suppression of charmonium due to Debye screening by free color charges was considered to be a key signature for the quark-gluon plasma [15]. Such a suppression indeed was observed by the NA50 experiment [146] on top of the expected “normal” absorption in hadronic matter. This normal absorption was studied by the same experiment in p+A collisions and found to follow an exponential attenuation law. Figure 3.24 shows the ratio of observed over

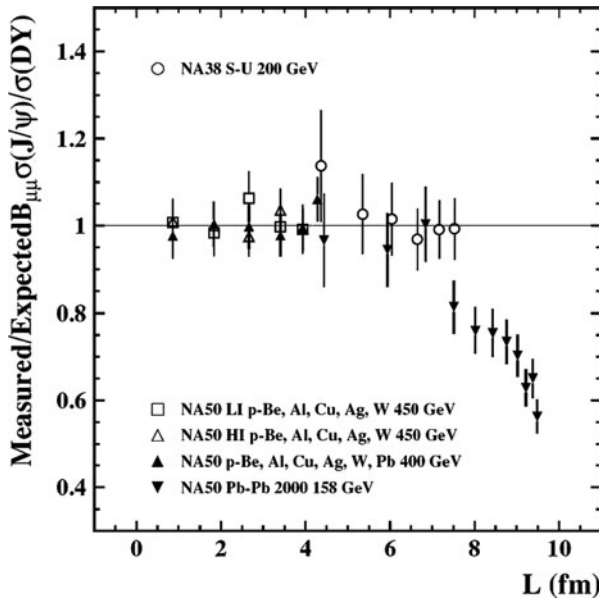


Fig. 3.24 Anomalous J/ψ suppression as a function of the nuclear thickness parameter L [146]

expected J/ψ yield as a function of the path length in cold nuclear matter L . While for peripheral collisions, the J/ψ production follows the expectations from normal nuclear absorption, additional suppression clearly sets in for more central events.

High-precision measurements performed by the NA60 experiment, the successor of NA50, confirmed these results and could pin down the onset of anomalous suppression at a number of participant nucleons of about 80 [163]. The corresponding initial energy density, again derived using the Bjorken formula, is approximately 1.5 GeV/fm^3 , strikingly close to the critical energy density predicted by lattice QCD.

3.3.5 In-medium modification of the ρ meson

In contrast to final-state hadrons, short-lived vector mesons decaying into lepton pairs, in particular the relatively abundant ρ , provide information on the entire evolution of the fireball due to the absence of final state interaction of the lepton daughters. Modifications of the properties of such vector mesons in a hot and dense environment were proposed as a signature for the restoration of chiral symmetry in quark matter [34].

The di-electron spectrum measured by the CERES collaboration in Pb+Au collisions at 158 AGeV showed no ρ peak at all, but a broad excess of electron pairs over the expectations from a hadronic cocktail [147]. This excess even increased at lower incident beam energy [148]. The excess is generally attributed to two-pion annihilation with an intermediate ρ meson, requiring a strong modification of the latter in the medium. Later results of the NA60 experiment in the di-muon channel [164] confirmed these findings and allowed to discriminate the various theoretical scenarios in favor of collisional broadening of the ρ through interaction with hadrons, while a shift of the ρ pole mass as expected from explicit connection to the chiral condensate seems to be excluded by the data.

3.3.6 Energy dependence of relative strangeness production

Since many experimental results obtained by the various experiments at top SPS energy (158 AGeV) suggest that in central collisions of heavy nuclei a deconfined state of strongly interacting matter is produced, the NA49 experiment embarked on an energy scan down to 20 AGeV in search for the onset of deconfinement. Figure 3.25 shows the most striking result of this programme, a narrow maximum in the K^+/π^+ ratio at around 30 AGeV bombarding energy. This ratio corresponds approximately to the total strangeness-to-

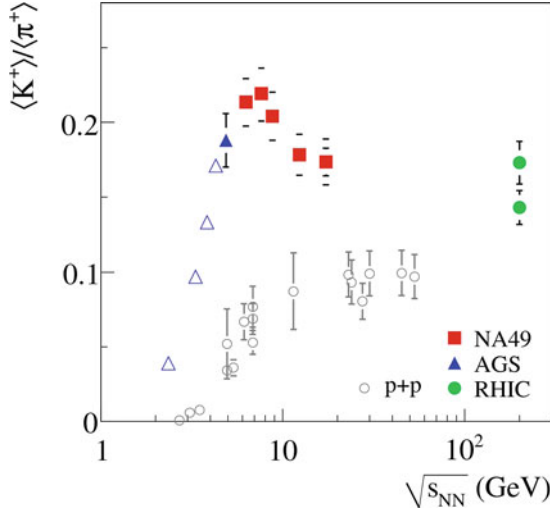


Fig. 3.25 Energy dependence of the K^+/π^+ ratio in central Pb+Pb/Au+Au collisions, and in p+p collisions (*open circles*) [159, 166]

entropy ratio. Such a feature was indeed predicted by the statistical model of the early stage assuming that the phase boundary between confined and deconfined matter is first crossed at that collision energy [165], while hadronic models fail to describe the detailed shape of the K^+/π^+ excitation function.

Further evidence is provided by the inverse slope parameters (or, alternatively, mean transverse masses) of the produced pions, kaons and protons which are found to be approximately constant over the entire SPS energy range, in contrast to the steep rise at AGS energies and the subsequent increase towards RHIC energies (see Fig. 3.26). This constancy can be interpreted as feature of a mixed phase with latent heat, where additional beam energy is converted into the phase transition instead of increasing pressure or temperature.

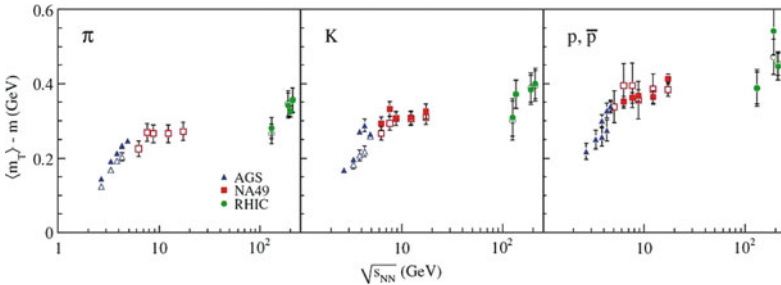


Fig. 3.26 Energy dependence of the mean transverse mass of pions, kaons and protons in central Pb+Pb/Au+Au collisions [159]

3.3.7 Conclusions and perspectives for FAIR

The results obtained in the SPS heavy-ion programme strongly support the conclusion that the matter created in central collisions of heavy nuclei at top SPS energy is transiently in a deconfined state of quarks and gluons. In addition, there are indications that the phase boundary is first reached at beam energies around 30 AGeV. Thus, the SIS-300 energy domain appears well suited for the in-depth study of the onset of deconfinement.

The SPS results show that both strangeness and charmonium production remain essential observables with direct connection to a phase transition. Systematic, high-precision measurements of these observables as function of collision energy appear the most promising strategy for the detailed investigation of the deconfinement phase transition, which can be expected to yield discontinuities in the excitation functions. A sudden change e.g. in the J/ψ suppression pattern would be a clear signal for such a phase transition. Open charm will add a new and important observable, which was not covered at the SPS at all.

Another possible signature is anisotropic flow of identified hadrons, including open charm. The results obtained at SPS, in particular in the context of the NA49 energy scan, were not conclusive, mostly because of insufficient statistics and precision. It will be a task for CBM to look for the possible breakdown of baryonic flow near the phase transition with high accuracy.

Effects of the medium on the properties of low-mass vector mesons seem to be governed by baryon density rather than by temperature. Hence, the maximal effects can be expected at the highest achievable net-baryon densities as created in heavy-ion collisions in the SIS-300 energy domain. Experience from SPS (and from RHIC) shows that for the discrimination of theoretical models, a good signal-to-background ratio, high resolution, and high statistics are essential. As a next-generation experiment, CBM should outperform its predecessors in these respects. It should be noted that the connection of in-medium modifications to the restoration of chiral symmetry is not yet unambiguous and subject to further theoretical developments.

The search at SPS for event-by-event fluctuations of several quantities like K/π ratio, mean transverse momentum, charged multiplicity etc. yielded no significant effects beyond the statistical expectations, with maybe the exception of the increase of dynamical fluctuations of the K/π ratio at lower beam energies as reported by NA49 [167]. Non-statistical fluctuations are expected in the vicinity of a critical point separating the region of a first-order phase transition from that of a smooth cross-over. Moreover, dynamical fluctuations might also develop in the coexistence phase of a first order phase transition. Therefore, the search for such fluctuations is an important part of the CBM research programme.

3.4 Probing partonic matter: results from RHIC

Over the past decade RHIC has established the existence of a strongly interacting collective partonic states, termed the sQGP [168]. The evidence is largely based on three fundamental measurements, the strong suppression of high momentum particles traversing the medium (jet quenching), the large azimuthal anisotropy of particle emission in non-central collisions (elliptic flow), and the scaling properties of the anisotropy for high momentum particles (constituent quark scaling). When nearing a critical point by lowering the collision energy one can assume that these indicators of a deconfined partonic state should weaken or disappear altogether. One of the main objectives of CBM will therefore be the mapping of these measurements as a function of collision energy. We will in the following detail the physics content of the RHIC QGP signatures. In addition we will propose the measurement of hadronic resonances, which were applied at RHIC energies to determine the lifetime and medium properties of the partonic and hadronic phases during the fireball evolution.

3.4.1 Jet quenching

The basic RHIC results regarding partonic energy loss in the medium are shown in Fig. 3.27.

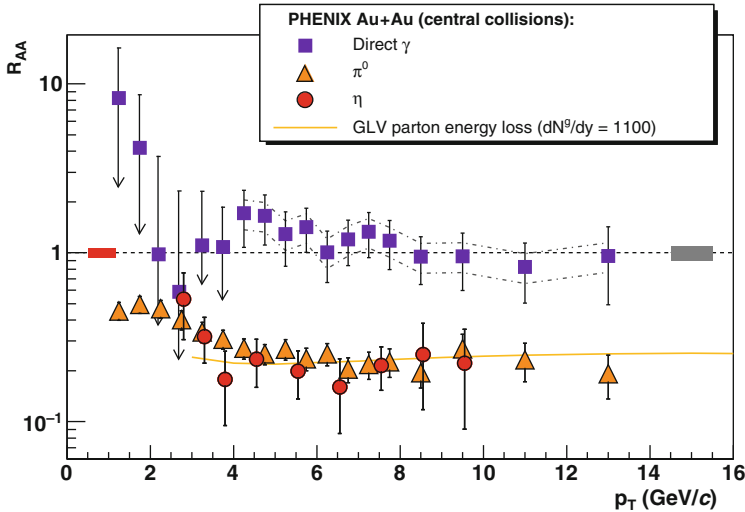


Fig. 3.27 $R_{AA}(p_T)$ measured in central Au+Au collisions at 200 AGeV for η , π^0 , and direct γ (from [169])

The so called nuclear suppression factor R_{AA} is shown as a function of particle transverse momentum. The suppression factor is the ratio of the particle spectrum measured in A+A collisions over the scaled particle spectrum measured in pp collisions. In case of a simple superposition of pp collisions, in order to describe the AA spectra, the ratio should be unity. High momentum particle suppression can be attributed to energy loss in the medium. A reference measurement even in central Au+Au collisions is given by determining the suppression factor for direct photons. Due to their negligible interaction cross section photons should not be suppressed at all, and the results shown in Fig. 3.27 confirm this assumption. The quantitative analysis of the suppression of hadrons can be used to determine the nature of the medium and its transport coefficient. It was shown [170] that the energy loss is about fifteen times higher than in cold nuclear matter, which unambiguously determined that the plasma is of partonic nature. The exact transport coefficient in the partonic medium is somewhat more difficult to determine and different theoretical approaches yield differing results [171, 172], but a recent detailed analysis of the available experimental data helps to constrain such models [173].

The relevant measurement for CBM is to determine the energy dependence of the quenching. RHIC has results for 22.4, 62.4 and 200 AGeV, and there are also some data from SPS, but they lack the statistics at high momentum. Figure 3.28 represents the present knowledge of the energy dependence based on Cu+Cu data [174]. It seems that at least for the π^0 the quenching effect disappears at SPS energies. CBM will be able to contribute a much more detailed measurement at even lower collision energy. We expect the charged particle momentum spectrum to reach out to 4–5 GeV/c.

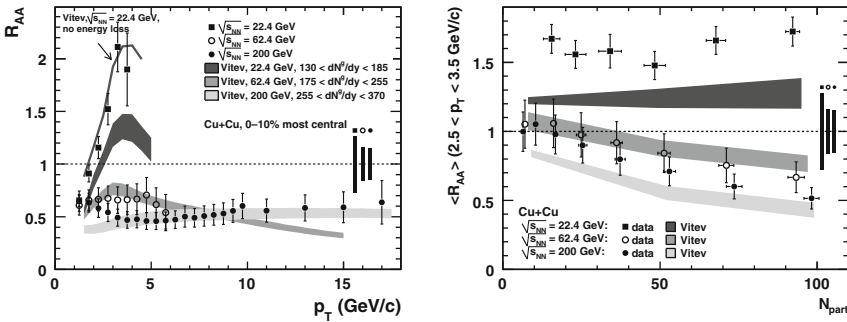


Fig. 3.28 (a) Measured π^0 R_{AA} as a function of p_T for the 0–10% most central Cu+Cu collisions at various collision energies, (b) average R_{AA} in the integral from $2.5 < p_T < 3.5$ GeV/c as a function of centrality for Cu+Cu collisions at various energies (from [174])

3.4.2 Hydrodynamical elliptic flow

One of the early discoveries of RHIC was that the magnitude of the azimuthal anisotropy in momentum space, measured by the second moment of the Fourier transform of the emission spectrum (v_2 = elliptic flow) reaches, for the first time, the hydrodynamical limit [175]. Figure 3.29 shows the collision energy dependence of the elliptic flow over eccentricity ratio in comparison to hydrodynamical calculations [176].

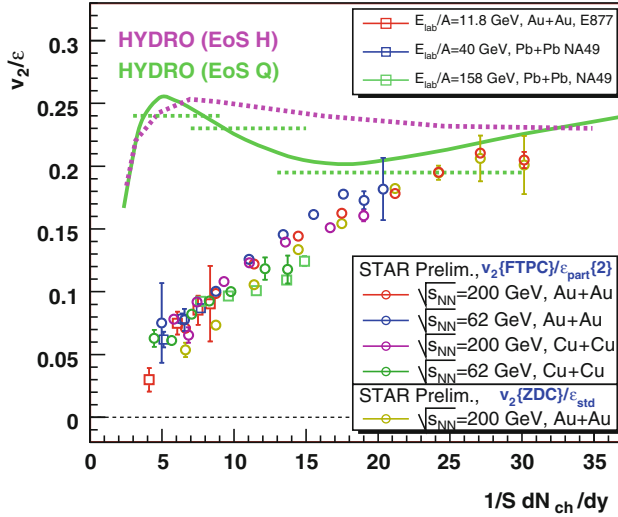


Fig. 3.29 v_2/ϵ as a function of the overlap density for various collision systems and collision energies compared to hydrodynamic model calculations (from [175])

The planned CBM experiment will cover the AGS and low energy CERN SPS regime. However, the high-rate capability of the CBM detector will result in superior statistics, and, hence, will open challenging perspectives even for multi-differential measurements. One of the interesting questions is, whether the elliptic flow just steadily drops as a function of collision energy or whether the existence of a critical point does not only affect the magnitude of v_2 but also its fluctuations [177, 178], see Sect. 9.8. Generally, hydrodynamic models assuming zero mean free path and negligible shear viscosity are capable of describing the elliptic flow data at RHIC [176]. Modified string models such as UrQMD are even successful in describing the general trend of v_2 as a function of collision energy [179]. The main new objective at CBM might thus be to investigate the evolution of the v_2 fluctuations. STAR was able to measure the v_2 fluctuations in $\sqrt{s_{NN}} = 200$ GeV Au+Au collisions [180] and found that the v_2 fluctuations are almost fully accounted for by assuming standard eccentricity fluctuations based on a Glauber model. The question

arises whether additional contributions will appear at lower energies. Several theory papers have related the level of fluctuations to the initial conditions in heavy ion collisions [181, 182].

3.4.3 Constituent Quark (NCQ) Scaling of elliptic flow

The remarkable scaling of the v_2 of high momentum hadrons with the number of constituent quarks has led to a general acceptance of the notion that the initial matter at RHIC is partonic. Figure 3.30 shows the latest results from STAR and PHENIX that include measurements from the pion all the way to the multi-strange hyperons [183].

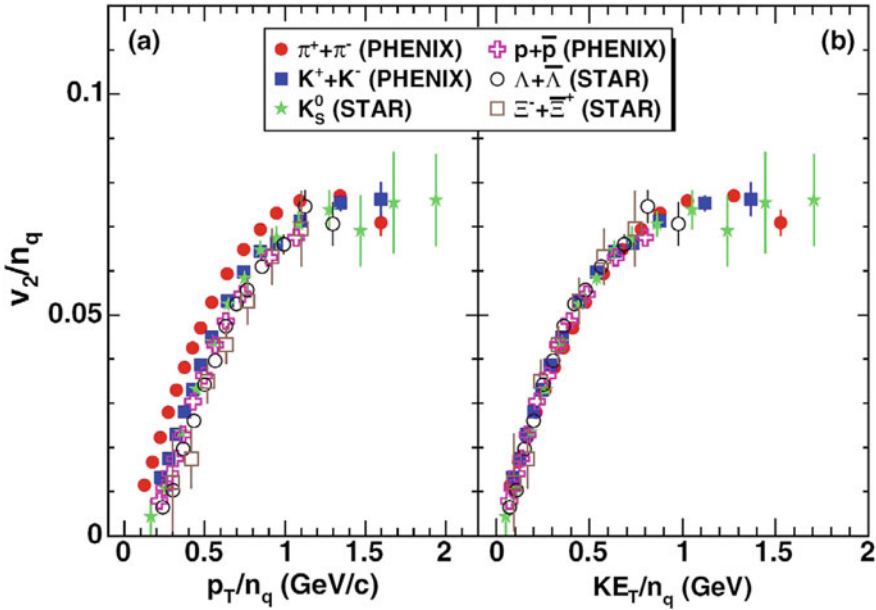


Fig. 3.30 Elliptic flow as a function of the transverse momentum (*left*) and of the transverse kinetic energy (*right*), both axes scaled with the number of constituent quarks (from [183])

The general consensus is that the quark scaling hints at a unique production mechanism for higher momentum particles, namely the recombination of quarks into hadrons in the deconfined phase [184, 185]. This mechanism is distinctly different from thermal production of lower momentum hadrons and fragmentation production of higher momentum hadrons. Neither hadronization mechanism is theoretically well described but the empirical evidence for recombination seems overwhelming at this point, and for quarks with negli-

gible quark masses the scaling formalism is well established. But the NCQ scaling of, in particular, the D meson is truly remarkable and not well understood (see [186]), because even if the charm quark is thermalized and flows with the light quarks, one should see a current quark mass scaling as long as the mass is not negligible compared to the particle momentum [187]. Thus, the determination of the validity of quark scaling at CBM energies, for particles ranging from light to heavy quark hadrons, will be very relevant. Figure 6.9 shows simulations of this effect at CBM/FAIR energies. One would assume that the recombination of partons from the medium should not be applicable below the critical point and then show a transition behavior at the critical point. How many of the produced particles species above the critical point will exhibit NCQ scaling will determine the level of strange and charm thermalization in the deconfined phase. It will also show whether, in particular, the charm quark results at RHIC are misinterpreted.

3.4.4 Hadronic resonance measurements

The advances in hadronic resonance reconstruction during the RHIC years have led to novel measurements of exotic resonances in relativistic heavy ion collisions. Besides the established results for ρ, ϕ and K^* , STAR was able to reconstruct strange baryonic resonances such as the $\Sigma(1385)$, $\Lambda(1520)$, and the $\Xi(1530)$ [188, 189]. By establishing such a long list of resonances with differing lifetime and decay properties STAR was able, in conjunction with its HBT measurements, to determine the lifetimes of the partonic and hadronic

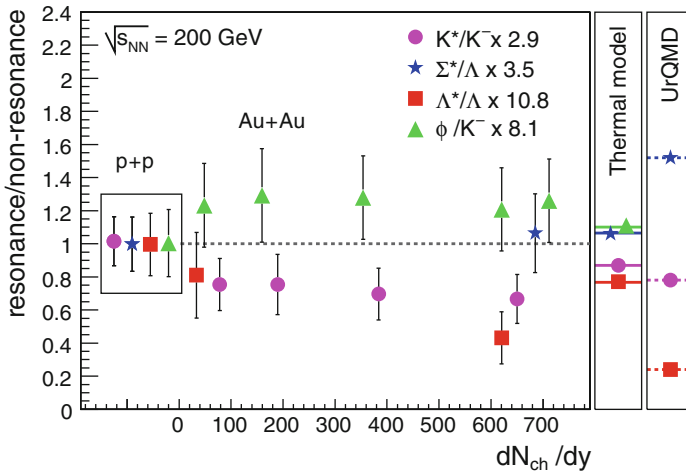


Fig. 3.31 Resonances to stable particle ratios for pp and Au+Au collisions at 200 AGeV (from [188])

phases at RHIC [188]. Furthermore the resonances can be used to establish interaction cross sections in medium by modeling the interplay of rescattering and regeneration during the hadronic de-excitation phase. Figure 3.31 shows the actual measurements of resonant over non-resonant ratios.

At CBM we expect the partonic phase to be shorter and the hadronic phase to last considerably longer. A systematic study of the resonance to particle ratios as a function of collision energy will determine the lifetime dependencies as well as the in-medium interaction cross sections, not only for light quark hadrons but also for the more exotic strange baryons.

Chapter 4

Hadron production

In this chapter we will discuss excitation functions of hadron production in heavy-ion collisions and their interpretations. As outlined in [Part I](#), particle yields and ratios can be analyzed with a statistical (thermal) model in order to extract the fireball freeze-out temperature T and the baryo chemical potential μ_b . [Figure 4.1](#) presents a recent compilation of thermal model fits to measured particle yields and ratios, and parameterizations of the energy dependence of T and μ_b [\[6\]](#).

It is worthwhile to note that the freeze-out temperature T exhibits a sharp rise up to $\sqrt{s_{NN}} = 7\text{--}8$ GeV and then stays constant, while μ_b sharply decreases all the way up to RHIC energies. The observation of a limiting freeze-out temperature is nontrivial, and may indicate a change of the degrees-of-freedom in the fireball which happens at FAIR (low SPS) beam energies. More detailed comparisons of thermal model calculations to particle yields and ratios, in particular for strange particles, are presented in this chapter. In order to obtain detailed information on the particle production mechanisms, and on the early, hot and dense phase of a nucleus-nucleus collision, the experimental data on hadron multiplicities have to be analyzed using microscopic transport models. Results will be discussed in this chapter.

4.1 Excitation functions of hadron yields

A compilation of measurements of yields at mid-rapidity for the most abundant hadron species is shown in [Fig. 4.2](#) for central nucleus–nucleus (Au+Au or Pb+Pb) collisions [\[26\]](#). These data have been used to extract the freeze-out temperature and the baryo chemical potential shown in [Fig. 4.1](#). As the centrality selection differs between various measurements, the data are scaled at the same number of participating nucleons, $N_{part}=350$. At AGS energies the fireball is dominated by the incoming nucleons, while the yield of the produced pions, with a strong energy dependence, dominates at higher ener-

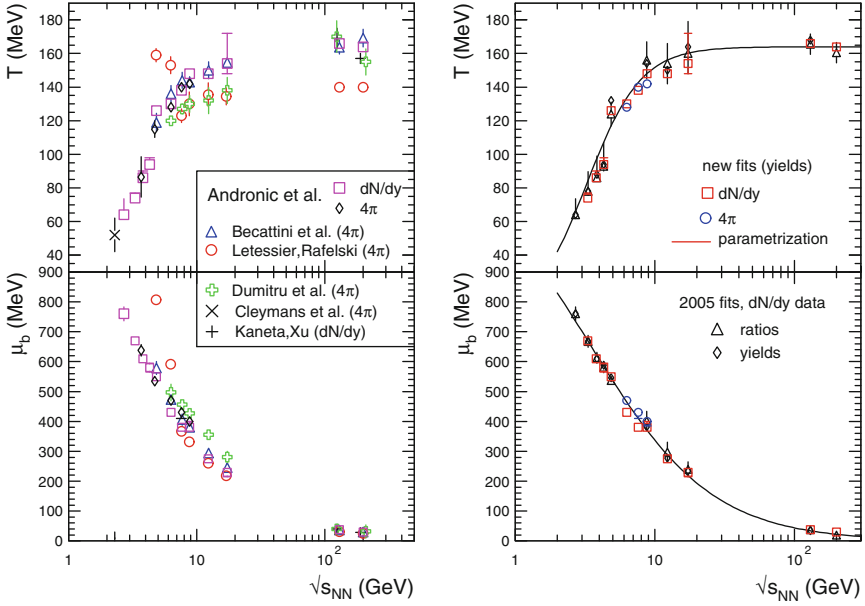


Fig. 4.1 The energy dependence of freeze-out temperature and baryo chemical potential. *Left panel:* comparison of various thermal model fits. *Right panel:* the results of fits using dN/dy data, both with ratios and yields. The *lines* are parameterizations for T and μ_b . Taken from [6]

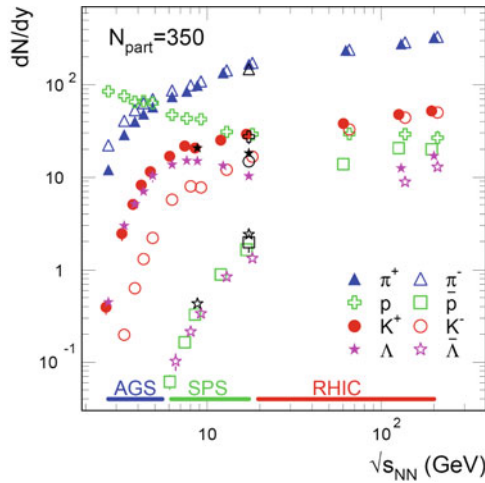


Fig. 4.2 The energy dependence of experimental hadron yields at mid-rapidity for various species produced in central nucleus-nucleus collisions. Taken from [26]

gies. The yield of strange hadrons shows a sharp rise at AGS energies, with characteristic features for various species, determined by their quark content. The yields of K^+ mesons and Λ hyperons (both with only the strange quark newly produced) are larger compared to K^- mesons, which has two newly produced quarks. The remarkable similarity of the yields of K^+ mesons and Λ hyperons, despite their large mass difference, is determined chiefly by their (anti)strange quark content, leading to their associated production. The yield of antiprotons and antihyperons (containing three newly produced quarks) is very similar and with a strong energy dependence (onset of production) at SPS energies. At the RHIC energies, due to a rather small net baryon content of the fireball, these differences almost disappear.

The excitation functions of hadron production in central collisions of heavy nuclei (Au+Au or Pb+Pb) measured in (or extrapolated to) the full solid angle are presented in Fig. 4.3 (taken from [35]). An interesting feature is the maximum of the Λ yield around $\sqrt{s_{NN}} = 7\text{--}10$ GeV which is caused by the decrease of the baryon-chemical potential indicating the transition from baryon to meson dominated matter.

The meson abundances measured in central Au+Au collisions from SIS to RHIC energies (solid symbols) are shown in Fig. 4.4 together with HSD transport model predictions. The multiplicities for π^+ , η , K^+ , K^- , ϕ as well

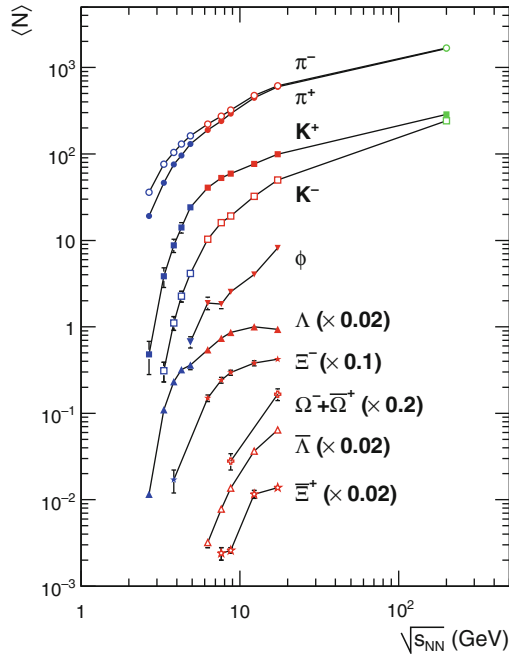


Fig. 4.3 Abundances of mesons and strange baryons measured in central nucleus–nucleus collisions as a function of the invariant energy \sqrt{s} (taken from [35])

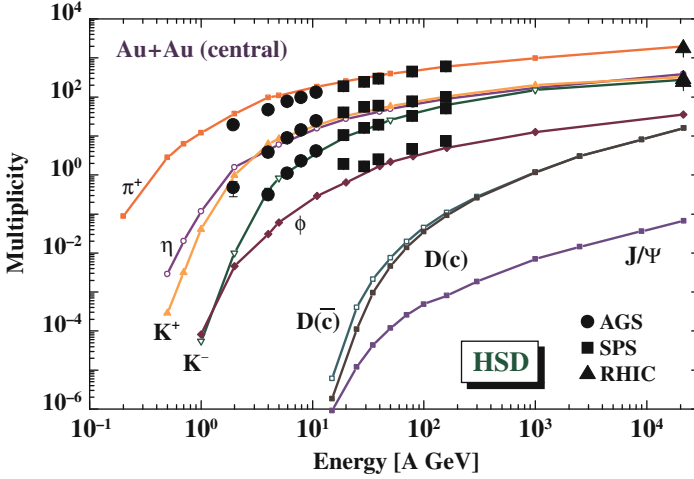


Fig. 4.4 Total multiplicities of π^+ , η , K^+ , K^- , ϕ , D , \bar{D} and J/ψ mesons for central Au+Au collisions as a function of bombarding energy from SIS to RHIC energies. *Full symbols*: experimental data. *Lines*: predictions of the HSD transport code. Taken from [190]

as D , \bar{D} , J/ψ mesons increase monotonically with bombarding energy. The increase is very steep at “subthreshold” energies, i.e. at beam energies per nucleon below the threshold for meson production in nucleon-nucleon collisions. The predicted cross sections for K^- merge at subthreshold energies with those for ϕ mesons since the antikaon is produced dominantly together with a kaon, i.e. the invariant mass of the K^+K^- or K^0K^- pair of ~ 989 MeV is close to the mass of the ϕ meson of 1020 MeV. On the other hand kaons (K^+ , K^0) are dominantly produced with a hyperon (Λ or Σ) since the relevant invariant mass is $m_K + m_\Lambda - m_n \approx 671$ MeV or $m_K + m_\Sigma - m_n \approx 745$ MeV and thus lower than the invariant mass of a $K\bar{K}$ pair of ~ 989 MeV.

The situation in the charm sector is rather similar except for the fact that the masses of the η_c and J/ψ (2.98 and 3.097 GeV, respectively) are well below the mass of a D meson pair which is 3.739 GeV. Accordingly, the formation of a η_c or a J/ψ from an initial $c\bar{c}$ pair is the only allowed process (in vacuum) close to the charm threshold since the production of a $D + \bar{D}$ pair is suppressed by its large invariant mass. But again the associated production of a \bar{D} meson (which contains a \bar{c} quark) with a charmed hyperon (Λ_c , Σ_c , Σ_c^*) is more favorable due to the effective invariant masses of 3.216 and 3.386 GeV, respectively, than the production of a $D\bar{D}$ pair. This explains why in Fig. 4.4 the \bar{D} cross section is larger than the D cross section at subthreshold energies and the J/ψ formation dominates in the far subthreshold domain. At higher bombarding energies the meson abundances group according to their quark content, i.e. the multiplicities are reduced (relative to π^+) by about a factor of 4–5 for a strange quark, a factor of ≈ 50 for $s\bar{s} \equiv \phi$ and a

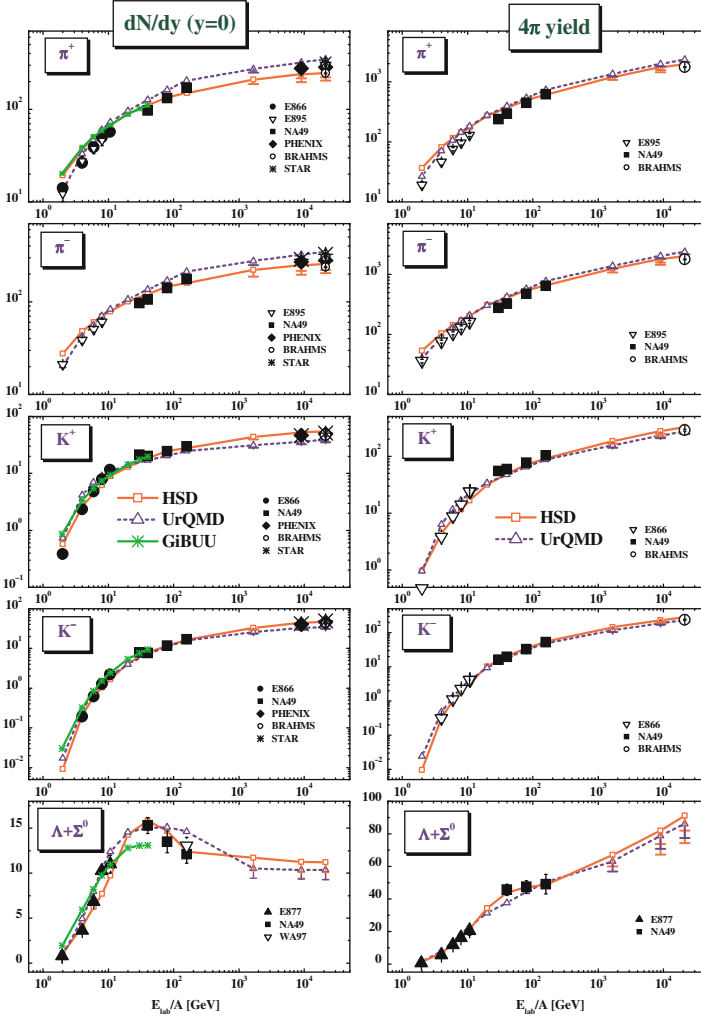


Fig. 4.5 The excitation function of π^+ , π^- , K^+ , K^- and $\Lambda + \Sigma^0$ yields from central Au+Au or Pb+Pb collisions in comparison to the experimental data from [191–194] (AGS), [159, 166, 195–198] (SPS) and [199–204] (RHIC) for midrapidity (left column) and rapidity integrated yields (right column). The solid lines with open squares show the results from HSD whereas the dashed lines with open triangles indicate the UrQMD calculations. (The HSD and UrQMD results are taken from [30].) The solid lines with the stars corresponds to the GiBUU calculations [205]

factor of $\approx 2 \cdot 10^4$ for $c\bar{c} \equiv J/\psi$. The early predictions of the HSD transport model for the production of light mesons [190] have been close to the actual experimental data, as illustrated in Fig. 4.4.

Figure 4.5 depicts the excitation functions of π^+ , π^- , K^+ , K^- and $\Lambda + \Sigma^0$ yields at midrapidity (left panel) and integrated over rapidity (right panel) for

central Au+Au (Pb+Pb) collisions. The symbols refer to experimental data, whereas the lines correspond to results of calculations [30] within the HSD [42, 206], UrQMD [124, 207], and the GiBUU model [205, 208]. As can be seen from Fig. 4.5 the differences between the different transport models are less than 20%; the maximum deviations between the models and the experimental data are less than $\sim 30\%$. In addition, a systematic analysis of model results and experimental data for central nucleus-nucleus collisions from 2 to 160 AGeV [209] has shown that also the rapidity distributions of protons, pions, kaons, antikaons and hyperons are quite similar and in reasonable agreement with available data. The exception are the pion rapidity spectra at the highest AGS energy and lower SPS energies, which are overestimated [209]. For a more detailed comparison of transport calculations with experimental data see [30, 205, 209–213].

Particle excitation functions have been also calculated within a 3-fluid hydrodynamical model [32] for a hadronic EoS. The results are shown in Fig. 4.6. The agreement with data is quite satisfactory except for the antikaons (and possibly $\bar{\Lambda}$'s).

4.2 Excitation functions of hadron ratios

In order to correct for temperature effects and to magnify the details of strangeness formation one can look at the ratios of the yields of strange particles over pions. Figure 4.7 depicts the excitation function of the particle ratios K^+/π^+ , K^-/π^- and $(\Lambda + \Sigma^0)/\pi$ from central Au+Au (Pb+Pb) collisions calculated with HSD [30], UrQMD [30] and GiBUU [205] in comparison to the experimental data available. The deviations between the transport models and the data are most pronounced for the midrapidity ratios (left column) since the ratios are very sensitive to actual rapidity spectra. The K^+/π^+ ratio in UrQMD shows a maximum at ~ 8 AGeV and then drops to a constant ratio of 0.11 at top SPS and RHIC energies. In the case of HSD (and GiBUU) a continuously rising ratio with bombarding energy is found for the midrapidity ratios. The 4π ratio in HSD is roughly constant from top SPS to RHIC energies, and is larger than the UrQMD ratio due to the lower amount of pion production in HSD. This effect essentially is caused by an energy-density cut of 1 GeV/fm³ in HSD which does not allow to form hadrons above this critical energy density [209]. Moreover, HSD produces a slightly higher K^+ yield than UrQMD (cf. Fig. 4.5). The experimental maximum in the K^+/π^+ ratio is missed both by the HSD and the UrMD calculation. The disagreement between data and model calculations can be dominantly attributed to an excess of pions in the transport codes at top AGS energies (for HSD) and above ~ 5 AGeV (for UrQMD). Qualitatively, the same argument – due to strangeness conservation – also holds for the $(\Lambda + \Sigma^0)/\pi$ ratio.

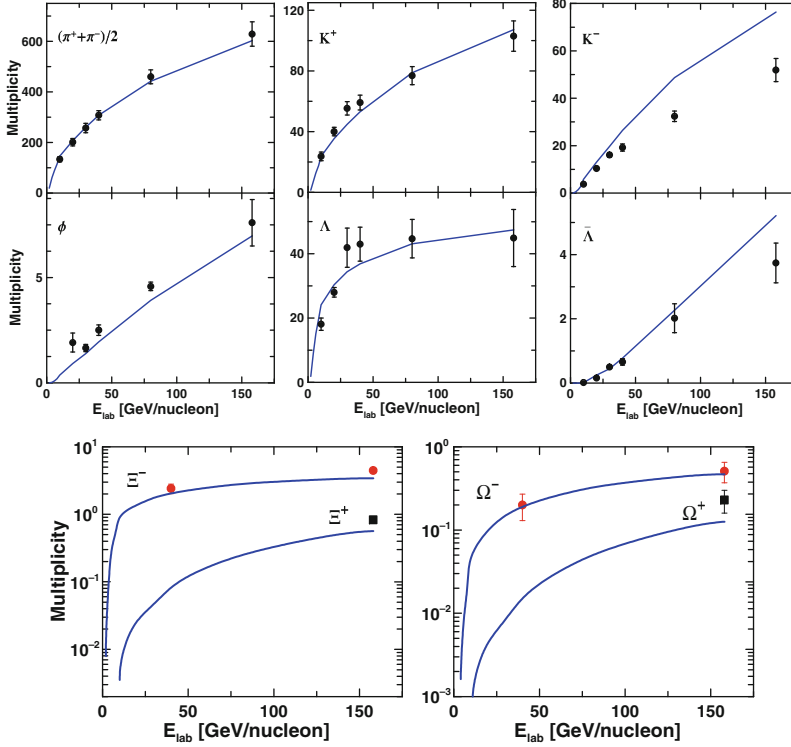


Fig. 4.6 The excitation function for the multiplicities of pions, K^+ , K^- , ϕ , Λ , $\bar{\Lambda}$ and multi-strange hyperons Ξ , Ω for central Au+Au (at AGS energies) and Pb+Pb (at SPS energies) reactions as calculated within the 3-fluid hydrodynamical model. The figures are taken from [32]

The maximum in the $(\Lambda + \Sigma^0)/\pi$ ratio is essentially due to a change from baryon to meson dominated dynamics with increasing beam energy. Similar arguments hold for the experimentally observed maxima in the ratio Ξ/π (cf. [214]). The enhancement in the measured K^+/π^+ ratio at ~ 30 AGeV cannot be described by hadron transport models.

Figure 4.8 depicts the $\bar{\Lambda}/\pi$ ratio as a function of collision energy $\sqrt{s_{NN}}$. The experimental data are confronted here with predictions from the statistical (hadron gas) model [20, 217–220] and from the microscopic transport models UrQMD [209] and HSD [221]. While UrQMD falls significantly low with respect to the data the HSD calculations perform better due to an inclusion of multi-meson fusion channels for baryon+antibaryon production. The experimental $\bar{\Lambda}/\pi$ ratio shows a monotonic increase up to RHIC energies [202–204] without any significant structure (similar to the K^-/π^- ratio).

The measured excitation functions of hadron abundances with respect to pion yields are presented in Fig. 4.9 in comparison to thermal model results

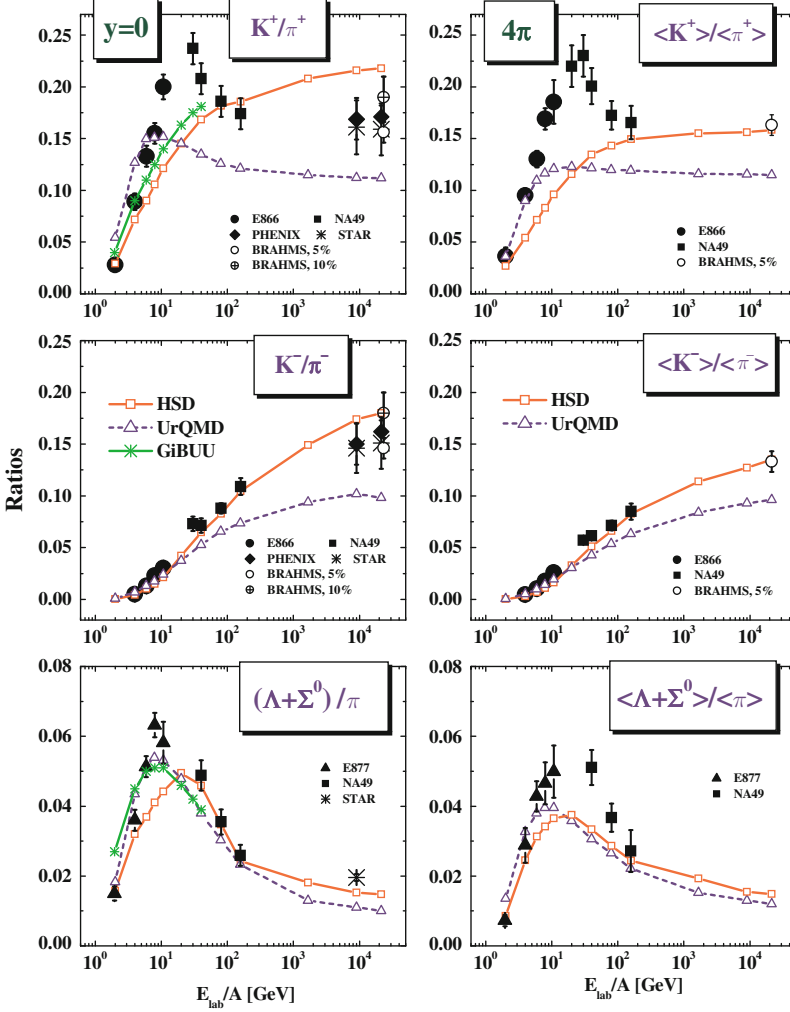


Fig. 4.7 The excitation function of K^+/π^+ , K^-/π^- and $(\Lambda + \Sigma^0)/(\pi^+ + \pi^-)$ ratios from 5% central (AGS energies, SPS at 160 AGeV and at RHIC energies), 7% central (20, 30, 40 and 80 AGeV), 10% central for $\Lambda + \Sigma^0$ at 160 AGeV Au+Au (AGS and RHIC) or Pb+Pb (SPS) collisions in comparison to the experimental data from [191, 193, 194] (AGS), [159, 166, 195–198] (SPS) and [199–204] (RHIC) for midrapidity (*left column*) and rapidity integrated yields (*right column*). The solid lines with open squares show the results from HSD whereas the dashed lines with open triangles indicate the UrQMD calculations. The solid line with the stars corresponds to the GiBUU results [205]

[6]. The calculations are based on the parameterizations of freeze-out temperature and baryon-chemical potential as shown in the right panel of Fig. 4.1. In contrast to previous studies [26], these thermal model fits include very high-mass resonances ($m > 2$ GeV), and the scalar σ meson (for details see [6]). No

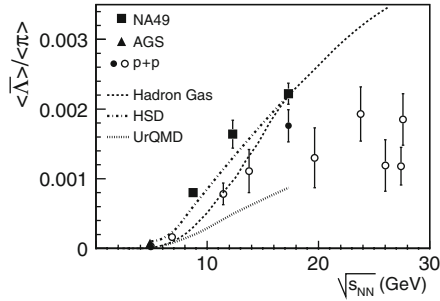


Fig. 4.8 The $\bar{\Lambda}/\pi$ ratio in full phase space versus energy from NA49 (*squares*), AGS [215] (*triangles*) and p-p reactions (*filled circle* from NA49 and *open circles* from [216]). The curves show predictions from the Hadron-gas model [20, 217–220] (*dashed*), UrQMD [209] (*dotted*) and HSD [221] (*dash-dotted*) including multi-meson fusion channels

contribution from weak decay feed-down is included in the model calculations as well as in the data. The ratios shown in Fig. 4.9 reflect the evolution of the fireball composition at freeze-out as a function of energy. The steep decrease of the p/π^+ ratio directly reflects the decrease as a function of energy of stopping of the incoming protons, implying a decrease of μ_b . The increase of pion production also plays a role in this ratio. Beyond $\sqrt{s_{NN}} \simeq 100$ GeV, the flattening is a consequence of the dominance of newly created baryons. The steep variation of the K^+/π^+ and K^-/π^- ratios at the lowest energies reflects the threshold for strangeness production, determined in the model by the steep increase of the temperature. The canonical suppression plays an important role as well. The ratio K^-/π^- shows a monotonic increase with energy followed by a saturation, essentially determined by the temperature (as both particles are newly created). In contrast, the ratio K^+/π^+ exhibits a peak around $\sqrt{s_{NN}} \simeq 8$ GeV which has been interpreted as a signature for the onset of QGP [165, 222, 223]. As the K^+ meson contains a u and a \bar{s} valence quark, it can be produced either associated with a Λ (or a Σ hyperon), or together with a K^- meson. Therefore, K^+ meson yield results from the convolution of two competing contributions as a function of energy: (i) the decreasing net light quark content (i.e. baryo-chemical potential), and (ii) the increasing production quark-antiquark pairs.

The thermal model predicts a rise and fall of the energy dependence of the relative hyperon yields Λ/π^- , Ξ^-/π^- and Ω^-/π^- which is caused by the interplay of rising temperature and decreasing baryon-chemical potential. Within the thermal model the peaks for the more massive hyperon species are less pronounced and located at higher energies, in agreement with the data. The mass hierarchy of the width and the location of the peaks, as recently discussed by Cleymans et al. [224], awaits experimental confirmation by improved data (see right panel of Fig. 4.9).

A more general way to represent the ratio of strange to non-strange hadrons is the strangeness (σ) to entropy (S) ratio [6]. Its excitation function

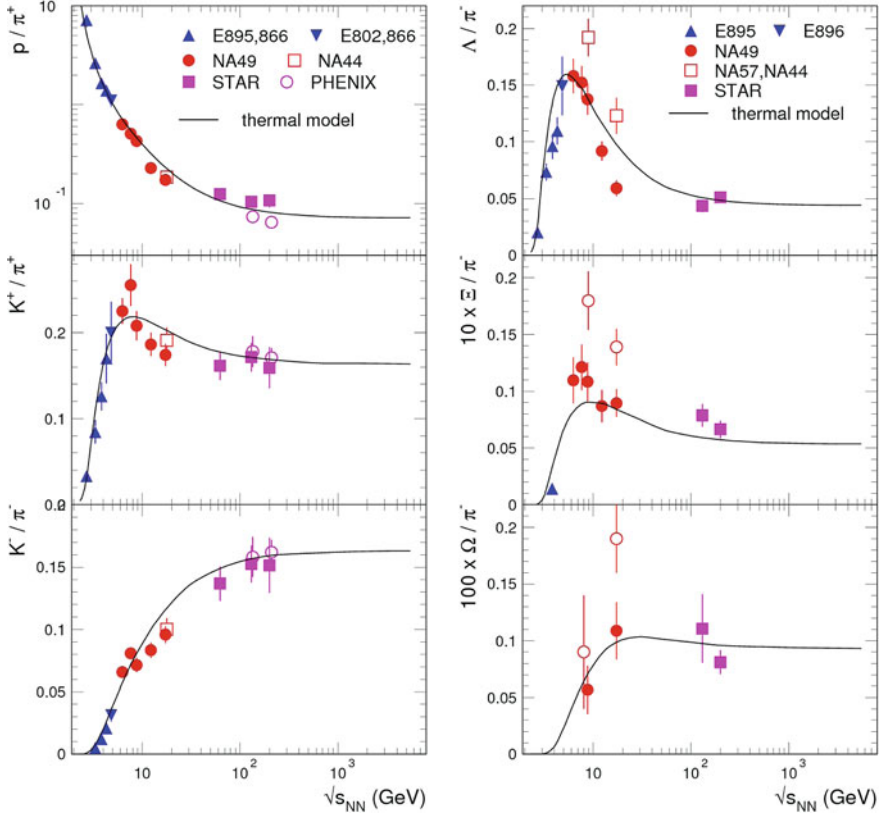


Fig. 4.9 The energy dependence of strange hadron yields relative to pions, including the most recent results from NA49 [166, 195] and RHIC [225]. In the *right panel*, note the scaling factors of 10 and 100 for the Ξ^-/π^- and Ω^-/π^- ratios, respectively. The measured yields at midrapidity are compared to the thermal model calculations of ref. [6]

is presented in Fig. 4.10. The two quantities have been calculated from the yields at mid-rapidity as:

$$\begin{aligned}\sigma &= 2(K^+ + K^-) + 1.54(\Lambda + \bar{\Lambda}) \\ S &= 1.5(\pi^+ + \pi^-) + 2\bar{p}\end{aligned}$$

The strangeness has in principle to be complemented with the yields of ϕ , Ξ , and Ω (and $\bar{\Xi}$, and $\bar{\Omega}$), but, since the measurements for these yields are scarce (as seen in Fig. 4.9) they were left out for the strangeness count. The factor 2 multiplying the kaon yields takes into account K^0 , while the factor 1.54 for Λ hyperons accounts for the contribution of Σ^\pm and was deduced from the model calculations (the yield of Σ^0 which decays with 100% branching ratio into $\Lambda\gamma$ is always included in the Λ yield.). The factor 1.5 for the pion yields accounts for the π^0 yield, while in case of \bar{p} yields the factor 2 is used to account for the produced protons. As expected from the individual particle

ratios studied above, the ratio strangeness to entropy is well reproduced by the model, with the exception of the NA49 data taken at high SPS energies.

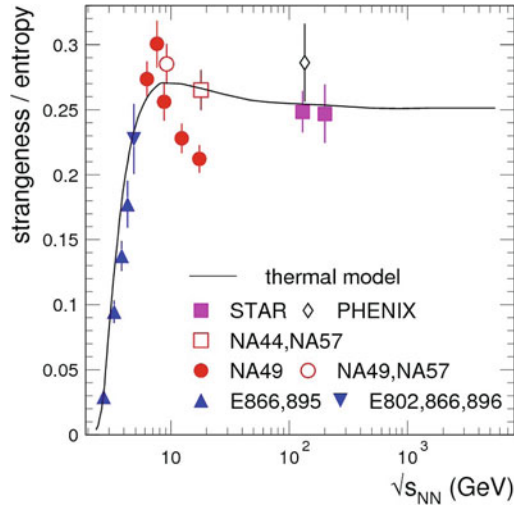


Fig. 4.10 Energy dependence of the strangeness to entropy ratio (see text). The *solid line* corresponds to a thermal model fit to the data, the model includes very high-mass resonances ($m > 2$ GeV), and the scalar σ meson [6]

4.3 Conclusions and perspectives for FAIR

The most intriguing feature in the excitation function of particle yields and ratios is the peak-like structure in the K^+/π^+ ratio at beam energies of 20–30 AGeV. A confirmation of these data by an independent experiment would certainly stir up the debate on a possible signature for the deconfinement phase transition at low SPS or FAIR energies. The excitation function of multi-strange hyperon production has to be measured with better accuracy in order to shed light on the strangeness production mechanisms. The measurements require a large detector acceptance over the full beam energy range, and excellent particle identification capabilities.

Chapter 5

Transverse mass spectra

Apart from particle yields also the phase space distributions of particles provide relevant information on the reaction dynamics. The transverse mass spectra of hadrons (heavier than pions) measured at AGS, SPS and RHIC energies can be parameterized by

$$\frac{1}{m_T} \frac{dN}{dm_T} \sim \exp\left(-\frac{m_T}{T}\right) \quad (5.1)$$

with $m_T = (p_T^2 + m^2)^{1/2}$. The m_T spectra measured in central Au+Au collisions exhibit substantial “harder” slopes as those from pp interactions (cf. [226]). This increase of the inverse slope parameter T (see Eq. (5.1)) for low transverse mass or momentum is commonly attributed to strong collective flow, which is absent in pp or pA collisions.

5.1 Beam energy dependence of transverse mass distributions

Figure 5.1 depicts the inverse slope parameters T as a function of \sqrt{s} extracted from K^+ and K^- meson transverse mass spectra measured for central Au+Au (Pb+Pb) collisions (l.h.s.) and pp reactions (r.h.s.) using Eq. (5.1) [226, 227]. The data are compared to results of various transport model calculations. The two solid lines with open circles on the l.h.s. in Fig. 5.1 represent results of HSD calculations corresponding to upper and lower limits due to the fit accuracy of the slope T , an uncertainty in the repulsive K^\pm potential, and the effect of possible string overlaps. The HSD calculations also demonstrate that the “partonic” Cronin effect plays a minor role at AGS and SPS energies for the parameter T . The slope parameters from pp collisions (r.h.s. in Fig. 5.1) increase smoothly with energy both in the experiment (full triangles) and in the transport calculations (full lines with open circles), and are

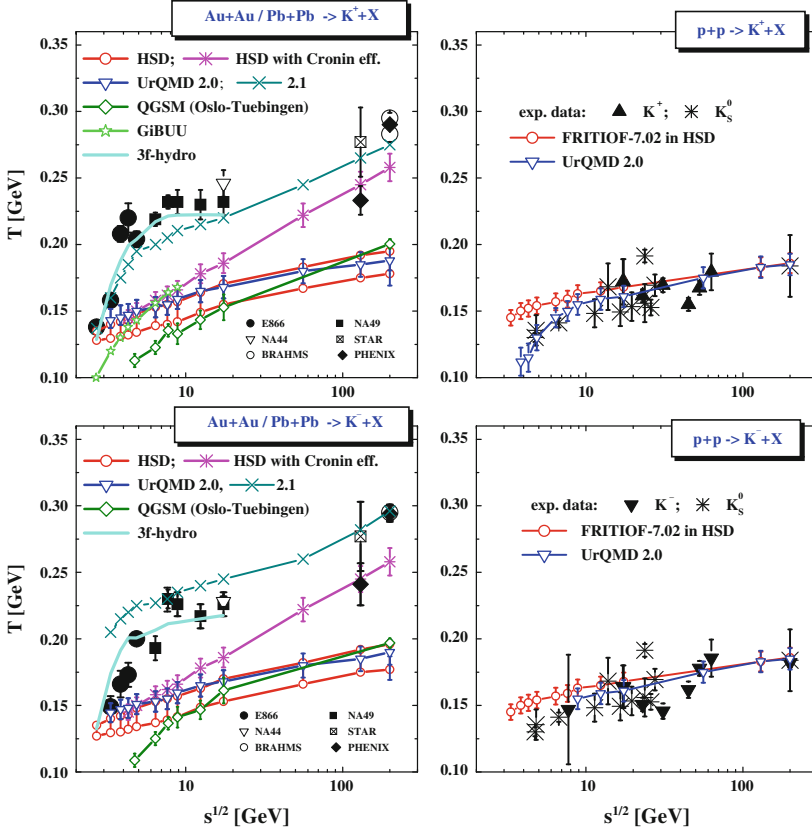


Fig. 5.1 Comparison of the inverse slope parameters T for K^+ and K^- mesons from central Au+Au (Pb+Pb) collisions (l.h.s.) and pp reactions (r.h.s.) as a function of the invariant energy \sqrt{s} from HSD (*upper and lower solid lines*) [30] and UrQMD (*open triangles*) [30] with data from [191, 199–204, 226, 228] for AA and [202–204, 227, 229] for pp collisions. The *open diamonds* show the Oslo-Tübingen QGSM [230–235] results, the *solid line with the stars* corresponds to the GiBUU calculations [205] while the *solid line* stands for the 3-fluid hydrodynamical model [236] that performs best at FAIR energies

significantly lower than those from central Au+Au reactions for $\sqrt{s_{NN}} > 3.5$ GeV.

The inverse slope parameters of kaon and antikaon transverse mass spectra measured in pp collisions satisfactorily agree with HSD and UrQMD transport calculations (see right panels of Fig. 5.1). The same is true for central C+C and Si+Si collisions [237]. For central Au+Au (or Pb+Pb) collisions, however, the situation is quite different (see left panels of Fig. 5.1). Whereas at a collision energy of $\sqrt{s_{NN}} = 3.3$ GeV (corresponding to a beam energy of 4 AGeV for fixed target experiments) the agreement between the transport model calculations and the data is still acceptable, the data are severely un-

derestimated by the transport models from $\sqrt{s_{NN}} = 7.7$ to 17.3 GeV (SPS energies 30 and 160 AGeV) [237]. Note that the π^\pm spectra are reasonably well described. Within the calculations, the increase of the inverse K^\pm slopes in heavy-ion collisions with respect to pp collisions is generated by rescattering of the produced hadrons. However, this effect provides only little additional transverse momentum at midrapidity because the elastic meson-baryon scattering is strongly forward peaked. Similar results are obtained with the GiBUU model [205] (up to 40 AGeV) and with the QGSM model [230–235]. For a more detailed discussion and other alternative scenarios implemented in the HSD, UrQMD and GiBUU models we refer to [30, 205].

The RQMD and UrQMD 2.1 models [30, 238] produce harder kaon spectra (i.e. larger inverse slope parameters) at AGS and SPS energies than HSD, UrQMD 2.0 and GiBUU. This effect essentially can be traced back to the implementation of effective resonances with masses above 2 GeV as well as “color ropes” which decay isotropically in their rest frame [239]. These heavy resonances preferentially decay into pions and nucleons or into kaons and nucleons (in UrQMD). In this way the pion number is reduced (which is in agreement with experimental data) and the hadron slope parameters are increased. However, in this case the pion and antikaon slope parameters are overestimated. Therefore, no conclusive picture emerges from the comparison of the experimental data to transport model calculations. One may speculate whether the additional pressure – which leads to the enhanced flow and, hence, to the large slope parameter – is generated in the early partonic phase of the collision. A more detailed discussion of this issue is presented in [30].

5.2 Particle mass dependence of transverse mass distributions

It was observed that the slope parameters do not follow a simple scaling with particle mass as expected for a radial collective flow. This finding is illustrated in Fig. 5.2 where the slope parameters T measured in $\sqrt{s_{NN}} = 200$ GeV Au + Au (full-circles) and $\sqrt{s_{NN}} = 17.2$ GeV Pb + Pb (open-circles) central collisions are presented as functions of the particle mass. The slope parameters rise with particle mass up to about 1 GeV, and then saturate for heavier particles. A similar observation has been made for particles decaying into lepton pairs (see Chap. 7). The light hadrons – up to masses of 1 GeV – get additionally accelerated in the hadronic phase by resonant rescattering. Multi-strange and charmed hadrons, however, cannot pick up flow in the hadronic phase as their hadronic reaction cross sections are too small. Therefore, the m_T spectra of multistrange and charmed hadrons are determined by the pressure in the early (partonic) phase of the collision.

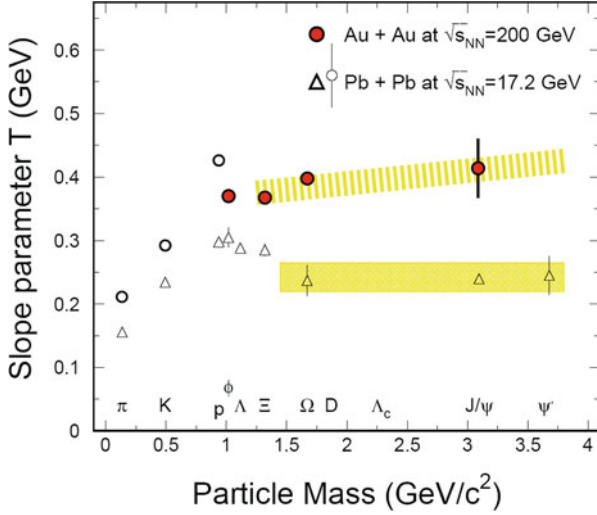


Fig. 5.2 Hadron inverse slope parameters T from $\sqrt{s_{NN}} = 200$ GeV Au + Au (*full-circles*) and $\sqrt{s_{NN}} = 17.2$ GeV Pb + Pb (*open-circles*) central collisions [240]

5.3 Conclusions and perspectives for FAIR

The transverse-mass inverse-slope parameters of strange particles measured in heavy-ion collisions are largely underestimated by hadron transport models for beam energies above 4 AGeV. Whether this discrepancy is due to missing heavy baryon resonances in the transport codes, or due to additional pressure generated in an early partonic phase, is still an open question. A possible experimental approach to study the early phase of the collision is to measure the phase-space distributions of ϕ mesons, multi-strange hyperons, D mesons and charmonium with high precision. These particles are only little affected by hadronic rescattering, and, therefore, their transverse mass distributions still reflect the initial conditions of a heavy-ion collision. Further progress requires the measurement of these rare probes in large data samples, and for various beam energies and collision systems.

Chapter 6

Collective flow

6.1 General considerations

Hydrodynamic flow and shock formation have been proposed early [241] as the key mechanism for the creation of hot and dense matter during relativistic heavy-ion collisions. However, the full three-dimensional hydrodynamical flow problem is much more complicated than the one-dimensional Landau model [242] used in many of the present hydrodynamical calculations. The 3-dimensional compression and expansion dynamics yields complex triple differential cross-sections, which provide quite accurate spectroscopic handles on the equation of state (EoS). The “bounce-off”, the “squeeze-out” and the “antiflow” [243] (third flow component [244]) have been suggested as differential barometers for the properties of compressed, dense matter from SIS to RHIC. Presently, the most employed flow observables are the “in-plane flow” and the “elliptic flow” [245]:

$$v_1 = \left\langle \frac{p_x}{p_T} \right\rangle, \quad v_2 = \left\langle \frac{p_x^2 - p_y^2}{p_x^2 + p_y^2} \right\rangle. \quad (6.1)$$

Here, p_x denotes the momentum in x -direction, i.e. the transverse momentum within the reaction plane and p_y the transverse momentum out of the reaction plane. The total transverse momentum is given as $p_T = \sqrt{p_x^2 + p_y^2}$; the z -axis is in the beam direction. Thus, v_1 measures the “bounce-off”, i.e. the strength of the directed flow in the reaction plane, and v_2 gives the strength of the second moment of the azimuthal particle emission distribution, i.e. “squeeze-out” for $v_2 < 0$ [241, 243].

Microscopic (pre-)hadronic transport models describe the formation and distributions of many hadronic particles from SIS to SPS energies reasonably well [209]. The observed proton flow v_2 below ~ 5 AGeV is less than zero, which corresponds to the squeeze-out predicted by hydrodynamics [241]. The AGS data exhibit a transition from squeeze-out to in-plane flow in the

midrapidity region. The change in sign of the proton v_2 at 4–5 AGeV is in accordance with transport calculations – UrQMD [246], HSD [247, 248], ART [249] and BUU [250]. Calculation without nuclear potentials severely underestimates the elliptic flow up to SPS energies as demonstrated by a UrQMD calculation (in the cascade mode) in Fig. 6.1 for midrapidity nucleons in comparison to the available data (cf. also [251]).

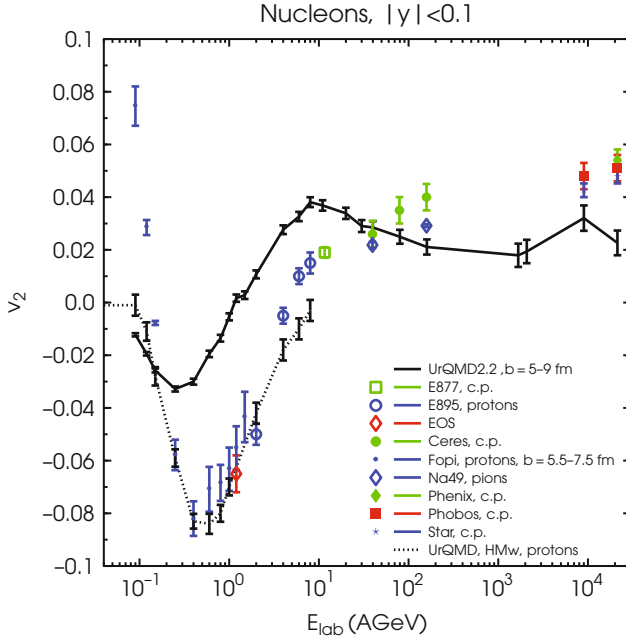


Fig. 6.1 Excitation function of v_2 for midrapidity nucleons in the UrQMD model in the cascade mode [252] in comparison to the available data

6.2 Nucleon flow and the nuclear equation-of-state

The directed and elliptic collective flow is generated in the very early phase of the collision, and thus is a promising probe for the properties of hot and dense matter. The disappearance or the “collapse” of flow has been discussed as a signature for a first order phase transition [243, 253]. The collective flow of nucleons is driven by the pressure in the reaction volume, and, hence, is sensitive to the equation-of-state (EoS) of (symmetric) nuclear matter. Values for the nuclear incompressibility have been extracted from flow data up to AGS energies by comparison to transport models [244, 246–248, 254, 255].

As discussed in [Part III](#), microscopic transport models reproduce the excitation function of the proton elliptic flow v_2 measured at SIS energies when incorporating a soft, momentum-dependent EoS [[212](#), [213](#), [256–258](#)]. This result is consistent with the interpretation of data on subthreshold kaon production. Both observables imply that the nuclear EoS is soft in the density range probed by heavy-ion collision at SIS energies, i.e. up to 2–3 times saturation density.

Proton flow data obtained in heavy-ion collisions at BEVALAC/SIS and AGS energies are shown together with the results of the transport model calculations in [Fig. 6.2](#). Values for the nuclear incompressibility of $\kappa = 170$ – 380 MeV have been extracted from the data [[132](#), [134](#)]. According to the model calculations, nuclear densities between $\rho = 2$ – $5 \rho_0$ are reached in the central fireball volume at these beam energies. The large range of κ values reflects the fact that the interpretation of proton flow data using transport models is not straight forward because the strength of the collective proton flow does not only depend on the EoS, but also on the in-medium nucleon-nucleon cross section, and on momentum-dependent interactions [[132](#)]. At SIS energies and below there is the additional complication that nucleonic clusters – which carry a substantial fraction of the nucleon flow – cannot be satisfactorily described by transport calculations.

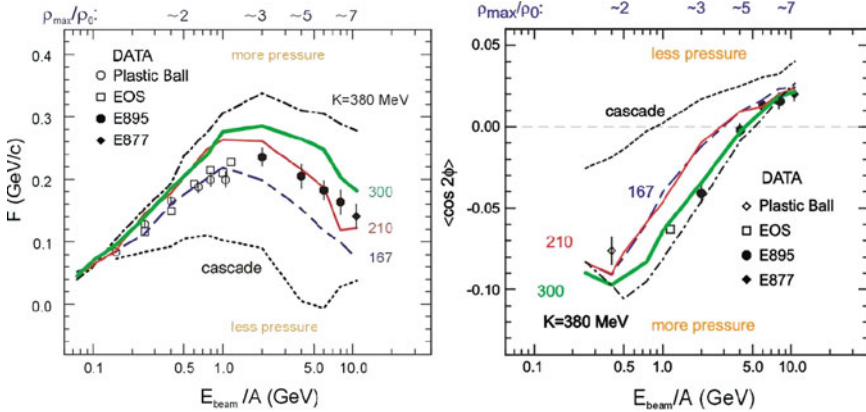


Fig. 6.2 *Left panel:* Sideward flow excitation function for Au+Au. Data and transport calculations are represented, respectively, by *symbols* and *lines*. *Right panel:* Elliptic flow excitation function for Au+Au. Data and transport calculations are represented, respectively, by *symbols* and *lines* (taken from [[132](#)])

6.3 Elliptic flow and partonic collectivity

One of the most intriguing observations at RHIC is the scaling of the strength of the elliptic flow v_2 with the number of constituent quarks n_q when studied as a function of transverse kinetic energy, as shown in the left panel of Fig. 6.3 for Au+Au at $\sqrt{s_{NN}} = 200$ GeV [259]. This scaling scheme has been extended to the v_2 of positive and negative pions, kaons and protons measured in Au+Au collisions at $\sqrt{s_{NN}} = 62.4$ GeV and Cu+Cu collisions at $\sqrt{s_{NN}} = 200$ GeV [260]. The middle panel of Fig. 6.3 shows that the constituent quark scaling of v_2 works well for π^\pm , K^\pm , p and \bar{p} in Au+Au collisions at $\sqrt{s_{NN}} = 62.4$ GeV. The scaling of v_2 is observed also for the smaller Cu+Cu system at $\sqrt{s_{NN}} = 200$ GeV (see right panel of Fig. 6.3). These observations suggest that partonic degrees of freedom exist in the matter formed at lower beam energy and in the smaller colliding system.

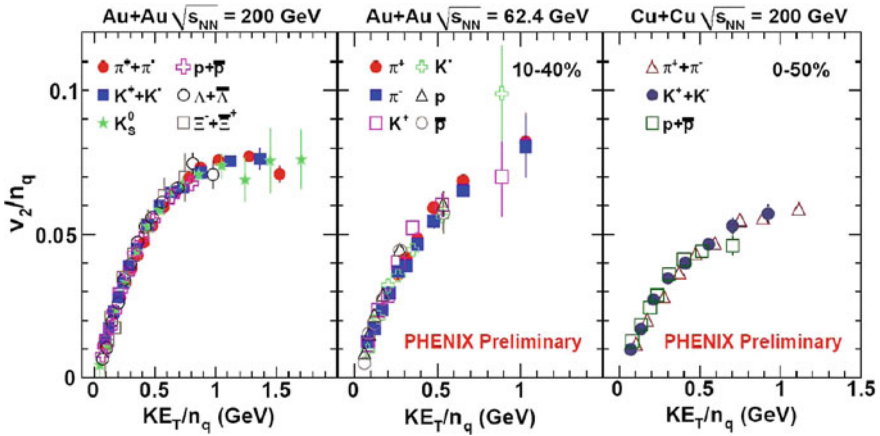


Fig. 6.3 Elliptic flow v_2/n_q as a function of transverse kinetic energy KE_T/n_q (both divided by the number of constituent quarks) for charged pions, kaons and protons in minimum bias Au+Au collisions at $\sqrt{s_{NN}} = 200$ GeV (left panel), in Au+Au collisions at $\sqrt{s_{NN}} = 62.4$ GeV for centrality 10–40% (middle panel) and Cu+Cu at $\sqrt{s_{NN}} = 200$ GeV for centrality 0–50% (right panel)

The elliptic flow of v_2 of ϕ mesons as measured in Au+Au collisions at $\sqrt{s_{NN}} = 200$ GeV is depicted in Fig. 6.4. The value of v_2 of ϕ mesons is surprisingly large. If the ϕ meson has a small cross-section with hadrons as suggested by the analysis of ϕ photo-production data ($\sigma_{\phi N} \approx 10$ mb [261]), it would not participate in the late stage hadronic interactions in contrast to hadrons such as pions, kaons and protons (or antiprotons) which freeze-out later. This indicates that the large elliptic flow of ϕ mesons must have been developed in the earlier partonic stage.

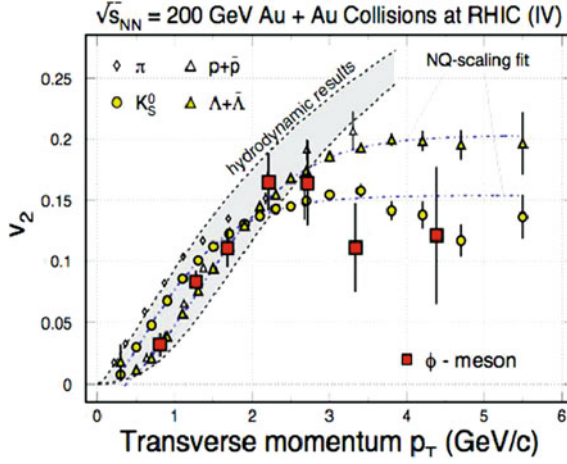


Fig. 6.4 Elliptic flow v_2 of mesons as function of transverse momentum measured at midrapidity in Au+Au collisions at $\sqrt{s_{NN}} = 200$ GeV [267]

The ϕ meson plays a particular role as a probe of the dense and hot nuclear medium. The proper lifetime of the ϕ meson is about 45 fm/c and it decays into charged kaons K^+K^- with a branching ratio of 49.2%, and more rarely into the dilepton pairs e^+e^- (B. R. of 2.97×10^{-4}) and $\mu^+\mu^-$ (B. R. of 2.86×10^{-4}). In an environment with many strange quarks, ϕ mesons can be produced through coalescence. Therefore, the enhancement of ϕ meson production due to the coalescence of $s\bar{s}$ pairs in the hot medium has been predicted to be a probe of the QGP in ultra-relativistic heavy-ion collisions [150, 262–264]. On the other hand, ϕ meson production via $K\bar{K} \rightarrow \phi$ in the hadronic rescattering stage may also lead to ϕ meson enhancement in heavy-ion collisions. Indeed, hadronic transport models such as RQMD [238] and UrQMD [207] have predicted an increase of the ϕ to K^- production ratio at midrapidity as a function of the number of participant nucleons. This prediction, however, was disproved for Au+Au collisions at $\sqrt{s_{NN}} = 200$ GeV by a measurement of the STAR collaboration [265, 266].

Figure 6.4 presents also the predictions of hydrodynamics (grey shaded area) and of quark number scaling (dashed-dotted lines). In the low p_T region (< 2 GeV/c), the v_2 value of the ϕ lies between that for the K_S^0 and the Λ in Au+Au 200 GeV collisions, consistent with the expectation of a mass ordering for v_2 in hydrodynamic models. These observations support the hypothesis of the development of partonic collectivity and possible thermalization in the early stages of heavy-ion collisions at RHIC. In the intermediate p_T region (≈ 2 –5 GeV/c), the v_2 of the ϕ meson is consistent with that for the K_S^0 rather than for the Λ . The fact that the $v_2(p_T)$ of ϕ is the same as that of other mesons indicates that the heavier s quarks flow as strongly as the lighter u and d quarks.

6.4 Collective flow and phase transitions

Several hydrodynamic models have been used in the past to calculate flow observables, starting with the one-fluid ideal hydrodynamic approach. It is well known that the latter model predicts far too large flow effects from SIS to SPS energies. To obtain a better description of the dynamics, viscous fluid models have been developed [271–273]. In parallel, so-called three-fluid models, which distinguish between projectile, target and the fireball fluids, have been introduced [32, 274, 275]. Here viscosity effects appear only between the different fluids, but not inside the individual fluid components. The future aim is to develop a reliable, three-dimensional, relativistic fluid model including viscosity [32, 272, 273].

Ideal hydro calculations predict the appearance of a so-called “third flow component” [244] or “antiflow” [269] in central collisions if the matter undergoes a first order phase transition to the QGP. In this case it is expected that

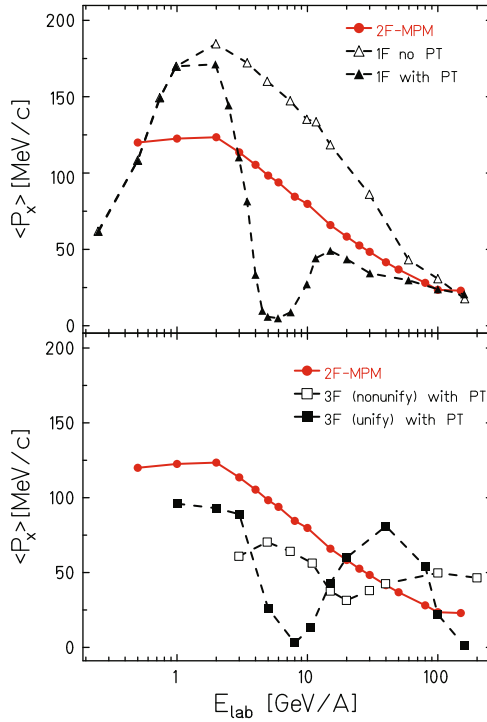


Fig. 6.5 Excitation function of the average directed flow for baryons from central Au + Au collisions calculated with two-fluid hydrodynamics with the EoS from the Mixed-Phase (MP) model, with one-fluid [268] with and without the phase transition (PT) (*upper panel*) and three-fluid [269] (*lower panel*) hydrodynamics with the bag-model EoS. (The figure is taken from [270])

the directed flow of protons $p_x(y)$ develops a negative slope around midrapidity [276]. This effect is not present in calculations based on a hadronic EoS without QGP phase transition. An example for an ideal hydrodynamics calculation with a first order phase transition is presented in Fig. 6.5 which illustrates the behavior of the directed proton flow p_x as function of beam energy: p_x becomes negative between 8 and 20 AGeV, and turns positive again with increasing energy when the compressed QGP phase is probed. These early hydrodynamical calculations have predicted the collapse of flow at the “softest point” to happen at beam energies of $E_{Lab} \approx 8$ AGeV; this has not been verified by the AGS data. However, a linear extrapolation of the AGS data suggest that a collapse of the directed proton flow might occur at $E_{Lab} \approx 30$ AGeV (see arrow in Fig. 6.6).

It should be noted that the hydrodynamical predictions for the negative values of $p_x(y)$ have to be taken with caution. Figure 6.5 demonstrates the sensitivity of the hydrodynamical calculations to the model ingredients, in particular to the initial and “freeze-out” conditions. For example, modifications of the “freeze-out” conditions such as the merging of the final 3 fluids to a single one, can lead to the disappearance of the “antiflow” effect.

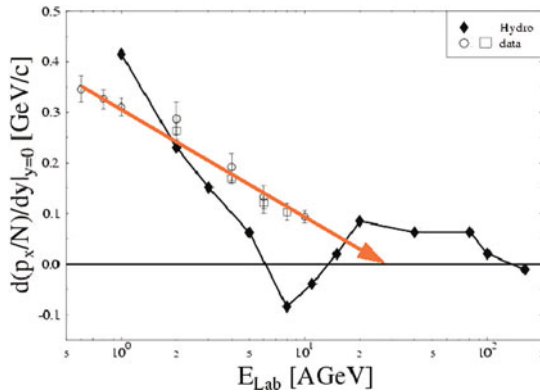


Fig. 6.6 Proton flow dp_x/dy as a function of beam energy. *Open symbols*: data measured at AGS. *Solid line*: (2+1)-fluid hydro calculation [276]. A linear extrapolation of the data (arrow) suggests a collapse of flow at $E_{Lab} \approx 30$ AGeV

Experimental indication for the collapse of proton flow has been found by the NA49 collaboration [277]. Figure 6.7 presents the directed flow v_1 (left) and elliptic flow v_2 (right) of protons as function of rapidity as measured in Pb+Pb collisions at 40 AGeV, in comparison to results of transport models. The 3-fluid hydrodynamic model [32, 236] with a hadronic EoS (solid line without symbols) overestimates both the slope of v_1 and the strength of v_2 for noncentral collisions. The hadronic transport models UrQMD and HSD explain reasonably well the v_1 flow component, but predict too large positive values for the elliptic flow v_2 . Future experimental studies will have to

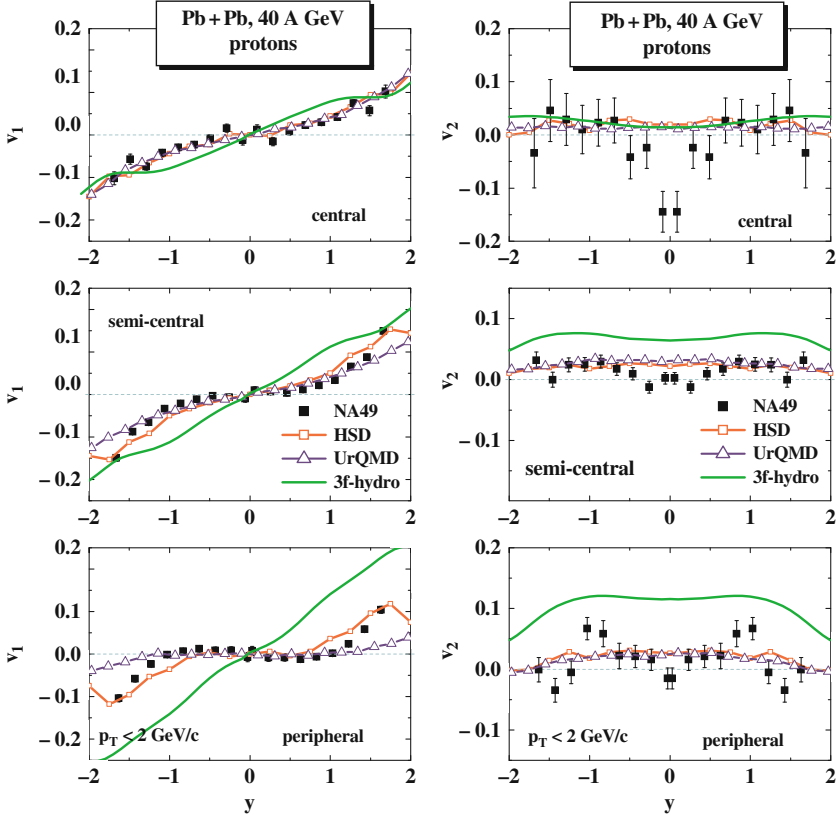


Fig. 6.7 Directed flow v_1 (left row) and elliptic flow v_2 (right row) of protons as function of rapidity measured in central, semi-central and peripheral (from *top to bottom*) Pb+Pb collisions at 40 AGeV in comparison to transport model results [277]

systematically map out the flow components in heavy-ion collisions at different bombarding energies in order to determine precisely the “softest point” of nuclear matter, and, eventually, to locate the first order phase transition between hadronic and partonic matter.

Though collective flow can be described very elegantly in hydrodynamics by a proper choice of initial conditions [278–281], most hydrodynamical calculations – describing flow – fail to reproduce the hadron spectra with the same initial conditions (and vice versa). Therefore, it is reasonable to consider also microscopic transport theory, e.g. models like UrQMD [124, 207], HSD [42, 206], GiBUU [208, 212, 213], RQMD [238], QGSM [230–235, 282, 283], or AMPT [284, 285] as complementary approaches to study the degree of equilibration, the in-medium particle properties, self energies, and cross sections. The comparison of data to hydrodynamical calculations with and without quark matter EoS, and to hadron transport models with and without early

partonic phase, will help to answer the question whether quark matter has been formed in heavy-ion collisions.

6.5 Conclusions and predictions for FAIR energies

The measurement of the collective flow of particles emitted in heavy-ion collisions provides unique information on the space-time evolution of the fireball. For example, the strength of the elliptic flow v_2 and its dependence on the particle transverse momentum sheds light on the degrees of freedom which prevail in the early stage of the collision. In particular, the scaling of v_2 with the number of constituent quarks observed at RHIC (see Figs. 3.30 and 6.3) is interpreted as a direct signature for partonic collectivity.

Large values of v_2 are expected due to the partonic pressure built up in the early phase of the collision. This effect is illustrated in Fig. 6.8 which depicts a compilation of transport model results on elliptic flow v_2 of charged hadrons at midrapidity for mid-central ($b = 7$ fm) Au+Au collisions at a typical FAIR beam energy of 25 AGeV. The figure includes results from AMPT [286] without and with string melting, QGSM/Dubna [287], QGSM/Oslo-Tübingen [230–235], UrQMD [252], HSD [288] and GiBUU [289]. The trans-

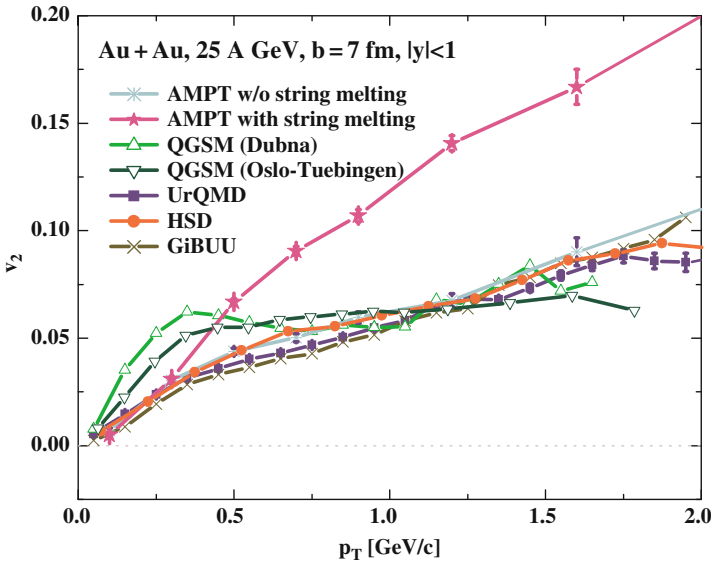


Fig. 6.8 Elliptic flow v_2 versus transverse momentum p_T of charged hadrons as calculated using various transport models: AMPT without and with string melting, QGSM (Dubna and Oslo-Tuebingen), UrQMD, HSD, and GiBUU. The calculations are performed at midrapidity $|y| < 1$ for mid-central Au+Au collisions (impact parameter $b=7$ fm) at 25 AGeV

port models based on hadron/string degrees of freedom predict very similar values for $v_2(p_T)$ (except for QGSM which predicts a larger v_2 value at transverse momenta of 0.3–0.4 GeV/c). However, when including “string melting” in AMPT, corresponding to partonic degrees of freedom in the early phase, the elliptic flow increases almost by a factor of 2, which results from partonic interactions prior to hadronization. Thus, the precise measurement of $v_2(p_T)$ as function of beam energy already may provide information on the onset of deconfinement.

The full string-melting option of the AMPT code assumes that the initially produced matter is 100% partonic. The hot and dense partonic medium generates a pressure which drives the quark flow. The v_2 flow component of hadrons is obtained from the v_2 of the corresponding quarks using the coalescence model. Figure 6.9 depicts the elliptic flow v_2 for charged hadrons normalized to the constituent quark number n_q as function of transverse momentum per constituent quark calculated at midrapidity ($|y| < 1$) with the AMPT transport code with string melting. The calculations were performed for mid-central Au+Au collisions at $\sqrt{s_{NN}} = 7$ GeV (corresponding to 25 AGeV fixed target beam energy).

The calculations presented in Fig. 6.9 demonstrate that approximate constituent quark number scaling is expected in the case of an early partonic phase. In order to locate the phase transition from hadronic to partonic

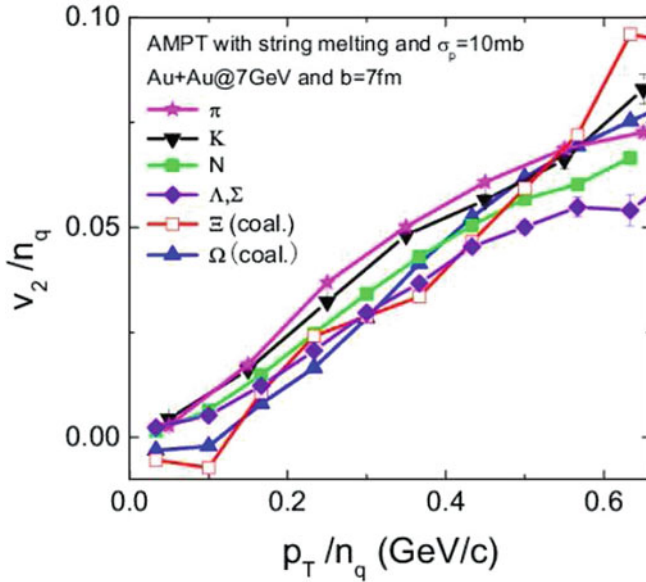


Fig. 6.9 Elliptic flow v_2 for charged hadrons normalized to the constituent quark number n_q versus transverse momentum per constituent quark as calculated with the AMPT transport model with string melting, for Au+Au collisions at a center of mass energy $\sqrt{s_{NN}} = 7$ GeV for an impact parameter $b=7$ fm (at midrapidity $|y| < 1$)

matter, future experiments will have to scan carefully the beam energies measuring the elliptic flow of many particles (including multi-strange and charmed particles), and search for the onset of constituent quark number scaling of the elliptic flow.

Chapter 7

Dileptons

7.1 General overview

Electromagnetic decays to virtual photons (decaying further into e^+e^- or $\mu^+\mu^-$ pairs) have been suggested long ago as a possible signature for a phase transition to the QGP [280, 290–293], or as a probe for in-medium vector meson properties and chiral symmetry restoration.

We recall that chiral symmetry restoration does not necessarily imply that vector-meson masses have to drop with baryon density, ρ_B , or temperature, T [294, 295]. More generally, chiral symmetry restoration dictates that the spectral functions in the vector-isovector and the axialvector-isovector channel (usually associated with the chiral partners ρ and a_1) become identical at high ρ_B and/or T . Possible realizations of chiral symmetry restoration, therefore, include [296] a “chiral mixing” of the ρ and a_1 spectral functions [297, 298] or a degeneracy via a strong broadening induced by hadronic many-body effects [299–302]. In either case, a direct experimental measurement of in-medium vector-meson properties is not easy and needs to be augmented by systematic theoretical analysis as outlined in Sect. 2.3 of Part II.

Dileptons provide the key to vector-meson measurements in the hot and/or dense medium. As pointed out in [301, 303, 304] the dilepton invariant mass spectra reflect the imaginary part of the ρ meson propagator which is proportional to the isovector current-current correlation function. Furthermore, the differential rate for dilepton radiation off hot and dense matter can be cast into a form [305] which highlights the direct connection between an observable (dilepton spectra) and the (in-medium) electromagnetic spectral function, which is dominated by the light vector mesons (ρ , ω , ϕ), especially the ρ , up to invariant masses of $M \simeq 1$ GeV.

Since dileptons can leave the reaction volume essentially undistorted by final-state interactions, they carry information about potential in-medium modifications of vector-meson properties out of the violent phases of a high-energy heavy-ion collision to the detectors. Indeed, the lepton-pair studies in

heavy-ion collisions by the DLS Collaboration at the BEVALAC [306–309], by the HADES Collaboration at GSI-SIS [310, 311], by the CERES [312, 313], HELIOS [314–316], NA38 [317, 318], NA50 [319], and NA60 Collaborations [320] at the CERN-SPS, and first results from the PHENIX Collaboration at RHIC [321, 322] have created a vivid interest in the nuclear physics community.

The experimental challenge of dilepton measurements is twofold. First, leptons need to be cleanly identified and separated from the large background of hadrons, mainly pions. Then, substantial physical and combinatorial backgrounds have to be determined and subtracted from the invariant pair-mass spectrum.

Electron measurements have been performed at all laboratories that have investigated dilepton production in heavy-ion collisions. Typically, electron identification relies on Cherenkov detectors, transition radiation radiators, and electromagnetic calorimeters. A dominant source of physical background of electron-positron pairs at all beam energies is the Dalitz decays of light neutral mesons, mainly π^0 and η mesons. At BEVALAC and SIS beam energies around 1 AGeV additional contributions from Δ resonance decays and from proton-neutron bremsstrahlung are important. At RHIC, even di-electron pairs from correlated charm decays can not be ignored towards higher pair mass. These (and other less important) sources compose the so called hadronic cocktail. A typical example from the CERES experiment at the CERN-SPS is shown in Fig. 7.1 for proton-gold collisions at 450 GeV. In general, this background has to be determined through independent measurements of the di-electron sources, e.g. the measurement of neutral pions and η mesons via their $\gamma\gamma$ decays. Another important contribution to the physical background is due to the conversion of photons in the target (in case of a fixed target experiment) and in the detector material. To minimize this background, di-electron experiments usually put special emphasis on designing their setups such that the amount of material within their acceptance is as small as possible. The remaining conversion background can partly be suppressed by removing electron-positron pairs with small opening angles which are dominated by γ conversions.

Non-physical background from the combination of uncorrelated electrons and positrons can overwhelm the physical signal by large factors. With increasing available energy the multiplicity of produced particles grows and, consequently, the combinatorial background rises rapidly, such that e.g. at RHIC signal to background ratios below one percent have to be dealt with. Techniques to determine combinatorial background with high precision include event mixing, where electrons are combined with positrons from different events, or the measurement of like-sign lepton pairs within the same event. The latter resemble the combinatorial background in case the geometrical acceptance of the apparatus is the same for unlike-sign and like-sign pairs.

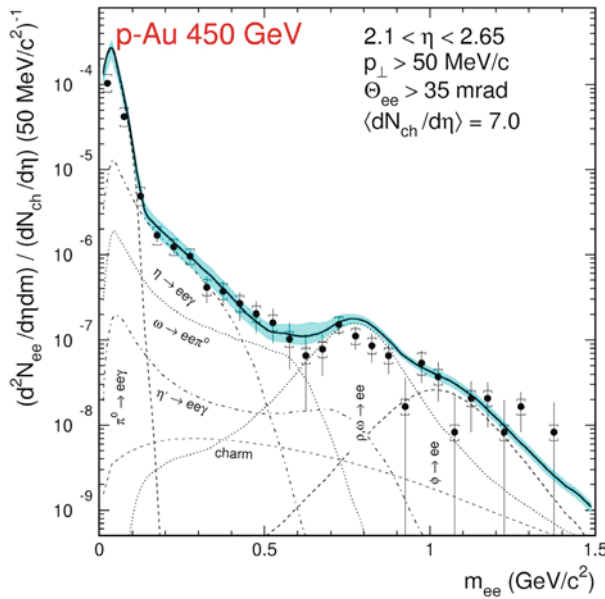


Fig. 7.1 Invariant mass spectrum of electron-positron pairs measured in p+Au collisions at 450 GeV. The contributions from known di-electron sources (“hadronic cocktail”) are indicated [323]

Dimuon measurements in the mass range relevant in the context of in-medium modifications of vector mesons have been done at the CERN-SPS. In these experiments muons are identified as the only charged particles punching through a thick hadron absorber located in front of a spectrometer. In the case of muon pairs the physical background is very much reduced compared to electron pairs. Since pion decays and photon conversions do not contribute to the muon-pair spectrum the most important source that remains is the Dalitz decay of η mesons. A large combinatorial background is created by muons from weak decays of pions and kaons, and by remaining hadrons which punch through the absorber and are misidentified as muons. As in the case of electron pairs the combinatorial background is determined by the analysis of like-sign pairs from the same event, and of unlike-sign pairs using particles from different events.

7.2 Lessons from the CERN-SPS

7.2.1 Invariant mass spectra

Until now, the most complete studies of dilepton production have been conducted at the CERN-SPS both in the electron and muon channel using pro-

ton, sulphur, indium, and lead beams incident on various nuclear targets. In proton induced reaction the measured dilepton invariant-mass distributions are in good agreement with the expected hadronic cocktail as shown in Fig. 7.1 for the CERES dielectron data measured in p+Au collisions at 450 GeV beam energy [323]. Dilepton continuum yields clearly beyond the hadronic cocktail were observed for the first time in sulphur induced reactions with heavy target nuclei. These early findings from the SPS are documented in Fig. 7.2 which shows dielectron spectra measured by the CERES Collaboration in S+Au collisions at 200 GeV/u [324] and dimuon spectra measured by the HELIOS-3 Collaboration in S+W reactions at the same energy [325].

Various microscopic transport calculations without in-medium modifications of the vector mesons but involving bare vector-meson masses only [326–333] are not able to reproduce the substantial enhancement observed in the low-mass region as demonstrated in the upper panels of Fig. 7.2. Only when dropping vector-meson masses in the dense nuclear medium are considered in the model calculations from [327, 332, 334], a reasonable agreement with the data is achieved as shown in the lower panels of Fig. 7.2.

However, this “dropping ρ mass” scenario is not the only possible explanation for the observed low-mass dilepton enhancement. It has been pointed out in [42, 295] that the previous experimental data can be described equally well within the “melting ρ ” picture, which implies a large spreading in mass of the ρ spectral function due to its couplings to baryons and/or mesons. This is demonstrated in Fig. 7.3, which shows a comparison of the dielectron spectrum measured by the CERES Collaboration in semicentral Pb+Au collisions at 158 AGeV [336] with results from a thermal evolution model [296, 337, 338]. In this calculation three different types of ρ spectral functions have been convoluted over a fireball expansion and the resulting dilepton spectra from the hadronic phase are supplemented with a hadronic decay cocktail accounting for final state decays after thermal freeze-out, as well as a small contribution due to dilepton emission from the QGP. The enhanced dielectron yield at low mass can be attributed to thermal radiation from the fireball which is dominated by the pion annihilation process $\pi^+\pi^- \rightarrow \rho \rightarrow l^+l^-$ with an intermediate ρ meson that is subject to strong in-medium modifications. However, the quality of these data in terms of statistics, invariant mass resolution and signal-to-background ratio neither allows to decisively distinguish between a dropping-mass and a broadening scenario nor is it sufficient to disentangle the contributions of the different vector mesons to the mass spectra or to perform a multi-differential analysis.

The experimental situation improved dramatically in 2005 when the NA60 Collaboration presented their dimuon spectra for In+In collisions at 160 AGeV [320]. The NA60 apparatus combines the previous NA50 muon spectrometer, which provides a very selective dimuon trigger, with a high granularity silicon pixel vertex spectrometer. The latter leads to a larger dimuon acceptance at low mass and low p_T with significantly improved mass resolution and a reduced combinatorial background. The measured unlike-sign

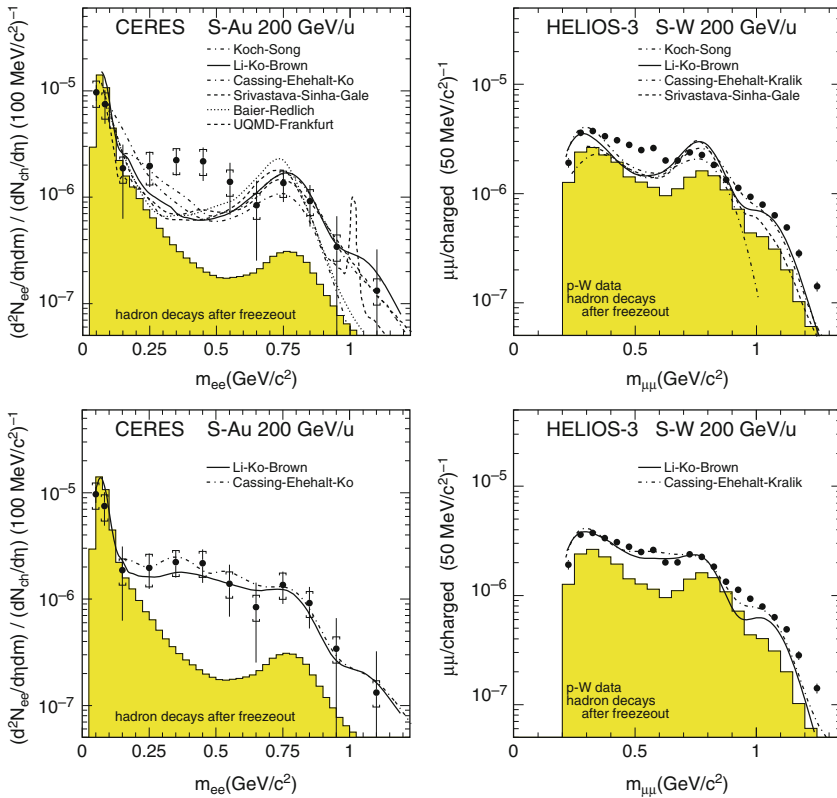


Fig. 7.2 Comparison of dilepton data from the CERES and HELIOS-3 Collaborations to various calculations [326–333]. The *upper panels* show the calculations with bare meson masses, whereas the *lower panels* show the results from [327, 332, 334] which assume dropping meson masses in the dense nuclear medium. The figures are taken from [335]

dimuon mass spectrum is shown in the left panel of Fig. 7.4 together with the combinatorial background, the contribution of fake tracks, and the signal muon pairs after background subtraction. The signal mass spectrum contains about 440,000 muon pairs. The ω mass resolution is 20 MeV. It is worthwhile to note that even the η meson is resolved. In the right panel of Fig. 7.4 the excess spectrum is shown which is obtained by subtracting known dimuon sources ($\eta \rightarrow \mu\mu\gamma$, $\eta' \rightarrow \mu\mu\gamma$, $\omega \rightarrow \mu\mu\pi_0$, $\eta \rightarrow \mu\mu$, $\omega \rightarrow \mu\mu$ and $\phi \rightarrow \mu\mu$) from the signal spectrum. The ρ meson is not subtracted. Due to the high statistic this procedure could be applied for several bins in centrality and transverse momentum.

The mass-difference spectrum in the right panel of Fig. 7.4 is qualitatively consistent with the interpretation that the excess is mainly due to $\pi\pi$ annihilation processes. For a quantitative analysis two theoretical scenarios for the in-medium spectral properties of the ρ , broadening [295] and dropping

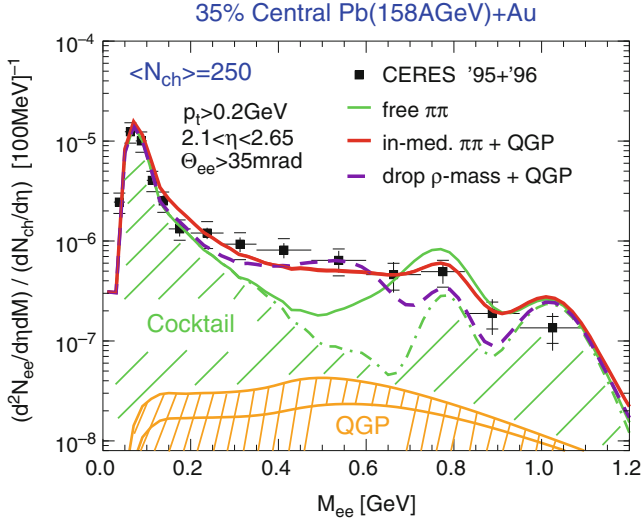


Fig. 7.3 Ceres/NA45 dielectron spectra from semicentral Pb+Au collisions at 158 AGeV [336] in comparison with thermal dilepton spectra evaluated in an expanding fireball model [296, 337, 338]. Thermal emission from the hadronic phase is calculated with three different models for the ρ spectral function (vacuum, dropping mass and hadronic many-body theory), and supplemented with the hadronic decay cocktail and QGP emission (assuming $T_c = 175$ MeV)

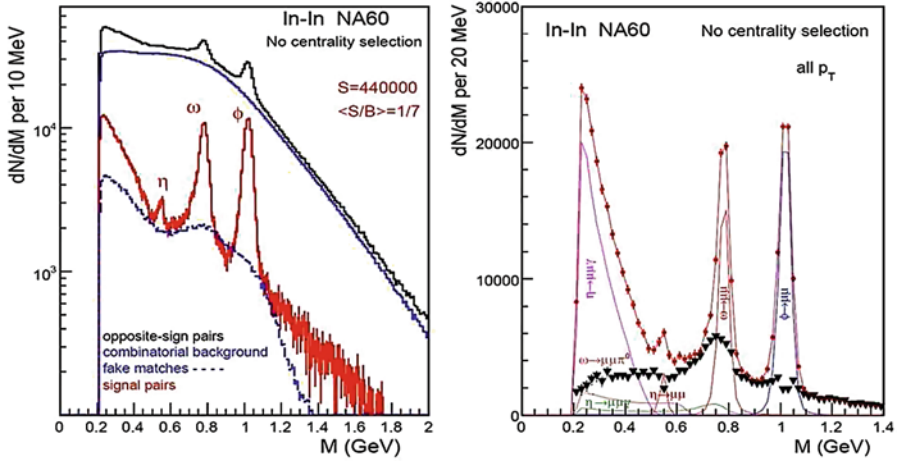


Fig. 7.4 NA60 dimuon invariant mass distributions measured in In+In collisions at 160 AGeV. *Left panel:* Mass spectra of the opposite-sign dimuons (*upper histogram*), combinatorial background (*dashed*), signal fake matches (*dashed-dotted*), and resulting signal (histogram with *error bars*). *Right panel:* Total data (*open circles*), individual cocktail sources (*solid*), difference data (*thick triangles*), sum of cocktail sources and difference data (*dashed*) (from [164])

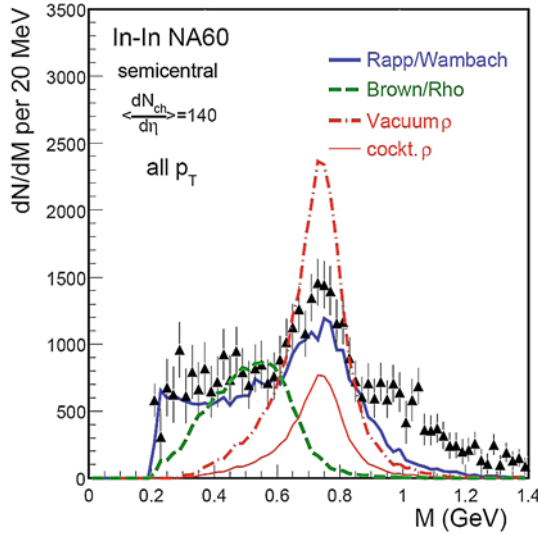


Fig. 7.5 NA60 dimuon excess mass spectrum measured in In+In collisions at 160 AGeV (full triangles). Thin solid line: cocktail ρ . The data are compared to calculations [339, 340] of the vacuum ρ (thick dashed-dotted line), in-medium broadened ρ (thick solid line), and the dropping mass of the ρ (dashed line). The calculations are absolutely normalized, taken from [341])

mass [342], have been calculated for the same fireball evolution keeping the original normalization [339, 340]. The results are shown in Fig. 7.5. The predictions based on the hadronic many-body ρ spectral function [296], are in good agreement with the experimental spectrum, while a schematic dropping-mass scenario describes only the low-mass tail of the NA60 data [343]. One should note, however, that a better agreement of the dropping-mass scenario with the data can be achieved when the outer corona of the collision zone is treated by a quasi-free production process. At masses beyond $M \simeq 1$ GeV, multi-pion annihilation as following from the free e.m. spectral function and contributions from the QGP have been identified as relevant sources.

The importance of baryon effects is highlighted in Fig. 7.6 where the results of the calculations with (left panel) and without (right panel) medium effects due to baryons are shown. In the latter case, the calculated dimuon invariant spectrum is too narrow, and misses yield at low masses. The average ρ broadening of the full in-medium ρ spectral function is approximately half of the ρ mass, $\bar{\Gamma}_\rho^{med} \simeq 350$ MeV, implying that in the early phases (i.e., close to the expected phase boundary), the ρ resonance has essentially melted, $\Gamma_\rho^{med}(T_c) \simeq m_\rho$. It is furthermore important to note that the absolute dilepton yield is a rather sensitive measure of the fireball lifetime, which for central In+In collisions at 158 AGeV amounts to about $\sim 7 \pm 1$ fm/c [339].

It should be noted that the CERES collaboration has provided dielectron excess spectra from their latest run in central Pb+Au collisions at

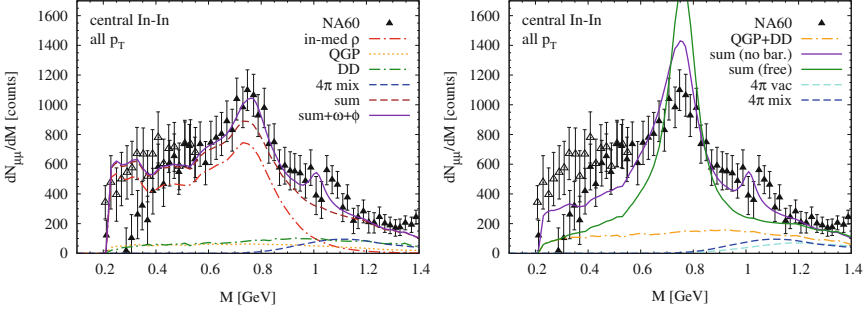


Fig. 7.6 Thermal dilepton emission evaluated in an expanding fireball model [339] in comparison to NA60 excess spectra [164] in central In+In collisions at 158 AGeV. Thermal emission from the hadronic phase includes both in-medium isovector (ρ meson) and isoscalar (ω and ϕ meson) channels, and is supplemented by open-charm decays and QGP emission (assuming $T_c = 175$ MeV). *Left panel*: employing the full hadronic many-body vector-meson spectral functions; *right panel*: employing vector-spectral functions without medium effects due to baryons, or without any medium effect, i.e. the vacuum e.m. spectral function

158 AGeV [344] as shown in Fig. 7.7. Although suffering from limited statistics these data may confirm the preference for the broadening over the dropping-mass scenario (left panel) as well as the importance of baryon-induced medium effects (right panel). Model calculations predict the latter to become particularly pronounced for small invariant masses, $M \leq 0.2$ GeV. It is noteworthy that this regime is not accessible with dimuon spectra. A recent analysis of the CERES and NA60 results within an off-shell transport model is presented in [345].

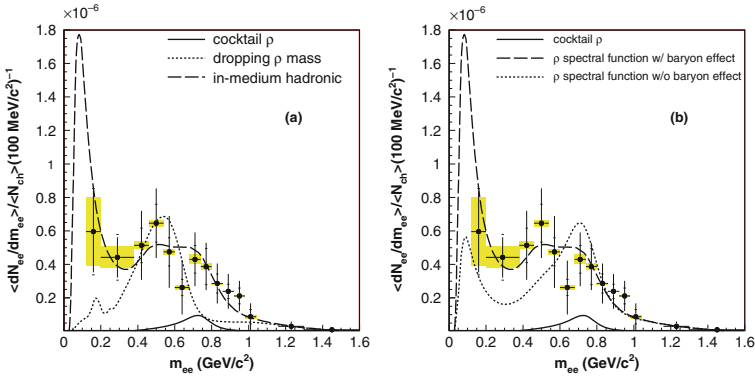


Fig. 7.7 Dielectron excess spectra in central Pb+Au collisions at 158 AGeV. CERES/NA45 data [344] are compared to thermal emission spectra using hadronic many-body and dropping-mass ρ spectral functions (*left panel*), as well as many-body ρ spectral functions with and without baryonic medium effects (*right panel*)

The NA60 data certainly pose a new constraint on the theoretical models which will have to simultaneously account for the CERES and NA60 results. But the deeper impact of these results is their possible relevance to the broader context of chiral symmetry restoration. If the system reaches, or is near to, chiral symmetry restoration then the dilepton results could be telling us whether the approach to such a state proceeds through broadening and eventually subsequent melting of the resonances or by dropping masses.

7.2.2 Transverse mass spectra

Lepton pairs are not only characterized by their invariant mass, but also by their transverse momentum. The latter contains information on the temperature and the radial flow of the expanding fireball. In contrast to hadrons which reach the full asymptotic flow at the moment of decoupling, lepton pairs are continuously emitted during the evolution. Therefore, lepton pairs reflect small flow and high temperatures from early times, and increasingly larger flow and smaller temperatures from later times. The resulting space-time folding over the temperature-flow history offers access, through the measurement of p_T spectra, to the emission region of the dileptons and may thus differentiate between a hadronic or a partonic nature of the emitting source.

Figure 7.8(left) displays the acceptance corrected and centrality integrated invariant transverse mass, m_T , spectra with $m_T = \sqrt{(p_T^2 + M^2)}$ for four mass windows measured in In+In collisions at 160 AGeV by the NA60 collaboration [346]. The inverse slope parameter T_{eff} extracted from the m_T spectra is shown in the right part of Fig. 7.8 as function of mass. The data for ω and ϕ mesons are also plotted. The parameter T_{eff} rises nearly linearly with mass up to the pole position of the ρ meson, followed by a sudden decline. The effective temperatures of the excess dileptons below the ρ pole mass are quite close to T_{eff} for ω and ϕ mesons which follow the entire evolution of the fireball until they decay. The rise and fall of T_{eff} as function of mass is very similar for dileptons and hadrons (see Fig. 5.2) where the effective temperatures of the Ω hyperon and of the J/ψ meson are found to be lower than the one for protons.

The sudden decline of T_{eff} at masses above 1 GeV is a very remarkable feature in Fig. 7.8. If the rise is due to flow, the rapid fall of T_{eff} indicates that the heavy dileptons are emitted prior to the development of collective hadron flow. The same explanation might hold for the heavy particles consisting of strange or charm quarks which decouple early from the collective expansion of the fireball (Fig. 5.2). Whether or not the fall of T_{eff} is related to an early phase with partonic degrees of freedom is discussed controversially. However, this intriguing interpretation would be supported by the model calculations which predict a substantial QGP contribution to the yield of heavy dileptons (see Fig. 7.6).

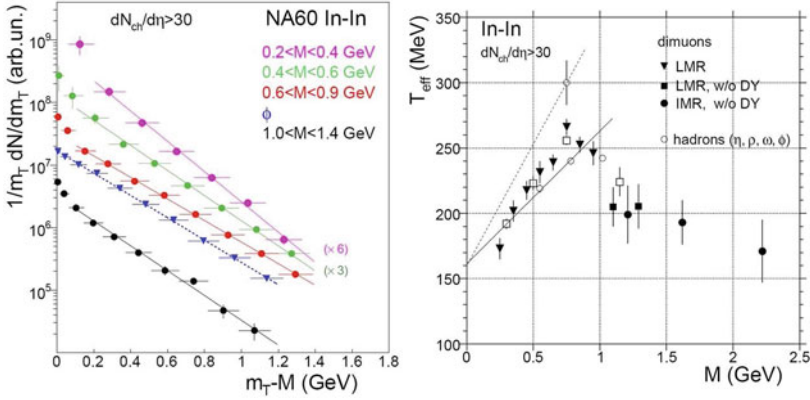


Fig. 7.8 *Left panel:* Acceptance corrected transverse mass spectra of excess dimuons (in four mass windows), the ω and the ϕ meson integrated over collision centrality. *Right panel:* Inverse slope parameter T_{eff} as function of dimuon mass M (taken from [346])

7.3 Dielectrons at RHIC

The situation becomes more complex at the higher RHIC energy, where the production of electron-positron pairs has been investigated by the PHENIX Collaboration in p+p and Au+Au collisions at a center-of-mass energy of $\sqrt{s_{NN}} = 200$ GeV per nucleon-nucleon pair. The data from p+p collisions [322] can fully be accounted for by the contribution from expected sources as demonstrated in Fig. 7.9. In addition to the light meson decays which dominate the cocktail at SPS energy, at RHIC additional sources become relevant, including open heavy flavor production as well as prompt virtual photon emission.

In contrast, as shown in Fig. 7.10 the Au+Au data exhibit significant additional contributions to the dielectron continuum over a wide range in mass and transverse momentum [321], which is currently discussed controversially. Qualitatively, the enhancement observed in the low-mass region between 0.15 and 0.75 GeV/ c^2 is quite consistent with the enhancement observed at the CERN-SPS, which was modelled successfully by $\pi\pi$ annihilation including a broadening of the ρ spectral function in medium. However, the enhancement observed at RHIC is significantly larger than predicted by such model calculations [345]. Furthermore, its yield increases significantly faster with collision centrality than the number of participating nucleons. Also the transverse momentum spectra of the excess dielectrons exhibit unusual features, in particular inverse slopes of about 100 MeV/ c only which is nearly independent on the dielectron mass.

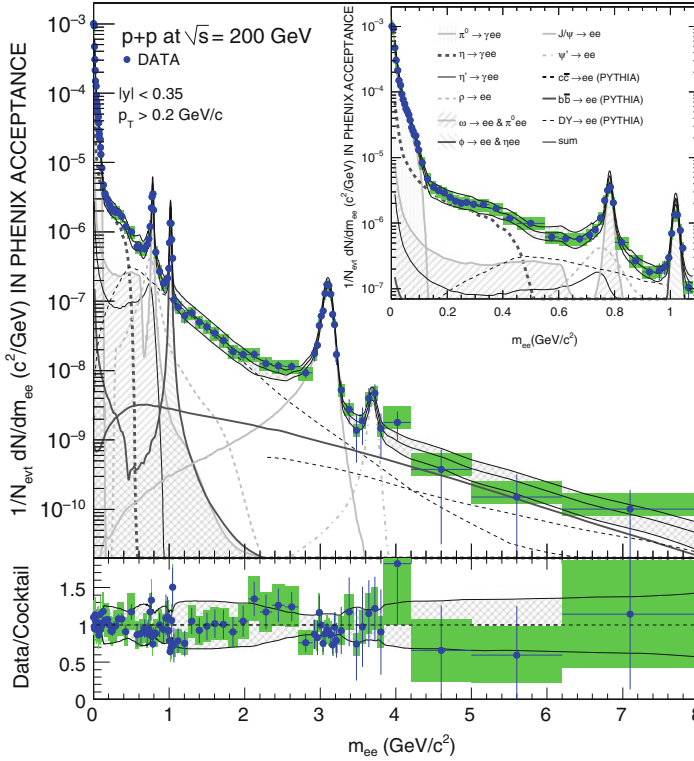


Fig. 7.9 Dielectron yield as function of mass as measured by PHENIX in p+p collisions at $\sqrt{s} = 200$ GeV. The data are compared to a cocktail of known sources (*upper panel*). The *lower panel* shows the ratio of data to cocktail (taken from [322])

7.4 Dielectrons at BEVALAC and SIS

Also in the BEVALAC and SIS energy range around 1 AGeV only dielectron measurements have been performed up to now. At the BEVALAC the DLS Collaboration has measured dielectron spectra in p+p and light ion collisions with limited statistics and mass resolution. As it is the case at higher energies, the dielectron data from p+p collisions in the beam energy range between 1 and 5 GeV [347] can be reasonably well accounted for with known hadronic sources [348–350]. In nuclear collisions with ions as light as carbon, an unexpected but significant low-mass dielectron enhancement was observed [306–309] that could neither be described in a dynamical spectral function approach [351] including collisional broadening nor in a dropping-mass scheme [349, 352].

This so called “DLS puzzle” was one of the motivations to build HADES as a second generation dielectron experiment with significantly improved mass

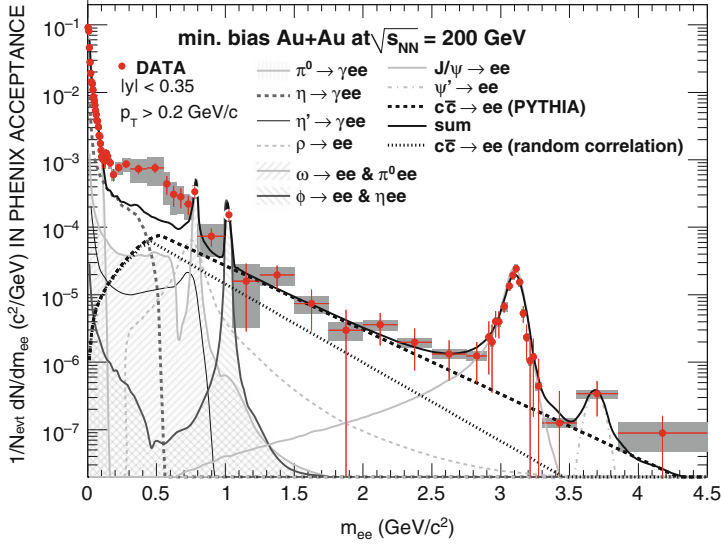


Fig. 7.10 Dielectron yield as function of mass as measured by PHENIX in Au+Au collisions at $\sqrt{s_{NN}} = 200$ GeV. The data are compared to a cocktail of known sources (taken from [321])

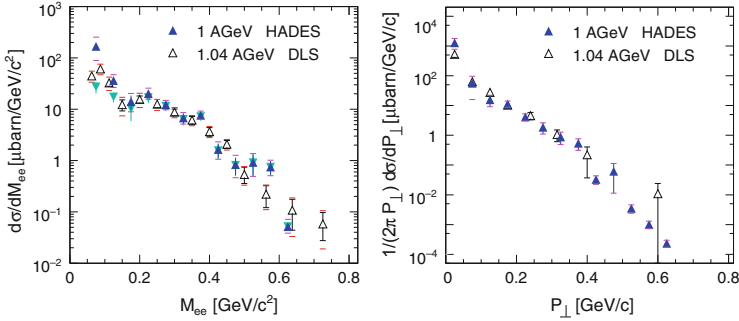


Fig. 7.11 Dielectron cross section as function of invariant mass (*left panel*) and invariant momentum distribution (*right panel*) as measured in C+C collisions by HADES at 1 AGeV [311] and by DLS at 1.04 AGeV [309] (taken from [311])

resolution and larger acceptance at the GSI-SIS, which would also allow to study heavier collision systems.

The present experimental studies of the HADES Collaboration for C+C collisions at 1 [311] and 2 AGeV [310] indeed confirm an excess of dilepton pairs from 0.3 to 0.7 GeV invariant mass as observed by DLS. In fact, the large acceptance of the HADES spectrometer allows for a direct comparison of the dielectron cross section and transverse momentum distributions measured in C+C collisions at 1 AGeV by HADES and at 1.04 AGeV by DLS within the smaller DLS acceptance as shown in Fig. 7.11. The two data sets are found to be in good agreement.

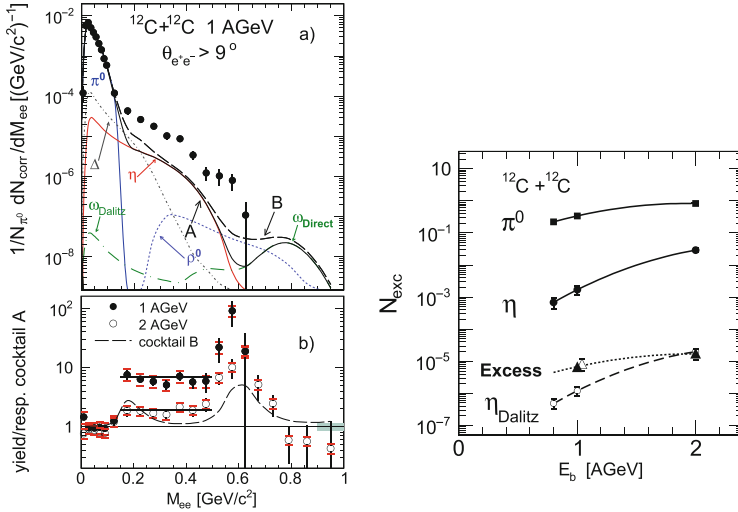


Fig. 7.12 *Left panel:* Dielectron mass spectrum as measured by HADES in C+C collisions at 1 AGeV in comparison with various expected sources (a), and the ratio of the data to the full cocktail (b). *Right panel:* Inclusive multiplicity of the excess pairs in the mass range $0.15 < m < 0.5 \text{ GeV}/c^2$ as function of beam energy, together with corresponding excitation curves for π^0 and η mesons. For comparison, the dotted curve shows the π^0 excitation curve scaled down by an arbitrary factor, and the dashed curve depicts the contribution from η Dalitz decays (taken from [311])

The dielectron mass spectrum measured in C+C collisions at 1 AGeV is shown in the left panel of Fig. 7.12 in comparison with two cocktails of known sources. Data and cocktails are in good agreement in the π^0 region but a strong enhancement of the data relative to the expected contributions from the decays of η and ω mesons (cocktail A) is observed for $M > 0.15 \text{ GeV}/c^2$. The addition of contributions from the decays of Δ resonances and ρ mesons (cocktail B) does not improve the agreement between cocktail and data significantly. The remaining enhancement relative to both cocktails is stronger at 1 AGeV compared to collisions at 2 AGeV. Going beyond the cocktail calculations, a comparison with various transport models has been published for the 2 AGeV case [310]. Microscopic models do not only treat the collision dynamics in a realistic way, in principle they also can deal with multistep processes, broad resonances, and related off-shell effects. While HSD, RQMD, and UrQMD calculations assuming vacuum spectral functions only qualitatively reproduce the trends observed in the data they fall short in a quantitative description of the excess yield over the full mass range [310]. In particular, all considered models overestimate the pair yield around the ρ and ω meson masses. Final conclusions have to wait for more refined calculations taking in-medium spectral functions into account.

A first quantitative assessment of the beam energy dependence of the excess dielectron yield has been published in [311] and is shown in the right

panel of Fig. 7.12 in comparison with the excitation function of π^0 and η mesons. It turns out that the shape of the excess dielectron excitation function is in good agreement with the shape of the π^0 excitation function, but not with the one of η mesons. From this observation one might conclude that in the BEVALAC/SIS energy range the dielectron excess is not driven by heavy resonances, which are relevant for the η meson yields, but maybe by the Δ resonance, which is the dominant source of neutral pions.

A prerequisite for further conclusions is to better constrain the elementary input, i.e. the elementary vector meson and dilepton production sources. Currently, these are partially based on data but to a large extent also on model assumptions, e.g. the resonance model [353–355], which show still some variance due to the lack of sufficient experimental constraints. The HADES program at the SIS will allow for a more thorough understanding of dilepton emission from elementary and complex reactions.

7.5 Conclusions and predictions for FAIR energies

Further progress in the understanding of the ρ meson dynamics in the hot and dense medium and its relation to the onset of chiral symmetry restoration requires detailed information on:

- the fireball evolution,
- the contribution of ρ mesons from the late and dilute stage of the collision (“freeze-out ρ ”),
- the contribution of ρ mesons from the very early non-equilibrated stage of the collision (“primordial ρ ”).

The experimental approach to achieve these goals seems straight forward. However, as discussed above, precision measurements of dileptons in heavy-ion collisions are notoriously difficult. In order to constrain the fireball evolution one has to measure – in addition to the vector mesons – the yields and phase space distributions of hadrons (pions, kaons, protons, lambdas, ...) under identical conditions as the vector mesons (projectile-target combination, beam energy, centrality). The yield, momentum and mass distribution of the “freeze-out ρ ” mesons can be determined by measuring their hadronic decays into pions and kaons. Information on the “primordial ρ ” can be obtained by measuring dilepton pairs in p+p and p+A collisions.

No experimental information on dilepton production in heavy-ion collisions is available in the FAIR beam energy range from 2 to 35 AGeV. Of particular interest are the highest FAIR energies where one expects to create the highest baryon densities that can be reached in heavy-ion collisions. Since baryon density has been identified as a crucial parameter related to the observed low-mass dilepton enhancement it is mandatory to investigate dilepton production in a systematic manner at FAIR.

This experimental program has to go hand in hand with a careful theoretical modelling of dilepton production at FAIR. As was shown, e.g. for

the CERN-SPS case, the interpretation of measured spectra relies heavily on theoretical guidance. In that respect, the FAIR energy range is a difficult one. Thermal evolution models that have been applied very successfully at SPS energy require that (local) thermal equilibrium is reached in the collisions studied. While there is ample evidence that equilibrium is reached already early in heavy-ion collisions at SPS and, in particular, at RHIC, this is not necessarily the case at FAIR energies and very questionable in the BEVALAC and SIS energy range. At these low energies microscopic transport model calculations are clearly the tool of choice. However, the proper treatment of in-medium spectral functions and the related off-shell effects is far from trivial and needs further development to be applicable for FAIR. A comprehensive discussion on the status of off-shell transport calculations and dilepton production at SIS energies is given in [356].

Some guidance is given by the only dielectron measurement that has been performed at a beam energy of 40 AGeV by the CERES Collaboration [148]. The obtained dielectron invariant mass spectrum is depicted in Fig. 7.13 in comparison with contributions from known sources and a calculation in a

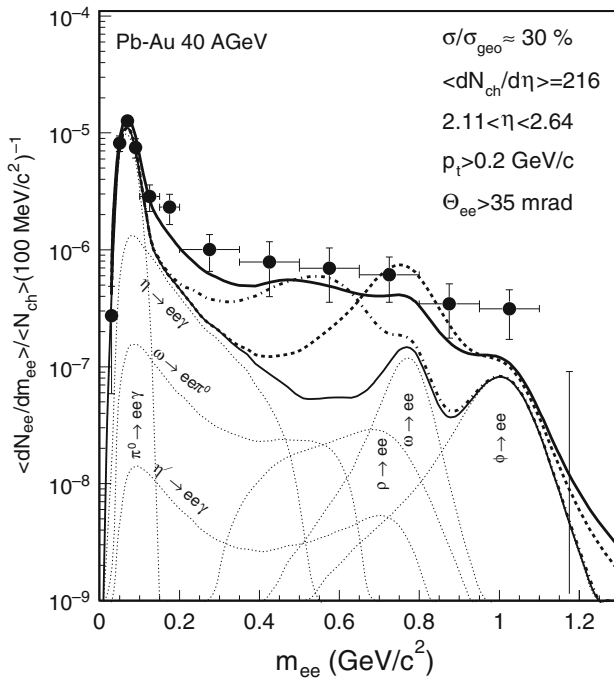


Fig. 7.13 Dielectron invariant mass spectrum measured by the CERES Collaboration in semicentral Pb+Au collisions at 40 AGeV [148] in comparison with the expectation from known sources and with predictions for thermal dilepton spectra. Thermal emission from the hadronic phase is calculated with three different models for the ρ spectral function (vacuum, dropping mass, and hadronic many-body theory), and supplemented with a hadronic decay cocktail and QGP emission (assuming $T_c = 175$ MeV)

thermal evolution model employing three different choices for the ρ meson spectral function, i.e. the vacuum spectral function, the dropping-mass scenario, and the hadronic many-body broadening scenario. The enhancement over the hadronic decay cocktail and the vacuum ρ evolution model appears to be even larger than at full SPS energy, albeit with rather large statistical errors. Given the fact that baryon density has been established as an important parameter driving the low-mass dilepton enhancement this observation is not surprising, but one is far from drawing any definite conclusion. Clearly, a measurement of the quality of the NA60 data could provide detailed information on the ρ line shape, potentially also a determination of the fireball lifetime, which, in turn, could carry valuable information on the onset of an extended QGP-hadronic mixed phase.

Finally, we want to comment on the question whether electrons or muons are better suited for low-mass dilepton spectroscopy. Electron-positron pairs can be measured down to almost zero invariant mass whereas the dimuon mass spectrum naturally starts at twice the muon mass. The advantage of muon measurements is the possibility to generate a trigger which is required for the collection of data with high statistics. The optimum strategy is to measure both electrons and muons, and to combine the advantages of both probes.

Chapter 8

Open and hidden charm

8.1 General overview

The investigation of the formation and propagation of particles containing charm and/or anticharm quarks in heavy-ion collisions opens the possibility to probe the early phase of the fireball due to the large mass of the charm quarks which can be produced in hard processes only. The suppression dynamics of charmonium, i.e. the dissociation of J/ψ and ψ' mesons is expected to be sensitive to the matter properties in the reaction volume, and the challenge is to disentangle absorption mechanisms in hadronic matter from color screening in a partonic phase. The elliptic flow of charm is another important diagnostic probe of the early fireball and its prevailing degrees of freedom. The propagation of open charm in the fireball provides information about the transport properties of hot and dense matter.

At FAIR energies the charm sector becomes accessible, and measurements of open and hidden charm will be performed for the first time in heavy-ion collisions close to (nucleon–nucleon) threshold energies. At low beam energies the charm production mechanisms and yields depend sensitively on the conditions inside the fireball, because the absolute production threshold for a $c\bar{c}$ pair in a partonic environment is lower than the minimum energy needed to create a pair of charmed hadrons. Therefore, both the total and the relative yields of hadrons containing charm quarks measured in heavy-ion collisions at threshold energies are very sensitive to the degrees of freedom in the early fireball.

Charm production cross sections have been measured in proton-proton, proton-nucleus and pion-nucleus collisions, mostly at top SPS energies [357–368]. Examples for charmonium measurements via $\mu^+\mu^-$ pairs in proton-nucleus collisions are shown in the left panel of Fig. 8.1 for p+W collisions at 200 GeV [315], and in the left panel of Fig. 8.2 for p+Ag collisions at 450 GeV [369]. One of the early dimuon measurement in nucleus-nucleus collisions is presented in the right panel of Fig. 8.1 for S+W collisions at 200

GeV [315]. The right panel of Fig. 8.2 depicts the most recent charmonium data measured in In+In collisions at 158 AGeV by NA60 [370].

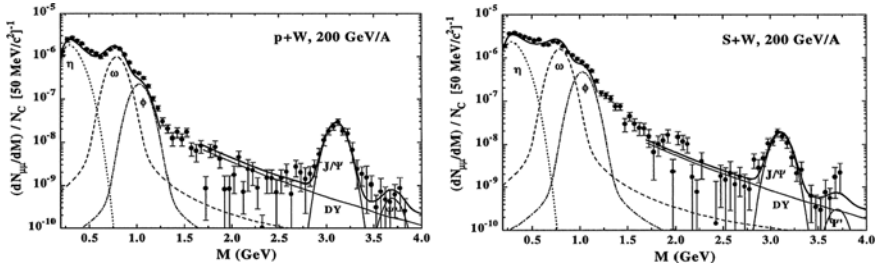


Fig. 8.1 Dimuon invariant mass spectra from p+W and S+W collisions at 200 AGeV measured by the HELIOS-3 Collaboration [315]. The lines represent calculations of the individual contributions [42]

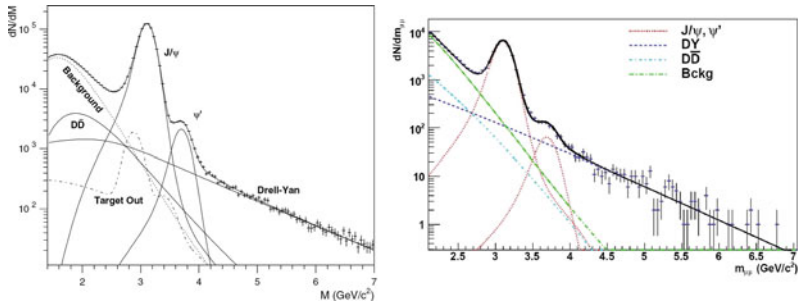


Fig. 8.2 $\mu^+\mu^-$ invariant mass spectra including the background contributions integrated over centrality measured in p+Ag collisions at 450 GeV (left panel, NA50 collaboration, [369]) and in In+In collisions at 160 AGeV (right panel, NA60 collaboration, [370])

The dissociation of charmonia J/ψ , χ_c , ψ' in the quark-gluon plasma due to color screening of $c\bar{c}$ states has been proposed as a signature for the deconfinement phase transition [15, 371]. In order to identify possible effects of color screening on the measured J/ψ meson yield one has to understand the absorption mechanisms in nuclear matter. These effects have been studied experimentally and theoretically in proton-nucleus collisions, and are used as a reference for data obtained in nucleus-nucleus collisions. Figure 8.3 depicts the ratio of measured over expected J/ψ mesons as a function of the number of participants. Here, “expected” refers to the number of J/ψ mesons which survive normal nuclear absorption processes as parameterized from p+A measurements. For semi-central and central collisions the ratio is smaller than unity, an effect which is called anomalous J/ψ suppression. This effect was observed in S+U and Pb+Pb collisions by the NA38 [372] and NA50 Collab-

orations [373, 374], and has been experimentally confirmed by NA60 [375] in In+In collisions at 160 AGeV (see Fig. 8.3).

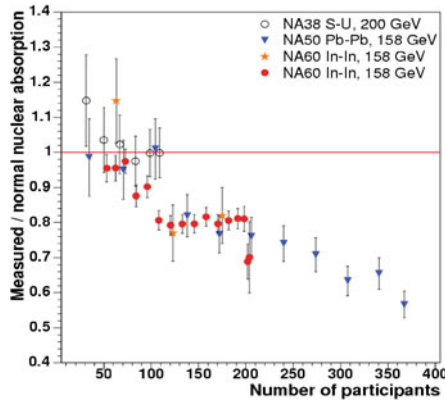


Fig. 8.3 Measured over expected J/ψ ratio versus number of participants in A+A collisions at SPS energies as function of the number of participants

In order to visualize absorption effects the medium, the charmonium yield in A+A collisions is often presented in terms of the nuclear modification factor, R_{AA} , which is the ratio between the charmonium yield in A+A collisions and that in p+p collisions scaled with the number of binary collisions,

$$R_{AA} = \frac{N_{AA}^{J/\psi}}{N_{pp}^{J/\psi} N_{coll}}.$$

The upper panel of Fig. 8.4 depicts the p_T integrated R_{AA} as a function of the number of participants N_{part} measured at mid and forward rapidity in Au+Au collisions at an energy of $\sqrt{s_{NN}} = 200$ GeV by the PHENIX collaboration at RHIC [376]. It was found that for each bin of rapidity, R_{AA} decreases with increasing N_{part} . For the most central collisions, R_{AA} is below 0.3 (0.2) at mid (forward) rapidity. The lower panel of Fig. 8.4 shows the ratio of forward/mid rapidity R_{AA} versus N_{part} . The ratio first decreases then reaches a plateau of about 0.6 for $N_{part} > 100$. A significant J/ψ suppression relative to binary scaling of proton-proton is observed for central Au + Au collisions at RHIC. The magnitude of the suppression is similar to that observed at the CERN-SPS and greater than the suppression expected by extrapolating the cold nuclear matter effects measured in d + Au collisions [377]. Models that describe the SPS data using a J/ψ and ψ' suppression based on the local density predict a significantly larger suppression at RHIC than at SPS, and more suppression at mid rapidity than at forward rapidity.

Apart from the total and relative abundances of charmonia and open charm mesons also their phase space distributions provide valuable insight in the collision dynamics. In particular, the transverse momentum (or mass)

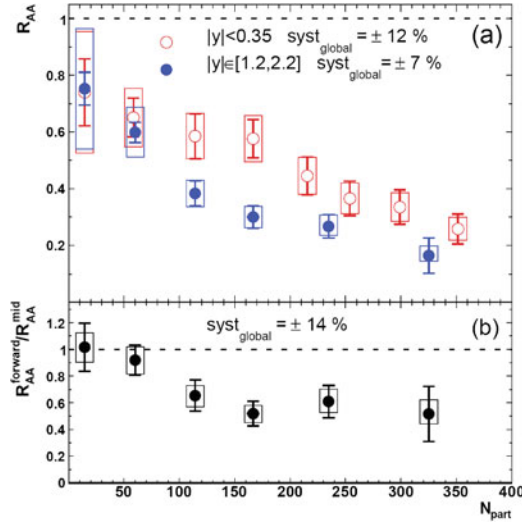


Fig. 8.4 Upper panel (a): R_{AA} vs. N_{part} for central Au + Au collisions at $\sqrt{s_{NN}} = 200$ GeV. Mid (forward) rapidity data are shown with *open* (*filled*) circles. Lower panel (b): Ratio of forward/mid rapidity J/ψ R_{AA} vs. N_{part} . For the two most central bins, mid rapidity points have been combined to form the ratio with the forward rapidity points. Taken from [376]

spectra are sensitive to the evolution and the degrees-of-freedom of the fire-ball [190, 378–380]. As discussed in the previous chapters, the spectral slopes of dilepton pairs with invariant masses above $1 \text{ GeV}/c^2$ do not follow the mass ordering of the radial flow. The same effect is observed for hadrons like multi-strange hyperons and charmonium. This observation supports the picture that these particles are emitted in the early (probably partonic) phase of the collision. The most recent data on acceptance corrected p_T distributions of J/ψ mesons measured in In+In collisions at 158 AGeV are shown in Fig. 8.5 for various centrality bins [381]. The plots refer to the rapidity region $0.1 < y_{CM} < 0.9$. The lines represent the function $(1/p_T)(dN/dp_T) = e^{-m_T/T}$ fitted to the data. The resulting T values increase with centrality and range from 204 to 234 MeV. The centrality integrated distribution corresponds to $T = 231 \pm 2 \text{ MeV}$.

8.2 Charm in transport models

Open charm and charmonium production at SPS and RHIC energies has been calculated within the AMPT [382], HSD [190, 210, 383, 384] and UrQMD [385, 386] transport approaches using parameterizations for the elementary production channels including the charmed hadrons $D, \bar{D}, D^*, \bar{D}^*, D_s, \bar{D}_s$,

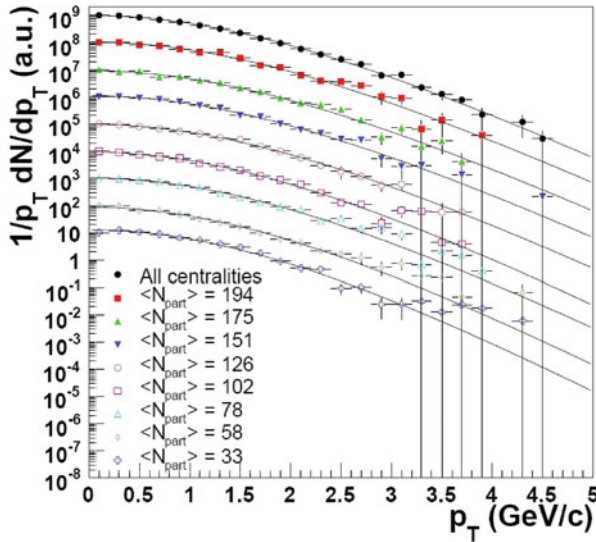


Fig. 8.5 The acceptance corrected p_T distributions of J/ψ mesons measured for different centralities in In+In collisions at 158 AGeV. The lines correspond to fits to the function $(1/p_T)(dN/dp_T) = e^{-m_T/T}$ [381]

D_s^* , \bar{D}_s^* , J/ψ , $\psi(2S)$, χ_{c2} from NN and πN collisions. The latter parameterizations have been fitted in [190] to PYTHIA [387] calculations above $\sqrt{s} = 10$ GeV and extrapolated to the individual thresholds, while the absolute strength of the cross sections has been fixed by the experimental data. For example, the lowest threshold for charm production in hadronic collisions is defined by the process $p + p \rightarrow \bar{D} + \Lambda_c + p$ resulting in a value of $\sqrt{s_{thr}} = 1.8646 \text{ GeV} + 2.285 \text{ GeV} + 0.938 \text{ GeV} = 5.07 \text{ GeV}$. In Fig. 8.6 the data from proton and pion induced reactions are presented as elementary production cross-sections for D mesons and charmonia. These “cross sections per nucleon” (see [368]) are used as input for calculations of charm production in nucleus-nucleus collisions [190].

The results of the UrQMD and HSD transport calculations for Pb+Pb collisions at 160 AGeV, both from , are in reasonably good agreement with the data of the NA50 Collaboration as illustrated in Fig. 8.7, where the cross-section ratio of muon pairs from J/ψ decays over Drell-Yan pairs is shown as a function of the transverse energy E_T . The ratio decreases with increasing transverse energy, indicating enhanced suppression of J/ψ mesons in central collisions. The solid line stands for the HSD result within the “comover absorption scenario” which describes the dissociation of charmonia via interaction with comoving mesons [388]. The symbols represent the NA50 data from the year 2000 (analysis A,B,C) that agree reasonably well with the HSD and UrQMD calculations [385, 386] (dashed histogram in Fig. 8.7). Note that the “comovers” should not be identified with hadronic states in vacuum,

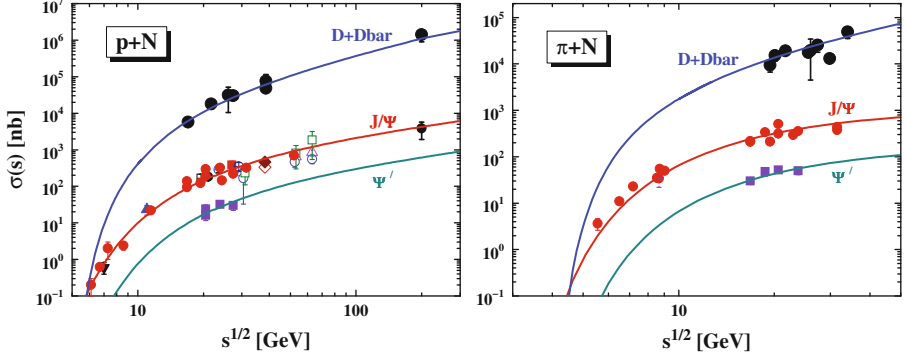


Fig. 8.6 Production cross sections for $D + \bar{D}$, J/ψ and ψ' mesons in pN (left part) and πN reactions (right part). The symbols represent the experimental data [357–367], whereas the solid lines correspond to the parameterizations used in the HSD transport code [190]. Note that the J/ψ cross sections include the decay from χ_c mesons

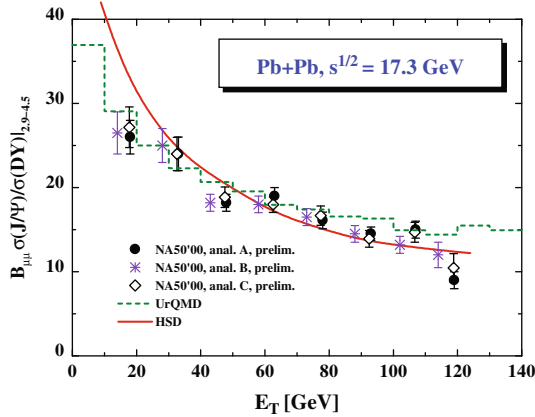


Fig. 8.7 $B_{\mu\mu}\sigma(J/\psi)/\sigma(DY)$ as a function of the transverse energy E_T in Pb + Pb collisions at 160 AGeV. $B_{\mu\mu}$ is the branching ratio of J/ψ mesons into $\mu^+\mu^-$ pairs, $\sigma(J/\psi)$ and $\sigma(DY)$ are the production cross-sections of J/ψ mesons and muon pairs from Drell-Yan processes, respectively. The different symbols represent the NA50 data [373] from the year 2000 (analysis A,B,C). The solid line corresponds to the HSD result within the co-mover absorption scenario [210], while the dashed histogram illustrates the UrQMD result [385, 386]

but rather should be considered as a common synonym for either strongly interacting (bound) quark-antiquark states in the high temperature hadronic phase, or resonant quark-antiquark correlators for temperatures above T_c . These correlators are expected to survive the transition in a similar fashion as e.g. the J/ψ up to rather high energy densities.

Lattice QCD calculations predict that at least the J/ψ may survive at temperatures above T_c (≈ 0.18 GeV). The predictions for the J/ψ dissocia-

tion temperature T_{diss} vary between $T_{diss} = 1.2\text{--}1.5 T_c$ such that the lowest $c\bar{c}$ states remain bound up to energy densities of about $2\text{--}5 \text{ GeV/fm}^3$ [16, 17, 389–391]. It is presently not clear if also the D or D^* mesons will survive at temperatures above T_c but strong correlations between a light quark (antiquark) and a charm antiquark (quark) are likely to persist also above T_c . One may speculate that similar correlations survive also in the light quark sector above T_c such that “hadronic comovers” – most likely with different spectral functions – might show up also at energy densities above 1 GeV/fm^3 , which is taken as a characteristic scale for the critical energy density.

In order to simulate effects of charmonium suppression in a partonic phase within hadron transport calculations, the “QGP threshold scenario” was implemented in HSD [392]. In this scenario the J/ψ and ψ' mesons dissociate if the energy density exceeds the critical values 16 and 2 (or 6.55) GeV/fm^3 , respectively. The charmonium yields for In+In and Pb+Pb collisions at 158 AGeV have been calculated using the HSD transport model within this “QGP threshold scenario”, and within the “hadronic comover scenario”. The comparison of the model results to the data is shown in Fig. 8.8 for J/ψ suppression, and in Fig. 8.9 for the ψ' to J/ψ ratio in Pb+Pb. The data can be described best by the comover absorption model with a single parameter $|M_0|^2$ for the matrix element squared for charmonium-meson dissociation [384, 392]. The “QGP threshold scenario” roughly reproduces the J/ψ suppression for both systems at 160 AGeV but fails in the ψ' to J/ψ ratio since too many ψ' already melt at a critical energy density of 2 GeV/fm^3 at 160 AGeV. Only when assuming the ψ' to dissolve above $\sim 6.5 \text{ GeV/fm}^3$ a reasonable description of all data is achieved in the “QGP threshold scenario”.

8.3 Charmonia from kinetic rate equations

Charmonium production and propagation has also been extensively studied in thermal fireball evolution models. In the same spirit as for dilepton production, rate equations for charmonium dissociation and regeneration are folded over a thermally evolving “background”. In a simplified form, the rate equation for the time evolution of charmonium state ψ , $N_\psi(\tau)$, can be written as

$$\frac{dN_\psi}{d\tau} = -\Gamma_\psi \left[N_\psi - N_\psi^{eq} \right]. \quad (8.1)$$

The first key quantity is the inelastic charmonium reaction rate, Γ_ψ , which, by detailed balance, governs both gain and loss terms. In the QGP, the leading-order (LO) process is the well known gluo-dissociation, $g+\psi \rightarrow c+\bar{c}$. However, as has been first emphasized in [394], the gluo-dissociation process becomes inefficient for small J/ψ binding energies as expected due to color screening in the QGP (and even without screening for ψ' and χ_c states). Therefore, the quasi-free dissociation process, $p + \psi \rightarrow c + \bar{c} + p$ ($p = q, \bar{q}, g$) has been

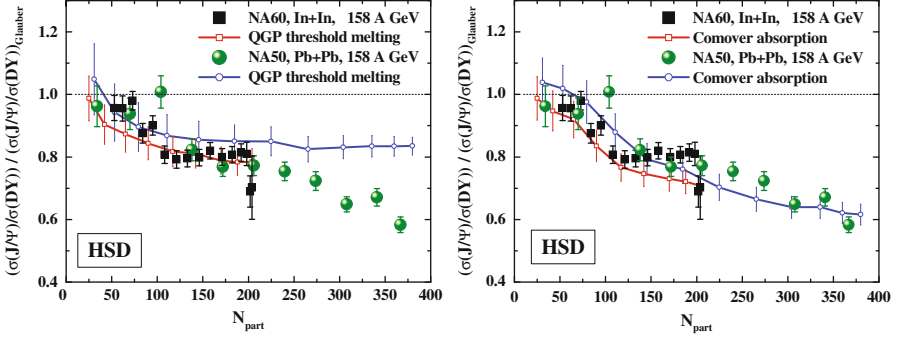


Fig. 8.8 The ratio of cross-sections for the production of J/ψ mesons over Drell-Yan muon pairs $\sigma(J/\psi)/\sigma(DY)$, divided by the same ratio as obtained by a Glauber calculation which represents the normal nuclear absorption. The double ratio is plotted as a function of the number of participants N_{part} for In-In and Pb+Pb collisions at 160 AGeV. The *straight (black) line* illustrates the expectation for nuclear absorption only. The *full dots and squares* correspond to data measured by the NA50 and NA60 Collaborations. The results of the HSD model are represented by *open squares* with (red) line for In-In, and by *open circles* with (blue) line for Pb+Pb. The calculations correspond to the comover absorption model (*right part*), and to the “QGP threshold scenario” (*left part*) with $\varepsilon_{J/\psi} = 16 \text{ GeV/fm}^3$, $\varepsilon_{\chi_c} = 2 \text{ GeV/fm}^3$, $\varepsilon_{\psi'} = 6.55 \text{ GeV/fm}^3$ neglecting comover absorption. The figure is taken from [392]

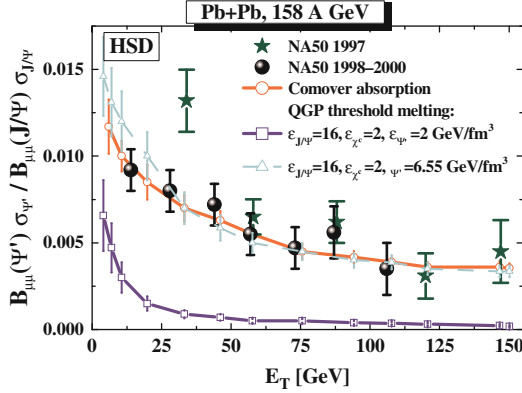


Fig. 8.9 The ψ' to J/ψ ratio as a function of the transverse energy E_T for Pb+Pb at 160 AGeV with $B_{\mu\mu}$ the branching ratios and σ the production cross-sections. The *full dots and stars* denote the data from the NA50 Collaboration [393]. The HSD result for the comover absorption model is shown as the (red) line with *open circles*, whereas the (blue) line with *open squares* correspond to the “QGP threshold scenario” with $\varepsilon_{J/\psi} = 16 \text{ GeV/fm}^3$, $\varepsilon_{\chi_c} = 2 \text{ GeV/fm}^3 = \varepsilon_{\psi'}$. The (light blue) line with open triangles reflect the “QGP threshold scenario” with $\varepsilon_{J/\psi} = 16 \text{ GeV/fm}^3$, $\varepsilon_{\chi_c} = 2 \text{ GeV/fm}^3$ and $\varepsilon_{\psi'} = 6.55 \text{ GeV/fm}^3$ while neglecting comover absorption. The figure is taken from [392]

introduced [394], which naively is of next-to-leading order in α_s but provides a much larger phase space, and, consequently the dominant dissociation rate for small charmonium binding (for gluo-dissociation, the phase space vanishes in the limit of vanishing binding energy). The other key quantity is the charmonium equilibrium limit, $N_\psi^{eq}(\tau)$, which depends on the charm content and temperature of the system. The typical procedure is to assume charm production to be a hard process and thus to be restricted to primordial N - N collisions. The statistical model is then used to distribute the fixed number of $c\bar{c}$ pairs over the available charmed states in the system (either quarks or hadrons). This introduces both temperature and volume dependences into $N_\psi^{eq}(T(\tau))$, as well as a sensitivity to medium modifications of the charm states (e.g., reduced D meson masses lead to a reduction in the charmonium equilibrium numbers) [395, 396].

In [397] the rate equation (8.1) has been solved for Pb+Pb collisions at 158 AGeV using the same fireball evolution as described above (including primordial nuclear absorption and suppression in the hadronic phase). The resulting centrality dependence for J/ψ production (including feed-down from χ_c and ψ') is shown in the left panel of Fig. 8.10. The only free parameter is the strong coupling constant figuring into the quasi-free dissociation cross section in the QGP which has been fixed to $\alpha_s \simeq 0.25$. The NA50 data [373] are fairly well reproduced, with a small contribution from regeneration. The main effect for the direct J/ψ 's is their suppression which is largely restricted to the QGP (after nuclear absorption as inferred from p -A data).

The investigation and interpretation of the transverse momentum spectra of J/ψ mesons will shed further light on charmonium production and suppression mechanisms. The average $\langle p_t^2 \rangle$ of J/ψ mesons is shown in the right panel of Fig. 8.10 as function of transverse energy. The symbols represent NA50 data [398, 399], whereas the lines correspond to results of a thermal fireball evolution model [397]. Most of the observed p_t dependence follows from the Cronin effect of the primordial component, represented by the dotted line. The QGP suppression, which is stronger at high p_t due to the increase of the dissociation rate with increasing momentum, leads to a slight reduction of $\langle p_t^2 \rangle$, improving the agreement with data. The coalescence component is rather insignificant.

According to the solution of rate equations within a thermal fireball evolution model, the ψ' suppression is substantially affected by the hadronic phase [396]. However, it is interesting to note that in this approach the NA50 data [400] can only be reproduced if in-medium D meson masses are implemented which open the direct $\psi' \rightarrow DD$ decay. The comparison of the data to the results of the calculations is shown in Fig. 8.11.

A widely debated issue is whether the NA50 data support the notion of a more or less sharp “onset behavior” of J/ψ suppression, possibly related to the formation of a deconfined medium. The NA60 collaboration has scrutinized this issue by measuring the J/ψ suppression pattern in a medium-size system, i.e., In+In at 158 AGeV. The data [381], normalized to the J/ψ

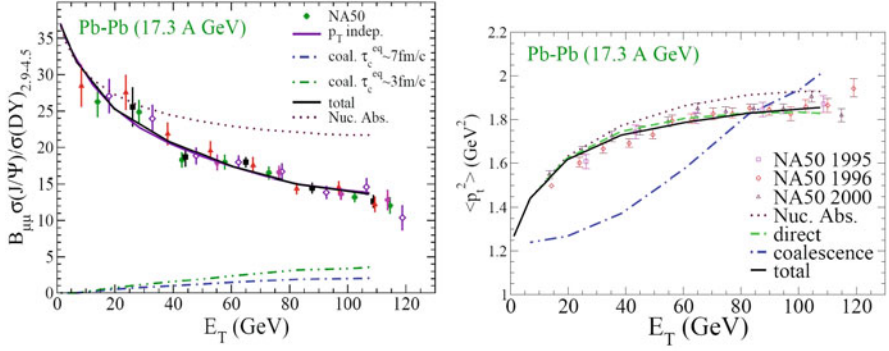


Fig. 8.10 J/ψ production in Pb+Pb collisions at SPS energies as a function of centrality quantified by the measured transverse energy of produced particles E_T . The *lines* correspond to results of the rate equation within an expanding thermal fireball with quasifree dissociation in the QGP and meson-induced break-up in the hadronic phase [397]. *Left panel*: NA50 data [373, 400] for J/ψ /Drell-Yan dimuons compared to the calculations. *Right panel*: Average $\langle p_t^2 \rangle$ of J/ψ mesons as a function of centrality. NA50 data [398, 399] are compared to results the model calculations. The $\langle p_t^2 \rangle$ for the direct component (*dashed line*) and coalescence component (*dash-dotted line*) are compared to the $\langle p_t^2 \rangle$ with nuclear absorption only including the Cronin p_t -broadening effect (*dotted line*)

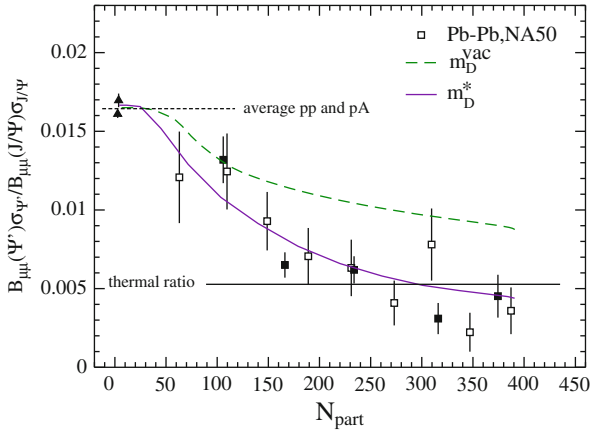


Fig. 8.11 NA50 data [373, 400] on the ψ' to J/ψ ratio in Pb(158 AGeV)+Pb collisions at the SPS, compared to solutions of a kinetic rate equation in a thermal fireball background [396] starting from initial yields subject to primordial nuclear absorption

yield expected after primordial nuclear absorption, are compared to theoretical predictions in Fig. 8.12. The latter approaches have been adjusted to the NA50 Pb-Pb data, but it turns out that none of them fully describes the In-In measurements. The hadronic comover scenario [401] over-predicts the suppression throughout, the schematic percolation model [402] misses the onset significantly, while the kinetic rate equation approach [403] somewhat

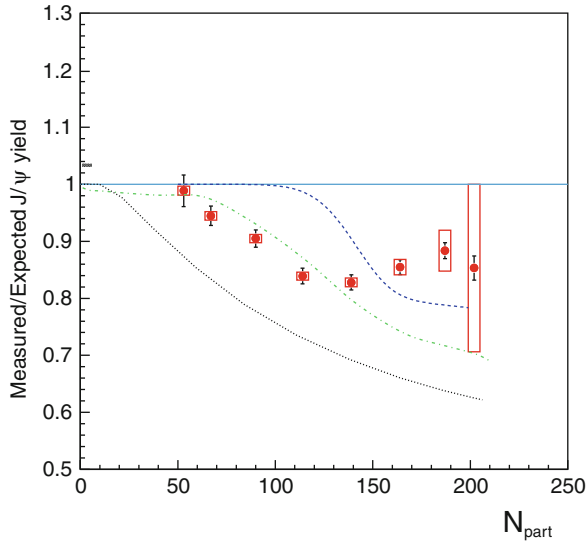


Fig. 8.12 NA60 data for J/ψ production in In(158 AGeV)-In [381] compared to theoretical model predictions that are in approximate agreement with the NA50 Pb-Pb data: percolation model (*upper (dashed) line*) [402], kinetic rate equation (*middle (dash-dotted) line*) [403] and hadronic comovers (*lower (dotted) line*) [401]. Data and theory curves are normalized to an “expected yield” which includes the effects of primordial nuclear absorption as extracted from p -A data

over-predicts the suppression for the most central collisions. Overall, the predictions of the kinetic approach (in a thermal fireball background) do not fare too badly with the data.

8.4 The statistical hadronization model

The statistical hadronization model (SHM) as described in Part II [19, 143, 404–406] is based on the following assumptions: (1) The charm and anticharm quarks are produced in primary hard collisions. (2) Primordial production of charmonia and D mesons is neglected, i.e. it is assumed that these particles are completely dissociated. (3) Charmonium suppression in cold nuclear matter (i.e. after hadronization) is also neglected.

One should note that the assumption of complete dissociation of charmonium and D mesons is fulfilled only if the plasma temperature exceeds the J/ψ dissociation temperature. In this sense the statistical hadronization model describes the extreme case that all of the hadrons containing charm quarks are born out of the QGP by hadronization, and do not suffer from interaction with cold matter afterwards.

The input parameters of the statistical hadronization model are the charm production cross section in pp collisions as shown in Fig. 8.13, and the chemical freeze-out parameters temperature, T , baryochemical potential, μ_b , and volume corresponding to one unit of rapidity $V_{\Delta y=1}$ (the calculations are for midrapidity). The charm production cross section is extrapolated towards the production threshold using the following expression:

$$\sigma_{c\bar{c}} = k(1 - \sqrt{s_{thr}}/\sqrt{s})^a (\sqrt{s_{thr}}/\sqrt{s})^b$$

with $k = 1.85 \mu\text{b}$, $\sqrt{s_{thr}} = 4.5 \text{ GeV}$ (calculated with a charm quark mass of $m_c = 1.3 \text{ GeV}$ assuming the process $p + p \rightarrow p + p + 2m_c$), $a = 4.3$, and $b = -1.44$. The parameters a , b , k were tuned to reproduce the low-energy part of the (scaled) NLO curve. The extrapolated curves for charm production cross section are shown with continuous lines in Fig. 8.13 [19, 143, 404–406].

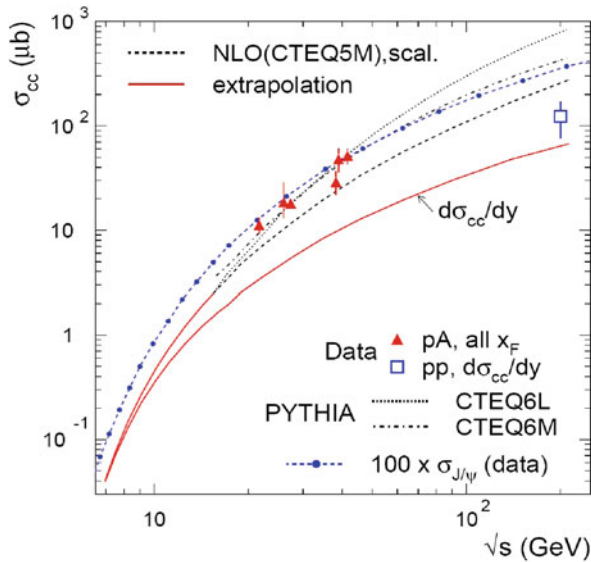


Fig. 8.13 Energy dependence of the charm production cross section in pp collisions. The NLO pQCD values [407] are compared to calculations using PYTHIA and to data in pA collisions, taken from [408]. The extrapolations for low energies are shown with *continuous lines*, for total and midrapidity ($d\sigma_{c\bar{c}}/dy$) cross section. The *open square* is a midrapidity measurement in pp collisions [409]. The *dashed line with dots* indicates a parameterization of the measured energy dependence of the J/ψ production cross section [410]

The results of the model are presented in Fig. 8.14. The left panel shows the predictions for the excitation functions of midrapidity yields for charmed hadrons. In the right panel of Fig. 8.14 the yields are normalized to the number of initially produced $c\bar{c}$ pairs. The striking feature is the decrease of the Λ_c^+ and Ξ_c^+ yields with increasing beam energy. This effect is caused by the decrease in baryo-chemical potential towards higher energies. In order to

prove these predictions experimentally it is necessary to measure the total charm production cross section which includes also the charmed baryons. The relative abundance of charmed hadrons, however, is independent of the absolute value of the $c\bar{c}$ yield within this model.

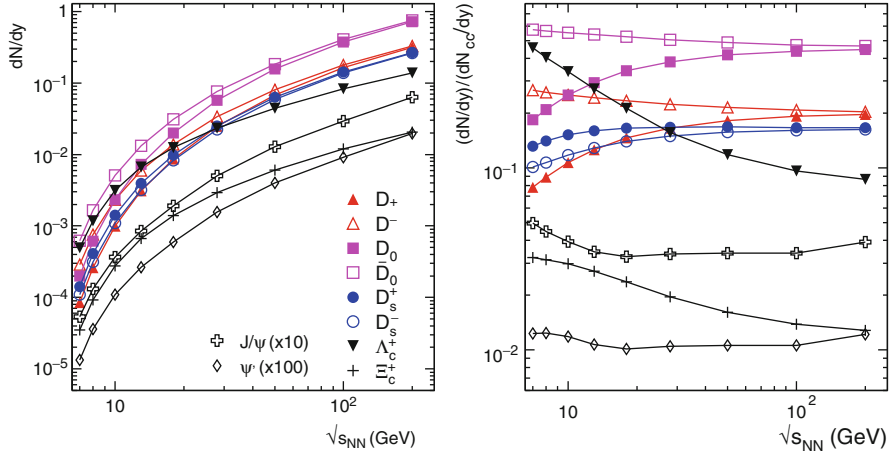


Fig. 8.14 Energy dependence of charmed hadron production at midrapidity. *Left panel:* absolute yields, *right panel:* yields relative to the number of $c\bar{c}$ pairs. Note, in both panels, the scale factors of 10 and 100 for J/ψ and ψ mesons, respectively

8.5 Open charm in dense matter

In the previous chapter we discussed charm production within the framework of the thermal fireball model which could explain the measured data on ψ meson production only when taking into account in-medium effects on open charm. The in-medium modification of D mesons opens the decay of ψ mesons into $D\bar{D}$ pairs, and, hence, contributes to the suppression of ψ mesons (see right panel of Fig. 8.11).

Within the SHM approach – which is a pure QGP model – in-medium mass modifications of open charm hadrons can be considered at the phase boundary. Two different scenarios¹ are assumed: (i) a common decrease of 50 MeV for all charmed mesons and their antiparticles and a decrease of 100 MeV for the Λ_c and Σ_c baryons (50 MeV decrease for Ξ_c); (ii) a decrease of

¹ The scenarios are constructed by modification of the constituent quark masses of light (u and d) quarks in the charmed hadrons by fixed amounts. Reducing, for example, the light quark masses by 50 MeV will lower D meson masses by 50 MeV and the $\Lambda_c(\Xi_c)$ mass by 100 (50) MeV.

100 MeV for all charmed mesons and a 50 MeV increase for their antiparticles, with the same (scaled with the number of light quarks) scenario as in (i) for the baryons. Scenario (i) is more suited for an isospin-symmetric fireball produced in high-energy collisions and was used in [190], while scenario (ii) may be realized at low energies. In both scenarios, the masses of the D_s mesons and of the charmonia are the vacuum masses. One should note that if one leaves all D meson masses unchanged but allows their widths to increase, the resulting yields will increase by 11% (2.7%) for a width of 100 MeV (50 MeV). If the in-medium widths exhibit tails towards low masses, as has been suggested by [411], to first order the effect on thermal densities is quantitatively comparable with that from a decrease in the pole mass.

In Fig. 8.15 it is demonstrated that the total open charm yield (sum over all charmed hadrons) exhibits essentially no change if one takes into account mass shifts, while the effect is large on charmonia. For this comparison, a third case has been added, namely considering that the mass change of charmed baryons is the same as for the mesons. Because of total charm conservation, with lowering of their masses the open charm hadrons eat away some of the charm quarks of the charmonia but, since the open charm hadrons are much more abundant, their own yield will hardly change.

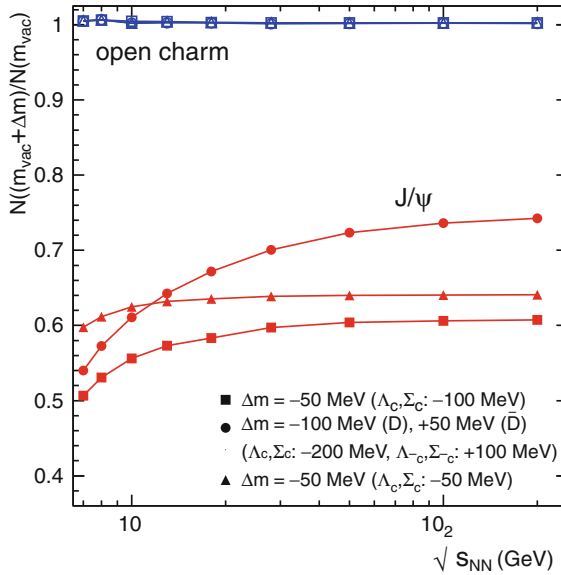


Fig. 8.15 Energy dependence of the relative change in the production yield of open charm hadrons and of J/ψ meson considering different scenarios for in-medium mass modifications (see text)

Within transport calculations one can calculate the effect of in-medium modifications of open charm both on their yields and spectral distributions.

HSD transport calculations predict that the m_T -spectra for pions, kaons, D mesons and J/ψ show a scaling behavior in central collisions of Au + Au at top SPS energies which is essentially due to an approximate m_T -scaling in pp collisions at $\sqrt{s} = 17.3$ GeV and D , \bar{D} and J/ψ final state interactions [190]. Furthermore, final state elastic scattering changes this result to a moderate extent since the relative meson abundances are not altered anymore and their spectra only get modified due to a common collective acceleration. The approximate m_T -scaling for pions, kaons, D mesons and J/ψ no longer holds well for central collisions of Au+Au at 25 A·GeV as shown in Fig. 8.16. Here the HSD calculations show a suppression of D mesons by a factor of ~ 10 relative to the global m_T -scaling – characterized by a slope of 143 MeV – if no D meson self energies are accounted for.

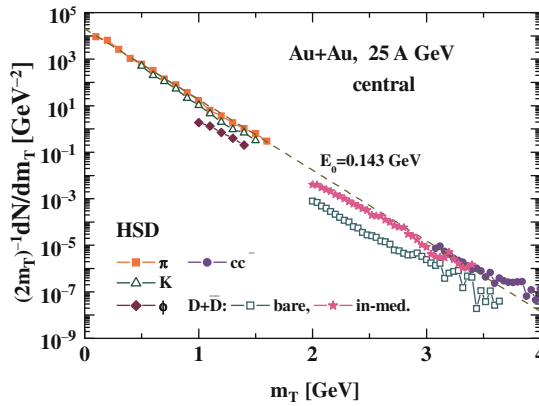


Fig. 8.16 The transverse mass spectra of pions (*full squares*), kaons (*open triangles*), ϕ mesons (*full rhombes*), $D + \bar{D}$ mesons (*open squares*) and $J/\psi, \psi'$ mesons (*full dots*) in the HSD approach for a central Au+Au collision at 25 AGeV without including self energies for the mesons. The *crosses* stand for the D meson m_T spectra when including an attractive mass shift of $-50\rho/\rho_0$ MeV. The thin dashed line shows an exponential with slope parameter $E_0 = 0.143$ GeV. Note that final state elastic scattering of kaons and ϕ mesons with pions has been discarded in the calculations

On the other hand, attractive mass shifts of D, \bar{D} mesons of -50 MeV at ρ_0 are expected due to hadronic interaction models when extending $SU(3)_{\text{flavor}}$ to $SU(4)_{\text{flavor}}$ symmetry. This is in analogy to the strange meson sector where the antikaon shows attractive mass shifts (or selfenergies). However, one should worry about an extrapolation of the hadronic interaction models to quark densities of $5-8 \rho_0$ since at these densities the effective degrees of freedom might be substantially different. This is guided by the idea that at these densities chiral symmetry should be restored, i.e. the large $\langle q\bar{q} \rangle$ condensate of the nonperturbative vacuum should have disappeared. Accordingly, the production of $c\bar{c}$ pairs in the “new” perturbative vacuum might be enhanced since only the invariant mass of a $c\bar{c}$ has to be produced e.g. by

gluon-gluon fusion. Note that in the perturbative vacuum no energy has to be spent for polarizing the nonperturbative vacuum. This vacuum polarization implies a generation of meson ($q\bar{q}$) clouds around the constituent quark-antiquark pairs which is no longer necessary in the perturbative vacuum of the chirally restored phase. Accordingly the threshold for $D\bar{D}$ production – which is ~ 3.739 GeV in vacuum – might be reduced by $\approx 2 \cdot 0.35$ GeV = 0.7 GeV in the chirally restored phase to about 3 GeV, only.

Such a reduction of the $c\bar{c}$ production threshold leads to an enhancement of open charm mesons by about a factor of 7 such that an approximate m_T -scaling for all mesons is regained. Thus, a global m_T scaling of all mesons may be regarded as a strong medium effect on the charmed hadrons, and as a signature for a chirally restored phase. As pointed out in [396] dropping D, \bar{D} masses lead also to an increase of J/ψ absorption by mesons and to a net lowering of the ψ' to J/ψ ratio for central collisions. So the ψ' to J/ψ ratio might also qualify as a probe of D meson in-medium effects.

One should note, however, that in the statistical model the ψ' to J/ψ ratio decreases below the value of 0.05 measured by NA50 with decreasing beam energy due to decreasing temperature. Moreover, the elementary cross sections for open charm and charmonia in pp and πN reactions have to be measured in the relevant kinematical regimes before reliable conclusions can be drawn in the nucleus-nucleus case. Experimental data in the 20–30 AGeV with light and heavy systems will have to clarify, furthermore, if the quasi-particle picture of open charm mesons at high baryon density is applicable at all or if the dynamics is already governed by partonic degrees of freedom rather than hadronic ones.

8.6 Conclusions and predictions for FAIR energies

The interpretation of charmonium yields measured in nuclear reactions and their relation to properties of the medium are a matter of ongoing investigations. In spite of more than 20 years of theoretical and experimental efforts no clear picture has emerged yet. Nonetheless, charmonium bound states are probably one of the most promising probes for the deconfined state of matter. However, further progress requires new data on the yields and phase-space distributions of charmonia, charmed mesons, and charmed baryons as function of beam energy and collision centrality in p+A and A+A collisions.

The measurement of ratios of hadrons containing charm quarks as a function of beam energy may provide direct evidence for a deconfinement phase transition. This is demonstrated in Fig. 8.17 which depicts the ratio of J/ψ over the sum of D and \bar{D} mesons (for central Au+Au collisions) as a function of available energy in the nucleon-nucleon system as predicted by the HSD hadronic transport model, and by the statistical hadronization model SHM. The SHM assumes complete dissociation of charmonium in the quark-gluon

plasma, followed by statistical production of J/ψ mesons (and particles with open charm) during hadronization.

For a typical FAIR beam energy of $\sqrt{s_{NN}} = 7$ GeV the hadronic transport model (HSD) predicts a J/ψ over $D + \bar{D}$ ratio which is about 5 times larger than the result of the statistical hadronization model (see Fig. 8.17). Within the HSD transport model both the J/ψ meson and the $D(\bar{D})$ meson production excitation functions are calculated using independent parameterizations which were fitted to experimental data (see Fig. 8.6). Within the SHM, the J/ψ over $D + \bar{D}$ ratio depends only on the temperature and the baryon chemical potential, and, hence, is in first order independent of the total abundance of charm and anticharm quarks in the fireball (at least at FAIR energies where this number is small). In fact, at a beam energy of $\sqrt{s_{NN}} = 7$ GeV the assumed abundance of $c\bar{c}$ pairs in the SHM is about 7 times higher than the abundance of $D\bar{D}$ pairs in HSD. This difference in the primordial charm + anticharm ($D+\bar{D}$) yields reflects the different threshold definitions in the cross-section parameterizations (see above).

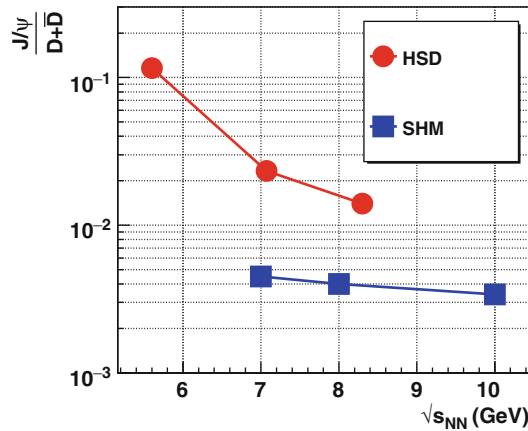


Fig. 8.17 Ratio of J/ψ over $D + \bar{D}$ mesons as a function of available energy in the nucleon–nucleon system predicted for central Au+Au collisions by the HSD hadronic transport model and by the statistical hadronization model SHM [19] which assumes a QGP initial state

In conclusion, the J/ψ over $D + \bar{D}$ ratio as shown in Fig. 8.17 is sensitive to the conditions inside the reaction volume, and the two models describe two extreme scenarios: a purely partonic fireball (SHM) versus a hadronic fireball (HSD). However, if only part of the fireball volume undergoes a deconfinement phase transition, or if the primordially produced J/ψ mesons are not fully suppressed by the plasma, the difference between the hadronic and partonic scenario will be reduced. Nevertheless, when measuring carefully the excitation function of J/ψ and $D(\bar{D})$ meson production in heavy-ion colli-

sions, their ratio should exhibit a discontinuity at the energy for which the deconfined phase is reached.

Charm production experiments at FAIR energies offer the possibility to disentangle the charmonium absorption processes in high-energy nucleus–nucleus collisions, such as the absorption on hadronic comovers and sequential melting in the partonic phase. The reason is that the average comover density increases only moderately with increasing bombarding energy, whereas the region in space-time with energy densities above critical values of 2 GeV/fm^3 increases rapidly for beam energies above 20 AGeV. Therefore, a precise measurement of the excitation function of the ψ' to J/ψ ratio in central Au+Au collisions will shed light on the charmonium absorption processes in dense matter. A smooth excitation function is expected for comover absorption, whereas sequential charmonium melting in the QGP would cause a structure in the excitation function of the ψ' to J/ψ ratio. The HSD predictions for Au+Au reactions at 25 AGeV are presented in Fig. 8.18 which depicts the survival probability $S(J/\psi)$ (left panel) and the ratio ψ' to J/ψ (right plot) as a function of the number of participants N_{part} which measures the centrality of the collision [384, 392].

The J/ψ nuclear modification factor R_{AA} calculated with the rate-equation approach for Pb+Pb collisions at 40 AGeV ($\sqrt{s} = 8.77 \text{ AGeV}$) is displayed the left panel of Fig. 8.19 as a function of collision centrality. In this model the fireball features a mixed phase of about 4 fm/c duration at $T_c = 160 \text{ MeV}$ for central Pb+Pb collisions [412]. According to these calculation the

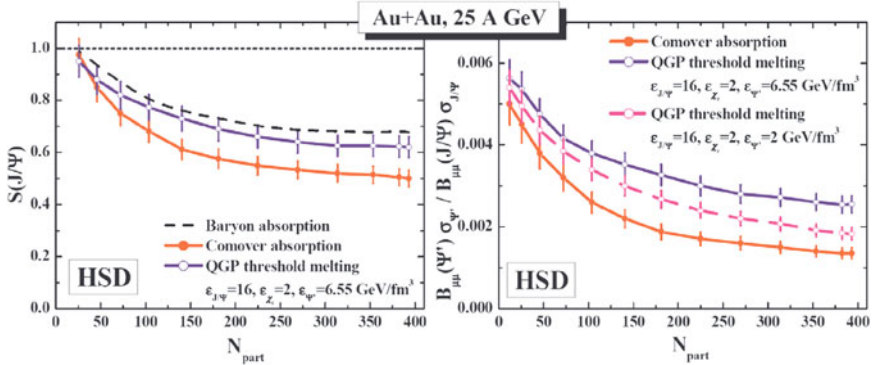


Fig. 8.18 The survival probability $S(J/\psi)$ (left panel) and the ratio ψ' to J/ψ (right panel) as a function of the number of participants N_{part} in Au+Au reactions at 25 AGeV. The (blue) lines with open dots reflect the “QGP threshold scenario” with $\epsilon_{J/\psi} = 16 \text{ GeV/fm}^3$, $\epsilon_{\chi_c} = 2 \text{ GeV/fm}^3$, $\epsilon_{\psi'} = 6.55 \text{ GeV/fm}^3$, while the (violet) lower line with open dots in the right panel represents the “QGP threshold scenario” with $\epsilon_{J/\psi} = 16 \text{ GeV/fm}^3$, $\epsilon_{\chi_c} = 2 \text{ GeV/fm}^3$, $\epsilon_{\psi'} = 2 \text{ GeV/fm}^3$. The solid (red) lines with the full dots denote the results for the comover absorption model with the standard matrix element squared $|M_0|^2 = 0.18 \text{ fm}^2/\text{GeV}^2$. The dashed line in the left panel represents the HSD calculations including only dissociation channels with nucleons. The figure is taken from [384, 392]

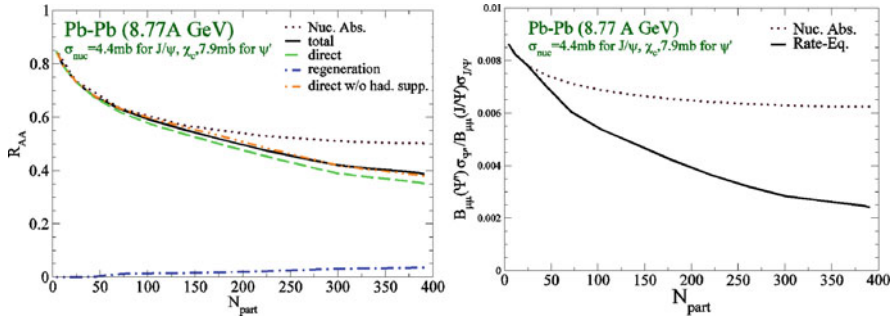


Fig. 8.19 *Left panel:* Results of the thermal kinetic approach for R_{AA} versus centrality at FAIR. *Solid line:* total J/ψ yield. *Dashed line:* suppressed primordial production. *Dot-dashed line:* regeneration component. *Dotted line:* primordial production with nuclear absorption only. *Double-dot-dashed line:* suppressed primordial production with QGP-induced anomalous suppression only (without hadronic suppression). *Right panel:* $\psi'/(J/\psi)$ ratio as computed in the thermal kinetic approach. *Solid line:* rate-equation. *Dotted line:* nuclear absorption [412]

suppression of the direct J/ψ component at FAIR energies is dominated by nuclear absorption. Therefore, the accurate measurement of nuclear absorption effects in peripheral nucleus–nucleus and proton–nucleus collisions will be essential to learn about the QGP suppression. Additional discrimination of charmonium production and suppression mechanisms can be obtained from the centrality dependence of the ψ' to J/ψ ratio as shown in the right panel of Fig. 8.19. The figure illustrates results of the thermal kinetic approach for Pb+Pb collisions at 40 AGeV. The ratio ψ' to J/ψ drops with increasing centrality below the ratios obtained for nuclear absorption (assuming that ψ' and J/ψ mesons are absorbed likewise). The strong anomalous suppression of ψ' in central collisions is due to the decay process $\psi' \rightarrow D + \bar{D}$ which is enhanced if the mass of the D mesons is broadened or reduced in hadronic matter (see also [396]).

Similar to RHIC energies [379, 380] the observation of strong collective flow for charm mesons will provide a strong indication for a new phase of matter at the top FAIR energies. In particular, the elliptic flow measured as a function of transverse momentum p_T may help to disentangle hadronic from partonic dynamics. The prediction of the hadronic transport model (HSD) for the D meson elliptic flow v_2 at midrapidity for Au+Au reactions at 25 A·GeV is shown in Fig. 8.20 in comparison to v_2 of charged hadrons. As seen from 8.20 the D, \bar{D} elliptic flow is smaller than the v_2 of the lighter hadrons. Such a low elliptic flow is due the small interaction cross section of D, \bar{D} mesons with hadrons. The observation of a much larger elliptic flow of D, \bar{D} mesons would be a signature for an increased pressure built up in an early partonic phase.

The transport properties of D mesons - as reflected in their collective flow and their spectral distributions - are instrumental in characterizing the dense

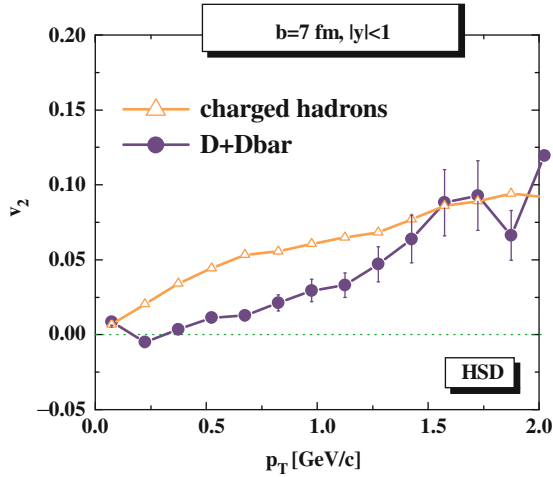


Fig. 8.20 The HSD predictions for the elliptic flow v_2 of $D + \bar{D}$ mesons (solid lines with full dots) and charged hadrons (solid lines with open triangles) for Au + Au collisions at 25 A GeV for $b = 7$ fm versus p_T for mid-rapidity

medium produced in the collision. The interaction of a baryon-dominated medium is stronger for D mesons than for \bar{D} mesons due to charm-exchange reactions which involve only c-quarks (for example $D + N \rightarrow \pi + \Lambda_c$). In consequence, the flow and the spectral distributions are expected to be stronger affected for D mesons than for \bar{D} mesons. On the other hand, interactions in the partonic stage via the excitation of mesonic resonances (such as $\bar{c} + q \rightarrow \bar{D} \rightarrow \bar{c} + q$) are stronger for \bar{D} than for D mesons. Moreover, medium modified D meson spectral functions also will have a large effect on the ψ' suppression pattern.

In conclusion, the measurement of charmonia and open charm hadrons in nucleus–nucleus collisions at FAIR energies has a wide discovery potential, and justifies the experimental efforts which are needed to obtain high quality data in spite of the low charm production cross sections and the huge background at threshold beam energies.

Chapter 9

Fluctuations and correlations

The occurrence of fluctuations (or thermal noise) is a normal concomitant in thermally excited systems. Caused by stochastic processes the actual (local) value of a certain observable may deviate from its average value. The average may be defined with respect to an average taken in a larger volume or averaged with respect to time or in (quantum) statistical systems with respect to an average over many events of a given statistical ensemble. In transport theoretical treatments the fluctuations display features characteristic of a diffusion process. Generally a created fluctuation will subsequently be damped out in time by those stochastic processes that lead to dissipation. The balance between the two counteracting processes is governed by the dissipation–fluctuation theorem which describes the (linear) response of the system upon an externally initiated fluctuation.

There are, however, interesting dynamical situations where such fluctuations are not damped out but rather grow and build up specific correlations. For example, the passage through a phase transition region causes a restructuring of the matter: certain modes become unstable and grow exponentially until the system is carried over into a new regime of stability with corresponding new structures. The presence of a phase transition is associated with a rapid change (with temperature and chemical potentials) of the thermodynamic susceptibilities, which reflect the corresponding fluctuations. The well known phenomenon of critical opalescence is a result of fluctuations at all length scales due to a second order phase transition. By contrast, the spinodal instabilities inside the first-order phase coexistence region tend to develop density patterns with a certain characteristic length scale. An instructive example is presented by the nuclear liquid-gas phase transition, cf. Sect. 2.2.3.4 in Part I, for which the spinodal formation of clusters (i.e. light nuclear fragments) has been studied by means of nuclear collisions. In the case of the first-order confinement transition, spinodal phase decomposition could generate kinematic correlations among particles and lead to enhanced fluctuations of e.g. strangeness.

The universe went through various transitions during its early evolution. At each stage, the pre-existing fluctuations largely determined the inhomogeneities of the subsequent matter distribution, leading finally to the present pattern of galaxies and its substructures. Prominent are the measurements of the cosmic microwave background radiation (CMB) [413], first carried out by the COBE satellite [414] and later refined by WMAP [415]. In inclusive single particle measurements, namely measuring the mean photon energy arriving on earth from different celestial angles, it was possible to resolve inhomogeneities in the resulting CMB temperature distribution on the level of 10^{-4} with respect to the angular averaged distribution. Though tiny, these inhomogeneities found their remarkable explanation in the primordial quantum fluctuations that were present prior to the inflation stage, thus confirming the Big Bang picture of the early universe.

In nuclear collision experiments, on the other hand, one collects results from many events. In addition to inclusive measurements that determine the asymptotic single-particle spectra, a variety of coincidence measurements permit the extraction of more detailed properties, such as sources sizes, jet propagation, or collective flow. Beyond these standard type of measurements one even has the chance and challenge to directly observe and exploit the fluctuations of a given observable from one event to another. In principle, any observable that is not globally conserved fluctuates. Most of these fluctuations, though, are trivial in nature, namely they are of pure statistical origin. The problem is to dig out the interesting and dynamically relevant event-to-event fluctuations, that e.g. enable the search for a possible critical point and for a first order co-existence region in the QCD phase diagram. Over the past two decades quite a number of such observables were suggested for clarifying the passage of the collision events through the quark-gluon plasma phase. These either refer to signals from the plasma that are supposed to survive the phase transition or to observables that experience strong fluctuations during the phase transition or close to the critical point. As the latter refer to the order parameters of the phase transition, which are given by conserved charges, such as baryon or strangeness number, special measures have to be taken in order to see the effects.

In this chapter we shall discuss these strategies and the experimental attempts to observe the proposed signals (which, however, so far were mostly unsuccessful). We start with a definition of the susceptibilities which reflect the fluctuations and correlations in Sect. 9.1. The limitations of measuring fluctuations and correlations of conserved quantities are outlined in Sect. 9.2. In Sect. 9.3 we discuss electric charge fluctuations for which no experimental indications of phase transitions have been found so far. The only event-by-event observable that shows a strong beam energy dependence is the fluctuation of the K/π ratio, as discussed in Sect. 9.4. The correlations between baryon number and strangeness are discussed in Sect. 9.5. In Sect. 9.6 we describe the advantage of measuring higher-order moments which provide a sensitive measure of the correlation length. The status of the investigation

of mean transverse momentum fluctuations – where the measured data do not show any non-monotonic behavior – is presented in Sect. 9.7. Finally, in Sect. 9.8 we discuss possible observables of a first-order transition which are based on clumping due to spinodal phase decomposition.

9.1 Fluctuations and correlations in a thermal system

As discussed in Part I a system in thermal equilibrium (for a grand-canonical ensemble) is characterized by its partition function

$$Z = \text{Tr} \left[\exp \left(-\frac{H - \sum_i \mu_i Q_i}{T} \right) \right] \quad (9.1)$$

where H is the Hamiltonian of the system, and Q_i and μ_i denote the conserved charges and the corresponding chemical potentials, respectively. In case of three flavor QCD these are strangeness, baryon-number, and electric charge, or, equivalently, the three quark flavors up, down, and strange. The mean and the (co)-variances are then expressed in terms of derivatives of the partition function with respect to the appropriate chemical potentials,¹

$$\langle Q_i \rangle = T \frac{\partial}{\partial \mu_i} \log(Z) \quad (9.2)$$

$$\langle \delta Q_i \delta Q_j \rangle = T^2 \frac{\partial^2}{\partial \mu_i \partial \mu_j} \log(Z) \equiv VT \chi_{i,j} \quad (9.3)$$

with $\delta Q_i = Q_i - \langle Q_i \rangle$. Here we have introduced the susceptibilities

$$\chi_{i,j} = \frac{T}{V} \frac{\partial^2}{\partial \mu_i \partial \mu_j} \log(Z) \quad (9.4)$$

which are generally quoted as a measure of the (co)-variances. The diagonal susceptibilities, $\chi_{i,i}$ are a measure for the fluctuations of the system, whereas the off-diagonal susceptibilities, $\chi_{i,j}$ with $i \neq j$ characterize the correlations between the conserved charges Q_i and Q_j .

One can define and study higher order susceptibilities or cumulants, by differentiating multiple times with respect to the appropriate chemical potentials

$$\chi^{n_i, n_j, n_k} \equiv \frac{1}{VT} \frac{\partial^{n_i}}{\partial (\mu_i/T)^{n_i}} \frac{\partial^{n_j}}{\partial (\mu_j/T)^{n_j}} \frac{\partial^{n_k}}{\partial (\mu_k/T)^{n_k}} \log(Z) \quad (9.5)$$

¹ Although in this section we will mostly concentrate on susceptibilities involving conserved charges, we note that one can define susceptibilities involving any well defined operator. One prominent example is the chiral susceptibility $\chi_{ch} = T/V \partial^2 / \partial m_q^2 \log(Z)$ which characterizes the chiral phase transition in QCD.

Higher order cumulants up to the sixth [416] and even eighth [417] order have been calculated in Lattice QCD which provide useful information about the properties of the matter above the critical temperature as will be discussed in one of the following sections.

9.2 Fluctuations and correlations of conserved quantities

The notion “fluctuation of conserved quantities” seems contradictory. Looking at the entire system, none of the conserved quantities will fluctuate. However, by studying a sufficiently small subsystem, the fluctuations of conserved quantities become meaningful. The small system may exchange conserved quanta with the rest of the system. This is similar to the assumptions which govern a thermal system in the grand-canonical ensemble, and Lattice QCD calculations are carried out in this ensemble. To illustrate this point in the context of heavy-ion collisions, consider a situation as depicted in Fig. 9.1.

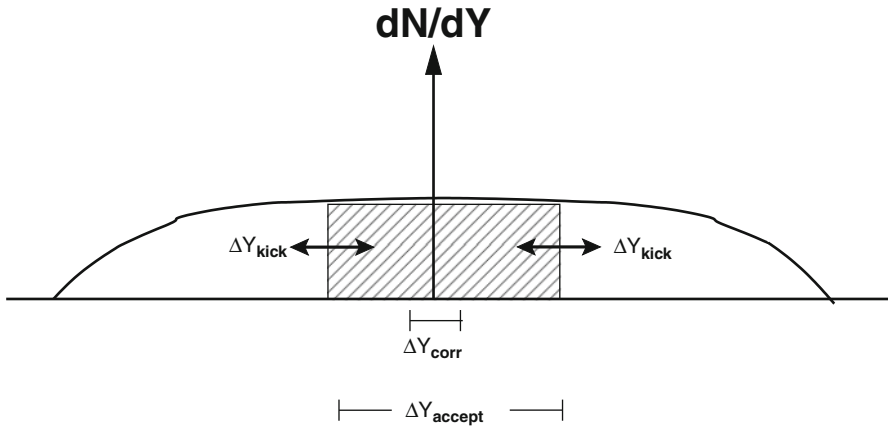


Fig. 9.1 The various rapidity scales relevant for fluctuations of conserved quantities (taken from [418]).

The total system corresponds to all particles distributed in rapidity Y over a range ΔY_{total} , whereas the small subsystem corresponds to the particles within the accepted rapidity interval ΔY_{accept} . For fluctuations of conserved quantities (charges) to be a meaningful observable the following scales need to be well separated:

- The range ΔY_{total} for the total charge multiplicity distribution.
- The interval ΔY_{accept} for the accepted charged particles.
- The charge correlation length ΔY_{corr} characteristic to the physics of interest.

- The typical rapidity shift ΔY_{kick} charges receive during and after hadronization.

Given these scales, fluctuations will be able to tell us about the properties of the early stage of the system, the QGP, if the following criteria are met:

$$\Delta Y_{\text{accept}} \gg \Delta Y_{\text{corr}} \\ \Delta Y_{\text{total}} \gg \Delta Y_{\text{accept}} \gg \Delta Y_{\text{kick}}$$

The first criterion is necessary in order to be sensitive to the relevant physics, whereas the second one ensures that the total charge conservation does not suppress the signal, and that the signal survives hadronization and the hadronic phase. In particular the condition $\Delta Y_{\text{accept}} \gg \Delta Y_{\text{kick}}$ is unique to conserved charges. For the charge of the system to change, charges need to be transported through the boundaries of the system. And if the condition $\Delta Y_{\text{accept}} \gg \Delta Y_{\text{kick}}$ is satisfied it requires many kicks to change the charge of the system. Consequently the relaxation time into a new equilibrium state may be very long, depending on how well the scales are separated. If the charges would not be conserved, on the other hand, they could be produced anywhere within the system leading to a much more rapid equilibration. For a detailed discussion see [418].

The main problematic in the chain of arguments is that the selection of the subsystem has to be done by the momenta or rapidities of the asymptotically observed particles. Stochastic processes that permit to explore the accessible fluctuations, however, are essentially caused by interaction partners in their spatial proximity irrespective of the momenta involved. Be it by collisions or even by the color neutralisation process itself. As these processes generally involve transfers of charges, one has a problem, whenever the asymptotic hadron resulting from the partner remains undetected. The correlation between momenta and spatial location, however, is significantly blurred due to the thermal motion of the particles. Thus a further constraint has to be [419]

$$\Delta Y_{\text{accept}} \gg \Delta Y_{\text{thermal}},$$

where for example

$$\Delta Y_{\text{thermal}}^{\text{f.w.h.m.}} = \begin{cases} 2.1 & \text{for massless quarks and gluons} \\ 1.7 & \text{for pions at } T = m_\pi \\ 0.8 & \text{for nucleons at } T = 120 \text{ MeV} \end{cases} \quad (9.6)$$

(all taken at full width half maximum). These are sizable rapidity spreads that imply a very fuzzy relation between the spatial origin of the particles and their final rapidity. For a clarification we refer to the discussion of the continuous freeze-out dynamics [420, 421] given in Sect. 5.8 of Part III in particular to the transport results shown in Fig. 5.5 [422].

Furthermore dynamical hadronisation calculations [423, 424], cf. Sect. 5.3.2 in Part III, showed that due to the significant drop in entropy density the hadronisation process itself proceeds during a significant time span of 6 fm/c

and more. This then leaves ample time for stochastic processes which can exchange charges with the rest of the system. Unfortunately no microscopic hadronisation calculations exist that could further quantify the issue.

9.3 Electric charge fluctuations

The fluctuations of conserved quantities in heavy-ion collisions was first discussed in the context of (electric) net-charge fluctuations [425, 426]. Here the simple observation was that charge fluctuations per entropy should scale with the square of the electric charge of the charge carrying particles and, consequently, they should be sensitive to the fractional charges of the quarks. In the following we discuss briefly the fluctuations of the ratio of positively over negatively charged particles, which is directly related to the net-charge fluctuations. The fluctuations of the ratio of positively over negatively charged particles

$$R_{+-} = \frac{N_+}{N_-} \quad (9.7)$$

are given by

$$\sigma_{+-}^2 = \frac{4}{\langle N_{ch} \rangle^2} \langle \delta N_+^2 + \delta N_-^2 - 2\delta N_+ \delta N_- \rangle = \frac{4\langle \delta Q^2 \rangle}{\langle N_{ch} \rangle^2} \quad (9.8)$$

in the limit of small net charge $\langle Q \rangle = \langle N_+ - N_- \rangle \ll \langle N_{ch} \rangle = \langle N_+ + N_- \rangle$.

The main assumption of the charge-fluctuation signal is that a well characterized subsystem of the plasma hadronises as if this subsystem is on the whole isolated from the rest. Then one can use entropy arguments to link the number of original quarks and antiquarks in the QGP essentially to the resulting number of mesons in the hadronic matter, since the formation of baryons is largely suppressed at mid-rapidity. Assuming a free gas of quarks and gluons for the QGP with a degeneracy ratio of $\langle N_g \rangle = \frac{16}{24} \langle N_q + N_{\bar{q}} \rangle$ and a pion gas at $T \approx m_\pi$, where $S_\pi/N_\pi \approx 4.2$, one finds within a few percent that

$$\langle N_{ch} \rangle \approx \langle N_q + N_{\bar{q}} \rangle. \quad (9.9)$$

Together with the neutral pions it implies that during hadronisation the number of plasma quarks and antiquarks is essentially tripled. Thus quark-antiquark pairs have to be created in order to form the constituents of the final mesons. Estimating the fluctuations of the total charge δQ^2 of the subsystem by employing Poisson statistics in both phases leads to

$$\langle \delta Q^2 \rangle_{\text{QGP}} = \frac{5}{18} \langle N_q + N_{\bar{q}} \rangle \approx \frac{1}{3.6} \langle N_{ch} \rangle \approx \frac{1}{3.6} \langle \delta Q^2 \rangle_{\text{hadrons}}. \quad (9.10)$$

where on the QCD side the fractional charges of the quarks enter. This displays the advocated signal: the charge fluctuations in the plasma are essentially a factor four smaller than those of the hadron gas. Even considering a couple of effects that can moderate the large factor in relation (9.10), like the inclusion hadronic resonances, Jeon et al. [425] still claims a suppression factor in the order of 3. Similar arguments were given for baryon number fluctuations [426], where one is sensitive to the fractional baryon number of the quarks. In this case an actual measurement would require the detection of neutrons, which is rather difficult. On the other hand, it may be sufficient to study proton number fluctuations, as the iso-vector channel does not show critical behavior [427]. This may also soften the limitations due to global baryon-number conservation.

Electric charge fluctuations have been measured in experiments both at the SPS and at RHIC [428–431] by the CERES, NA49, PHENIX, and STAR collaborations. The results at the SPS are difficult to interpret as the necessary separation of rapidity scales at these energies is not satisfied and global charge conservation effects dominate the signal. The RHIC measurements by PHENIX and STAR were still found consistent with the predictions for a hadron resonance gas. Here the main obstacle for an observation of the QGP fluctuations are certainly the narrow pseudo-rapidity windows of $\Delta\eta = 0.7$ and 1.0 [430, 431], in comparison to the thermal spread (9.6) induced by the pions. Even for the $\Delta\eta = 2$ window investigated in [432] a sizable fraction of the particles emitted from the central collision volume remained undetected.

Electric charge fluctuations have also been investigated by microscopic event-by-event transport calculations using the HSD code [433]. The charge fluctuations $\Delta\Phi_q$ are defined as

$$\Delta\Phi_q = \Phi_q - \Phi_{q,GCC}, \quad (9.11)$$

$$\Phi_q = \sqrt{\frac{\langle Z^2 \rangle}{\langle N \rangle}} - \sqrt{z^2}, \quad z = q - \bar{q}, \quad Z = \sum_{i=1}^N (q_i - \bar{q}), \quad (9.12)$$

where q denotes a single particle variable, i.e. electric charge q ; N is the number of particles of the event within the acceptance, and over-line and $\langle \dots \rangle$ denote averaging over a single particle inclusive distribution and over events, respectively. The trivial fluctuations due to the global charge conservation (GCC) is

$$\Phi_{q,GCC} = \sqrt{1 - P} - 1, \quad \text{where } P = \frac{\langle N_{ch} \rangle}{\langle N_{ch} \rangle_{tot}} \quad (9.13)$$

with $\langle N_{ch} \rangle$ and $\langle N_{ch} \rangle_{tot}$ the mean charged multiplicity in the detector acceptance and in full phase space (excluding spectator nucleons), respectively.

The HSD results [433] show a good agreement with the NA49 data at SPS energies (Fig. 9.2). Thus, this observable is dominated by the final stage dynamics, i.e. the hadronization phase and the resonance decays, and rather insensitive to the initial QGP dynamics.

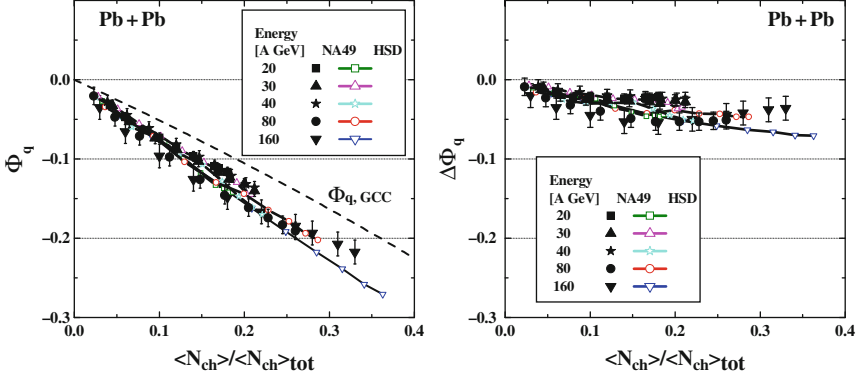


Fig. 9.2 The dependence of the Φ_q (l.h.s.) and $\Delta\Phi_q$ (r.h.s.) on the fraction of accepted particles for central Pb+Pb collisions at 20–158 AGeV. The NA49 data [428] are shown as *full symbols*, whereas the *open symbols* (connected by *lines*) stay for the HSD results. The *dashed line* shows the dependence expected for the case if the only source of particle correlations is the global charge conservation $\Phi_{q,GCC}$.

As mentioned above, microscopic transport simulations should be performed in order to properly account for detector geometries and centrality classes of events in accordance with the experimental setup and analysis. To this aim the event-by-event multiplicity fluctuations in Pb+Pb collisions at 158 AGeV have been studied within the HSD and UrQMD transport models in [434].

The average values of negative, positive, and all charged hadrons $\langle N_i \rangle$, ($i = +, -, ch$) and variances $\sigma^2(N_i) \equiv \langle N_i^2 \rangle - \langle N_i \rangle^2$ have been calculated for samples of collision events with fixed values of projectile participants, N_P^{proj} [435]. The scaled variances are by definition

$$\omega_i \equiv \sigma^2(N_i) / \langle N_i \rangle \quad (9.14)$$

Note that $\omega = 1$ for a Poisson multiplicity distribution: $P(N) = e^{-\bar{N}} \bar{N}^N / N!$. In Fig. 9.3 the HSD and UrQMD results are shown and compared with the NA49 data.

The samples with $N_P^{proj} = 20-60$ show large fluctuations of the number of target nucleons, N_P^{targ} , which participate in inelastic collisions, $\omega_P^{targ} \geq 2$. The final hadron multiplicity fluctuations exhibit an analogous behavior, which explains the large values of the HSD and UrQMD scaled variances ω_i in the target hemispheres and in the full 4π acceptance. On the other hand, the asymmetry between the projectile and target participants – introduced in the data samples by the trigger condition of fixed N_P^{targ} – can be used to explore different dynamics of nucleus–nucleus collisions by measuring the final multiplicity fluctuations as a function of rapidity. This analysis reveals that the recent NA49 data might indicate a rather strong mixing of the

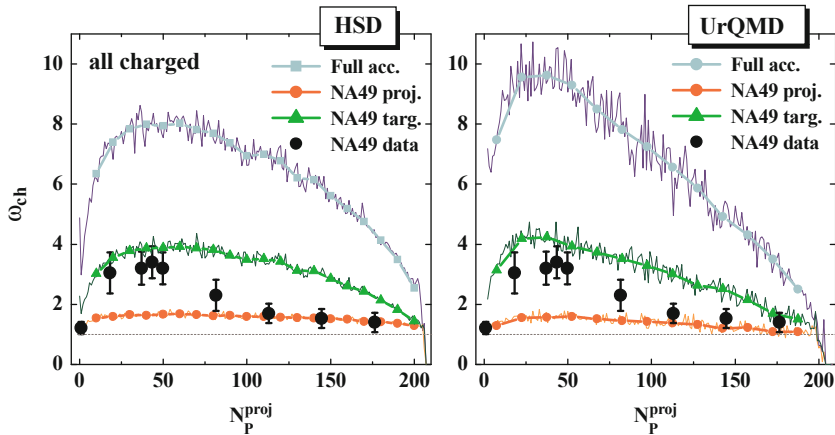


Fig. 9.3 The results of the HSD (*left*) and UrQMD (*right*) simulations are shown for ω_- , ω_+ , and ω_{ch} in Pb+Pb collisions at 158 AGeV as functions of N_P^{proj} . The black points are the NA49 data. The different lines correspond to the model simulations with the original NA49 acceptance, $1.1 < y < 2.6$, in the projectile hemisphere (*lower lines*), the NA49-like acceptance in the mirror rapidity interval, $-2.6 < y < -1.1$, in the target hemisphere (*middle lines*), and full 4π acceptance (*upper lines*).

longitudinal flows of the projectile and target hadron production sources. This is so not only for central collisions – in line with the HSD and UrQMD approaches – but also for rather peripheral reactions.

Nevertheless, the first study in [434] (cf. Fig. 9.3) has also demonstrated that trigger conditions have a large impact on fluctuation observables and imply conditional fluctuations that are not easy to interpret. Only in case of ‘full’ acceptance this might be the case.

9.4 Particle multiplicity ratio fluctuations

The first study of event-by-event fluctuations in a heavy-ion collision experiment was the measurement of the K/π fluctuations by the NA49 collaboration [436]. The original motivation for this analysis was to look for separate event classes, for example, those with enhanced strangeness and those without. The observed fluctuations, however, are rather small, $\approx 2\%$, indicating that the events generated in these collision are rather similar. Subsequently, the NA49 collaboration has measured the K/π fluctuations over the entire CERN-SPS energy range [437], and together with the preliminary measurements from STAR at RHIC [438] we have an excitation function for this observable over a wide range of energies. The difference between the actual variance of the system and that of an uncorrelated (mixed event) ensemble is usually referred to as

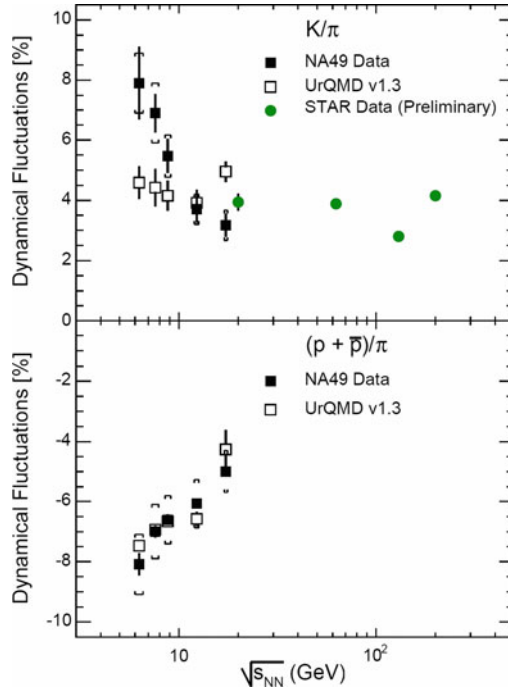


Fig. 9.4 Energy dependence of the event-by-event nonstatistical fluctuations of the K/π ratio (*top panel*) and the $(p + \bar{p})/\pi$ ratio (*bottom panel*). *Filled symbols* show data, *open symbols* show calculations with the UrQMD transport code, using NA49 acceptance tables. Systematic uncertainties are shown as *brackets*. (taken from [437]).

$$\sigma_{\text{dynamic}}^2 = \sigma^2 - \sigma_{\text{uncorrelated}}^2. \quad (9.15)$$

This observable is depicted in the upper panel of Fig. 9.4 for the K/π ratio as measured at the SPS and RHIC. The K/π fluctuations increase steeply as the center of mass energy is decreased below $\sqrt{s_{NN}} = 10$ A GeV. This rise coincides with a maximum of the inclusive K/π ratio. In contrast, the fluctuations of the $(p + \bar{p})/\pi$ ratio measured at SPS decrease with decreasing beam energy as shown in the lower panel of Fig. 9.4. Both the data sets are compared to results of UrQMD transport calculations which fail to reproduce the K/π fluctuations but agree with the fluctuations of the $(p + \bar{p})/\pi$ ratio.

The question is whether the increase of the K/π fluctuation is related to the critical point. However, in this case one would expect the fluctuations of the pion number to be enhanced. But this would imply also enhanced fluctuations of the proton-to-pion ratio, which is not observed in experiment, as shown in the lower panel of Fig. 9.4.

In Fig. 9.5 the fluctuations of the K/π ratio are compared to results of HSD calculations [439]. In contrast to the UrQMD calculations the HSD model at least reproduces the trend of the data towards lower beam energies,

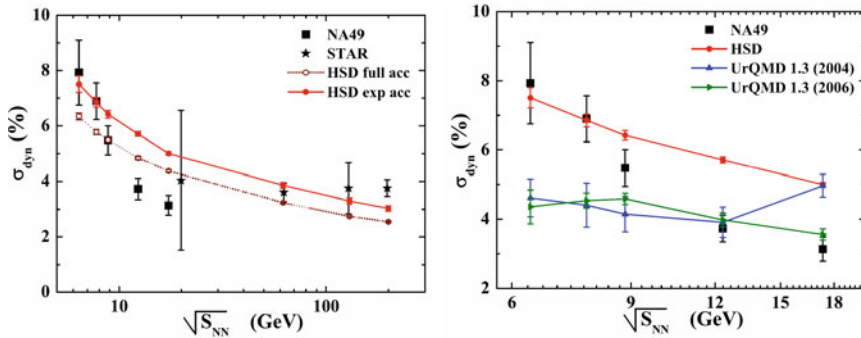


Fig. 9.5 *Left panel:* The excitation function of σ_{dynamic} measured by the NA49 Collaboration at the SPS CERN [437] and by the STAR Collaboration at BNL RHIC [438], together with results from HSD calculations for the K/π ratio for full acceptance (*dotted line*) and within the experimental acceptance (*solid line*). *Right panel:* The HSD results (*circles*) and two different versions of UrQMD (*triangles*) calculations for σ_{dynamic} in comparison to the NA49 data. Statistical uncertainties in the transport calculations are shown by *error bars* (taken from [439]).

although the data points taken at high SPS energies cannot be reproduced. While the increase of the K/π fluctuations towards lower beam energies might indeed be a first experimental indication for interesting structures in the QCD phase diagram, one should raise a note of caution. As discussed in [440], ratio fluctuations scale roughly as the inverse of the accepted multiplicity,

$$\sigma_{\text{dynamic}}^2 \approx \frac{1}{\langle N \rangle_{\text{accepted}}} \quad (9.16)$$

Consequently, the observed rise may partially be due to the change of the actual acceptance with beam energy, which is always the case in a fixed target experiment such as NA49. As proposed in [440], the observed rise in the fluctuations would be more convincing if it showed up in the ratio of the measured variance over that from mixed events:

$$F \equiv \frac{\sigma^2}{\sigma_{\text{uncorrelated}}^2}. \quad (9.17)$$

This ratio does not exhibit any trivial multiplicity dependence, and is much less sensitive to acceptance effects.

9.5 Correlation between baryon number and strangeness

The correlation between the strangeness S and the baryon number B provides a useful diagnostic for the presence of strong correlations between quarks and antiquarks [441]. To understand this, consider first a situation in which the

basic degrees of freedom are weakly interacting quarks and gluons. Then strangeness is carried exclusively by the s and \bar{s} quarks which in turn carry baryon number in strict proportion to their strangeness, $B_s = -\frac{1}{3}S_s$, thus rendering strangeness and baryon number strongly correlated. This feature is in strong contrast to a hadron gas in which the relation between strangeness and baryon number is less intimate. For example, at small baryon chemical potential the strangeness is carried primarily by kaons, which have no baryon number. Thus one expects baryon number and strangeness to be stronger correlated in a Quark Gluon Plasma than in a hadron gas.

Such elementary considerations suggest the introduction of the following correlation coefficient [441],

$$C_{BS} \equiv -3 \frac{\sigma_{BS}}{\sigma_S^2} = -3 \frac{\langle BS \rangle - \langle B \rangle \langle S \rangle}{\langle S^2 \rangle - \langle S \rangle^2} = -3 \frac{\langle BS \rangle}{\langle S^2 \rangle}. \quad (9.18)$$

In terms of quark flavors the correlation coefficient C_{BS} can be written as

$$C_{BS} = -3 \frac{\langle BS \rangle}{\langle S^2 \rangle} = \frac{\langle (u + d + s)(s) \rangle}{\langle s^2 \rangle} = 1 + \frac{\langle us \rangle + \langle ds \rangle}{\langle s^2 \rangle} = 1 + \frac{\chi_{us} + \chi_{ds}}{\chi_{ss}} \quad (9.19)$$

since the baryon number of a quark is $\frac{1}{3}$ and the strangeness of a strange quark is -1 . Note that the quark operators u, d, s here represent the net-quark number of a given flavor, i.e. $\langle u \rangle \equiv \langle u - \bar{u} \rangle$ etc. The last expression in Eq. (9.19) is obtained by using the definition for the susceptibilities as defined in the previous section. For uncorrelated quark flavors like in a simple Quark-Gluon-Plasma we have

$$\langle us \rangle = \langle ds \rangle = 0 \quad (9.20)$$

and hence

$$C_{BS} = 1 \quad (9.21)$$

In contrast, a gas of uncorrelated hadron resonances gives

$$C_{BS} \approx 3 \frac{\langle A \rangle + \langle \bar{A} \rangle + \dots + 3\langle \Omega^- \rangle + 3\langle \bar{\Omega}^+ \rangle}{K^0 + \bar{K}^0 + \dots + 9\langle \Omega^- \rangle + 9\langle \bar{\Omega}^+ \rangle}. \quad (9.22)$$

Here, the numerator receives contributions from only (strange) baryons (and anti-baryons), while the denominator receives contributions also from (strange) mesons. As a result, one obtains $C_{BS} = 0.66$ for $T = 170$ MeV and $\mu_B = 0$. On the other hand, at very high μ_B and low T where strangeness is carried exclusively by lambdas and kaons, the correlation coefficient increases to $C_{BS} \approx 3/2$ due to strangeness neutrality ($\langle A \rangle = \langle K \rangle$). This dependence of C_{BS} on the hadronic environment is in sharp contrast to the simple Quark-Gluon Plasma where the correlation coefficient remains strictly one for all temperatures and chemical potentials. The left panel of Fig. 9.6 depicts the result for C_{BS} as function of μ_B for both an ideal Quark-Gluon Plasma as well as for a hadron gas along the empirical chemical freeze-out line [441].

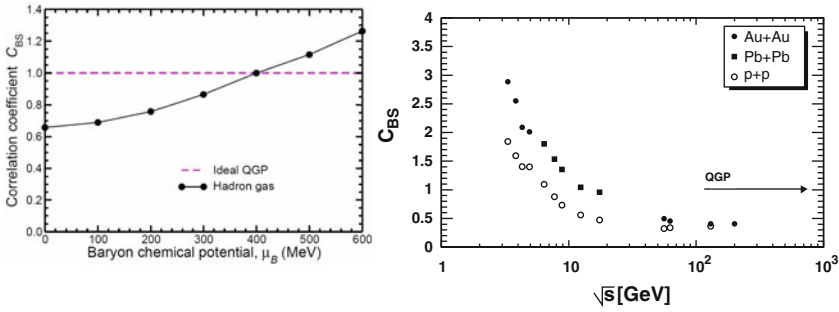


Fig. 9.6 *Left panel:* The correlation coefficient C_{BS} for a hadron gas along the empirical chemical freeze out line as determined in [20] (*full line*). The *dashed line* corresponds to an ideal quark-gluon plasma. The figure is from [441]. *Right panel:* The excitation function of the correlation coefficient C_{BS} for central Au+Au (Pb+Pb) (*full symbols*) and minimum bias $p + p$ collisions (*open symbols*) calculated within the UrQMD model. The maximum rapidity accepted is $y_{max} = 0.5$ (figure taken from [442]).

The right panel of Fig. 9.6 depicts the predicted energy excitation function of C_{BS} in both $p+p$ and central Au+Au (Pb+Pb) collisions as calculated in the UrQMD model [442]. As shown in the left panel, C_{BS} increases with increasing baryon chemical potential μ_B which is the case when going to lower beam energies. With increasing collision energy, and therefore decreasing μ_B , C_{BS} decreases to $C_{BS} \approx 0.4$ at the highest RHIC energy available. Surprisingly, the general trend is the same for both $p+p$ and Au+Au (Pb+Pb). Measuring the energy dependence of C_{BS} correlation around midrapidity might therefore allow to map out the onset of QGP production.

9.6 Higher-order moments of the fluctuations

Most fluctuation measures discussed to-date can be related to quadratic variances of event-by-event observables, such as particle multiplicities, net charge, baryon number, particle ratios, or mean transverse momentum. In the vicinity of the QCD critical point, these variances are proportional to the square of the correlation length which is expected to diverge at the critical point. However, the magnitude of the correlation length is limited by the system size and by finite time effects (critical slowing down), and could be as small as 2–3 fm. Hence, the contribution to the fluctuations from the critical point might be too weak as to be discovered experimentally, if only the second moments are measured. Therefore, it has been proposed to measure higher, non-Gaussian moments of the fluctuations which are expected to be much more sensitive to the critical point [443]. For example, it has been estimated that the third and fourth moment (“skewness” and “kurtosis”) of the event-wise measured pion and proton multiplicity distribution are proportional to

the 4th–5th and 7th power of the correlation length [443]. Thus if the correlation length increases only by 10% in the vicinity of the critical point, one should see an enhancement by a factor of two in the fourth order cumulant, whereas the second order cumulant, i.e. the fluctuations, would only increase by 20%.

For example, the ratio of the fourth order susceptibility (kurtosis) over the second order susceptibility for baryon number

$$R_{4,2}^B \equiv \frac{\chi_B^{(4)}}{\chi_B^{(2)}} \quad (9.23)$$

has been determined by lattice QCD calculations with three flavors and almost physical light quark masses [444]. The result is shown in Fig. 9.7. The full line indicates the estimate for a hadron gas (labelled “HRG”) at low temperatures, and the limit of non-interacting quarks at high temperatures (labelled “SB”). The peak close to the transition temperature softens considerably when going to smaller lattice spacings, i.e. from $N_\tau = 4$ to $N_\tau = 6$.

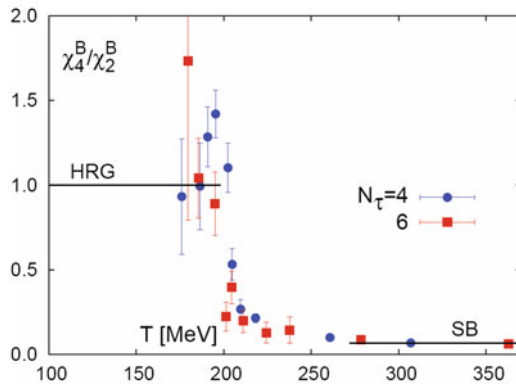


Fig. 9.7 Ratio of fourth order to second susceptibilities for baryon number. The line at low temperature, labelled “HRG” indicates the results for a hadron gas. The limit of free quarks is shown on the right and denoted by “SB” (figure taken from [444]).

The results shown in Fig. 9.7 can be easily understood in terms of hadrons on the low temperature side and independent quarks on the high temperature side. Consider a classical ideal gas of particles with baryon number b . Then we have

$$\chi_B^{(2)} = b^2 \left(\chi_N^{(2)} + \chi_{\bar{N}}^{(2)} \right) \quad (9.24)$$

$$\chi_B^{(4)} = b^4 \left(\chi_N^{(4)} + \chi_{\bar{N}}^{(4)} \right) \quad (9.25)$$

where $\chi_N^{(2)}$ and $\chi_{\bar{N}}^{(2)}$ are the particle-number cumulants for particles and anti-particles, respectively.

$$\chi_N^{(2)} = \langle N^2 \rangle - \langle N \rangle^2 = \langle N \rangle \quad (9.26)$$

$$\chi_N^{(4)} = \langle N^4 \rangle - 3\langle N \rangle^2 = \langle N \rangle \quad (9.27)$$

Consequently, the ratio of the cumulants is $R_{4,2}^B = b^2$, and since all baryons in the hadronic phase have baryon number $|B_{hadronic}| = 1$ and all quarks have baryon number $|B_{quark}| = 1/3$ the final result is $R_{4,2}^B = 1$ for the hadronic phase and $R_{4,2}^B = 1/9$ for the quark-Gluon Plasma. Since baryons are fermions, one would have to correct the above result for quantum statistics. In case of massless particles this can be done analytically and one would have to multiply the results by a factor of $6/\pi^2 \simeq 0.6$. The effect of quantum statistics for the massive baryons in the hadronic phase can only be evaluated numerically and for baryons with mass $M = 1 \text{ GeV}$ and a temperature of $T = 170 \text{ MeV}$ the correction is less than 1%. The results of this simple estimate are also shown in Fig. 9.7 as the full lines at low (hadron gas) and high (QGP) temperatures.

According to Fig. 9.7 the system is well described by a gas of independent quarks above $\sim 1.5T_c$. If the calculation with $N_\tau = 6$ is indeed close to the continuum limit, then we see a rapid change from hadrons to independent quarks, both in the flavor off-diagonal susceptibilities as well as in the fourth order baryon number cumulants. This would lend theoretical support of the rather surprising finding of the so-called quark number scaling at RHIC which can be simply understood within a recombination/coalescence picture. In this picture hadrons are formed at T_c by simple phase-space coalescence, which is consistent with the rather rapid buildup of correlations around T_c seen in the lattice results for the susceptibilities as discussed here.

Finally, it is important to note that non-Gaussian moments of the fluctuations like skewness and kurtosis may receive contributions from other sources like remnants of initial fluctuations, flow, and jets – to name just a few obvious contributors. The experimental challenge will be to identify and evaluate these background contributions, and to extract the genuine critical point effect.

9.7 Fluctuations of the mean transverse momentum

Event-by-event fluctuations of the mean transverse momentum p_t have been discussed in the literature as a measure of energy fluctuations, which should show a peak close to the QCD phase transition, where the specific heat has a maximum [445]. Transverse momentum fluctuations have also been discussed in the context of a search for the QCD critical point where one expects long range fluctuations which would result in enhanced transverse momentum

fluctuations, especially for small momenta [446]. The signature in this case would be a maximum in the excitation function of p_t -fluctuations at the energy corresponding to the location of the critical point.

Experimentally, p_t -fluctuations have been investigated by the CERES collaboration [447], the NA49 collaboration [448, 449] at the CERN SPS and by the STAR [450], and the PHENIX [451, 452] collaborations at RHIC. These measurements cover a wide range of beam energies. The resulting p_t -fluctuations are shown in Fig. 9.8 They are small and show virtually no beam-energy dependence.

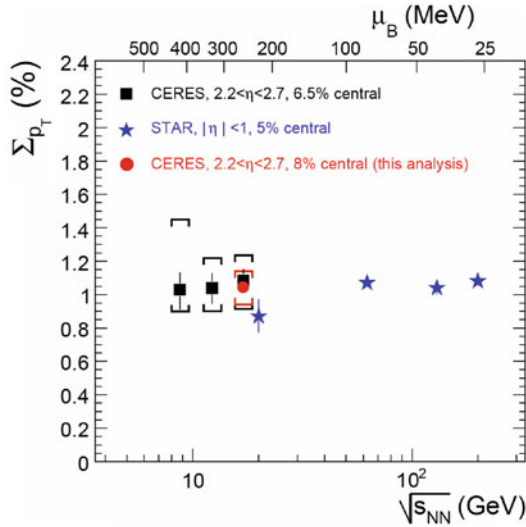


Fig. 9.8 Transverse momentum fluctuations for different center of mass energies. Here $\Sigma_{p_T} = \sigma_{\text{dynamical}}$ (the figure is adapted from [453]).

In addition to the transverse momentum fluctuations for all charged particles, one can investigate the p_t fluctuations of the negative and positive charges independently as well as the cross correlation between them. This aspect is discussed in detail in [454]. Such an excitation function has been measured by the NA49 collaboration, and it is shown in Fig. 9.9 for different charge combinations and different cuts on the transverse momentum [455]. Critical fluctuations, corrected for critical slowing down and expansion of the system, would lead to a bump which should be at least a factor of two larger than the statistical background [456]. Obviously, the data shown in Fig. 9.9 do not show such a behavior, even for small transverse momenta. The results at RHIC [43], shown in Fig. 9.8, are consistent with the data from SPS. Hence, so far there is no indication of a critical point in the transverse momentum fluctuation measurements. Of course it could be that the signal is too weak to be seen and it may also be washed out by subsequent

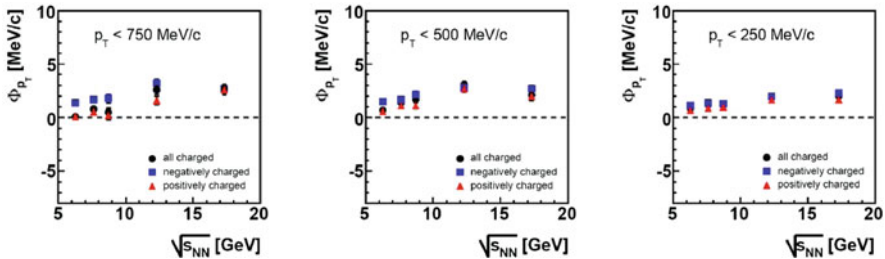


Fig. 9.9 Preliminary data on the energy dependence of p_t fluctuations from the NA49 collaboration [455] for all charged particles and for positively and negatively charged particles. The panels show the fluctuations for different cuts in the transverse momentum (the figure is adapted from [455]).

hadronic interactions. To address this issue, higher cumulants, as discussed above, need to be measured as they should show a stronger enhancement close to the critical point. Furthermore, on the theoretical side, one needs to get a better understanding of the degradation of the proposed signals in the hadronic phase.

9.8 Observable consequences of a first-order transition

The presence of a first-order phase transition may, if the bulk of the system can be brought into the associated spinodal region, cause a clumping to develop. We discuss here how such a phenomenon may have observable consequences that could form the basis for an experimental investigation of the phase structure of strongly interacting matter. However, it is important to recognize that our quantitative understanding of the equation of state and the collision dynamics is still only rudimentary. Therefore, the development of practical experimental signals requires more precise calculations of the equation of state in the relevant baryon-rich environments, to better locate the expected phase coexistence region. Furthermore, refined calculations of the collision dynamics are needed to help ascertain whether the spinodal region is in fact likely to be encountered and, if so, to what degree the phase decomposition may actually develop and lead to signals that survive the further expansion dynamics. The discussion below should therefore be regarded as only qualitative.

Moreover, it should be emphasized that the hadrons considered have not (yet) been propagated from their creation through the expanding hadronic-gas stage until no further interactions or decay processes occur. Such “afterburner” simulations could be carried out with fairly good confidence by existing hadronic transport codes.

9.8.1 Kinematic observables

The development of clumping may affect the final momenta of the resulting hadrons. The discussion below is based on the schematic studies made in [457], which addressed scenarios where the expanding system has (somehow) transformed itself into an assembly of plasma “blobs” that proceed to hadronize separately. These blobs are formed at different locations in space and the local flow velocities will differ correspondingly. Thus, blobs formed at different longitudinal locations will tend to move with different rapidities and they may also be endowed with a transverse motion reflecting their transverse location.

In order to facilitate illustrative calculations, it is assumed that these blobs hadronize statistically, with the emerging hadrons being boosted by the flow velocity of the mother blob. Since the thermal velocity of the hadrons will tend to wash out the clumped structure of the multi-blob source, it is advantageous to consider relatively heavy hadrons. Thus pions are unsuitable, while protons, which are relatively abundant, may be preferable. For any type of hadron considered, it is then elementary to calculate the resulting single-particle spectrum and the projected rapidity distribution of protons. The studies in [457] suggest that it will generally be difficult to discern the clumpiness of the source from single-particle observables. One may thus expect that correlation observables need to be considered.

Various candidate correlation observables were introduced and analyzed in [457], as briefly summarized below. A relatively simple correlation observable that exhibits a sensitivity to a clumping of the source is the distribution of the rapidity difference between two hadrons, $y_{12} \equiv y_1 - y_2$. As one would expect, the resulting distribution, $P_{1D}(y_{12})$, when divided by the corresponding mixed-event result, $P_{1D}^{\text{mix}}(y_{12})$, exhibits a peak at $y_{12} = 0$, with a width reflecting the thermal width of a single source (see Fig. 9.10, left).

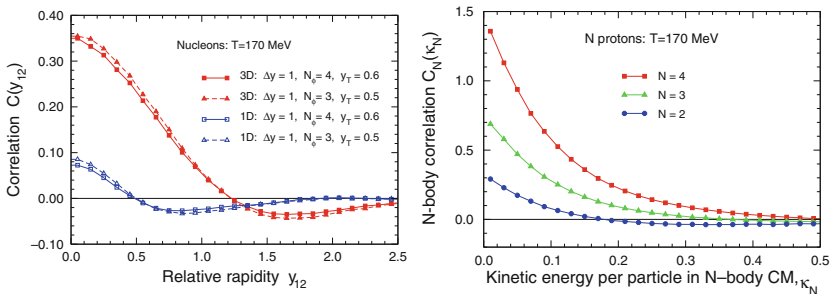


Fig. 9.10 *Left:* The reduced 1D and 3D rapidity correlation functions for the standard clumping scenario having $N_\phi = 4$ (see text) or a modified scenario using $N_\phi = 3$ with the transverse flow reduced to $y_T = 0.5$ in order to approximately preserve the recession speed between neighboring sources. *Right:* The corresponding relative distribution of the internal kinetic energy per particle, κ_N , for $N = 2, 3, 4$ protons in the same standard clumping scenario (from [457]).

When the individual sources are endowed with transverse flow motion as one would usually expect, one may obtain a stronger signal by generalizing the relative rapidity to three dimensions and thus consider

$$y_{12}(p_1, p_2) \equiv \ln[\gamma_{12} + \sqrt{\gamma_{12}^2 - 1}] , \quad (9.28)$$

where γ_{12} is the Lorentz factor for the relative motion of the two observed hadrons, $m_1 m_2 \gamma_{12} = p_1 \cdot p_2 = E_1 E_2 - \mathbf{p}_1 \cdot \mathbf{p}_2$. The resulting correlation function, $C_{3D}(y_{12}) \equiv P_{3D}(y_{12})/P_{3D}^{\text{mix}}(y_{12}) - 1$ is shown in Fig. 9.10, left for a number of scenarios considered in Ref. [457]. While the detailed behavior of the correlation function depends on the particular clumping scenario, the enhancement around zero remains a rather robust feature, thus suggesting that this kind of observable may be useful.

The relative-rapidity observables have been examined in a number of schematic scenarios that incorporate some degree of transverse flow in addition to the overall longitudinal expansion. For this purpose, ensembles of source configurations are generated by making random variations relative to suitable scaffold configurations of individual thermal sources in rapidity space. A scaffold configuration consists of sources situated at the vertices of N_ϕ -sided equilateral polygons (e.g. squares) that are oriented perpendicular to the z axis and placed with regular spacings Δy in longitudinal rapidity. (The (mean) azimuthal separation between two neighboring scaffold sources in a given polygon is thus $\Delta\phi = 2\pi/N_\phi$ and each polygon is rotated by half that amount relative to its neighbors.) On the average, each individual thermal source emits the same number of particles $\bar{\nu}_n$, and the magnitude of its transverse flow rapidity is y_T . The mean rapidity density is thus $d\bar{\nu}/dy = N_\phi \bar{\nu}_n / \Delta y$. Relative to the scaffold configuration, the actual velocity of each source n is obtained by adding a random deviation with regard to both its longitudinal rapidity and its transverse flow vector, as well as to the number of particles emitted.

As a standard illustrative scenario, let us take the polygons to be squares (i.e. $N_\phi = 4$) that are placed with rapidity separations of $\Delta y = 1$ and whose corners are endowed with a transverse flow rapidity of $y_T = 0.6$. It then follows that the relative rapidity between two neighboring sources in the same polygon is approximately the same as that between neighboring sources in adjacent polygons (namely ≈ 1.20). Relative to this scaffold configuration, the actual number of protons emitted by a given source is governed by the corresponding Poisson distribution, and the dispersion of the longitudinal rapidity of a given source, σ_\parallel , as well as the dispersion of its transverse flow rapidity, σ_\perp , are taken to be 0.3.

The sensitivity to a clumping structure of the source can generally be enhanced by considering correlations of ever higher order. A particularly simple N -body observable is the invariant mass of the detected N hadrons [457]. Specifically, in each particular event, one may extract the kinetic energy per particle in the CM system of the observed N -particle system,

$$\kappa_N\{p_n\} \equiv \frac{1}{N} \left[\left[\left(\sum_{n=1}^N E_n \right)^2 - \left(\sum_{n=1}^N \mathbf{p}_n \right)^2 \right]^{\frac{1}{2}} - \sum_{n=1}^N m_n \right], \quad (9.29)$$

where the N observed particles have four-momenta $\{p_n = (E_n, \mathbf{p}_n)\}$, with $E_n^2 = \mathbf{p}_n^2 + m_n^2$. The motivation for considering this observable is the expectation that when the N -body momentum distribution is clumped, the sampling of κ_N will yield an enhancement around the typical (i.e. thermal) kinetic energy in the individual source, relative to what would occur for a structure-less distribution. In order to bring out this signal, we compare the correlated distribution $P_N(\kappa)$, obtained by sampling all the N particles from the same event, with the corresponding uncorrelated distribution $P_N^{\text{mix}}(\kappa)$ obtained by sampling the N particles from N different events. This yields the reduced correlation function for the internal kinetic energy, $C_N(\kappa) \equiv P_N(\kappa)/P_N^{\text{mix}}(\kappa) - 1$. The result is illustrated in Fig. 9.10, right for $N = 2, 3, 4$ protons. The correlation signal grows more prominent as the correlation order N is increased (its strength approximately doubles for each “detector” added), as expected because it becomes increasingly unlikely that N momenta sampled from a structure-less distribution would all be nearly similar. This feature is the reason why higher-order correlations may be advantageous.

However, generally, the correlation signal receives its support from a relatively small region of the N -body phase space and the required counting statistics therefore increases factorially with N , thus presenting a practical limit to the order of correlation that can be addressed with a given set of data. However, the information conveyed by the higher-order correlations is progressively more effective as a discriminator between various possible underlying dynamical mechanisms.

9.8.2 Chemical observables

We turn now to the effect of a dynamical clumping on the abundances of the various hadron species and, following [223], we specifically consider the distribution of strangeness. The basic picture is as follows: If the clumping is sufficiently rapid, then whatever net strangeness happens to reside within the region of the plasma that forms a given blob will effectively become trapped within that blob and, consequently, the resulting hadronization of the blob will be subject to a corresponding constraint on the net strangeness. Such a canonical constraint will enhance the multiplicity of strangeness-carrying hadrons, relative to the conventional (grand-canonical) scenario where global chemical equilibrium is maintained through the hadronic freeze-out. [The enhancement is qualitatively easy to understand, since a non-zero amount of strangeness in the hadronizing blob enforces the production of a corresponding minimum number of strange hadrons.] The fluctuations in the multiplicity

of strange hadrons, such as kaons, are enhanced even more, thus offering a possible means for the experimental exploration of the phenomenon.

Of particular interest is the ratio between the number of kaons and the number of pions in a given event. When μ_B is positive there is a preference for K^+ over K^- and hence $\langle K^+/\pi^+ \rangle$ will increase while $\langle K^-/\pi^- \rangle$ decreases. This dependence of the average ratios on the chemical potential is practically linear, because although an increase of the freeze-out value of μ_B implies a decrease in the corresponding freeze-out value of the temperature, the suppression from the decreasing temperature affects all hadrons species. However, the effect of the canonical constraint is rather small for the ratio averages. Furthermore, since there is a (small) tendency for the π and K multiplicities to vary in concert, the difference between the scenarios is further reduced. In particular, there is hardly any difference to be seen for $\langle K^-/\pi^- \rangle$.

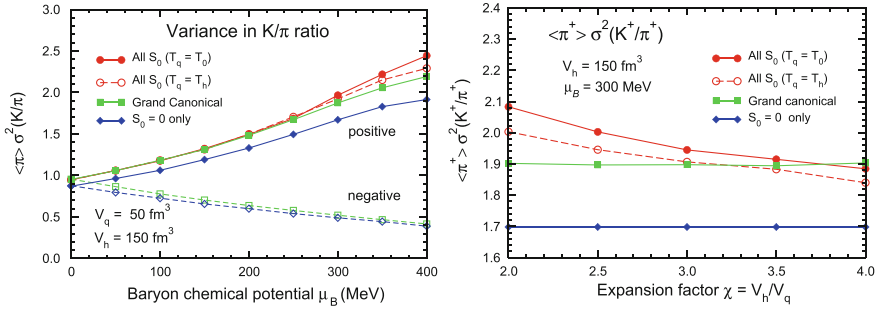


Fig. 9.11 The variance in the K/π ratio (multiplied by the average pion multiplicity to make the result size invariant) for either positive (increasing) or negative charges (decreasing) as a function of the baryon chemical potential μ_B for an expansion factor of $\chi \equiv V_h/V_q = 3$ (l.h.s.) and as a function of χ for $\mu_B = 300$ MeV (r.h.s.) (from [223]).

The situation is more favorable for the corresponding fluctuations, as shown in Fig. 9.11, left. Since the variance of the K/π ratio decreases in inverse proportion to the size of the system, it is convenient to multiply by the mean pion multiplicity and thus consider a quantity that approaches a constant for large volumes, $\langle \pi^\pm \rangle \sigma^2(K^\pm/\pi^\pm)$. The resulting ratio variances for the positively charged hadrons are qualitatively similar to the ratio averages $\langle K^\pm/\pi^\pm \rangle$. But although the variances in the ratios are less sensitive to the specific scenario than the kaon variances themselves, the differences are still clearly brought out, as seen in Fig. 9.11, left. Furthermore, if the clumping occurs at a higher temperature than assumed here, the fluctuation in the blob strangeness would increase and, as a result, the ratio variances would be larger. The fluctuations in the K^+/π^+ ratio may thus offer a suitable observable that is sensitive to a clumping-induced trapping of strangeness in the expanding matter prior to the hadronization.

The above results were obtained for a given value of the expansion factor, the relative increase in the volume from the time of the blob formation to the thermal freeze-out, $\chi \equiv V_h/V_q = 3$. Since the results are sensitive to this yet poorly known quantity, it is of interest to consider also other values of χ . This aspect is illustrated in Fig. 9.11, right, where the variance of the K^+/π^+ ratio is shown as a function of χ for $\mu_B = 300$ MeV.

It is easy to see that $\langle \pi^+ \rangle \sigma^2(K^+/\pi^\pm)$ is a decreasing function of χ , though this dependence is not dramatic: a doubling of χ from 2 to 4 reduces the variance by less than 10%. Thus the results in the left panel are fairly robust against changes in χ .

Thus, the studies made in [223] suggest that a spinodal decomposition might indeed lead to enhancements of the magnitude observed by NA49. However, before any statements could be made with confidence, further studies would be required. In particular, both strong resonance decays and weak decays should be taken into account. Moreover, the enhancement of the K/π fluctuations should be correlated with other expected effects, such as N -body kinematic correlations (such as those studied in [457] and discussed above or those put forward by Mishustin in [458]).

9.9 Observable consequences of a critical end point

The above discussion addresses the challenge of identifying signals of a first-order phase transition, focussing on the fact that bulk matter is unstable inside the associated spinodal region. A complementary approach is to explore signals of the critical endpoint. Below we critically review an example of the latter, recently suggested by Asakawa et al. [459].

The work of Asakawa et al. is based on the idea that the presence of a critical end point may distort the expansion trajectories in the $\mu - T$ plane, resulting in a focussing towards the end point in the cross over region. Such a focussing effect was first suggested by Nonaka and Asakawa [177], who considered an isentropic fluid dynamical expansion for various equations of state. As illustrated in the left panel of Fig. 9.12, slightly supercritical trajectories may exhibit a local deflection towards the critical end point.

Such a modification of the expansion trajectory may lead to observable effects in the hadron spectra. For a given (observed) freeze-out condition, a system which follows a distorted trajectory has experienced a different thermodynamical environment, than a reference system, where the expansion trajectory smoothly cuts across the transition region, as illustrated in the right panel of Fig. 9.12. A distorted trajectory passing near the critical end point, has experienced an environment of higher entropy per baryon than in the reference case. As a consequence, hadron abundances may differ.

In particular, in [459] it is suggested that the expected modification of the transverse rapidity dependence of the \bar{p}/p ratio may be observable. Since fast

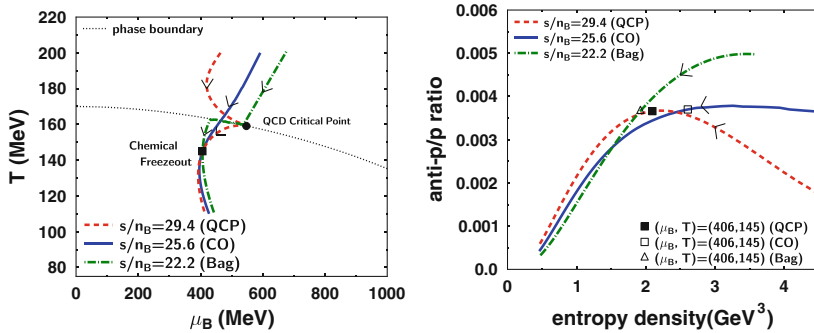


Fig. 9.12 *Left:* Isentropic ideal-fluid trajectories in the $\mu - T$ phase plane. Trajectories in the absence of a critical end point are shown for a crossover phase transformation (solid line) and a first-order phase transition (dash-dotted line). The dashed line shows the trajectory when the critical point is present. *Right:* The \bar{p}/p ratio along the phase trajectories shown in the left panel, as a function of the evolving entropy density [459].

hadrons (those having a high transverse rapidity) are emitted earlier, they would be more sensitive to the bending of the trajectories near the critical end point. Consequently, for an expansion trajectory, which passes close to the critical end point, the \bar{p}/p ratio would *fall* with increasing transverse rapidity rather than rise or stay constant, as would otherwise be expected. (For instance, UrQMD, which does not describe the QCD phase transition, yields a steady increase of the \bar{p}/p ratio with y_T .) The transverse rapidity is particularly well suited for exhibiting this effect, since it readily permits the observer to distinguish between fast and slow baryons.

We conclude this section with a critical assessment of the robustness of this effect. In [177] it was argued that the focussing of the isentropic trajectories is a universal property. Hence, all systems with a critical end point in the same universality class as the three-dimensional Ising model, in particular hot and dense QCD matter, would exhibit focussing near the critical end point. However, this conclusion was recently challenged in the work of [178], where the isentropic trajectories were explored in a renormalization group approach applied to a model of the same universality class, the quark-meson model. These authors find smooth isentropic trajectories also near the critical end point. They point out that while the critical behaviour at the critical end point is universal, this does not mean that the focussing effect is also universal. The point is that the entropy per baryon does not diverge at the critical end point. Hence, the appearance of the focussing effect depends on the competition between the singular but finite contribution to the entropy per baryon, which is universal, to the background, which is model dependent. Consequently, it is not impossible that in QCD the singular part dominates over the background and the isentropic trajectories are focussed towards the critical endpoint, as suggested in [177]. On the other hand, the isentropic trajectories in QCD matter may well be smooth, just like in the quark meson

model. As noted above, universality arguments are not useful for addressing this particular problem; this issue can only be settled by studying QCD, e.g. in lattice gauge theory.

9.10 Summary and concluding remarks

As far as observables are concerned we have discussed electric charge fluctuations, transverse momentum fluctuations, and the fluctuations of the kaon-to-pion ratio. All these have been measured over a wide range of beam energies, from the CERN SPS to RHIC, and none of the excitation functions, with the possible exception of the kaon-to-pion ratio, show any significant beam energy dependence. In the case of the event-by-event fluctuation of the kaon-to-pion ratio a rapid rise towards the lowest energies is observed, which may or may not be due to simple scaling of the observable with the acceptance. If the observed rise is real, then this may very well be the first hint for some non-trivial phase structure probed at these lowest energies.

Concerning the QCD critical point there is only limited theoretical guidance clarifying the relevant beam-energy range for an experimental search. The model predictions for its location in the phase diagram vary quite a bit. Employing the proposed strategies the present data set does not provide any hint for the critical point's location in the region probed so far. The transverse momentum fluctuations do not show any non-monotonic behavior, as originally predicted. However, it could very well be that the signal is too weak, as there is not sufficient time to develop a large correlation length in these finite size systems. Therefore, it is imperative to measure the higher cumulants as well. For example, the fourth order cumulant scales like the seventh power of the correlation length, whereas the second order, which controls the transverse momentum fluctuations, only scales like the square of the correlation length [443].

It is important to note that a first-order phase-coexistence region might be much easier to detect than the critical point. Both phenomena are equally important for our understanding of the QCD phase diagram. The first-order phase transition corresponds to a large region in the $T - \rho$ phase diagram, and the system most probably spends sufficient time in this region to develop measurable signals. Moreover, fluctuations caused by spinodal instabilities [460] – which are a generic phenomenon of first-order phase transitions – may be much less suppressed by the finite size and the short lifetime of the system, as compared to critical fluctuations. Spinodal instabilities have been studied and successfully identified in the context of the nuclear liquid-gas phase transition [461]. In the case of the QCD first-order transition, spinodal instabilities could lead to kinematic correlations among particles [457] and to enhanced fluctuations of strangeness [223]. And indeed the observed enhancement of the kaon-to-pion fluctuations may be due to these enhanced

fluctuations in the strangeness sector [223]. Therefore, the search for kinematical and chemical observables which reflect the clumping of the system in the coexistence region is a promising experimental task.

Nevertheless, one should keep in mind that the fluctuations and correlations induced by the critical point or by a phase transition may be masked by other effects like impact parameter (or volume) fluctuations, and correlations due to collective flow. Moreover, the signals may be severely degraded by subsequent hadronic processes such as rescattering and resonance interactions and decays. Therefore, the hadronic effects and the background sources should be carefully studied in transport simulations in order to correct the measurements for, and to reveal the primordial information. However, the existing transport codes need further development before they can reliably treat scenarios where a phase transition is present. This presents several distinct challenges, particularly the following three: (1) The development of a realistic equation of state that displays the expected phase structure with a first-order phase transition and an associated critical end point at a finite chemical potential. (2) The ability to describe the change in the active degrees of freedom as the system enters and leaves the deconfined phase region. (3) The proper dynamical evolution of the system as it encounters the thermodynamic and mechanical instabilities associated with the presence of a phase transition, in particular the growth and further development of the correlated fluctuations that ultimately form the basis for observable signals.

Although in the case of heavy-ion collisions one observes correlations in momenta rather than in space, the situation may be quite similar. To first order thermal spectra and radial flow are measured. Next, one observes a large quadrupole correlation due to elliptic flow. The interesting question then remains whether it will be possible to identify smaller correlations due to a phase transition and the QCD critical point after subtracting the two dominant backgrounds, namely thermal emission and elliptic flow.

Chapter 10

Dibaryons, hypernuclei and strange nuclear systems at FAIR

Massive heavy-ion reactions provide an abundant source of strangeness. More than 50 hyperons and about 30 Anti-Kaons (i.e. $K^- + \overline{K^0}$ carrying the strange quark) are produced in a single central collisions of lead nuclei at the CERN-SPS low energy program and before that at the AGS (see e.g. [462]). In the near future, the Facility for Anti-proton and Ion Research (FAIR) will start to investigate this energy regime closer with much higher luminosity and state-of-the-art detector technology. This opens the exciting perspective to explore the formation of composite objects with multiple units of strangeness so far not achievable with conventional methods.

Exotic forms of deeply bound objects with strangeness have been proposed long ago (see [463]) as collapsed states of matter, either consisting of baryons or quarks. For example the H di-baryon (a six quark state) was predicted by Jaffe [464]. Later a multitude of bound di-baryon states with strangeness were proposed using quark potentials [465, 466] or the Skyrme model [467]. However, the (non-)observation of multi-quark bags, e.g. strangelets and (strange) di-baryons is still one of the open problems of intermediate and high energy physics. Most noteworthy in this respect has been the hunt for the Pentaquark over the last 10 years, which re-stimulated this field and resulted in a reported observation at the CERN SPS accelerator [468].

The early theoretical models based on SU(3) and SU(6) symmetries [469, 470] and on Regge theory [471, 472] suggest that di-baryons should exist. More recently, even QCD-inspired models predict di-baryons with strangeness $S = 0, -1$, and -2 . The invariant masses range between 2 and 3 GeV [464, 473–479]. Unfortunately, masses and widths of the expected 6-quark states differ considerably for these models. Nevertheless, most QCD-inspired models predict di-baryons and none seems to forbid them.

On the conventional hadronic side, however, hypernuclei are known to exist already for a long time [480, 481]. The double Λ hypernuclear events reported so far are closely related to the H di-baryon [482] and recent simulations of the strongly attractive $\Lambda\Xi$ interaction suggest that the ${}_{\Lambda\Xi}^6\text{He}$ hypernuclei marks the onset of nuclear stability for Ξ hyperons [483]. Metastable exotic

multi-hypernuclear objects (MEMOs) as well as purely hyperonic systems of Λ 's and Ξ 's were introduced in [484, 485] as the hadronic counterparts to multi-strange quark bags (strangelets) [486, 487]. The Nijmegen soft-core potential was extended to the full baryon octet and bound states of $\Sigma\Sigma$, $\Sigma\Xi$, and $\Xi\Xi$ di-baryons were predicted [488]. In addition it has been shown that the hyperon-hyperon binding energy in bulk matter is considerably enhanced [489].

There are several searches in heavy-ion collisions for the H -dibaryon [490–492] and for long-lived strangelets [493, 494] with high sensitivities. The hypernuclei ${}^3_\Lambda\text{H}$ and ${}^4_\Lambda\text{H}$ have been detected in heavy-ion reactions at the AGS by the E864 collaboration [495, 496]. The invariant yields of the hypernuclei were determined, by the invariant mass reconstruction of decay products (${}^3_\Lambda\text{H} \rightarrow \pi^- + {}^3\text{He}$ and ${}^4_\Lambda\text{H} \rightarrow \pi^- + {}^4\text{He}$), to be of the order of 10^{-4} per event.

A major uncertainty for the detection of such speculative states is their (meta)stability. Metastable exotic multi-hypernuclear objects (MEMOs), for example, consist of nucleons, Λ 's, and Ξ and are stabilised due to Pauli's principle, blocking the decay of the hyperons into nucleons. The presented MEMO candidates are expected to possess binding energies up to $E_B/A_B \approx -22$ MeV [487] due to attractive hyperon-hyperon interactions.

Only few investigations about the weak decay of di-baryons exist so far: In [497], the H -di-baryon was found to decay dominantly by $H \rightarrow \Sigma^- + p$ for moderate binding energies. While the $(\Lambda\Lambda)$ bound state, which has exactly the same quantum numbers as the H -di-baryon, was studied in [498]. Here, the main non-mesonic channel was found to be $(\Lambda\Lambda) \rightarrow \Lambda + n$. If the life time of the $(\Lambda\Lambda)$ correlation or H^0 particle is not too long, the specific decay channels might be used to distinguish between both states.

For a detection in heavy-ion experiments one is mainly interested in candidates whose final decay products are charged: as

$$\begin{aligned} (\Sigma^+ p)_b &\rightarrow p + p \\ (\Xi^0 p)_b &\rightarrow p + \Lambda \\ (\Xi^0 \Lambda)_b &\rightarrow p + \Xi^- \text{ or } \Lambda + \Lambda \\ (\Xi^0 \Xi^-)_b &\rightarrow \Xi^- + \Lambda \end{aligned}$$

It has been shown that the decay lengths for all of the above strange dibaryons is between $c\tau \approx 1 - 5$ cm [478].

$(\Sigma^+ p)_b$: There is only one non-mesonic decay channel for $(\Sigma p)_b \rightarrow p + p$ dominant above 5 MeV binding energy. The dibaryon should show up in the invariant pp mass spectrum after background subtraction from event-mixing at $M = 2.128 \text{ GeV} - \epsilon$ where ϵ is the binding energy. With this method the weak decay of the lightest hypernucleus ${}^3_\Lambda\text{H} \rightarrow {}^3\text{He} + \pi^-$ has been detected in heavy-ion collisions by the E864 collaboration [495].

$(\Xi^0 p)_b$: For the $(\Xi^0 p)_b$ bound state only one mesonic but three different non-mesonic channels contribute. The dominant non-mesonic decay turns out to be $(\Xi^0 p)_b \rightarrow \Lambda + p$ already for a binding energy of 2 MeV or more. The decay itself resembles the one for the weak decay of the Ξ^- or Ω^- ,

which have already been detected by several experiments (see contributions in [462]). Instead of an outgoing π^- or K^- there is a proton leaving the first weak vertex.

$(\Xi^0 p)_b$: The dibaryon $(\Xi^0 \Lambda)_b$ decays to $\Xi^- + p$ and, with a small fraction, to two Λ 's. Therefore, it can be seen in $\Xi^- p$ or $\Lambda\Lambda$ invariant mass plots.

$(\Xi^0 \Xi^-)_b$: The $(\Xi^0 \Xi^-)_b$ dibaryon has been predicted to be bound [488] and its decay to $\Xi^- + \Lambda$ has a branching ratio of a few percent.

Another way of identifying possible MEMO candidates is by directly observing their decay systematics (i.e. a charged particle decaying in two equally charged particles, a strong 'kink' in the track of a charged particle or two charged particles created from nowhere). See [479] for a full discussion and new estimates for the weak nonleptonic decays of strange di-baryons.

The production rate of multi-strange objects has been studied within the UrQMD model (v2.3) [124, 499] and a micro+macro hybrid approach [124, 499–501] to heavy ion reactions, as well as in a thermal model [26]. In the hybrid model, a full (3+1) dimensional ideal hydrodynamic evolution is performed using the SHASTA algorithm [502, 503]. An equation of state for a free hadron gas without any phase transition is used [504]. The EoS includes all hadronic degrees of freedom with masses up to 2 GeV, which is consistent with the effective degrees of freedom present in the UrQMD model. The mass of a MEMO was assumed to be the sum of the masses of all hadrons it is composed of. Similarly the total chemical potential is the sum of the constituents, and is composed of baryon and strange-quark chemical potentials μ_B and μ_s . Table 10.1 gives the properties of all multibaryonic states considered in this analysis.

Figure 10.1, left provides the total multiplicities per degeneracy factor of various types of MEMOs and strangelets in central Pb+Pb reactions at $E_{\text{lab}} = 30$ AGeV. The yields obtained are in good agreement to the statistical model analysis [505], which is describing strange cluster production at AGS energies.

Table 10.1 Properties of light multibaryonic states with strangeness.

Cluster	Mass [GeV]	Quark content	Cluster	Mass [GeV]	Quark content
H^0	2.020	$4q + 2s$	$\{2\Xi^-, 2\Xi^0\}$	5.268	$4q + 8s$
$\{\Xi^-, \Xi^0\}$	2.634	$2q + 4s$	${}^6_{\Lambda\Lambda}\text{He}$	5.982	$16q + 2s$
${}^4\text{He}$	3.750	$12q$	$\alpha_q\{6\Lambda\}$	6.060	$12q + 6s$
${}^4_{\Lambda\Lambda}\text{H}$	4.206	$10q + 2s$	${}^6_{\Lambda\Xi}\text{He}$	6.183	$15q + 3s$
$\{4\Lambda\}$	4.464	$8q + 4s$	$\{2n, 2\Lambda, 2\Xi^-\}$	6.742	$12q + 6s$
$\{2\Lambda, 2\Sigma^-\}$	4.610	$8q + 4s$	${}^7_{\Xi^0\Lambda\Lambda}\text{He}$	7.297	$16q + 2s$
${}^5_\Lambda\text{He}$	4.866	$14q + 1s$	$\{2\Lambda, 2\Xi^0, 2\Xi^-\}$	7.500	$8q + 10s$
$\{2\Lambda, 2\Xi^-\}$	4.866	$6q + 6s$			

Because local, as well as global, thermal equilibration are assumptions not necessarily justified in heavy ion collisions, a microcanonical description,

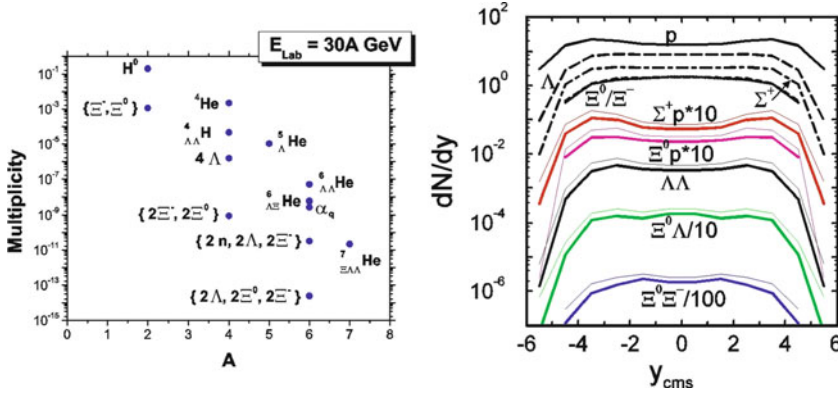


Fig. 10.1 *Left*: Multiplicities of various types of MEMOs and strangelets in central Pb+Pb reactions at $E_{\text{lab}} = 30A$ GeV from the hybrid approach. *Right*: Rapidity distribution of baryons (*upper curves*) and strange dibaryons (*lower curves*) using RQMD2.4 with wavefunction coalescence for Au+Au collisions at $\sqrt{s} = 200$ AGeV. *Upper curves* are for a binding energy of $E_b = 5$ MeV, lower ones for $E_b = 1$ MeV.

combined with MEMO production by coalescence, has been proposed. Due to the restrictions of energy and momentum conservation, resulting in a phase space reduction for produced strange particles, a (micro)canonical description of the system strongly decreases strange particle yields at the lowest energies [506, 507]. Thermal model analysis however show, that canonical corrections are negligible for all hadron species already for the highest AGS energies ($\sqrt{s_{NN}} \approx 5$ GeV) [26].

In [478] MEMO production by coalescence was investigated for RHIC energy regime ($\sqrt{s} = 200$ GeV). The obtained total yields of strange clusters are of similar magnitude compared to the hybrid model calculation. Figure 10.1, right shows the rapidity spectra for several strange dibaryons from the RQMD2.4 model with wavefunction coalescence. Another study predicted strange cluster formation at AGS energies within a simplified coalescence model [508]. Compared to data [495, 496] and thermal production [509], the production of strange clusters within this approach was overpredicted by orders of magnitude.

Investigating strange-cluster production over a range of beam energies shows a distinct maximum in the yields of several multi strange objects. Figure 10.2, left displays the excitation function of the multiplicities of various MEMOs in central Pb+Pb reactions from the hybrid approach. In the right panel of Fig. 10.2 we show a prediction within the thermal model [26] for the energy dependence of the production yield of multi-strange light hypernuclei [505]. Shown is the yield relative to that of Λ hyperons, calculated using the parametrizations for the temperature (T) and baryochemical potential (μ_b) established in [26] based on fits of midrapidity data in central collisions. The production shows a pronounced maximum in the FAIR energy regime, which

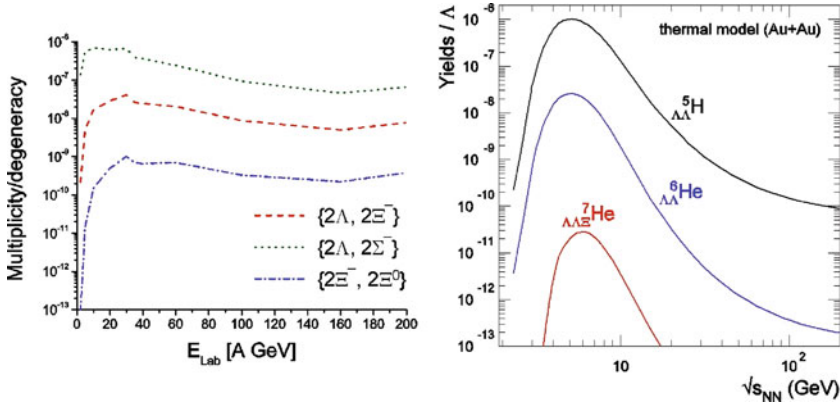


Fig. 10.2 *Left*: Excitation functions of the multiplicities of various MEMOs in central Pb+Pb reactions from the hybrid approach. *Right*: The energy dependence of multistrange Λ hypernuclei yields relative to the yields of Lambdas at midrapidity for central nucleus-nucleus collisions, calculated with the statistical model.

is the consequence of a competition between a strong increase (followed by saturation) of T and a strongly decreasing μ_b . In addition, the canonical suppression leads to reduced yields at low energies. One easily observes that the upper FAIR energy region ($\sim E_{\text{lab}} = 10 - 40$ AGeV) is ideally placed for the search of exotic multi-strange baryon clusters.

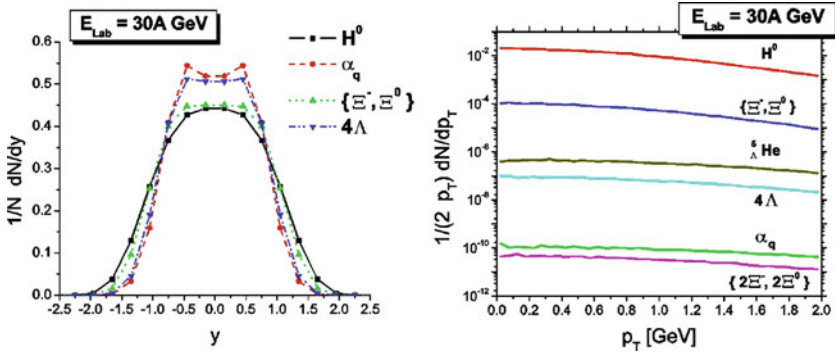


Fig. 10.3 *Left*: Normalized rapidity density of various MEMOs in central Pb+Pb reactions at $E_{\text{lab}} = 30$ AGeV from the hybrid approach. *Right*: Transverse momentum spectra at midrapidity ($|y| < 0.5$) of various MEMOs in central Pb+Pb reactions at $E_{\text{lab}} = 30$ AGeV from the hybrid approach.

Figure 10.3 shows the normalized rapidity distribution of various MEMOs in central Pb+Pb reactions at $E_{\text{lab}} = 30$ AGeV from the hybrid approach. The production of baryon rich clusters is most pronounced in the high baryon

density rapidity region. The rapidity distributions for MEMOs with a larger strangeness to baryon number fraction tend to look more gaussian like.

Figure 10.3, right depicts the transverse momentum distribution of various MEMOs at midrapidity in central Pb+Pb reactions at $E_{\text{lab}} = 30$ AGeV from the hybrid approach. The p_T spectra are rather broad as compared to usual hadrons. This is due to the large boost the MEMOs acquire due to their large mass and the fact, that they are produced predominantly in the hottest regions of the expanding system.

Another project, dedicated to the study of hypernuclei, formed out of projectile fragments from heavy ion collisions at the CBM experiment, is the HypHI project at GSI and FAIR. The secondary beams of exotic nuclei with unprecedented intensity and clarity will become available at the Super-Fragment-Separator.

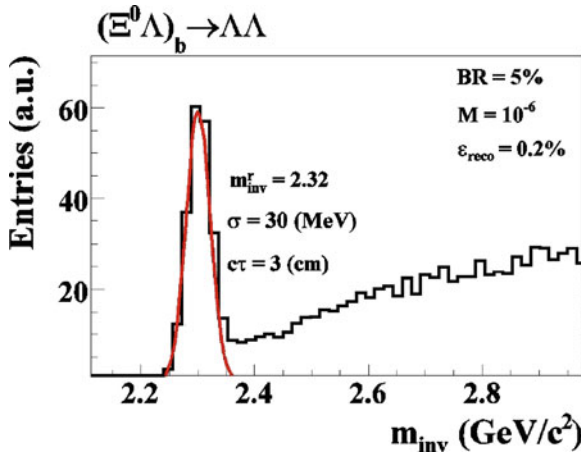


Fig. 10.4 Simulation of a possible reconstruction of a multi strange di-baryon.

In summary, the presented excitation functions for various MEMO multiplicities show a clear maximum at the upper FAIR energy regime making this facility the ideal place to study the production of these exotic forms of multi-strange objects. Detector simulations have shown that the CBM experiment is well suited for the search of exotic multihypernuclear objects either by invariant mass reconstruction of strange di-baryons (Fig. 10.4) or observation decay systematics. This opens the unique opportunity to study the evolution of nuclear structure into the yet unexplored territory of the nuclear chart and to determine the properties of many short-lived nuclei which are produced in explosive astrophysical events and crucially influence their dynamics and associated nucleosynthesis processes.

Chapter 11

Summary

The investigation of nuclear matter at extreme conditions, i.e. at high temperatures and/or at high baryon densities, is a fascinating, growing field of modern physics. Worldwide, major efforts are devoted to the exploration of the phase diagram of strongly interacting matter using high-energy nucleus-nucleus collisions. While the experiments at the Relativistic Heavy Ion Collider (RHIC) at BNL and at the future Large Hadron Collider (LHC) at CERN focus on the study of high temperatures, the experiments with high-energy heavy-ion beams at the future Facility for Antiproton and Ion Research will concentrate on the investigation of the highest baryon densities achievable in the laboratory.

The physics of high baryon densities is of elementary importance for nuclear and subnuclear physics, for astrophysics and cosmology. The fundamental theory of strong interaction, Quantum Chromodynamics (QCD) has just recently succeeded in throwing a first glance at the phase diagram of QCD matter at finite baryo-chemical potential μ_b . Lattice QCD calculations find a crossover transition at $\mu_b = 0$, but expect a critical endpoint and a first order phase transition at $\mu_b > 0$. The experimental discovery of these prominent landmarks of the QCD phase diagram would be a major breakthrough in our understanding of the physics of strongly interaction matter. Equally important is quantitative experimental information on the properties of hadrons in dense matter which may shed light on the effects of chiral symmetry restoration and the origin of hadron masses.

Several experimental programs are planned to explore the QCD phase diagram at large baryo-chemical potentials. The STAR and PHENIX collaborations at RHIC propose to scan the beam energies, and to search for the QCD critical endpoint [510]. For the same reason, future measurements are envisaged at CERN-SPS with the upgraded NA49 detector (NA61) using light and medium size beams [511]. At the Joint Institute for Nuclear Research (JINR) in Dubna, a heavy-ion collider project (NICA) is discussed with the goal to search for the coexistence phase of nuclear matter [512]. However, due to luminosity limitations these experiments are constrained to

the investigation of bulk observables. In contrast, the Compressed Baryonic Matter (CBM) experiment at the Facility for Antiproton and Ion Research (FAIR) in Darmstadt is designed for the detection of bulk and rare probes, and will benefit from the high-intensity heavy-ion beams provided by the FAIR accelerators.

The CBM experiment will enter a new era of nuclear matter research by measuring rare diagnostic probes never observed before at FAIR energies, and thus has a unique discovery potential. In order to obtain a complete picture, a comprehensive set of observables will be measured in proton-proton, proton-nucleus, and nucleus-nucleus collisions over the full FAIR energy range. The observables include:

- *Hadron yields, transverse mass spectra and rapidity distributions:* The excitation function (from 2 to 45 AGeV) of hadron yields and phase space distributions (including multi-strange hyperons) will provide information about the fireball dynamics and the nuclear matter equation of state over a wide range of baryon densities. A non-monotonic behavior of the inverse slope as function of beam energy would signal a change in the nuclear matter properties at a certain baryon density. The inverse-slope distribution as a function of particle mass is related to the particle freeze-out time, and, hence, may help to disentangle the early from the late collision stages.
- *Collective flow:* The strength of the elliptic flow v_2 measured as a function of transverse momentum for various particle species reflects the initial pressure of the system. The vanishing of directed flow at a certain beam energy would indicate a strong softening of the equation-of-state. The scaling of v_2 with the quark content of the particles may serve as indication for flow generation in a partonic phase. The onset (or the disappearance) of the scaling behavior at a certain beam energy would signal a change in the degrees-of-freedom of the matter. Of particular importance with respect to quark number scaling is the flow of ϕ mesons and Ω hyperons which are only little affected by final state interaction.
- *Open and hidden charm:* The transport properties of open charm mesons in dense matter – which depend on the interaction with the medium and, hence, on the structure of the medium – can be studied via the yields, the elliptic flow and the momentum distributions of charmed particles. In a baryon-dominated medium these observables are expected to differ for D and \bar{D} mesons. A global m_T -scaling of all mesons – in particular for strange and charmed particles – indicates in-medium modifications which may be related to effects of chiral symmetry restoration. The crossing of the phase boundary may be indicated by sudden changes of charm particle ratios such as the ψ' to (J/ψ) ratio and the J/ψ to D ratio, when measured as function of beam energy. The elliptic flow of charmonium and open charm is sensitive to the initial pressure which might be of partonic nature.
- *Dileptons:* A precise measurement of the dilepton invariant mass spectrum up to about 1 GeV provides information on the in-medium properties of the vector-meson spectral function as a signal of the chiral symmetry restora-

tion in the hot and dense matter. At higher invariant masses the spectrum contains a substantial contribution from thermal dileptons from the early partonic phase. The different origin of the dileptons is also reflected in the inverse slopes of their transverse momentum spectra. The experimental determination of dileptons emitted from the high-density phase of the collision requires the measurement (and subtraction) of contributions from very early nucleon-nucleon collision, from the dilute corona, and from post freeze-out decays.

- *Fluctuations and correlations:* Lattice calculations indicate large variations of the baryon, charge and strangeness susceptibilities in the vicinity of the QCD critical endpoint. These phenomena can be related to event-by-event fluctuations of conserved quantities such as net baryon number, net charge, and net strangeness. Fluctuations of the kaon, pion and proton multiplicities, in particular of their higher moments, measured as a function of beam energy, are expected to be sensitive indicators for the location of the critical point. A promising experimental task is the search for fluctuations and correlations caused by a first-order phase transition, focussing on the fact that bulk matter is unstable inside the associated spinodal region.
- *Exotica:* Exotic forms of deeply-bound multi-strange objects have been proposed many years ago, but have not been found experimentally. Future experiments should focus on the search for short-lived (weakly decaying) objects.

Most of the predictions discussed in this part are based on hadron-string or hydrodynamical model considerations without including the phase transition to the QGP (except for thermal evolution models and for the AMPT model which includes parton interactions in a perturbative way). The goal is to extract information about the initial partonic phase of the collision from the measurement of hadronic observables. The QGP signals might be strongly distorted by the hadronization process and by final state interactions of the hadrons. Moreover, the finite size of the fireball and its very short lifetime might blur the signatures from the partonic matter, in particular the possible remnants of critical fluctuations near the QCD critical endpoint.

In order to trace the final observations back to the early phase of the collisions, and to subtract the hadronic contribution from the QGP signal, one needs dynamical models containing the proper degrees of freedom – quarks and gluons in the initial phase and hadrons in the final phase – and dynamics which includes the phase transition according to the Lattice QCD EoS. The development of such approaches is in progress [284, 285, 513–515]. Finally, the progress in dense matter research using high-energy heavy-ion collision definitely relies on both, novel theoretical tools and a comprehensive set of high-quality experimental data.

References

1. A. Bazavov, et al., Phys. Rev. D **80**, 014504 (2009) [684](#)
2. J.D. Bjorken, Phys. Rev. D **27**, 140 (1983) [684](#), [716](#)
3. H. Stöcker, W. Greiner, Phys. Rep. **137**, 277 (1986) [684](#)
4. W. Cassing, E.L. Bratkovskaya, S. Juchem, Nucl. Phys. A **674**, 249 (2000)
5. I.C. Arsene, L.V. Bravina, W. Cassing, et al., Phys. Rev. C **75**, 034902 (2007) [684](#)
6. A. Andronic, P. Braun-Munzinger, J. Stachel, Phys. Lett. B **673** (2009) [684](#), [687](#), [688](#)
7. F. Karsch, PoS (CPOD07) 026. ArXiv:0711.0661 [685](#), [689](#)
8. Z. Fodor, PoS (CPOD07) 027 [685](#), [689](#)
9. Y. Aoki, G. Endrodi, Z. Fodor, S. Katz, K. Szabo, Nature **443**, 675 (2006) [685](#)
10. K. Rajagopal, F. Wilczek, arXiv:hep-ph/0011333 (2000) [685](#)
11. Z. Fodor, S.D. Katz, JHEP **404**, 50 (2004) [685](#), [687](#), [688](#)
12. P. de Forcrand, O. Philipsen, JHEP 0701:077 (2007)
13. P. de Forcrand, O. Philipsen, JHEP 0811:012 (2008) [685](#)
14. R. Rapp, Nucl. Phys. A **782**, 275 (2007) [686](#)
15. T. Matsui, H. Satz, Phys. Lett. B **178**, 416 (1986) [686](#), [715](#), [720](#), [776](#)
16. H. Satz, Nucl. Phys. A **783**, 249 (2007) [686](#), [781](#)
17. A. Mocsy, P. Petreczky, Phys. Rev. D **77**, 014501 (2008) [686](#), [781](#)
18. R. Rapp, H. van Hees, The Physics of Quarks: New Research, Horizons in World Physics, Vol. 265 (N.L. Watson and T.M. Grant (Eds.)), (Nova Publishers, 2009) [686](#)
19. A. Andronic, P. Braun-Munzinger, K. Redlich, J. Stachel, J. Phys. G **35**, 104155 (2008) [686](#), [785](#), [786](#), [791](#)
20. P. Braun-Munzinger, K. Redlich, J. Stachel, *Quark Gluon Plasma 3* (R. C. Hwa, X.-N. Wang (Eds.)), (World Scientific, Singapore, 2004) [687](#), [737](#), [739](#)
21. M.A. Stephanov, Prog. Theor. Phys. Suppl. **153**, 139 (2004)
22. O. Philipsen, PoS **LAT2005**, 016 (2005) [687](#)
23. P. Braun-Munzinger, J. Stachel, Nucl. Phys. A **638**, 3c (1998) [687](#), [705](#)
24. J. Cleymans, K. Redlich, Phys. Rev. Lett. **81**, 5284 (1998) [689](#), [690](#)

25. J. Cleymans, K. Redlich, Phys. Rev. C **60**, 054908 (1999) [687](#), [689](#), [690](#)
26. A. Andronic, P. Braun-Munzinger, J. Stachel, Nucl. Phys. A **772**, 167 (2006) [687](#), [731](#), [732](#), [738](#), [823](#), [824](#)
27. F. Becattini, J. Manninen, J. Phys. G **35**, 104013 (2008) [688](#)
28. L.V. Bravina, et al., Phys. Rev. C **60**, 024904 (1999) [688](#), [689](#)
29. L.V. Bravina, et al., Nucl. Phys. A **698**, 383 (2002) [689](#)
30. E.L. Bratkovskaya, et al., Phys. Rev. C **69**, 054907 (2004) [688](#), [735](#), [736](#), [744](#), [745](#)
31. H. Stöcker, et al., J. Phys. G **31**, S929 (2005) [689](#)
32. Y.B. Ivanov, V.N. Russkikh, V.D. Toneev, Phys. Rev. C **73**, 044904 (2006) [689](#), [690](#), [736](#), [737](#), [752](#), [753](#)
33. Z. Fodor, S.D. Katz, JHEP **0203**, 014 (2002) [690](#)
34. R.D. Pisarski, Phys. Lett. B **110**, 155 (1982) [690](#), [721](#)
35. C. Blume, J. Phys. G **31**, S57 (2005) (and privat communication) [691](#), [733](#)
36. G. Stephans, J. Phys. G: Nucl. Part. Phys. **35**, 044050 (2008) [691](#)
37. J. Aichelin, C.M. Ko, Phys. Rev. Lett. **55**, 2661 (1985) [693](#), [700](#)
38. G.Q. Li, C.M. Ko, Phys. Lett. B **349**, 405 (1995) [693](#), [701](#)
39. C. Fuchs, Prog. Part. Nucl. Phys. **56**, 1 (2006) [693](#), [695](#), [698](#), [701](#), [702](#), [703](#)
40. J. Schaffner-Bielich, J. Bondorf, I. Mishustin, Nucl. Phys. A **625**, 325 (1997) [693](#)
41. G.E. Brown, et al., Phys. Rev. C **43**, 1881 (1991)
42. W. Cassing, E.L. Bratkovskaya, Phys. Rep. **308**, 65 (1999) [693](#), [702](#), [736](#), [754](#), [762](#)
43. G.Q. Li, C.H. Lee, G.E. Brown, Phys. Rev. Lett. **79**, 5214 (1997) [693](#), [695](#)
44. G.E. Brown, H.A. Bethe, Astrophys. J. **423**, 659 (1994) [693](#)
45. M.F.M. Lutz, C.L. Korpa, M. Moeller, Nucl. Phys. A **808**, 124 (2008) [693](#), [694](#)
46. N.K.T. Waas, W. Weise, Phys. Lett. B **379**, 34 (1996)
47. M.F.M. Lutz, C. Korpa, Nucl. Phys. A **700**, 209 (2002) [704](#)
48. L. Tolos, A. Ramos, E. Oset, Prog. Theor. Phys. Suppl. **168**, 635 (2007) [694](#), [704](#)
49. C. Fuchs, A. Faessler, E. Zabrodin, Y.M. Zheng, Phys. Rev. Lett. **86**, 1974 (2001) [695](#), [701](#), [702](#)
50. C.M. Ko, G.Q. Li, J. Phys. G **22**, 405 (1996) [695](#)
51. C. Hartnack, J. Aichelin, J. Phys. G **28**, 1649 (2002) [695](#), [699](#), [701](#)
52. A. Mishra, E.L. Bratkovskaya, J. Schaffner-Bielich, S. Schramm, H. Stöcker, Phys. Rev. C **70**, 044904 (2004) [695](#), [696](#)
53. D. Best, et al. [FOPI Collaboration], Nucl. Phys. A **625**, 307 (1997) [695](#)
54. M. Menzel, et al. [KaoS Collaboration], Phys. Lett. B **495**, 26 (2000) [695](#)
55. L.W. Chen, C.M. Ko, Y. Tzeng, Phys. Lett. B **584**, 269 (2004) [695](#), [696](#)
56. S. Pal, C.M. Ko, Z. wei Lin, Phys. Rev. C **64**, 042201 (2001) [695](#)
57. C. Hartnack, H. Oeschler, J. Aichelin, Phys. Rev. Lett. **93**, 102302 (2003). [Erratum *ibid.* **93**, 149903(E) (2004)] [695](#)
58. W. Cassing, L. Tolos, E.L. Bratkovskaya, A. Ramos, Nucl. Phys. A **727**, 59 (2003) [695](#), [696](#), [704](#)
59. J. Schaffner-Bielich, V. Koch, M. Effenberger, Nucl. Phys. A **669**, 153 (2000) [696](#)
60. M.F.M. Lutz, C.L. Korpa, Nucl. Phys. A **700**, 309 (2002) [696](#)
61. J. Ritman, et al. [FOPI Collaboration], Z. Phys. A **352**, 355 (1995) [696](#), [697](#)

- 62. N. Herrmann, et al. [FOPI Collaboration], Prog. Part. Nucl. Phys. **42**, 187 (1999) [696](#)
- 63. G.Q. Li, C.M. Ko, B.A. Li, Phys. Rev. Lett. **74**, 235 (1995) [696](#)
- 64. G.Q. Li, C.M. Ko, Nucl. Phys. A **594**, 460 (1995) [696](#)
- 65. E.L. Bratkovskaya, W. Cassing, U. Mosel, Nucl. Phys. A **622**, 593 (1997) [697](#)
- 66. E.L. Bratkovskaya, W. Cassing, U. Mosel, Phys. Lett. B **424**, 244 (1998)
- 67. Z.S. Wang, A. Faessler, C. Fuchs, V.S.U. Maheswari, D. Kosov, Nucl. Phys. A **628**, 151 (1998)
- 68. G.Q. Li, G.E. Brown, Nucl. Phys. A **636**, 487 (1998) [697](#)
- 69. C. Fuchs, D. Kosov, A. Faessler, Z.S. Wang, T. Waindzocho, Phys. Lett. B **434**, 254 (1998) [697](#)
- 70. Y.M. Zheng, C. Fuchs, A. Faessler, K. Shekhter, Y.P. Yan, C. Kobdaj, Phys. Rev. C **69**, 034907 (2004) [697](#)
- 71. A. Larionov, U. Mosel, Phys. Rev. C **72**, 014901 (2005) [697](#), [698](#)
- 72. T. Gaitanos, C. Fuchs, H.H. Wolter, A. Faessler, Eur. Phys. J. A **12**, 421 (2001) [697](#)
- 73. A. Hombach, W. Cassing, S. Teis, U. Mosel, Eur. Phys. J. A **5**, 157 (1999)
- 74. C. Fuchs, T. Gaitanos, H.H. Wolter, Phys. Lett. B **381**, 23 (1996)
- 75. T. Gaitanos, C. Fuchs, H.H. Wolter, Nucl. Phys. A **650**, 97 (1999) [697](#)
- 76. P. Crochet, et al. [FOPI Collaboration], Phys. Lett. B **486**, 6 (2000) [697](#)
- 77. D. Brill, et al. [KaoS Collaboration], Phys. Rev. Lett. **71**, 336 (1993) [697](#)
- 78. L.B. Venema, et al. [TAPS Collaboration], Phys. Rev. Lett. **71**, 835 (1993) [697](#)
- 79. Y. Shin, , et al. [KaoS Collaboration], Phys. Rev. Lett. **81**, 1576 (1998) [698](#)
- 80. G.Q. Li, C.M. Ko, G.E. Brown, Phys. Lett. B **381**, 17 (1996)
- 81. Z.S. Wang, C. Fuchs, A. Faessler, T. Gross-Boelting, Eur. Phys. J. A **5**, 275 (1999) [698](#), [699](#)
- 82. F. Uhlig, A. Förster, et al. [KaoS Collaboration], Phys. Rev. Lett. **95**, 012301 (2005) [698](#), [699](#)
- 83. E.L. Bratkovskaya, private communication (2005) [698](#), [700](#)
- 84. G.Q. Li, C.M. Ko, Phys. Rev. C **54**, R2159 (1996) [699](#)
- 85. C. Hartnack, et al., Eur. Phys. J. A **1**, 151 (1998) [699](#)
- 86. M. Nekipelov, et al. [ANKE-Collaboration], Phys. Lett. B **540**, 207 (2002) [700](#), [703](#)
- 87. M. Büscher, et al. [ANKE-Collaboration], Eur. Phys. J. A **22**, 301 (2004) [700](#)
- 88. Z. Rudy, W. Cassing, L. Jarczyk, B. Kamys, P. Kulessa, Eur. Phys. J. A **15**, 303 (2002) [700](#)
- 89. Z. Rudy, W. Cassing, L. Jarczyk, B. Kamys, A. Kowalczyk, P. Kulessa, Eur. Phys. J. A **23**, 379 (2005) [700](#)
- 90. W. Scheinast, et al., Phys. Rev. Lett. **96**, 072301 (2006) [700](#), [703](#), [704](#)
- 91. R. Stock, Phys. Rep. **135**, 259 (1986) [700](#)
- 92. S.A. Bass, C. Hartnack, H. Stöcker, W. Greiner, Phys. Rev. C **51**, 3343 (1995) [700](#)

93. S. Teis, W. Cassing, M. Effenberger, A. Hombach, U. Mosel, G. Wolf, *Z. Phys. A* **356**, 421 (1997)
94. V.S.U. Maheswari, C. Fuchs, A. Faessler, L. Sehn, D. Kosov, Z. Wang, *Nucl. Phys. A* **628**, 669 (1998) [700](#)
95. A. Lang, W. Cassing, U. Mosel, K. Weber, *Nucl. Phys. A* **541**, 507 (1992) [701](#)
96. S.W. Huang, A. Faessler, G.Q. Li, R.K. Puri, E. Lehmann, D.T. Khoa, M.A. Matin, *Phys. Lett. B* **298**, 41 (1993)
97. C. Hartnack, J. Jaenicke, L. Sehn, H. Stöcker, J. Aichelin, *Nucl. Phys. A* **580**, 643 (1994) [701](#)
98. D. Miskowiec, et al. [KaoS Collaboration], *Phys. Rev. Lett.* **72**, 3650 (1994) [701](#)
99. R. Barth, et al. [KaoS Collaboration], *Phys. Rev. Lett.* **78**, 4007 (1997)
100. F. Laue, et al. [KaoS Collaboration], *Phys. Rev. Lett.* **82**, 1640 (1999) [701](#)
101. F. Laue, et al. [KaoS Collaboration], *Eur. Phys. J. A* **9**, 397 (2000)
102. C. Sturm, et al. [KaoS Collaboration], *Phys. Rev. Lett.* **86**, 39 (2001) [701](#), [702](#)
103. C. Fuchs, A. Faessler, S. El-Basouny, E. Zabrodin, *J. Phys. G* **28**, 1615 (2002) [701](#)
104. C. Hartnack, H. Oeschler, J. Aichelin, *Phys. Rev. Lett.* **96**, 012302 (2006) [701](#), [702](#)
105. K. Tsushima, A. Sibirtsev, A.W. Thomas, G.Q. Li, *Phys. Rev. C* **59**, 369 (1999) [702](#)
106. H.W. Barz, L. Naumann, *Phys. Rev. C* **68**, 041901 (2003) [704](#)
107. L. Tolos, A. Polls, A. Ramos, J. Schaffner-Bielich, *Phys. Rev. C* **68**, 024903 (2003) [704](#)
108. L. Tolos, A. Ramos, A. Polls, T.T. Kuo, *Nucl. Phys. A* **690**, 547 (2001) [704](#)
109. J. Stachel, *Nucl. Phys. A* **610**, 509c (1996) [705](#)
110. B.B. Buck [E917 Collaboration], *Phys. Rev. C* **66**, 054901 (2002) [705](#), [706](#)
111. M. Cheng, et al., *Phys. Rev. D* **74**, 054507 (2006) [705](#)
112. C. Ogilvie, et al. [E866/E917 Collaboration], *Nucl. Phys. A* **698**, 12c (2002) [706](#)
113. F. Wang, *J. Phys. G* **27**, 283 (2001) [706](#), [707](#), [709](#)
114. R. Bellwied, et al. [E896 Collaboration], *Nucl. Phys. A* **698**, 499c (2002) [707](#)
115. G. Bunce, et al., *Phys. Rev. Lett.* **36**, 1113 (1976) [707](#)
116. J. Felix, et al., *Phys. Rev. Lett.* **82**, 22 (1999) [707](#)
117. A.D. Panagiotou, *Phys. Rev. C* **33**, 1999 (1986) [707](#)
118. P. Chung, et al. [E895 Collaboration], *Phys. Rev. Lett.* **85**, 940 (2000) [707](#), [708](#)
119. P. Chung, et al. [E895 Collaboration], *Phys. Rev. Lett.* **91**, 202301 (2003) [707](#), [708](#), [714](#)
120. T. Armstrong, et al., *Phys. Rev. C* **59**, 2699 (1999) [708](#)
121. B. Back, et al. [E917 Collaboration], *Phys. Rev. Lett.* **87**, 242301 (2001)
122. C. Alt, et al. [Na49 Collaboration], *Phys. Rev. C* **73**, 044910 (2006) [708](#)
123. G.J. Wang, et al., arXiv:nucl-th/9807036 [709](#)
124. S.A. Bass, et al., *Prog. Part. Nucl. Phys.* **41**, 255 (1998) [709](#), [736](#), [754](#), [823](#)
125. K. Barish, et al. [E941 Collaboration], *Nucl. Phys. A* **698**, 599 (2002) [709](#)

126. J. Barrette, et al., Phys. Lett. B **458**, 319 (2000) [709](#)
127. M.A. Lisa, et al., Ann. Rev. Nucl. Part. Sci. **55**, 357 (2005) [710](#)
128. M. Lisa, et al. [E895 Collaboration], Phys. Rev. C **66**, 054906 (2002) [709](#)
129. M. Lisa, et al. [E895 Collaboration], Phys. Rev. Lett. **84**, 2798 (2000) [709](#)
130. R. Lacey, Braz. J. Phys. **37**, 893 (2007) [710](#)
131. C. Pinkenburg, et al. [E895 Collaboration], Phys. Rev. Lett. **83**, 1295 (1999) [711](#), [712](#)
132. P. Danielewicz, R. Lacey, W.G. Lynch, Science **298**, 1592 (2002) [711](#), [712](#), [749](#)
133. H. Liu, et al. [E895 Collaboration], Phys. Rev. Lett. **84**, 5488 (2000) [712](#), [713](#)
134. P. Danielewicz, 50th Symposium on Nuclear Physics, Dec 12–16, 2005, Bhabha Atomic Research Centre, Mumbai, India (2005) [712](#), [749](#)
135. G. Zeeb, M. Reiter, M. Bleicher, Phys. Lett. B **586**, 297 (2004) [713](#)
136. J.W. Harris, et al., Nucl. Inst. Meth. A **315**, 33 (1992) [714](#)
137. A. Bialas, W. Czyz, Phys. Lett. B **58**, 325 (1975) [714](#)
138. A. Bialas, M. Bleszynski, W. Czyz, Nucl. Phys. B **111**, 461 (1976) [714](#)
139. T. Alber, et al. [NA49 Collaboration], Phys. Rev. Lett. **75**, 3814 (1995) [715](#), [717](#)
140. H. Appelshäuser, et al. [NA49 Collaboration], Eur. Phys. J. C **2**, 661 (1998) [715](#), [717](#), [718](#)
141. R. Hagedorn, Nuovo Cim. Suppl. **3**, 147 (1965) [715](#)
142. J. Sollfrank, M. Gazdzicki, U. Heinz, J. Rafelski, Z. Phys. C **61**, 659 (1994) [715](#)
143. P. Braun-Munzinger, J. Stachel, J.P. Wessels, N. Xu, Phys. Lett. B **344**, 43 (1995) [715](#), [785](#), [786](#)
144. P. Braun-Munzinger, I. Heppe, J. Stachel, Phys. Lett. B **465**, 15 (1999) [715](#), [719](#)
145. F. Becattini, J. Manninen, M. Gazdzicki, Phys. Rev. C **73**, 044905 (2006) [715](#), [720](#)
146. P. Cortese, et al. [NA60 Collaboration], J. Phys. G: Nucl. Part. Phys. **31**, S809 (2005) [715](#), [720](#)
147. G. Agakichiev, et al. [CERES Collaboration], Phys. Lett. B **422**, 405 (1998) [715](#), [721](#)
148. D. Adamova, et al. [CERES/NA45 Collaboration], Phys. Rev. Lett. **91**, 042301 (2003) [715](#), [721](#), [773](#)
149. H. Appelshäuser, et al. [NA49 Collaboration], Phys. Lett. B **444**, 523 (1998) [715](#)
150. J. Rafelski, B. Müller, Phys. Rev. Lett. **48**, 1066 (1982) [716](#), [751](#)
151. CERN, Press Release (February 10, 2000) [716](#)
152. C. Alt, et al. [NA49 Collaboration], Phys. Rev. C **77**, 064908 (2008) [716](#)
153. M. Aggarwal, et al. [WA98 Collaboration], Nucl. Phys. A **610**, 200c (1996) [717](#)
154. P. Seyboth, et al. [NA49 Collaboration], Acta Phys. Polon. B **36**, 565 (2005) [717](#), [718](#)
155. F. Antinori, et al. [NA57 Collaboration], J. Phys. G **30**, 823 (2004) [717](#)
156. P. Koch, B. Müller, J. Rafelski, Phys. Rep. **142**, 167 (1986) [718](#)
157. F. Antinori, et al. [NA57 Collaboration], J. Phys. G **32**, 427 (2006) [718](#), [719](#)

158. S.V. Afanasiev, et al., Phys. Lett. B **538**, 275 (2002)
159. S.V. Afanasiev, et al. [NA49 collaboration], Phys. Rev. C **66**, 054902 (2002) [718](#), [722](#), [735](#), [738](#)
160. C. Alt, et al. [NA49 Collaboration], Phys. Rev. Lett. **94**, 052301 (2005) [718](#)
161. R. Hagedorn, K. Redlich, Z. Phys. C **27**, 541 (1985) [718](#)
162. R. Stock, Phys. Lett. B **456**, 277 (1999) [720](#)
163. R. Arnaldi, et al. [NA60 Collaboration], Phys. Rev. Lett. **99**, 132302 (2007) [721](#)
164. R. Arnaldi, et al. [NA60 Collaboration], Phys. Rev. Lett. **96**, 162302 (2006) [721](#), [764](#), [766](#)
165. M. Gazdzicki, M.I. Gorenstein, Acta Phys. Polon. B **30**, 2705 (1999) [722](#), [739](#)
166. C. Alt, et al. [NA49 Collaboration], Phys. Rev. C **77**, 024903 (2008) [722](#), [735](#), [738](#)
167. C. Alt, et al. [NA49 Collaboration], Phys. Rev. C **78**, 044907 (2008) [723](#)
168. M. Gyulassy, L. McLerran, Nucl. Phys. A **750**, 30 (2005) [724](#)
169. S. Adler, et al. [PHENIX Collaboration], Phys. Rev. Lett. **96**, 202301 (2006) [724](#)
170. E. Wang, X.N. Wang, Phys. Rev. Lett. **89**, 162301 (2002) [725](#)
171. C. Loizides, Eur. Phys. J. C **49**, 339 (2007) [725](#)
172. I. Vitev, Phys. Lett. B **639**, 38 (2006) [725](#)
173. A. Adare, et al. [PHENIX Collaboration], Phys. Rev. C **77**, 064907 (2008) [725](#)
174. A. Adare, et al. [PHENIX Collaboration], Phys. Rev. Lett. **101**, 162301 (2008) [725](#)
175. S. Voloshin, et al. [STAR Collaboration], J. Phys. G **34**, S883 (2007) [726](#)
176. P. Kolb, et al., Phys. Rev. C **62**, 054909 (2000) [726](#)
177. C. Nonaka, M. Asakawa, Phys. Rev. C **71**, 044904 (2005) [726](#), [816](#), [817](#)
178. E. Nakano, B.J. Schaefer, B. Stokic, B. Friman, K. Redlich, Phys. Lett. B **682**, 401 (2010). DOI 10.1016/j.physletb.2009.11.027 [726](#), [817](#)
179. H. Petersen, et al., Phys. Rev. C **74**, 064908 (2006) [726](#)
180. P. Sorensen, et al. [STAR Collaboration], J. Phys. G **34**, S897 (2007). [726](#)
181. S. Mrowczynsky, E. Shuryak, Acta Phys. Polon. B **34**, 4241 (2003) [727](#)
182. S. Vogel, M. Bleicher, G. Torrieri, arXiv:nucl-th/0703031 (2007) [727](#)
183. A. Adare, et al. [PHENIX Collaboration], Phys. Rev. Lett. **98**, 162301 (2007) [727](#)
184. R.J. Fries, et al., Phys. Rev. Lett. **90**, 202303 (2003) [727](#)
185. V. Greco, et al., Phys. Rev. Lett. **90**, 202302 (2003) [727](#)
186. R. Lacey, A. Taranenko, PoSCFRNC2006:021 (2006) [728](#)
187. R. Bellwied, PoSCPOD07:015 (2007) [728](#)
188. B.I. Abelev, et al. [STAR Collaboration], Phys. Rev. Lett. **97**, 132301 (2006) [728](#), [729](#)
189. R. Witt, et al. [STAR Collaboration], J. Phys. G **34**, S921 (2007) [728](#)
190. W. Cassing, E.L. Bratkovskaya, A. Sibirtsev, Nucl. Phys. A **691**, 753 (2001) [734](#), [735](#), [778](#), [779](#), [780](#), [788](#), [789](#)
191. L. Ahle, et al. [E866 and E917 Collaboration], Phys. Lett. B **476**, 1 (2000). [Ibid. **490**, 53 (2000)] [735](#), [738](#), [744](#)

192. J.L. Klay, et al. [E895 Collaboration], Phys. Rev. C **68**, 054905 (2003)
193. S. Ahmad, et al. [E891 Collaboration], Phys. Lett. B **382**, 35 (1996) [738](#)
194. C. Pinkenburg, et al. [E866 Collaboration], Nucl. Phys. A **698**, 495c (2002) [735](#), [738](#)
195. C. Alt, et al. [NA49 Collaboration], Phys. Rev. C **78**, 034918 (2008) [735](#), [738](#), [740](#)
196. A. Mischke, et al. [NA49 Collaboration], J. Phys. G. **28**, 1761 (2002)
197. A. Mischke, et al. [NA49 Collaboration], Nucl. Phys. A **715**, 453 (2003)
198. F. Antinori, et al. [WA97 Collaboration], Nucl. Phys. A **661**, 130c (1999) [735](#), [738](#)
199. D. Ouerdane, et al. [BRAHMS Collaboration], Nucl. Phys. A **715**, 478 (2003) [735](#), [738](#), [744](#)
200. J.H. Lee, et al., J. Phys. G **30**, S85 (2004)
201. S.S. Adler, et al. [PHENIX Collaboration], Phys. Rev. C **69**, 024904 (2004). [Ibid. **69**, 034909 (2004)]
202. C. Adler, et al. [STAR Collaboration], Phys. Rev. Lett. **87**, 262302 (2001) [737](#), [744](#)
203. O. Barannikova, et al., Nucl. Phys. A **715**, 458 (2003)
204. K. Filimonov, et al. [STAR Collaboration], in Proc. I. Ya. Pomeranchuk and Physics at the Turn of Centuries, January 24–28, 2003, MOSCOW (2003) p. 58, arXiv:hep-ex/0306056 (2003) [735](#), [737](#), [738](#), [744](#)
205. M. Wagner, et al., Phys. Rev. C **71**, 034910 (2005) [735](#), [736](#), [738](#), [744](#), [745](#)
206. W. Ehehalt, W. Cassing, Nucl. Phys. A **602**, 449 (1996) [736](#), [754](#)
207. M. Bleicher, E. Zabrodin, C. Spieles, S.A. Bass, C. Ernst, S. Soff, L. Bravina, M. Belkacem, H. Weber, H. Stocker, W. Greiner, J. Phys. G: Nucl. Part. Phys. **25**, 1859 (1999) [736](#), [751](#), [754](#)
208. M. Effenberger, E. Bratkovskaya, U. Mosel, Phys. Rev. C **60**, 044614 (1999) [736](#), [754](#)
209. H. Weber, E.L. Bratkovskaya, W. Cassing, H. Stöcker, Phys. Rev. C **67**, 014904 (2003) [736](#), [737](#), [739](#), [747](#)
210. E.L. Bratkovskaya, W. Cassing, H. Stöcker, Phys. Rev. C **67**, 054905 (2003) [778](#), [780](#)
211. S. Soff, et al., Phys. Lett. B **551**, 115 (2003)
212. A.B. Larionov, W. Cassing, C. Greiner, U. Mosel, Phys. Rev. C **62**, 064611 (2000) [749](#), [754](#)
213. A.B. Larionov, et al., Phys. Rev. C **71**, 034910 (2005) [736](#), [749](#), [754](#)
214. K. Redlich, J. Cleymans, H. Oeschler, A. Tounsi, Acta Phys. Pol. B **33**, 1609 (2002) [737](#)
215. B.B. Back, et al., Phys. Rev. Lett. **87**, 242301 (2001) [739](#)
216. M. Gaździcki, D. Röhrich, Z. Phys. C **65**, 215 (1995). [Ibid. **71**, 55 (1996)] [739](#)
217. P. Braun-Munzinger, J. Stachel, Phys. Lett. B **490**, 196 (2000) [737](#), [739](#)
218. P. Braun-Munzinger, J. Stachel, Nucl. Phys. A **690**, 119c (2001)
219. P. Braun-Munzinger, J. Cleymans, H. Oeschler, K. Redlich, Nucl. Phys. A **697**, 902 (2002)
220. P. Braun-Munzinger, J. Stachel, C. Wetterich, Phys. Lett. B **596**, 61 (2004) [737](#), [739](#)

- 221. W. Cassing, Nucl. Phys. A **700**, 618 (2002) [737](#), [739](#)
- 222. M. Gaździcki, J. Phys. G **30**, S161 (2004) [739](#)
- 223. V. Koch, A. Majumder, J. Randrup, Phys. Rev. C **72**, 064903 (2005) [739](#), [814](#), [815](#)
- 224. J. Cleymans, H. Oeschler, K. Redlich, S. Wheaton, Phys. Lett. B **615**, 50 (2005) [739](#)
- 225. B.I. Abelev, et al. [STAR Collaboration], Phys. Rev. C **79**, 034909 (2009) [740](#)
- 226. V. Friese, et al. [NA49 Collaboration], J. Phys. G **30**, 119 (2004) [743](#), [744](#)
- 227. I. Kraus, et al. [NA49 Collaboration], J. Phys. G **30**, 5583 (2004) [743](#), [744](#)
- 228. I.G. Bearden, et al. [NA44 Collaboration], Phys. Rev. C **66**, 044907 (2002) [744](#)
- 229. M. Kliemant, B. Lungwitz, M. Gaździcki, Phys. Rev. C **69**, 044903 (2004) [744](#)
- 230. E.E. Zabrodin, C. Fuchs, L.V. Bravina, A. Faessler, Phys. Rev. C **63**, 034902 (2001) [744](#), [745](#), [754](#), [755](#)
- 231. E.E. Zabrodin, C. Fuchs, L.V. Bravina, A. Faessler, Phys. Lett. B **508**, 184 (2001)
- 232. G. Burau, J. Bleibel, C. Fuchs, A. Faessler, L.V. Bravina, E.E. Zabrodin, Phys. Rev. C **71**, 054905 (2005)
- 233. J. Bleibel, G. Burau, A. Faessler, C. Fuchs, Nucl. Phys. A **767**, 218 (2006)
- 234. L. Bravina, K. Tywoniuk, E. Zabrodin, G. Burau, J. Bleibel, C. Fuchs, A. Faessler, Phys. Lett. B **631**, 109 (2005)
- 235. L.V. Bravina, L.P. Csernai, A. Faessler, C. Fuchs, E.E. Zabrodin, Phys. Lett. B **543**, 217 (2002) [744](#), [745](#), [754](#), [755](#)
- 236. V.N. Russkikh, Y.B. Ivanov, Phys. Rev. C **74**, 034904 (2006) [744](#), [753](#)
- 237. E.L. Bratkovskaya, S. Soff, H. Stöcker, M. van Leeuwen, W. Cassing, Phys. Rev. Lett. **92**, 032302 (2004) [744](#), [745](#)
- 238. H. Sorge, Phys. Rev. C **52**, 3291 (1995) [745](#), [751](#), [754](#)
- 239. H. van Hecke, et al., Phys. Rev. Lett. **81**, 5764 (1998) [745](#)
- 240. N. Xu, Int. J. Mod. Phys. E **16**, 715 (2007) [746](#)
- 241. W.G.W. Scheid, H. Müller, Phys. Rev. Lett. **32**, 741 (1974) [747](#)
- 242. L.D. Landau, E.M. Lifshitz, *Fluid Mechanics* (Pergamon Press, New York, 1959) [747](#)
- 243. H. Stöcker, J. Hofmann, J.A. Maruhn, W. Greiner, Prog. Part. Nucl. Phys. **4**, 133 (1980) [747](#), [748](#)
- 244. L.P. Csernai, D. Rohrich, Phys. Lett. B **458**, 454 (1999) [747](#), [748](#), [752](#)
- 245. S. Voloshin, Y. Zhang, Z. Phys. C **70**, 665 (1996) [747](#)
- 246. S. Soff, S.A. Bass, M. Bleicher, H. Stöcker, W. Greiner, arXiv:nucl-th/9903061 [748](#)
- 247. P.K. Sahu, W. Cassing, Nucl. Phys. A **672**, 376 (2000) [748](#)
- 248. P.K. Sahu, W. Cassing, Nucl. Phys. A **712**, 357 (2002) [748](#)
- 249. B.A. Li, et al., Phys. Rev. C **60**, 01191 (1999) [748](#)
- 250. P.D. et al., Phys. Rev. Lett. **81**, 2438 (1998) [748](#)

- 251. M. Isse, A. Ohnishi, N. Otuka, P.K. Sahu, Y. Nara, Phys. Rev. C **72**, 064908 (2005) [748](#)
- 252. H. Petersen, M. Bleicher, **PoSCPOD2006**, 025 (2006) [748](#), [755](#)
- 253. J. Hofmann, H. Stöcker, U.W. Heinz, W. Scheid, W. Greiner, Phys. Rev. Lett. **36**, 88 (1976) [748](#)
- 254. A. Andronic, et al., Phys. Rev. C **67**, 034907 (2003) [748](#)
- 255. A. Andronic, et al., Phys. Rev. C **64**, 041604 (2001) [748](#)
- 256. A. Andronic, et al., Nucl. Phys. A **679**, 765 (2001) [749](#)
- 257. A. Andronic, et al., Phys. Lett. B **612**, 173 (2005)
- 258. A. Andronic, Nucl. Phys. A **661**, 333 (1999) [749](#)
- 259. C. Adler, et al. [STAR Collaboration], Phys. Rev. Lett. **90**, 082302 (2003) [750](#)
- 260. M. Issah, [PHENIX Collaboration], J. Phys. G **35**, 104103 (2008) [750](#)
- 261. A. Sibirtsev, H.W. Hammer, U.G. Meissner, A.W. Thomas, Eur. Phys. J. A **29**, 209 (2006) [750](#)
- 262. J. Rafelski, Nucl. Phys. A **418**, 215c (1984) [751](#)
- 263. P. Koch, J. Rafelski, Nucl. Phys. A **444**, 678 (1985)
- 264. A.J. Baltz, C. Dover, Phys. Rev. C **53**, 362 (1996) [751](#)
- 265. J. Adams, et al. [STAR Collaboration], Phys. Lett. B **612**, 181 (2005) [751](#)
- 266. B.I. Abelev, et al. [STAR Collaboration], Phys. Rev. C **79**, 064903 (2009) [751](#)
- 267. B. Mohanty, N. Xu, J. Phys. G **36**, 064022 (2009) [751](#)
- 268. D.H. Rischke, Y. Pürsün, J.A. Maruhn, H. Stöcker, W. Greiner, Heavy Ion Phys. **610**, 88c (1996) [752](#)
- 269. J. Brachmann, et al., Phys. Rev. C **61**, 024909 (2000) [752](#)
- 270. Y.B. Ivanov, E.G. Nikonov, W. Nörenberg, A.A. Shanenko, V.D. Toneev, Heavy Ion Phys. **15**, 117 (2002) [752](#)
- 271. W. Schmidt, et al., Phys. Rev. C **47**, 2782 (1993) [752](#)
- 272. A. Muronga, Heavy Ion Phys. **15**, 337 (2002) [752](#)
- 273. A. Muronga, Phys. Rev. C **69**, 034903 (2004) [752](#)
- 274. J. Brachmann, et al., Nucl. Phys. A **619**, 391 (1997) [752](#)
- 275. V.D. Toneev, et al., Phys. Part. Nucl. Lett. **2**, 288 (2005). ArXiv:nucl-th/0309008 [752](#)
- 276. K. Paech, M. Reiter, A. Dumitru, H. Stöcker, W. Greiner, Nucl. Phys. A **681**, 41 (2001) [753](#)
- 277. C. Alt, et al., Phys. Rev. C **68**, 034903 (2003) [753](#), [754](#)
- 278. P.F. Kolb, et al., Nucl. Phys. A **696**, 197 (2001) [754](#)
- 279. D. Teaney, Phys. Rev. C **68**, 034913 (2003)
- 280. E. Shuryak, J. Phys. G **30**, S1221 (2004) [759](#)
- 281. T. Hirano, Y. Nara, J. Phys. G **31**, S1 (2005) [754](#)
- 282. K.K. Gudima, M. Ploszajczak, V.D. Toneev, Phys. Lett. B **328**, 249 (1994) [754](#)
- 283. N.S. Amelin, L.V. Bravina, L.P. Csernai, V.D. Toneev, K.K. Gudima, S.Y. Sivoklokov, Phys. Rev. C **47**, 2299 (1993) [754](#)
- 284. B. Zhang, et al., Phys. Rev. C **61**, 067901 (2000) [754](#), [829](#)

285. Z.W. Lin, et al., Phys. Rev. C **64**, 011902 (2001) [754](#), [829](#)
286. L.W. Chen, C.M. Ko, private communication (2006) [755](#)
287. V.D. Toneev, private communication (2006) [755](#)
288. E.L. Bratkovskaya, private communication (2006) [755](#)
289. A.V. Larionov, private communication (2006) [755](#)
290. K. Kajantie, J. Kapusta, L. McLerran, A. Mekjian, Phys. Rev. D **34**, 2746 (1986) [759](#)
291. P.V. Ruuskanen, Nucl. Phys. A **544**, 169c (1992)
292. J. Cleymans, K. Redlich, H. Satz, Z. Phys. C **52**, 517 (1991)
293. U. Heinz, K.S. Lee, Phys. Lett. B **259**, 162 (1991) [759](#)
294. C.M. Ko, V. Koch, G.Q. Li, Ann. Rev. Nucl. Part. Sci. **47**, 505 (1997) [759](#)
295. R. Rapp, J. Wambach, Adv. Nucl. Phys. **25**, 1 (2000) [759](#), [762](#), [763](#)
296. R. Rapp, J. Wambach, Eur. Phys. J. A **6**, 415 (1999) [759](#), [762](#), [764](#), [765](#)
297. M. Dey, V.L. Eletsky, B.L. Ioffe, Phys. Lett. B **252**, 620 (1990) [759](#)
298. G. Chanfray, J. Delorme, M. Ericson, M. Rosa-Clot, nucl-th/9809007 (1998) [759](#)
299. R. Rapp, G. Chanfray, J. Wambach, Nucl. Phys. A **617**, 472 (1997) [759](#)
300. B. Friman, H.J. Pirner, Nucl. Phys. A **617**, 496 (1997)
301. F. Klingl, N. Kaiser, W. Weise, Nucl. Phys. A **624**, 527 (1997) [759](#)
302. W. Peters, M. Post, H. Lenske, S. Leupold, U. Mosel, Nucl. Phys. A **632**, 109 (1998) [759](#)
303. J.V. Steele, H. Yamagishi, I. Zahed, Phys. Lett. B **384**, 255 (1996) [759](#)
304. J.V. Steele, H. Yamagishi, I. Zahed, Phys. Rev. D **56**, 5605 (1997) [759](#)
305. L.D. McLerran, T. Toimela, Phys. Rev. D **31**, 545 (1985) [759](#)
306. G. Roche, et al., Phys. Rev. Lett. **61**, 1069 (1988) [760](#), [769](#)
307. C. Naudet, et al., Phys. Rev. Lett. **62**, 2652 (1989)
308. G. Roche, et al., Phys. Lett. B **226**, 228 (1989)
309. R. Porter, et al., Phys. Rev. Lett. **79**, 1229 (1997) [760](#), [769](#), [770](#)
310. G. Agakichiev, et al. [HADES Collaboration], Phys. Rev. Lett. **98**, 052302 (2007) [760](#), [770](#), [771](#)
311. G. Agakichiev, et al. [HADES Collaboration], Phys. Lett. B **663**, 43 (2008) [760](#), [770](#), [771](#)
312. G. Agakichiev, et al., Phys. Rev. Lett. **75**, 1272 (1995) [760](#)
313. G. Agakichiev, et al., Phys. Lett. B **422**, 405 (1998) [760](#)
314. M.A. Mazzoni, [HELIOS/3 Collaboration], Nucl. Phys. A **566**, 95c (1994) [760](#)
315. M. Masera, [HELIOS/3 Collaboration], Nucl. Phys. A **590**, 93c (1995) [775](#), [776](#)
316. T. Åkesson, et al., Z. Phys. C **68**, 47 (1995) [760](#)
317. C. Baglin, et al. [NA38 Collaboration], Phys. Lett. B **220**, 471 (1989). *ibid.* **251** 465 (1990); **270** 105 (1991); **345** 617 (1995) [760](#)
318. S. Ramos, Nucl. Phys. A **590**, 117c (1995) [760](#)
319. M. Gonin, et al., Nucl. Phys. A **610**, 404c (1996) [760](#)
320. S. Damjanovic, N. Collaboration], Nucl. Phys. A **774**, 715 (2006) [760](#), [762](#)
321. S. Afanasiev, et al. [PHENIX Collaboration], arXiv:nucl-ex/0706.3034 [760](#), [768](#)
322. A. Adare, et al. [PHENIX Collaboration], Phys. Lett. B **670**, 313 (2009) [760](#), [768](#), [769](#)

- 323. G. Agakichiev, et al. [CERES Collaboration], *Eur. Phys. J. C* **4**, 249 (1998) [761](#), [762](#)
- 324. G. Agakichiev, et al. [CERES Collaboration], *Phys. Rev. Lett.* **75**, 1272 (1995) [762](#)
- 325. A.L.S. Angelis, et al. [HELIOS-3 Collaboration], *Eur. Phys. J. C* **13**, 433 (2000) [762](#)
- 326. G.Q. Li, C.M. Ko, G.E. Brown, *Phys. Rev. Lett.* **75**, 4007 (1995) [762](#), [763](#)
- 327. W. Cassing, W. Ehehalt, C.M. Ko, *Phys. Lett. B* **363**, 35 (1995) [762](#), [763](#)
- 328. G.Q. Li, C.M. Ko, G.E. Brown, H. Sorge, *Nucl. Phys. A* **611**, 539 (1996)
- 329. V. Koch, C. Song, *Phys. Rev. C* **54**, 1903 (1996)
- 330. D.K. Srivastava, B. Sinha, C. Gale, *Phys. Rev. C* **53**, R567 (1996)
- 331. L.A. Winckelmann, C. Ernst, L. Gerland, J. Konopka, S. Soff, et al., RHIC-Theory Workshop, BNL July 8–19, 1996 (1996)
- 332. W. Cassing, W. Ehehalt, I. Kralik, *Phys. Lett. B* **377**, 5 (1996) [762](#), [763](#)
- 333. R. Baier, M. Dirks, K. Redlich, *Phys. Rev. D* **55**, 4344 (1997). [*Ibid.* **56**, 2548 (1997)] [762](#), [763](#)
- 334. C.M. Ko, G.Q. Li, G.E. Brown, H. Sorge, *Nucl. Phys. A* **610**, 342c (1996) [762](#), [763](#)
- 335. A. Drees, *Nucl. Phys. A* **610**, 536c (1996) [763](#)
- 336. G. Agakichiev, et al. [CERES Collaboration], *Eur. Phys. J. C* **41**, 475 (2005) [762](#), [764](#)
- 337. R. Rapp, *Phys. Rev. C* **66**, 017901 (2002) [762](#), [764](#)
- 338. R. Rapp, *Pramana* **60**, 675 (2003). ArXiv:hep-ph/0201101 [762](#), [764](#)
- 339. H. van Hees, R. Rapp, *Phys. Rev. Lett.* **97**, 102301 (2006) [765](#), [766](#)
- 340. R. Rapp, private communication (2007) [765](#)
- 341. S. Damjanovic, [NA60 Collaboration], *J. Phys. G* **35**, 104036 (2008) [765](#)
- 342. G.E. Brown, M. Rho, *Phys. Rep.* **363**, 85 (2002) [765](#)
- 343. H. van Hees, R. Rapp, in *Proc. 22nd Winter Workshop on Nuclear Dynamics*, Budapest 2006, arXiv:hep-ph/0604269 (2006) [765](#)
- 344. D. Adamova, et al., *Phys. Lett. B* **666**, 425 (2008) [766](#)
- 345. E.L. Bratkovskaya, W. Cassing, *Phys. Lett. B* **670**, 428 (2009) [766](#), [768](#)
- 346. R. Arnaldi, et al. [NA60 Collaboration], *Phys. Rev. Lett.* **100**, 022302 (2008) [767](#), [768](#)
- 347. W.K. Wilson, et al., *Phys. Rev. C* **57**, 1865 (1998) [769](#)
- 348. E.L. Bratkovskaya, W. Cassing, M. Effenberger, U. Mosel, *Nucl. Phys. A* **653**, 301 (1999) [769](#)
- 349. C. Ernst, S.A. Bass, M. Belkacem, et al., *Phys. Rev. C* **58**, 447 (1998) [769](#)
- 350. K. Shekhter, C. Fuchs, et al., *Phys. Rev. C* **68**, 014904 (2003) [769](#)
- 351. E.L. Bratkovskaya, W. Cassing, R. Rapp, J. Wambach, *Nucl. Phys. A* **634**, 168 (1998) [769](#)
- 352. E.L. Bratkovskaya, C.M. Ko, *Phys. Lett. B* **445**, 265 (1999) [769](#)
- 353. M.I. Krivoruchenko, B.V. Martemyanov, A. Faessler, C. Fuchs, *Ann. Phys.* **296**, 299 (2002) [772](#)
- 354. A. Faessler, C. Fuchs, M.I. Krivoruchenko, B.V. Martemyanov, *Phys. Rev. C* **70**, 035211 (2004)

355. A.I. Titov, B. Kämpfer, B. L. Reznik Phys. Rev. C **65**, 065202 (2002) [772](#)
356. E.L. Bratkovskaya, W. Cassing, Nucl. Phys. A **807**, 214 (2008) [773](#)
357. M. Aguilar-Benitez, et al. [NA16 Collaboration], Phys. Lett. B **135**, 237 (1984) [775](#), [780](#)
358. M. Aguilar-Benitez, et al. [NA27 Collaboration], Z. Phys. C **40**, 321 (1988)
359. R. Ammar, et al. [E743 Collaboration], Phys. Rev. Lett. **61**, 2185 (1988)
360. K. Kodama, et al. [E653 Collaboration], Phys. Lett. B **284**, 461 (1991)
361. M.J. Leitch, et al. [E789 Collaboration], Phys. Rev. Lett. **72**, 2542 (1994)
362. S. Barlag, et al. [NA32 Collaboration], Z. Phys. C **39**, 451 (1988)
363. S. Barlag, et al. [NA32 Collaboration], Phys. Lett. B **247**, 113 (1990)
364. G.A. Alves, et al. [E769 Collaboration], Phys. Rev. Lett. **77**, 2388 (1996). [Ibid. 2392]
365. M. Adamovich, et al. [WA92 Collaboration], Nucl. Phys. B **495**, 3 (1997)
366. E.M. Aitala, et al. [E791 Collaboration], Eur. Phys. J. C **4**, 1 (1999)
367. S.S. Adler, et al. [PHENIX Collaboration], Phys. Rev. Lett. **92**, 051802 (2004). [Ibid. **96**, 012304 (2006); arXiv:hep-ex/0609032] [780](#)
368. C. Lourenco, Nucl. Phys. A **610**, 552c (1996) [775](#), [779](#)
369. B. Alessandro, et al. [NA50 Collaboration], Eur. Phys. J. C **33**, 31 (2004) [775](#), [776](#)
370. R. Arnaldi, et al. [NA60 Collaboration], Phys. Rev. Lett. **99**, 132302 (2007) [776](#)
371. H. Satz, Rept. Prog. Phys. **63**, 1511 (2000) [776](#)
372. M.C. Abreu, et al. [NA38 Collaboration], Phys. Lett. B **449**, 128 (1999) [776](#)
373. L. Ramello, et al. [NA50 Collaboration], Nucl. Phys. A **715**, 243 (2003) [777](#), [780](#)
374. B. Alessandro, et al. [NA50 Collaboration], Eur. Phys. J. C **39**, 335 (2005) [777](#)
375. A. Förster, et al. [NA60 Collaboration], J. Phys. G **32**, S51 (2006) [777](#)
376. A. Adare, et al. [PHENIX Collaboration], Phys. Rev. Lett. **98**, 232301 (2007) [777](#), [778](#)
377. S. Adler, et al. [PHENIX Collaboration], Phys. Rev. Lett. **96**, 032301 (2006) [777](#)
378. A. Dumitru, C. Spieles, Phys. Lett. B **446**, 326 (1999) [778](#)
379. N. Xu, Prog. Part. Nucl. Phys. **53**, 165 (2004) (And references therein) [793](#)
380. V. Greco, C.M. Ko, R. Rapp, Phys. Lett. B **595**, 202 (2004) [778](#), [793](#)
381. E. Scomparin, [NA60 Collaboration], J. Phys. G **34**, S463 (2007) [778](#), [779](#), [783](#), [785](#)
382. B. Zhang, C.M. Ko, B.A. Li, Z. Lin, B.H. Sa, Phys. Rev. C **62**, 054905 (2000) [778](#)
383. W. Cassing, K. Gallmeister, E.L. Bratkovskaya, C. Greiner, H. Stöcker, Prog. Part. Nucl. Phys. **53**, 211 (2004) [778](#)
384. O. Linnyk, E.L. Bratkovskaya, W. Cassing, Int. J. Mod. Phys. E **17**, 1367 (2008) [778](#), [781](#), [792](#)
385. C. Spieles, et al., Eur. Phys. J. C **5**, 349 (1998) [778](#), [779](#), [780](#)
386. C. Spieles, et al., Phys. Rev. C **60**, 054901 (1999) [778](#), [779](#), [780](#)
387. T. Sjöstrand, et al., Comput. Phys. Commun. **135**, 238 (2001) [779](#)
388. O. Linnyk, E.L. Bratkovskaya, W. Cassing, Nucl. Phys. A **807**, 79 (2008) [779](#)

- 389. H. Satz, J. Phys. G **36**, 064011 (2009) [781](#)
- 390. S. Datta, F. Karsch, P. Petreczky, I. Wetzorke, Phys. Rev. D **69**, 094507 (2004)
- 391. M. Asakawa, T. Hatsuda, J. Phys. G **30**, S1337 (2004) [781](#)
- 392. O. Linnyk, E.L. Bratkovskaya, W. Cassing, H. Stöcker, Nucl. Phys. A **786**, 183 (2007) [781](#), [782](#), [792](#)
- 393. B. Alessandro, et al. [NA50 Collaboration], Eur. Phys. J. C **49**, 559 (2007) [782](#)
- 394. L. Grandchamp, R. Rapp, Phys. Lett. B **523**, 60 (2001) [781](#), [783](#)
- 395. R. Rapp, L. Grandchamp, J. Phys. G **30**, S305 (2004) [783](#)
- 396. L. Grandchamp, R. Rapp, G.E. Brown, Phys. Rev. Lett. **92**, 212301 (2004) [783](#), [784](#), [790](#), [793](#)
- 397. X. Zhao, R. Rapp, Phys. Lett. B **664**, 253 (2008) [783](#), [784](#)
- 398. M.C. Abreu, et al. [NA50 Collaboration], Phys. Lett. B **499**, 85 (2001) [783](#), [784](#)
- 399. N.S. Topilskaya, et al. [NA50 Collaboration], Nucl. Phys. A **715**, 675 (2003) [783](#), [784](#)
- 400. L. Ramello, et al. [NA50 Collaboration], Nucl. Phys. A **638**, 261 (1998) [783](#), [784](#)
- 401. A. Capella, E.G. Ferreira, Eur. Phys. J. C **42**, 419 (2005) [784](#), [785](#)
- 402. S. Digal, S. Fortunato, H. Satz, Eur. Phys. J. C **32**, 547 (2004) [784](#), [785](#)
- 403. L. Grandchamp, R. Rapp, G.E. Brown, J. Phys. G **30**, S1355 (2004) [784](#), [785](#)
- 404. P. Braun-Munzinger, I. Heppe, J. Stachel, Phys. Lett. B **465**, 15 (1999) [785](#), [786](#)
- 405. R. Averbeck, R. Holzmann, V. Metag, R.S. Simon, Phys. Rev. C **67**, 024903 (2003)
- 406. P. Braun-Munzinger, J. Stachel, J.P. Wessels, N. Xu, Phys. Lett. B **365**, 1 (1996) [785](#), [786](#)
- 407. R. Vogt, Int. J. Mod. Phys. E **12**, 211 (2003) [786](#)
- 408. C. Lourenco, H. Wöhri, Phys. Rep. **433**, 127 (2006) [786](#)
- 409. A. Adare, et al. [PHENIX Collaboration], Phys. Rev. Lett. **97**, 252002 (2006) [786](#)
- 410. I. Abt, et al. [HERA-B Collaboration], Phys. Lett. B **638**, 407 (2006) [786](#)
- 411. L. Tolos, J. Schaffner-Bielich, H. Stöcker, Phys. Lett. B **635**, 85 (2006) [788](#)
- 412. X. Zhao, R. Rapp, arXiv:1008.5328 [792](#), [793](#)
- 413. G.F. Smoot, Rev. Mod. Phys. **79**, 1349 (2007) [796](#)
- 414. G.F. Smoot, et al., Astrophys. J. **396** (1992) [796](#)
- 415. D.N. Spergel, et al. [WMAP Collaboration], Astrophys. J. Suppl. **170**, 377 (2007) [796](#)
- 416. C.R. Allton, et al., Phys. Rev. D **71**, 054508 (2005) [798](#)
- 417. R.V. Gavai, S. Gupta, Phys. Rev. D **78**, 114503 (2008) [798](#)
- 418. V. Koch, arXiv:nucl-th/0810.2520 (2008) [798](#), [799](#)
- 419. J. Knoll, private communication (2009) [799](#)
- 420. J. Knoll, Nucl. Phys. A **821**, 235 (2009) [799](#)
- 421. J. Knoll, Acta Phys. Polon. B **40**, 1037 (2009) [799](#)
- 422. S. Pratt, Phys. Rev. Lett. **102**, 232301 (2009) [799](#)
- 423. H.W. Barz, B.L. Friman, J. Knoll, H. Schulz, Nucl. Phys. A **484**, 661 (1988) [799](#)

- 424. H.W. Barz, B.L. Friman, J. Knoll, H. Schulz, Nucl. Phys. A **519**, 831 (1990) [799](#)
- 425. S. Jeon, V. Koch, Phys. Rev. Lett. **85**, 2076 (2000) [800](#), [801](#)
- 426. M. Asakawa, U.W. Heinz, B. Müller, Phys. Rev. Lett. **85**, 2072 (2000) [800](#), [801](#)
- 427. Y. Hatta, M.A. Stephanov, Phys. Rev. Lett. **91**, 102003 (2003) [801](#)
- 428. C. Alt, et al. [NA49 Collaboration], Phys. Rev. C **70**, 064903 (2004) [801](#), [802](#)
- 429. H. Appelshäuser, et al. [CERES Collaboration], Nucl. Phys. A **752**, 394 (2005)
- 430. K. Adcox, et al. [PHENIX Collaboration], Phys. Rev. Lett. **89**, 082301 (2002) [801](#)
- 431. B.I. Abelev, et al. [STAR Collaboration], Phys. Rev. C **79**, 024906 (2009) [801](#)
- 432. J. Adams, et al., Phys. Rev. C **68**, 044905 (2003) [801](#)
- 433. V.P. Konchakovski, M.I. Gorenstein, E.L. Bratkovskaya, H. Stoecker, Phys. Rev. C **74**, 064911 (2006) [801](#)
- 434. V.P. Konchakovski, M. Gorenstein, E.L. Bratkovskaya, M. Bleicher, H. Stöcker, Phys. Rev. C **73**, 034902 (2006) [802](#), [803](#)
- 435. M. Rybczynski, et al. [NA49 Collaboration], J. Phys. Conf. Ser. **5**, 74 (2005) [802](#)
- 436. S.V. Afanasiev, et al. [NA49 Collaboration], Phys. Rev. Lett. **86**, 1965 (2001) [803](#)
- 437. C. Alt, et al. [NA49 Collaboration], Phys. Rev. C **79**, 044910 (2009) [803](#), [804](#), [805](#)
- 438. S. Das, et al. [STAR Collaboration], J. Phys. G **32**, S541 (2006) [803](#), [805](#)
- 439. M. Gorenstein, M. Hauer, V. Konchakovski, E. Bratkovskaya, Phys. Rev. C **79**, 024907 (2009) [804](#), [805](#)
- 440. S. Jeon, V. Koch, Phys. Rev. Lett. **83**, 5435 (1999) [805](#)
- 441. V. Koch, A. Majumder, J. Randrup, Phys. Rev. Lett. **95**, 182301 (2005) [805](#), [806](#), [807](#)
- 442. S. Haussler, H. Stöcker, M. Bleicher, Phys. Rev. C **73**, 021901 (2006) [807](#)
- 443. M.A. Stephanov, Phys. Rev. Lett. **102**, 032301 (2009) [807](#), [808](#), [818](#)
- 444. C. Miao, C. Schmidt, [RBC-Bielefeld Collaboration], PoS **LAT2008**, 172 (2008) [808](#)
- 445. E.V. Shuryak, Phys. Lett. B **423**, 9 (1998) [809](#)
- 446. M.A. Stephanov, K. Rajagopal, E.V. Shuryak, Phys. Rev. D **60**, 114028 (1999) [810](#)
- 447. H. Sako, H. Appelshäuser, [CERES Collaboration], J. Phys. G **30**, S1371 (2004) [810](#)
- 448. H. Appelsäuser, et al. [NA49 Collaboration], Phys. Lett. B **459**, 679 (1999) [810](#)
- 449. M. Rybczynski, et al. [NA49 Collaboration], J. Phys. G **35**, 104091 (2008) [810](#)
- 450. J. Adams, et al. [STAR Collaboration], Phys. Rev. C **71**, 064906 (2005) [810](#)
- 451. K. Adcox, et al. [PHENIX Collaboration], Phys. Rev. C **66**, 024901 (2002) [810](#)
- 452. S.S. Adler, et al. [PHENIX Collaboration], Phys. Rev. Lett. **93**, 092301 (2004). ArXiv:nucl-ex/0310005 [810](#)

- 453. D. Adamova, et al. [CERES Collaboration], Nucl. Phys. A **811**, 179 (2008) [810](#)
- 454. S. Jeon, V. Koch, *Quark Gluon Plasma 3* (R. Hwa, X. Wang (Eds.), World Scientific, Singapore), p. 430 (2004) [810](#)
- 455. K. Grebieszko, et al. [NA49 Collaboration], PoS **CPOD2007**, 022 (2007) [810](#), [811](#)
- 456. B. Berdnikov, K. Rajagopal, Phys. Rev. D **61**, 105017 (2000) [810](#)
- 457. J. Randrup, Acta Phys. Hung. **22**, 69 (2005) [812](#), [813](#), [816](#), [818](#)
- 458. I.N. Mishustin, Eur. Phys. J. A **30**, 311 (2006) [816](#)
- 459. M. Asakawa, S. Bass, B. Müller, C. Nonaka, Phys. Rev. Lett. **101**, 122302 (2008) [816](#), [817](#)
- 460. P. Chomaz, M. Colonna, J. Randrup, Phys. Rep. **389**, 263 (2004) [818](#)
- 461. B. Borderie, et al. [INDRA Collaboration], Phys. Rev. Lett. **86**, 3252 (2001) [818](#)
- 462. M. Morando (Ed.), International Symposium on Strangeness in Quark Matter 1998, J. Phys. G **25**, 1 (1999) [821](#), [823](#)
- 463. A.R. Bodmer, Phys. Rev. D **4**, 1601 (1971) [821](#)
- 464. R.L. Jaffe, Phys. Rev. Lett. B **38**, 195 (1977). [Erratum-ibid. **38**, 617 (1977)] [821](#)
- 465. J.T. Goldman, K. Maltman, G.J. Stephenson, K.E. Schmidt, F. Wang, Phys. Rev. Lett. **59**, 627 (1987) [821](#)
- 466. J.T. Goldman, K. Maltman, G.J. Stephenson, J.L. Ping, F. Wang, Mod. Phys. Lett. A **13**, 59 (1998) [821](#)
- 467. B. Schwesinger, F.G. Scholtz, H.B. Geyer, Phys. Rev. D **51**, 1228 (1995) [821](#)
- 468. C. Alt, et al. [NA49 Collaboration], Phys. Rev. Lett. **92**, 042003 (2004) [821](#)
- 469. R.J. Oakes, Phys. Rev. **131**, 2239 (1963) [821](#)
- 470. F.J. Dyson, N.H. Xuong, Phys. Rev. Lett. **13**, 815 (1964) [821](#)
- 471. L.M. Libby, Phys. Lett. B **29**, 345 (1969) [821](#)
- 472. S. Graffi, V. Grecchi, G. Turchetti, Lett. Nuovo Cim. **2**, 311 (1969) [821](#)
- 473. A.T.M. Aerts, P.J.G. Mulders, J.J. de Swart, Phys. Rev. D **17**, 260 (1978) [821](#)
- 474. C.W. Wong, K.F. Liu, Phys. Rev. Lett. **41**, 82 (1978)
- 475. A.T.M. Aerts, C.B. Dover, Phys. Lett. B **146**, 95 (1984)
- 476. Y.S. Kalashnikova, I.M. Narodetsky, Y.A. Simonov, Sov. J. Nucl. Phys. **46**, 689 (1987). [Yad. Fiz. **46**, 1181 (1987)]
- 477. J.T. Goldman, K. Maltman, G.J. Stephenson, K.E. Schmidt, F. Wang, Phys. Rev. C **39**, 1889 (1989)
- 478. J. Schaffner-Bielich, R. Mattiello, H. Sorge, Phys. Rev. Lett. **84**, 4305 (2000) [822](#), [824](#)
- 479. J. Schaffner-Bielich, Nucl. Phys. A **691**, 416 (2001) [821](#), [823](#)
- 480. J.K. Ahn, et al., Phys. Rev. Lett. **87**, 132504 (2001) [821](#)
- 481. H. Takahashi, et al., Phys. Rev. Lett. **87**, 212502 (2001) [821](#)
- 482. R.H. Dalitz, D.H. Davis, P.H. Fowler, A. Montwill, J. Pniewski, J.A. Zakrzewski, Proc. Roy. Soc. Lond. A **426**, 1 (1989) [821](#)
- 483. I.N. Filikhin, A. Gal, Phys. Rev. C **65**, 041001 (2002) [821](#)

484. J. Schaffner, H. Stoecker, C. Greiner, Phys. Rev. C **46**, 322 (1992) [822](#)
485. J. Schaffner, C.B. Dover, A. Gal, C. Greiner, H. Stoecker, Phys. Rev. Lett. **71**, 1328 (1993) [822](#)
486. E.P. Gilson, R.L. Jaffe, Phys. Rev. Lett. **71**, 332 (1993) [822](#)
487. J. Schaffner-Bielich, C. Greiner, A. Diener, H. Stoecker, Phys. Rev. C **55**, 3038 (1997) [822](#)
488. V.G.J. Stoks, T.A. Rijken, Phys. Rev. C **59**, 3009 (1999) [822](#), [823](#)
489. J. Schaffner-Bielich, A. Gal, Phys. Rev. C **62**, 034311 (2000) [822](#)
490. J. Belz, et al. [BNL-E888 Collaboration], Phys. Rev. Lett. **76**, 3277 (1996) [822](#)
491. J. Belz, et al., Phys. Rev. C **56**, 1164 (1997)
492. H.J. Crawford, Nucl. Phys. A **639**, 417 (1998) [822](#)
493. G. Appelquist, et al. [NA52 (NEWMASS) Collaboration], Phys. Rev. Lett. **76**, 3907 (1996) [822](#)
494. T.A. Armstrong, et al. [E864 Collaboration], Phys. Rev. Lett. **79**, 3612 (1997) [822](#)
495. L.E. Finch, [E864 Collaboration], Nucl. Phys. A **661**, 395 (1999) [822](#), [824](#)
496. T.A. Armstrong, et al. [E864 Collaboration], Phys. Rev. C **70**, 024902 (2004) [822](#), [824](#)
497. J.F. Donoghue, E. Golowich, B.R. Holstein, Phys. Rev. D **34**, 3434 (1986) [822](#)
498. M.I. Krivoruchenko, M.G. Shchepkin, Sov. J. Nucl. Phys. **36**, 769 (1982). [Yad. Fiz. **36**, 1328 (1982)] [822](#)
499. M. Bleicher, et al., J. Phys. G **25**, 1859 (1999) [823](#)
500. H. Petersen, J. Steinheimer, G. Burau, M. Bleicher, H. Stöcker, Phys. Rev. C **78**, 044901 (2008)
501. J. Steinheimer, M. Bleicher, H. Petersen, S. Schramm, H. Stöcker, D. Zschesche, Phys. Rev. C **77**, 034901 (2008) [823](#)
502. D.H. Rischke, S. Bernard, J.A. Maruhn, Nucl. Phys. A **595**, 346 (1995) [823](#)
503. D.H. Rischke, Y. Pursun, J.A. Maruhn, Nucl. Phys. A **595**, 383 (1995). [Erratum-ibid. **596**, 717 (1996)] [823](#)
504. D. Zschesche, S. Schramm, J. Schaffner-Bielich, H. Stoecker, W. Greiner, Phys. Lett. B **547**, 7 (2002) [823](#)
505. P. Braun-Munzinger, J. Stachel, J. Phys. G **21**, L17 (1995) [823](#), [824](#)
506. F. Becattini, U.W. Heinz, Z. Phys. C **76**, 269 (1997). [Erratum-ibid. **76**, 578 (1997)] [824](#)
507. J. Cleymans, K. Redlich, E. Suhonen, Z. Phys. C **51**, 137 (1991) [824](#)
508. A.J. Baltz, C.B. Dover, S.H. Kahana, Y. Pang, T.J. Schlagel, E. Schneidermann, Phys. Lett. B **325**, 7 (1994) [824](#)
509. J. Steinheimer, M. Mitrovski, T. Schuster, H. Petersen, M. Bleicher, H. Stöcker, arXiv:hep-ph/0811.4077 (2008) [824](#)
510. T. Satogata, Pos **CPOD07**, 051 (2007) [827](#)
511. A. Laszlo [NA61 Collaboration], Pos **CPOD07**, 054 (2007) [827](#)
512. V. Toneev, Pos **CPOD07**, 057 (2007) [827](#)

- 513. W. Cassing, Nucl. Phys. A **791**, 365 (2007) [829](#)
- 514. W. Cassing, Nucl. Phys. A **795**, 70 (2007)
- 515. W. Cassing, E.L. Bratkovskaya, Phys. Rev. C **78**, 034919 (2008) [829](#)

Part V

CBM Experiment

Conveners:

C. Höhne^{1,2,a} and P. Senger^{2,a}

Authors, who contributed to the various chapters or sections given in brackets:

A. Andronic² [A.15], F. Antinori³ [A.8], R. Averbeck² [A.12], R. Bellwied⁷ [A.14], V. Friese² [A.7], J. Heuser² [A.9], C. Höhne^{1,2} [1–4, A.1, A.5, A.13], R. Holzmann² [A.3], Y. Leifels² [A.2], D. Miśkowiec² [A.6, A.15], T. Peitzmann⁵ [A.10], D. Röhrich⁶ [A.11], E. Scapparini⁴ [A.9], P. Senger² [1–4, A.4], F. Uhlig² [A.4]

Affiliations:

¹University of Gießen, Gießen, Germany; ²GSF Helmholtzzentrum für Schwerionenforschung, Darmstadt, Germany; ³Istituto Nazionale di Fisica Nucleare, Padova, Italy; ⁴Università di Torino and INFN, Torino, Italy; ⁵Utrecht University, Utrecht, The Netherlands; ⁶University of Bergen, Bergen, Norway; ⁷Wayne State University, Detroit, Mi, USA

Support:

^aEU, FP6 Hadron Physics (I3HP) under Contract number RII3-CT-2004-506078

Chapter 1

Introduction

1.1 Exploring dense baryonic matter in the laboratory

High-energy heavy-ion collision experiments worldwide are devoted to the investigation of strongly interacting matter under extreme conditions. At the Relativistic Heavy Ion Collider (RHIC) at BNL intriguing observations have been made which support the picture that partonic degrees of freedom prevail in the early phase of the fireball evolution. These studies will be continued at even higher energies at the Large Hadron Collider (LHC) at CERN. The goal of the experiments at RHIC and LHC is to investigate the properties of deconfined QCD matter at very high temperatures and almost zero net baryon densities. This is a domain of the QCD phase diagram where modern Lattice-QCD calculations anticipate a smooth crossover from hadronic to partonic matter, leading to predictions for the critical temperature which vary between 150 and 190 MeV.

The region of the QCD phase diagram with the highest net-baryon densities can be reached in heavy-ion collisions at moderate collision energies which are and will be available at the Super-Proton-Synchrotron (SPS) at CERN, and at the Facility for Antiproton and Ion Research (FAIR) in Darmstadt. Structures observed in the excitation functions of strange-to-nonstrange particles, and of the inverse slope parameters of strange particles stimulated lively discussions on the possible onset of deconfinement at low SPS energies. At the high net-baryon densities reached in this energy range, the phase transition between hadronic and partonic matter is expected to be first order, featuring a region of phase coexistence and a critical end-point. The experimental discovery of these prominent landmarks of the QCD phase diagram would be a major breakthrough in our understanding of the properties of nuclear matter. Equally important is quantitative experimental information on the properties of hadrons in dense matter which may shed light on chiral symmetry restoration and the origin of hadron masses.

According to an analysis of particle yields in heavy-ion collisions, the maximum net-baryon density at freeze-out is reached at low CERN-SPS or FAIR energies [1]. This is illustrated in Fig. 1.1 which depicts the chemical freeze-out line as function of temperature and net-baryon density. The numbers refer to either the total collision energy (from 2+2 to 100+100 AGeV), or to laboratory kinetic energies for fixed target experiments (from 5 to 40 AGeV). The calculations indicate, that beam energies between 30 and 40 AGeV (on fixed target), or total energies between $\sqrt{s}=6$ and 10 AGeV are best suited to create the highest net-baryon densities in the laboratory.

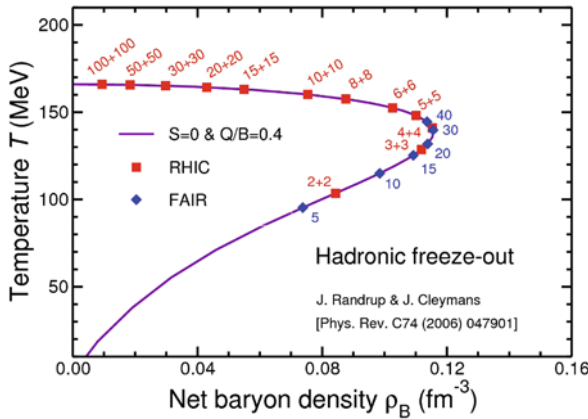


Fig. 1.1 The hadronic freeze-out *line* in the plane temperature versus net-baryon density as obtained in the statistical model with the values of μ_B and T that have been extracted from the experimental data in [2]. The *curve* corresponds to Au+Au collisions. The symbols represent beam energies (in AGeV) at either RHIC (total energy in each beam), or FAIR (kinetic energy of the beam for a stationary target). The figure is taken from [1].

In order to explore the QCD phase diagram at high net-baryon densities, several experimental programs are planned all over the world. The STAR and PHENIX collaborations at RHIC propose to scan the beam energies, and to search for the QCD critical endpoint [3]. For the same reason, future measurements are envisaged at CERN-SPS with the upgraded NA49 detector (NA61-SHINE) using light and medium size beams [4]. At the Joint Institute for Nuclear Research (JINR) in Dubna, a heavy-ion collider project (NICA) is discussed with the goal to search for the coexistence phase of nuclear matter [5]. Due to luminosity limitations these experiments are constrained to the investigation of bulk observables which are – except for elliptic flow – predominantly sensitive to the late and dilute phase of the collision when most of the particles freeze out. In contrast, the research program of the Compressed Baryonic Matter (CBM) experiment at FAIR is focused on the measurement of diagnostic probes of the early and dense phase of the fireball evolution. This approach offers the possibility to find signatures of partonic degrees-

of-freedom, and to discover the conjectured first order deconfinement phase transition and its critical endpoint. Another important goal is the study of in-medium modifications of hadron properties in order to shed light on the phenomenon of chiral symmetry restoration in dense hadronic and partonic matter.

Figure 1.2 depicts three snapshots of the evolution of a heavy-ion collision at FAIR energies, and illustrates the time of emission of various particle species. Particles containing charm quarks are expected to be created in the very first stage of the reaction. Vector mesons like ω , ρ and ϕ mesons are produced continuously via $\pi\pi$ annihilation during the course of the reaction, and decay either again into mesons, or into a pair of leptons. The latter decay channel is suppressed by about 4 orders of magnitude (corresponding to the square of the electromagnetic coupling constant $(1/137)^2$). However, as leptons are not affected by final-state interactions, this decay offers the possibility to look into the fireball. In particular the short-lived ρ meson is a promising diagnostic probe of hot and dense nuclear matter. Due to their small hadronic cross sections, also multi-strange hyperons and ϕ mesons carry information on the dense phase of the collision, in particular via their collective flow. Finally, the bulk of the particles freezes out at densities below saturation density. Up to date, essentially these freeze-out probes have been measured in heavy-ion collisions at beam energies between 2 and 40 AGeV (on stationary target). The CBM experiment is designed for the detection of signals from the high-density phase. These signals, however, are produced very rarely, either because of the low cross section (charm) or because of the small branching ratios into lepton pairs (low-mass vector mesons). Therefore,

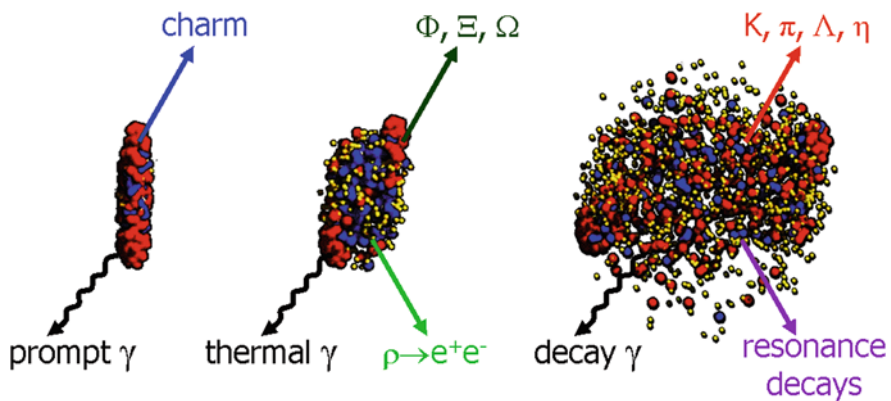


Fig. 1.2 Sketch of the expansion phase of a U+U collision at a laboratory beam energy of 23 AGeV at different time steps: initial stage where the two Lorentz-contracted nuclei overlap (*left*), high density phase (*middle*), and final stage (“freeze-out”) when all hadrons have been formed (*right*). Different particles are created in different stages of the collisions or escape from the interaction region at different times (see text). Almost 1,000 charged particles are created in such a collision, most of them are pions.

the CBM experimental program can only be realized with a combination of fast detector systems and high beam luminosity as provided by the FAIR accelerators [6].

The CBM research program comprises a comprehensive scan of observables, beam energies and collision systems. The observables include low mass dilepton pairs, charmonia and open charm, but also collective flow of rare and bulk particles, correlations and fluctuations. The experimental goal is to measure these rare probes with unprecedented precision in spite of the very low multiplicities. Figure 1.3 quantifies the notation “rare probes” in terms of the product of particle multiplicity times branching ratio. The points are calculated for central Au+Au collisions at 25 AGeV using either the HSD transport code [7], or a thermal model assuming values for temperature and baryon chemical potential corresponding to a beam energy of 25 AGeV [8]. Mesons containing charm quarks are suppressed by about 9 orders of magnitude with respect to the pions (the ψ' meson is even more suppressed). The yield of lepton pairs from vector meson decays is about 6 orders of magnitude below the pion yield, similar to the yield of multi-strange hyperons.

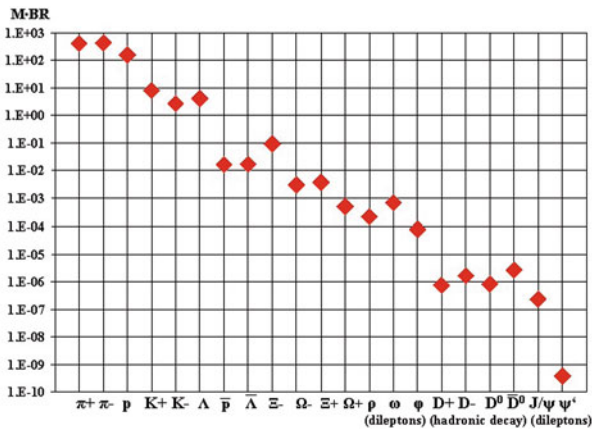


Fig. 1.3 Particle multiplicities times branching ratio for central Au+Au collisions at 25 AGeV as calculated with the HSD transport code [7] and the statistical model [8]. For the vector mesons (ρ , ω , ϕ , J/ψ , ψ') the decay into lepton pairs was assumed, for D mesons the hadronic decay into kaons and pions.

In order to compensate for the low yields the measurements will be performed at exceptionally high reaction rates (up to 10 MHz for certain observables). These conditions require the development of ultra fast and extreme radiation hard detectors and electronics. A particular challenge for the detectors, the front-end electronics and the data acquisition is the online selection of displaced vertices with extraordinary high speed and precision which is needed for open charm measurements.

The CBM detector is designed as a multi-purpose device which will be able to measure hadrons, electrons and muons in heavy-ion collisions. The optimization of the detector design is carried out through extensive feasibility studies which are performed within a newly developed software framework. The results of the simulations demonstrate that the anticipated observables including the rare probes can be measured with the proposed setup. Hardware development concentrates on highly granular, fast and radiation-hard detectors, on data-driven and fast read-out electronics, and on a high-speed data acquisition. In conclusion, the CBM experimental setup is optimized to reinvestigate with new probes a very promising territory of the QCD phase diagram, and thus has a unique discovery potential.

The experimental studies of dense baryonic matter at FAIR will be synchronized with the availability of the accelerators. In the first stage of the realization of FAIR the beams will be delivered by the SIS100 accelerator with energies up to 11 AGeV for Au, 14 AGeV for Ca, and 29 GeV for protons. In order to measure electron-positron pairs in heavy-ion collisions at energies up to 8 AGeV the HADES detector will be installed. For the measurement of multi-strange hyperons in heavy-ion collisions, and of charmed particles in proton induced reactions at SIS100, a reduced version of the CBM detector will be sufficient. Once the beams from SIS300 will be available (35 AGeV for Au and 89 GeV for protons) the full CBM detector system will be ready.

1.2 The facility of antiproton and ion research

A sketch of FAIR together with the existing GSI facilities is presented in Fig. 1.4. FAIR comprises two synchrotrons with rigidities of 100 and 300 Tm (SIS100/300), the Superconducting Fragment Separator (Super-FRS), the storage ring for antiprotons (High-energy Storage Ring HESR), the Collector Ring (CR), and the New Experimental Storage Ring (NESR). The experimental facilities include the CBM experiment, the PANDA detector for hadron physics experiments using cooled high-energy antiproton beams, the NUSTAR detectors used for experiments on the structure of unstable nuclei and on nuclear astrophysics, and experimental setups for Plasma Physics (PP) and Atomic Physics (AP). First beams delivered from SIS100 are scheduled for the year 2018, from SIS300 about 2 years later.

Beams to HADES and CBM will be delivered by the SIS100 and SIS300 synchrotrons. The available kinetic beam energy per nucleon depends essentially on the bending power $B \cdot r$ provided by the dipole magnets:

$$E/A = \sqrt{(0.3 \cdot B \cdot r \cdot Z/A)^2 + m^2} - m \quad (1.1)$$

With Z and A being the charge and atomic number of the ion, and m the mass of the nucleon. The beam energies obtained for the maximum beam

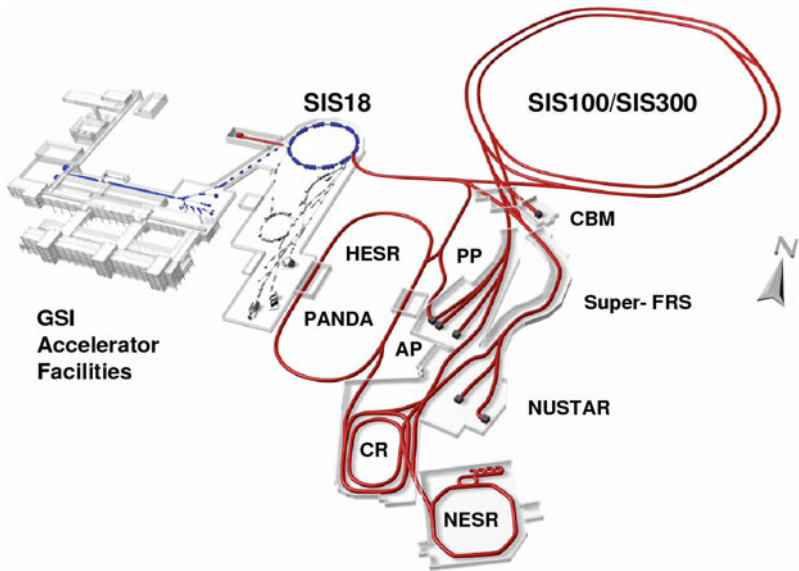


Fig. 1.4 Layout of FAIR [6].

Table 1.1 Ion species and their kinetic energy per nucleon for a beam rigidity of 100 Tm at the SIS100 and 300 Tm at the SIS300.

Beam	Z	A	E/AGeV SIS100	E/AGeV SIS300
p	1	1	29	89
d	1	2	14	44
Ca	20	40	14	44
Ni	28	58	13.6	42
In	49	115	11.9	37
Au	79	197	11	35
U	92	238	10.7	34

rigidity of SIS300 ($B \cdot r = 300 \text{ Tm}$) are listed in Table 1.1 for different ion species. The minimal available ion beam energy is about 2 AGeV.

1.3 Nuclear matter research at FAIR

1.3.1 Experiments at SIS100

Heavy-ion beams in the energy range between 2 and about 14 AGeV are ideally suited to explore the properties of dense baryonic matter. According to transport calculations, energy densities up to 2.5 GeV fm^{-3} and baryon

densities of 2–7 times saturation density ρ_0 are expected to be reached in the center of the reaction zone. Such conditions prevail in core collapse supernovae and in the core of neutron stars. Measurements at SIS100 energies will focus on the investigation of the properties of resonance matter in the vicinity of the phase boundary, and, therefore, will provide important information on this transition region of the QCD phase diagram. The following fundamental questions can be addressed experimentally with heavy-ion collisions at SIS100:

- What is the electromagnetic structure of dense baryonic matter?
- What are the properties of hadrons in dense baryonic matter?
- Is chiral symmetry restored at very high baryon densities?
- What is the equation-of-state of nuclear matter at neutron star core densities?
- What are the relevant degrees-of-freedom in the vicinity of the deconfinement phase transition?
- Does strange matter exist in the form of heavy multi-strange objects?
- How is charm produced at threshold beam energies?
- How does charm propagate in nuclear matter?

The heavy-ion experiments at SIS100 will concentrate on the measurement of the following observables:

As discussed in [Part IV](#) the production of multi-strange hyperons at threshold beam energies proceeds via strangeness exchange reactions in multi-step processes. The “cooking” of Ξ and Ω hyperons is favored at high densities where the mean free path between consecutive collisions is short. Therefore, the yield of multi-strange hyperons depends very much on the density, and, hence, on the compressibility of baryonic matter at these particular densities. In conclusion, a detailed measurement of the excitation function of the multiplicities and the collective flow of multi-strange hyperons in heavy-ion collisions at beam energies between 2 and 11 AGeV will provide new information on the equation-of-state of nuclear matter at high densities. No multi-strange particles have been measured in heavy-ion collisions in this energy range (except for a Ξ data point at 6 AGeV).

According to model calculations, the yield of meta-stable exotic multi-hypernuclear clusters (consisting of nucleons and hyperons) increases with increasing baryon density, and has a maximum in heavy-ion collisions at FAIR energies (see [Part IV](#)). Therefore, the search for composite objects with multiple units of strangeness is very promising at SIS100. These objects can be identified e.g. via their weak decay into a pair of lambda hyperons.

The yields and momenta of hadrons will be analyzed event-wise in order to search for nonstatistical fluctuations which are predicted to occur when the system passes through the coexistence phase of the anticipated first order deconfinement phase transition. In order to subtract the (dominant) contributions from resonance decays one has to measure the yields of the relevant short-lived particles such as the ϕ and the K^* mesons. Measurements of

hadrons including multi-strange hyperons will be performed with a start version of CBM comprising the dipole magnet, the silicon tracking system, and a time-of-flight wall.

Measurements of dilepton pairs permit to investigate the in-medium spectral functions of low-mass vector mesons which are expected to be modified due to effects of chiral symmetry restoration in dense matter. So far no dilepton measurements have been performed in this energy range. Electron-positron pairs will be measured with the HADES setup for energies up to 8 AGeV and further on with the CBM startup version supplemented by a RICH detector.

In addition to the experiments with heavy ion beams pioneering measurements on charm production in nuclear collisions will become possible with proton beams of energies up to 29 GeV. These experiments address important questions such as the production mechanism of charm-anticharm pairs at threshold energies, and the properties of charmed particles in nuclear matter at saturation density. In addition, the propagation of charm in cold nuclear matter can be investigated by varying the size of the target nucleus. These measurements are complementary to the PANDA research program on charm in nuclear matter. Moreover, the charm data obtained in proton induced reactions serve as a reference for nucleus-nucleus collisions. Up to date, no data on charmonium production have been measured in nuclear collisions below top SPS energies. Open charm has not been measured at all in heavy-ion collisions, except for an excess of high energy electrons observed at RHIC which is attributed to the semi-leptonic decays of D mesons.

The identification of particles with open charm requires the CBM start version equipped with an additional small micro-vertex detector for reconstruction of displaced vertices of D mesons. For the identification of charmonium in proton-nucleus collisions a reduced version of the planned CBM muon detection system has to be installed.

1.3.1.1 HADES at SIS100

HADES will be placed in front of the CBM detector as sketched in Fig. 1.5. The beam enters from the lower left corner of the picture. The beam can be focused either at the target position of HADES (left setup), or at the CBM target (right setup). In order to study the physics performance of HADES for SIS100 beam energies, simulations of dilepton and hadron production have been performed for Au+Au collisions at 8 AGeV (for details see [9]). It turns out that the phase space acceptance for hadrons and for dielectrons from ω meson decays is shifted towards target rapidity but still covers midrapidity. The overall acceptance for dielectron pairs at 8 AGeV beam energy is 21% compared to 33% at 2 AGeV. In order to handle the high multiplicities in Au+Au collisions HADES is being upgraded with a highly segmented TOF detector based on Resistive Plate Chamber (RPC) technology. The data acquisition has been already upgraded to a bandwidth of 20 kHz. Moreover,

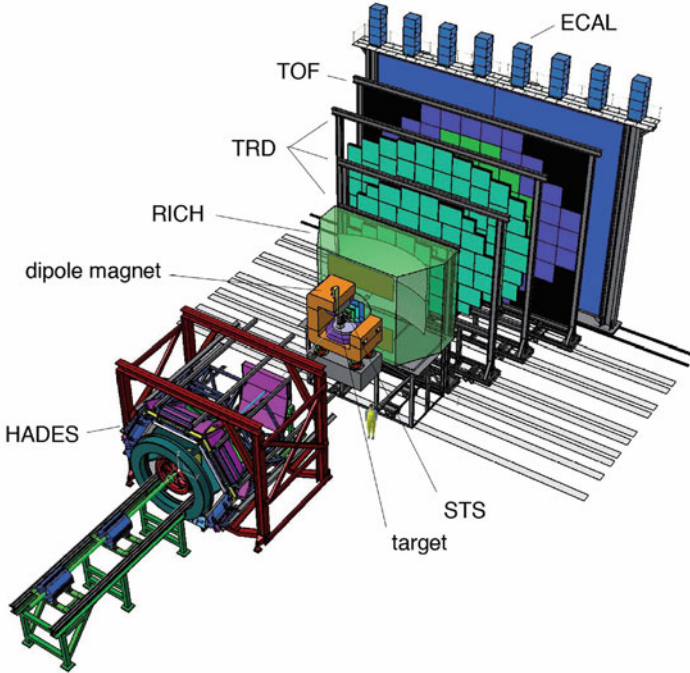


Fig. 1.5 Sketch of the planned Compressed Baryonic Matter (CBM) experiment together with the HADES detector.

the HADES Pre-Shower detector will be replaced by a lead-glass calorimeter which also will enable the measurement of η mesons via photon decays.

The performance of HADES for electron-positron measurements at SIS100 beams energies is illustrated in Fig. 1.6 which depicts the di-electron invariant mass spectrum for Au+Au collisions at 8 AGeV as simulated in a Monte-Carlo study. For this simulation all meson sources were generated simultaneously with proper weights using the PLUTO code (version 4.08) [10]. The multiplicities were taken from data (if available): π^0 and η yields were calculated according to the TAPS measurement for C+C and Ca+Ca collisions at 1–2 AGeV beam energy [11]. Probabilities for ω and ϕ production were obtained from an m_t -scaling ansatz. For a beam energy of 8 AGeV the production probabilities of π^0 per participant were derived from the experimental data published in [12]. As experimental data for the other mesons are missing at this energy, the ratios for η , ω and ϕ mesons were obtained from a thermal model [13].

The HADES geometry is included in these simulations by filtering the generated events with acceptance matrices that take into account the momenta, azimuthal and polar angles of the leptons. Lepton momenta were smeared in order to take into account the detector resolution. Close lepton pairs are rejected by an opening angle cut of 9° . No misidentified particles or

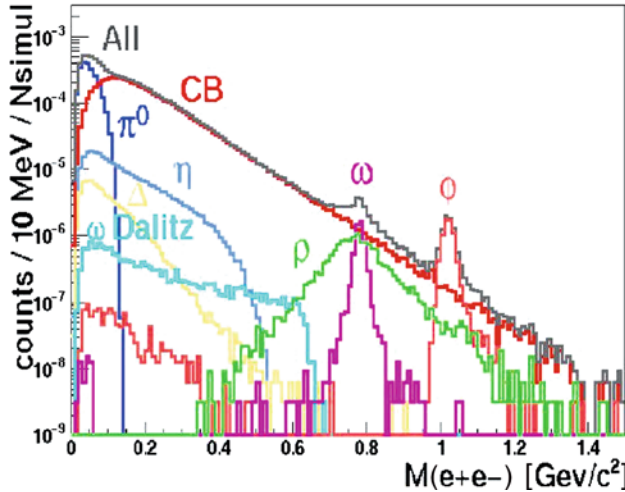


Fig. 1.6 Simulated invariant-mass distribution of dilepton pairs in the HADES experiment per minimum bias Au+Au collision at 8 AGeV beam energy. The simulated cocktail (*black line*) and combinatorial background (*red line*), as well as various cocktail components are shown.

reconstruction efficiencies, nor electrons from γ conversion in the target are taken into account. The spectrum represents $3.2 \cdot 10^7$ minimum bias Au+Au collisions at 8 AGeV beam energy ($b=0-8$ fm, 228 participants on average).

1.3.1.2 CBM at SIS100

The yields, spectra and collective flow of (multi-)strange hyperons are sensitive diagnostic probes of the early and dense fireball, and, therefore, are prime observables in heavy-ion collisions at SIS100. Λ , Ξ , and Ω hyperons can be identified via the topology of their weak decays ($\Lambda \rightarrow p\pi$, $\Xi \rightarrow \Lambda\pi$, $\Omega \rightarrow \Lambda K$) as illustrated in Fig. 1.7. Such a measurement requires a tracking detector inside a magnetic field.

Figure 1.8 depicts the invariant mass spectra for Λ , Ξ , and Ω hyperons simulated for central Au+Au collisions at 6 AGeV after applying cuts on the decay topology without particle identification. The simulation is based on full track reconstruction of UrQMD events transported through the CBM Silicon detector stations using the GEANT code. The combinatorial background can be further reduced by identifying the decay protons by a time-of-flight measurement.

The total efficiencies for multi-strange hyperons including geometrical acceptance, track reconstruction efficiency, and after applying cuts for background reduction are $\epsilon(\Lambda) = 7.4\%$, $\epsilon(\Xi) = 2.6\%$, and $\epsilon(\Omega) = 2.0\%$ for

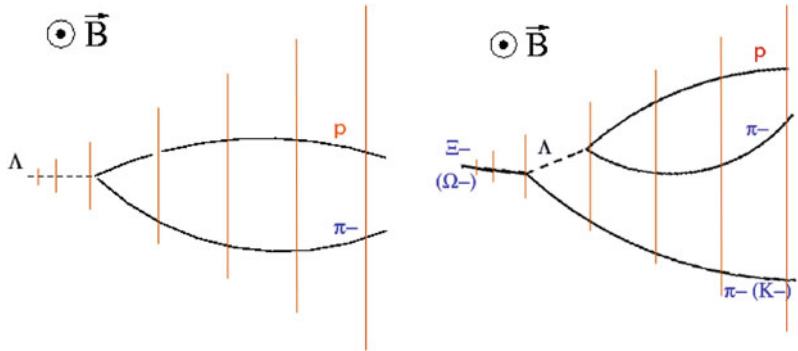


Fig. 1.7 Decay topologies of hyperons. Detector planes are indicated as *lines*, the magnetic field is perpendicular to the plane.

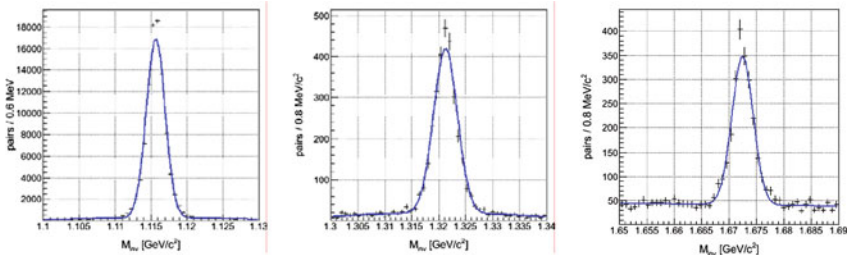


Fig. 1.8 Reconstruction of Λ , Ξ^- , and Ω^- hyperons (from *left to right*) in central Au+Au collisions at 6 AGeV after applying topological cuts only. Further background reduction can be achieved by proton identification with a time-of-flight wall.

central Au+Au collisions at 6 AGeV. The proposed measurements require a slowly extracted heavy-ion beam from SIS100 with an intensity of about 10^7 ions/s and a 1% interaction target, corresponding to a rate of 10^4 /s for the 10% most central events. The resulting yields per week are listed in Table 1.2 for central A+Au collisions at energies between 4 and 10 AGeV, taking into account multiplicities as calculated with a statistical model, and using the total detection efficiencies mentioned above.

Table 1.2 Hyperon yields per week at a reaction rate of 10^4 /s central Au+Au collisions. The multiplicities per event have been calculated with a statistical model.

Beam energy (AGeV)	Ξ^-	Ω^-	Anti- Λ	Ξ^+	Ω^+
4.0	1.7×10^7	2.3×10^5	9.8×10^4	8.9×10^4	1.2×10^3
6.0	4.3×10^7	6.8×10^5	2.5×10^5	2.3×10^5	3.6×10^3
8.0	6.9×10^7	1.9×10^6	3.6×10^6	3.7×10^6	8.0×10^4
10.7	9.2×10^7	3.0×10^6	6.8×10^6	7.1×10^6	1.6×10^5

The identification of D mesons produced in 30 GeV proton–carbon collisions has been simulated for the CBM start version. In this case, the average multiplicities are very low, about 2–3 tracks per event. The setup comprised 8 layers of silicon micro-strip detectors, and a micro-vertex detector consisting of two layers of Monolithic Active Pixel Sensors (details see next chapter). The background was generated by the UrQMD code, the D meson multiplicities were calculated with the HSD event generator, the particles were transported through the detector system inside the magnetic dipole field using GEANT3, and the tracks were reconstructed with a Cellular Automaton algorithm and a Kalman filter. D mesons are identified via their hadronic decays into pions and kaons. In order to reduce the background of mesons which are directly produced in the collision, promptly emitted particles have to be suppressed. However, due to the low particle multiplicity, the primary vertex cannot be determined with good precision. Therefore, only vertices are selected which are located at a distance between 400 and 1,000 μm downstream of the center of the target which has a thickness of 400 μm . The resulting invariant mass spectra of $K^-\pi^+\pi^+$ and $K^+\pi^-\pi^-$ are shown in Fig. 1.9. For the multiplicities given by HSD, a yield of 183 D^+ mesons and 327 D^- mesons can be obtained in 10^{12} collisions, corresponding to a measuring time of about 2 days.

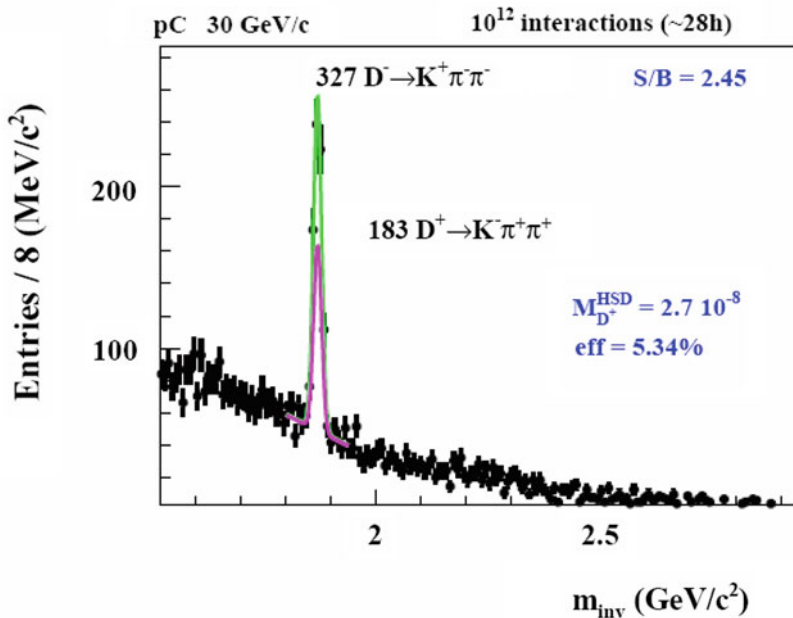


Fig. 1.9 Invariant mass spectrum of $K^-\pi^+\pi^+$ and $K^+\pi^-\pi^-$ simulated for 30 GeV p+C collisions. The spectrum can be obtained in a beam time of about 2 days.

1.3.2 Experiments at SIS300

The heavy-ion beams from SIS300 are required for the CBM core research program which is the search for the most prominent landmarks of the QCD phase diagram at high net baryon densities: the first order deconfinement phase transition and the critical endpoint. Moreover, the research program at SIS300 includes the study of the equation-of-state of high-density baryonic matter, and the search for modifications of hadronic properties in the dense baryonic medium as signatures for chiral symmetry restoration.

As pointed out in the previous chapters, the most promising observables from nucleus-nucleus collisions in the SIS300 energy range are:

- particles containing charm quarks (D mesons and charmonium): heavy quarks are created in the early phase of the collision and, hence, probe the highly compressed baryonic matter.
- low-mass vector mesons decaying into dilepton pairs (ρ , ω and ϕ mesons): electron and muon pairs are penetrating probes which carry undisturbed information on hadron properties in the dense and hot fireball.
- the collective flow of identified hadrons: the flow is driven by the pressure created in the early phase of the collision and carries information on the equation-of-state of dense matter.
- kaons, hyperons (Λ , Ξ , Ω and their antiparticles) and hadronic resonances (as ϕ , K^* , Λ^*): the yield of particles carrying strange quarks is expected to be sensitive to the fireball evolution.
- dynamical fluctuations of particle multiplicities and momenta: event-wise fluctuations are expected to occur if the system passes a first order phase transition or the critical endpoint.
- photons: photons are penetrating probes and can provide information on direct radiation from the early fireball
- two-particle correlations: two-particle correlations carry information on the source size and time evolution of the fireball and particle production

Phase transitions occur above a critical energy density and can only be observed if the matter extends over a certain volume. Therefore, a key feature of the CBM experimental program is a systematic and comprehensive measurement of excitation functions and system size dependencies of all observables.

Particular emphasis will be put on rare diagnostic probes which are not accessible by other experiments in this energy range. The identification of rare probes requires high beam intensities, a large duty cycle, excellent beam quality, and running times of several months per year. Observables like event-by-event fluctuations require full azimuthal coverage of the produced particles in a wide acceptance of rapidity and transverse momentum and excellent centrality determination.

In the following we review the CBM detector concept and the results of the feasibility studies for the various observables.

Chapter 2

The CBM detector concept

The goal of the experiment is to measure multiplicities, phase-space distributions and flow of protons, pions, kaons, hyperons, hadronic resonances, light vector mesons, charmonium and open charm including their correlations and event-by-event fluctuations in heavy-ion collisions. The technical challenge of the CBM experiment is to identify both, hadrons and leptons, and to filter out rare probes at reaction rates of up to 10 MHz with charged particle multiplicities of up to 1,000 per event. Measurements at these high rates cannot be performed with slow detectors like Time-Projection Chambers (TPC), but rather require extremely fast and radiation hard detector (and electronic) components. Moreover, the experiment has to provide lepton identification, high-resolution secondary vertex determination and a high speed trigger and data acquisition system. The CBM detector system will have the capability to measure both electrons and muons. This approach combines the advantages of both methods, and guarantees reliable results as in the end both data sets should agree to each other in spite of the very different background sources. Details of the CBM research program and of the setup can be found in the FAIR Baseline Technical Report [6]. The layout of the CBM experimental setup is sketched in Figs. 2.1 and 2.2.

The heart of the experiment will be a silicon tracking and vertex detection system installed in a large acceptance dipole magnet. The Silicon Tracking System (STS) consists of low-mass silicon micro-strip detectors possibly complemented by one or two hybrid-pixel detector layers providing unambiguous space point measurements. The STS allows for track reconstruction in a wide momentum range from about 100 MeV up to more than 10 GeV with a momentum resolution of about 1%.

The Micro-Vertex Detector (MVD) is needed to determine secondary vertices with high precision for D meson identification. The MVD consists of two layers of ultra-thin and highly-granulated Monolithic Active silicon Pixel Sensors (MAPS) which are located close to the target.

The measurement of electrons will be performed with a Ring Imaging Cherenkov (RICH) detector (for momenta below 8–10 GeV/c) together with

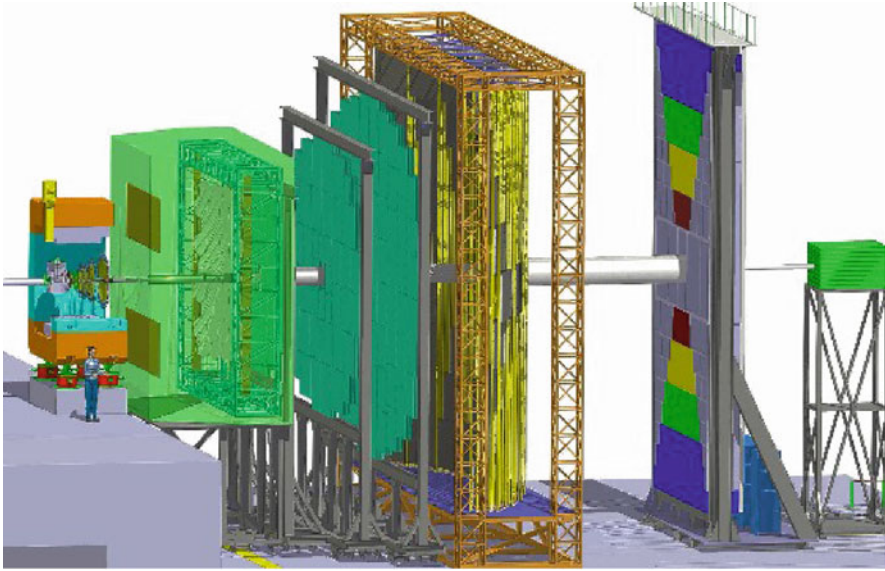


Fig. 2.1 The Compressed Baryonic Matter (CBM) experiment. The CBM setup consists of a large acceptance dipole magnet, radiation-hard Silicon pixel/strip detectors for tracking and vertex determination (STS, MVD), a Ring Imaging Cherenkov detector (RICH) and Transition Radiation Detectors (TRD) for electron identification, Resistive Plate Chambers (RPC) for time-of-flight measurement, an Electromagnetic Calorimeter (ECAL) for photon identification, and a Projectile Spectator Detector (PSD) for centrality and reaction plane determination.

Transition Radiation Detectors (TRD) for electrons with momenta above 1.5 GeV/c.

Muons will be measured with an active hadron absorber system consisting of iron layers and muon tracking chambers (MuCh). For muon measurements the MuCh will be moved to the position of the RICH.

Charged hadron identification will be performed by a time-of-flight (TOF) measurement with a wall of RPCs located at a distance of 10 m behind the target.

The setup is complemented by an Electromagnetic Calorimeter (ECAL) in selected regions of phase space providing information on photons and neutral particles, and by a Projectile Spectator Detector (PSD) needed for the determination of the collision centrality and the orientation of the reaction plane.

A key feature of the CBM experiment is online event selection which requires free streaming read-out electronics and fast algorithms running on computer farms based on future many-core architectures.

The CBM detector components required for the measurement of the different observables are listed in Table 2.1.

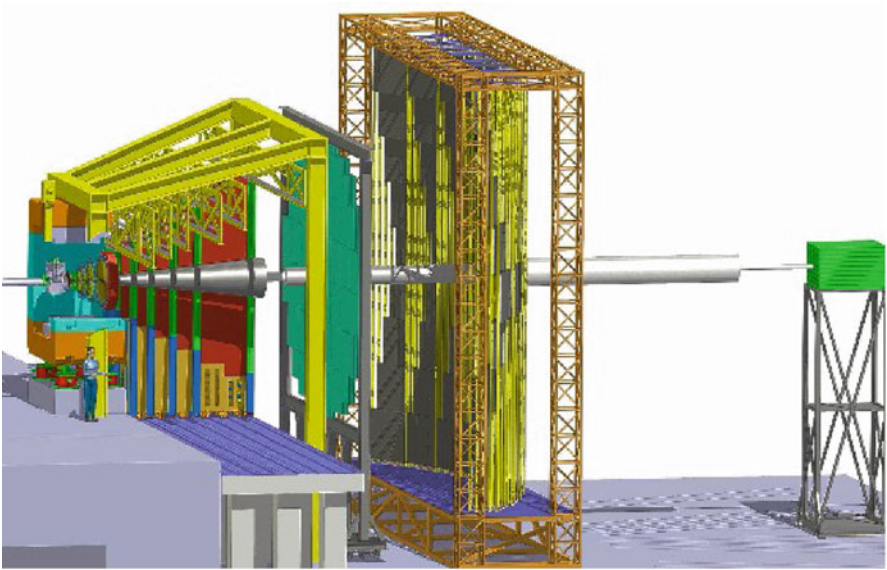


Fig. 2.2 The Compressed Baryonic Matter (CBM) experiment with a muon detection system (MuCh) with alternating absorber and detector layers instead of the RICH as shown in Fig. 2.1.

Table 2.1 Observables and required detectors: Micro-Vertex Detector MVD, Silicon Tracking Station STS, Ring Imaging Cherenkov detector RICH, Muon Chambers MuCh, Transition Radiation Detector TRD, timing Resistive Plate Chambers RPC, Electromagnetic Calorimeter ECAL, Projectile Spectator Detector PSD. Detectors marked as (x) can be used to suppress background.

Observables	MVD	STS	RICH	MuCh	TRD	RPC	ECAL	PSD
π , K, p		x	(x)		(x)	x		x
Hyperons		x			(x)	(x)		x
Open charm	x	x	(x)		(x)	(x)		x
Electrons	x	x	x		x	x		x
Muons		x		x		(x)		x
Photons							x	x
Photons via e^\pm conversion	x	x	x		x	x		x

2.1 The Silicon Tracking System (STS)

The task of the STS is to provide track reconstruction and momentum determination of charged particles. The multiplicity of charged particles is up to 600 per event within the detector acceptance. In its currently studied versions the STS consists of up to 8 tracking layers of silicon detectors. They are located downstream of the target at distances between 30 and 100 cm in

a magnetic dipole field of about 1 Tm bending power. The required momentum resolution is of the order of $\Delta p/p = 1\%$. This performance can only be achieved with an ultra low material budget of the stations, imposing particular restrictions on the location of power-dissipating front-end electronics in the fiducial volume. The concept of the STS tracking is based on silicon micro-strip detectors on lightweight ladder-like mechanical supports. The sensors will be read out through multi-line micro-cables with fast electronics at the periphery of the stations where cooling lines and other infrastructure can be placed. The development of the components of the tracking stations are subject to focussed R&D activities. The micro-strip sensors will be double-sided with a stereo angle of 15° , a strip pitch of $60\text{ }\mu\text{m}$, strip lengths between 20 and 60 mm, and a thickness of $250\text{--}300\text{ }\mu\text{m}$ of silicon. The micro-cables will be built from sandwiched polyimide-Aluminum layers of several $10\text{ }\mu\text{m}$ thickness. The total material budget including support structures and cables may amount to about $400\text{--}800\text{ }\mu\text{m}$ silicon equivalent, but is not homogeneous. The typical hit resolution achieved will be of the order of $25\text{ }\mu\text{m}$. As the projective geometry of the micro-strip detectors results in a combinatorial hit point pattern, the first two stations might be built from LHC-type hybrid pixel detectors, providing unambiguous hit points in pixels of 70 by $100\text{ }\mu\text{m}$ size where the track densities are highest. The material of a pixel detector station, including support structures, may be of about $800\text{ }\mu\text{m}$ silicon equivalent.

2.2 The Micro-Vertex Detector (MVD)

The identification of D mesons via their weak hadronic decay into pions and kaons requires a dedicated Micro-Vertex Detector in addition to the STS. The D meson lifetimes are $\tau = 123\text{ }\mu\text{m}/c$ for D^0 and $\tau = 314\text{ }\mu\text{m}/c$ for D^\pm . In order to suppress the background of promptly emitted pions and kaons one has to determine the secondary decay vertices of D mesons with extremely high precision. This task requires detectors with excellent position resolution and a very low material budget in order to reduce multiple scattering. These requirements are met by Monolithic Active Pixel Sensors (MAPS). The pixel size will be between $25 \times 25\text{ }\mu\text{m}^2$ and $40 \times 40\text{ }\mu\text{m}^2$. For the latter size a position resolution of $\sigma = 3\text{ }\mu\text{m}$ can be achieved. The goal of the detector development is to construct MAPS detector stations with a total thickness of about $300\text{ }\mu\text{m}$ silicon equivalent for sensors and support structures, however, $500\text{ }\mu\text{m}$ silicon equivalent might be more realistic in particular for the larger stations. The MVD consists of 2 MAPS layers located 10 and 20 cm downstream the target. A 3rd MAPS station might be located at only 5 cm behind the target. Due to its smallness this station could be particularly thin, i.e. less than $300\text{ }\mu\text{m}$, because less material is required for cables and cooling. This detector arrangement permits to determine the secondary decay vertex of a D mesons with a resolution of about $(50\text{--}100)\text{ }\mu\text{m}$ along the beam axis,

the actual resolution depending on the thickness of the first MAPS station and its distance to the target.

The MAPS detector R&D is focused on the improvement of radiation tolerance and readout speed. The goal is to develop detectors which survive a radiation dose of 10^{13} n_{eq} which corresponds to 10^{12} minimum bias Au+Au collisions at 25 AGeV. The design value for the readout speed is 10 μs . As the beam from SIS 300 will not come in bunches but continuously, we expect few events piling up randomly in one readout frame of the MAPS detector if running with 100 kHz interaction rate. Simulations demonstrate that a pile-up of up to 10 events in the MAPS detectors can be tolerated with only minor deterioration of the performance. At this reaction rate the detector can run about 4 months before the inner part of the first MAPS has to be replaced.

The MVD will be installed for dedicated measurements of open charm where the secondary vertex has to be determined with high resolution, and for electron measurements where close pairs have to be rejected in order to reduce the combinatorial background (see Sect. 3.5 and 3.6.1). The MVD information improves hyperon identification and the detector might be used also for this purpose.

2.3 The Ring Imaging CHerenkov detector (RICH)

The RICH detector is designed to provide identification of electrons and suppression of pions in the momentum range below 8 GeV/c. The version of the RICH detector used in the feasibility studies presented in this chapter comprises the following components: a 2.9 m long gas vessel filled with nitrogen as a radiator material (pion threshold for Cherenkov radiation is 5.6 GeV/c), a glass mirror (radius of curvature 4.5 m, thickness 3 mm), and two photodetector planes (each $(1.7 \times 0.7) \text{ m}^2$) consisting of Hamamatsu multi-anode photo multipliers. In the simulations discussed below values for photon absorption in the radiator gas, the reflectivity of the mirror and the quantum efficiency of the photodetector have been taken from literature. Entrance and exit windows of the gas vessel are taken into account. The number of measured photons per ring is about 20. Due to pair conversion of gamma rays in the material in front of the RICH about 100 rings are detected per central Au+Au collision at 25 AGeV. With the current setup a pion suppression on the order of 500–1,000 is achieved for $p \lesssim 10 \text{ GeV/c}$. Including TRD and RPC information this factor can be increased considerably up to 10^4 . Further simulations are being performed to optimize the size and geometry of the RICH with respect to performance and costs. The same performance can e.g. be kept when reducing the overall size by a factor 2–3 by choosing CO_2 as radiator gas and a mirror of radius 3 m.

2.4 The Transition Radiation Detector (TRD)

Three Transition Radiation Detector stations each consisting of 3–4 detector layers will serve for particle tracking and for the identification of electrons and positrons with $p > 1.5 \text{ GeV}/c$ ($\gamma > 1,000$). The detector stations are located at appr. 5, 7.2 and 9.5 m downstream the target, the total active detector area amounts to about 1100 m^2 . The detector development concentrates on the improvement of the electron identification performance, and on the development of highly granular and fast gaseous detectors in particular for the inner part of the detector planes covering forward emission angles. For example, at small forward angles and at a distance of 5 m from the target, we expect particle rates on the order of $100 \text{ kHz}/\text{cm}^2$ for 10 MHz minimum bias Au+Au collisions at 25 AGeV. In a central collision, particle densities of about $0.05/\text{cm}^2$ are reached. In order to keep the occupancy below 5% the minimum size of a single cell should be about 1 cm^2 . The TRD detector readout will be realized in rectangular pads giving a resolution of $300\text{--}500 \mu\text{m}$ across and $3\text{--}30 \text{ mm}$ along the pad. Every second TR layer is rotated by 90° . Prototype gas detectors based on MWPC and GEM technology have been built and tested with particle rates of up to $400 \text{ kHz}/\text{cm}^2$ without deterioration of their performance. The pion suppression factor obtained with 12 TRD layers is estimated to be well above 100 at an electron efficiency of 90%.

2.5 The Muon Chamber system (MuCh)

The experimental challenge for muon measurements in heavy-ion collisions at FAIR energies is to identify low-momentum muons in an environment of high particle densities. The CBM concept is to track the particles through a hadron absorber system, and to perform a momentum-dependent muon identification. This concept is realized by segmenting the hadron absorber in several layers, and placing triplets of tracking detector planes in the gaps between the absorber layers. The absorber/detector system is placed downstream of the Silicon Tracking System (STS) which determines the particle momentum. In order to reduce meson decays into muons the absorber/detector system has to be as compact as possible.

The actual design of the muon detector system consists of 6 hadron absorber layers (iron plates of thickness 20, 20, 20, 30, 35, 100 cm) and 15–18 gaseous tracking chambers located in triplets behind each iron slab. The definition of a muon depends on its momentum which varies with the mass of the vector mesons and with beam energy. For example, for beam energies above 15 AGeV muons from the decay of J/ψ mesons have to pass all 6 absorber layers with a total iron thickness of 225 cm corresponding to 13.4 interaction length λ_I . The muons from the decay of low-mass vector mesons (ρ , ω , ϕ)

only have to penetrate through 5 iron absorber layers with a total thickness of 125 cm (corresponding to $7.5 \lambda_I$).

The challenge for the muon chambers and for the track reconstruction algorithms is the huge particle density of up to 1 hit/cm² per event in the first detector layers after 20 cm of iron. Therefore, the detector development concentrates on the design of fast and highly granulated gaseous detectors based on GEM technology. In total, the muon chambers cover an active area of about 70 m² subdivided into about half a million channels. Ongoing studies concentrate on the optimization of the muon absorber system in terms of absorber thicknesses, number of absorbers and tracking stations, and required hit resolution, i.e. pad size of the detector.

The low particle multiplicities behind the muon absorber enables the implementation of a trigger on muon pairs. The trigger concept is based on the measurement of short track segments in the last tracking station triplet, and extrapolation of these tracks to the target. After selection of tracks with good vertices the event rate can be reduced already by a factor of about 600 for J/ψ measurements in minimum bias Au+Au collisions.

2.6 The timing Resistive Plate Chambers (RPC)

An array of Resistive Plate Chambers will be used for hadron identification via TOF measurements. The TOF wall is located 10 m downstream of the target and covers an active area of about 120 m². The required time resolution is on the order of 80 ps. For 10 MHz minimum bias Au+Au collisions the innermost part of the detector has to work at rates up to 20 kHz/cm². At small deflection angles the pad size is about 5 cm² corresponding to an occupancy of below 5% for central Au+Au collisions at 25 AGeV. With the proposed pad readout a position resolution of 0.6 cm across the pads is expected. Along the pads the resolution depends on the padlength which increases from the center to the outer regions of the TOF wall. The development of timing RPCs is focused on high rate capability, low resistivity material, long term stability and the realization of large arrays with overall excellent timing performance. Prototype timing RPCs with ceramic electrodes have been built and tested. A time resolution of better than 90 ps was obtained with rates up to 70 kHz/cm².

2.7 The Electromagnetic CALorimeter (ECAL)

A “shashlik” type calorimeter as installed in the HERA-B, PHENIX and LHCb experiments will be used to measure direct photons and neutral mesons (π^0 , η) decaying into photons. The ECAL will be composed of modules which

consist of 140 layers of 1mm lead and 1mm scintillator, with cell sizes of $3 \times 3 \text{ cm}^2$, $6 \times 6 \text{ cm}^2$, and $12 \times 12 \text{ cm}^2$. The shashlik modules can be arranged either as a wall or in a tower geometry with variable distance from the target. Ongoing studies concentrate on an optimization of the layout, in particular in terms of required azimuthal coverage.

2.8 The Projectile Spectator Detector (PSD)

The PSD will be used to determine the collision centrality and the orientation of the reaction plane. A very precise characterization of the event class is of crucial importance for the analysis of event-by-event observables. The study of collective flow requires a well defined reaction plane which has to be determined by a method not involving particles participating in the collision. The detector is designed to measure the number of non-interacting nucleons from a projectile nucleus in nucleus-nucleus collisions. The PSD is a full compensating modular lead-scintillator calorimeter which provides very good and uniform energy resolution [14]. The calorimeter comprises 12×9 individual modules, each consisting of 60 lead/scintillator layers with a surface of $10 \times 10 \text{ cm}^2$. The scintillation light is read out via wavelength shifting (WLS) fibers by Multi-Avalanche Photo-Diodes (MAPD with an active area of $3 \times 3 \text{ mm}^2$ and a pixel density of $10^4/\text{mm}^2$).

2.9 Online event selection and data acquisition

High statistics measurements of rare probes require high reaction rates. The CBM detectors, the online event selection systems, and the data acquisition will be designed for event rates of 10 MHz, corresponding to a beam intensity of 10^9 ions/s and a 1% interaction target, for example. Assuming an archiving rate of 1 Gb/s and an event volume of about 40 kB for minimum bias Au+Au collisions, an event rate of 25 kHz can be accepted by the data acquisition. Therefore, measurements with event rates of 10 MHz require on-line event selection algorithms (and hardware) which reject the background events (which contain no signal) by a factor of 400 or more.

The event selection system will be based on a fast on-line event reconstruction running on a PC farm equipped with many-core CPUs and graphics cards. Different many-core architectures developed by Intel, IBM, NVIDIA and AMD are under investigation. Track reconstruction, which is the most time consuming combinatorial stage of the event reconstruction, will be based on parallel track finding and fitting algorithms, implementing the Cellular Automaton and Kalman Filter methods. Novel languages, such as CUDA,

Ct and OpenCL, can be used for parallel programming on the heterogeneous CPU/GPU on-line event selection system.

For open charm production the trigger will be based on an online search for secondary vertices which requires high speed tracking and event reconstruction in the STS and MVD. The highest suppression factor has to be achieved for J/ψ mesons where a high-energetic pair of electrons or muons is required in the TRD or in the MuCh. For low-mass electron pairs no online selection is possible due to the large number of rings/event in the RICH caused by the material budget of the STS. In the case of low-mass muon pairs some background rejection on the trigger level seems to be feasible.

Chapter 3

Feasibility studies

The CBMRoot simulation framework [15] has been developed for feasibility studies and optimization of the detector layout. As event generator we use the UrQMD (version 1.3) [16] code. This code does not include rare probes as e.g. the vector mesons and charmed hadrons, therefore we implement their multiplicities using the HSD [17] model. For feasibility studies the rare probes are then added on top of the UrQMD events with kinematic distributions also guided by HSD. Vector mesons decaying into dileptons are embedded using the PLUTO generator [10] which in particular provides correct decay kinematics of the hadronic and electromagnetic decays. Particles are propagated through a CBM detector model as has been introduced in the previous section using the transport code GEANT 3 [18]. Simulated events are reconstructed using different track and ring reconstruction routines as well as secondary vertex finding algorithms. For particle identification RICH, TRD and TOF information is combined for the single tracks. Realistic detector response is taken into account as far as possible. Detector resolution and granularity are still implemented in a generic way not yet taking into account the detailed structures and the supporting material.

3.1 Track and vertex reconstruction

Track reconstruction for high multiplicity events in a fixed target geometry poses severe challenges to the tracking detectors and to the reconstruction algorithms. The central tracking detector in the CBM experiment is the STS. In order to optimize the STS layout we perform simulations of central Au+Au collisions which produce the highest track densities envisaged for the experiment. The events are generated with the UrQMD code, transported through the STS with GEANT3. The simulated tracks of a central Au+Au collision at 25 AGeV are shown in Fig. 3.1.

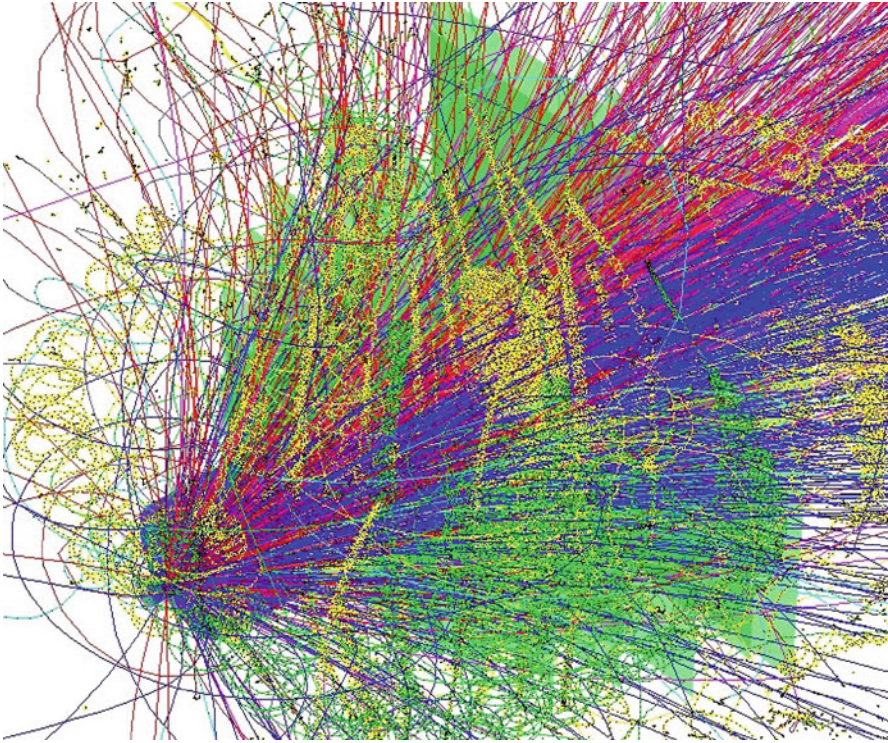


Fig. 3.1 Particle tracks in the STS simulated for a central Au+Au collision at a beam energy of 25 AGeV. The particles are produced with the UrQMD event generator, and transported through the STS with the GEANT3 code which calculated the hits in the detector layers.

The simulated tracks are reconstructed with a Cellular Automaton algorithm and a Kalman filter. The resulting track reconstruction efficiencies and the momentum resolution are shown in Fig. 3.2, top row. In the next step, STS tracks are extrapolated through the TRD stations and matched to hits of the RPC-TOF detector. A global track reconstruction efficiency for charged particles of 86% is reached including matching to TOF hits (Fig. 3.2, lower left plot). In case the STS is followed by the muon absorber system, STS tracks are extrapolated through the iron absorbers with its intermediate tracking stations. The lower right figure of 3.2 shows the global tracking efficiency for the reconstruction of muons embedded into UrQMD events for a total absorber length of 1.25 and 2.25 m.

The current concept of the Micro-Vertex detector (MVD) is based on MAPS (CMOS) technology which limits the maximum interaction rates due to constraints in readout speed and radiation hardness. The MVD is required for high precision secondary vertex reconstruction in open charm measurements, and for the rejection of close di-electron pairs from pion Dalitz decays.

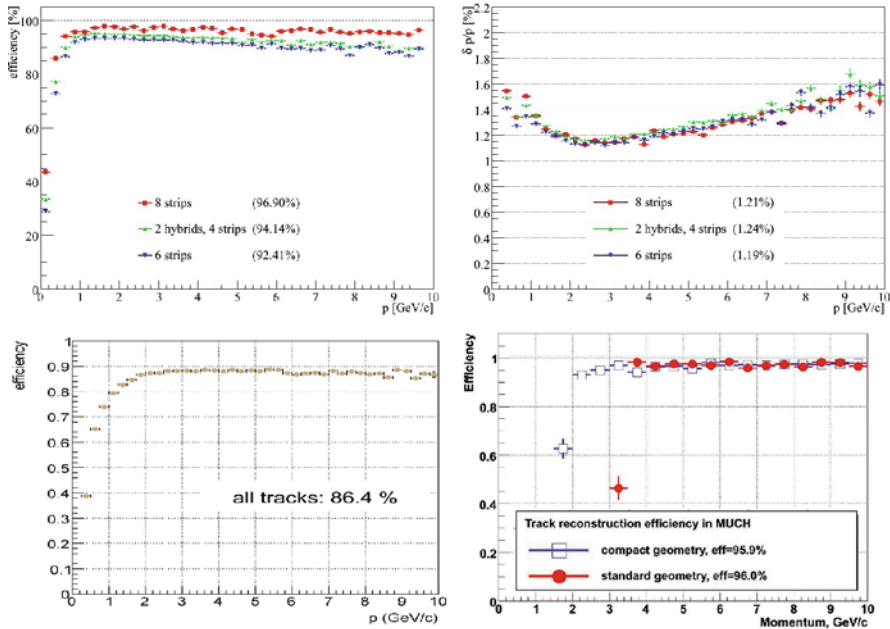


Fig. 3.2 Track reconstruction efficiency for primary vertex tracks (more than 75% of maximum number of hits) in the Silicon Tracking System (STS) for different STS configurations (*top left panel*); momentum resolution in the STS (*top right panel*); global track reconstruction efficiency for the combined STS-TRD-TOF system (*bottom left panel*); global track reconstruction efficiency for muons embedded into UrQMD events for the combined STS-MuCh system for 1.25 m (compact geometry) and 2.25 m (standard geometry) total absorber length (*bottom right panel*).

The MVD hits are attached to the track after the STS track reconstruction has been performed. The high position resolution of the detectors in combination with their location close to the target results in a vertex resolution of better than $60 \mu\text{m}$ along the beam axis. The quality of vertex reconstruction is robust against a limited event pile-up (<10 events) in the MVD which is likely to happen at interaction rates of 100 kHz for the open charm measurement.

3.2 Hadron identification

The identification of pions, kaons and protons over a large phase space interval is a prerequisite for a deeper understanding of the collision process. The identification of the bulk hadrons is also required for the reconstruction of hadronic resonances such as the $K^*(892)$, ϕ -mesons or even $\Lambda(1520)$. Fluctuation and correlation measurements without particle identification are difficult

to interpret. Hadron identification will also improve background suppression in D mesons or hyperon measurements.

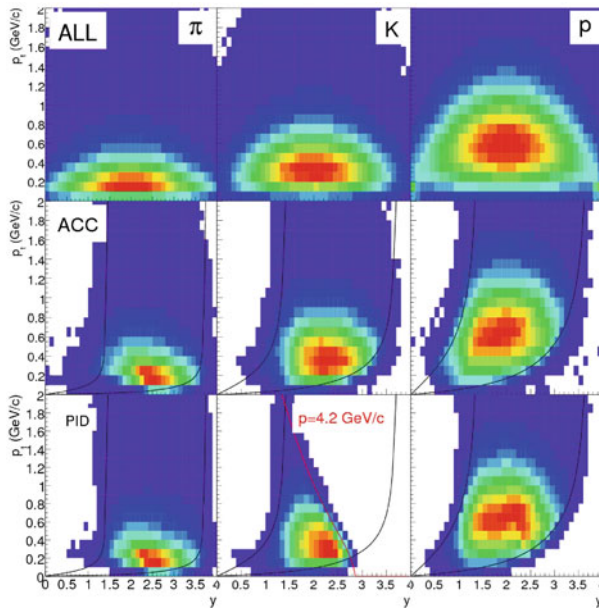


Fig. 3.3 Phase-space distributions of generated (*top*), geometrically accepted (*middle*), and identified pions, kaons and protons (*bottom*) for Au+Au collisions at 25 AGeV. The reconstructed particles are identified by time-of-flight measured with the RPC detector located 10 m downstream of the target. The time resolution is assumed to be 80 ps. For kaons a purity of 90% defined by the mass resolutions is required leading to the upper momentum cutoff close to 4.2 GeV/c. For pions and protons a momentum cutoff of 10 GeV/c is used. Midrapidity for 25 AGeV beam energy lies at 2, for 15 and 35 AGeV at 1.75 and 2.16, respectively.

The CBM detector accepts charged particles emitted at polar angles between 2.5 and 25 degrees in the laboratory. The resulting phase-space coverage for reconstructed pions, kaons and protons produced in Au+Au collisions at 25 AGeV is illustrated in Fig. 3.3 as function of transverse momentum and rapidity. The CBM phase space coverage allows the extrapolation to 4π with good precision for beam energies from 15 to 35 AGeV. For a beam energy of 25 AGeV, for example, 38% of the generated kaons are geometrically accepted, and 18.4% of the emitted kaons can be reconstructed and identified with a purity of 90%.

Hadron identification is performed in several steps. First, track reconstruction and momentum determination in the Silicon Tracking System is performed (no MVD required). These tracks are extrapolated to the Transition Radiation Detector (TRD) stations where the TRD hits are included in the track reconstruction, and finally these reconstructed tracks are matched to

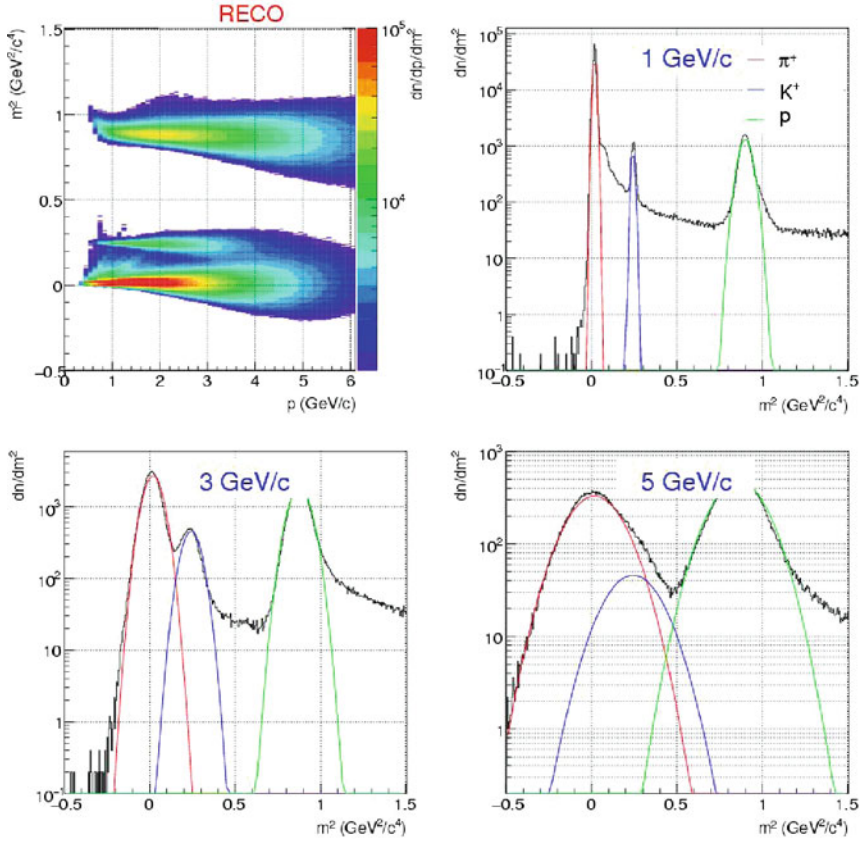


Fig. 3.4 Mass² versus momentum plot for reconstructed tracks assuming 80 ps time resolution (200 k events, central Au+Au collisions at 25 AGeV). In addition mass spectra for momentum bins at $p = 1, 3$, and 5 GeV/c are shown. Tails are due to mismatches and double hits in TOF.

the nearest hit in the RPC-TOF detector. The track reconstruction efficiencies are shown in Fig. 3.2. For mass determination a time-of-flight resolution of 80 ps is assumed. The mass spectra for different momentum bins are shown in Fig. 3.4. The tails in the mass distributions at low particle momenta are caused by the energy loss of the low-momentum tracks, ghost tracks, mismatches of tracks and TOF-hits as well as double hits in TOF. For laboratory momenta up to 3 GeV/c pions, kaons and protons are well separated, for higher momenta the different yields can still be extracted from a statistical unfolding of the spectra. This technique will allow the extraction of $pt - y$ spectra and a flow measurement at midrapidity up to transverse momenta of a few GeV/c. The number of generated, accepted, and identified kaons (99% purity) is shown as a function of transverse momentum at midrapidity in Fig. 3.5.

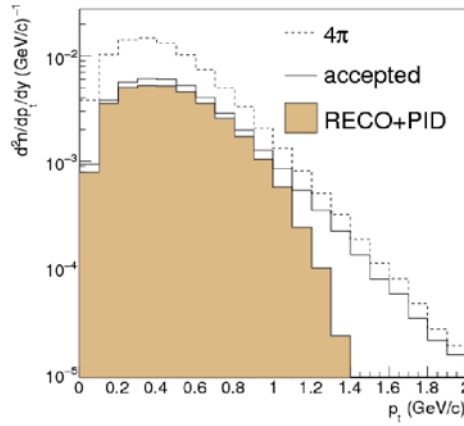


Fig. 3.5 Distribution of generated, accepted, and identified kaons (99% purity) as a function of transverse momentum.

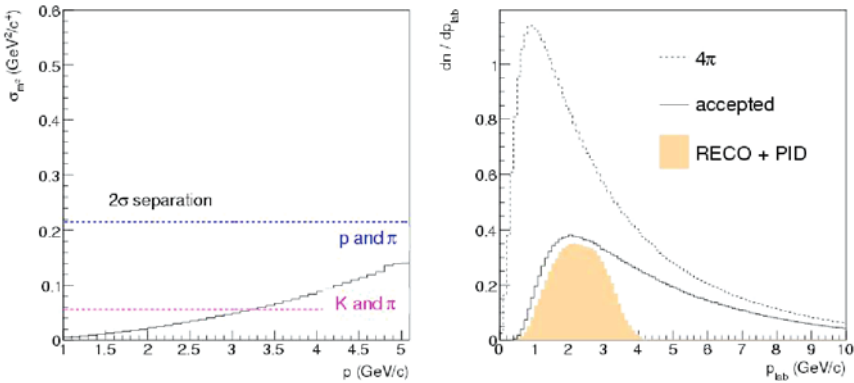


Fig. 3.6 *Left:* Mass resolution versus momentum (time resolution 80 ps) for reconstructed tracks; *dashed lines* indicate the mass resolution for a 2σ separation between kaons and pions or protons and kaons, respectively. *Right:* Distribution of generated, accepted, and identified kaons (99% purity) as a function of laboratory momentum.

The measurement of event-by-event particle ratio fluctuations requires kaon identification with high purity. Figure 3.6 demonstrates that pions and kaons are separated by 2σ of the mass resolution up to laboratory momenta of 3.2 GeV/c (left panel). The requirement of a kaon purity of 99% restricts the efficiency to laboratory momenta below to about 3.5 GeV (see right panel of Fig. 3.6). Depending on the required purity for kaon identification using a $\pm 2\sigma_m$ cut in each momentum bin, a momentum cutoff at appr. 5 GeV/c (50% kaon purity), 4.2 GeV/c (90%), 3.5 GeV/c (99%) or even 2.2 GeV/c (100%) is introduced to the selected kaon sample. As the event-by-event fluctuations connected to the first order phase transition or to the critical point are gen-

erally expected to occur predominantly at low particle momenta, this range of purely identified kaons is expected to be sufficient.

3.3 Hyperon reconstruction

The abundance and phase space distributions of strange particles, in particular of multi-strange hyperons, are expected to be sensitive to the evolution of the fireball. The hyperons can be identified via their charged particle decay channels $\Lambda \rightarrow p + \pi^-$, $\Xi^- \rightarrow \Lambda + \pi^-$, and $\Omega^- \rightarrow \Lambda + K^-$ via their decay topology using only STS information without requiring hadron identification.

The simulation discussed in the following assume a STS layout consisting of 2 hybrid pixel and 4 silicon strip detectors. The first detector is placed 30 cm downstream of the target. The silicon strip detectors were implemented with a pitch of 50 μm and a stereo angle of only 5° . No MVD was included although it certainly would increase the resolution of track parameters and secondary vertex reconstruction. The STS track finder was specifically tuned in order to provide a good efficiency for tracks from secondary vertices. Typically, the resolution of the secondary vertices is of order 3–4 mm. The momentum averaged reconstruction efficiencies for two different beam energies are given in Table 3.1. The reconstruction efficiency of 63% for Λ hyperons

Table 3.1 Acceptance and efficiencies, mass resolution, and signal-to-background ratio (S/B) for hyperon reconstruction in central Au+Au collisions at 25 and 6 AGeV beam energy. No hadron identification is used. The total efficiency is calculated from the product of geometrical acceptance, reconstruction and cut efficiency.

	Λ^a	Ξ^-	Ω^-
Detected decay channel	$p + \pi^-$	$\Lambda + \pi^-$	$\Lambda + K^-$
Branching ratio into detected channel	63.9%	99.9% ^b	67.8% ^b
25 AGeV beam energy			
Multiplicity	36.6	0.983	0.022
Geometrical acceptance	28.5%	16.3%	14.6%
Reconstruction efficiency	62.8%	40.6%	46.2%
Cut efficiency	59.4%	32.3%	15.4%
Total efficiency	10.6%	2.1%	1.0%
σ_m [MeV/c ²]	1.34	1.87	2.04
S/B	30.2	12.8	2.5
6 AGeV beam energy			
Multiplicity	12.8	0.118	$7.2 \cdot 10^{-4}$
Geometrical acceptance	25.1%	13.6%	13.9%
Reconstruction efficiency	73.4%	53.5%	64.9%
Cut efficiency	40.1%	35.1%	21.7%
Total efficiency	7.4%	2.6%	2.0%
σ_m [MeV/c ²]	1.341	2.21	1.96
S/B	65	17.8	4.3

^a Includes Λ s from the electromagnetic decay $\Sigma^0 \rightarrow \Lambda + \gamma$ (BR 100%)

^b Branching ratio of $\Lambda \rightarrow p + \pi^-$ not included

at 25 AGeV beam energy, for example, results from a track finding efficiency of 86% for the decay protons and 73% for the decay pions only slightly depending on momentum. In addition to the secondary vertex finding a set of mostly topological cuts is applied in order to further reduce the background. Their effect on the signal efficiency is included in the table (“cut efficiency”). Total efficiencies are given as product of acceptance, reconstruction, and cut efficiency. For Λ baryons the resulting high total efficiency of more than 10% leads to the fact, that at 25 AGeV beam energy 3–4 Λ s will be reconstructed per event. It should be noted that the cuts used in this analysis are tuned to achieve a large signal/background ratio which results in a low reconstruction efficiency. In order to study, for example, Λ – Λ correlations one would relax the cuts, and thus increase the efficiency to 25% corresponding to about 11 Λ s reconstructed per event.

Figure 3.7 (left column) illustrates the quality of hyperon reconstruction using the STS only. The reconstructed invariant mass distributions simulated for central Au+Au collisions at 25 AGeV are almost free of background. The STS detector acceptance is depicted in the right column of Fig. 3.7.

3.4 Event-by-event fluctuations

Event-by-event fluctuations of particle yields, ratios or kinematical properties are expected to occur in the vicinity of a critical point or a first order phase transition as discussed in the first parts of this book. In order to perform a robust measurement of these fluctuations, a detector layout is needed which covers uniformly the full phase space without introducing additional fluctuations due to acceptance or identification limitations. This requirement is difficult to fulfill in a fixed target geometry. In order to ensure a nearly full azimuthal coverage the width of the detectors are not kept at a fixed angle but are enlarged in the bending plane of the magnet. As example for feasibility studies on the CBM performance for fluctuations we will report here on investigations of particle ratio fluctuations, in particular concerning the K/π ratio.

Detailed studies are performed in order to understand the bias introduced by the CBM detector layout due to the finite geometrical acceptance and particle identification capability. Hadron identification is performed using time-of-flight information, see e.g. Figs. 3.3 and 3.4. Hadrons are selected by a momentum dependent mass cut of $\pm 2\sigma_m$ for kaons and $\pm 3\sigma_m$ for pions and protons where σ_m is the mass resolution. A purity of identified kaons of 99% is required in each momentum bin in addition thus restricting the kaon identification at higher momenta. For 99% purity this momentum cutoff poses an upper momentum cutoff for kaons close to 3.5 GeV/c (see Fig. 3.6, right panel). Fluctuations related to the critical point or a first order phase

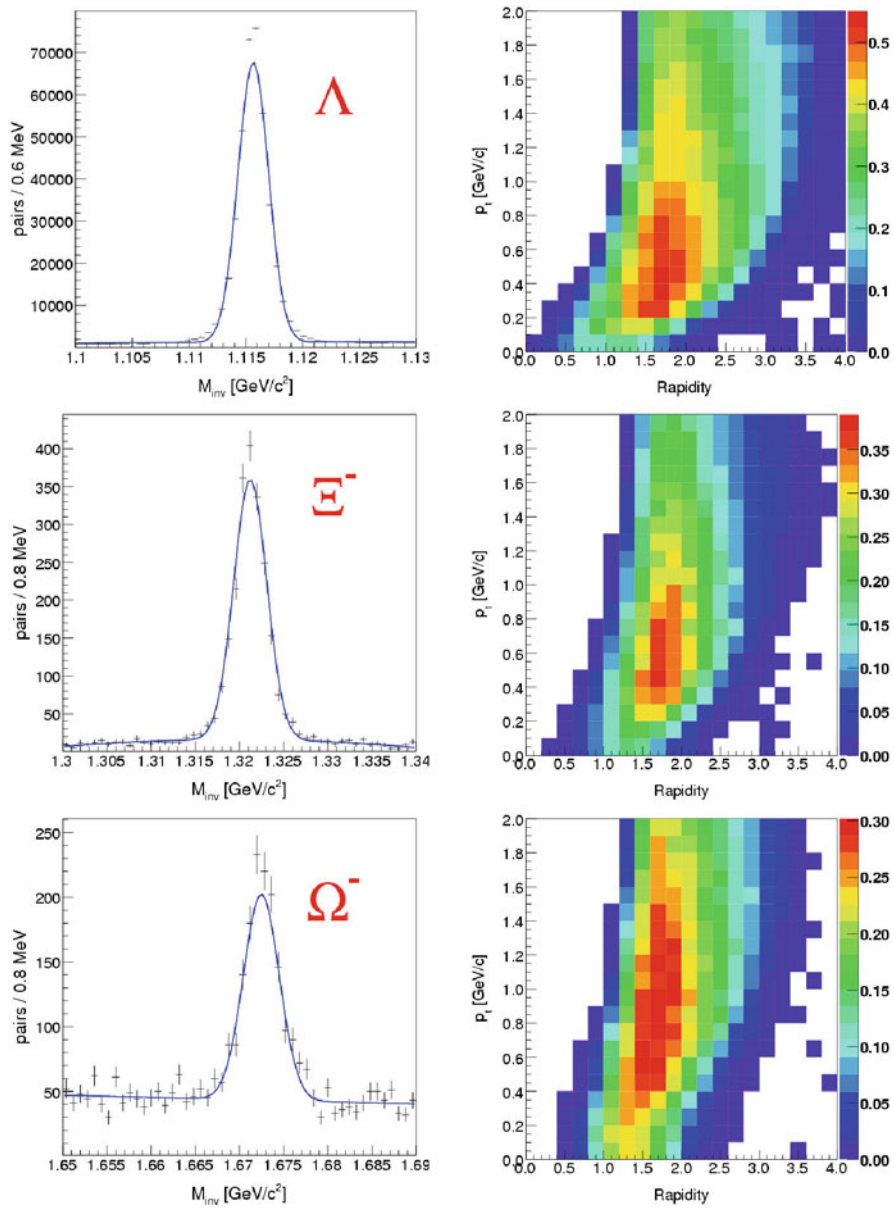


Fig. 3.7 *Left column:* Invariant mass spectra of hyperons simulated for 10^5 (Λ and Ξ^-) and $4.5 \cdot 10^6$ (Ω) central Au+Au collisions at 25 AGeV using the UrQMD event generator. The identification is based on track reconstruction only, no hadron identification is applied. *Right column:* Geometrical acceptance of the STS detector in transverse momentum versus rapidity for the corresponding hyperon.

transition are expected at low p_t ($p_t \lesssim 0.5$ GeV/c) where the CBM acceptance is very good.

Systematic errors due to the event characterization (for example centrality) are reduced considerably when calculating ratios of particle yields event-by-event. Then, the width of the distribution is mainly determined by statistical fluctuations, detector resolution and particle identification effects. Subtracting these effects by event mixing methods, the remaining “dynamical” fluctuations can be defined as

$$\sigma_{\text{dyn}} = \text{sign}(\sigma_{\text{data}}^2 - \sigma_{\text{mixed}}^2) \sqrt{|\sigma_{\text{data}}^2 - \sigma_{\text{mixed}}^2|} \quad (3.1)$$

An example for an event-by-event K/π ratio from UrQMD and mixed events is shown in Fig. 3.8 for fully reconstructed and identified particles in CBM in central Au+Au collisions at 25 AGeV beam energy requiring a kaon purity of 99 %. The particle ratio fluctuations extracted from UrQMD are summarized in Table 3.2. The results show some dependence on the acceptance restrictions due to particle identification for kaons. The higher purity of kaons is required, the lower is the momentum cutoff for their identification and the more fluctuations are added compared to the result in the full acceptance. This observation is summarized in plot 3.10 showing that by phase space restrictions additional fluctuations on the % level can easily be introduced. Such a dependence is seen for all particle ratio fluctuation signals where kaons are involved. Compared to this effect misidentification of kaons seems to have a lower impact.

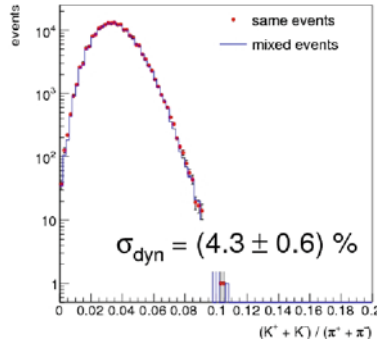


Fig. 3.8 Ratio of $(K^+ + K^-)/(\pi^+ + \pi^-)$ calculated event-by-event for central Au+Au collisions from UrQMD at 25 AGeV requiring reconstruction, full particle identification and a kaon purity of 99% in CBM.

The negative σ_{dyn} values obtained in particular for $(p + \bar{p})/(\pi^+ + \pi^-)$ fluctuations can be explained by correlated particle production through baryonic resonance decays, e.g. $N(1440), \Delta \rightarrow N + \pi$, present in the data but

Table 3.2 Particle ratio fluctuations as defined in Eq. (3.1) for different conditions in 25 AGeV in central Au+Au collisions from UrQMD. In the first 2 columns particles are purely identified from the MC simulation but the acceptance is restricted in the second step. For reconstructed and identified kaons requiring $\geq 99\%$ purity in each momentum bin an upper momentum cutoff of 3.5 GeV/C is introduced. The effect of this is seen in Fig. 3.10. For this last column full reconstruction and particle identification is used, i.e. mismatches and misidentified particles are included.

	4π (%)	geom. acc. particles (MC) (%)	Reco. and id. particles in CBM (%)
$(K^+ + K^-)/(\pi^+ + \pi^-)$	(2.6 ± 0.2)	(2.3 ± 0.4)	(4.3 ± 0.6)
$(K^+)/(\pi^+)$	(-6.2 ± 0.1)	(-6.4 ± 0.2)	(-4.4 ± 0.8)
$(K^-)/(\pi^+)$	(-8.4 ± 0.2)	(-9.6 ± 0.4)	(-9.3 ± 1.1)
$(K^+)/(\pi^-)$	(-8.0 ± 0.1)	(-8.3 ± 0.2)	(-6.8 ± 0.5)
$(K^-)/(\pi^-)$	(-6.9 ± 0.3)	(-8.1 ± 0.5)	(-6.7 ± 1.6)
$(p + \bar{p})/(\pi^+ + \pi^-)$	(-5.53 ± 0.03)	(-6.03 ± 0.04)	(-5.33 ± 0.07)
$(K^+ + K^-)/(p + \bar{p})$	(-3.2 ± 0.2)	(-3.9 ± 0.3)	(0.8 ± 3.8)

not in the mixed events. The interpretation of the negative values found in the $(K^+)/(\pi^+)$ and $(K^+)/(\pi^-)$ cases is more subtle. For example the decay channels $K^* \rightarrow K\pi$ or $K_1 \rightarrow K\rho \rightarrow K\pi\pi$ and $K_1 \rightarrow K^*\pi \rightarrow K\pi\pi$ feed these ratios. In order to understand the relative importance of resonance feeddown for the fluctuation signal, the relevant resonances have to be known in detail. Indeed, investigations using simple model assumptions show that for the interpretation of dynamical fluctuation signals a detailed understanding of the relevant resonance abundances is needed [19].

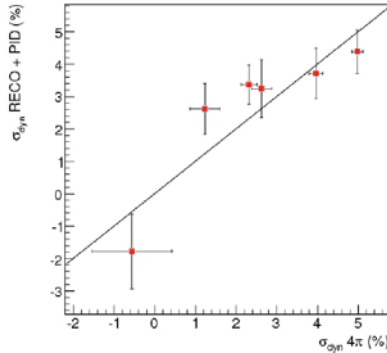


Fig. 3.9 Sensitivity study on dynamical fluctuations in the CBM detector: Extracted fluctuations versus dynamical fluctuations in 4π added to input data.

In order to study the sensitivity of the CBM detector on additional dynamical particle ratio fluctuations, simulations were performed in which single particles were added or removed to a fixed K/π ratio in order to generate additional fluctuations. Figure 3.9 shows the fluctuation signal extracted from

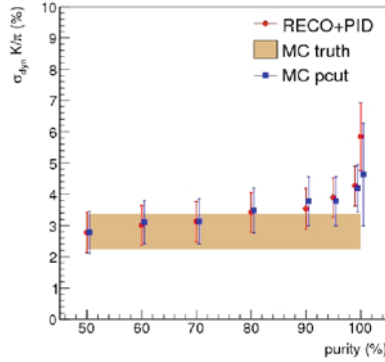


Fig. 3.10 Dynamical K/π fluctuations in central Au+Au collisions at 25 AGeV beam energy from UrQMD for various purity requirements for kaons. Simulation data employing full event reconstruction and particle identification are compared with the MC truth in the CBM acceptance (band) and within the CBM acceptance but employing the upper momentum cutoff due to the purity restriction of kaons as well (MC pcut): 5 GeV/c for 50% purity, 4.2 GeV/c (90%), 3.5 GeV/c (99%), and 2.2 GeV/c (100%).

these data versus the input fluctuations. These studies show that CBM should be sensitive on dynamical fluctuations on the % level.

3.5 Open charm

Charm production and propagation is expected to be sensitive to the conditions in the early stage of the collision. The experimental challenge is to identify the very rare D mesons or even Λ_c baryon via their hadronic decay modes $D^0 \rightarrow K^-\pi^+$ and $D^0 \rightarrow K^-\pi^+\pi^+\pi^-$, $D^\pm \rightarrow K^\mp\pi^\pm\pi^\pm$, or $\Lambda_c \rightarrow pK^-\pi^+$, even $D_s^+ \rightarrow K^+K^-\pi^+$. The D^0 , the D^\pm , the D_s^+ -mesons and the Λ_c have lifetimes of 124.4, 317, 150 μm , and 61.8 μm , respectively. In order to suppress the background of kaons and pions emitted from the primary vertex a high resolution Micro-Vertex Detector (MVD) is required to precisely determine the secondary decay vertex of particles with open charm.

The feasibility studies presented in the following are based on a MVD which consists of two MAPS stations located 10 and 20 cm downstream of the target. The total material budget of one MAPS station is assumed to be 150 μm silicon equivalent. The STS comprises 6 stations of silicon micro-strip detectors. With a single hit resolution in the MAPS detectors of 5 μm , the primary vertex was reconstructed with a precision of 6 μm along the beam axis and the D^0 -decay vertex ($D^0 + \bar{D}^0 \rightarrow K^\mp\pi^\pm$) with 53 μm . In addition to the 2-particle decay channel of the D^0 meson, a 4-particle decay channel was investigated; $D^0 \rightarrow K^-\pi^+\pi^+\pi^-$. The 4-particle decay vertex can still be reconstructed with a precision of 82 μm along the beam axis. The vertex

resolution for the 3-particle decay vertices of D^+ and Λ_c hadrons is about 60 and 70 μm , respectively. The measurement of the different D mesons and of the Λ_c is necessary to determine the total charm production cross section.

In order to reconstruct the charmed hadrons with a good signal-to-background ratio, a set of topological cuts is applied to single tracks as well as to the reconstructed vertices. Single tracks are extrapolated to the target, and are rejected if they point to the primary vertex. In contrast, the reconstructed track of the D meson is required to originate from the primary vertex. As an example, Fig. 3.11 presents the resulting background suppression of such cuts for the 3-particle decay of the D^+ meson. Although these cuts also reject a large fraction of the charmed hadrons (see efficiencies in Table 3.3), they are required to suppress the overwhelming background. Please note that no kaon or pion identification with TOF is applied, however, it is important to use the time-of-flight measurement in order to reject proton tracks from the sample. The fully reconstructed invariant mass spectra of all investigated charmed hadrons and decay channels are shown in Fig. 3.12 for central Au+Au collisions at 25 AGeV beam energy. Numbers for efficiency and acceptance are presented in Table 3.3. The results for the D^\pm meson are somewhat better than for the D^0 mesons, because the D^\pm lifetime is longer by a factor 2.5, and the combinatorial background is suppressed more efficiently because the secondary vertex is defined by 3 particles. The identification of Λ_c s is particularly challenging due to its extremely short lifetime. This measurement requires an exceptionally precise vertex determination. Figure 3.13 illustrates the large phase space coverage for Λ_c -baryons in CBM.

The identification of particles carrying open charm requires an excellent vertex resolution which in turn can only be achieved with detectors which have an extremely low material budget (small multiple scattering), and which are positioned close to the target (small extrapolation error). The simulations

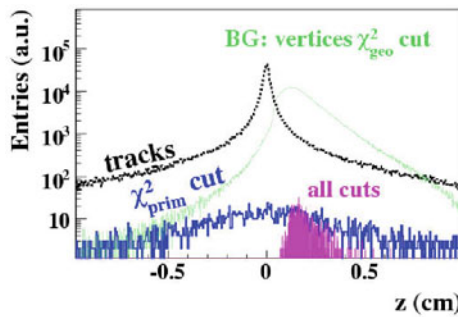


Fig. 3.11 Distribution of single tracks and secondary vertices along the beam line for $D^+ \rightarrow K^- \pi^+ \pi^+$ reconstruction: All primary tracks (black line) and those selected by χ^2 cuts as single track candidates for D^+ daughters (blue). 3-particle secondary vertices after first geometrical cuts (light green), and finally selected D^+ candidates including more stringent topological cuts (magenta).

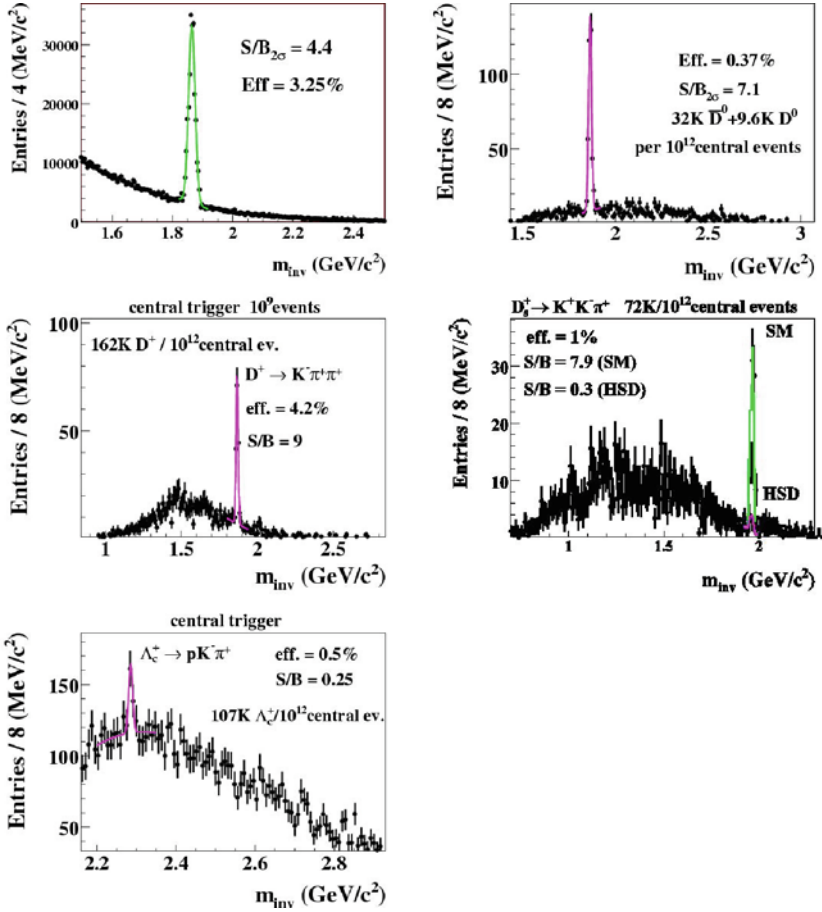


Fig. 3.12 Reconstructed charmed hadrons in 10^{12} central Au+Au collisions at 25 AGeV. From upper left to lower left: $D^0 + \bar{D}^0 \rightarrow K^\mp \pi^\pm$, $D^0 \rightarrow K^- \pi^+ \pi^+ \pi^-$, $D^+ \rightarrow K^- \pi^+ \pi^+$, $D_s^+ \rightarrow K^+ K^- \pi^+$, and $\Lambda_c \rightarrow p K^- \pi^+$.

discussed above were performed with two MAPS detector stations with a material budget of $150 \mu\text{m}$ silicon equivalent, located at 10 and 20 cm downstream of the target. In order to study the influence of the material budget on the vertex resolution, we increased the material budget of each MAPS station to $500 \mu\text{m}$ silicon. Due to the increased multiple scattering the primary vertex resolution along the z-axis decreases to $10 \mu\text{m}$. Moreover, the secondary decay vertex resolution decreases considerably for all investigated decays (about $110 \mu\text{m}$ for D^0 and Λ_c , and about $170 \mu\text{m}$ for D^+ and D_s^+). It turns out that in particular the identification of Λ_c requires MAPS stations with a material budget below $200 \mu\text{m}$ silicon. On the other hand, the material budget of the MAPS stations strongly depends on their size, as it is dominated by read-out and cooling structures. Therefore, the stations will

Table 3.3 Acceptance and efficiencies, mass resolution, and signal-to-background ratio (S/B) in a $2\sigma_m$ region around the peak for open charm reconstruction in central Au+Au collisions at 25 AGeV beam energy for 2 MAPS stations with 150 μm Si equivalent at 10 and 20 cm behind the target. The total efficiency is calculated from the product of geometrical acceptance, reconstruction and cut efficiencies. Multiplicities are taken from the HSD model [17] or from the statistical model (SM) [20].

	$D^0 + \bar{D}^0$	D^0	D^+	D_s^+	Λ_c
Multiplicity (HSD)	$1.5 \cdot 10^{-4}$	$4 \cdot 10^{-5}$	$4.2 \cdot 10^{-5}$	$5.4 \cdot 10^{-6}$	$4.9 \cdot 10^{-4}$
Multiplicity (SM)			$8.4 \cdot 10^{-5}$	$1.4 \cdot 10^{-4}$	($\Delta y = 1$)
Lifetime $c\tau$	124 μm	124 μm	317 μm	150 μm	62 μm
Decay channel	$K^\mp \pi^\pm$	$K^- \pi^+ \pi^+ \pi^-$	$K^- \pi^+ \pi^+$	$K^+ K^- \pi^+$	$p K^- \pi^+$
Branching ratio	3.85%	7.5%	9.5%	5.3%	5%
Geom. acceptance	55.7%	19.3%	39.6%	29.6%	53%
Reconstr. efficiency	96%	97.7%	97.5%	97.5%	97.6%
z-resol. of decay vertex	53 μm	82 μm	60 μm	67 μm	70 μm
Cut efficiency (mainly topological cuts)	6.1%	2%	10.9%	3.5%	1%
Total efficiency	3.25%	0.37%	4.2%	1%	0.5%
σ_m [MeV/c^2]	11.0	12.0	11.0	12.0	12.0
S/B $_{2\sigma}$ (HSD)	4.4	7.1	9	0.3	
S/B $_{2\sigma}$ (SM)				7.9	0.25

become thinner the closer to the target they are. For example, if the first MAPS detector is positioned 5 cm downstream of the target, its thickness reduces to 300 μm silicon. This scenario has been implemented in simulations as well, and the resulting efficiencies and signal-to-background ratios are close to those which were obtained with the two 150 μm silicon-equivalent MAPS layers at 10 and 20 cm distance from the target. The results for the different scenarios are summarized in Table 3.4 for D^0 and D^+ mesons.

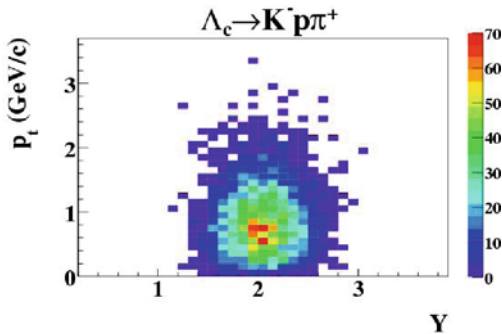


Fig. 3.13 Phase space coverage of reconstructed Λ_c -baryons in transverse momentum versus rapidity.

Table 3.4 Total efficiency, secondary vertex resolution and signal-to-background ratio (S/B) in a $2\sigma_m$ region around the peak for open charm reconstruction in central Au+Au collisions at 25 AGeV beam energy, for different MVD configurations. Multiplicities are taken from the HSD model [17], see Table 3.3.

MAPS configuration			
Position of 1st MAPS	10 cm	10 cm	5 cm
Thickness of 1st MAPS	150 μm Si-equiv.	500 μm Si-equiv.	300 μm Si-equiv.
Position of 2nd MAPS	20 cm	20 cm	10 cm
Thickness of 2nd MAPS	150 μm Si-equiv.	500 μm Si-equiv.	500 μm Si-equiv.
D^0+D^0			
z-resol. of decay vertex	53 μm	105 μm	47 μm
total efficiency	3.25%	3.05%	4.4%
S/B $_{2\sigma}$	4.4	0.25	5.4
D^+			
z-resol. of decay vertex	60 μm	165 μm	47 μm
total efficiency	4.2%	1.05%	2.6%
S/B $_{2\sigma}$	9	0.93	1.1

As mentioned above the MAPS detectors are limited in readout time to about 10 μs . Therefore, the pile-up of several events in the MAPS detectors is very likely to occur at interaction rates of 100 kHz. This scenario was studied by superimposing a certain number of minimum bias events on top of one central Au+Au collision at 25 AGeV beam energy in the MAPS detectors (for a material budget of 150 μm silicon equivalent). It was found that even when piling up 10 minimum bias events the secondary vertex resolution degrades only slightly by 7.5% to 57 μm , and the mass resolution increases by 12% to 12.3 MeV/ c^2 . Therefore, the precise measurement of the D^0 meson is not limited by a moderate event pile up.

3.6 Identification of vector mesons via lepton pairs

The identification of lepton pairs in heavy-ion collisions is notoriously difficult because of their low multiplicity and the large background of charged particles. In the case of electrons one has to deal with an overwhelming physical background of electron pairs from γ conversions in the target and from π^0 and η Dalitz decays. For example, the 365 π^0 produced in central Au+Au collisions at 25 AGeV beam energy (UrQMD) lead to about 7 e^\pm pairs at the target; 4 from π^0 Dalitz decay, and 3 from γ conversion in the target (25 μm thick Au-foil, 0.1% interaction probability). The most important source of combinatorial background are pions misidentified as electrons because of the limited $e - \pi$ separation in the detector. The suppression of this background requires excellent electron identification capabilities which cannot be achieved with one electron detector only. Simulations show that with a pion

suppression factor on the order of 10^4 the remaining background is dominated by physical sources of electron-positron pairs.

In the case of muon measurements the background from physical muon pair sources is much less important than the combinatorial background caused by weak meson decays and by misidentified hadrons. Muons are usually identified as charged particles measured behind thick layers of hadron absorbers. However, this absorber technique works well only for high momentum muons. At FAIR beam energies, however, the muon momenta are rather low, and the soft muons are absorbed as well. The CBM muon detection concept is based on an instrumented absorber which allows for a momentum-dependent muon identification. The particles are measured by tracking chambers located between the absorber layers, and the reconstructed tracks which pass a certain amount of absorber material are counted as muons if hadrons with the given momentum should have been absorbed. The experimental challenge is to reconstruct the tracks for high hit densities in the tracking chambers. The resulting muon sample is mainly contaminated by charged particles punching through the absorber, and by muons from pion or kaon decays which are matched to their mother track in the STS. A minor contribution to the combinatorial background are muons from weak decays happening in front of the STS which cannot be distinguished from muons from vector meson decays.

In the following we present results of simulations which demonstrate that for FAIR energies the performance of dielectron and dimuon measurements is rather similar despite of the completely different background conditions. Electron measurements provide access to lowest invariant masses (i.e. below the mass of a muon pair), whereas muon measurements allow to generate a trigger which is required for the collection of data with high statistics. The CBM strategy is to measure both electrons and muons in order to combine the advantages of both probes, and to provide a comprehensive and consistent set of data.

3.6.1 Electron simulations

3.6.1.1 Electron identification

In the CBM experiment the electrons and positrons are identified via their Cherenkov radiation measured with the RICH, and via their transition radiation measured with the TRD. The Cherenkov ring positions and radii are determined by dedicated ring recognition algorithms, and the ring centers are attached to the reconstructed particle tracks. The ring radius resolution is better than 3%. The radius of the reconstructed rings is shown in the left panel of Fig. 3.14 as a function of the particle momentum. Up to particle momenta of about 10 GeV/c the RICH detector provides a good pion suppression. The main source of background in the electron sample at low-

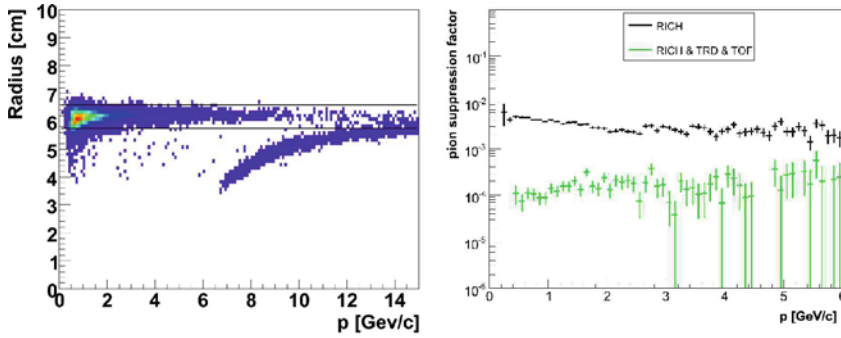


Fig. 3.14 Electron identification in the RICH detector for central Au+Au collisions at 25 AGeV. *Left panel:* Reconstructed ring radius as function of momentum for 10^4 UrQMD events. The band indicates a $\pm 3\sigma$ range around the mean radius of electrons. *Right panel:* Pion suppression factor as function of momentum for RICH only, and for the combination of RICH, TRD and TOF.

momenta is a mismatch of soft pion tracks from the primary vertex, and rings from secondary electrons. Most of the electron rings measured in the RICH are not produced by electrons emitted from the primary vertex, but rather stem from secondary electrons which are produced by gamma conversion in the detector material or in the magnet yoke. As their tracks cannot be reconstructed, there is a certain probability of matching these background electron rings to pion, kaon or proton tracks from the primary vertex.

The contamination of the electron sample by misidentified hadrons is strongly reduced when the energy loss information from the TRD (Fig. 3.15), and the timing information from the TOF detector is included into the analysis. In the current simulation 12 TRD layers are implemented, and the electron-to-pion separation is performed by a statistical analysis of the energy losses in each layer. The time-of-flight condition suppresses pions with momenta mainly below 1 GeV/c, and rejects the kaons and protons from the electron sample. The total electron identification efficiency is 50% for $p = 1$ GeV/c, rising to about 80% for momenta between 3 and 8 GeV/c. When combining the information from RICH, TRD, and TOF the hadron yield is reduced by a factor of 10,000. If the pions are suppressed by a factor of 5,000–10,000, the remaining background is dominated by electrons from γ -conversion in the target and π^0 -Dalitz decays.

3.6.1.2 Invariant mass spectra and phase-space coverage

The invariant mass distributions of electron-positron pairs simulated for central Au+Au collisions at 25 AGeV are shown in Fig. 3.16. The background is generated by UrQMD, the multiplicity of vector mesons is calculated with the HSD code, and the phase space distributions of the vector mesons and their

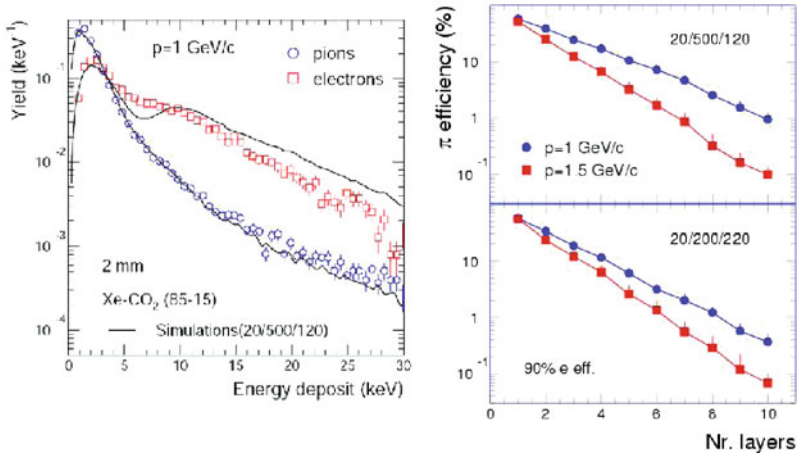


Fig. 3.15 Electron identification by the TRD detector. *Left panel:* Energy loss of pions and electrons of 1.5 GeV/c measured for a single TRD layer. *Right panel:* simulated pion efficiency for an electron efficiency of 90% as function of the number of TRD layers for 2 different types of detector material composition.

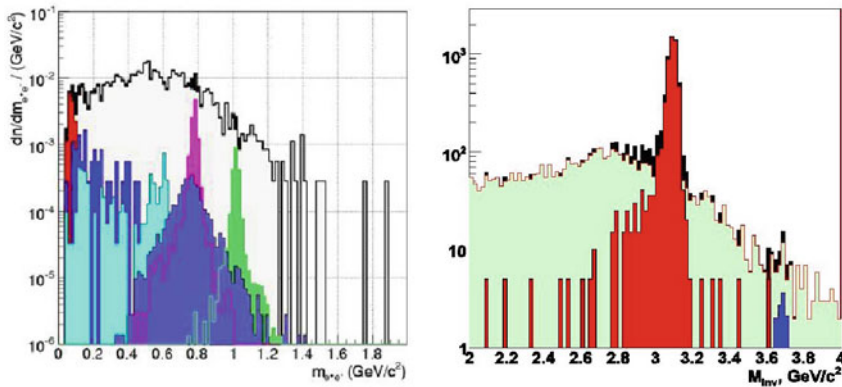


Fig. 3.16 Invariant mass spectra of electron-positron pairs simulated for central Au+Au collisions at 25 AGeV. The target thickness is 25 μ m. The analysis is based on full track reconstruction (STS-TRD-TOF), and on electron identification using information from RICH (ring recognition and ring-track matching), using energy loss signals in the TRD layers, and timing information from the RPC. *Left panel:* low mass dielectrons simulated for 200k central collisions with a cut on $p_t > 0.2$ GeV/c for single electrons. Different sources are shown with different color; from left to right: π^0 , η , and ω Dalitz decays, ρ , ω , and ϕ meson. *Right panel:* J/ψ and ψ' for $4 \cdot 10^{10}$ central events, $p_t > 1.2$ GeV/c for single electrons.

decay into dielectrons is simulated with the PLUTO (thermal source) generator. The dominating electron background contribution is from γ -conversion in the target. Thus, both for low-mass vector meson and for charmonium simulations, an Au-target of 25 μ m (0.1% interaction length) is used. When

implementing this thin target the remaining background is dominated by electrons from π^0 -Dalitz decays. In order to enhance the statistics for J/ψ mesons a segmented target will be used in the experiment. The phase-space coverage of the CBM detector for the measurement of vector mesons decaying into electron pairs is illustrated in Fig. 3.17.

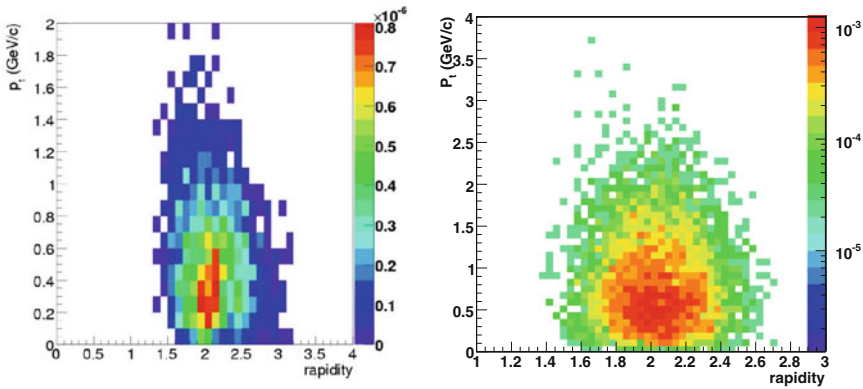


Fig. 3.17 Phase space distribution in transverse momentum versus rapidity for reconstructed and identified ρ mesons (*left*) and J/ψ meson (*right*) in central Au+Au collisions at 25 AGeV beam energy (midrapidity = 2).

Several modifications of the CBM detector setup have been studied in order to reduce the combinatorial background of electron–positron pairs from π^0 -Dalitz decays and γ -conversion. As already mentioned, the target thickness was limited to 25 μm to suppress γ -conversion. The magnetic field was reduced to 70% of its nominal value in order to increase the reconstruction efficiency of low-momentum tracks. For this field the momentum resolution is still well below 2%. In order to improve the rejection power of close dielectron pairs the MVD detector is included in this setup. To further increase the reconstruction efficiency of low-momentum tracks both MVD and the first 4 of the 6 STS stations were enlarged by a factor 1.5 in the bending plane. In this way the reconstruction efficiency for tracks with momenta of 150 and 200 MeV/c was increased to 15% and 45%, respectively.

The resulting dielectron invariant mass spectrum is shown in the left panel of Fig. 3.16, and the reconstruction efficiencies of the vector mesons are listed in Table 3.5. For the analysis, single electrons with transverse momenta below 0.2 GeV/c were rejected. This cut strongly reduces the background, but also restricts the acceptance for low transverse momentum pairs at low invariant masses. However, some theoretical models expect that very soft dilepton pairs are particularly sensitive probes of the chiral and deconfinement phase transition and the critical point. Figure 3.18 illustrates that the CBM acceptance indeed covers a wide range of dielectron transverse momenta for the

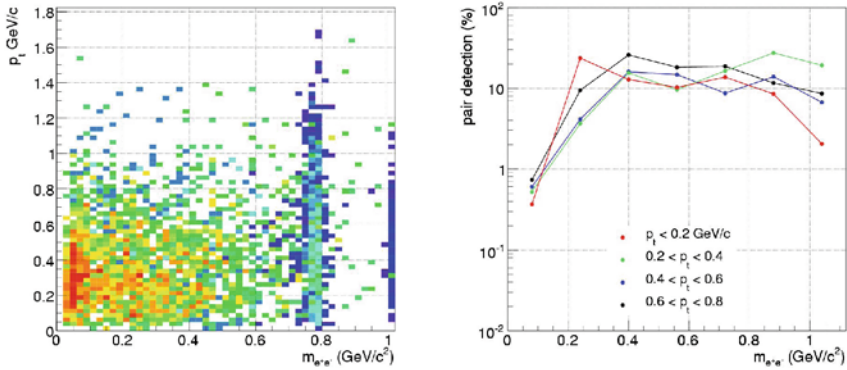


Fig. 3.18 Dielectron pair detection in CBM without p_t -cut on single electrons. *Left:* Transverse momentum of signal pairs versus their invariant mass. *Right:* Pair detection probability versus invariant mass for different p_t ranges.

Table 3.5 Efficiencies and signal-to-background ratios for vector mesons in the dielectron decay channel for central Au+Au collisions at 15, 25, and 35 AGeV. The presented efficiencies include geometrical acceptance, reconstruction and particle identification efficiencies. The S/B ratio is determined in a 2σ region around the peak, for the ρ a mass range of 0.2–0.9 GeV/c² was chosen. The mass resolution does not change with energy as the magnetic field is kept constant.

	ρ	ω	ϕ	J/ψ	ψ'
Branching ratio (e^+e^-)	$4.5 \cdot 10^{-5}$	$7.1 \cdot 10^{-5}$	$3 \cdot 10^{-4}$	6%	0.88%
15 AGeV beam energy					
Multiplicity	15	27	0.5	$2.44 \cdot 10^{-6}$	
efficiency (p_t cut ^a)	4.7%	6.7%	9.4%	12%	
S/B (p_t cut ^a)	1/100	0.39	0.32	7	
25 AGeV beam energy					
Multiplicity	23	38	1.28	$1.92 \cdot 10^{-5}$	$2.56 \cdot 10^{-7}$
σ_m [MeV/c ²]	–	14	16	27	29
Efficiency (no p_t -cut)	5.4%	7.2%	9.6%		
S/B (no p_t -cut)	0.003	0.32	0.3		
Efficiency (p_t cut ^a)	4.6%	6.8%	9.8%	13%	14%
S/B (p_t cut ^a)	1/130	0.48	0.32	12	0.4
35 AGeV beam energy					
Multiplicity	26	46	1.5	$5.45 \cdot 10^{-5}$	$9.96 \cdot 10^{-7}$
efficiency (p_t cut ^a)	4.3%	6.7%	9.4%	10%	9%
S/B (p_t cut ^a)	1/71	0.8	0.29	12	0.15

^a Low-mass vector mesons $p_t > 0.2$ GeV/c, J/ψ and ψ' $p_t > 1.2$ GeV/c

lowest invariant masses. The goal of future studies is to further reduce the background in this region, and to improve the signal-to-background ratio.

The J/ψ simulations are performed with 8 silicon micro-strip detectors only, no MVD was implemented. In order to reduce the contribution of electrons from γ -conversion in the target (which is the dominant background source for a 1% interaction target) the thickness of the gold target was

chosen to 25 μm corresponding to an interaction probability of 0.1%. The combinatorial background is drastically reduced by rejecting single electrons with transverse momentum below 1.2 GeV/c. The remaining background is due to electrons from π^0 -Dalitz decays. The results of the simulations are presented in Fig. 3.16 and in Table 3.5 for different beam energies. In order to perform high statistics measurements for charmonium a segmented target will be used, and a trigger concept has to be developed.

3.6.2 Muon simulations

The CBM muon detection system is designed to measure muon pairs from the decay of vector mesons ($\rho, \omega, \phi, J/\psi$) produced in heavy-ion collisions. At FAIR energies the muon momenta can be rather low, and, therefore, we develop a muon detection concept with a dynamical definition of absorber thickness according to the muon momentum. The actual design of the muon detector system consists of 6 hadron absorber layers (iron plates of thickness 20, 20, 20, 30, 35, 100 cm) and 18 gaseous tracking chambers located in triplets behind each iron slab. The absorber/detector system is placed downstream of the Silicon Tracking System (STS) which determines the particle momentum. The definition of a muon depends on its momentum which varies with the mass of the vector mesons and with beam energy. For example, muons from the decay of J/ψ mesons have to pass all 6 absorber layers with a total iron thickness of 225 cm corresponding to 13.4 interaction length λ_I . The muons from the decay of low-mass vector mesons (ρ, ω, ϕ) only have to penetrate through 5 iron absorber layers with a total thickness of 125 cm (corresponding to 7.5 λ_I).

3.6.2.1 Absorber optimization and background studies

In a first step we studied the survival probability of muons from vector meson decays in comparison to hadrons as function of the thickness of an iron absorber. The result is presented in the left panel of Fig. 3.19 for central Au+Au collisions at an energy of 25 AGeV. The particle yields are normalized to the respective yields in front of the absorber. The high energetic muons from decay of J/ψ mesons penetrate the absorber almost without any losses. The muons from ω meson decays are absorbed stronger, but still not as much as the hadrons. The simulations demonstrate that for absorber layers thicker than 1 m the remaining background is completely dominated by muons from weak meson decays. In order to suppress this contribution, the muon detection system should be as close to the target and as compact as possible.

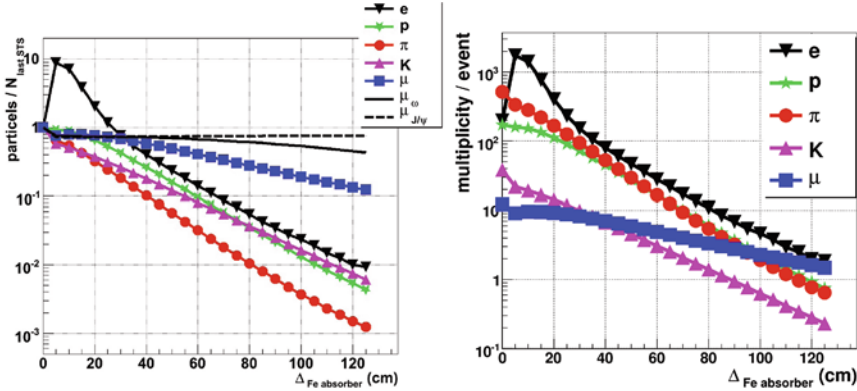


Fig. 3.19 Particle multiplicity behind an iron absorber as function of absorber thickness simulated for central Au+Au collisions at 25 AGeV. The muons from weak decays are labelled as μ . *Left*: Number of particles normalized to their respective yield in front of the absorber. *Right*: particle multiplicity per event.

The experimental challenge is to reconstruct the tracks of charged particles which penetrate the segmented hadron absorber. In this respect, the thickness of the first absorber layer plays a particular role. With increasing absorber thickness the particle multiplicity decreases, but the multiple scattering increases. The total particle multiplicities per event (including secondaries) after the first absorber layer is shown in the right panel of Fig. 3.19. The multiplicity at thickness zero corresponds to the number of particles in front of the absorber. The yield behind the absorber is dominated by secondary electrons. In order to reduce the hit density in the first muon tracking detector to a tolerable level the absorber should have a thickness of at least 20 cm.

The feasibility studies discussed below are performed for central Au+Au collisions. The background is generated using UrQMD events. The multiplicities of vector mesons are taken from the HSD code. The momentum distributions of the vector mesons and of their decay products are calculated using the thermal source generator PLUTO. Finally the muon pairs are embedded into UrQMD events and are transported through the detector setup using the GEANT3 transport code. The analysis of the simulated data is based on full track reconstruction in the Silicon Tracking System (STS) and in the muon chambers. The events are reconstructed using a Cellular Automaton algorithm for track finding, and a Kalman filter for track fitting. The STS consists of 8 stations of micro-strip detectors. The muon detectors are subdivided into pads which grow in size both with increasing polar angle and detector distance from the target in order to keep the occupancy for central Au+Au collisions below 5%. The pad size varies between $0.14 \times 0.28 \text{ cm}^2$ and $2.22 \times 4.44 \text{ cm}^2$.

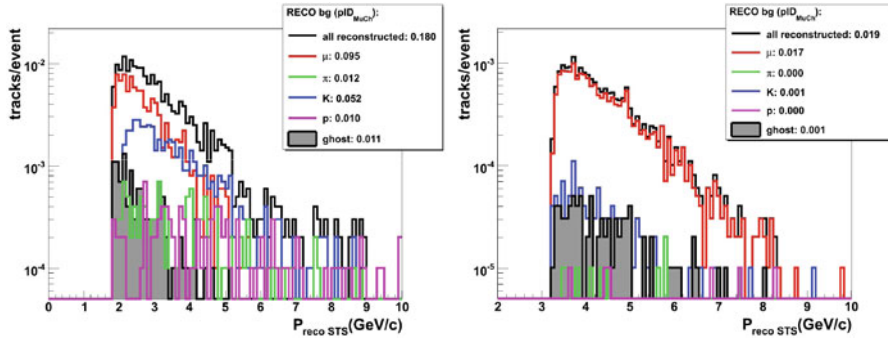


Fig. 3.20 Reconstructed background tracks per event simulated for central Au+Au collision at a beam energy of 25 AGeV. The integrated yields of the different background contributions are given in the insert. The calculations are performed for a total iron absorber thickness of 1.25 m (*left panel*) and for a thickness of 2.25 m (*right panel*).

In order to study the performance of the CBM muon detection system we have analyzed the reconstructed particle tracks which pass the absorbers. The simulations were performed for a total iron absorber thickness of 1.25 m of iron which is used for the measurement of muons from low-mass vector mesons, and for a thickness of 2.25 m of iron used for charmonium measurements. The results are presented in Fig. 3.20 which depicts the composition of reconstructed particles per central Au+Au collision. For the thin absorber in total about 0.2 tracks are reconstructed per event, the dominating contribution (about 50%) are muons from weak decays which are wrongly matched to the tracks of their mother particles. For an absorber thickness of 2.25 m only 0.02 tracks are reconstructed per event, 90% of them being muons.

The background contribution from muons from weak decays is surprisingly small as compared to the 800 charged pions produced in the collision. The reason is that most of the weak pion and kaon decays are recognized (and rejected) by the track reconstruction routines of the STS. This is illustrated in Fig. 3.21 where the number of muons from weak decays is shown as function of the z -position of the decay vertex. It turns out that in average 2.4 muons from weak decays are reconstructed per event in the STS, and only 0.4 muons survive the cut on the primary vertex. These muons stem from decays which happen shortly downstream of the target, and, hence, their tracks are perfectly reconstructible in the STS. The first STS station is located 30 cm downstream of the target.

The kaons and protons with punch through the absorber can be further rejected by a condition on their time of flight. This information can be obtained from the TOF wall for the J/ψ analysis where the full absorber (2.25 m iron) is required. For the detection of muons from low-mass vector mesons an additional RPC-TOF detector can be installed in front of the last iron block of 1 m thickness. The additional condition on time-of-flight reduces

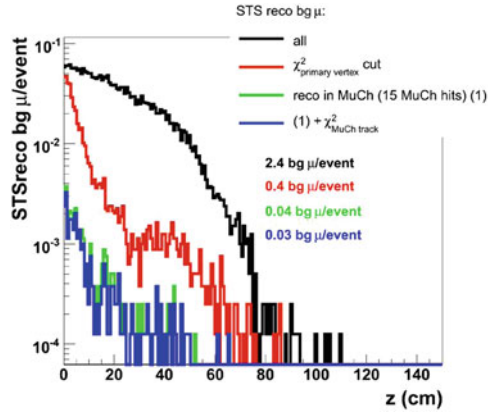


Fig. 3.21 Production vertex in z -direction of secondary muons reconstructed in the STS (central Au+Au collision, 25 AGeV); from *top to bottom*: all (*black*), muons surviving the χ^2 cut for selecting those from the target (*red*), muons reconstructed in the muon detector (*green*) and surviving a χ^2 cut on the track quality in the MuCh detector (*blue*).

the efficiency for the signal, but increases the signal-to-background ratio (see Table 3.6).

3.6.2.2 Invariant mass spectra and phase-space coverage

The combined performance of the STS and the muon detection system as described above is illustrated in Fig. 3.22 which displays the invariant mass spectra of muon pairs in the region of low-mass vector mesons (left panel) and for charmonium (right panel) simulated for central Au+Au collisions at a beam energy of 25 AGeV. In the analysis of low-mass vector mesons not only pairs of “hard” muons are included, i.e. muons which pass 1.25 m of iron, but also pairs of “hard” and “soft” muons where the latter only pass 0.9 m of iron. In this way the reconstruction efficiency for low-mass vector mesons is increased, with only little effect on the signal-to-background ratio. For the analysis of charmonium only pairs of “hard” muons (penetrating 2.25 m of iron) are considered, no cut on transverse momentum is applied. The signal-to-background ratio is on the order of 10 for J/ψ mesons, and about 0.1 for ψ' mesons. The latter value is based on a background extrapolation using a Gaussian distribution fitted to the spectrum. The values for efficiencies and signal-to-background ratios are listed in Table 3.6 for different vector mesons and beam energies.

The phase-space coverage of the CBM muon detection system is shown in Fig. 3.23 for ρ mesons (left panel) and for J/ψ mesons (right panel) in the plane transverse momentum versus rapidity. In the case of the ρ mesons both “hard + hard” and “soft + hard” muon pairs are taken into account. Note,

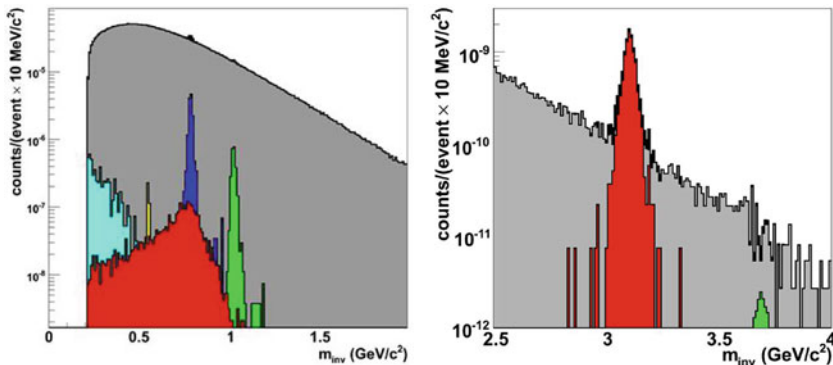


Fig. 3.22 Invariant dimuon mass spectra calculated for $4 \cdot 10^8$ (left) and $3.8 \cdot 10^{10}$ (right) central Au+Au collisions at 25 AGeV beam energy. *Left panel:* low-mass range including as dimuon signals η -Dalitz decays, ρ , η , ω , and ϕ meson (from left to right). The data include “hard-hard” as well as “hard-soft” pairs without any cuts on momentum. “Hard” muons traverse 1.25 m of iron, “soft” muons pass only 0.9 m of iron. *Right panel:* charmonium mass range. A minimal transverse momentum of $p_t > 1$ GeV/c is required for single muons. No time-of-flight information is used for these spectra.

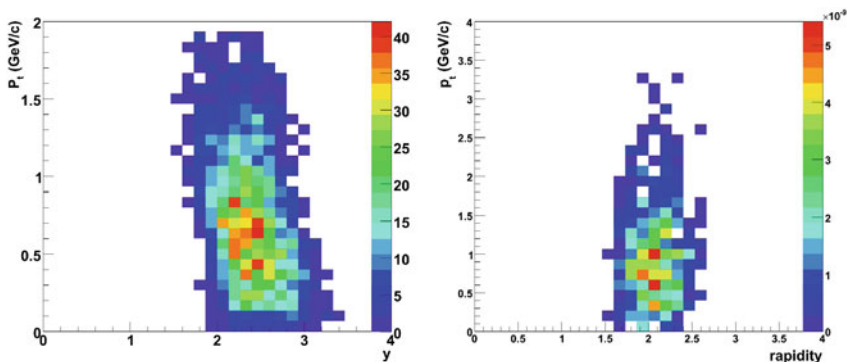


Fig. 3.23 Phase space coverage for dimuon pairs as a function of transverse momentum and rapidity calculated for central Au+Au collisions at 25 AGeV beam energy (midrapidity is at $y = 2$). *Left panel:* ρ mesons, both “hard-hard” and “hard-soft” muon pairs were included in the analysis. *Right panel:* J/ψ meson.

that “hard” muons which traverse 1.25 m of iron have laboratory momenta of more than $p_{lab} = 1.5$ GeV/c. This intrinsic momentum cutoff is reduced to $p_{lab} = 1.2$ GeV/c for “soft” muons which have to pass only 0.9 m of iron. Due to the absorption of muons with laboratory momenta below 1.2 GeV/c the acceptance for ρ mesons is slightly shifted to forward rapidities (midrapidity is at $y=2$ for 25 AGeV). In contrast, the acceptance for charmonium does not suffer from the momentum cutoff which is at $p_{lab} = 2.8$ GeV/c for an iron absorber of 2.25 m thickness.

Table 3.6 Efficiencies and signal-to-background ratios for vector mesons in the dimuon decay channel for central Au+Au collisions at 15, 25, and 35 AGeV. The efficiencies contain geometrical acceptance, reconstruction and particle identification. The analysis was made for pairs of “hard” muons (hh) which are required to pass 1.25 m Fe for low-mass vector mesons, or 2.25 m of iron in case of charmonia. For the beam energy of 25 AGeV also pairs of a “hard” and a “soft” muon (hs) for low-mass vector mesons are analyzed, with the soft muons passing only 0.9 m of iron. Moreover, the results including TOF information (hh+hs+TOF) are shown. The S/B ratio is extracted in a 2σ region around the peak, for the ρ a mass range of 0.2–0.9 GeV/ c^2 was chosen. The mass resolution does not change with energy as the magnetic field is kept constant.

	ρ	ω	ϕ	J/ψ	ψ'
Branching ratio ($\mu^+\mu^-$)	$4.5 \cdot 10^{-5}$	$7.1 \cdot 10^{-5}$	$3 \cdot 10^{-4}$	5.9 %	0.73%
15 AGeV beam energy					
Multiplicity	15	27	0.5	$2.44 \cdot 10^{-6}$	
efficiency (hh)	1.4 %	1.3 %	2.2 %	11.8 %	
S/B (hh)	0.002	0.08	0.01	3	
25 AGeV beam energy					
Multiplicity	23	38	1.28	$1.92 \cdot 10^{-5}$	$2.56 \cdot 10^{-7}$
geometrical acceptance	9%	12%	19%	36%	41%
σ_m [MeV/ c^2]	-	10	12	24	28
Efficiency (hh)	1.9 %	1.9%	4.3%	16%	19%
S/B (hh)	0.002	0.1	0.03	7	0.09
Efficiency (hh+hs)	2.7 %	3.7%	6%		
S/B (hh+hs)	0.001	0.08	0.03		
Efficiency (hh+hs+TOF)	1.6 %	2.3%	3.9%		
S/B (hh+hs+TOF)	0.002	0.16	0.08		
35 AGeV beam energy					
Multiplicity	26	46	1.5	$5.49 \cdot 10^{-5}$	$9.96 \cdot 10^{-7}$
efficiency (hh)	1.8 %	3.3 %	5.4 %	16%	19%
S/B (hh)	0.001	0.09	0.03	11	0.2

The acceptance for low-mass vector mesons as a function of their transverse momentum and the invariant mass of the muon pairs is shown in the left panel of Fig. 3.24. The analysis includes “hard + hard” as well as “hard + soft” muon pairs. The right panel of Fig. 3.24 depicts the efficiency for muon pairs from ρ meson decays as a function of invariant mass for different thresholds in transverse momentum.

The performance of the CBM muon detection system for low-mass vector mesons can be considerably improved when installing a time-of-flight detector between the second last and the last absorber of 1 m thickness. Figure 3.25 presents the invariant mass spectra of muon pairs calculated for central Au+Au collisions at 25 AGeV. In the analysis only “hard+hard” muon pairs are taken into account. Figure 3.25 presents results obtained without (left panel) and with an additional condition on the time-of-flight information (right panel) assuming a time resolution of 80 ps. In the latter case the reconstruction efficiencies are 1% for ρ and ω mesons, and 2.8% for ϕ mesons.

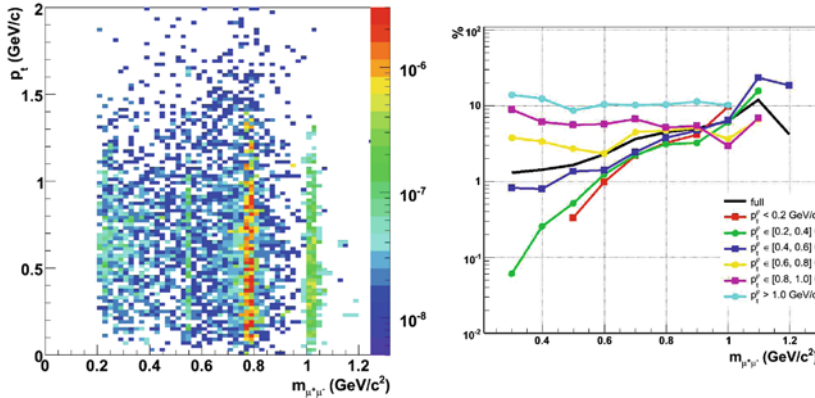


Fig. 3.24 *Left panel:* Transverse momentum of muon pairs versus their invariant mass. *Right panel:* Efficiency for muon-pairs from the ρ meson as a function of invariant mass for cutoffs in transverse momentum p_t . In both cases the analysis includes “hard+hard” as well as “hard+soft” muon pairs without momentum cuts. No time-of-flight information is used.

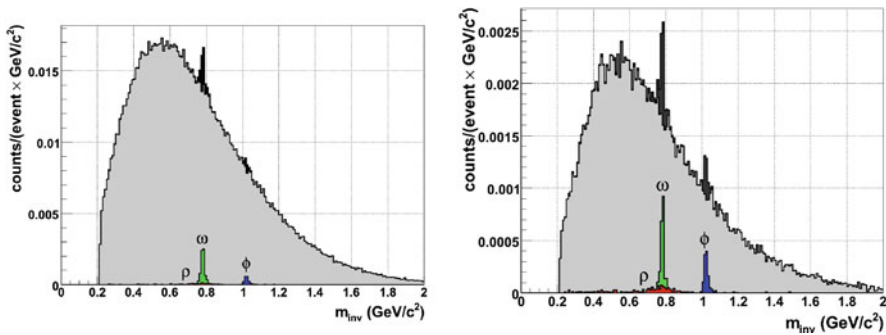


Fig. 3.25 Invariant dimuon mass spectra calculated for central Au+Au collisions at 25 AGeV beam energy. The analysis includes pairs of “hard” muons only. *Left panel:* no time-of-flight information used. *Right panel:* with a condition on time-of-flight given by a TOF wall installed in front of the last iron absorber of 1 m thickness. The time resolution was assumed to be 80 ps.

3.6.2.3 Dimuon Trigger studies

High statistics measurements of lepton pairs from the decay of vector mesons ($\rho, \omega, \phi, J/\psi$) produced in heavy-ion collisions require high reaction rates, and, hence, a selective trigger. The low particle multiplicities behind the hadron absorber of the CBM muon detection system enable the implementation of a fast trigger on muon pairs. The CBM trigger concept is flexible with respect to the muon momentum which depends on the mass of the vector meson and on the beam energy. Only the last 3 muon chambers located behind the full absorber of 225 cm iron will be used for the generation of a

charmonium trigger. The trigger on low-mass vector mesons will be derived from hits in the 3 muon tracking chambers in front of the last absorber (after 125 cm of iron). In this case, the tracks stop in the last absorber, and no hits are measured behind. The trigger generation proceeds via the following steps: (i) selection of events with at least 6 hits in the last (or second last) detector triplet, (ii) calculation of a track segment by a linear fit of the hit positions, (iii) extrapolation of the track segment to the vertex, and selection of tracks according to the fit parameters (χ^2 and vertex). Optionally, the time-of-flight information is included in the trigger on charmonia. The event selection will be performed online by the CBM computer farm based on many-core processors.

The quality of the track extrapolation depends on the position resolution of the muon trigger chambers. Therefore, the trigger performance has been investigated for different granularities of the muon chambers. The results shown below were obtained with a pad size of 2.23×4.48 cm². The track selection criteria are the χ^2 of the fit, the X - and Y -distributions at $Z = 0$. The trigger performance is quantified by the background suppression factor (which is the fraction of minimum bias events which survive the trigger cuts) and by the efficiency for J/ψ mesons which pass the trigger conditions. The background suppression factor and the J/ψ trigger efficiency for minimum bias Au+Au collisions at 25 AGeV are listed Table 3.7. The background suppression factor decreases by about a factor of 2 if the pad size of the muon detectors is increased by a factor of 2. The trigger performance is increased by more than a factor of three if the ToF information is included (see last column of Table 3.7).

Table 3.7 Background suppression factor for minimum bias Au+Au collisions at 25 AGeV and detection efficiency for J/ψ mesons after different trigger conditions (see text).

Trigger cuts	No cuts	MuCh	MuCh+ToF
Background suppression factor	1	606	2222
J/ψ efficiency (%)	20.3	15.2	13.7

The CBM data acquisition system is able to process minimum bias Au+Au collisions up to a reaction rate of 25 kHz without trigger reduction. Hence, the CBM experiment can be operated at the full design luminosity of 10 MHz if the event rate is reduced by a factor of 400. This factor is easily achieved by the dimuon trigger even without time-of-flight selection (see Table 3.7). In order to test the robustness of the trigger concept with respect to additional detector noise we added 10 hits in each muon chamber of the trigger triplet. It turns out that the background reduction factor is reduced by about 15% only.

For low-mass vector mesons only the selection criteria based on the track quality is applied. Due to the high hit density in detector triplet in front of

the last absorber layer a background suppression factor of about 20 can be achieved without appreciable loss of signals. This factor would permit to run the CBM experiment with about 0.5 MHz. Studies are in progress to improve the trigger concept for low-mass vector mesons by taking into account the track and momentum information from the STS.

3.7 Direct photons

The measurement of photon production from the fireball, the so-called direct photons, is together with the dileptons another penetrating probe giving access to direct radiation from the early created, dense medium. In particular the transverse momentum spectra of single photons are suggested to provide information on the (highest) temperature of the system. In CBM, so far two ways of direct photon measurements have been investigated in simulations: the classical method using the electromagnetic calorimeter, and the possibility to reconstruct in particular the low momentum photons by γ -conversion in the target and measurement of the resulting electrons.

The ECAL provides photon identification via an energy loss measurement from electron-photon showers in the sampling scintillator-lead structures of the ECAL modules. In simulations, selected isolated clusters of calorimeter cells not matching with any reconstructed (charged) track are fitted in order to extract the energy of the photon. An energy resolution of approximately 7.5% is reached integrating over all momenta. The average photon reconstruction efficiency for energies $E > 0.5$ GeV is (35–40)% depending on the photon production angle. Currently a setup with two arms covering $\pm 45^\circ$ on both sides for $9^\circ < \theta_{\text{lab}} < 20^\circ$ at a distance of 12 m from the target is investigated. With such a setup approximately 80 photons are detected per central Au+Au collision at 25 AGeV beam energy out of which 90% are from π^0 decays but also 3% from η -decay. Invariant mass spectra for the extraction of π^0 mesons from the combination of two photons are shown in Fig. 3.26. The huge combinatorial background is still a lower estimate as not all background sources are included yet. With a signal-to-background ratio on the order of 0.01 the background can be well estimated by even-mixing methods and subtracted. The reconstruction probabilities depending on energy cutoffs are on the order of (1–2)%. Similar conditions concerning signal-to-background ratios and efficiencies are expected for the reconstruction of the η meson.

As the energy resolution of the ECAL increases below energies of 5 GeV, a detection of low momentum photons by the conversion into an e^\pm pair might be favorable as the momentum resolution from tracking is at a 1% level down to momenta of 0.5 GeV/c. Electrons are identified as described above for the di-electron measurements, only pairs from conversion in the target are selected for this analysis. For the combined pairs the momentum

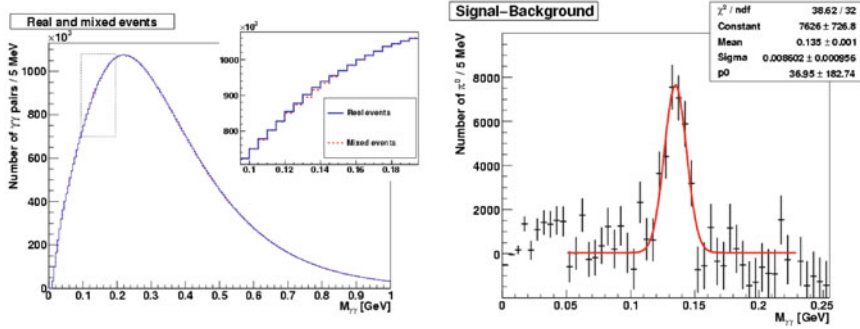


Fig. 3.26 Invariant mass spectra for momentum integrated π^0 mesons for 5,000 central Au+Au collisions at 25 AGeV beam energy. *Left*: Full spectrum with combinatorial background. *Right*: Background subtracted spectrum.

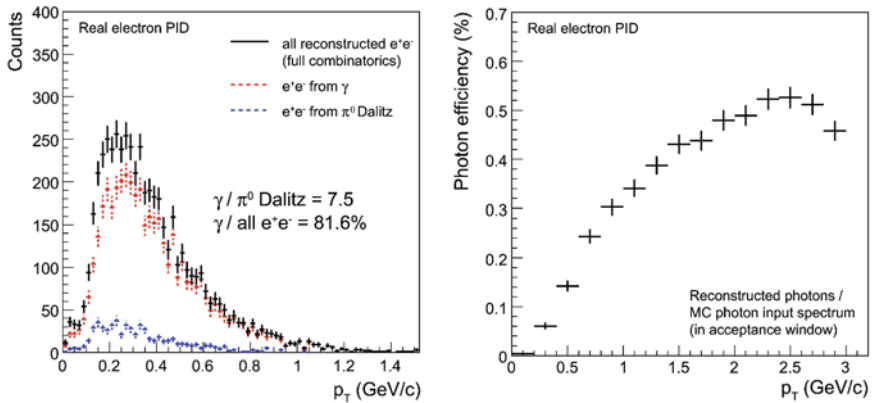


Fig. 3.27 *Left*: Transverse momentum spectrum of reconstructed photons from the target identified by their conversion into dielectrons (central Au+Au collisions at 25 AGeV, 20,000 events). An opening angle cut of $\theta < 1^\circ$ is applied. The contributions of the two main sources (γ conversion (red), π^0 -Dalitz decay (blue)) are shown separately (*top to bottom*). *Right*: Combined reconstruction and identification efficiency of photons in the acceptance window of CBM ($2.5^\circ < \theta_{25^\circ}$ for embedded π^0).

resolution is about 2%. A cut on the opening angle of the dilepton pair is done ($\theta < 1^\circ$) in order to enhance dielectrons from γ conversion above those from π^0 -Dalitz decay. The resulting transverse momentum spectrum of the photons is shown in Fig. 3.27. Dominant contributions clearly come from photons and π^0 decays, misidentifications play a minor role. The overall identification probability of photons via conversion in the target is on the order of 0.5 % (Fig. 3.27). By combining two reconstructed photons π^0 mesons can be identified in the invariant mass spectrum, however their identification probability goes quadratically with the single-photon efficiency. Measuring photons from π^0 decay in addition to the inclusive ones is an important tool

to extract direct photons as this allows the construction of double ratios as $(\gamma_{\text{incl}}/\gamma_{\text{decay}})_{\text{meas.}}/(\gamma_{\text{incl}}/\gamma_{\text{decay}})_{\text{sim.}}$ in data analysis.

With the same experimental setup as used for the measurement of hadron and strange hyperon production, both photon and π^0 measurements can be done in parallel with sufficient statistics. The presented spectrum for the ECAL is for 5,000 central Au+Au collisions only corresponding to less than 1 s beamtime of CBM. One day of data taking will e.g. provide on the order of 1,500 well measured π^0 at 2 GeV/c ($S/B \sim 0.6$) in central Au+Au collisions with the conversion method. With separate conversion runs using a thick target statistics can of course be enhanced.

3.8 Expected particle yields

In the following we estimate rates and yields of various particles to be measured with CBM under typical running conditions. The estimates are based on particle multiplicities predicted by the Hadron-String-Dynamics (HSD) transport code version V2.4 for Au+Au collisions at different beam energies. The multiplicities were calculated for central collisions ($b = 0$ fm) and scaled down by a factor of 5 corresponding to minimum bias collisions. This factor was derived from the pion multiplicities which were calculated for both central and minimum bias collisions. Acceptances and efficiencies were determined by full detector simulations including event reconstruction and particle identification as explained in the previous paragraphs.

The yields are based on a data archiving rate of 1 Gb/s. If no online event selection can be performed, this rate corresponds to about 25 kHz minimum bias Au+Au collisions at FAIR energies. This is the case for the measurement of hadrons (including multi-strange hyperons) and of low-mass dielectrons. Online event selection is possible for the measurement of low-mass dimuons, D mesons, and of charmonia (both in the electron and muon channel). For low-mass dimuons an event-suppression factor of 20 can be achieved for min. bias collisions allowing for a primary reaction rate of 500 kHz. For open charm, the online track reconstruction algorithms select events with displaced vertices, and are able to reject about 99% of the reactions. This would allow to run with a primary reaction rate of about 2.5 MHz. However, the read-out speed of the CMOS sensors in the Micro-Vertex Detector limits the reaction rate to 100 kHz. In this case the event-pile up in the MAPS detectors is well below 10, a number which can be handled by the track reconstruction algorithms. Once faster and radiation harder ultra-thin pixel detectors are available, the performance of the online trigger system will be fully exploited. For the measurement of charmonia via the dimuon decay the online event selection is based only on the information provided by the last muon chamber triplet where the hit rate is very low. In case of charmonium measurements via the di-electron channel the generation of a trigger signal requires information

from the TRD and the STS. Both for the electron and muon channel an online event suppression factor of 400–1000 is achievable, thus permitting to increase the primary reaction rate up to 10 MHz.

Table 3.8 Estimated particle yields for minimum bias Au+Au collisions at 25 AGeV based on HSD calculations. For all measurements except for low-mass vector mesons in the dielectron channel a 1% interaction target is assumed.

Particle	N	Decay mode	BR	R/s (MHz)	T	ϵ (%)	Y/s	Y/10 w
η	6.6	$\mu^+\mu^-$	$5.8 \cdot 10^{-6}$	0.5	y	3	0.56	$3.4 \cdot 10^6$
K^+	8	—	—	0.025	n	18.4	$3.7 \cdot 10^4$	$2.2 \cdot 10^{11}$
K^-	2.6	—	—	0.025	n	18.4	$1.2 \cdot 10^4$	$7.2 \cdot 10^{10}$
K_s^0	5.4	$\pi^+\pi^-$	0.69	0.025	n	10	$9.3 \cdot 10^3$	$5.6 \cdot 10^{10}$
ρ	4.6	e^+e^-	$4.7 \cdot 10^{-5}$	0.025	n	4.6	0.25	$1.5 \cdot 10^6$
ρ	4.6	$\mu^+\mu^-$	$4.6 \cdot 10^{-5}$	0.5	y	2.7	2.8	$1.7 \cdot 10^7$
ω	7.6	e^+e^-	$7.1 \cdot 10^{-5}$	0.025	n	6.8	1	$5.5 \cdot 10^6$
ω	7.6	$\mu^+\mu^-$	$9 \cdot 10^{-5}$	0.5	y	3.7	12.6	$7.6 \cdot 10^7$
ϕ	0.256	e^+e^-	$3 \cdot 10^{-4}$	0.025	n	9.8	0.19	$1 \cdot 10^6$
ϕ	0.256	$\mu^+\mu^-$	$2.9 \cdot 10^{-4}$	0.5	y	6	2.	$1.3 \cdot 10^7$
Λ	6.4	$p \pi^-$	0.64	0.025	n	10.6	$1.1 \cdot 10^4$	$6.5 \cdot 10^{10}$
Ξ^-	0.096	$\Lambda \pi^-$	0.999	0.025	n	2.1	50.4	$3 \cdot 10^8$
Ω^-	0.0044	ΛK^-	0.68	0.025	n	1	0.75	$4.5 \cdot 10^6$
D^0	$7.5 \cdot 10^{-6}$	$K^- \pi^+$	0.038	0.1	y	3.25	$8.5 \cdot 10^{-4}$	$5.1 \cdot 10^3$
D^0	$7.5 \cdot 10^{-6}$	$K^- \pi^+ \pi^+ \pi^-$	0.075	0.1	y	0.37	$2.1 \cdot 10^{-4}$	$1.3 \cdot 10^3$
D^0	$2.3 \cdot 10^{-5}$	$K^+ \pi^-$	0.038	0.1	y	3.25	$2.6 \cdot 10^{-3}$	$1.6 \cdot 10^4$
D^+	$8 \cdot 10^{-6}$	$K^- \pi^+ \pi^+$	0.092	0.1	y	4.2	$3.1 \cdot 10^{-3}$	$1.9 \cdot 10^4$
D^-	$1.8 \cdot 10^{-5}$	$K^+ \pi^- \pi^-$	0.092	0.1	y	4.2	$7 \cdot 10^{-3}$	$4.2 \cdot 10^4$
D_s^+	$1.08 \cdot 10^{-6}$	$K^+ K^- \pi^+$	0.053	0.1	y	1	$5.7 \cdot 10^{-5}$	$3.5 \cdot 10^2$
Λ_c	$4.9 \cdot 10^{-4}$	$p K^- \pi^+$	0.05	0.1	y	0.5	$1.2 \cdot 10^{-2}$	$7.4 \cdot 10^4$
J/ψ	$3.8 \cdot 10^{-6}$	e^+e^-	0.06	10	y	13	0.32	$1.9 \cdot 10^6$
ψ'	$5.1 \cdot 10^{-8}$	e^+e^-	$7.3 \cdot 10^{-3}$	10	y	14	$5.2 \cdot 10^{-4}$	$3.2 \cdot 10^3$
J/ψ	$3.8 \cdot 10^{-6}$	$\mu^+\mu^-$	0.06	10	y	16	0.36	$2.2 \cdot 10^6$
ψ'	$5.1 \cdot 10^{-8}$	$\mu^+\mu^-$	$7.3 \cdot 10^{-3}$	10	y	19	$7.1 \cdot 10^{-4}$	$4.3 \cdot 10^3$

N = multiplicity in minimum bias collisions (= 1/5 of central collisions), BR = branching ratio, R/s = reaction rate, T = trigger needed (y/n), ϵ = acceptance and efficiency for central collisions, Y/s = particle yield per second, and Y/10 w = particle yield per 10 weeks. The masses of the listed particles are as follows: η (547), K^\pm (494), K_s^0 (497), ρ (770), ω (782), ϕ (1020), Λ (1115), Ξ^- (1321), Ω^- (1672), d^0 (1864), D^\pm (1869), Λ_c (2285), J/ψ (3097), ψ' (3686).

Chapter 4

Experiments complementary to CBM

4.1 The NICA/MPD project at JINR

At JINR (Dubna) a new Nuclotron based Ion Collider fAcility (NICA) including a Multi-Purpose Detector (MPD) is proposed in order to investigate heavy-ion collisions at $\sqrt{s_{NN}} = 3\text{--}9$ GeV [5]. NICA will consist of several accelerator stages: Multi-charged ions will be generated in the KRION ion source, and then accelerated in a RFQ injector up to energies of 6 AMeV. Then, the ions are injected into a new Booster-Synchrotron, accelerated, extracted and stripped. Then, the beam is transferred to the existing Nuclotron, and accelerated up to the energy required by the experiment. Finally, the beam is injected into the collider rings. The beams will be cooled in order to reach the average design luminosity of $10^{27} \text{ cm}^{-2}\text{s}^{-1}$ which corresponds to an interaction rate of 10 kHz for U+U collisions.

The scientific goal of the NICA/MPD project is to search for phase transitions, the coexistence phase, and critical phenomena in nuclear matter. The experimental approach is to measure the multiplicity and the phase-space distributions of identified hadrons including multi-strange hyperons. This program includes the measurement of event-by-event fluctuations of multiplicities and transverse momenta, of directed and elliptic flow, HBT and particle correlations.

According to the conceptional design the MPD consists of an inner tracker based on silicon micro-strip detectors and a time-projection chamber, and of an outer tracker based on straw-tube technology. The detectors are arranged in barrels to fully cover azimuthal angles, complemented by end-cap trackers (straw tube wheels). The detector system is located inside a solenoidal magnetic field with a field strength of 0.5 T. Possible detector upgrades include a time-of-flight barrel based on RPC technology to improve the capability of particle identification, and an electromagnetic calorimeter for electron and gamma measurements. Beam counters will provide a trigger and information on the interaction point. Zero-degree calorimeters will measure the energy of

the spectator nucleons in order to obtain information on the collision centrality.

The commissioning of the accelerator complex and of the detector system is scheduled for 2014.

4.2 The NA61 experiment at the CERN-SPS

As discussed in [Part IV](#) the NA49 collaboration found distinct structures in the excitation functions of the K^+/π^+ ratio and in the mean transverse particle momenta around a beam energy of 30 AGeV. In order to provide a complete data set it has been proposed to extend these measurements to smaller collision systems, and to measure inclusive spectra of identified hadrons in C+C, Si+Si and In+In collisions at beam energies from 10 to 158 AGeV with an upgraded NA49 apparatus [21]. The proposal includes the measurement of particle production cross sections in $p + p$, $p + A$ and $\pi + A$ interactions needed for the interpretation of neutrino experiments and cosmic shower data.

The proposed heavy-ion program includes the measurement of particle yields, transverse momenta, fluctuations and collective flow in collision systems smaller than Pb+Pb with good statistics, in particular for beam energies below 40 AGeV. Typical systematic errors of 5–10% on particle yields and of 10 MeV for T and $\langle m_t \rangle$ are expected. The excitation function of anisotropic flow will be measured for charged pions, protons, K_S^0 mesons and Λ baryons.

In order to reduce the statistical errors, to increase the detector acceptance, and to improve the centrality and event-plane determination the following detector upgrades have been or will be implemented:

- The TPC readout has been replaced by an ALICE-like system providing an increased event rate by a factor of about 20.
- A new projectile spectator detector (PSD) is being built in order to improve the selection of the event centrality and the determination of the reaction plane for high precision measurements of flow and event-by-event fluctuations. This development is done in collaboration with CBM.
- The NA49 acceptance can be enlarged for NA61 by redesigning the field cages of the vertex TPCs.

Since 2006 the measurements of $p+p$ and $p+A$ collisions at energies from 10 to 158 GeV beam energy related to the neutrino and cosmic ray physics program have been started. Once heavy-ion beams will become available at CERN-SPS it is proposed to run for about 30 days per year at energies between 10 and 158 AGeV for 3 years in order to collect $2 \cdot 10^6$ events at each energy. NA61 will use the Pb-beam provided by the SPS in order to produce a fragmentation beam of C-, Si-, and In- projectiles needed for the planned system-size study. The efficient use of the fragmentation beam has still to be

proven in order to get full recommendation for this research program from CERN. In addition, 4 weeks of proton beam are required per year.

4.3 The RHIC energy scan program

As discussed in [Part IV](#) the experiments at RHIC found evidence for partonic degrees-of-freedom in the early fireball of a heavy-ion collision: the large azimuthal anisotropy of particle emission in non-central collisions (elliptic flow), the scaling of the strength of the elliptic flow with the constituent quark content of the measured hadrons (quark number scaling), and the strong suppression of high momentum particles traversing the medium (jet quenching). No signature of a chiral phase transition has been found. In order to search for indications of phase transitions and for the QCD critical endpoint, the RHIC community has started to prepare an energy scan, as these features of the QCD phase diagram are predicted to be located in the region of large baryon-chemical potentials. The experimental approach at RHIC is to reduce stepwise the collision energy, and to look for the disappearance of the phenomena related to the early partonic phase. In the vicinity of the QCD critical endpoint critical phenomena are expected to appear, such as dynamical event-by-event fluctuations.

The PHENIX and STAR detectors are ideally suited for an energy scan program as their acceptance does not vary with the collision energy. In addition, the experiments are preparing detector upgrades to improve their particle identification capabilities. The most important upgrade of the STAR detector is the installation of the full TOF barrel providing clean K/π separation up to 1.6 GeV/c. This improvement will be essential for the measurement of event-by-event fluctuations of particle ratios. The upgrade of the PHENIX detector includes the Hadron-Blind Detector (HBD) which will improve the electron identification considerably, and the barrel silicon vertex tracker for direct charm and bottom measurements. This detector could perform triggering, centrality determination and reaction plane determination for the low energy runs.

On the other hand, the measurements will suffer from the limited luminosity of the colliding beams which drops dramatically with decreasing beam energy, in particular below injection energy. Therefore, major efforts of the RHIC accelerator experts are devoted to the improvement of the quality of the low energy beams. In 2007 a test run at $\sqrt{s_{NN}} = 9.3$ GeV (Au-beam) was performed in order to get first experience with technical challenges as magnetic field quality at low currents, RHIC harmonic number changes, inefficiencies due to RF acceptances, and intra-beam scattering. In a further test beam in 2008 first data at $\sqrt{s_{NN}} = 9.2$ GeV has been taken by the STAR experiment with an event rate of 0.7 Hz. Without further upgrades, a first energy scan is feasible.

For energies above injection energy ($\sqrt{s_{NN}} = 19.6$ GeV/c) interaction rates will be sufficiently high for the measurement of rare probes such as dileptons and charm by PHENIX and STAR. At lower collision energies, however, the measurements most probably will be limited to bulk observables like hadron yields, elliptic flow of abundant particles, and event-by-event fluctuations. Here, the goal is to reduce the statistical error of the particle yields with respect to the existing data taken at low SPS beam energies. Major improvements are expected for data on elliptic flow and fluctuations, in particular by the STAR experiment which has a large, uniform acceptance and excellent particle identification capability.

The STAR collaboration estimates that $5 \cdot 10^6$ events are needed per collision energy for the measurement of pions, kaons, and protons including spectra, yields, p_t -dependent elliptic flow, and fluctuations in order to reduce the statistical errors significantly below those from NA49. Such a number of events would even allow for averaged elliptic flow measurements of Ω baryons and ϕ mesons with an error of 1% only. Due to the excellent event plane resolution of STAR, the systematic error on flow measurements will be significantly smaller than the one of the NA49 data. The preliminary planning of the STAR collaboration foresees an energy scan in 8 steps from $\sqrt{s_{NN}} = 5$ to 39 GeV. The reaction rates are expected to increase with energy from 0.5 to 50 Hz, and the number of collected events per energy step will increase from $1 \cdot 10^6$ to $1 \cdot 10^7$. The beam time request for the full energy scan with the STAR detector is expected to be about 100 days. The PHENIX experiment will also measure global observables with high reaction plane resolution. Sufficient statistics for a low-mass dielectron spectrum at $\sqrt{s_{NN}} = 17.2$ GeV would require about $50 \cdot 10^6$ events which could be taken within 2 weeks of running. The start of the energy scan program is planned for 2010.

References

1. J. Randrup, J. Cleymans, Phys. Rev. C **74**, 047901 (2006) [852](#)
2. J. Cleymans, et al., Phys. Rev. C **73**, 034905 (2006) [852](#)
3. T. Satogata, PoS **CPOD07**, 051 (2007) [852](#)
4. A. Laszlo, [NA60 collaboration], PoS **CPOD07**, 054 (2007) [852](#)
5. V. Toneev, PoS **CPOD07**, 057 (2007) [852](#), [909](#)
6. FAIR Baseline Technical Report, <http://www.gsi.de/fair/reports/btr.html> (2006) [854](#), [856](#), [865](#)
7. E. Bratkovskaya, privat communication (2009) [854](#)
8. A. Andronic, privat communication (2009) [854](#)
9. A. Kugler, et al., Proceedings of XLIV International Winter Meeting on Nuclear Physics, Bormio, **125**, 282 (2006) [858](#)
10. M. Kagarlis, <http://www-hades.gsi.de/computing/pluto> [859](#), [875](#)
11. R. Auerbeck, et al., Z. Phys. A **359**, 65 (1997) [859](#)
12. R. Klay, et al., Phys. Rev. C **68**, 054905 (2003) [859](#)
13. J. Cleymans, H. Satz, Z. Phys. C **57**, 135 (1993) [859](#)
14. M. Golubeva, et al., Nucl. Instr. Meth. A **598**, 268 (2009) [872](#)
15. CbmRoot, <http://cbmroot.gsi.de> (2006) [875](#)
16. S. Bass, et al., Prog. Part. Nucl. Phys. **41**, 255 (1998) [875](#)
17. W. Cassing, E. Bratkovskaya, S. Juchem, Nucl. Phys. A **674**, 249 (2000) [875](#), [889](#)
18. R. Brun, GEANT – Detector Description and Simulation Tool, CERN Program Library Long Writeup W5013 [875](#)
19. D. Kresan, V. Friese, PoS **CFRNC2006**, 017 (2006) [885](#)
20. A. Andronic, et al., J. Phys. G **35**, 104155 (2008) [889](#)
21. Letter of Intent for the NA61 experiment, CERN-SPSC-2006-001 **SPSC-I-235** (2006) [910](#)

Appendix A

Overview of heavy-ion experiments

A.1 Introduction

Results from various heavy-ion experiments at SIS (GSI), AGS (BNL), SPS (CERN), and RHIC (BNL) have been discussed and reviewed in [Part IV](#) of this book. Several heavy-ion experiments were built at the mentioned accelerators and each of the experiments had a special focus which determined the layout. With the new accelerators becoming available, LHC and FAIR, this strategy has had to change: Only one dedicated heavy-ion experiment has to cover all observables. It thus is a useful exercise to review previous experiments, in particular their advantages and deficiencies. Besides, some knowledge on the experimental setup helps to understand and acknowledge the results.

A.2 FOPI – a 4π detector for heavy ion collisions at SIS

A.2.1 Introduction

The beam energies of the Heavy Ion Synchrotron SIS (0.1–2 AGeV) at GSI span the range from where nuclear mean-field effects dominate up to the excitation of internal nucleonic degrees of freedom for a sizeable fraction of the collisional system. Over this energy regime, the measurable signals from heavy ion collisions include heavy nuclear fragments (up to $Z \approx 20$), individual nucleons, mesons and hadronic resonances probing different stages of the reaction. Measuring these various particle types requires a large dynamic range and the combination of various particle identification concepts. The FOPI system has been built with a modular design where each component has been optimized for the detection of a particular type of particle.

A.2.2 The detector

The full FOPI detector,¹ shown in Fig. A.1, has been constructed and operated in three stages:

The main detector system in the first phase of FOPI is the Forward Plastic Wall (764 scintillators). The Forward Wall [1] measures the energy loss (ΔE) and velocity of all charged particles emitted from the reaction zone with laboratory polar angles between $1^\circ < \Theta_{Lab} < 30^\circ$. Time of flight resolution is around 220–250 ps for the inner Wall ($< 7^\circ$) and 80–150 ps for the outer Wall. Since the scintillators are thick enough to stop slower and/or heavier fragments an additional thinner shell of energy loss detectors (ionization chambers beyond 7° , scintillators below) were placed in front of the Forward Wall to reduce the particle identification thresholds. Using this arrangement it is possible to measure fragments up to charge ≈ 20 and down to beam energies of 90 MeV.

The installation of the Superconducting Solenoid marks the beginning of the second phase [2]. The magnet has a diameter of 2.4 m and a length of 3.3 m. In the central volume a field of 0.6 T is produced with a homogeneity of 1.5%. A drift chamber of jet type (CDC) is covering the polar angle range $30^\circ < \Theta_{Lab} < 150^\circ$. The resolutions in determining the laboratory angles Φ and Θ are $\sigma_{Phi} \approx 0.6^\circ$ and $\sigma_{Theta} \approx 6^\circ$. The relative momentum resolution σ_{p_t}/p_t ranges between 4 and 12% rising with momentum. Particle identification is achieved by combining specific energy loss with the momentum. The low transverse momentum acceptance of the CDC is 70 MeV/c for pions and 120 MeV/c for protons. To improve the particle identification properties the CDC is surrounded by a scintillator barrel. In phase 2 the Barrel consists of

¹ <http://www-fopi.gsi.de>

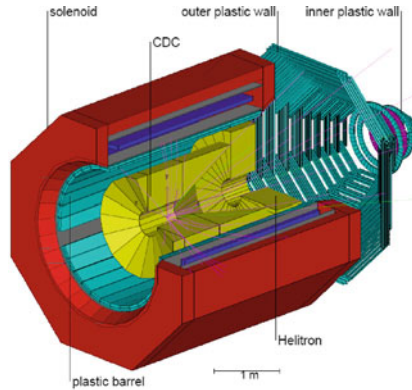


Fig. A.1 FOPI detector set-up phase 2. The beam is entering from the left into the set-up.

180 individual plastic scintillators ($240 \times 4 \times 3 \text{ cm}^3$) arranged in a cylindrical pattern with each aligned parallel to the beam axis. The plastic strips cover the laboratory angular range $40^\circ < \Theta_{Lab} < 140^\circ$ and almost the full azimuth. Charged kaon identification became possible for momenta from 0.1 to 0.6 GeV/c. The forward drift chamber HELITRON adds isotope separation to the particles identified by the Forward Wall within the angular range $7^\circ < \Theta_{Lab} < 30^\circ$ allowing for identification of isotopes up to $Z=4$.

In phase 3 of FOPI the scintillator barrel surrounding the CDC was shortened and the region from $37^\circ < \Theta_{Lab} < 70^\circ$ was equipped with Multi-strip Multi-gap Resistive Plate Chambers (MMRPCs). The MMRPC-ToF-barrel has an active area of 5 m^2 and 2,400 individual strips ($900 \times 1.6 \text{ mm}^2$) [3] which are readout on both sides by custom designed electronics. The efficiency of the MMRPCs is above 95%. The installation of the MMRPC was completed in 2007 and in a first experiment a system time resolution of the complete MMRPC barrel of $< 100 \text{ ps}$ was demonstrated. Identification of charged kaons is now possible up to $p = 1 \text{ GeV/c}$.

A.2.3 Experimental program and results

Aiming at the experimental determination of fundamental properties of hadronic systems at finite temperatures and densities like the equation of state (EOS), the in-medium cross sections and the effective masses of the constituents systematic measurements are necessary.

Table A.1 lists the systems which have been or will be investigated by FOPI.

The experimental program of FOPI concentrates on the measurement of complete phase space distributions of nucleons and heavy fragments in central and mid-central heavy ion collisions, their radial and directed flow, the in-

Table A.1 Summary of FOPI production beam times

Year	Phase	Exp	System	Energy	Comment
1991	1	S018	Au+Au	90–800 AMeV	Fragment production, flow, neutron meas. with LAND
1992	2 w/o Helitron	S109	Au+Au	1 AGeV	Pion production
1993/1994	2 w/o Helitron	S119	Ni+Ni Xe+Sn Au+Au	90–400 AMeV	Cluster production
1994	2	S119	Ni+Ni	1–1.9 AGeV	Pion, K^+ production
1996	2	S183	Ru/Zr	0.4 AGeV 1.5 AGeV 1.6 AGeV	Isotopic ratios, mixing and stopping, K^+ production
1997	2	S183	Ca+Ca Au+Au	0.4–2.0 AGeV 0.4–1.5 AGeV	Flow systematics, meson production
2003	3 w/o RPC	S261	Ni+Ni	1.9 AGeV	Ξ^- Production
2003	3 w/o RPC	S263	Ni/Pb	0.4 AGeV 0.8 AGeV 1.16 AGeV	Stopping
2004	3 w/o RPC	S273	π +A	1.15 GeV/c	Medium mod. at $\rho = \rho_0$
2005	3 w/o RPC	S279	Al+Al	1.91 AGeV	Exotic resonances
2005	3 w/o RPC	S297	p+d/p+C	3.5 GeV	ppn K^- bound state
2007/2008	3	S325	Ni+Ni	1.91 AGeV	K^- flow
2009	3	S341	Ni+Pb	1.9 AGeV	K^- flow, prod. of strange resonances
2009	3	S349	p+p	3.2 GeV	pp K^- bound state
2010	3	S341	Ru+Ru	1.6 AGeV	K^- flow, prod. of strange resonances
2010	3	S344	π +p,A	1.7 GeV/c	K^+ / K^- production

vestigation of produced particles like pions, kaons and short lived resonances that are reconstructed by their decay into charged particles, e.g. strange resonances (like Ξ^-) or more exotic states like strange clusters (predicted by [4]).

The main results published by the FOPI collaboration comprise:

- The identification of a mid-rapidity source for intermediate mass fragments in highly central Au–Au collisions [5].
- The first measurement of neutron squeeze-out in heavy ion collisions showing that neutrons and protons show a similar flow pattern [6,7].
- First determination of collective radial flow in heavy collisions from the kinetic energy distributions of intermediate mass fragments in Au+Au collisions [8,9].
- Extensive studies on the correlations of protons and intermediate mass fragments and their interplay with collective flow phenomena [10,11], determination of the emission order of p, d, t, ^3He and α particles [12].

- Reconstruction of $\Delta(1,232)$ resonances in heavy ion reactions, determination of the resonance shape and the mean transverse energy of their phase space distribution during freeze out [13,14].
- Extensive data on directed and elliptic flow phenomena in mid central collisions [15,16,17,18] as a function of particle species, system size and impact parameter are confronted with transport model predictions. FOPI presented the first analysis of flow with Lee-Yang Zeros [19].
- The in-plane to out-of plane enhancement has been studied and the transition energy was determined for Au+Au collisions as a function of impact parameter and particle species [15,16,17,18]. The azimuthal distribution of the collective expansion is sensitive to the equation of state [20].
- First investigation of nuclear stopping using the isospin tracing method [21] proving that even in the most central collisions the colliding partners are not stopped.
- Nuclear stopping investigations [22,23,24,25,26]: The degree of stopping shows a maximum with a plateau at around $E_{beam}=500$ AMeV with a sharp drop on both sides and is never reaching the hydrodynamical limit even for the heaviest systems [27] and nuclear stopping in central collisions is highly correlated with side flow [27].
- Comprehensive summary on the pion production in heavy ion collisions between 0.4 and 2.0 AGeV [28].
- Direct comparison of K^+ and K^- phase space distributions are sensitive to in-medium modifications of kaons [29].
- Measurements of directed Flow of kaons and Λ s in Ni+Ni collisions [19]. It was shown that the transverse momentum dependence of v_1 of Kaons is sensitive to the in-medium effects [30,31].
- Phase space distributions of K^0 and Λ in Ni+Ni collisions at 1.93 AGeV [32] and the first measurement of the K^0/K^+ yield ratio to determine the symmetry term of the nuclear EOS [33].
- First measurements of Φ mesons in HI – collisions close to threshold [34] and $\Sigma(1,385)$ resonances [35].

A final unambiguous conclusion about the stiffness of the EOS and on the existence of in-medium effects and their connection to the partial restoration of chiral symmetry has not been achieved yet. It seems, however, possible to further discriminate the theoretical models especially for the latter point by enhancing the rate capability of future experiments by a factor of 100. With the closure of the FOPI facility in 2010 this task will have to be covered by CBM experiments at SIS100.

References

1. A. Gobbi [The FOPI collaboration], Nucl. Instrum. Methods A **324**, 156 (1993) 916

2. J.L. Ritman [The FOPI collaboration], Nucl. Phys. B - Proc. Supp. **44**, 708–715 (1995) [916](#)
3. A. Schütttauf [The FOPI collaboration], Nucl. Phys. B **158**, 52–55 (2006) [917](#)
4. T. Yamazaki, Y. Akaishi, Phys. Lett. B **533**, 70 (2002) [918](#)
5. J.P. Alard [The FOPI collaboration], Phys. Rev. Lett. **69**, 889 (1992) [918](#)
6. Y. Leifels [The LAND/FOPI collaborations], Phys. Rev. Lett. **71**, 963 (1993) [918](#)
7. D. Lambrecht [The LAND/FOPI collaborations], Z. Phys. A **350**, 115 (1994) [918](#)
8. D. Lambrecht [The LAND/FOPI collaborations], Phys. Rev. Lett. **72**, 3468 (1994) [918](#)
9. G. Poggi [The FOPI collaboration], Nucl. Phys. A **586**, 755 (1995) [918](#)
10. B. Kämpfer [The FOPI collaboration], Phys. Rev. C **48**, R955 (1993) [918](#)
11. R. Kotte et al., Phys. Rev. C **51**, 2686 (1995) [918](#)
12. R. Kotte [The FOPI collaboration], Eur. Phys. J. A **6**, 185 (1999) [918](#)
13. M. Eskef [The FOPI collaboration], Eur. Phys. Journ. A **3**, 335 (1998) [919](#)
14. B. Hong et al., Phys. Rev. C **71**, 034902 (2005) [919](#)
15. A. Andronic [The FOPI collaboration], Phys. Rev. C **64**, 041604 (2001) [919](#)
16. A. Andronic [The FOPI collaboration], Phys. Rev. C **67**, 034907 (2003) [919](#)
17. A. Andronic [The FOPI collaboration], Phys. Lett. B **612**, 173–180 (2005) [919](#)
18. A. Andronic [The FOPI collaboration], Nucl. Phys. A **679**, 765 (2001) [919](#)
19. N. Bastid [The FOPI collaboration], Phys. Rev. C **72**, 011901 (2005) [919](#)
20. G. Stoicea [The FOPI collaboration], Phys. Rev. Lett. **92**, 072303 (2004) [919](#)
21. F. Rami [The FOPI collaboration], Phys. Rev. Lett. **84**, 1120 (2000) [919](#)
22. B. Hong [The FOPI collaboration], Phys. Rev. C **57**, 244 (1998) [919](#)
23. B. Hong [The FOPI collaboration], Phys. Rev. C **58**, 603 (1998) [919](#)
24. B. Hong [The FOPI collaboration], Phys. Rev. C **66**, 034901 (2002) [919](#)
25. W. Reisdorf et al., Phys. Rev. Lett. **92**, 232301 (2004) [919](#)
26. W. Reisdorf [The FOPI collaboration], Phys. Lett. B **595**, 118–126 (2004) [919](#)
27. W. Reisdorf [The FOPI collaboration], Phys. Rev. Lett. **92**, 232301 (2004) [919](#)
28. W. Reisdorf [The FOPI collaboration], Nucl. Phys. A **781**, 459 (2007) [919](#)
29. K. Wisniewski [The FOPI collaboration], Eur. Phys. Journ. A **9**, 515 (2000) [919](#)
30. J.L. Ritman [The FOPI collaboration], Z. Phys. A **352**, 355 (1995) [919](#)
31. P. Crochet [The FOPI collaboration], Phys. Lett. **486**, 6 (2000) [919](#)
32. M. Merschmeyer [The FOPI collaboration], Phys. Rev. C **76**, 024906 (2007) [919](#)
33. X. Lopez [The FOPI collaboration], Phys. Rev. C **75**, 011901 (2007) [919](#)
34. A. Mangiarotti [The FOPI collaboration], Nucl. Phys. A **714**, 89 (2003) [919](#)
35. X. Lopez [The FOPI collaboration], Phys. Rev. C **76**, 052203 (2007)

A.3 The HADES detector at SIS/GSI

The High Acceptance Dielectron Spectrometer HADES² was designed to measure electromagnetic radiation emitted out of moderately hot and dense nuclear matter as it is formed in reactions of heavy ions in the few-GeV bombarding energy regime. Important design criteria were (1) a large and uniform acceptance, (2) the use of low mass tracking chambers combined with a toroidal field generated by six superconducting coils and (3) the capability for real-time electron recognition using a hadron-blind RICH detector and a dedicated two-level trigger system [1,2]. Beside its main purpose to study dielectron emission, HADES is also very well suited for investigating purely hadronic probes and in particular the production of open and hidden strangeness.

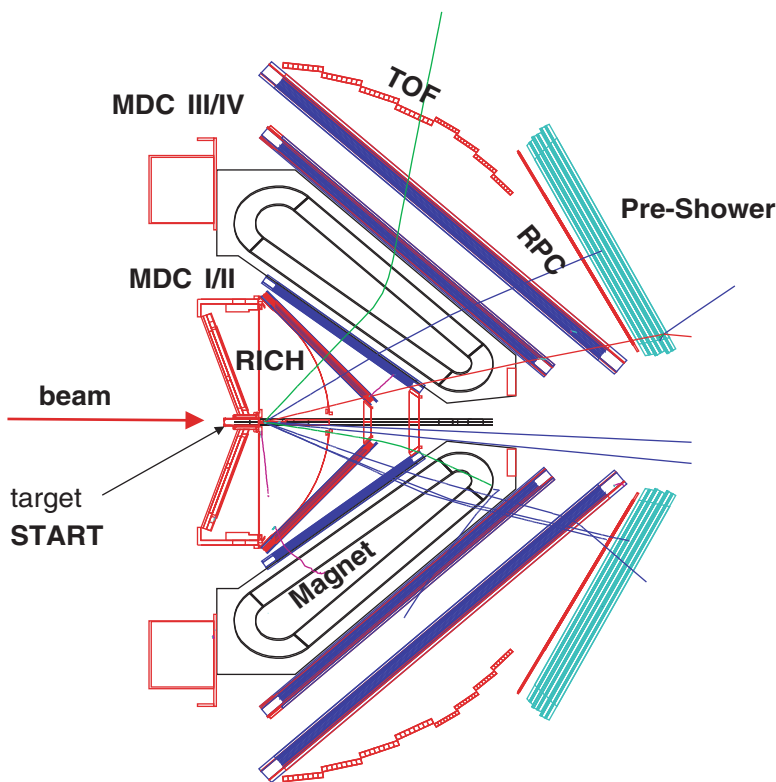


Fig. A.2 Schematic layout of the HADES detector with its six-sector toroidal geometry. For the sake of clarity, only tracks from a low-multiplicity C+C event are shown overlaid.

² Home: <http://www-hades.gsi.de/>

HADES is a rotationally symmetric large acceptance toroidal spectrometer with almost complete azimuthal coverage. The spectrometer acceptance covers polar angles between $\theta = 18^\circ$ and $\theta = 85^\circ$ with respect to the target placed inside a RICH detector. HADES features six identical sectors framed by the six coils of the super-conducting magnet. Figure A.2 shows the cross section of the device in the vertical plane containing the beam axis, together with the simulation of a low-multiplicity C+C event. The angular and momentum acceptance of HADES has been optimized for the detection of di-electron decays of hadrons produced at SIS18 energies, and in particular the vector-meson decays ρ, ω , and $\phi \rightarrow e^+e^-$ [3,4].

Momentum reconstruction is carried out by measuring the deflection angle of particle trajectories derived from the hit positions in two sets of Mini Drift Chambers (MDC) placed before and behind the magnetic field region, totalling four chambers per sector.

Electron identification is performed with a hadron-blind Ring Imaging Cherenkov detector (RICH), operating in the field-free region, as well as a Multiplicity and Trigger Array (META) providing time-of-flight (TOF scintillators + RPC, the latter to be installed in 2009) and electromagnetic shower detection (Pre-Shower).

For precise reaction-time measurements, a radiation-hard diamond start detector system is located in the beam line.

A powerful multi-level trigger system is able to select events within a pre-defined charged-particle multiplicity interval (LVL1 trigger), as well as single-lepton candidates or lepton pairs within a selectable invariant-mass window (LVL2 trigger). After the upgrade of the readout and trigger electronics (to be completed in 2009) the system will permit data-taking rates of 20 kHz up to the largest event sizes (e.g. in Au+Au collisions). This corresponds to a maximum beam intensity of $10^7/\text{s}$ on a 2% interaction target at 10% LVL1 selectivity.

HADES exploits ion-, proton- and pion-beam induced reactions on nuclear and hydrogen targets and covers both, hadron physics and nuclear matter physics aspects. The spectrometer became operational in 2002 and is run by an international collaboration comprising in 2008 more than 100 scientists from 14 European countries.

The following reactions have been investigated since startup in 2002:

- 1 and 2 GeV/u C+C
- 1.75 GeV/u Ar+KCl
- 1.25, 2.2, and 3.5 GeV p+p
- 1.25 GeV/u d+p
- 3.5 GeV p+Nb

The results of the C+C run at 2 GeV/u provide evidence for a substantial contribution to the pair yield in the mass range between 0.15 and 0.5 GeV/c² from the early phase of the collision. Electron pairs from this phase are as abundant as pairs from the Dalitz decay of η mesons [5]. The data from the

1 GeV/u carbon run reveal an excess yield even six times higher than the contribution from η mesons, corroborating earlier findings of the former DLS collaboration [6]. Comparing the two measurements at 1 and 2 GeV/u, one can conclude that the medium contribution grows with beam energy like pion production. This finding supports the conjecture that the excess radiation stems predominantly from decays of baryonic resonances. The comparison of the 1.25 GeV/u p+p and d+p results suggests that pn bremsstrahlung plays a much more important role than hitherto suspected [7]. The 2.2 and 3.5 GeV p+p runs provided a wealth of information on various inclusive and exclusive meson production channels, also of prime importance to improve the various transport codes involved in the interpretation of the heavy-ion data gained at comparable bombarding energies. The most recent p+Nb run was dedicated to the investigation of omega production in cold nuclear matter, the former 3.5 GeV p+p data serving thereby as a baseline.

These investigations will be continued over the next years with more data-taking periods using, on the one hand, truly heavy ion beams (e.g. Ni and Au) and, on the other hand, pion-induced reactions to further the understanding of the underlying elementary processes.

The main reason hampering presently the systematic investigation of in-medium production and propagation of the light vector mesons is, however, the limited bombarding energy available from SIS18, allowing heavy-ion reactions only at or even below production threshold. Here the move of HADES to SIS100 will open definitely a more efficient approach to the study of in-medium effects. It is hence evident that in the energy range of 2–10 GeV/u the HADES detector will remain for a foreseeable future *the* state-of-the-art device able to address and answer the relevant physics questions. Beyond 10 GeV/u, in order to make connection with the data from the former SPS experiments, a measurement around 25 GeV/u will, however, remain desirable. This would then be the realm of the planned CBM experiment.

References

1. HADES Collaboration, Nucl. Instrum. Methods Phys. Res. A **380**, 586 (1996) [921](#)
2. HADES Collaboration, Nucl. Instrum. Methods Phys. Res. A to be published (2009) [921](#)
3. HADES Collaboration, Prog. Part. Nucl. Phys. **53**, 49 (2004) [922](#)
4. HADES Collaboration, Nucl. Phys. A **749**, 150 (2005) [922](#)
5. HADES Collaboration, Phys. Rev. Lett. **98**, 052302 (2007) [922](#)
6. HADES Collaboration, Phys. Lett. B **663**, 43 (2008) [923](#)
7. HADES Collaboration, Phys. Rev. Lett. to be published (2009)

A.4 The KaoS experiment at SIS/GSI

The mission of the **Kaon Spectrometer (KaoS)** experiment at GSI/SIS18 was to explore the properties of dense nuclear matter, and to study the in-medium properties of strange particles [1]. The experimental approach was to produce dense fireballs in heavy-ion collisions, and to measure the production and propagation of K^+ and K^- mesons which serve as diagnostic probes. The experimental challenge was to identify the strange particles in heavy-ion collisions at SIS18 energies. This is because the strangeness production cross section is very small at beam energies below or close to the strangeness production threshold, and the background of charged particles like pions and protons is very high. The experimental task was to identify the particles, to measure their momentum, and to generate a trigger on charged kaons. This task could be fulfilled with a magnetic spectrometer which could be moved to different polar angles to scan a large range of rapidity. The spectrometer was equipped with detectors for event characterization to determine the centrality and the orientation of the reaction plane for flow measurements.

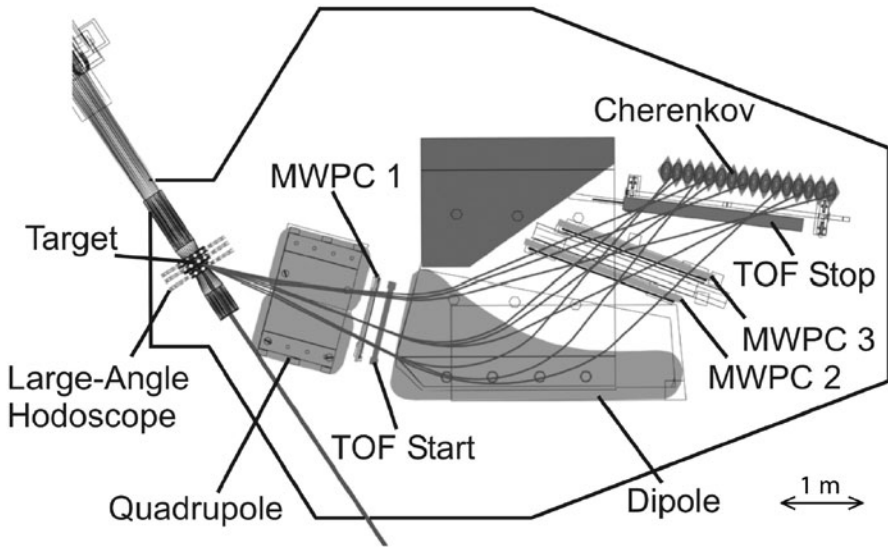


Fig. A.3 Top view of the Kaon Spectrometer KaoS with its various detector components

The experimental setup is shown in Fig. A.3. The spectrometer consists of a quadrupole and a dipole magnet providing a large acceptance in solid angle and in momentum ($\Omega \approx 30$ msr, $p_{\max}/p_{\min} \approx 2$). The short distance of 5 – 6.5 m from the target to the focal plane minimizes the number of kaon decays in flight. The acceptance of the magnets and the detectors for charged particles have been determined by Monte Carlo simulations using

the GEANT code. The particle identification is based on separate measurements of the momentum and of the time-of-flight (TOF). The trigger signal is generated from the time-of-flight measurement in conjunction with a threshold Cherenkov detector which rejected high momentum pions. The trigger rejection factor was about 10^2 for pions and about 10^3 for protons.

The time is measured three times with segmented plastic scintillator arrays: The TOF Start wall between the quadrupole and the dipole (16 modules), the TOF Stop wall in the focal plane of the spectrometer (30 modules), and the Large-Angle Hodoscope (LAH) around the target point covering polar laboratory angles of $12^\circ \leq \theta_{\text{lab}} \leq 48^\circ$ (84 modules). The information from the LAH is used to determine the collision centrality. Moreover, the LAH provides a "time zero" measurement for background rejection.

The background due to spurious tracks and pile-up is removed by a trajectory reconstruction based on three large-area multi-wire proportional counters (MWPC 1 – 3), one of them located between the quadrupole and the dipole, and two chambers behind the dipole magnet. The beam intensity was monitored using two telescopes at $\theta_{\text{lab}} = \pm 110^\circ$. Each of these telescopes consists of 3 plastic scintillators which were read out in coincidence. The flux of charged particles measured by these detectors is proportional to the beam intensity. The absolute normalization was obtained in measurements with low beam intensities using a plastic scintillation detector directly in the beam line.

The spectrometer can be pivoted around the target point on air cushions. The setup was equipped with a forward hodoscope 7 m downstream of the target to measure the orientation of the reaction plane. This detector consists of 380 plastic scintillator modules covering polar emission angles from 0.5° to 11° .

The highlights of the scientific results obtained with the KaoS experiment have been published in the following papers:

- First measurement of the elliptic flow of pions in symmetric heavy-ion collisions for several beam energies [2]
- First observation of enhanced K^+ production in central collisions between heavy nuclei [3]
- Evidence for different freeze-out radii of high- and low-energy pions emitted in Au+Au collisions at 1 AGeV [4]
- Observation of enhanced out-of-plane emission of K^+ mesons in Au+Au collisions at 1 AGeV [5]
- Observation of medium effects in kaon and antikaon production in nuclear collisions at subthreshold beam energies [6]
- Measurement of the emission pattern of high-energy pions as a new probe for the early phase of heavy ion collisions [7]
- First measurement of antikaon phase-space distributions in nucleus–nucleus collisions at subthreshold beam energies [8]
- Evidence for a soft nuclear equation-of-state from kaon production in heavy ion collisions [9]

- First evidence for different freeze-out conditions for kaons and antikaons observed in heavy-ion collisions [10]
- Observation of different azimuthal emission patterns for K^+ and of K^- mesons in heavy-ion collisions at 1–2 AGeV [11]

In 1998 the American Physical Society has cited the KaoS results to be among the ten “top physics stories” in particle, nuclear and plasma physics.

The KaoS experiment started to operate in 1990 and finished data taking in 2001. In 2003 the spectrometer was moved to the electron accelerator MAMI at Mainz University to serve as a kaon trigger for the study of hyper-nuclei.

References

1. P. Senger, et al., Nucl. Instrum. Methods Phys. Res. B **327**, 393 (1993) 924
2. D. Brill, et al., Phys. Rev. Lett. **71**, 336 (1993) 925
3. D. Miskowiec, et al., Phys. Rev. Lett. **72**, 3650 (1994) 925
4. A. Wagner, et al., Phys. Lett. B **420**, 20 (1998) 925
5. Y. Shin, et al., Phys. Rev. Lett. **81**, 1576 (1998) 925
6. F. Laue, et al., Phys. Rev. Lett. **82**, 1640 (1999) 925
7. A. Wagner, et al., Phys. Rev. Lett. **85**, 18 (2000) 925
8. M. Menzel, et al., Phys. Lett. B **495**, 26 (2000) 925
9. C. Sturm, et al., Phys. Rev. Lett. **86**, 39 (2001) 925
10. A. Förster, et al., Phys. Rev. Lett. **91**, 152301 (2003) 926
11. F. Uhlig, et al., Phys. Rev. Lett. **95**, 012301 (2005) 926

A.5 Summary of AGS experiments

At the AGS at BNL a variety of fixed target heavy-ion collision experiments were performed from end of the 1980s until RHIC became available in 1999. O, Si and Au beams at energies from 2 to 14.5 AGeV were used with a variety of different targets. As experiments had to re-apply for beamtime when an approved program was accomplished, certain long standing collaborations were renumbered several times. Very often, with renumbering also detector upgrades went along in particular when Au beams became available at AGS in 1992. A brief overview of the main experiments data of which were discussed in [Part IV](#) is given here (valuable information taken from [1]), for physics results an extended review is given in [Part IV](#).

A.5.1 E802 – E859 – E866 – E917

The experiment E802 was a single arm magnetic spectrometer [2], see [Fig. A.4](#). The spectrometer consisted of a dipole magnet and a set of tracking (drift) chambers before and behind the magnet of 1.5 Tm bending power. A set of Cherenkov and time-of-flight counters allowed for a clean $\pi - K - p$ separation up to momenta of 4.7 GeV/c. The spectrometer had a geometric solid angle of 25 msr. An additional small solid angle (1 msr) arm, the Cherenkov Complex (CC), extended the $\pi - K - p$ separation up to 15 GeV/c. The spectrometer could be rotated to cover reaction angles from 5° to 58° , and the CC could rotate independently of the spectrometer from 5° to 35° . E802 employed event characterization detectors: a charged-particle

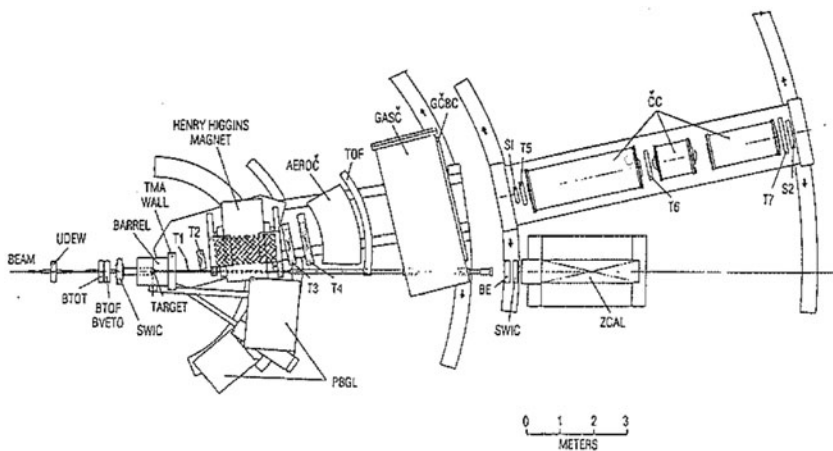


Fig. A.4 Sketch of E802. Picture taken from [1]

multiplicity array close to the target, a highly segmented lead-glass detector, and a zero degree calorimeter.

Particle momentum spectra were measured for π^\pm , K^\pm , p , \bar{p} as function of collision centrality in the approximate rapidity interval $0.5 \leq y \leq 2.1$. Data on Bose–Einstein correlations of pions and kaons were also measured. Beams of p, O and Si were used with a variety of targets.

E859 carried on with these experiments adding a Phoswich Detector at the target for the measurement of $Z = 1$ fragments for $50^\circ < \theta < 150^\circ$. E866 was then an extension for use with Au beams (Fig. A.5): The old E802/E859 spectrometer was used for $20^\circ < \theta < 60^\circ$ where multiplicities with Au beams were similar to the previous for Si beams. In the forward direction a new small spectrometer had been built covering the high multiplicity region $6^\circ < \theta < 20^\circ$. The E917 experiment was the last in this series and continued the physics program of E866.

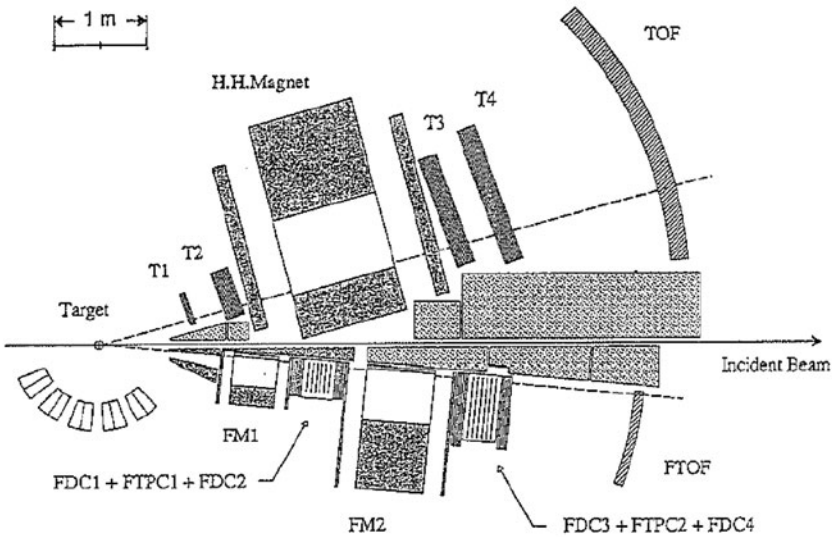


Fig. A.5 Sketch of E866. Picture taken from [1]

E866/E917 did systematic measurements of baryon stopping and strange particle production for a variety of beam energies and collision centralities including Λ , $\bar{\Lambda}$ and ϕ production.

A.5.2 E814 – E877

Experiments E814 [3] and E877 which was the upgrade of E814 for the usage of Au beams had a large target calorimeter with azimuthal coverage and pseu-

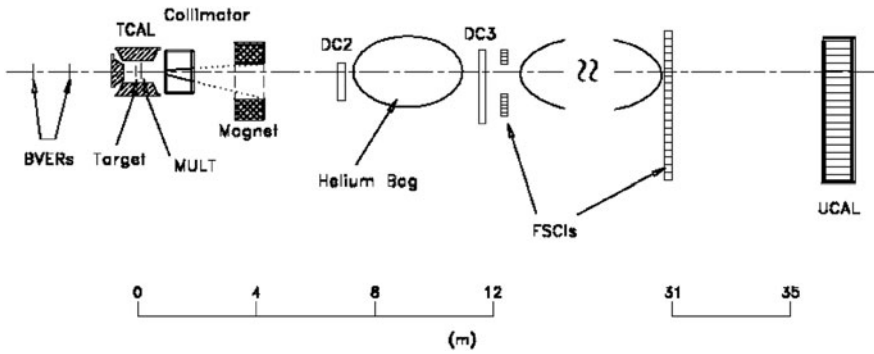


Fig. A.6 Sketch of E814. Picture taken from [1].

dorapidity range $-0.5 < \eta < 0.8$ for the measurement of transverse energy including flow (Fig. A.6). It was complemented by a participant calorimeter with a coverage of $0.9 < \eta < 3.9$. A further forward calorimeter was used for the measurement of zero degree energy and neutrons. Si-Pad detectors could measure charged particle multiplicity for $0.86 < \eta < 3.86$. A forward spectrometer with tracking (drift) chambers, a dipole magnet and two time-of-flight walls provided momentum determination and particle identification for $-115 < \theta_x < 14$ mr and $-21 < \theta_y < 21$ mr. Pions and kaons could be separated up to 5 GeV/c, kaons and protons up to 7 GeV/c. For E877 more tracking chambers were added in order to cope with the higher multiplicities becoming available with the usage of Au beams.

E814/E877 did systematic studies of transverse energy distributions and particle production including two-particle correlations and flow.

A.5.3 E810 – E891

The experiment E810 was the first experiment using a TPC in heavy-ion collisions [4], see Fig. A.7. Three TPC modules were placed in the MPS magnetic field providing a uniform 0.5 T field in the TPC volumes. Angles and momenta of charged particles emitted in the forward hemisphere of heavy-ion collisions were measured with the TPCs. Each module of the TPC contained twelve rows of short anode wires which gave 3-D space points on each track, but no dE/dx information useable for particle identification. Charged particle tracks had been measured in the TPCs including the reconstruction of secondary vertices from Λ and K_S^0 . Particle identification was approximately accomplished by assuming that all negative particles are “pions” and positive-negatives are \approx “protons”. Antiprotons could be identified by a time-of-flight

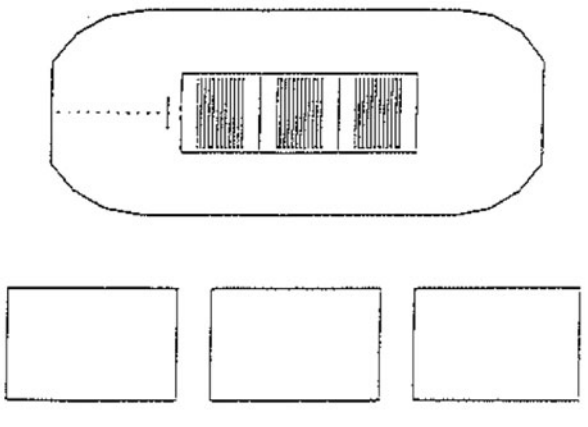


Fig. A.7 Sketch of E810 with the three TPC modules in the magnetic field. In addition a time-of-flight wall (not shown) identified antiprotons. Picture taken from [1].

wall. More central collisions were selected by choosing event samples with higher charged particle multiplicity as measured in the TPCs.

E810 measured rapidity spectra and transverse momentum distributions for π^- , Λ and K_S^0 with Si beams on a variety of targets. E810 also searched for strangelet candidates.

E891 went on to Au beams and used a geometric rearrangement of the TPCs to better adopt to the higher track multiplicities.

A.5.4 E895

E859 fully explored particle identification capabilities using the large EOS TPC from Bevalac which was placed in the MPS magnet (see E810) [5]. The active drift volume was 150 cm long, 96 cm wide and 75 cm high. Most produced particles and nuclear fragment species could be measured and identified over a substantial fraction of 4π solid angle. Due to the good tracking capabilities secondary vertices from the decay of K_S^0 , Λ , $\bar{\Lambda}$, and even Ξ^- could be identified. Using the measured dE/dx , charged pions, kaons and protons could be identified in the $1/\beta^2$ region. Nuclear fragments up to Oxygen could also be measured by their energy loss in the TPC. The Multiple Sampling Ionization Chamber (MUSIC) was positioned to intercept projectile spectator fragments, and could easily resolve charge for relativistic ions up to gold and beyond.

Particle production with emphasis on longitudinal and elliptic flow as well as two-particle correlations were systematically measured in Au+Au colli-

sions over the full range of AGS energies and for different centralities. E895 also did a measurement of the Ξ^- multiplicity at 6 AGeV near threshold.

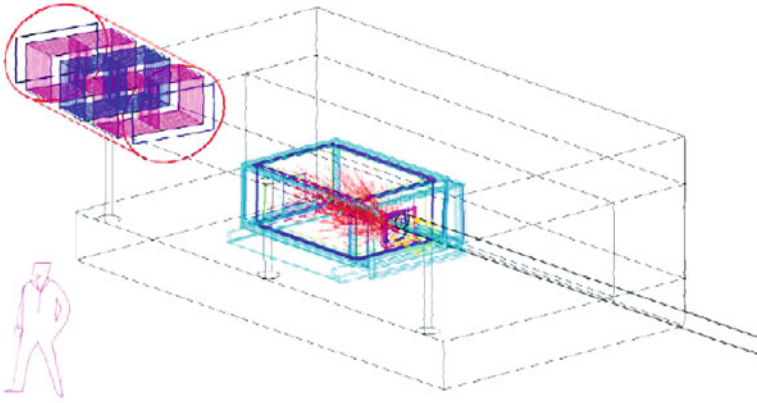


Fig. A.8 Layout of experiment E895. The EOS TPC in the MPS magnet with a typical 4 AGeV Au+Au event is seen as well as the MUSIC detector upstream (not located to scale)

A.5.5 E910

The E910 experiment also used the large EOS TPC placed inside the MPS magnet (see E810, E895) [6] (Figs. A.8 and A.9). With this TPC dE/dx information could be used for particle identification for $p \lesssim 2$ GeV/c ($1/\beta^2$ region). Additional charged particle tracking was done with drift chambers. Particle identification for higher momenta could be performed using a Cherenkov counter at the exit of the magnet and a time-of-flight wall further downstream. The good tracking capabilities inside the TPC allowed for Λ and K_S^0 reconstruction.

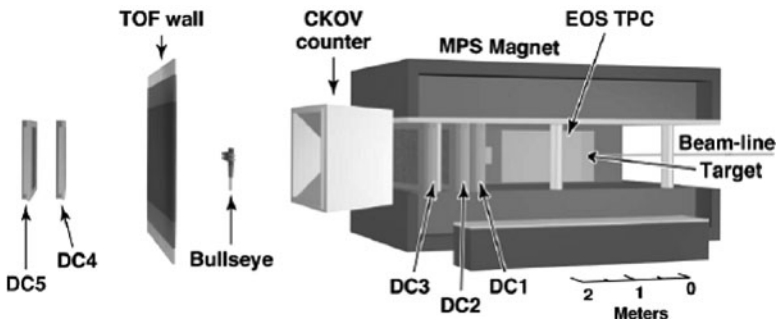


Fig. A.9 Layout of E910 [E910]

E910 specifically studied p+A collisions in order to investigate multiple collisions and re-interactions of the projectile nucleon within the target nucleus. In order to investigate particle production, specifically strangeness production as a function of the number of projectile collisions, slow protons and deuterons measured in the TPC were counted and related to the number of projectile collisions. Systematic investigations were done using different energies of proton beams and a variety of targets.

References

1. “High energy heavy ion experiments”, Booklet distributed at QM93, Borlänge, Sweden [927](#), [928](#), [929](#), [930](#)
2. T. Abbott, et al., [E802], Nucl. Instrum. Methods A **290**, 41 (1990) [927](#)
3. J. Barrette, et al., [E814], Phys. Rev. Lett. **64**, 1219 (1990) [928](#)
4. A. Etkin, et al., [E810], Nucl. Instrum. Methods A **283**, 557 (1989) [929](#)
5. E895 homepage: <http://phys.kent.edu/e895/> [930](#)
6. I. Chemakin, et al., [E910], Phys. Rev. C **60**, 024902 (1999) [931](#)

A.6 The CERES (NA45) experiment at the SPS/CERN

The experiment, built in the early nineties and upgraded by a radial-drift TPC in 1998, is mainly known for its observation of enhanced production of low mass e^+e^- pairs in heavy ion collisions. Figure A.10 represents the final setup. The target consists of 13 thin (25 μm) gold disks, separated by 2 mm, to minimize gamma conversion pairs into the acceptance. Two silicon radial drift detectors give the charged particle multiplicity and event vertex within $\Delta z = 0.2$ mm (in central Pb+Au) and the angles of individual tracks within $\Delta\theta=0.2$ mrad and $\Delta\phi=2$ mrad. Two RICH detectors provide electron identification with a combined efficiency of about 70%. Finally, the TPC yields momentum of charged particles within $\Delta p/p = 2\% \oplus 1\% \cdot p/\text{GeV}$ and dE/dx within 9%. Combining rings in the RICHs and dE/dx in the TPC to identify electrons results in a pion suppression factor of 4,000.

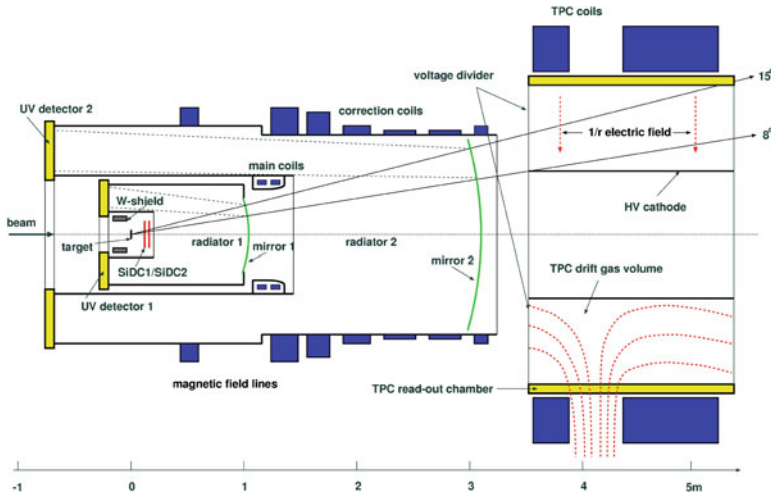


Fig. A.10 The final setup of the CERES/NA45 experiment at CERN SPS.

The detectors cover polar angles of $8^\circ < \theta < 14^\circ$ ($2.1 < \eta < 2.65$) and all azimuthal angles and allow to identify electrons (via rings and dE/dx), K_S^0 , Λ , $\bar{\Lambda}$ (via pion-pion and pion-proton decay), K^+ , K^- (via three-pion decay), photons (via conversions), π^0 (via two-photon decay), and pions/protons (partly, via dE/dx). The collision centrality is determined via charged particle multiplicity and the reaction plane angle via elliptic flow ($\Delta\Psi = 30\text{--}34^\circ$). The runs are listed below. The typical Pb-beam intensity in 1999/2000 was 10^6 ions per 4 s spill and the event rate was 400–1,000 per spill, depending on centrality; typical duration of an SPS heavy ion run was 4–5 weeks in a year.

The highlights of the experiment include, in addition to dilepton spectra [1–5], papers on strange particle spectra [6], flow [7], fluctuations [8], and

two-particle correlations [9–11]. Cylindrical symmetry and an acceptance identical for positive and negative particles proved useful in dilepton (background) and flow analyses. The main problems of the dilepton and hadron analyses were the high background (signal to background of 1/20) caused by unrecognized conversion and Dalitz pairs and lack of good hadron identification system, respectively.

Year	System	Energy	Trigger and collected statistics
1992	S+Au	200 AGeV	$4 \cdot 10^6$ central, $3 \cdot 10^6$ e^+e^- pairs
1993	p+Be	450 GeV	10^7 e^+e^- pairs
1993	p+Au	450 GeV	$3 \cdot 10^6$ e^+e^- pairs
1995	Pb+Au	158 AGeV	10^7 central
1996	Pb+Au	158 AGeV	$5 \cdot 10^7$ central
1999	Pb+Au	40 AGeV	10^7 central
2000	Pb+Au	158 AGeV	$3 \cdot 10^7$ central
2000	Pb+Au	80 AGeV	10^6 central

References

1. G. Agakichiev, et al., Phys. Rev. Lett. **75**, 1272–1275 (1995) [933](#)
2. G. Agakichiev, et al., Eur. Phys. J. C **4**, 231 (1998)
3. D. Adamová, et al., Phys. Rev. Lett. **91**, 042301 (2003)
4. G. Agakichiev, et al., Eur. Phys. J. C **41**, 475 (2005)
5. D. Adamová, et al., Phys. Lett. B **666**, 425–429 (2008) [933](#)
6. D. Adamová, et al., Phys. Rev. Lett. **96**, 152301 (2006) [933](#)
7. G. Agakichiev, et al., Phys. Rev. Lett. **92**, 032301 (2004) [933](#)
8. D. Adamová, et al., Nucl. Phys. A **727**, 97–119 (2003) [933](#)
9. D. Adamová, et al., Phys. Rev. Lett. **90**, 022301 (2003) [934](#)
10. D. Adamová, et al., Nucl. Phys. A **714**, 124 (2003)
11. D. Adamová, et al., Phys. Rev. C **78**, 064901 (2008) [934](#)

A.7 The NA49 experiment at the SPS/CERN

NA49 [1] (see Fig. A.11) is a fixed-target hadron spectrometer which was operated at the CERN-SPS from 1994 to 2002. Its main elements are four large-volume time-projection chambers (TPC), two of which are operated inside the field of two superconducting dipole magnets with a total bending power of 9 Tm. Two time-of-flight walls are located behind the TPCs to improve kaon identification at mid-rapidity. A zero-degree calorimeter measured the energy carried by the projectile spectators.

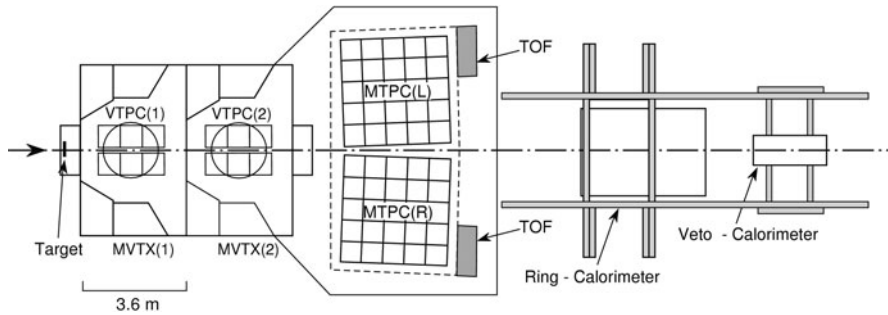


Fig. A.11 The NA49 detector layout.

The NA49 experiment covered a large range of hadronic observables:

- spectra and yield of hadrons ($\pi^\pm, p, \bar{p}, K^\pm, K_S^0, \Lambda, \bar{\Lambda}, \Xi^\pm, \Omega^\pm, \phi, \Lambda^*, K^*$);
- production of light nuclei ($d, \bar{d}, {}^3\text{He}$);
- anisotropic flow of identified hadrons;
- particle interferometry;
- transverse and forward energy;
- event-by-event fluctuations of particle yield ratios, mean transverse momentum, net charge and charged multiplicity;
- exotic baryonic resonances (pentaquarks).

Particle identification is achieved by the energy loss measurement of charged hadrons in the TPC gas. In addition, hadrons are identified by time-of-flight in a restricted acceptance range. Weak decays are identified by the decay topology and invariant mass, resonances by invariant mass.

The event centrality is estimated using the measurement of the projectile spectator energy in the zero-degree calorimeter. An online centrality trigger is used to select central events. The event plane is determined from the azimuthal distribution of produced particles.

The NA49 acceptance covers almost the complete forward rapidity hemisphere. The full p_t range is accessible. Typical acceptance values are 50% for Λ , 40% for Ξ and 20% for Ω and ϕ . The reconstruction and identification efficiency is larger than 95% for charged hadrons identified by dE/dx ; it is

about 70% in case of identification by time-of-flight. Typical efficiencies for other particles are 75% for ϕ , 4–8% for Λ , 2–5% for Ξ and 2–3% for Ω . The signal-to-background ratio is of the order of 10^{-2} for resonances and of the order of unity for hyperons.

The focus of the NA49 data taking were Pb+Pb collisions, both centrality selected and minimum bias, at various beam energies (20, 30, 40, 80 and 158 AGeV). In addition, lighter collision systems like C+C and Si+Si were investigated, as well as p+A interactions (C, Al, Pb) and p+p reactions. Also, pion and deuteron beams were used.

The experiment was operated at beam intensities from 10^4 to 10^5 Hz. Typical event rates were of the order of 1 Hz. In total, about 60 weeks of beam time were recorded. Table A.2 summarises the event statistics obtained for various collision systems.

Table A.2 Event statistics recorded by the NA49 experiment for some collision systems and trigger settings

System	Beam energy (AGeV)	Trigger	Number of events
Pb+Pb	158	Central	3,730,000
Pb+Pb	158	Min. bias	650,000
Pb+Pb	80	Central	305,000
Pb+Pb	40	Central	710,000
Pb+Pb	40	Min. bias	840,000
Pb+Pb	30	Central	440,000
Pb+Pb	30	Semi-central	230,000
Pb+Pb	20	Central	360,000
Pb+Pb	20	Semi-central	310,000
p+p	158		7,900,000
p+Pb	158		2,950,000
p+Al	158		355,000
C+C	158	Min bias	560,000
Si+Si	158	Min. bias	410,000

The main scientific outcomes of the NA49 experiments are [2–8]:

- The initial energy density in central Pb+Pb collisions at top SPS energy is about 3 GeV/fm^3 .
- The measured transverse mass spectra can be described by a blast-wave parametrisation. Hadron-string transport models fail to reproduce the observed transverse spectra.
- From HBT, strong radial flow is observed, which is largely independent of the beam energy.
- The measured hadron abundances can be described by statistical models. The thermal freeze-out occurs on a smooth curve in the $T-\mu_B$ plane which approaches the hadron-parton phase transition line as predicted by lattice QCD at top SPS energy.

- Anomalies in the energy dependence of hadron production (“horn”, “step”, “kink”) suggest that deconfinement sets in at low SPS energy.
- The yields of strange hadrons per participant nucleon is enhanced in central Pb+Pb collisions with respect to p+p. This enhancement is already present in relatively small systems (C+C, Si+Si).
- No distinct event classes are observed in the event-by-event analysis of mean transverse momentum or the K/π ratio. The fluctuations are close to the statistical limit as obtained from mixed events. Non-statistical K/π fluctuations seem to increase when lowering the beam energy.
- A narrow $S=-2$, $Q=-2$ baryonic resonance was observed in the $\Xi^-\pi^-$ decay channel in p+p reactions at 158 GeV beam energy.

Due to its large acceptance, the NA49 detector allows to extract hadron yields in full phase space, in contrast to most other heavy-ion experiments. The track measurement in the large TPCs gives rise to a high track reconstruction efficiency, excellent momentum resolution and good resolution of secondary decay vertices. On the other hand, the rather slow detector response of the TPCs limits the event rates considerably. The precision of track reconstruction in the TPCs is not sufficient for the detection of displaced vertices from open charm decays. NA49 does not cover leptonic observables due to the lack of devices for electron or muon identification.

References

1. S. Afanasiev, et al. [NA49], Nucl. Instrum. Methods Phys. Res. A **430**, 210 (1999) [935](#)
2. T. Alber, et al. [NA49], Phys. Rev. Lett. **75**, 3814 (1995) [936](#)
3. H. Appelshaeuser, et al. [NA49], Eur. Phys. J. C **2**, 661 (1998)
4. C. Alt, et al. [NA49], Phys. Rev. C **68**, 034903 (2003)
5. C. Alt, et al. [NA49], Phys. Rev. C **77**, 023903 (2008)
6. C. Alt, et al. [NA49], Phys. Rev. Lett. **94**, 052301 (2005)
7. S. Afanasiev, et al. [NA49], Phys. Rev. Lett. **86**, 1965 (2001)
8. C. Alt, et al. [NA49], Phys. Rev. Lett. **92**, 042003 (2004) [936](#)

The acceptance covered the midrapidity region with a lower cut on transverse momenta of $p_t > 0.4$ GeV. The acceptance of course depends on the decay topology, however, typical values are on the order of 1% for the Λ for example. Once in the acceptance the reconstruction efficiency is as high as 75 – 95% depending on the event multiplicity. The invariant mass spectrum of the reconstructed hyperons and K_S^0 is almost background free.

A clear advantage of the WA97/NA57 setups was the precise tracking and the clean identification of weak decays by topology. A limitation was the restriction of their measurement to the midrapidity region and the missing identification of the decay products.

A.8.2 Results

The number of recorded events is summarized in Table A.3

Table A.3 Event statistics recorded by the NA57 experiment.

System	Beam energy (AGeV)	Number of events
p+be	158	$180 \cdot 10^6$
p+Pb	158	$290 \cdot 10^6$
Pb+Pb	40	$290 \cdot 10^6$
Pb+Pb	158	$460 \cdot 10^6$
p+Be	40	$170 \cdot 10^6$

WA97/NA57 were the first experiments to employ silicon pixel detectors, 10^6 channels have successfully been operated. This has been an essential milestone on the way to Si pixel detectors for the LHC experiments.

The main observation of WA97/NA57 was the enhancement of strange hadron abundances in central Pb+Pb collisions at 160 AGeV/c beam energy compared to p+Pb and to p+Be. This enhancement grows with the strangeness of the produced hadrons and amounts up to 20 for Ω -baryons. Such a pattern had been predicted as a signature of the transition between hadronic matter and a plasma of quarks and gluons. The enhancements were found to increase with the number of nucleons participating in the collision, across the whole explored centrality range, from rather peripheral (about 50 participant nucleons) to central. NA57 has also measured the strangeness enhancement pattern in Pb–Pb collisions at 40 AGeV/c beam momentum: the effect is found to be slightly larger than at top energy for central collisions and to have a steeper centrality dependence. So far, it has not been possible to reproduce the WA97/NA57 results within conventional hadronic models of nucleus–nucleus collisions.

Besides midrapidity yields NA57 also performed an analysis of the transverse mass distributions of strange particles. A study of the hydrodynamic behaviour of matter emerging from Pb–Pb collisions at the SPS indicates

that a thermal distribution is superimposed to a collective hydrodynamical expansion at a speed close to $0.5c$. This suggests the generation of a very strong pressure as it would be expected in case of deconfinement due to the large increase in the number of degrees of freedom. The collective expansion velocity and the duration of the expansion of the system before the final decoupling appears to increase with the number of participants. The interest for evaluating the hydrodynamical conditions for semi-central collisions at SPS stems from the observation of an azimuthal anisotropy in the momentum distribution. At RHIC, in semi-central collisions this observation is close to calculations near the hydrodynamical limit and thus one of the main pillars for the “perfect liquid” claim.

Recently, NA57 analyzed the centrality dependence of p_t spectra of K_S^0 and Λ at 158 AGeV/c in terms of the so called “nuclear modification factor” (RCP). The RCP pattern measured at the SPS is found to be similar to that observed at RHIC which has been interpreted as due to energy loss in the medium formed in the collision. The emerging picture, also considering that the values of the hyperon enhancements measured at RHIC are similar to those measured at the SPS, is that there does not seem to be evidence of a qualitative difference between the mechanisms at work in strangeness production in the systems created in heavy-ion collisions at the two machines.

References

1. F. Antinori, et al., J. Phys. G **30**, 823–840 (2004)
2. F. Antinori, et al., Phys. Lett. B **595**, 68–74 (2004)
3. F. Antinori, et al., J. Phys. G **31**, 321–335 (2005)
4. F. Antinori, et al., Phys. Lett. B **623**, 17–25 (2005)
5. F. Antinori, et al., J. Phys. G **31**, 1345–1357 (2005)
6. F. Antinori, et al., J. Phys. G **32**, 427–441 (2006)
7. F. Antinori, et al., J. Phys. G **32**, 2065–2080 (2006)
8. F. Antinori, et al., J. Phys. G **34**, 403–429 (2007)

A.9 The NA60 experiment at the SPS/CERN

A.9.1 *Experimental setup*

The fixed-target experiment NA60, schematically shown in Fig. A.13, consists of a muon spectrometer and a zero-degree calorimeter, previously used by the NA50 experiment, that were complemented with two state-of-the-art silicon detectors in the target region. The muon spectrometer consists of a hadron absorber made from carbon and iron discs followed by two groups of multi-wire tracking chambers and trigger stations in front and behind of a toroid magnet. The zero-degree calorimeter, positioned at the entrance of the hadron absorber, determines the centrality of the collisions. The target region is newly instrumented with two detector systems:

1. A radiation hard beam tracker, made from four stations of single-sided silicon microstrip detectors operated at cryogenic temperatures, placed on the ion beam in front of the targets. The beam tracker identifies for each beam particle impact time and impact point on the target.
2. A highly granular radiation tolerant silicon pixel detector telescope installed in a dipole magnet downstream of the targets. This vertex spectrometer tracks all charged particles in front of the hadron absorber and determines their momenta independently of the muon spectrometer. Planes of silicon micro-strip detectors have also been used when running with proton beams.

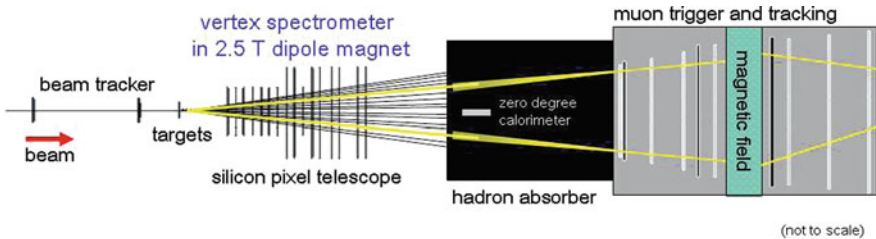


Fig. A.13 Schematic view of the NA60 experiment: Beam tracker, targets, vertex spectrometer, hadron absorber, zero degree calorimeter, and muon spectrometer

A.9.2 Observables, event characterization

Observables:	Dimuon mass and transverse momentum spectra; Charged-particle multiplicity and momenta; Centrality; Displaced vertices, open charm; Low-mass vector mesons (ρ , ω , ϕ), J/ψ , Drell-Yan.
Particle identification:	Muon spectrometer.
Event-plane:	Determination using the pixel detector telescope.
Centrality:	Determination using the zero-degree calorimeter and track multiplicity in the vertex spectrometer.

A.9.3 Performance

Acceptance:	$3.3 < y < 4.3$ (at low p_T), $3 < y < 4$ (high p_T , J/ψ).
Signal/background:	From no background at high masses (J/ψ and beyond) to ≈ 0.1 for central In-In collisions at low masses.

A.9.4 Running conditions

in year 2002:	p+A (Be, In, Pb), 400 GeV beam (“commissioning run”, 5 days, $\approx 3 \times 10^5$ dimuon events); Pb+Pb, 20 and 30 GeV/u, (“SPS-LHC test”, “commissioning run”, 10 days, $\approx 2.5 \times 10^7$ minimum bias events).
in year 2003:	In+In, 158 GeV/u beam (35 days, 2×10^8 dimuon events).
in year 2004:	p+A (U, W, Cu, In, Be, Pb), 158 GeV beam (3 days, 3×10^4 J/ψ events); p+A (U, W, Cu, In, Be, Pb), 400 GeV beam (≈ 70 days, 3×10^5 J/ψ events).

A.9.5 Results and outcomes

The experiment has provided important new results that have helped to sharpen our understanding of heavy-ion physics at SPS energies. For In–In collisions, in the low-mass dimuon sector, a significant broadening of the ρ meson, without any mass shift, has been observed, ruling out models that connect hadron masses directly to the chiral condensate. In the intermediate mass region, between the ρ and the J/ψ , the presence of an excess in the dimuon yield has been confirmed and it has been discovered that this excess is of a prompt nature (i.e. not connected with open charm decays). The study of the transverse momentum distributions of excess dimuons at low and intermediate mass implies that, beyond $m = 1 \text{ GeV}/c^2$, the yield is dominated by a thermal-like contribution, mainly of partonic origin. Finally, the J/ψ suppression has been studied as a function of centrality in In–In collisions. The onset of the anomalous J/ψ suppression (i.e. suppression beyond the expectations from cold nuclear matter absorption) has been found to occur for a very similar number of participant nucleons for both In–In and Pb–Pb collisions. A signal of J/ψ elliptic flow has also been observed, concentrated in semi-peripheral collisions and at transverse momentum values larger than $1 \text{ GeV}/c$.

Publications as of mid 2008 (for an up-to-date list, see <http://na60.cern.ch>):

1. First measurement of the ρ spectral function in high-energy nuclear collisions; [NA60], Phys. Rev. Lett. **96**, 162302 (2006)
2. J/ψ production in Indium-Indium collisions at 158 GeV/nucleon; [NA60], Phys. Rev. Lett. **99**, 132302 (2007)
3. Evidence for radial flow of thermal dileptons in high-energy nuclear collisions; [NA60], Phys. Rev. Lett. **100**, 022302 (2008)
4. Evidence for the production of thermal-like muon pairs with masses above $1 \text{ GeV}/c^2$ in 158 A GeV Indium-Indium collisions; [NA60], Eur. Phys. J. C **59**, 607 (2009)

A.9.6 Advantages and limitations

The NA60 experiment has been conceived as an upgrade of the NA50 experiment, that studied muon production in p-A and nucleus–nucleus collisions at the CERN SPS. In that experiment, it was possible to perform a high-statistics study of dimuon production thanks to an extremely selective trigger system. The mass resolution was of the order of 100 MeV for the J/ψ and of $\approx 80 \text{ MeV}$ for the ϕ and ω . However, there were severe limitations in the study of the muon pair continuum. At low masses, the p_T acceptance was essentially zero below $1 \text{ GeV}/c$, making it impossible to access the low p_T region where thermal dimuon production may become sizeable. Furthermore,

in the mass region beyond the ϕ , the vertexing capabilities did not allow to distinguish between prompt muon pairs and dimuons coming from open charm decays.

In NA60, adding a silicon pixel telescope in the target region, it becomes possible to perform a matching of the muon tracks before and after the hadron absorber, both in angular and momentum space. This way it is possible to improve the dimuon mass resolution in the region of the vector mesons ω and ϕ from ≈ 80 to $20 \text{ MeV}/c^2$, to significantly reduce the combinatorial background due to π and K decays and to measure the muon offset with respect to the interaction vertex. The additional bend by the dipole field in the target region deflects soft muons into the acceptance of the muon spectrometer, thereby strongly enhancing the opposite-sign dimuon acceptance at low mass and low transverse momentum with respect to all previous dimuon experiments. Furthermore, the selective dimuon trigger and the fast readout speed of the vertex tracker allow the experiment to run at very high luminosities, leading to an unprecedented level of statistics for low-mass lepton pairs.

A.10 The WA98 experiment at the SPS/CERN

A.10.1 Experimental setup

The WA98 experimental setup (see Fig. A.14) consisted of large acceptance hadron and photon spectrometers, detectors for photon and charged particle multiplicity measurements, calorimeters for transverse and forward measurements, and detectors for triggering purposes.

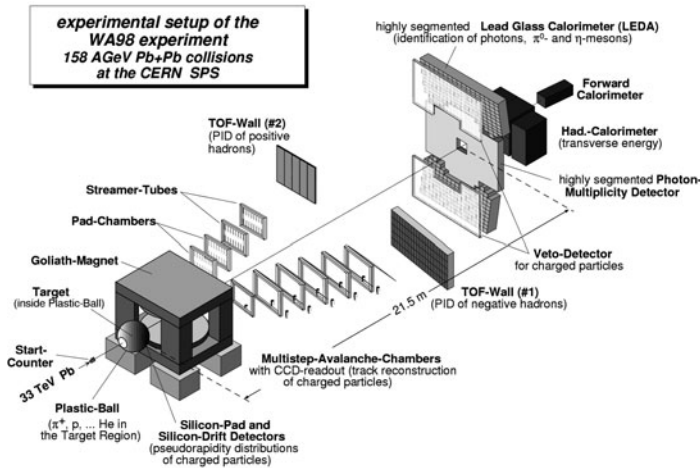


Fig. A.14 The WA98 experimental setup

The photon spectrometer LEDA was located at 21.5 m from the target in two halves above and below the beam plane. It consisted of 10,080 lead glass modules readout by individual phototubes with custom-developed Cockcroft-Walton bases and ADCs, and a monitoring system based on LEDs and photodiodes. Arrays of streamer tubes with pad readout were placed directly in front of the photon spectrometer as a charged particle veto detector.

The photon multiplicity detector (PMD), a preshower detector covered the region between the two halves of LEDA at the same distance. The sampling calorimeters MIRAC and ZDC were placed further downstream to register the transverse and forward energy, resp. The Plastic Ball consisted of 655 $\Delta E - E$ detectors arranged in a sphere surrounding the target. Just downstream of the Plastic Ball a circular silicon pad multiplicity detector (SPMD) was placed at 32.8 cm from the target. It counted charged particles with $\approx 1,000$ pads. The charged particle spectrometer was divided into a negative and a positive tracking arm. Both used the GOLIATH magnet, a large aperture dipole magnet positioned directly behind the Plastic Ball and providing 1.6 Tm bending power. Both arms were complemented with scintillator time-of-flight walls positioned behind the chambers.

A.10.2 Trigger and observables

The minimum bias trigger required a valid signal of the beam counters and a minimum amount of transverse energy measured in MIRAC. For Pb+Pb collisions it selected a cross section of $\sigma_{\text{min-bias}} \approx 6,300$ mb. A central trigger with a higher transverse energy threshold was used to enhance the $\approx 10\%$ most central collisions. In hadron-induced reactions a high-energy photon (HEP) trigger based on the sum energy signal of overlapping 4×4 groups of towers in the lead-glass calorimeter was used to enhance the sample of high p_T events. The experiment had implemented an *interleaved* readout, where the faster detectors could be read out multiple times during the dead time of slower systems to enhance the statistics, in particular, for high p_T photon measurements.

The WA98 experiment allowed to measure

- the calorimetric transverse energy, and multiplicity, pseudorapidity and azimuthal distributions of charged particles and inclusive photons close to mid-rapidity,
- slow target fragments and positive pions at target rapidity, and charged hadrons at mid-rapidity with particle ID for low transverse momentum,
- and photons, neutral pions and η mesons at mid-rapidity out to high transverse momentum.

The event centrality could be determined from the measurements of transverse energy (preferred method), forward energy and the multiplicity of charged particles and photons. Reaction plane determination was possible with the full azimuthal coverage of the PMD and SPMD at mid-rapidity and of the Plastic Ball at target rapidity.

A.10.3 Performance

Figure A.15 shows the acceptance ranges of the WA98 detectors for charged particle multiplicity (SPMD), photon multiplicity (PMD) and calorimetric energy (MIRAC and ZDC). The detection efficiencies in the active areas for charged hadrons and energy were essentially 100%. The PMD had an average photon counting efficiency of $\sim 70\%$ with about 15% of the charged hadrons misidentified as photons.

Figure A.16 shows the acceptance for identified particles. The resolution for tracking was $\Delta p/p = 0.5\%$ at $p = 1.5$ GeV/c and $\sigma_{TOF} < 120$ ps for the negative arm (Arm 1), and $\Delta p/p = 1\%$ at $p = 2$ GeV/c and $\sigma_{TOF} < 90$ ps for the positive arm (Arm 2). The single photon detection efficiency of LEDA was essentially 100% above a low energy threshold. However, the energy resolution of $\sigma/E = 5.5\%/\sqrt{E/\text{GeV}} + 0.8\%$ and particle overlaps in high multiplicity

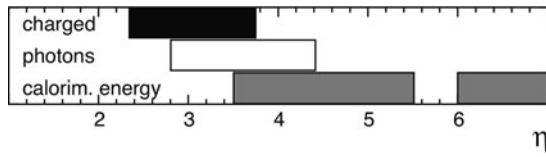


Fig. A.15 Acceptance ranges in pseudorapidity for global observables (charged multiplicity, photon multiplicity and calorimetric energy)

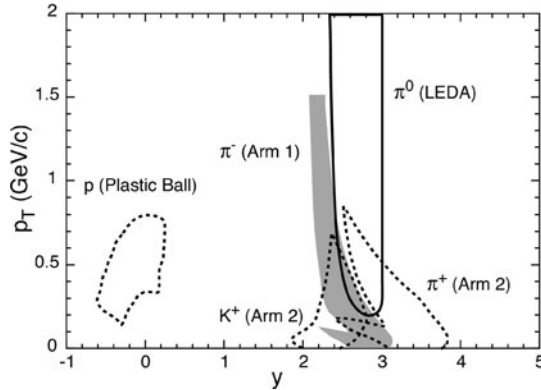


Fig. A.16 Acceptances for identified particles as a function of rapidity and transverse momentum

events lead to distortions of the momentum spectra, which had to be corrected. The contamination of the photon sample from charged hadrons and (anti-)neutrons was smaller than 10% each for $p_T > 0.2$ GeV/c. The total conversion probability for photons in material in front of the photon spectrometer was 8.6% in the last run period with Pb+Pb collisions (including target, vacuum exit window, and air). The largest single source of uncertainty of the measurement with LEDA is the absolute energy scale, which translates to uncertainties on the total cross section measurement of up to 20% at $p_T = 4 - 5$ GeV/c.

A.10.4 Results

The WA98 experiment focussed on the study of direct photons in heavy ion collisions (see Table A.4). The observation of direct photons in central Pb+Pb collisions at the SPS from statistical subtraction of decay photons for intermediate and high p_T is the major achievement of the experiment [1]. This was possible only by keeping the total systematic error on the direct photons below 10%. This result has led to a reinvestigation of theoretical predictions of photon production. Most of the high p_T direct photons can be explained

Table A.4 Investigated reaction systems with target thickness and collected statistics.

Beam	Energy	Target and thickness (mg/cm ²)	No. of events	Enhanc.
Pb	158 AGeV	Pb 239 or 495	$6.7 \cdot 10^6$ (central) $4.3 \cdot 10^6$ (periph.)	
Pb	158 AGeV	Nb 217	$0.5 \cdot 10^6$	
Pb	158 AGeV	Ni 223	$0.55 \cdot 10^6$	
p	160 GeV	Pb 495	$1.0 \cdot 10^6$ (min.bias) $1.5 \cdot 10^6$ (HEP)	$\times 26$
p	160 GeV	C 1,879	$1.2 \cdot 10^6$ (min.bias) $0.5 \cdot 10^6$ (HEP)	$\times 16$

by state-of-the-art prompt photon calculations. A thermal component at intermediate p_T is not excluded but cannot yet be proven to be significant. Later, the first measurement of direct photon interferometry in high-energy heavy-ion collisions was performed [2]. This provided evidence for a direct photon signal at low p_T .

Related studies of neutral meson production have been performed and resulted in neutral pion spectra out to very high transverse momentum ($x_T \sim 0.4$) in Pb+Pb [3–5], p+Pb and p+C [6] reactions and more limited results on η meson production [1]. The comparison of these results shows first hints of jet quenching effects already at the SPS.

WA98 has also performed the first search for disoriented chiral condensates (DCC) in heavy ion collisions by studying the relative fluctuations of the multiplicities of charged hadrons and photons (dominantly representing charged and neutral pions) [7]. An upper limit for DCC production was obtained. Elliptic flow has been studied via target fragments, and unidentified charged hadrons, photons and identified K and π at mid-rapidity [8, 9]. Most of these results are in line with the general trend of elliptic flow at the SPS. Interestingly, kaons show out-of-plane flow unlike the other particles. Detailed studies of the scaling of global variables with centrality have been performed [10, 11], showing a stronger increase of these variables than expected from the wounded nucleon model. A large number of other studies has been performed, which can not be covered in this summary.

A.10.5 Advantages and limitations

The strong asset of the WA98 experiment were the very good photon and neutral pion detection capabilities. Of crucial importance were the low material budget in front of the photon detector including a thin target, and the excellent performance of the photon spectrometer regarding in particular its calibration and gain stability.

Furthermore, both centrality and reaction plane measurement capabilities were very good. The redundant systems for centrality related measurements allowed a good systematic understanding, such that the observables allowed centrality cuts as stringent as 1% of the cross section in Pb+Pb. The reaction plane studies could profit from relevant detectors well separated in rapidity which allows to reduce the influence of non-flow.

The major limitation of the measurements was the available statistics, in particular for the high p_T measurements. Reasons for this were in part unavoidable, caused e.g. by the choice of a thin target or by the radiation limits in the experimental area, but also by external circumstances like limited total amount of beam time.

References

1. M.M. Aggarwal, et al., Phys. Rev. Lett. **85**, 3595 (2000) [947](#), [948](#)
2. M.M. Aggarwal, et al., Phys. Rev. Lett. **93**, 022301 (2004) [948](#)
3. M.M. Aggarwal, et al., Phys. Rev. Lett. **81**, 4087 (1998); [948](#)
[Erratum-ibid. **84**, 578 (2000)]
4. M.M. Aggarwal, et al., Phys. Rev. Lett. **83**, 926 (1999)
5. M.M. Aggarwal, et al., Eur. Phys. J. C **23**, 225 (2002) [948](#)
6. M.M. Aggarwal, et al., Phys. Rev. Lett. **100**, 242301 (2008) [948](#)
7. M.M. Aggarwal, et al., Phys. Lett. B **420**, 169 (1998) [948](#)
8. M.M. Aggarwal, et al., Phys. Lett. B **469**, 30 (1999) [948](#)
9. M.M. Aggarwal, et al., Eur. Phys. J. C **41**, 287 (2005) [948](#)
10. M.M. Aggarwal, et al., Phys. Lett. B **458**, 422 (1999) [948](#)
11. M.M. Aggarwal, et al., Eur. Phys. J. C **18**, 651 (2001) [948](#)

A.11 The BRAHMS experiment at RHIC/BNL

A.11.1 Experimental setup

A perspective view of the BRAHMS detector layout is presented in Fig. A.17. Two rotatable magnetic spectrometers, the Forward Spectrometer (FS) and the Mid-Rapidity Spectrometer (MRS) are augmented by global detectors: a two-component multiplicity array surrounding the interaction vertex, the beam–beam counters (BBC) located 220 cm away from the vertex and close to the beam pipe and the zero-degree calorimeters (ZDC) 18 m from the interaction point. The FS contains four dipole magnets for sweeping and analyzing particles emerging from the reaction in a solid angle of 0.8 msr.

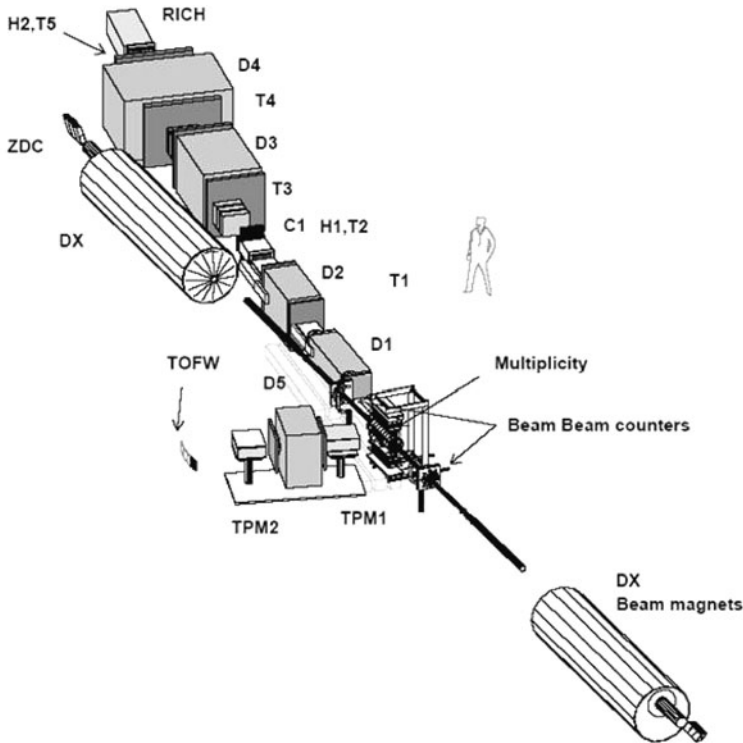


Fig. A.17 The BRAHMS detectors in perspective. The spectrometer magnets are denoted D1–D5, the TOF hodoscopes in the FS are H1 and H2, and the tracking counters T1–T5, where T1 and T2 are TPCs and T3, T4 and T5 are multi-wire DCs. The two Cherenkov counters in the FS are C1 and RICH. TPM1 and TPM2 are the tracking chambers of the MRS, while the TOF system is the TOFW. The global detectors are denoted as BBCs and multiplicity. The ZDCs are situated beyond the DX beam magnets. The distance between the front of the two DX beam magnets is 18 m

The first two tracking detectors are Time Projection Chambers (TPC) which provide good three-dimensional track recognition and a high degree of background rejection in a high multiplicity environment; the remaining tracking detectors are Drift Chambers (DC). Particle identification in the FS is based on two Time-Of-Flight (TOF) hodoscopes, and two Cherenkov detectors: a threshold detector and a ring imaging Cherenkov detector. The MRS is a single dipole magnetic spectrometer with a geometric acceptance of 6.5 msr and it covers the angular range between 30° and 95° . Two TPCs provide the tracking information in the MRS; particle identification is accomplished with a highly segmented scintillator TOF wall.

A.11.2 Observables

The BRAHMS detectors are designed to cover the widest possible range in polar angle relative to the beam direction with precise momentum determination and good particle identification. Two separate spectrometers, one for low to medium momenta and one for high momenta (25–30 GeV/c around 2°), both with comparatively small solid angles, measure and identify charged pions, kaons and protons.

A left-right coincidence of the ZDC timing signals with a narrow time overlap of about 5 ns provides a zero level trigger. The BBCs provide the second zero level trigger input, the start time for the TOF measurements and the primary collision vertex position to an accuracy of approximately 1 cm. The Multiplicity Array is used to establish overall charged particle multiplicities. An inner barrel of Si strip detectors and an outer barrel of plastic scintillator tile detectors measure the energy loss of particles passing through the array. The detectors are only modestly segmented so they can provide both a pseudo-rapidity density of charged particles and an event plane. The Si strip detectors and scintillator tiles give quasi-independent measurements of the event-by-event charged particle multiplicities, the latter being fast enough to be part of the level 1 trigger.

A.11.3 Performance

The rapidity coverage of the entire spectrometer is from $y \approx 0$ to $y \approx 4$ (for comparison the beam rapidity is 5.37 at the maximum RHIC collision energy of 100 GeV/nucleon). The p_T coverage is optimized for soft physics, i.e. the region around the mean p_T , starting from about 200 MeV/c and approaching 3–4 GeV/c. Since both spectrometers have small solid angles many polar angles and magnetic field settings have to be systematically combined in order to obtain a broad rapidity coverage.

The highly segmented scintillator TOF wall of the MRS provides π/K separation to momenta of 2 GeV/c and K/p separation to momenta of 3.5 GeV/c (at 3σ). Particle identification in the FS is based on TOF hodoscopes that achieve a 3σ -separation of π/K and K/p up to momenta of 3.3 and 5.7 GeV/c, respectively, for H1 and to 5.8 and 8.5 GeV/c, respectively, for H2. The threshold Cherenkov detector, C1 extends the $\pi/K/p$ identification behind H1 to 9 GeV/c while the RICH detector allows $\pi/K/p$ separation in the high momentum configuration up to 25 GeV/c.

A.11.4 Running conditions

BRAHMS participated in the RHIC running periods from 2000 until 2006 and took the following data sets:

- 200 GeV
 - Au+Au (80 M, min. bias and central collisions, 200 M sampled min. bias events) (2001, 2004)
 - Cu+Cu (1.75 nb^{-1} , 160 M events) (2005)
 - d+Au (120 M min. bias events) (2003)
 - p+p (sampled 2.5 pb^{-1} min. bias events) (2002, 2003, 2005)
- 62.4 GeV
 - Au+Au (18 M min. bias events, sampled) (2004)
 - Cu+Cu (0.12 nb^{-1} , 25 M events) (2005)
 - p+p (sampled 0.21 pb^{-1} min. bias events) (2006)

At full luminosity the Au–Au nuclear collision rate is about 1.2 kHz (2001). A centrality trigger was implemented to select the 20% most central collisions. The pp collision rate was 50 kHz. In the later runs in 2003–2006 specific spectrometer and vertex range triggers were implemented allowing to sample the full luminosity thus enriching the physics data samples. Event rates of 60 Hz with an event size of 60 kB have been achieved for AuAu, while pp runs were taken typically with 120 Hz and 30 kb event size.

A.11.5 Results

Some of the results specific to BRAHMS are listed below:

- Pseudo-rapidity density distribution and total multiplicity of charged particles [3, 4, 9]: The pseudo-rapidity density at mid-rapidity in central Au+Au collisions, normalised to the number of nucleon-pairs exceeds the

one observed in p+p collisions but is surprisingly small when compared to model predictions.

- Rapidity distribution of identified charged hadrons [2, 5, 10]: The rapidity distribution can be described by a Gaussian shape, the width agrees with predictions based on the Landau model. The rapidity dependence of particle ratios has been studied for small and large systems at 64 and 200 GeV. Large K^+/π^+ and small K^-/π^- ratios at forward rapidities in central Au+Au collisions have been observed – values which are similar to those at the SPS at mid-rapidity (and in 4π) when compared at the same \bar{p}/p ratio.
- Net proton rapidity distribution [8]: The kinetic energy that is removed from the beam and which is available for the production of states such as the sQGP depends on the amount of stopping between the colliding ions. This value has been determined to be 73% for central Au+Au collisions at 200 GeV. The process of stopping itself is not really understood, not even for small systems like p+p and d+Au.
- Nuclear modification factor [6, 7, 11, 12]: Due to the p_T coverage up to 4 GeV/c suppression effects at intermediate transverse momenta could be studied. The nuclear modification factor for pions changes from a Cronin-like enhancement at mid-rapidity to a suppression at forward rapidities in d+Au collisions. This effect could be interpreted as an indication of gluon saturation. In central Au+Au no rapidity dependence of the suppression of pions was observed. This could be an indication of corona emission of jets or may be due to interplay between initial (saturation) and final (parton energy loss) state effects.
- Transverse Single Spin Asymmetries of π and K in pp collisions [13]: The high x_F coverage allowed measurements of single spin asymmetries at 62 and 200 GeV. Large values are observed for both pions and kaons. In particular the almost identical asymmetry for K^+ and K^- is surprising. These data will contribute to the understanding of the orbital angular momentum in the proton.

A.11.6 Advantages and limitations of the experimental approach

The BRAHMS detector is the only detector system at RHIC that can study both stopping and production of pions, kaons and protons at forward rapidities. The excellent momentum measurement and particle identification capability at small angles and large momenta has a drawback: the small solid angle of the spectrometers introduce limitations which result in low statistics for rare particles (antiprotons at forward rapidities) and restrict correlation studies, e.g. in HBT the limited spectrometer acceptance restricts the Q-side range; resonance (e.g. Λ) studies are practically impossible (with the exception of a limited acceptance for ϕ decaying into charged kaons).

References

1. BRAHMS Collaboration, Nucl. Instrum. Methods A **499**, 437 (2003)
2. BRAHMS Collaboration, Phys. Rev. Lett. **87**, 112305 (2001) [953](#)
3. BRAHMS Collaboration, Phys. Lett. B **523**, 227 (2001) [952](#)
4. BRAHMS Collaboration, Phys. Rev. Lett. **88**, 202301 (2002) [952](#)
5. BRAHMS Collaboration, Phys. Rev. Lett. **90**, 102301 (2003) [953](#)
6. BRAHMS Collaboration, Phys. Rev. Lett. **91**, 072305 (2003) [953](#)
7. BRAHMS Collaboration, Phys. Rev. Lett. **93**, 242303 (2004) [953](#)
8. BRAHMS Collaboration, Phys. Rev. Lett. **93**, 102301 (2004) [953](#)
9. BRAHMS Collaboration, Phys. Rev. Lett. **94**, 032301 (2005) [952](#)
10. BRAHMS Collaboration, Phys. Rev. Lett. **94**, 162301 (2005) [953](#)
11. BRAHMS Collaboration, Phys. Lett. B **650**, 219 (2007) [953](#)
12. BRAHMS Collaboration, Phys. Rev. Lett. **98**, 252001 (2007) [953](#)
13. BRAHMS Collaboration, Phys. Rev. Lett. **101**, 042001 (2008) [953](#)

A.12 The PHENIX experiment at RHIC/BNL

The Pioneering High Energy Nuclear Interaction eXperiment (PHENIX) is located at Brookhaven National Laboratory's Relativistic Heavy Ion Collider (RHIC). PHENIX is designed for a broad study of (polarized) p-p, p(d)-A, and A-A collisions to search for and characterize new states of strongly interacting matter as well as to measure the spin structure of the proton. While rare probes, i.e. electromagnetic probes and phenomena at high transverse momentum, are considered a priority for the physics program, global observables and soft identified hadron spectra are measured in PHENIX as well.

A.12.1 Experimental setup

The PHENIX setup was optimized for rare probe measurements in a limited acceptance and integrates a large number of subsystems for excellent tracking and particle identification with a high-bandwidth trigger and data-acquisition system. At RHIC, this approach is complementary to the main focus of the STAR experiment which emphasizes the tracking of almost all charged particles in a large acceptance time projection chamber.

PHENIX uses a set of global detectors to characterize the collisions, a pair of central spectrometer arms to measure electrons, hadrons, and photons around mid-rapidity, and a pair of forward spectrometers to measure muons. The detector setup in its configuration from the 2007/2008 run at RHIC is sketched in Fig. A.18. The overall design parameters of PHENIX as well as detailed descriptions of the various subsystems have been published in a dedicated volume of *Nuclear Instruments and Methods in Physics Research* [1].

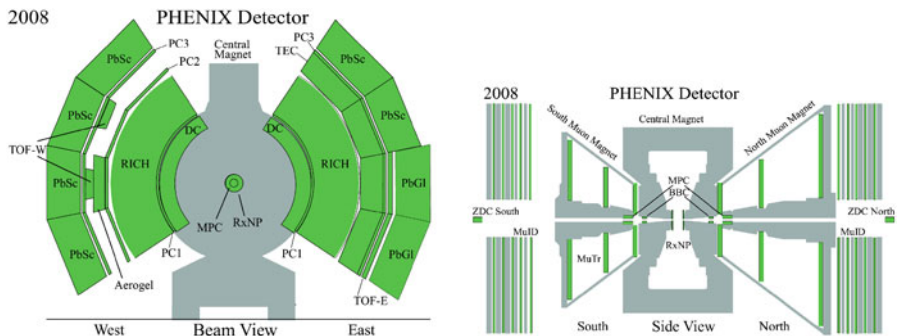


Fig. A.18 Sketch of the PHENIX setup in its configuration from the 2007/2008 run at RHIC in beam view (*left*) and side view (*right*)

For event characterization a set of global detectors is used. A pair of Zero-Degree hadronic Calorimeters (ZDC) measures neutrons from beam fragments downstream of the interaction region. A pair of Beam-Beam Counters (BBC) covers the full azimuth in pseudo-rapidity intervals $\Delta\eta = \pm(3.1 - 3.9)$ and measures the time and position of an interaction along the beam direction via the time of flight of prompt charged particles. The ZDC and/or BBC provide interaction triggers and contribute to the centrality measurement for nuclear collisions. The orientation of the reaction plane is measured with the BBC and a dedicated Reaction-Plane Detector which covers the full azimuth in the range $\Delta\eta = \pm(1.0 - 2.8)$.

An axial magnetic field (field integral up to 1.15 Tm) is provided for the central spectrometers parallel to the beam and around the interaction vertex. The central spectrometers cover the pseudo-rapidity range $\Delta\eta = \pm 0.35$ and combine a tracking system for charged particles with electromagnetic calorimetry. The tracking system ($\Delta\phi = 90^\circ \times 2$) comprises a pair of Drift Chambers (DC), which allow for projective tracking of charged particles, and three sets of Pad Chambers (PC), which add three-dimensional space points for pattern recognition and tracking in the non-bending plane. A momentum resolution of $\sigma_p/p \simeq 0.7\% \oplus 1.0\%p$ (GeV/c) is achieved, which translates into an invariant mass resolution of $\Delta m/m \simeq 1.0\%$ at $m = 1$ GeV/ c^2 . A Time Expansion Chamber (TEC) in one of the spectrometers ($\Delta\phi = 90^\circ$) provides additional tracking and particle identification capabilities.

Particle identification is achieved by a set of dedicated detectors. For hadron identification two time of flight (TOF) detector systems are in place which both provide a time resolution of better than 100 ps, i.e. the scintillator based TOF-E ($\Delta\phi = 45^\circ$) in one spectrometer arm and the multi-gap resistive plate chamber based TOF-W ($\Delta\phi = 14^\circ$) in the other arm. These detectors provide a 4σ π/K and K/p separation up to transverse momenta p_T of 2.5 and 4.5 GeV/c, respectively. An additional aerogel Cherenkov detector ($\Delta\phi = 14^\circ$) allows to separate pions from kaons in the range $1 < p_T < 5$ GeV/c. A pair of CO₂ filled Ring-Imaging Cherenkov detectors (RICH) covering both spectrometers ($\Delta\phi = 90^\circ \times 2$) identifies pions for $p_T > 5.5$ GeV/c and is crucial for clean electron identification up to momenta of 4.7 GeV/c. To further extend the p_T range of the electron measurement to $\simeq 10$ GeV/c the information from the RICH is combined with the energy and shower shape measured in the electromagnetic calorimeters for electron candidate tracks. A pion contamination in the electron sample of better than one part in 10^4 is obtained over a wide momentum range.

Two electromagnetic calorimeters are used in PHENIX, i.e. a lead-scintillator (PbSc) sampling calorimeter ($\Delta\phi = 90^\circ + 45^\circ$) with a nominal energy resolution of $8.1\%/\sqrt{E(\text{GeV})} \oplus 2.1\%$ and an intrinsic time resolution of better than 200 ps for electromagnetic showers, and a lead-glass (PbGl) Cherenkov calorimeter ($\Delta\phi = 45^\circ$) providing a nominal energy resolution of $6\%/\sqrt{E(\text{GeV})}$ and a time resolution of better than 300 ps for electromagnetic showers. The main purpose of the calorimeters is the measurement of

photons and energetic electrons. The segmentation and position resolution of the calorimeters is sufficient to resolve the two electromagnetic showers from the decay $\pi^0 \rightarrow \gamma + \gamma$ up to p_T of ≈ 25 GeV/c. At forward rapidities ($\Delta\eta = \pm(3.1-3.65)$), an additional pair of lead-tungstate crystal based muon piston calorimeters (MPC) covering the full azimuth allows to measure cross sections and spin asymmetries of neutral pions in d–Au and polarized p–p collisions.

Two muon spectrometers at rapidities of $-2.25 < y < -1.15$ and $1.15 < y < 2.44$ cover the full azimuth and are optimized for the measurement of J/ψ di-muon decays. Both spectrometers comprise a muon tracker (MuTr) inside a radial magnetic field followed by a muon identifier system to reject hadron background. In the muon trackers three stations of multi-plane drift chambers provide precision tracking. The muon identifiers are made from alternating layers of steel absorbers and tracking layers of Iarocci streamer tubes. Typically, the pion contamination in the identified muon sample is about 3×10^{-3} .

The trigger and data acquisition systems were optimized for the study of rare event physics. In addition to minimum bias collision triggers from the BBC and/or ZDC level-1 hardware and level-2 software trigger system are in place. Various triggers were implemented, including triggers on the collision centrality, single electrons or muons above a given energy threshold or penetration depth into the muon identifier, respectively, energy deposit in the calorimeters above a given threshold, or more sophisticated triggers, e.g. on electron or muon pair candidates above a given invariant mass. Up to now a maximum throughput of 8 kHz has been achieved in the data acquisition.

PHENIX has recorded data in all runs at RHIC. The colliding species and energies per nucleon–nucleon pair, as well as the size of the recorded data sets and the number of total collisions sampled by the level-1 and/or level-2 triggers are summarized in Table A.5.

A.12.2 Main results and publications

As multi-purpose experiment with a focus on rare probes PHENIX has contributed significantly to the characterization of the medium produced in relativistic nucleus–nucleus collisions at RHIC as a form of dense partonic matter [2]. A selection of results from the heavy-ion program demonstrates the broad spectrum of observables accessible by PHENIX:

- *global observables*: PHENIX has systematically studied the centrality and $\sqrt{s_{NN}}$ dependence of the charged particle pseudo-rapidity density $dN_{ch}/d\eta$ and the transverse energy $dE_T/d\eta$ in Au–Au collisions [3].
- *identified hadrons*: PHENIX has measured π^\pm , K^\pm , p , and \bar{p} spectra in Au–Au collisions at $\sqrt{s_{NN}} = 130$ [4] and 200 GeV [5]. An anomalously large (anti)proton yield was observed at intermediate p_T [4,5]. The elliptic

Table A.5 Summary of basic running conditions and data samples recorded by PHENIX until RHIC run 8.

RHIC run	Year	Species	$\sqrt{s_{NN}}$ (GeV)	Int. luminosity	Sampled events	Data volume
1	2000	Au–Au	130	$1 \mu\text{b}^{-1}$	10×10^6	3 TB
2	2001/2002	Au–Au	200	$24 \mu\text{b}^{-1}$	170×10^6	10 TB
		Au–Au	19		$< 1 \times 10^6$	
		p–p	200	0.15 pb^{-1}	3.7×10^9	20 TB
3	2002/2003	d–Au	200	2.71 nb^{-1}	5.5×10^9	46 TB
		p–p	200	0.35 pb^{-1}	6.6×10^9	35 TB
4	2003/2004	Au–Au	200	$241 \mu\text{b}^{-1}$	1.5×10^9	270 TB
		Au–Au	62.4	$9 \mu\text{b}^{-1}$	58×10^6	10 TB
5	2005	Cu–Cu	200	3 nb^{-1}	8.6×10^9	173 TB
		Cu–Cu	62.4	0.19 nb^{-1}	0.4×10^9	48 TB
		Cu–Cu	22.4	$2.7 \mu\text{b}^{-1}$	9×10^6	1 TB
		p–p	200	3.8 pb^{-1}	85×10^9	262 TB
6	2006	p–p	200	10.7 pb^{-1}	233×10^9	310 TB
		p–p	62.4	0.1 pb^{-1}	28×10^9	25 TB
7	2007	Au–Au	200	$813 \mu\text{b}^{-1}$	5.1×10^9	650 TB
8	2007/2008	d–Au	200	80 nb^{-1}	160×10^9	437 TB
		p–p	200	5.2 pb^{-1}	115×10^9	118 TB
		Au–Au	9.2		$\text{few} \times 10^3$	

flow of hadrons was measured at various energies [6,7] and a quark number scaling of the azimuthal anisotropies was observed [8].

- *high p_T probes*: PHENIX has observed a substantial suppression of neutral pions and charged particles at high p_T [9] in Au–Au collisions which is absent in d–Au collisions [11]. This indicates partonic energy loss in the medium produced in nucleus nucleus collisions at RHIC [10]. Direct photons from hard scattering processes have been measured in p–p [12] and Au–Au collisions [13]. Away-side di-jet induced azimuthal correlations of hadron pairs have been observed to be significantly modified in nuclear collisions [14].
- *heavy flavor*: PHENIX has measured electrons from semileptonic heavy-flavor decays in Au–Au collisions which show that the total charm yield scales with the number of binary collisions [15]. The nuclear modification of electron spectra at high p_T , observed together with a substantial azimuthal anisotropy of electron emission, indicates a strong interaction of heavy flavor with the medium produced in Au–Au collisions, which can be characterized as an almost perfect fluid with partonic degrees of freedom [16, 17]. In addition, PHENIX has systematically measured J/ψ production in p–p [18], d–Au [19], Cu–Cu [20], and Au–Au [21] collisions at $\sqrt{s_{NN}} = 200$ GeV. Medium effects in cold and hot matter leave their footprint on the centrality, p_T , and rapidity dependence of J/ψ production in nuclear collisions at RHIC [22].
- *electromagnetic probes*: PHENIX has measured correlated dielectron production in p–p [23] and Au–Au [24] collisions at $\sqrt{s_{NN}} = 200$ GeV. In par-

ticular, a significantly enhanced low-mass pair yield is observed in Au–Au collisions compared to the expectation from hadronic sources and relative to the binary collision scaled p–p reference [24, 25].

Further information about PHENIX as well as a complete record of all publications can be found at <http://www.phenix.bnl.gov>.

References

1. K. Adcox, et al., Nucl. Instrum. Methods A **499**, 469 (2003), and the following papers in the same journal issue up to page 602 955
2. K. Adcox, et al., Nucl. Phys. A **757** 184 (2005) 957
3. S.S. Adler, et al., Phys. Rev. C **71** 034908 (2005) 957
S.S. Adler, et al., Phys. Rev. C **71** 049901 (2005) [Erratum]
4. K. Adcox, et al., Phys. Rev. Lett. **88** 242301 (2002) 957
5. S.S. Adler, et al., Phys. Rev. C **69** 034909 (2004) 957
6. K. Adcox, et al., Phys. Rev. Lett. **89** 212301 (2002) 958
7. S.S. Adler, et al., Phys. Rev. Lett. **91** 182301 (2003) 958
8. A. Adare, et al., Phys. Rev. Lett. **98** 162301 (2007) 958
9. K. Adcox, et al., Phys. Rev. Lett. **88** 022301 (2002) 958
10. S.S. Adler, et al., Phys. Rev. Lett. **91** 072301 (2003) 958
11. S.S. Adler, et al., Phys. Rev. Lett. **91** 072303 (2003) 958
12. S.S. Adler, et al., Phys. Rev. D **71** 071102R (2005) 958
13. S.S. Adler, et al., Phys. Rev. Lett. **94** 232301 (2005) 958
14. S.S. Adler, et al., Phys. Rev. Lett. **97** 052301 (2006) 958
15. S.S. Adler, et al., Phys. Rev. Lett. **94** 082301 (2005) 958
16. S.S. Adler, et al., Phys. Rev. Lett. **96** 032301 (2006) 958
17. A. Adare, et al., Phys. Rev. Lett. **98** 172301 (2007) 958
18. S.S. Adler, et al., Phys. Rev. Lett. **92** 051802 (2004) 958
19. S.S. Adler, et al., Phys. Rev. Lett. **96** 012304 (2006) 958
20. A. Adare, et al., Phys. Rev. Lett. **101**, 122301 (2008); arXiv:0801.0220 958
21. S.S. Adler, et al., Phys. Rev. C **69** 014901 (2004) 958
22. A. Adare, et al., Phys. Rev. Lett. **98** 232301 (2007) 958
23. A. Adare, et al., Phys. Lett. B **670**, 313 (2009); arXiv:0802.0050 958
24. S. Afanasiev, et al., arXiv:0706.3034 958, 959
25. A. Adare, et al., Phys. Rev. Lett. **104**, 132301 (2010); arXiv:0804.4168 959

A.13 The PHOBOS experiment at RHIC/BNL

The PHOBOS experiment is the smallest in size of the four heavy-ion collision experiments at RHIC. It has been designed to perform comprehensive studies of global parameters of ultra-relativistic heavy-ion collisions with almost complete coverage of the solid angle. The multiplicity of charged particles can be measured over the pseudorapidity interval $-5.4 < \eta < 5.4$. At midrapidity special focus was set on the measurement and identification of low p_t particles. The detector system has been mainly used for charged particle multiplicities, spectra, two-particle correlations, and collective flow characteristics.

A.13.1 Experimental setup

The PHOBOS setup as depicted in Fig. A.19 and described in detail in [1] consists of four subsystems: a Multiplicity array, a Vertex detector, a two-arm Spectrometer including time-of-flight walls, and several trigger detectors which also determine the centrality of the collisions. The detector is rather compact; almost all elements are located within 1 m of the beam line with the first detectors located in the closest proximity (appr. 10 cm) to the interaction region. A Be beampipe with a wall thickness of only 1 mm was chosen in order to minimize the effect of particle decays and multiple scattering in material near the collision region, which is especially important at low p_t .

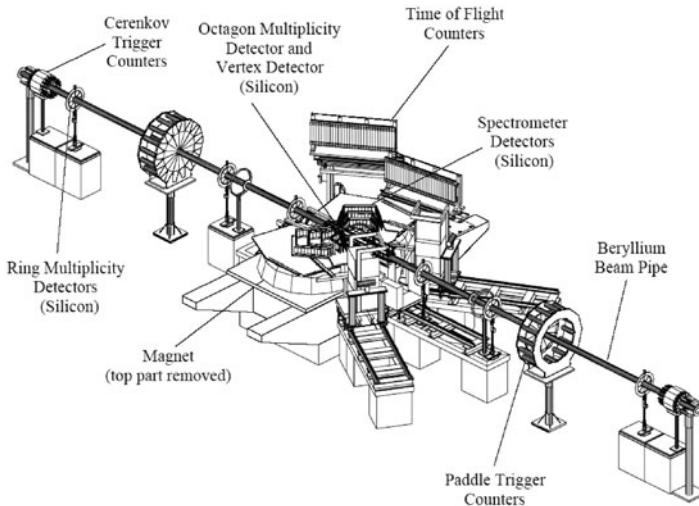


Fig. A.19 Schematic layout of the PHOBOS detector. The top yoke of the magnet is not shown [1]

The Multiplicity array consists of single layer silicon detectors used to measure the number and angular distribution of charged particles over a pseudorapidity range of $|\eta| \leq 5.4$. It consists of a central, octagon-shaped barrel of 1.1 m length and 9 cm diameter around the beam pipe covering $|\eta| \leq 3.2$ and six ring detectors at distances of ± 1.13 , ± 2.35 , and ± 5.05 m from the interaction point along the beam axis extending the coverage to $|\eta| \leq 5.4$. Above and below the interaction region additional double layers of finely segmented Si sensors are used for precise vertex determination. For collisions that take place within ± 10 cm of the nominal center of the apparatus, the vertex position can be determined with an accuracy of better than 0.2 mm along the beam line. The geometrical acceptance of these Si detectors is depicted in Fig. A.20. Apart from the opening for the Spectrometer arms these detectors provide almost complete coverage for $|\eta| \leq 5.4$.

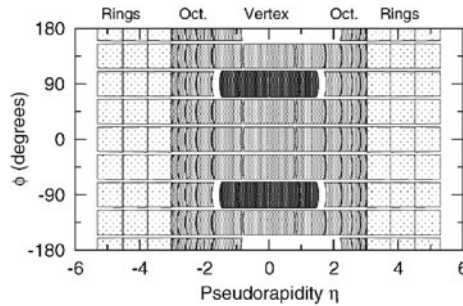


Fig. A.20 The geometrical acceptances of the Ring (*light*), Octagon (*medium*) and Inner Vertex (*dark*) detectors for particles emitted from the nominal interaction point are shown as a function of η and ϕ [1]

The Spectrometer consists of two arms of 15 silicon layers each located on either side of the beam axis. This subsystem provides tracking and particle identification of roughly 2% of the charged particles emitted in a typical interaction. It covers a span of approx. 0.7 units of pseudorapidity for a given vertex location with a total coverage of approximately $0 \leq \eta \leq 2$. The orientation of the spectrometer was designed to allow tracking of very low p_t particles, i.e. from 30 MeV/c on. Particle identification is achieved using the energy loss in the Si layers as well as additional time-of-flight information from two arrays of scintillator TOF counters (120 scintillators each) with photomultiplier tubes (Hamamatsu R5900). The combined π/K separation reaches up to 1.4 GeV/c, the one for p/K up to 3.0 GeV/c.

With these detectors the PHOBOS apparatus makes thus extensive use of silicon pad detector technology (135,168 channels in total). Although the pad sizes and shapes vary greatly among the different components, a common AC-coupled, single sided, silicon pad design was used for all sensors.

For trigger detectors PHOBOS employs paddle counters from BC-400 plastic scintillators as primary event trigger and a high- p_T particle trigger system

(for d+Au collisions), Cherenkov counters to produce the interaction vertex trigger, and a zero degree calorimeter which is common to the other RHIC experiments as minimum bias trigger and for centrality selection.

The PHOBOS data acquisition is capable of accepting data from 150,000 silicon and a total of 2,000 scintillation detector channels at an event rate of 200 Hz, and sending the data over a Gigabit network to the RHIC central data storage system at a sustained rate of 30 MB/s. The detector was successfully commissioned and used to measure Au+Au, p+p, d+Au and Cu+Cu collisions at RHIC from the first run in 2000 until Run 5 in 2005.

A.13.2 Main results and publications

The PHOBOS experiment is focussed on the measurement of global observables and multiplicities. Amongst its main outcome are charged particle pseudorapidity distributions over 11 units in η for all RHIC energies and collisions systems, see e.g. the first RHIC publication [2] and an overview of the first 5 RHIC years in [3]. Detailed analysis of elliptic flow data, including the study of correlations and fluctuations of the initial source eccentricity were performed [4–6]. PHOBOS also contributed identified particle spectra extending the measured p_t -spectra from the other RHIC experiments to lowest p_t [7]. Studying two-particle correlations with a high transverse momentum trigger particle, not only a broadening of the away-side azimuthal correlation ("jet quenching") is observed compared to p+p, but also an additional correlation on the trigger particle side extended over $\Delta\eta \sim 4$ [8]. Overall, the measured values of charged particle pseudorapidity density and elliptic flow were found to be independent of energy over a broad range of pseudorapidities when effectively viewed in the rest frame of one of the colliding nuclei, a property described as "extended longitudinal scaling". The centrality and energy dependence of several observables were found to factorize to a surprising degree [3].

Further information about PHOBOS as well as a complete record of all publications can be found at <http://www.phobos.bnl.gov/>.

References

1. B.B. Back, et al., Nucl. Instrum. Methods A **499**, 603 (2003) 960, 961
2. B.B. Back, et al., Phys. Rev. Lett. **85**, 3100 (2000) 962
3. B.B. Back, et al., Nucl. Phys. A **757**, 28 (2005) 962
4. B.B. Back, et al., Phys. Rev. Lett. **97**, 012301 (2006) 962
5. B. Alver, et al., Phys. Rev. Lett. **98**, 242302 (2007)
6. B. Alver, et al., Phys. Rev. C **77**, 014906 (2008) 962
7. B.B. Back, et al., Phys. Rev. C **75**, 024910 (2007) 962
8. B. Alver, et al., Phys. Rev. Lett. **104**, 062301 (2010) 962

A.14 The STAR experiment at RHIC/BNL

The Solenoidal Tracker At RHIC (STAR) is one of the two large experiments at the Relativistic Heavy Ion Collider at BNL. The experiment started taking data in 2000 and is running since then.

A.14.1 Experimental setup

STAR was designed primarily for measurements of hadron production over a large solid angle, featuring detector systems for high precision tracking, momentum analysis, and particle identification at the center of mass (c.m.) rapidity. The large acceptance of STAR makes it particularly well suited for event-by-event characterizations of heavy ion collisions and for the detection of hadron jets. The detector was build, unlike PHENIX, to measure the maximum information content from the abundant probes in a single heavy ion collisions rather than rare probes. Therefore its capabilities in photons and leptons are limited. The layout of the STAR experiment is shown in Fig. A.21. All detector components are described in detail in a dedicated NIM volume [1].

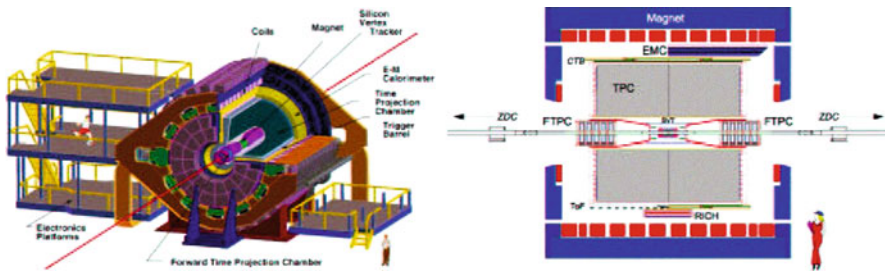


Fig. A.21 Schematic of STAR in its complete configuration as of 2007, beam view (*left*) and side view (*right*)

A room temperature solenoidal magnet with a uniform magnetic field of maximum value 0.5 T provides momentum for charged particles. A Silicon Vertex Tracker (SVT) close to the interaction allows precision localization of the primary interaction vertex and identification of secondary vertices from weak decays of strange and charmed hadrons. The SVT is arranged in three cylindrical layers at distances of approximately 7, 11 and 15 cm from the beam axis. A 4th layer of Silicon Strip Detectors (SSD) has been added to the inner tracker in 2002. The silicon detectors cover a pseudo-rapidity range $\eta = \pm 1$ with complete azimuthal symmetry ($\phi = 2\pi$).

At the heart of STAR is the world's second largest Time Projection Chamber (behind the new ALICE-TPC), which has been used reliably and successfully for the past eight years. The TPC enables charged particle tracking and particle identification in a volume from 50 to 200 cm radially from the beam axis. The TPC is 4 m long and it covers a pseudo-rapidity range $\eta = \pm 1.8$ for tracking with complete azimuthal symmetry ($\phi = 2\pi$). The TPC contributes to particle identification using ionization energy loss, with an energy loss resolution (dE/dx) of 7%. The combined momentum resolution of the SVT and TPC reach a value of $dp/p = 0.02$ for a majority of the tracks in the TPC. The dp/p resolution improves as the number of hit points along the track increases and as the particle's momentum decreases.

To extend the tracking to the forward region, STAR features a radial-drift TPC (FTPC) covering $\eta = \pm 2.5$ –4, also with complete azimuthal coverage and symmetry. A full-barrel electromagnetic calorimeter (EMC) was installed over a period of years together with an endcap electromagnetic calorimeter (EEMC) yielding a coverage of $-1 < \eta < 2$ and $\phi = 2\pi$. This system allows the measurement of the transverse energy of events, and trigger on and measure high transverse momentum photons, electrons, and electromagnetically decaying hadrons. The EMCs include shower-maximum detectors to distinguish high momentum single photons from photon pairs resulting from π and η meson decays. The EMCs also provide prompt charged particle signals essential to discriminate against pileup tracks in the TPC, arising from other beam crossings falling within the 40 μ s drift time of the TPC, which are prevalent at RHIC pp collision luminosities ($> 10^{32} \text{ cm}^{-2} \text{ s}^{-1}$).

In the early years of STAR particle identification at large momenta has been achieved over a small solid angle for identified single-particle spectra at mid-rapidity using a Ring Imaging Cherenkov detector which covered $\eta < \pm 0.3$ and $\phi = 0.11\pi$. A new Time-Of-Flight (TOF) detector covering $\eta \pm 1$ over the full azimuth is one of two main upgrades to STAR, which will be completed in the next few years. The other device is the so-called Heavy Flavor Tracker (HFT) which replaces the SVT in an attempt to reconstruct the hadronic decays of charm and bottom hadrons. The HFT is based on active pixel sensor technology and will improve the positions resolution in the SVT by about a factor 5 down to below 10 μ m.

The STAR trigger system is a 10 MHz pipelined system with different trigger levels which is based on input from fast detectors to control the event selection (level 0) for the much slower tracking detectors. In particular STAR has a 3rd level trigger which performs complete online reconstruction of the events in a dedicated CPU farm also providing an online display (Fig. A.22) for visual inspection of individual events in real time. The level 3 trigger can process central Au+Au collisions at a rate of 50 Hz including simple analysis of physics observables such as particle momentum and rate of energy loss.

The fast detectors that provide input to the trigger system are a central trigger barrel (CTB) at $\eta < 1$ and zero-degree calorimeters (ZDC) located in the forward direction at $\theta < 2$ mrad. The CTB surrounds the outer cylinder

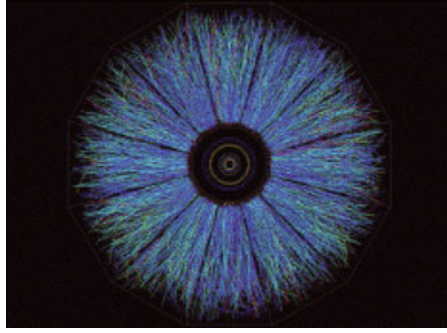


Fig. A.22 STAR online display for a typical central Au+Au collision

of the TPC, and triggers on the flux of charged-particles in the midrapidity region. The ZDCs are used for determining the energy in neutral particles remaining in the forward directions. Each experiment at RHIC has a complement of ZDCs for triggering and cross-calibrating the centrality triggering between experiments.

STAR's data volume for a single event is considerably larger than PHENIX's and it utilizes significantly slower detector components (drift detectors), in terms of readout speed. In particular the TPC limits STAR's bandwidth in terms of data volume and readout speed. Therefore the initial event collection speed in STAR was 1 Hz with an average data volume of 20 MB for a central AuAu collision. Since then the TPC readout electronics has been upgraded, the DAQ and Trigger frameworks have been optimized and STAR's latest setup is running at a few hundred Hz. The final goal for STAR is to run all detector components at 1 kHz, a goal that should be achievable within the next two years pending certain further improvements to the data compactification in the data acquisition.

STAR has recorded data in all eight runs at RHIC since 2000. The colliding species and energies per nucleon–nucleon pair, as well as the size of the recorded data sets and the number of total collisions sampled are summarized in Table A.6.

A.14.2 Main results and publications

The main publications of STAR deal mostly with hadronic and global observables, see [2] for a summary on results leading to the announcement of the discovery of a strongly coupled QGP in 2005 often referred to as a perfect liquid. STAR collects and reconstructs most of the hadronic particle emission from heavy ion collisions, due to its almost complete pseudo-rapidity coverage and its high resolution vertexing capabilities which enable reconstruction

Table A.6 Summary of basic running conditions and data samples recorded by STAR from 2000 to 2008.

RHIC run	Year	Species	$\sqrt{s_{NN}}$ (GeV)	Sampled events
1	2000	Au–Au	130	2×10^5
2	2001/2002	Au–Au	200	10×10^6
		Au–Au	19	5×10^4
		p–p	200	8×10^6
3	2002/2003	d–Au	200	31×10^6
		p–p	200	50×10^6
4	2003/2004	Au–Au	200	60×10^6
		Au–Au	62.4	18×10^6
		p–p	200	13×10^6
5	2005	Cu–Cu	200	75×10^6
		Cu–Cu	62.4	40×10^6
		Cu–Cu	22.4	4×10^6
		p–p	200	250×10^6
6	2006	p–p	200	400×10^6
		p–p	62.4	50×10^6
7	2007	Au–Au	200	100×10^6
8	2007/2008	d–Au	200	1.2×10^9
		p–p	200	300×10^6
		Au–Au	9.2	1×10^6

of short lived hadronic resonances, as well as strange and potentially heavy quark hadrons. More specific highlights of the STAR pool of publications can be characterized as follows:

- *directed and elliptic flow*: STAR has measured the directed (v_1) and elliptic flow (v_2) parameters as well as higher order harmonics for charged particles and identified particles, including resonances, all the way up to the Ω . These measurements have established evidence for near ideal hydrodynamic behavior of the partonic phase. In addition the quark scaling behavior at intermediate p_T proves the partonic nature of the collective phase and gives evidence for recombination as a prime hadronization mechanism at RHIC energies [3–12].
- *identified hadrons*: A detailed analysis of the identified spectra in STAR yields strong evidence for radial flow with expansion velocities in excess of $0.6c$ for the bulk matter, plus evidence for recombination for matter at intermediate p_T [13–15]. Source sizes measured through HBT are surprisingly small though [16–19]. Simultaneous analysis of hadronic resonances and stable particles sets constraints on the partonic and hadronic lifetimes at RHIC [20, 21]. Strangeness enhancement and the behavior of the ϕ meson in the context of hadron production has been measured extensively [22–27].
- *high p_T probes*: STAR has measured jet quenching in charged and identified particle spectra to a level that is only achievable in a deconfined partonic system. The disappearance of the high momentum away-side jet

components in di-jet correlation measurements was an early highlight at RHIC which again confirmed the partonic nature of the medium. Measurements of the quenching strength as a function of reaction planes proved the anticipated path length dependence of radiative energy loss. Punch-through measurements of very high away-side jets quantify the surface bias of the leading hadron correlation method and constrain the measurements of the in-medium modification of the fragmentation process, plus the determination of transport coefficients and gluon densities at RHIC. Several high momentum correlation structures (e.g. the same-side ridge) have been discovered at RHIC which suggest enhanced interactions between the jet and the partonic medium [28–34].

- *heavy flavor*: Heavy flavor quenching at RHIC is still not well understood but it gives rise to the possibility of enhanced collisional energy loss, plus it constrains the measurements of the shear viscosity (η/s) to values near the quantum limit and far away from the pQCD limit (i.e. sQGP) [35, 36]. Separate measurements of fully reconstructed D and B mesons will be one of the highlights of future heavy ion measurements in STAR [37].
- *fluctuations and correlations*: STAR has an extensive program of fluctuation and correlation measurements. Although strong evidence for critical fluctuations has not been found, recent correlation measurements seem to hint at transitional behavior at a given energy/particle density in mid-central heavy ion collisions at RHIC [38–41].

References

1. STAR collaboration, Nucl. Instrum. Methods A **499**, 624 (2003) 963
2. J. Adams, et al., Nucl. Phys. A **757**, 102 (2005) 965
3. B.I. Abelev, et al., Phys. Rev. C **75**, 54906 (2007) 966
4. J. Adams, et al., Phys. Rev. Lett. **95**, 122301 (2005)
5. J. Adams, et al., Phys. Rev. C **72**, 14904 (2005)
6. J. Adams, et al., Phys. Rev. Lett. **93**, 252301 (2004)
7. J. Adams, et al., Phys. Rev. Lett. **92**, 062301 (2004)
8. J. Adams, et al., Phys. Rev. Lett. **92**, 52302 (2004)
9. C. Adler, et al., Phys. Rev. C **66**, 34904 (2002)
10. C. Adler, et al., Phys. Rev. Lett. **89**, 132301 (2002)
11. C. Adler, et al., Phys. Rev. Lett. **87**, 182301 (2001)
12. C. Adler, et al., Phys. Rev. Lett. **86**, 402 (2001) 966
13. J. Adams, et al., Phys. Rev. Lett. **97**, 152301 (2006) 966
14. J. Adams, et al., Phys. Rev. Lett. **92**, 112301 (2004)
15. J. Adams, et al., Phys. Rev. C **70**, 41901 (2004) 966
16. J. Adams, et al., Phys. Rev. C **71**, 44906 (2005) 966
17. J. Adams, et al., Phys. Rev. Lett. **93**, 12301 (2004)
18. J. Adams, et al., Phys. Rev. Lett. **91**, 262301 (2003)

19. C. Adler, et al., Phys. Rev. Lett. **87**, 82301 (2001) [966](#)
20. J. Adams, et al., Phys. Rev. Lett. **97**, 132301 (2006) [966](#)
21. J. Adams, et al., Phys. Rev. Lett. **92**, 92301 (2004) [966](#)
22. B.I. Abelev, et al., Phys. Rev. C **77**, 44908 (2008) [966](#)
23. B.I. Abelev, et al., Phys. Rev. Lett. **99**, 112301 (2007)
24. B.I. Abelev, et al., Phys. Rev. Lett. **98**, 62301 (2007)
25. J. Adams, et al., Phys. Lett. B **612**, 181 (2005)
26. J. Adams, et al., Phys. Rev. Lett. **92**, 182301 (2004)
27. C. Adler, et al., Phys. Rev. Lett. **89**, 92301 (2002) [966](#)
28. J. Adams, et al., Phys. Rev. Lett. **97**, 162301 (2006) [967](#)
29. J. Adams, et al., Phys. Rev. Lett. **95**, 152301 (2005)
30. J. Adams, et al., Phys. Rev. Lett. **91**, 072304 (2003)
31. J. Adams, et al., Phys. Rev. Lett. **91**, 172302 (2003)
32. C. Adler, et al., Phys. Rev. Lett. **90**, 82302 (2003)
33. C. Adler, et al., Phys. Rev. Lett. **89**, 202301 (2002)
34. C. Adler, et al., Phys. Rev. Lett. **90**, 032301 (2003) [967](#)
35. B.I. Abelev, et al., Phys. Rev. Lett. **98**, 192301 (2007) [967](#)
36. J. Adams, et al., Phys. Rev. Lett. **94**, 62301 (2005) [967](#)
37. J. Kapitan, et al., arXiv:0806.2266 [967](#)
38. J. Adams, et al., Phys. Rev. C **71**, 64906 (2005) [967](#)
39. J. Adams, et al., Phys. Rev. C **68**, 44905 (2003)
40. C. Adler, et al., Phys. Rev. Lett. **90**, 172301 (2003)
41. M. Daugherty, et al., J. Phys. G **35**, 104090 (2008), arXiv:0906.2121 [967](#)

A.15 The ALICE experiment at the LHC/CERN

ALICE (A Large Ion Collider Experiment) is a dedicated heavy ion experiment at the CERN LHC, designed to address the physics of strongly interacting matter and the quark-gluon plasma at extreme values of energy density and temperature in nucleus–nucleus collisions. The most stringent design constraint is to cope with the extreme particle multiplicity anticipated in central Pb–Pb collisions (up to $dN_{ch}/dy=8,000$). The detector has been built by a collaboration including currently over 1,000 physicists and engineers from 105 institutes in 30 countries. Its overall dimensions are $16 \times 16 \times 26 \text{ m}^3$ with a total weight of approximately 10,000 t. The experimental setup is shown in Fig. A.23. A solenoid magnet with an inner length of 12.1 m and a radius of 5.75 m, inherited from the L3 experiment at LEP, provides a field of 0.5 T at the nominal current of 30 kA. The field uniformity is better than 2%. The solenoid houses the full azimuthal acceptance central barrel detectors ITS, TPC, TRD, and TOF, as well as several special purpose smaller detector systems.

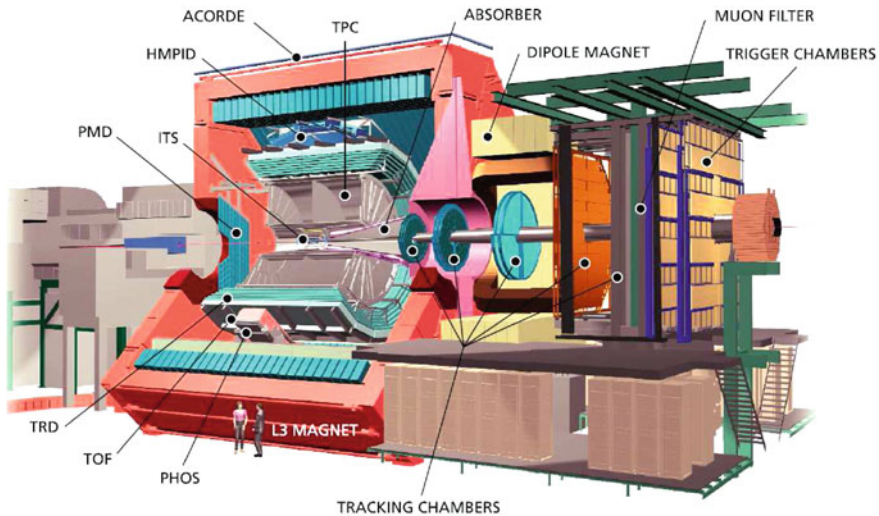


Fig. A.23 The ALICE experiment at the CERN LHC. See the text for the description of subdetectors

The tasks of the Inner Tracking System (ITS) are to localize the primary vertex with a resolution better than $100 \mu\text{m}$, to reconstruct the secondary vertices from the decays of hyperons and D and B mesons, to track and identify particles with momentum below $200 \text{ MeV}/c$, and to improve the momentum and angle resolution for particles reconstructed by the TPC. The six cylindrical layers of ITS (two pixel, two drift, and two strip detectors) are located at radii between 4 and 43 cm, have a resolution in the bending plane

of $r\Delta\phi = 12 - 35 \mu\text{m}$, and cover the rapidity range of $|\eta| < 0.9$ for all vertices located within the length of the interaction diamond ($\sigma = 5.3 \text{ cm}$ along the beam direction). The four outer layers have analogue readout and hence can be used for particle identification via dE/dx . The overall thickness of the ITS is $8\% X_0$. The expected total radiation dose for the inner layer is 270 krad .

The Time-Projection Chamber (TPC) is the main tracking detector of the central barrel and provides, together with the other central barrel detectors, charged-particle momentum measurements with good two-track separation, particle identification, and vertex determination. The active volume has an inner radius of about 0.85 m , an outer radius of about 2.5 m , and an overall length along the beam direction of 5 m and is filled with 90 m^3 of $\text{Ne-CO}_2\text{-N}_2$ [90-10-5]. The drift potential is 100 kV . With a field (oriented along the beam axis) of 400 V/cm the drift velocity is $2.7 \text{ cm}/\mu\text{s}$. The ionization electrons drift over a distance of up to 2.5 m on either side of the central electrode to the end plates. Multi-wire proportional chambers with cathode pad readout are mounted into 18 trapezoidal sectors at each end plate. The TPC covers $-0.9 < \eta < 0.9$ for tracks with full length; short tracks can be detected within $|\eta| < 1.5$. It is expected that in Pb-Pb runs the TPC can be operated at central collision rates of up to 300 Hz at which point the space charge due to the ion feed-back during gate-open time starts to be comparable to the space charge due to the ionisation in the TPC drift volume itself, resulting in tracking distortions of the order of a few mm . For proton-proton collisions, trigger rates of up to 1 kHz seem realistic. The position resolution in the bending plane ($r\phi$) is between 400 and $1,100 \mu\text{m}$, depending on momentum and drift length. The dE/dx resolution is $5.0\text{--}6.8\%$ depending on multiplicity. The Ne/CO_2 has a steep dependence of drift velocity on temperature. For this reason, the TPC is aiming for a thermal stability with $\Delta T \approx 0.1 \text{ K}$ in the drift volume. The CO_2 and N_2 fractions are kept stable to 0.1% , necessary to ensure stable drift velocity and gas gain of the readout chambers. The O_2 impurity as achieved with a reduced flow during commissioning is extrapolated to be about 1 ppm or lower in the final installation in the cavern, limiting the signal reduction due to attachment for the maximum drift length of 2.5 m to less than 5% . The TPC thickness is $3\% X_0$.

The Transition Radiation Detector (TRD) will provide electron identification in the central barrel for momenta above $1 \text{ GeV}/c$. Electrons passing a 4.8 cm thick polypropylene fibre and Rohacell foam radiator produce X-rays which are detected in a Xe/CO_2 filled drift chamber with pad readout. The X-rays, combined with the 30% higher dE/dx of electrons, provide the basis to distinguish them from pions. Six layers of radiator/readout chamber modules result in a pion rejection factor of 100 . The TRD will, moreover, provide a fast ($6.5 \mu\text{s}$) trigger for charged particles with high momentum. The momentum resolution of TRD in the standalone mode is $3.5\text{--}4.7\%$ at $5 \text{ GeV}/c$. The radiation thickness is $23\% X_0$. The TRD, in conjunction with the ITS and the TPC, will enable the measurement of light and heavy vector-meson

resonances and the dilepton continuum in pp and Pb–Pb collisions. Exploiting the excellent impact parameter resolution of the ITS it is furthermore possible to reconstruct open charm and open beauty in semi-leptonic decays.

The Time-Of-Flight (TOF) detector, based on the multi-gap Resistive Plate Chamber technology, provides particle identification in the intermediate p_t region below about 2.5 GeV/c for pions and kaons, up to 4 GeV/c for protons, with a p/K and K/p separation better than 3σ . The intrinsic time resolution is about 40 ps and the efficiency close to 100%. The radiation thickness is 30% X_0 .

The High-Momentum Particle Identification Detector (HMPID) is dedicated to inclusive measurements of identified hadrons at $p_t > 1$ GeV/c. The aim is to extend, within 5% of the central barrel acceptance, the range for π/K and K/p discrimination up to 3 and 5 GeV/c, respectively. Identification of light nuclei and anti-nuclei (d, t, ^3He , α) at high transverse momenta in the central rapidity region can be performed as well. The HMPID is based on proximity-focusing Ring Imaging Cherenkov (RICH) detectors. The radiator, which defines the momentum range covered by the HMPID, is a 15 mm thick layer of low chromaticity C_6F_{14} (perfluorohexane) liquid with an index of refraction of $n=1.30$ at $\lambda=175$ nm, corresponding to $\beta_{\min} = 0.77$. The Cherenkov photons are detected by MWPCs with CsI coated pads.

The PHOTon Spectrometer (PHOS) is a high-resolution electromagnetic spectrometer for low p_t direct photon measurements and for study of jet quenching through the measurement of high- p_t π^0 and γ -jet correlations. The high-energy resolution and granularity is provided by using dense scintillator material (lead-tungstate, PbWO_4) of 20 X_0 with high photo-electron yield. The two-photon invariant mass resolution at the π^0 peak is 3.5%. The fast scintillator and preamplifier result in a time resolution of 2 ns at energies above 1.5 GeV. A MWPC with pad readout, placed 5 mm before the calorimeter, provides a charged-particle veto (CPV) with an efficiency of better than 99%. The material budget of the CPV is less than 5% of X_0 .

The construction of a large ElectroMagnetic Calorimeter (EMCal) began in 2008 with the aim to enable ALICE to explore in detail the physics of jet quenching (interaction of energetic partons with dense matter) over the large kinematic range accessible in heavy-ion collisions at the LHC. The EMCal is a 20 X_0 Pb-scintillator sampling calorimeter with cylindrical geometry, located adjacent to the ALICE magnet coil at a radius of 4.5 m. It covers $|\eta| < 0.7$ and $\Delta\phi = 107^\circ$, and is positioned opposite in azimuth from PHOS.

ACORDE, the ALICE cosmic ray detector, is an array of plastic scintillator counters placed on the upper surface of the L3 magnet and covering $-1.3 < \eta < 1.3$ and $-60^\circ < \phi < 60^\circ$. It provides a fast (Level-0) trigger signal, for the commissioning, calibration and alignment of the ALICE tracking detectors, and it will detect, in combination with the TPC, TRD and TOF, single atmospheric muons and multi-muon events (so-called muon bundles) thus allowing the study of high-energy cosmic rays in the energy region of the knee in the cosmic ray spectrum.

The Muon Spectrometer covers $-4.0 < \eta < -2.5$ and consists of a carbon/concrete absorber, a dipol magnet with 0.67 T and 3 Tm, and 10 detection planes with a resolution of 70 μm . With this detector, the heavy quarkonia J/ψ , ψ' , Υ , Υ' , Υ'' will be addressed via their muon decay channel. The minimum muon momentum is 4 GeV/c and the system aims at an invariant mass resolution of 1% at 10 GeV/c².

The ALICE detector suite is complemented by two Zero Degree Calorimeters (ZDC) for centrality and reaction plane angle, a Photon Multiplicity Detector (PMD) for γ and charged particle measurement within $2.3 < \eta < 3.7$, a Forward Multiplicity Detector (FMD) covering $-3.4 < \eta < -1.7$ and $1.7 < \eta < 5.0$, two vertex detectors (V0A and V0C) for interaction trigger, and two TOF start detectors (T0) with 50 ps which also provide the longitudinal event vertex position within 1.5 cm.

The High-Level Trigger (HLT) computer farm, consisting of 1,000 multi-processor machines, will perform fast online processing and provide trigger for rare signals and/or data compression on the fly.

ALICE will address the heavy ion reaction dynamics via studies of multiplicities, spectra, two-particle correlations, and collective flow. The Quark-Gluon Plasma will be probed by heavy flavours, photons, and jets. The QCD phase transition will be investigated by hadron abundances and by charge fluctuations, with the corrections for momentum conservation being less important than at lower energies. Besides running with Pb ions, the physics programme includes collisions with lighter ions, lower energy running, and dedicated proton-nucleus runs. ALICE will also take data with proton beams at the top LHC energy to collect reference data for the heavy-ion programme and to address several QCD topics for which ALICE is complementary to the other LHC detectors.

References

1. ALICE Collaboration, J. Phys. G: Nucl. Part. Phys. **30**, 1517–1763 (2004)
2. ALICE Collaboration, J. Phys. G: Nucl. Part. Phys. **32**, 1295–2040 (2006)
3. ALICE Collaboration, JINST **3**, S08002 (2008)

Index

A

accelerator \rightarrow experiment
 adiabatic expansion/ index 227, 620ff
 adiabatic trajectory \rightarrow isentrop
 AdS/CFT (anti de Sitter space/ conformal field theory) 5, 297, 298, 301
 Anderson-Higgs mechanism 185
 anomalous channels 397
 anomalous J/ψ suppression 483
 anomaly 57ff, 353
 antikaon 419, 422, 425, 695
 antiproton 24, 855, 930
 AMPT (a multi-phase transport) 591, 642, 755f
 ART (a relativistic transport) 590
 astrophysics 6, \rightarrow compact star
 asymptotic freedom 19, 52
 axialvector 62f, 348f, 360

B

baryon

\sim density 18, 98, 196, 203, 213, 220, 359, 389, 534, 637, 688, 852
 baryo-chemical potential 98, 131, 138, 205, 732
 \sim multiplet 49, 539
 dibaryon 821
 BCS theory 182
 Beth-Uhlenbeck 566
 Bethe-Salpeter eq. 416, 581
 Bjorken expansion 619, 645
 black hole 287
 charged \sim 299
 blast wave 619, 645
 Boltzmann equation 552, 585
 Boltzmann-Langevin 553

Boltzmann-Uehling-Uhlenbeck \rightarrow BUU
 boost invariance 619
 Bose-Einstein condensation 194
 Bose-Einstein distribution 560 562
 boson 12, 56f, 150, 185, 501, 560f
 Botermans-Malfliet approximation 565
 Breit-Wigner function 357, 402
BUU (Boltzmann-Uehling-Uhlenbeck) 553, 588, 589, 646
 BEM (Boltzmann eq. model MSU) 585
 BRoBUU (Budapest-Rosendorf) 587
 GiBUU (Giessen) 586, 641, 698, 735 - 744
 RBUU (relativistic) 588, 589, 641, 643, 695

C

cascade models

 linear cascade 544
 parton cascade 546
 intra-nuclear cascade 543
 center symmetry (\rightarrow Polyakov loop) 56, 60, 239
 charge density fluctuation \rightarrow fluctuation

charm

\sim baryon 462
 \sim chemistry 449
 \sim diffusion 441
 \sim dilepton decay 448
 charm-quark interaction 438
 charm-quark production 431, 434
 charmonium 465, 466, 470, 481, 495, 781, 900f
 hidden \sim 775
 J/ψ 454, 472ff, 483ff, 720ff, 734, 777 - 793, 893 - 907

- regeneration of \sim **489**, **793**
- suppression of \sim **483**, **720**,
- open \sim **429**, **440**, **451**, **480**, **766**, **775**,
787, **886**
- ψ' **478f**, **784** - **793**, **895**
- chemical potential**
 - baryo \sim **98**, **131**, **138**, **205**, **732**
 - quark \sim **42**, **131ff**, **187** - **196**, **213**, **246** -
263, **396**, **499**, **505**
- chemical rates **612**
- chiral**
 - \sim condensate \rightarrow condensate **126**, **244**,
254, **354**
 - chirality **19**, **61**
 - \sim mixing **349**
 - \sim partners **20**, **338**, **442**
 - \sim perturbation theory (χ PT) **44**, **54**, **407**
 - \sim symmetry **20**, **56**, **74**, **85**, **92**, **363**,
375, **405**, **425**
- coalescence **445f**, **627**, **784**, **824**
- coexistence phase **18**, **66ff**, **534**, **613**
- collaboration \rightarrow experiments
- collective flow \rightarrow flow
- collective modes/ excitation **17**, **614**
- collision geometry **536**
- collision term **563**
- color**
 - \sim charge **14**
 - \sim neutral **14**, **500**
 - \rightarrow screening **466**
 - \rightarrow superconductor (CFL, CSC)
- comover **488**, **494**, **780** - **792**
- compact star (neutron star)** **18**, **158**,
 - \sim cooling **173**
 - \sim mass **163**, **164**, **165**, **166**
 - \sim moment of inertia **170**
 - \sim radius **167**
 - \sim rotation **171**
 - \sim structure **160**
- compression **22**, **643ff**, **693**, **701ff**, **711**
- condensate**
 - Bose-Einstein \sim **194**
 - chiral \sim **126**, **244**, **254**, **354**
 - diquark \sim **57**, **295**
 - four-quark \sim **93**, **355f**
 - gluon \sim **57ff**, **98**, **354**
 - QCD \sim **405**
 - quark \sim **57**, **93ff**, **256**, **355ff**
 - spin-zero \sim **114**
- confinement **13**, **48**, **293**
- conserving approximation **564**
- Cooper pair **182**
- Cooper-Frye **623**
- correlation**
 - \sim function **290ff**, **345**, **387**, **812**
 - final-state \sim **628**
 - HBT \sim **632**
 - short range \sim **550**
 - strangeness to baryon number \sim **140**,
805
- correlator**
 - current-current \sim **557**
 - Euclidean \sim **469**
- cosmology **6**
- coupled channel dynamics **416**
- critical phenomena**
 - \sim end point **5**, **16**, **44**, **224**, **260**, **690**, **817**
 - \sim point **15**, **42**, **89**, **91**, **133**, **134**, **203**,
639, **688**, **817**
 - \sim region **283**
- precritical **503**
- precursor (effect) **503ff**
- tricritical point **86**, **90**, **261**
- crossover **16ff**, **42**, **87**, **136ff**, **180**, **248ff**, **817**
- D**
 - Debye screening/ mass **109**, **442**, **484**
 - deconfinement **18**, **172**, **197**, **209**, **228**,
229, **254**, **295**
 - degrees of freedom **209**, **228**, **539**, **662**
 - detailed balance **574**
 - detector**
 - MuCh (muon chamber) **870**, **877**, **899**
 - MVD (micro vertex) **866f**, **868**, **890**
 - PSD (projectile spectator) **866**, **872**
 - RICH (ring imaging Cherenkov) **867**,
869, **892f**, **950**
 - RPC (timing resistive plate chamber)
867, **878**, **893**
 - STS (silicon tracking system) **867**, **867**,
876ff, **899**
 - TRD (transition radiation) **867**, **870**,
877, **892f**
 - dibaryon \rightarrow baryon
 - diffusion **291**, **441**
 - dilepton **348**, **375**, **386ff**, **448**, **507**, **759ff**,
860
 - dielectron **764ff**, **768**, **769**
 - dimuon **764** - **776**, **784ff**
 - dimensional transmutation principle **2**
 - Dirac-Brueckner-Hartree-Fock (DBHF)
147 - **180**
 - Dirac
 - \sim Γ matrix **184ff**, **50**
 - \sim monopole **288**
 - \sim particle **61**
 - \sim spinor **50**

direct photon [394](#), [904](#)

distorted wave [621](#)

distribution function

Bose-Einstein distribution [562](#)

Fermi-Dirac distribution [562](#)

Drell-Yan process [347](#), [780ff](#)

Dyson(-Schwinger) equation/ resummation
[182ff](#), [266ff](#), [368ff](#), [559ff](#)

E

early universe [18](#), [126](#), [624](#)

effective action [268](#), [277](#)

effective mass [148](#), [564](#)

electromagnetic

~ correlator [345](#)

~ decay [881](#)

~ form factor [380](#), [391](#)

~ probe [343](#)

energy density [98](#), [127ff](#), [203](#), [224](#), [242](#),
[304](#), [534](#), [648](#), [688](#), [716](#), [852](#)

entropy [66](#), [125ff](#), [208](#), [220](#), [242](#), [287f](#), [302](#),
[608](#), [741](#), [817](#)

conservation of ~ [608](#)

→ isentropes

EoS (equation of state) [66ff](#), [101](#), [124](#),
[131](#), [132](#), [146](#), [151](#), [158](#), [215](#), [223](#),
[541](#), [700](#), [748](#)

astrophysical constraints on ~ [158](#), →
compact star

bag model ~ [223f](#), [612](#), [752](#)

Skyrme model ~ [154](#), [703](#)

Walecka model ~ [148](#), [612](#)

equilibrium distribution [562](#)

Euclidean action [51](#)

Euclidean correlator [469](#)

Euclidean space [51](#)

event-by-event fluctuations → fluctuations

excitation function [648ff](#), [701](#) - [712](#), [731](#),
[736](#), [748ff](#), [805ff](#), [825](#)

exotica [429](#)

experiments, collaborations

BNL Brookhaven AGS [23](#), [650](#), [704ff](#),
[737ff](#), [749ff](#), [927](#)

BNL Brookhaven RHIC

BRAHMS [735ff](#), [950](#)

PHENIX [290](#), [440ff](#), [652](#), [769f](#), [955](#)

PHOBOS [652](#), [960](#)

STAR [290](#), [402f](#), [440ff](#), [648](#), [805](#), [963](#)

CERN LHC

ALICE [969](#)

CERN SPS

CERES [763ff](#), [773](#), [933](#)

NA49 [651](#), [708](#), [739ff](#), [754](#) - [811](#), [935](#)

NA60 [390](#), [764ff](#), [776](#), [782ff](#), [941](#),
WA98 [394](#), [945](#)

GSI SIS18

FOPI [650](#), [695f](#), [916](#)

HADES [770f](#), [858](#), [921](#)

KaoS [695ff](#), [924](#)

GSI SIS100/300

CBM [24](#), [793](#), [849](#), [860](#), [865](#), [884](#) -
[895](#), [905](#), [909](#)

JINR Dubna

NICA [909](#)

LBL Berkeley BEVALAC [22](#), [683](#), [749](#),
[769](#)

DLS [770](#)

F

FAIR [24f](#), [375](#), [540](#), [712](#), [723](#), [741](#), [746](#),
[755](#), [772](#), [790](#), [821](#), [852ff](#), [856](#)

Fermi-Dirac distribution [562](#)

Feshbach resonances [194](#), [292](#)

field theory

→ gauge theory

non-equilibrium ~ [559](#)

quantum ~ [12](#)

final state interaction [621](#), [630](#)

fireball [290](#), [390ff](#), [625](#), [764ff](#), [784f](#)

flavor kinetics [611](#)

flavor symmetry [49](#), [184](#), [426](#)

flow

antiflow [708](#), [747](#)

bounce-off [747](#)

collective flow [644](#), [747](#), [752](#)

conical flow [288](#)

directed flow [647](#), [711](#), [752ff](#)

elliptic flow [179](#), [288](#), [440ff](#), [647ff](#), [712](#),
[726](#), [727](#), [749](#), [750ff](#), [794](#)

in-plane flow [696](#)

out-of-plane flow [697](#)

squeeze-out [645ff](#)

transverse flow [812](#)

flow equation (renormalization group ~)
[271](#), [274](#), [278](#)

proper time flow [274](#)

fluctuations [795](#)

charge density ~ [210](#), [212](#), [260](#), [262](#),
[800](#)

~ of conserved quantities [798](#)

event-by-event ~ [804](#), [882](#)

higher order moments of ~ [807](#)

K to π ~ [803](#)

particle multiplicity ~ [803](#)

susceptibility and ~ [138](#), [142](#)

thermal ~ [797](#)

transverse momentum \sim **809**
fluid dynamics **607**, **615**, **619**, **662**
 Bjorken model **619**, **645**
 \rightarrow freeze-out
 multi-fluid hydrodynamics **609**
 one-fluid hydrodynamics **608**
 3FD ($3 \sim$) **647ff**
 viscous \sim **615**
 Fokker-Planck equation **441**
 formfactor **367f**
 four-quark condensate **93**, **355f**
 freeze-out **22**, **131**, **203ff**, **534**, **620ff**, **688ff**,
706, **732**, **807**, **852**
 continuous **624f**
 friction **440**, **447**
G
 gapless spectrum/ phase **17**, **56**, **182**, **191ff**
gauge theory **50**, **126**, **132**, **212**, **229**
 color (gauge) transformation **57**
 Coulomb gauge **467**
 covariant derivative **50**
 gauge invariance **50**
 \rightarrow lattice gauge theory
 non-Abelian \sim **50**, **290**
 Yang-Mills $SU(N)$ **229**
 Gell-Mann matrices **50**
 Gell-Mann–Oakes–Renner relation **93**, **414**
 Ginzburg-Landau theory/ potential **77**, **91**
 Glauber model **544**, **726**, **782**
 gluon condensate **57ff**, **98**, **354**
 Goldstone boson/ mode/ theorem **56f**, **185**,
501
 gradient expansion **556ff**, **562**
 gradient terms **564**
 Greens function **268**, **559**
H
hadron
 hadronic model **44**, **364**, **427**
 hadronic phase **121**, **295**, **764ff**, **773**, **784**
 hadronic resonances **209**, **401**, **728**
 resonance gas **98**, **105**, **127**, **212**, **224**, **719**
 HSD (hadron-string dynamics) **592**, **642**,
651ff, **698**, **734 - 744**, **755**, **780 - 805**,
889ff, **907**
 HBT (Hanbury-Brown–Twiss effect) **206**,
628, **709**
 Hawking temperature **302**
 Hellmann-Feynman theorem **353**
 Higgs mechanism/ phase **185**, **293**
 HTL(PT) (hard thermal loop (perturbation
 theory)) **109**, **217**, **296**
 hybrid models **617**

hybrid star \rightarrow compact star **167 - 180**
 hydrodynamics \rightarrow fluid dynamics
 hypernuclei **821**
hyperon **49**, **719**, **737**, **861ff**, **881**
 Λ **52**, **61**, **77**, **111**, **225**, **367**, **414**, **427**,
455f, **705ff**, **735ff**, **825**, **861**, **881ff**, **907**
 $\Lambda(1405)$ **414**
 Ω^- **172**, **207**, **225**, **280**, **627**, **737ff**, **861**,
907
 Σ **708**, **735ff**, **810**, **881**
 Ξ **207**, **225**, **708**, **737ff**, **861**, **883**, **907**
 hypersurface **623**

I

imaging \rightarrow source imaging **628**, **866f**, **869**
 in-medium potential **420**, **696ff**
instabilities
 gravitational instabilities **172**
 dynamical instabilities **614**
 invariances \rightarrow symmetries
 isentrops **130ff**, **226**, **264ff**, **615**, **817**
 isentropic spinodals **264f**, **615**

J

jet **290**, **304**, **724**
 jet quenching **724**, **911**
 Jüttner function **562**
 $J/\psi \rightarrow$ charm, charmonium

K

Kadanoff-Baym equation **557ff**
kaon **97**, **412ff**, **423**, **694**, **700**, **722**, **750**,
789ff, **924**
 antikaon **419**, **422ff**, **695**
 \sim mass **412**, **413**
 \sim potential **421**, **701**
 \sim production **700**
 K^\pm **414ff**, **425**, **627**, **695ff**, **722**, **734ff**,
744, **862**
 K^- nucleon scattering **417**
 Kaplan-Nelson term **412**, **425**
 Klein-Gordon particles **413**, **560**
 Kubo formula **616**

L

laboratory cites \rightarrow experiments
Lagrangian
 effective Lagrangian **242**
 QCD Lagrangian **50**, **127**
 chiral Lagrangian **263**, **412**, **694**
 Λ \rightarrow hyperon
 $\Lambda_{\text{QCD}} \rightarrow$ QCD

Landau damping 109
 Landau-Ginzburg \rightarrow Ginzburg-Landau
 Langevin equation/ force 440ff, 553, 604
 \rightarrow Boltzmann-Langevin
 latent heat 16, 613, 626
lattice gauge theory (QCD) 8, 44, 54,
 116, 124, 203, 220ff, 248, 387, 447,
 466, 688ff
 finite chemical potential 111, 119, 243
 lattice action 133
 lattice lattice gauge theory 9
 quenched 105, 141, 290, 387, 468, 469
 staggered fermion 127ff, 138ff
 Wilson fermion 128
 linear cascade model 544
 linear-density approximation 95
 liquid-gas phase transition 15, 19, 42 68 84
 LPM (Landau-Pomeranchuk-Migdal)
 effect 446, 578, 582

M

Mach angle/ cone 290, 609
 many-body collisions 578
 many-body models 595
 Maxwell construction 264
 McLerran-Toimela formula 570
 mean-field dynamics 412, 642
 mean-field potential \rightarrow potential
 Meissner mass 58, 193
meson 13
 D meson 431, 450 - 479, 789
 J/ψ meson \rightarrow charm, charmonium
 K meson \rightarrow kaon
 $\omega, \phi, \rho \rightarrow$ vector meson
 π meson \rightarrow pion
 σ meson 395
 Minkowski space/ metric 51
molecular dynamics
 AMD (antisymmetrized \sim) 603
 FMD (fermionic \sim) 601
 quantum $\sim \rightarrow$ QMD
 momentum distribution 492, 648, 770
 monopoles 288
 multiplicity 409, 648, 701f, 734ff, 771, 803,
 815ff, 861, 889ff, 907, 947ff

N

Nambu-Goldstone phase/ theorem 56f, 581
 Navier-Stokes 615
 neutron star \rightarrow compact star 18, 167 - 180
 NJL (Nambu-Jona-Lasinio) model 167ff,
 179, 196 237ff, 264, 396, 499
 Noether currents/ theorem 564, 581

non-Abelian 50, 290

nuclear matter

baryons in \sim 407f
 equation of state of \sim 151
 experiments probing dense \sim 693ff, 856
 pairing gaps in \sim 174
 phase diagram of \sim 18, 42, 68, 82, 203,
 688
 mesons in \sim 366, 369, 383, 425f, 455,
 458

O

off-shell 563, 577
 omega meson \rightarrow vector meson
 on-shell 556
 OPE (operator product expansion) 352,
 452
 optical potential \rightarrow potential
 order parameter 57, 92, 229

P

participant 536, 777, 782, 792
 particle production 197
 partition function 51, 73, 117
 \rightarrow grand canonical \sim 51
 path integral 51
 Pauli principle/ blocking 420, 553
 Pauli matrices 238
 penetrating probes 22, 338
perturbative
 \sim degrees of freedom 662
 \sim expansion 111, 363, 431, 569
 \sim QCD 44, 53, 102, 111, 276
phases of matter 14
 \rightarrow coexistence phase
 deconfined phase \rightarrow QGP 19
 \rightarrow hadronic phase
 \rightarrow nuclear matter
 \rightarrow Nambu-Goldstone phase
 \rightarrow plasma phase
 quark-gluon plasma \rightarrow QGP
 \rightarrow superconducting phase
 \rightarrow Wigner-Weyl phase
 phase equilibrium 67
 phase space 402, 596, 706, 739, 878 - 894,
 899,
 phase shift 97, 369, 566, 567
phase transition
 crossover 16ff, 42, 87, 136ff, 180, 248ff,
 817
 critical point 15, 42, 89, 91, 133, 134,
 203, 639, 688, 817
 critical region 283

- first order *16ff*, *66ff*, *87*, *136ff*, *187*, *234*,
248, *256*, *263ff*, *282*, *396*, **811**, *817*
→ liquid-gas ~
→ phases
phase boundary *15*, *73f*, **260**, *639*
phase coexistence *18*, *68*, *534*
phase diagram *15ff*, *42ff*, *68*, *81ff*, *90*,
121 - *138*, *180*, *192* - *203*, **237**, *248*,
255, *264*, **281**, *295f*, **499**, *613*, **687**
phase mixture (→ coexistence phase) *16*,
66ff
second order **76**, **77**, *87*, *248*, *282*
transition line *42*, *121*, **133**, **215**, *282*
transition temperature *132*, **132**, *187*,
234
tricritical point **86**, **90**, *261*
- ϕ meson → meson
- Φ -derivable approximation *110*, *575*
→ two particle irreducible
- photon**
diphoton **395**
photon rate **392**
single photon **392**
- pion**
pion cloud *366ff*, *385*
pion-decay constant *92*, *362*
pion mass *134*, *138*, **233**, *282*
pion matter **423**
- Pisarski-Wilczek argument **85**
- plasma phase *16*
- polarisation function *557*
- Polyakov loop *59*, *126*, **229**, *242* - *256*, *293*
center symmetry *56ff*
PNJL (Polyakov–Nambu–Jona-Lasinio
model) **237**, **239**
PQM (Polyakov–quark-meson model)
237, *255ff*
- potential**
mean-field potential **550**
heavy quark potential *127ff*
optical potential *153f*, *568*
- pressure *15*, *66*, *97*, **101**, **104**, *110*, *127ff*,
179, *213* - *263*, *648*
- ψ' → charm, charmonium
- pulsar → compact star
- Q**
- QCD** (Quantum Chromodynamics)
ChPT → chiral perturb. theory *54*, *97*,
152, *415*
 Λ_{QCD} *52*, *61*, *77*
LQCD → lattice ~
PQCD (perturbative ~) *3ff*, *44*, *53*
~ action *51*
~ flavor *13*, *47*
~ Lagrangian *50*, *127*
QCDLite *3*, *81*
~ phase diagram *42*, **81**, *88ff*, *131*, **499**,
687
~ sum rules *351ff*, **426**, **451**,
phases of ~ **182**
running coupling *53*
symmetries of ~ **56**
- QGP** (quark-gluon plasma) *19*, *42*, *295*,
389, **438**, **441**, *764* - *793*
sQGP (strongly coupled ~) **286**, **293**,
298, **301**
- QL (quantum Langevin) **604**
- QMD** (quantum molecular dynamics) **596**
IQMD (isospin ~) **597**, *627*, *641*,
*695ff**699*,
RQMD (relativistic ~) **598**, *627*, *641*,
695 - *708*, *824*
UrQMD (ultra-relativistic ~) **599**, *637ff*,
651, *689*, *709*, *735* - *755*, *780ff*, *807* -
892
- quantum chromodynamics → QCD
- quark**
~ condensate *57*, *93ff*, *256*, *355ff*
quark-gluon plasma → QGP
~ mass *47*, **87**, **89**, **104**, *118*, *126ff*, *137ff*,
234, *242ff*, *263*, *434ff*, *500*
~ meson model **249**, **277**, **281**,
~ number scaling *751*, *756*, *911*
~ number susceptibility *258*, *265*, *282*
~ recombination *450*
- quark matter → QGP **83**, *167* - *195*,
*499ff***89**, *118*, *126*, *137*, *140*
~ star → compact star
- quarkonium (→ charm, charmonium, J/ψ)
466, *490*
- quasiparticle *17*, *191*, **215ff**, *222ff*, **292**
415, *460*, **579**
- R**
- rare probe **653**
- rate equation *492*, *612*, **781**, *793*
- RG (renormalization group) **266**, **267**, **375**
→ flow equation
- resonance** *96ff*, *105*, *127*, *194*, **209**, **212ff**,
292, **369**, *383*, *401ff*, *440ff*, **500**, **555**,
567, **577**, *719*, **728**, *741*
 Δ ~ *111*, *222ff*, *290*, *367ff*, *385*, *406ff*,
476, *500*, *567f*, *623*, *637*, *802*
meson ~ **402**
baryon ~ **22**, **404**, **407**

\sim gas [98ff](#), [127](#), [212](#), [224](#), [719](#)
 restoration [87](#), [89](#), [363](#), [425](#), [442](#)
 resummation [108](#), [296](#), [432](#)
 rho meson \rightarrow vector meson
 rows-on-rows [545](#)
S
 Schwinger-Dyson \rightarrow Dyson
 screening [109](#), [296](#), [466](#), [484](#)
selfenergy [424](#), [427](#), [368](#), [447](#) [455ff](#), [506](#),
 [550f](#), [789](#)
 imaginary part of \sim [551](#)
 relativistic \sim [551](#)
 semi-classical approximation [621](#)
 σ meson [395](#)
 source imaging [628](#)
 source radii (R_{out} , R_{side} , R_{long}) [629ff](#), [710](#)
 spectators [536](#), [866ff](#), [872](#)
 spectral function [346](#), [360](#), [363](#) - [375](#), [383](#) -
 [422](#), [457ff](#), [469](#), [470](#), [555](#), [562](#), [577](#),
 [764ff](#)
spinodal [68](#), [262](#), [263ff](#), [615](#)
 isentropic \sim [264f](#), [615](#)
 spin wave [17](#)
 SPT (screened perturbation theory) [109](#)
 sQGP (strongly coupled QGP) [286](#), [293](#),
 [298](#), [301](#)
 squeeze-out [645ff](#)
 staggered fermion [127](#) - [141](#)
statistical ensembles
 microcanonical [66](#)
 canonical [51](#), [70](#), [198](#), [200](#), [278](#), [476](#)
 grand canonical [51](#), [71](#), [198](#), [278](#), [280](#)
 statistical hadronisation [471f](#), [785](#), [791](#)
 statistical model (\rightarrow thermal model) [197](#),
 [825](#), [852](#), [861](#), [889](#)
 Stephan-Boltzmann [245ff](#), [302](#)
 strangeness [141](#), [200](#), [208](#), [411](#), [412](#), [718](#),
 [721](#), [741](#), [805](#), [823](#)
string models [547](#), [593](#)
 HSD (hadron-string dyn.) [592](#), [641](#), [651](#),
 [695ff](#), [734](#) - [744](#), [780](#) - [805](#), [889ff](#), [907](#)
 QGSM (quark-gluon-string model) [593](#),
 [637ff](#), [652](#), [744](#), [755](#)
 strong interaction/ force [12](#), [18](#)
 strong charge [14](#)
 subthreshold processes [700](#)
 sum rules [350](#)
 chiral (Weinberg) \sim [360](#)
 QCD \sim [351ff](#), [426](#), [451](#),
 TRK (Thomas-Reiche-Kuhn) \sim [351](#)
superconductor
 2SC (two flavor \sim) [167](#) - [193](#), [499ff](#)

CFL (color-flavor locked \sim) [4](#), [83](#), [185ff](#)
 CSC (color superconductor) [42ff](#), [114](#),
 [170](#), [179](#), [182](#), [183](#), [188](#), [194](#), [389](#),
 [499](#), [503](#)
 supernova [158ff](#), [164ff](#), [683](#)
 susceptibility [57](#), [136](#), [138](#), [213](#), [220](#), [227](#),
 [258ff](#), [282ff](#), [808](#)
symmetry [12](#), [20f](#),
 center \sim [56ff](#), [239](#)
 chiral \sim [3](#), [20](#), [56](#), [74](#), [85](#), [92](#), [261](#), [363](#),
 [375](#), [405](#), [425](#)
 explicitly broken \sim [57](#)
 flavor \sim [49](#), [184](#), [426](#)
 isospin \sim [179ff](#), [424](#), [499](#)
 \sim of QCD [47](#), [56](#)
 \sim restoration [87](#), [89](#), [363](#), [425](#), [442](#)
 spontaneously broken \sim [17](#), [74](#)
 SU(3) \sim [49](#), [126](#), [132](#), [426f](#), [539](#)
 SU(N) \sim [229](#)
 U_A(1) \sim [57](#)
 Z(3) \sim [59](#), [239](#)
 Z(N) \sim [233](#)

T

thermal model (\rightarrow statistical model) [207](#),
 [449](#), [690](#), [732](#), [740ff](#)
 thermalisation [225](#), [443](#), [495](#), [690](#)
 thermodynamic stability [68f](#)
 Tolman-Oppenheimer-Volkoff (TOV) Eq.
 [162](#)
 trace anomaly [61](#), [353](#)
transport models [549](#), [641](#) - [652](#), [713](#) -
 [756](#), [778](#), [791](#)
 \rightarrow AMPT, ART, BUU, cascade models,
 QMD, string models
 charmonium transport [481](#)
 dynamical spectral function [555](#), [562](#),
 [577](#)
 resonance transport [555](#)
transport coefficient
 diffusion [291](#), [441](#)
 \rightarrow viscosity
transversality
 four transverse [367](#), [581](#)
 four longitudinal [368](#)
 transverse mass [718](#), [722](#), [743](#), [745](#), [767](#),
 [789](#)
 transverse momentum [225](#), [402ff](#), [492](#),
 [648ff](#), [711ff](#), [727](#), [751ff](#), [809](#), [880](#) -
 [905](#), [947](#)
 two-body collision [552](#)
 two-particle irreducible (2PI) [555](#), [574](#)

two-quark condensate \rightarrow condensate,
diquark \sim

U

universality class [16](#), [78](#), [89](#), [91](#)
unitary correlation operator method
(UCOM) [602](#)
Urca process [173](#)

V

VDM (vector dominance) [347](#)
vector meson [343](#), [364](#), [379](#), [390](#), [766](#),
[890](#), [895](#) - [907](#)
 \rightarrow charmonium, J/ψ
 ω meson [357](#), [382](#),
 ϕ meson [384](#), [766f](#), [789](#), [893](#), [900](#)
 ρ meson [356](#), [366](#), [367](#) - [383](#), [398](#), [572f](#),
[721](#), [894](#), [900](#)
vector manifestation [375](#), [390](#)
vertex reconstruction [875](#)
virial limit [566](#)
viscosity [287ff](#)

viscous fluid dynamics [615](#)
viscosity-entropy ratio [287](#)

W

Ward-Takahashi identity [581](#)
Weinberg sum rules [361](#)
Weinberg-Tomozawa term [412ff](#), [425](#)
Wigner function [560](#)
Wigner-Weyl phase [56](#)
Wigner transformation [560](#)
Wilczek \rightarrow Pisarski-Wilczek argument
Wilson coefficients \rightarrow OPE [352](#), [452](#)
Wilson line/ loop [59](#), [228](#), [303](#)
Wilson fermions [128](#)
Wilsonian RG approach [267](#)

Y

Yang-Mills theory [58](#), [229](#), [288](#), [393](#)
 \rightarrow gauge theory
massive \sim [393](#)
supersymmetric \sim [288](#)

Z

$Z(3)$, $Z(N) \rightarrow$ symmetry